DISCLAIMER

This version is for the use of the annual seminar only.

In case of discrepancy, the proceedings on Advanced International Journals of Research, (AIJR) which will be published in Jul 2022 will prevail.

Any opinions, findings, conclusions, or recommendations expressed in this material do not reflect the views of The Hong Kong Institution of Engineers.

Published by:
Geotechnical Division
The Hong Kong Institution of Engineers
9/F., Island Beverley, 1 Great George Street, Causeway Bay, Hong Kong
Tel: 2895 4446   Fax: 2577 7791

Prepared in Hong Kong

THE HONG KONG INSTITUTION OF ENGINEERS
香港工程師學會

Geotechnical Division
岩土分部

THE HKIE GEOTECHNICAL DIVISION 42ND ANNUAL SEMINAR 2022

Published on 13th May 2022

A New Era of Metropolis and Infrastructure Developments in Hong Kong – Challenges and Opportunities to Geotechnical Engineering

Proceedings of the 42nd Annual Seminar

Geotechnical Division, The Hong Kong Institution of Engineers

A New Era of Metropolis and Infrastructure Developments in Hong Kong –

Challenges and Opportunities to Geotechnical Engineering

13 May 2022

Hong Kong

Supported by:

The Association of Consulting Engineers of Hong Kong

Association of Geotechnical and Geoenvironmental Specialists (Hong Kong)

Construction Industry Council

The Geological Society of London (Hong Kong Regional Group)

The Hong Kong Geotechnical Society

Civil Division, The Hong Kong Institution of Engineers

Structural Division, The Hong Kong Institution of Engineers

The Institution of Civil Engineers (Hong Kong Association)

The Institute of Materials, Minerals & Mining (Hong Kong Branch)

Click here to download the softcopy.

ACKNOWLEDGEMENTS

The Organising Committee would like to acknowledge the support of the following sponsors for their generous support of the Seminar:

Diamond Sponsor

HKUST Department of Civil and Environmental Engineering cum
Civil and Environmental Engineering Alumni Association

Platinum Sponsor

AECOM Asia Co. Ltd.

Atkins China Ltd.

Gold Sponsor

Adrian Construction Ltd.

Arcadis Design & Engineering Ltd.

Arup

C M Wong & Associates Ltd.

China Geo-Engineering Corporation

Fugro Geotechnical Services Ltd.

Fraser Construction Co., Ltd.

G and E Co., Ltd.

Intrafor Hong Kong Ltd.

MTR Corporation Ltd.

Pan Kee Construction Ltd.

Reinforced Earth Pacific Ltd.

Shanghai Tunnel Engineering Co., Ltd.

WSP (Asia) Ltd.

Silver Sponsor

Aurecon Hong Kong Ltd.

Dix Construction & Transportation Ltd.

Fong On Geotechnics Ltd.

Geotech Engineering Ltd.

Lambeth Associates Ltd.

Meinhardt Consulting Engineers

Paul Y. Engineering Group

Tysan Foundation Ltd.

Vibro (H.K.) Ltd.

香港科技大學
THE HONG KONG UNIVERSITY OF SCIENCE AND TECHNOLOGY

土木及環境工程學系
DEPARTMENT OF CIVIL AND ENVIRONMENTAL ENGINEERING

Department of Civil and Environmental Engineering of The HKUST

BEng in Civil Engineering (CIVL)
BEng in Civil and Environmental Engineering (CIEV)
MSc in Civil Infrastructural Engineering and Management (CIEM)
MSc in Environmental Engineering and Management (EVEM)
MPhil and PhD in Civil Engineering (CIVL)
MPhil and PhD in Environmental Engineering (EVNG)

CIVL's vision : 'Smart' and 'Sustainability'

- Energy and Environment
- Great Smart Cities
- Carbon Net Zero
- Next Generation Infrastructure

Subject Areas :

- Geotechnical Engineering
- Water Resource Engineering
- Systems Engineering and Management
- Structural & Material Engineering
- Environmental Engineering
- Transportation Engineering
- Smart City

QS World University Rankings:

HKUST 34th globally*

*In QS World University Rankings 2022

HKUST CIVL 16th globally**

**In QS World University Rankings by Subject 2021

HKUST Engineering & Technology 20th globally**

(1st in Hong Kong, 11 years in a row)

**In QS World University Rankings by Subject 2021

What do we offer?

- Industrial Training
- Internship
- Capstone Design Project
- Final Year Project
- Minor in Environmental Sustainability & Management
- Academic and Professional Development
- In-depth Specialty Courses
- Exchange
- Competitions

Impact Cases :

- Green Technologies for Mitigating Urban Landslide and Debris Flow Risks
- Risks SANI® process - A Paradigm - Shift Technology for Hong Kong Sewage Management

Research Highlights :

- Area of Excellence - Centre for Slope Safety
- Smart Urban Water Supply Systems - Defect Detection and Pipe Condition Assessment
- PRAISE-HK - Empower the Public with Personalized Air Quality Information
- Intelligent Transportation
- Digital Twins
- Building Information Modelling
- Intranet of Tree Things


AECOM
Leading the change towards a better future
Everything we do is designed to deliver a better world
Uplifting communities, improving access and sustaining our planet. We partner with clients to turn ambitions into action.
aecom.com
Delivering a better world

ADRIAN CONSTRUCTION LIMITED
毅 源 建 築 有 限 公 司

我們主要業務包括：
Our Bussiness includes:

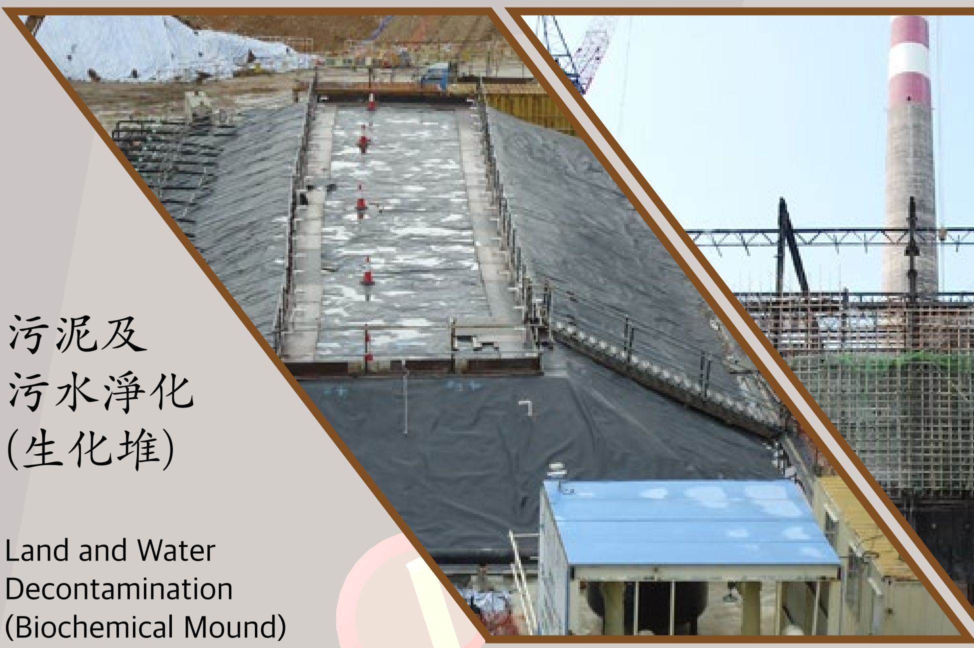

污泥及
污水淨化
(生化堆)

Land and Water
Decontamination
(Biochemical Mound)

樓宇拆卸 (煙囪拆卸)

Demolition of Building
(Demolition of
Chimney)

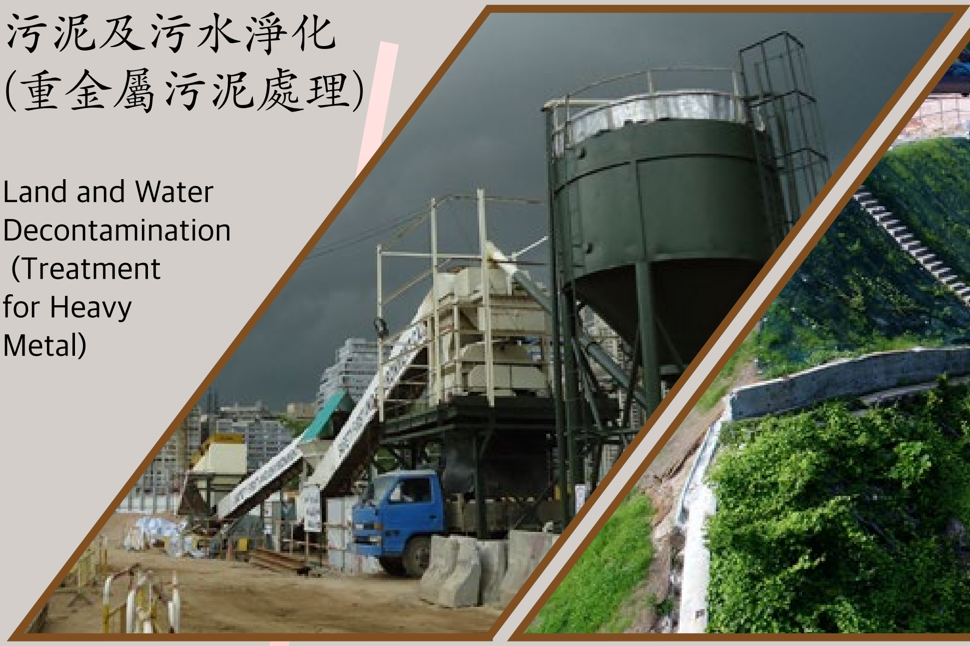

污泥及污水淨化
(重金屬污泥處理)

Land and Water
Decontamination
(Treatment
for Heavy
Metal)

斜坡鞏固
及修葺
(斜坡鞏固)

Slope Stabilisation Works
and Remedial/
Preventive Works for
Dangerous Hillside
(Slope Stabilisation Works)

香港新界葵涌葵昌路50號葵昌中心10樓1006室
Unit 1006, 10/F, Kwai Cheong Centre, 50 Kwai Cheong Road, Kwai Chung, NT, Hong Kong

Tel：+852 2428 8923　　Fax：+852 2484 1622

Underpinning world-class infrastructure

From underground space strategies to railway networks, from offshore wind facilities to community water systems, and from the airport gateway to cross-border connectivity, Arup's geotechnical expertise enables world-class infrastructure projects that make our city a better place to live, work and do business.

Image Shatin-Central Link, Hong Kong

C M WONG & ASSOCIATES LTD
黃志明建築工程師有限公司

11/F Universal Trade Centre
3-5A Arbuthnot Road, Hong Kong
Tel: (852)2522-1068
Fax: (852)2526-3111
www.cmwal.com
cmwal@cmwal.com

C M Wong & Associates Ltd is a Hong Kong based consulting engineer in providing a full range of professional services including feasibility studies, planning, design and supervision in relation to building and infrastructure projects. Our clients include various Hong Kong Government departments, institutions and major developers.

We adopt a flexible approach to suit clients' needs. We are also renowned for providing innovative engineering solutions for challenging projects especially for those with difficult ground conditions.

Sustainable Slope Excellence Award 2020 Champion
11NW-A/C597 Reservoir Dam of Kowloon Byewash Reservoir

Sustainable Slope Excellence Award 2020 Special Merit
11SW-A/CR1113 Hornsey Road near Chater Hall

ISO 9001 : 2015 Certificate No.: CC 801

ISO 14001 : 2015 Certificate No.: CC 5408

ISO 45001 : 2018 Certificate No.: CC 7033


MTR
caring for life's journeys
Connecting People To New Possibilities Around The World
All across the world, cities are expanding. People need better connections to access new places. MTR makes it happen in Hong Kong, the United Kingdom, Sweden, Australia, as well as in the Mainland of China and Macao.
With our sophisticated approach of integrating railways and urban development, we continue to grow and connect vibrant communities for a better future.
For more details

盼記建設有限公司
PAN KEE CONSTRUCTION LIMITED
Unit 7, 3/F, Block 2, Tak Fung Industrial Centre,
No.168 Texaco Road, Tsuen Wan
Phone : +852 2818 6811 / Fax : +852 2818 6899

PAN KEE CONSTRUCTION LIMITED, as a construction company main business engaged on slope improvement works in Hong Kong, was established in 2013. Our goal is to develop a safer environment for living with professions and sincere.

License

- **Relevant Government departments or public organizations**
  - Buildings Department Site
  - Construction Industry Council in geotechnical works
- **Registration and qualification**
  - Registered Specialist Contractor
  - Registered Subcontractor
- **Category**
  - Formation Category
  - General civil works with specialty

Certifications for compliance with ISO requirements

Nature	Certification
Quality Management System	ISO 9001:2015
Environmental Management System	ISO14001:2015
Occupational Health and Safety Management System	ISO45001:2018


AECOM


wsp
Elevating urban landscape with our ingenuity
Integrating our geotechnical expertise with data and digital technologies, our Future Ready solutions for mega infrastructure optimise land use and escalate connectivity, making our city a better, more vibrant place to live and work.
Project
Hung Shui Kiu Station

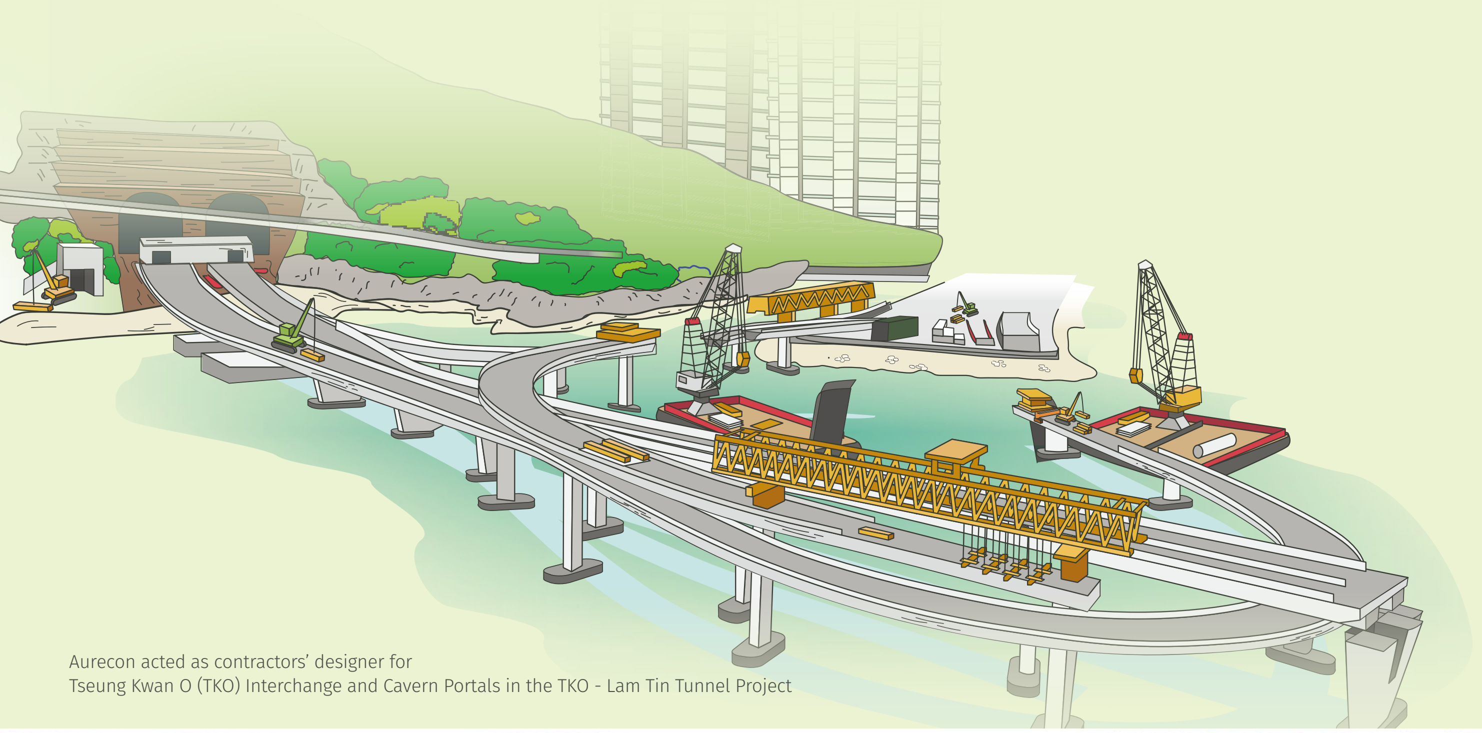

ORGANISING COMMITTEE

Chairman

Ir Clifford Phung

Members

Ir Joanne Ko

Ir Carmen Lau

Dr Andy Leung

Ir David Mak

Ir Candy Tsoi

Ir Victon Wong

Ir W C Yip

Mr Mickey Goh

Mr Alex Leung

Published by:
Geotechnical Division
The Hong Kong Institution of Engineers
9/F., Island Beverley, 1 Great George Street, Causeway Bay, Hong Kong
Tel: 2895 4446   Fax: 2577 7791

Prepared in Hong Kong

EDITORS

Panel Chair

Ir Dr SW Lee

Reviewer

Prof Andy Y F Leung

Prof Anthony K Leung

Prof Louis N Y Wong

Ir Dr Tony Chen

Ir Y C Lam

Ir Jack Yiu

Ir Terence L Y Yau

Ir David C W Mak

Ir Roy K C Hung

Published by:
Geotechnical Division
The Hong Kong Institution of Engineers
9/F., Island Beverley, 1 Great George Street, Causeway Bay, Hong Kong
Tel: 2895 4446 Fax: 2577 7791

Prepared in Hong Kong

FOREWORD

I am most delighted to extend a warm welcome to all distinguished guests, speakers and participants of the 42nd HKIE Geotechnical Division Annual Seminar.

The HKSAR Government has announced a suite of mega development projects including the Northern Metropolis, Lantau Tomorrow Vision, new railway projects, along with the ten-year public housing plan, twenty-year hospital development plan as well as other land supply and infrastructure projects in the pipeline. This visionary blueprint offers huge opportunities to the construction industry in Hong Kong. At the same time, our challenges are also enormous, particularly in the face of ascending construction volume, extremely tight project schedules and higher technical requirements. Geotechnical professionals, being one of the key contributors, play a pivotal role in the implementation of this master plan and we should leverage our expertise and the latest advances in the technologies to rise to the challenges.

Under the theme of “A New Era of Metropolis and Infrastructure Developments in Hong Kong – Challenges and Opportunities to Geotechnical Engineering”, this seminar provides a platform for the practitioners and academia to share their wisdoms and generate new ideas for further enhancing our capability to shape the new future of Hong Kong. Over 40 technical papers have been received, covering a variety of geotechnical topics relevant to the theme. We are particularly grateful to Ir John Kwong, JP (the Head of Project Strategy and Governance Office, Development Bureau) and Ir Barry Sum (the General Manager - New Territories (Projects), Capital Works Business Unit, MTR Corporation Limited) for delivering two insightful and inspiring keynote lectures. I wish that all participants would find the event fruitful and stimulating, with knowledge gained to move towards the new chapter.

On behalf of the Geotechnical Division, I would like to express my gratitude to the speakers and authors contributing to this seminar. My special thanks also go to members of the Organising Committee, under the leadership of Ir Clifford Phung, for their commitment and hard work in making this event a great success. In particular, I do appreciate the idea of introducing a new session called ‘GED Talk’ into the seminar so as to enable more quality papers to be presented in an interactive way. Last but not least, I would like to thank all supporting organisations and sponsors for their continuous support to this annual event.

Ir Tony Ho
Chairman, Geotechnical Division
The Hong Kong Institution of Engineers (2021/22 Session)
May 2022

THE HKIE GEOTECHNICAL PAPER AWARD 2022

The HKIE 2022 Geotechnical Paper Award has received 25 nominations. The number of entries in previous years are 2014 (36 nos.), 2016 (17 nos.), 2018 (24 nos.) and 2020 (13 nos.). With the endorsement of the Geotechnical Division Committee (GDC), a seven-member Assessment Board was formed to select the winning papers. It comprises Ir Tony Ho (Chairman), Ir Dr Johnny Cheuk (Deputy Chairman), Ir Dr Daman Lee, Ir H N Wong, Ir Dr S W Lee, Ir Prof George Tham and Ir Dr C K Lau (Coordinator). Ir Tony Ho and Ir Dr Johnny Cheuk are ex-officio members of the Board, who are the Chairman and Deputy Chairman of GDC. The other five members are selected from the 20-member Assessment Board Panel taking account of the subject nature of the contending papers and the need to avoid potential conflict of interest.

The Assessment Board follows the practices set up since inauguration to ensure the confidentiality of identity of participants and fair but critical judgment on the contending papers. Hence, members would receive information on a need-to-know basis, and only the winning papers are made known publicly. The Board members share views through a hub that remove identity tags. Deciding winners in the Assessment Board meeting is by blind voting.

The Assessment Board has decided to confer the Award for 2022 to the following two papers:

"Design Recommendations for Single and Dual Flow Barriers with and without Basal Clearance" in WLF Kyoto Japan (2021)

Charles W W Ng, Clarence E Choi, Haiming Liu, Sunil Poudyal and Julian S H Kwan

Citation:
This paper provides details of a new analytical framework for assessing the runup, overflow, and landing of granular debris intercepted by multiple rigid barriers. The framework is evaluated by using flume model tests, which simulate dry sand, water, and typical debris flow materials. Related studies using flume model tests to investigate the impact dynamics of debris flow on a rigid barrier with a basal clearance and flexible barrier are also reported. Based on the findings, design recommendations for single and dual debris flow barriers are described and explained. These include optimized design impact coefficients to predict the impact force for: (i) single rigid barriers with and without basal clearance; (ii) single flexible barrier; and (iii) dual rigid barriers. The recommendations can be used for the design of safe and cost-effective barrier systems to protect human lives and infrastructure against debris flow hazards in mountainous regions globally.

And

"Development and applications of debris mobility models in Hong Kong" in Proceedings of the Institution of Civil Engineers - Geotechnical Engineering (2021)
Julian S H Kwan, Eric H Y Sze, Carlos Lam, Raymond P H Law and Raymond C H Koo

Citation:
The paper reviews a comprehensive range of numerical approaches for modelling the mobility and dynamics of landslide debris as part of the continuously improving landslide risk assessment and debris-resisting barrier design in Hong Kong. One of Hong Kong's major contributions to the world is the meticulous post-landslide investigations carried out by GEO over the years. The paper reports on how the high quality findings and reliable data collected from the investigations have been made to good use in validating and calibrating the advanced numerical tools in debris mobility modelling. The paper also explains the principles and practices for analyzing the mobility of landslide debris and deriving the relevant design parameters as well as extending the work to debris-barrier interaction. The materials presented in the paper are reliable, rigorous and suitably explained with due consideration of their scientific context and relevance.

The prize presentation ceremony was held at the HKIE Geotechnical Division Annual Seminar on 13 May 2022. The authors of the winning papers is presented with a trophy and a crystal plaque each. A certificate is also presented to each of the coauthors.

The authors of the winning papers will be invited to give presentation on the key highlights of the papers at technical seminars to be held separately.

For further information on The HKIE Geotechnical Paper Award 2022, please visit the website of the HKIE Geotechnical Division.

Ir Dr C K Lau
Coordinator, Assessment Board
The HKIE 2022 Geotechnical Paper Award

PROGRAMME RUNDOWN

Time (GMT+8)	Agenda
09:00 – 09:05	**Welcome Speech** *Ir Tony Ho, Chairman, The HKIE Geotechnical Division*
09:05 – 09:10	**Sponsor Acknowledgement**
09:10 – 10:25	**Session 1 | Keynote Presentation**
09:10 – 09:40	A New Era of Metropolis and Infrastructure Developments in Hong Kong - The Road Ahead *Ir John Kwong, JP, Head of Project Strategy and Governance Office, Development Bureau*
09:40 – 10:10	Opportunities of New Railway Projects *Ir Barry Sum, General Manager - New Territories (Projects), Capital Works Business Unit, MTR Corporation Ltd.*
10:10 – 10:15	Souvenir Presentation
10:15 – 10:25	**Prize Presentation for The HKIE Geotechnical Paper Award 2022**
10:25 – 10:35	**Break**
10:35 – 11:45	**Session 2 | Session Chairman: Ir Dr Richard Pang** **Theme: Geotechnical Exploration**
10:35 – 10:50	A Sustainable Approach to Marine Reclamations Using Local Dredged Marine Soils and Wastes: Soft Soil Improvement, Physical Modelling Study, and Settlement Prediction-Control *Ir Prof J H Yin, The Hong Kong Polytechnic University*
10:50 – 11:05	Advanced Design and Construction Method of Marine Cut & Cover ELS Tunnel Cofferdam *Ir Dr Raymond Cheung, Gammon Construction Ltd.*
11:05 – 11:20	Developing Hong Kong's First Materials Testing Laboratory and Archives Centre in Caverns - Technical Challenges and Solutions *Ir Ivan Chan, Geotechnical Engineering Office, Civil Engineering and Development Department*
11:20 – 11:35	A Critical Review of the Current Practice of Design and Construction of Offshore Foundations in Hong Kong *Ir Dr Daman Lee, CLP Power Hong Kong Ltd.*

Time (GMT+8)	**Agenda**
11:35 – 11:45	Q&A Session & Souvenir Presentation
11:45 – 13:00	**Lunch**
13:00 – 13:55	**Session 3 | Session Chairman: Ir Dr Johnny Cheuk** **Theme: Digital Technologies for Geotechnical Applications**
13:00 – 13:15	3-D Hong Kong Geological Modelling and Management System *Mr Matthew Liu, The Hong Kong University of Science and Technology*
13:15 – 13:30	A New Digital-based Approach to Automate and Optimize Geotechnical Design *Ir Alvin Lam, Arup*
13:30 – 13:45	Machine Learning-based Natural Terrain Landslide Susceptibility Analysis – A Pilot Study *Ir Helen Li, Geotechnical Engineering Office, Civil Engineering and Development Department*
13:45 – 13:55	Q&A Session & Souvenir Presentation
13:55 – 14:50	**Session 4 | Session Chairman: Ir Tony Ho** **Theme: Advances in Underground Development**
13:55 – 14:10	Underground Development - Adoption of Systematic Pipe Curtain with Jack-in Place Rectangular Tunnel Boring Machine Methodology *Ir K M Chiang, Shanghai Tunnel Engineering Co., Ltd.*
14:10 – 14:25	Active Site Supervision to Enhance Drilling & Blasting *Ir Simon Leung, AECOM Asia Co. Ltd.*
14:25 – 14:40	Two Major Technical Solutions on the Lung Shan Road Tunnel - Pilot TBM Tunnel Enlargement and TBM U-turn in Cavern *Mr Xavier Monin, Dragages Hong Kong Ltd.*
14:40 – 14:50	Q&A Session & Souvenir Presentation

Time (GMT+8)	Agenda
14:50 – 15:50	**Session 5 | Session Chairman: Ir Chris Lee** **Theme: New Materials and Testing Standards**
14:50 – 15:05	Novel Cementitious Materials for Geotechnical Applications - Vibration Resistant Sprayed Concrete for Rock Tunnel Lining and Self-compacting Backfill for Slope Upgrading Works *Ir Martin Kwong & Mr Eric Chen, Nano and Advanced Materials Institute*
15:05 – 15:20	Technical Developments Related to Deep Cement Mixing Method in Hong Kong *Ir Prof Philip Chung, Geotechnical Engineering Office, Civil Engineering and Development Department*
15:20 – 15:35	Pilot Use of Alternative Compliance Criterion for Cement-soil in a Slope Upgrading Works Project *Ir Dr Dominic Lo, Geotechnical Engineering Office, Civil Engineering and Development Department*
15:35 – 15:45	Q&A Session & Souvenir Presentation
15:45 – 15:55	**Break**
15:55 – 16:30	**Session 6 | Session Chairman: Ir Lawrence Shum** **GED Talk: Design and Construction Technologies**
15:55 – 16:15	1. Digital Classification of Anthropogenic Features for Natural Terrain Hazard Assessment in the Quasi-natural Heritage Landscape of the Lin Ma Hang Lead Mine *Ms Petra Lee, Meinhardt Infrastructure and Environment Ltd.*
	2. Deep Cement Mixing - The Experience in Tung Chung East Reclamation and Challenges Ahead *Ir C H Yan, Sustainable Lantau Office, Civil Engineering and Development Department* 3. Marine Deep Cement Mixing (Cutter Soil Mixing Technique) *Mr Ricky Pang, Bachy Soletanche Group Ltd., Hong Kong*
16:15 – 16:30	Panel Discussion, Q&A Session & Souvenir Presentation

Time (GMT+8)	**Agenda**
16:30 – 17:15	**Session 7 | Session Chairman: Ir Clifford Phung** **GED Talk: Smart and Digital Technologies**
16:30 – 16:55	1. Use of Smart Devices in Civil and Geotechnical Works for Vibration, Noise and Temperature Measurement *Ir Dr Thomas Lam, Construction Industry Council* 2. GIS-BIM Adoption for Construction Digitalisation *Mr Simon Leung, Esri China (Hong Kong) Ltd.* 3. Monitoring of a Peanut-shaped TBM Launching Shaft Excavation Using Fibre Optics and Remote Sensing Techniques *Ir Ivan Li, Geotechnical Engineering Office, Civil Engineering and Development Department* 4. Are We Ready to Use AI Technologies for the Prediction of Soil Properties? *Ir Dr Ryan Yan, AECOM Asia Co. Ltd.*
16:55 – 17:15	Panel Discussion, Q&A Session & Souvenir Presentation
17:15 – 17:50	**Session 8 | Session Chairman: Ir Y C Lam** **GED Talk: Advances in Underground Development**
17:15 – 17:35	1. An Unprecedented Land Supply Means in Hong Kong: Underground Quarrying-cum-Cavern Development *Ir Leslie Tsang, Geotechnical Engineering Office, Civil Engineering and Development Department* 2. Rock Breaking Using Supercritical Carbon Dioxide (SC-CO_2) Technology – a Safe, Efficient, and Sustainable Approach *Dr Garfield Guan, G & K Consultancy Ltd.* 3. Evaluation of Digital Rock Mass Discontinuity Mapping Techniques for Applications in Tunnels *Mr Philip Wu, Aurecon Hong Kong Ltd.*
17:35 – 17:50	Panel Discussion, Q&A Session & Souvenir Presentation
17:50 – 17:55	**Closing Remarks** *Ir Clifford Phung, Organising Committee Chairman, The HKIE Geotechnical Division 42nd Annual Seminar, 2022*

TABLE OF CONTENTS

Theme: Advances in Underground Development (I)

Theme: New Materials and Testing Standards

A Sustainable Approach to Marine Reclamations Using Local Dredged Marine Soils and Wastes: Soft Soil Improvement, Physical Modelling Study, and Settlement Prediction-Control

J H Yin[1], W B Chen, D Y Tan, P C Wu
Department of Civil and Environmental Engineering, The Hong Kong Polytechnic University, Hong Kong, China

ABSTRACT

Housing is currently one of the burning social issues in Hong Kong. There is an urgent need for providing large areas of suitable lands for residential houses and other infrastructures. In 2018, the Hong Kong Government proposed a major reclamation project in Hong Kong waters, i.e., "Lantau Tomorrow" vision, the main concerns of which are the short supply of fill materials, long construction time, and high cost. To tackle these concerns, the authors have proposed to use local dredged Hong Kong Marine Deposits (HKMD) and construction wastes to fill a reclaimed area on the seabed in a major Research Impact Fund project in 2019 with HK$15M funding. The use of local HKMD and construction wastes can significantly save the costs for fill material and shorten the construction time. In this paper, successful reclamation projects using soft soils will be briefly reviewed. The state-of-the-art research findings in PolyU, including the results from two ongoing physical model tests, turning construction wastes into the competent filling materials, and a well-verified new simplified Hypothesis B method for predicting soft soil settlements will be presented. Lastly, the methodologies for controlling the post-construction settlement will be discussed.

1 INTRODUCTION

Hong Kong ranks among the top in the world in terms of population density and the least affordable housing market. The average waiting time to get the government-subsidized houses has been increased to 6 years, equaling the highest record in history. There is an urgent need for providing a large area of suitable lands for residential housing and other infrastructures. In the Chief Executive's 2018 Policy Address, "Lantau Tomorrow" reclamation in Hong Kong waters was proposed with a total 1700 hectares of land for 700,000 to 1,100,000 people. The detailed planning and engineering study for the artificial islands of about 1000 hectares around Kau Yi Chau is in progress. One of the biggest challenges for "Lantau Tomorrow" reclamation is a short supply of fill materials. The construction time and cost are also a concern.

Marine reclamations have a long history in Hong Kong and the technologies used for marine reclamations vary widely. As part of the Hong Kong-Zhuhai-Macau Link Project, two artificial islands were reclaimed using sandfill and vertical drains with sandfill surcharge surrounded by 120 steel pipe piles (22m in diameter and 50.5 m in length). In the reclamation of Hong Kong Airport Runway 1 and Runway 2, the reclamation was done by dredging and removing all Hong Kong Marine Deposits (HKMD) which caused marine environmental problems. For the new Third Runway, all HKMD have been kept in situ and surrounded by seawalls constructed on Deep Cement Mixed (DCM) soil foundations. Imported sandfills (or crushed stones) have been used to fill the reclaimed area and vertical drains with preloading have been used to improve the HKMD. However, there is a severe shortage of sand for marine reclamations in Hong Kong. The cost of crushed stones is high and

[1] E-mail: cejhyin@polyu.edu.hk

takes time. Therefore, there is an imperative need to identify an alternative reclamation method, that is economical, efficient, and sustainable, for Hong Kong.

In view of the limited and expensive sand resources, the dredging and filling method using local soft soils has become the most prevalent method for marine reclamation projects in many other coastal cities. The dredged soft soils are from the basin of harbor, lake or river, the sea channel. These soft soils have normally high water content, high compressibility, low permeability, and low strength. In Hong Kong, maintenance dredging of HKMD for harbor and navigation channels is periodically conducted. The dredged HKMD are naturally dewatered and transported to the Mainland for disposal. In our approach, these HKMD can be used for marine reclamation in Hong Kong. In addition, HKMD in seabed in Hong Kong waters, where marine ecology is not much affected, can be dredged and used for reclamations in Hong Kong.

Among many existing soft soil ground improvement techniques, prefabricated vertical drains (PVDs) with vacuum/surcharge preloading have gained their popularity due to their high efficiency, high safety, low contamination and low cost. Yan and Chu (2005) reported a case study of using the combined vacuum and fill surcharge preloading method to improve the recently dredged clay slurry with a thickness of 16 m for a storage yard at Tianjin Port. Wang et al. (2016) presented an improved vacuum preloading method with an air-pressurizing system to accelerate the consolidation of Wenzhou clay slurry through a field pilot test. Another field test in Shenzhen that investigated the feasibility of under water vacuum preloading method in treating soft clay is reported by Kwong et al. (2008). Similar studies were also conducted in other countries, for example, in Singapore (Chu et al. 2000), Australia (Indraratna et al. 2004), Thailand (Artidteang et al. 2011), and Japan (Chai et al. 2012). Though the performance of vacuum preloading with PVDs has been widely validated so far, the limitations of this method can be seen from: (1) serious bending and clogging of PVDs, reducing dewatering efficiency; (2) obvious deterioration of vacuum pressure along with the depth, resulting in insufficient consolidation at deeper positions; and (3) requirement of a working platform for the installation of PVDs and the application of the preloading, which extends the construction duration.

This paper aims to introduce a novel reclamation method for treating local HKMD slurry in a feasible, efficient and economical way. The detailed procedures of this novel method will be presented. In addition, two ongoing physical models, one is a large cylinder model and the other is a large plane strain model, will be described in detail, followed by the demonstration of initial test results and data interpretation. Turning wastes into competent filling and/or strengthening materials for marine reclamation in Hong Kong will be presented briefly. Besides, a well-verified new simplified Hypothesis B method will be introduced as well. Lastly, the methodology for controlling the post-construction settlement will also be presented. All the works are from our recent studies and will contribute to research development, the design and construction of marine reclamations, and make a positive impact on Hong Kong society.

2 A NEW RECLAMATION METHOD USING DREDGED MARINE SOILS

To solve the problem of the short supply of lands, the authors have advocated using local dredged marine soils or construction wastes with a combined ground improvement method to achieve a super-fast, large-area and low-cost marine reclamation in Hong Kong or even Guangdong-Hong Kong-Macau Greater Bay Area.

Figure 1: Tian Kun dredging and blow-filling ship

The super-fast construction is contributed in four ways: (i) fast dredging and blow-filling local marine deposits, (ii) use of local general soil fill or even construction wastes instead of using imported sand, (iii) fast consolidation by using horizontal and vertical drains with vacuum preloading rather than using imported sand as surcharge; and (iv) fast installation of steel (or FRP/FRP concrete) pipe pile walls rather than the slow method using concrete blocks. Chinese Mainland has had the newest dredging blow-filling ship Tian Kun (Figure 1) which has a blow filling speed of 6000 m^3/hour, operating 24 hours per day. Take the 1700 hectares of "Lantau Tomorrow" reclamation as an example. If we assume that the average water depth is 15 m and the final filled land is +6 m above sea level, the total volume of the fills needed, considering added fill for 2 m settlement compensation, will be 3.91×10^8 m^3. If 20 Tian Kun ships are employed for the reclamation, the time required will be 1.39 years. If 20 conventional 4000-ton ships are utilized to move sand from a site in Mainland, say, the time required will be 133.9 years.

"Large-area" and "low-cost" of the new method are contributed in two ways: (i) blow filling a large area, say, a few square kilometers is easy and (ii) since no imported sand is needed, the economical benefit of the new method of using local free marine soils or general soil fills/construction wastes for reclamation is obvious. The estimated cost saving for imported sand only will be HK$60 billion dollars for the 1700 hectares of "Lantau Tomorrow" reclamation.

3 A COMBINED GROUND IMPROVEMENT METHOD FOR HKMD SLURRY

The local dredged marine soils are mainly HKMD. In order to facilitate the blow-filling process, dredged HKMD will be mixed with water to reach a certain slurry state. Due to the high water content, high compressibility, and extremely low bearing capacity of blow-filled HKMD slurry, ground improvement techniques have to be integrated with the blow-filling process to speed up the consolidation and enhance the shear strength.

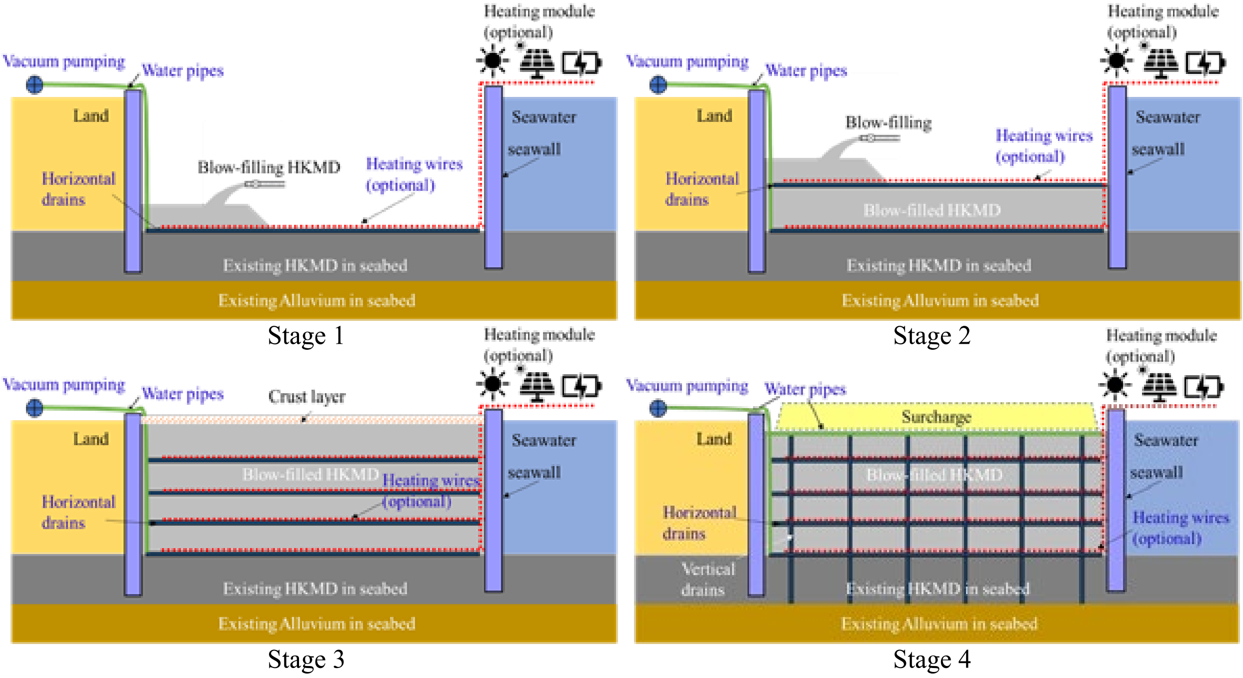

Figure 2: Illustration of a combined ground improvement method for HKMD slurry in stages

A ground improvement method combining horizontal and vertical drains with vacuum and/or surcharge preloading is recommended by the authors to improve the HKMD slurry in stages, as illustrated in Figure 2.

In Stage 1, a layer of prefabricated horizontal drains (PHDs) is placed on the existing seabed before blow-filling HKMD slurry. Vacuum pressure is applied to the PHDs after significant self-weight consolidation of the HKMD slurry. In Stage 2, the second layer of PHDs is placed on the blow-filled HKMD slurry followed by filling the second layer of HKMD slurry. The newly filled HKMD slurry is subjected to a self-weight consolidation followed by a vacuum preloading, while the HKMD slurry filled in Stage 1 is subjected to both the vacuum preloading and the vertical surcharge from the self-weight of the newly filled HKMD slurry. In Stage 3, a multi-layer HKMD ground is formed by blow-filling and improved by PHDs with vacuum preloading technique. Once a crust layer with sufficient strength is formed on the surface of the HKMD ground, PVDs are installed in Stage 4 to further improve the HKMD ground with the help of vacuum and/or surcharge preloading. The surcharge preloading can be applied by filling construction wastes. Optional heating techniques can be used to tackle marine soils with very low permeability or significant viscosity.

For a PVDs-installation crawler with a working load of 80 kPa and a working area of around 6 m^2, a crust layer possessing an average undrained shear strength of 35 kPa and a thickness of 0.5~1 m is most likely to meet the requirement of FOS>3. For a light crawler with a working loading of 30 kPa and a working area of around 6 m^2, a crust layer with an average undrained shear strength of 15 kPa and a thickness of 0.5~1 m is most likely to satisfy the requirement of FOS>3. Crust layers can be formed by sun-dry or mixing the surface layer with cementitious binders (presented in Section 5). It should be noted that the abovementioned ground improvement methods are proposed with the purpose of fast reclamation. Post-construction settlements shall be controlled by other measures, which are discussed in Section 7.

4 TWO TYPES OF ONGOING PHYSICAL MODEL TESTS

4.1 Testing material

The soil used in the physical model tests was HKMD, which is mud-like soil dredged from a construction site in Tuen Mun, Hong Kong. In accordance with the British standard BS 1377:2016, basic properties were determined and listed in Table 1. Particle size distribution was determined by the wet sieving method and hydrometer method and showed that the soil mainly consists of clay (36%), silt (33%) and sand (31%). It should be noted that the initial water content was increased to 220% in the following physical model tests.

Table 1: Basic properties of the HKMD

Property	Value
Natural water content (%)	86.31
Liquid limit (%)	63.88
Plastic limit (%)	28.23
Plasticity index	25.22
Specific gravity	2.63
Void ratio	2.27
Salinity (%)	3.30

4.2 Cylindrical physical model tests

Figure 3(a) presents the photos of the cylindrical physical model, which consists of several short Perspex tubes called sub-columns. Each sub-column is 100 mm in height and 170 mm in internal diameter. Eight sub-columns can be assembled together to have an 800 mm initial height for each test. There are three holes opened at the middle height of each sub-column. Two of them serve as sampling ports with valves and the third one is for pore pressure monitoring. During the test, soil samples were extracted from sampling ports at different heights and different time points so that the water content profile during the test can be captured. Meanwhile, pore pressure was monitored via the pressure transducers installed on the sidewall. Settlement of the soil surface was observed by a digital camera due to the transparent feature of the Perspex material. There were two outlet channels in the bottom plate. One was for measuring the pressure at the bottom, and the other one connected the vacuum system to apply vacuum loading through the bottom. Two pieces of geotextiles were placed on the bottom plate and a porous stone was put between the geotextiles to form a sandwich permeable layer as a horizontal drain (Figure 3(b)). The sandwich layer was used instead of the prefabricated drain (PD) so that the vacuum loading can be uniformly applied on the whole cross-section of soils. In this model test, only one horizontal drainage was placed at the bottom. In fact, multiple PHDs can be installed at different soil depths, for example, in our large physical model test and the field trial. Two model tests were designed and completed: namely, Test 1 and Test 2. Test 1 was a control test of vacuum preloading with PHD, and multi-staged vacuum pressure from 20 kPa to 80 kPa was applied in order to reduce clogging effect by lower initial vacuum pressure. Both tests started with 4 days of self-weight consolidation. The total period of applying vacuum pressure in Test 1 was 19 days. Test 2 was the test combining PVD and PHD, with

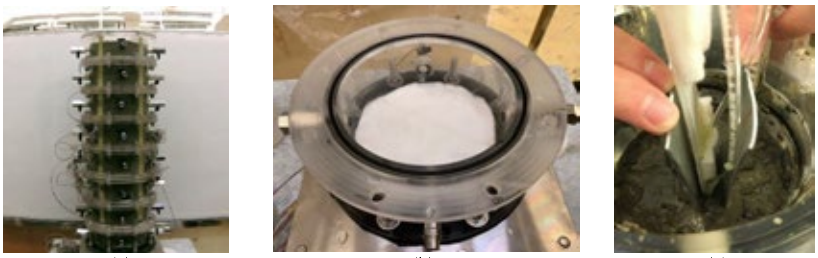

(a) (b) (c)

Figure 3: Photos of a cylindrical physical model: (a) the segmented settling columns, (b) geotextile laid on the bottom as PHD, and (c) PVD installation

14 days for vacuum application on PHD only and another 14 days for vacuum pressure on both PHD and PVD. The installation of PVD is shown in Figure 3(c). The initial height of soil slurry was 800mm.

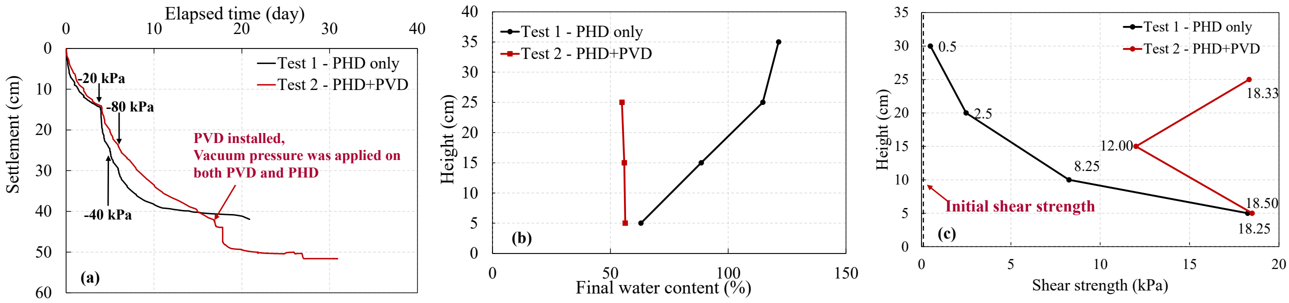

Figure 4: Plots of cylindrical physical model tests: (a) settlement versus elapsed time, (b) final water content versus soil height, and (c) shear strength versus soil height

As can be seen in Figure 4(a), the HKMD slurry settled significantly in the first 4 days due to self-weight consolidation and followed by a sudden drop induced by -20 kPa vacuum pressure at the bottom. -40 kPa and -80 kPa were applied after 5 and 6 days, respectively. It can be observed that in Test 1 the settlement tended to level off after -80 kPa was held for 9 days. And the settlement in Test 2 generally kept increasing with a decreasing rate. While, for Test 2, an obvious sudden drop on settlement curve was observed immediately after the PVD was inserted with -20 kPa applied for 1 day. Another large sudden increase occurred when vacuum pressure was further increased to -80 kPa on both PHD and PVD. The settlement, then, started to stabilize quite quickly after 3 days with no obvious further increase. The final settlements for Test 1 and Test 2 were 0.46 m and 0.53 m, respectively. The final water content along soil height at the end of each test was shown in Figure 4(b). As expected, the final water contents at different heights in Test 2 were lower than those in Test 1, with an even distribution for Test 2 and decreasing trend with decreasing height for Test 1. Figure 4(c) shows the shear strength along the soil height measured by a hand-held vane shear device. The shear strength in Test 1 increased with decreasing soil height and kept more or less stable along with soil height in Test 2, which corresponds to the change of water content in Figure 4(b). After the combined PHD and PVD with vacuum preloading, the shear strength generally increased from almost zero to around 18 kPa at the top and bottom boundary and to 12 kPa at the middle height of soil. The test results imply that the dewatering capacity can be largely improved using the vacuum preloading method with both PHD and PVD, compared to the case with PHD only.

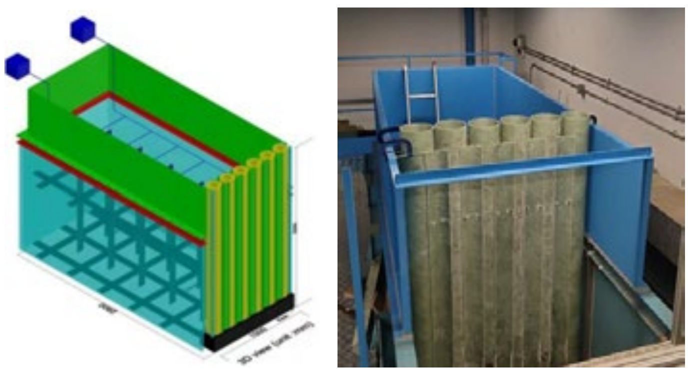

(a) (b)

Figure 5: (a) Schematic drawing and (b) photo of plane strain physical model

4.3 Plane strain physical model tests

The plane strain physical model is aimed to simulate the real case of reclamation projects, including the dredging process, self-consolidation process, fast consolidation process by vacuum preloading with prefabricated band drains. This large model test was built in a water tank with the dimension of 1.5 m in width, 2.5 m in length, and 2.3 m in height. The details of the model are shown in Figure 5. The filled soil was surrounded by steel plate wall and FRP pipe wall, which consists of 6 FRP pipes with a length of 2.3 m, a diameter of 0.21 m, and a thickness of 0.005 m. The vacuum pressure was applied through PVDs and PHDs.

The test procedure is as follows:

Step 1: Place PHD grid first at the bottom, then pump HKMD slurry into the tank, and apply vacuum pressure on PHD grid layer.

Step 2: After consolidation, place another PHD grid layer at the soil surface in Step 1, then pump in the second layer of slurry, then apply vacuum pressure on both PHD grid layers.

Step 3: After consolidation, place the third layer of PHD grid layer at the soil surface in Step 2, then pump in the third layer of slurry, then apply vacuum pressure on three PHD grid layers together.

Step 4: After consolidation, install PVDs at predetermined positions and cover the soil with a geomembrane, then apply vacuum pressure on all PHD grid layers and PVDs.

The development of the settlement of the bottom layer of soil in Step 1 with time is shown in Figure 6(a). It can be observed that a sharp increase in settlement occurred after the vacuum preloading was applied. The height of the bottom layer of HKMD was decreased from 1 m to 0.634 m. Figure 6(b) presents a general decreasing trend of water content with the decrease of the soil height at all time points and the average water content in the physical model decreased from 181% to 101% during the period of applying vacuum pressure on the PHD layer at the bottom. Special emphasis should be paid to the fact that the difference of water content between the soil at the bottom and the surface increased with time, which indicates that a better dewatering effect can be achieved for the soil with a closer distance to the PHDs.

After the second layer of soil was pump-filled on top of the bottom layer, vacuum pressure was applied on both PHD layers. The development of settlement with time is shown in Figure 7(a). A sudden increase in the settlement of the bottom layer of soil can be observed because the second layer of soil served as a surcharge on the bottom layer of soil and the second layer of PHD with vacuum pressure also accelerated the dewatering of the bottom layer of soil. Comparisons of water content and shear strength are shown in Figure 7(b) and Figure 7(c), respectively. A general decreasing trend of water content and a general increasing trend of shear strength along with decreasing soil height can be observed. An obvious inflection point at a height of 47cm (the height of the second layer of PHDs) can be observed in both figures, proving that a better improvement performance can be obtained at a closer distance with the PHDs. It can be seen that the average water content of two layers of soil was decreased from 155% to 76% with the final water content of 60% at the bottom and the final shear strength of 27 kPa at the bottom. In the following test schedule, the third layer of soil will be placed on top and treated by PHDs. After the stabilization of settlement of soil due to PHDs, PVDs will then be inserted and applied with vacuum pressure.

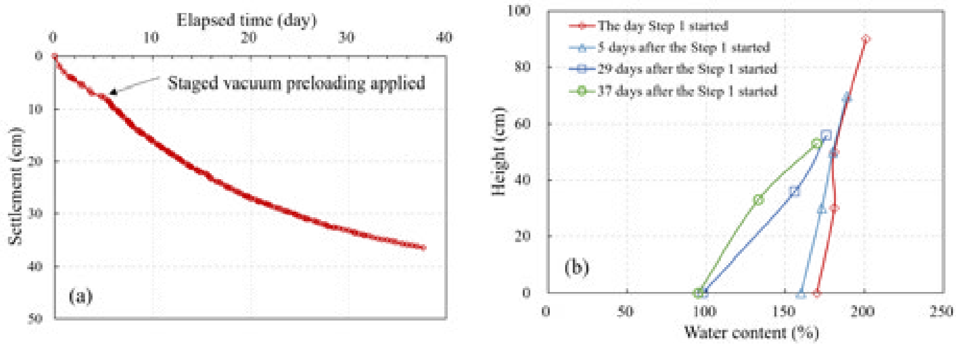

Figure 6: (a) Settlement versus time under staged vacuum preloading and (b) water content along soil height at different times after vacuum pressure applied

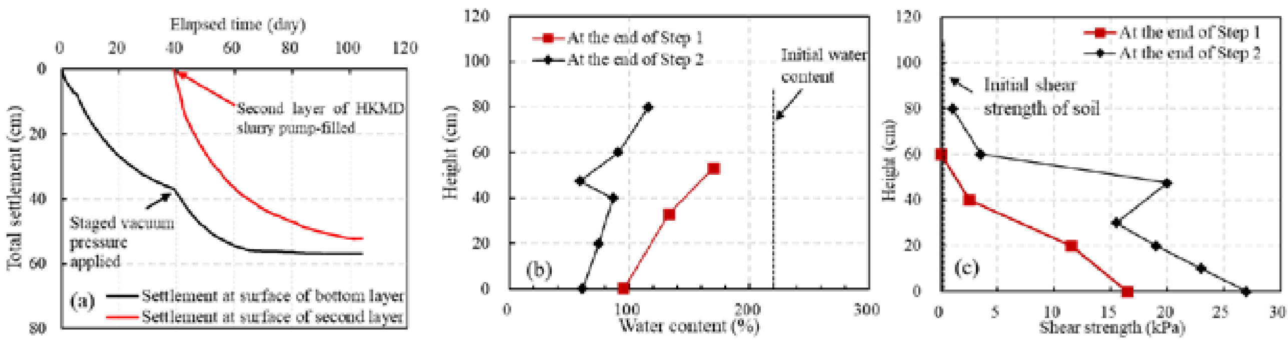

Figure 7: Plots of (a) the settlement versus time of two layers of soil in Step 2, (b) the water contents along soil height after Step 1 and Step 2, and (c) the shear strength along soil height after Step 1 and Step 2

5 USE OF WASTE INTO FILLING MATERIALS FOR MARINE RECLAMATION

HK now produces approximately 1200 tonnes/day (2000 tonnes in 2030) of dewatered sewage sludge. The sludge will then be converted into Incinerated Sewage Sludge Ash (ISSA) which has to be disposed of at landfills, which will be fully filled within 5 years. ISSA is a by-product from the burning dewatered sewage sludge in furnaces in Hong Kong. The use of a combination of ISSA with traditional binders including cement or lime on soil improvement has been studied and showed that ISSA has great potential to be utilized in geotechnical application. Therefore, a "win-win" strategy of turning large volumes of dredged HKMD into fill materials using ISSA and certain alkali activators is expected to be of high economic and social benefits. This sustainable fill material can be used to form a competent crust layer quickly on top of HKMD slurry treated by PHD vacuum preloading for the easy access of personnel and light machinery to insert PVD.

The authors have adopted lime-activated ISSA as a binder, which is mixed into HKMD slurry to decrease the water content and increase the strength. In order to further increase the strength, another industrial by-product, i.e., ground-granulated blast-furnace slag (GGBS) is also added into binder material with different mixing ratios to ISSA. So far, two series of unconfined compression (UC) tests have been conducted: (1) dry mass of binder (ISSA only) to dry mass of HKMD is equal to 30%, and the activator ratio (AR) (a dry mass ratio of lime to binder) is 20%, 30%, and 40%, respectively; (2) dry mass of binder (ISSA and GGBS) to dry mass of HKMD is equal to 30%, the mass ratio between ISSA to GGBS is 0, 1, 2, 3, and 5 respectively, and the addition of lime is kept at 30% in dry mass to the binder. The initial water content of all specimens is 200%, defined as the ratio of water mass to dry mass of soil. All the mixed specimens were cured under an environmental chamber with humidity of 90% and a temperature of 24 °C. The specimen dimension is 50mm in diameter and 100mm in height.

Figure 8(a) shows the unconfined compressive strength (UCS) of ISSA-based specimens, i.e., the first series of tests. The UCS with an AR of 20% showed no obvious change with the increase of curing time, which implies that the low content of lime is incapable of providing a sufficient alkali environment for activating ISSA. When AR was increased to 30% and 40%, the effect of curing time became more significant. The hydration of lime will decrease the water content by a large extent and provide hydration products to bond soil particles. This explains the reason why only 10% change of AR would lead to a double in UCS when AR changed from 30% to 40%. As discussed in Section 3, with AR of 30%, the treated specimen achieved a strength level of soft clay, which generally fulfills the strength requirement for a light crawler to insert PVD with a FOS>3 (UCS>30 kPa). While with 40%, the specimen achieved a level of medium stiff clay, which is competent to sustain a crawler with working load of 80 kPa to meet the requirement of FOS>3 (UCS>75 kPa). In order to further increase the strength, GGBS can be added by different ratios to ISSA as binder. As can be seen in Figure 8(b), the UCS keeps increasing with the addition of GGBS and the increasing curing time. The obvious increase in UCS implies that there would be a great potential of alkali-activated ISSA+GGBS treated HKMD to be used in road pavement applications, provided that further studies can be conducted on the long-term reliability influenced by environmental change and

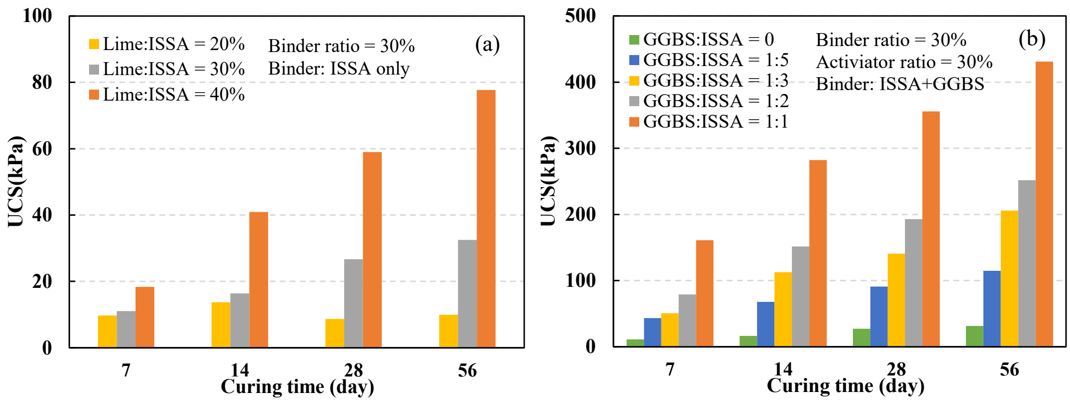

Figure 8: UCS of (a) ISSA-based and (b) ISSA+GGBS-based specimens at 7, 14, 28, 56 days

degradation behavior under cyclic loading due to moving vehicle. As the following work, a mechanical-chemical combined method, which incorporates binder stabilization and vacuum preloading with PHD at the same time, will be further implemented in PolyU to propose an efficient and sustainable way in the marine reclamation project.

6 A NEW SIMPLIFIED HYPOTHESIS B METHOD

It is well known that creep compression shall be considered in both "primary" consolidation and "secondary" consolidation periods. For an accurate settlement calculation, a rigorous Hypothesis B method coupling the dissipation of excess pore water pressure and viscous deformation of soil skeleton has been used based on a proper Elastic Visco-Plastic (EVP) constitutive model (Yin and Graham 1996 and 1999). However. this method needs to solve a set of nonlinear partial differential equations which is not easy to be used by engineers. Yin and his coworkers have done many works to simplify the rigorous Hypothesis B method by partially de-couple the dissipation of excess pore water pressure and have proposed a simplified method for multi-layered soils with/without drains under complicated loadings (Yin and Feng 2017; Feng et al. 2020). Recently, a general simplified Hypothesis B method (Yin et al. 2022) was proposed and verified.

In many cases, the consolidation of soils is very close to or can be approximated as a one-dimensional (1D) problem, that is, strain and water flow occur in vertical direction only as assumed in Terzaghi's 1D consolidation theory. In this case, a simple method for consolidation analyses of clayey soils exhibiting viscous behaviour is available to use. The simple method for a single-layer case is presented below.

$$S = S_{primary} + S_{creep} = \\ = \begin{cases} US_{pf} + \alpha U^{\beta} S_{creep,f} & for \quad t_0 \le t \le t_{EOP,field} \\ US_{pf} + [\alpha U^{\beta} S_{creep,f} + (1-\alpha U^{\beta}) S_{creep,d}] & for \quad t \ge t_{EOP,field} \end{cases} \tag{1}$$

Here S is total settlement. $S_{primary} = US_{pf}$ is "primary" consolidation settlement. U is average degree of consolidation. S_{pf} is settlement at the end of the "primary" consolidation. $S_{creep} = \alpha U^{\beta} S_{creep,f}$ or $S_{creep} = [\alpha U^{\beta} S_{creep,f} + (1-\alpha U^{\beta}) S_{creep,d}]$ is viscous (creep) settlement. $S_{creep,f}$ is creep settlement under the final total vertical effective stress assuming the excess porewater pressure zero. $S_{creep,d}$ is creep settlement delayed to occur by $t_{EOP,field}$, that is, $t \ge t_{EOP,field}$ for $S_{creep,d}$. t_0 is a creep parameter and is equal to 1 day since all points in the compression curve in Figure 9 have the load duration of 1 day in a conventional staged oedometer test. $t_{EOP,field}$ is the time at the End-of-Primary consolidation for the field condition, calculated using $U = 98\%$. α and β are two constants with $\alpha = 0.8$ and $\beta = 0.3$ recommended for all clayey soils. Small ranges of $0.75 \le \alpha \le 0.85$ and $0.2 \le \beta \le 0.4$ are possible and can be verified by using the rigorous Hypothesis B method.

In the above equation, S_{pf} is the final primary consolidation settlement and is caused by an applied load. S_{pf} depends on the relative magnitudes of the initial vertical effective stress acting on the soil and the effective preconsolidation pressure, and can be estimated as follows, based on oedometer test condition or one-dimensional (1D) strain condition:

For $\sigma'_{v0} = \sigma'_p < \sigma'_{v0} + \Delta\sigma'_v$: $S_{pf} = H_s\left(\frac{C_c}{1+e_0}\log\frac{\sigma'_{v0} + \Delta\sigma'_v}{\sigma'_{v0}}\right)$

(2a)

For $\sigma'_{v0} < \sigma'_p < \sigma'_{v0} + \Delta\sigma'_v$: $S_{pf} = H_s\left(\frac{C_r}{1+e_0}\log\frac{\sigma'_p}{\sigma'_{v0}} + \frac{C_c}{1+e_0}\log\frac{\sigma'_{v0} + \Delta\sigma'_v}{\sigma'_p}\right)$

(2b)

For $\sigma'_{v0} < \sigma'_{v0} + \Delta\sigma'_{v} < \sigma'_{p}$: $S_{pf} = H_s\left(\frac{C_r}{1+e_0}\log\frac{\sigma'_{v0}+\Delta\sigma'_{v}}{\sigma'_{v0}}\right)$

(2c)

Here σ'_{v0} is initial vertical effective stress in the soil layer. e_0 is initial void ratio in the soil layer. σ'_{p} is effective preconsolidation pressure, which is the maximum vertical effective stress that has acted on the soil layer in the past and can be determined from laboratory oedometer tests. $\Delta\sigma'_{v}$ is the change in vertical effective stress due to the fill and future imposed load on the soil layer. H_s is thickness of the soil layer to be considered. $C_c/(1+e_0) = CR$ is compression ratio, equal to the slope of the virgin compression portion of the $\varepsilon_v - \log\sigma'_{v}$ plot as shown in Figure 9 and C_c is compression index which can be estimated from laboratory oedometer tests. $C_r/(1+e_0) = RR$ is recompression ratio, equal to the average slope of the recompression portion of the $\varepsilon_v - \log\sigma'_{v}$ plotted in Figure 9 and C_r is recompression index which can be estimated from laboratory oedometer tests, and ε_v is vertical strain caused by $\Delta\sigma'_{v}$. Note that the curve of $\varepsilon_v - \log\sigma'_{v}$ plotted in Figure 9 is normally measured from an oedometer test under multiple staged load increments with one day duration under each load increment.

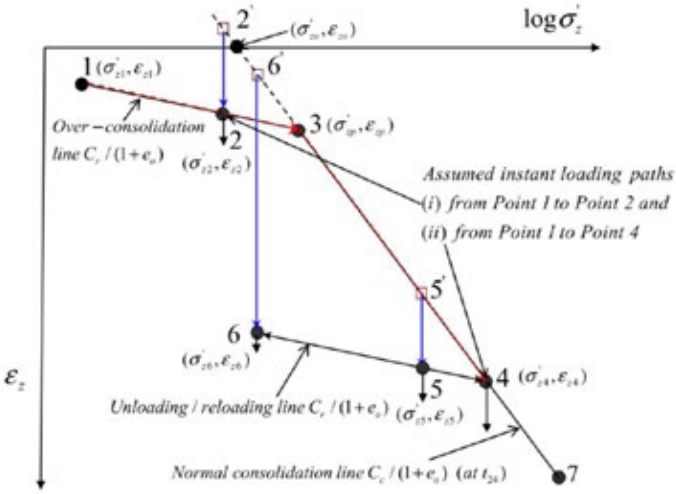

Figure 9: Relationship of strain and log(effective stress) with different consolidation states (after Yin et al. 2022)

Referring to Figure 9 and consider one soil layer with thickness H_s, Point 1 is considered to be the original starting condition with initial stress and strain $(\sigma'_{v1}, \varepsilon_{v1})$ in the field. Here σ'_{v1} has the same meaning as σ'_{v0} in the above equations. Due to gravity, the initial vertical effective stress increases with depth. In this case, the initial stress σ'_{v1} may be calculated at the mid-height $H_s/2$ of this soil layer. The initial strain ε_{v1} is normally taken as zero. Point 1 to Point 3 in Figure 9 is in an Over-consolidation (OC) line with slope $C_r/(1+e_0)$. The average line slope of the expansion-recompression loop in Figure 9 has the same slope $C_r/(1+e_0)$ as that of this OC line. Point 3 is considered the pre-consolidation pressure point $(\sigma'_p, \varepsilon_p)$ in the soil profile, also at the mid-depth $H_s/2$ of the layer. The preconsolidation pressure σ'_p is normally measured in an oedometer test with one-day duration for each staged load on a soil sample taken from the mid-depth. The strain ε_p can be calculated as $\varepsilon_p = [C_r/(1+e_0)]\log(\sigma'_p/\sigma'_{v1})$. The line from Point 3 to Point 4 in the figure is a Normal Consolidation (NC) line with slope $C_c/(1+e_0)$. This is measured from the same oedometer test with one-day duration for each staged loading. From Point 4 to Point 6 is an unloading/reloading line with same slope $C_r/(1+e_0)$ as the over-consolidated line from Point 1 to Point 3.

The above equation can also be used for the case with vertical drains. In this case, $U = 1-(1-U_v)(1-U_r)$ where U_v and U_r are average degree of consolidation for vertical and radial directions respectively. The values of $\alpha = 0.8$ and $\beta = 0.3$ are obtained from the best-fitting the calculated settlement curve to the settlement curves computed by the fully coupled consolidation analyses and use $U = 98\%$ to calculate $t_{EOP,field}$. The U is related to a time factor, for example, $T_v = tc_v/d^2$ for 1D consolidation. The parameter d is the maximum drainage distance. If the layer with thickness H_s has top and bottom drainages, then $d = H_s / 2$. Many charts and equations are available for using the value of T_v to find U. For ramp loading, Terzaghi's correction method can be applied for finding the corrected U. The c_v used in the expression for T_v is related to hydraulic conductivity k and the coefficient of volume compressibility m_v by $c_v = k/(m_v \gamma_w)$. The value of m_v is not a constant. For each stress increment $\Delta\sigma_v^{'}$, the value of m_v can be calculated from strain increment $\Delta\varepsilon_v$ using $m_v = \Delta\varepsilon_v / \Delta\sigma_v^{'}$. For example, if the load increment is from Point 1 to Point 4, the stress increment is $\Delta\sigma_v^{'} = \sigma_{v4}^{'} - \sigma_{v1}^{'}$ and the strain increment $\Delta\varepsilon_v = [C_r/(1+e_0)]\log(\sigma_p^{'}/\sigma_{v1}^{'}) + [C_c/(1+e_0)]\log(\sigma_{v4}^{'}/\sigma_p^{'})$. In this simple method, m_v is back-calculated using $\Delta\varepsilon_v$ and $\Delta\sigma_v^{'}$ in order to obtain U.

Both $S_{creep,f}$ and $S_{creep,d}$ are calculated as follows for different final stress-strain points.

(i) If the final stress level is in the NC range (for example Point 4 in Figure 9), the final creep settlement is:

$$S_{creep,f} = \frac{C_\alpha}{1+e_0}\log(\frac{t}{t_o}) \times H_s \quad for \;\; t \ge t_o = 1 \text{ day} \tag{3}$$

where C_α is the conventional "coefficient of secondary compression" defined as $C_\alpha = -\Delta e / \Delta \log \sigma_v^{'}$ from an oedometer test on a soil specimen in an NC state. The time *t* is the duration of the applied load of interest, in which the corresponding total settlement is to be calculated. Note that t_o in the equation is soil-related parameter and has the value of one day because the compression relation in Figure 9 has a one-day duration for each load increment. The delayed creep settlement is:

$$S_{creep,d} = \frac{C_\alpha}{1+e_0}\log(\frac{t}{t_{EOP,field}}) \times H_s \quad for \;\; t \ge t_{EOP,field} \tag{4}$$

(ii) If the final loading stress level is in an OC range (for example, Points 2, 5, 6), the final creep settlement is:

$$S_{creep,f} = \frac{C_\alpha}{1+e_0}\log(\frac{t+t_{eOC}}{t_o+t_{eOC}}) \times H_s \quad for \;\; t \ge t_o = 1 \text{ day} \tag{5}$$

where t_{eOC} is the "equivalent time" for the final point in an OC state. The t_{eOC} is calculated from:

$$t_{eOC} = t_o \times 10^{\left[(\varepsilon_{OC}-\varepsilon_p)\frac{V}{C_\alpha}\right]} (\frac{\sigma_{OC}^{'}}{\sigma_p^{'}})^{-\frac{C_c}{C_\alpha}} - t_o \tag{6}$$

where $V = (1+e_0)$ is specific volume. For example, for Point 2 with stress and strain point in Figure 9 $(\sigma_{v2}^{'}, \varepsilon_{v2})$, the time $t_{eOC} = t_{e2}$ can be calculated using the above equation by letting $\varepsilon_{OC} = \varepsilon_{v2}, \sigma_{OC}^{'} = \sigma_{v2}^{'}$, that is, $t_{e2} = t_o \times 10^{\left[(\varepsilon_{v2}-\varepsilon_p)\frac{V}{C_\alpha}\right]} (\frac{\sigma_{v2}^{'}}{\sigma_p^{'}})^{-\frac{C_c}{C_\alpha}} - t_o$. If the NC line in Figure 9 is extended to Point $2^{'}$ and above, Point $2^{'}$ has the same stress $\sigma_{v2}^{'}$. The physical meaning of $t_{eOC} = t_{e2}$ is that the time for creep compression from Point $2^{'}$ to Point 2 is equal to t_{e2}. For Point 5 $(\sigma_{v5}^{'}, \varepsilon_{v5})$, the time $t_{eOC} = t_{e5}$ can be calculated by letting $\varepsilon_{OC} = \varepsilon_{v5}, \sigma_{OC}^{'} = \sigma_{v5}^{'}$; for Point 6 $(\sigma_{v6}^{'}, \varepsilon_{v6})$, $t_{eOC} = t_{e6}$ can be calculated letting $\varepsilon_{OC} = \varepsilon_{v6}, \sigma_{OC}^{'} = \sigma_{v6}^{'}$. It should be noted that the same value of C_α from NC state can be used to calculate the creep settlement of the same soil layer in the OC state. In fact, the creep settlement of the same soil layer in OC state is smaller than that in an NC state. This smaller creep settlement is considered by t_{eOC} in the above equation for $S_{creep,f}$. The $S_{creep,d}$ for the final point at an OC state (for example Points 2, 5, 6) is calculated using:

$$S_{creep,d} = \frac{C_\alpha}{1+e_0}\log\left(\frac{t+t_{eOC}}{t_{EOP,field}+t_{eOC}}\right)\times H_s \qquad for \quad t \geq t_{EOP,field} \tag{7}$$

where t_{eOC} is calculated in the same way as that explained before.

In summary, all parameters used in this simple method are listed in the table below.

Table 2: Basic parameters used in the simple method

C_r	C_c	$\sigma_p^{'}$ (kPa)	C_α	$t_o = 1$ day	e_0	$\alpha = 0.8$	$\beta = 0.3$	k (m/day)

It is helpful to note that ε_p is calculated using $\sigma_p^{'}$ and C_r. The m_v is back-calculated using $\Delta\varepsilon_v$ and $\Delta\sigma_v^{'}$ using C_r and C_c; and $c_v = k/(m_v\gamma_w)$ is calculated using k and m_v. The U in the equation of this simple method can be obtained using existing charts and equations.

Generally speaking, the equation of the simple method is used for a 1D straining condition simulated in a oedometer test. If vertical drains are installed in soils with uniform spacing, the consolidation for each equivalent cylindrical cell is in both vertical and radial directions. However, the vertical compressions for the soil layers with such vertical drains can be approximated by 1D straining. In cases of true 2D and 3D cases, such as a rectangular or strip foundation, the settlement calculated using the simple method is still useful, but shall be multiplied by a settlement correction coefficient. If the effective stresses in a soil layer are not uniform, for example, the vertical effective stress increasing with depth, this soil layer should be divided into a number of sub-layers for calculating S_f, $S_{creep,f}$, and $S_{creep,d}$. Similarly, if there are multiple soil layers with non-uniform effective stresses and soil parameters, these layers should be divided into sub-layers (Feng et al. 2020; Yin and Zhu 2020; Yin et al. 2022). A general simple method has been developed based on the simplified Hypothesis B method in Eq.(1) to the cases of multiple layers with or without vertical drains under complicated loading conditions (Yin et al. 2022) with verifications and applications.

7 POST-CONSTRUCTION SETTLEMENT CONTROL

Post-construction settlements of dredged Hong Kong Marine Deposits (HKMD) can be calculated or predicted using the simplified Hypothesis B method (or the newly extended general simple method)) or fully coupled consolidation analysis with a suitable Elastic Visco-Plastic (EVP) model. The control of the post-construction settlement can be achieved in two ways.

(i) Make the dredged HKMD over-consolidated using PVDs with vacuum preloading with additional water/fill surcharge:

As shown in Figure 9, assuming the initial stress-strain point in a soil layer is at Point 1. Under the action of additional design loading pressure, the state point will move from Point 1 to Point 5'. Since Point 5' is on NC line, the creep settlement will be large. The post-construction settlement will be large since the creep settlement contributes significantly, provided that the long-term settlement is of interest. However, if we can use vacuum preloading with additional water/fill surcharge, we can make the HKMD over-consolidated. For example, the state point will move from Point 1 to Point 4, then unload to Point 5 under the same design loading pressure. Point 5 is on OC line, so that the creep settlement is much smaller, resulting much smaller post-construction settlement. The simplified Hypothesis B method can calculate such creep settlements/post-construction settlements on OC line.

(ii) Improvement of the dredged HKMD by deep cementing mixing (DCM) technique:

Generally, DCM can reduce the viscosity, increase the stiffness and shear strength of the HKMD so that the post-construction settlement can be reduced (Yin and Lai 1998; Yin and Fang 2006; Ho et al. 2021). In practice, the DCM technique is implemented by forming columns, clusters, walls, blocks, etc. (Kitazume and Terashi 2013). For example, DCM columns exhibit good efficiency in controlling settlements and transferring load from surrounding soil to DCM columns. The load transfer can induce an unloading process on surrounding soil, which makes the soil into an overconsolidated state with a smaller creep strain rate (Wu et al. 2020).

8 CONCLUSIONS

Systematic research works are ongoing in PolyU from element tests and physical model tests to theoretical modelling and engineering applications, on the development of a sustainable reclamation method using local dredged marine deposits. The works will contribute to research development, the design and construction of marine reclamations, and make a positive impact on Hong Kong society. The main conclusions can be drawn as follows:

(a) The marine reclamation method using local dredged marine deposits has been approved as a cost-saving and time-reduction effective method in Hong Kong and other coastal cities, with more test and field evidences coming up on the effectiveness of this method using dredged Hong Kong Marine Deposits (HKMD).

(b) A new soft soil improvement method combining horizontal and vertical drains with vacuum and/or surcharge preloading is proposed to strengthen the dredged HKMD slurry for marine reclamation works.

(c) Two types of physical model tests are ongoing in PolyU's laboratory in order to simulate the whole process of implementing the new soft soil improvement method. Both of the tests well proved that the new improvement method is capable of decreasing water content and increasing soil strength effectively.

(d) Stabilizing HKMD slurry using alkali-activated industrial waste, like ISSA and/or GGBS, has a great potential for forming the crust layer on the top of vacuum preloading-treated slurry in an efficient and sustainable way.

(e) A new simplified Hypothesis B method is proposed. This method has been verified to be accurate and easy to use by engineers. This method can be used to predict the settlement of HKMD or other soft soils in layers and installed with/without drains subjected to staged loading unloading/reloading and even vacuum loading.

(f) The methodology of controlling the post-construction settlement by making the HKMD overconsolidated through vacuum preloading with additional water/fill surcharge or deep cement mixing method is also presented and discussed.

ACKNOWLEDGEMENTS

The work in this paper is supported by a Research Impact Fund (RIF) project (R5037-18), and three General Research Fund (GRF) projects (PolyU 152209/17E; PolyU 152179/18E; PolyU 152130/19E; PolyU 152100/20E) from Research Grants Council (RGC) of Hong Kong Special Administrative Region Government of China. The authors also acknowledge the financial supports from Research Institute for Sustainable Urban Development and Research Institute of Land and Space of The Hong Kong Polytechnic University and four grants (BBAG, ZDBS, ZVNC, CD82) from The Hong Kong Polytechnic University.

REFERENCES

Artidteang, S., Bergado, D.T., Saowapakpiboon, J., Teerachaikulpanich, N. & Kumar, A. 2011. Enhancement of efficiency of prefabricated vertical drains using surcharge, vacuum and heat preloading. *Geosynthetics International*, 18(1): 35-47.

Carrillo, N. 1942. Simple two and three dimensional case in the theory of consolidation of soils. *Journal of Mathematics and Physics*, 21(1-4): 1-5.

Chai, J.C., Carter, J.P. & Liu, M.D. 2012. Vacuum consolidation and deformation analyses–case studies in Japan. Indraratna, Rujikiatkamjorn and Vinod (ed.), *Proceedings of the International Conference. On Ground Improvement and Ground Control*, *University of Wollongong*, *Australia*, 30 Oct -2 Nov 2012.

Chu, J., Yan, S.W. & Yang, H. 2000. Soil improvement by vacuum preloading method for an oil storage station. *Géotechnique*, 50(6): 625-632.

Feng, W.Q., Yin, J.H., Chen, W.B., Tan, D.Y. & Wu, P.C. 2020. A new simplified method for calculating consolidation settlement of multi-layer soft soils with creep under multi-stage ramp loading. *Engineering Geology*, 264: 105322.

Ho, T.O., Chen, W.B., Yin, J.H., Wu, P.C. & Tsang, D.C. 2021. Stress-Strain behaviour of Cement-Stabilized Hong Kong marine deposits. *Construction and Building Materials*, 274: 122103.

Indraratna, B., Bamunawita, C. & Khabbaz, H. 2004. Numerical modelling of vacuum preloading & field applications. *Canadian Geotechnical Journal*, 41: 1098-1110.

Kitazume, M. & Terashi, M. 2013. *The deep mixing method*. CRC press.

Kwong, A.K.L., Han, X.F., Tham, L.G., Lee, P.K.K. & Zhao, W.B. 2008. A Field Test Study on under Water Vacuum Preloading Method. *Proceedings of the 6th International Conference on Case histories in Geotechnical Engineering and Symposium*, *Arlington*, *VA*, 14 Aug. 2008.

Walker, R. & Indraratna, B. 2009. Consolidation analysis of a stratified soil with vertical and horizontal drainage using the spectral method. *Géotechnique*, 59: 657-663.

Wang, J., Cai, Y., Ma, J., Chu, J., Fu, H., Wang, P. & Jin, Y. 2016. Improved vacuum preloading method for consolidation of dredged clay-slurry fill. *Journal of Geotechnical and Geoenvironmental Engineering*, 142(11): 06016012.

Wu, P.C., Feng, W.Q. & Yin, J.H. 2020. Numerical study of creep effects on settlements and load transfer mechanisms of soft soil improved by deep cement mixed soil columns under embankment load. *Geotextiles and Geomembranes*, 48(3): 331-348.

Yan, S.W. & Chu, J. 2005. Soil improvement for a storage yard using the combined vacuum and fill preloading method. *Canadian Geotechnical Journal*, 42(4): 1094-1104.

Yin, J.H., Chen, Z.J. & Feng, W.Q. 2022. A general simple method for calculating consolidation settlements of layered clayey soils with vertical drains under staged loadings. *Acta Geotechnica*, 1-28.

Yin, J.H. & Fang, Z. 2006. Physical modelling of consolidation behaviour of a composite foundation consisting of a cement-mixed soil column and untreated soft marine clay. *Géotechnique*, 56(1): 63-68.

Yin, J.H. & Feng, W.Q. 2017. A new simplified method and its verification for calculation of consolidation settlement of a clayey soil with creep. *Canadian Geotechnical Journal*, 54(3): 333-347.

Yin, J.H. & Graham, J. 1989. Viscous-elastic-plastic modelling of one-dimensional time-dependent behaviour of clays. *Canadian Geotechnical Journal*, 26(2): 199-209.

Yin, J. H. & Graham, J. 1994. Equivalent times and one-dimensional elastic viscoplastic modelling of time-dependent stress-strain behaviour of clays. *Canadian Geotechnical Journal*, 31(1): 42-52.

Yin, J.H. & Graham, J. 1996. Elastic visco-plastic modelling of one-dimensional consolidation. *Géotechnique*, 46(3): 515-527.

Yin, J.H. & Graham, J. 1999. Elastic viscoplastic modelling of the time-dependent stress-strain behaviour of soils. *Canadian Geotechnical Journal*, 36(4): 736-745.

Yin, J.H. & Lai, C.K. 1998. Strength and stiffness of Hong Kong marine deposits mixed with cement. *Geotechnical Engineering*, 29(1): 29-44.

Yin, J.H. & Zhu, G.F. 2020. ***Consolidation Analysis of Soils***. CRC Press.

Zhu, G.F., Yin, J.H. & Graham, J. 2001. Consolidation modelling of soils under the test embankment at Chek Lap Kok International Airport in Hong Kong using a simplified finite element method. *Canadian Geotechnical Journal*, 38(2): 349-363.

Advanced Design and Construction of Marine Cut & Cover ELS Tunnel Cofferdam

Raymond W M Cheung, Sam H S Liu
Gammon Construction Limited, Hong Kong, China

Gavin S H Toh, Steven Jenkins, M K Chong, Michael Chak
Lambeth Associates Limited, Hong Kong, China

ABSTRACT

The most challenging aspect of the CKR-KTW Contract is the construction of maximum 35m deep Underwater Tunnel (UWT) submerged in Kowloon Bay which is a typhoon shelter with marine constraints from several stakeholders such as Hong Kong China Gas requiring 60m wide navigation channel for refueling tankers, Kowloon City Ferry Pier (AMO Grade 2 Historic Structure) operations for public ferry service and the marine traffic impact to Kowloon Bay. To overcome the substantial adverse impact to the environment and marine traffic of Kowloon Bay area from the conforming scheme of full temporary reclamation, an optimized scheme was employed for the marine cut & cover ELS cofferdam using only partial temporary reclamation. The use of this advanced design and construction method not only provided robust structural design with water-tight cofferdam, it also resulted in substantially less cost, construction risks / time and reduced disturbance to marine environment and traffic at Kowloon Bay due to substantially less temporary reclamation required.

1 INTRODUCTION

The CKR-KTW Contract no. HY/2014/07 is located at Kai Tak West and comprised of 125m long depressed road, 200m long underpass, 160m long cut & cover tunnel and a 370m long submerged tunnel under KWB including a separate 360m long underground ventilation adit connecting to the CKR-BEM contract. The most challenging aspect of the CKR-KTW Contract is the construction of the 370m long Underwater Tunnel (UWT) submerged in Kowloon Bay which is a typhoon shelter with marine constraints from several stakeholders such as Hong Kong China Gas requiring 60m wide navigation channel for refueling tankers, Kowloon City Ferry Pier (AMO Grade 2 Historic Structure) operations for public ferry service and the marine traffic impact to KWB as shown in Plate 1 below.

Plate 1: Marine Cut & Cover ELS at KTW

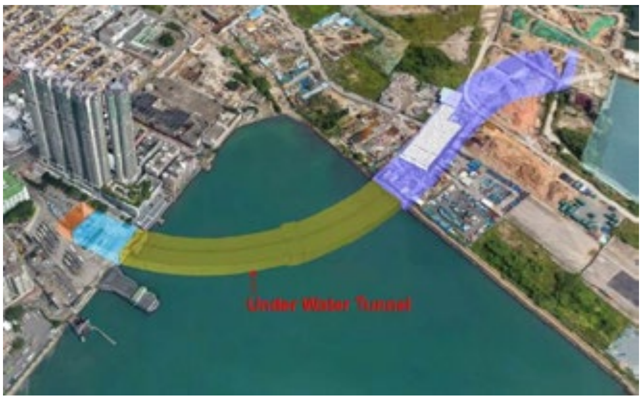

In the conforming scheme for construction of the UWT, substantial temporary reclamation is proposed over the entire 35,511 m^2 footprint of the UWT. This was completed in 2 stages named UWT1 and UWT2 in order to maintain the 60m marine navigation channel and function as a large marine working platform for installation of diaphragm wall cofferdam and subsequent staged Excavation and Lateral Support (ELS) and tunnel construction works. The two stages of cofferdam for 60m wide navigation channel shown in Figure 1 below:

Figure 1: Provision of 60m wide Navigation Channel within KWB

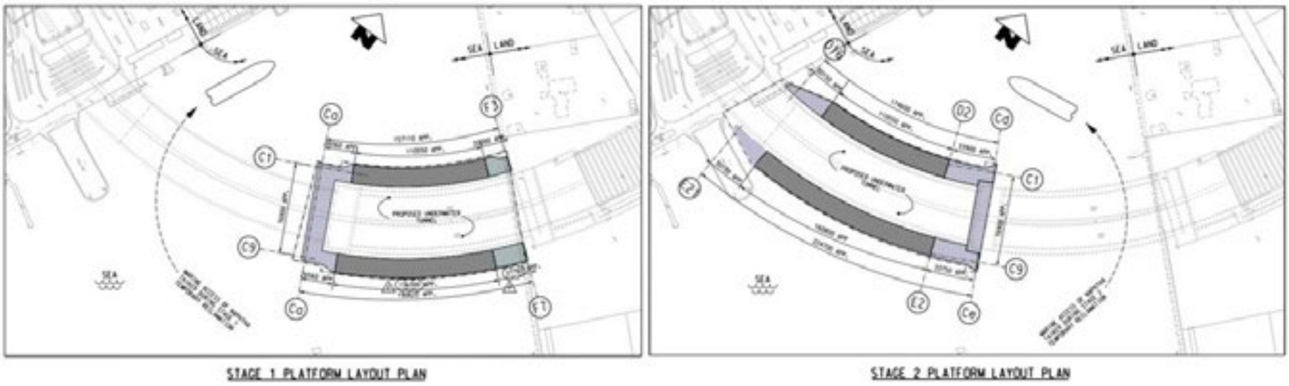

Reclamation on marine deposit will result in on-going settlement and require to accelerate consolidation by surcharging to ensure a safe working platform. To overcome the expense and time consuming resources required for the temporary reclamation works and the substantial adverse impact to the environment and marine traffic of KWB area from the conforming scheme, an advanced design and construction method was proposed for the marine cut & cover ELS cofferdam with by using a reduced temporary reclamation method. A reduced temporary reclamation scheme was proposed for the tunnel construction works comprised of a double wall tied system of 16m width reclamation area built up by FSPVL sheet pile on the seawall side and interlocking 813 Dia. Clutch Pipe Pile (CPP) wall on the tunnel excavation side. The design of the FSPVL outer wall functioned as the seawall while the CPP inner wall served as the ELS cofferdam wall. The double wall system was tied together at the top by waler / wall tie system at 6m c/c spacing prior to backfilling of the temporary reclamation works. The typical cross section of UWT is shown in Figure 2 below.

Figure 2: Typical Cross Section of UWT Stage 1 ELS Arrangement

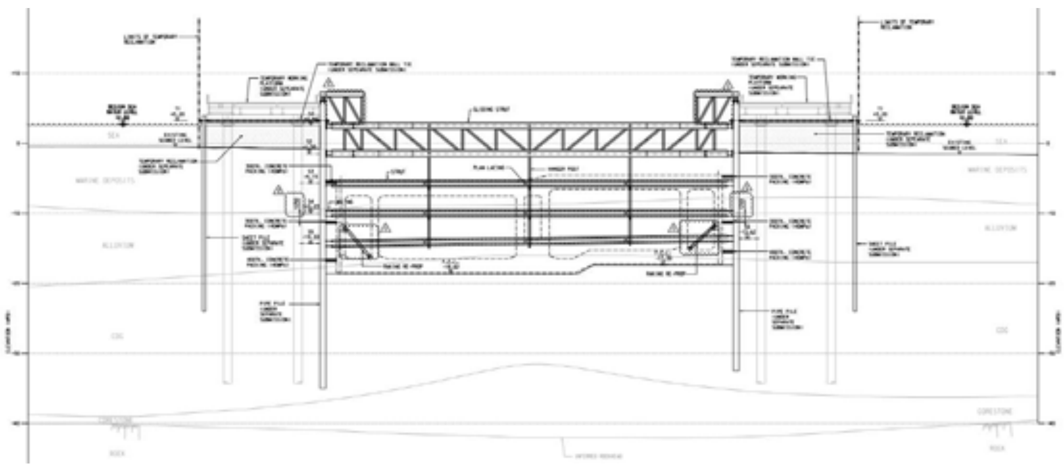

This overall arrangement reduced the temporary reclamation impact by 62.9% in UWT1 and 52% in UWT2 compared to the conforming scheme. In order to carry out the piling works before the temporary reclamation is completed, a marine working platform all around each UWT1 / UWT2 cofferdam was constructed. These platforms were supported by 2 rows of 1.2m diameter staging piles that are vibrated by crane barges until the pile toe is founded firmly on hard Completely Decomposed Granite (CDG). The marine platform allowed for several work fronts of CPP piling rigs for inner cofferdam wall, installation of the innovative skidding system for S1 / S2 mega trusses with hanging king posts, telescopic excavators and crawler cranes for the installation of the modular ELS system and tunnel construction works. The temporary reclamation between the CPP and Sheet Pile walls were set close to high tide for two purposes. First was to provide a soil medium that could allow remedial grouting outside the CPP wall in the event of localized leaking. The second was to provide significant mass to mitigate berthing marine barges or accidental impact. The tie between outer and inner walls was envisaged as a fuse, acting only in tension but not transferring direct compression loads from berthing vessels to the ELS struts. Another benefit of the steel working platform was founded on piles was that the reclamation backfill would not be subjected to heavy construction surcharge loading which helped reduced lateral loading to the ELS cofferdam walls and shoring system. The use of this advanced design and construction method resulted in substantially less cost, construction risks / time and reduced disturbance to marine environment and traffic at KWB.

2 ADVANCED DESIGN AND CONSTRUCTION OF MARINE CUT & COVER ELS TUNNEL COFFERDAM

2.1 Key Constraint

The reduced temporary reclamation scheme along with the temporary steel working platform above allowed the CPP cofferdam wall to be installed along the platform deck and eliminated the need to form full temporary reclamation from the conforming scheme where it was used as a temporary earth working platform. This greatly reduced the material required to complete excavation of the cut and cover tunnel meaning reduced transporting and disposal of fill material. By removing the temporary reclamation within the excavation area of the two inner CPP walls, a reduction in the temporary reclamation backfilling volume of 62.9% in UWT Stage 1 and 52% in UWT Stage 2 could be achieved. The construction sequence employed the use of skidding mega trusses for installation of strutting layers S1 and S2 with hanging king post which eliminates the necessity of piling works of lateral shoring vertical mid span supports. The skidding mega truss struts also allowed installation without dewatering within the cofferdam. Once the skidding mega trusses are installed, the dewatering works commence and the remaining modular struts are installed by traditional staged excavation, mucking out and bolt and nut fixing of modular struts to the final excavation level. The reinforced concrete tunnel box is cast from the bottom up within the CPP walls with staged backfilling and strut removal up to the existing seabed level. The Contract requirement for removal of minimum 2m of the temporary cofferdam wall below seabed level is another benefit of the CPP wall compared to the diaphragm wall of the conforming scheme. A combination of proprietary Water Cutting Jet (WCJ) machine and traditional Divers was employed, the WCJ is installed inside each CPP and remotely rotates and cuts the CPP walls while divers with plasma torches along excavated side of CPP wall cut the clutches and remaining CPP not cut by WCJ. The use of the above design and construction method allowed significant mitigation of the key constraints and benefited by reducing the working time and impact to the live marine traffic at existing Kowloon Bay area, the marine traffic includes Ferry operations in Kowloon City Ferry Pier, vessel traffic in To Kwa Wan Typhoon Shelter. The mitigation measures to key constraint is outline in Table 1.

Table 1: Key Constraint and Mitigation Measures for Marine Cofferdam

Key Constraint	Proposed Mitigation Measures
Working in live marine traffic conditions of busy Kowloon Bay	• Reduce marine construction traffic by reducing extent of temporary reclamation. • Use crawler crane on temporary steel deck for excavation and tunnel construction; reduces requirement for derrick barges and improves access. • Implement Marine Traffic Management Plan and coordinate through the Marine Traffic Working Group. • Maintain 60m-wide navigation channel for each ferry service. • Dedicated staff for coordination of marine craft movements and coordination with Marine Department (MD) and Vessel Traffic Centre (VTC).
Impact on marine traffic	• A dedicated team will be responsible for coordination with Kowloon City Ferry, Hong Kong China Gas and the MD. • Light buoys to clearly identify works area. • Maintain a minimum 60m-wide navigation channel during construction as per "Final Updated Marine Traffic Impact Assessment Report" • Marine traffic deck to assist transportation of materials to ELS by land.
Vessel damage temporary reclamation	• Install outer piles wall with reclamation soil fill to re-distribute ship impact load. • Install light buoys to clearly identify works area.
Ferry operations and mooring	• Recommend, provide a pontoon system for the ferry operation and mooring of standby vessels. • Closely liaise with marine ferry operator, obtain ferry timetable, and plan our movements to maintain normal ferry services.
Maintain access to Hong Kong China Gas pier for Naphtha delivery	• Maintain marine access by using guard boats and light buoys to demarcate the navigation channel. • Liaise with HKCG on their requirements and obtain naphtha delivery schedule. Plan our marine movements to maintain smooth tanker route.

2.2 Site Set up

The general design of the UWT ELS cofferdam comprise of an inner and outer retaining wall backfilled with temporary reclamation all around the tunnel excavation area. A temporary steel working platform founded on steel tubular vibrated piles is installed within the temporary reclamation area. The double retaining walls are tied back at the top of the 16m width reclamation area with outer wall of interlocking FSPVL sheet pile retaining wall as the seawall side and inner interlocking 813mm Dia. Clutch Pipe Pile (CPP) retaining wall at the tunnel excavation side. The FSPVL outer wall is designed to function as a seawall while the CPP inner wall served as the ELS cofferdam wall, providing a watertight seal against water ingress and prevent any loss of reclamation material into surrounding waters. The overall view of the double wall cofferdam ELS of UWT Stage 1 and installation of marine working platforms and CPP piling works for UWT Stage 2 are shown in Plate 2 below.

Plate 2: General View of Marine Cut & Cover ELS UWT Stage 1 and UWT Stage 2 installing CPP wall

UWT Stage 1 UWT Stage 2

The temporary reclamation for both stages 1 and 2 was reduced by eliminating the temporary reclamation within the area of tunnel excavation footprint as shown in Figure 3 below.

Figure 3: Reduced temporary reclamation area

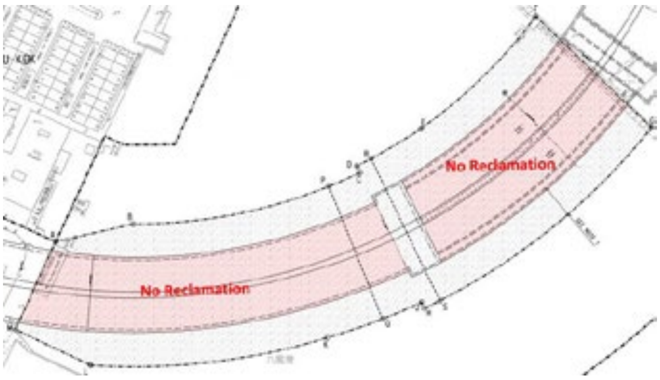

The reduced volume and percentage of reclamation works compared to the Conforming scheme is shown in Table 2 below:

Table 2: Temporary Reclamation for under water tunnel.

	Conforming Scheme	Gammon's Scheme	Reduction in Temporary Reclamation
Stage 1	16,832m^2	6,244m^2	62.9%
Stage 2	18,679m^2	8,973m^2	52.0%

An added advantage of this reduction of the total area of temporary reclamation is that the environmental carbon footprint is also substantially reduced for noise impact, air impact, visual impact, land and marine traffic impact to the residents of Ma Tau Kok as well as the massive soil stockpile management and disposal impacts. The proposed use of CPP cofferdam wall is able to be installed directly from the marine working platforms as compared to earth work platform required for the conventional diaphragm wall method of conforming scheme. The ability to quickly install CPP by erecting a marine working platform saves considerable time compared to backfilling the central portion of the cofferdam with temporary reclamation just to install the ELS vertical members and reduces the total reclamation fill requirement of the project by some 69%. If the need for additional fill material is required due to consolidation effect of the marine mud layer, the total reclamation fill project reduction may well be in excess of 75%. Reduced fill quantities translate into direct programme benefits to the project and eliminates over 300 barge journeys for material delivery (124 journeys for stage 1 and 190 journeys for stage 2). Reducing the number of barge journeys means less disruption to public marine traffic, less congestion in Kowloon Harbour, improved carbon footprint through reduced emissions (1,269 tonnes embodied carbon saving). The reduction of temporary reclamation fill greatly benefits the environment and reduces the overall volume of backfill material to be imported and later disposal.

2.3 Robustness of the Cofferdam against Marine Impact

The continuous CPP wall is known for its inherent water tightness due to the clutched system, as illustrated in Figure 4 below.

Figure 4: Clutch Pipe Pile Wall

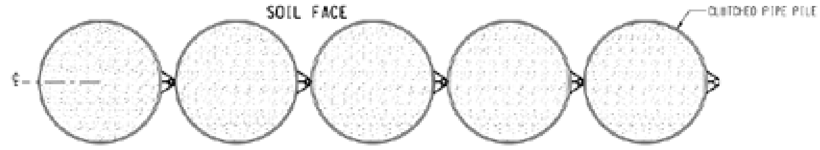

- The ELS is designed as top down staged excavation and lateral shoring method with bottom up for tunnel construction and backfilling / strut removal works with consideration for constraints of marine environment.
- Internal loads from accidental plant or impact loading on the ELS is considered at any point and in any direction. This is intended to cover situations such as accidental contact by excavation machinery and crane lifts where objects and equipment have routine movements within the excavation and in close proximity to ELS structural members.
- External dynamic loads due to berthing, mooring and accidental impact are included in the ELS wall and strut design. 3D finite element analysis has been used to quantify magnitude and distribution of accidental impact forces through the reclamation fill mass and residual loading passing through to the ELS wall and struts.
- Dynamic environmental loads from the marine environment in accordance with the Port Works Design Manual.
- The top two layers of struts in the marine section are of a robust modular mega truss design which are skidded into position. They are connected together to form a rectangular mega truss of 4m depth by 2.5m width with free span of 57.7m for UWT Stage 1 and 48.1m of UWT Stage 2. The depth to span ratio means these mega trusses can support 3 nos. of hanging king post running longitudinally across the cofferdam to provide vertical support and restraints for all the strut layers below.

The skidding mega trusses combine the top two strut layers S1 and S2 and simply supported at each end on skidding rails installed at top of CPP cofferdam wall. The mega truss depth and width were designed with beam deflection 75% less than the deflection limit of L/200 required by local code requirement. For the strut layers below S3 level, the compression loads induced during excavation required the use of lateral restraints provided by the 3 rows of hanging kingposts and longitudinal runner beams with plan bracing to control strut buckling and sway. The strut spacing was determined based on the clear width required for mucking out operations of the telescopic excavators and crawler crane grabs as well as provide windows for material delivery to construct the permanent works. The mega trusses hanging king post avoid requiring driven piles as king posts and thus provides for a wide clear working area for the reinforced concrete tunnel construction works and travelling formwork system. The UWT cofferdams are located in marine area and material delivery or excavated material disposal will require the use of barges or marine vessels which will subject the double cofferdam wall system to berthing and mooring loads or accidental impact collision loads from other marine vessels. The marine impact traffic assessment report outlines the existing vessel fleet that typically operates in this area of the harbour. Together with the construction barges to be used as part of Kai Tak West

Contract PS requirements, a deterministic 2000T vessel was selected to carry out analysis. These berthing and collision loadings and the impact to the ELS system were considered in the ELS cofferdam wall design. The mass of the temporary reclamation fill and plasticity of the soil provide robust mass to absorb the impacts due to berthing loads and accidental ship impact. Since the deformation is largely absorbed by the soil mass of the temporary reclamation area, the CPP wall and its water tightness of its clutched system is not compromised from the event as shown in Figure 3 below.

Figure 3: Peak displacement analysis for accidental ship impact

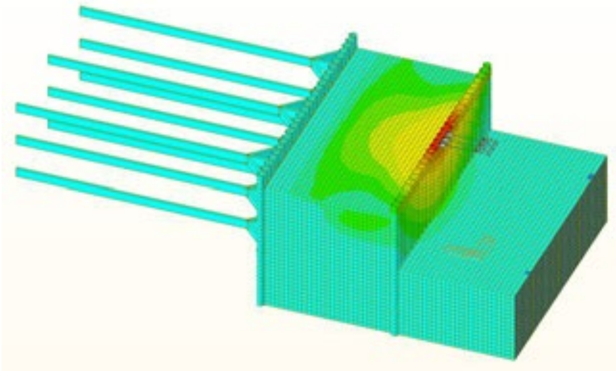

The method of deriving impact loading follows the Port Works Design Manual to evaluate the impact energy. A 3D soil structure interaction analysis is carried out to assess the displacements of the reclamation and derive the distribution and magnitude of loads that develop through the fill and transferred onto the ELS struts. Despite plasticity in the soil mass and load spread from the patch of impact, the analysis concludes that 30% of the load may be passed into each of the top three layers of ELS struts of the excavation and that this is an important provision to include in their design for overall robustness. In addition, The ELS ties within the reclamation is designed as one way ties and only work for tension loads avoiding direct compression loads transferring through the steel ties to the CPP wall in the event of accidental ship impact. The steel working platform deck and CPP cofferdam wall was designed with free tolerance (no-touch) for vessel berthing and typical environmental background movements. The ship impact collision load as maximum displacement or deformation were modelled in computer programme OASYS GSA and the induced force was checked against the moment bending and buckling capacity of the CPP wall as shown in Figure 4 below:

Figure 4: OASYS GSA computer modelling of accidental collision to temporary marine working platform

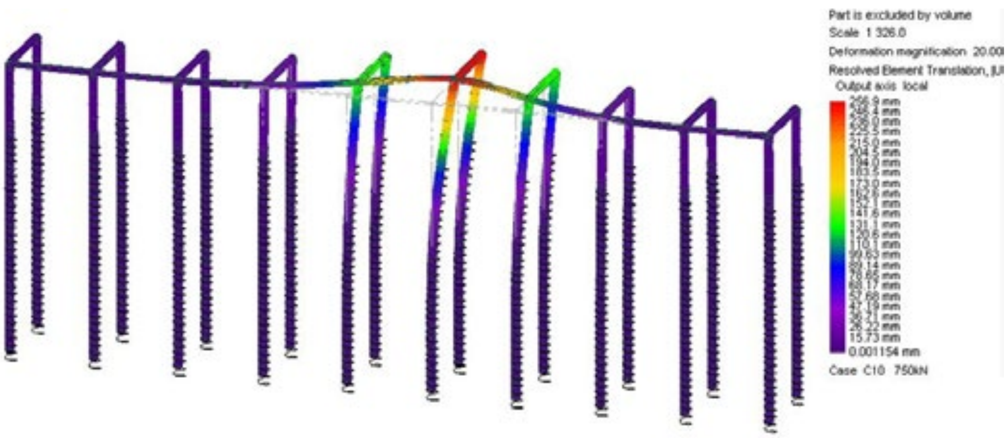

Together, both the ELS cofferdam wall and steel marine working platform provides significant robustness in the design to safely allow berthing and mitigate catastrophic events such as ship collision into the design.

2.4 Temporary Steel Working Platform

In order to construct ELS walls in the reclamation and provide working space for the subsequent earthworks and tunnel construction, temporary steel working platform deck built up from 3 nos. of modular decks with widths of 4m, 6m, 6m by 11.5m lengths to form 1 bay were constructed around the outer edge of the tunnel box. The assembled marine platform will have an overall deck width of 15.4m, and is designed to carry all plant, materials and equipment needed for our operations as shown in Plate 3 below.

Plate 3: General View of UWT Stage 1 Temporary Marine Working Platform

The temporary working platform is wide enough to accommodate plant movements and maneuvering with 1 clear lane of 3m width for simultaneous access of delivery trucks. The crawler crane boom turning also remains clear of the designated barriers and separated personnel walkways as shown in Figure 5 below.

Figure 5: Modular marine platform arrangement

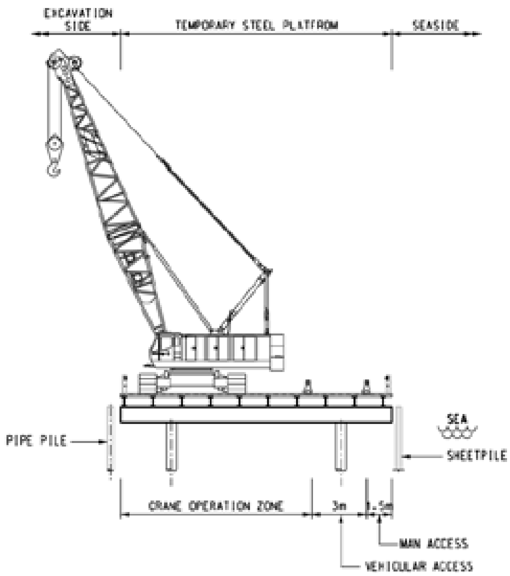

Construction of the temporary steel working platform will involve installation of the prefabricated standard size modules of 4m, 6m and 6m by 11.5m as mentioned above. Primary beams for the temporary steel working platform will be installed and span across the completed 1200 dia. pipe piles installed by vibro hammer. The pre-fabricated platform modules lifted on top will comprise of secondary beams and sections of sheet pile and pre-fixed edge protection, similar to what Gammon has done at Tuen Mun Chek Lap Kok Link. All of pre-fabricated platform modules have a standard sizes which are fabricated in Gammon wholly owned steel fabrication yard in the PRC. This engineering solution simplify onsite fixing and save more than 3,886 man-hours of labour. The platform geometry was set to maximize deck panel sizes to suit the backfilling and removal of reclamation fill while allowing the crawler crane to pass over the temporary reclamation works on the platform. The handling logistics and our selected crane sizes drove the geometric designand also reduce total marine traffic for delivery of materials and shorten the mooring durations in Kowloon Bay, minimizing the potential for impacting marine traffic and providing an overall safer working environment. Gammon have extensive experience working with the construction of temporary marine platforms and using them for successful delivery of major civil works projects. They include Shenzhen Western Corridor, Central Wanchai Bypass and Tuen Mun Chek Lap Kok Link projects, altogether totaling more than 30,000m2 of temporary working platforms installed in the last 15 years.

2.5 Clutched Pipe Pile (CPP) Wall

All piles for construction of temporary reclamation on this project will be made fully continuous using CPPs. CPP will be installed from the steel working platform. We will commence installation of the CPP after we have completed 40m of the temporary steel deck. The inner layer of CPP will be installed using Gammon's modified down-the-hole drilling equipment, enabling pre-boring of the CPP into rock with a minimum of ground disturbance during installation. Gammon was the pioneer Contractor in Hong Kong and continues to develop this technology for the excellent water-tightness the system provides. The CPP wall is able to provide a relatively stiff retaining wall for the compact diameter of 813mm due to the inherent geometric strength of circular sections along with the selected CPP wall thickness with thickness varies with depth and design requirement. Where additional rigidity is required for areas of large bending moments, the thickness of the CPP wall and bending capacity is locally increased. Together with water tightness of the fully clutched system, the CPP wall allows for a very cost effective, programme beneficial and constructible cofferdam wall at marine area of KWB. Another advantage of the CPP system is that during installation it can drill through hard obstructions compared to an older method where clutched pipes were vibrated in. At the outer wall, sheet piles were proposed and if any hard obstruction were encountered, they can be overcome locally by changing to pipe piles or pre-bored sheet piles. However, if the drilling encountered a steel anchor, a sunken ship or even dumped vehicles in the sea such as by historic British Army, the CPP drill bit would be unlikely to overcome such obstruction and design review would need to be carried out for the as-built CPP's with short toe levels in the ELS Cofferdam wall design. The CPP clutch system and splicing is shown in Plate 3 below.

Plate 3: Clutch Pipe Pile Wall

As the CPP wall is proposed on the tunnel excavation side and design of the FSPVL outer wall functioned as the seawall. The double wall system was tied together at the top by waler / wall tie system at 6m c/c spacing prior to backfilling will provide the dual purpose of acting as an impact protection fender and as a working surface for TAM grouting for additional sealing should it be required.

2.6 Modular Strut for ELS

The design of the lateral shoring system for the UWT Stage 1 and 2 cofferdams considered all the loadings mentioned above inputted PLAXIS computer model to determine the strut forces at each design section. The layout of the lateral strut shoring arrangement for UWT Stage 2 and UWT Stage 2 are shown in Figure 6 below.

Figure 6: UWT Stage 1 and 2 ELS Layout Plan

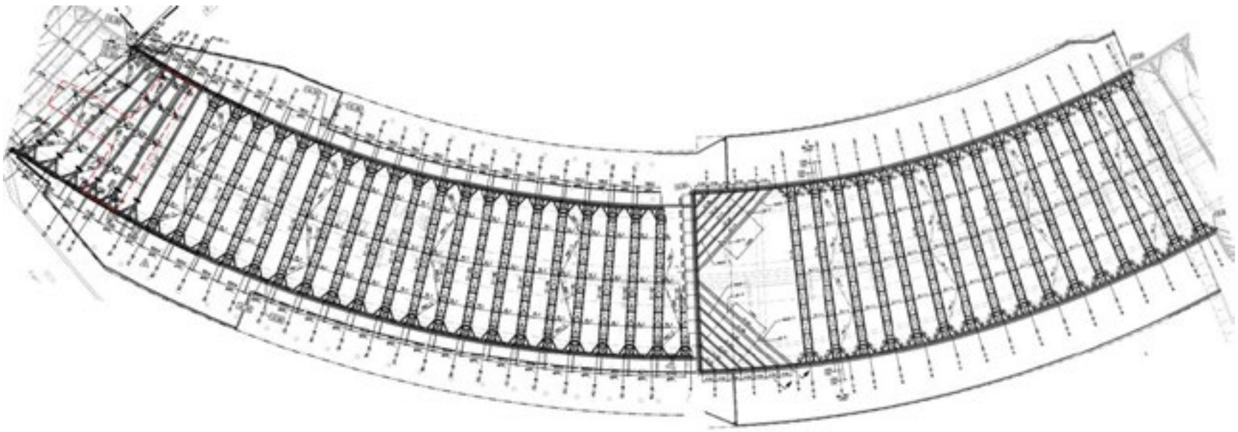

This was modelled along with the double tie back wall and marine working platforms directly in the PLAXIS computer simulation. Several design cross sectional slices were analyzed by the PLAXIS model and the strut forces were assessed to determine the range of standard sizes to be used for the modular strut fabrication. The typical PLAXIS model geometry of one section is shown in Figure 7 below.

Figure 7: PLAXIS modelling of ELS and Mega Truss Strut

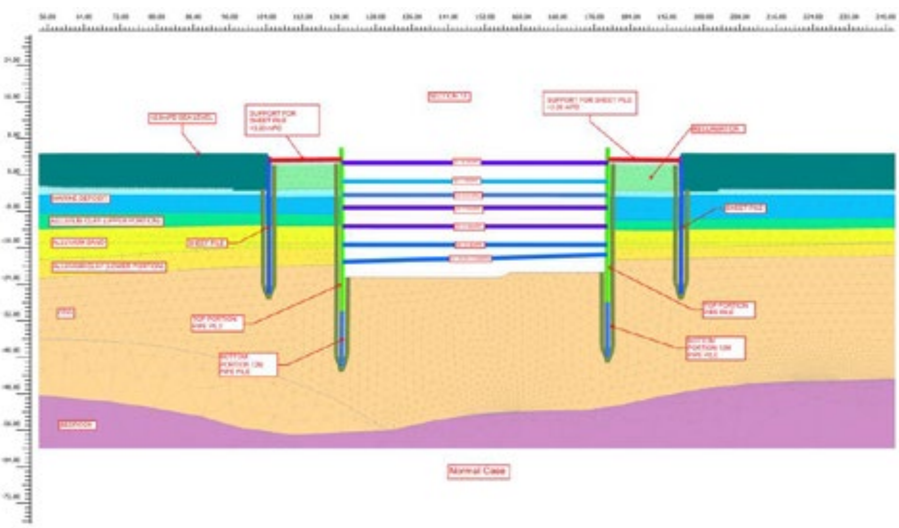

Since the CPP wall effectively functions as both a retaining wall and vertical support for the mega trusses above, the CPP wall was modelled as a retaining wall. The vertical load applied at the top was checked against the structural and geotechnical capacity of the CPP. Additionally, the predicted maximum wall deflection at the top after would need to be known to allow suitable tolerance for the skidding system upon the time for the removal of struts. The actual performance of the ELS UWT Stage 1 was in fact better than the design prediction with actual maximum deflection of the CPP cofferdam wall at 40% less than that predicted by the computer model which indicates that the ELS cofferdam is indeed very robust. The reason of better performance is due to the conservative estimation of stiffness contribute from both the mega trusses system and the adoption of double wall tie back scheme. The aerial view of UWT Stage 1 ELS works is shown in Plate 4 below.

Plate 4: Ariel view of UWT Stage 1 ELS works

Construction of the temporary steel struts and wailing will involve installation of standard size, pre-fabricated modular struts and traditional non-modular struts. The main struts are installed directly underneath each of the mega trusses spanning across the CPP cofferdam wall. Over 90% of all pre-fabricated steel strut and wailing modules will have a standard size of 914 series Twin UB and length of 12m, which are fabricated in Gammon's factory in the PRC. The modular standard size of strut and wailing in UWT Stage 1 have been design for re-used in UWT Stage 2. A typical span of each main strut is comprised of several straight main beams with preload module located slightly mid span and forks on each end connected to modular walers as shown in Figure 7 below.

Figure 7: UWT Stage 2 Modular Strut Layout Plan

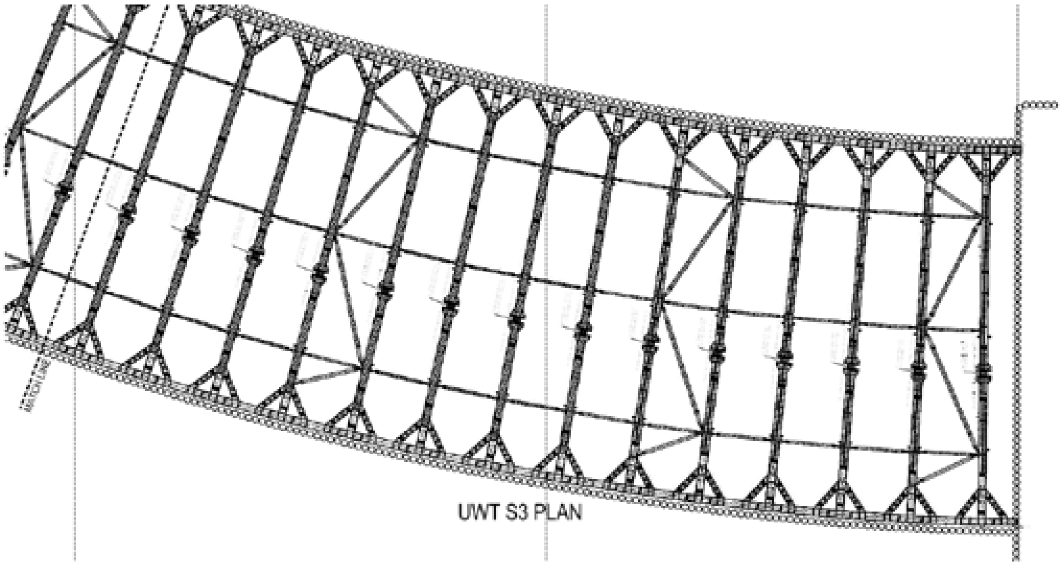

The modules are fixed by bolt and nut which saves substantial time if welding were used and reduces the safety risk of these hot works at height. The modular struts reduce the installation time and provide an overall safer working environment. The modular strut layouts were inputted into the 3D BIM model to ensure optimum fit of the fabricated modules and the reused strut shown in grey color in Figure 8 below.

Figure 8: 3D BIM model of UWT Stage 2 Reusable Modular Strut arrangement

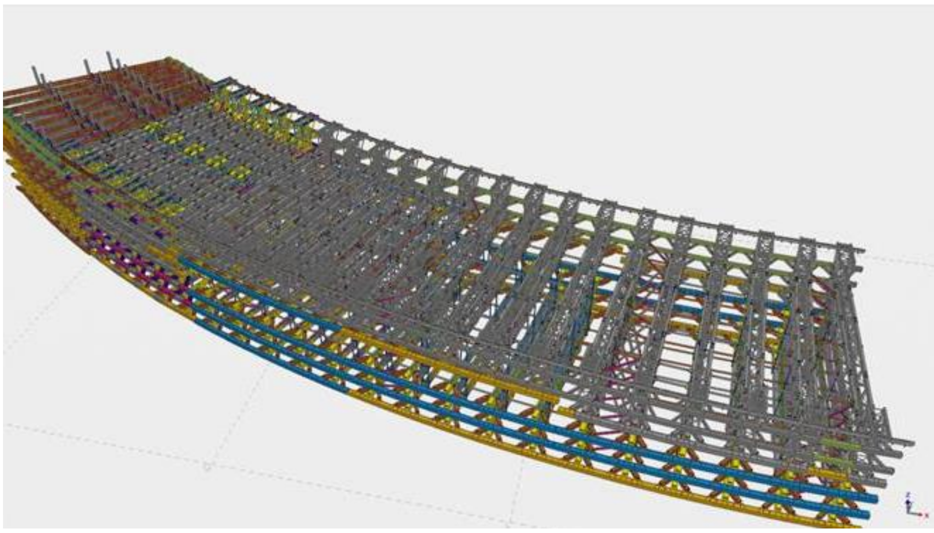

As the modular struts were to be used in a marine environment and designed to be reusable, corrosion due to the marine environment was a real concern. All reusable modular struts were painted with corrosion protection paint and prior to reuse of modular struts, they were inspected to ensure the sacrificial corrosion thickness did not exceed the designed capacity. Any struts with excess corrosion were checked, repaired, modified and repainted before reuse.

Figure 9: Modular Strut with corrosion check and awaiting for re-paint.

2.7 References

Clark et al. (2011)

3 CONCLUSIONS

The reduced reclamation scheme between the CPP and sheet pile double tied back wall system, the modular temporary steel working platform deck, the skidding modular mega truss strut system with hanging king posts and the ELS design comprised of reusable modular struts provides benefits to the Contractor, environment and project. The advanced design and construction of the ELS Cut and Cover cofferdam for the UWT submerged tunnel greatly reduces the material and time required to complete construction of the 370m length tunnel despite the constraints such as stakeholders, provision of navigation channel requiring works carried out in two stages and substantially less cost, construction risks / time and reduced disturbance to marine environment and traffic at Kowloon Bay from the substantially reduced temporary reclamation design.

ACKNOWLEDGEMENTS

Special gratitude and appreciation is expressed for all the contributions from the CKR Site Teams below:

Hong Kong Highways Department Major Works Division – LAM M.S. Roy (CE1/MW), CHAN M.K. (SE3/CKR), WONG Y.P. Arthur (E15/CKR), LEE K.S. Victor (PC1/CKR)

Arup - Mott MacDonald Joint Venture (AMMJV) – LO K.C. Patrick (CRE), WONG Y.K. Antony (SRE), LAU Jeffrey (SRE), NG M.Y. May (RE), KWOK H.Y. Kevin (RE)

Gammon Construction Limited – TAM K.F. (CM), LUI Y.F. Niki (SPM), LEE H.H. (SPM), FUNG C.S. Julian (PM)

REFERENCES

Clark & Askew, Thoren, 2011, Safety by Design – Clearance of buried sea wall at Marina Bay, Singapore, Underground Singapore

Developing Hong Kong's First Materials Testing Laboratory and Archives Centre in Caverns - Technical Challenges and Solutions

Ivan H H Chan
Geotechnical Engineering Office, Civil Engineering and Development Department, The Government of the HKSAR, Hong Kong, China

Y K Ho
Development Bureau, The Government of the HKSAR, Hong Kong, China

Carrie Cheung
Geotechnical Engineering Office, Civil Engineering and Development Department, The Government of the HKSAR, Hong Kong, China

ABSTRACT

In Hong Kong, cavern development is entering a new era, from a narrow range of uses in the past to the recent widespread applications in the territory (Ho et al. 2020). Rock caverns are now engineered to become a viable source of land supply for sustainable development of Hong Kong. With four decades of knowledge and experience accumulation, Hong Kong has proclaimed its readiness in taking on a new path following the launch of the award-winning Cavern Master Plan along with a suite of enabling measures to foster wider applications of rock caverns in Hong Kong. A number of cavern projects are in the pipeline, covering not only traditional "Not In My Back Yard" (NIMBY) uses but also some new types of facilities. Among all, the Geotechnical Engineering Office of the Civil Engineering and Development Department is now undertaking a joint cavern development project at Anderson Road Quarry Site, which involves two first-of-its-kind cavern facilities in Hong Kong — a materials testing laboratory and an archives centre.

This paper will introduce the background of the project and use it as an illustration to highlight various challenges encountered when housing facilities in caverns, such as operation requirements of the facilities, fire safety considerations, site constraints, and the need for preserving the future potential of Strategic Cavern Area concerned. This paper will also discuss some novel design approaches contemplated and other potential solutions to tackle these challenges.

1 INTRODUCTION

The Joint Cavern Development project at Anderson Road Quarry Site comprises two government facilities, namely the Public Works Central Laboratory (PWCL) of the Civil Engineering and Development Department (CEDD) and the Archives Centre (AC) of the Government Records Service (GRS). These facilities, given their nature and requirement for a stable environment, are particularly suitable to be housed in rock caverns.

The Public Works Laboratories of the CEDD comprise PWCL and five Public Works Regional Laboratories (PWRLs). The Public Works Laboratories, including the PWCL and five PWRLs, are accredited by Hong Kong Accreditation Service under the Hong Kong Laboratory Accreditation Scheme (HOKLAS) for testing and calibration services. The quality management system of Public Works Laboratories meets the requirements of international standard ISO/IEC 17025. Pursuant to the policy directive as set out in WBTC No. 14/2000, the Public Works Laboratories are to provide quality testing services in the capacity of an Employer laboratory and to ensure that reliable, efficient and effective construction materials testing is accessible to all public works projects.

The PWCL is currently accommodated in a four-storey purpose-built building at Cheung Yip Street, Kowloon Bay, with a site area of 3850 m^2. A picture of the existing PWCL building is shown in Figure 1. The total covered floor area of the building is 7088 m^2 with a usable area of 5782 m^2. The PWCL offers an extensive range of compliance and investigative testing services, covering soil and rock tests, concrete and cement tests, general materials and steel tests, chemical tests and calibration services. In the past few years, the Public Works Laboratories delivered about 600,000 tests/year on average on various construction materials. Apart from routine testing, the PWCL also provides expert testing services to forensic investigations and sets technical standards for construction material testing in Hong Kong (e.g. Geospec 3, CS1, CS2 and CS3). Furthermore, the PWCL undertakes technological development work relevant to construction materials and devises new testing techniques and standards to meet industry needs. The laboratory compartment is equipped with special ventilation provisions, dangerous goods stores and loading bays. Currently, there are about 120 staff working in the PWCL Building.

Figure 1 Existing PWCL Building at Kowloon Bay

It was stated in the 2013 Policy Address that the Government would take forward the initiative of rock cavern development as a viable source of long-term land supply. As the existing site occupied by the PWCL Building will be made available for land disposal in years to come, it has become the Government's target to relocate the PWCL and release the site in the future. Throughout the process, it is essential to maintain quality, efficient and effective construction material testing services for public works projects in Hong Kong.

The other government facility to be housed in Joint Cavern Development caverns is the GRS' AC. Records are valuable resources of the Government. They are evidence of decisions made, support for operational and regulatory requirements and are essential for an open and accountable government. GRS, established in 1989, is tasked to oversee the overall management of government records and ensure that government records are properly managed and those of archival value are selected for preservation and public access. At present, GRS is providing archival facilities for public records, i.e. records appraised as having historical value for long-term preservation. The Public Records Office of GRS is responsible for appraising and acquiring government records and material of enduring value and making them available for public inspection. A photo of the Public Records Building at Kwun Tong and one of its archival repositories are shown in Figure 2. The Public Records Office offers a rich heritage resource consisting of documents, photographs, movies, posters and other records tracing the governance and evolution of Hong Kong. These archival records are stored under tightly controlled climatic conditions in terms of temperature, relative humidity and light for protection against deterioration such that they could be preserved and retained permanently, and are available for public viewing. The current storage capacity of the Public Records Building at Kwun Tong is close to saturation. To increase the maximum capacity in meeting the expected storage demands of government archival materials in the future, there is an imminent operational need to expand the existing archival storage facilities by means of building a new AC in caverns.

Figure 2 Public Records Building at Kwun Tong and one of its archival repositories

2 INCENTIVES TO ADOPT CAVERN OPTION AND SELECTION OF THE SUITABLE SITE

Surface land is a scarce resource, particularly for those in the urban area. A parcel of land should always be planned for the most effective and beneficial land use taking into account socio-economic needs, demand-supply balance, engineering factors and various district and regional land development considerations vis-à-vis the nature of the planned facility.

Based on the findings of CEDD's study on "Long-term Strategy for Cavern Development" completed in 2018, PWCL and GRS' AC are two potential facilities highly suitable to be housed in caverns (Ho et al. 2020) with reasons below:-

(i) *Preservation of valuable surface land for other beneficial use*
Both facilities require the occupancy of a relatively large floor area with limited flexibility for vertical development due to operational needs (e.g. efficiency in testing material delivery in PWCL and inventory arrangement / retrieval logistics in AC, both of which are essential for providing quality service). A convenient centralised location is preferrable for the ease of access by facility users. However, any large surface land in urban area would be better utilised for other higher priority usages, such as residential developments. The cavern option allows surface land to be designated for other value-added developments.

(ii) *Stable environmental condition*
The stable environment in rock caverns is ideal for laboratory testing operation and storage of testing specimen (e.g. sheltered from shock and vibration, constant humidity, steady temperature, etc.). These conditions are also advantageous to the storage of archival holdings. In an ordinary surface building, a large amount of energy is required for indoor climatic control in order to satisfy the stringent preservation requirements of the archives repositories. The stable humidity and lower temperature in caverns are beneficial to operate the facilities in a higher energy efficient manner, hence is more environmentally friendly and will cost less in the long run.

(iii) *Isolation from the surface*
Some of the tests and calibration process as well as fragile items from the archival holdings are sensitive to vibration. Rock caverns offer a natural isolation which can effectively shield off / minimise the vibration caused by adjacent users.

(iv) *Flexibility for future extension*
Due to higher public expectation for enhancement in quality service of the Government with time, there is an increasing demand for preservation of heritage resources in archival repositories and for public inspection (for GRS' AC) and more space is required for advanced laboratory testing by automation and expansion of service (for PWCL). Surface buildings in an urban setting are usually surrounded by occupied buildings, infrastructures, utilities, etc. These physical constraints, together with the potential construction impacts as well as other planning and development restrictions, would normally increase the difficulty, hence the cost and time, for any further extension. Caverns, if under a proper initial planning, would allow a higher flexibility in layout design which facilitates future expansion.

After deciding on the cavern option, a site identification and selection exercise was carried out during the feasibility studies. Considering a basket of factors including operation and location requirements of the facility itself, site characteristics (e.g. planning conditions, accessibility, geology, hydrogeology, traffic, environmental aspects, etc.), project programme and cost for development, etc., Tai Sheung Tok overlooking Anderson Road Quarry Site Development was selected as the most cavern suitable location for relocating the PWCL and building the new AC. This site falls within the Strategic Cavern Area (SCVA) No. 28 of the Cavern Master Plan (CEDD 2017). The selected site at SCVA No. 28 and the preliminary footprint layout of the Joint Cavern Development project is shown in Figure 3.

The schematic design of the Joint Cavern Development project comprises four main caverns in 3 to 4 floor levels with portal structures of similar heights. The rendering of the outline scheme is shown in Figure 4 for illustrative purpose. Preliminarily, the size of the caverns would be 30 m (H) x 90 m (L) with span ranging from 30 m to 35 m. Offices and the necessary mechanical plant rooms are planned at the portal structure while the laboratory testing areas and archive repositories will be accommodated inside the main caverns.

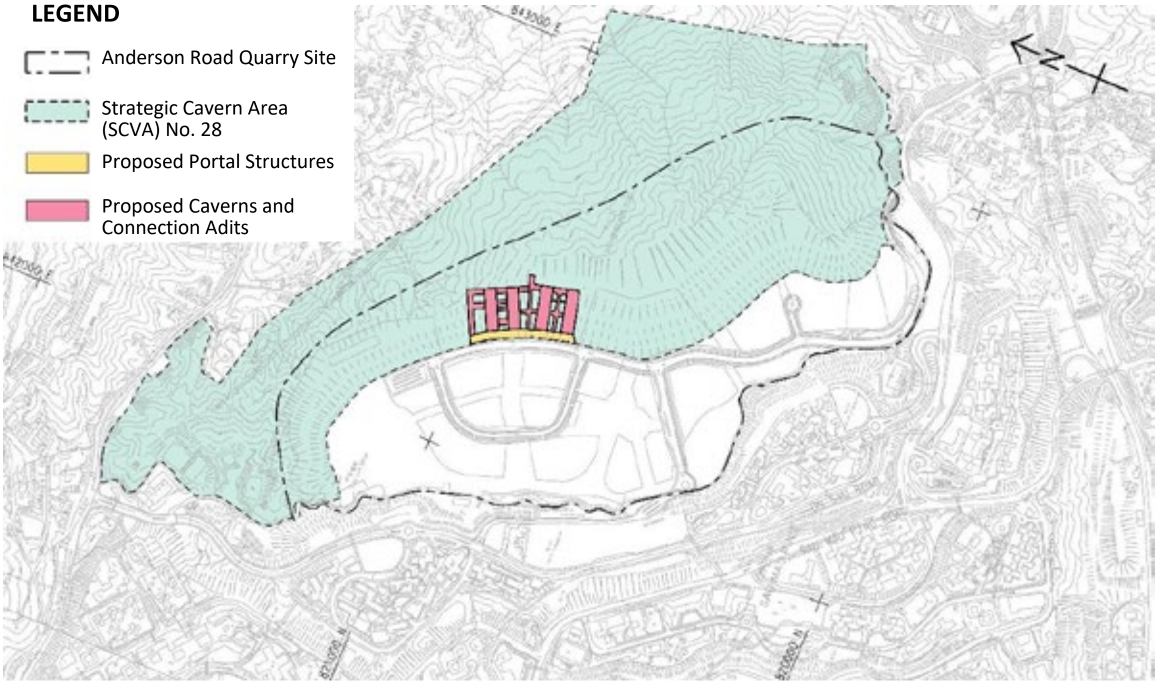

Figure 3 Location plan showing the selected site at SCVA No. 28 and the preliminary footprint layout of the Joint Cavern Development project

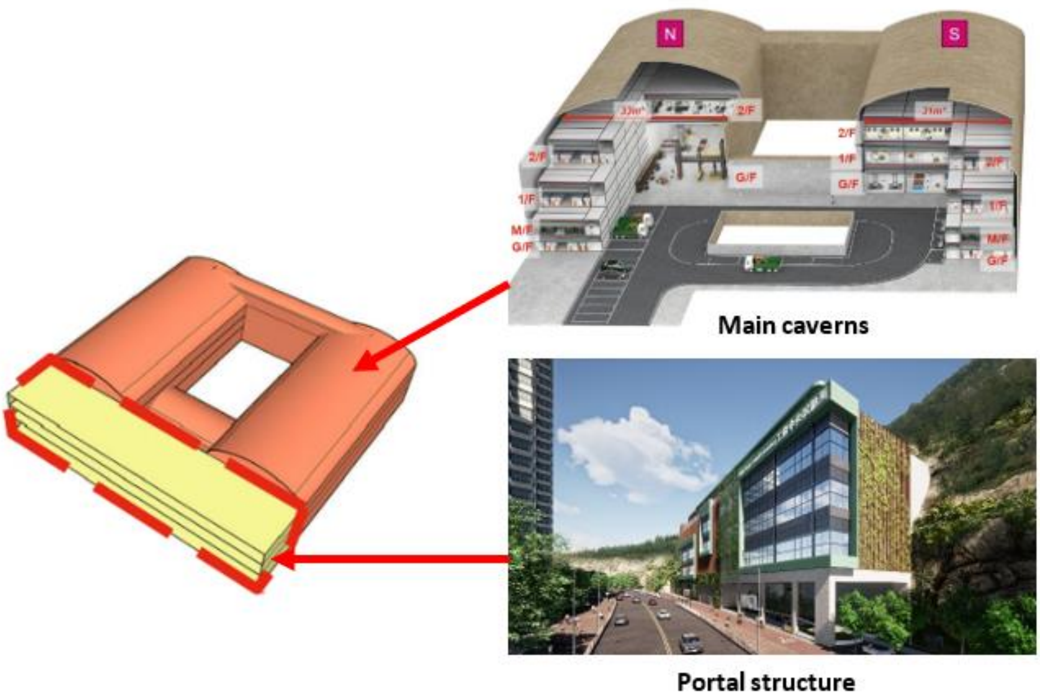

Figure 4 Indicative model of main caverns and portal structure

3 CHALLENGES OF CAVERN DEVELOPMENT

Since 1980's, the Government has successfully implemented a few cavern projects in Hong Kong, including the Stanley Sewage Treatment Works, Island West Transfer Station and Western Salt Water

Services Reservoirs. Although cavern development is not new in Hong Kong, caverns were mostly used to house limited types of facilities (mainly NIMBY) in the past. The issue of the Cavern Master Plan has provided more opportunities for extended land use in caverns. In the Joint Cavern Development project, the relocated PWCL will be the world's first cavern material testing laboratory of such scale and the new AC will pioneer cavern archives facilities in Asia Pacific.

Along with these extended uses, new challenges also emerge. One of them is the applicability of prevailing design codes and practice to these new types of facilities. For instance, the Guide to Fire Safety Design for Caverns 1994 (BA & FSD 1994) sets out the design rules for rock caverns intended for low population occupancy (e.g. those for public utilities in the 1980's). There is also a lack of established fire safety guidelines and regulations tailored for the current purpose in overseas countries with advanced application of rock caverns. It is considered not appropriate to apply directly local and overseas fire safety codes to the Joint Cavern Development project or any other cavern facilities of similar scale in terms of population occupancy. A customised fire safety guideline based on sound fire engineering principles has to be tailored for these projects. In this connection, the establishment of an appropriate vetting mechanism is also required to ensure top-level design for fire safety in all relevant aspects.

The biggest project-specific challenge is the extremely tight development time frame in relation to (1) the staged population intake schedule of the residential housing at Anderson Road Quarry Site Development from mid-2023 to 2026 tentatively and (2) the target land disposal schedule for the site occupied by the existing PWCL Building at Kai Tak. In short, every stage in the Joint Cavern Development project is competition against an extremely aggressive programme.

There are still site-specific challenges at Tai Sheung Tok in spite of its favourable factors for cavern development (e.g. geology, accessibility, readiness of development, etc.). The construction team has to resolve the problem of limited work areas near the proposed portals and within the network of caverns and connecting adits while racing for progress under a tight programme. Innovative construction methods are called for to enable work on multiple fronts with a view to achieving programme merits.

Land, both surface and underground, is a valuable yet expendable asset. In every cavern development project, sustainability is of the essence given the limited length of available portal access versus the comparatively large developable cavern space. It is HKSAR Government's policy to safeguard the development potential of SCVAs. Taking SCVA No. 28 as an example (Figure 5), once the whole lengths of the three potential portal areas are depleted, further cavern development by other project proponents or extension of completed caverns will become extremely difficult if not impossible. As such, suitable enabling measures have to be explored and implemented to safeguard the future development potential of the unused space. Such provisions to foster sustainable and continuous rock development will form part of the current project.

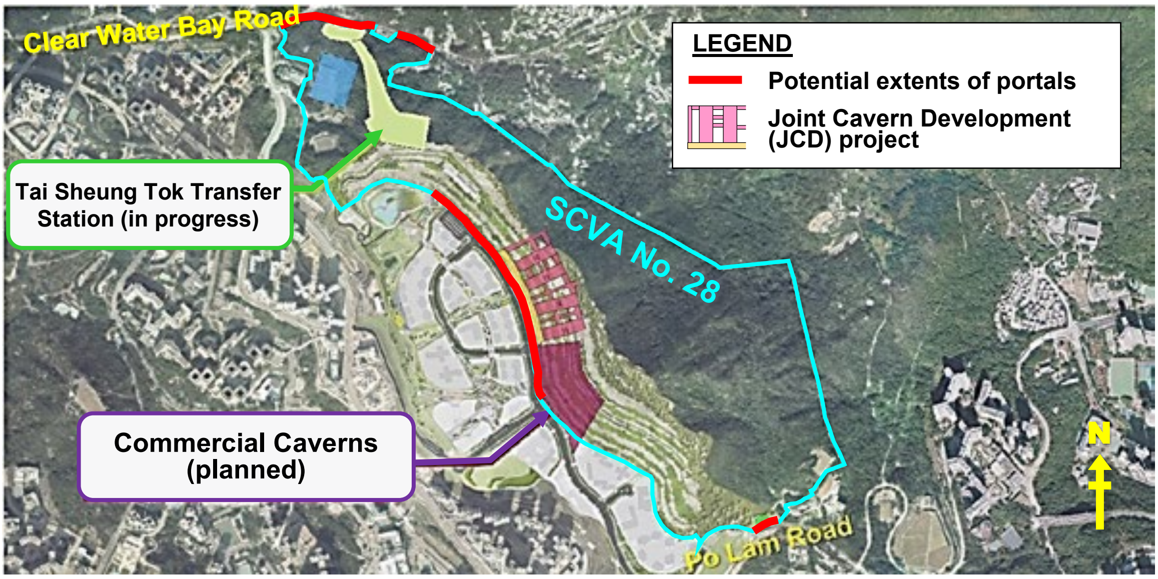

Figure 5 Extent of potential portal locations of Strategic Cavern Area No. 28 and the planned / ongoing cavern projects

4 BUNDLING ARRANGMENT

PWCL and GRS' AC were initially two distinct projects. The CEDD has coincidentally undertaken as the works agent for both projects. In separate site identification and selection exercises, Tai Sheung Tok was chosen as the suitable site for both facilities, because of similar location requirements (e.g. centralised with good accessiblility) and operational needs (e.g. stable environment). In working out the implementation plans for the PWCL project and the AC project, the following are observed:-

(i) Similar nature of works — both projects are cavern development to house government offices and facilities;
(ii) Project implementation time frame largely overlapped with staggered completion;
(iii) Extremely close geographically (i.e. with project boundary adjoining each other) — significant construction challenges in interface coordination, resources planning and constraints in division/sharing of works area; and
(iv) The need to install full noise enclosure before first population intake scheduled for mid-2023 at Anderson Road Quarry Site to mitigate the environmental impact during the construction stage of the projects.

With due consideration to the above, the most effective project delivery approach is to adopt a combined arrangement, so as to tackle the above-mentioned construction challenges and to achieve synergy effects. One significant benefit of this bundling arrangement is the reduction in consultancy and contract administrative efforts. It is also envisaged that there would be savings related to economies of scale in excavation volume, shared use of building services provisions, optimisation of cavern size, etc.

In particular, a single consultancy agreement covering both the PWCL project and AC project can facilitate design coordination and harmonisation, optimise cavern design and layout (e.g. reduction of excavation volume, better layout of the connecting tunnel, etc.), reduce study efforts on technical aspects of similar nature and maximise cost-effectiveness.

Delivering the works of both facilities under one contract can minimise works interfaces and enable better planning and site coordination, which is beneficial to systematic safety planning and implementation of impact mitigation measures particularly in a congested site environment. There will be more efficient deployment of contractors and supervision teams. A single contract can also reduce the risk of programme delay.

5 USE OF MODULAR INTEGRATED CONSTRUCTION (MiC) IN CAVERNS

Unless for special reasons, it is normally conducive to take forward cavern excavation and construction of the associated building (including portal building if any) in an integrated manner. This requires more comprehensive consideration of design, construction, operation and maintenance aspects for the whole facility.

The adoption of MiC is one of the key measures for meeting the tight programme. On-site cavern formation and off-site manufacture of structure modules at the MiC yard are to be carried out in parallel. Using MiC inside caverns to build a structure of such a scale is unprecedented in the world. Innovative ideas are called for to tackle the challenges, including headroom limitation in caverns, logistic planning, customised room requirements vis-à-vis standardised units, design for fire safety and space optimisation, etc. In particular, a material testing laboratory housed in caverns demands stringent environmental control, sophisticated ventilation system, ample fire service installation, exhaust gas emission control from experiments, etc. Archive repositories require a high-rate temperature and humidity control system for preservation of valuable archival records, an effective automatic storage/retrieval system, and a custom-made fire safety system of high reliability. The MiC must be able to incorporate/accommodate all these features.

6 APPLICATION OF EARLY CONTRACTOR INVOLVEMENT (ECI)

In the engineering industry, the expertise of MiC lies with the contractors and their suppliers. To ensure effective use of MiC and reaping its greatest benefits, ECI is introduced. It is intended to bring about constructive proposals that would allow refinement of the Employers Requirements, which may in turn enhance the overall buildability and achieve greater certainty in the works programme. In this project, an ECI stage is included between the prequalification stage and the tendering stage. The ECI process would allow the Government to capture contractors' expertise in approaching the technical challenges envisaged for this project.

7 PROVISION OF ENABLING ADITS

Today, several cavern projects are under planning at SCVA No. 28 (Figure 5). These projects plan to utilise, as construction portal, and subsequently occupy, as portal buildings, the two portal areas facing Clear Water Bay Road to the north and the one facing Anderson Road Quarry Site to the southwest, leaving a relatively small portal facing Po Lam Road to the south. One can easily imagine that, upon the completion of these projects, two of the three portal areas will be fully occupied. The remaining portal in the south can hardly support any extensive development due to its small size (i.e. limited work space and difficulty in mucking out), long distance from the centre of the SCVA, i.e. space with sufficient rock cover for cavern development of larger scale.

Population intake at Anderson Road Quarry Site Development is anticipated to commence in mid-2023 with full intake after 2026. This adds to the challenges. Construction of additional portals at existing rock slopes, which needs the set up of blast doors and noise enclosures before any drill and blast operation can take place, will be extremely difficult if not impossible in view of the noise and vibration caused by mechanical excavation. From the perspective of preservation of the development potential, a project should be aware of such constraint to any subsequent projects in this SCVA. To address this, one should consider the potential implication of his proposal holistically and strategically and reserve/provide the necessary measures to safeguard the future cavern development potential in order not to jeopardise effective use of cavern space in general.

In the Joint Cavern Development project, the detailed proposal for safeguarding measures is still being developed. One of the preliminary ideas is to provide reserve tunnels or retain the construction adits as enabling works of future projects. The layout and alignment of these tunnels/adits would be designed meticulously such that, whereby achieving the objective of SCVA preservation, the work front or blast face in particular, is sufficiently far from the commissioned PWCL and AC. This essentially reduces the risk of excessive vibration due to future construction to PWCL and AC vibration-sensitive operations. Also, as the reserve tunnels/construction adits will probably serve as the mucking out point during cavern construction in the future, their locations should be chosen strategically to minimise the potential construction traffic impact towards the local community.

The above is only one of the many options that may fulfil the SCVA preservation requirements as set out by the Government. It is always worthwhile to explore other innovative measures, or by integration of more than one option, in the upcoming phases of the Joint Cavern Development project. Despite details of measures will vary by projects, the essence is to foster sustainable caverns development within the SCVA concerned during the early stage of a project.

8 ROCK REINFORCEMENT APPROACH AND NEW CONSTRUCTION MATERIAL

The concept of Rock Reinforcement Approach (RRA) is to mobilise the strength of rock to form a natural rock arch with adequate stability. The common support elements comprise (1) rock bolts which tie the rock blocks together to form an arch, and (2) a layer of sprayed concrete which provides a confinement pressure on the rock face. The lining system adopting RRA is illustrated in Figure 6.

Figure 6 Illustrative diagram for the concept of RRA

In Hong Kong, it has long been a common practice to adopt cast-in-situ concrete lining as the permanent support of tunnels/caverns, no matter whether there is a shotcrete/sprayed concrete lining (i.e. the first pass lining) serving as the temporary support or not. It is totally understandable that in the past, local practitioners might find the support contribution by sprayed concrete lining skeptical, thereby neglecting it, due to immature technique and lack of internationally-recognised standard and specifications then. However, engineering knowledge also tells us that competent rock mass could be stronger and stiffer than artificial material. A design taking into account rock strength contribution will be more rational.

Following the improvement of sprayed concrete technique in recent years, high quality sprayed concrete lining had been constructed in tunnel projects around the world, including the renowned Crossrail project in UK (Stark et al. 2016). While the international counterparts are consolidating their experience in literatures and publications (e.g. Thomas (2009), the series of papers in ICE's 5 volume set publication for the Crossrail Project (Crossrail 2016), etc.), the local industry is left with some easier tasks by specifying the sprayed concrete for tunnel/cavern use and the local application of the RRA.

Riding on the successful application of the RRA in Drainage Services Department's project to relocate Sha Tin Sewage Treatment Works to caverns, the Joint Cavern Development project team aims for enhancing the application of RRA. Among the potential options, the most promising is the application of composite lining concept. By applying this concept, the first pass lining will form part of the permanent works, and the overall lining thickness could be reduced. Given the same usable space in the completed structure, the total volume of rock requiring excavation could be reduced.

In order to implement this approach, suitable specifications on the first pass lining with reference to relevant international practice have to be developed. One of the key concerns that led to the disregard of first pass lining in the past was the potential damage caused by subsequent blasting vibration to the completed portions. To ensure the structural integrity of the first pass lining, the CEDD has initiated a study on the development of a Vibration Resistant Sprayed Concrete (VRSC). It is of aspiration that the novel material could have stronger resistance against blasting vibration such that the sprayed concrete lining using this material could withstand rounds of blasting operation and remain intact and durable for permanent use. The development of VRSC is still in progress. Trial use and full application of the material as sprayed concrete lining are probable in the Joint Cavern Development project depending on the time frame for material development in times to come.

9 CONCLUSIONS

The Joint Cavern Development project is a pioneer project which realises the initiative of versatile use of caverns. Rock cavern is regarded as a valuable source of land supply in the middle to long term, contributing to alleviation of the intense demand for surface land in Hong Kong. It is envisaged that by expanding the potential applications of rock caverns to house wider range of government facilities, more surface land could be released for other beneficial uses.

The Joint Cavern Development project at SCVA No. 28 involves two first-of-its-kind cavern facilities in Hong Kong — a materials testing laboratory and an archives centre. This paper illustrates the challenges of the Joint Cavern Development project, including the extremely tight implementation time frame, site constraints, project interfaces, fire safety considerations, novel construction techniques and technical design requirements arisen from pilot applications of design concepts and unconventional project implementation strategies, and the way-forward options which aim at surmounting the challenges and at the same time creating synergy for cost-effectiveness and minimising the risks of programme delay.

It is our mission to ensure the sustainability of cavern development where strategic planning and implementation of enabling measures are highly necessary. To this end, it is always important to maintain holistic considerations for the implications on future development potential of the SCVA concerned. The spirit of cavern development is to be progressive and systematic, in lieu of individual project-based implementation.

10 ACKNOWLEDGEMENT

This paper is published with the permission of the Head of Geotechnical Engineering Office and the Director of Civil Engineering and Development, Government of the Hong Kong Special Administrative Region, China.

11 REFERENCES

BA & FSD 1994. *Guide to Fire Safety Design for Cavern 1994*. Building Authority and Fire Services Department, Hong Kong Government, Hong Kong.

CEDD 2017. *Cavern Master Plan*. Civil Engineering and Development Department, Government of the Hong Kong Special Administrative Region, Hong Kong, China. See https://www.cedd.gov.hk/eng/topics-in-focus/index-id-27.html. Accessed 08/04/2022.

Crossrail 2016. *Crossrail Project: Infrastructure Design and Construction – 5 Volume set*. ICE Publishing, United Kingdom.

Ho, Y.K., Tsang, W.H. & Chan, C.C. 2020. Rock cavern development in Hong Kong: past, present and future. *Proceedings of the Institution of Civil Engineers – Civil Engineering*, 173(5): 25-31.

Stark, A., Rangel, L.J. & Wade, C. 2016. Analyses of convergence and utilization of SCL – tunnels during excavation. In: Black, M. (editor), Crossrail Project: Infrastructure design and construction - Vol. 3: 89-104. ICE Publishing, United Kingdom.

Thomas, A.H. 2009. *Sprayed Concrete Lined Tunnels*. Taylor & Francis Group, CRC Press.

A Critical Review of the Current Practice of Design and Construction of Offshore Foundations in Hong Kong

Daman Lee
CLP Power Hong Kong Ltd., Hong Kong, China

K T Hung
Hongkong Electric Co. Ltd., Hong Kong, China

Samuel Lee
Hutchison Ports Yantian, Hong Kong, China
(Formerly CLP Power Hong Kong Ltd.).

Victor Li
Victor Li & Associates Ltd., Hong Kong, China

ABSTRACT

Large diameter driven tubular piles have recently been used as the foundation system for the Hong Kong Offshore LNG Terminal located in the southern waters of Hong Kong SAR, to the east of the Soko Islands. At present, there are limited guidelines in local codes or guides for the design of offshore foundations in Hong Kong. It is observed that the current practice of regulatory control in Hong Kong will often cause great difficulties in planning and construction of foundation works. Moreover, it is of paramount importance to have experience in offshore pile installation, which is severely lacking in local industry, in order to produce safe and efficient foundation designs to handle the much more hostile site conditions. Some suggestions for revising the current practice are suggested to bring it more in line with accepted international practices for offshore foundations.

1 INTRODUCTION

To support the HKSAR Government's Climate Action Plan 2050 on the increasing use of natural gas in Hong Kong to reduce carbon emission, CLP Power Hong Kong Limited (CLP) and The Hongkong Electric Co., Ltd. (HKE), are jointly developing an offshore liquefied natural gas (LNG) facility called the Hong Kong Offshore LNG Terminal (HKOLNGT) to receive and convert LNG into gas for supply to the gas receiving stations at CLP's power station at Black Point and HKE's power station at Lamma Island for power generation.

The foundations for the HKOLNGT comprise 6 pile groups each with 4 raking piles for the mooring dolphins, named MD1 to MD6; 3 pile groups each with 8 vertical piles for the breasting dolphins, named BD1 to BD3, and two pile groups each with 3 vertical piles located adjacent to MD1 for the fireboat mooring dolphins, named FD1 and FD2. The piles for MD1 to MD6 and BD1 to BD6 are 1.83m outer diameter open-end driven steel tubular piles and those of the FD1 and FD2 are similar piles but with a smaller outer diameter of 1.26m. There are a total of 54 piles for the Terminal. The foundation works for the HKOLNGT have recently been completed. Figure 1 shows a photograph of the completed foundation of the Terminal. Details of the design and installation of the foundations for HKOLNGT are presented in a companion paper by Shea et al (2022) published in the proceedings of this seminar.

Figure 1: Photograph of the completed foundations of HKOLNGT

The design and installation of the foundations for HKOLGNT are subject to the regulatory control of the Buildings Department (BD). There are difficulties faced in fulfilling some of the regulatory requirements for the foundation works in the project. This paper aims to present a critical review of the current practice of design and construction of offshore foundations in Hong Kong and suggest some changes that can be made to reduce these difficulties. Although the suggestions made in this paper are mainly related to the foundation type used for HKOLNGT, the ideas may also be applicable generally to other types of offshore foundations.

2 CURRENT GOVERNMENT CONTROL ON DESIGN AND CONSTRUCTION OF FOUNDATIONS

The design and construction of foundation for private development projects in Hong Kong, including those of power supply companies, are subject to the control of the Buildings Ordinance. The designs of foundation for such projects require approval by the BD. In addition, consent for constructing the foundation works needs to be applied for and granted by the BD before such works can be commenced.

The BD implements a central processing system for foundation submissions. For offshore foundations, the BD will usually refer the design submissions to relevant government departments such as the Geotechnical Engineering Office (GEO) and Port Works Division (PWD) of the Civil Engineering and Development Department (CEDD) for comments. The BD will consider comments from these departments in addition to the guidelines promulgated by its own department before granting approval of the foundation plans.

In Hong Kong, the design of foundations for private development projects usually follow the guidelines of the Code of Practice for Foundations (CoPF) (BD 2017). The GEO Publication No. 1/2006 (GEO 2006), which supersedes the earlier GEO Publication No. 1/1996 (GEO 1996) is also commonly used as a guide for foundation design, particularly for design submissions that also require acceptance by the GEO. The two GEO publications are hereafter named GEO-2006 and GEO-1996 for ease of reference.

The CoPF and GEO-2006 give guidelines only for the design of more common foundation types including footings and pile foundations such as bored piles founding on rock, driven steel piles, socketed H-piles and mini-piles. Offshore foundations often involve driven large diameter tubular piles. There is virtually no guideline in CoPF and GEO-2006 for such a foundation type and it is strongly recommended not to simply adapt these for use in offshore foundation designs. The BD implements a system of recognized pile types. At present, there are 13 recognized pile types on the approved list (BD, 2022). Currently, there is only one recognized pile type, of Reference Number BD-RP018, that is related to driven pipe piles. According to BD (2022), this pile type covers "Driven Steel Bearing Piles including H-piles and Pipe Piles (sections of yield strength not more than 355 MPa to BD EN 10025-2 or equivalent)". Unfortunately, this recognized pile type does not cover large diameter driven tubular piles commonly used for offshore foundations.

The CoPF gives the following guidelines for the design of driven piles.

"For driven piles, the ultimate bearing capacity of driven piles may be assessed by any one or more of the following methods:

(a) a dynamic formula based on the data obtained from test driving the pile on site;
(b) a static formula based on design parameters of the supporting soil obtained from suitable tests; or
(c) loading test of the pile on site.

A suitable factor of safety should be adopted when deriving the allowable bearing capacity of the piles. In general, a factor of safety not less than 3 should be used for a static formula and those formulae for which lower factors of safety have not been established. In no cases should the factor of safety be less than 2."

All the above three methods are normally required by the BD for assessing and confirming the capacity of a non-recognized pile type. For driven tubular piles, this will usually mean that the required pile length to attain the design capacity of the piles needs to be assessed by soil mechanics principles with a factor of safety (FoS) of 3 and that final set tables need to be developed using a suitable pile driving formula for ascertaining that the target FoS can be achieved at final set. In addition, one or more trial piles may be required to be installed and subjected to a static loading test to verify the design capacity with a FoS of 3. The trial piles may be selected from the working piles or they can be purposely constructed piles to be abandoned after loading test.

According to the current practice, approval of and/or consent for the working piles or remaining working piles not selected as trial piles may not be granted until the results of trial pile(s) have satisfactorily confirmed the design pile capacity or principles of the foundation design.

Based on past experience, it will usually take 5 months or more before the design and consent of the trial piles of a non-recognized pile type can both be obtained from the BD. Once the installation of trial piles has been completed, works on site may need to be suspended until approval and/or consent for the remaining piles have been granted by the BD depending on the conditions stated in the approved foundation plans or approval letters.

Similar to the CoPF, the GEO-1996 and GEO-2006 also stipulate higher FoS for piling design unless trial piles have been used to increase the confidence of the design method. GEO-1996 recommends that the minimum FoS should be 3 for compression and lateral resistance and 3.5 for tension capacity if the method of determining pile capacity is based on theoretical or semi-empirical method not verified by load tests on trial piles. The corresponding FoS can be reduced to 2 and 2.5 if the design method is verified by a sufficient number of load tests on trial piles. In GEO-2006, the recommended FoS are reduced to 3 throughout for pile designs not verified by trial piles and 2 throughout when there are sufficient load tests on trial piles.

3 DIFFICULTIES FACED IN DESIGN OF OFFSHORE FOUNDATIONS

In the preceding section, an overview of the current practice regarding regulatory control of design and construction of larger diameter tubular piles has been presented. Such practices, when applied to offshore foundations, will impose extreme difficulties on the design and construction as explained below.

3.1 Dynamic formula

In Hong Kong, the pile driving formula developed by Hiley (1922) and enshrined in the CoPF is essentially the only pile driving formula that will be accepted by the BD for developing the final set tables. The Hiley formula which has served the industry well in times of uncertainty is long overdue for retirement. As discussed by Li et al. (2003a), the Hiley formula predicts that the energy transmitted to a driven pile after hammer impact will decrease with pile length. However, there are abundant data to indicate that the energy transferred to a driven pile after impact will remain relatively constant and independent of pile length for a given pile type, pile driving hammer and ground condition (e.g. Li et al. 2003a). The Hiley formula is therefore flawed, or at least problematic for long piles.

The Hiley formula contains three input parameters, namely the hammer efficiency α, the coefficient of restitution e, and the elastic compression of pile cushion C_c. Usually, the formula is not sensitive to the magnitude of C_c, but highly dependent on α and e. The parameter e is not a fundamental parameter and essentially an artifact of the theoretical model. One has to rely on past experience of similar pile types and hammer types for the selection of a suitable design value of e. For offshore piles, there are rarely sufficient past experience for the choice of a suitable site specific design value of e for meaningful application of the Hiley formula for prediction of pile capacity.

3.2 Static formula for assessing of pile capacity

There is little guideline in the CoPF on assessing the static capacity of piles except for some presumed allowable bearing pressure for soils and rocks. The GEO-2006 does discuss some textbook methods on assessment of the static capacity of piles. For shaft resistance, the suggested methods are largely confined to the conventional approaches based on the so-called α-method for clayey soils and β-method for sands. For end-bearing resistance of a solid pile, the bearing capacity factor can be obtained from a design chart in GEO-2006. Limiting values are suggested in the GEO-2006 for both the shaft and end bearing resistance.

When a foundation design is subject to the scrutiny of regulatory authorities, it is not surprising that reasonably conservative values and assumptions need to be adopted for estimating the static capacity of piles. For instance, the design strength profiles should be reasonably close to the lower bound envelope of test results, soil layers with interbedding layers of sands, silts and clays should be treated as purely a clay layer using undrained parameters, design values of adhesion factor α and shaft resistance factor β should be sufficiently conservative and perhaps close to the recommended lower bound values, and shaft and end-bearing resistance to be capped at the limiting values such as those suggested in GEO-2006 or even lower values. Given these various sources of conservatism, the end results are usually that the pile length required to achieve the required static capacity with a FoS of 3 may become exceedingly long, making installation of offshore piles more difficult as more site welding will be necessary for splicing of longer piles and heavier hammer will be required for installing the longer and thicker piles.

The situation may become worse if the estimated pile length to achieve the calculated ultimate pile capacity turns out to be a requirement of the approval. If the design static length is obtained from conservative design assumptions and parameters or when a stiffer stratum is encountered earlier than expected due to local variation of ground conditions, the required minimum pile length may not be achievable during construction. This will trigger new design submissions for justifying the adequacy of a shorter pile and, if necessary, re-design of the foundation. Worse still, preboring may be required for the purpose of achieved the specified minimum pile length. All these problems will no doubt cause severe interruption of and delay in pile installation.

3.3 Multiple approvals and consents

As discussed above, trial piles are usually required for non-recognized pile types. If the design and installation of trial piles need to be separate from working piles, foundation works on site need to be suspended for months after the construction and testing of trial pile until approval and consent for the working piles have been obtained.

3.4 Loading tests

Except for mono-piles, stability of offshore piles installed in deep waters is typically maintained by pile jackets or steel frames. To ensure safety of the pile foundation and the pile jacket under adverse or extreme weather and wave impact, it is always desirous to connect the piles to the pile jacket by welding and to also seal the gap between the pile and the pile jacket if necessary as soon as practicable after the satisfactory completion of pile installation. This will make static loading test of a working pile a difficult task.

Even if the welded connection of the working pile selected for loading test can be temporarily removed to free up the pile for loading test, the pile jacket may not be sufficiently strong to act as the supporting flame for the kentledge. It may not be feasible nor environmentally friendly to design the pile jacket to also serve as a supporting frame for static loading test to be conducted for any possible working piles, including edge piles, to be selected by the BD for loading test. Also, the layout of the working piles may be such that they will not be adequate in supporting a kentledge load in excess of three times the design working load of the test pile.

If a static loading test is to be carried out for the trial pile or a working pile, a separate temporary supporting frame similar to a pile jacket and perhaps also new reaction piles may need to be constructed for the purpose of static loading test. Such supporting frames and reaction piles cannot be commenced until the location of test pile(s) to be selected by the BD for loading test is known after completion of all working piles. This will make the task of conducting a static loading test much more difficult as the presence of installed pile jackets and working piles will impose severe limitations in maneuvering the marine vessels for such works. Moreover, reaction piles and temporary supporting frame may need to be removed after static loading test as they may affect the intended operation of the offshore facility. Perhaps most importantly, creating a large set up of kentledge for pile testing is inherently very risky for offshore environment as when adverse weather arrives such as strong winds and waves, the monsoons or the typhoons, complete evacuation would need to take place in good time.

For the above reasons, static loading tests are not practical for offshore foundation works and are therefore seldom used in international practice because of safety, the long delay they may cause to an offshore project and the high costs involved.

3.5 Suspension of works

As discussed earlier, the design and construction of offshore foundation often require multiple approvals and consents for different stages of works. Sometimes, when conditions are imposed in the approved foundation plans and/or approval letters, such conditions may need to be complied with before the next stage of construction can be started. For instance, if a condition that working piles cannot be started after satisfactory completion of the trial pile(s) has been imposed, installation of working piles will need to be severely delayed. As will be explained later, idling is extremely costly and unsafe for offshore foundation works. There is a great need for simplifying the regulatory control procedures to make offshore works a less difficult task.

3.6 Understanding of Construction in Offshore

Designers of offshore foundation must also be experienced in dealing with the various constraints and difficulties in construction. This is indeed why typical foundations codes for land works cannot be easily applied to works in offshore. The sea state due to the weather conditions often dictates the method of construction and hence the design. Typically, it is essential to estimate the window of opportunities to carry out the piling works using the right type of Principle Installation Vessel (PIV). This often means that the designer will focus on how to ensure the installation time spent at offshore site is as short as possible. The preference will therefore be for large diameter driven piles to reduce the installation time. The piles would be thicker than those used on land to fully utilize the capacities from the friction and end bearing of the long piles. The need for splicing would also be kept to a minimum and hence single segment of pile of >50m long is quite common and usually limited by the size of the transportation vessels. For similar reasons, it is also not preferred to have pile lengths that need to be determined on site, for example, driving to a set table. The designers would also need to take into account during the design stage the type of PIVs that are likely to be used for installation in order to tackle the sea state such as wind, wave and in particular where it might be susceptible to long period swells. For the more heavy duty offshore piling works, the PIVs may need to be secured well in advance and this, in turns, could also affect the tender strategy and the design process.

4 INTERNATIONAL PRACTICE

The international practice for offshore foundations is no doubt influenced by the difficulties and high costs in carrying out both ground investigation and foundation works in deep waters. The tubular piles and pile jackets are usually pre-fabricated in whole or in parts in fabrication yards and shipped to site for installation.

In addition to boreholes that are sunk for obtaining soil samples for confirming the soil types of founding soils and laboratory testing for measurement of soil parameters, cone penetration test (CPT) soundings can be used more economically to supplement the boreholes for delineating variation of the soil profile and for inferring the soil properties.

The information obtained from ground investigation and CPT tests will be used for estimating the variation of pile resistance with pile length. This exercise is useful in planning the lengths of individual segments of tubular piles to be fabricated. It is equally important in assisting the contractor in selecting a suitable hammer for pile driving and evaluating of the drivability of piles, something which are commonly performed with a popular program GRLweap developed by Pile Dynamic, Inc. (PDI).

The estimated pile length required to achieve the target capacity is seldom used as a rigid design requirement unless there are other design considerations such as tension capacity which dictates the design pile length. Designers usually rely on a dynamic pile testing method for estimating the pile capacity of installed piles, and not counting fully on the calculated pile length needed to achieve the target static capacity. The piling testing equipment Pile Driving Analyzer (PDA) and the program CAPWAP which predicts the pile capacity based on data obtained from a PDA test, both developed by PDI, are popular tools that can be used for monitoring the pile capacity during driving, at end of driving (EOD) or after installation. Static loading tests are rarely used for determining the static capacity of offshore piles.

The design guidelines published by the American Petroleum Institute (API) are some of popular design standards adopted worldwide for design of offshore foundations. In the code API-RP 2A-WSD developed by API (2014), it is recommended that the FoS for pile design should be determined in accordance with the risk level of the structure. FoS of 1.5 or 2.0 have been recommended as general guidelines for the *design environmental condition* and *operating environmental condition* respectively, which can be treated as equivalent to the *Normal* and *Extreme Conditions* in Port Works Design Manual

(PWDM), Part 1 (CEO 2002). The recommended FoS for pile design in API-RP 2A-WSD are shown in Table 1.

Table 1: Pile Factors of Safety for Different Load Conditions (from Table 9.1 of API-RP 2A-WSD)

Condition Number	Load Condition	Factors of Safety
1	Design environmental conditions with appropriate drilling loads	1.5
2	Operating environmental conditions during drilling operations	2.0
3	Design environmental conditions with appropriate producing loads	1.5
4	Operating environmental conditions during producing operations	2.0
5	Design environmental conditions with minimum loads (for pullout)	1.5

The *design environment conditions* in Table 1 is recommended to be determined based on the design life of the structures, likelihood, and consequence of its failure following API design philosophy. In general, 100-year oceanographic design criteria should be adopted for structures that are manned during the event or whose failure will result in a high consequence. For structures that are unmanned or evacuated during a storm event, with a short design life of say 20 years or when loss or severe damage will not result in a high risk to life, a reduced factor can be allowed. The *operating environment conditions* generally refers to a 1-year to 10-year storm for the Gulf of Mexico, though the design conditions for a specific project will depend on the site-specific metocean condition and project-specific requirements.

In contrast, design load conditions for offshore works in Hong Kong usually follows the guidelines in Section 5.10.2 of the PWDM, Part 1 (CEO 2002). A 100-year return period for wave, current and water levels and 50-year return period for wind are generally required for the extreme condition, which is consistent with recommendations in API-RP 2A-WSD. For the normal condition, a design 2-year storm event can be adopted in the absence of more meaningful wave information. It should be noted that this recommendation should be consistent with the definition of normal condition in PWDM and it refers to the "wave condition at no.3 or within a first few hours of hoisting of no.8". The applicability of 2-year storm event as the *Normal Condition* should be reviewed for future offshore development for which the effect of climate change over the structure's design life may need to be considered in the choice of design return period.

The recommended FoS in Section 3.5.2 of PWDM Part 2 (CEO 2004) does not distinguish the Normal and Extreme Conditions and are based on the older GEO-1996 which requires a higher design FoS for piling design than GEO-2006 for tension piles.

As discussed earlier, large diameter driven steel tubular piles are regarded by the BD as a non-recognized pile type for which a design FoS of 3 and loading tests on trial piles may also be required. This, coupled with a similar requirement in PWDM Part 2, will mean that the design requirements for offshore pile foundations are much more stringent than international practice in terms of proof testing and design FoS.

The α-method for clay and β-method for sands are both discussed in GEO-2006 and in the main text of API standard API RP GEO (API 2011), although the recommended values of β and limiting shaft friction values are different. In international practices, the pile capacity of offshore piles are more commonly estimated directly from CPT results. Further discussions in this respect are given in Shea et al. (2022).

5 BEHAVIOUR OF OFFSHORE PILES

It is well established that large diameter driven tubular piles will exhibit increase in capacity with time, a phenomenon usually called the set-up effect. The set-up effect can be attributed to kinematically restrained dilation of soils close to the pile shaft and soil ageing (Bowman & Soga 2003, 2005). Set-up effects can be significant for large diameter tubular piles. Sze et al. (2014) reported a case study in which significant pile resistance increase had been observed during re-strike after the installation of closed-end tubular piles were temporarily suspended for extension of the pile before continuing the pile installation.

The set-up effect can be characterized by the ratio of $r = R_t/R_{EOD}$, where R_t and R_{EOD} are the pile capacities at time t after installation and at EOD respectively. In the literature, the set-up curve which describes the variation of r with time is commonly modelled as a logarithmic function. This relationship is theoretically deficient as it predicts an unbounded limit for r. An alternative relationship based on a hyperbolic function which caps the ratio r at a limiting value at large time t is suggested by Shea et al. (2022) and found to give a good fit to the data obtained from the HKOLNGT project.

Sometimes, foundation contractors will take advantage of set-up effect and stop pile driving before reaching the target FoS at EOD, allowing the required FoS to be attained due to set-up effect before the deck structure is built above the pile foundations.

The set-up effect also has implications on planning the driving operation. To enable the design pile length to be reached with the minimum of pile driving energy, the installation of piles should be completed with as little interruption as possible to avoid increased pile resistance that will develop during interruptions.

The set-up effect may be different for the toe resistance and shaft resistance and may also vary along the pile length. The effect tends to be more significant for the shaft resistance than the toe resistance. Care should therefore be taken when back-analyzing the pile resistance obtained from CAPWAP analyses or instrumented piles. A higher mobilization ratio can often be attained for the toe resistance in the initial periods after pile installation when the shaft resistance is still low due to its slower rate of set-up. With time, a higher shaft resistance will be developed. For the same pile driving energy, the pile toe displacement that can be mobilized will be reduced and it may not be able to fully mobilize the toe resistance during the PDA test, giving a wrong impression that the toe resistance has dropped with time. When assessing the pile capacity, one should take account of all the estimated toe and shaft resistances measured at different times. The total capacity should be better assessed by summing the maximum measured toe resistance and shaft resistance although they may not occur at the same time (Hussein et al. 2002).

6 UNCERTAINTY OF FOUNDATION DESIGN

As remarked by Li et al. (2003b), the current practice of calculating the static capacity of piles is fraught with problems because the conventional, simple textbook theories described in most design guidelines, including GEO-2006, often fail to give accurate prediction of pile capacity. This can be illustrated using the data in Figure 2(a) which presents the data and design lines marked with A, D, K, M, P T and W recommended by various researchers for adhesion factor of clay and Figure 2(b) which shows the bearing capacity factor for the toe resistance of a solid pile proposed by different renowned researchers. It can be observed from Figure 2 that there is a high degree of uncertainty in soil mechanics theories and it is justifiable to adopt a higher factor of safety of 3 or higher when predicting the geotechnical pile capacity purely on the basis of theoretical or semi-empirical methods.

The technology of dynamic pile testing, such as PDA tests and CAPWAP analyses, has now become very mature after almost 50 years of development. The pile capacity predicted by such techniques are proven to be much more reliable than that estimated by conventional soil mechanics theories. Figure 3 shows the result published by Likins & Rausche (2004) for a correlation between pile capacities predicted by CAPWAP analyses (denoted by CW) and static loading test (denoted by SLT) based on a database of 303 results. The data cover results for a large range of piles including H-piles, bored piles, reinforced concrete piles, prestressed concrete piles, open-end and closed-end tubular piles, and auger piles. The results give a ratio of CW/SLT with a mean value of 0.98 and a coefficient of variation (COV) of16.9%. The CAPWAP analyses can therefore give an essentially unbiased and reasonably accurate prediction of the static capacity of piles.

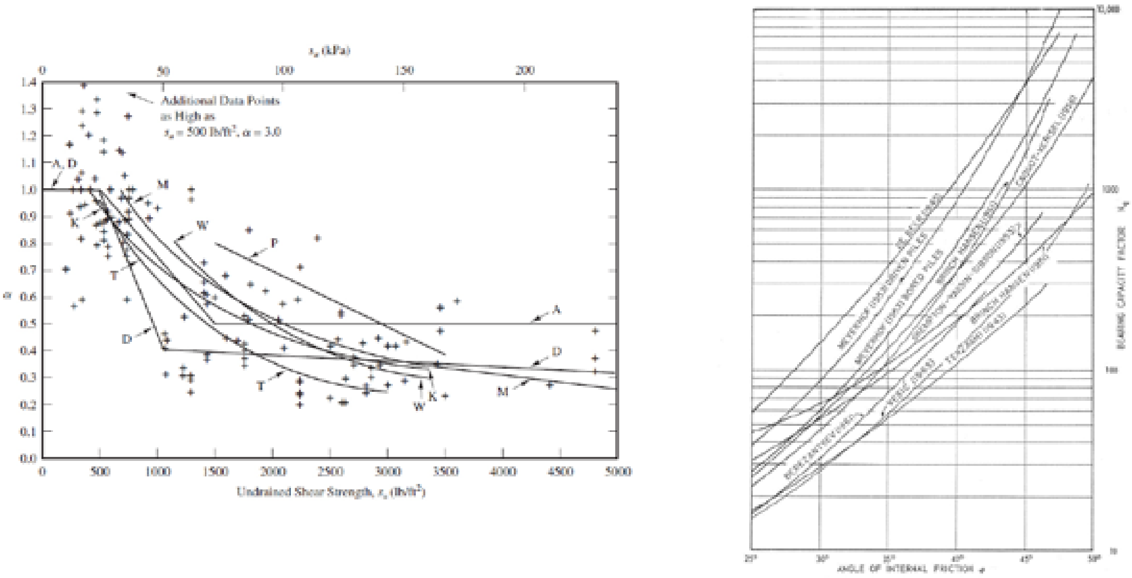

(a)

(b)

Figure 2: (a) Adhesion factor α for clay (after Coduto et al, 2016) and (b) bearing capacity factor N_q for toe resistance of pile (after Vesic, 1967)

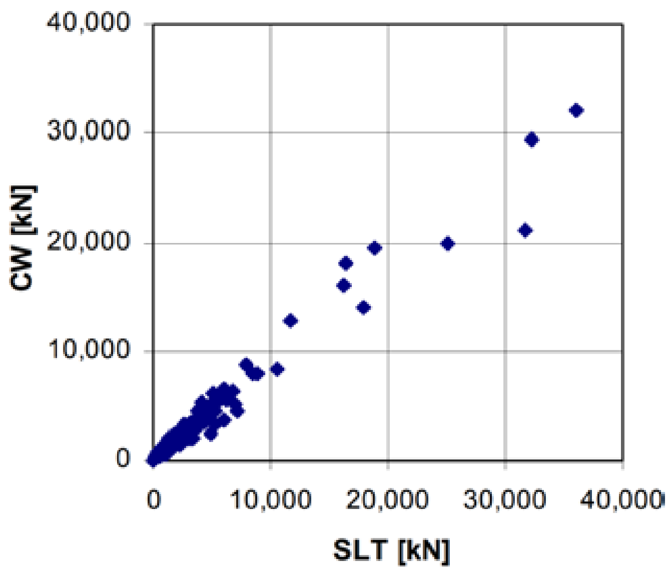

Figure 3: Comparison of pile capacity measured by CAPWAP analysis (CW) versus static loading test (SLT) (after Likins & Rausche 2004)

The reliability of the method for estimating the pile capacity has a significant bearing of the required FoS for piling design. This can be discussed by way of a simple analysis. Consider a group of n piles with a similar design and installed in similar ground conditions. One can assume that the failure probability p of each pile is the same. The system failure probability of the pile group, defined as the failure probability of one or more piles within the group (denoted by P_S), is given by:

$$P_S = 1 - (1 - p)^n$$

Eq.1

Consider two design approaches. In the first approach, the pile capacity is predicted using theoretical method with a target FoS of 3. The distribution of the actual FoS of pile under this design approach is denoted by R_1. As the design FoS is 3, it is convenient to assume that R_1 is a normally distributed random variable with a mean value of 3.0. Given the high uncertainty of predicting the pile capacity using a theoretical approach, it is reasonable to adopt a higher COV of, say, 30% for R_1, giving a standard deviation of $0.3 \times 3 = 0.9$ for R_1.

In the second design approach, PDA tests are conducted and CAPWAP analyses performed for all piles and each pile will achieve a FoS of 2.0 at EOD. The actual FoS of pile designed based on the second approach is denoted by R_2. Again, it is also assumed for convenience that R_2 is a normally distributed random variable, but now with a smaller mean value of 2. As CAPWAP analysis is a proven reliable tool for predicting the actual pile capacity, it is reasonable to adopt a smaller COV of 17% for R_2 based on the study by Likins & Rausche (2004). This gives a standard deviation of 0.17 x 2 = 0.34 for R_2.

A pile will fail if its FoS fall below a value of 1.0. The failure probability of a single pile, p, can then be evaluated using the cumulative distribution function of a normal distribution. For the first design approach, the value of p is given by p = Prob ($R_1 < 1$) = 0.013. For the second approach, the failure probability of a single pile is p = Prob ($R_2 < 1$) = 1.64×10^{-3}.

Suppose there are 40 piles in the pile group. Assuming that a loading test has been conducted successfully for a working pile as trial pile before commencement of foundation works and another working pile after completion of works, the pile capacities of these two tested piles are confirmed to be satisfactory by the loading tests. However, there is still a chance that one or more of the remaining 38 piles may fail. Taking $p = 0.013$ and $n = 38$, Eq.1 gives a system failure probability of $P_S = 0.395$ for the pile group designed using the first approach.

For the second design approach, all the 40 piles have been subjected to PDA tests and confirmed to have a CAPWAP capacity with FoS higher than 2.0. There is still a chance that any of the 40 pile may fail when subjected to a static loading test. The system failure property will then be evaluated based on $p = 1.64 \times 10^{-3}$ and $n = 40$, giving a result of $P_S = 0.063$.

It can be observed from the above simple analysis that the system failure probability is much lower for the second design approach despite the use of a lower FoS. Although the above analyses are over-simplified, it serves to illustrate the main point that, from a system reliability point of view, it is much more preferable to adopt a lower FoS for design coupled with the use of a reliable testing technique for indirect verification of the pile capacity for all or a significant proportion of the piles than to adopt a less reliable method of design but with a more reliable load testing method implemented for just a few piles.

The information that one or more piles have passed the static loading tests or PDA tests is useful in updating the probability distribution using the well-known Bayesian method (see Ang & Tang, 2007) to produce a more accurate prediction of failure probability. For the first approach, there is only limited information based on the results of a few static loading test and it will not produce a much more reliable posterior probability distribution after updating. For the second design approach, PDA tests are to be carried out for all piles and the posterior probability distribution so obtained based on such vast information of successfully completed PDA tests will lead to a much more accurate and smaller predicted failure probability. The contrast between the two design approaches will become much larger in actuality when considering the updating of probability distribution based on proof testing results and it will give a much stronger theoretical support to the notion that the second design approach is the much more preferred option.

Given the higher reliability of the PDA test, it will be overly conservative to require offshore piles to achieve a high FoS of 3 for the CAPWAP capacity when the second approach is adopted for pile installation and proof testing. If such a high FoS is stipulated, stronger tubular sections will be required to withstand the higher driving stress and the piles will have to be driven to deeper levels to achieve a higher geotechnical capacity. This is not a satisfactory situation when there is a global trend towards more sustainable construction and the aim to reduce the installation time in the risky offshore environment.

7 DIFFICULTIES ENCOUNTERED IN THE HKOLNGT PROJECT

The foundation system for the HKOLNGT project is the first of its kind in Hong Kong. It was anticipated from the outset that the BD would treat the larger diameter driven tubular piles for this project as a non-recognized pile type. It was also expected that the design of large-scale pile jacket for holding the piles during installation and maintaining stability of the pile under permanent conditions would also be something novel and the BD might take a longer period of time for reviewing the design before approval. For this reason, the design of the foundation works for the HKOLNGT project were divided into a few smaller packages to ensure smoother and hopefully more timely approval by the BD. The first submission package covered only the design of foundation of 4 piles and the associated pile jacket for mooring dolphin MD2, which is located on the northern side of the Terminal.

As expected, the proposed pile foundation system for the HKOLNGT was categorized as a non-recognized pile type and the design approval required a review by the Structural Engineering Committee (SEC) of the BD before approval. The review by SEC could not be initiated until comments from other concerned government departments or offices, including the GEO and PWD, had been received by the BD and there were no major objections from such parties in approving the design. In the event, it took about 5 months before approval of the foundation plans for MD2 could be obtained. At the time of submission, it was proposed that PDA tests and CAPWAP analyses would be conducted for all the piles of MD2 as an alternative to dynamic formula for pile driving and also as an alternative to static loading test of pile. It was initially hoped that a design FoS of 2.0 could be adopted in line with international practice for design of offshore foundations. In the event, the following requirements would need to be fulfilled for the foundation works after approval.

- PDA with CAPWAP analyses to be conducted for all the piles of MD2.
- Unless a FoS of 3 can be achieved for the CAPWAP capacity at EOD, restrike PDA tests should be carried until a FoS of at least 3 is attained.
- The piles have to reach the minimum pile length required to achieve the design static capacity, with a FoS of 3
- Back-analyses should be carried out using CAPWAP results to verify the design assumptions and soil parameters used for evaluating the static capacity.
- A performance review of the foundation works should be carried out upon completion of the foundation works for MD2.

The same requirements were also imposed on later submissions of the foundation works of other mooring dolphins and breasting dolphins.

Although trial pile and static loading test of working pile(s) are not required in the approved foundation plans, the need for achieving a CAPWAP capacity with a FoS higher than 3 for all piles is in essence a replacement for static loading test and arguably an equally stringent requirement for this project due to significant increase in weather risk with the prolonged installation.

One of the key constraints for the piling works on this jetty was to avoid the peak occurrence season of the Finless Porpoise that lasts a total of 6 months within the year. This was stated in the original Environmental Permit (EP) to be between December and May (both months inclusive) and later adjusted to be from January to June under a variation to the EP.

Due to the lengthy procedure required to secure approval and consent for the foundations, the first offshore installation of mooring dolphin MD1 could only be started in early December 2020. However, it was considered extremely important to complete at least one jacket and the associated 4 piles before the end of December so that during the non-piling period, the installation data could be analyzed in detail to gain more confidence in completing the rest of the piling works in the following year. The installation and subsequent PDA tests took approximately 15 days to complete just in time for the suspension of works at the end of December 2020. The installation of the foundations for MD1 was found to be slower than the contractor's experience in carrying out similar foundations in similar geology internationally by some 40%. This is largely attributed to a higher FoS adopted for this project and a longer waiting time for the set-up effect to develop to enable a CAPWAP capacity with FoS higher than 3 to be attained for all piles.

An idling time of nearly 5 days waiting for proof load test is rare in offshore installation practice due to the aim to achieve safe construction by limiting the offshore works duration as well as the expensive installation vessels and sizable crew and technical people onboard normally required for offshore installation works. Luckily, the development of set-up effect for this site has been consistent and fast enough to enable the pile installation for MD1 to be completed before the end of piling window with only a few days to spare. Otherwise, the partially completed piles would need to be temporarily fixed onto the pile jacket by welding and the piling works could only be resumed half a year later when the new piling window begins the following year.

The significance of being able to complete MD1 within 2020 cannot be overstated. During the peak porpoise activity season, the project team was able to make good use of the data collected on the behaviour of the pile / soil interactions and made suitable amends to the design to be in a much better position to complete the remaining piling and testing works within 2021. Further discussions on the observed pile capacity set-up for this project are presented in the work of Shea et al. (2022).

Like all other offshore works, the offshore lifting, installation and piling operations for this project were heavily controlled by the forecasted and prevailing weather conditions and sea states at the time. Figure 4 shows examples of instances when the offshore construction works have been particularly challenging during the installation of MD1. Lifting of the heavy piling hammer from the congested vessel deck could be difficult under seemingly good weather often due to the long period wave from afar. Heaving, pitching and rolling motions of the crane vessel and/or high winds could potentially cause the piling hammer to swing making it difficult to slot its sleeve over the raking piles. Lifting operations were therefore suspended for 1-2 days until an improved weather window became available. This highlights the construction difficulties unique to large-scale marine construction compared to conventional land-based projects.

For reasons discussed earlier, it is always desirable to reduce the idling time as far as possible to enable the piling works to be completed as quickly as feasible while the metocean conditions are good. The duration of the jacket installation work cycle, including jacket lowering, piling, proof testing, welding and grouting, should be reduced as far as practical so that there is certainty that the majority of the installation can be completed within a seven-day forecast of reasonable weather. It is important to note that once the jacket is lowered on the seabed and the piling works have commenced, the work cycle cannot be interrupted. In the event of adverse weather conditions such as strong wind from monsoon or hoisting of typhoon signal No. 3 or above, the installation vessel will need to evacuate from site and take shelter because it would be unsafe for it to remain in the open sea under such conditions. Hence, it is of paramount importance to limit the installation cycle to around 7 days when the weather is ‘forecastable’, so that the jacket substructure can be well-secured to the seabed by completed piles to ensure the site safety.

(a) (b)

Figure 4: Difficulties of installation caused by weather (a) heavy piling hammer needs to be lifted from congested deck and (b) difficulty to slot piling hammer into raking piles.

Soon after resuming piling works in the summer of 2021, with due consideration of the duration needed for installing and testing MD1, the early optimism of being able to complete the remaining piling works in 2021 was quickly eroding away with the arrivals of typhoons at poor timing. As explained by Shea et al. (2022), the offshore construction sequence and vessel maneuverability for this project are limited by the anchorage spread arrangement, making it difficult/infeasible for the installation vessel to readily return to the previous location(s) due to interference between anchorage lines and the completed mooring/breasting dolphins. Also, it will not be possible to mobilize one additional installation vessel to speed up the foundation works. Faced with this big difficulty, the project team decided to put forward the following proposal to the BD to relax the proof testing requirement so as to speed up the construction programme.

- Only some instead of all piles will be selected for restrike PDA tests to achieve a FoS of 3.
- The set-up curve is constantly updated as more information on CAPWAP capacities of installed piles becomes available.
- For the remaining piles not selected for achieving a CAPWAP capacity with FoS higher than 3, the longer-term pile capacity can be inferred from the updated set-up curve. The pile capacities of all such remaining piles inferred from the set-up curve should attain a FoS higher than 3 when reporting completion of foundation works to the BD.

The above proposal, if accepted, will save a lot of time in having to wait for achieving a FoS higher than 3 during restrike tests for all piles. A second SEC meeting was held by the BD to consider the above proposal. Figure 5 shows the relaxed proof testing regime by PDA tests for the project finally accepted by the BD.

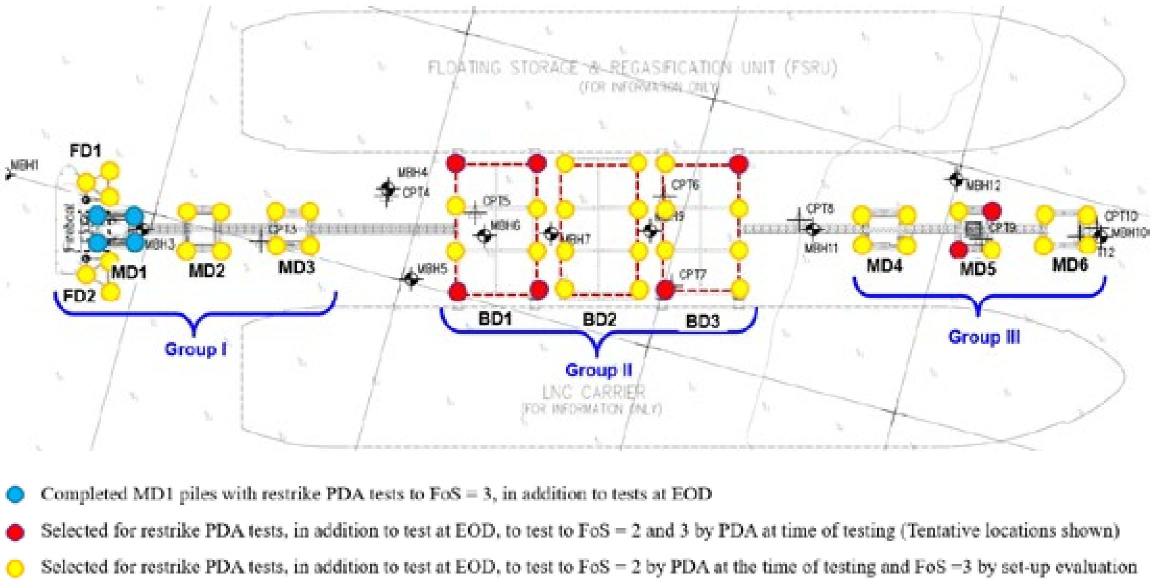

Figure 5: Optimised Testing Proposal for Proof Load Tests at Remaining Dolphins

The piles are grouped into Group 1 to 3 according to similarity in geological conditions as shown in Figure 5. For Group 1 piles, the 4 piles of MD1 completed earlier have already achieved CAPWAP capacities with a FoS higher than 3. No more pile will be selected from this group for restrike PDA tests to achieve this higher FoS. For Group 2 piles, 4 piles have been selected for restrike PDA tests until a FoS higher than 3. For Group 3 piles, the number of selected piles is reduced to 2. With the revised proof testing arrangement, it was possible to complete the foundation works largely within the original construction programme.

8 CONCLUSIONS

The following recommendations are made after reviewing the current practice of design and regulatory control of offshore foundations in Hong Kong.

a. PDA tests with CAPWAP analysis are proven reliable techniques for predicting the pile capacity and can be used as a convenient alternative to pile driving formula for final setting of piles and as replacement for static loading test for verifying the geotechnical capacity of piles. For this reason, the requirement of trial piles should be dropped for offshore piles and the requirement of static loading test for working piles can be waived without jeopardizing safety.

b. From a system reliability point of view, it is much better to design piles with a lower FoS with more extensive PDA testing than to use a less reliable design method with a higher FoS and static loading test for a just a few piles. The current practice should be critically reviewed and revised to cater for the special conditions of offshore foundations.

c. If pile installation and acceptance are based on PDA tests, it will no longer be necessary to rely systematically on theoretical or semi-empirical methods for predicting the geotechnical capacity of piles. A FoS of 3, which is intended to cover the higher uncertainty of such theoretical methods, is considered not necessary and extremely conservative for offshore foundations installed with

PDA testing. Lower FoS as suggested in API codes are considered reasonable and in line with international practice.

d. If the pile capacity predicted by theoretical methods is not reliable, it is unreasonable to require the installed piles to achieve the minimum pile length corresponding to the calculated static capacity. PDA tests can give a much more reliable indicator as to whether the installed pile length is sufficient to achieve the required capacity.

e. For offshore foundation projects, it is important that the installation of piles can be completed quickly and with as little interruption as possible to reduce the risks of damage to unfinished substructure during adverse weather and ocean conditions. Imposed conditions that may cause interruptions to foundation works should be kept to the minimum when approving the foundation plans.

ACKNOWLEDGEMENTS

This paper is published with the permission of CLP Power Hong Kong Ltd. and Hongkong Electric Co. Ltd. The assistance from Mr. Victor Shea in preparing this paper is gratefully acknowledged.

REFERENCES

Ang, A.H-S. and Tang, W.H. 2007. *Probability Concepts in Engineering: Emphasis on Applications to Civil and Environmental Engineering*, 2nd Edition. John Wiley & Sons.

API. 2011. *RP2 GEO: Geotechnical and Foundation Design Considerations*. American Petroleum Institute.

API. 2014. *Planning, Designing and Constructing Fixed Offshore Platforms - Working Stress Design. API Recommended Practice 2A-WSD*. American Petroleum Institute.

Bowman, E.T. and Soga, K. 2003. Creep, ageing and microstructural change in dense granular materials. *Soils and Foundations*, 43(4), 107-117.

Bowman, E.T. and Soga, K. 2005. Mechanisms of setup of displacement piles in sand: laboratory creep tests. *Canadian Geotechnical Journal*, 42, 1391-1407.

Buildings Department (BD). 2022. List of recognized types of piles (downloaded from https://www.bd.gov.hk/doc/en/resources/pre-accepted-materials/CDBRPT.pdf 12 April 2022).

Civil Engineering Office (CEO). 2002. *Port Works Design Manual Part 1 - General Design Considerations for Marine Works*. Civil Engineering Office, Civil Engineering Department, Hong Kong SAR.

Civil Engineering Office (CEO). 2004. *Port Works Design Manual Part 2 - Guide to Design of Piers and Dolphins*. Civil Engineering Office, Civil Engineering Department, Hong Kong SAR.

Coduto, D.P., Kitch, W.A. and Yeung, M-C. R. 2016. *Foundation Design Principles and Practices*, 3rd Edition. Pearson Education, Inc.

Geotechnical Engineering Office (GEO). 1996. GEO Publication No. 1/1996: Pile Design and Construction.

Geotechnical Engineering Office (GEO). 2006. GEO Publication No. 1/2006: Foundation Design and Construction.

Hiley, A. 1922. The efficiency of the hammer blow. Engineering, 673-674, 711-714, 745.

Hussein, M.H., Sharp, M.R. and Knight, W.F. 2002. The use of superposition for evaluating pile capacity. *Geotechnical Special Publication No. 116*, ASCE, 6-21.

Li, K.S., Chan, S.T. and Lam, J. 2003a. An alternative pile driving formula – a preliminary study. *Proc. HKIE Geotechnical Division Annual Seminar*, 179-189.

Li, K.S., Lee, P.K.K. and Lam, J. 2003b. *Chapter 1: Introduction. Design and Construction of Driven and Jacked Piles*, (Editor: K.S. Li). Centre for Research & Professional Development.

Likins, G. and Rausche, F. 2004. Correlation of CAPWAP with static load tests. *Proc. 7th International Conf. on Application of Stresswave Theory to Piles*, 153-165.

Sze, J.W.C., Li, J.C.Y. and Lau, C.K. 2014. Foundation design for a residential development in adverse ground condition at Designated Area of Northshore Lantau. Proc. HKIE Geotechnical Division Annual Seminar, 143-149.

Shea, V., Li, D., Shum,D and Chu, F. 2022. Large diameter open-end steel piled foundations for the Hong Kong Offshore LNG Terminal – design and installation. *Proc. HKIE Geotechnical Division Annual Seminar*.

Vesic, A.S. 1967. Ultimate loads and settlements of deep foundation in sand. *Proc. Symposium on Bearing Capacity and Settlement of Foundations*, (Editor: A.S. Vesic), 53-68.

Effect of Slope Geometries on 3D Slope Stability under the Influence of Infiltration

M S K Hassan, V H Loo

Department of Civil and Construction Engineering, Curtin University Malaysia; CDT 250, 98009 Miri, Sarawak, Malaysia

ABSTRACT

Rainfall-induced slope failure is the most common type of slope failure in Malaysia. Many studies have been carried out to assess the correlation of infiltration to 2D geometric features such as slope inclination. However, the relationship between infiltration and 3D slope geometric features has not yet been widely studied. The aim of this study is to assess the effect of varying slope geometries on slope stability with the influence of rainfall, and to compare the results of the 2D and 3D slope analysis. Seepage and slope stability analysis of homogenous slopes for normal, curved surface and turning corner slopes of varying angles were modelled using the numerical software PLAXIS LE. The 3D analysis demonstrated that multiple shallow failures spread across the sloped surface, which could not be captured by the 2D analysis. The failure modes are similar for the various geometric types of slopes. The results also indicate that the safety factor from the 3D analysis decreases more significantly with the rainfall duration as compared to the 2D analysis. This study changes the perception that a 2D analysis is more conservative than a 3D analysis, which is not always true.

1 INTRODUCTION

Rainfall-induced slope failure is a common type of slope failure that occurs frequently in tropical regions such as East Malaysia, where the annual rainfall ranges from 3300 mm to 4600 mm (Sarawak Government 2021). Slope failures pose a considerable threat to human beings in the surrounding vicinity and cause damages to infrastructure, which result in severe economic losses. Global warming has led to an increase in the frequency and intensity of rainfall events (Huggel et al. 2013) and a surge in the extreme rainfall event conditions (Hausfather 2018). Figure 1 illustrates the variation of the average global temperature and precipitation with their respective trends over the last 120 years (NASA/GISS 2019). The increase in precipitation has caused a rise in the number of annual landslide occurrences (Petley 2012). Therefore, this is a concern as landslides will only increase with time and hence, it must be diligently investigated.

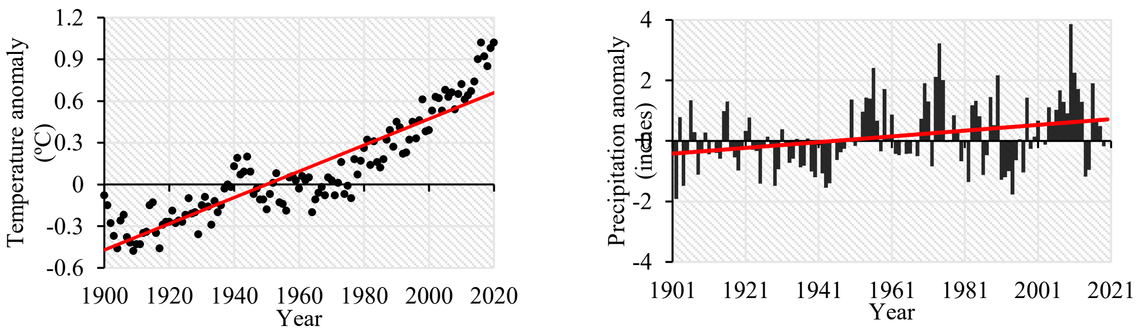

(i) *(ii)*

Figure 1 (i) Average global temperature change and (ii) average global precipitation change (NASA/GISS 2019)

Intensity of rainfall is one of the major factors that affects the stability of the slope. The study carried out by Gasmo, Rahardjo, and Leong (2000) showed that a rainfall event with an intensity of approximately 16 mm/hr would decrease the factor of safety (FoS) by around 10%, while the rainfall intensity of 55 mm/hr would cause a decrease of around 25%. This highlights that an increase in the rainfall intensity has a detrimental effect on the factor of safety. This finding is in line with the study carried out by researchers such as Hossain, Hossain, and Hoyos (2013) and Kristo, Rahardjo, and Satyanaga (2017). It is anticipated that the increase of rainfall intensity would induce more severe slope failures.

Another key characteristic that influences slope stability is the geometry of the slope. Several studies on two-dimensional (2D) slope geometries have been conducted to investigate the effect of slope angle on the stability of the slope (Zakaria et al. 2018; Chatterjee and Murali Krishna 2019; Zhou et al. 2020). In addition, Chatterjee and Murali Krishna (2019) investigated the correlation of 2D slope geometries with infiltration. Their results indicate that an increase in slope angle would decrease the amount of infiltration into the sloped surface, thus reducing the decrease in the FoS during the rainfall event.

Three-dimensional (3D) slope geometric features such as curved surfaces, turning corners, etc can be observed in several man-made slopes in slope engineering, road engineering, etc. Examples of these features have been illustrated in Figure 2. The study carried out by Zhang et al. (2013) showed that these geometrical features can influence the FoS by as much as 20% and affect the failure surface. Based on the literature review, it has been identified that a majority of the studies focused on 2D slope geometry but the correlation between 3D geometric features and infiltration has not yet been well-studied.

Figure 2 Example of (i) curved surfaced slopes at Canada Hill at Miri, Sarawak and (ii) turning corner slopes (Call and Nicholas 2021)

In current industrial practices, running a 3D analysis is not compulsory on the account that a 2D analysis will generally lead to a conservative result, of which the most critical 2D cross-section is identified and analysed. However, studies indicate that a 2D analysis could lead to an inadequate representation of the conditions of slope failures (Stark and Eid 1998; Chaudhary, Fredlund, and Lu 2016). This is because a 2D analysis assumes plane strain conditions and hence, it does not consider the effects of 3D geometry such as convex and concave configurations. Therefore, the actual extent of the failure surface and volume cannot be captured. The understanding that FoS_{3D} is higher than FoS_{2D} is based on research that has not considered the factor of seepage due to rainfall.

Over the last decade, the commercially available 3D slope stability analysis software and advancement in computing technology has seen a major development. Therefore, running a 3D analysis has become affordable as it is cost and time efficient. The objective of this study is to assess the effect of varying 3D slope geometries on slope stability by the influence of rainfall, and to compare the results of the 2D and 3D slope analysis. Three slope geometries: normal, curved surface and turning corner slopes of varying angles were modelled. The following sections will introduce the method used and discuss the results obtained.

2 MATERIAL AND METHODS

The analyses were carried out using the Groundwater and Slope Stability modules of PLAXIS LE by Bentley Systems (Bentley Systems 2022). A seepage analysis was first carried out to obtain the pore pressure distribution, followed by a slope stability analysis to assess the factor of safety of the slope. The methodology can be classified into three stages. The first stage is to validate the model to ensure the ability to perform the required tasks with acceptable accuracy. The second stage involves an analysis of a 3D idealized slope with and without rainfall infiltration. The final stage involves a comparative analysis where 2D slices of the 3D models were extracted and analysed, subjected to the same conditions as the 3D models.

2.1 Validation

A case study by Fredlund, Rahardjo, and Fredlund (2012) was selected to validate the seepage flow of the model. This case was tested and verified experimentally and numerically by the original authors and hence, is of high value for validation purposes. The case involves a 2D multi-layered slope subjected to a constant rainfall flux of 756 mm/hr into the slope. Surface runoff was not considered in the model. A transient analysis with a total duration of 280 seconds was carried out. The total head contours at various timesteps were compared with the original results and identical results were obtained with only minor discrepancies. Figure 3 illustrates a sample of the original and obtained result.

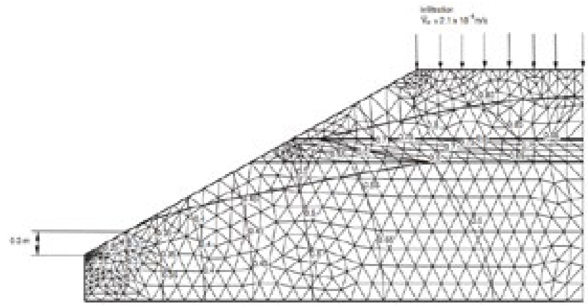

(i)

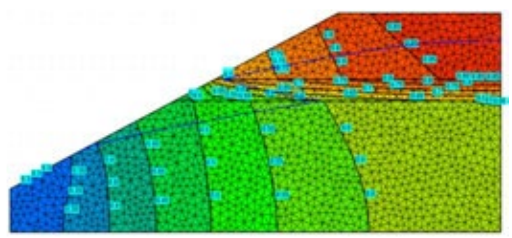

(ii)

Figure 3 (i) Original seepage result at t = 260s (Fredlund, Rahardjo, and Fredlund 2012) and (ii) recreated seepage model

To test the slope stability module, a case study by Leong and Rahardjo (2012) has been selected. The case involves a 3D, single-layered slope overlying bedrock with the water table at the ground surface. An effective stress analysis with varying shear strength parameters was conducted and the soil shear strength was modelled using the Mohr-Coulomb failure criterion. Some of the FoS results have been listed in Table 1 below. The obtained failure surface was comparable to the original result. The accuracy of the validation results obtained from both analyses were acceptable.

Table 1: Comparison of the FoS results of validated model and the case studies

Soil Parameters		Factor of safety (method of analysis)		
Effective friction angle	Effective cohesion	Bishop*	Morgenstern and Price*	Current Study (Morgenstern and Price)
32.0	2.0	0.560	0.660	0.603
32.0	10.6	0.895	0.908	0.942
36.4	10.6	0.990	1.006	1.051

* represents results taken from Leong and Rahardjo (2012)

2.2 Slope geometrical variants

The three types of varying 3D slope geometries include normal, curved surfaces and turning corners. The slope inclination is 45 degrees for all the types. The geometries will be further elaborated in the following paragraphs.

Type 1 is the normal slope. Figures 4 (i) and 4 (ii) illustrate the cross section in 2D (with dimensions in meters) and 3D, respectively. The length and width of the slope was taken as 180 m and 120 m, respectively.

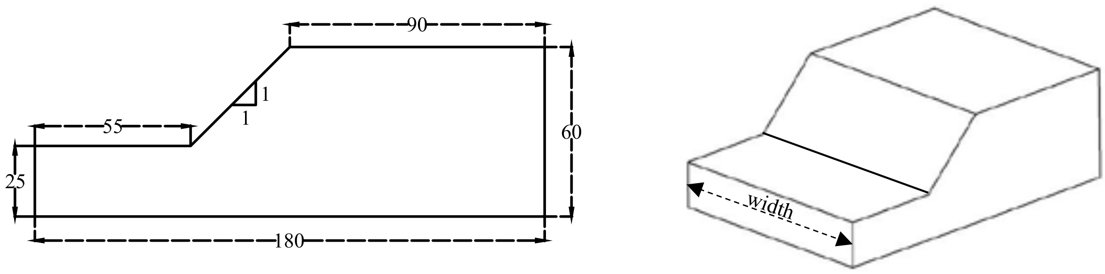

(i) *(ii)*

Figure 4 (i) Cross-sectional view and (ii) 3D view of normal slope

Type 2 is the curved surface slope. Concave and convex curved surface slopes of various curvatures were modelled. The degree of curvature was expressed by the parameter R_{cur} (Zhang et al. 2013) as shown in the following formula:

$$R_{cur} = \frac{L}{W}$$

In equation (1), L is the distance that the sloped surface bulges in (concave) or out (1) (convex) at the toe and crest, and W is the width of the slope which is 120m. The slope retains the same cross-sectional dimensions illustrated in Figure 4. Figure 5 illustrates an example of a concave curved surface slope, convex curved surface and a 3D model of a concaved slope surface. The annotations A, B and C represent the region behind the crest of the slope, the region in front of the slope toe and the sloped surface, respectively. Table 2 (second row) summarizes all the curved surface slope variants that were included in the analysis. The negative values in the table refer to curved surfaces that are in the outward direction.

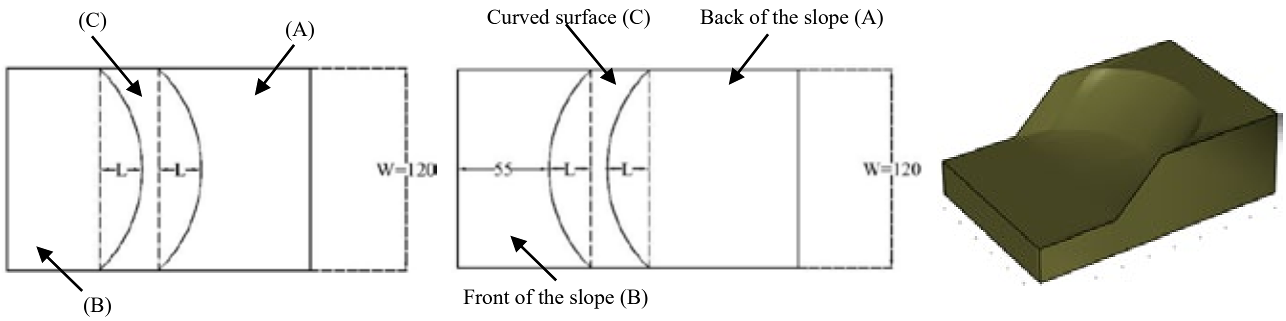

(i) *(ii)* *(iii)*

Figure 5 Plan view of (i) concave, (ii) convex and (iii) 3D concave curved surface slope

Type 3 is the turning corner slope. The turning corner angle (α) is measured from the outside of the slope as displayed in Figure 6. The slope retains the same cross-sectional dimensions as illustrated in Figure 4. Table 2 (third row) summarizes all the variants that were included in the analysis.

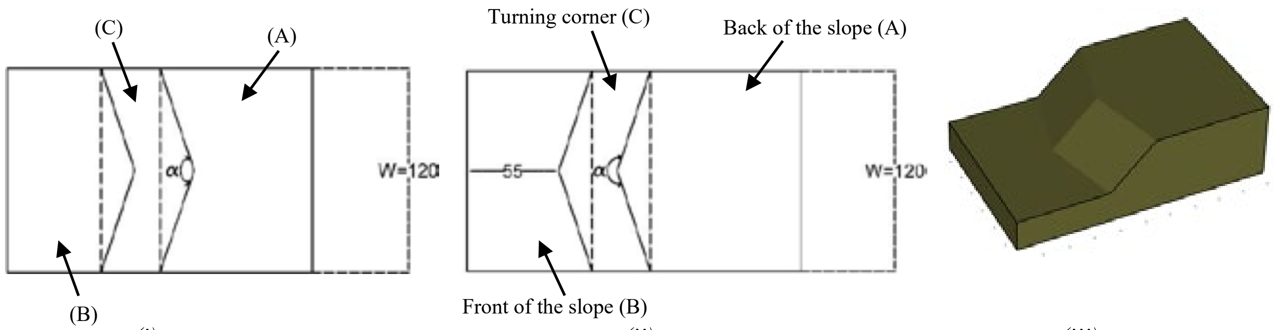

(i) *(ii)* *(iii)*

Figure 6 Plan view of (i) concave, (ii) convex and (iii) 3D convex turning corner slope

Table 2: Curved surface and turning arc slope variants

Geometrical variant type	Shape parameter	Concave			Normal	Convex		
Curved surface slope (ref. Figure 5)	R_{cur}	3/6	2/6	1/6	0	-1/6	-2/6	-3/6
Turning corner slope (ref. Figure 6)	α	90°	120°	150°	180°	210°	240°	270°

2.3 Seepage analysis

The Groundwater module of PLAXIS LE is a finite element (FEM) analysis software that has been used for the seepage analysis.

2.3.1 Hydraulic soil properties

The study adopted the soil properties of sand from West Malaysia referring to research from Gofar and Lee (2008). Table 3 lists the hydraulic properties of soil. The soil water characteristic curve (SWCC) and permeability function curves were based on the van Genuchten (1980) model as illustrated in Figure 7.

Table 3: Hydraulic properties of sand soil (Gofar and Lee 2008)

Soil parameters	Symbol	Value	Unit
Saturated volumetric water content	w_s	0.450	-
Saturated permeability	k_s	3.4×10^{-4}	m/s

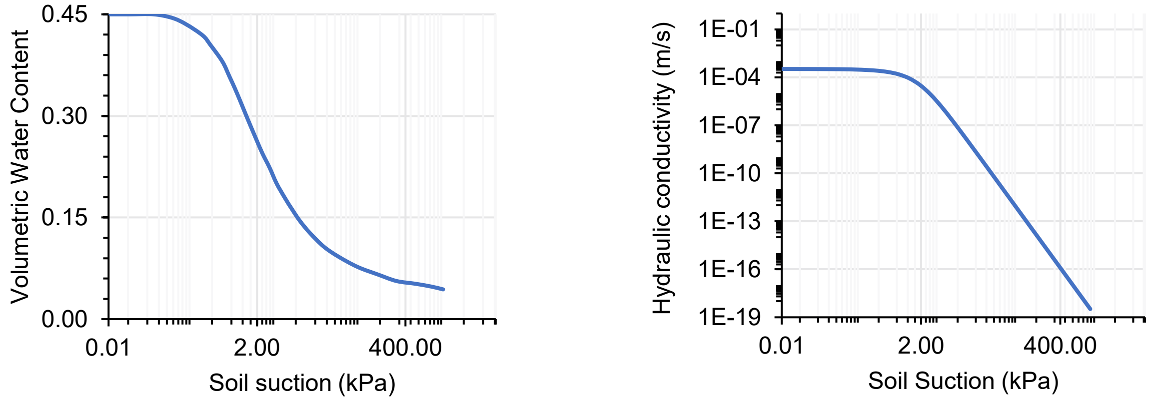

(i) *(ii)*

Figure 7 Recreated (i) SWCC and (ii) permeability function curve of the sand soil (Gofar and Lee 2008)

2.3.2 Hydraulic boundary conditions

Figure 8 illustrates the seepage model of the 2D and 3D normal slope. The initial water table was set at the mid heights of each of the sides, in which a constant head (A) was applied below the water table at both side regions of the slope. The side regions above the water table were set to zero nodal flux (B). To model rainfall, a vertical flux (C) with a constant intensity of 35 mm/hr for a total duration of 6 hours was applied to the ground surface.

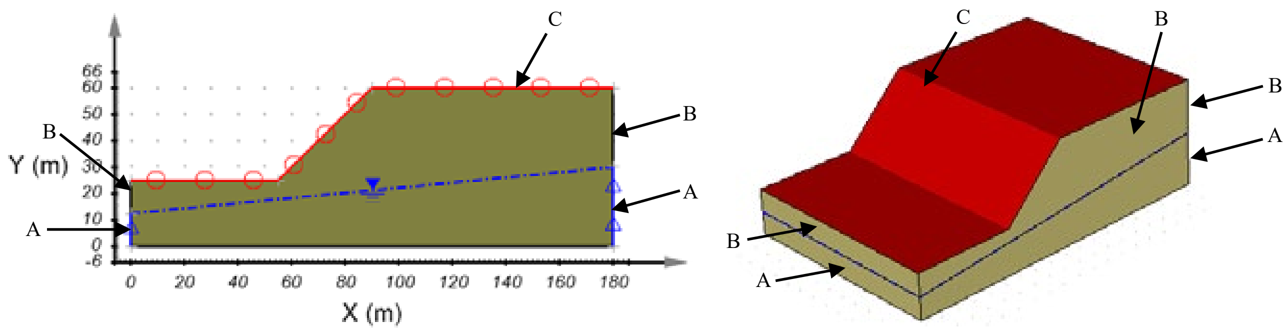

(i) *(ii)*

Figure 8 Hydraulic boundary conditions for (i) 2D normal slope and (ii) 3D normal slope

2.4 Slope stability analysis

The Slope Stability module of PLAXIS LE is a limit equilibrium (LEM) analysis software under Bentley systems. The linear Phi-b model (Bentley Systems 2020) enables the modelling of unsaturated shear strength taking into account the matric suction and has been adopted for this study.

2.4.1 Mechanical and material soil properties

Table 4 lists the bulk unit weight and shear strength parameters used for the modelling, referring to the study by Gofar and Lee (2008).

Table 4: Soil mechanical and material properties based on Gofar and Lee (2008)

Parameter	Symbol	Value	Unit
Unit weight	γ	19.44	kN/m^3
Effective friction angle	ϕ'	35.0	°
Unsaturated friction angle	ϕ^b	14.0	°
Effective cohesion	c'	1.0	kN/m^2

2.4.2 Search method for critical slip surface and calculation methods

The most critical failure surface was identified through a trial-and-error slip search process known as the grid and tangent method, which assumes circular failure surfaces. For each 3D analysis, over 103,000 trial surfaces were analysed, while for the 2D analysis, over 1500 surfaces were evaluated. For the calculation method, the Morgenstern and Price's method, which satisfies both the force and moment equilibrium equations, was used. Morgenstern and Price's method assumes that the interslice shear forces are a function of normal forces. The half-sine function, which has been commonly used Rawat and Gupta (2016) and Beyene (2017) was adopted.

3 RESULTS AND DISCUSSION

3.1 Distribution of pore pressure

Figure 9 illustrates a comparison of the 3D (elevation view) and 2D normal slope seepage analysis result at the 0-hr and 6-hr rainfall duration. For the 2D results, it was observed that with the duration of the rainfall, there is a decrease in the matric suction near the sloped surface (annotation A on Figure 9 (iii) and (iv)). This is because as rainfall infiltrates the soil, the volumetric water content increases which results in a decrease in the matric suction as illustrated in Figure 7 (i). In addition to this, the water table rose minorly (yellow line indicated by annotation B in Figure 9 (iii) and (iv)) and the formation of the wetting front at the sloped surface was observed (yellow line indicated by annotation C in Figure 9 (iii)). These findings are in line with the 3D seepage results. These observations are common for all the geometric variants.

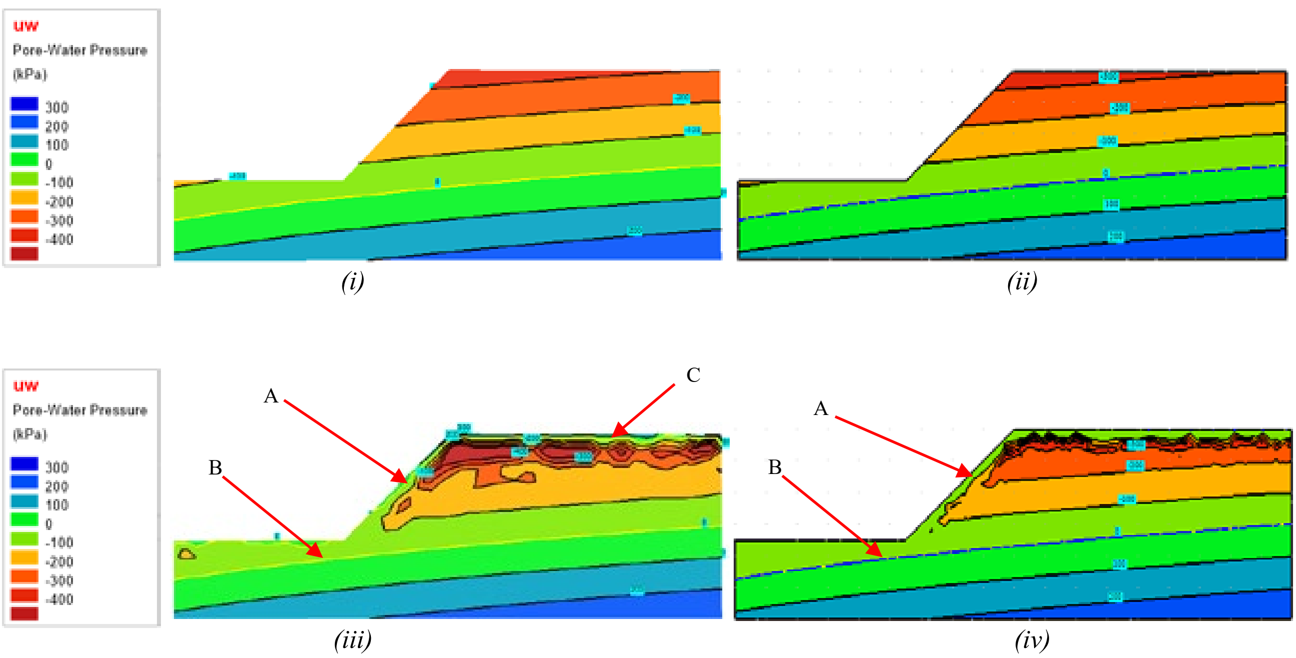

Figure 9 Pore pressure distribution of the (i) 0-hr timestep for the 3D (elevation view) normal slope, (ii) 0-hr timestep for the 2D normal slope, (iii) 6-hr timestep for the 3D (elevation view) normal slope and (iv) 6-hr timestep for the 2D normal slope

3.2 Comparison of failure surfaces when utilizing a 3D analysis over a 2D analysis

Figure 10 demonstrates a comparison of the slope stability results at the 1.5-hr and 6-hr rainfall duration for the 3D and 2D normal slope. Initially, the FoS of both 3D and 2D results are similar and their critical slip surfaces behave as a global failure (Figures 10 (i) and (iii)). However, with the rainfall infiltration, the slip surface becomes localized and shallow for both cases. The 3D results show numerous shallow failure surfaces (FoS < 1) spreading throughout the sloped surfaces (critical slip surface for the 3D model has been marked in black in Figure 10 (ii)).

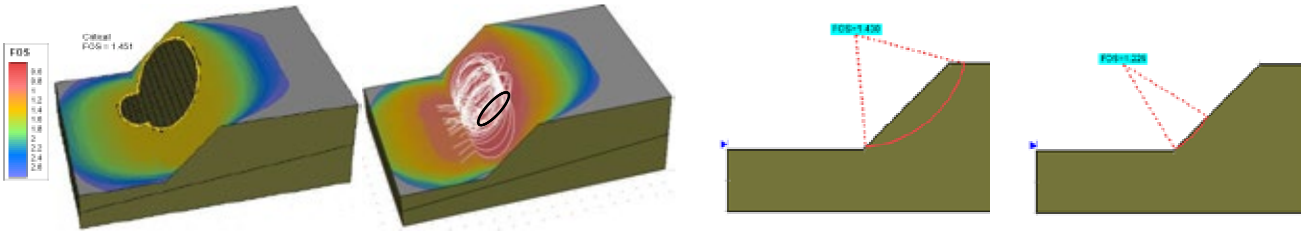

(i) *(ii)* *(iii)* *(iv)*

Figure 10 Failure surface for the 3D normal slope at (i) 1.5-hr and (ii) 6-hr, and the 2D model at (iii) 1.5-hr and (iv) 6-hr

Figure 11 displays an example of the spread of the failures with the duration of rainfall for a 3D curved surface slope. Similar to the 2D models, the slope initially experiences a global failure. However, as the rainfall event progresses, instead of a single slip surface, the result demonstrates several shallow failures (FoS < 1) spreading across the sloped surface (critical slip surface has been marked in black in Figures 11 (ii) and (iii)). This is due to the continuous decrease in matric suction as the rainfall duration increases. The normal, curved surface and turning corner slopes exhibited identical features. This result is significant as it highlights that a 3D analysis is able to detect the spread of multiple shallow failures.

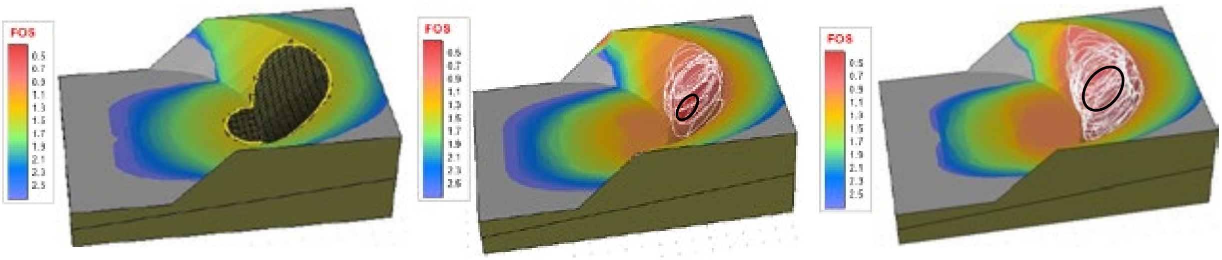

(i) *(ii)* *(iii)*

Figure 11 Failure surfaces (FoS<1) for concave curved surface with R_{cur} = 3/6 at (i) 1.5-hr, (ii) 4.5-hr and (iii) 6-hr

The failure surface for the turning corner slopes was unique where the failure surfaces varied with change in the turning corner angle. Figures 12 (i) and (ii) demonstrate that for concave turning corner slopes of decreasing turning angle, the failures were spread across both sides of the slope. Conversely, Figures 12 (iii) and (iv) illustrate that for convex turning corners of increasing turning angle, the failures were concentrated at the ridge of the slope (critical slip surface has been marked in black in Figure 12). A potential cause for this observation is that a higher concentration of positive pore pressures is distributed near the ridge of the slope for the convex variants than the concave variants, resulting in a narrow extent of slope failures at the ridge of the slope. This demonstrates how the geometry of the slope will affect the distribution of rainfall as well as the distribution of slope failure surfaces. This finding could not have been observed from a 2D analysis as it assumes plane strain conditions.

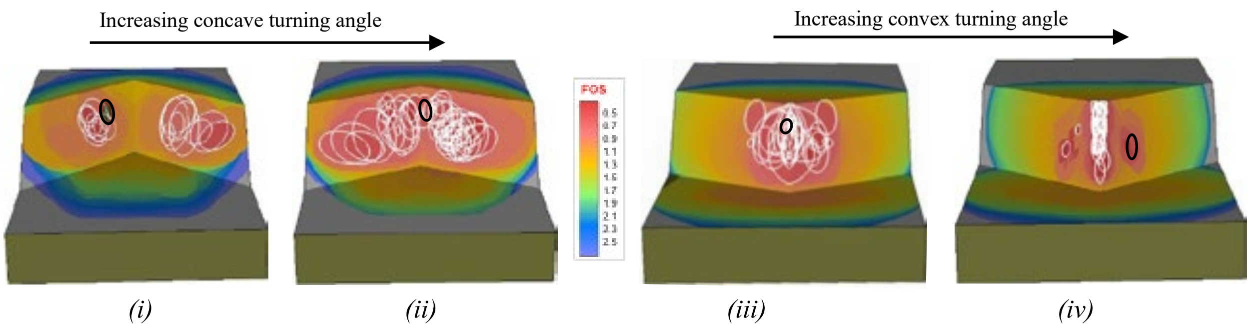

Figure 12 Spread of failures of slip surfaces (FoS<1) for turning corner slopes at the 6-hr duration for (i) concave 90, (ii) concave 120, (iii) convex 240 and (iv) convex 270

3.3 Changes of FoS for 3D analysis

For the models in which multiple shallow failures were observed, the 10 most critical failures were selected to evaluate the FoS of the slope. The range of the critical FoS values for these models were considered using range bars in the graph with the average critical FoS represented by the points in the graph. The type of turning corner has been selected to illustrate the changes of FoS with the duration of the rainfall event as illustrated in Figure 13. It is observed that the FoS decreases nonlinearly as the rainfall event progresses. This is due to the decrease in the shear strength that occurs due to the decrease in the matric suction. A greater decrease in the FoS for convex variants when compared to the concave variants was also observed. This is potentially because the convex slopes have a greater surface area behind the slope crest when compared to the concave counterparts, giving a larger area of infiltration for the convex slopes. These findings are common amongst all the geometric variants.

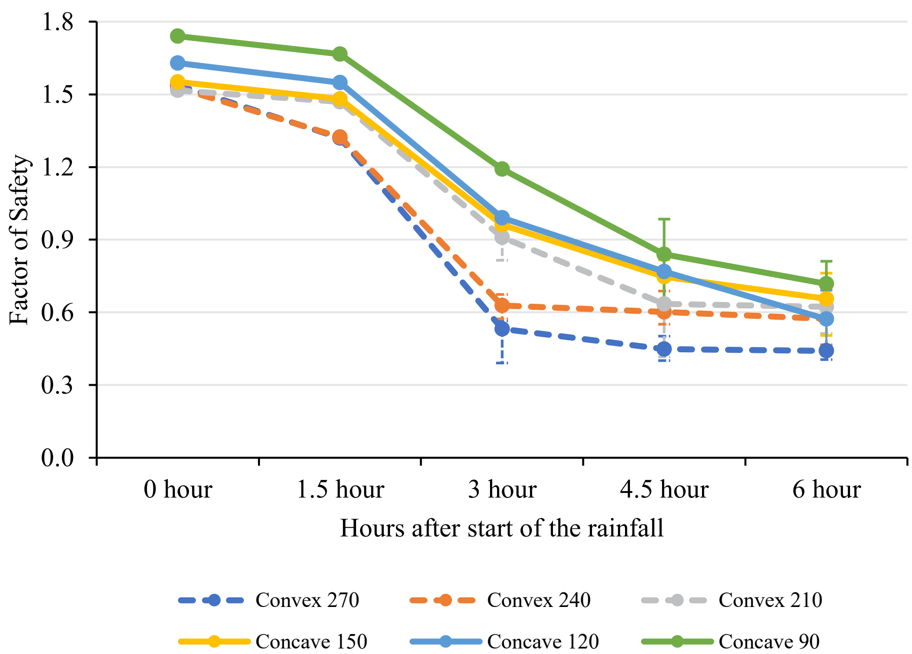

Figure 13 Variation of the factor of safety for the turning corner slopes

3.4 Changes of FoS for 3D analysis and 2D analysis

To illustrate the comparison between the 2D and 3D analysis results, a single case has been selected from each geometric variant type. The results have been plotted in Figure 14. The changes in the FoS for 2D analysis is much more gradual compared to the 3D analysis. The FoS for the critical slip surface of the 3D analysis decreases by around 51%, 54% and 71% for the normal, curved surface and turning corner slope, respectively. However, the FoS decrease for the 2D analysis is only around 16%, 17% and 11% for the normal, curved surface and turning corner slope respectively. As the rainfall event progresses, the FoS of the 3D results are below 1 but the FoS of 2D results are still above 1. While the conservative 3D results were observed for failures that are shallow in depth and small in volume, it is nonetheless a substantial finding as it changes the perception of our common understanding that a 2D slope stability analysis will always yield a conservative result when compared to a 3D analysis. The 3D analysis enables the distribution of pore water in 3 dimensions, which increases various potential failure surfaces of slope. The trend in the change of the FoS for the other models are similar.

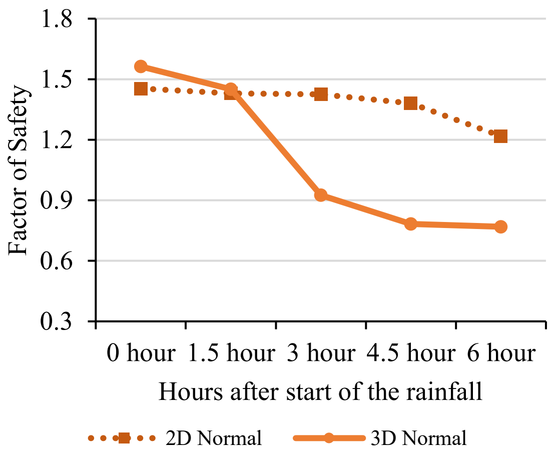

(i)

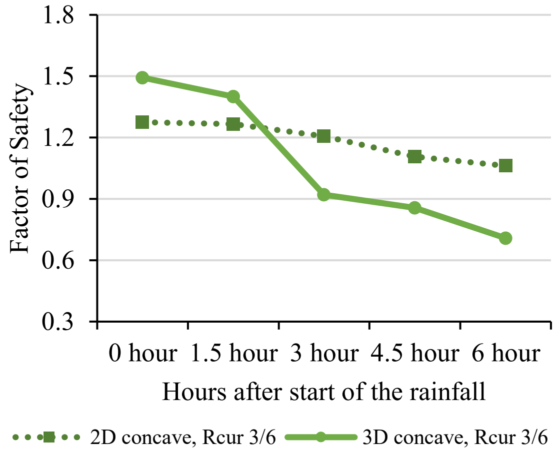

(ii)

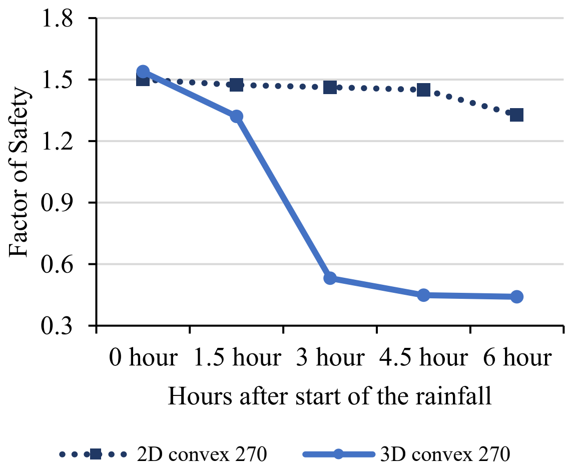

(iii)

Figure 14 Comparison of the factor of safety for the (i) 2D and 3D normal slope, (ii) 2D and 3D concave R_{cur} 3/6 curved surface slope and (iii) 2D and 3D concave 270 turning corner slope

4 CONCLUSIONS

Rainfall-induced slope failure is the most common type of slope failure in Malaysia. In the past, most of the studies' focus on rainfall-induced slope failures are in 2D analysis. The influence of rainfall to the 3D geometric features has not yet been well-studied. The objective of this study is to evaluate the effect of utilizing a 3D analysis over a 2D analysis for slopes of varying geometry subjected to rainfall. Homogenous sandy slopes with a 1:1 (horizontal to vertical) slope inclination was modelled using the numerical software PLAXIS LE. A seepage analysis was carried out to obtain the pore pressure distribution for a specific rainfall event. The slope stability analysis was then assessed using Morgenstern and Price's limit equilibrium method. During rainfall, for all slope geometries, the 3D analysis indicated that several shallow failures occur across the sloped surfaces. Similar trends in the decrease of the FoS with the duration of the rainfall were observed for slope geometries such as the normal, curved surface and turning corner slopes. When comparing the 2D and 3D analysis results without rainfall, the FoS from the 2D analysis is generally lower. However, the FoS from the 3D analysis decreases more significantly as the rainfall event progresses while the FoS from the 2D analysis decreases gradually. Hence, resulting in a conservative result from the 3D analysis. This study demonstrated that a 3D analysis is advantageous to capture shallow and localized slope failures spreading across the sloped surface. This study gives new insights of understanding slope failures under the influence of rainfall, which ultimately highlights the fact that running a 3D seepage and slope stability analysis is of paramount importance. Furthermore, affordable computing technology has become more accessible over the last decade and is continuing to advance even now. Therefore, running a 3D analysis should be encouraged amongst the engineers to provide a more sustainable and cost-effective design in the industry.

ACKNOWLEDGEMENTS

This research was supported under the budget for final year projects by Faculty of Engineering and Science, Curtin University Malaysia. The authors would also like to thank Ir. Dr. Wong Kwong Soon, the unit leader, and the lecturers Dr. Tang Fu Ee and Dr. Yong Leong Kong for their constructive comments during the proposal and final presentation. The authors would also like to express gratitude towards Dr. Choo Chung Siung of Swinburne University for his comments during the final presentation. Also, special thanks to Mr. Sheikh Zaffrullah, who aided in providing technical support.

REFERENCES

Bentley Systems. 2020. SVSLOPE 2D/3D limit equilibrium slope stability analysis - Theory manual. 1–235.

Bentley Systems. 2022. PLAXIS LE - Limit equilibrium geotechnical application. https://www.bentley.com/en/products/product-line/geotechnical-engineering-software/plaxis-le.

Call and Nicholas. 2021. Open Pit Mining Geotechnical Consulting Services - Call & Nicholas, Inc. 2021. https://www.cnitucson.com/openpit.html.

Chatterjee, D. & Murali Krishan, A. 2019. Effect of slope angle on the stability of a slope under rainfall infiltration. *Indian geotechnical journal,* 49(6): 708–17. https://doi.org/10.1007/s40098-019-00362-w.

Chaudhary, K.B., Fredlund, M. & Lu, H. 2016. Three-dimensional slope stability: Geometry effects. In *Tailings and mine waste '16*. Colorado.

Fredlund, D. G., Rahardjo, H. & Fredlund, M.D. 2012. *Unsaturated soil mechanics in engineering practice*. John Wiley & Sons, Inc. https://doi.org/10.1002/9781118280492.

Gasmo, J. M., Rahardjo, H. & Leong, E.C. 2000. Infiltration effects on stability of a residual soil slope. *Computers and Geotechnics*, 26(2): 145–65. https://doi.org/10.1016/S0266-352X(99)00035-X.

Genuchten, M. Th. van. 1980. A closed-form equation for predicting the hydraulic conductivity of unsaturated soils. *Soil science society of America journal*, 44(5): 892–98. https://doi.org/10.2136/sssaj1980.03615995004400050002x.

Gofar, N. & Lee, M.L. 2008. Extreme rainfall characteristics for surface slope stability in the Malaysian peninsular. *Georisk,* 2(2): 65–78. https://doi.org/10.1080/17499510802072991.

Hossain, J., Hossain, M.S. & Hoyos, L. R. 2013. Effect of rainfall on stability of unsaturated earth slopes constructed on expansive clay. In *Geo-Congress 2013: Stability and Performance of Slopes and Embankments III,* 417–25. American Society of Civil Engineers (ASCE). https://doi.org/10.1061/9780784412787.042.

Huggel, C., Khabarov, N., Korup, O. & Obersteiner, M. 2013. Physical impacts of climate change on landslide occurrence and related adaptation. In *Landslides*, 121–33. Cambridge University Press. https://doi.org/10.1017/cbo9780511740367.012.

Leong, E. C. & Rahardjo, H. 2012. Two and three-dimensional slope stability reanalyses of bukit batok slope. *Computers and geotechnics,* 42: 81–88. https://doi.org/10.1016/j.compgeo.2012.01.001.

NASA/GISS. 2019. Global temperature | Vital signs – climate change: vital signs of the planet. https://climate.nasa.gov/vital-signs/global-temperature/.

Petley, D. 2012. Global patterns of loss of life from landslides. *Geology*, 40(10): 927–30. https://doi.org/10.1130/G33217.1.

Sarawak Government. 2021. Geography. sarawak.gov.my. https://sarawak.gov.my/web/home/article_view/159/176/?id=159.

Singh, R., Umrao, R.K. & Singh, T.N. 2017. Hill slope stability analysis using two and three dimensions analysis: A comparative study. *Journal of the geological society of India*, 89(3): 295–302. https://doi.org/10.1007/s12594-017-0602-2.

Stark, Timothy D. & Hisham T. Eid. 1998. Performance of Three-Dimensional Slope Stability Methods in Practice. *Journal of Geotechnical and Geoenvironmental Engineering* 124 (11): 1049–60. https://doi.org/10.1061/(asce)1090-0241(1998)124:11(1049).

Zakaria, Z., Sophian, I., Sabila, Z.S. & Jihadi, L. H. 2018. Slope safety factor and its relationship with angle of slope gradient to support landslide mitigation at Jatinangor education area, Sumedang, West Java, Indonesia." *IOP conference series: Earth and environmental science*, 145(1): 0–8. https://doi.org/10.1088/1755-1315/145/1/012052.

Hausfather, Z. 2018. Explainer: What Climate models tell us about future rainfall. *Carbon brief.* https://www.carbonbrief.org/explainer-what-climate-models-tell-us-about-future-rainfall.

Zhang, Y., Chen, G., Zheng, L., Li, Y. & Zhuang, X. 2013. Effects of geometries on three-dimensional slope stability. *Canadian geotechnical journal*, 50(3): 233–49. https://doi.org/10.1139/cgj-2012-0279.

Zhou, Y., Qi, S.C., Fan, G., Chen, M.L. & Zhou, J.W. 2020. Topographic effects on three-dimensional slope stability for fluctuating water conditions using numerical analysis. *Water (Switzerland)*, 12(2): 615. https://doi.org/10.3390/w12020615.

3D Geological Modelling and Management System

Y B Liu[1], T Xiao[2], L M Zhang[3]
Department of Civil and Environmental Engineering, The Hong Kong University of Science and Technology, Hong Kong SAR, China

ABSTRACT

A three-dimensional (3-D) geological model has been established for Hong Kong using existing borehole data in order to facilitate detailed site investigations for future engineering projects. This study aims to digitalise ground investigation data in Hong Kong, develop easy-to-use tools for 3-D borehole management and visualisation, and eventually establish 3-D geological models for Hong Kong. The modelling capabilities include geological data retrieval and processing, geological cross-section creation, fence diagrams and 3-D model construction. With approximate 90,000 boreholes processed, 3-D virtual boreholes can be created and managed using ArcGIS Pro. Further, cross-sectional diagrams, fence diagrams and 3-D models can be created and presented. The 3-D geological model established shows the complexity of Hong Kong geological formation layers. Building a 3-D geological model based on machine learning or artificial intelligence is proved to be a feasible way to provide an accurate evaluation of soil layering. The interpreted cross-sections and constructed fence diagrams help engineers and geologists to better understand the complicated sub-surface profiles in a 3-D way, and provide estimates of the volumes of different types of soil locally. The 3-D model will become a design tool for future city and infrastructure planning and constructions.

1 INTRODUCTION

Hong Kong has a high population density and lacks the supply of flat lands, inducing associated social issues such as housing shortages. To meet the demand, decentralize the population from over-occupied urban areas and alleviate social problems, a series of land reclamation projects or new town projects have been launched. However, since the enactment of the Protection of the Harbour Ordinance in 1997, environmental problems associated with land reclamation have been a concern and land reclamation has dropped around 80% (CEDD, 2022). To accommodate more citizens and growing urbanization, the development of more land is initiated again in recent years. In particular, the feasibility of the East Lantau Metropolis or Lantau Tomorrow, has been evaluated recently. A regional geological map of East Lantau is shown in Figure 1, which mainly consists of rhyolite dykes and granite. Still, land reclamation requires thorough ground investigations, assessment of related risks and satisfaction of sustainability principles. To simultaneously reach the objectives of sustainability and minimising the risks resulted from the lack of understanding of subsurface conditions, it is crucial to understand the seabed conditions before conducting land reclamation (Dong et al., 2014; Hack et al., 2005).

A huge number of reports from ground investigations has been obtained over the years in Hong Kong, including borehole data and results of laboratory tests. If these data are processed and managed properly, it will be valuable in preventing or mitigating ground risks at an early stage, and facilitating project management by a robust and realistic evaluation of project proposal and costs.

[1] E-mail: yliued@connect.ust.hk
[2] E-mail: xiaote@ust.hk
[3] E-mail: cezhangl@ust.hk

It is understood that advanced computations empower faster data collection, management and modelling in multi-dimensions (Aleksandrov et al., 2019; Balsa-Barreiro and Fritsch, 2018). Taking advantage of technological advances, 3-D geological visualisation is ubiquitous around the world (Self et al., 2012; Pan et al., 2018). However, the engineering community in Hong Kong mainly uses 2-D maps (Xiao et al., 2017), such as borehole sections, geological profiles and plans. It is rare for engineers or geologists to visualise in 3-D format or construct 3-D geological models using common modelling platforms, such as RockWorks, Leapfrog, GOCAD, and Civil 3D. These platforms are not very satisfactory for large-scale, complicated geological modelling. Hence, it is beneficial and essential to develop user-friendly toolboxes involving data management and 3-D geological modelling for Hong Kong. 3-D modelling and visualisation enables better understanding of the geological environment because of direct representation of data in 3-D space, which is more exact, direct and dynamic (Shao et al., 2011). Not only 3-D modelling provides innovation to geological and geotechnical study, it also analyses the geological formation, geological structures, attributes associated with geology and geotechnical parameters (Gong et al., 2004; Collon et al., 2015; Wang et al., 2015). Therefore, the 3-D modelling technique will bring significant changes in geological data management and display, providing a scientific basis and technical support for engineering decisions (Shao et al., 2011; Wu and Xu, 2004).

Developing methodologies, proposing standards of 3-D geological model and facilitating the ability of decision making on geo-environmental implications hence become the driving force of this study. Several digital databases, including buildings, road network, drainage system, land use planning, marine traffic density, marine resources, terrain elevation and seabed level, marine ecological system, geohazards, geology and ground investigation records, are collected (Figure 1), with the help of several governmental departments, such as Civil Engineering and Development Department, Lands Department, and Marine Department. The development of the geological modelling and management system is presented, taking a 3-D marine geological model of East Lantau as an example. Further possibilities and limitations of the developed analytical toolbox and 3-D modelling capabilities are evaluated in this study.

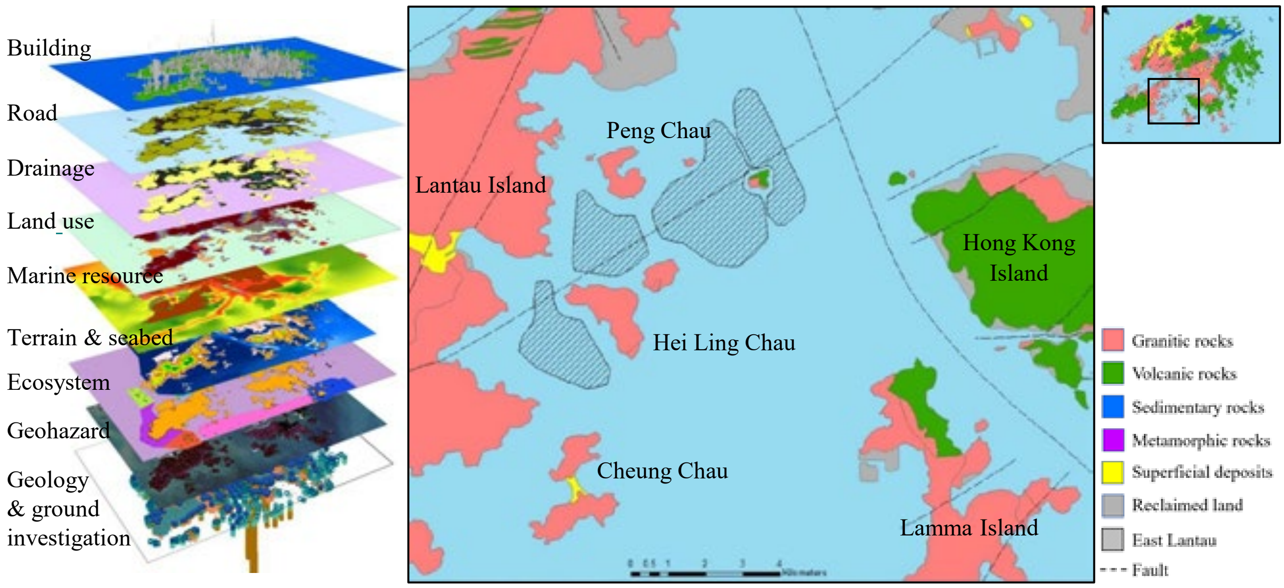

Figure 1: Hong Kong geo-databases and digitalised geology for East Lantau

2 DEVELOPMENT OF 3-D GEOLOGICAL MODELLING AND MANAGEMENT SYSTEM

The 3-D geological modelling and management system is developed for entire Hong Kong. East Lantau is presented as a case study to demonstrate the functions of the system. The methodology is implemented in three phases (Figure 2), including data preparation, development of associated toolboxes and 3-D geological model construction. All the development is based on ESRI ArcGIS Pro which provides various geoprocessing tools for 2-D and 3-D interactions and supports Python programming and web-based data visualisation and sharing, although it is not originally designed for 3-D geological modelling. Considering that ArcGIS platform has been widely used in the industry, it is the most suitable platform for the development of the geological modelling and management system.

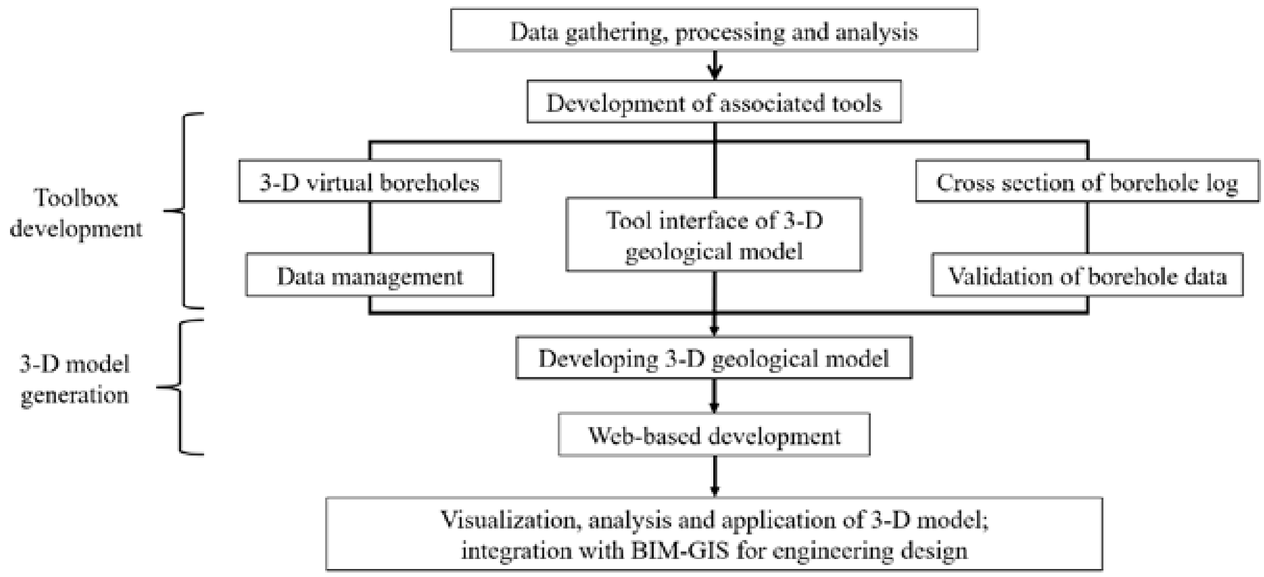

Figure 2: Methodology for developing a 3-D geological model

2.1 Borehole data preparation

We first digitalise available borehole data in AGS files and ground investigation reports from the Geotechnical Engineering Office, and conduct data clearance by correcting errors in coordinates, depth and material type and removing repeated records. Data verification is then performed by checking the conformity between borehole logs and geological maps, and between borehole collars and topographic maps. A total of approximately 90,000 boreholes with 667,000 records is finally verified in the entire Hong Kong, of which East Lantau has about 780 marine boreholes with 4,900 records, and converted into a ".csv" file for importing to ArcGIS. A verified record consists of location ID, report ID, hole ID, coordination, ground level, final depth, top depth, bottom depth, and geology code, as shown in Figure 3. Top and bottom elevations of each record in the toolbox are obtained by subtracting top depth and bottom depth from the ground level, respectively.

	A	B	C	D	E	F	G	H	I	J	Y	Z
1	Location ID	Report No	Hole ID	Location Type	Easting	Northing	Ground Le	Final Dept	Depth Top	Depth Bas	Geology Code	Geology Code 2
2	R_19722 H_BH-02	R_19722	H_BH-02	CP+RO+RC	821926.48	815848.66	-1.9	21.93	0	4.95	SAND	Marine deposit
3	R_19722 H_BH-02	R_19722	H_BH-02	CP+RO+RC	821926.48	815848.66	-1.9	21.93	4.95	9	CLAY	Marine deposit
4	R_19722 H_BH-02	R_19722	H_BH-02	CP+RO+RC	821926.48	815848.66	-1.9	21.93	9	13	SAND	Marine deposit
5	R_19722 H_BH-02	R_19722	H_BH-02	CP+RO+RC	821926.48	815848.66	-1.9	21.93	13	14.5	SAND	Alluvium
6	R_19722 H_BH-02	R_19722	H_BH-02	CP+RO+RC	821926.48	815848.66	-1.9	21.93	14.5	17.9	SAND	Grade V-IV rocks
7	R_19722 H_BH-02	R_19722	H_BH-02	CP+RO+RC	821926.48	815848.66	-1.9	21.93	17.9	20.23	GRANITE	Grade III-I rocks
8	R_19722 H_BH-02	R_19722	H_BH-02	CP+RO+RC	821926.48	815848.66	-1.9	21.93	20.23	21.93	GRANITE	Grade III-I rocks

Figure 3: Examples of borehole records in an Excel file

Figure 4 presents the frequency of 12 geological types in the borehole records of East Lantau, including N/A, fill, beach deposit, marine deposit, estuarine deposit, debris flow deposit, alluvium, colluvium, residual soil, grade V-IV rock, grade III-I rock and others. During modelling, the non-informative N/A and others are directly removed. Some geological groups, such as beach deposit, debris flow deposit, estuarine deposit, colluvium and residual soil, account for only small percentages comparing with the dominant groups, such as marine deposit, alluvium and grade V-IV rock. They are combined with the dominant group according to the stratigraphic property, forming five main groups, namely fill, marine deposit, alluvium, grade V-IV rock and grade III-I rock.

In addition, each borehole record has different lengths (for example, the first record in Figure 3 is 4.95 m and the fourth record is 1.5 m) and they should take different weights in geological modelling. For this purpose, every section of borehole log (i.e., a record in Figure 3) is discretised into a series of points with the same geological type. For example, if vertical resolution is 1 m, the first and forth records will be discretised as 5 and 2 points.

The geo-databases in Figure 1, such as territory boundary and seabed level, are useful in shaping the 3-D geological model into the region of interest and controlling the groundwater level of the model. When constructing the whole geological model for Hong Kong, terrain elevation is helpful in defining the boundary between mountain and air. Note that geological structures are not explicitly modelled in the current study, and they will be considered in the future.

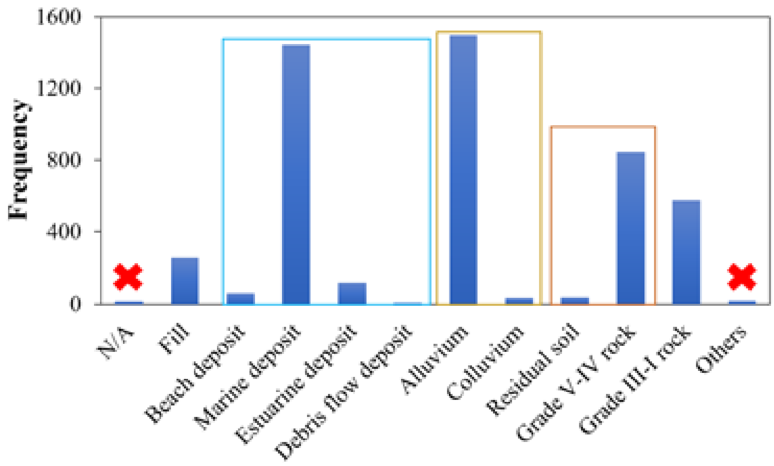

Figure 4: Distribution of geological type in borehole data

2.2 Toolbox development

This study develops three ArcGIS toolboxes through Python programming, including 3-D virtual borehole toolbox, cross-section profiling toolbox and 3-D geological modelling toolbox, to enhance the capability of ArcGIS Pro in geological modelling and management. It is also flexible for users familiar with basic Python skills to customize the toolboxes.

2.2.1 3-D virtual borehole

This tool helps to manage borehole data systematically and visually in 3-D space. The primary principle is to make use of “arcpy.Array” and “arcpy.Polyline” in ArcGIS Pro to form 3-D polylines of boreholes by connecting 3-D points of records. The first step is to convey the delimited files containing borehole data in “.csv” to dBASE table by “arcpy.conversion.TableToTable” so that the borehole data is easier to be managed and searched in ArcGIS Pro as a geodatabase. Linking the top elevation and bottom elevation point together of each row from the borehole log table with functions of "arcpy.SearchCursor" and "arcpy.UpdateCursor" enables 3-D virtual borehole visualisation.

2.2.2 Cross-section profiling

This tool allows users to focus on geological profile of interest by generating a 2-D cross-section of borehole log, elevation profile and groundwater level. The first phase is to obtain Z values and M values along the cross-section line using the function of "arcpy.StackProfile_3d", where Z defines the elevation value along the cross-section line while M implies the measured distance from the beginning of the cross-section line (Figure 5). With the points at the beginning and at the end of the cross-section line, coordinates of each borehole log (existing x and y value) could be converted into M values by applying the Euclidean distance. Top and bottom elevations are transformed into Z values simultaneously by ensuring conversion under the same Borehole ID to avoid mixing up borehole logs.

Horizontal and vertical exaggerations are optional if users would like to expand or squeeze the section view. It is suggested that users compress the horizontal distance by inputting a number smaller than 1 as the horizontal distance is usually much greater than the vertical distance. The temporary feature class output is a cross-section polyline profile. With the temporary polyline feature and function of "arcpy.analysis.Buffer", borehole logs in the cross-section view hence could be constructed as polygons, together with the polyline feature of terrain.

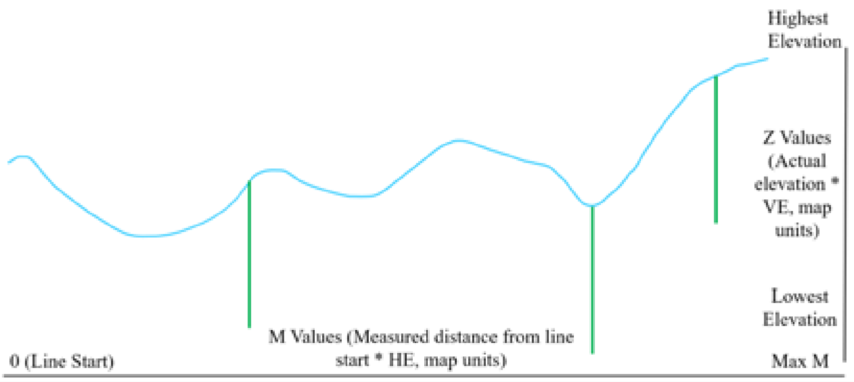

Figure 5: A surface profile and borehole log using M and Z values obtained

2.2.3 3-D geological modelling

This tool aims to provide automatic modelling of 3-D geological conditions in a region defined by users, lessening the coding requirements. The first step is to set up an interface for users to define the boundary where they would like to model. A 3-D geological modelling algorithm is then selected with necessary model parameters. The output file extension is ".nc", Network Common Data Form (NetCDF), which supports the storage of 3-D array data (Unidata, 2022). With a designated output path and file name, the 3-D geological model could be added and viewed in ArcGIS Pro.

This study makes use of three machine learning algorithms including k-nearest neighbours (kNN), support vector machine (SVM) and random forest (RF) (scikit-learn, 2022) for 3-D geological modelling. In the toolbox, parameters of each algorithm are set at default values, in which the number of neighbours used in kNN is 15, the kernel coefficient gamma of SVM is 0.5 and the number of trees in RF is 45. The borehole data is randomly divided into 7:3 for training and test sets. A unified parameter, anisotropy ratio δ, is introduced to eliminate the anisotropic effect between the horizontal scale and vertical scale in geological setting, as:

$$x' = \frac{x}{\delta} \quad (1)$$

where x = the horizontal coordinates and x' = the transformed horizontal coordinates.

The F-1 score is used for model comparison, which is defined as a harmonic mean of the precision and recall of model performance. The precision accounts for the ratio of true positive outcomes to all the positive outcomes, and the recall means the ratio between the true positive results and the number of results that should have been positively identified. Specifically, the F-1 score is calculated as follows:

$$F1 = \frac{2(precision \times recall)}{(precision + recall)} \quad (2)$$

F-1 score value of 1 is the best while 0 is the worst performance, reflecting the goodness of the interpolated geological model.

In addition to the 3-D geological modelling, the information entropy at each location is also estimated to measure the uncertainty of the interpolated model (Zhao and Wang, 2019; Xiao et al., 2021). The entropy shows the level of "surprise" with respect to the possible results, and is defined as:

$$H(Y) = -\sum_{i=1}^{n} P(y_i) \log P(y_i) \quad (3)$$

where $P(y_i)$ = probability of possible geological condition, estimated from the machine learning algorithms; y_i = possible geological condition (i.e., fill, marine deposit, alluvium, grade V-IV rock and grade III-I rock); n = number of possible geological conditions (i.e., 5 in this study). A larger information entropy means a higher geological modelling uncertainty.

3 CASE STUDY OF EAST LANTAU

East Lantau, one of the major future developments in Hong Kong, is taken as a case study. The selected region is between 820,000 and 830,000 Easting, and between 810,000 and 819,000 Northing (Figure 6). Within the selected region, about 780 marine boreholes with average drillhole depth of 33 m and an average water depth of 6 m are employed for demonstration. After combining the stratigraphy types as mentioned in section 2.1, the ratio of fill : marine deposit : alluvium : grade V-IV rock : grade III-I rock is 5:33:32:18:12, showing that marine deposit and alluvium are the top two strata in East Lantau.

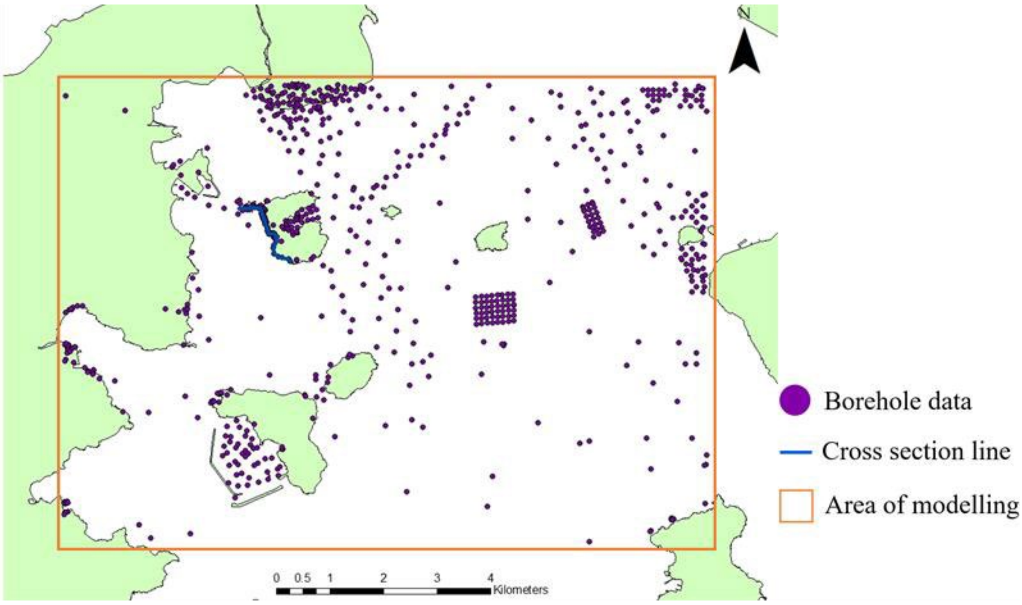

Figure 6: Boreholes in East Lantau

3.1 3-D borehole data management

The interface of the 3-D virtual borehole toolbox is illustrated in Figure 7(a). This tool creates 3-D virtual drillholes from the borehole log table, offering easier borehole data management and searching functions of the borehole information, as shown in Figure 7(b). If users would like to review boreholes information that they are interested in, they can click the created 3-D drillholes to view the details, as illustrated in Figure 7(c). The soil or stratigraphic layer is symbolized by a different colour, supporting another method of validation on the 3-D geological model.

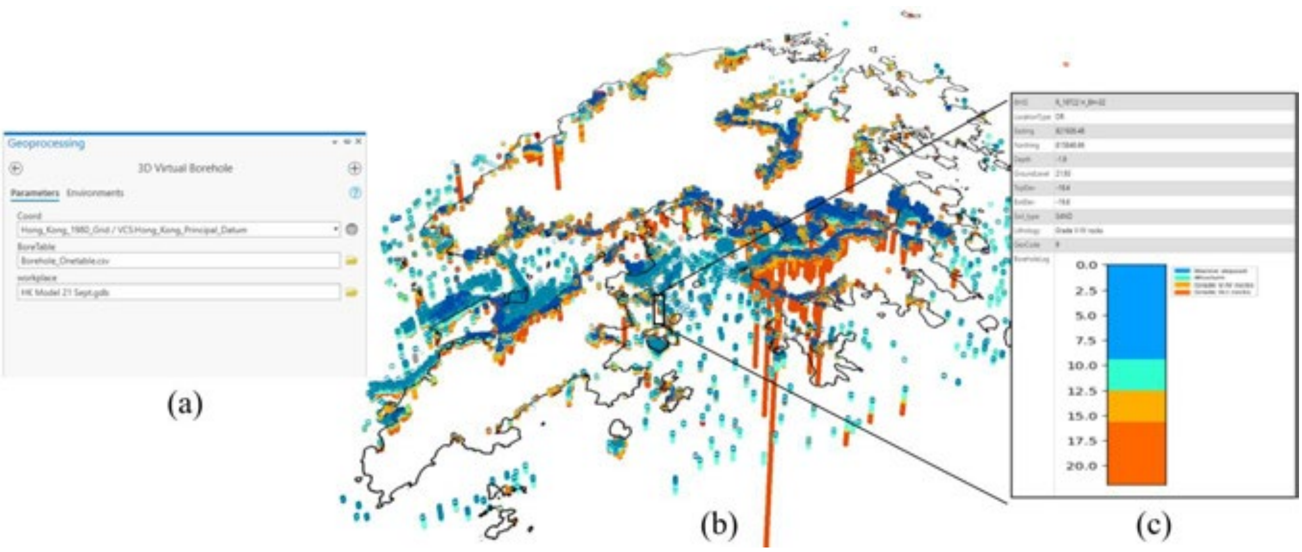

Figure 7: 3-D virtual boreholes: (a) toolbox interface; (b) all digitalised boreholes; (c) details of one borehole

3.2 Cross-section of borehole logs

The interface of the cross-section profiling toolbox is shown in Figure 8(a), which chooses borehole data within 100 m along the west Peng Chau (i.e., the cross-section line in Figure 6) to produce borehole logs with 10 times vertical exaggeration and 0.5 times horizontal exaggeration. Figure 8(b) presents the cross section, in which the reference elevation profile is obtained from the digital terrain and seabed elevation model and boreholes are selected within the specified searching radius. It is important to accurately trace the position of each exploration and the related borehole log along the cross-section line. The thickness of each layer in each borehole is depicted, which is derived from the distance between the top and bottom elevation field.

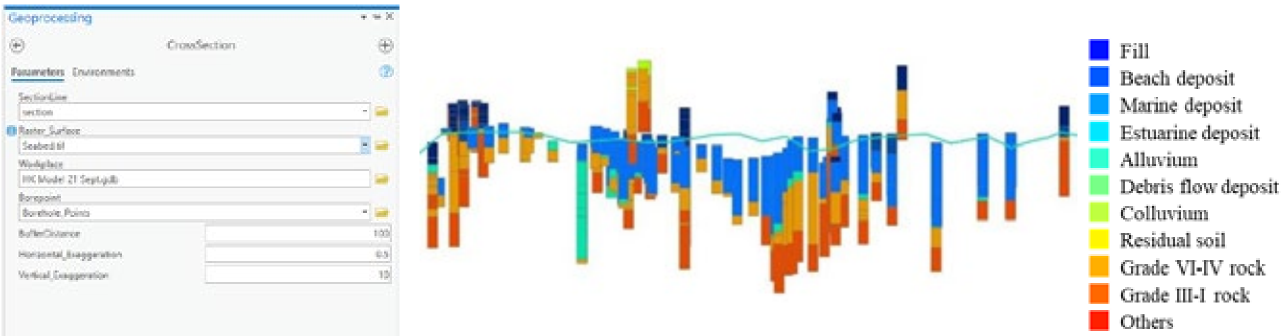

(a) (b)

Figure 8: Cross-section of borehole logs: (a) toolbox interface; (b) an example along the west Peng Chau

3.3 3-D geological model and associated modelling uncertainty

The toolbox interface of the 3-D geological model is shown in Figure 9(a), allowing users to choose the boundary that they are interested in and a specified machine learning algorithm (available algorisms: kNN, SVM, and RF). Figure 9(b) show a 3-D geological model with space resolution of 50 m by 50 m by 1 m and the fence diagram of the East Lantau generated from kNN with an anisotropy ratio of 100 and a neighbour size of 15. Anisotropy ratio refers to the scale weight difference between the horizontal scale and vertical scale. Positions of the faces can also be adjusted to locations of interest using sliders in ArcGIS Pro when users need to focus on specified subsurface sections.

This toolbox also measures the modelling uncertainty through information entropy. Figure 9(c) demonstrates the information entropy of the geological model in Figure 9(b). The uncertainty of bedrock is much smaller than other stratigraphic layers. This is reasonable since the unknown points in deeper elevation are predicted from observed points that mostly belong to grade III-I rock. The zone between Lantau Island and Hei Ling Chau, the area around Peng Chau and the open area of the East of Hong Kong Island have higher uncertainties. Hence, more detailed site investigation works could be considered on these areas, bringing about higher affirmation on the subsurface conditions.

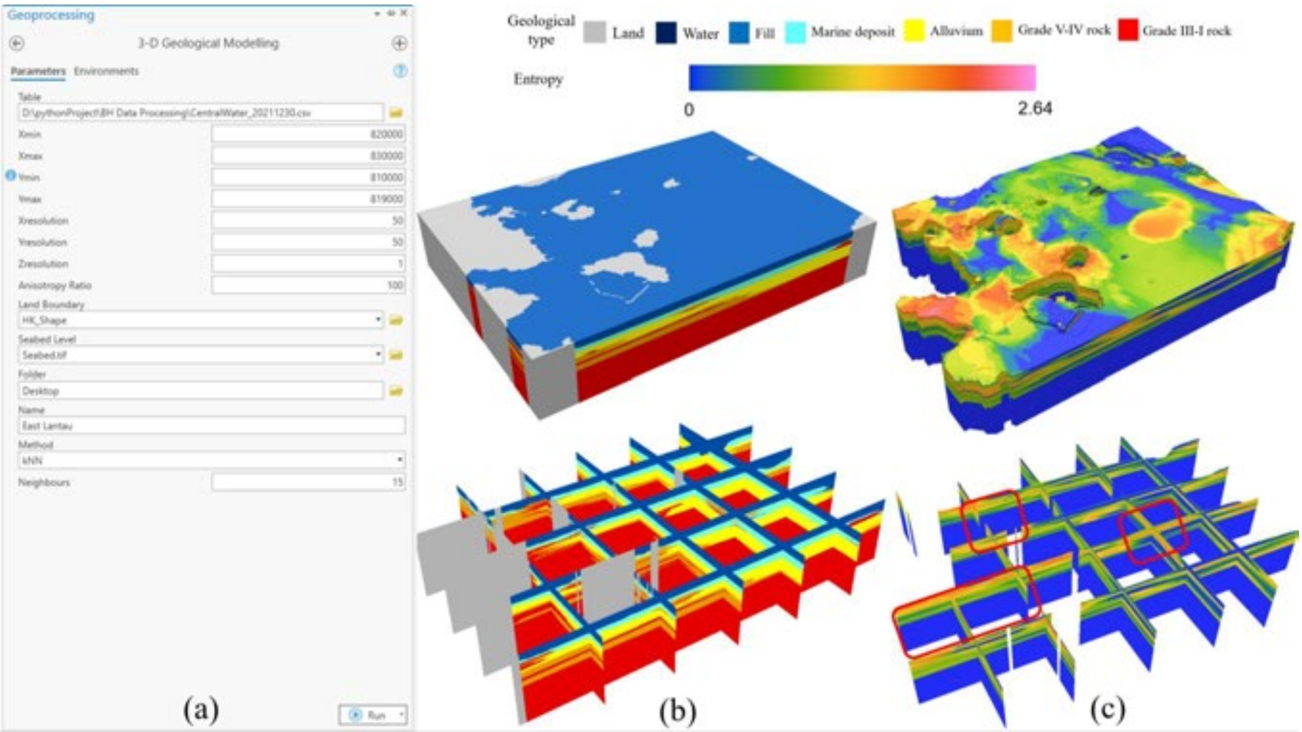

Figure 9: 3-D geological model: (a) toolbox interface; (b) a 3-D model of East Lantau using kNN; (c) associated information entropy of the 3-D model

4 IMPACT OF ANISOTROPY RATIO IN GEOLOGICAL MODELLING

This section compares the geological models of East Lantau generated using all the three implemented algorithms (i.e., kNN, SVM, and RF) with five typical anisotropy ratios (i.e., δ = 1, 10, 100, 1000, and 10000 in Eq. (1)). Figure 10 provides their F-1 scores for both training and test sets. Note that a weighted average of F-1 score for each class is applied to avoid the effect of the imbalance classification. The F-1 score of kNN and RF algorithms for the training set at different anisotropy ratio is highly overlapped at 0.95. Meanwhile, the F-1 score of kNN for the test set reaches the maximum value (i.e., 0.7) at an anisotropy ratio δ of 100. Such an anisotropy ratio means that two borehole points with horizontal separation distance of 100 m is equivalent to two borehole points with vertical separation distance of 1 m. This is similar to many studies on characterising spatial variability of soils, which found that the horizontal scale of fluctuation is about one or two orders of magnitude larger than the vertical scale of fluctuation (Phoon and Kulhawy, 1999).

Figure 11 further compares the detailed geological profiles of west Peng Chau using kNN with three anisotropy ratios. The original borehole logs are shown in Figure 11(a) for reference. Visually, when δ is less than 100 (Figure 11(b)), the estimation of stratigraphy is more dominated by vertical separation of observed samples, and the information from nearby boreholes (e.g., 100 m away) are not fully used. On the other hand, if δ is greater than 100 (Figure 11(d)), the horizontal separations provide higher importance than the vertical separations, which undermines the nature of the geological formation and leads to the overfitting of stratigraphy. As a result, to prevent modelling from wrongly predicted by the dominance of vertical separations and overfitting from horizontal separations, an optimal anisotropy ratio δ should be determined during the construction of a 3-D geological model and δ = 100 appears most reasonable in this case study (Figure 11(c)).

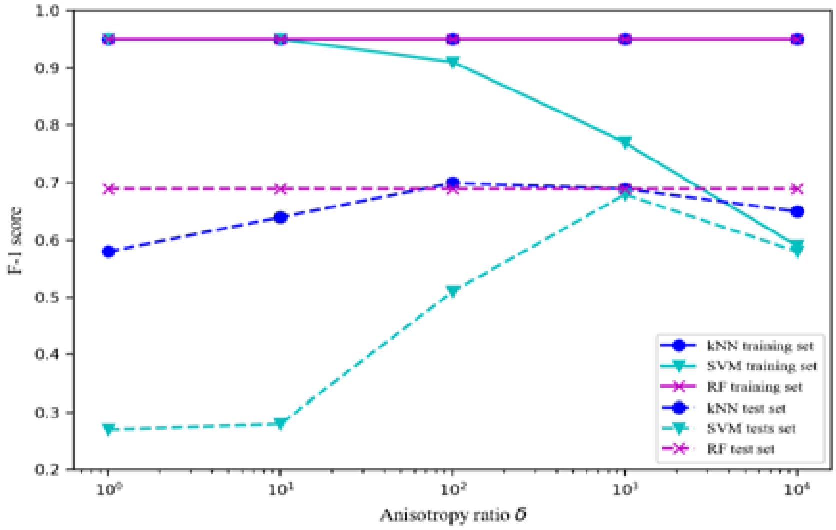

Figure 10: Comparison of weighted average of F-1 score among algorithms

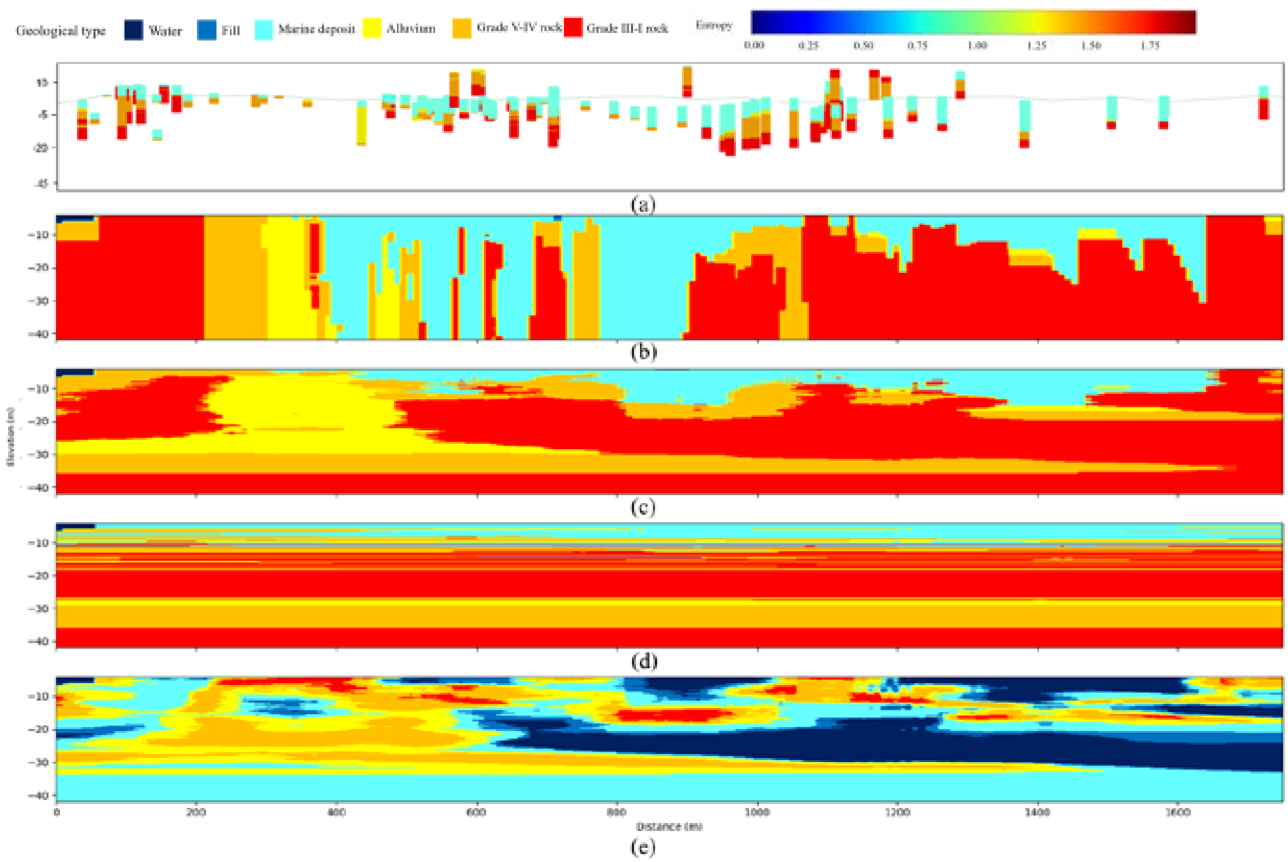

Figure 11: Example of west Ping Chau: (a) original borehole log; (b)-(d) predicted geological profiles using kNN with anisotropy ratio $\delta = 1$, 100, and 10,000, respectively; (e) information entropy of the geological model with $\delta = 100$

5 CONCLUSIONS AND RECOMMENDATIONS

A set of ArcGIS tools have been developed for territory-wide borehole data management and 3-D geological model visualisation in Hong Kong. East Lantau is used as an example to illustrate the results of toolboxes and 3-D geological model construction.

Data clearance is required to eliminate duplicates or typographical errors before applying the toolbox and building the 3-D geological model. The 3-D borehole log and cross-section borehole log further provide visualised tools to validate the borehole data, enhancing the quality and quantity of the input data.

The 3-D geological model is established by machine learning algorithms. An anisotropy ratio is introduced to eliminate the anisotropic effect between the horizontal scale and vertical scale in geological setting. Information entropy is provided to quantify the uncertainty of the model. With the aid of fence diagrams or cross sections obtained from the 3-D model, geologists or engineers can have a better understanding of the local geological conditions and the complex subsurface profiles. In addition, it is reminded that a geological model is a tool for conducting a more effective site investigation work instead of substitution. Whenever new borehole data is acquired from site investigation, they in turn can be employed to verify or improve the geological model so that the reliability of subsequent geotechnical or structural design can be enhanced due to a great reduction in uncertainties.

Web-based ArcGIS map service can be further developed in the future so that the public can access and view the borehole data or 3-D geological model and use the developed toolboxes without installing ArcGIS platforms, providing much smoother interactions among engineers, governmental agencies and the public.

ACKNOWLEDGEMENTS

The authors acknowledge the financial support from Eunsung O&C Offshore Marine and Construction (project No. EUNSUNG19EG01) and the data support from the Geotechnical Engineering Office of the Civil Engineering and Development Department, the Government of the Hong Kong Special Administrative Region.

REFERENCES

Aleksandrov, M., Diakité, A., Yan, J., Li, W., and Zlatanova, S. 2019. Systems architecture for management of BIM, 3D GIS and sensors data. *ISPRS Annals of the Photogrammetry, Remote Sensing and Spatial Information Sciences*, IV-4/W9: 3–10.

Balsa-Barreiro, J., and Fritsch, D. 2018. Generation of visually aesthetic and detailed 3D models of historical cities by using Laser Scanning and digital photogrammetry. *Digital Applications in Archaeology and Cultural Heritage*, 8: 57–64.

Civil Engineering and Development Department (CEDD). 2022. *Role of Reclamation in Hong Kong Development*, <https://www.cedd.gov.hk/filemanager/eng/content_954/Info_Sheet3.pdf> (accessed March 15, 2022).

Collon, P., Steckiewicz-Laurent, W., Pellerin, J., Laurent, G., Caumon, G., Reichart, G., and Vaute, L. 2015. 3D geomodelling combining implicit surfaces and Voronoi-based remeshing: A case study in the Lorraine Coal Basin (France). *Computers & Geosciences*, 77: 29–43.

Dong, M., Neukum, C., Hu, H., and Azzam, R. 2014. Real 3D geotechnical modeling in engineering geology: A case study from the inner city of Aachen, Germany. *Bulletin of Engineering Geology and the Environment*, 74(2): 281–300.

Gong, J., Cheng, P., and Wang, Y. 2004. Three-dimensional modeling and application in geological exploration engineering. *Computers & Geosciences*, 30(4): 391–404.

Hack, R., Orlic, B., Ozmutlu, S., Zhu, S., and Rengers, N. 2005. Three and more dimensional modelling in geo-engineering. *Bulletin of Engineering Geology and the Environment*, 65(2): 143–153.

Pan, X., Guo, W., Aung, Z., Nyo, A. K. K., Chiam, K., Wu, D., and Chu, J. 2018. Procedure for establishing a 3D geological model for Singapore. *Proceedings of GeoShanghai 2018 International Conference: Transportation Geotechnics and Pavement Engineering*, 81–89.

Phoon, K. K. and Kulhawy, F. H. 1999. Characterization of geotechnical variability. *Canadian Geotechnical Journal*, 36(4): 612–624.

scikit-learn. 2022. <https://scikit-learn.org/stable/user_guide.html> (accessed March 15, 2022).

Self, S. J., Entwisle, D. C., and Northmore, K. J. 2012. *The Structure and Operation of the BGS National Geotechnical Properties Database. Version 2.* British Geological Survey Report IR/12/056.

Shao, Y., Zheng, A., He, Y. and Xiao, K. 2011. 3D geological modeling and its application under complex geological conditions. *Procedia Engineering*, 12: 41–46.

Unidata. 2022. Network Common Data Form (NetCDF). Boulder, CO: UCAR/Unidata, <https://www.unidata.ucar.edu/software/netcdf/> (accessed March 15, 2022).

Wang, Y., Zhao, H., Sheng, Y., and Kang, N. 2015. Construction and application of 3D geological models for attribute-oriented information expression. *Journal of Applied Science and Engineering*, 18(4): 315-322.

Wu, Q., and Xu, H. 2004. On three-dimensional geological modeling and visualization. *Science in China Series D: Earth Sciences*, 47(8): 739–748.

Xiao, T., Zhang, L. M., Li, X. Y. and Li, D. Q. 2017. Probabilistic stratification modeling in geotechnical site characterization. *ASCE-ASME Journal of Risk and Uncertainty in Engineering Systems, Part A: Civil Engineering*, 3(4): 04017019.

Xiao, T., Zou, H. F., Yin, K. S., Du, Y. and Zhang, L. M. 2021. Machine learning-enhanced soil classification by integrating borehole and CPTU data with noise filtering. *Bulletin of Engineering Geology and the Environment*, 80(12): 9157–9171.

Zhao, T. and Wang, Y. 2019. Determination of efficient sampling locations in geotechnical site characterization using information entropy and Bayesian compressive sampling. *Canadian Geotechnical Journal*, 56(11): 1622–1637.

A New Digital-based Approach to Automate and Optimize Geotechnical Design

Alvin K M Lam, Andrew T F Wong, K P Chan
Arup, Hong Kong, China

ABSTRACT

Geotechnical engineers always work with complicated terrains and geologies, which are usually interpreted from the topographical survey, LiDAR data, geophysical survey and ground investigation boreholes. In the old days, these data were mapped or modelled but could only be visualized or transformed to 2D sections for subsequent design, which may not be easily visualized in a 3D space. With the advancement of computing power and the development of digital tools, they enable engineers to work and visualize their design in a 3D environment. This paper will showcase the application of Rhinoceros 3D (Rhino) in various geotechnical designs. With the aid of Grasshopper, which is a visual programming language running within Rhino, some traditional spreadsheet-based designs can be automated in a new digital-based platform. This paper will discuss the workflow and algorithms of applying the Grasshopper visual program to assist in site formation and foundation designs supplemented by case examples, which include the determination of the pile rockhead level, the calculation of the rock and soil cone volumes, the visualization of the borehole stratigraphy, the automation of soil nail arrangement over complex terrain, the development of the excavation profile with multiple platforms and the full excavation and lateral support (ELS) system, etc. The application will also be extended to create model inputs for geotechnical analysis such as Oasys PDisp through COM Interface and PLAXIS through Jupyter Notebook.

1 INTRODUCTION

We are living in a Digital Era benefited from the advancement of the computer power. The development of digital tools enables engineering industry being evolved to a new level of 3D visualization and design environmental. It improves the design capability to handle complex geotechnical problems in a holistic manner. It also enables design optimization and engineering analysis to be carried out in an efficient way.

Rhinoceros 3D (Rhino) is one of the 3D modeling programs available in the market. Rhino has been widely used in architectural and product designs. It can create, edit, analyze, document, render, animate, and translate curves, surfaces, solids, point clouds, and polygon meshes with no limits on complexity, degree, or size, which are particularly suitable for dealing with complex topographies and geological profiles of the geotechnical works. Grasshopper is a graphical algorithm editor included with Rhino. It is a visual programming tool, which requires no knowledge of programming or scripting, but still allows designers to develop algorithms to deal with geometries in various shapes. In this paper, the Author will showcase the applications of Rhino with Grasshopper in various geotechnical designs. The application will also be extended to create model inputs for geotechnical analysis. However, the adopted programs for geotechnical applications in this Paper are not unique and exhaustive.

2 DESIGN WORKFLOW AND ALGORITHM

2.1 Mapping design workflow

Mapping of the current design workflows can assist in identifying areas that could most benefit from the design automation. The workflow interface starts with data "Sources" from different disciplines or clients as inputs and the design product "Receivers" as outputs. These inputs and outputs are in the form of "Data Sets", which are generally represented by drawing, spreadsheet, analytical model, etc. The workflow processes will consist of dataset being transformed or manipulated to a new dataset by means of a "Process". Data sets shall be connected to processes and the processes shall generate new data sets, one after the other. The "Processes" generally consists of calculation, data extraction, decision making, etc. Figure 1 shows an example of design workflow for determination of the pile founding level.

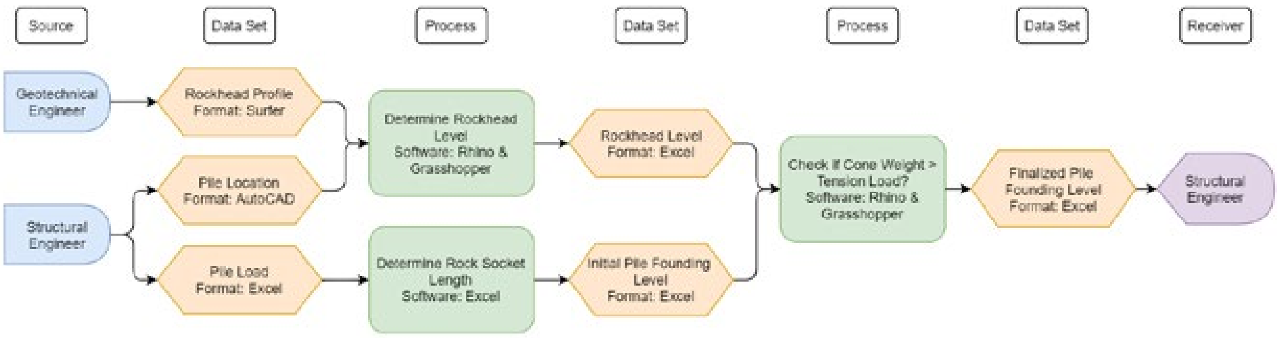

Figure 1: Example of design workflow for determination of rockhead level for rock socketed pile

2.2 Design Algorithm in Grasshopper

Once the design processes are identified, the adequate tools to automate the processes shall be selected. Following the example in Figure 1, the "Process" to determine the pile founding level can be automated by Grasshopper algorithm. First, define the circles representing the piles as a set of curves and the rockhead surface as a boundary representation (BREP) object. The rockhead surface can be generated from programmes such as Surfer as a set of points or Leapfrog as a mesh imported into Rhino and converted into BREP object or a patch surface. Second, project the circular curves onto the BREP surface. Third, find the lowest points of the projected circles onto the BREP using the bounding box function in Grasshopper. Finally, extract the z-coordinates of the lowest points, which represent the rockhead level of the piles. The algorithm is illustrated in Figure 2. Once the algorithm is set, it can generally be applied to other projects with no limit on number of piles.

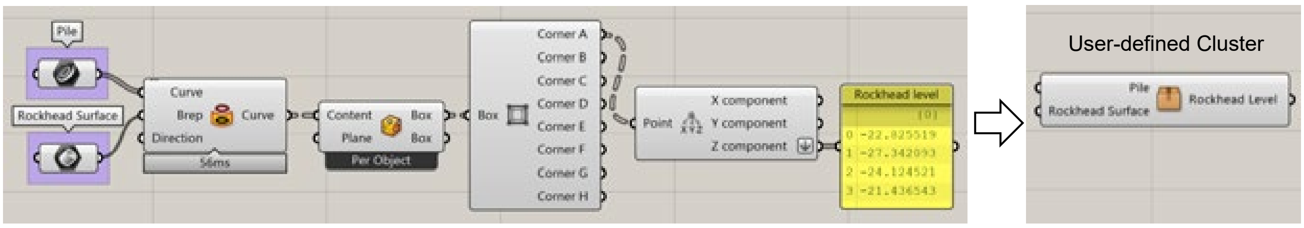

Figure 2: Algorithm in Grasshopper to determine rockhead level for 4 numbers of piles

Geotechnical design often involves complex geometries. The function categories of "Surface", "Mesh" and "Intersect" in Grasshopper are highly applicable for geotechnical works. These enable the design engineer to create site topography, geological stratum, site formation and excavation profiles as surfaces or meshes in various shapes. It can evaluate the surface and mesh properties such as the area, centroid, dimension, relationships with nearby points, curvature, direction, etc. The "Intersect" function also enables splitting/trimming and the determination of union, difference and intersection of regions, meshes and BREPs. Clash analysis can also be performed on a set of shapes.

In routine foundation design, assessment of the effective weight of the tension cone, which comprises rock cone and soil columns, is required for piles subject to uplift forces according to the Code of Practice for Foundations 2017. However, precise calculation of the tension cone is difficult and time consuming as the boundary for tension cone calculation depends on the pile spacing and is limited by the lot boundary. The Voronoi function in Grasshopper can be applied in this situation. In mathematics, a Voronoi diagram is a partition of a plane into regions close to each of a given set of points. For each point, there is a corresponding region, called a Voronoi cell, consisting of all points of the plane closer to that point than to any other. The

Voronoi diagram of a set of points is dual to its Delaunay triangulation. Figure 3 illustrates the algorithm in Grasshopper to determine the soil and rock cone volumes given the limiting boundary of the cone weight, the pile layout, the pile cut-off level, the rockhead level and the pile founding level. The angle of soil and rock cones can also be specified. Once defined, the rock cone for individual pile can be developed by offsetting the pile circle at the rockhead level. A ruled surface is then extruded from the pile base circle to the offset circle at the rockhead level, which is then capped at the top and bottom to form a solid rock cone. The same is performed for the soil cone. Using the Voronoi function and intercepted by the cone weight boundary, the Voronoi cells are then extruded over the same depth of the rock and soil cones and capped to form the solid cells for individual pile. Using the intersect function, the intersection as well as the volume between the solid cell and the solid cone can be determined for individual pile. The general view of the soil and rock cones in Rhino is illustrated in Figure 4. The algorithm in Grasshopper can be grouped and converted into a cluster, which can subsequently be created as a new category in Grasshopper for future use.

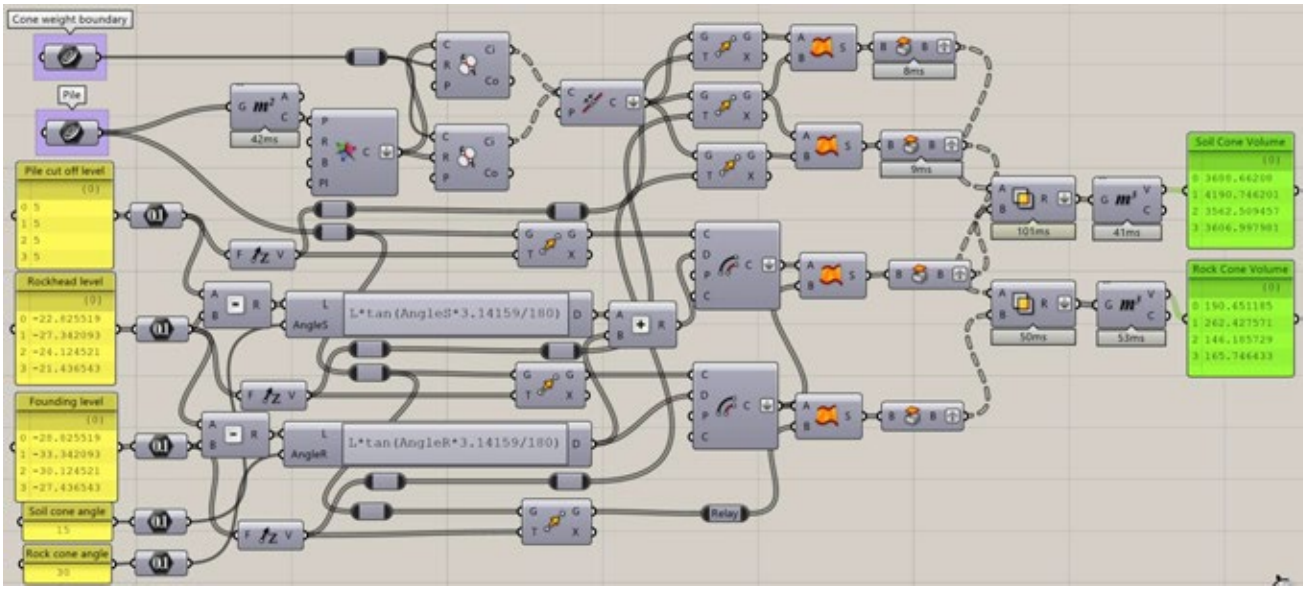

Figure 3: Algorithm in Grasshopper to determine soil and rock cones for 4 numbers of piles subject to uplift

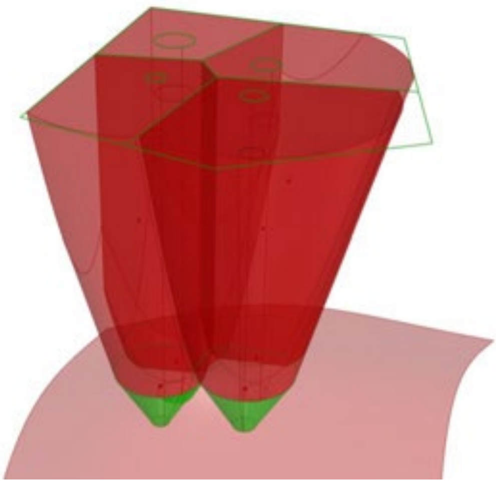

Figure 4: General view of soil and rock cones for a group of 4 numbers of piles bounded by a boundary in Rhino

3 APPLICATION OF AUTOMATION IN GEOTECHNICAL DESIGN

3.1 Geological Profile

Proper ground model to represent the ground condition is essential for geotechnical design. There are some software programs in the market which can generate borehole sticks for visualization. However, the borehole information is usually limited to visualization and cannot be easily extracted to other platform for subsequent design application. Rhino and Grasshopper indeed provide a platform not only to visualize the borehole data in 3D space but also enable design engineers to integrate the geological model with the design models including the foundation, site formation and excavation and lateral support works created in Rhino. As such, the stratum information as well as the proposed geotechnical works can be reviewed holistically in a unified platform. The presentation style is also highly flexible and can be designed by the users to suit their design purpose. This concept of integrating the Ground Information Management (GIM) and the Building Information Management (BIM) models is also discussed in Mak et al (2021).

The author has imported the borehole data from Microsoft Excel spreadsheets in a designed format through Grasshopper to generate the borehole sticks in Rhino. The borehole sticks are mainly extruded from circles to represent each stratum based on the input levels for visualization. The modelling format is consistent with the Construction Industry Council (CIC) BIM Standard, which enables the integration with BIM model and BIM submission in the next stage. The individual strata from each borehole can be grouped to form a surface or solid to represent the generalized strata. This process can be automated in Grasshopper. The top and bottom points of the generalized strata can be sorted for individual borehole in Grasshopper. A mesh or BREP can then be generated based on these points to represent each stratum. Other information such as stratum labels, SPT N-values and total core recovery can also be imported. The borehole sticks as well as the imported information can be plotted in a geological section. An illustration of borehole sticks and the geological section are shown in Figures 5 & 6 respectively. When the data in Excel are updated, the borehole sticks and the geological sections will also be updated instantly. In addition, the geological profile can be uploaded to Rhino through Speckle, which is an open-source programme and can extract and exchange data in a real time manner between the most popular architectural, engineering and construction applications.

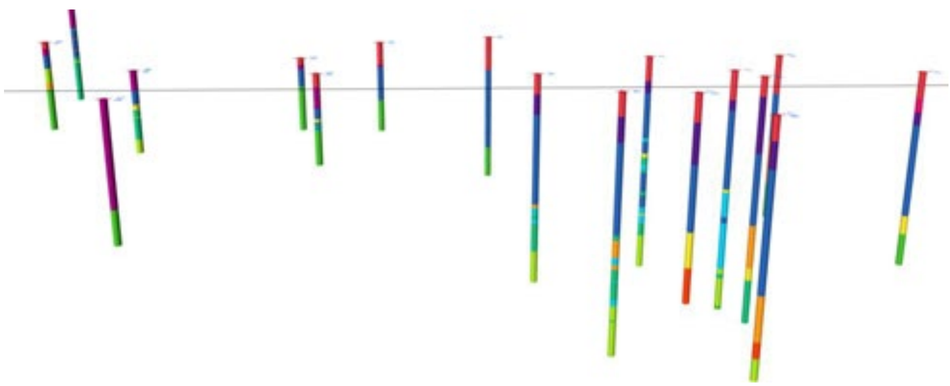

Figure 5: 3D View of borehole sticks generated by Rhino using Grasshopper algorithm

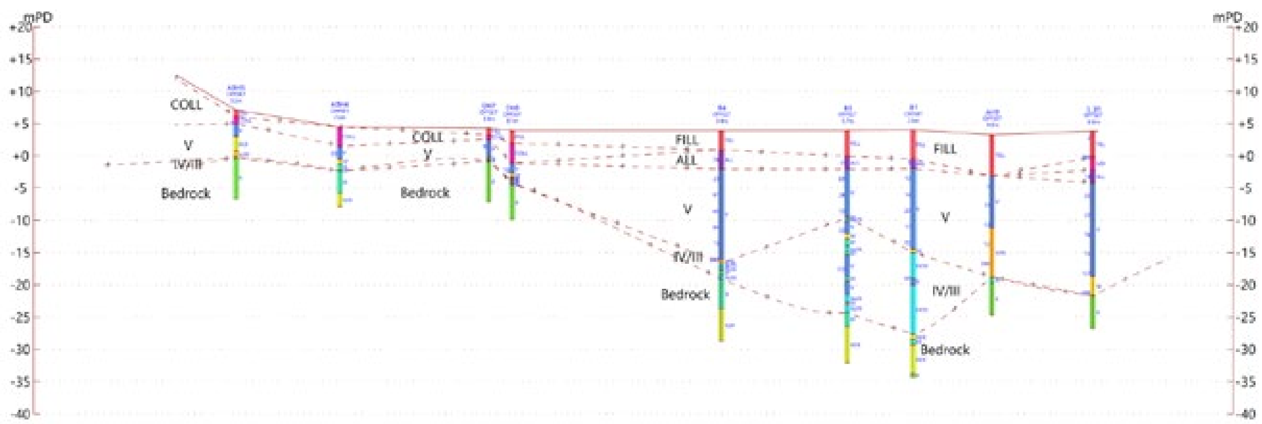

Figure 6: Typical geological section generated by Rhino using Grasshopper algorithm

3.2 Excavation and Lateral Support Works

Deep excavation over sloping terrain is challenging to geotechnical engineer. Sometimes, excavation involves hundreds of platforms at various levels, which makes the excavation profile highly complicated. The intersection with the existing topography will also enable the design engineer to decide if a perimeter pile wall is required or the formation level shall be adjusted to confine the excavation within the lot boundary. The "Intersect" function in Grasshopper enables multiple open cut excavation profiles to form a solid union, which is then trimmed by the existing topography in the form of BREP to obtain the excavation profile. Indeed, the formation of the open cut excavation profile is similar to the formation of the solid rock cone in previous example. Figure 7 illustrates an example of generating the excavation profile for more than a hundred platforms over a buildup terrain in a 3D space.

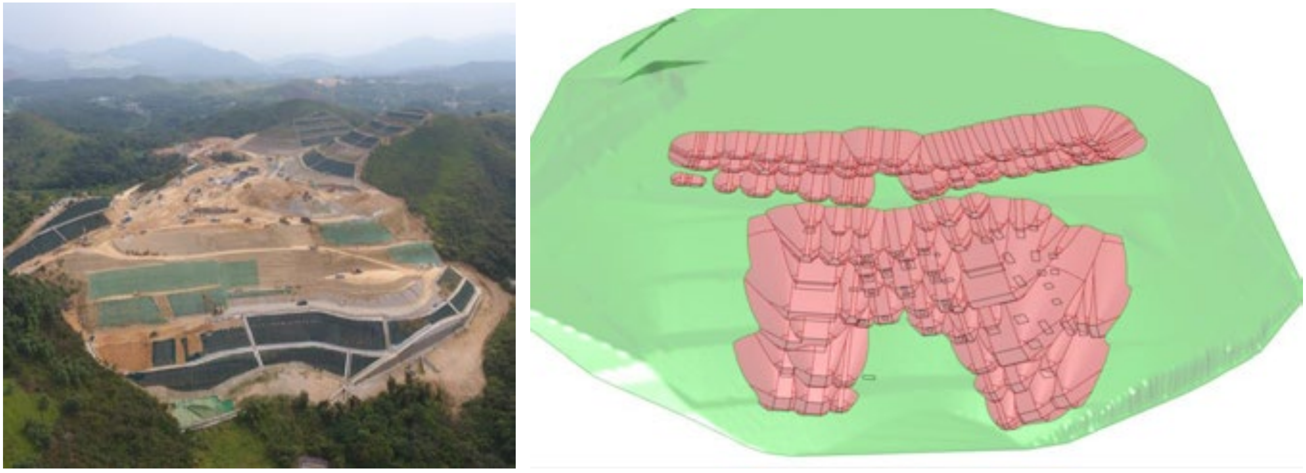

Figure 7: Automated open cut excavation profile for multiple platforms over existing slope

Deep excavation in bottom-up excavation sequence generally involves two main components: the pile wall and the steel shoring. Using the algorithm in Grasshopper, a series of point can be evenly distributed along a curve or polyline at given spacing to set out the centroid of the pile wall. The wall geometry can then be built and extruded to the existing ground and to the required toe level to achieve the required toe stability and to provide effective groundwater cut-off during excavation. For the shoring layout, the author has created a logic to automate the shoring arrangement. First, identify the corner areas with two lines of equal length where corner struts will be placed. Second, group the remaining curve or polylines into two groups such that the strut at one side of the group will support against the one at the other side of the other group. Third, based on the spacing of the main strut, corner struts and diagonal struts, determine the number of nodes for placement of struts and distribute them uniformly. Figure 8 illustrates an example of generating the preliminary shoring layout for a complex basement outline.

Figure 8: Automated shoring layout using Grasshopper algorithm

For uneven topography, the waling and the struts are not normally levelled. In such case, the strut members can be projected to the waling and create a space frame. This space frame contains the spatial information of the strut, such as the length, the inclination to horizontal, the planar angle normal to the waling, strut spacing, etc. Once the normal forces to the waling are determined from staged analysis, such as Oasys FREW or PLAXIS, the force for individual strut members can be readily determined for subsequent structural design using Grasshopper. With the lowest waling line being defined and the groundwater and geological profiles represented by BREPs in Rhino, cutting a section through the pile wall using the Grasshopper intersection function for BREPs and a plane will be able to retrieve the curves representing the groundwater table and geological stratum. These curves can then be converted into corresponding levels for toe stability check. The mathematical operation can indeed be carried out in Grasshopper such that the wall toe level can be optimized. Figure 9 illustrates an example of an ELS cofferdam with optimized wall toes in Grasshopper with consideration of the geological and groundwater conditions over a sloping ground.

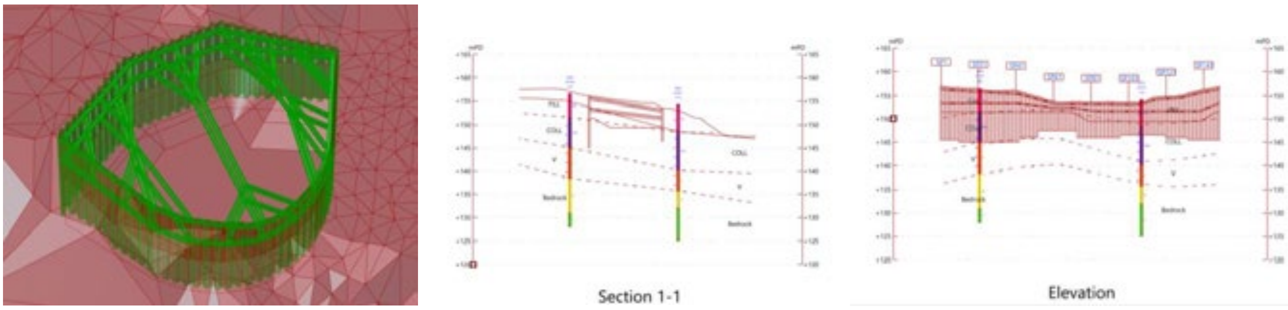

Figure 9: Example of ELS cofferdam over uneven terrain with optimized wall toe levels

3.3 Soil Nail Works

Soil nailing is an effective slope stabilization method widely adopted in Hong Kong. Typically, the spacing of soil nail varies from 1.5m to 2m both vertically and horizontally. A soil nail head is also required to enhance local stability. When placing soil nails over uneven terrain, it is difficult to be visualized in a 3D environment. Grasshopper has a category of vector function, which enables user to position the soil nail normal to the face of the terrain at a specified dip angle. First, define a series of horizontal surface planes and set the level of the planes as the vertical spacing of the soil nails. Second, intercept those horizontal surface planes with the existing topography represented by BREP (see Figure 10). Third, smoothen the intercepted curve to minimize sharp turning point of the uneven terrain. Forth, split the smoothened curve with nodes at equal horizontal spacing. Finally, position a line normal to the smoothened curve and dip at a specified angle to represent the soil nail. The length of the line is the length of the soil nail. Given the diameter of the soil nail, a circle can be extruded along the line to represent the physical dimension of the soil nail. Figure 11 illustrates the automated soil nail arrangement over an uneven terrain in 3D space. In Grasshopper, there is a function to carry out clash checking. This function enables user to identify the clashed soil nails so that their orientation and dip angle can be further refined.

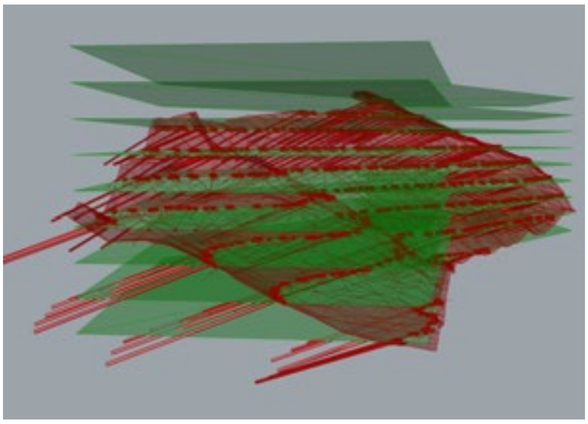

Figure 10: Intersect of the horizontal planes and the existing topography

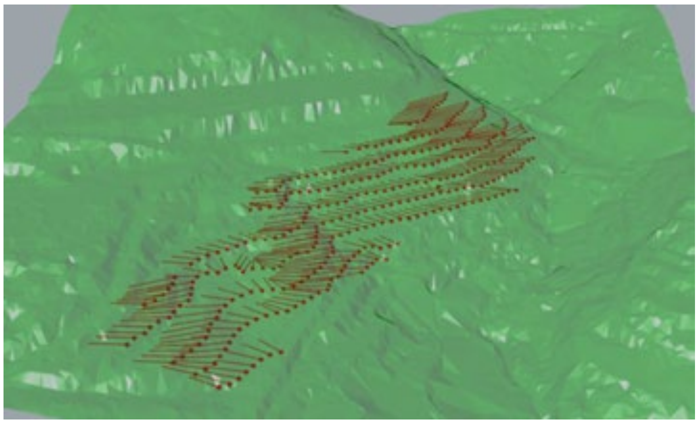

Figure 11: Automated soil nail arrangement on existing topography

4 AUTOMATION IN COMPUTER ANALYSIS

The Rhino model contains all the geological, groundwater as well as the topographical information. These profiles can be easily manipulated through Grasshopper to extract the desired input data in a designated format for computer analysis. The data can first be extracted to an Excel spreadsheet to facilitate the inputs. One of the applications is to provide input data for Oasys PDisp by converting various geological profile to discrete sets of stratum levels under a given grid pattern. This process is particularly useful for simplifying the complicated geological profile to a generalized flat plane as inputs in PDisp. In PDisp, the analysis area needs to be divided into soil zones in a grid pattern. Each soil zone shall specify a soil profile with soil stratum levels. Traditionally, the stratum levels need to be read off manually from the inferred contours for different soil layers in every grid. While the geological profile is usually non-uniform, it is tedious and time-consuming to produce a high-resolution geology in PDisp.

With the aid of Grasshopper, the geological profiles represented by BREP in Rhino at each soil zone can be intersected by the cells of the grid pattern and the centroids of the intersected profiles can be obtained. The cell coordinates, which represents the soil zones, and the levels of the centroids, which represents the levels of the soil profiles, can then be extracted to an Excel spreadsheet. Figures 12 illustrates the cells of the grid pattern projected onto the geological profile.

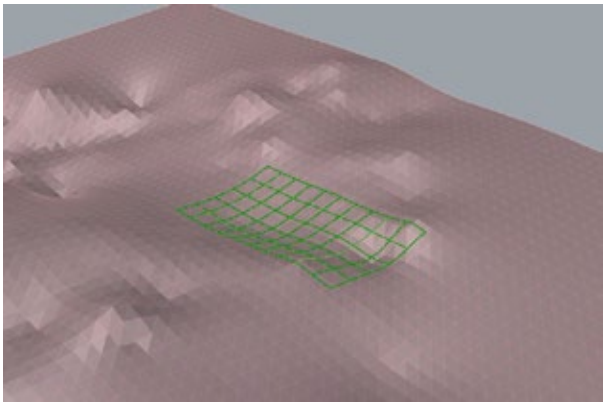

Figure 12: Projection of grid on geological profile in Rhino model

In order to import the data objects into PDisp, this can be achieved via the Component Object Model (COM) Interface. This enables external programs to pass information and instructions to and from PDisp, including the Visual Basic for Applications (VBA) in Excel. As such, the design process can be streamlined and automated from data input from Rhino through COM Interface in Excel to PDisp. Using this process, the time saving is substantial, and the model can be effectively refined by reducing the size of the grid to achieve a more accurate and prompt estimate. Figures 13 and 14 demonstrate the soil zone and soil profile in PDisp model automatically generated using the COM Interface. The COM Interface is also available in other geotechnical software under Oasys and similar design process can be established.

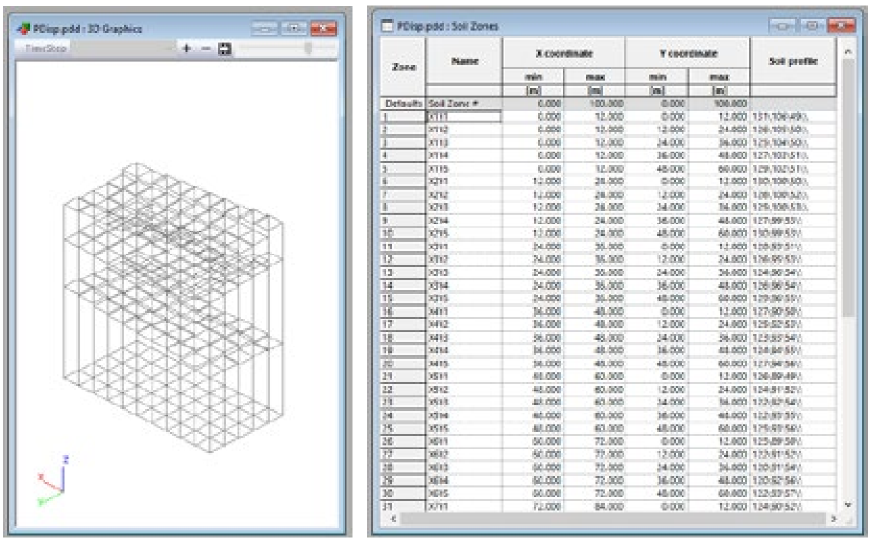

Figure 13: Soil zones with soil profile in PDisp using COM Interface

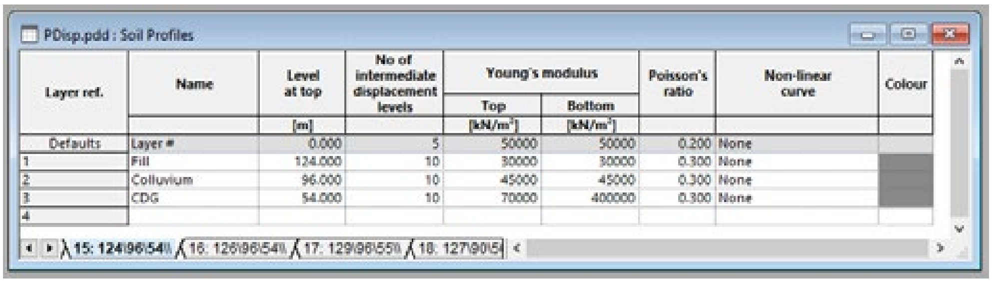

PDisp.pdd : Soil Profiles

Layer ref.	Name	Level at top	No of intermediate displacement levels	Young's modulus Top	Young's modulus Bottom	Poisson's ratio	Non-linear curve	Colour
		[m]		[kN/m²]	[kN/m²]			
Defaults	Layer #	0.000	5	50000	50000	0.200	None	
1	Fill	124.000	10	30000	30000	0.300	None	
2	Colluvium	96.000	10	45000	45000	0.300	None	
3	CDG	54.000	10	70000	400000	0.300	None	
4								

Figure 14: Soil profile with assigned geotechnical parameters

In addition to Oasys, remote scripting enables PLAXIS analysis to be run through Jupyter Notebook. It is a web-based open-source interactive computing platform. It can control PLAXIS in a remote manner through the python scripting. The geometries in Rhino are first converted into polygons, polylines and lines, which are then exported to a pre-defined format in Excel with all the input parameters required in PLAXIS. These parameters include the soil polygons representing the geological stratum and the excavation profile, the lines representing the wall plate and node-to-node elements, and the polyline representing the groundwater profile. The python script in Jupyter Notebook can then read the Excel data and run PLAXIS commands to drive the staged inputs and analysis in PLAXIS. Figure 15 illustrates the use of Jupyter Notebook to connect with PLAXIS and automate staged excavation input in PLAXIS.

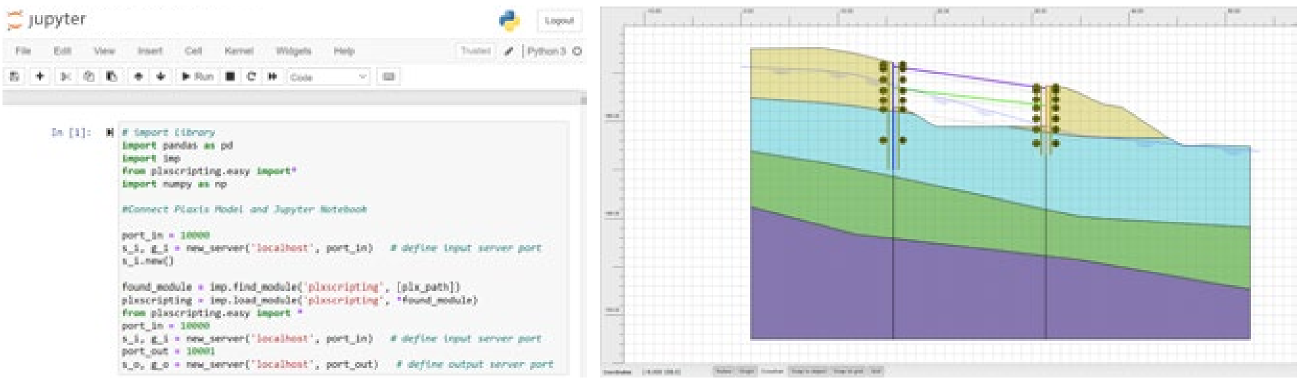

Figure 15: Example of using Jupyter Notebook to automate staged excavation input in PLAXIS

5 DESIGN EFFICIENCY

Traditionally, the BIM model is generated after the design is nearly finalized or frozen. With the capability of visual programming and the pre-defined algorithms as presented in this paper, a preliminary 3D model can be built within couple hours or a day depending on the project scale at the beginning of the design stage to integrate the ground model, geological profile as well as the intended geotechnical design into a single 3D platform. Once the integrated 3D model is built, it enables the geotechnical engineers to extract useful design data such as rockhead level, shoring and soil nail arrangements as illustrated in previous examples for subsequent design and to facilitate prompt quantity estimation. The algorithms also enable the generation of input data for geotechnical analysis such as toe stability check, settlement check, slope stability analysis, finite element modelling, etc. The greater benefit is that once the 3D model and the design workflow and algorithms are set, any changes in geological condition due to additional ground investigation boreholes or any update of geotechnical design in the 3D model can provide instant update to all the input data for repeated geotechnical analysis. Based on the experience of the author, it is believed that the time saving by using the pre-defined algorithms on routine engineering design is enormous and could possibly be in the order of 25% to 50% for beginners to greater than 75% for experienced users.

6 BENEFITS OF AUTOMATION

The benefits grained on design automation not only enable faster delivery of the design, but also enable better and optimized design to be produced. The visualization of the integrated geological and design models in 3D space enables the design engineer to have a better understanding of the site and the geological constraints. During the design development, these constraints can be considered holistically such that the ground risk can be addressed at early design stage. The integrated model also facilities better communication with the clients and coordination among the engineering team and the BIM coordinator. The integrated model in Rhino enables computer inputs to be generated for analysis in a more efficient and accurate manner. Any changes in Rhino can also be automatically updated following the same workflow and algorithm in Grasshopper to re-create the model as well as the data inputs for computer analysis. The enhanced digital capability also enables more design sections to be created for analysis and optioneering to drive data-driven decisions. Ultimately, it can provide optimal design outcomes and high-quality outputs for clients in lesser time.

7 CONCLUSION

The development of digital tools enables design engineer to visualize, automate and optimize their design under a digital-based platform. Mapping of the design workflows and identifying the time-consuming processes can maximize the effectiveness of the design automation. The Author has showcased the applications of using Rhino with Grasshopper to automate various geotechnical designs, including pile foundation, excavation and lateral support and soil nailing works, create model inputs for computer analysis and perform design calculation and stability check. Grasshopper is easy to learn and use. It requires minimum knowledge of programming or coding. There are plenty Grasshopper plug-ins available for downloading. Besides, the designers can create their own clusters and categories in Grasshopper and they are transferable and applicable to multiple projects. These clusters can always be replaced individually if a better one is created or developed without affecting the entire algorithm. The future development of design automation is to link the results of the computer analysis back to update the design model in Rhino. The finalized design model shall then be transformed to 3D BIM model for design submission and drawing production.

REFERENCES

BD 2017. *Code of Practice for Foundations 2017*, Buildings Department, Hong Kong.

Mak, D.Y.Y., Millis, S.W., Li, P. (2021), *A BIM-based Ground Information Management (GIM) Framework to Manage Ground Risk for Construction Projects*, Proceedings of the HKIE Geotechnical Division Annual Seminar 2021, HKIE, 158-168.

Machine Learning-based Natural Terrain Landslide Susceptibility Analysis – A Pilot Study

H W M Li, R H L Li, C C J Wong, F L C Lo
Geotechnical Engineering Office, Civil Engineering and Development Department, Government of HKSAR, Hong Kong SAR, China

ABSTRACT

Recently, the Geotechnical Engineering Office has initiated a pilot study on data-driven landslide susceptibility analysis (LSA) using a machine learning (ML) approach. A study area covering about one-fifth of the total natural hillside area of Hong Kong on and around the Lantau Island was considered. Three common tree-type ML classifiers: Decision Tree, Random Forest and XGBoost have been used. Conditioning factors (or features) including rainfall, geological and topography-related features were considered. In the study, the domain knowledge on natural terrain landslides in Hong Kong were critically incorporated into the susceptibility models through feature engineering to ensure that the resulted models are physically meaningful. In addition, an approach proposed to resolve the serious data imbalance problem, which is common in LSA, will be highlighted. Under this approach, the predicted probabilities of the positive class (i.e. landslide) can also be taken as a proxy to the landslide probability. This paper reports the methodology and key findings of this pilot study. The approach can be extended to cover other ML algorithms and features, and to a territory-wide scale with a view to enhancing the resolution and accuracy of the current susceptibility model of natural hillsides in Hong Kong.

1. INTRODUCTION

Much of the natural terrain in Hong Kong is steeply sloping with a surface mantle of weak saprolite, residual soil or colluvial deposits. These hillsides are susceptible to shallow rain-induced landslides with a typical depth of less than 3m. As part of its slope safety management system, the Geotechnical Engineering Office (GEO) has been conducting technical development work pertaining to landslide hazards. Landslide susceptibility analysis (LSA) has been one of the key areas of technical development work for improving our understanding of the nature and characteristics of natural terrain hillsides, their potential risk and approaches for risk management (Wong, 2009).

Landslide susceptibility refers to the spatial likelihood of a landslide occurring in an area on the basis of local terrain conditions (Brabb, 1984). While previous studies on landslide susceptibility for Hong Kong were mainly based on the data-driven analysis using conventional statistical approach (e.g. Evans & King, 1998; Ko & Lo, 2016), a few recent studies were based on the machine learning (ML) approach (e.g. Dai & Lee, 2002; Ng et al., 2021; Wang et al., 2021). The ML techniques are becoming popular to model complex landslide problems and starting to demonstrate promising the predictive performance compared to conventional methods (Tehrani et al., 2021). In light of this, the GEO carried out a pilot study to explore the potential of applying ML on natural terrain LSA. With reference to Ko & Lo (2016), landslides and conditioning factors covering the same period from year 1985 to 2008 were adopted. Under this pilot study, a study area covering about one-fifth of the total natural terrain areas in Hong Kong has been considered. Although it is a regional study, the methodology has been developed with a view to extending it to a territory-wide study. This paper presents the preliminary findings of this ML-based natural terrain LSA using three different ML algorithms.

2. PREVIOUS STATISTICAL-BASED NATURAL TERRAIN LSA FOR HONG KONG

The first territory-wide natural terrain LSA of Hong Kong conducted by the GEO is reported in Evans & King (1998). The territory was catergorised into five classes of susceptibility, with slope angle (13 classes) and geology (19 groups) accounted as the conditioning factors for landslide occurrence. The susceptibility classes were differentiated by one order of magnitude in terms of landslide frequency (i.e. 0.1 to 1 no. of landslide/km^2/year). This resolution was considered limited and insufficient in differentiating more vulnerable areas for risk management applications (Wong, 2003; Wong, 2009). Also, the effect of rainfall, a key contributory factor to landslide occurrence, was not considered in this study.

An updated territory-wide natural terrain susceptibility model was developed by Ko & Lo (2016) taking into account the effect of rainfall, together with the consideration of the enhanced landslide in the Enhanced Natural Terrain Landslide Inventory (ENTLI), and enhanced topography data from the territory-wide multi-return airborne Light Detection and Ranging (LiDAR) survey undertaken in 2010 (2010 LiDAR data) respectively. The three conditioning factors considered: slope gradient, solid geology and rainfall intensity were categorized into eight, three and six classes respectively and correlated to landslide susceptibility using conventional statistical approach. The analysis resulted in an improved resolution spanning across four to five orders of magnitude in terms of landslide density (no./km^2) (see Figure 1). In particular, natural terrain landslides were found to be highly sensitive to rainfall (two to three orders of magnitude between the lowest and highest rainfall classes, for one slope angle class). They further predicted the number of landslides that may occur in an anticipated rainfall event and generated a possible landslide frequency map (Ko and Lo, 2018). Based on the work by Ko & Lo (2016), a pilot study has been undertaken to explore the potential of applying ML on natural terrain LSA, taking advantage of the powerful performance of ML in data analytics. The following sections present the methodology and key findings of this ML-based study.

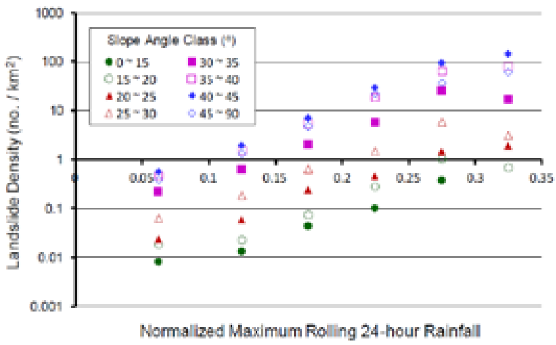

Figure 1: Year-based Rainfall Landslide Correlation by Ko & Lo (2016)

3. MACHINE LEARNING ALGORITHMS

Since the first use of ML in the field of landslide studies in early to mid-2000s, a wide range of conventional ML and deep learning (e.g. neural networks) algorithms have been developed for classification and regression purposes. They have been used in various landslide studies yet there is still no consensus on which algorithm is the 'best' suited for predicting landslide prone areas (Dou et al., 2020). In this pilot study, ML algorithms which suit our purposes and the adopted approach of the study were identified based on the key factors below.

(i) interpretability of the algorithms,
(ii) balance between bias and variances,
(iii) suitability for handling correlated conditioning factors, and
(iv) computational efficiency.

Interpretability refers how easy is it to explain the results from the input data by a ML model, or to understand the patterns that models use to link to the training datasets (Ma et al., 2021). It is essential for detecting bias and debugging of the ML models. We also considered it is important for us to be able to explain the model predictions in combination with our professional knowledge (domain knowledge) on landslide occurrence. Balance between bias and variances refers whether the algorithm is able to form a predictive model that is generalized enough to give consistent yet accurate forward predictions. Algorithms which are prone to overfitting should be avoided. The ability of an algorithm to handle correlated conditioning factors, or more commonly referred as features in ML terminology, provide additional flexibility in selection of features and is thus more preferable. Lastly, computational efficiency is related to the time spent on the LSA and is taken as one of the considerations as well.

With reference to the above considerations, three tree-based ML algorithms, namely: Decision Tree, Random Forst and XGBoost were chosen. Decision Tree algorithm (Breiman et al., 1984) is known as one of the most commonly used algorithms in the studies of similar nature. Despite it is a less robust algorithm and sensitive to the predictive data, it is adopted for its computational efficiency and high interpretability to facilitate the understanding of the other two algorithms. Random forest (Breiman, 2001) and XGBoost (Chen & Guestrin, 2016) are tree-based ensemble learning algorithms. With different ensemble methods adopted, their performance has been much enhanced in terms of robustness and generalizability. While tree-based ensemble algorithms are widely recognized to achieve excellent results compared to other ML algorithms, Ma et al. (2021) in particular remarked that Random Forest algorithm offers robust performance for accurate susceptibility mapping with only a small number of adjustments required before training the model. On the other hand, the performance of XGBoost has been widely recognized in a number of ML and data mining challenges (e.g. Kaggle competitions). XGBoost is one of the Gradient Boosting algorithms. While Gradient Boosting become popular very recently such that they are less routinely used in LSA, it has been reported to be able to improve the accuracies of ML models for landslide susceptibility analyses (Merghadi et al., 2020).

The architecture of the adopted algorithms are not elaborated in this paper. Readers may refer to the original papers of the algorithms for more details.

4. MODELLING APPROACH AND FEATURE ENGINEERING

4.1. Modelling Approach

The LSA in this pilot study was treated as a grid-based binary classification problem in ML. In other words, given the set of condition factors possessed by a grid, the ML classifier predicts the landslide occurrence within the cell as a binary dependent variable comprising positive value (with landslide) or negative value (without landslide) only. The same approach was adopted by similar studies in Hong Kong (Dai & Lee, 2001; Ng et al., 2021; Wang et al., 2021). A grid size of 5m x 5m was adopted as in the previous work by Ko & Lo (2016). Reichenbach et al. (2018) also remarked that grid-based approach is the most common type of mapping units for LSA modelling.

One of the major challenges commonly encountered in applying binary classification in LSA is the sample bias due to the highly imbalance dataset, as there is always a scarce proportion of positive value grids within a study area. The ratio of positive value to negative value grids the dataset for this pilot study area is in the order of 1:30,000. Such imbalances can cause a model to be biased towards classifying the susceptible area as safe (i.e. negative value), jeopardizing the accuracy of the minority class prediction (the class of interest in our study). With a view to improving the binary classification result of the minority class, data-level techniques which refer to selecting a 1:1 ratio (or other ratio as appropriate) of landslide data points to non-landslide data points using different sampling techniques were commonly adopted (Dai & Lee, 2001; Ng et al., 2021; Ma et al., 2021). However, there is concern that sampling of data would bias the predicted probabilities of a classifier, resulting in a significantly high proportion of false positive when applying the classifier trained and tested using sampled datasets to an unsampled domain. This manifest as a substantial over-prediction of landslide potential when practically applying such models to forward prediction of the landslide potential of the entire study areas.

In view of the above, this pilot study adopted a different ML approach to handle an imbalance dataset (referred as the adopted approach in this paper). Under this approach, while the analysis was still handled as a binary classification problem, no data sampling was applied to avoid biasing the predicted class probabilities of a classifier. The issue of sample bias was overcome by taking the 'predicted class probabilities' (e.g. the probability of having a landslide), instead of the 'predicted classes' (i.e. with or without landslide), as the key prediction result obtained from the ML classifier. Since the predicted probabilities of the classifier were not biased by data sampling, the predicted probability of the positive class [P(+ve)] could be taken as a proxy to the landslide probability directly. In addition, the information loss in model training can be minimized as the entire dataset except those saved for validation and testing can be utilised without sampling. Similar approach was adopted in Xiao & Zhang (2021) in forecasting the number of man-made slope failures in response to rainstorms with machine learning technique for slope-based analysis.

4.2. Feature Engineering

The nature and number of features adopted in ML modelling vary significantly among different literatures on LSA. While the introduction of redundant or irrelevant features may create noise that decreases the overall predictive capability of the models, no universal agreement on the principle of selecting relevant features among the literatures could be found. In particular, some of the features adopted in the literatures lack physical relevance with landslide occurrence. As a result, it is preferable to identify appropriate features through understanding their roles on landslide occurrence and the adoption of conventional engineering which involves a substantial amount of prior knowledge (Reichenbach et al., 2018; Ma et al., 2021).

In view of the above, a framework which ensures the quality, and the statistical and physical relevance of the features was adopted in selecting proper features for inclusion in this pilot study.

4.2.1. The Feature Selection Framework

Feature selection is the process of reducing the dimensionality of input variables and creating summary measures to encapsulate the information in the entire dataset. Domain knowledge would be used in the process to extract the characteristics and attributes from raw data. Under the feature selection framework, potential features were assessed against the criteria given in Table 1. In particular, while ML belongs to algorithmic modelling which provides prediction based on the available data only and treat the data mechanism as an unknown (Tehrani et al., 2021), we emphasised on the inclusion of our domain knowledge for the development of physically meaningful ML models.

Table 1 Feature Selection Criteria

Criterion	Consideration
(i) quality of the feature datasets	• good spatial and temporal coverage, resolution and accuracy of the feature data • crucial to ensuring the performances of ML models are not adversely affected by the quality of their training data • avoid underrepresentation due to scarcity of the available data
(ii) statistical correlation between the feature and landslide occurrence	• prevent the introduction of less relevant or redundant features to the ML model, as they create noise that decreases the overall predictive capability of the models • facilitate understanding of the data structure • aid the data preprocessing by revealing underrepresentative data (e.g. the response of the hillsides under heavy rainfall with a low probability of occurrence, characteristics of the terrain covering a small land area) • assessed by means of descriptive analytics (see Table 2)
(iii) consistency of the statistical correlation with domain knowledge on landslide susceptibility	• allows the incorporation of domain knowledge, past experience and expert judgment on landslide susceptibility to the ML model by reviewing the consistency of the correlation observed in Criterion (ii) against the existing engineering knowledge on landslide occurrence

A feature selection priority matrix (the matrix) shown in Figure 2 was created for assessment against Criteria (ii) and (iii) in this pilot study. Potential features that fall within Quadrant 1 would have higher priority to be included in the susceptibility models, follow by those falling in Quadrant 2. Features found in Quadrants 3 and 4 reveal statistical correlations that do not tally with the existing engineering knowledge and should be well considered and tested with due consideration of the data representativeness before inclusion.

Further elaborations on the application of the matrix is given based on three topography-related example features: slope gradient, profile curvature and aspect. The vertical axis of the matrix is determined with reference to Table 2, which summarises the correlations of the example features with the density of past landslide occurrences ($\delta_{Landslide}$, no./km^2) and their distribution of area. Territory-wide data of Hong Kong instead of the study area solely were used with a view to extend the pilot study to territory-wide in future.

Strong statistical correlation with $\delta_{Landslide}$ increases by about five times from 30° to 45° is observed from slope gradient. The increase of $\delta_{Landslide}$ with slope gradient is attributable to its effects on the balance of stabilizing and destabilizing forces, and thus the overall stability of a slope. Areas steeper than 45° possess lower $\delta_{Landslide}$ as they are more rocky or composed of denser soil, having a higher stabilizing force. This feature is thus placed near the high ends of both the vertical and horizontal axes in the matrix.

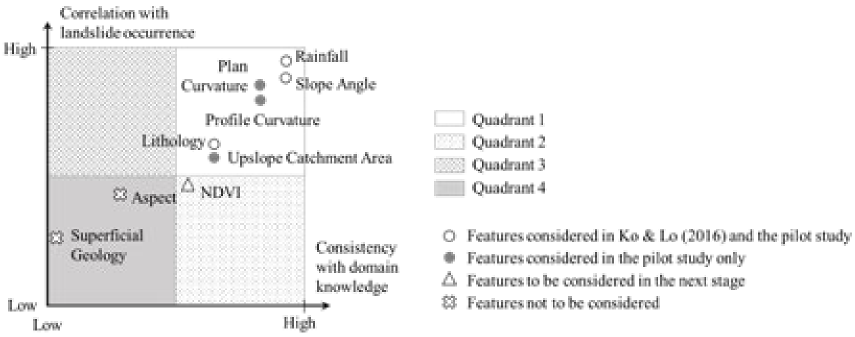

Figure 2: Feature Selection Priority Matrix

Areas with greater magnitude of profile curvature are about four times more susceptible to landslide, illustrating a relatively strong statistical correlation. As profile curvature refers the rate of change of slope gradient along the vertical directions, it can be considered as a proxy to the break in slope which is landslide related (Ho & Roberts, 2016). This feature is thus placed in Quadrant 1 of the matrix, at a less extreme position as compared to slope gradient.

Aspect shows certain degree of statistical correlation with landslide, with the south or southeast aspects being two times more susceptible than the north. Nonetheless, this correlation cannot be justified based on domain knowledge. As such, aspect falls within Quadrant 4 and is not considered in this pilot study.

Table 2 Area and Landslide Density Distribution of Example Features

Slope Gradient (deg)	Area (%)	$\delta_{Landslide}$ (no./km^2)	Profile Curvature	Area (%)	$\delta_{Landslide}$ (no./km^2)	Aspect	Area (%)	$\delta_{Landslide}$ (no./km^2)
0 - 15	12.5%	1.20	≤ -7	2.1%	77.75	N	12.2%	20.19
15 - 20	12.0%	2.19	-7 - -5	2.7%	61.65	NE	12.3%	25.75
20 - 25	17.4%	4.61	-5 - -3	7.5%	43.08	E	12.7%	31.35
25 - 30	22.6%	12.57	-3 - -1	20.7%	25.06	SE	12.6%	38.63
30 - 35	19.3%	42.21	-1 - 1	36.1%	17.29	S	12.5%	39.05
35 - 40	10.2%	102.36	1 - 3	18.7%	27.32	SW	12.5%	34.88
40 - 45	4.1%	141.68	3 - 5	6.3%	52.28	W	12.6%	30.82
45 - 90	2.0%	95.36	5 - 7	2.6%	76.90	NW	12.5%	25.37
			≥ 7	3.4%	58.08			

4.2.2. The Selected Features

Table 3 summarizes the features identified based on the feature selection framework. As can be seen, compared with the three basic features considered by Ko & Lo (2016) (i.e. rainfall, lithology, slope gradient), this study considered three additional features (i.e. plan curvature, profile curvature and upslope catchment area). These features are briefly described as follows.

Table 3: Summary of Features Considered in this Study

Feature	Rainfall	Lithology	Slope gradient	Plan Curvature	Profile Curvature	Upslope Catchment Area
Ko & Lo (2016)	✓	✓	✓	-	-	-
This Study	✓	✓	✓	✓	✓	✓

4.2.2.1. Rainfall

The natural terrain landslides in Hong Kong were characterized as rainfall-induced. Since 1980s, the GEO and the Hong Kong Observatory (HKO) have installed a total of more than 120 automatic rain gauges across Hong Kong, with an average density of about one rain gauge per 10 km^2. In particular, the GEO rain gauges (90 nos.) capture real-time data which would be transmitted to the servers automatically at up to 1-minute intervals. This network of rain gauges provide a reasonably good spatial and temporal coverage of rainfall data across Hong Kong.

Year-based rainfall intensities quantified in terms of normalised maximum rolling rainfall (NMRR) was adopted in this pilot study. NMRR is determined by normalizing the maximum rolling rainfall as recorded at a location with the mean annual rainfall of the same location of a 30-year period from year 1977 to 2006. The normalisation of rainfall intensity is a common approach to better characterise extremity or anomalies of the rainfall (Ko, 2005; Ko & Lo, 2016). The statistical correlation of 24-hour and 4-& 24-hour NMRR with landslide susceptibility was thoroughly studied in Ko & Lo (2016), which concluded that landslide occurrence is highly sensitive to rainfall with a strong statistical correlation up to five orders of magnitude observed. With reference to Ko & Lo (2016), rolling durations of 24-hour was considered in this pilot study.

4.2.2.2. Topography-related Features

Topography-related features refer to the list of features which could be determined with reference to the topography of the study area. A total of four topography-related features (i.e. slope gradient, plan curvature, profile curvature and upslope catchment area) were identified for incorporation in this pilot study. The data of these features obtained from the 2010 LiDAR data. The 0.5m x 0.5m digital terrain model (DTM) developed was first resampled to form a 5m x 5m DTM, and then converted into the feature dataset using ArcGIS applications. Given LiDAR data shows promising results in producing high resolution DTM that can 'see through' vegetation, topography-related feature dataset derived from territory-wide LiDAR survey results are of good quality fulfilling feature selection Criterion (i).

Statistical correlations of two to six folds are observed from these features. In terms of physical significance, slope gradient plays a significant role on the overall stability of a slope. Plan and profile curvatures are related to the mass-wasting and runoff processes. The upslope catchment area indicates the amount of flow that would be concentrated to the grid in event of precipitation.

4.2.2.3. Lithology

Lithology has been adopted in both generations of the territory-wide natural terrain landslide susceptibility analysis by Evans & King (1998) and Ko & Lo (2016). The lithology is related to the engineering properties of the soils derived from the parent rocks and is thus considered to be physically relevant to the landslide potential. The lithology of the study area was categorised into three main groups (namely intrusive, volcanic, and sedimentary) with reference to the 1:20,000 solid and superficial geology maps of Hong Kong (https://www.cedd.gov.hk/eng/publications/geo/hong-kong-geological-survey/index.html). The same categorization was adopted in Ko & Lo (2016).

4.2.3. The Landslide Data

In this pilot study, landslide data as recorded in the ENTLI was adopted. The ENTLI provides year-based landslide information which were collected through the interpretation of available high-flight (≥ 2,400m altitude) and low-flight aerial photos (< 2,400m altitude). As compared with the reported landslides or field-mapped landslides which are commonly adopted in other LSA, landslide data based on ENTLI provided a more complete picture of landslide occurrence over the study area which is not biased by the accessibility of the landslide locations. On the other hand, the temporal resolution of the data was limited by the frequencies of aerial photo-taking and interpretation. Year-based LSA was considered as a result. In the dataset, grids containing the crowns of the landslides were identified as the landslide area and denoted as '1'; remaining grids were considered as non-landsliding area and denoted as '0'.

5. MACHINE LEARNING-BASED NATURAL TERRAIN LANDSLIDE SUSCEPTIBILITY ANALYSIS

5.1. The Pilot Study Area

The pilot study area comprises the natural terrain areas of the Lantau Island, as well as those of the adjacent outlying islands as indicated in Figure 3. It is 130 km^2 by area, over 30% of the study area is steeper than 30^o, with the elevation varied from sea level to 930m above sea level. It is mainly underlain by volcanic and intrusive rock, with a small area of sedimentary rock. There were over 6,100 recent natural terrain landslides recorded within the study area in the ENTLI. The study area has experienced intense rainfall in 1993 and 2008, with the 24-hour maximum rolling rainfall of over 500 mm and 600 mm respectively. The rainstorm on 7 June 2008 alone has resulted in over 2,500 natural terrain landslides. Given the high variabilities in topography-related and rainfall data available within the pilot study area, as well as its rich history of past landslides, it is considered as an ideal study area for this pilot study.

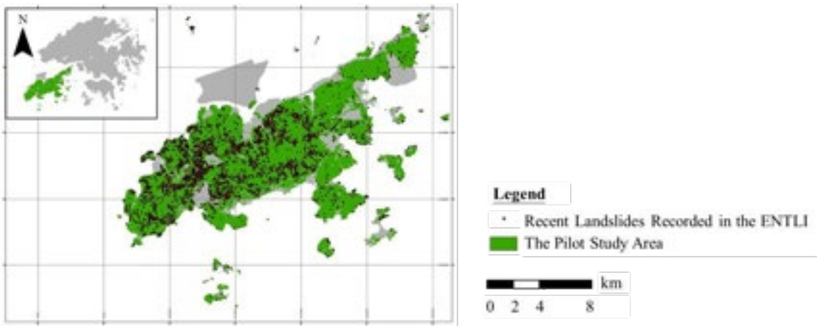

Figure 3: Extent of the Study Area and Recent Landslides in Enhanced Natural Terrain Landslide Inventory (ENTLI)

5.2. The Workflow

The workflow of this ML-based analysis mainly comprises data preprocessing and resampling, model construction and performance evaluation stages.

5.2.1. Data Preprocessing and Resampling

With a grid-based approach adopted in this pilot study, the entire pilot study area discretized into about 5.2 million numbers of 5m x 5m grids, each of which contains 24 years (year 1985 to 2008) of rainfall and landslide data on top of the geological and topography-related features. Under the adopted approach, most of the data in grids were used for either the construction or the evaluation of the ML models. Given the amount of data to be handled, the model construction and evaluation works of this pilot study were carried out on web service platform using python programming language.

Data preprocessing refers to the preparation of data for model construction. Key actions include the cleansing of data, the encoding of categorical data, as well as the resampling of data for model training and evaluation. Data cleansing forms part of the feature engineering works, which involves the removal of null or undesirable data from the dataset to ensure only representative and unbiased data are fed into the models. For instance, data associated with rainfall intensities beyond the range of 0.025 to 0.3 for 24-hour NMRR were removed since only a limited portion of the pilot study area had encountered these extreme rainfall intensities in rare events, such that the associated data would not be representative enough for incorporation. Data points associated with the extreme values of plan and profile curvatures were discarded for similar reasons. The encoding of categorical data involved the lithological data only, with one-hot encoding adopted.

The resampling of the dataset along with the workflow of this pilot study is illustrated in Figure 4, the dataset was resampled into training dataset, validation dataset and testing dataset. The testing dataset comprised 1) all the data from years 1993 and 2007, and 2) 10% of the data randomly selected from the remaining 22 years in a stratified manner. Stratified random sampling is a commonly adopted sampling technique in which the data is divided into smaller groups or strata and then randomly selected from each of the strata by the same proportion. The data were stratified based on landslide occurrences in this pilot study such that the ratio of landsliding to non-landsliding data in each of the dataset could be maintained.

The two sets of testing data are referred as Testing Data 1 (TD1) and Testing Data 2 (TD2) respectively. While TD2 pertained the type of testing data commonly adopted in other similar studies, TD1 comprised data that possess unseen rainfall patterns during the model construction such that it served as a more stringent test which tested the models' ability in making forward predictions. Of note, the intensity of rainfall in year 1993 is one of the highest one among the 24 years, whilst that in year 2007 is a moderate one. The remaining data served as training and validation datasets.

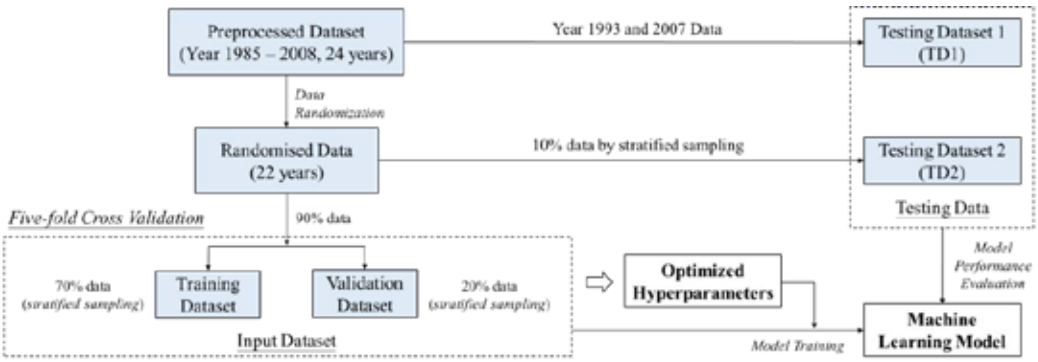

Figure 4: Resampling of Data in the Pilot Study

5.2.2. Model Construction

Construction of the ML model mainly involves the optimization, or tuning, of the hyperparameters. Hyperparameters are parameters that control the learning process of a ML model, the optimal set of hyperparameters to be used varies by cases as it is dependent on the algorithm and dataset involved. Although some ML-based studies adopt the default values of hyperparameters, Tehrani et al. (2021) remarked that hyperparameter tuning plays a significant role on the performance and the predictive ability of a ML model. The tuning of hyperparameters is a process of trial and error, which can be done in either systematically (e.g grid search) or randomly. For each set of the hyperparameters considered in this pilot study, their performances were assessed using five-fold cross-validation. A five-fold cross validation involved the key steps below:

(1) shuffling of dataset in a random manner
(2) splitting of the shuffled dataset into nine groups in a stratified manner
(3) from (2), select seven groups of the split data as training dataset to fit the model
(4) evaluate the trained model using the remaining two groups of split data, i.e. the validation dataset, with reference to the area under the receiver operating characteristic (ROC) curve
(5) repeat (3) and (4) for a total of five times

Each of the analysis cases were trained and evaluated with the set of preprocessed data based on the same workflow. Scikit learn packages were used for the implementation of the Decision Tree and Random Forest algorithms, whereas the XGBoost package was adopted for the XGBoost algorithm.

5.2.3. *Performance Evaluation*

Performances of the ML models in this pilot study were evaluated using the Area Under Curve (AUC) of the receiver operating characteristic (ROC) curves (see Figure 5). An ROC curve plots the true positive rate (TPR) against the false positive rate (FPR) for different classification thresholds, such that the pre-determination of the threshold is not required. A higher ROC AUC value indicates a better performance of the model over the whole range of the classification threshold. This evaluation metric is chosen since it does not require a predetermined classification threshold, which is non-trivial given the modelling approach adopted in this pilot study, to define the splitting of the model predictions in binary classification.

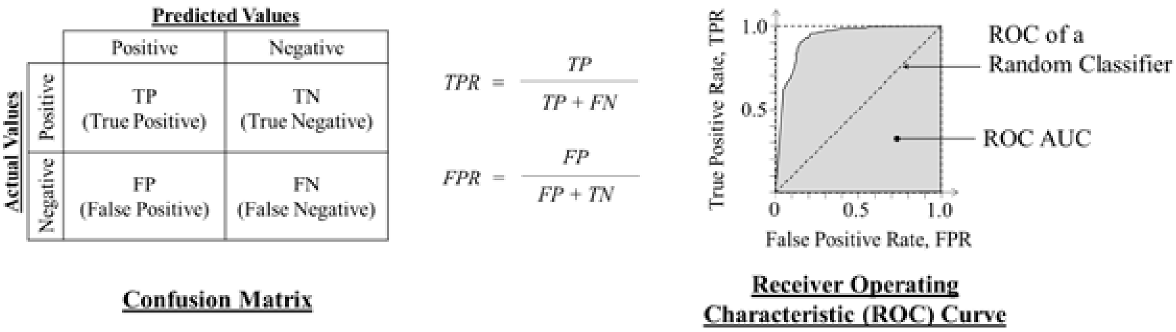

Figure 5 Definition of ROC AUC and Confusion Matrix

The ROC AUC of the ML models assessed based on the different data are summarised in Table 4. A set of ML models considering the features adopted in Ko & Lo (2016) only are also included as reference case.

Table 4 ROC AUC of the Predictive Models

Evaluation Data	Training Data			Testing Data 1 (TD1)			Testing Data 2 (TD2)		
ML Algorithms	Decision Tree	Random Forest	XGBoost	Decision Tree	Random Forest	XGBoost	Decision Tree	Random Forest	XGBoost
Pilot Study	0.9674	0.9965	0.9808	0.8764	0.9083	0.9149	0.9443	0.9670	0.9732
Reference case	0.9571	0.9881	0.9660	0.8770	0.8836	0.8867	0.9499	0.9593	0.9627

On top of the ROC AUC evaluation, Tehrani et al. (2021) suggested to further examine the accuracy of a ML model by validating the areal extent of each susceptibility class against the density distribution of landslides in the landslide inventory. A model is accurate when the landslide density ratio increases moving from low to high susceptibility classes, and when the high susceptibility classes cover small extent of areas only. Table 5 validates the XGBoost model which gives the highest ROC AUC for both TD1 and TD2 among the models tested as an illustration. The pilot study area is divided into eight groups based on the P(+ve) as predicted by the model in a log cycle. The (a) distribution of actual landslides from year 1985 to 2008 as recorded in the ENTLI, and the (b) areal distribution of the study area in each year is tabulated by group. The actual landslide density, $\delta_{Landslide}$, in each of the groups is calculated as dividing (a) by (b).

Table 5 Distribution of Actual Landslide Occurrences and Area by Predicted P(+ve)

Group	I	II	III	IV	V	VI	VII	VIII
Predicted P(+ve)	10^{-8}-10^{-7}	10^{-7}-10^{-6}	10^{-6}-10^{-5}	10^{-5}-10^{-4}	10^{-4}-10^{-3}	10^{-3}-10^{-2}	10^{-2}-10^{-1}	10^{-1}-1
Area (km^2)	117.6 (3.8%)	1486.8 (48%)	1056.8 (34%)	318.8 (10%)	100.9 (3.3%)	19.1 (0.6%)	1.4 (0.05%)	0.004 (0.0001%)
Landslide no.	1 (0.02%)	30 (0.69%)	167 (3.82%)	484 (11.1%)	1268 (29.0%)	1586 (36.2%)	817 (18.7%)	24 (0.55%)
$\delta_{Landslide}$ (no./km^2)	0.009	0.020	0.158	1.518	12.57	83.09	564.3	5,962.7
Actual P(+ve)*	2.13×10^{-7}	5.04×10^{-7}	3.95×10^{-6}	3.80×10^{-5}	3.14×10^{-4}	2.08×10^{-3}	1.41×10^{-2}	1.49×10^{-1}

*Actual P(+ve) refers the actual probability of landslide, which is the product of actual landslide density and grid size.

6. Discussion

6.1. Accuracy

Key observations from the performance evaluation results are summarised below.

(a) The ROC AUC based on training data of all cases are over 96%, indicating that the ML models fit the training data very well.

(b) The ROC AUC based on testing data TD1 and TD2 are over 87%. The maximum ROC AUC were up to 91.5% and 97.3% respectively for the XGBoost models. The ROC AUC based on TD1 is obviously lower than that based on TD2 for all of the cases as the former served as more stringent test on the models' abilities in making forward predictions. All in all, the ROC AUC values achieved reveal that all of the ML models are able to make fairly accurate predictions.

(c) XGBoost and Random Forest models perform better than Decision Tree models based on the testing data. The results are also shown in Table 4. As compared with the reference case, the introduction of additional features improved the performance of the ML models, the effect is more obvious when the models were tested with TD2.

(d) In Table 4, about 85% (3,695 out of 4,377 nos.) of the landslides fall within 4% of area of the highest landslide susceptibility (Susceptibility Classes V to VIII), demonstrating that the ML model is giving fairly accurate susceptibility predictions.

6.2. Predicted Probability vs Actual Probability

Under the adopted approach, the predicted P(+ve) is directly taken as the predicted landslide probability. This section validates this assumption. Figure 6 plots the actual landslide probability [Actual P(+ve) in Table 5] of the pilot study area from year 1985 to 2008 by P(+ve) as predicted by the XGBoost model. A linear relationship with a gradient of unity is observed, indicating that the two quantities are close to each other. As such, the predicted P(+ve) of the ML model under the adopted approach provides a fairly realistic indication of, and can been taken as a proxy to, the predicted landslide probability for practical applications.

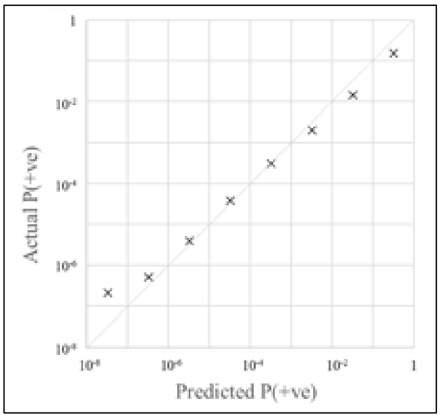

Figure 6 Actual Landslide Probability by Positive Classification Scores (XGBoost model)

6.3. Spatial Resolution

The spatial forecast of landslide susceptibility models is often presented as susceptibility maps. Each of the grids on the map represents the reclassified or calibrated landslide occurrence prediction of the location covered. Table 6 compares the range of the landslide probability of the entire pilot study area as predicted by the XGBoost model under rainfall intensities corresponding to the mean normalized 24-hour NMRR intensities of 24-hour NMRR Classes I to V in Ko & Lo (2016). The range of the landslide probability based on an XGBoost model considering the three features adopted in Ko & Lo (2016) only is also included for reference (the reference model). With the additional topography-related features considered in the former model, it differentiates the landslide susceptibility of terrain with a higher spatial resolution by two to three orders of magnitude for each of the rainfall intensity classes considered.

Figure 7 shows an extract of the landslide susceptibility maps near the Tai O area as predicted by the reference model and the XGBoost model under a hypothetical constant rainfall scenario with 24-hour NMRR Class IV to illustrate the difference. Again, the XGBoost model is able to distinguish landslide susceptibility with a much higher resolution as compared with FS1-24hr-XGB.

Table 6 Range of Predicted Probability of the Pilot Study Area

24hr NMRR		Rainfall Class I	Rainfall Class II	Rainfall Class III	Rainfall Class IV	Rainfall Class V
XGBoost	Min	9.89×10^{-9}	1.17×10^{-8}	4.17×10^{-8}	1.35×10^{-7}	2.17×10^{-7}
Model	Max	1.57×10^{-3}	1.63×10^{-3}	1.34×10^{-2}	9.59×10^{-2}	2.71×10^{-1}
Reference	Min	2.12×10^{-7}	2.54×10^{-7}	6.35×10^{-7}	3.45×10^{-6}	9.61×10^{-6}
Model	Max	2.04×10^{-5}	3.36×10^{-5}	2.10×10^{-4}	2.68×10^{-3}	2.56×10^{-3}

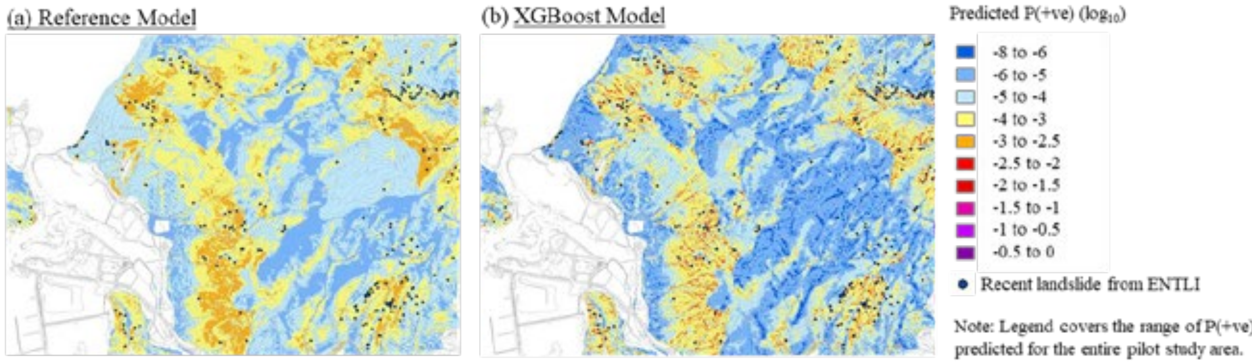

Figure 7 Landslide Susceptibility Map of the Tai O Area (24h-NMRR Class IV)

7. CONCLUDING REMARKS

Over the years GEO has been conducting technical development work on LSA for natural hillsides. This pilot study is carried out to explore the potential improvement to the existing landslide susceptibility model of natural terrain that can be brought about by the application of ML analysis. It is different from the other ML-based LSA on two aspects: 1) the adoption of a different modelling approach instead of data sampling to tackle the issue of acutely imbalanced dataset, and 2) the placing of emphasis on the incorporation of domain knowledge throughout entire workflow of the study.

The adopted modelling approach is proven to work fairly well, with the ML models giving accurate susceptibility predictions which can be taken as a proxy to landslide probability. ML-models allow a systematic way to include additional features for LSA. The results of the study show that the resolution of the susceptibility map is enhanced by two to three orders of magnitude upon the introduction of three critically assessed additional features. The degree of improvement to the spatial resolution of the landslide susceptibility map is similar for the range of rainfall intensity considered.

However, a fine balance should be struck between the predictive performance and the interpretability of the model. While being powerful, the ML algorithms learn the association between landslide occurrences and the set of features in various manner without considerations on the physical mechanism of slope failure behind. As such, the use of ML does not guarantee better susceptibility models that is physically meaningful unless it is applied with the input of sound professional knowledge. In this pilot study, we have demonstrated the introduction of domain knowledge to machine learn-based models through critical feature engineering works, proper selection of suitable algorithms, and detailed assessment of the model performances.

As a pilot study, the conducted analyses focused on the group of the most promising features and algorithms, based on rainfall and landslide data up to year 2008 only. Before the study is expanded to a territory-wide scale, we believe the models can be further enhanced on various aspects. Suitable additional features fulfilling the same feature selection framework will be introduced in a step-wise manner with a view to maximizing the amount of information gain while maintaining the feature space of the dataset in a reasonable dimension. Additional ML algorithms may also be considered. As this pilot study considered rainfall and landslide data up to year 2008 only, the dataset will be expanded to cover data of nearer years for testing of the ML models. Retraining of the ML models will also be carried out if necessary, especially when data associated with high rainfall intensity become available. Rainfall intensity characterised in different rolling durations may be considered. Scale effect and effect of post-landslide topography may also be explored.

ACKNOWLEDGEMENTS

This paper is published with the permission of the Head of the Geotechnical Engineering Office and the Director of Civil Engineering and Development, the Government of the Hong Kong Special Administrative Region, China.

REFERENCES

Brabb, E.E. 1984. Innovative approaches to landslide hazard mapping. *Proceedings of 4th International Symposium on Landslides,* 1, 307-324.

Breiman, L., Friedman, J.H., Olshen, R.A.& Stone, C.J. (1984). *Classification and Regression Tree.* Wadsworth, New York.

Breiman, L. (2001). Random Forest. *Machine Learning*, 45, pp. 4-32 (2001).

Chen, T. & Guestrin, C. (2016). XGBoost: A Scalable Tree Boosting System. *Proceedings of the 22nd ACM SIGKDD International Conference on Knowledge Discovery and Data Mining. San Francisco, CA:* 785-794.

Dai, F.C. & Lee, C.F. (2001). Terrain-based mapping of landslide susceptibility using a geographical information system: a case study. *Canadian Geotechnical Journal*, 38, 911-923.

Dou, J., Yunus, A.P., Merghadi, A., Shirzadi, A., Nguyen, H., Hussain, Y., Avtar, R., Chen, Y., Pham, B.T., Yamagishi, Ho., (2020). Different sampling strategies for predicting landslide susceptibilities are deemed less consequential with deep learning. *Science of The Total Environment*, 720, 137320.

Evans, N.C. and King, J.P. (1998). *The Natural Terrain Landslide Study - Debris Avalanche Susceptibility (TN 1/98)*, Geotechnical Engineering Office, Hong Kong.

Ko, F.W.Y. & Lo, F.L.C (2016). Rainfall-based landslide susceptibility analysis for natural terrain in Hong Kong - A direct stock-taking approach. *Engineering Geology*. 215: 95-107.

Ko, F.W.Y. & Lo, F.L.C (2018). From Landslide Susceptibility to Landslide Frequency: A territory-wide study in HK. *Engineering Geology*. 242: 12-22.

Li, H.W.M., Lo, F.L.C., Wong, T.K.C & Cheung, R.W.M. (2022). Machine Learning-Powered Rainfall-Based Landslide Predictions in Hong Kong - An Exploratory Study. *Not yet published.*

Ma, Z., Mei, G. & Piccialli, F. (2021). Machine Learning for Landslides Prevention: A Survey. *Neural Computing and Applications*. 33(17), 10881–10907.

Merghadi, A., Yunus, A.P., Dou, J., Whiteley, J., Pham, B.T., Bui, D.T., Avtar, R., Abderrahmane, B. (2020). Machine learning methods for landslide susceptibility studies: A comparative overview of algorithm performance. *Earth-Science Reviews*, 207, 103225.

Ng, C.W.W., Yang, B., Liu, Z.Q., Kwan, J.S.H., Chen, L. (2021). Spatiotemporal modelling of rainfall-induced landslides using machine learning. *Landslides*, 18: 2499-2514.

Reichenbach, P., Rossi, M., Malamud, B.D., Mihri, M., Guzzetti, F. (2018). A review of statistically-based landslide susceptibility models. *Earth-Science Reviews 2018*, 180: 60-91.

Tehrani, F.S., Calvello, M., Liu, Z.Q., Zhang, L., Lacasse, S. (2021). Machine learning and landslide studies: recent advances and applications, *Not yet published.*

Wang, H., Zhang, L., Lau, H., He, J., Cheung, R.W.M. (2021). AI-powered landslide susceptibility assessment in Hong Kong. *Engineering Geology*, 288, 106103.

Wong, H.N. (2003). Natural Terrain Management Criteria – Hong Kong Practice and Experience. *Thirty Years of Slope Safety Practice in Hong Kong*. Geotechnical Engineering Office, Hong Kong.

Wong, H.N. (2009). Rising to the challenges of natural terrain landslides. *HKIE Geotechnical Division Annual Seminar 2009*, Hong Kong, 15–53.

Xiao, T. & Zhang, L. (2021). Storm-based forecasting of man-made slope failures using machine learning. *Proceedings of the 20th International Conference on Soil Mechanics and Geotechnical Engineering*, Sydney 2021.

3D Wireless Seismic Survey Technology and its Application in Hong Kong

A Cunningham, Y Sitanggang
Geophysical Services Singapore Pte Ltd, Singapore

K M Chiang
Shanghai Tunnel Hong Kong Co., Ltd., Hong Kong, China

D Remus
Palladin Phuket Co. Ltd., Thailand

D Voss
Mint Seismic, Australia

ABSTRACT

Design and construction of underground structures, such as basements and tunnels, always face the risk of unforeseen ground conditions, which are difficult to determine based on preliminary GI information. Traditionally, GI information, such as desk study, trial pits, and boreholes can only provide discrete details. This leads to unnecessary design review and introduces additional time and cost implications to the project. Seismic surveys, commonly used in the "Oil & Gas" industry, may provide an alternative solution to allow the interested parties to acquire valuable underground information through a non-destructive approach. In this paper, an advanced 3D wireless seismic survey technology will be introduced, which has recently been conducted in Hong Kong to collect additional underground information for the construction work.

The technology uses unique seismic sources combined with an expandable wireless multi-channel seismic data acquisition system and GPS to collect comprehensive seismic data. These recordings are taken and, using specialised seismic data processing, transformed into 3D visual images of the earth's subsurface in the survey area. And geoscientists can indirectly use those seismic data to obtain a picture of the structure and nature of the stratum and rock layers' structure and character. The technology is instrumental in urban areas as it possesses the flexibility and mechanism to scan the location where the surface is obstructed by structures.

1 INTRODUCTION

Mapping the shallow near-surface geology for construction purposes in a "City" environment has always been a challenge. In the case of this subject matter, we are engaged to construct a subway tunnel beneath the major high-speed road (RED route) by the trenchless method, where the road comprises eleven lanes of highway lanes, one small side road, one wide pedestrian path and several central reservations and verges.

The subway will be constructed by the Jack-in place segment RTBM method; it is essential fully understand the underground geology condition before the machine design. As the highway structure is the primary route for vehicular traffic in the East Kowloon area, any lane closure for the destructive survey is impossible. A seismic survey is then deployed as an alternative approach to achieve the objective.

The challenge, therefore, was to acquire high resolution, high-quality geophysical data, to a depth of 100+ meters, beneath a highway that is subject to 24 hours heavy traffic flow, where the random acoustic noise that such an environment creates needed to be attenuated, and where the artificial seismic source signal needs to be amplified.

This project had demonstrated that with the advanced wireless seismic devices and details work planning, a comprehensive seismic survey (3D mapping) to the area of interest, which is obstructed by existing structures or even inaccessible, can be done. The team included a task force in Hong Kong which was responsible for field equipment and facilities setup and operation; the acquired data were positioned by GPS and instantaneously sent to the data centre in Singapore, which was supported by a crew of geophysics technicians, verifying and accepting the data and gave a real-time response in case abnormality was found during the operation. The results from the survey are sent to geophysics experts for analysis and interpretation in Australia. The whole process was a joint effort by specialists worldwide, and the findings will benefit designers / interested parties in the project.

2. WIRELESS SEISMIC SURVEY TECHNOLOGY AND ITS APPLICATION IN HONG KONG

In land seismic surveying, sound waves are mechanically generated and sent into the earth. Some of this energy is reflected back to recording sensors, measuring devices that record accurately the strength of this energy and the time it has taken for this energy to travel through the various layers of geological layers and back to the locations of the sensors. Some of this energy is also refracted back to the recording sensors, giving precise velocity information of the underlying strata as well as a velocity profile picture.

These recordings are then taken and, using specialised seismic data processing, are transformed into visual images of the subsurface of the earth in the seismic survey area. Geoscientists use seismic surveying to obtain a picture of the structure and nature of the rock layers indirectly.

Energy from a sound source is released. The magnitude of the pressure is called 'amplitude', and the excited waves are P-waves or compressional waves. The energy source will propagate P-waves, and the sensors that will make accurate measurements of the amplitudes of P-waves are geophones. P-waves will hit the rock, and the reflected signals will be recorded.

In Land 2D operations, a single land seismic array is deployed together with a single seismic source. The reflections from the subsurface are assumed to lie directly below the line, providing an image in two dimensions (horizontal and vertical). In Land 3D operations, two or more land seismic arrays are deployed together with single or multiple seismic sources. The reflections from the subsurface are collected through a range of azimuths delivering what is generally known as wide azimuth 3D data. The two operations supplement each other.

Where obstructions and impediments prevent continuous/contiguous data acquisition, use a wireless seismic recording system to either "shoot around" or "undershoot" any such obstructions. This array layout shall be designed on a case by case basis based on experience in acquiring data in such conditions.

To meet the geophysical objectives, a high-density spread of geophones was deployed and placed in closed lanes. The geophones were positioned to give wide azimuth, near, mid & far offsets from the seismic source, delivering (>1,500,000) common data points across the entire area of interest. The whole survey took 17 days to acquire, where one "traffic lane" of data and two "verges" of data was obtained during each nighttime data acquisition period (2 hours only per night) to minimise disturbance to the traffic flow.

<u>Geological objectives of this survey are summarised as follows:-</u>

a) Measure the interface between the Fill, Alluvium, Weathered Granite and Fresh Granite.
b) Geological target depth of interest was 5 meters to 100+ meters depth range.
c) Identify any geological anomalies, including boulders > 250 mm in size, cavities and voids
d) Compare results with known geological data, including borehole data.
e) Deliver an accurate geological interpretation of the seismic survey results showing the geological profile, identified and unidentified objects, cavities, voids, faults and fracture zones.

<u>The Resulting "Survey plan and method" to meet the geological objectives:-</u>

a) The most appropriate identified geophysical method was a 3D seismic survey, using a wireless seismic recording system with a portable seismic energy source.
b) Seismic spread layout required to meet geological objective was;
    i. 1 x Floating geophone sub-array patch comprising 48 Geophones (arranged in a 3 x 16 Geophone array) (rolling across 13 traffic lanes) and
    ii. 2 x Fixed geophone sub-array patches comprise 96 Geophones (arranged in two separate 3 x 16 Geophone arrays) (Placed on the central verges) across the defined survey area.
c) Source to receiver offsets were arranged such that the shallow to deeper geological target ranges could be imaged with a wide range of offsets and a broad range of azimuths.
d) Conduct 3D reflection seismic data processing and data interpretation.
e) Survey Geometry requirement; Receiver interval 1 meter, Shot interval 0.5 metres, asymmetrically derived CMP interval was 12.5 centimetres, and resulting CMP bin size of 12.5. x 12.5 centimetres.
f) Deliver the investigation results and interpretation in a compiled report with supporting documentation.

(More conventional seismic methods (i.e. Cabled reflection, refraction, MASW, downhole cross-hole, GPR were all excluded as viable geophysical methods as a) they Cannot be deployed across a highway, b) Resulting data would not be conducive to nor meet the prescribed geological objectives, i.e. depth, accuracy, resolution, wide azimuth 3D spatial coverage and resolution.)

Technical Objectives:

a) Acquire high-quality seismic data within or exceed manufacturers' specifications and capabilities.
b) Record data within 0 - 100+ m below ground level.

Operational Objectives:

a) Acquire data set on time, with no accidents, no harm to people and no damage to the environment.
b) To implement all necessary HSE measures according to Industry and regulatory authorities.

Survey Area overview

The survey area was located in Hong Kong, beneath the Prince Edward Road East highway. See Figures 1 & 2.

Figure 1; Showing survey location in Hong Kong (Red marker)

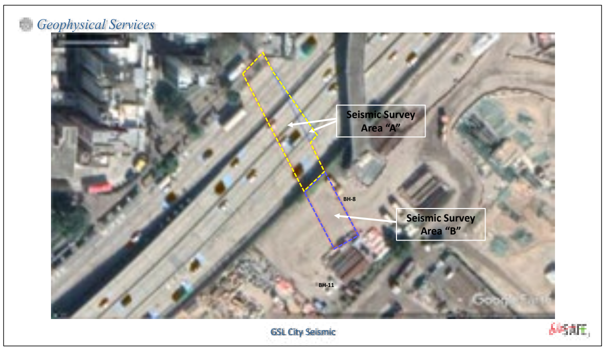

Figure 2; Showing satellite view of survey area across the Prince Edward Road East highway

The area can be described as residential on the north side of the highway, with many high-rise residential apartment blocks on the periphery of the work area. This presents environmental challenges concerning the noise emitted by the seismic energy source.

The main issue was balancing heavy vehicular traffic noise interference with the seismic signals versus disturbance to the residents during the early hours when the noise created by the seismic source could disturb the residents' sleep.

The geology based on borehole information and historical geological information indicates that the area comprises the following:

a) Reclaimed land, road tarmac and path surface; b) Land Fill; c) Alluvium; d) Weathered Hong Kong Granite; e) Fresh Hong Kong Granite

Figures 2 & 3 show the survey area depicted across the PERE Highway. One can clearly understand from this satellite picture the operational challenges involved with acquiring geophysical data across an extremely busy highway. Figure 4 is an excerpt from the Geological Interpretive Baseline Report showing the work area versus the roads and local building infrastructure, including three nearby boreholes.

Figure 3; Showing satellite view of survey area across the Prince Edward Road East highway

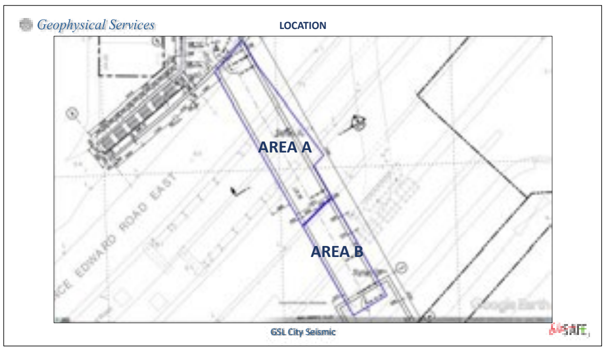

Figure 4; Showing GIBR plan of seismic survey area overlay onto topo map

The local environmental situation as described above clearly shows the physical limitations imposed on the survey design and survey acquisition teams. Further to this, there are practical limitations imposed upon the planned survey, including the following:-

a) Working hours are limited to 2 hours per day between 2 a.m. to 4 a.m.
b) Noise limitations imposed during night hours. (**Use noise enclosure**)
c) Traffic disruption, one traffic lane, for 2 hours/day during off-peak hours.

Final resulting survey patch layout (See figures 5, 6, 8 & 9) comprised the following:-

Array Type	**Patches**	**Geophone Arrangement**	**Location**
Floating Sub-Array	13	One x 48 geophones laid out in a symmetrical 3 x 16 geophone array with 1 meters receiver spacing	Traffic lanes 1 to 13
Fixed Sub-Array	2	Two x 48 geophones laid out in a symmetrical 3 x 16 geophone array with 1 meters receiver spacing	Verges 1 & 2
Offset ranges		0 - 75 meters Shot to Receiver, horizontal distance	

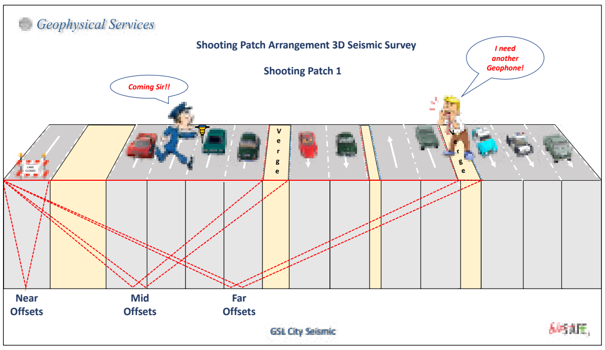

Figure 5; Showing Geophone sub-arrays and seismic ray-paths where seismic source is in lane 1

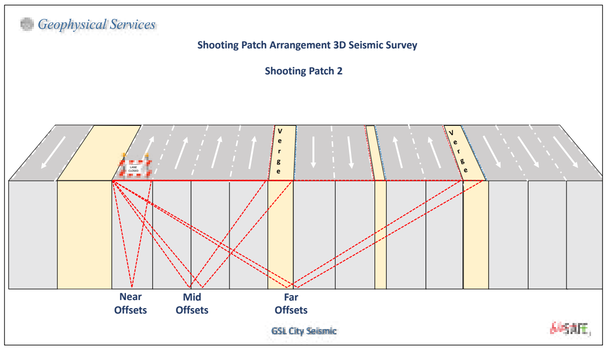

Figure 6; Showing Geophone sub-arrays and seismic ray-paths where seismic source is in lane 3

The resultant Geophone plan and shooting arrangement based on area access and geological objectives are described as follows:

a) Geophones (Floating Sub-array) were placed in the one (1) closed traffic lane, and this sub-array was moved across the traffic lanes, one new lane each night, onto a newly closed lane. (See figs 8 & 9)

b) Geophones (Fixed sub-arrays) were placed in two of the central verges, permanent throughout the survey. (See figs 8 & 9)

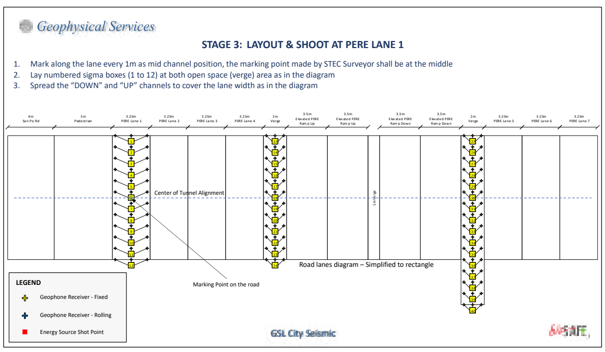

Figure 8; Showing Seismic survey sub-array(s) geophone deployment

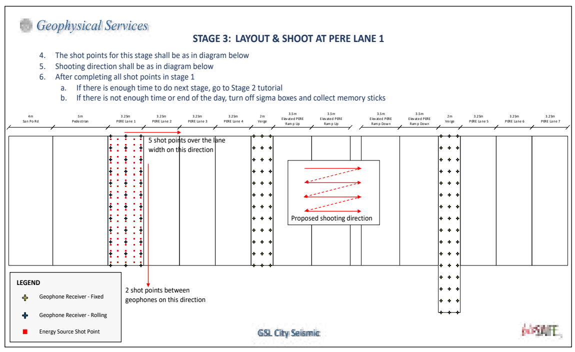

Figure 9; Showing Seismic survey sub-array(s) geophone point and shot point arrangement

2.1. Data acquisition

For this survey, the following survey parameters were used:-

Type of Seismic Survey:	3D Land / Onshore
Recording System:	i-Seis Sigma
Recording Length:	1 second
Sampling Rate:	0.25 ms
Energy Source Type:	PSS-100 Portable Source
Thumps Per Shot:	3 thumps per shot point
No. of Groups:	3 x 48 GS-One geophones sub-arrays (15 meters x 3.5 meters)
Shot Interval:	0.5 m
Group Interval:	1.0 m
CMP Bin Size:	12.5 x 12.5 cms

Access to the survey area was restricted to two hours per day (between 2 a.m. to 4 a.m.).
The receivers were laid out in the pattern shown in figure 8, where one (1) road lane was closed for the Floating Sub-array (Near seismic channels) during each data acquisition period and where two Fixed Sub-arrays (mid and far seismic channels) were placed permanently in the centre of the highway on easily accessible road verges. (See figure 10 & figure 11)
There were 13 x Floating sub-array rolls across the highway (figure 2. Seismic Survey Area "A"), with additional patches shot in the waste ground to the south of the highway (figure 2. Seismic Survey Area "B").

Figure 10; Showing Seismic survey Floating sub-array & Fixed Sub-array geophone deployment

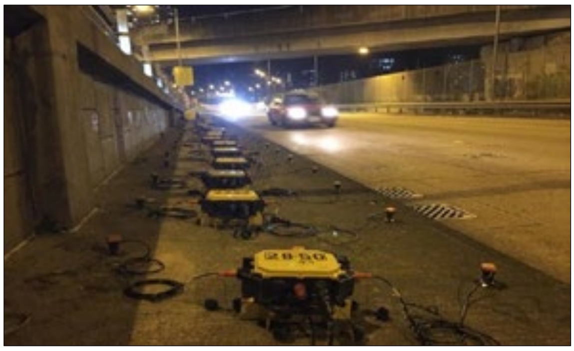

Figure 11; Showing Seismic survey Fixed sub-array(s) geophone deployment

Resulting data, Raw data, 3D binning & Fold coverage;

- At each shot point, three (3) thumps were emitted from the energy source.
- The three thumps were stacked into a single V-Stack in processing, thus eliminating a significant amount of the surrounding area generated ambient noise, i.e. improving the signal to noise ratio by a factor of 3:1
- The fold coverage achieved was in the order of 150 fold, further eliminating the ambient noise.
- The entire survey area was a rectangle of dimensions 15m x 100m. For seismic survey purposes, this rectangle was further sub-divided (in processing) into small squares (12 cms x 12 cms). The common midpoints were accurately binned, resulting in an almost perfectly symmetrical binned data set.
- Figure 12 shows the midpoint distribution of the acquired 3D seismic data set.
- Figure 13 shows Raw Shot data
- Figure 14 shows the final post-plot shot & receiver points across the entire area

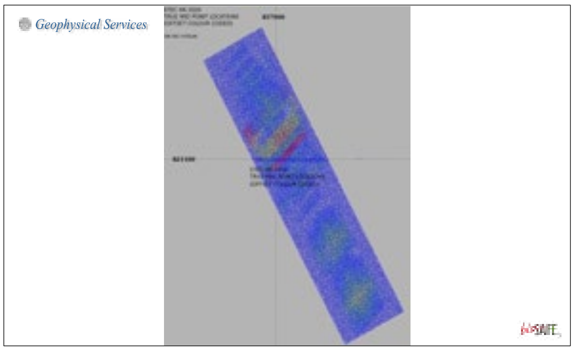

Figure 12; Showing True Mid-Point scatter of CMP data.

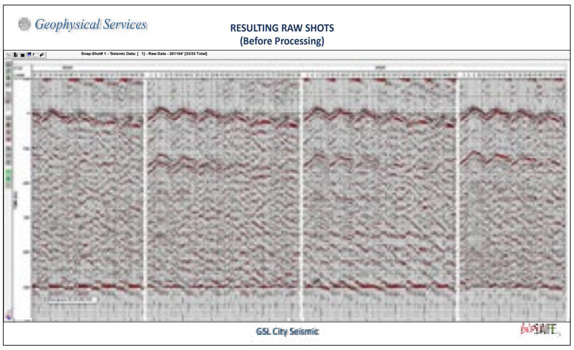

Figure 13; Raw Shot records across 3 Sub-Arrays

Figure 14; Post-Plot diagram showing each and every shot point and receiver points across the entire survey area

3. DATA PROCESSING

Acquisition and survey parameters

3D survey description

The 3D survey consisted of approximately 11300 shot records acquired at 3876 shot locations over an area of 1435 square metres.

Trace parameters		**Source parameters**	
Record length:	600 milliseconds	Source type:	Accelerated weight drop
Sample interval:	0.25 milliseconds	Thumps per shot location:	3 (nominal)

	AREA "A" (Northern Area)	**AREA "B" (Southern Area)**
Receiver line spacing:	1.25 metres	2.0 metres
Receiver interval:	1.0 metres	1.0 metres
Source line spacing:	0.6 metres	1.0 metres
Source interval:	0.5 metres	0.5 metres

The live patch typically consists of 9 receiver lines, with up to 144 live channels.

2D survey description

Line length:	54 metres	Shot interval:	1.0 metre
Receiver interval:	1 metre	CMP interval:	0.5 metres

Output grid was aligned with the planned tunnel, and the Bin dimensions were: 0.5m x 0.5m

Comments on input data, output data, and processing

The survey consisted of a full-azimuth, high-density, high-quality 3D field. The receiver and source arrays were filled-grid, apart from a small number of gaps due to obstacles.

The polarity convention used is such that a positive impedance change results in a positive deflection.

The ambient noise was moderate. The hard tarmac surface in places was a cause for high-frequency reverberation, largely ameliorated by adaptive noise removal techniques. To suit various purposes, three different versions of the data were produced with different spectral weighting, referred to as non-spectral weighting, milder spectral weighting and stronger spectral weighting. The strong spectral weighting option resulted in a volume with a dominant frequency of 290 Hz at the target depth, and the milder option had a dominant frequency of 215 Hz. In the target area, the maximum frequency of useful reflection data was approximately 400 Hz.

Processing sequence summary

Three different versions of the output were produced, referred to as the non-spectral weighting, milder spectral weighting, and stronger spectral weighting options, to give the interpreters a choice of which frequency balance was suitable for various aspects of the analysis.

1. Reformat to Globe Claritas internal format
2. Apply geometry headers from observer's logs, apply 0.5 x 0.5 rectilinear grid geometry
3. ad shot and trace edit
4. Shot summation (diversity summation)
5. First break picking and refraction model calculation
6. Spherical divergence correction (G=V^2*T) using regional velocities
7. Random & linear noise attenuation (Mintox ANA)
8. Gap deconvolution (adaptive deconvolution used in some areas)
9. Refraction statics application
10. First-pass velocity analysis at 10 m x 10 m intervals
11. Residual statics calculation
12. Second pass velocity analysis at 5 m x 10 m intervals
13. NMO using 2nd pass velocities
14. Residual statics application
15. CMP trim statics calculation and application
16. Stacking mute, hand-picked
17. Pre-stack scaling
18. Stack
19. Post-stack spectral weighting, coherency filtering, bandpass filtering, scaling
20. Phase correction
21. Shift to final datum
22. -> SEG-Y out time-domain stacks
23. Depth conversion using a simple velocity model
24. -> SEG-Y out depth domain stacks at final datum

4. 3DATA INTERPRETATION

4.1. Geology of the area

The geology of Hong Kong is described in detail in the "Geology Of Hong Kong (Interactive On-line)" publication of the Civil Engineering and Development Department (CEDD) of the Government of the Hong Kong Special Administrative Region. Figure 1 is taken from that report and is a map of the geology of Hong Kong.

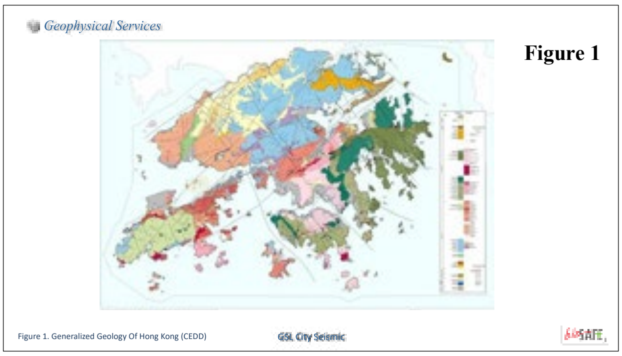

Figure 1. Generalized Geology Of Hong Kong (CEDD)

The survey was in the Kowloon area (Figure 2), where granite is exposed at the surface north and west of the survey area. Granite is also found underfill and Quaternary alluvial and colluvial sediments in the specific survey area. A marine survey map of 1841 (Figure 3) shows the presence of granite cored islands just offshore of the survey area in an area now entirely covered by fill. It is possible that similar pinnacles of fresh granite could be present in the survey area.

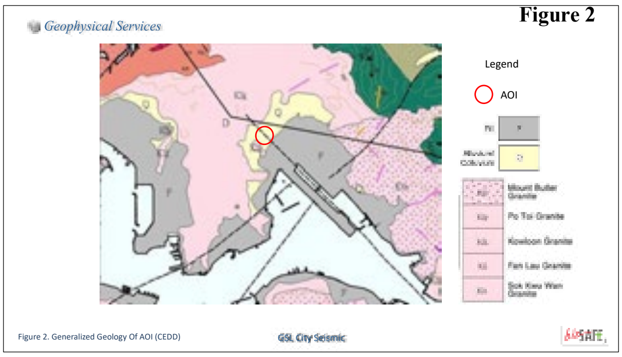

Figure 2. Generalized Geology Of AOI (CEDD)

Figure 3. 1841 Marine Chart HMS Sulphur

Mesozoic granitic and volcanic rocks make up almost 85% of the rock outcrop on land. Several distinct granitic terrains are recognised. The remaining area is comprised of Pleistocene to recent colluvial and alluvial deposits. Colluvium covers most hillsides in thin layers and can be thick in granitic terrains. Cobbles and boulders can be present. Alluvium can be found in river valleys, coastal floodplains, and deltas. In the survey area, 15 to 30 meters of alluvium is measured. Figure 4 is taken from K. W. Lai and shows an outcrop of alluvium with abundant cobbles present.

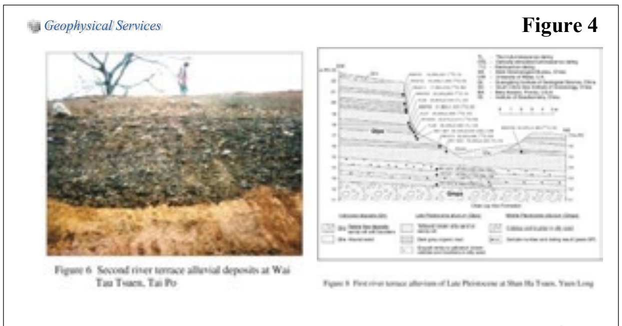

Figure 4. Examples Of ALLUVIUM. L. W. Lai, 2011

4.2. *Kowloon and mt butler granites*

The survey area is underlain by the Kowloon and Mount Butler Granites that form sub-circular plutons centred on Kowloon and Hong Kong Island. The Kowloon Granite is uniform in texture and composition and is typically a biotite monzogranite. The Mount Butler Granite, a subcircular leucocratic monzogranite, intrudes the Kowloon Granite. Pegmatite patches and miarolitic cavities are common, particularly close to the granite–volcanic contact.

4.3. *Weathering profiles*

The weathering profile of the Kowloon and Buter Granites has been established (Shaw, 1997) using borehole records supported by field mapping. The correlation between the topography of the weathered profile base and the main structural trends is evident. Zones of deep weathering have been preferentially eroded to create valleys, which subsequently became sites of alluvial and colluvial accumulation. Variations in weathering patterns are primarily a function of the geometry and infilling of relict jointing, which determines local hydrogeology and hence the intensity of weathering. Corestones are generally restricted to weathered profiles over topographically high areas, the locations of which are controlled by regional joint spacing and orientation. Corestone-bearing profiles are rare, and more commonly, deeply weathered granite without corestones passes abruptly into relatively fresh rock. This has important implications for engineering ground models derived from borehole interpretation.

Granite exhibits a multi-layered weathering profile near the surface, as described in Figure 5. In engineering terms, the GIII is generally considered the "Rockhead", although GIV is a transition zone that may comprise highly weathered intact rock, fractured rock or a mix of GV and GIII rocks. In some cases, GIV is considered "Rockhead". While GV and GVI are considered soils, they are often described as hard, dense to very dense and may impact engineering projects such as dredging.

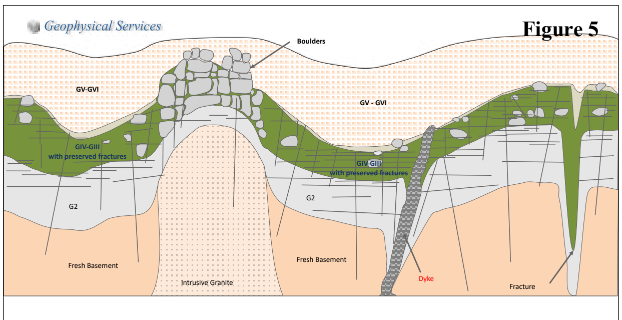

Figure 5. Granite Weathering Cross-section

The Rockhead granite (GIII/GIV or greater) is typically undulating, with frequent domes and valleys as seen. Intrusive granite domes may cause harder rock to be nearer the surface, and occasionally, intrusive dykes may be present. Fractures can often result in a deeper weathering profile.

4.4. *Data*

- Three boreholes, BH-5, BH-8 and BH-11, which prove relevant to the survey, were provided. Additional boreholes that are not within the survey were also offered. The borehole locations are shown in Figure 6a.
- Potential Hazard objects were also provided. These included five pipeline locations with depths Figure 6b.
- An elevation model derived from the seismic survey data.

- The 3D seismic survey comprised 1435 square meters of high-resolution seismic reflection and velocity data coverage. The data was provided in Time and Depth domains with a low-frequency 3D cube for event mapping and a high-frequency 3D cube for attribute analysis. The data quality is good to very good.
- Interval Velocity Volume for the 3D cube.
- A 2D seismic profile crossing the 3D and tying to BH-8 and BH-11. Also, in Time and Depth. The data quality is good to very good.
- Various geological and geophysical data available in the public domain were collected and referenced herein.

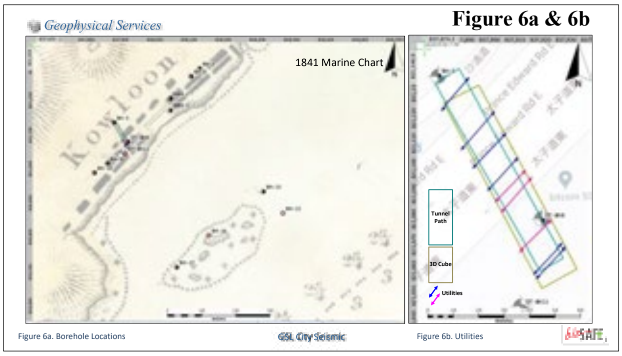

Figure 6a & 6b

Figure 6a. Borehole Locations

Figure 6b. Utilities

5. ANALYSIS

5.1. Borehole descriptions

The boreholes describe mixed fill comprised of rock and concrete fragments, some asphalt and clayey sand, silty sand and gravels to a thickness of 6.6 meters. There are thin layers of pavement in places. The alluvium comprised of mixed sand, gravel, clayey sand, and silty sand is encountered. The alluvium is up to 30 meters in thickness. There is no mention of cobbles or boulders being encountered in the alluvium. Marine deposits encountered in BH 11 are sandy with shell fragments. Completely decomposed granite Grade V is described as extremely weak, white and pink to dark brown-grey to spotted white, medium-grained. It reaches 36 meters in thickness. Grade IV granite is described as white to pink and medium-grained. This is transitional to Rockhead (Grade III). The granite is described as pink, spotted white to yellowish-brown, moderately strong to strong with weaker intervals. Jointing and fractures are observed.

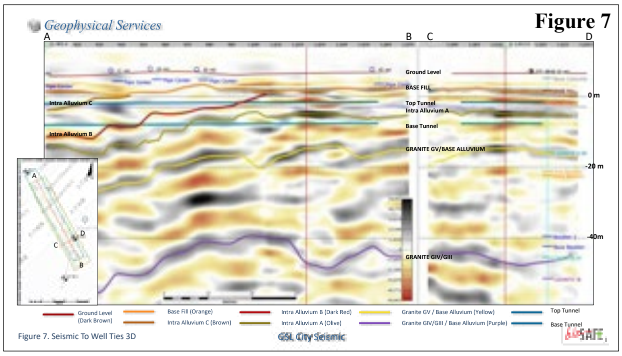

Figure 7

Figure 7. Seismic To Well Ties 3D

5.2. Borehole to seismic ties

Borehole 8 ties to both the 3D volume and the 2D profile. Borehole 11 ties to the 2D profile only. Figure 7 shows the tie to BH 8 within the 3D cube. The key surfaces identified are Base Fill (orange), Granite GV/Base Alluvium (yellow) and "Rockhead" Granite GIII/GIV (Purple). Additionally, three intra alluvium events A, B, and C, are identified. Boreholes 8 and 11 are tied to the 2D seismic profile in Figure 8. The same key surfaces are tied to both boreholes, while an additional Base Marine E surface can be mapped in the BH-11 area. In 2D, the GIV and GIII GRANITE grades can be differentiated, while in 3D, the surface is more gradational between the two grades.

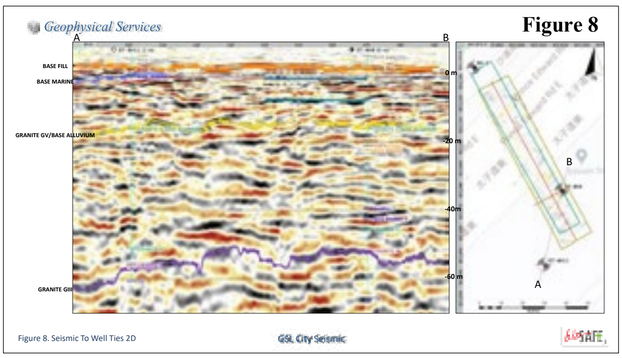

Figure 8

Figure 8. Seismic To Well Ties 2D

The pre-survey analysis of the three boreholes indicated that the tunnel would pass through alluvium with some possible marine deposits in the southern end. This finding is supported by the Borehole to Seismic ties.

5.3. Resolution

A good seismic signal is observed down to at least -50 meters HKPD. This is well below the base of the zone of interest, which is roughly -1 to -7 m HKPD. The "Rockhead" granite is observed at -40 to -50 m HKPD.

Figure 9

In high-resolution seismic surveying for Civil Engineering, understanding the limits of resolvability vs detection is critical. In general, seismic data can resolve the top and base of an event or feature, such as a boulder bed, if the feature is >=λ/4, where Lambda is the dominant wavelength. To calculate Lambda, use λ= v/f where v = velocity of feature to be resolved, and f is the dominant frequency. Figure 9 shows the calculated frequency spectra in the data. The dominant frequency is 270 Hz. A wedge model often used to explain resolution and detection is also displayed. Given a peak frequency of 270 Hz, cobbles or boulders of hazardous size are assumed to be resolvable in the tunnel path.

5.4. Seismic Attributes

The interpretation methodology uses seismic attributes. The following is a discussion of some of the attributes used (Tanner et al.).

Seismic attributes are measurable properties of seismic data such as amplitude, dip, frequency, phase and polarity. Attributes can be measured at one instant in time or over a window of data. They can be calculated on a single seismic trace (one x, y, z data point), a set of paths, or on a seismic surface (geological event) interpreted on the seismic data. Seismic attributes reveal features, relationships and patterns in seismic data that may otherwise not be noticed.

The instantaneous phase attribute is a physical attribute and can be effectively used as a discriminator for geometrical shape classifications, such as lateral continuity, sequence boundaries, bedding configuration and edges. The instantaneous amplitude measures the reflectivity strength, which is proportional to the square root of the total energy of the seismic signal at an instant of time.

It is a measure of reflection strength and can be used to identify lithological contrasts, bedding continuity, bed spacing (thickness), and gross porosity.
The instantaneous frequency is a seismic attribute, which is defined to be the time rate of change of the instantaneous phase. Instantaneous frequencies relate to the wave propagation and depositional environment; hence they are physical attributes and can be used as effective discriminators such as seismic character correlation in the lateral direction, Indication of the edges of low impedance thin beds, fracture zone indicator; they may appear as lower frequency zones, Chaotic reflection zone indicator, due to excessive scatters, bed thickness indicator. Higher frequencies indicate sharp interfaces or thin bedding; lower frequencies indicate thicker bedding. Sweetness is calculated by dividing the instantaneous amplitude (amplitude envelope) by the square root of the instantaneous frequency. The Sweetness attribute reduces the contribution of the higher frequencies. And is useful for the identification of thicker, hard rock units (such as boulders or cobble zones), which will be seen as high amplitude/low-frequency values (DUG Insight software (v.5.1, 2021).

6. SEISMIC EVENTS IDENTIFIED, HORIZONS MAPPED AND LAYERS DESCRIBED

In Figure 7, the key surfaces were identified. These are Base Fill (orange), Intra Alluvium C (brown), Intra Alluvium B (dark red), Intra Alluvium A (olive), Granite GV/Base Alluvium (yellow) and Granite Grade GIV/GIII (purple). The ground level is o displayed as dark brown. The ground level surface was derived from the surveying operation undertaken for the 3D shot/receiver layout.

The Base Fill map (Figure 10) defines the bottom of the Fill layer. The surface is fairly flat but slightly undulating. The depth ranges from 0 mPD to almost 5 mPD. The Fill comprises rock and concrete fragments, some asphalt and clayey SAND, silty SAND and gravels. It varies from 1.6 to 6.6 meters in thickness. Cobbles of rock fragments cemented with concrete are mentioned in BH-8.

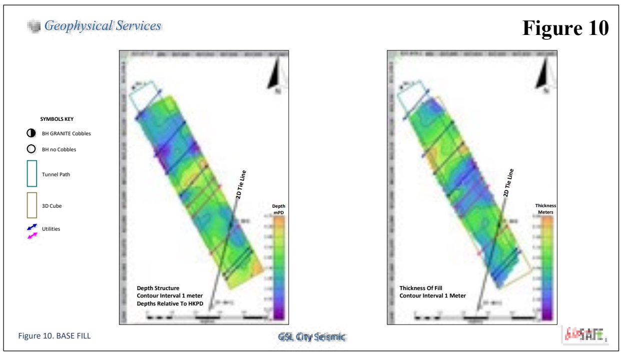

Figure 10. BASE FILL

The upper portion of the fill layer will comprise concrete and asphalt road materials in the PERE area of the survey. Additionally, many utilities, including electricity cables, water and other pipes, are present in the FILL. These utilities can be seen in Figure 6b. No attempt to resolve these utilities was attempted.

6.1. *The Alluvium Layers*

Alluvium is described as consisting of unconsolidated detrital rock material deposited in stream beds or on a flood plain (K. W. Lai.). Three depositional layers are recognised in the outcrop. These are Middle Pleistocene, Late Pleistocene, and Holocene.

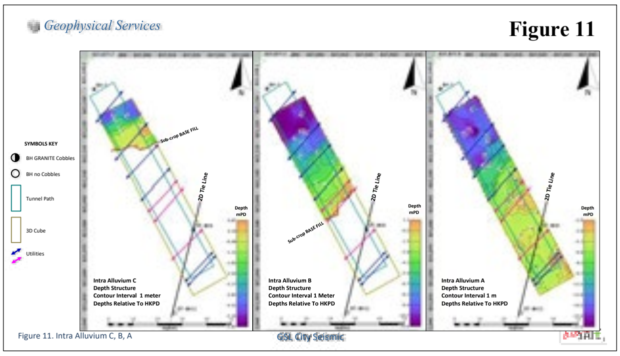

Figure 11. Intra Alluvium C, B, A

The alluvium can be sub-divided into three layers based on seismic data interpretation. This corresponds with what is observed in the outcrop. We have defined these layers as A, B and C from base to top (Figure 7). Layer A, which is considered to correspond to the Middle Pleistocene outcrop, is present throughout the survey area, while Layers B, Late Pleistocene and C Holocene, sub-crop the Base Fill (Figure 11).

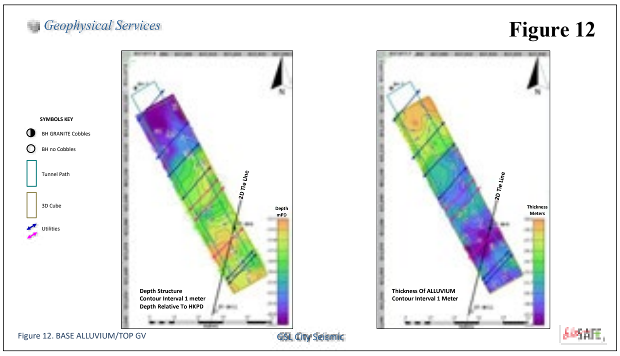

Figure 12. BASE ALLUVIUM/TOP GV

The alluvium ranges from 16 to 31 meters (Figure 12) and thickens and plunges towards the NW. The depth ranges from -28 to -33 mPD. The alluvium, as described in outcrop and boreholes, is comprised of mixed sand, gravel, clayey sand and silty sand. Detailed descriptions of outcrop are found in K. W. Lai.

6.2. *Weathered Granite*

The GV weathered granite is between 18 and 36 meters thick (Figure 13). It is the thinnest in the centre of the survey. The granite is described in BH-8 as extremely weak, reddish yellow to dark brown-grey to spotted white, and medium-grained. Cobbles and boulders are present.

6.3. *Granite*

The granite GIII/IV) is mapped at between -38 and – 59 mPD. It is at its shallowest in the survey centre, where it rises to -37.7 mPD. The GRANITE is described as pink to spotted white and black, moderately strong to strong. Jointing and fractures are observed. While the granite GIII/GIV does rise into a dome in the survey centre, it never reaches heights that could impact the tunnel boring (Figure 13).

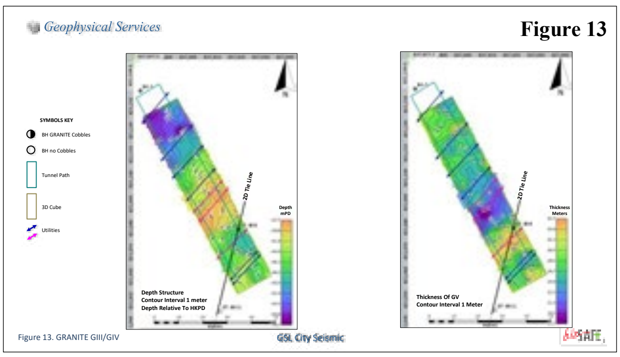

Figure 13. GRANITE GIII/GIV

7. DISCUSSION OF RESULTS

7.1. Known And Unknown Potential Hazards

Known hazards in the area include water and electrical utilities pipelines, as seen in Figure 7b. Utilities are known to be much shallower than the top tunnel and do not impact the tunnelling project.

The alluvium will be comprised of eroded and weathered GRANITE from the Mt Butler and Kowloon GRANITE suites. Cobbles and boulders, although not identified in boreholes, could be present in the tunnel path. The presence of these could present problems for the tunnelling project.

It has already been determined that granite pinnacles are not present in the survey area.
The following analysis aims to determine the probable presence of alluvial boulders.

7.2. Discussion of Objectives and Process

The survey's main objective was to analyse the presence of and location of potential hazards. The analysis has shown that granite is too deep to be a concern, and no granite pinnacles have been identified. The utilities are all in the artificial fill layer and are too shallow to be of concern. Of remaining concern is the presence of large cobbles or boulders.

Once the basic interpretation and identification of the key surfaces are completed, a set of attribute volumes are created or extracted from the Fullstack 3D Depth high-frequency amplitude volume of the 3D data. DUG Insight software (v.5.1, 2021) was used for seismic visualisation, interpretation and analysis. The attributes calculated, and referred to previously in the Seismic Attributes section, include Sweetness, Instantaneous Amplitude, Instantaneous Phase and Instantaneous Frequency.

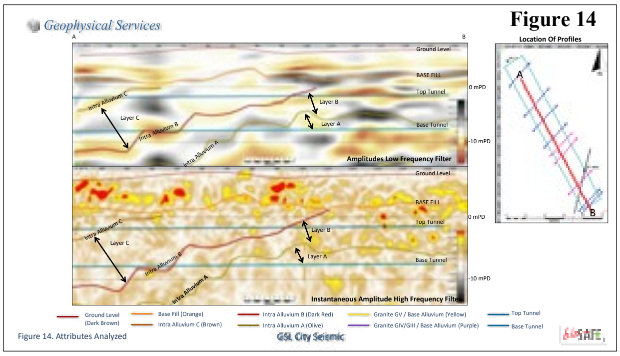

Figure 14. Attributes Analyzed

Figures 14 through 16 are examples of the attributes used in the analysis. In all attribute extractions, the hot colours green to red are higher values. The Amplitude and Sweetness attribute can be equated with higher relative densities. For the Frequency attribute, this indicates higher frequency.

In Figure 14, the upper section is an Amplitude section taken from the low frequency filtered data cube. The lower section is an Instantaneous Amplitude section derived from the high frequency filtered data cube. Within the tunnel pathway (shown by the two cyan coloured lines), three distinct layers of alluvium can be identified. This fits closely with the alluvium as described in K. W. Lai.

The attribute analysis was windowed around these layers and examined Layer A, which is from the base tunnel to Intra Alluvium A, Layer B, which is from Intra Alluvium A to Intra Alluvium B and clipped at the top tunnel and Layer C, which is from Intra Alluvium B to top tunnel.

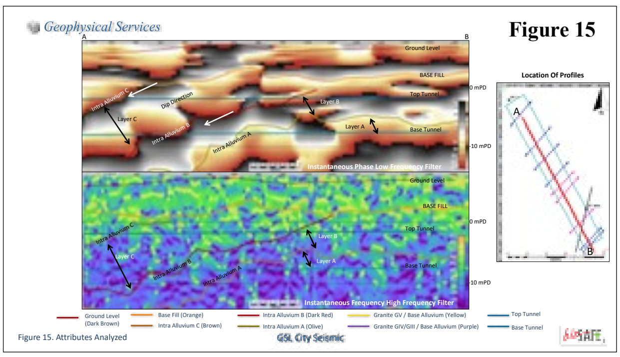

Figure 15. Attributes Analyzed

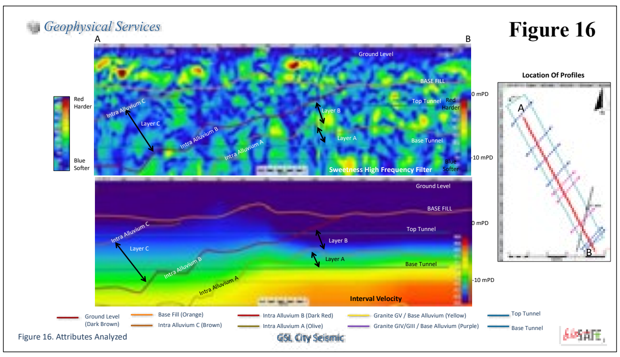

Figure 16. Attributes Analyzed

Figure 15 has an Instantaneous Phase section, which was derived from the low-frequency 3D cube and an Instantaneous Frequency section derived from the high-frequency 3D cube. Figure 16 contains a Sweetness section from the high-frequency 3D cube and an Interval Velocity section.
Figures 17 through 19 display extracted attributes for Layers A, B and C.
Windowed depth slices of each attribute are calculated for layers A through C. Layer A is calculated from Base Tunnel to Intra Alluvium A, Layer B is calculated from Intra Alluvium A to Intra Alluvium B and clipped at Top Tunnel, Layer C is calculated from Intra Alluvium B to Top Tunnel (Figures 17 to 19). Intra Alluvium C to Top Tunnel is included in Layer C as the area is extremely small. These attributes are subsequently analysed for subtle discrete anomalies. The Instantaneous Phase attribute is used here for structural measures of dip and strike.

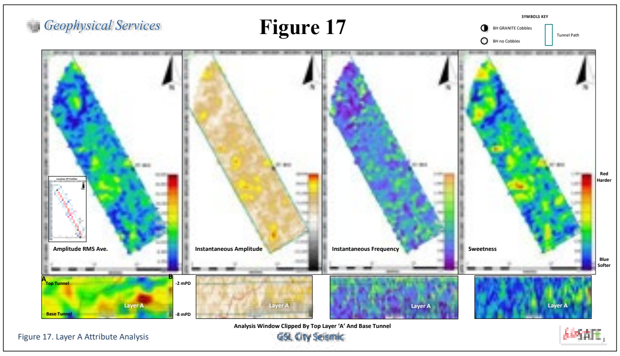

Figure 17. Layer A Attribute Analysis

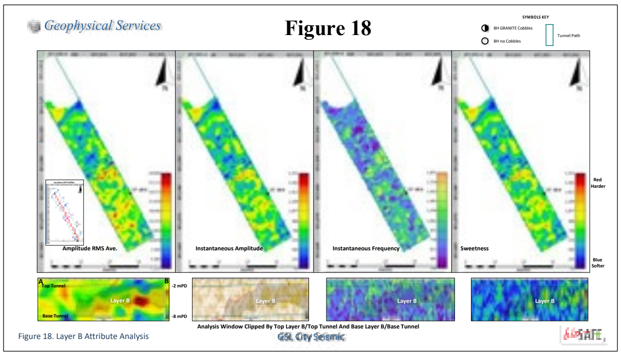

Figure 18. Layer B Attribute Analysis

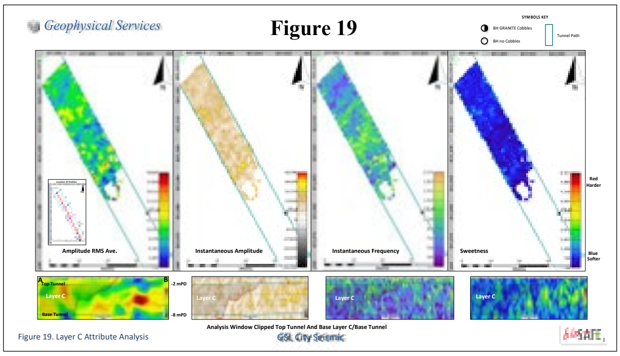

Figure 19. Layer C Attribute Analysis

7.2.1. Correlation of attributes to surface and borehole descriptions

Knowledge of outcrop geology is directly applicable to the understanding of subsurface geology. Outcrop analogues and borehole descriptions are used to provide a qualitative check on the subsurface model. Outcrop data coupled with borehole descriptions provide a good source of information on structural and sedimentological geometries at sub-seismic scales. K. W. Lai described in detail the Alluvial and Colluvial deposits of Hong Kong. Three layers or periods of deposition have been described.

Layer A, Middle Pleistocene, is described at Lam Tsuen River. Age Range 157,500 +/- 36,500 years BP. Layer B, Late Pleistocene, is described northwest of Yuen Long. Age Range 30,400+/- 8,000 to 81,000 +/- 13,500 years BP. Layer C, Holocene. Age Range 520 +/- 112 to 6,700 +/-700 years BP.

Holocene alluvium occurs mainly along narrow stream courses incised into fluvial terraces. The Holocene deposits are yellowish-brown clayey, silty sand with thin layers of organics.

The outcrop data describe thin cobbley and boulder zones with cobbles ranging from 20 to 170 mm. These sized cobbles and boulders are beneath the desired resolution size of 250 mm and are below seismic resolution with a peak frequency of 270 Hz.

No cobbles or boulders are described in boreholes 5, 8, 9, 10 and 11. These are the nearest boreholes to the survey area.

It is unlikely that cobbles or boulders are distributed as individuals. It is more likely that cobbles and boulders are confined to specific beds. Such as identified in Figure 4. K. W. Lai describes the cobbles as generally 20 to 170 mm. Cobbles of this size range are too small to detect, even with a peak frequency of 270 Hz.

Given that the alluvium has been described as layered and outcrop evidence points to cobbley intervals, it is likely that the denser Layer B could contain such cobble beds. An interval of up to 60-70% cobbles or boulders could provide enough of an impedance contrast to result in the layered intervals seen.

No cobbles or boulders are described in boreholes 5, 8, 9, 10 and 11. These are the nearest boreholes to the survey area.

Integration of outcrop analogues, borehole data and attributes allows a geological interpretation to be made. Figure 20 is a geological interpretation of the analysis. The profile is taken from the survey centre and runs from NW on the left to SE on the right. It has been smoothed to simplify the interpretation. Three distinct layers are identified. These correlate to surface geology and borehole descriptions as Layer A, Middle Pleistocene, Layer B, Late Pleistocene and Layer C, Holocene.

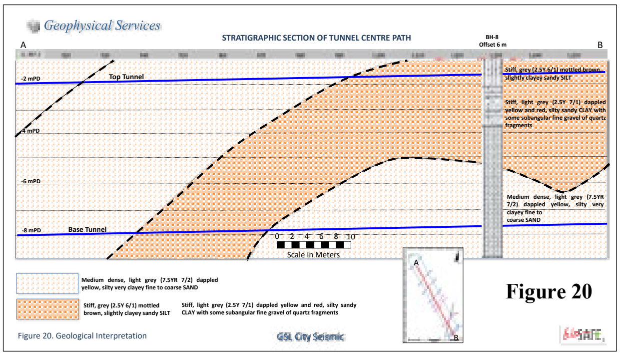

Figure 20

Figure 20. Geological Interpretation

From the Instantaneous Phase section and general structural mapping, the dip and strike are derived. The dip is to the NW, and the strike is NE-SW. Analysis of the other attributes, Instantaneous Frequency, Instantaneous Amplitude and Sweetness, of both vertical and interval extractions indicate that Layer A and Layer C contain lower attribute values than the middle Layer B. This suggests that these layers are less dense than the intermediate Layer B.

The horizontal depth slices also support the interpretation of denser material in the SE. All displays indicate high attribute value and higher relative density in this area.

8. EFFECTIVENESS OF METHOD

The data quality of the 3D volumes and 2D seismic profile is good to very good. The seismic data ties to boreholes with little or no shift required. Six surfaces have been identified and mapped across the 3D volume. Mapping the Granite GIII/GIV indicates a dome in the centre of the survey, but the Granite does not reach high enough to impact the tunnelling. The Alluvium is layered. Three distinct layers are seen through the tunnel path.

The middle Layer B appears to be denser and may have cobble beds.
However, outcrop mapping suggests alluvial cobbles to be in the range of 20 to 170 mm. These are too small to detect as individual items. No individual cobbles or boulders of a size greater than 250 mm have been identified in the zone of interest. This analysis suggests that the tunnel path will pass through lower density sediments in the NW, pass through a higher density interval in the middle where cobble layers could be encountered, and then pass into a zone of higher density sediments over lower density sediments in the SE.

This method is unique because it can deliver a **complete geological profile in 3-Dimensions** in areas where access is either severely limited or denied. This is particularly useful in Hong Kong urban development, where existing structures may obstruct the areas of interest.

For the subject project, the findings and conclusion in the report are adopted for the RTBM design in the selection of cutterhead, cutting tools and screw conveyor to suit the geological character of the existing ground. The application of this technology can benefit other substructures construction projects, such as basement and piling, in which the complete mapping results can supplement the discrete site investigation findings to allow both designer/contractor to have a complete picture of the variation of ground condition, thus minimising the potential dispute of the project and avoid the potential hazard in geology complex location.

9. REFERENCES

- *Geology Of Hong Kong (Interactive online). Civil Engineering and Development Department (CEDD) of the Government of the Hong Kong Special Administrative Region.*
- *Geotechnical Properties of Colluvial and Alluvial Deposits In Hong Kong. K. W. Lai. The 5th Cross-strait Conference on Structural and geotechnical engineering. Hong Kong, July 2011*
- *Guide To Rock And Soil Descriptions. Geotechnical Engineering Office, Civil Engineering Department of the Government of the Hong Kong Special Administrative Region. 1988*
- *Variations in sub-tropical deep weathering profiles over the Kowloon GRANITE, Hong Kong. R Shaw, Journal of the Geological Society, 154, 1077-1085, 1 November 1997.*
- *British Admiralty hydrographic chart 1466; 1841, Surveyed by Captain Sir Edward Belcher, in HMS Sulphur.*
- *British Admiralty hydrographic charts 3279 & 3280; 1886 & 1893, Surveyed by W.U.Moore, in HMS Rambler & HMS Penguin.*
- *Hong Kong Ordnance Survey Map 1947, 1949*
- *Historic Maps available and archieved on https://www.hkmaps.hk/mapviewer.html*
- *Assessment of Hydraulic Conductivity and Groundwater Flow Models in Bukit Timah GRANITE. Andrew Forsythe and Nina Pearse Hawkins. 2014.*
- *Taner, M.T., Koehler, F., and Sheriff, R.E. 1979. Complex Seismic Trace Analysis. Geophysics 44 (6): 1041.*
- *DUG Insight (version 5.1). 2021. Windows/Linux/Mac. Perth, Western Australia: DUG Technology Ltd (http://www.dug.com).*

LIST OF ABBREVIATIONS FOUND IN THIS REPORT:

AOI:	Area of Interest
BH:	Borehole
CMP:	Common Mid-Point
GIBR:	Geological Interpretive Baseline Report
GEOPHONE ARRAY:	An assembly of Geophones arranged in symmetrical or asymmetrical form
HSE:	Health, Safety, Environment
i-SEIS:	i-Seis digital data acquisition system
NMO:	Normal Move Out
PATCH:	An area containing geophone and source points. (i.e. 15 * 50 meters)
PERE:	Prince Edward Road East
PSS-100:	Portable Seismic Source 100
RECORDING SENSORS:	Geophones, Hydrophones
ROLLING:	The moving or leapfrogging of a geophone or energy array from one location to a new location.
SOURCE:	Seismic Energy Source
SUB-ARRAY:	A smaller array of Geophones or source points. Several of which form a FULL ARRAY

Engineering Geological Assessment of Lin Ma Hang Mine Caverns Using Handheld LiDAR Scanner

Samson Leung, Geoffrey Pook, Ming Kwok, Cloud Lo, Michael Wright
Meinhardt Infrastructure and Environment Ltd., Hong Kong, China

ABSTRACT

Lin Ma Hang Mine, in the former closed border zone in the northeast New Territories, rewards intrepid visitors with impressive 19^{th} century mine caverns. As part of the planned establishment of the Robin's Nest Country Park, the caverns have been earmarked for revitalization to increase public awareness and accessibility. A key aspect of the scheme is to assess the stability of the accessible caverns. Maintaining the natural heritage and appearance of the historical mine workings is forefront in tailoring specific solutions. Faced with a highly irregular cavern layout due to a complex history of mining activities, the engineering geological assessment was facilitated by 3D digitalisation of the cavern developed from handheld and aerial LiDAR scanning. Point cloud data obtained provided a fast and efficient means to form models for 3D and 2D assessment and visualisation. The ability to handle data through GIS and Common Data Environments (CDE) means management of vast point cloud sets is no longer a daunting task. The digital model developed will be showcased as part of the planned public engagement and educational information about the capabilities of digital geoscience and also to further explore in virtual reality the mine cavern extent.

1 INTRODUCTION

1.1 Site description

The Government of the Hong Kong Special Administrative Region (HKSAR) plans to revitalize the Lin Ma Hang Lead Mine site as a Country Park Outdoor Education Site showcasing the heritage mining history and ecology of the area to the general public. This includes the revitalization of an existing mine cavern, natural terrain hazard mitigation and other necessary works such as to promote access to the cavern for visitors. The Lin Ma Hang Lead Mine is an abandoned mine site operated intermittently from the 1860s until 1962. It is a significant historical mining site with a rich heritage linked to the local villages and military conflict legacy that contains one of Hong Kong's most complex mining operations in a remote wilderness area. Located in the Sha Tau Kok area of Hong Kong east of Heung Yuen Wai and north of Robin's Nest, the lower slopes of the mine abut the Lin Ma Hang Road and Sha Tau Kok Closed Frontier Road at the border between Hong Kong and Shenzhen (SEZ). The Lin Ma Hang Lead Mines SSSI is related to the caverns and contains one of the most important bat colonies in Hong Kong (Figure 1).

The mineralisation that gives the mine its significant resource results from metamorphism of the coarse ash tuff with a series of en-echelon, northwest-southeast striking, north-easterly dipping vein deposits. The ore veins generally dip between 15° and 60°, with some veins nearly vertical. The veins are lenticular along strike and down dip, with widths of a few millimetres to several metres and a strike length of some 2km.

Figure 1: Lin Ma Hang Mine Location

General view of the mining compound in 1938; looking from the Chinese border (Williams 1991).

Plate 1: Lin Ma Hang Mine Mill Processing Buildings 1938, Williams 1991

The mine was developed by a series of adits at different levels and locations. Since the mine has been worked and reworked by different parties at different times during the past, there are varying accounts about the extent and locations of the mine workings. The mine level number referencing system has also changed over the years but at least five major levels are recorded: Levels 1, 2, 3, 5 and 6. Level 1 access is on the Lin Ma Hang "Border Road", with other levels at progressively higher elevations. The caverns which are the subject of this study are mainly on the uppermost level – Level 6.

A substantial development of mill buildings and ore processing plant with tailings dump area was constructed to the northeast of the mining area (Plate 1). Several transport adits were driven from the underground workings towards the mine-processing plant buildings. During WWII, the Japanese mined most of the ore in the eastern section of the mine by robbing pillars, resulting in some caving of the roof. They also drove an additional intermediate level between the pre-War uppermost Levels 5 and 6. The mine eventually shut down during the period 1958-1962. Since then, the Lin Ma Hang Mine has been abandoned without operations or any maintenance. Up to 2016, the mine was within the Frontier Closed Area (FCA) and so out of bounds for most members of the public. In 2019, steel grilles were installed at selected adit entrances of Level 3 and Level 6 to prevent public entry and disturbance of the bat colonies. No abandonment mine plans have been located and the contemporary documentation of the mine workings is fragmentary. Davis et al (1956 and 1964) includes a plan based on a somewhat schematic and generalized map prepared by S.K. Wong in 1953 showing Level 5 and Level 6 and several presumed surface buildings in the Caverns area (Figure 2). Williams et al (1991) consolidated the available information supported by inspection and survey within Level 2 and 3 by the Geotechnical Control Office (GCO now GEO). A detailed recent account of the mine history is provided in Mellor, T. (2018a, 2018b, 2018c, 2021).

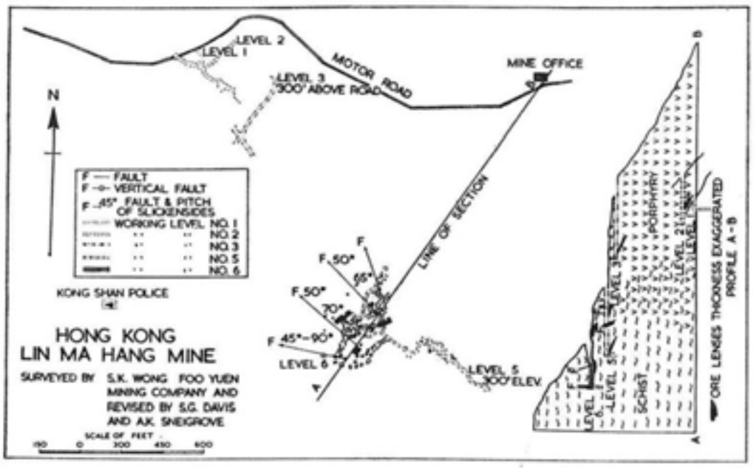

FIG. 2. Map of Lin Ma Hang Lead Mine with profile of the four main levels of exploitation.

Figure 2: Lin Ma Hang Mine Plan, Davis et al 1964

2 OBJECTIVES

2.1 Geotechnical assessment

The geotechnical study aims to assess the existing layout, condition and stability of the accessible cavern at Level 6 and adjacent related adits and shafts such that any necessary stabilization works can be designed to reduce the risk to public visitors whilst at the same time preserving the existing industrial heritage and ecology of the area. The study is based on the following steps: (i) understanding the existing cavern network; (ii) evaluating the rock mass condition within the cavern; and (iii) conducting analytical and numerical analysis.

2.2 Understanding the existing cavern network

The generalized mine plan prepared by S.K. Wong in 1953 suggests the Level 6 cavern was an E-W trending opening/ mine stope surrounded by several sub-rounded shaped rock pillars. Subsequent mine mapping by handheld laser scanner reveals the Level 6 cavern is part of an inter-connected room- and pillar- mine workings with several branches of adits trending S-N and E-W, as well as several production shafts connected to the ground surface and the lower mine levels. Mine mapping provides fundamental information for geotechnical assessment namely the numbers of rock pillars supporting the cavern, dimension of the rock pillars, and the spatial relationship between the cavern and the pillars. Preliminary geotechnical assessment was conducted by calculating pillar width-height ratio and estimating applied pillar stress due to overburden. Empirical stability graph method was applied to assess the pillar stability with respect to the minimum FOS required in Hong Kong.

2.3 Evaluation of rock mass condition

Engineering rock mapping was carried out in the cavern and adits to evaluate the rock mass condition as well as recording rock discontinuities data. Rock mass classification systems namely Q-System, RMR, and GSI were used to evaluate the general rock mass quality. Rock stability kinematic analysis by conventional stereographic projection was conducted based on the discontinuities data extracted by handheld laser scanner. Potential failure mechanism namely planar failure on the sidewall and gravity-driven wedge fallout from the crown was examined as part of the geotechnical assessment. The bedrock of the caverns area is characterised by dark grey to brownish grey, moderately weathered, strong to moderately strong, Grade II/III coarse ash Tuff. A relatively thin soil layer comprising colluvium overlies rock head with limited in-situ weathering profile developed above the Caverns. The entrance into the main cavern gallery and several adit entrances are excavated into the face of a steep, locally overhanging rock cut slope (Plate 2). The rock cut slope (Feature no. 3NE-A/C79) up to 10.5m high surrounds a bowl-shaped excavation, “the atrium”.

Plate 2: The rock slope and entrances into the main Level 6 cavern

2.4 Analytical and numerical analysis

Subsequent analysis will be based on the results of field surveys and planned GI. Limit equilibrium method will be used to calculate FOS against different potential failure mechanisms. Loading condition will be based on mapped block size and overburden pressure with rock strength parameters derived from in-situ tests and field measurement. Numerical analyses by computer software Phase^2 will be carried out for critical cavern sections. Generalized Hoek-Brown failure criterion will be used to evaluate the rock mass with a range of GSI values.

2.5 Potential stabilisation measures

Typical measures, including rock dowels, wire mesh and buttresses, will be considered as enhancement of the local stability of the caverns. The key approach for exploring necessary stability measures in Lin Ma Hang Cavern aims to maintain wherever practical the natural and mining heritage of the site and to preserve the authentic appearance and impression of the caverns. The scheme aims to protect the natural ecological niche currently notably occupied by several species of bats whilst also utilizing the rock strength and cavern layout to reduce the requirements for any conventional systematic support, as well as providing safe walkways for public access. The enhancement works will include sympathetic finishes and styles to ensure that the natural heritage and appearance of the caverns can be preserved.

3 METHODOLOGY

3.1 Data collection

The site is remote and largely covered with dense vegetation and tree cover. To build up the site history and existing topography, information from various sources was gathered and collated. Due to the site constraints and large site area a traditional site specific topographical survey was impractical within the desk study time frame. The existing data gathering processes are listed in Table 1.

Table 1: Existing data gathering process

	Data	Sources	Description
1	Open Data		
1.1	Topographical Maps iB1000	Retrieved from Lands D Map Service 2.0	Traditional base maps in CAD format with contours presented every 2m interval
1.2	2010 LiDAR Dataset	Requested from GEO	Hong Kong territory-wide Light Detection and Ranging Survey in 2010 with 0.50m Point Density
1.3	2020 LiDAR Dataset	Requested from GEO	Hong Kong territory-wide LiDAR in 2020 with 0.25m Point Density
2	Desk Study Data		
2.1	Aerial Photographs (AP) from 1924	Borrowed from GEO AP Library	Aerial survey undertaken by the Government or the British Royal Air Force (RAF) in a yearly bases.
2.2	Old maps or old mine plans	Various sources, most importantly from Williams (1991)	Summary of the Lin Ma Hang Lead Mine from GEO revisit including the history and the conditions back in year 1991. (Williams, 1991)
3	Project Specific Data		
3.1	Traditional site walkover survey	Meinhardt Team	Major site walkover survey tasks include but not limited to: ▪ Making notes on LiDAR generated contoured topographic maps, record with sketches and descriptions of significant observations ▪ Measuring dimensions with measuring tape, laser detector, directions and orientation with geological compasses. ▪ Recording the absolute location with GPS or relative location with reference to the pre-existing topographical plan

Data		Sources	Description
3.2	UAV (Drone) Data	Meinhardt Team	Drones are applied to take vertical, oblique aerial HD video and still photographs to discover significant detectable features on the ground surface and understanding the area and its context
3.3	Traditional topographical survey	Surveyor Team	Major topographical survey tasks include: ▪ Production of topographical contours of 1m interval, which may include computer smoothing and modification ▪ Outline significant structures, utilities and trees. And in the special case of cavern, the top and bottom of the cavern entrance and cave in, if any
3.4	Point Cloud Data	Meinhardt Team	GeoSLAM handheld scanner is applied to collect Point Cloud data with range up to 100m with in-built video camera and using georeference spheres. Two sets of data are collected during the scanning: ▪ Points with relative geometry with reference to the initial starting location (Local XYZ) & ▪ Video of throughout the scanning to record visual data (RGB / actual conditions seen in the study area) The cavern area and adits are scanned in separate parts due to topographical difference, accessibility & safety issues, namely: ▪ Atrium area of different elevation ▪ Rock Slopes ▪ Main cavern gallery ▪ Adits & other massive cavern areas behind grilles ▪ Adits & cavern areas at other mine levels ▪ Shafts/ surface collapses

3.2 Data processing

Following gathering of data from the sources outlined in Table 1, data processing and analysis are undertaken to generate ground models and extract geotechnical design parameters (Table 2).

Table 2: Data processing

Steps		Software	Description
1	Forming Overall Point Cloud Cavern Model		
1.1	Initial Processing	GeoSlam Hub & CloudCompare Stereo v. 2.12	▪ Retrieve all point cloud data parts, check and choose the best possible scan in multiple scan trials. ▪ Convert point cloud from .geoslam format to .laz format via GeoSlam Hub ▪ Subsample the point cloud in order to process further in a reasonable speed
1.2	Georeferencing	CloudCompare Stereo v. 2.12	Since the point cloud data are collected in a series of scan portions, there are two major parts in Georeferencing, namely ▪ Absolute Georeferencing - the major scan of the Cavern area is put to its absolute spatial location based on the Georeference spheres and their GPS readings ▪ Point Cloud merging (Relative Georeferencing) - other point cloud scan parts are merged onto the major scan with absolute spatial location by recognition of distinct site geometry and reference points at the Cavern area. ▪ Additional Checking - afterwards, the exposed surface part of the point cloud model is checked against the LiDAR Data to match the overall surface topography layout
1.3	Noise cleaning	CloudCompare Stereo v. 2.12	A series of noise cleaning methods are adopted in the Cavern Model: ▪ Typical built-in noise cleaning in CloudCompare to remove statistical outliers, including the SOR Filter and Noise Filter Scan time clipping - noise/ inaccurate point data in particular scan time are removed. The inaccuracy is usually associated with data collection

Steps		Software	Description
			errors where relative spatial references cannot be recognized by the scanner at particular time intervals. In the case of this cavern study, the error usually occurs when (1) traversing in and out of confined areas, (2) scanning involves trees and/or moving objects in the surroundings ▪ Elevation clipping- noise/ inaccurate point data on particular range and values of elevation are removed. This is particularly useful with reference with the LiDAR data to remove vegetation cover at the atrium ▪ Manual clipping - in the end, the point cloud model is checked, any noise/inaccurate point data left are removed with reference to actual field observations by professional judgement
2	Using Overall Point Cloud Cavern Model		
2.1	Extracting the Cavern geometry	CloudCompare Stereo v. 2.12 & CAD Softwares (Microstation and AutoCAD)	After the overall point cloud model is built, 2D views such as cavern sections (cutting along the X or Y axis) and layouts (cutting along the Z axis) can be formed freely by slicing and sampling a certain thickness of the point cloud via "Cross Section" and extracting contours. Whereas elevations can also be extracted, but require unfolding of the point cloud along an elevation section line. The extracted sections, layouts and elevations are in CAD (.dxf) format for further edits or use.
2.2	3D Cavern Model	CloudCompare Stereo v. 2.12 & Leapfrog Works	Overall point cloud model can be meshed using functions and plugins in CloudCompare – "Delaunay for 2.5D Clouds" and "Poisson Surface Reconstruction for 3D Clouds". Afterwards, the mesh can be extracted and imported in Leapfrog Works for better visualization with a 3D topographical model.
2.3	Rock Joint Analysis	CloudCompare Stereo v. 2.12 & Dips v6.0	Different portions of the point cloud model, such as rock slope faces, can be isolated. The portion can then be classified into planes via plug-in "Facet/fraction detection" in CloudCompare. The orientation and dip direction of the planes can then be transformed and analysed in Dips v6.0, to identify any potential kinematic hazards
2.4	Cavern Stress Analysis	CloudCompare Stereo v. 2.12 & Phase^2 v9.0	Critical profiles of the cavern are extracted into CAD files and the profiles are imported and analysed with Phase^2 to simulate 2D Stress conditions of the cavern and identify potential areas of concern.

4 ANALYSIS & DISCUSSION

The point cloud data obtained from the cavern and mine area was used in various ways to provide engineering geological assessment. The value of this data is in the ease of the collection, as well as the quality and quantity of data obtained. As the aim of the works was to verify the stability and provide necessary enhancement schemes, it was critical that the point cloud provided both a highly accurate and fully interactive representation of the accessible mine. The following areas are discussed with reference to how the 3D scanning process produced high quality output in an atypical working environment.

4.1 Geospatial

The existing documentation on the extent and layout of the mine is very limited; however, it is important to understand the original context of the mining to be able to re-create the network. The mines were excavated over a series of stages by different operators for various purposes and using different mining techniques. This has left a rather haphazard arrangement of openings, shafts, adits, pillars and rooms. By scanning and reproducing the 3D mesh in relation to the latest high resolution 2020 aerial LiDAR data (Wong, 2021), the extent of the excavation in relation to the surface features, rock and soil overburden, clearance between mine levels, potential shaft and adit connections is revealed, as well as relating findings to desk stuzdy data obtained through old mine maps and layout drawings (Figure 3). Hillshade and aerial photos draped over LiDAR generated DTM were created (Figure 4).

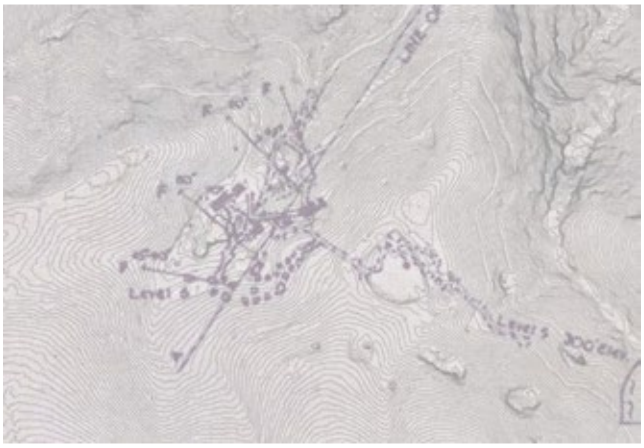

Figure 3: Lin Ma Hang Mine Level 5 & 6 plan from Davis et al 1964 and contoured 2020 aerial LiDAR

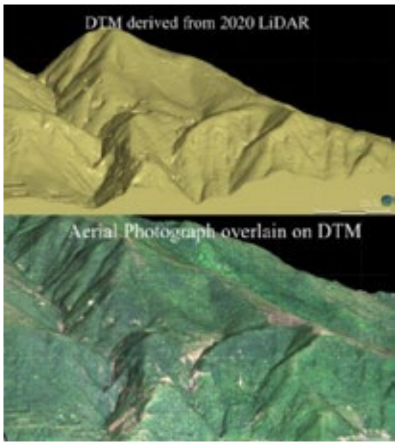

Figure 4: Lin Ma Hang Mine 2020 aerial LiDAR DTM and photo drape

As with a traditional survey, the surfaces can be mapped but in this case the task involves a 3D excavation with pillars and arched crowns up to 6m high (Figure 5). The irregular shape, thickness and orientation can be accurately modelled in georeferenced space with respect to the surface topography and control points. It is noted that slight offset of data may arise during the point cloud merging during relative georeferencing. In order to enhance the accuracy, each point cloud scan was to contain at least one locally fixed feature, such as the Grilles, for matching purposes. By developing a 3D ground model in GIS/ LeapFrog software, the scan data is easily matched to the surface expressions. The extent of the Level 6 sub layer could be determined as well as the proximity of unconnected adits beneath the hiking trail. It is important to correlate the surface expressions with the subsurface features and, by utilizing the 2020 LiDAR, drone surveys and site reconnaissance, it was possible to develop a better) understanding of the mine layout above and below ground (Figure 6).

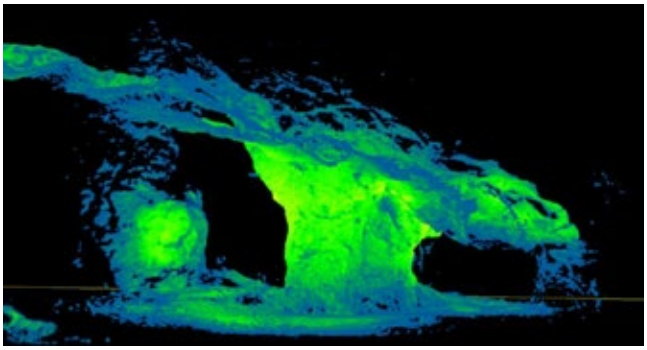

Figure 5: Lin Ma Hang Mine 3D scanning point cloud heat map

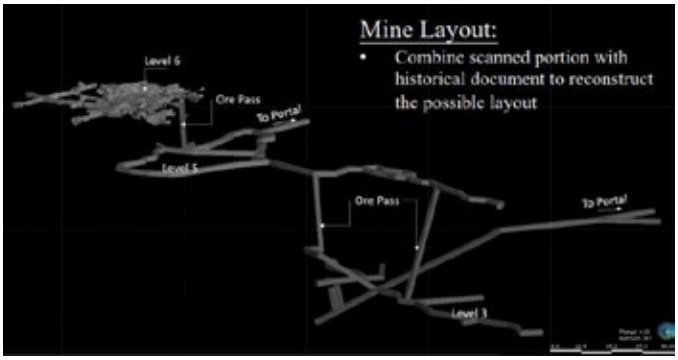

Figure 6: Lin Ma Hang Mine 3D layout with the Level 6 caverns area at top left. The model for Level 5 and Level 3 are based on interpretation of plans in Davies et all 1964 and Williams 1991.

The cavern is entered through three rock arches separated by four substantial rock pillars at the southern edge of the atrium (Plate 3). The ground level of the cavern gallery varies between +180 to +185 mPD, similar to that of the atrium level. The inner southern part of the gallery is marked by entrances to several adits separated by rock pillars or ribs. Adits are fenced off by lockable metal grilles installed in 2019, where the grille openings are large enough to allow passage of bats and uninterrupted natural ventilation (Plate 4). One adit terminates at a vertical unlined shaft, which is open at the ground surface next to the footpath access to the caverns.

Plate 3: The Level 6 cavern

The lateral span of the gallery has a maximum dimension of 19m. The maximum crown height in the gallery is around 6m near the entrance archway. The typical crown height is around 4m, descending to 3m against the eastern wall, Site surveys identifies several rounded to square shaped rock pillars and some elongated rib pillars around the cavern gallery. Pillars forming the entrance archways are formed in jointed volcanic Tuff rock. They exhibit occasional slickensided surfaces and open joints. Existing rock rubble packing are found around the bases of some pillars. A total of 10 major adits, some of which are interconnected have been identified (Figure 7).

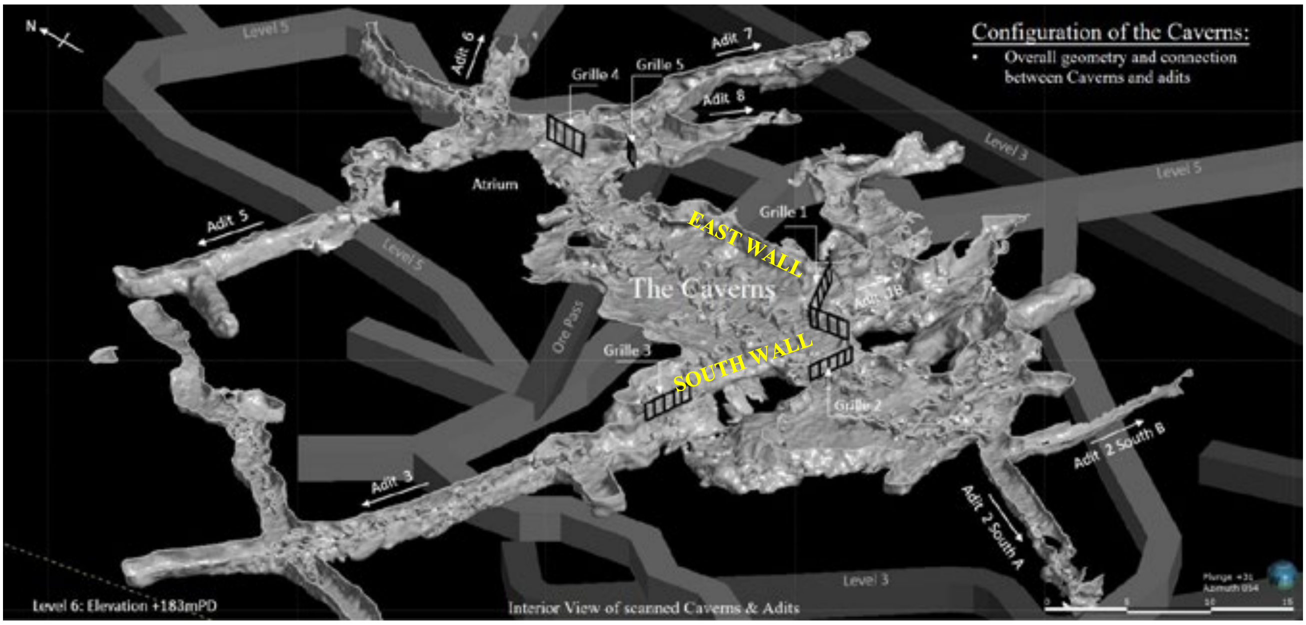

Figure 7: Lin Ma Hang Mine Level 6 cavern and adits 3D meshed model

The adits observed are mostly sub-horizontal at around +180mPD. These adits are part of the previously described Level 6. A lower level at +174 mPD approx. was also identified. This is suspected to be the intermediate level between Level 5 and Level 6. The major adits fork or branch into multiple galleries, forming an inter-connected room and pillar mine network. Site inspection identifies mortar cemented rock rubble walls are built between some pillars, blocking the connection between adits. All accessible adits are excavated in rock and are unlined. The remnants of disused vertical timber prop supports are present in the adits. Site inspections also confirmed a lower level (Level 5) mine network, accessible via two adit entrances at approximately +157mPD, northeast of the caverns. A total of 4 shafts connected to Level 6 have been located. The shafts are formed in rock, square or rectangular in plan and unlined. One of the shafts connects to the surface while three are suspected to connect to lower level workings (Plate 4).

Plate 4: A shaft in Level 6 connecting to lower level workings

The results of scanning and site inspection reveal the cavern gallery entrance of rock arches within the rock cut slope. These details were captured in 3D for use in the model from the point cloud scanning. The southern extent of the Level 6 cave is bounded by a persistent sub-vertical plane trending WNW- ESE which forms the northern faces of some pillars and the southern wall of an adit. The plane represented in the 3D model can be tentatively correlated with fault/shear zones, indicated on the 1950s mine plan, Davis et al (1964) (Figures 2 and 3).

4.2 Geotechnical

The point cloud model created from the 3D scanning was incorporated in the assessment of the design sections and elevations as well as for using in the empirical assessment of rock mass classification Q-system and as direct input in 2D FEM. As the project scope required an assessment of the overall stability of the existing caverns, the point cloud model is particularly useful in providing actual cavern geometry, such as Cavern spans and areas of high and low cover, and joint measurements. Critical spans and areas of stability concerns are identified and sections can be readily extracted for further review, analysis and markup. These methods allowed a comprehensive review of the stability of the opening in terms of stress and spans. Without a comprehensive 3D model detailing the extent and arrangement of pillars, openings and adits, the identification of critical spans and areas of high or low cover would have been challenging to determine.

Based on site inspection and details obtained from the scan, Q-value and RMR parameters were determined for the cavern areas (Table 3 and Table 4). RMR rating is calculated as 58.

Table 3: Q-values for the caverns

	Cavern Portion (Refer to Figure 10 for the Location)		
Parameter	Wall (East)	Wall (South)	Roof (crown)
RQD	75	75	80
Jn	9	12	9
Jr	1.5	0.5	1.5
Ja	2	4	2
Jw	0.66	1	1
SRF	2.5	2.5	2.5
Calculated Q	1.65	0.32	2.67

Table 4: RMR parameters for the caverns

Parameter	Value	Rating
UCS	Estimated 50 MPa	7
RQD	50 – 75%	13
Joint Spacing	0.6 – 2m	15
Joint Condition - Persistence	Most joints are 3 – 10m long	2
Joint Condition – Separation	Most joints have 1 – 5mm aperture	1
Joint Condition – Roughness	Most joints have slightly rough to smooth surface	1
Joint Condition – Infilling	Most joints are clean	6
Joint Condition – Weathering	Most joints are moderately weathered with stained surface	3
Groundwater	Damp	10

GSI values ranging from 50 to 60 were considered in our simulation to reflects the nature of moderately weathered with interlocked undisturbed blocky rock mass occurs in the cavern.

A series of rubble walls or surface protection were identified during site inspection as part of the original mine workings. The exact purpose of these features is lost to time but they appear to backfill undercut pillars or to provide rubble walls between pillars. It is not clear if these are designed as storage of the mine tailings or to provide a stabilizing function. The extent, thickness and shape, was better understood and illustrated with the benefit of scanning and viewing in 3D.

4.3 Kinematic analysis

A feature of the point cloud data is the ability to carry out statistical analysis of the points to derive facets, or surfaces, which can be correlated to rock joints of the exposed mine faces. As the mine is already fully excavated, the scanning data was ideal for obtaining the joints in a fully 3D space. This allowed an accurate representation of joints in rock faces and within the pillars and also those that interface with both walls and crown of the adits and cavern. This is an invaluable tool to assist the traditional rock joint mapping (Figure 8).

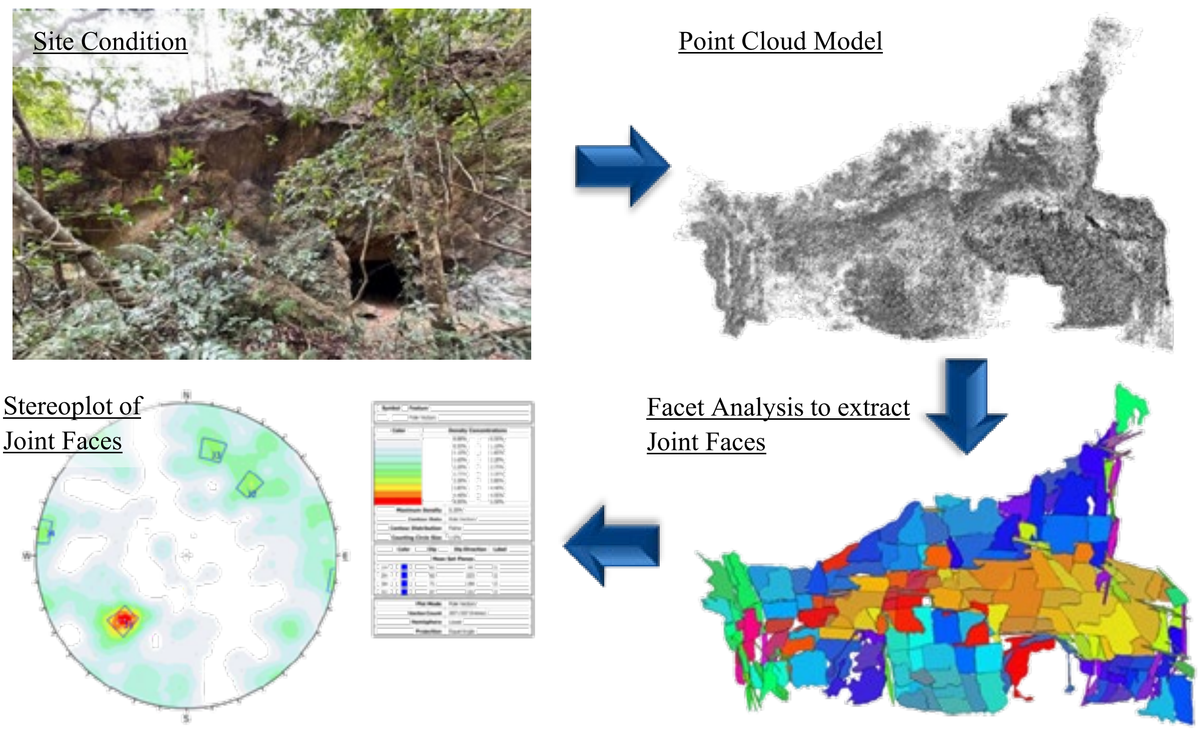

Figure 8: Lin Ma Hang Mine (Northeast side of the Atrium). Facets and stereoplot generated from 3D scanning point cloud

Portable laser scan and conventional manual discontinuity survey were carried out for the rock faces (Table 5 and Table 6). Facets extracted from 3D point cloud laser scanning and manual mapped discontinuities consisting of rock joints with occasional shear planes and quartz veins are plotted into stereonets. Separate stereonet plots representing manual survey data and laser scan data are produced for northeast, southeast, and northwest slope faces. Pillars near the archway entrance exhibit adverse joint orientations that can be mapped through the pillar shape by facet identification (Figure 9), while one pillar is characterised by longitudinal cracks (i.e. crack formed by spalling along the long axis of the pillar) and associated fractured rock materials. Irregular cracks and open joints are not as clear to identify in the scanning data and require visual inspection. Other pillars in the cavern gallery show no sign of adverse jointing or intense cracking and fracturing. Due to the quantity of the data, the major joints sets are predominantly determined through the scanning data with traditional mapping providing an additional assessment through contextual site observation.

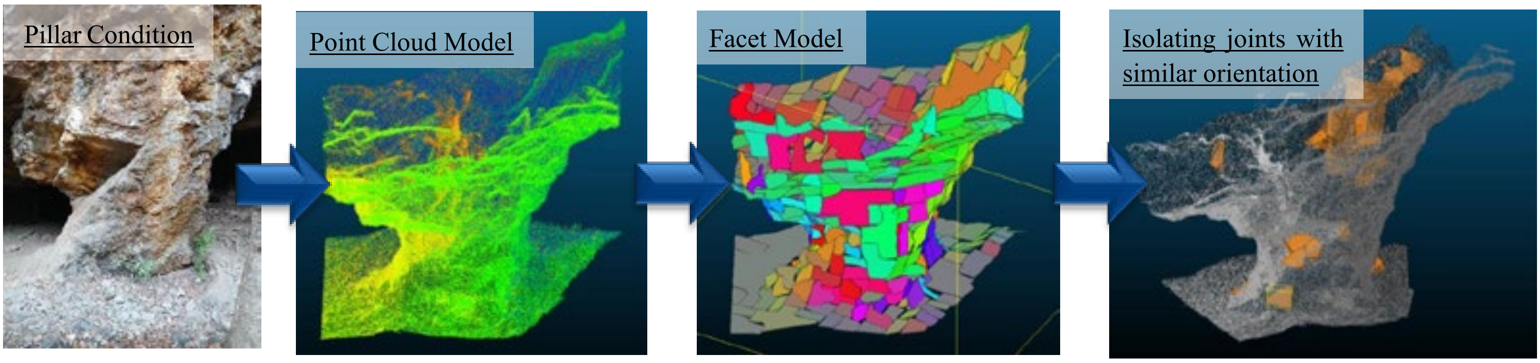

Figure 9: Process of facet identification through a pillar

Table 5: Major joint set data from discontinuity survey for the overall Cavern Area

Major Joint Set	Manual Discontinuity Survey	
	Dip Angle	Dip Direction
J1	43	117
J2	76	023
J3	42	044
J4	79	183

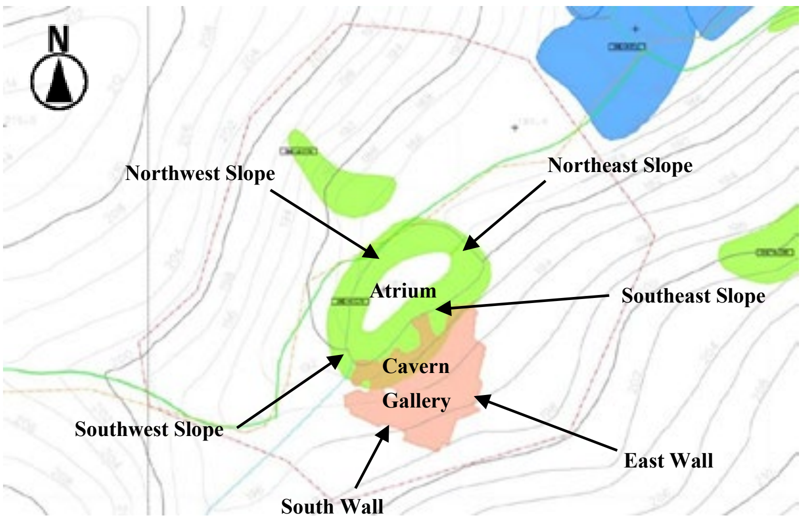

Figure 10: Location plan of slope faces and cavern walls

Table 6: Discontinuity data from manual and laser scan processing

Slope Face (Refer to Figure 10)	Joint Set	Manual Discontinuity Survey		Laser Scan derived Discontinuity Survey	
		Dip Angle	Dip Direction	Dip Angle	Dip Direction
Southeast	J1	43	102	47	129
	J2	45	043	46	039
	J3	85	312	79	295
	J4	25	116	88	172
	J5	48	142	87	098
Northwest	J1	30	100	37	119
	J2	63	116	62	121
	J3	48	052	35	067
	J4	52	144	90	309
Northeast	J1	70	062	60	045
	J2	50	200	63	223
	J3	76	180	74	191
Southwest	J1	72	092	/	/
	J2	51	113	/	/
	J3	70	338	/	/
	J4	85	270	/	/
	J5	75	120	/	/

For the southeast slope face (i.e. Rock cut slope at the atrium outside Cavern), both laser scan and manual survey identify similar major joint sets (J1, J2, and J3) with fairly consistent orientation. For the northwest slope face, both laser scan and manual survey identify similar major joint sets (J1, J2, and J3) with fairly consistent orientation. For the northeast slope face, both laser scan data and manual survey identify similar major joint sets (J1, J2, and J3) with fairly consistent orientation. For the southwest slope face, no laser scan discontinuity data is available due to dense vegetation. Manual discontinuity survey identifies four major joint sets. J1 represents the shear plane parallel to the slope face, while J2 and J3 are the dominant joint sets identified within the cavern gallery and in other slope faces.

A kinematic stability assessment of the rock cut slope was carried out based on the major joint sets identified by portable laser scan and manual discontinuity survey. Kinematic analysis was completed using Rocscience computer software DIPS (v.6.0), the results of which are graphically presented in equal area stereoplots (lower hemisphere) using methods discussed by Hoek and Bray. The lateral limits of planar and toppling failure were set at ±20° and ±10°, respectively.

5 CONCLUSIONS

Portable laser scanning supported by high resolution aerial LiDAR surveys, desk study, API and site inspection and mapping have provided complementary information to develop an accurate 3D model of part of the Lin Ma Hang Mine. The caverns are confirmed to be part of a complex inter-connected network of abandoned mine workings. The workings include sub-horizontal adits, inclined stopes, pillar and room workings, as well as vertical shafts and inclined ore passes. The caverns form a part of the Level 6 workings, the highest recorded level of workings. Within the former mining area as a whole, aerial LiDAR has also greatly helped identify anthropogenic features on the natural hillsides surrounding the caverns such as abandoned building platforms, in particular those related to suspected mine workings. Site observations confirmed the presence of ruins and several suspected openings into the mine. The caverns of Level 6 are accessed from the surface via adits and archway openings excavated into a rock cut slope. A large "gallery" with span up to 19m and height of up to 6m is supported by several rock pillars.

Portable laser scanning enabled development of a detailed geo-referenced 3D model of the existing cavern, rock pillars and connected adits and openings augmented by a detailed aerial LiDAR derived DTM. It is anticipated that subsequent rock stress analysis of the cavern opening geometry and associated openings and adits will be greatly facilitated. Automated recognition of joint face facets from the 3D model enabled capture of discontinuity data from otherwise inaccessible faces such as the cavern roof (crown). The detailed 3D model will be used to tailor the design of necessary but sympathetically selected and installed local stabilisation measures. The model can also form the baseline for subsequent cavern monitoring as well as future educational interactive or display use.

ACKNOWLEDGEMENTS

The 2020 LiDAR survey data has been used with the consent of the Geotechnical Engineering Office of the Civil Engineering and Development Department, of the Government of the Hong Kong SAR

REFERENCES & BIBLIOGRAPHY

Chu, J., & Chan, J. 2015. Hong Kong Mining History (1st ed., pp. 19-41). ProjecTerrae.

Davis, S. G., and Snelgrove, A. K. 1956. Geology of the Lin Ma Hang Lead Mine, New Territories, Hong Kong.

Davis, S. G. and Snelgrove, A. K. 1964. The Geology of the Lin Ma Hang Lead Mine, New Territories, Hong Kong, carried in Symposium on land use and mineral deposits in Hong Kong Southern China and South-East Asia: proceedings of Golden Jubilee Congress of University of Hong Kong. Hong Kong University Press

Dewez, T. J., Girardeau-Montaut, D., Allanic, C., and Rohmer, J. 2016. Facets: A Cloudcompare Plugin to Extract Geological Planes from Unstructured 3D Point Clouds. International Archives of the Photogrammetry, Remote Sensing & Spatial Information Sciences, 41.

GEO. 1991. Hong Kong Geological Survey (HKGS) Map Sheet 3, Solid and Superficial Geology, Sheung Shui, 1: 20,000 – scale, HGM20 series.

GEO. 1996. Hong Kong Geological Survey Memoir No.5 - Geology of the Northeastern New Territories. pp. 28,99-100,119,122 Government of Hong Kong.

GEO. 2018. Guide to Cavern Engineering. Geoguide 4. Geotechnical Engineering Office, Civil Engineering and Development Department, HKSAR Government, 262 p.

Grimstad, E. 1993. Updating the Q-system for NMT. In Proceedings of the International Symposium on Sprayed Concrete-Modern use of wet mix sprayed concrete for underground support, Fagemes, Oslo, Norwegian Concrete Association, 1993.

Idrees, M. O. and Pradhan, B. 2018. Geostructural Stability Assessment of Cave Using Rock Surface Discontinuity Extracted from Terrestrial Laser Scanning Point Cloud. Journal of Rock Mechanics and Geotechnical Engineering, 10(3), 534-544.

Kazhdan, M., Chuang, M., Rusinkiewicz, S. and Hoppe, H. 2020. Poisson Surface Reconstruction with Envelope Constraints. In Computer graphics forum (Vol. 39, No. 5, pp. 173-182).

Martin, C. D. and Maybee, W. G., 2000. The Strength of Hard Rock Pillars. Int. Jnl. Rock Mechanics & Min. Sci. 37:1239-1246.

Mellor, T. 2018a, April 27. Lin Ma Hang Mine Part 3 – Exploitation. The Industrial History of Hong Kong Group. https://Industrialhistoryhk.Org/Lin-Ma-Hang-Part-3-Exploitation/.

Mellor, T. 2018b, January 30. Lin Ma Hang Mine Part 2 – The Yung Years. The Industrial History of Hong Kong Group. https://industrialhistoryhk.org/lin-ma-hang-mine-part-2-the-yung-years/

Mellor, T. 2018c, May 30. Lin Ma Hang Mine Part 4 – Decline and Closure. The Industrial History of Hong Kong Group. https://industrialhistoryhk.org/lin-ma-hang-part-4-decline-and-closure/.

Mellor, T. 2021, January 9. Lin Ma Hang Mine Part 1 – The Early Years. The Industrial History of Hong Kong Group. https://industrialhistoryhk.org/lin-ma-hang-mine-part-1-the-early-years/

Norwegian Geotechnical Institute. 2015. Using the Q-system: Rock Mass Classification and Support Design.

Williams, T. 1991. The Story of Lin Ma Hang Lead Mine, 1915-1962. GSHK Newsletter, 9(4). pp. 3-26.

Wong, Jeffrey. 2021. Detector in the Air – 2020 Airborne LiDAR Survey. Joint Technical Symposium on Digital Geosciences & Geotechnology. 16 September 2021.

阮志 2012。《中港邊界的百年變遷：從沙頭角蓮蔴坑村說起》。香港：三聯書店（香港）有限公司。

Smart Construction Monitoring Using Photogrammetry and LiDAR-derived 4D Digital Model: A Case Study from the Tung Chung New Town Development of Hong Kong

S Y N Cheng, L Liu
The Chinese University of Hong Kong, Hong Kong, China

W Hou, J R Hart
GeoRisk Solutions Limited, Hong Kong, China

Y M T Yong
Arup, Hong Kong, China

ABSTRACT

The conventional practice of construction site monitoring in Hong Kong relies heavily on in-person site inspection, which is inherently subject to limitations in human resources, health, safety and time. Additionally, given that the advent and application of new digital technologies in the construction industry predominantly occurred after 2010 in Hong Kong, it is more challenging to review/ monitor the changes of a construction site with respect to its historical (pre-2010) status. To overcome these limitations, in this paper, we present the use of the 4D model monitoring method on a case study from the Tung Chung New Town (TCNT) and its extension development in Hong Kong. Nine 3D digital surface models covering a 57-year time period from 1963 to 2020 were built from the historical aerial photographs using the Structure from Motion technique and from the territory-wide airborne LiDAR data. These models were used for monitoring the process of land reclamation, site formation and the subsequent works during the TCNT development. In addition, a preliminary ground model was constructed from approximately 500 Nos. of drillholes to provide an engineering geological background for the study site. It is promising that our innovative 4D digital model and the associated sub-surface rockhead model can be integrated with the Building Information Modelling (BIM) system at a later stage to constituent a Smart Built Environment and to facilitate a smart construction site monitoring practice in near future.

1 INTRODUCTION

1.1 Background

The conventional industry practice in construction monitoring, particularly for site formation works, involves an in-person site inspection and the use of site photos or videos taken by unmanned aerial vehicles (UAV). These aerial photographs will be taken at different altitudes, different angles, different resolutions, and at different locations of the construction site at certain time intervals as stated in the contract. The details of the construction progress and site overview can be recorded and tracked from these monthly photographs. However, limitations were found with carrying out the monitoring in an oversimplified 2D format. Even with the adoption of some advanced technological methods in recent years for construction monitoring, including thermal surveys using thermal cameras mounted on UAV, handheld LiDAR surveys, and the use of online platforms (e.g., Aerial Cloud) for data acquisition and management, some are subject to significant limitations in time and cost, especially when it is necessary to monitor a relatively large construction site for a prolonged period of time. Besides, challenges were also found in monitoring changes in a construction site with its historical status due to limitations in technologies at that time. With the rapid development of different geospatial and geotechnical software together with more open geospatial data available in recent years, a more advanced technological approach can be used in tackling some of the constraints present in the latest construction monitoring practice. In this paper, we present the use of the 4D digital model monitoring method on a case study from the Tung Chung New Town (TCNT) and its extension development, by building and comparing multi-temporal 3D digital ground surface models from historical aerial photographs and the available airborne, territory-wide LiDAR data. Nine surface models were built for the years 1963, 1993, 1998, 2000, 2001, 2004, 2010, and 2020 (two models for 2020). The pre-2010 and one of the 2020 surface models were built from historical aerial photographs using the Structure from Motion (SfM) technique. The remaining two recent models were built from the available 2010 and 2020 airborne LiDAR data respectively.

1.2 Study Area

The study area is located in the northern part of Lantau Island, which includes the existing Tung Chung New Town Centre, Tung Chung North, and Tung Chung (East) New Town Extension, which is now undergoing reclamation and construction (Figure 1). The constructed 3D digital models would mainly focus on land reclamation and site formation of Tung Chung Town Centre, Tung Chung North, and Tung Chung (East) New Town Extension under the Tung Chung New Town Development Project.

1.3 Construction Process of the Tung Chung New Town Development

The study area is part of the general new town programme launched in 1973 with TCNT being the ninth new town developed in this programme. The existing TCNT is situated on the northern side of Lantau Island (ARUP, 2015). The engineering construction work for Tung Chung New Town Development Plan has been divided into four major phases since its commencement. Phase 1 of Tung Chung Development was part of the Airport Core Programme Project and was completed in January 1997. The engineering work in Phase 1 includes site formation, construction of different infrastructure including roads, drains, and sewage treatment facilities (Civil Engineering and Development Department, 2020). This phase of construction work involved reclamation work of a total of 67 hectares.

Phase 2 of Tung Chung Development was divided into Phase 2A and Phase 2B. Each of the phases was completed in May 2000 and February 2001, respectively. Phase 2A involved reclamation works and construction of the associated infrastructure. They were completed in January 1997 and May 2000 respectively (Civil Engineering and Development Department, 2020). The reclamation work involves 35 hectares of reclaimed land, located due north of Yat Tung Estate (Hong Kong Place, 2021). Phase 2B involved engineering works including site formation and infrastructure. This phase was completed in February 2001.

Phase 3A of Tung Chung Development mainly focused on reclamation work which was completed in April 2003. This involved 26 hectares of reclaimed land located due north of Ying Hei Road with the use of public fill (Civil Engineering and Development Department, 2020; Hong Kong Place, 2021).

The last phase of Tung Chung New Town Development, which is the Tung Chung New Town Extension project involves a total possible development areas of about 240 hectares with about 124 hectares of reclaimed area at Tung Chung East and Tung Chung West (ARUP, 2015). Apart from reclamation work, this stage of construction work will also involve construction of associated infrastructure.

1.4 Geological conditions

According to the studies on the geological conditions of Northshore Lantau carried out by the Geotechnical Engineering Office (GEO), Tung Chung (East) New Town Extension is located within the Northshore Lantau Designated Area, which is potentially underlain by complex geological conditions (GEO, 2021). Those complex geological features include anomalously deep and inclined rockhead with mainly weathered intrusive igneous rocks, carbonate-bearing rocks which would give rise to cavities and cavity-fill deposits, massive marble with a karstic upper surface displaying solution features, and superficial deposits which indicate the potential occurrence of other complex ground features (GEO, 2004, 2021). In view of the complex geological conditions, it is suggested that detailed geophysical (gravity) survey instead of the conventional ground investigation techniques (drilling and seismic reflection profiling) shall be used for identifying the location of the deeply weathered zones (Environment, Transport and Works Bureau, 2004). Besides, the complex geological conditions may also give rise to problems associated with construction involving deep foundations. Adequate resources and geotechnical input would be required in designing and constructing the foundations (GEO, 2021).

One of the signature obstacles in engineering work of TCNT associated with the complex ground conditions is the abandonment of proposed tower 5 due to the problematic geological conditions found in 1996 when drilling for Tung Chung Town Lot 3 (Figure 2) (Sewell & Kirk, 2002). Both cavity-filled facies and collapsed facies were found below 100m from ground, indicating the presence of cavities formed from dissolution of marble-bearing granite (Sewell & Kirk, 2002).

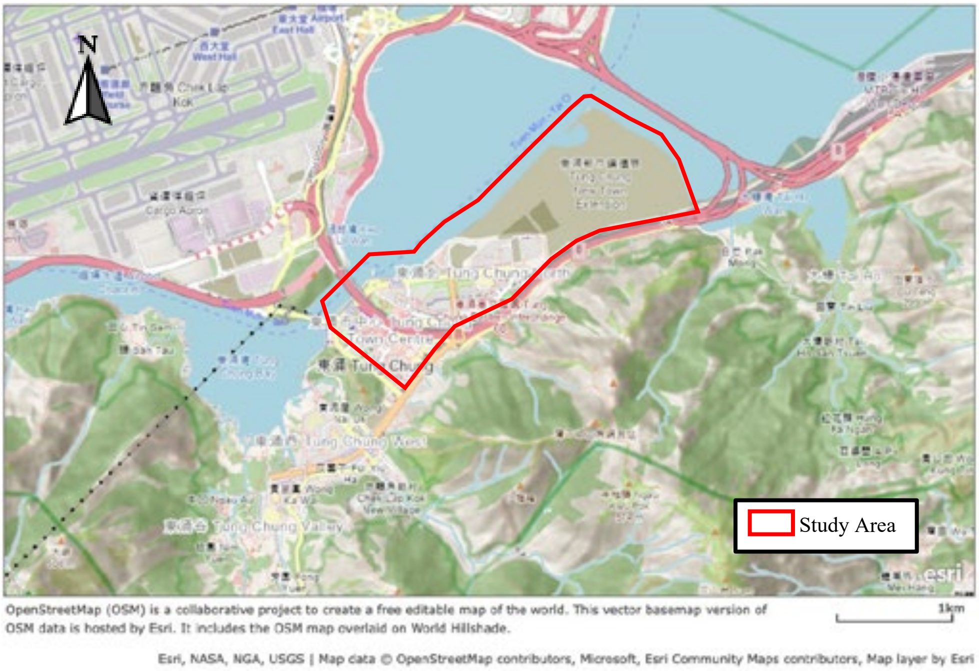

Figure 1: Location of the study area. Basemap is from Esri OpenStreetMap.

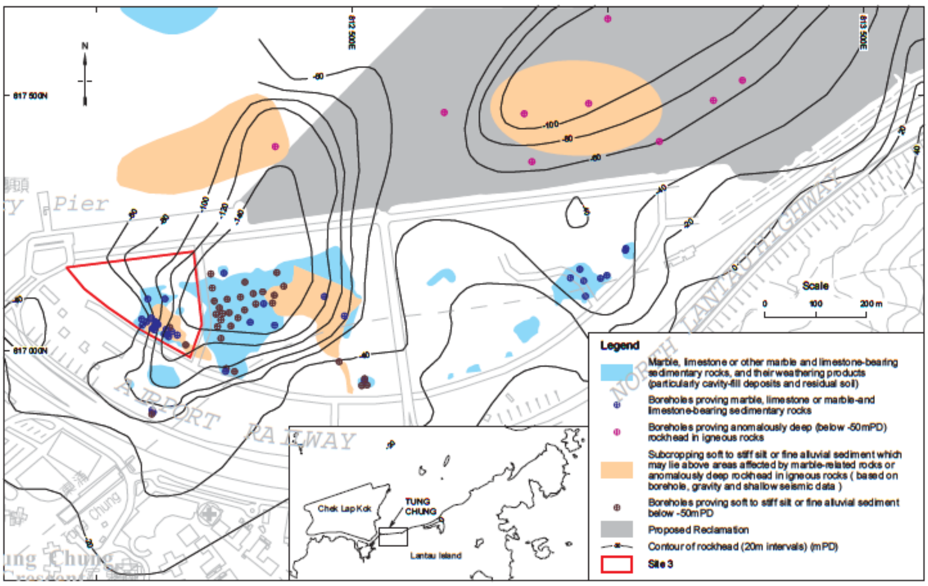

Figure 2: Map showing complex geological conditions in part of Tung Chung East (Sewell & Kirk, 2002).

2 METHODOLOGY

The generation and analysis of multi-temporal 3D digital models mainly comprised 4 major works including (1) Generation of historical aerial photographs-derived 3D surface model (non-georeferenced), (2) Generation of LiDAR-derived 3D surface model, (3) Generation of 3D engineering rockhead mesh model, and (4) Georeferencing the historical aerial photographs-derived 3D models.

2.1 Photogrammetry-derived 3D surface model

The 3D Digital surface model for years 1963 (Figure 3a), 1993 (Figure 3b), 1998 (Figure 3c), 2000 (Figure 3d), 2001(Figure 3e), 2004 (Figure 3f), and 2020 (photogrammetry)[1] (Figure 3i) were built from historical aerial photographs using the SfM technique. The historical aerial photos were obtained via the online geospatial data provided by the Hong Kong Map Service 2.0[2] (HKMS 2.0) at a resolution of 300 dpi. A total of 263 aerial photos taken at height from 2800 ft. to 8000 ft., were used in generation of 3D surface models for the seven models. (24 photos for 1963; 38 photos for 1993; 25 photos for 1998; 15 photos for 2000; 39 photos for 2001; 26 photos for 2004; 96 photos for 2020). The models were built in a point cloud format (.las) using the software Agisoft Metashape Pro. To remove point cloud noise from the models, data cleansing is performed by using the “Segment” tool in the software CloudCompare, for better visualization and qualitative analysis in the later stage.

2.2 LiDAR-derived 3D surface model

The 3D Digital surface model for years 2010 (Figure 3g) and 2020 (LiDAR) (Figure 3h) were built from the available 2010 and 2020 airborne LiDAR survey data from the Geotechnical Engineering Office (GEO), HKSAR. The “Ground” and “Any first returns” LiDAR data points were selected for building the 2010 model; whereas the “Ground”, “Building”, and “Vege” LiDAR data points were selected for building the 2020 (LiDAR) model.

2.3 3D Engineering Rockhead Mesh Model

To understand the engineering geological conditions of TCNT, a mesh model of rockhead level (Figure 4) was generated from 514 No. of drillholes by using the ground modelling software Leapfrog Works. The drillhole data were obtained from 43 Geotechnical Information Unit (GIU) ground investigation reports in Geotechnical Information Infrastructure (GInfo). The resolution of the subsurface model was set to 15m. The subsurface model was exported as file type .dxf for further visualization and analysis, together with the 3D surface model, in CloudCompare, ArcGIS Pro, and AutoCAD.

2.4 Georeferencing

Since the historical aerial photographs obtained from HKMS 2.0 were lack of geospatial information, the scale and the coordinate system of the photogrammetry-derived 3D surface models were incorrect. Georeferencing process were performed on all the seven photogrammetry-derived 3D surface model using CloudCompare, with 2020 LiDAR-derived 3D surface model serving as the referencing frame for coordinate point input. They were all projected using Hong Kong 1980 Grid as the coordinate system.

Six points had been selected as ground control points (GCPs) for georeferencing in 1963 models. Due to the lack of man-made infrastructures at that time, the selection of GCPs would mainly focus on picking points of recognizable mountain peaks. Five other points were selected as GCPs for georeferencing in 1993 model. The GCPs selected were mainly focusing on different corners of the newly reclaimed land for better georeferencing quality of the study area.

The selection of GCPs for 1998, 2000, 2001, and 2004 were mainly focus on the man-made infrastructures as more buildings and lands were built and reclaimed since 1998. The GCPs were

[1] 2020 photogrammetry-derived model was built as supplementary part of 2020 LiDAR-derived model due to the lack of reclamation information of Tung Chung (East) Extension in the 2020 LiDAR data.

[2] The historical aerial photographs were retrieved from HKMS 2.0 webpage (with category of aerial photo and image product) at https://www.hkmapservice.gov.hk/OneStopSystem/map-search?product=OSSCatA

selected at corners on different high-rise and low-rise buildings. Seventeen GCPs were picked for georeferencing in these four models.

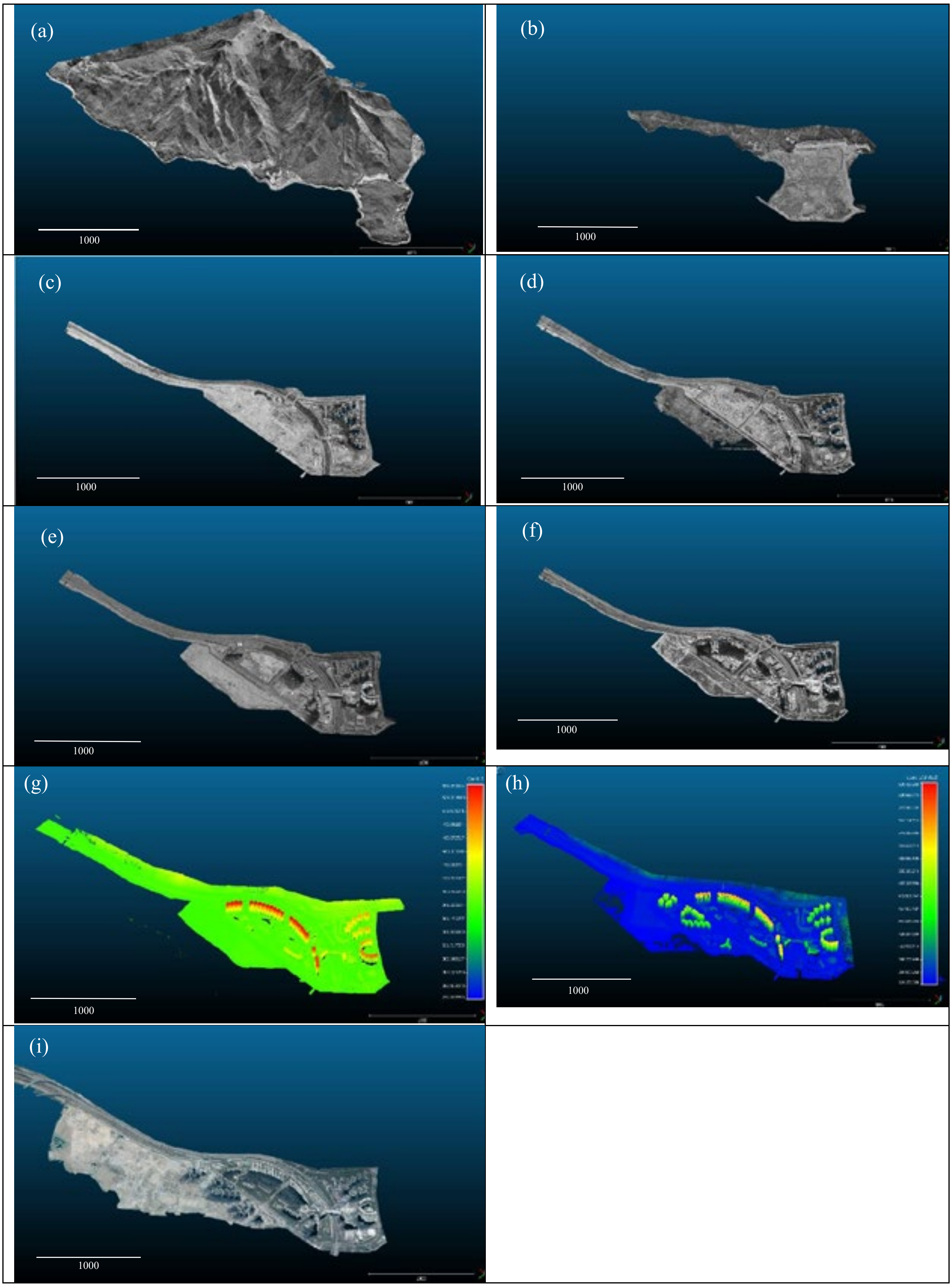

Figure 3: Photogrammetry-derived 3D surface models of (a) 1963; (b) 1993; (c) 1998; (d) 2000; (e) 2001; (f) 2004; (i) 2020; LiDAR-derived 3D surface model of (g) 2010;, and (h) 2020.

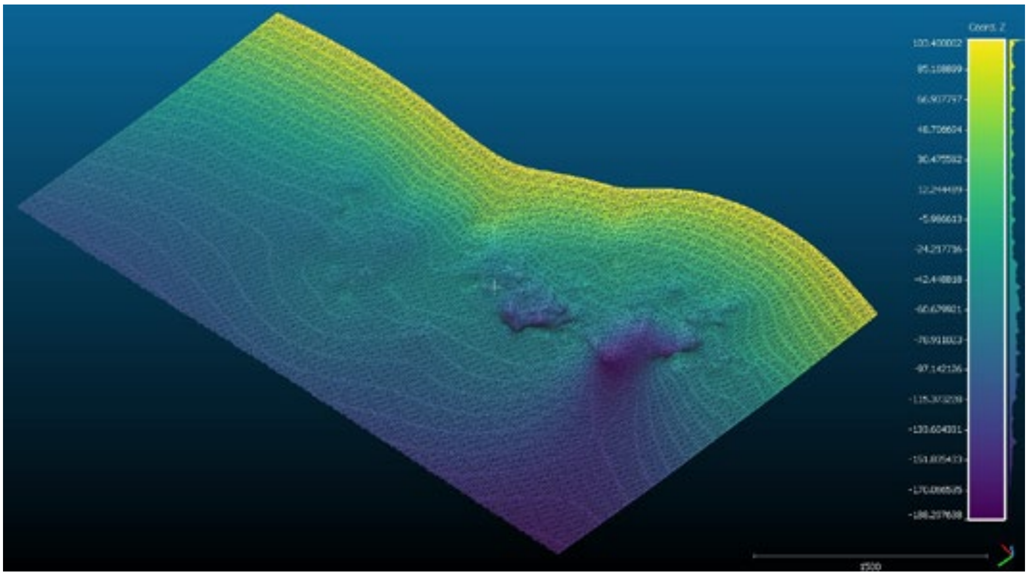

Figure 4: 3D Engineering Rockhead Mesh Model indicating general rock head level of the study area

2.4.1 Georeferencing Quality Assessment

To assess the georeferencing quality of the photogrammetry-derived models, a method called Multiscale Model to Model Cloud Comparison (M3C2) (Lague et al., 2013) was used for 3D direct point cloud comparison of the models. This method could accurately calculate and measure the orthogonal distance between two point clouds, and thus their 3D variations with consideration of cloud roughness.

This method was applied with the use of CloudCompare in computing the mean offset between the georeferenced photogrammetry-derived models and the reference model, i.e. 2020 LiDAR-derived model. For a more accurate assessment on models of early-stage TCNT Development, buildings were filtered out in the 2020 LiDAR model when performing M3C2 with the 1963, 1993, and 1998 models. This is to avoid counting of buildings from 2020 model as offsets on the undeveloped land of 1963, 1993, and 1998 models. The mean offsets for the 1963, 1993, 1998, 2000, 2001, and 2004 models are listed in Table 1.

Table 1: Mean offset of photogrammetry-derived 3D surface model with reference model.

Photogrammetry-derived 3D surface model (year)	Mean Offset (m)
1963	0.440057
1993	0.800728
1998	1.612809
2000	1.354278
2001	0.798643
2004	0.021451

3 AERIAL PHOTOGRAPH INTERPRETATION (API)

Aerial Photographs taken from 1963 to 2010 have been reviewed to assess the site development history within the Study Area for verifying the validity of the 4D model in this study. A total of 24 paper copy aerial photographs were acquired from the Lands Department, The Government of HKSAR for assessment. API was completed using digital methods with 6 orthorectified aerial photographs (with scale of 1:13000) retrieved from Geotechnical Information Infrastructure (Ginfo). The key observations from API for the study area from 1963 to 2010 are shown in Table 2.

Table 2: Key observations from API for 1963 to 2010

Year	Observations
1963	• The Study Area essentially comprises sea and coastal area. • Agricultural terraces are evident to the southeast portion of the Study Area.
1993	• Land reclamation works had been conducted for Phase 1 Tung Chung New Town Development to the Southwest of the Study Area. • A footpath had been constructed at the southeastern portion of the Study Area. • Vegetation clearance is observed at the southeastern portion of the Study Area.
2000	• Phase 1 Tung Chung New Town reclaimed land had been formed in the central portion of the Study Area. • Land reclamation works had been conducted for Phase 3 Tung Chung New Town Development in the northern portion of the Study Area. • Tung Chung Waterfront Road had been constructed at the western portion of the Study Area. • Tung Chung MTR station, Tat Tung Footbridge, Tung Chung Crescent, Fu Tung Estate, Yu Tung Court, Fu Tung Plaza, schools, Tung Chung Wan Telephone Exchange, and Tung Chung Sewage Pumping Station had been built at the southern portion of the Study Area. • Ling Liang Church Sau Tak Primary School and Ling Liang Church E Wun Secondary School had been built in the central portion of the Study Area. • Construction works had been conducted for Citygate in the central portion of the Study Area. • North Lantau Highway, Man Tung Road, Yi Tung Road, and Ying Hei Road had been constructed in the central portion of the Study Area. • Construction works had been conducted for Coastal Skyline in the central portion of the Study Area.
2001	• More lands were reclaimed for Phase 3 Tung Chung New Town Development in the northern portion of the Study Area. • Commercial Complex of Coastal Skyline, Man Tung Footbridge, Citygate, Tower 1 to 5 of Coastal Skyline had been built in the central portion of the Study Area. • Site formation works had been conducted for Seaview Crescent, Le Bleu Deux-Coastal Skyline Phase 4, Coastal Skyline Le Bleu House, and Caribbean Coast Phase 2 to 4 in the central portion of the Study Area. • Construction work had been conducted for Caribbean Coast Phase 1 at the eastern portion of the Study Area.
2004	• More lands were reclaimed for Phase 3 Tung Chung New Town Development's reclamation work at the northern portion of the Study Area. • Seaview Crescent Block 1 to 3 had been built at the northwestern portion of the Study Area. • Construction works had been conducted for Seaview Crescent Block 5 at the northwestern portion of the Study Area.
2010	• Phase 3 Tung Chung reclaimed land had been formed with vegetation growth at the northern portion of the Study Area. • Man Tung Road Park, Ngong Ping Cable Car Tung Chung Station, and Tung Chung Swimming Pool had been built at the western portion of the Study Area. • Novotel Citygate Hong Kong Hotel, Tung Chung Man Tung Road Sports Centre, Tung Chung Community Hall, Coastal Skyline Tower 6 and 7, Tung Chung North Pet Garden, Tung Chung North Park, Chinese Herb Garden, Caribbean Coast Phase 1 to 4, Bermuda Park, Ho Yu College, Coastal Skyline Le Bleu house, La Mer Block, Le Bleu Deux-Coastal Skyline, and Orange Zone Park had been built in the central portion of the Study Area.

4 RESULTS AND DISCUSSIONS

The 4D digital surface model illustrating site changes of the study area are presented in Figure 5. To better illustrate the site condition and changes in different years, the surface model of 1963 is used as the background model with models from different years overlayed. Quantitative analyses involving extraction of two cross section profiles are presented in Figure 6.

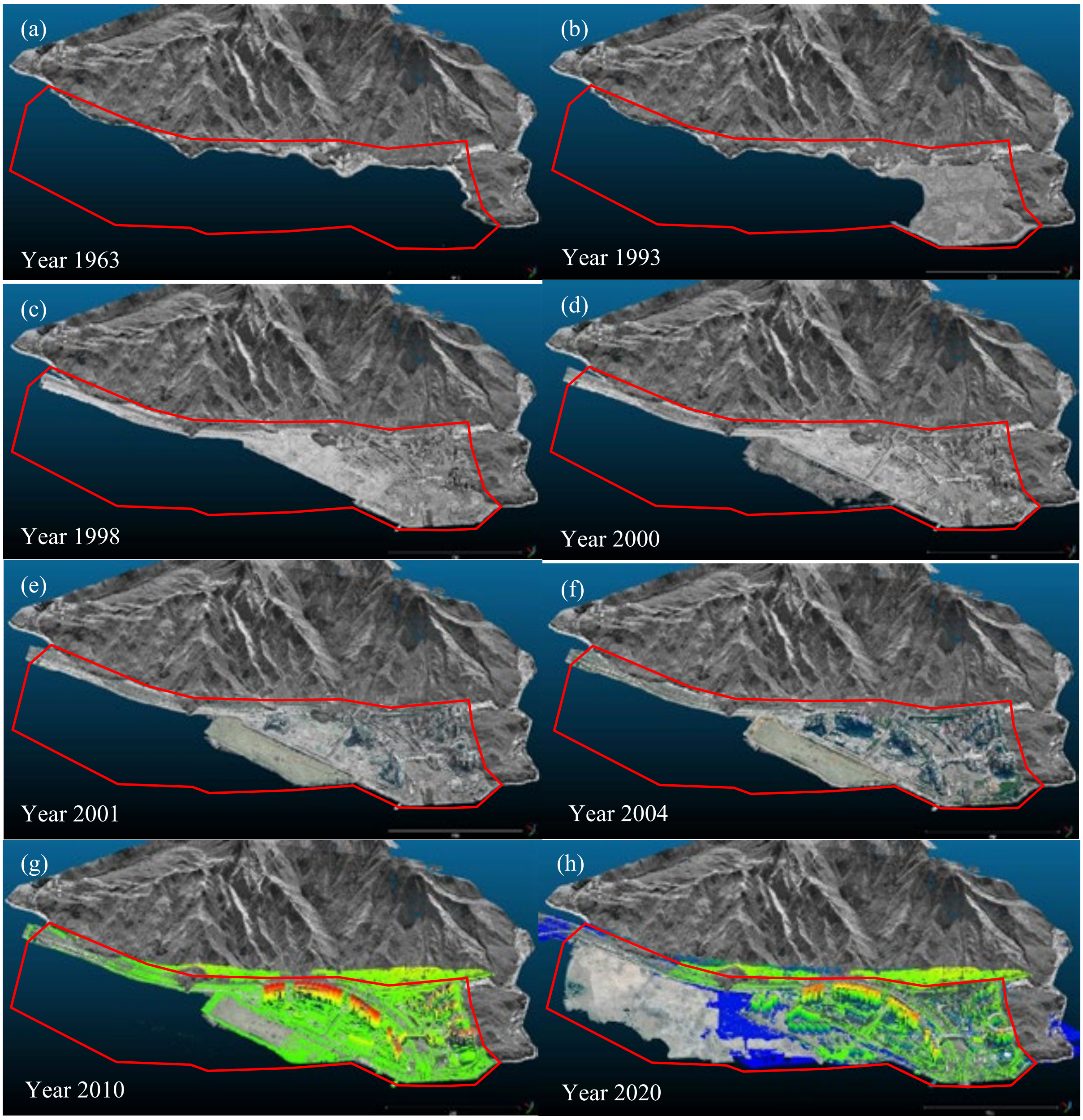

Figure 5: 4D digital surface model illustrating site changes from 1963 to 2020 (Year 1963 model is used as background model with models from different years overlayed). Site conditions in (a) 1963, (b) 1993, (c) 1998, (d) 2000, (e) 2001, (f) 2004, (g) 2010 and (h) 2020. The study area is outlined in red.

4.1 Cross Section Profiles

Two cross sections AA' (Figure 6b) and BB' (Figure 6c) were drawn across the study area using ArcGIS Pro. For better illustration, only the years with significant changes in cross section were shown in the profiles. A general comparison between the results obtained from cross section profiles and API are presented in Table 3.

Table 3: Comparison of results obtained from cross section profiles and API

Cross Section	Results from Cross Section of 4D Digital Surface Model	Results from API
AA' (Figure 6b)	(1) Phase 1 reclaimed land was observed in 1998 (2) Completion of Phase 3 reclaimed land and progressing construction work of Caribbean Coast Phase 4 Crystal Cove Tower 5 between 1998 to 2004 (3) The Coastal Skyline Clubhouse and Caribbean Coast Phase 4 Crystal Cove Tower 5 were built by 2010	(1) Central portion Phase 1 reclamation work was done by 2000. (2) Phase 3 reclamation work was started in 2000, with most of the reclaimed land formed in 2001. (3) Caribbean Coast Phase 4 Crystal Cove Tower 5 was built by 2010
BB' (Figure 6c)	(1) Phase 1 reclamation work was observed in 1993 (2) Completed Phase 1 reclamation, Tung Chung Crescent Clubhouse, Tung Chung Crescent Block 3, and Tat Tung Footbridge were found and built between 1993 to 1998 (3) Phase 3 reclaimed land was formed between 1998 to 2000 (4) Le Bleu House was built between 2000 to 2010 (5) Century Link was built between 2010 and 2020 (6) Progressing reclamation work of Tung Chung West found in 2020	(1) Southwestern part of Phase 1 reclamation work was in progress in 1993. (2) Formation of southeastern part of Phase 1 reclaimed land and completed construction of Tung Chung Crescent and Tat Tung footbridge by 2000 (3) Phase 3 reclamation work had been conducted in 2001. (4) Le Blue House was built between 2004 and 2010. (5) N/A (6) N/A

4.2 Complex Geological Conditions

Complex offshore geological ground conditions including weathered granite and rhyolite featuring some block xenoliths with dissolution features and cavities, was found with highly variable and occasionally extremely deep and steeply inclined rock head levels as illustrated from the 4D digital model. The mean rock head level of the study area is around - 48 mPD, with maximum depth at around -188 mPD. A cross segment is extracted from the 4D digital model (Figure 7) to illustrate the specially planned locations of different buildings' and facilities' heights in relations to the rockhead level of the study area. In Figure 7, it is evident that high-rising buildings are present in areas with shallower rockhead levels (at around -40 mPD). In contrast, those areas with the deepest rockhead levels (at around -100 to -188 mPD) contain open areas (i.e. park) without significant structures. The models match the actual situation given the limitations and cost of construction of deep foundations for high-rise buildings in areas with deep rockhead levels and with complex ground conditions.

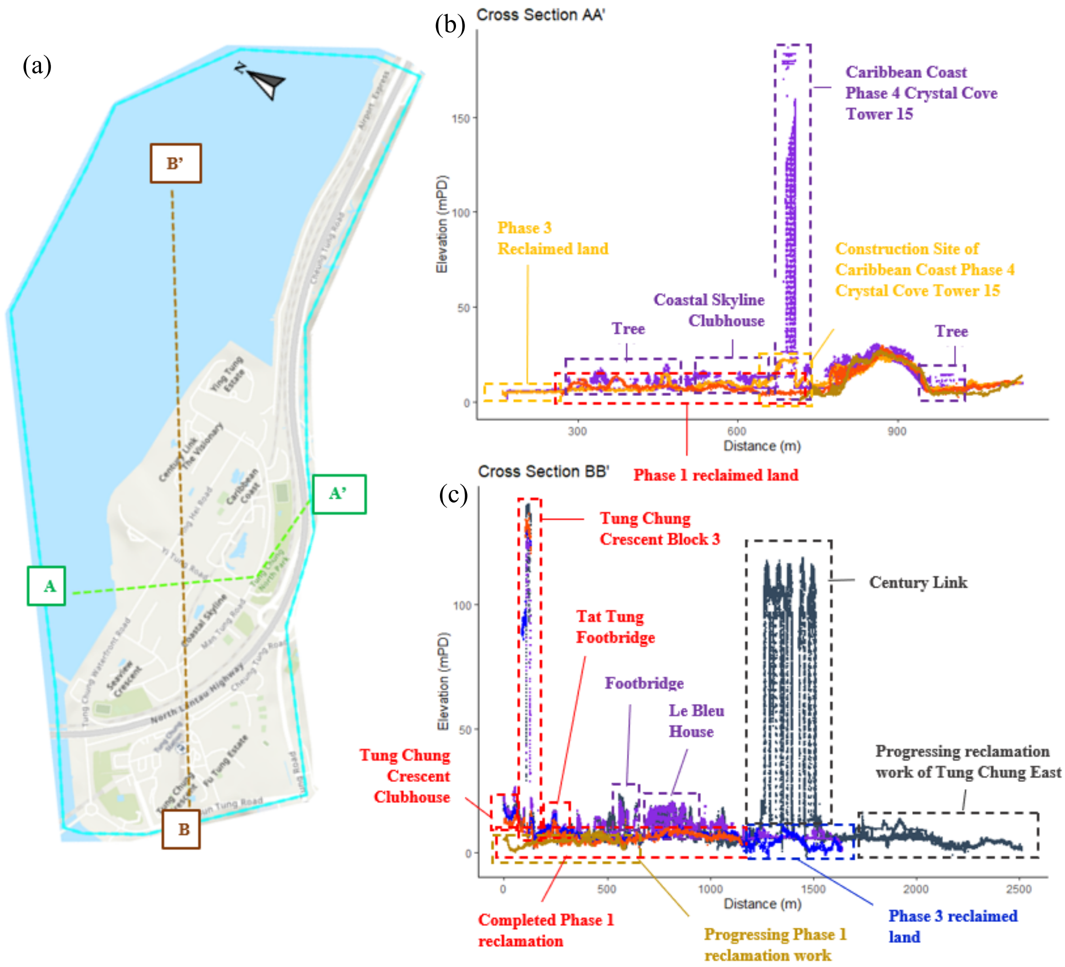

Figure 6: Cross section profiles of the study area. (a) Map showing the locations of cross sections AA' and BB'; (b) Cross section AA' across Tung Chung North; (c) Cross section BB' from Tung Chung Centre to Tung Chung East.

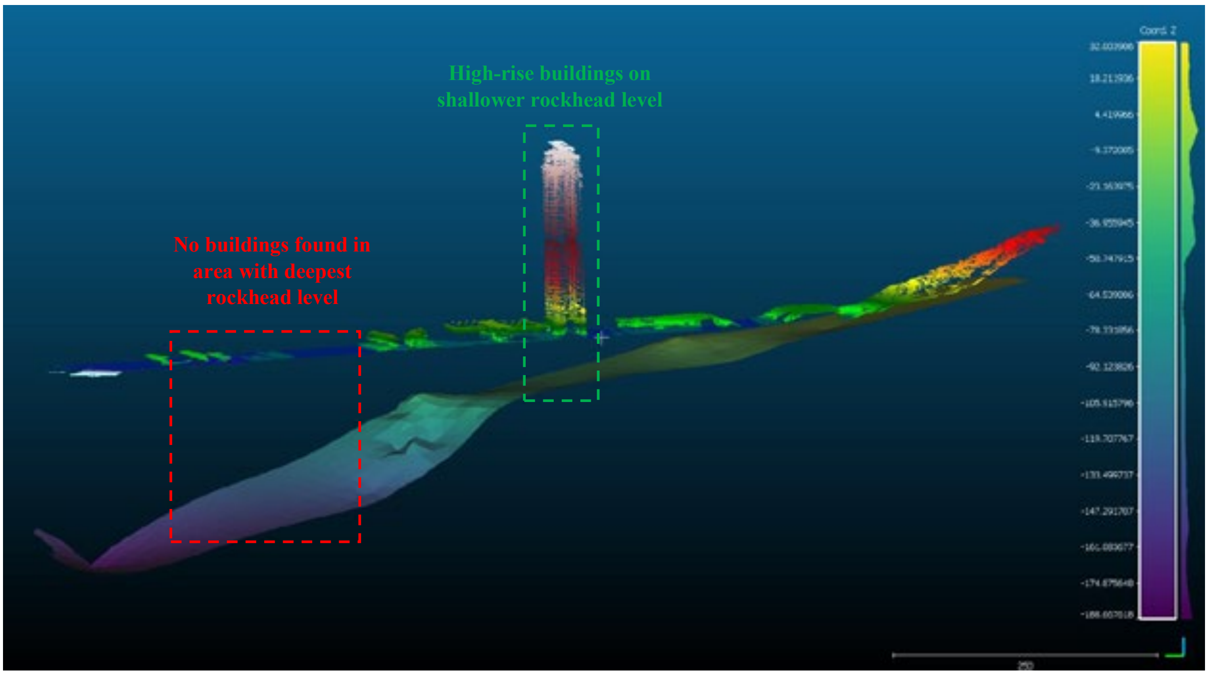

Figure 7: Cross segment of the 2020 surface model with the engineering rockhead model. The colour scale displays the elevation of rockhead level.

4.3 Summary

From the result obtained from the surface model and both the integration of surface and engineering rockhead mesh model, most of the results match with what have been obtained from both API and the literature review. The changes in site conditions including reclamation work and construction of different infrastructures are accurately illustrated and presented from the 4D digital model with its special geological conditions shown. This final result shows that the use of 4D model monitoring method is feasible in monitoring major changes of a site even for prolonged periods.

4.4 Limitations and Suggestions

While the 4D digital model monitoring method described in this paper is feasible in construction monitoring, limitations are found in the model building process in which improvements can be made in future works. Since the historical aerial photographs obtained from HKMS 2.0 in this study were in the format of DAP-L0 version[3], resolution and geospatial information of the images are limited. The resolution of the images is further reduced with photos taken at high flying heights. Thus, limitations in quality are found in the generation of 3D point cloud surface models using SfM.

In addition, as the digital aerial photos were taken from different months of the same year, the incoherence of features shown in the photos might also affect the completeness in the generation of 3D point cloud surface models. For example, model distortion was encountered in the 2004 surface model, which resulted in incomplete building structure in part of the model. Since geospatial information is also absent from the raw model, further georeferencing is necessary. The missing points in the point cloud model might increase the difficulty in performing geo-referencing manually (GCPs picking), and thus the accuracy and quality of the model.

For future improvements, it is suggested that UE Version of digital aerial photographs can be used for model building. The UE Version of digital aerial photographs are stored in the format of TIFF format with larger range of colour information from 8-bit to 12-bit, and with relevant geospatial information provided (Lands Department, 2021). It is believed that the quality, including resolution and georeferencing accuracy of the model can be greatly improved with the use of UE version of digital aerial photographs. Besides, it is also suggested that digital aerial photographs taken at lower altitudes should be chosen in priority to higher altitudes when generating 3D surface models. This can ensure that more features can be captured and illustrated clearly on 3D models. Aerial photos should also chosen with similar shooting date. This is to maintain the coherence of the photos used in model building.

5 CONCLUSIONS AND FUTURE USES

The case study shows that the use of the 4D digital model monitoring method is feasible and efficient in monitoring changes in construction site. It could provide a more comprehensive view and allow both qualitative and quantitative analyses of site changes in a systematic way. Cross section profiles can be extracted from the 4D digital model with its elevation change presented clearly. The changes in respective elevations could illustrate the corresponding construction and reclamation works in a given year. These numerical data might be useful in other stage of site planning and keep track of the construction progress and overall site development changes. The use of this smart construction monitoring method could greatly overcome limitations brought by conventional practice of construction monitoring in a more time-efficient and cost-effective manner. It is promising that our innovative 4D digital model and the associated sub-surface engineering rockhead model can be integrated with the Building Information Modelling system at a later stage to constituent a Smart Built Environment and to facilitate a smart construction site monitoring practice in near future.

[3] Digital aerial photo in L0 version is a free version aerial photographs which can be downloaded from HKMS 2.0 in JPEG format. The images are at an resolution of 300 dpi scanned from paper copy of the aerial photographs (Lands Department, 2021)

ACKNOWLEDGEMENTS

We would like to thank Prof. Richard MARTIN for his support and provision of useful background information for this study, and Mr. Ivan KWONG for his assistance in point cloud presentation of the cross section profile. We acknowledge the provision of LiDAR survey data and other relevant information from the Geotechnical Engineering Office of the Civil Engineering and Development Department, of the Government of HKSAR.

This paper is extracted from the undergoing graduate Final Year Project (FYP) of one of the authors Natalie Cheng. This FYP is a collaboration project between the Earth System Science Programme (ESSC), Chinese University of Hong Kong and the Hong Kong based engineering geological consultant, GeoRisk Solutions Limited (GRS). This project is supervised by Prof. Lin LIU of ESSC, CUHK and co-supervised by Dr. Wenzhu HOU of GRS.

REFERENCES

ARUP. 2015. *Civil Engineering and Development Department Tung Chung New Town Extension Project Profile (REP-128-00)* (Draft). Hong Kong.

Civil Engineering and Development Department. 2020. L1 Tung Chung New Town Background and Project Objective. Civil Engineering and Development Department, Government of the Hong Kong SAR. From https://www.cedd.gov.hk/eng/about-us/achievements/land/regional-development/l1-tung-chung-new-town/index.html, accessed March, 2022.

Environment, Transport and Works Bureau. 2004. Checking of Foundation Works in the Scheduled Areas of Northwest New Territories and Ma On Shan and the Designated Area of Northshore Lantau. *Environment, Transport and Works Bureau Technical Circular (Works) No. 4/2004*. Hong Kong: Environment, Transport and Works Bureau, The Government of Hong Kong SAR.

Geotechnical Engineering Office (GEO). 2021. *Complex Geological Conditions in Northshore Lantau (Information Note 09/2021)*. Hong Kong.

Geotechnical Engineering Office (GEO). 2004. The Designated Area of Northshore Lantau. *GEO Technical Guidance Note No.12.* Hong Kong: Geotechnical Engineering Office, Civil Engineering and Development Department, The Government of the Hong Kong SAR.

Hong Kong Place. 2021. *Place-Land Reclamation Work*. Hong Kong Place. [In Chinese] From https://www.hk-place.com/view.php?id=119#top, accessed March, 2022.

Lague, D., Brodu, N.,& Leroux. J. 2013. Accurate 3D comparison of complex topography with terrestrial laser scanner: Application to the Rangitikei Canyon (N-Z). *ISPRS Journal of Photogrammetry and Remote Sensing*, 82: 10-26.

Lands Department. 2021. *Aerial Photographs*. Lands Department, The Government of Hong Kong SAR. From https://www.landsd.gov.hk/en/survey-mapping/mapping/aerial-photo-photogrammetric-products/aerial-photo.html, accessed March, 2022.

Lands Department. 2021. *Aerial Digital Photo*. Lands Department, The Government of Hong Kong SAR. From https://www.landsd.gov.hk/en/survey-mapping/mapping/aerial-photo-photogrammetric-products/digital-aerial-photo.html, accessed March, 2022.

Land Department. 2021. Photogrammetric Survey and Remote Sensing. Lands Department, The Government of Hong Kong SAR. From https://www.landsd.gov.hk/en/spatial-data/imagery-intelligence-collection.html, accessed March, 2022.

Sewell, R. J. & Kirk, P.A. 2002 Geology of Tung Chung and Northshore Lantau Island. *Hong Kong Geological Survey Sheet Report No. 6*, pp.48-55. Hong Kong: Geotechnical Engineering Office, Civil Engineering and Development Department, The Government of the Hong Kong SAR

Digital Solutions to Improve Workflows of 3D Ground Modelling

P K K Wu, J Chin, C Ng, R Tsui
Aurecon Hong Kong Limited, Hong Kong, China

ABSTRACT

3D ground modelling often starts with importing digitised ground investigation (GI) data into modelling software. This first step is very vital for further ground interpretation with meaningful result. Since the invention of digitised GI data, any data obtained on site can be electronically transferred by adopting the AGS format (*.AGS).

To utilise any digital GI data for this purpose, engineering geologists must go through manual data clean up to suit the import format of modelling software. Otherwise, details will be lost such that risks could potentially be overlooked in the interpretation of the data.

Aurecon has developed a new tool specifically to automate the manual process to restructure any AGS data, streamlining the process of 3D ground modelling. After any AGS files are processed by this tool, the likelihood of overlooking any details or important information has been greatly minimized. From our experience, the time saving between using this tool and manually processing digital data to build up a 3D ground model is often more than 50%.

This paper will first discuss challenges of 3D ground modelling from AGS data, followed by discussion on preferred data structure for ground modelling and capabilities of the tool to overcome these challenges.

1 INTRODUCTION

A well-established ground engineering design needs to be based on relevant and detailed ground model where most of the geotechnical risks are carefully determined and properly handled.. Building up a detailed ground model involves cross-checking of different data and descriptions from ground investigation (GI) data, which may include grain size and type of soil material, strength and weathering grade of rocks, rock mass descriptions and characteristics of localized weak zones. The focus of each ground model may be very different depending on each project requirements. For example, the ground model for a cut-and-cover tunnel focuses on soil properties while the ground model for a deep rock tunnel focuses on rock mass characteristics.

At the start of every project, a new ground model needs to be developed to ensure that the ground model is serving the project's specific needs and that all project-specific GI data, or related archival GI data, are included. Depending on the scale of projects, hundreds or even thousands of GI data may be involved. Although GI data can be transferred in bulk in electronic format with the help of AGS data format, one cannot assume that the process of building up a ground model can be easily automated.

This is because only factual data collected from GI sites and laboratories is stored in AGS data. Without manual input from engineering geologists or geotechnical engineers, which involves checking and putting relevant data together and adding sensible interpretations, raw AGS data is far from having sufficient information required in building up a detailed ground model for any project. In large projects in which a large number of GI data is involved, it is often required for a team of engineering geologists or geotechnical engineers to work for a certain period (from days to weeks) to process all the data.

Therefore, in an attempt to reduce the time required in projects to work on repetitive tasks, a tool has been developed to semi-automatically process and refine AGS data for the need of a detailed ground model. The following section will explain in detail the challenges encountered when a detailed ground model is built from

AGS data. The subsequent section will explore how these challenges can be overcome with the help of the tool. The benefits and future developments of the tool will be discussed in the final section.

2 COMMON CHALLENGES OF BUILDING GROUND MODEL WITH AGS DATA

Compared with building up a ground model based on the GI reports in hardcopies or pdf format, AGS data, which is saved in a format convenient for data storage and transfer, can save a huge amount of time for manual data input. Nevertheless, some challenges may be encountered when directly using the AGS data for ground modelling.

2.1 Reliance on Commercial Software

AGS data handling often relies on commercial software. AGS data is stored as a text file with specific format. It is almost like a combined csv file of all the groups. Although it can be opened with text-reading software, only a few commercial software can decode this specific format back to its spreadsheet-like format as designed. Though these pieces of commercial software allow reading, editing and visualizing of the data in different groups directly (Figure 1), no commercial software to-date enables query of data across different groups and restructuring of AGS data. These two tasks are often done out of commercial software and can only be done in spreadsheets which are output from the software. If performed manually, they could be extremely time-consuming tasks.

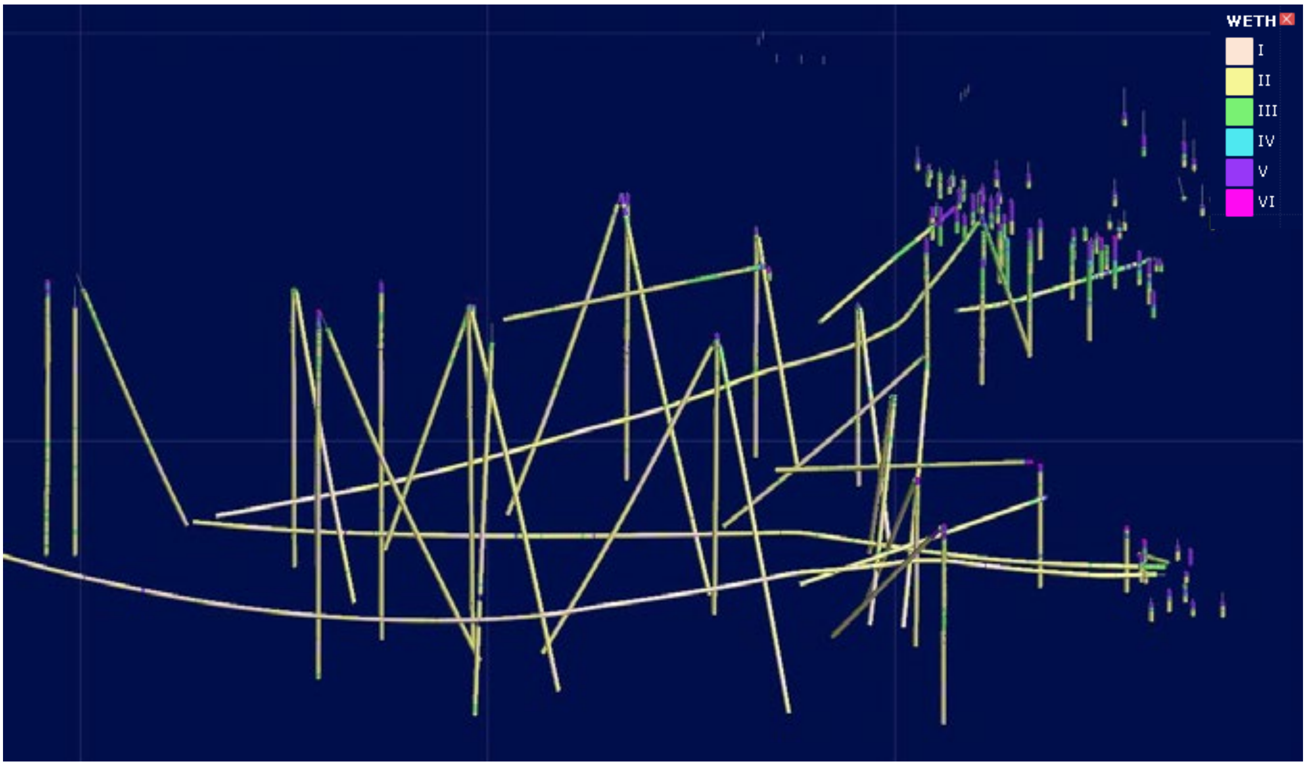

Figure 1 Raw AGS data visualized by commercial software, Leapfrog Works

2.2 Purpose as Electronic Transfer Format

The goal of AGS data format is to make electronical transfer and storage of ground investigation data possible (AGS, 2022; Caronna & Wade, 2005). AGS data format was introduced by the Association of Geotechnical and Geoenvironmental Specialists in 1991 to store GI data in digital format. This format stores data in Group Hierarchy, or a tree-like structure where a group on top is called parent group and groups below it are called child groups. Each group can have more than 1 child groups but at most 1 parent group. At the top of the hierarchy is PROJ group. Below PROJ group are LBSG and HOLE (which is renamed to LOCA in the latest (4th) version of AGS data format) groups which lab testing schedule and location details of each GI point respectively (see Figure 2 and Figure 3 for a better visualization of the structure).

This format is easy for any party using GI data (e.g., GI contractors, main contractor, consultant, etc.) as any data can be added or removed simply by editing a single group. It is also a great transfer format due to its small file size. It made transfer of more and more, if not all, GI data available since its introduction. However, when it comes to ground modelling when data from different groups should be read concurrently, problems may arise with data in different groups stored independently without relationship to other groups except their own parent group.

HOLE_ID	HOLE_TYPE	HOLE_NATE	HOLE_NATN	HOLE_GL	HOLE_FDEP	HOLE_STAR	HOLE_LOG	HOLE_REM	HOLE_LETT	HOLE_
BH1	W+RC	839956.27	828994.35	5.43	17.27	14/04/1999	K.M. To	1. Piezometer tip installed at 10.50m depth.		
BH2	W+RC	840083.86	829135.56	6.55	37.4	17/04/1999	K.M. To			
BH3	W+RC	840216.28	829280.88	4.91	27.48	22/04/1999	K.M. To	1. Piezometer tip installed at 21.45m depth.		
BH4	W+RC	840230.82	829195.83	6.31	22.82	9/4/1999	K.M. To	1. Piezometer tip installed at 16.10m depth.		
BH5	W+RC	840660.75	829638.92	5.54	37.16	21/04/1999	K.M. To	1. Piezometer tip installed at 25.00m depth.		
BH6	W+RC	840753.76	829649.59	4.99	46.06	12/4/1999	K.M. To			
TP1	TP	839921.45	828956.41	4.1	2.3	12/4/1999	K.M. To			
TP2	TP	840026.09	829073.55	5.63	2.4	12/4/1999	K.M. To			
TP3	TP	840115.37	829094.16	6.11	2.2	20/04/1999	K.M. To			
TP4	TP	840148.59	829203.17	6.78	1.2	15/04/1999	K.M. To			
TP5	TP	840217.7	829267.36	5.07	2	14/04/1999	K.M. To			
TP6	TP	840277.51	829222.71	5.78	1.3	15/04/1999	K.M. To			
TP7	TP	840387.15	829287.28	6.24	1.6	15/04/1999	K.M. To			
TP8	TP	840384.65	829381.94	5.77	2.1	3/5/1999	K.M. To			
TP9	TP	840474.73	829340.17	7	2	17/04/1999	K.M. To			
TP10	TP	840469.68	829496.15	6.24	2.1	5/5/1999	K.M. To			
TP11	TP	840566.68	829402.48	7.39	2	16/04/1999	K.M. To			
TP13	TP	840671	829475.05	5.78	2	16/04/1999	K.M. To			
TP14	TP	840816.46	829690.73	7.41	2.3	12/4/1999	K.M. To			
TP15	TP	840897.38	829793.95	8.41	2.3	13/04/1999	K.M. To			
TP16	TP	840988.85	829972.06	5.99	2.3	14/04/1999	K.M. To			
TP17	TP	841044.39	830096.51	5.67	2.3	13/04/1999	K.M. To			

PROJ | HOLE | HDIA | PTIM | SAMP | GEOL | DETL | FRAC | CORE | ISPT | PREF | POBS | WETH | IDEN

Figure 2 Example of structure of AGS file (converted to Excel spreadsheet by commercial software gINT)

Figure 3 Structure of AGS data (from AGS, 2022)

2.3 Loss of Detailed Variations in Ground Conditions in Grouped Data

Raw AGS data alone does not directly show the detailed variations in ground conditions, due to its grouped structure. Detailed ground conditions may be described in numerous types of data, which may be continuous qualitative descriptions like field geological descriptions, continuous numeric data like coring information (core recovery, RQD etc.), discrete descriptions at certain depths like stratum detail descriptions, or discrete data at certain depths like field or lab test data.

Every type of data is stored in individual groups. Groups commonly used in ground modelling in Hong Kong include:

- DETL: Stratum Detail Descriptions
- FRAC: Fracture Spacing
- GEOL: Field Geological Descriptions
- WETH: Weathering Grade
- CORE: Coring Information

Interpretation of ground conditions cannot rely on any single group alone. For example, in the interpretation of engineering rockhead, other than reading the WETH group, the geologist must also check the CORE group for TCR and GEOL and DETL groups for descriptions to ensure all requirements for rockhead as described in the Code of Practice of Foundations are met.

2.4 Laborious Cross-group Analysis

Analyzing AGS data across numerous groups is a laborious process, because data are often stored in different intervals across different groups and querying capabilities are lost (Caronna & Wade, 2005).

Data in each group are often stored in depth intervals and only depths where there are changes in that particular group is recorded. As a result, the depth intervals often do not match with each other. In the example shown in Figure 4, main geological descriptions are stored in a large interval between 541.48m and 546.45m. RQD is stored in slightly smaller intervals: 541.30m – 542.85m, 542.85m – 544.38m etc. Weathering grade and fracture index are stored in smaller, yet completely different intervals. Detailed descriptions are then added in specific intervals.

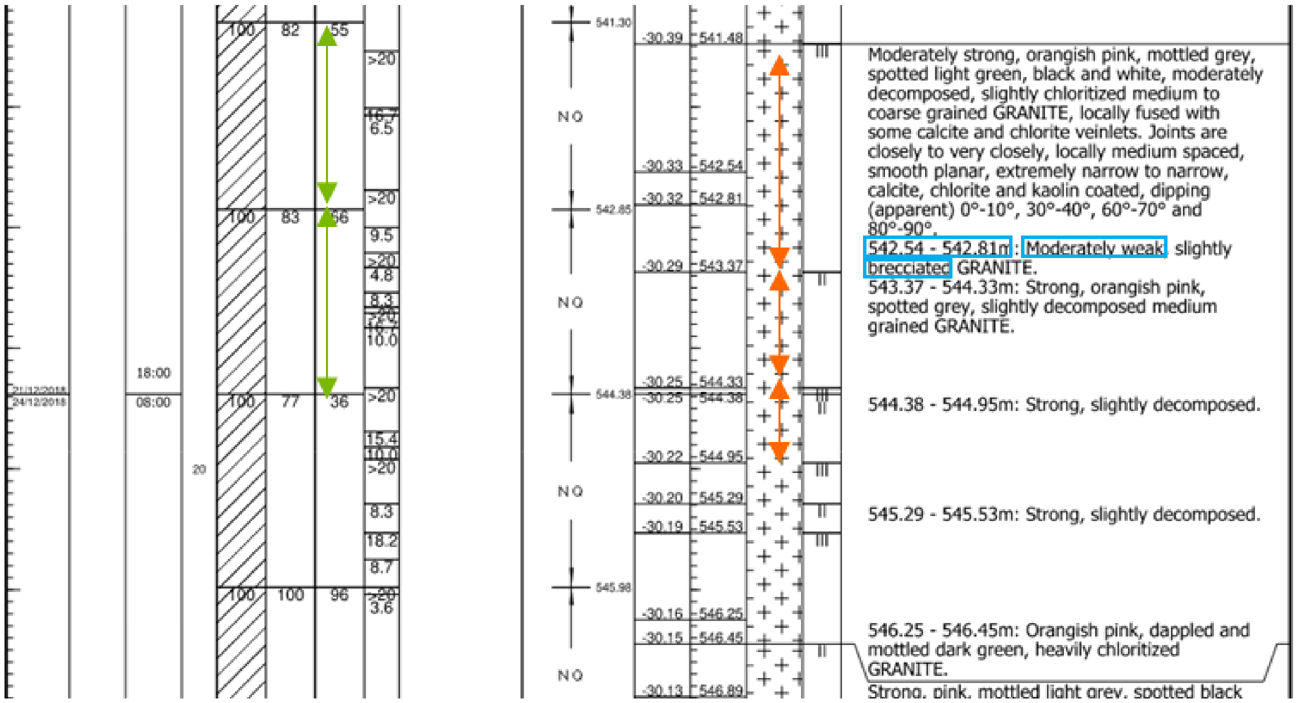

Figure 4 Example of common borehole log where data are stored in different intervals

If data in two or more different groups are to be compared, the intervals must be combined and broken down to smaller intervals. For example, if one wishes to find out the SPT-N value of different soil type (e.g. fill, marine deposits, alluvium, etc.) and grain size (e.g. sand, silt, clay, etc.), one may first transfer ISPT group data and the descriptions in GEOL group into an Excel spreadsheet. The soil type and grain size of each SPT test may be correlated manually by either reading the GEOL group descriptions one by one, or by combining data in both groups into a single table and then matching the soil types and grain size of each test at once. This process may still be easy if only few boreholes are involved and only data from two groups are to be correlated. If data from more than 2 groups are to be compared or combined, though not impossible, a large amount of repetitive data lookup and/or copy-pasting is required.

2.5 Overlooked Risk of Directly Imported AGS

Building up a ground model with AGS data directly may lead to geotechnical risks being potentially missed by overlooking data in other groups. As data are stored in different intervals in different groups, no one single group is comprehensive enough to reflect all the detailed changes of ground conditions. Whenever ground conditions are to be characterized by using data stored in more than one groups, correlating and combining the data is inevitable. If only selected groups are assessed, potential geotechnical risks represented in other unassessed groups may be overlooked.

For example, if only the WETH group is directly used for finding the engineering rockhead, localized weak materials described in DETL group and the presence of the description of corestone, which should not be considered as engineering rockhead, will highly likely be missed. And occasionally, in depths much below the engineering rockhead where mostly Grade II or Grade III rock is present, if only weathering grade is checked, localized weak zone or fault materials, which may be described in DETL or GEOL groups, will likely be missed, unless detailed manual checking is done on borehole logs or excel spreadsheets.

3 PREFERRED DATA STRUCTURE FOR GROUND MODELLING

For the purpose of developing a database for a comprehensive ground model, it is suggested to further process the AGS data by restructuring the Group Hierarchy structure. One single depth-related table (instead of separated groups) should be constructed to allow easier correlation of depth-related data across different groups. Depth intervals from all groups, which should be considered in the detailed ground model, shall be taken and broken down to merge data from all groups. Qualitative descriptions, such as field geological descriptions and stratum detail descriptions, should be included. Key descriptions, such as rock and soil types and soil grain size, should be extracted as well.

Important geological features, such as fault zones, shear zones and corestone zones, should then be extracted from descriptions. Continuous numeric data such as TCR, RQD, fracture index and weathering grade, should also be populated. Other depth-dependent data such as field test and lab test data, standpipe and piezometer installation records, can then be correlated with geological descriptions and coring information to enhance the efficiency of data interpretation. Subsequently, further interpretation of ground conditions (such as fault zones, weak seams) can also be added into this detailed database. With such database structure, any GI data can be correlated and interpreted with ease. Interpretations can also be visualized and related to factual data easily.

4 CAPABILITIES OF “AGS PROCESSOR”

With the aim of using AGS format data for ground modelling more efficiently, the authors developed a number of excel spreadsheets with complicated equations to process the AGS data. However, the authors soon realised that such excel spreadsheets are not user-friendly at all and this approach cannot support to process large amount of GI information. As a result, a python-based tool called AGS Processor (Figure 5 has been developed to solve the aforementioned problems. It aims at transforming AGS data files to a format ready for development of a detailed ground model.

4.1 Data Reconstruction

Similar to commercial software, this AGS Processor can read and parse (decode) AGS files. Excel files output from commercial software gINT can also be read. The widely adopted modified AGS 3rd version (AGS3) data format for Hong Kong industry can be read, checked and inspected. The Combine function allows the user to restructure AGS data from various groups, such as GEOL, CORE, DETL, FRAC and WETH, into a single depth-correlated table as suggested in Section 3. Depth intervals from all the groups are combined and data from all groups are automatically populated into the combined table (Figure 5).

HOLE_ID	DEPTH_FROM	DEPTH_TO	GEOL	GEOL_DESC	THICKNESS_M	TCR	RQD	WETH_GRAD	FI	Details
28066_DH1-1	0.0	3.3	SANDSL	Extremely weak, yellowish brown, completel	3.3	N/A	N/A	V	N/A	N/A
28066_DH1-1	3.3	4.14	SANDSLGR	Extremely weak, yellowish brown, completel	0.84	N/A	N/A	V	N/A	N/A
28066_DH1-1	4.14	4.22	GRANITE	Moderately strong to strong, pinkish grey anc	0.08	100.0	89.0	III	12.5	4.14m to 4.22m and 6.18m to 6.60m : V
28066_DH1-1	4.22	4.84	GRANITE	Moderately strong to strong, pinkish grey anc	0.62	100.0	89.0	III/II	1.4	N/A
28066_DH1-1	4.84	5.61	GRANITE	Moderately strong to strong, pinkish grey anc	0.77	98.0	89.0	III/II	1.4	N/A
28066_DH1-1	5.61	5.68	GRANITE	Moderately strong to strong, pinkish grey anc	0.07	98.0	89.0	III/II	14.3	N/A
28066_DH1-1	5.68	6.18	GRANITE	Moderately strong to strong, pinkish grey anc	0.5	98.0	89.0	III/II	1.9	N/A
28066_DH1-1	6.18	6.21	GRANITE	Moderately strong to strong, pinkish grey anc	0.03	98.0	89.0	III	1.9	4.14m to 4.22m and 6.18m to 6.60m : V
28066_DH1-1	6.21	6.3	GRANITE	Moderately strong to strong, pinkish grey anc	0.09	98.0	89.0	III	10	4.14m to 4.22m and 6.18m to 6.60m : V
28066_DH1-1	6.3	6.41	GRANITE	Moderately strong to strong, pinkish grey anc	0.11	99.0	99.0	III	10	4.14m to 4.22m and 6.18m to 6.60m : V
28066_DH1-1	6.41	6.6	GRANITE	Moderately strong to strong, pinkish grey anc	0.19	99.0	99.0	III	0.7	4.14m to 4.22m and 6.18m to 6.60m : V
28066_DH1-1	6.6	7.52	GRANITE	Moderately strong to strong, pinkish grey anc	0.92	99.0	99.0	III/II	0.7	N/A
28066_DH1-1	7.52	7.87	GRANITE	Moderately strong to strong, pinkish grey anc	0.35	100.0	100.0	III/II	0.7	N/A
28066_DH1-1	7.87	7.92	GRANITE	Moderately strong to strong, pinkish grey anc	0.05	97.0	93.0	III/II	0.7	N/A
28066_DH1-1	7.92	9.25	GRANITE	Moderately strong to strong, pinkish grey anc	1.33	97.0	93.0	III/II	3.8	N/A
28066_DH1-1	9.25	9.41	GRANITE	Moderately strong to strong, pinkish grey anc	0.16	97.0	93.0	III/II	1.4	N/A
28066_DH1-1	9.41	10.0	GRANITE	Moderately strong to strong, pinkish grey anc	0.59	96.0	96.0	III/II	1.4	N/A
28066_DH1-1	10.0	10.27	GRANITE	Moderately strong to strong, pinkish grey anc	0.27	96.0	96.0	III/II	0	N/A
28066_DH1-2	0.0	3.95	SANDSLGR	Extremely weak, pinkish grey, spotted brown	3.95	N/A	N/A	V	N/A	N/A
28066_DH1-2	3.95	4.0	SANDSLGR	Extremely weak, pinkish grey, spotted brown	0.05	N/A	N/A	V	N/A	Becoming very dense at 4.00m.

Figure 5 Preliminary Interface of AGS Processor, showing reconstructed AGS data

4.2 Information Extraction and Matching

To enhance the efficiency to cross-check the information and minimize the potential risks of missing important information in the geological descriptions (GEOL) and detailed descriptions (DETL), one of the functions of AGS Processor is to automatically extract and combine information from geological descriptions and detailed descriptions. Key descriptions, such as soil type and grainsize (e.g., marine clay, alluvial sand etc.) are extracted from geological descriptions and automatically matched. Other soil-related data, such as field test and lab test data, can then be matched with the corresponding soil type and grain size directly. For example, given a list of SPT data in the list of boreholes in the combined table, the soil types and grain sizes can be matched automatically. All the SPT data can then be sorted and plotted for evaluation directly. Another example of using this function is the packer test results can be matched with the RQD and fracture index (FI) which are stored in different group of the AGS data automatically for ease of review and further analysis.

Detailed descriptions are also checked. For instance, in rock portion, descriptions are also automatically checked in GEOL and DETL groups to locate any weak materials by searching for key words such as *moderately weak*, *weak*, *extremely weak*, or *no recovery*. Important geological descriptions such as *corestone*, *fault*, *fault gauge*, *fault breccia* can also be automatically located (Figure 6).

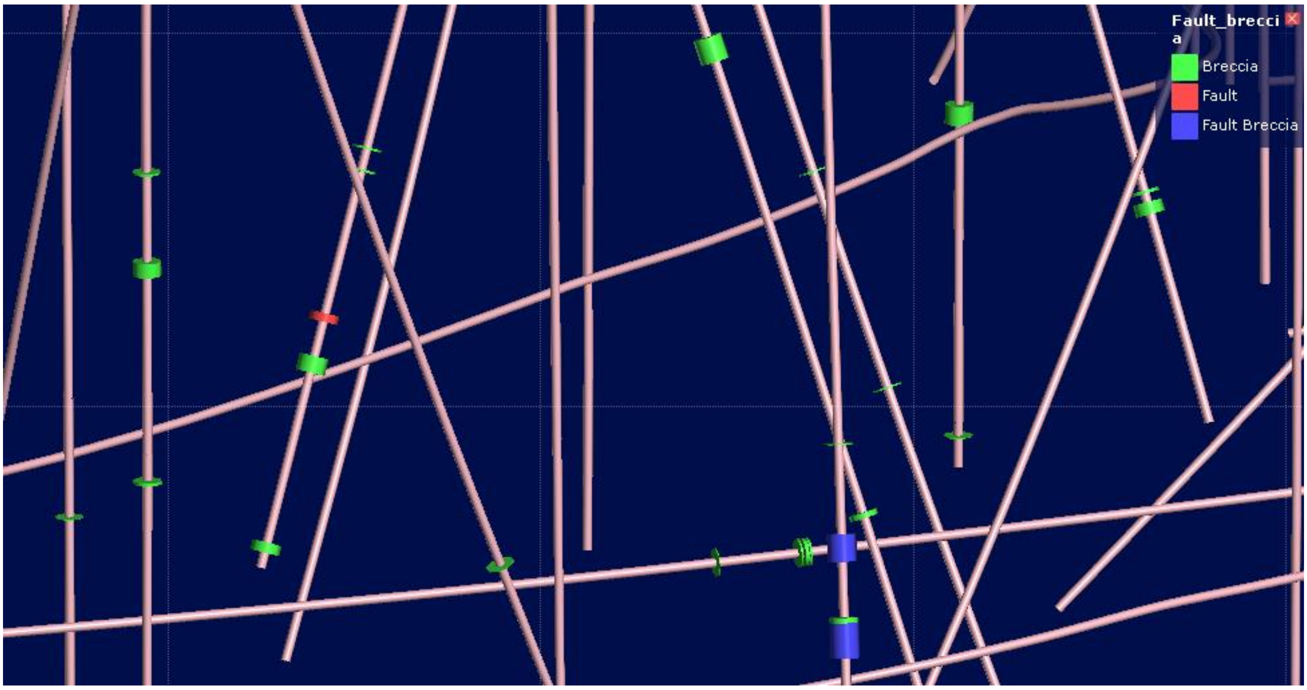

Figure 6 Example of "fault" (red), "breccia" (green) and "fault breccia" (blue) extracted from AGS Processor

4.3 Characterization of Ground Conditions

4.3.1 Engineering Rockhead

AGS Processor can also characterize ground conditions in different ways. The function of "Calculate Rockhead" can determine the depth of engineering rockhead of any boreholes. Conditions defining engineering rockhead can be specified and changed according to project requirements if needed. It is understood that some of the cases of determining the engineering rockhead can be complicated (even for manual interpretation) and this automatic function may not be able to determine the engineering rockhead for these complicated cases with 100% accuracy. Therefore, every calculated rockhead point will be further classified as either simple or complicated case. The user will be given alerts when complicated cases are encountered. For example, the user will be notified when corestone exists above rockhead, and when weak materials exist below rockhead.

Once the engineering rockhead has been determined based on user-defined conditions, the function of "Corestone Percentage" can then be used to calculate the percentage of rock above rockhead to estimate the percentage of corestones intercepted at each borehole.

4.3.2 Zones of Weakness

AGS Processor can also help the users to characterize rock mass conditions by looking for the zones of weakness in the rock mass. After engineering rockhead has been defined, all weak materials below the engineering rockhead can be extracted and characterized. Depending on project requirements, for example in Geotechnical Baseline Reports or definitions defined by the users, the weak seams can be defined with editable parameters (e.g. weathering grade, RQD, FI, etc.), hence thicknesses of all the weak seams can be automatically calculated. Identified weak seams can then be grouped and characterized into wider zones of weakness based on criteria defined by the user such as width of widest seam, maximum separation, accumulated length along the borehole and density (Figure 7). Localized zones of weakness encountered at each borehole can then be outlined with a consistent definition with much less manual input and subsequently the users can interpret the zone of weaknesses located in the site area. The users can also do the interpretation with different trials using various definitions of weak seams and zones of weakness. This function is particularly useful when the zones of weaknesses are not discrete, and the weak materials shown in the boreholes distributed dispersedly in the site area.

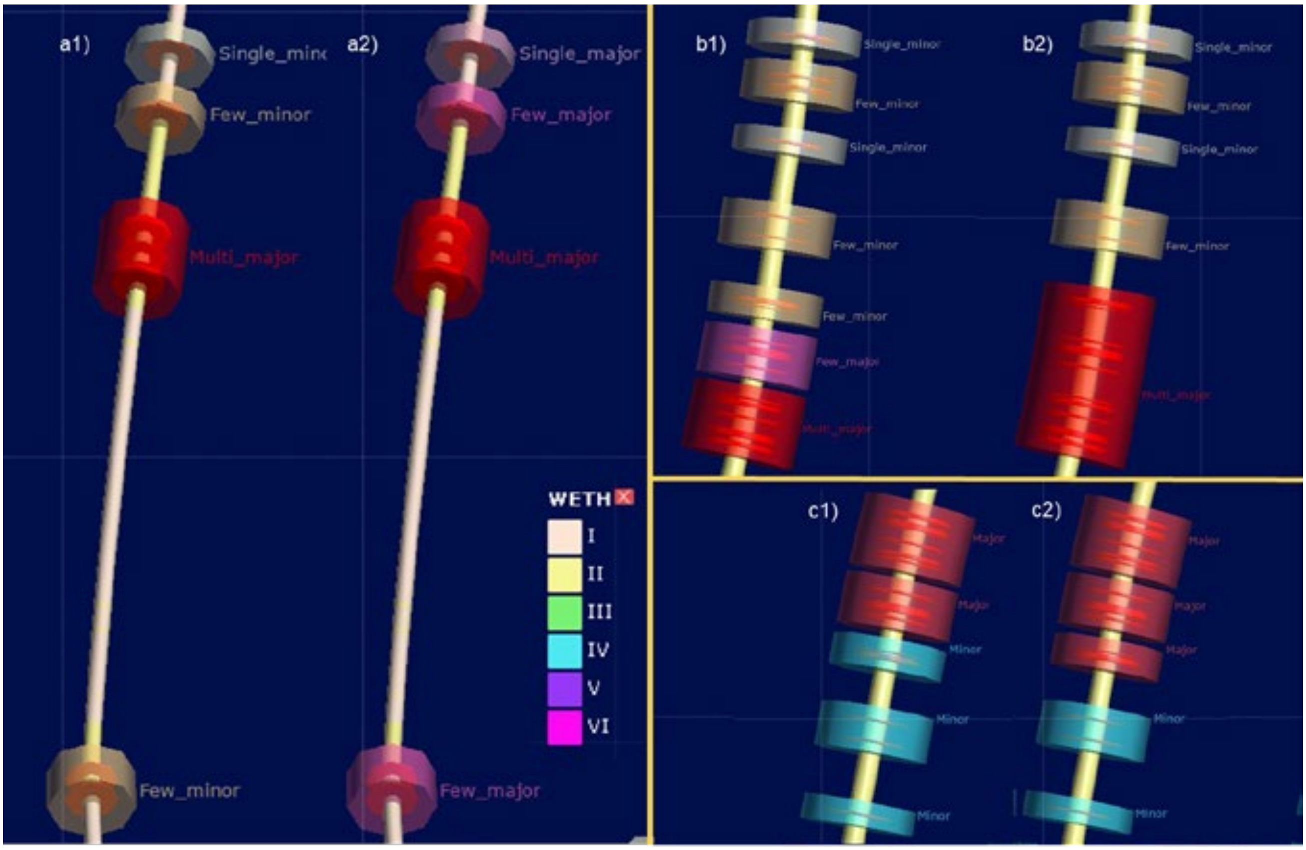

Figure 7 Example of zones of weakness extracted by AGS Processor: (a) classifying as major zone of weakness by width of widest seam (a1)>500mm or (a2)>350mm; (b) changing definition of zones by maximum separation of (b1)2m or (b2)3m between seams; (c) classifying as major/minor weak zone with density (c1)>0.2 or (c2)>0.15. Weak seams are denoted smaller red discs. Weathering grade is displayed at the background.

4.3.3 Rock Mass Quality

Rock mass quality such as the NGI-Q method is based on six parameters each defining different characteristics of the rock mass, and it can also be calculated from the reconstructed database (Figure 8). According to the authors' experience on site, parameter Jn can be estimated by numerical correlation with RQD or other correlation. Rock joint friction parameters, Jr and Ja, can be estimated from extracted rock joint descriptions based on RQD, Jn, Jr and Ja; the application of Jw and SRF as defined by the user, Q-value for each interval of the boreholes can then be calculated effectively from the reconstructed data for subsequent manual interpretation for estimating the rock mass quality of the site area. The rock mass quality using other rock mass classification systems such as GSI and RMR can also be calculated.

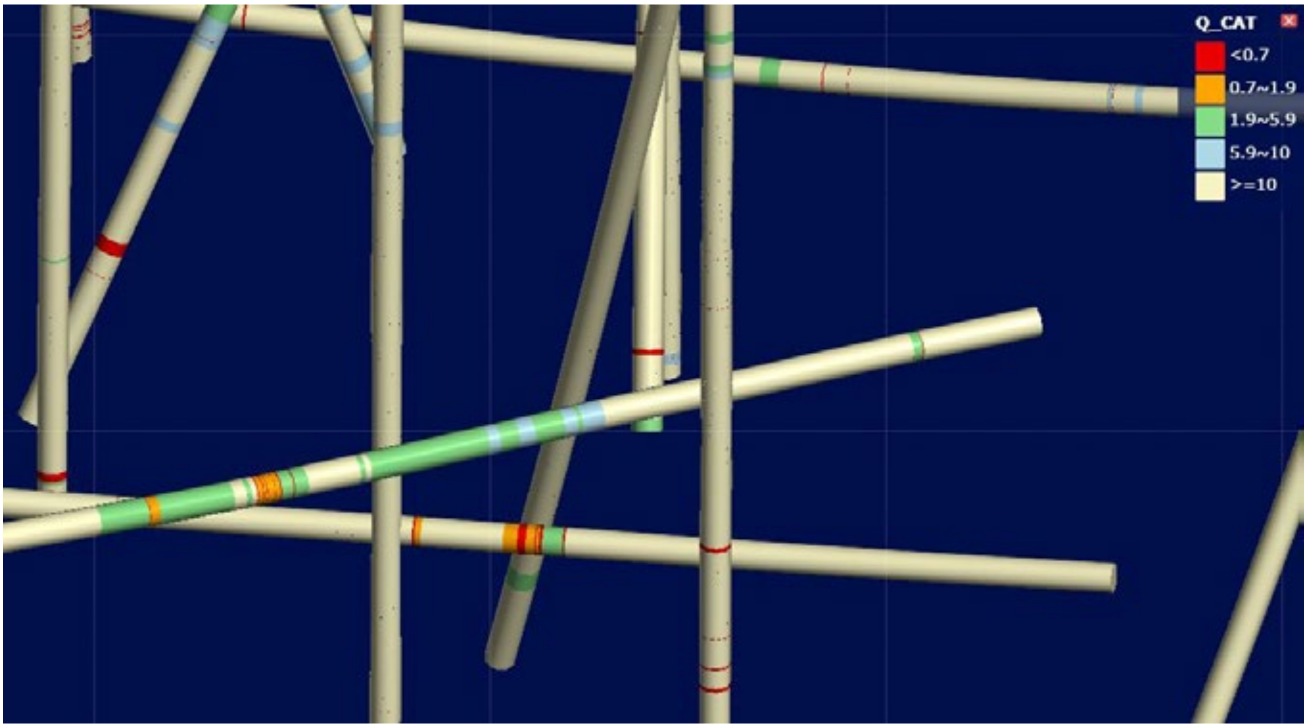

Figure 8 Example of NGI-Q values calculated by AGS Processor

4.3 Data Export

Processed data can be exported in a few ways. For the convenience of viewing all raw data and further processing, the combined database, instead of separated in groups, can be exported as a unified spreadsheet. Selected columns can then be imported to commercial ground modelling software such as Leapfrog to create 3D ground model. Since all the data are combined, data from different groups, including all details can be visualized, correlated and interpreted conveniently in 3D view. Data can also be transformed into AutoCAD or Civil 3D format for drafting or exported to ArcGIS platforms (ArcMap, ArcGIS Pro and ArcScene) for further spatial analysis.

5 DISCUSSION

As a partially automated means of data preparation, AGS Processor brings significant benefits in the process of building up a detailed ground model. Most routine and repetitive manual processing and restructuring of data has been replaced by AGS Processor. From the experience of projects, it is estimated that more than 50% of time can be saved in the entire process of ground modelling (Figure 9). AGS Processor can especially enhance the efficiency in the steps of data reconstruction, information extraction and matching for different test results and corresponding geological information, calculation of engineering rockhead and interpretation of zones of weakness. More resources can then be redirected to evaluating and mitigating the risks of ground conditions. This can bring great savings, in terms of human resources, to ground engineering teams. This is especially useful during tendering or proposal of large underground projects where vast amount of GI data has to be processed to build a ground model as detailed as possible in a short time.

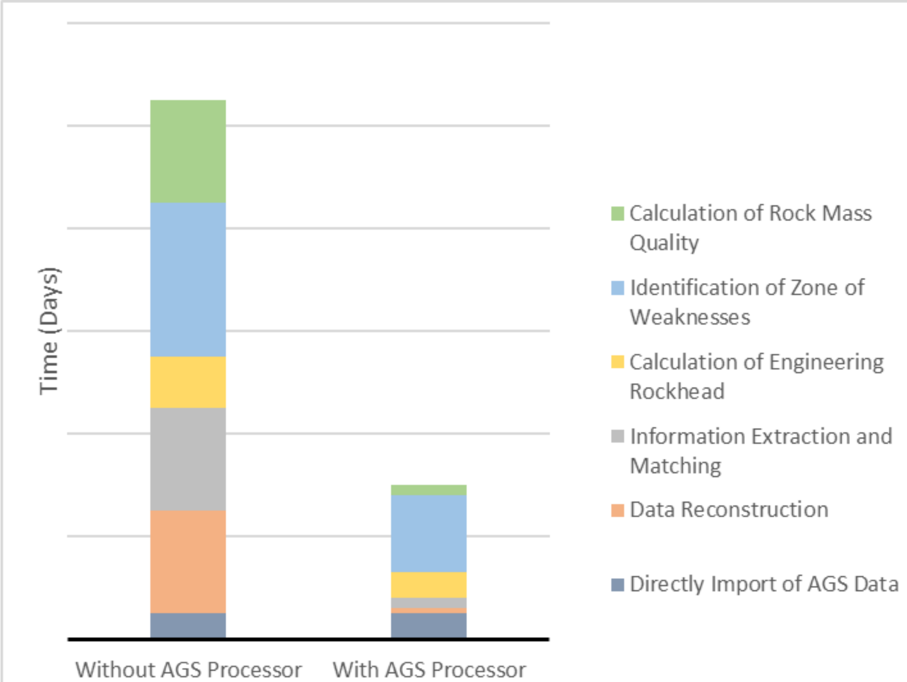

Figure 9 Estimated time savings of AGS Processor based on a recent cavern project (may differ among different projects)

It should be noted that although data processing can be automated, human interpretation and judgement should not be replaced (Gibbons & Kirk, 2019). The ground conditions, underlying risks and concerns for each site or project may not be the same. One method of characterization of data may not be directly applied to the other project or site. Though AGS Processor may help on characterizing ground conditions from raw data, detailed interpretations should always be led by experienced engineering geologists in order to prevent overlooking of risks.

Other than variation in ground conditions and identification of features critical to stability such as faults, a robust ground model may also include more extensive information such as groundwater monitoring data and other field and lab test data such as Borehole Televiewer Survey data. Unfortunately, these data are not always included in the AGS files in Hong Kong practice. Once these data are more broadly available in the industry, more functions and processes will be developed for AGS Processor, providing additional values to the detailed ground model.

6 CONCLUSION

AGS data format is a highly convenient data format for data storage and transfer. Yet building up a very simple ground model by directly importing and visualizing AGS data, such as showing RQD and weathering grade, may be fast and simple, but often cannot provide sufficient ground information for any meaningful engineering purposes. A more detailed ground model, such as one that includes descriptions of localized zones of weakness and rock mass characteristics, is usually required especially in the detailed design and construction stages.

As AGS data format was designed for efficient storage and transfer of GI data, challenges may arise when building detailed ground model with AGS format data due to its reliance on commercial software and its grouped structure. Detailed variations in ground conditions and risks may be easily overlooked unless additional manual efforts are paid in restructuring the data.

To suit the needs of building detailed ground models, AGS Processor can help as a semi-automated means of restructuring AGS format data and help to enhance the efficiency of ground modelling using its functions of information extraction and characterization of ground conditions. Based on our experience, it is estimated that over 50% of time can be saved in the entire process of preparing ground modelling for engineering purpose.

REFERENCES

Association of Geotechnical and Geoenvironmental Specialists. 2022. *Electronic Transfer of Geotechnical and Geoenvironmental Data AGS4 (Edition 4.1.1 – March 2022).* Association of Geotechnical and Geoenvironmental Specialists.

A.C.S. Lai, A.C.T. So & S.C. Mok. 2019. AGS Data – Subsurface Data in Digital Format in Hong Kong. The *HKIE Geotechnical Division Annual Seminar 2019.*

S. Caronna & P.M. Wade. 2005. Problems with Using the AGS Format as a Working Database Structure. *Geotechnical and Geoenvironmental Data in Electronic Format Production, Management and Application, Format Conference, Association of Geotechnical and Geoenvironmental Specialists.*

C. Gibbons & P. Kirk. 2019. Three dimensional geological models in ground engineering: when to use, how to build and review benefits and potential pitfalls. *NZ Geomechanics News.*

Photogrammetry- and LiDAR-based Multi-temporal Point Cloud Models and Digital Elevation Models for Landslide Investigation in Hong Kong - Feasibility and Challenges

Y T A Chan, L Liu
The Chinese University of Hong Kong, Hong Kong, China
W Hou
GeoRisk Solutions Limited, Hong Kong, China
R Tsui
Aurecon Hong Kong Limited, Hong Kong, China

ABSTRACT

In adapting to rapid urban development and changing climate, the geotechnical industry is shifting towards harnessing digital technologies in Natural Terrain Hazard Study (NTHS) for landslide investigation. In this paper, we adopted a new digital method using multi-temporal point cloud models and digital elevation models derived from various available resources for the assessment of landslide source volume and dimensions. These resources include (1) historical aerial photographs from territory-wide aerial photographic survey carried out by the Lands Department, (2) project-specific UAV photographic and video surveys, and (3) the territory-wide airborne LiDAR surveys data. Two case studies from the Fei Ngo Shan area, Hong Kong, were carried out. Case 1 involves two recent landslides that occurred in 2005, and Case 2 involves a cluster of eight recent landslides that occurred in 2020. All these ten landslides were carefully investigated using conventional methods (e.g., field measurement or API) by GEO and GeoRisk Solutions, respectively. These investigation results were taken as legacy records for a comparison with the results derived from our adopted digital method. The comparison shows that the landslide source volume derived from the digital method is similar to the legacy record. This paper assessed the feasibility and accuracies of aligning and comparing digital models derived from multi-sources for landslide studies.

1 INTRODUCTION

1.1 Background

Landslides are a common and devastating type of natural disasters which often cause loss of life and irreparable damage. In Hong Kong, 60% of its terrain is hilly or mountainous with steep slopes. As a result, NTHS is a compulsory risk management strategy for the safe and cost-effective utilization and development of lands.

Conventional approaches to investigate the landslide source volume typically utilize direct field-based measurements, i.e., hand-held tape measures, to estimate and record the extent and the dimensions of a landslide scar. In spite of the long history of this application, several major limitations still exist. First, the unavailability of instant measurement after the landslide, given the time required to gain a safe field access to the scar, slows down the response in risk mitigation. Second, the conventional assumption of ellipsoidal landslide geometry may not fit the actual natural terrain landslides in Hong Kong (Hou et al., 2021).

With the rapid advancement in technology, the potential to take new approaches and utilize innovative developments in landslide studies arises. Airborne photogrammetry and LiDAR in particular, can overcome some of the limitations of the conventional methodology. By building and analyzing a multi-temporal digital model, a fast, cost-effective, relatively accurate and safe remote survey for landslide features can be provided.

The key objective of this paper is to construct pre- and post-failure high-resolution and accurately georeferenced point cloud models (PCM) and digital elevation models (DEM) for the 2005 and 2020 landslides in Fei Ngo Shan area. By aligning and comparing these 3D models (i.e. pre- and post-failure), the landslide failure volume together with its source dimensions can be computed, section profiles can be generated and 3D presentations can be provided. This paper aims to show the potential of digital measures and to encourage the NTHS practitioners in Hong Kong to adopt relevant digital measures.

1.2 Study Area

This paper studies ten landslide features in total, i.e., two features from the 2005 Fei Ngo Shan landslides and eight features from the 2020 Fei Ngo Shan landslides (Figure 1).

The 2005 Fei Ngo Shan landslide occurred on the natural hillside near Fei Ngo Shan service reservoir at about 6 a.m. on 21 August 2005 (Maunsell, 2008), which was possibly triggered by heavy and prolonged rainfall. The landslide event comprised a major channelized debris flow landslide (i.e. Landslide No. 1) involving a failure volume of about 3,350 m³, and a smaller landslide (i.e. Landslide No. 2), involving a failure volume of about 180 m³ (Maunsell, 2008). A Landslide No. 3 was reported by Maunsell (2008). However, this Landslide No. 3 is not covered by this paper due to its comparatively distant location.

The 2020 Fei Ngo Shan landslide comprised a cluster of eight landslides (i.e. RC15 to RC22), which were most likely triggered by a heavy rainstorm between 2:00 am and 6:00 am on 6 June 2020 (GRS, 2021). These landslides were debris avalanches with estimated source volumes ranging from 13 m³ to 144 m³ (GRS, 2021).

1.3 Regional Geology

The study area was predominantly underlain by fine ash vitric tuff from the Mount Davis Formation that forms part of the Lower Cretaceous Repulse Bay Volcanic Group. The Mount Davis Formation is at least 500 m thick and comprises variably lapilli-bearing, coarse ash crystal tuff, with some eutaxite and sandstone beds at the type locality. Bands of eutaxitic crystal-bearing fine ash vitric tuff and thin bands of quartzphyric rhyolite dykes are aligned sub-parallel to the strike of the volcanic strata (Figure 1).

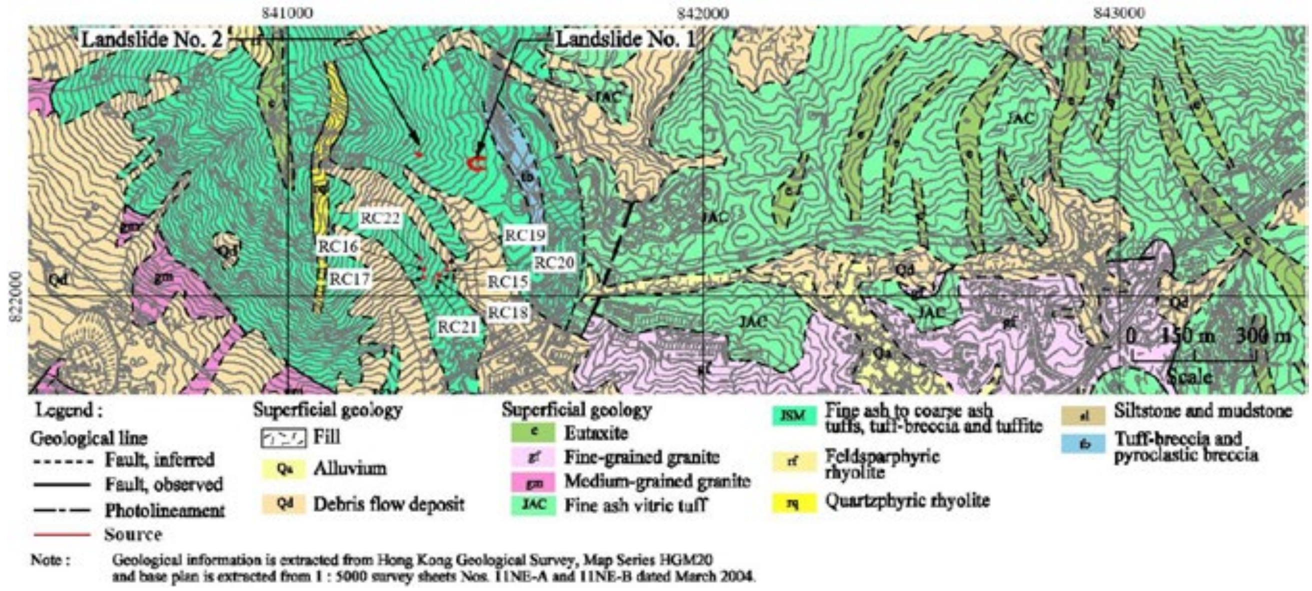

Figure 1: Location of landslide source areas indicated on the regional geological map

2 METHODOLOGY & DATA COLLECTION

2.1 Data Collection

For case study 1 (i.e. the 2005 features), pre- and post-failure point cloud models were constructed using historical aerial photographs. For case study 2 (i.e. the 2020 features), the pre-failure point cloud model was obtained directly from the 2020 territory wide airborne LiDAR survey. The post-failure point cloud model was constructed from project-specific UAV survey (including photos and videos). More details are provided in Table 1 and Table 2.

Table 1: Digital sources applied for each 3D model

	Pre-failure model	**Post-failure model**
The 2005 landslide	Historical aerial photos taken in Mar, Apr, May 2005 & Sep 2004 (Lands Department, 2021)	Historical aerial photos taken in Oct 2005 (Lands Department, 2021)
The 2020 landslide	The 2020 LiDAR survey (GEO, n.d.)	UAV survey in Sep 2021 (Hou et al., 2021)

Table 2: Historical aerial photos applied for the 2005 point clouds modelling (Lands Department, 2021)

	Pre-failure model				**Post-failure model**	
Date	07/05/05	03/04/05	08/03/05	11/09/04	25/10/05	
Flying Height (ft.)	3500	2500	4000	4000	4000	
Selected Aerial Photograph No.	CW64629 CW64630 CW64631 CW64632	CW64003 CW64004 CW64005	CW63614 CW63615 CW63616 CW63617 CW63618 CW63619	CW58943 CW58944 CW58945 CW58946 CW58947 CW58948	CW66184 CW66185 CW66186 CW66187 CW66210 CW66211 CW66212 CW66213	CW66214 CW66215 CW66216 CW66217 CW66224 CW66225 CW66226 CW66227

2.1.1 Historical Aerial Photographs

In order to construct point cloud models on Agisoft Metashape Professional Edition (Agisoft Metahsape Pro), we adopted four sets of aerial photographs from several flying heights on four different dates before the occurrence of the landslide on 21st August 2005. For the post-failure point cloud, the aerial photos were taken on 25th October of the same year, more than two months after the debris flow, from 4,000 feet flying height.

Obviously, the lower the flying height, the closer to our study feature, meaning a higher resolution: 4,000 feet flying height produces a high enough resolution for our purpose. Originally, we intended to use aerial photographs taken at the same height and date on a single flying path, but there were not enough of these photographs to provide a full coverage of the study area. Therefore, we decided to select aerial photos taken from different flying heights of several flying paths on different dates. Although they have different flying heights from more than one time periods, this does not violate the principle of SfM photogrammetry and has been shown to have limited impact on the quality of the constructed point cloud for our purpose.

The study used the freely available digital version colour frames (DAP-L0) aerial photographs at 300 dpi resolution downloaded from Lands Department (2021).

2.1.2 UAV

We adopt the UAV survey of the 2020 Fei Ngo Shan landslide conducted by GRS (2021), with a DJI Mavic Air 2 equipped with a camera. A series of photos and several videos were taken during the survey. UAV photos and a series of consecutive frames extracted from video clips were used to build the model with software Agisoft Metahsape Pro. The photos acquired from the UAV are accompanied by GPS coordinates stored as metadata embedded in the photo files.

2.1.3 Airborne LiDAR (ALS)

LiDAR mounted on an airborne platform produces higher frequency EM pulses, typically Near-infrared (wavelength 1064 nm) or Green (wavelength 532 nm), then records the reflectance from the ground surface. The light's travel time is then measured by an optical telescope mounted on the same platform. After that, the travel time is converted to distance, from which a LiDAR point cloud can be constructed.

The 2020 territory-wide Airborne LiDAR survey in Hong Kong is an open-source data provided by Geotechnical Engineering Office (GEO), Civil Engineering and Development Department. The data was collected from Dec 2019 to Feb 2020. LAS format of the LiDAR Data was used and data covering the map sheets nos. 11NE8A, 11NE8B, 11NE8C and 11NE8D were required to cover the regional area of the study landslide features.

2.2 Methodology

2.2.1 Structure from Motion (SfM) Data Processing

Structure from Motion (SfM), with multiview stereo, is a crucial technique derived from photogrammetry, surveying and computer vision, using overlapping images to establish hyper-scale three-dimensional landform models for observing multi-temporal geomorphic processes (Eltner & Sofia, 2020).

Traditionally, landslide inventory maps are prepared by stereoscopic aerial photograph interpretations (API) and field validation. Fiorucci et al (2018) claimed that API by stereoscope can be interrupted by shadows, obstructing the photographic elements typical of landslides. This hinders the recognition and mapping of the landslides (Fiorucci et al., 2018). Furthermore, the detailed observations made from an interpretation of aerial photographs are qualitative and subjective, making it impossible to perform precise analytic data analysis.

By contrast, photogrammetry technique, along with LiDAR geodetic observations method, offers detailed topographic information for hazards analyses and possible instantaneous monitoring through observing large morphological changes (Chan, 2021). Depending on the desired level of accuracy, aerial photography can be converted into a PCM or a DEM for further calculations and analysis within a short period of time in general cases.

2.2.2 Georeferencing

Georeferencing of the 3D point cloud models was carried out in software CloudCompare (CC). Two georeferencing tools, i.e., Align and Transformation, were applied in the study.

For the 2005 landslide models, both the pre-failure and the post-failure models were aligned to the LiDAR point cloud (i.e., the reference cloud). For point-pair registration, a minimum of three ground control points (GCP) can exactly map each raster point to the target location with a first-order transformation (Esri, n.d.). In this study, four control points with one at each corner were used for covering the area of the study features. These control points were selected from corners of man-made features.

The 2020 UAV model was initially generated with Agisoft Metahsape Pro, and possessed correct x, y coordinates and inaccurate z coordinates due to the limitation of the drone equipment. Therefore, adjustment of z-value was completed in CC. A z-axis translation of 298.5 upward was applied to align the 2020 UAV model to the LiDAR model (i.e. the reference model). The accuracy of the translation was validated by professional judgment of the good matching of the landslide crowns and the pre-failure ground.

2.2.3 Digital Elevation Model (DEM)

DEM is defined as the ground, or bare earth, and contains only topography, whereas a Digital Surface Model (DSM) is a first return surface and includes tree canopy and buildings (Esri, n.d.). In our study, DEM is constructed for volume calculation since only the non-vegetated landslide scars are of concern, compared against the bare surface model, for source volume calculation.

After all the preparation works of point cloud processing, point cloud cleaning, and georeferencing of the pre- and post-failure landslide 3D models of 2005 and 2020, a DEM with 0.01 m resolution can finally be derived through rasterization on ArcGIS.

Due to the 2020 LiDAR survey adopting the Hong Kong 1980 Grid Coordinate System, we must convert the Coordinate Reference System (CRS) to Hong Kong 1980 Grid before making other calculations or measurements. This step is crucial because LiDAR is either used for comparison directly or as a reference model indirectly.

2.2.4 Volume and Dimension Estimation

To estimate the landslide source volume, two platforms, i.e., CloudComapre (CC) and ArcGIS Pro (ArcGIS), were used. The main purpose of comparing the CC-computed with the ArcGIS-computed source volumes is to confirm that the point cloud-based volume calculations obtained in CC are as reliable as calculating volume using DEM (raster) data in ArcGIS. To estimate the landslide source length, width and depth, “Point Picking” tool on CC were used. Once determined to be accurate by comparing to legacy, the whole process including both volume and dimension estimation can be simplified into only working on CC after deriving PCMs on Agisoft Metahsape Pro.

In CC, the pre-failure and the post-failure model of each year was compared to deduce the 2.5D Volume of the landslides. 2.5 spatial dimensions defines as a uniformly spaced grid that records the elevation on a cell-by-cell basis (Verhoeven et al., 2021). According to the same study, truly 3D digital surfaces are less used in geo-sciences because of the limitations of most GIS software till this very day with their display and analysis. The first step of pre-processing is to segment the source volume of each landslide. Then, it is necessary to segment or filter the vegetation and the noise from the landslide scar given that these signals sum the contribution of each cell and affect the calculation. After that, the “2.5D Volume” tool rasterized the point clouds, generated the 2.5D raster with one height value added to each grid cell, projected the clouds inside, and deduced the volume between two 2.5D clouds (CloudCompareWiki, 2015).

In ArcGIS Pro, the segmented source areas of the landslides in LAS format were firstly converted into rasters. After the conversion, the spatial analyst tool, Raster Calculator, was used to execute a Map Algebra expression: (Pre-failure model – Post-failure model) * Pixel Area. Finally, data within this volume raster was exported into a table for further analysis.

2.2.5 Accuracy Assessment

Ultimately, the failure volume, the profiles of the landslides and the calculated source area dimensions are compared to the legacy records in “*Geo Report No. 233*” for the 2005 landslides and “*Using UAV-based Technology to Enhance Landslide Investigation*” for the 2020 landslides, as a follow-up georeferencing uncertainty analysis adopting two different methods.

For the alignment accuracy of the 2005 landslide PCMs to the LiDAR reference PCM, root mean square error (RMSE) is used to describe how consistent the transformation is between the different control points (Esri, n.d.). RMSE is one of the standard ways to measure the error of a model, lower values indicating better accuracy and thus a better model performance.

Another method for assessing the accuracy of the 2005 and the 2020 landslide PCM is by the Gaussian (Normal) distribution of the signed distances directly between the stable region, i.e., excluding the landslides scars, of the pre- and post-failure point clouds. The mean value in Gaussian distribution fitting indicates the statistics on how close the cloud distances are to one another and 0 denotes a perfect fit with no gap. Thus, the convergence towards 0 signals an ideal model. The standard deviation (SD) simply conveys the dispersion of the points in clouds.

3 RESULTS

3.1 Volume Estimation and Area Dimension

Table 3: A comparison of source volumes (in m^3), widths (in m), lengths (in m) and depths (in m) of the 2005 and 2020 landslides, using point cloud data processed by CC and DEM data processed by ArcGIS.

Year	Landslide	Legacy Volume	Estimated Volume by CC	ΔVolume (Legacy-CC)	Estimated Volume by ArcGIS	ΔVolume (CC-ArcGIS)	Legacy Width	Estimated Width	ΔWidth (Legacy-CC)	Legacy Length	Estimated Length	ΔLength (Legacy-CC)	Legacy Depth	Estimated Depth	ΔDepth (Legacy-CC)
2005	NO1	3350.0	2679.5	670.5	2677.9	1.6	32.0	48.8	-16.8	54.0	64.2	-10.2	5.0	5.0	0.0
2005	NO2	180.0	160.4	19.6	159.6	0.8	10.0	12.1	-2.1	18.0	23.3	-5.3	2.0	1.9	0.1
2020	RC15	144.0	139.0	5.0	130.8	8.2	11.0	11.4	-0.4	10.0	8.3	1.7	2.5	2.1	0.4
2020	RC16	81.6	81.0	0.6	78.2	2.8	12.0	10.0	2.0	13.0	7.9	5.1	1.5	2.6	-1.1
2020	RC17	70.0	36.5	33.5	39.3	-2.8	8.5	7.2	1.3	10.5	9.3	1.2	1.5	1.4	0.1
2020	RC18	13.1	1.3	11.8	-2.1	3.4	5.0	2.1	2.9	5.0	2.2	2.8	1.0	-1.0	2.0
2020	RC19	41.2	43.2	-2.0	49.2	-6.0	7.5	7.2	0.3	7.0	4.5	2.5	1.5	1.9	-0.4
2020	RC20	57.8	55.5	2.3	62.6	-7.1	13.0	10.1	2.9	8.5	5.7	2.8	1.0	2.0	-1.0
2020	RC21	15.7	16.7	-1.0	14.1	2.6	5.0	4.2	0.8	6.0	5.1	0.9	1.0	1.3	-0.3
2020	RC22	61.8	58.4	3.4	54.7	3.7	7.5	7.2	0.3	10.5	10.3	0.2	1.5	1.7	-0.2

The source volumes are derived by ArcGIS and CC respectively while the widths, lengths and depths are all measured in CC. The changes in volume and dimensions are computed by the results generated on CC subtracted from legacy records. An additional comparison between the CC-derived and the ArcGIS-derived volume is shown in Table 3.

Regardless of the computing software, subtracting the post-failure model from the pre-failure model gives us a reduction in volume. Take RC18, for example: its negative estimated volume by ArcGIS indicates a source volume increase, which reveals an anomaly in the result because landslides should normally be associated with a volume drop. The cause of this will be further explained in the upcoming Discussion section. For any negative delta volume, width, length or depth, it means that particular result acquired via CC is larger than legacy.

It is observed that the difference in the estimated source volume between the two methods ranges from 0.8 to 8.2 m^3. For 2005 landslide No.1, our digital approach of the estimated source volume by CC is 670.5 m^3 less than the physical measurement record in the *GEO Report No. 233* whereas landslide No.2 is only 19.6 m^3 less than legacy. However, the large variation in landslide No.1 is due to the concrete cover on its landslide scar with unknown thickness summing to a certain volume. For the 2020 Fei Ngo Shan landslides, the mean of the volume difference is 6.7 m^3 and the median is 2.8 m^3. Among all the 2020 landslides, RC16 has the smallest difference of 0.6 m^3 while RC17 has the largest difference of 33.5 m^3. The source volumes are summarized in Figure 2.

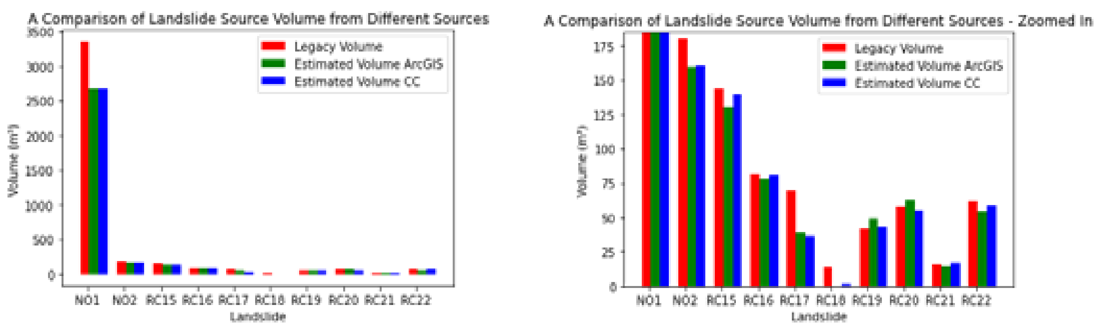

Figure 2: Bar charts of the estimated source volumes. The left is the overview while the right is zoomed in to 180 m^3.

Out of the 10 landslides, only the legacy volumes in landslides No.1, No.2, RC17 and RC18 are intuitively larger than our estimations.

The overall performance in source area measurement is reasonable and not far from the past records if excluding the significant longer length and width of the 2005 No.1 landslide. In general, the mean of the difference in width is -0.9 m, in length is 0.2 m, in depth is 0.04 m.

3.2 Landslide Profiles

Applying terrain profile for analytical analysis is a common application for observing the failure from the side view. Instead of the traditional line profile, Cross Section in CC was used to extract polygonal contours in each slice to give a more realistic look to the profiles of the point clouds.

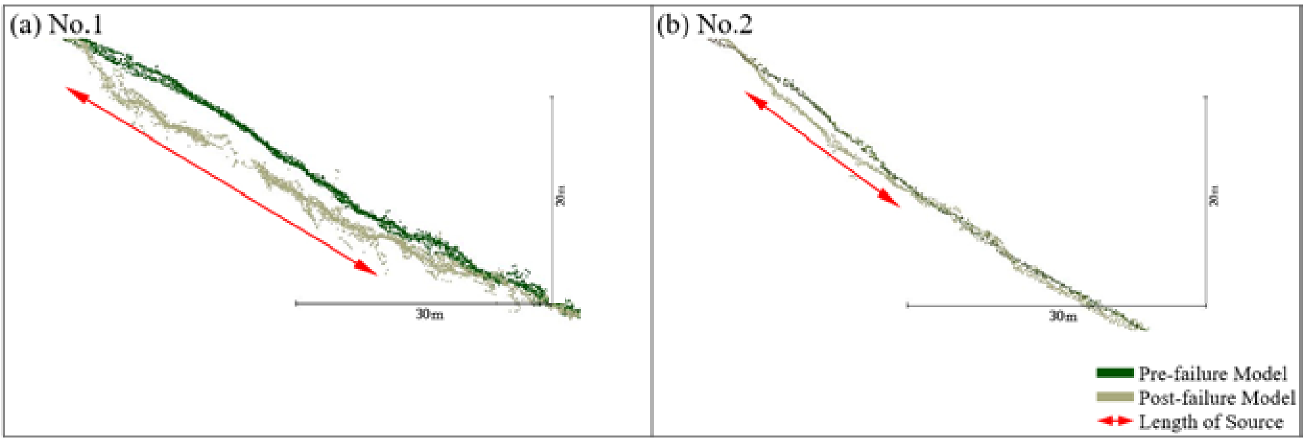

Figure 3: Source area profiles of the 2005 landslides, showing the pre-failure model compared against the post-failure model, derived from historical aerial photographs.

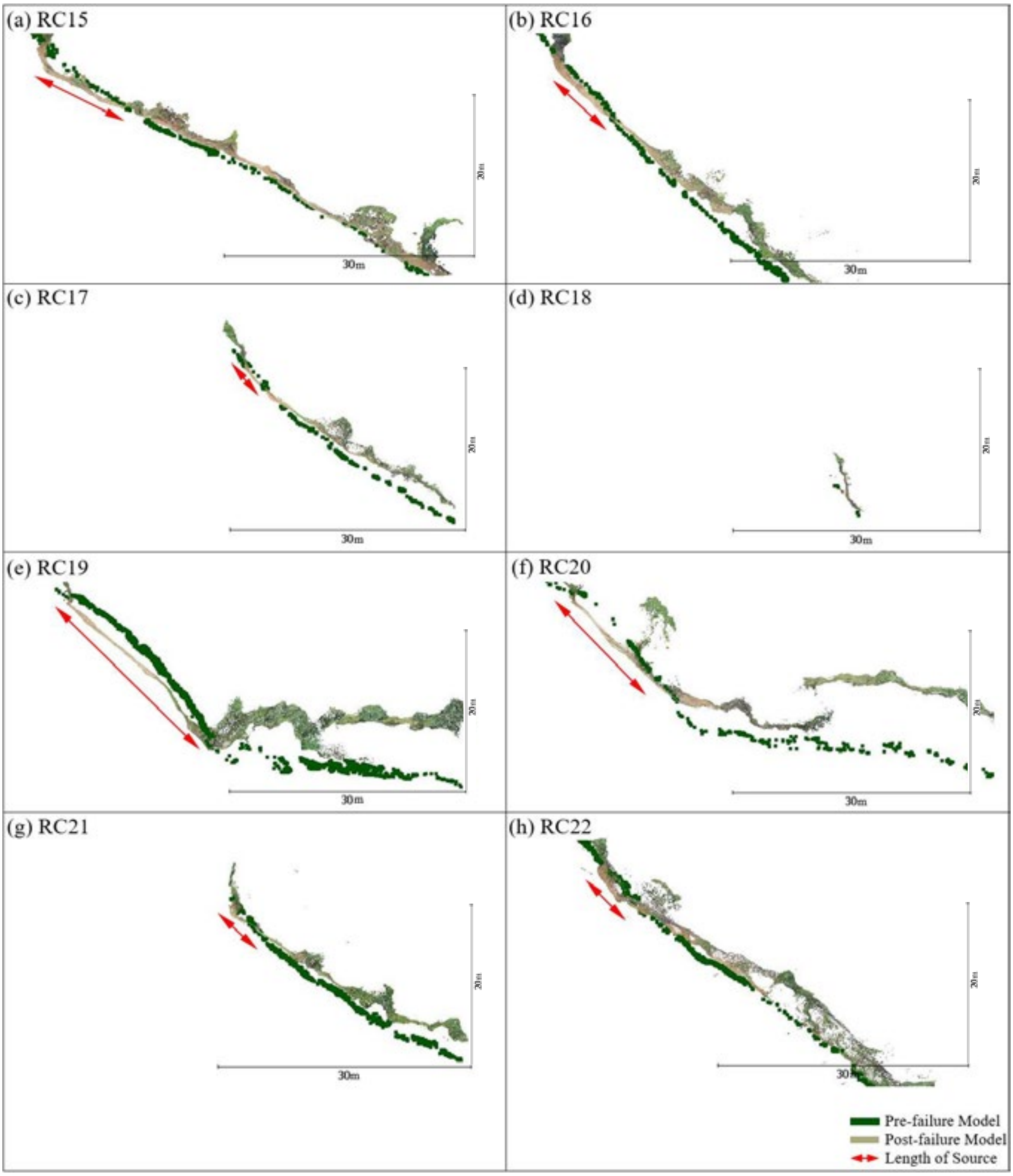

Figure 4: Source area profiles of the 2020 landslides, showing the LiDAR pre-failure model compared with the UAV-SfM-derived post-failure model. For (f) RC18, since the pre-failure model is lying beneath the post-failure model, no source area can be found.

3.3 Georeferencing Uncertainty

The georeferencing accuracy of the 2005 pre- and post-failure PCMs aligned to the LiDAR reference PCM assessed by RMSE, as well as the 2005 and the 2020 landslide PCMs assessed by Gaussian distribution, are summarized into Table 4 and 5 respectively.

Table 4: The final RMSE of the 2005 pre-failure and the post-failure models aligned to LiDAR respectively

	Pre-failure Model aligned to LiDAR (m)	**Post-failure Model aligned to LiDAR (m)**
The 2005 landslide	0.91	2.30

Table 5: The Gaussian mean and standard deviation of the signed distances of the 2005 and the 2020 pre- and post-failure PCMs

	Mean (m)	**Standard Deviation (m)**
The 2005 landslide	-2.85	1.22
The 2020 landslide	-0.65	1.04

4 DISCUSSIONS

4.1 Use of Data

The sensory data used in this study, Airborne LiDAR and aerial photographs acquired from various remote sensing platforms such as UAV, contain potential estimation errors originating from their data generation methods and flight operations (Hsieh et al., 2016). According to the same study, the elevation error of airborne LiDAR survey is about 0.15-0.3 m and for aerial photogrammetry is about 0.2-1.3 m. The inaccuracy in the elevation of the UAV-derived point clouds is encountered in the study but the difference is 298.5 m lower than the actual. The explanation for this is that UAV relies on the Inertial Measuring Units and the Global Navigation Satellite System (GNSS) for positioning and orientation. If GNSS signals suffer from interference, it also affects the entire pose estimation of the UAV and causes altitude errors (Forte et al., 2021). To conclude, the constraint in this study is the variation of positional accuracy of various techniques, i.e., aerial photos, LiDAR used, which affects the result of parameter estimation.

4.2 Georeferencing Uncertainty

Recalling the RMS accuracy of the pre-failure model aligned to LiDAR is 0.91 m and the final RMSE of the post-failure model aligned to LiDAR is 2.30 m. The positive RMSE indicates the predicted value overestimates the actual value, which partly can be contributed by the variations between the vegetated SfM PCM and the bare ground LiDAR model. The larger RMSE of the post-failure model, comparing to the pre-failure model, can be attributable to the elevation difference of the landslide scars between the post-failure PCM and the reference LiDAR model.

Despite such RMSE values providing valuable insight into overall georeferencing performance, they do not expose the spatial variability for detailed PCM or DEM analyses as uncertainty estimates for topographic change detection can lose validity in regions of steep topography (James et al., 2017). Therefore, the RMSE values above do not necessarily mean the positioning accuracy is unsatisfactory for the purpose of studying geomorphological changes caused by landslides and its insight is currently restricted by our limited understanding of SfM survey uncertainties (James et al., 2017). Although the positioning accuracy directly depends on the accuracy of GCPs, it is challenging to achieve perfect georeferencing. Furthermore, a low RMSE should not be confused with an accurate registration, because the transformation may still contain significant errors due to a poorly entered control point. The significant transformation errors can be improved by selecting more GCPs with equal quality (Esri, n.d.).

Reciting the georeferencing accuracy for 2005 landslides models, the Gaussian mean is -2.85 m with a SD of 1.22 m, meaning that the post-failure PCM is 2.85 m lower than the post-failure PCM with a dispersion of 1.22 m relative to its mean. For the 2020 UAV-derived point cloud versus the vegetated LiDAR point cloud, the mean is -0.65 m with a SD of 1.04 m, meaning that the LiDAR model is 0.65 m lower than the SfM PCM with a dispersion of 1.04 m relative to its mean. To sum up, the general georeferencing performance of the 2020 3D models is better than the 2005's. It is because the horizontal georeferencing uncertainty of the UAV-derived PCM has been reduced given that the horizontal GPS positioning of the UAV source is accurate, neglecting the data generation and the operation errors. By contrast, the uncertainties of the pre- and the post-failure 3D models of 2005 based solely on aerial photos at natural hillsides are uncertain, as it depends on the time to take the photos and the quality of the photos, or other potential human errors involved. Thus, the analysis of 2005 landslides may involve a higher degree of uncertainty in landslide volume determination.

When it comes to the georeferencing methodology, Airborne LiDAR has a key role in this study by acting as a reference cloud, as well as acting as a post-failure model in 2020 for generating source volume. However, the above methodologies were based on the assumption of LiDAR being both horizontally and vertically accurate. In reality, the LiDAR collection process consists of positional (X-Y-Z) error, where the horizontal (X-Y) error is typically much greater than the vertical error (Hodgson & Bresnahan, 2004). The height accuracy of airborne LiDAR measurement technology may be as high as 13 cm while horizontal accuracy may be as high as 20 cm (Ren et al., 2016). Moreover, it is worth noting that the LiDAR point cloud may be sparse at some depth and thus provide insufficient point cloud data, preventing precise computing of the landslide volume.

4.3 Volume and Dimension Estimation

The estimated volumes computed by ArcGIS Pro and CC are not the same, but as close as a difference of 0.8 - 8.2 m^3. Both platforms undergo point cloud rasterization before calculation, adopting the same segments of source area input, with the same rationale of the formula: product of the difference in elevation and the grid or pixel area. Despite all those similarities, the variations between the two software algorithms may have triggered the distinct values in landslide source volumes. The range of difference has been proven to be reasonable, in such case, it fulfils the main objective of comparing the CC-computed source volume with the ArcGIS-computed source volume is to verify that the results obtained in CC are indeed as reliable. Therefore, we would recommend taking the CC methodology, which has the simplest procedure, as a common practice in digital approaches to measuring landslide source volumes.

For record comparison, there is a relatively large difference in the 2005 No.1 and No.2 landslides, together with the 2020 RC17 and RC18 landslides, among all the legacy volumes and our estimated volumes. Only the landslides with a difference of larger than 10 m^3 have been evaluated for possible improvements. Landslide No.1 can be explained by the concrete cover on its landslide scar with unknown thickness which could have counted towards the 670.5 m^3 difference, even though its width and length are 16.8 and 10.2 m larger than the records stated in GEO Report No. 233. The volume gap of landslide No.2 still could not be narrowed down further from 19.6 m^3 since it already adopts a wider and longer dimension. Similarly, RC17 in 2020 already has a wider and longer dimension than the legacy but the volume estimation is still 30.7 m^3 smaller than the result obtained by GRS (2021). Based on other volumes being mostly consistent, the actual RC17 source volume may be controversial. On the other hand, RC18 can be rejected as a null result, not only because the LiDAR density is exceptionally sparse in that particular shadow position resulting in poor airborne LiDAR survey coverage, but also because the post-failure model has a higher elevation than the pre-failure model. In other words, this creates an anomalous source volume increase, as estimated by ArcGIS Pro, or an atypically low volume as measured by CC.

4.4 Possible Improvements

There are two possible improvements can be made in future applications. First, purchase of GeoTIFF, defined as a tagged image file format with geographic information, from the Lands Department would be an option for constructing a point cloud model or a DEM. This could save time from 3D point cloud georeferencing, together with providing a higher resolution of the digital aerial photos than the freely available 300 dpi version.

Second, to achieve a more accurate source volume estimation, filtering the vegetation signals from the landslide scars is another optional procedure; the detailed steps can be referenced in Hou et al. (2021).

Within this context, the photogrammetry and LiDAR-based methodologies used to construct 3D models in this study are far from maturity, and still have great potential for development.

5 CONCLUSION & FUTURE APPLICATION

Among all the landslides, 2020 RC16 has the smallest difference of 0.6 m³ while 2005 No.1 has the largest difference of 670.5 m³. 60% of the investigated landslides have variations of less than 10 m³ from the legacy records. For the georeferencing accuracy, the Gaussian mean and the SD of the signed distances directly between the 2005 pre- and the post-failure point cloud models are -2.85 m and 1.22 m while 2020 has an even better mean of -0.65 m with a SD of 1.04 m. The outcomes of the study are therefore robust.

All in all, NTHS requires professional knowledge and expertise, and thus the source area dimension segmentation is subject to individual professional judgements. Nevertheless, this study serves as a comprehensive guide and a comparison to past results. The consistent records from the traditional field-based measurements in *GEO Report No. 233* have validated the feasibility of this remote sensing approach. On the other hand, by applying the same digital method of using a UAV-based SfM photogrammetry to construct a landslide 3D model, the acceptable range of result variations between this study and Hou et al. (2021) has proven the consistency of this methodology. Therefore, not only has this adventurous digital approach demonstrated its practicability, but also it reveals a trend of shifting from rasters towards point clouds, more dependence in the future on processing voxels directly instead of pixels.

On top of industrial application, generating accurate landslide volumes will be important for risk management and future research, in adapting to new challenges brought by growth and development in Hong Kong, and global climate change. It is worth mentioning that the importance of the landslide clusters in Fei Ngo Shan is that they were triggered by a 1-in-2000-year rainfall event (GRS, 2021; Hou et al., 2021). Under the conventional practice, the total volume of the 2020 cluster can be treated as a 1-in-2000-year landslide event. Therefore, all the data acquired and processed, along with and the relevant analysis, revealed can be used as a benchmark for a future Quantitative Risk Assessment (QRA) practice.

These remote sensing digital modelling techniques aided by GIS can possibly complement the NTHS and enhance future investigations, bringing lower costs but higher efficiency, accuracy and effectiveness.

ACKNOWLEDGEMENTS

We would like to express our special thanks to Mr. Ken Grimes from the English Language Teaching Unit, The Chinese University of Hong Kong (CUHK), for his language advice throughout the project, and Dr. WONG Kwan Kit from Department of Geography and Resource Management, CUHK, for his advice on georeferencing methodology. We acknowledge the provision of LiDAR survey data and other relevant information from the Geotechnical Engineering Office of the Civil Engineering and Development Department of the HKSAR Government. This paper is extracted from the undergraduate Final Year Project (FYP) of one of the authors, Y. T. Agnes CHAN. This FYP is a collaboration project between the Earth System Science Programme (ESSC), CUHK and the Hong Kong based geotechnical engineering consultant, GeoRisk Solutions Limited (GRS). The project is supervised by Prof. Lin LIU of ESSC, CUHK and co-supervised by Dr. Wenzhu HOU of GRS.

REFERENCES

Chan, A. (2021). Volcano Geodesy [Unpublished manuscript]. The Chinese University of Hong Kong.

CloudCompareWiki. (2015, October 19). 2.5D Volume. 2.5D Volume - CloudCompareWiki. Retrieved March 27, 2022, from https://www.cloudcompare.org/doc/wiki/index.php?title=2.5D_Volume

Eltner, A., and G. Sofia (2020), Chapter 1 - Structure from motion photogrammetric technique, Developments in Earth Surface Processes, 23, 1–24, doi:10.1016/b978-0-444-64177-9.00001-1.

Esri (n.d.), Creating raster DEMs and DSMs from large lidar point collections, Lidar solutions in ArcGIS. Available from: https://desktop.arcgis.com/en/arcmap/10.3/manage-data/las-dataset/lidar-solutions-creating-raster-dems-and-dsms-from-large-lidar-point-collections.htm#ESRI_SECTION1_7ABD98654A49411FB44CF0920B23F427 (Accessed 7 December 2021)

Esri. (n.d.). Overview of georeferencing. Overview of georeferencing-ArcGIS Pro | Documentation. Retrieved March 28, 2022, from https://pro.arcgis.com/en/pro-app/latest/help/data/imagery/overview-of-georeferencing.htm

Fiorucci, F., F. Ardizzone, A. C. Mondini, A. Viero, and F. Guzzetti (2018), Visual interpretation of stereoscopic NDVI satellite images to map rainfall-induced landslides, Landslides, 16(1), 165–174, doi:10.1007/s10346-018-1069-y.

Forte, M., Neto, P., Thé, G., & Nogueira, F. (2021). Altitude Correction of an UAV assisted by Point Cloud Registration of LIDAR SCANS. Proceedings of the 18th International Conference on Informatics in Control, Automation and Robotics, 485–492. https://doi.org/10.5220/0010583004850492

GeoRisk Solutions Limited (GRS) 2021. Study Of Natural Terrain Hazards For A Major Drainage Catchment (MDC), At Fei Ngo Shan, Kowloon [internal report for GEO]

Geotechnical Engineering Office (GEO) (n.d.). GEO Data For Public Use. Open data - geo, CEDD, HKSARG. Retrieved March 30, 2022, from https://www.geomap.cedd.gov.hk/GEOOpenData/eng/Default.aspx

Geotechnical Engineering Office (GEO) 2021. Landslide Risk Management and the Role of Quantitative Risk Assessment Techniques. Geotechnical Engineering Office, Civil Engineering and Development Department, Hong Kong Government.

Hodgson, M. E., & Bresnahan, P. (2004). Accuracy of airborne lidar-derived elevation. Photogrammetric Engineering & Remote Sensing, 70(3), 331–339. https://doi.org/10.14358/pers.70.3.331

Hou, W., J. R. Hart, R. Tsui, A. Ng, and C. Cheung (2021), Using UAV-based technology to enhance landslide investigation, Available from: https://www.researchgate.net/publication/352177443_Using_UAV-based_Technology_to_Enhance_Landslide_Investigation (Accessed 3 December 2021)

Hsieh, Y.-C., Chan, Y.-C., & Hu, J.-C. (2016). Digital Elevation Model differencing and error estimation from multiple sources: A case study from the Meiyuan Shan landslide in Taiwan. Remote Sensing, 8(3), 199. https://doi.org/10.3390/rs8030199

James, M. R., Robson, S., & Smith, M. W. (2017). 3-D uncertainty-based topographic change detection with structure-from-motion photogrammetry: Precision maps for ground control and directly georeferenced surveys. Earth Surface Processes and Landforms, 42(12), 1769–1788. https://doi.org/10.1002/esp.4125

Maunsell Geotechnical Services Limited (Maunsell) (2008). Detailed Study of the 21 August 2005 Debris Flow on the Natural Hillside near Fei Ngo Shan Service Reservoir. GEO Report No. 233.Geotechnical

Lands Department (2021), Hong Kong Map Service 2.0, Available from: https://www.hkmapservice.gov.hk/OneStopSystem/home (Accessed 5 December 2021)

Ren, H. C., Yan, Q., Liu, Z. J., Zuo, Z. Q., Xu, Q. Q., Li, F. F., & Song, C. (2016). Study on analysis from sources of error for Airborne Lidar. IOP Conference Series: Earth and Environmental Science, 46, 012030. https://doi.org/10.1088/1755-1315/46/1/012030

Verhoeven, G. J., Santner, M., & Trinks, I. (2021). From 2d (to 3D) to 2.5D – not all gridded digital surfaces are created equally. ISPRS Annals of the Photogrammetry, Remote Sensing and Spatial Information Sciences, VIII-M-1-2021, 171–178. https://doi.org/10.5194/isprs-annals-viii-m-1-2021-171-2021

An Alternative Approach for Semi-Automatic Delineation of Rock Blocks on 3D Meshes and Engineering Application

Regine Tsui
Aurecon Hong Kong Limited, Hong Kong, China

Jonathan Hart, Wenzhu Hou, Alan Ng
GeoRisk Solutions Ltd., Hong Kong, China

ABSTRACT

Auto-identification of rock blocks on 3D models is a useful new tool for rock engineering. It has the potential, when undertaken with rock engineering professionals, to delineate remotely, potentially unstable rock blocks associated with adverse discontinuities. An alternative approach is proposed to semi-automatically delineate rock blocks on 3D meshes, which does not require prior extraction and fitting of discontinuity planes. The proposed approach starts with trace extraction, exploiting the fact that the contact between two rock blocks is most often manifested by a trace (i.e., an exposed line) on the rock surface. Geometrically, the trace is usually either a concave edge or a depressed line. These traces are first extracted due to their higher concavity or darkness compared to their neighbouring mesh faces. After post-processing, the mesh is segmented into sub-meshes around the extracted trace lines. The algorithms are implemented in Python and are tested on three rock slopes, including: (1) a rock slope in Ouray, USA; (2) a natural rock outcrop in Ma Shi Chau, Hong Kong; and (3) a rock slope in a former quarry currently being redeveloped as part of a large-scale site development in Hong Kong. Our approach can enrich the rock mapping results and help identify critical rock blocks which may be at risk of planar failure.

1. INTRODUCTION

In recent years, due to the increase in the capability of 3D data acquisition techniques, such as structure-from-motion (SfM) photogrammetry and laser scanning, accurate 3D models can be readily produced for rock surfaces. Auto-identification of rock blocks on 3D models is a useful new tool for rock engineering. It has the potential, when undertaken with rock engineering professionals, to delineate remotely, potentially unstable rock blocks associated with adverse discontinuities.

Compared with numerous research focused on discontinuity plane extraction and computation on 3D surface models (e.g., Vöge et al., 2013; Assali et al., 2014; Riquelme et al., 2014; Dewez et al., 2016; Kong et al., 2020; Zhang et al., 2018; Tsui et al., 2021), research centered on rock blocks on 3D surface models is at an early stage. Relevant research is largely motivated by attempts to estimate the block size, which is important in various rock mass classification schemes. For example, by statistical modelling, Mavrouli et al. (2015), Wichmann (2019), and Buyer et al. (2020) can estimate the rock block size distribution from characteristics of major discontinuity sets derived from the 3D models, either using equations or a stochastic discrete fracture network (DFN) generator. However, identification of the actual rock blocks from the 3D model is not required and is not a focus in the above research.

Chen et al. (2017) proposed a method that can extract regular, six-sided rock blocks formed by 3 discontinuity sets. Long et al. (2021) and Kong et al. (2021) further developed methods to detect rock blocks with more complex shapes (i.e. those formed by > 3 discontinuity sets), also by examining the intersection relationship of the discontinuities extracted. By considering discontinuity intersections, some of these methods are not only able to extract the exposed portions of the rock blocks, but also able to reasonably predict the shape of the hidden portion of the rock blocks for volume calculation. However, these methods can only detect rock blocks wholly bounded by planar discontinuities. Under actual conditions, exposed rock blocks are frequently bounded by uneven, irregular surfaces on one or more sides, such as curved fractures formed by blasting, or portions of weathered rock. Whilst these surfaces may form part of the rock blocks, they may not be planar or persistent enough to be extracted automatically. This is particularly relevant in Hong Kong, where the granitic and volcanic rock slopes often contain extensive yet wavy and undulating sheeting joints.

Whilst an estimation of rock block volume is useful, if this is not part of the objective, it is unnecessary to predict hidden parts of the rock blocks. In this way, we propose an alternative approach to semi-automatically delineate rock blocks on 3D meshes, which does not require prior extraction and fitting of discontinuity planes. This is particularly applicable to irregular rock blocks not wholly bounded by planar discontinuities.

2. APPROACH AND ASSUMPTIONS

Since only the surface of the rock can be seen, the connectedness of the concealed portions of the rock blocks is uncertain. When geologists identify rock blocks on the rock surface, the identification is interpretive, with assumptions on the subsurface block contacts. Similarly, our semi-automatic block delineation approach is also interpretive and is based on the following two principal assumptions:

1. The contact between two adjacent exposed rock blocks will be exposed as a trace (i.e., an exposed line) on the rock surface. Geometrically, the trace is usually either a concave rock edge or a line of narrow opening. In terms of color, the line is often darker than its surroundings due to shadow. An example is shown in Figure 1.
2. Blocks are fully separated from adjacent rock blocks by the exposed traces on the rock surface.

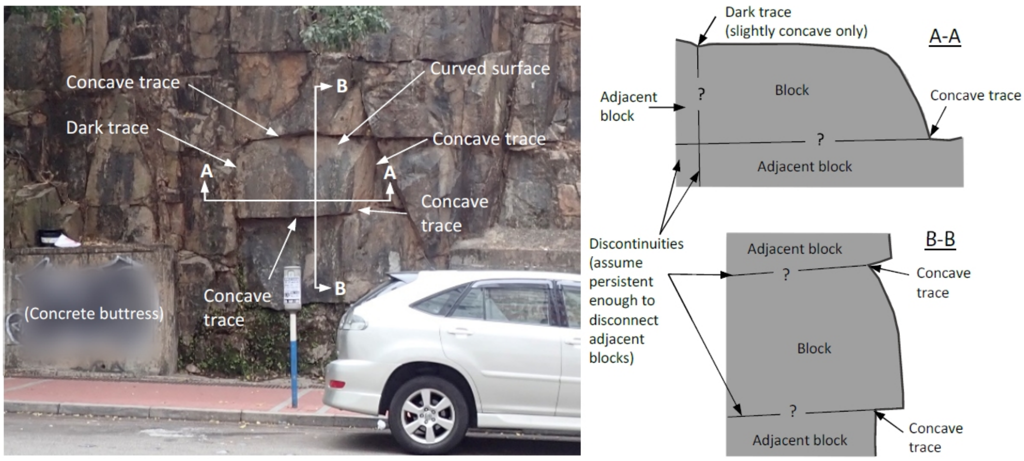

Figure 1: Example of a rock block with curved surfaces on a granite cut slope and the interpreted cross-sections. The contacts between the rock block and adjacent blocks are either concave edges or dark traces

The procedures of the proposed block delineation are summarized in Figure 2. Following assumption (1), the proposed approach starts by extracting traces, i.e. mesh faces representing concave rock edges or dark lines on the rock surface. These initial traces comprising the concave edges and the dark lines and are then combined. A threshold is set on the minimum number of faces contained by a connected trace group to reduce small, scattered noise. At this stage, some traces may not be extracted fully and are disconnected at place. In order to enhance the connection, dilation is then applied to the traces. In other words, a mesh face is recognized as part of the traces as long as any one of its closest *k* neighbors (where *k* is user-defined based on the resolution of the mesh) is classified as part of the traces. At the end of this stage, the final traces form connected networks spanning most of the mesh to separate individual blocks.

In the next stage, the extracted traces are removed from the mesh. Individual rock blocks are then separated into isolated mesh components. Each isolated component of the mesh is then labelled as an individual rock block.

The initial result of the block delineation contains holes left by the traces. For noise reduction, a threshold is set on the minimum number of faces contained by the blocks to avoid tiny groups of mesh faces from being labelled as blocks. To restore the blocks' boundaries and to fill holes in the delineated mesh, mesh faces belonging to the traces or the discarded rock blocks are simply grouped into their closest labeled blocks.

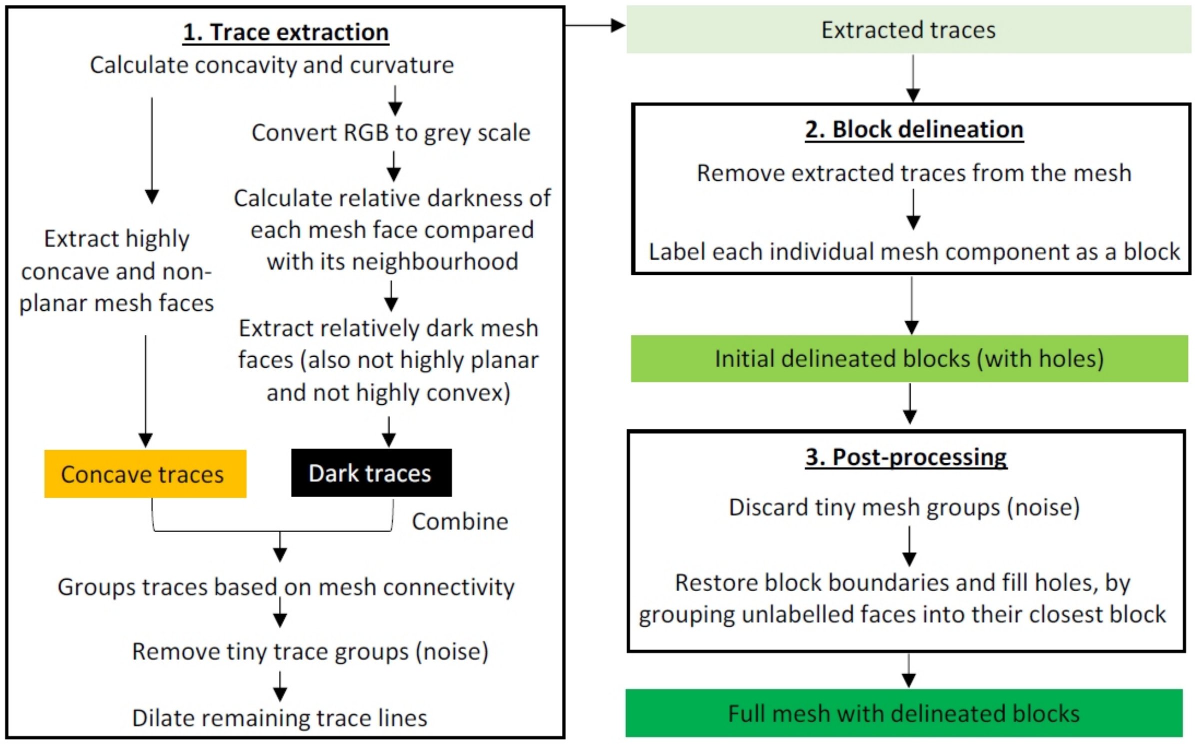

Figure 2: Procedures of block delineation

Our approach is implemented in Python scripts. The analysis relies heavily on the following widely used, well tested and free Python packages, as shown in Table 1:

Table 1: Python packages used in the analysis

Python packages	Usage
Trimesh (Dawson-Haggerty et al. 2019)	Mesh input / output, general mesh manipulations
NumPy (Harris et al. 2020)	Principal component analysis, and other operations on matrices
SciPy (Virtanen et al. 2020)	Finding connected components on meshes; k-nearest neighbor search

3. APPLICATION OF BLOCK DELINEATION

The most crucial part of our approach is trace extraction. Various semi-automatic trace extraction workflows have already been proposed for 3D surface models of rock mass, which operate on meshes (Umili et al. 2013, Li et al. 2016, Cao et al. 2017, Guo et al. 2019, Zhang et al. 2020), point clouds (Thiele et al. 2017, Guo et al. 2018), grid cells (Bolkas et al 2018), or a combination of point clouds and images (Zhang et al. 2019, Lee et al. 2022). Comprehensive reviews of most of the above trace extraction techniques can be found in Battulwal et al. (2020) and Umili (2021).

Most trace extraction methods are based on geometry (e.g. curvature) alone, while some are based on colours (i.e. RGB values) alone. Few (e.g. Guo et al. 2019) consider both geometry and colours at the same time. While most point clouds produced by SfM photogrammetry or terrestrial laser scanning are coloured nowadays, occasionally the RGB values are not available. Therefore, we tried two cases, one only extracts concave edges based on geometry, while the other also extracts dark lines by considering RGB values.

3.1 Block delineation based on concave trace

The point cloud data generated from terrestrial laser scanning of a quartzite rock slope in Ouray, Colorado, USA was selected as a trial. The point cloud was originally hosted in the Rockbench repository (Lato et al. 2013) and has been widely used in digital rock mass research (e.g., Riquelme et al. 2014, Li et al. 2016, Guo et al. 2018). The rock slope is approximately 20m long by 15m high. The retrieved point cloud was not colored. Meshing was performed in CloudCompare (CloudCompare 2017).

Figure 3: Roadside cut slope in Ouray, Colorado. Originally hosted in the Rockbench repository (Lato et al. 2013)

However, for block delineation purpose, we need to extract concave faces only. To extract concave mesh faces as traces, we estimated the concavity c of each face by

$$c = \left(\overline{\boldsymbol{f_k}} - \boldsymbol{f}\right) \cdot \boldsymbol{n} \tag{1}$$

Where $\boldsymbol{f}$ is the position vector ([x, y, z]) of the centroid of the mesh face, $\overline{\boldsymbol{f_k}}$ is the mean position of the centroids of the k-nearest neighbours of the face, and $\boldsymbol{n}$ is the unit vector along the direction normal to the mesh face.

The computed concavity on the mesh is shown in Figure 4 (Right). However, the results contain significant noise which is difficult to be differentiated from the true edges, mostly due to natural undulations which create concave spots and patches (i.e. irregularities) on the rock surface.

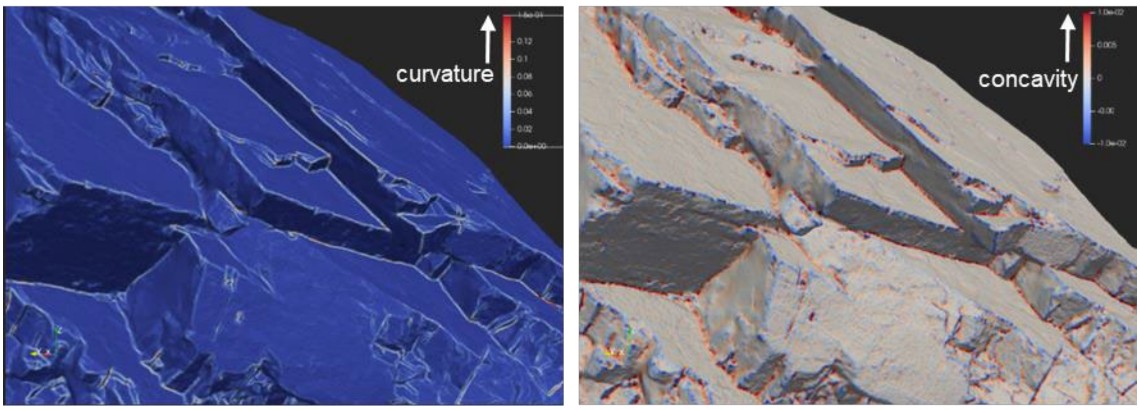

Figure 4: Calculated curvature (Left) and concavity (Right) values on the mesh

It is found that incorporating the curvature can improve the results, as the neighbourhood of the concave undulations are in fact generally planar. Due to ease of computation, the method used in Riquelme et al. (2014) and Wang et al. (2017) for checking planarity was used to estimate the curvature. To estimate the local curvature (σ) of a face, eigendecomposition is carried out on the covariance matrix of the centroids of its neighbouring faces. This gives three pairs of orthogonal eigenvectors and eigenvalues (λ_1, λ_2 and λ_3, where $\lambda_1 \geq \lambda_2 \geq \lambda_3$). Curvature σ can then be estimated by Pauli et al. (2002):

$$\sigma = \frac{\lambda_3}{\lambda_1 + \lambda_2 + \lambda_3} \quad (2)$$

The calculated curvature on the mesh is shown in Figure 4. Based on trial and error, mesh faces with the 30% highest concavity and the 40% highest curvature are extracted as concave traces. After refining the traces and delineating the blocks following procedures as discussed in Figure 2, the final traces and the block delineation results are shown in Figure 5.

The results show that the delineation is overall satisfactory and that the larger blocks, such as the three rock slabs on the crest of the slope, are extracted rather accurately. In the more fractured areas, e.g. close to the left toe of the rock slope, the block boundaries are less accurate.

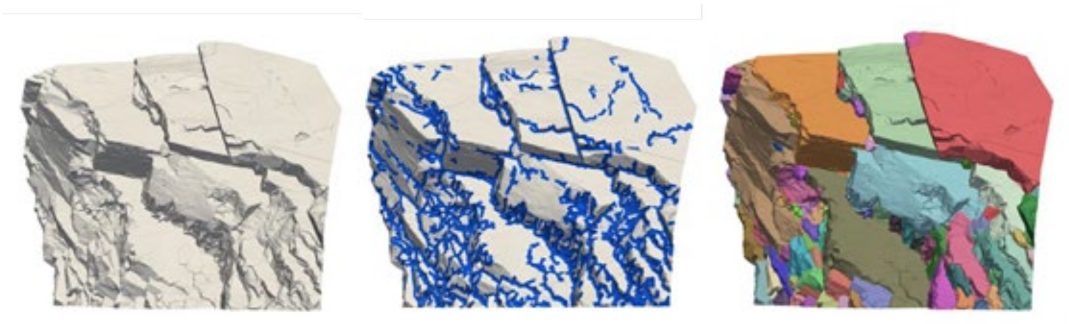

Figure 5: Results of block delineation on the rock cut in Ouray

3.2 Block delineation based on concave trace and dark trace

A rock outcrop in Ma Shi Chau, Hong Kong, is selected to test block delineation based on concave and dark traces. The rock outcrop is approximately 2m long and comprises sandstone from the Permian Tolo Harbour Formation. Since the outcrop is located along the coast, the surface is weathered and relatively rounded due to coastal erosion. The outcrop contains multiple sets of discontinuities which form networks of traces on the surface (Figure 6). The point cloud was generated by SfM photogrammetry from 24 photos using the software Agisoft Metashape Standard. The point cloud was scaled and orientated accurately based on reference objects in the field. Meshing was carried out in CloudCompare (CloudCompare, 2017).

Trace-extraction methods based on colours (Guo et al. 2018, Zhang et al. 2019, Lee et al. 2022) make use of sophisticated edge-detection algorithms on 2D images to extract the edges or dark lines and map the traces back to the 3D surface models. In this study, we just compute the relative darkness (i.e. opposite of brightness) of individual faces by comparing their brightness to the average brightness of their k-nearest neighbourhood directly, which appears to work well enough to recognize the dark traces (Figure 7). To simplify the calculation, the RGB values are first converted to grey-scale brightness by taking average of the RGB values. The equation for the relative darkness is simply as follows:

$$\text{Relative darkness} = B_k / B \quad (3)$$

Where B is the brightness of the mesh face and B_k is the average brightness of the k-nearest neighborhood of the mesh face.

In this study, traces with the 35% highest relative darkness are extracted, based on trial and error. Extraction of traces based on relative darkness are capable of extracting traces which are less concave compared to those extracted purely based on geometry, i.e. concavity and curvature (as shown in Figure 7).

However, since a few locally dark areas (such as weathering stains) are still extracted inaccurately as traces, we further add constraints based on the concavity and the curvature on the dark traces to filter faces with low concavity and curvature. Finally, these are combined with the extracted concave traces and are refined according to procedures in Figure 2. The final traces and the block delineation results are presented in Figure 6 and these are in overall good agreement with the visual interpretation. The results show that our approach can work on rock blocks bounded by weathered surfaces as well.

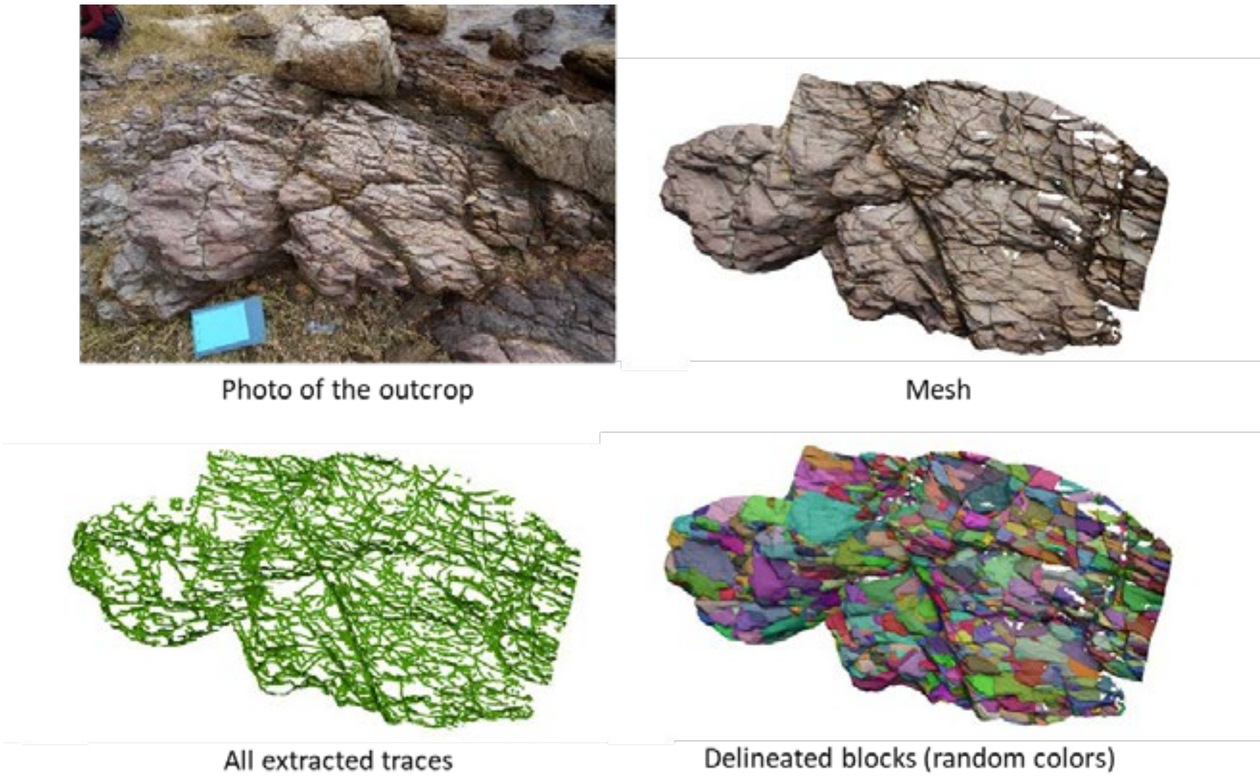

Figure 6: Block delineation of the rock outcrop in Ma Shi Chau

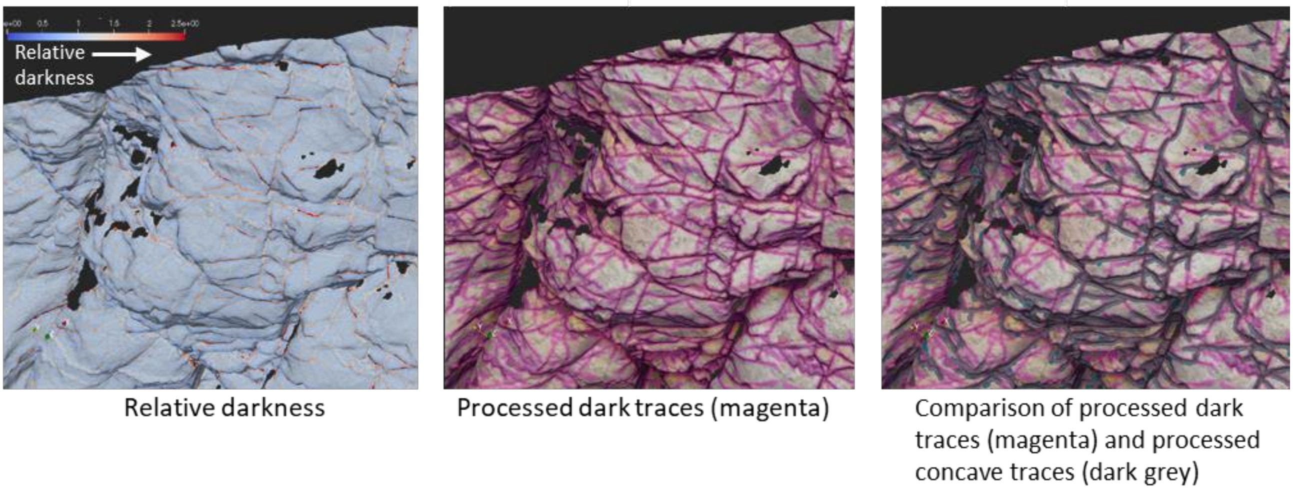

Figure 7: Extraction of traces based on relative darkness

4. ENGINEERING APPLICATION – POTENTIALLY UNSTABLE BLOCKS

A possible engineering application of block delineation is to delineate potentially unstable rock blocks. Previously we presented an approach to detect intersections which indicate potential planar sliding blocks in Tsui et al. (2021). The technique has the advantage of not requiring to assume a uniform slope orientation, compared to traditional kinematic analysis based on stereonets. In the case study provided below, we use the technique in conjunction with block delineation to give more relevant results.

This application is tested on an existing rock slope at a former quarry in Hong Kong. The rock slope was formed with a slope face dipping at 60° and predominantly comprises Grade II granite. The slope was surveyed by an unmanned aerial vehicle (UAV). A point cloud was constructed from the UAV photos by SfM photogrammetry using the software Agisoft Metashape Standard. Georeferencing was carried out with reference to ground control points. An area measuring approximately 15m long by 8m high, which does not contain vegetation and man-made structures, was selected for analysis (red box in Figure 8). The slope was also mapped manually on an elevated working platform.

Figure 8: Photo of the studied existing slope at a former quarry in Hong Kong. Red box: studied portion

Following the procedures in Figure 2, we extracted both concave traces and dark traces on the mesh (50% highest in concavity and 40% highest in curvature, with 10% highest in relative darkness) based on trial and error. The delineated blocks are shown in Figure 9. Overall, the results are consistent with our visual interpretation, except that the block boundaries are less accurate at the right toe of the slope where the rock is more heavily fractured.

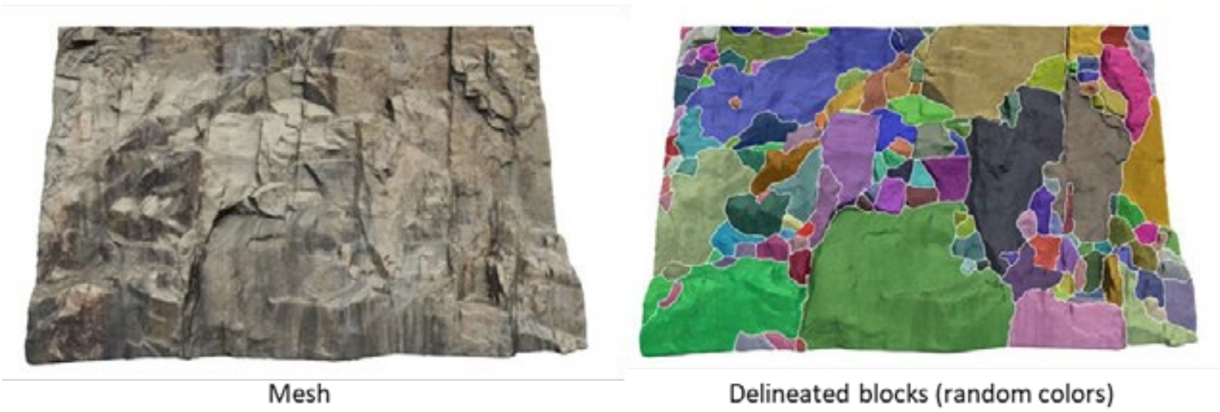

Figure 9: Results of block delineation

Our intersection-based planar sliding detection approach works by checking whether concave edges exist above an extracted discontinuity, as this indicates that the discontinuity is “daylighting” and a block may be present on top of it. If a daylighting discontinuity dips steeper than the friction angle, the block may slide along its surface. Our first step is to extract the discontinuities on the slope by the approach used in Tsui et al. (2021). The results are shown in Figure 10. For demonstration purposes only, a low friction angle (25°) was adopted to search for any potentially adverse daylight-indicating intersections, such that more unstable blocks are yielded in the demonstration exercise.

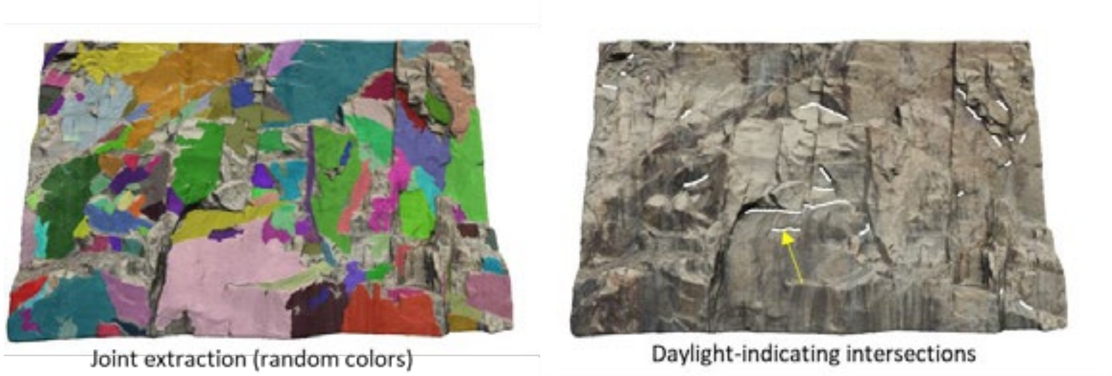

Figure 10: Results of joint extraction and search for potentially adverse daylight-indicating intersections (yellow arrow: invalid intersection)

In the next stage, we check whether the daylight-indicating intersections are really located at the base of any blocks. This step is carried out because the search for daylight-indicating intersections often picks up rock undulations which have no apparent side release mechanism (e.g. yellow arrow in Figure 10). To some extent, by checking with the block delineation results, this step also takes into consideration the availability of side release surfaces.

The interpreted, potentially unstable blocks are shown in Figure 11. Overall, the results are similar to those from our mapping, although the mapping also identified areas with potential ravelling and rockfall mechanisms, which are not checked in this semi-automated approach. A few small blocks were also missed in the semi-automated approach, due to inaccurate discontinuity or block boundaries.

Figure 11: Highlighting potentially unstable blocks associated with adverse discontinuities

5. DISCUSSIONS

5.1 Advantages

Our approach of block delineation has the following advantages:

1. It does not require prior discontinuity plane extraction and it is not affected by the performance of the plane extraction process. In addition, block detection techniques based on plane extraction may not be applicable when the exposed discontinuity planes are limited, for example, the rock outcrop in Ma Shi Chau (Section 3.2). Extraction of traces is a more versatile solution in this situation.
2. Rock blocks not wholly bounded by planar discontinuities (e.g. partially bounded by weathered surfaces) can also be delineated. This is particularly relevant in Hong Kong where rock blocks may be located above irregular sheeting-like joints in weathered granite and volcanic rocks.

3. In rock slope mapping, it is not routine to interpret the block boundaries on the whole slope. Our approach provides a semi-automated way to do so, which may enhance the mapping results. In addition, delineating blocks on the rock slope can assist in rock mass characterization.
4. When linked with kinematic analysis, the results may help locate potentially unstable planar blocks for stabilization. A quick analysis can be carried out remotely as a preliminary safety check before direct rock slope mapping is undertaken. This is also an alternative solution when only remote (i.e. indirect) mapping can be carried out.
5. The entire block delineation process from trace extraction to post processing is very quick (completed under 3 minutes) on a computer with Intel Core i7-9750H and 32 GB RAM. For reference, the meshes in the case studies contain 1.9 million to 8.8 million faces, with surveyed areas ranging from approximately 3m^2 (for the rock outcrop) to 120m^3 and 300m^2 (for the rock slopes).

5.2 *Limitations*

1. This approach assumes that the contact between two adjacent exposed rock blocks will be exposed as a trace on the rock surface. However, extremely narrow joints (i.e. with small aperture) which appear as very thin dark lines and are not obviously concave may still be missed in the trace extraction. As a result, two blocks may be labelled as one.
2. This approach assumes that blocks are fully separated by exposed traces on the rock surface. However, in reality, the true subsurface persistence of these discontinuities is not known. In addition, these are also likely to contain rock bridges which still connect the adjacent blocks. Whether or not there are discontinuities 'hidden' at the back of the block to disconnect it from the overall rock mass, is also not known. Figure 12 illustrates the above uncertainties. Therefore, the delineation is a conservative interpretation.

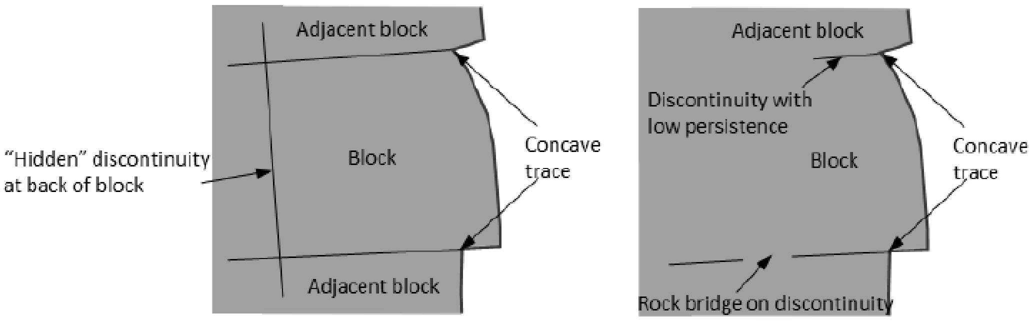

Figure 12: Schematic cross-sections showing two possible scenarios when a block is seemingly enclosed by concave traces on the surface. Left: The block is isolated. Right: The block is still connected with adjacent blocks.

3. The approach works for concave rock blocks (Figure 13, left). However, if the rock block contains areas enclosed by sharp concave edges, these areas may be misidentified as separate blocks (Figure 13, right). In addition, the approach does not perform well for highly fractured areas, as these areas are full of extracted traces that mask the blocks.

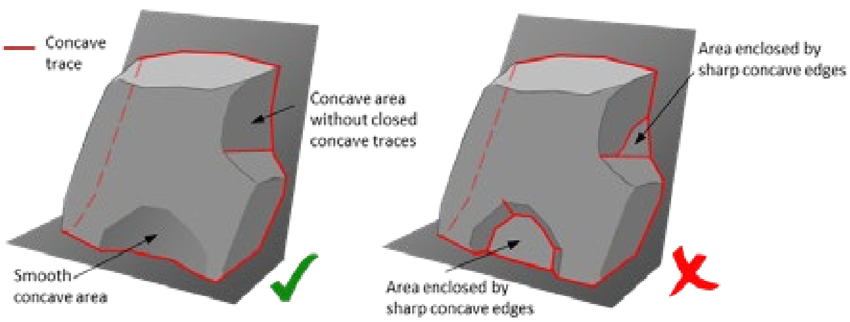

Figure 13: Example of a rock block with areas enclosed by sharp concave edges (Right) and one which does not (Left)

4. The approach relies on the user to set various thresholds to extract the traces and the post-processing steps. These thresholds need to be fine-tuned as these are specific for each site and depends on the resolution of the mesh.
5. In our last case study (Section 4), we only focused in planar sliding, which is just one mode of block failure mechanism. Other mechanisms, like toppling and wedge failures, are not considered at present, especially for small blocks or discontinuities of very low persistence. In addition, the discontinuity characteristics such as infilling, roughness, and alteration, are not taken into account.

5.3 Further investigations

Potential further investigations to improve the method include:
1. To carry out more case studies to find automatic ways to define the thresholds. Machine-learning approaches can be explored.
2. To modify the approach such that it can be applied on point clouds directly instead of meshes. Point clouds retain more information than meshes.
3. To estimate the volumes of the extracted blocks, for example, by using convex hull on the exposed portions of the rock blocks. Our current approach cannot directly calculate the block volume, as it does not predict hidden parts of the rock blocks.

6. CONCLUSIONS

This study proposes and describes an alternative, semi-automatic approach to delineate rock blocks on 3D meshes of rock surfaces based on traces. The proposed block delineation approach relies on the extraction of concave traces and dark traces based on curvature and colours respectively. An area on the mesh which is enclosed by concave or dark traces is then interpreted as a block. Our approach is demonstrated satisfactorily for three case studies involving a natural outcrop and two rock cut slopes, one of which is a mapped rock slope in Hong Kong. In one case study, we identified intersections associated with potential planar failure and linked these with the delineated blocks to highlight those blocks that are potentially unstable. Although these semi-automatic techniques cannot replace field verification by geologists, our approach can enhance the field mapping results, assist in locating areas which require stabilization and enhance the site safety.

ACKNOWLEDGEMENTS

The point cloud data from the Ouray rock cut was retrieved from Dr. Riquelme's personal website (https://personal.ua.es/en/ariquelme/a-new-approach-for-semi-automatic-rock-mass-joints-recognition-from-lidar-data.html). The dataset was formerly hosted on the Rockbench open repository (www.rockbench.org).

We would like to thank Miss Sonia Hui and others for their kind field assistance in Ma Shi Chau, and Mr Chison Cheung for part of the mapping work of the granite rock slope.

REFERENCES

Assali, P., Grussenmeyer, P., Villemin, T., Pollet, N. & Viguier, F. 2014. Surveying and modeling of rock discontinuities by terrestrial laser scanning and photogrammetry: Semi-automatic approaches for linear outcrop inspection. *Journal of Structural Geology*, 66, 102-114

Battulwar, R.; Zare-Naghadehi, M.; Emami, E. & Sattarvand, J. 2021. A state-of-the-art review of automated extraction of rock mass discontinuity characteristics using three-dimensional surface models. *Journal of Rock Mechanics and Geotechnical Engineering*, 13, 920-936

Bolkas, D.; Vazaios, I.; Peidou, A. & Vlachopoulos, N. 2018. Detection of Rock Discontinuity Traces Using Terrestrial LiDAR Data and Space-Frequency Transforms. *Geotechnical and Geological Engineering*, 36, 1745-1765

Buyer, A., Aichinger, S. & Schubert, W. 2020. Applying photogrammetry and semi-automated joint mapping for rock mass characterization. *Engineering Geology*, 264, 105332

Cao, T.; Xiao, A.; Wu, L. & Mao, L. Automatic fracture detection based on Terrestrial Laser Scanning data: A new method and case study. 2017. *Computers & Geosciences*, 106, 209-216

CloudCompare (version 2.9). 2017. Retrieved from http://www.cloudcompare.org/

Chen, N., Kemeny, J., Jiang, Q. & Pan, Z. 2017. Automatic extraction of blocks from 3D point clouds of fractured rock. *Computers & Geosciences*, 109, 149 – 161

Dawson-Haggerty et al. 2019. Trimesh (version 3.2.0). https://trimsh.org/

Dewez, T. J. B., Girardeau-Montaut, D., Allanic, C. & Rohmer, J. 2016. Facets: A CloudCompare Plugin To Extract Geological Planes From Unstructured 3d Point Clouds. Int. Arch. Photogramm. Remote Sens. Spatial Inf. Sci., XLI-B5, 799-804

Guo, J.; Wu, L.; Zhang, M.; Liu, S. & Sun, X. 2018. Towards automatic discontinuity trace extraction from rock mass point cloud without triangulation. *International Journal of Rock Mechanics and Mining Sciences*, 112, 226 - 237

Guo, J.; Liu, Y.; Wu, L.; Liu, S.; Yang, T.; Zhu, W. & Zhang, Z. 2019. A geometry- and texture-based automatic discontinuity trace extraction method for rock mass point cloud. *International Journal of Rock Mechanics and Mining Sciences*, 124, 104132

Kong, D., Wu, F. & Saroglou, C. 2020. Automatic identification and characterization of discontinuities in rock masses from 3D point clouds. *Engineering Geology*, 265, 105442

Kong, D., Wu, F., Saroglou, C., Sha, P. & Li, B. 2021. In-Situ Block Characterization of Jointed Rock Exposures Based on a 3D Point Cloud Model. *Remote Sensing*, 13

Lato, M., Kemeny, J., Harrap, R. & Bevan, G. 2013. Rock bench: Establishing a common repository and standards for assessing rockmass characteristics using LiDAR and photogrammetry. *Computers & Geosciences*, 50, 106 – 114

Lee, Y.-K.; Kim, J.; Choi, C.-S. & Song, J.-J. 2022. Semi-automatic calculation of joint trace length from digital images based on deep learning and data structuring techniques. *International Journal of Rock Mechanics and Mining Sciences,* 149, 104981

Li, X.; Chen, J. & Zhu, H. 2016. A new method for automated discontinuity trace mapping on rock mass 3D surface model. *Computers & Geosciences*, 89, 118-131

Long, Y., Huang, Q., Wu, F., Yi, H., Guan, S. & Sha, P. 2021. Automatic identification of irregular rock blocks from 3D point cloud data of rock surface. IOP Conference Series: Earth and Environmental Science, IOP Publishing, 861, 022048

Mavrouli, O., Corominas, J. & Jaboyedoff, M. 2015. Size Distribution for Potentially Unstable Rock Masses and In Situ Rock Blocks Using LIDAR-Generated Digital Elevation Models. *Rock Mechanics and Rock Engineering*, 48, 1589-1604

Pauly, M., Gross, M., & Kobbelt, L. P. 2002. Efficient simplification of point-sampled surfaces. In IEEE Visualization, October 2002. VIS 2002. IEEE.

Riquelme, A. J., Abellán, A., Tomás, R. & Jaboyedoff, M. 2014. A new approach for semi-automatic rock mass joints recognition from 3D point clouds. *Computers & Geosciences*, 68, 38-52

Thiele, S. T.; Grose, L.; Samsu, A.; Micklethwaite, S.; Vollgger, S. A. & Cruden, A. R. 2017. Rapid, semi-automatic fracture and contact mapping for point clouds, images and geophysical data. *Solid Earth*, 8, 1241-1253

Tsui, R., Cheung, C., Hart, J., Hou, W. & Ng, A. 2021. Intersection-based potential plane failure detection on 3D meshes for rock slopes. In Proceedings of the HKIE Geotechnical Division 41st Annual Seminar, pp. 256-268.

Virtanen, P., Gommers, R., Oliphant, T.E., Haberland, M., Reddy, T., Cournapeau, D., . . .SciPy 1.0 Contributors. 2020. SciPy 1.0: Fundamental Algorithms for Scientific Computing in Python. *Nature Methods*, 17, 261–272.

Vöge, M., Lato, M. J. & Diederichs, M. S. 2013. Automated rockmass discontinuity mapping from 3-dimensional surface data. *Engineering Geology*, 164, 155-162

Wang, X.; Zou, L.; Shen, X.; Ren, Y. & Qin, Y. 2017. A region-growing approach for automatic outcrop fracture extraction from a three-dimensional point cloud. *Computers & Geosciences*, 99, 100 - 106

Wichmann, V., Strauhal, T., Fey, C. & Perzlmaier, S. 2019. Derivation of space-resolved normal joint spacing and in situ block size distribution data from terrestrial LIDAR point clouds in a rugged Alpine relief (Kühtai, Austria). *Bulletin of Engineering Geology and the Environment*, 78, 4465-4478

Umili, G.; Ferrero, A. & Einstein, H. H. A new method for automatic discontinuity traces sampling on rock mass 3D model. 2013. *Computers & Geosciences*, 51, 182-192.

Umili, G. Methods for sampling discontinuity traces on rock mass 3D models: state of the art. IOP Conference Series: Earth and Environmental Science, IOP Publishing, 2021, 833, 012050

Zhang, P., Du, K., Tannant, D. D., Zhu, H. & Zheng, W. 2018. Automated method for extracting and analysing the rock discontinuities from point clouds based on digital surface model of rock mass. *Engineering Geology*, 239, 109 – 118.

Zhang, P.; Zhao, Q.; Tannant, D. D.; Ji, T. & Zhu, H. 2019. 3D mapping of discontinuity traces using fusion of point cloud and image data. *Bulletin of Engineering Geology and the Environment*, 78, 2789-2801

Zhang, K.; Wu, W.; Zhu, H.; Zhang, L.; Li, X. & Zhang, H. 2020. A modified method of discontinuity trace mapping using three-dimensional point clouds of rock mass surfaces. *Journal of Rock Mechanics and Geotechnical Engineering*, 12, 571 - 586

Large Diameter Open-end Steel Piled Foundations for the Hong Kong Offshore LNG Terminal – Design and Installation

Victor Shea, Dazhong Li, Dora Shum, Freda Chu

Arup, Hong Kong, China

ABSTRACT

Large diameter tubular piles are the most common offshore foundation type in the energy sector due to their relatively easy installation compared to other methods, yet local experiences with regards to their design and offshore installation are still limited. Successful installation of pile foundation on the Hong Kong Offshore LNG Terminal (HKOLNGT) Project provides valuable experience for future offshore developments in the territory. Unlike onshore piling works, offshore piling works are heavily limited by the available machinery, site constraints and weather conditions. This Paper shares the experiences gained on the HKOLNGT Project and draws together solutions to several challenges pertaining to the design and offshore installation of large diameter pile foundations, such as limitations arising from offshore environmental conditions.

INTRODUCTION

To support the energy transition in Hong Kong, and as part of the HKSAR Government's Climate Action Plan 2050 that targets to increase the use of natural gas for power generation, the two local power companies, CLP Power Hong Kong Limited and The Hongkong Electric Co., Ltd., are jointly developing an offshore liquefied natural gas (LNG) import facility using Floating Storage Regasification Unit (FSRU) technology. The proposed Hong Kong Offshore LNG Terminal (HKOLNGT) will enable procurement of LNG from global markets improving Hong Kong's long-term natural gas supply stability.

When in operation, a FSRU vessel of up to 263,000m³ storage capacity and a supplying LNG carrier will be double berthed in parallel at the proposed offshore jetty, located in the southern waters of Hong Kong SAR, to the east of the Soko Islands. The offshore Jetty Terminal, totalling approximately 385m in length, is formed by six steel mooring dolphin substructures (also termed jackets) and three larger central breasting dolphin substructures, each measuring 50m by 30m on plan housing all the equipment for operating the facility. The breasting dolphins are supported on vertical 1.83m OD cold-formed steel tubular piles driven to tentative 65m depth below the seabed. While, the mooring dolphins are supported on piles of the same diameter but raked at 1v:6.25h and of slightly shallower embedment. The smaller dolphin substructures provide mooring anchorage points for the berthed vessels. Each dolphin substructure will be decked over by prefabricated steel topside superstructures, which will be interconnected by access walkways at the topside level at nearly 16m above sea level. In addition, vertical 1.26m OD steel tubular piles support two smaller mooring dolphins at the northern end of the jetty to provide mooring for larger crew boats, including fireboats, visiting the jetty. The regasified natural gas will be delivered to the Black Point Power Station and Lamma Power Station via 45km and 18km subsea pipelines, respectively. **Figure 1** to **Figure 3** show the location and general arrangement of the proposed jetty.

The following sections start with the overall geological setting of the Project, followed by design aspects of the offshore pile foundations with focus on the capacity analysis as the deformation of offshore structure is generally less of a concern compared for example to onshore buildings and is not the focus of this paper. The paper moves on to the discussion of the high-strain dynamic loading tests using Pile Driving Analyzer (PDA) and CAPWAP (Case Pile Wave Analysis Program) analysis and comparison with CPT-based design methods. An observed site-specific pile capacity set-up is discussed and a site-specific set-up curve developed during the project is presented, followed by a discussion of the construction methodology at the end of this paper.

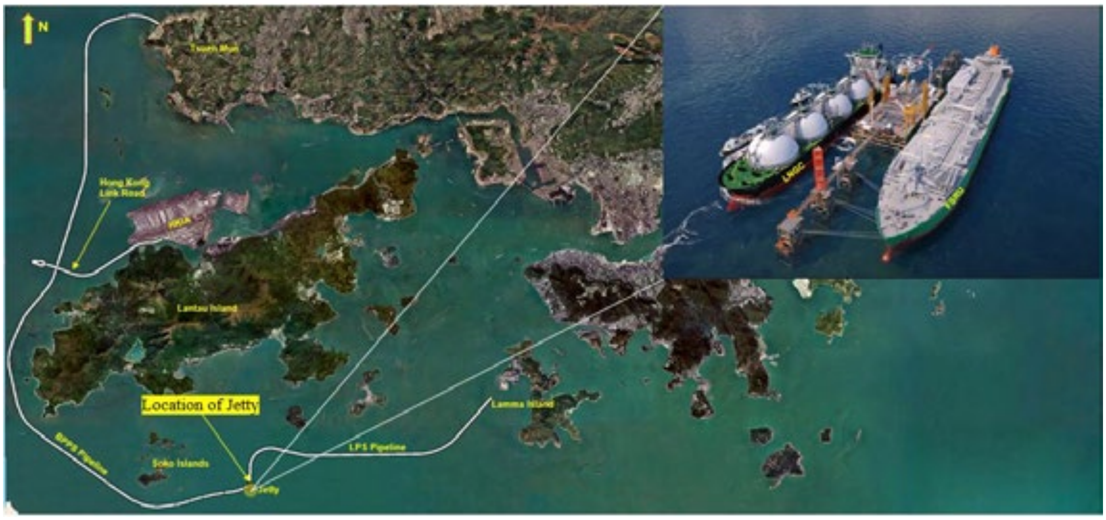

Figure 1: Location Plan of Jetty and Associated Pipelines

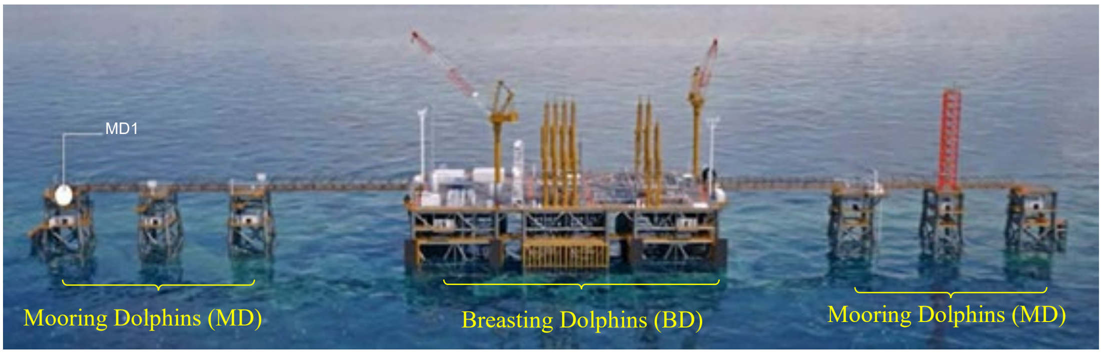

Figure 2: General Arrangement of Jetty

Figure 3: Site Photo of Jetty

1 SITE GEOLOGICAL CONDITION

Site investigation results indicate that the seabed is underlain by 10m to 15m of Marine Deposits (plastic Clays), followed in sequence by Upper Alluvium (Clay/Silt), Interbedded Alluvium (plastic Clay/Sand and Silts), Alluvial Sand (thick dense Sand) and Lower Alluvium (consists of Clays, Silts and Sands). Completely Decomposed Granite (CDG) is encountered at approximately -100mPD, whilst rockhead (Grade III or better) is typically greater than 90m depth (at approx. -110mPD).

The piles of the Jetty are all founded on the dense to very dense Alluvial Sand. A geological longitudinal section based on the available ground investigation stations at the Jetty location is shown in **Figure 4**.

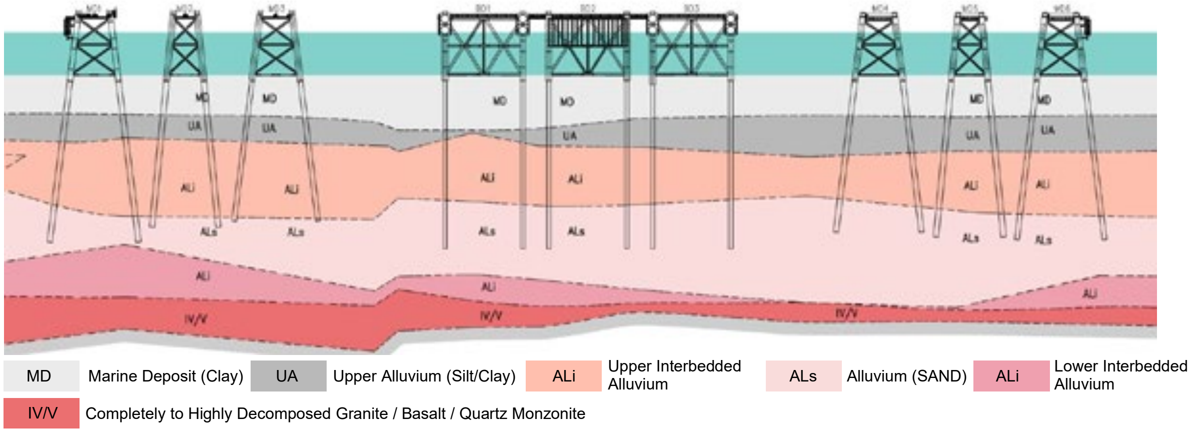

Figure 4: Geological Condition Over the Jetty Site

2 DESIGN OF THE OFFSHORE PILE FOUNDATION

Tubular piles are the most commonly used offshore foundation type in the oil and gas industry, and considerable experiences of designing such foundation type are reflected in the international codes (API, 2011; DNVGL, 2017). However, the use of large diameter tubular piles in offshore geological condition is less common in local practice and tubular piles are considered non-recognised pile type by the local authority. In this project, two separate designs have been undertaken satisfying the relevant international codes and standards to align the design to international practice, as well as a separate design following the Hong Kong SAR local code of practice to conform to the established local practice, make use of established local experience and obtain design approval by local authorities. In terms of the geotechnical design of the piled foundation, the American Petroleum Institute (API) codes (API, 2011, 2014) are primarily adopted. Reference is also made to the Hong Kong SAR local codes/standards where appropriate to perform checking to fulfil the requirements of local authorities for obtaining statutory approvals.

2.1 Design Factor of Safety

For a pile foundation design according to GEO Publication No. 1/2006 (GEO, 2006), static load test should be performed on preliminary piles, which is usually not practical for offshore developments at project level. This is because the required test loads for offshore piles would be large due to substantial design environmental loading from wave and wind, and the test itself can be both impractical and costly. In offshore foundation practice, a design factor of safety (FOS) of 2.0 is usually adopted for the normal condition. For more onerous extreme design environmental conditions, a lower FOS of 1.5 is deemed acceptable considering the likelihood of the extreme case is less compared to normal operating conditions. If a higher test load to achieve a higher FOS of 3 is desired, static loading test will become practically impossible to conduct for high-capacity offshore piles.

The recommended FOSs in the offshore practice are acknowledged to be less than those typically adopted for onshore foundation practice, which may be due to offshore platforms being less sensitive to displacement for serviceability limit state conditions and are usually unmanned during the design storm events (Lehane et al., 2005).

In Hong Kong, a larger design FOS of 3 and preliminary pile(s) to be load tested are usually required (GEO, 2006) for new or less commonly used pile types to increase the confidence of the design. For piles which will be subjected to some form of proof testing to verify their pile capacities, a high FOS of 3 may not be necessary from a technical point of view. For offshore piles, PDA tests with CAPWAP analyses can be and are often conducted during and after installation for assessing the capacities of installed piles. Such pile testing technique is now a widely accepted reliable proof loading test method in the offshore piling industry as an alternative to static loading test (Webster et al., 2008; Yu et al., 2013). In this project, the jetty will be unmanned, all vessels will be disconnected from the dolphins when typhoon signal No. 3 or higher is hoisted and all the piles have been tested by PDA with CAPWAP analysis during driving and restrike after a period of time as proof load tests. In order to satisfy local practice, it is required that all piles in the Project be designed and tested by PDA with CAPWAP analysis to a FOS of 3.0 for the long-term loading conditions. However, as suggested in the following discussions, site-specific pile set-up behaviour could be considered as a part of the pile capacity verification process to achieve cost-effective offshore pile foundation designs in Hong Kong.

2.2 Pile Axial Load-carrying Capacity

Tubular piles can behave plugged or unplugged depending on the pile configuration and soil resistance distribution (**Figure 5**Error! Reference source not found.). A plugged condition refers to the situation when the internal shaft friction of the soil plugged inside the tubular pile is greater than the base resistance and no relative movement between the soil plug and internal surface of the tubular pile is possible. Generally, for large diameter piles, they are rarely plugged during installation by continuous driving (Rausche et al., 2010) due to the inertia of the soil plug inside and the shaft friction is considerably disturbed by the installation process, whereas under static loading condition, plugged condition can be more dominant for pile with sufficient embedment. The pile capacity derived from the two different assumed mechanisms are given in Eq. (1) & (2).

$$Q_{c_{\mathrm{plugged}}} = Q_{\mathrm{f,c,o}} + Q_{\mathrm{b,p}} = \pi D_{\mathrm{o}} \int_{\mathrm{L}} \tau_f(\mathrm{z})\mathrm{dz} + q_b A_{\mathrm{p}} \tag{1}$$

$$Q_{c_{\mathrm{unplugged}}} = Q_{\mathrm{f,c,o}} + Q_{\mathrm{f,c,i}} + Q_{\mathrm{b,wall}} = \pi D_{\mathrm{i}} \int_{\mathrm{L}} \tau_f(\mathrm{z})\mathrm{dz} + \pi D_{\mathrm{o}} \int_{\mathrm{L}} \tau_f(\mathrm{z})\mathrm{dz} + q_{\mathrm{b}} A_{\mathrm{wall}} \tag{2}$$

where, $Q_{\mathrm{f,c,o}}$ = shaft friction at pile outer surface, $Q_{\mathrm{f,c,i}}$ = shaft friction at pile inner surface, $Q_{\mathrm{b,p}}$ = toe resistance from gross area of pile base, $Q_{\mathrm{b,wall}}$ = toe resistance from pile wall area, $\tau_f(\mathrm{z})$ = shear stress developed at failure along shaft, q_b = base resistance pressure, A_p, A_{wall} = pile gross bases area and wall area respectively, and D_i and D_0 are the inner and outer diameters of the pile.

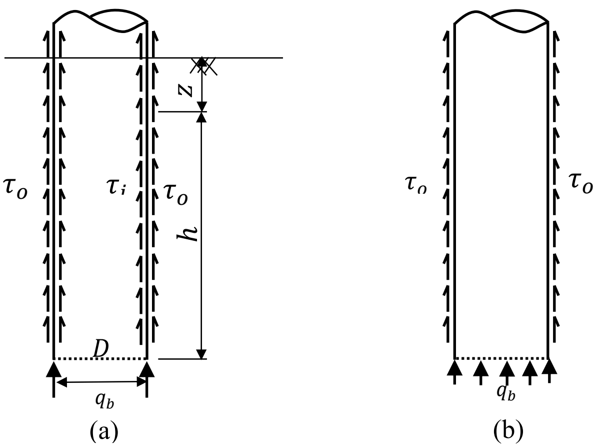

Figure 5: Load-transferring mechanism for tubular piles (a) unplugged case and (b) plugged case

In the API RP 2GEO Code, the traditional pile capacity calculation method is referred to as the Main Text Method. For the simplicity of design, the API Main Text method recommends both cases be checked and the lesser of the calculated capacities shall be adopted in the design. Furthermore, the same shaft friction is assumed for both internal and external friction at a given depth in the calculations, which is conservative as some degrees of arching will be developed by the driving process that tends to create higher inner shaft friction than the outer.

2.3 Conventional Driven Pile Design Approach

In terms of the effective stresses, the shaft friction τ_f along a pile can be expressed as Eq.(3).

$$\tau_f = \eta \cdot \sigma'_{r0} \cdot \tan\delta_f \;= \eta \cdot K_c \cdot \sigma'_{v0} \cdot \tan\delta_f \tag{3}$$

where, σ'_{r0} = radial effective stress, $K_c = \sigma'_{rc}/\sigma'_{v0}$, η = resistance adjustment factor, and δ_f = interface angle.

For cohesive soils, a total stress analysis method is conventionally adopted for its simplicity without considering the complex stress development. The shaft friction can be related directly to the undrained shear strength of soils s_u, known as the alpha method. Such simplification has been stated to have limitations in principle (Jardine et al., 2005). However, such formulation is the current industry standard in design and have been adopted both in the main text of API as well as referenced in the GEO Publication 1/2006. For the granular soils, the term $\eta \cdot K_c \cdot \tan\delta_f$ is lumped to β and it is known as the beta method, which directly relates the shaft friction to vertical effective stresses. The pile shaft friction can be expressed as Eq.(4).

$$\tau_f = \begin{cases} \alpha \cdot s_u \leq \tau_{s,\text{lim,clay}} & for\ cohesive\ soil \\ \beta \cdot \sigma'_{v0} \leq \tau_{s,\text{lim,sand}} & for\ granularsoil \end{cases} \tag{4}$$

In addition, a limiting shaft resistance $q_{b,\text{lim}}$ is further introduced to cap the shaft friction that can be utilised in design. Using the limiting shaft friction could be misleading (Kulhawy, 1984) but nonetheless it has been used in the present design in accordance with the common practice in Hong Kong. API RP 2GEO recommends a limiting shaft friction of 120kPa for very dense sand, whereas in GEO Publication No. 1/2006 higher shaft friction of 150kPa has been suggested for bored piles in granite saprolites. The seemingly larger observed shaft limits suggested for onshore piles could be attributed to a) API Main Text Method developed the limiting values based on un-instrumented piles, the limiting values are more of a fitting tool rather than the actual shaft friction and b) discussion within GEO Publication No 1/2006 are based primarily on land piles tested at a much later time after installation, whereas the loading test for marine piles referenced in API are usually conducted only a few days after driven due to the harsh offshore environment and machinery availability. Such time-dependence could have a significant effect on the apparent pile capacity, which will be further elaborated on in the later **Section 3.1** of this paper. To assess the long-term pile axial compression capacity, a limiting value of 140kPa has been adopted.

For the base pressure, it is calculated according to Eq.(5).

$$q_b = N_q \cdot \sigma'_{v0} \leq q_{b,\text{lim}} \tag{5}$$

where, N_q = bearing capacity coefficient and σ'_{v0} = vertical effective stress acting on soil at pile base.

For this project, the piles have an embedment of approximately 60m below the seabed level, it is found the that $q_{b,\text{lim}}$ will be triggered for most of the piles. API Main Text recommends a limit of 10~12MPa for dense to very dense sand. A conservative value of 10MPa has been adopted in the design.

The applicability of limiting values heavily relies on the calibration with the accumulated database. It has been reported in the literature that since the α and β design approaches fail to capture the fundamental failure mechanism of a pile, it is considered less reliable than the modern CPT-based methods (Randolph & Gourvenec, 2011), which have also been compared in this study in **Section 3.2** .

2.4 *Consideration of Cyclic Degradation of Pile Capacity*

Cyclic effects are commonly researched for monopiles supporting wind turbine generators, which in addition to cyclic environmental loading by predominantly waves, will impose millions of rotating blade cycles onto the foundations (Buckley et al, 2018). As discussed by Jardine (2020), there is currently no internationally recognised design method for the cyclic design for piles. A design workflow chart has been proposed following the Project SOLCYP and involves a screening stage using the concept of cyclic interactive chart or stability chart, which classes the cyclic loading response as stable, meta-stable or unstable (Jardine, 2020; Poulos, 1988; Puech, 2013). When the loading data points fall within the stable zone, it can be decided that a static design approach is adequate without further considering the potential of cyclic load degradation effect on the pile axial capacity.

The foundation system of HKOLNGT is subjected to relatively mild cyclic load amplitude compared to their design ultimate pile capacities. Unlike common offshore piled foundations that are typically designed to FOS of 2, a conservative design FOS of 3 has been used in this Project. This means that the mean and cyclic axial forces under working conditions will be considerably lower than the pile ultimate capacity and soil strains will be limited to a small range that will not be sufficient to trigger cyclic shaft degradation (**Figure 6**).

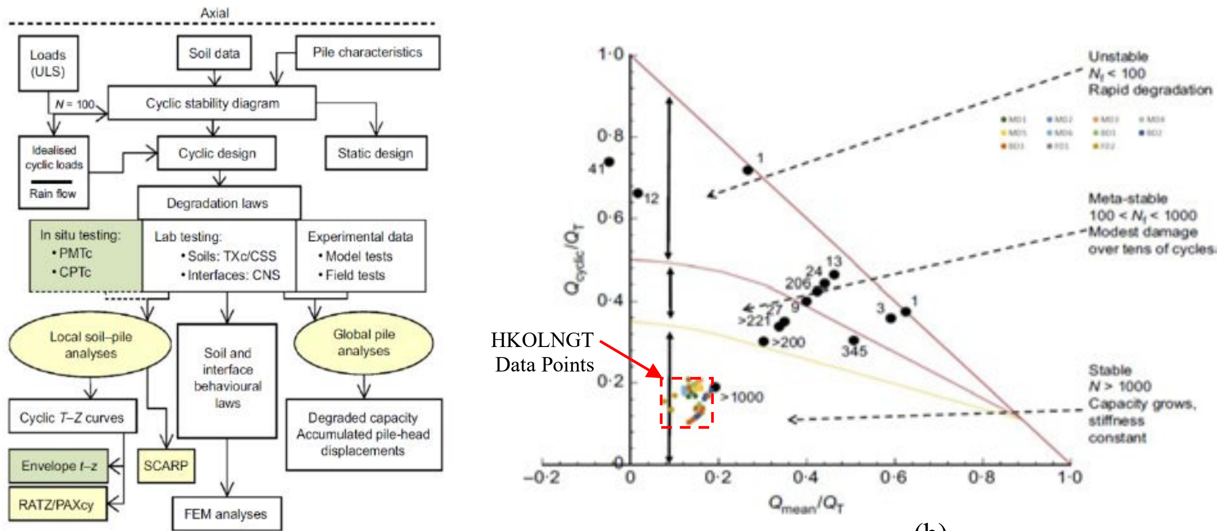

(a) (b)

Figure 6: SOLCYP Workflow Process for Use in Design of Pile to Carry Axial Pile Loading (Extracted from Jardine (2020)); and (b) Interaction Diagram Developed at Dunkirk test Site (Jardine and Standing 2012, Jardine 2020) with Data Points at HKOLNGT Added

3 PROOF LOAD TEST AND DESIGN VERIFICATION

For large load-carrying capacity offshore piles, it is generally impractical to perform static pile load tests. A series of high-strain dynamic load tests using PDA were carried out as proof load tests and CAPWAP analyses used to derive their static pile capacities. Dynamic load tests have been performed at various times after the end of driving (EOD) to capture the site-specific pile capacity set-up behaviour.

3.1 Review of Site-specific Set-up Curve

Pile capacity set-up is primarily due to an increase in the shaft capacity over time as indicated by both field and model tests (Bullock et al., 2005; Chow et al., 1998). To represent the set-up behaviour, i.e., an increase in capacity with a decreasing rate, a logarithmic relationship has been proposed for its simplicity in the literature (Axelsson, 1998; Hosseinzadeh Attar & Fakharian, 2013; Komurka et al., 2003; Rausche et al., 2010). Alternatively, a hyperbolic function in the form of Eq.(6) has also found wide application in geotechnical engineering for predicting geotechnical behaviours from available field data, e.g., settlement predictions over time (Chung et al., 2009; Tan, 1995) as well as ultimate pile capacity prediction in Chin's method (Chin, 1972). The hyperbolic function has two unknowns and further caps to $1/b$ as time (t) approaches to infinity as opposed to conventional logarithmic relationship used to assess set-up behaviour on international offshore projects, and thus the former can be viewed as being more reasonable. It should be noted that the actual pile capacity set-up behaviour is complex with an initial relatively faster recovery of pile capacity within the first one to two days after EOD. This is believed to be the result of excess porewater pressure dissipation as well as collapsing of soil arching formed during to pile driving with time. The continual slower growth in the pile capacity can be more attributed to the ageing effect of the soil.

Attempt has been made to capture the set-up behaviour after an initial stage post-EOD, when the set-up response tends to be more consistent and less prone to uncertainties introduced by the driving process. Hyperbolic function in the form of Eq. (6) has been used in this project. It is recommended that for other sites a site-specific predictive curve should be developed based on the observed set-up trend in the available test data over a particular period of development. As shown in **Figure 7(a)**, data presented in the (t/τ_f ,t) space show a good linearity indicating a hyperbolic function is a reasonable representation of the trend.

The project consists of 54 nos. of piles with varying penetration at different dolphins and diameters. To make use of all tested pile capacities, the shaft resistances are normalised by their respective pile outer surface area using Eq.(7). The resultant $\tau_{f,i}$ can be regarded as a representative shaft friction stress. Test data have been plotted in **Figure 7(b)**, which exhibits a consistent trend that can be well described by a hyperbolic function.

$$Q(t) = \frac{t}{a+b\cdot t}\ for\ t > t_0 \text{ (a, b are constants to be determined by data regression)} \tag{6}$$

$$\tau_{f,i}(t) = \frac{Q_{s,i}(t)}{\pi D_{o,i} H_i} \quad \left(Q_{s,i}(t), \text{measured shaft resitance for } ith \text{ pile at time t}\right) \tag{7}$$

where, $Q_{s,i}$(t) = the measured shaft resistance at time t after EOD for i-th pile, $D_{o,i}$ and H_i refer to the pile outer diameter and the embedment, respectively. Re-arranging the data in the (t/τ_f ,t) space and performing a linear regression, the set-up of average shaft resistance can be expressed as Eq.(8) with a coefficient of determination of R^2 approximately 0.90.

$$\tau_f(t) = \frac{t}{0.0079\cdot t + 0.2711}\ for\ t > 48\text{hours and } \tau_f \text{ in kPa} \tag{8}$$

The set-up effect ratio $\xi(t)$ at a particular time t referencing to a testing time t_0 can therefore be written as Eq.(9). Using a reference t_0 = 48 hour, the set-up curve in terms of a set-up ratio $\xi(t)$ can be derived in Eq.(10).

$$\xi(t) = \frac{\tau_f(t)}{\tau_f(t_0)} = \frac{t(0.0079\cdot t_0 + 0.2711)}{t_0(0.0079\cdot t + 0.2711)}\ for\ t > 48\text{hours and } \tau_f \text{ in kPa} \tag{9}$$

The predicted total pile capacity at any given time t can also be calculated by applying the set-up factor to the measured shaft friction at the time of the testing. Toe resistance set-up was observed at this site, but it is much less significant when compared to the shaft resistance set-up effect, and therefore has been ignored when further interpolating the pile capacities to 5 days, which is conservative.

$$Q(t) = Q_{b,0} + \xi(t)\cdot Q_{s,0} \quad (Q_{b,0} \text{ and } Q_{s,0} \text{ are base and shaft resistances measured at time } t_0) \tag{10}$$

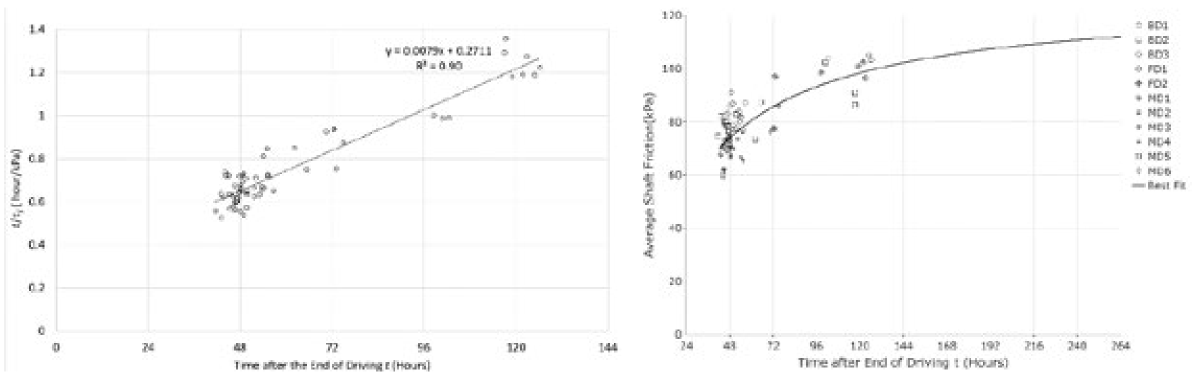

(a) (b)

Figure 7: Shaft Set-up Behaviour (a) t/q vs. t and (b) average shaft friction vs. time

Though pile capacity set-up is a well recognised phenomenon, there has been no consensus in the local industry on how such time-dependent features of pile capacity could be considered in design. It can be seen from this work that pile capacity set-up could be significant in the pile design as well as in the proposal of the proof load test regime for future offshore development in Hong Kong.

3.2 Cone Penetration Test (CPT) Based Design Method

To remove the inherent limitation of the current design approach, as highlighted in the preceding section, many international design codes are moving towards CPT-based pile design. In these methods, the concept of the shaft and toe resistance limit has been removed and a length factor h/D has been introduced to account for the effect of pile installation as well as the loading phases (Randolph, 2003). Several direct CPT methods have been proposed in the literature and four (4) CPT methods have been included in API RP 2GEO. Among the four methods, Method 1, ICP -05 (Jardine et al., 2005) and Method 2 UWA-05 (Lehane et al., 2005) have received more research attention in subsequent developments.

It should be noted that the four API CPT methods are developed for silt/sand. Typical Hong Kong offshore geology consists of a layer of marine deposit overlying alluvial deposits which are more variably composed. At the site of Jetty Terminal, the alluvial layer consists of interbedded silts and sands, occasionally clay followed by a relatively uniform dense to very dense alluvial sand where the tubular piles are toed in.

Given the layered geological profile at HKOLNGT, both CPT methods fitted for the clay site and sand sites are considered for the respective layers. Discussion on design method within clay has been provided in Jardine et al. (2005) and a simplified version adopting CPT methods is then described in the works of Lehane (Lehane et al., 2000; Lehane et al., 2013). The UWA-13 method (Lehane et al., 2013) developed for clay is appropriate where clay is encountered, and the same approach has been employed in the work of Lehane et al.(2017) for sites with the presence of both sand and clay. As the UWA-05 is largely developed for silt/sand from the ICP-05 with several modifications and have been demonstrated to provide a better predictive performance with the available field test results (Labenski & Moormann, 2016; Schneider et al., 2008), this method has been adopted in this study to provide an indication of the pile axial capacities. The simplified version of UWA-05 as presented in API RP 2GEO is shown in Eq.(12), which is considered a reasonable simplification in offshore applications (API, 2011).

$$\text{UWA}-13\ \text{(Clay)}:\ \tau_f = 0.055q_t\left[\max\left(\frac{h}{R^*},1\right)\right]^{-0.2}\ \text{where}\ R^* = (R^2-R_i^2)^{0.5}\quad for\ shaft\ resistance \tag{11}$$

$$\text{UWA}-05\ \text{(Sand)}:\begin{cases}\tau_f = 0.03\cdot q_c\cdot A_r^{0.3}\cdot\max\left(\frac{h}{D},2\right)^{-0.5}\tan\delta_{cv} & for\ shaft\ resistance\\ q_b = q_{c,av1.5D}(0.15+0.45A_r) & for\ toe\ resistance\end{cases} \tag{12}$$

where, h = the distance between the points at z and the pile tip. δ_{cv} is the constant volume friction angle, $A_r = 1-(D_i/D_o)^2$, the pile displacement ratio, $q_{c,av1.5D}$= average cone resistance q_c over 1.5D above and 1.5D below the pile tip. q_t= corrected cone resistance.

As shown in Eq.(12) , UWA-05 does not distinguish the plugged or unplugged case for the toe resistance and an average of q_c over 1.5D above and below the toe tip has been used. In addition, as discussed earlier, as the unplugged case under the working condition is atypical for large diameter piles. It should also be noted the shaft friction derived from the CPT-based design method does not differentiate the internal and external resistances for the design equations which are derived from fitting the database of pile load tests.

12 nos. of CPTs are available over the jetty area, five (5) of which have a penetration deeper than 60m below the seabed level and can be used for the estimate of the static pile capacity. The calculated pile capacities based on CPT method across the jetty are generally in a range of 35~40MN depending on the local variation in geological conditions as well as the pile length. It is noted that the calculated FOSs are between 2.03 and 2.63, greater than 2.0 required in international practice for normal conditions. The subsequent PDA tests on site indicate that the pile capacities typically attained a FOS greater than 2 at around two days after EOD, which suggests that CPT-based method can provide a reasonable estimate of the pile capacities after a relatively short time after installation.

The further dynamic load tests had demonstrated that all piles achieved at least FOS of 3 at the time of around five (5) days after pile installation due to the additional pile capacity set-up effect. It is noted that the site-specific set-up behaviour and the time elapsed after EOD have important influence on the pile capacity obtained at the time of PDA testing. The extensive high-strain dynamic loading tests at HKOLNGT indicate that the CPT-based design methods provide a reasonably conservative estimate of long-term pile capacity. It is suggested that the CPT-based method can be explored in future offshore pile foundation designs in Hong Kong SAR along with a FOS of 2.0 to align the designs with the international offshore practice.

Table 1: Pile Axial Compression Capacity using CPT-based Design Method

Pile Location	Maximum Working Compression Load [kN]	CPT-based Capacity* [kN]	FOS
MD1	14,919	30,253	2.03
MD2	12,177	27,025	2.22
MD3	11,911	26,070	2.19
MD4	11,397	29,952	2.63
MD5	12,351	30,811	2.49
MD6	12,645	31,584	2.50
BD1~BD3	18,446	38,351	2.08

*Note: * Compression capacities based on UWA-05 and UWA-13*

4 INSTALLATION

The dolphin jackets and piles were fabricated in Qingdao, Mainland China, which were towed to site on large delivery barges for installation. During the installation, the jacket was first lowered onto the seabed, and was temporarily supported on the seabed by two large mudmats prefabricated onto the base of the jackets, **Figure 8(a) & (b)**. Once the jacket was lowered to be seabed, it would be difficult to adjust its location or orientation hence for this reason and to ensure safety of the lifting works, the offshore installation required a calm sea state.

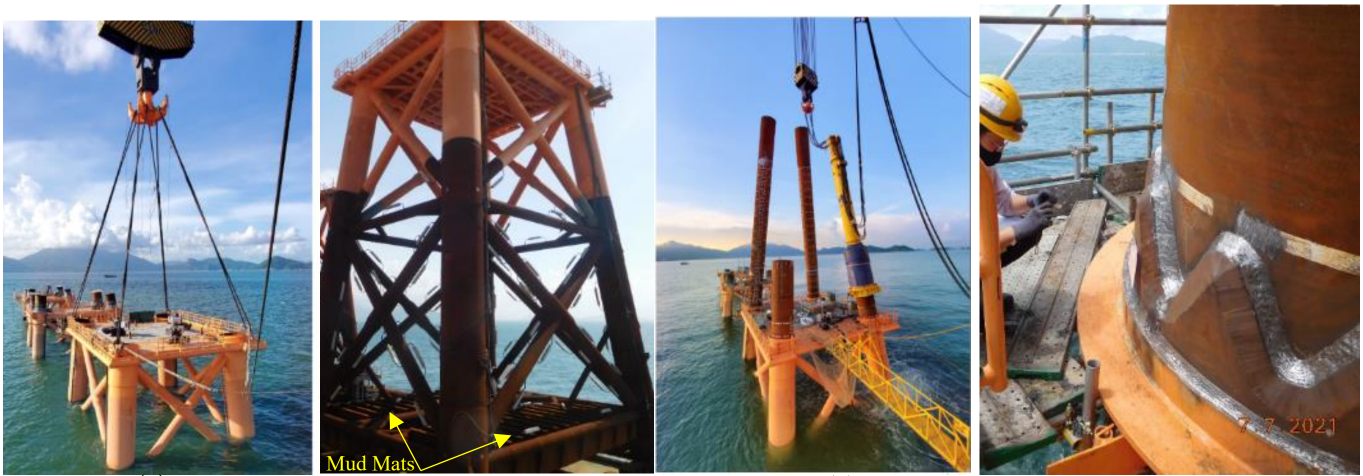

(a) (b) (c) (d)

Figure 8: Jacket Structure Installation (a) Lowering Jacket; (b) Temporary Mud Mats; (c) Pile Driving; and (d) Welding of the Crown Shim Plate

After the jacket was placed at the design location, the first segments of the corner piles were pitched into the jacket legs and driven to their specified levels using offshore hydraulic hammers. The second pile segments are stabbed into the first segments, welded together, tested by non-destructive tests and driven to their design founding levels, **Figure 8(c)**. The driving process was monitored using the PDA system to check that the maximum driving force did not exceed the allowable limit and on this project 0.9 times the steel yield strength has been adopted. When the PDA test results are proven satisfactory, the annulus between the jacket leg and pile is grouted and the top of the jacket connected to the piles by 100mm thick steel crown shim plates, **Figure 8(d)**.

4.1 Limitation due to Environmental Condition

Based on the Contractor's international offshore experiences, site characteristics and heavy-duty installation vessel, with up to 3,800te lifting capacity, deployed on this Project, the limiting environmental conditions for various construction activities are shown in **Table 2**. The significant wave height, H_s, heavily restricts jacket installation works. During the construction of dolphin MD1, only the first 4 days out of the 14-day construction period from 10 to 24 December 2020 recorded H_s < 1.0m, suitable for jacket lowering, which caused a considerable impact on the construction programme.

Long waves (typically peak wave periods, T_p > 6.7s) have a significant impact on the rolling motion of the installation vessel. Several precautions had to be implemented during the installation because of adverse weather conditions. For example, the primary hook was removed as it collided with the ancillary hook under severe rolling, slight adjustment of vessel orientation, and deployment of additional anchorage to achieve better stability of the vessel. Despite these enhancement measures, some of the hammer lifting and pile splicing works still had to be temporarily halted because of excessive vessel heave/roll.

Table 2: Limiting Environmental Condition of Installation Vessel

Construction Activity	Wind Speed	Significant Wave Height, H_s	Current Speed
	[m/s]	[m]	[knot]
Jacket Lifting	≤10.0	≤1.5	≤2
Jacket Lowering	≤13.8	≤1.0	≤0.88
Piling	≤12.0	≤1.5	-

4.2 Limitation due to the Anchorage Extent

Unlike onshore piling works, the offshore construction sequence and vessel manoeuvrability are limited by the anchorage spread arrangement making it difficult/infeasible for the installation vessel to readily return to the previous location(s) due to interference between anchorage lines and completed dolphins. In addition, the long extent of the anchorage spread of the installation vessel, shown in **Figure 9**, means that it is not physically feasible to mobilise a second installation vessel of equal size to work concurrently to accelerate the works. Therefore, the dolphin jackets and piling works must be carried out in a predefined sequence with the required proof testing completed at each location before moving to the next one.

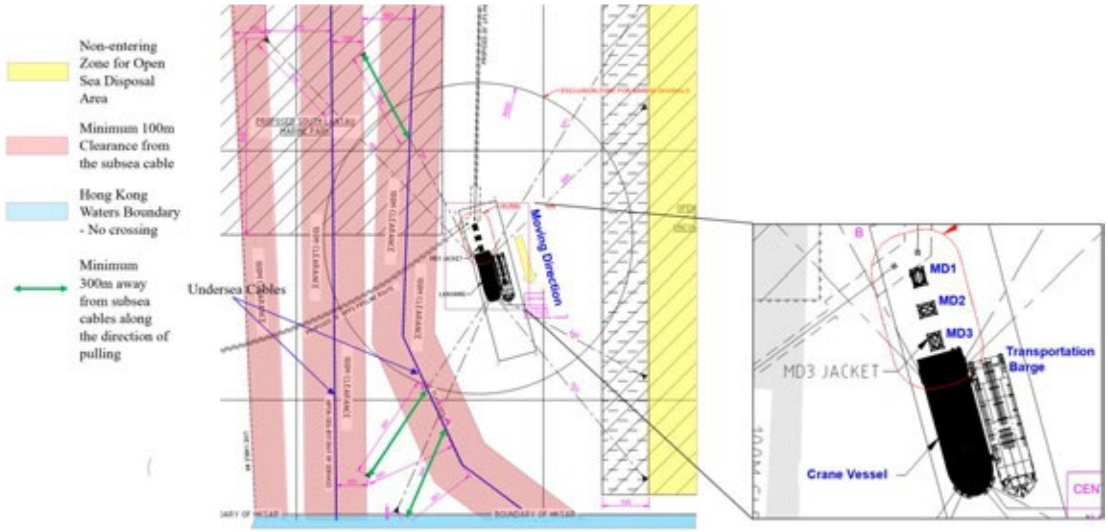

Figure 9: Marine Installation Constraints

The installation vessel will have to stay idle for a period until the pile capacity recovers after driving, which may require multiple restrike PDA tests. This could generate considerable loss of valuable fair-weather windows. Consequently, the installation sequence must be well-planned in advance with adequate allowance in the programme for weather related downtime, so that the programme can be adjusted with some flexibility against the closely monitored offshore weather forecast.

5 CONCLUSIONS AND RECOMMENDATION

This paper discusses the design and installation aspects of a jetty foundation supported by large-diameter steel tubular piles. Experiences drawn by the authors in this project include:

1. The international offshore codes have been shifting to CPT-based design methods for the design of offshore pile foundations. The modern CPT-based methods provide a reasonable estimate of pile axial capacities soon after completion of pile installation, which at the HKOLNGT site approximate to the CAPWAP capacities obtained at around two days after end of driving.
2. The established local experience on onshore piles should be considered together with the time-dependent effect of pile set-up, which will affect the proof loading test proposal. An appreciable pile capacity set-up has been observed in this project. A hyperbolic set-up curve has been developed that shows a consistent set-up behaviour across the site.
3. It is suggested that CPT-based methods could be used along with a FOS of 2.0 in future offshore developments in Hong Kong SAR to assess the design pile capacity soon after pile installation coupled with the consideration of site-specific pile capacity set-up behaviour to determine the longer-term pile capacity.
4. The use of PDA testing with CAPWAP analysis could be maximised to obtain field data on the pile capacity development at various times after end of driving to verify the set-up response, which can be very site dependent. In this way, safe and cost-effective offshore piled foundation designs can be achieved in Hong Kong SAR.
5. The installation of offshore pile foundations is heavily affected by the harsh marine environmental condition, which is further restricted by non-piling window requirements implemented to protect marine mammals, therefore a flexible and adaptive construction programme is critical to the successful completion of the project.

ACKNOWLEDGEMENTS

The data presented in this paper had been collected during the construction of the jetty terminal. The authors wish to thank Hong Kong LNG Terminal Limited for the permission to publish the data. The supports from the Engineering Procurement and Construction (EPC) Contractor, Offshore Oil Engineering Co. Ltd, are also gratefully acknowledged.

REFERENCE

API. 2011. RP2 GEO: Geotechnical and Foundation Design Considerations. American Petroleum Institute.

API. 2014. RP2A:Planning, Designing and Constructing Fixed Offshore Platforms - Working Stress Design. American Petroleum Institute.

Axelsson, G. 1998. Long-term increase in shaft capacity of driven piles in sand. In *Proceedings of 4th International Conference on Case Histories in Geotechnical Engineering*, *St. Louis, Missouri.*

Buckley, R., Jardine, R., Kontoe, S., Parker, D., & Schroeder, F. 2018. Ageing and cyclic behaviour of axially loaded piles driven in chalk. *Géotechnique*, 68(2), 146-161.

Bullock, P. J., Schmertmann, J. H., McVay, M. C., & Townsend, F. C. 2005. Side shear setup. II: Results from Florida test piles. *Journal of Geotechnical Geoenvironmental Engineering,* 131(3), 301-310.

Chin, F. K. 1972. *The inverse slope as a prediction of ultimate bearing capacity of piles.* In *Proceedings of 2nd SE Asia Conference on Soil Engineering*, 1972.

Chow, F., Jardine, R., Brucy, F., & Nauroy, J. 1998. Effects of time on capacity of pipe piles in dense marine sand. *Journal of Geotechnical Geoenvironmental Engineering,* 124(3), 254-264.

Chung, S. G., Lee, N. K., & Kim, S. R. 2009. Hyperbolic method for prediction of prefabricated vertical drains performance. *Journal of Geotechnical and Geoenvironmental Engineering,* 135(10), 1519-1528.

DNV GL2017. DNVGL-RP-C212: Offshore Soil Mechanics and Geotechnical Engineering.

GEO. 2006. GEO Publication No. 1/2006: Foundation Design and Construction. Geotechnical Engineering Office, Civil Engineering Development Department, Hong Kong SAR.

Hosseinzadeh Attar, I., & Fakharian, K. 2013. Influence of soil setup on shaft resistance variations of driven piles: Case study. *International Journal of Civil Engineering* 11(2), 112-121.

Jardine, R. J. , Chow, F., Overy, R., & Standing, J. 2005. *ICP design methods for driven piles in sands and clays* (Vol. 112). Thomas Telford London.

Jardine, R. J., & Standing, J. R. 2012. Field axial cyclic loading experiments on piles driven in sand. *Soils and Foundations*, 52(4), 723-736.

Jardine, R. J. 2020. Geotechnics, energy and climate change: the 56th Rankine Lecture. *Géotechnique,* 70(1), 3-59.

Komurka, V. E., Wagner, A. B., & Edil, T. B. 2003. A review of pile set-up. In *51st Annual Geotechnical Engineering Conference*.

Kulhawy, F. H. 1984. *Limiting tip and side resistance: fact or fallacy?* In J. R. Meyer (ed.), *Analysis and design of pile foundations, New York: ASCE, 80-98.*

Labenski, J., & Moormann, C. 2016. A parametric study of different analytical design methods to determine the axial bearing capacity of monopiles. *Geomechanics for Energy the Environment,* 6, 70-80.

Lehane, B., Lim, J. K., Carotenuto, P., Nadim, F., Lacasse, S., Jardine, R., & Van Dijk, B. 2017. Characteristics of unified databases for driven piles. In *Proceedings of the 8th International Conference of Offshore Site Investigation and Geotechnics OSIG, London, UK.*

Lehane, B. M., Schneider, J., & Xu, X. 2005. The UWA-05 method for prediction of axial capacity of driven piles in sand. *Frontiers in Offshore Geotechnics: ISFOG*, 683-689.

Lehane, B. M., Chow, F., McCabe, B., & Jardine, R. 2000. Relationships between shaft capacity of driven piles and CPT end resistance. In *Proceedings of the Institution of Civil Engineers-Geotechnical Engineering,* 143(2), 93-101.

Lehane, B. M., Li, Y., & Williams, R. 2013. Shaft capacity of displacement piles in clay using the cone penetration test. *Journal of Geotechnical Geoenvironmental Engineering,* 139(2), 253-266.

Lehane, B. M., Schneider, J., & Xu, X. 2005. *A review of design methods for offshore driven piles in siliceous sand*. The University of Western Australia.

Poulos, H. G. 1988. Cyclic stability diagram for axially loaded piles. *Journal of Geotechnical Engineering,* 114(8), 877-895.

Puech, A. 2013. Design for Cyclic Loading: Piles and other Foundations. In *Proceedings of TC 209 workshop-18th ICSMGE, Paris*.

Randolph, M. F., & Gourvenec, S. 2011. *Offshore Geotechnical Egineering*. CRC Press.

Randolph, M. F. 2003. Science and empiricism in pile foundation design. *Geotechnique,* 53(10), 847-875.

Rausche, F., Goble, G. G., & Likins, G. E. 2010. *GRLWEAP 2010 Background Report*.

Schneider, J. A., Xu, X., & Lehane, B. M. 2008. Database assessment of CPT-based design methods for axial capacity of driven piles in siliceous sands. *Journal of Geotechnical Geoenvironmental Engineering,* 134(9), 1227-1244.

Tan, S. A. 1995. Validation of hyperbolic method for settlement in clays with vertical drains. *Soils and Foundations,* 35(1), 101-113.

Webster, S., Givet, R., & Griffith, A. 2008. Offshore pile acceptance using dynamic pile monitoring. In *Proceedings of the Eighth International Conference on the Application of Stress Wave Theory to Piles*. *Lisbon, Portugal*, 2008.

Yu, W., Qin, L., Li, X., Wang, A. M., Liang, L., & Givet, R. 2013. Application of high strain dynamic testing technique to underwater skirt pile foundation. In *The Twenty-third International Offshore and Polar Engineering Conference*. *Anchorage, Alaska, June 2013.*

Frost Depth Prediction for Seasonal Freezing Area in Lithuania

Mindaugas Zakarka, Šarūnas Skuodis
Department of Reinforced Concrete Structures and Geotechnics,
Vilnius TECH, Vilnius, Lithuania

ABSTRACT

The calculation of the frost depth is included in the geotechnical design for the Lithuanian region. The average temperature could be below zero for three months a year and maximum seasonal frost depth reaches more than 1.5 m. The analysis has shown that the frost has been declining for the last 200 years, which has intensified particularly in recent years. The purpose of this study is to review two different methods (LST EN ISO 13793 and RSN 156-94) for determining frost depths. The frost depth calculations performed for dry and saturated sandy soils, which are mainly observed in road construction. Obtained results are compared with frost depth map based on road weather stations data

1 INTRODUCTION

Frost depth is very actual for the countries in which territories experiencing negative temperature during winter time. One of the countries, where design rules demand to evaluate seasonal frost depth is Lithuania. The depth of frozen ground in Lithuania was started to be measured in 1923 (Juknevičiūtė et al. 2008). In Lithuania, since 1994 there have been national frost depth evaluation rules according to RSN 156-94, which were update in 2002. Before issue of RSN 156-94 in Lithuania, SNirT 2.01.01-82 was valid. Later, when Lithuania became a European Union member in 2004, soil frost depth can be also evaluated by LST EN ISO 13793. Permafrost (Slade et al. 2020; Tinivella et al. 2019) in territory of Lithuania does not exist and it is not evaluated.

Two different technical documents of freezing depth evaluation (RSN 156-94 and LST EN ISO 13793) give two different results. The difference is also obtained between theoretical frost depth evaluation according to technical documents (RSN 156-94 and LST EN ISO 13793) and data measured at weather stations (Vaitkus et al. 2016). Also, due to climate change (Rimkus et al. 2006) and average annual temperature increase, more freezing thawing cycles (Shirmohammadi et al. 2021; Sadeghi et al. 2018) appear during one winter period. According to weather prognosis in Lithuania, maximum precipitation quantity will also increase up to 15% and largest precipitation increment will be during winter with increment up to 24% (Skuodis et al. 2021). Due to rising annual average temperatures (Galvonaitė et al. 2013), increasing amounts of winter precipitation will be drizzle and sleet (Skuodis et al. 2021).

This research paper is oriented to soils, which are mostly used in road construction. That means, soil frost depth must be evaluated without snow coverage (Roustaei et al. 2022; Iwata et al. 2018). Main Lithuanian roads are divided into different temperature and freezing index areas and calculations of frost depths are provided. Obtained results are compared with existing data collected at road weather stations (Vaitkus et al. 2016). After comparison of theoretical and measured frost depth results, most suitable frost depth theoretical method is suggested, which gives similar results to measured data.

2 ENVIRONMENTAL CONDITIONS

Average annual temperature in Lithuania in 1981-2010 was 6.9 °C and average decadal air temperature since 1961–1970 increased from 5.8 °C up to 7.3°C in 2001–2010 (Galvonaitė et al. 2013). Officially measured absolute minimum air temperature in Lithuania is -42.9 °C, but in most parts of Lithuania, negative maximum air temperature is observed 50–60 days per year, the lowest number of such days is on the coast (30 days per year), and highest number is in the north-eastern part (70 days) (Galvonaitė et al. 2013). Kabailienė (2006) prepared Lithuania average annual temperature map (Fig. 1) for period in 1961-1990. Lithuanian Hydrometeorological Service (2021) prepared Lithuania average annual temperature map (Fig. 1) for period in 1991-2020.

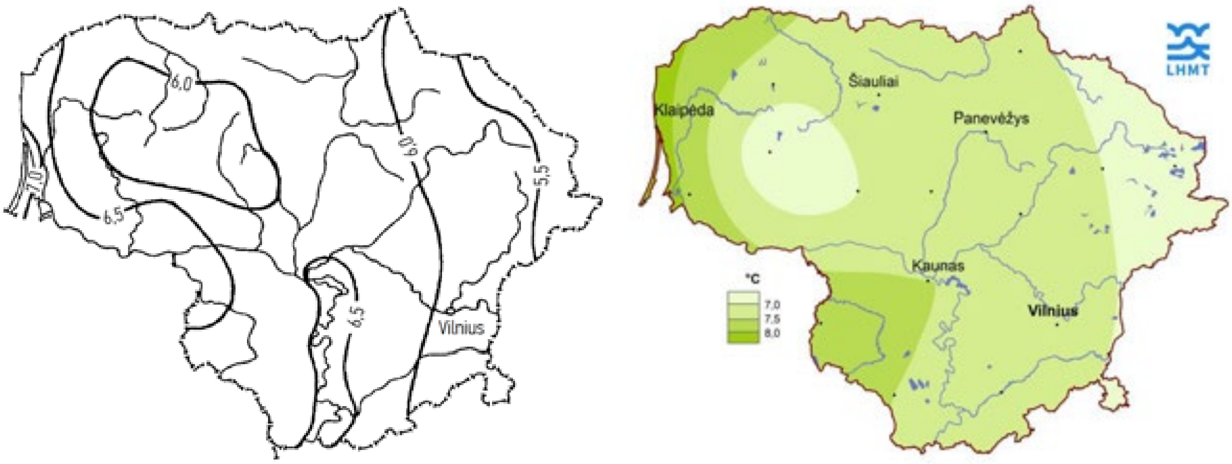

Figure 1. Lithuania average annual air temperature °C in different periods: on the left – 1961-1990 (Kabailienė, 2006), on the right – 1991-2020 (Lithuanian Hydrometeorological Service, 2021)

Sližytė et al. (2012) prepared freezing index (FI) map for Lithuanian area (Fig. 2). This map of FI is based on average decadal air temperature since 1961–1970 (average temperature 5.8 °C). Later, Vaitkus et al. (2016) prepared FI map for Lithuania territory (Fig. 2), which is less accurate (only three areas are included), but based on 2012–2014 average annual temperature.

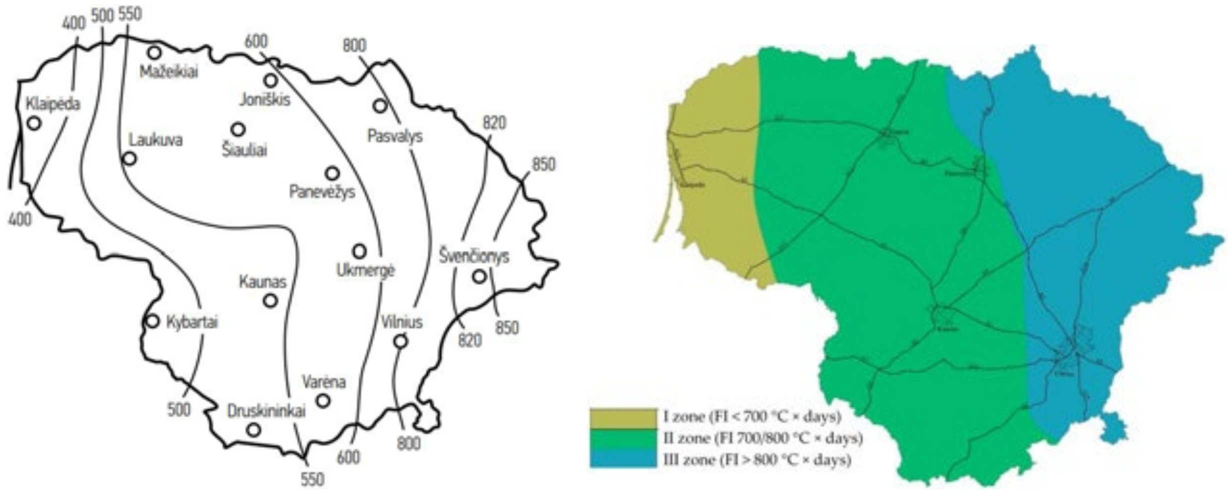

Figure 2. Lithuania territory division to FI: on the left – according to average annual air temperature in 1961–1970 (Sližytė et al. 2012), on the right – according to average annual air temperature in 2012–2014 (Vaitkus et al. 2016)

Vaitkus et al. (2016) performed statistical analysis of 2012–2014 data pertaining to 26 road weather stations and prepared Lithuania frost depth map (Fig. 3). The real-time data from road weather stations are automatically registered every 30 min in a warm period and every 12 min in a cold period (Žilinksienė et al. 2015). Frost depth analysis showed that maximum frost depths vary from 110.4 cm to 179.1 cm.

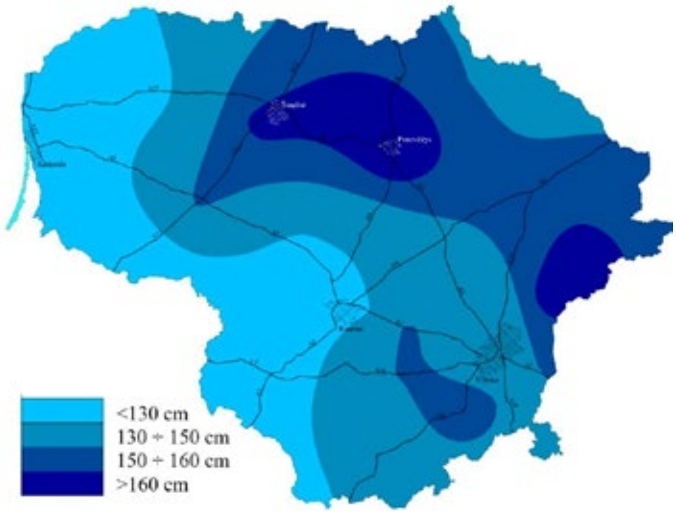

Figure 3. Lithuania frost depth map based on road weather stations data (Vaitkus et al. 2016)

3 FROST DEPTH EVALUATION

As it was mentioned in the introduction part, frost depth evaluation in the Area of Lithuania can be evaluated according to RSN 156-94 and LST EN ISO 13793. First of all, in this manuscript it is presented LST EN ISO 13793 frost depth evaluation methodology. LST EN ISO 13793 provides formula for calculating the frost depth H_0:

$$H_0 = \sqrt{\frac{7200 \cdot F_d \cdot \lambda_f}{L + C \cdot \theta_e}} \tag{1}$$

where freezing index F_d:

$$F_d = 24 \sum (\theta_f - \theta_{d,j}) \tag{2}$$

where:

Symbol	Description	Units of measurement
F_d	Design freezing index	K·h
λ_f	Thermal conductivity of frozen soil	W/(m·K)
L	Latent heat of freezing of water in the soil per volume of soil	J/m^3
C	Heat capacity of unfrozen soil per volume	J/(m^3·K)
θ_e	Annual average external air temperature	°C
θ_f	Equal to 0°C	°C
$\theta_{d,j}$	Daily mean external air temperature for day j	°C

It is generally accepted to use daily mean external air temperature data ($\theta_{d,j}$) under Lithuania average annual temperature map (Fig. 1) for period in 1961-1990. Data have been updated in the face of climate change. Lithuanian Hydrometeorological Service (2021) prepared Lithuania average annual temperature map (Fig. 1) for period in 1991-2020.

It is worth to note that LST EN ISO 13793 standard does not provide thermal properties for different soil types. The recommended characteristics λ_f, L and C are given in the general case based on homogeneous frost-susceptible soil (Table 1). For different soils, actual thermal property λ_f can be found in VDI 4640-4 (Table 2).

Table 1: Thermal properties of frost-susceptible soil (LST EN ISO 13793)

Description	Thermal properties
Thermal conductivity (unfrozen)	$\lambda = 1.5$ W/(m·K)
Thermal conductivity (frozen)	$\lambda_f = 2.5$ W/(m·K)
Heat capacity per volume (unfrozen)	$C = 3 \cdot 10^6$ J/(m^3·K)
Heat capacity per volume (frozen)	$C_f = 1.9 \cdot 10^6$ J/(m^3·K)
Latent heat of freezing per cubic meter of soil dry density	$L = 150 \cdot 10^6$ J/m^3

Table 2: Thermal properties for different soils (VDI 4640-4)

Ground type	Thermal conductivity λ_f, in W/(m·K)	Typical calculated value
Sand, dry	0.3 to 0.8	0.4
Sand, water-saturated	1.7 to 5.0	2.4
Gravel, dry	0.4 to 0.5	0.4
Gravel, water saturated	Approx. 1.8	1.8
Clay or silt, dry	0.4 to 1.0	0.5
Clay or silt, water-saturated	0.9 to 2.9	1.7
Peat	0.2 to 0.7	0.4

Calculation of the frost depth d_f can be realized according to RSN 156-94:

$$d_f = d_0 \cdot \sqrt{M_t} \tag{3}$$

where d_0 = frost depth when $M_t = 0$, M_t = sum of non-dimensional coefficient of negative monthly temperatures, absolute value.

The frost depth d_0 depends on the soil type and is equal to:

Clay and sandy loam – 23 cm;

Clayey or silty sand, silt and fine sand – 28 cm;

Medium coarse sand, coarse sand and gravelly sand – 30 cm.

Frost depth d_0 calculations lead to the problem related to classification of soil based on non-valid normative documents. According to the actual normative documents (LST EN ISO 14688-1), clay and sandy loam classified as sandy clay (saCl) and clayey or silty sand, silt and fine sand classified as sandy clay (saCl), clayey sand (clSa) or silty sand (siSa). Also, there is a difference between geotechnical and road soil classification (Table 3).

Table 3: Compliance with soil labeling (LST 1331:2015)

LST 1331:2015	LST EN ISO 14688-1
ŽB, ŽG, ŽP, ŽD, ŽM	Gr
SB, SG, SP, SD, SM	Sa
ŽD0	siGr
ŽM0	clGr
SD0	siSa
SM0	clSa
DL, DV, DR	Si
ML, MV, MR	Cl
OD, OM, OH	orSi, orCl, orSa
HU, HN	Or

In order to find the M_t (3), it is necessary to evaluate monthly air temperatures. For this investigation it was chosen to analyze four main cities in Lithuania territory, namely: Klaipėda, Kaunas, Vilnius and Utena (Table 4).

Table 4: Average monthly air temperature in °C (RSN 156-94)

Air measuring station	Months											
	1	2	3	4	5	6	7	8	9	10	11	12
Klaipėda	-2.8	-2.6	0.3	5.0	10.6	14.3	16.6	16.8	13.3	9.0	3.9	-0.1
Kaunas	-5.2	-4.3	-0.4	5.8	12.4	15.8	16.9	16.4	11.9	7.1	1.8	-2.3
Vilnius	-6.1	-4.8	-0.6	5.7	12.5	15.8	16.9	16.3	11.6	6.6	1.2	-2.9
Utena	-6.0	-5.2	-1.2	5.5	12.2	15.6	16.8	15.9	11.4	6.6	1.4	-3.2

The design value of frost depth d_{fd} can be found:

$$d_{fd} = k_h \cdot d_f \tag{4}$$

where k_h = temperature coefficient (the frost depth was calculated for a road structure that is not affected by constant heat (as it could be for buildings case), therefore $k_h = 1$).

The results of frost depths calculated by five different methods (Figure 4). First calculation is realized according to LST EN ISO 13793 using 1961-1990 temperature data. Second calculation is provided by LST EN ISO 13793 using 1991-2020 temperature data. Third and fourth calculations are based on LST EN ISO 13793 methodology, but it used VDI 4640-4 actual thermal properties for different soils (dry and saturated cases). The last calculation of frost depth is accomplished with RSN 156-94 methodology. For all cases it was assumed, that frost depth is evaluated for sandy soil type.

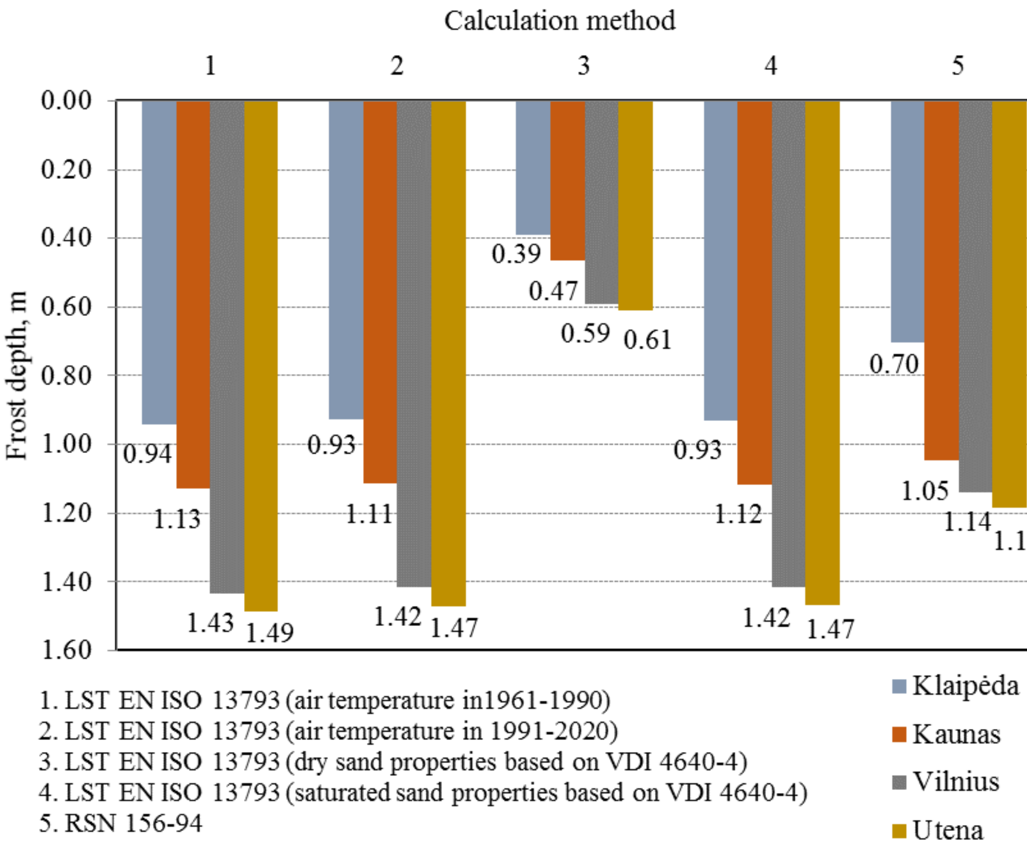

Figure 4: Summary of frost depth evaluation in different cities

The results of frost depths evaluation by different methods (Figure 4) showed that Lithuania's average annual temperature increased approx. 1.5 °C, but frost depth decreased about 1-2 cm (Figure 4, calculation methods 1 and 2). The smallest frost depth is obtained for dry sand (Figure 4, calculation method 3). Evaluating actual thermal properties given in VDI 4640-4 and using those properties in LST EN ISO 13793 methodology for frost evaluation (Figure 4. Calculation method 4), very similar results are obtained for Figure 4 (calculation methods 1 and 2). Frost depth evaluation by RSN 156-94 (Figure 4, calculation method 5) gives smaller frost depth results comparing with LST EN ISO 13793 (Figure 4, calculation methods 1 and 2). Comparison of Lithuania frost depth map based on road weather stations data (Figure 3) and calculated frost depths (Figure 4) are presented in Table 5.

Table 5: Summary of frost depth evaluation in different cities

Area\Method	Road weather stations data (Vaitkus et al. 2016)	LST EN ISO 13793 (air temperature in 1961-1990)	LST EN ISO 13793 (air temperature in 1991-2020)	LST EN ISO 13793 (dry sand properties based on VDI 4640-4)	LST EN ISO 13793 (saturated sand properties based on VDI 4640-4)	RSN 156-94
Klaipėda	<1.30 cm	0.94 cm	0.93 cm	0.39 cm	0.93 cm	0.70 cm
Kaunas	<1.30 cm	1.13 cm	1.11 cm	0.47 cm	1.12 cm	1.05 cm
Vilnius	1.30-1.50 cm	1.43 cm	1.42 cm	0.59 cm	1.42 cm	1.14 cm
Utena	1.50-1.60 cm	1.49 cm	1.47 cm	0.61 cm	1.47 cm	1.18 cm

The most similar frost depth evaluation results are obtained by using LST EN ISO 13793 method using actual saturated soil thermal properties according to VDI 4640-4. Evaluation of dry sand thermal properties is not recommended, because calculated frost depths are almost three times smaller than those measured at the road weather stations. Frost depth results obtained by RSN 156-94 method are lower than those obtained by LST EN ISO 13793. For road construction frost depth evaluation, it is not recommended to use RSN 156-94 method, because calculated frost depth values are too small.

4 CONCLUSIONS

Frost depth evaluation methodology is very important for final results. Realized different calculations of frost depth showed main differences between LST EN ISO 13793 and RSN 156-94. Frost depth calculations according to LST EN ISO 13793 showed that for sandy soil it is obtained almost the same results in both evaluated cases: 1) calculating by LST EN ISO 13793 suggested soil thermal properties; 2) calculating by LST EN ISO 13793 and using actual saturated soil thermal properties, which can be found in VDI 4640-4. It is not recommended to use dry soil thermal properties given in VDI 4640-4, because predicted frost depth decreases approx. 3 times. Frost depth results obtained by RSN 156-94 method are lower than those obtained by LST EN ISO 13793. For evaluation of road construction frost depth, it is recommended to use LST EN ISO 13793 based on air temperature in 1961-1990 and applying actual saturated soil properties, which are given in VDI 4640-4. Such evaluation gives the most similar frost depth results to those measured at road weather stations.

REFERENCES

Galvonaitė, A., Valiukas, D., Kilpys, J., Kitrienė, Z. & Misiūnienė, M. 2013. Climate atlas of Lithuania. *Lithuanian Hydrometeorological Service*, 176 p.

Iwata, Y., Yanai, Y., Yazaki, T. & Hirota, T. 2018. Effects of a snow-compaction treatment on soil freezing, snowmelt runoff, and soil nitrate movement: A field-scale paired-plot experiment. *Journal of Hydrology*, 567(2018): 280-289.

Juknevičiūtė, L. & Laurinavičius, A. Analysis of the change in the depth of frozen ground in different soils under Lithuanian conditions. *The 7th International Conference Environmental Engineering, Vilnius, 22-23 May, 2008*. Vilnius Gediminas Technical University.

Kabailienė, M. 2006. Gamtinės aplinkos raida Lietuvoje per 14 000 metų. *Vilnius: Vilniaus universiteto leidykla*, 471 p.
Lithuanian Hydrometeorological Service 2021. Map of mean annual air temperature in Lithuania (1991–2020) http://www.meteo.lt/en/web/guest/weather-temperature
LST EN ISO 13793:2002 Šiluminės statinių charakteristikos. Pamatų šiluminių parametrų apskaičiavimas siekiant išvengti pamatų peršalimo. *Vilnius: Lietuvos standartizacijos departamentas*, 48 p.
LST EN ISO 14688-1:2018 Geotechniniai tyrinėjimai ir bandymai. Gruntų atpažinimas ir klasifikavimas. 1 dalis. Atpažinimas ir aprašymas. *Vilnius: Lietuvos standartizacijos departamentas*, 25 p.
LST 1331:2015 Gruntai, skirti keliams ir jų statiniams. Klasifikacija. *Vilnius: Lietuvos standartizacijos departamentas*, 13 p.
Rimkus, E., Bukantis, A. & Stankūnavičius, G. 2006. Klimato kaita: faktai ir prognozės. *Geologijos akiračiai*, 2006: 10-20.
Roustaei, M., Hendry, M.T. & Roghani, A. 2022. Investigating the mechanism of frost penetration under railway embankment and projecting frost depth for future expected climate: A case study. *Cold Regions Science and Technology*, 197(2022): 1-16.
RSN 156-94. Statybinė klimatologija. 1995. *Vilnius*, 136 p.
Sadeghi, S.H., Raeisi, M.B. & Hazbavi, Z. 2018. Influence of freeze-only and freezing-thawing cycles on splash erosion. *International Soil and Water Conservation Research*, 6(2018): 275-279.
Sladen, W.E., Wolfe, S.A. & Morse, P.D. 2020. Evaluation of threshold freezing conditions for winter road construction over discontinuous permafrost peatlands, subarctic Canada. *Cold Regions Science and Technology*, 170(2020): 1-11.
Shirmohammadi, S., Jahromi, S.G., Payan. M., & Senetakis, K. 2021. Effect of lime stabilization and partial clinoptilolite zeolite replacement on the behavior of a silt-sized low-plasticity soil subjected to freezing–thawing cycles. *Coatings*, 11(994): 1-21.
Skuodis, Š., Michelevičius, D., Damušytė, A., Valivonis, J., Medzvieckas, J., Šneideris, A., Jokubaitis, A. & Daugevičius, M. 2021. The engineering geological and geotechnical conditions of Gediminas Hill (Vilnius, Lithuania): an update. *Geological Quarterly*, 65(42): 1-13.
Sližytė, D., Medzvieckas, J. & Mackevičius R. 2012. Pamatai ir pagrindai. *Technika*, 248 p.
SNirT 2.01.01-82 „Statybinė klimatologija ir geofizika“.
Tinivella, U., Giustiniani, M. & Marin-Moreno, H. 2019. A Quick-Look method for initial evaluation of gas hydrate stability below subaqueous permafrost. *Geosciences*, 9: 1-13.
Vaitkus, A., Gražulytė, J., Skrodenis, E. & Kravcovas, I. 2016. Design of frost resistant pavement structure based on road weather stations (RWSs) data. *Sustainability*, 8: 1-13.
VDI 4640-4:2004 Thermal use of the underground direct uses. *Verein Deutscher Ingenieure, Düsseldor*, 40 p.
Žilinskienė, L.J. & Laurinavičius, A. 2015. Evaluation of frost depth for the climatic distribution of regions from the point of view of road construction. *The Baltic journal of Road and Bridge Engineering*, 10(3): 262-268.

Underground Development - Pipe Curtain with Jack-in place Rectangular Tunnel Boring Machine Technology

Zhang Zhen, K M Chiang, Leo Man
Shanghai Tunnel Engineering Co., Ltd., Hong Kong, China

ABSTRACT

With the recent successful application of Rectangular Tunnel Boring Machine (RTBM) Jack-in place technology in Hong Kong, more interest is put into its wider use. However, the application of RTBM is restrained by geological limitations, such as shallow overburden depth, limited span depth ratio of the tunnel (< 2), etc. Advanced underground construction technology – the adoption of systematic pipe curtain with Jack-in place RTBM methodology- was introduced recently in China and Overseas to construct underground railway tunnels, stations, pedestrian subways, and underpass in challenging congested urban areas. This advanced methodology focuses on underground structures construction in which stringent settlement control with shallow overburden cover is required. It also possesses the flexibility to adapt to different sizes of cross-sections, which makes wide span (>20m) underground structures can be constructed by the trenchless method. Given the future of Hong Kong infrastructure development, this paper is aimed to explore the potential for developing underground space based on this advanced solution to resolving problems in an old and congested urban area. Taking past successful project experiences in Mainland China as examples, this paper has discussed the geological requirements, construction method, sequence, ground settlement performance, etc. It also provides consideration that should be aware of the adoption of technology in typical Hong Kong geological conditions. The RTBM technology offers a new solution to the infrastructure development projects in Hong Kong with better buildability, safety and productivity.

1. Introduction

With the continuous urban development, a large number of existing facilities (roads, railways, municipal pipelines, etc.), three-dimensional intersection projects and underground passage projects have emerged. These projects can resolve the traffic bottlenecks formed by the construction of existing facilities, which are of great significance for alleviating the problem of regional traffic congestion and can substantially improve the travel efficiency of the entire transportation network. However, the surrounding environment of such projects is complex, often characterised by heavy regional traffic, limited construction land and underground space availability. With the increasing public engagement in modern society, when constructing the underpass structures under the existing facilities, the public demands stringent requirements on construction safety and less impact on the surrounding environment, which makes the trenchless technology face high challenges.

The successful completion of a subway structure using the jack-in-place RTBM technology has proved that mechanical construction methodology can effectively fulfil safety and environmental concerns. This paper is aimed to explore another dimension of this automated technology by discussing the limitation of the technology itself, introducing an advanced approach, a combination of systematic pipe curtain technology together with RTBM to deal with the more complex underground condition. Case studies for projects in Mainland China have demonstrated the potential for broader application of RTBM methodology to achieve higher productivity, better safety and environmental control in a construction project that benefits future development in Hong Kong.

2. Limitation of Jack-in-place RTBM methodology

auxiliary	Trenchless methodology		
	Jack-in-place Segment RTBM	**New Austrian Tunnelling Method (NATM)**	**Large dia. TBM**
Cross-section span	Width W ≤ 12m	Unlimited in theory	Dia. $D \leq$ 17m
Shallowest overburden	1.0 *D*	3 m	1.0 *D*
Cross-section utilization	★★★★	★★★★	★★
Flexibility of cross-section	★★★	★★★★★	★★
Disturbance to ground	★★★	★★	★★★★
Site utilisation	Less demanding	Less demanding	Demanding
Safety	★★★★	★★	★★★★
Construction cost	★★★★	★★★★★	★★★★
Construction period	Short for <200m	Long	Short for long tunnel

Figure 1 Comparison of common trenchless methodology

Figure 1 compares three trenchless technologies in terms of several important elements for a construction project. The advantages of using the jack-in-place segment RTBM method to construct underground structures are significant, especially in short distances (< 200m) in subway structures construction; its effectiveness is outstanding. In mainland China, the technology has been applied in other scenarios, such as vehicular underpass, underground podium construction, etc. In a recent project in HK using this technology, the internal structure envelope formed by the machine is 9m in width, and 5m in height (on average), which has demonstrated its potential usage in other underground structures construction. However, this leads to two major limitations. The first is the overburden depth. In general, 1.0D overburden depth is required when designing using the jack-in-place segment RBM structure, which implies a deep structure invert level for the pedestrian subway or a longer slip road for the vehicular underpass. The second one is the span width of the structure to be built; due to the potential hazard of the "Segment-crown soil carrying effect" (a phenomenon observed in jack-in-place segment RTBM technology that can cause severe ground structure disturbance), the span width of the machine is limited to 12m. Those two constraints limit the technology usage flexibility and its potential to apply in structures where a wider cross-section is needed.

Advanced technology is introduced to overcome these two shortfalls, known as the systematic pipe-curtain method. In simple terms, this is an upgraded version of the pipe roofing method. The combination of systematic pipe-curtain with jack-in-place segment RTBM method has the characteristics of minimum environmental impact, strong soil adaptability, and flexible cross-section layout. By adjusting the layout of the pipe curtain and the prefabrication of the segment lining components, tunnel or subway structures passing through complex existing structures or utilities is feasible and has very high cost-effectiveness for short-distance crossing in congested urban areas.

3. Characteristics of the pipe curtain construction method

The pipe curtain with jack-in-place segment RTBM construction method refers to the methodology of using the rectangular TBM drilling through an underground horizontal section which is protected by the formed pipe curtain to construct the underground structure. The pipe curtains are connected by standard male and female sockets with grouting, which can create a watertight curtain closure. It is different from the typical interlocking pipe pile in which special design steel pipes connect each other without any protruding part.

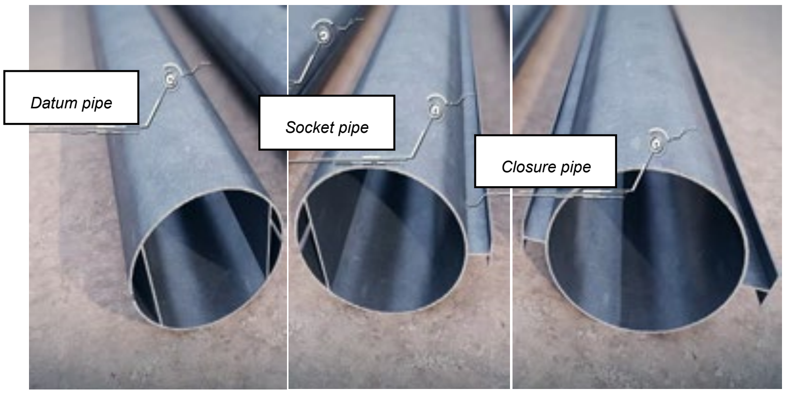

Special pipe locking design

The high precision hidden type pipe interlocking design effectively controls the alignment of the pipes installation

Figure 2 Hidden type interlocking pipeline arrangement

Figure 2 shows the typical arrangement of the unique design pipelines, which are installed by a mini-pipe jacking machine with laser target alignment control. The machine is equipped with a multi-level articulation system to control the pipe installation, as shown in Figure 3. With the systematic interlocking pipe arrangement, the technology can ensure the pipe curtain is formed precisely and with minimum impact on the surrounding environment.

Figure 3 Mini-pipe jacking machine for pipe installation

The pipe curtain can be formed in a different shape to suit the structure requirement. Once these pipelines protection is formed, the jack-in place segments by the RTBM can be installed within this protected zone.

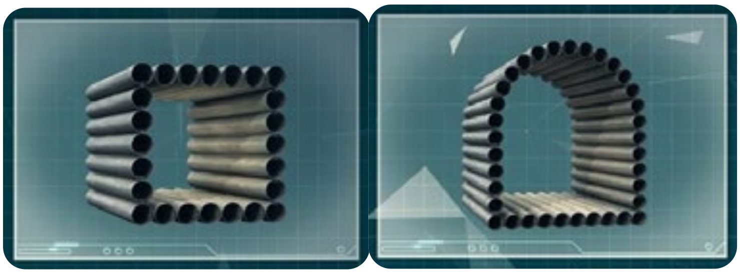

The pipe curtain effectively controls the impact on the ground caused by the segment jacking operation. Combining two technologies, five advantages for underground structure construction can be achieved, as shown in Figure 4.

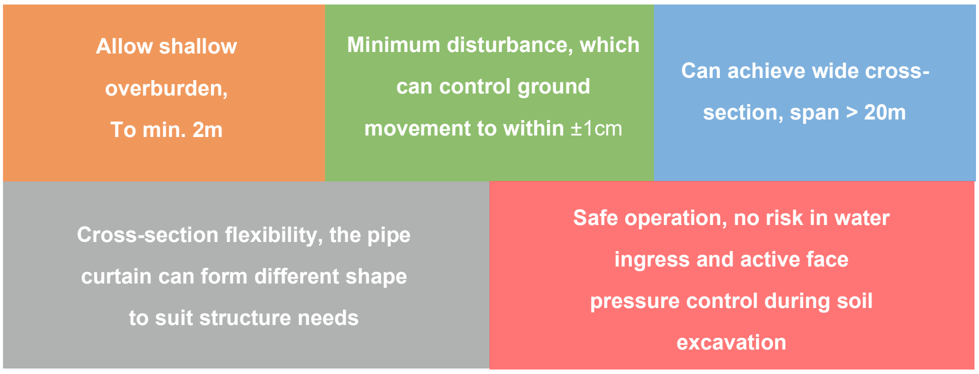

Figure 4 Five major advantages of systematic pipe curtain with RTBM methodology

4. Construction Sequences

The construction sequences for pipe curtain RTBM methodology are mainly divided into two stages: One is pipe curtain installation and segment installation. The other is a common launching and receiving shaft that will be constructed for both activities, and its setup requirement is similar to a RTBM construction site.

Step 1 - Setup

Setup a jacking platform inside the launching shaft. The tunnel eye seal will be installed at each break-out location. Remove the sheetpile or RC wall at each break out position. Install and commission the pipe jacking machine and the supporting system. After the preparations are completed, pipe jacking will commence.

Step 2 – Jack in the datum pipe

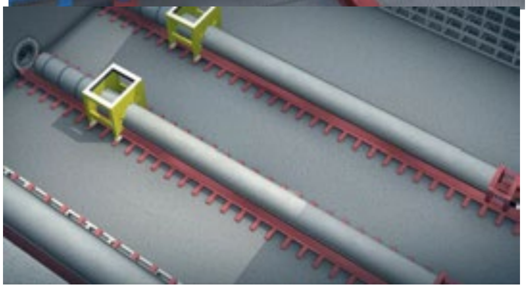

Pipe curtain steel pipe can be divided into three types: datum pipe, socket pipe and closure pipe. Both sides of the datum pipe are female locks, which is the starting point of the pipe curtain's construction, so it requires high precision control.

Step 3 – Jack in socket pipe

The lock of the socket-intubation pipe consists of a male lock and one or more female locks. After the jacking of the datum pipe is completed, insert the male lock of the first socket pipe into the female lock of the adjacent datum pipe, and then start the jacking of the subsequent socket pipes one by one. During the process, insert the male locks of the socket pipe into the female locks of the adjacent socket pipe in turn until the entire pipe curtain is about to close.

Step 4 – Jack in closure pipe

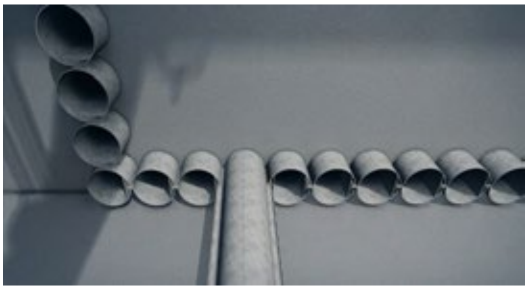

The lock of the closure pipe consists of one or more male locks. Each male lock of the closure pipe needs to be inserted into the female lock of the adjacent steel pipe to form a closed-up structure. In the process of pipe curtain construction, a pipe curtain system generally consists of one reference pipe and a closed pipe. In case of achieving a shorter construction period, multiple datum pipes and closure pipes can also be configured according to the programme to allow numerous pipes to be jacked simultaneously. In order to reduce the jacking resistance, lubricant grout will be injected into the female lock during the jacking process.

Step 5 – Replacement grouting

After the whole pipe curtain system is installed, replace the lubricant grout with high strength cementitious grout to reduce the post-construction settlement and improve the water tightness of the pipe curtain system.

Step 6 – Concrete infill

To ensure that the pipe curtain has good rigidity in the subsequent excavation process, self-compacting concrete is filled into the steel pipes. If stringent monitoring requirement is needed, monitoring devices can also be embedded into several steel pipes of the curtain together with the concrete infill to act as a monitoring datum before subsequent excavation work is conducted.

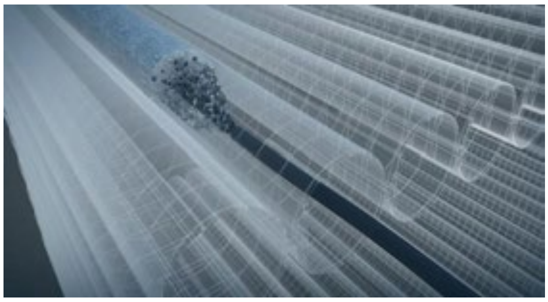

Step 7 – Tunnel eye portal

Finally, a tunnel eye portal will be constructed to join all the steel pipes together to form a pipe curtain ring beam. Thus, the closed steel pipe curtain is completed.

After the pipe curtain is completed, the soil within the curtain will be excavated. The excavation method can refer to the other technical paper regarding the jack-in-place segment RTBM methodology.

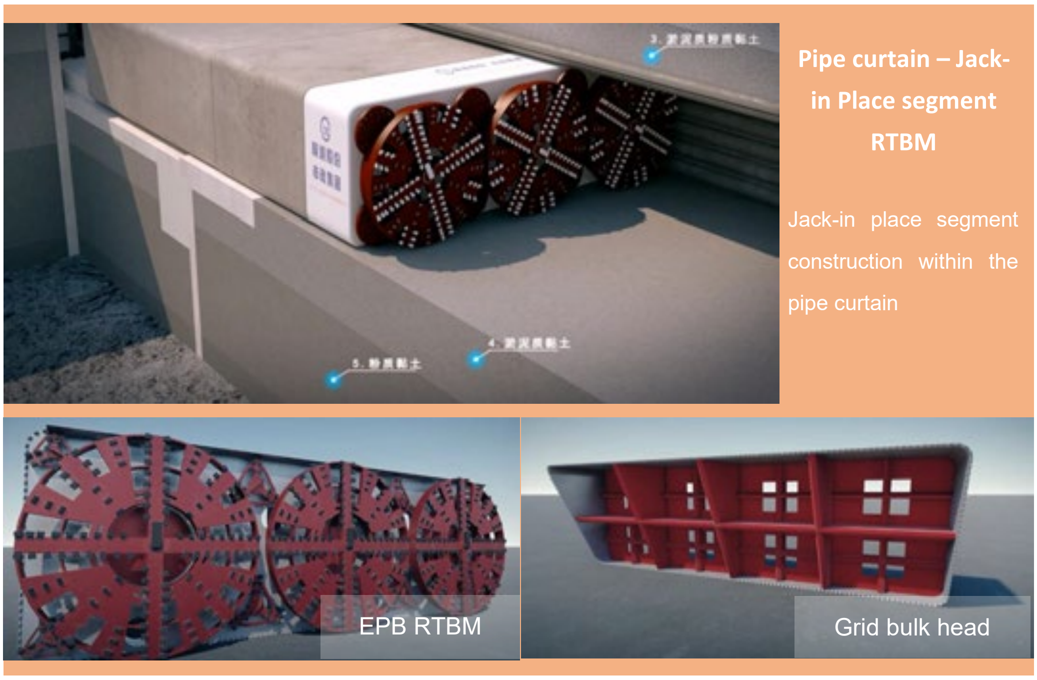

Figure 5 Jack-in place segment RTBM

According to the ground conditions, different types of drilling machines can be selected. The permanent structure can be cast in situ, prefabricated, or combined depending on the availability of construction space, logistics and lifting capacity. During the structure jacking process, the posture of the excavation machine can be precisely controlled by adjusting the synchronous jacking system and the front face pressure developed at the bulkhead of the excavation machine. The pipe curtain system, together with the RTBM technology, will provide double assurance to prevent excessive ground settlement even for wide span rectangular structures. Similar to the normal RTBM process, lubricant grouting will be injected during the process. Once all the permanent structures are jacked in place, the whole lubricant grouting will be replaced by annulus replacement grout to complete the entire process.

5. Case Study

1) Project Overview

Tian Lin Road underpass under the Middle Ring Road (Transportation Node Improvement Project on the Middle Ring Line)

Figure 6 Site setup on Tian Lin Road

The project is located in the middle of Cao He Jing Development Zone, Xuhui District (City center) in Shanghai, China. It is part of the transportation improvement project on Middle Ring Road and Tian Lin Road interchange which is a 1032.78 meters long expressway across the Shanghai city center. The starting and ending chainage of the underpass structure intersecting with the Middle Ring Road is at chainage K0+663~ K0+749, the underpass length is 86m, with the structure's top soil cover is 6.3m. The design cross-section of the underpass structure is 19.8m in width and 6.4m in height to allow three traffic lanes for two directions and two subway passages. In general, the whole structure is located in silty clay geology conditions.

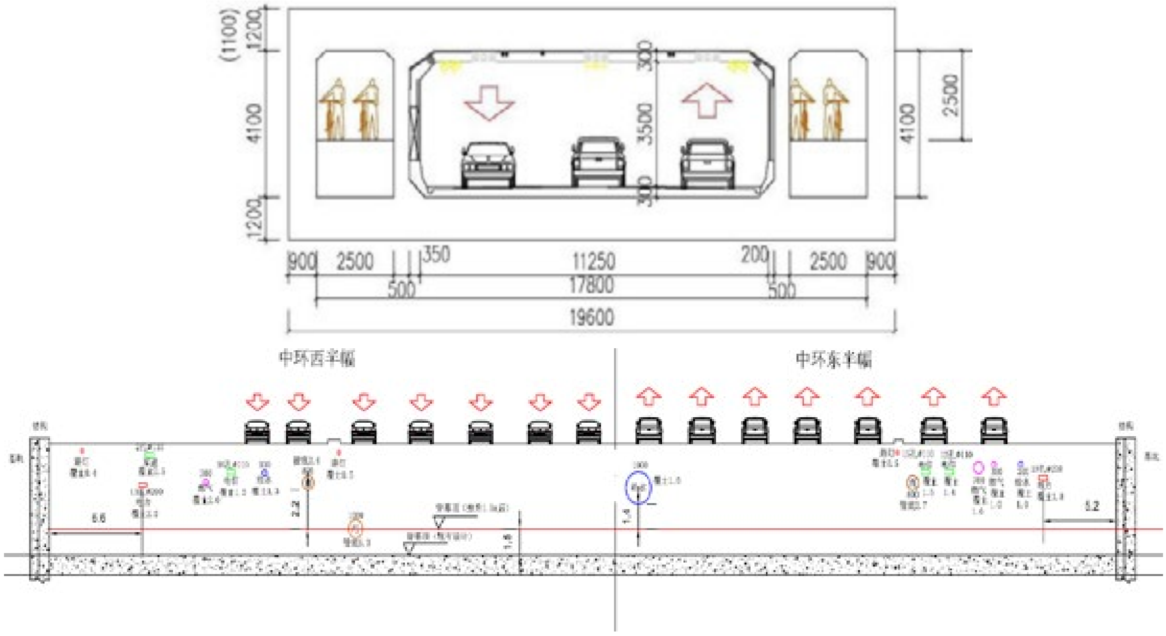

Figure 7 Tin Lin Road Underpass General arrangement

As shown in Figure 7, there are more than 20 nos of existing utilities/pipelines on the Middle Ring Road, which had intersected with the Tian Lin Road underpass structure, including electric power cables, communication cables, water supply pipelines, coal-gas supply pipelines, storm drain, sewage drain, and national defense optical cables. Among them the 1000mm dia. sewage pipe on the auxiliary road on the west side of the Middle Ring Road (the covering depth is about 4.2m) and the 1800mm dia. water supply pipe at the lower part of the central green verge of the Middle Ring Road (the covering soil depth is about 2.0m) are the closest to the top of steel pipe curtain. The minimum clear distance between the sewage pipe foundation and the top of the steel pipe curtain is only 0.5m.

2) <u>Construction process design of the pipe curtain</u>

A mini pipe jacking machine was used in advance to jack 62 steel pipes one by one at the outer periphery of the underpass. During the construction stage, four monitoring pipes were set up according to the jacking sequence of the steel pipe curtain. At the same time, in order to ensure the jacking accuracy of the pipe curtain and reduce the deformation of the underground pipeline and the settlement of the Middle Ring Road caused by multiple pipe jacking, the jacking sequence of the pipe curtain is as

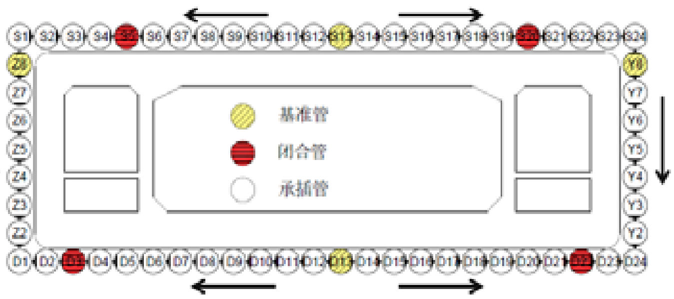

Figure 8 Pipe curtain jacking sequence

follows, first installing the lower row, then the upper row, from the middle pieces toward both sides. The side rows are installed from top to bottom.

Figure 9A Pipe curtain jacking in process

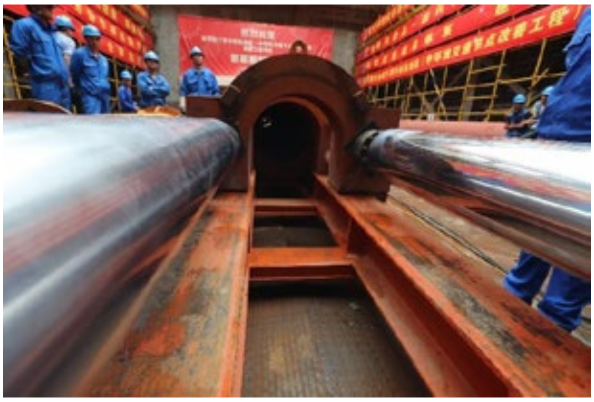

Figure 9B Close up view of jacking cylinder

The construction tolerance between the steel pipe curtain and the underpass structure is set as follows: the upper row to the structure's top level is 10 cm, and the left and right sides are 10 cm.

The whole underpass structure is divided into five sections, the first section is 12.4m, and the last four sections are 18.8m each. Every section is constructed within the launching shaft and jacked forward one by one. A wide span EPB RTBM is deployed to muck out the soil within the steel pipe curtain. By controlling the active front face pressure of the machine, it can effectively control the deformation and settlement of the pipe curtain section during the excavation process. It is assumed that the surrounding frictional resistance to the circumference of the underpass structure is 20 kN/m2. During the construction stage, the actual measured maximum jacking force is 6,687 tons when the last section of the underpass structure (section 5) is jacked, which is equivalent to frictional resistance 5 kN/m2 on the circumference of the underpass structure. It has been proved that by using the automatic lubricant injection system, a lubricant layer is established between the pipe curtain and the underpass structure.

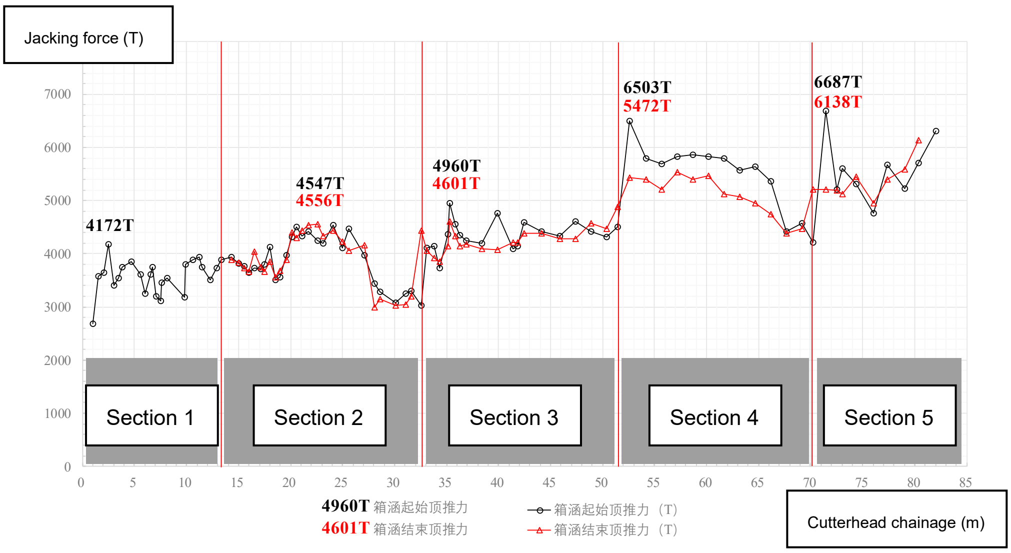

Figure 10 Measured jacking force during the segment jack-in process

The pipe curtain effectively reduces the loss of lubricant to the surrounding soil, thus reducing the requirement of total jacking force for the operation.

3) Equipment selection

The pipe jacking machine for the pipe curtain adopts the special pipe jacking machine for the 824mm dia. slurry machine.

Major components	Unit	Spec.
Machine dia.	mm	824
Length of machine	mm	3,600
Cutterhead power	kW	15
Torque	kN.m	23.3
Rotation speed	r/min	0—8
No. for articulation cylinder	Pcs	4
Articulation force	kN	375
Articulation cylinder stroke	mm	30
Re-adjusting angle	°	±2
Slurry pipe dia.	mm	100

Figure 11 Specification for the mini pipe jacking machine

The selection of the cutter head of the pipe jacking machine for the pipe curtain takes into account that the foundation of the underground pipeline is only 0.5m away from the pipe curtain. As the machine is relatively small in size using 100mm dia. slurry pipe, the gravel/cobbles fill near the pipeline foundation, which may block the slurry discharge pipeline during the construction, will be treated by the secondary crushing devices equipped with the machine to crush it down to less than 20mm. The opening ratio is adjusted to 8%, which effectively supports the front soil and reduces the settlement. The opening ratio is the percentage of opening portion on cutterhead to the total area of the cutterhead.

The RTBM's section is 19.84m×6.42m, and there is a 20mm overcut to the top and both sides of the underpass structure. There are three 6360mm dia. main cutterheads and eight small cutterheads setup at the blind spots, and the coverage reaches 92% of the whole section. The blind spots are provided

Figure 12 RTBM cutterhead and jacking arrangement

with a splitting device and a high-pressure water injection port, further enhancing mucking out ability of the machine.

The main jacking system for the RTBM uses 70nos of 250T hydraulic cylinders, which are divided into seven groups. Each group of hydraulic cylinders is driven and controlled by an independent hydraulic pump station. The deviation value is monitored in real-time according to the laser target installed on both sides of the underpass. The output data of each group of pump stations are synchronously adjusted through the specialised PID control algorithm, and the hydraulic cylinder propulsion speed is controlled to achieve synchronous propulsion.

4) <u>Data Analysis</u>

i) Monitoring Plan on Middle Ring Road

A total of 12 cross-sections of ground vertical displacement monitoring points are set on Tian Lin Road and Middle Ring Road junction. Each section consists of 16 nos of monitoring points spanned across the main road and auxiliary road.

ii) Observation during the pipe curtain installation stage

Ground settlement upto approx. 10mm was observed during the initial stage of pipe curtain installation. The subsequent review had concluded that this was induced by the high opening ratio on the cutterhead of the machine and high jacking speed during the initial drive. After the minor modification to the cutterhead and adjustment to the jacking operation, including the settlement control injection, the

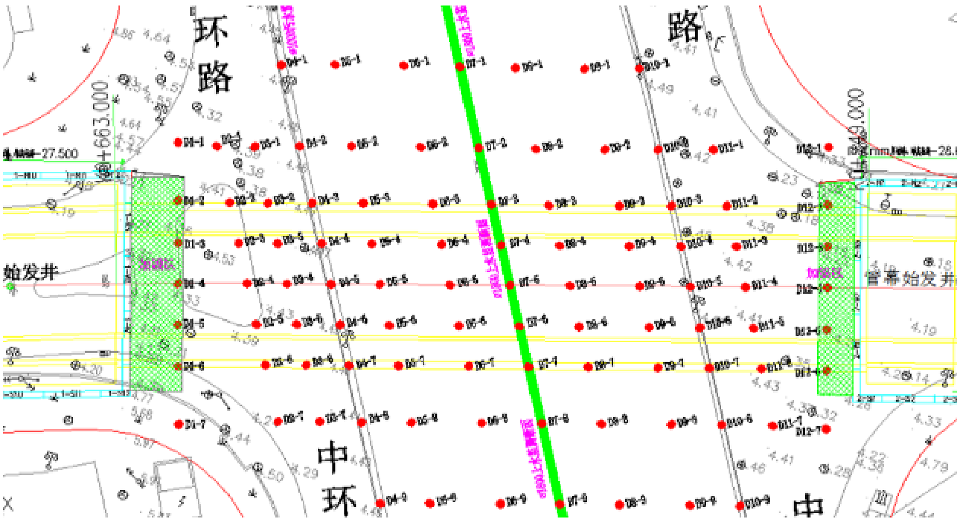

Figure 13 Monitoring plan on Tian Lin Road

ground settlement is effectively controlled after the initial drive. When all the pipe curtains work was completed, the total accumulated ground settlement was not exceeded 10mm. The monitoring points on the D4, D5, and D6 sections have indicated that about 15mm ground heave occurred, which is caused by the subsequent replacement grouting during the final stage of pipe curtain installation.

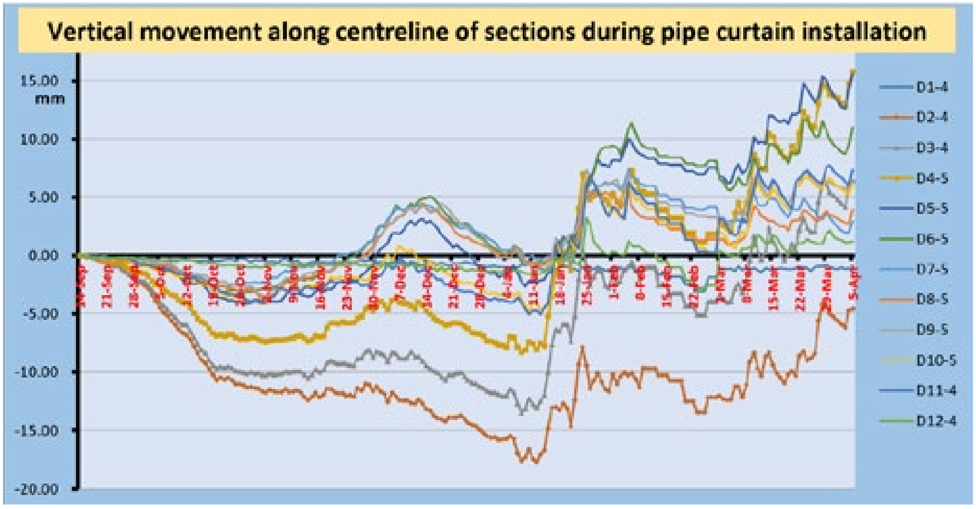

Figure 14 Ground settlement monitoring during pipe curtain installation stage

iii) Ground settlement and observations during the RTBM jacking stage

The segment jacking is protected by the pipe curtain and the face pressure developed by RTBM; thus, the ground settlement can be effectively controlled. The maximum ground settlement during the process was limited to within 10mm.

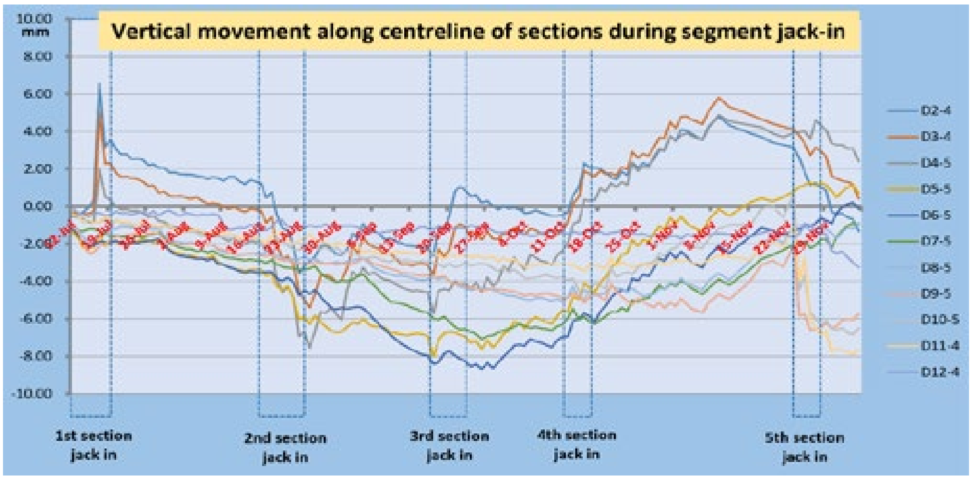

Figure 15 Ground settlement monitoring during RTBM jacking stage

The face pressure monitoring mainly relied on the pressure sensors installed along the vertical centerline portion of the machine. As multiple cutterheads were used for the machine, in reality, it can anticipate that uneven face pressure will be developed across the span of the machine. However, with the presence of pipe curtain, the adverse effect was minimized. The ground settlement of each cross-section of monitoring points along the main portion of the Middle Ring Road was further reviewed. It had revealed that the actual ground settlement is not affected by the potential uneven pressure during the segment jacking. The settlement curve across the underpass section still shows the settlement along the vertical centerline had the maximum value, which is in line with impact assessment prediction. It can be concluded with the protection of the pipe curtain, the ground settlement caused by the uneven active face pressure developed during the jacking operation, even for the wide-span section underpass, can be effectively alleviated.

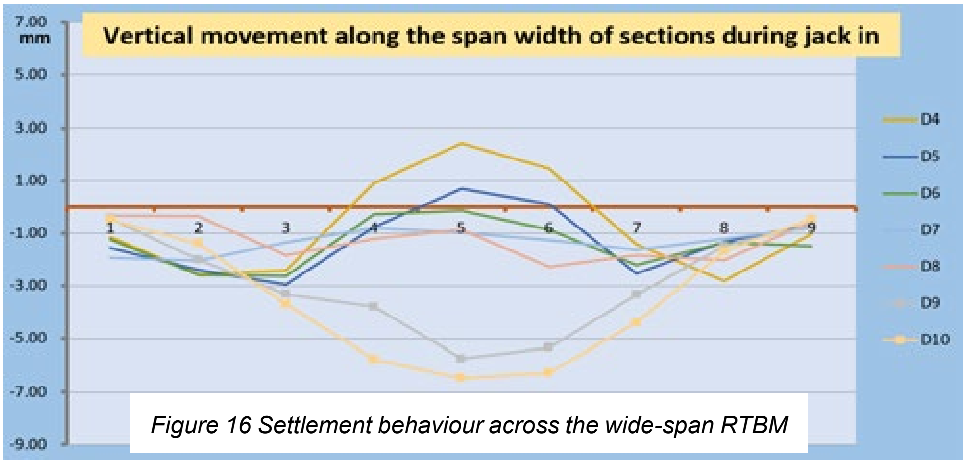

Figure 16 Settlement behaviour across the wide-span RTBM

6. Summary

1) The pipe curtain with jack-in place RTBM construction method can effectively solve the settlement effect caused by the “Segment Crown Soil Carrying Effect" induced during the rectangular TBM jacking operation and allow the trenchless construction of the underground structure with shallow soil cover and large section (>20m).

2) During the pipe curtain jacking stage, a minor settlement will occur to the ground surface due to the multiple disturbances resulting from pipe installation. The effect is minimal due to the fact that a small size jacking machine is in use. The effect can be further reduced by the replacement grout at the final stage of the work.

3) Special design pipe interlocking system can prevent the loss of the synchronous grouting slurry in the gap between the segment and the pipe curtain during the jacking stage, thus reducing peripheral friction resistance.

4) When constructing a large section box culvert, the protection of the pipe curtain can effectively reduce the risk of ground settlement caused by the uneven front face earth pressure developed by the machine induced by the disturbance of the multiple cutterheads arrangements.

5) In Hong Kong, we generally encounter fill, alluvium or colluvium with boulder mixed ground conditions. By the experience obtained from the local jack-in place segment RTBM projects, these typical Hong Kong geological profiles can be overcome by various cutterhead designs. With the enhancement of pipe curtain, we believe the RTBM technique can apply to underground space construction and provide a solution to overcome the current restraints that hinder the potential development, especially a structure with shallow soil cover and a wide cross-section area is required, for example, developing an underground shopping street that connects buildings in the town centre, and construction of vehicular underpass structures at a major road junction etc. This technique allows challenging projects to be built in a safe, high quality and high productivity manner.

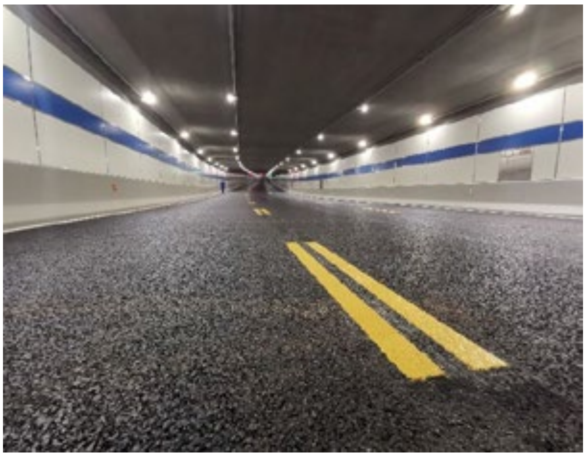

Figure 17A The completed underpass

Figure 17B Operation room of RTBM

REFERENCES

- Park I J, Kwak C W, Kim S W, et al. Verification and general behaviour of Tubular Roof & Trench method (TR&T) by numerical analysis in Korea[J]. Tunnelling and Underground Space Technology, 2006,21(3/4):394.
- Xing Kai,Chen Tao,Huang Changbo. 2009. On new tubular roof method[J]. Urban Rail Transit Research,2009,12(8):63–67.
- Li Yongsuo,Zhang Keneng,Hu`1ang Changbo,et al. 2011. Analysis of surface subsidence of tunnel built by pipe-roof pre-construction method[J]. Rock and Soil Mechanics,2011,32(12):3701–3707
- DOU Xiaotian, WANG Hekun, CAO Weiming, WANG Jinbo, ZHAO Liyong, RAN Jingpeng. 2019. Cause Analysis and Treatment Measures for Overall-Carrying-Soil Effect of Shallow-buried Rectangular Pipe Jacking. Tunnel Construction 2019/3.
- Wilfred So K.M. Chiang & R.W. Yu H.S. Kan Davis Lee. 2021. Geotechnical Challenges during Design and Construction of a Jacked-in-Place Pedestrian Subway using the First Rectangular Tunnel Boring Machine Technology in Hong Kong. HKIE Geotechnical annual seminar 2021.
- JIANG Xiaotian. 2019. Study on Construction of a Super-large Pipe-roofing and Box-culvert. Construction technology 2019/8:102-106

Active Site Supervision to Enhance Drilling & Blasting

Simon Leung
AECOM Asia Co., Ltd., Hong Kong, China

Elton M Y Ko
Drainage Services Department, HKSARG, Hong Kong, China

ABSTRACT

In Hong Kong, the steep hilly terrain is a significant constraint on surface development but provides good opportunities for underground rock caverns. The systematic use of rock caverns will be the long-termed options to increase the land supply, and drill-and-blast is still the most commonly adopted excavation method in underground. However, the technology adopted in site supervision of drill-and-blast excavation has no significant advancement along the time-tunnel of development in Hong Kong. The checking on the as-built blast holes is not comprehensive enough as only the layout on the blast face and the depth of only reachable blast holes can be checked. The alignment of blast holes behind the blast face is unknown, which is however important. In addition, no qualitative and quantitative review on the geological condition ahead of the blast face can be carried out continuously while drilling.

"The relocation of Sha Tin Sewage Treatment Works to Caverns" is a pioneering project for the cavern development in Hong Kong. It showcases the use of rock cavern to unlock the precious land resources in congested urban area. The project team endeavours in adopting Measure-While-Drilling technique to uplift the current practice of site supervision. Sensors and routers are installed at the drilling jumbos to collect valuable drilling data, including the as-built alignment in three dimensions for 100% blast holes, such that live-monitoring of drilling operations could be carried out anytime and anywhere such as in office as well as on site. In case of any as-built blast holes were found to be significantly deviated from the original alignment, review on the drilling operation and rectification could be carried out immediately. Geo-mechanical data is also live-collected for rock mass analysis while drilling of each blast hole, serving like ground investigation drillholes to reveal the geological condition ahead blast face in a fast and an efficient way. The geological condition is one of the major factors in controlling the overbreak in drill-and-blast excavation as well as the blasting factors. The blast design can be reviewed and can be optimized to cope with the changing geological conditions. The huge volume of data generated will be stored into a Big Data database, which is versioned to share all the data obtained with the local construction industry. In long term, the use of Big Data would be the way in predicting the potential risks and its root cause instead of being traditionally merely responsive to an already happened event.

The site supervision for underground construction under public works projects has become more active than ever before, for which the client departments and Resident Site Supervisors (RSS) actively master the use of live data as to enhancing the safety and quality of drill-and-blast operation. The full adoption of Measure-While-Drilling are leading the site supervision sector towards a more productive, more effectively managed digital age where real time data and reporting will be available for key elements of future tunnel and cavern projects.

1. Introduction

In Hong Kong, drill-and-blast excavation is commonly adopted excavation method in rocks considering its low investment cost, high adaptability to very varied ground condition and large flexibility to deal with different shapes and sizes of openings. However, the drill-and-blast excavation method will inevitably damage the peripherical rock mass due to the formation of a network of fine cracks which may lead to safety and stability concerns. In case of too large damaged zone, it would endanger the safety of front-line workers and RSS due to the reduction of stand-up time, especially for poor rock mass. It also leads to escalation of time and cost due to the increase in rock fragment being mucked out and larger extent of permanent support. In addition, functionality and post-construction performance of the structures get affected due to the large extent of the damage zone if not taken care in time.

The overbreak/underbreak zone and damaged zone have significant impact on the project cost, construction period, safety and performance of the underground opening. They are mainly influenced by the quality of the rock mass, the validity of the blast design and the workmanship of blast hole drilling. In addition, it is not uncommon encountering that the actual pull length is less than the designed pull length, as a result the project would suffer and require a longer or more round of blasting to mitigate the lost pull length causing an out-of-blasting cycle or progamme problem. Such problem is usually attributed, among other geotechnical factors, by the mis-alignment of the inner blast holes as well as the surface blast holes. With such an insight, it is of paramount importance to control the quality of blast holes in a workmanlike manner as similar for the workmanship of other civil engineering works supervised by RSS team. The supervision of drill-and-blast operations by RSS team, who endeavours to uplift the supervision practice by adopting Measure-While-Drilling (MWD), has become more direct and active than ever before.

2. Incomprehensive Current Practice on Supervision of Blast Holes Drilling

The current practice for the quality supervision of the blast hole drilling is not comprehensive enough and remains much rooms for improvement without evolving with the fast-developing tunnel technology. The layout of as-built blast holes on the blast face can only be checked briefly by visual inspection to an approximate extent. No qualitative checking of the deviation of as-built blast holes from the designed layout is carried out. There was no way to check the correctness of the alignment of as-built blast holes behind the blast surface, i.e. the inner blast holes. During drilling, drilling error may be caused by collaring, alignment and trajectory deviation. However, the blast hole deviation changes the burden, spacing and plane of holes, which is particularly critical for the contour holes. This results in overbreak/underbreak at the perimeter of the opening, for which it induces significant direct and indirect cost to the project. However, the RSS team is compelled to ignore the checking of the alignment of the as-built blast holes due to the time and practical constraints. In addition, the depth of the blast holes is important to check to ensure that the actual depth conforms with the design and no internal collapse subsequent to drilling, thereby affecting the quantity of explosive. The depth of blast holes is checked manually by a worker inserting a rod into the as-built blast holes sometimes with the aid of a cherry picker, and then measure the inserted length by a ruler **(Photo 1)**. The checking is time consuming and is also limited to those reachable blast holes. In view of this, the RSS could only conduct spot checks on the depth of as-built blast holes at easily accessible locations and the checking covers very low percentage of the total blast holes per round **(Photo 2)**. The checking is however considered not effective as a higher possibility of significant deviation is anticipated to occur at blast holes having difficulties to access, e.g. the perimeter holes at the crown level, which usually got skipped during checking. Furthermore, the checking of as-built blast holes by RSS was usually carried out after the whole round of drilling and right before the blasting in regard of the tight blasting cycle to facilitate the completion of the project on time. Sometimes the explosive has already been ordered and being delivered on the way to the site while the drilling of blast holes is still in progress. Therefore, it is considered too late for the checking and implementing any corrective action to rectify the largely deviated blast holes. The overall quality of the blast hole drilling is somehow deemed to be self-controlled by the contractor and RSS had been difficult to provide input on the quality supervision of the blast hole drilling before.

Photo 1. Depth Checking of As-built Blast Holes by Inserting a Ruler Manually

Photo 2. Depth Checking Covers Few As-built Blast Holes Only

3. Limited Geological Information

For civil engineers, dealing with the drill & blast activities can be an extraordinary task. There are so many known and unknown geological details that must be observed, understood and act upon by RSS in order to achieve a qualitative supervision. There are no two blasts having exactly the same geotechnical conditions and so are the challenges and concerns. The level and extent of these challenges and concerns can vary substantially for each blast. Even in a situation where an experienced RSS may have a profound knowledge on the drill and blast, there are still many unpredictable risks arising from the known and unknown geological details behind the blast face. In view of this, we should not only rely heavily on the mapping information appears visually on the surface, but should be explored as to how we can obtain those geological conditions exist behind the blast face and be aware of those associated potential risks, then stay vigilant during our supervision.

The underground project is normally started with a site investigation to determine the in-situ rock mass condition and it provides the basis for the tunnel and the blast design. However, the site investigation is often based on limited information such as surface mapping, geophysical profile, few drill holes, etc. The estimation of the rock mass conditions may contain inaccuracies, resulting in inappropriate designs. During the excavation, the predicted rock mass conditions is verified by observational method (Peck 1969). Geological mapping is conducted on the blast surface after each round of blasting at 3m to 5m interval normally. The determination of rock mass condition is based on the mapped sections discretely. An assumption has been made that the rock mass condition beyond the blast face could be represented by the blast face, which may not be applicable to some locations with complex geological setting. In addition, the geological mapping is recorded individually for each blast face, which is inconvenient for geotechnical engineers who try to understand the trend of changing rock mass condition over a tunnel portion. As the information of geological mapping report is not digitalized, it hinders the sharing and utilization of the information by other future underground projects in Hong Kong.

4. A Pioneer Project with Pioneer Supervision Skills

The Relocation of Sha Tin Sewage Treatment Works (STSTW) to Caverns is a showcase cavern project in Hong Kong commenced in 2019. The aerial photo the project site is shown in **Photo 3**. After its completion, the cavern hall is around 380m x 350m with span up to 32m. It consists of five parallel caverns along the longitudinal axis of the cavern complex. The future cavern complex for the relocated STSTW will be the largest of its type ever built in Hong Kong and it needs to be implemented in stages. BIM model of future cavern complex is shown in **Figure 1**. The first stage of the project involved construction of 260m long Main Access Tunnel (MAT) and 90m Main Access Tunnel West (MAT-W). The MAT and MAT-W are formed as a horseshoe shape with approximate excavated span 18m and cross section area around 270m2. The majority of the tunnels and caverns are in rock with more than half span of rock cover above the tunnel crown and will be formed using the drill-and-blast method and the general view inside MAT is shown in **Photo 4**.

Photo 3. Aerial Photo of the Project Site

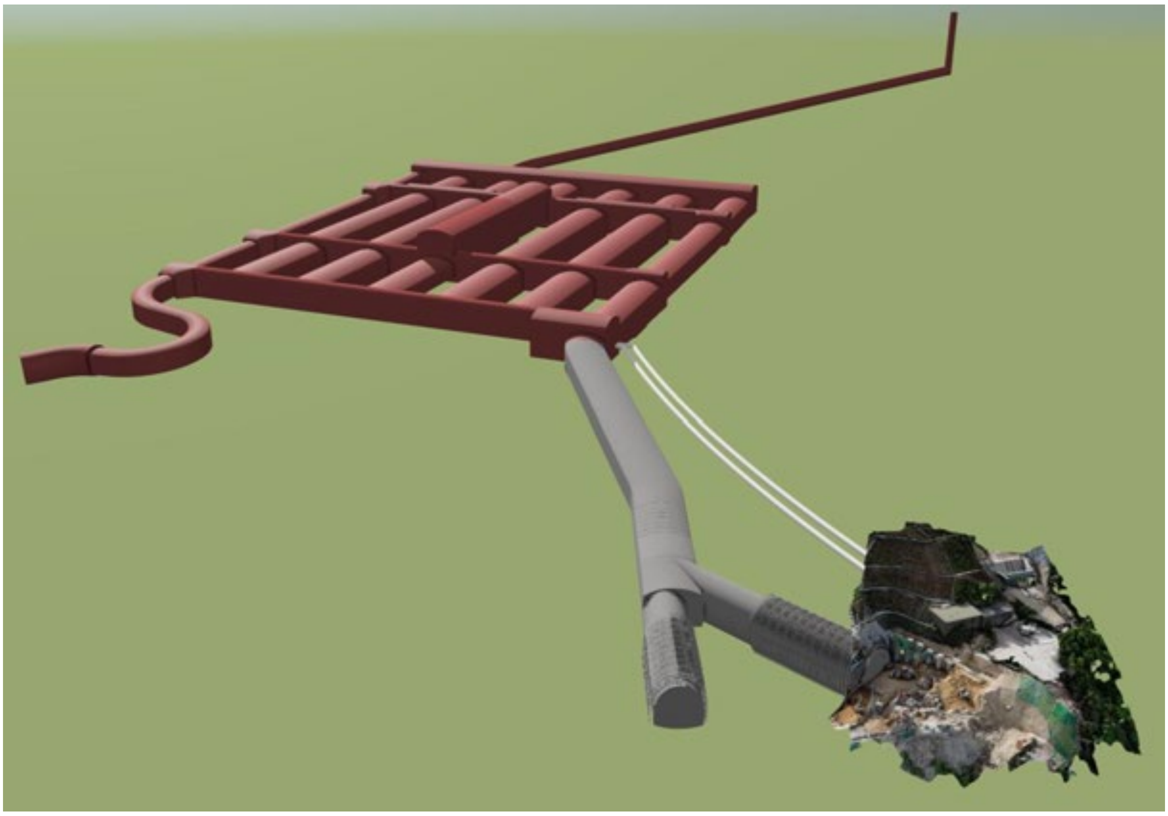

Figure 1. BIM Model of Future Cavern Complex

Photo 4. General View inside MAT

"The adoption of digital supervision workflow can streamline many of the repetitive paperwork associated with current practices. It allows real-time monitoring of inspection status so management can much more easily spot any potential problems before they are manifested." (CIC 2020). As the Review Report recommended under Recommendation 3, "……site supervision personnel should focus more on results-oriented inspections for assuring that quality and design intent are being delivered rather than mechanistic checking and administrative procedures…… It is worth exploring the need for preparing a relevant document spelling out the good practices and guidelines for rationalizing the relevant requirements for the industry's general reference." (CIC 2020). Somehow in this context, the recommendation triggers the exploration of what really need for a step up by an active supervision for a drill and blast projects.

To facilitate live monitoring by RSS with the aid of MWD, various sensors for collecting the drilling data are installed at the booms of jumbos **(Photo 5)**. The current application of the MWD sensor could only provide for an on-site monitoring inside the cabinet of the jumbo. In order to achieve a "supervision-anytime-anywhere" concept, RSS installed a router at the jumbo as for the data transmitting directly from the booms of jumbo to site office, thanks to the dedicated RSS innovation team. A site specific 5G network with the advantages of low latency, high-speed transmission, and high device capacity has been brought in to the whole tunnels and construction site by the project team. The drilling data collected at the jumbos is then transmitted via the 5G network to anywhere outside the tunnels such as office as well as spot on site for live monitoring of the blast holes drilling. A round report summarizing all the drilling data including as-built layout, geological and geo-mechanical data, etc. is generated and is stored in the hard disk at the jumbos and can be downloaded to the computer server at office, thanks to 5G network.

Photo 5. Jumbo Equipped with MWD Sensors

5. MWD and Chief Resident Engineer (CRE) Report

A CRE report after each round of blasting was prepared by RSS for review and endorsement by CRE under this the project. The CRE report recorded some further pre-blasting and post-blasting checks, which is meant to supplement the statutory required Resident Explosives Supervisor (RES) report and post blasting report. There are three main sections including pre-blasting check, post blasting check and kinematic analysis of the unstable wedges. In this paper, the CRE report for blasting number MAT-066 is chosen to demonstrate the enhanced supervision developed by our project team through adopting MWD in pre-blasting check. The location of MWD data for MAT-066 is shown in **Figure 2**. All the MWD data obtained from the project can be combined together in BIM, which allows the access of all the project participants. It provides a convenient way for the engineers of RSS and the contractor to access and review the data for improved blasting control and outcomes.

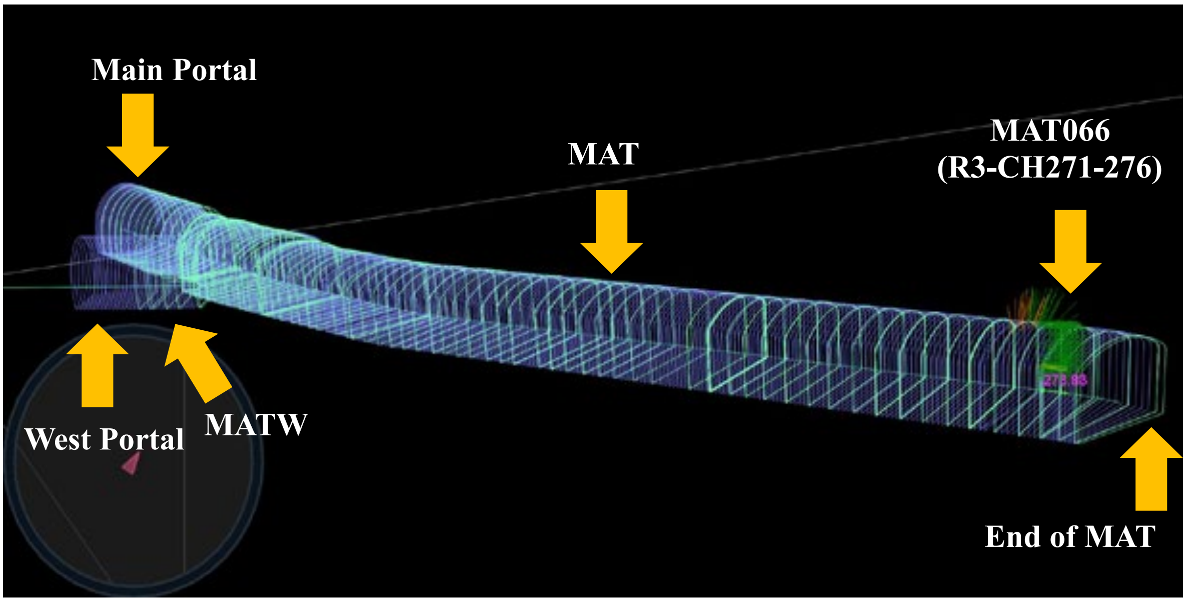

Figure 2. Location of MWD for Blast No. MAT-066

Pre-Blasting Check – Enhancing the Supervision of Blast Hole Drilling

The total number of blast hole for MAT-066 was 252 nos., which contained 170 nos. production holes, 60 nos. perimeter holes and 22 nos. lifter holes. In the pre-blasting check, live checking for the profile on blasting surface, alignment and depth of total 252 nos. of as-built blast holes were performed by the works supervisors, which helps prevent the occurrence of significant deviation of as-built blast holes from the designed profile by immediate notification to the contractor for rectifying promptly. The deviation between the designed (blue coloured) and the as-built blast holes (red coloured) on the blasting face can be easily identified from MWD as shown in **Figure 3**. As a result, the profile checking of the as-built blast holes on the blasting surface resulted in 100% production holes, 93% perimeter holes and 100% lifter holes within the deviation range between 0mm and 400mm. For the profile check of the end point of the as-built blast holes, 93% production holes, 99% perimeter holes and 50% lifter holes were drilled within the deviation range between 0mm and 400mm. For the depth checking, 100% production holes, 99% perimeter holes and 100% lifter holes were drilled longer than the designed depth. The results are plotted in **Figure 4 – Figure 7** respectively. The graphical representation of as-built blast holes in MWD in 3-dimension is shown in Figure 5.

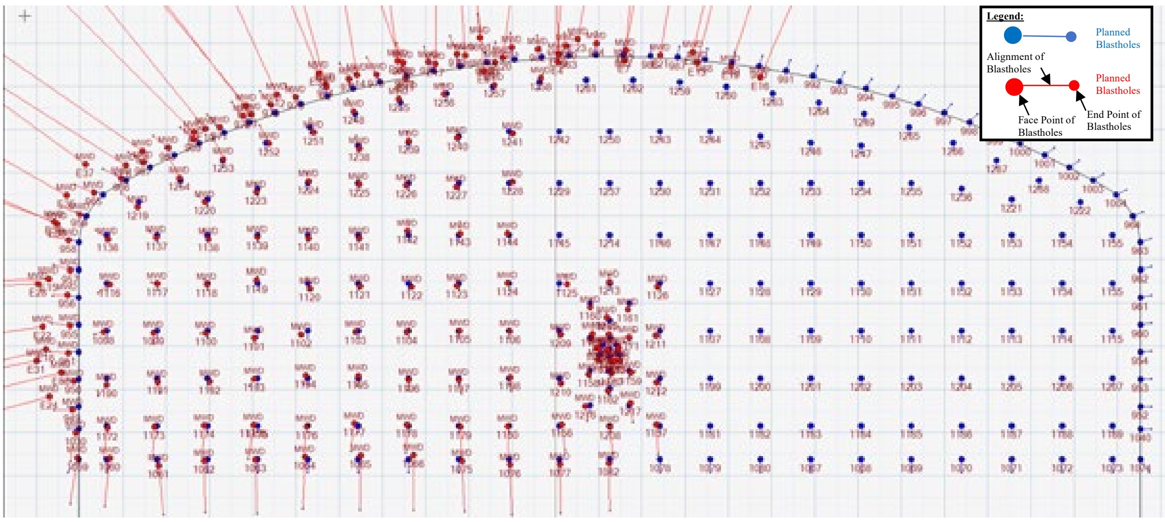

Figure 3. The deviation between the designed and as-built blast holes on the blasting face

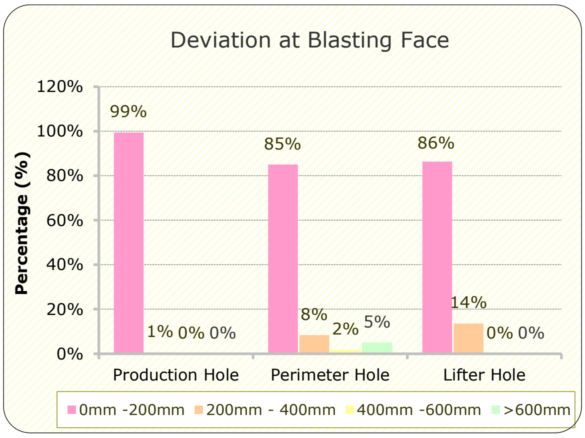

Figure 4. Profile Checking of the As-built Blast Hole on the Blasting Surface

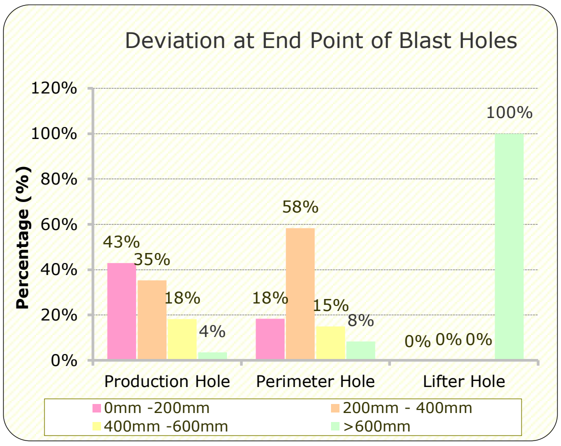

Figure 5. Profile Checking of the End Point of As-built Blast Holes

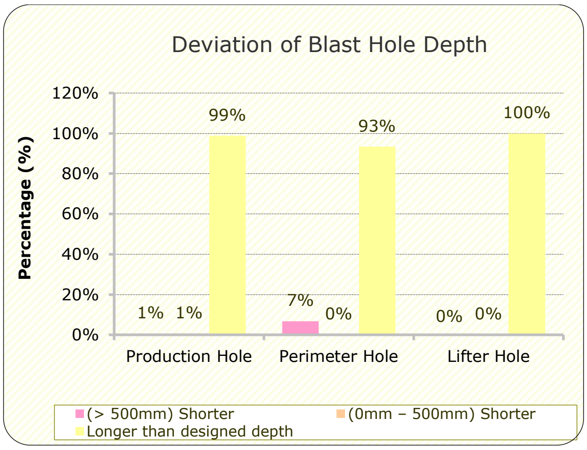

Figure 6. Depth Checking of As-built Blast Holes

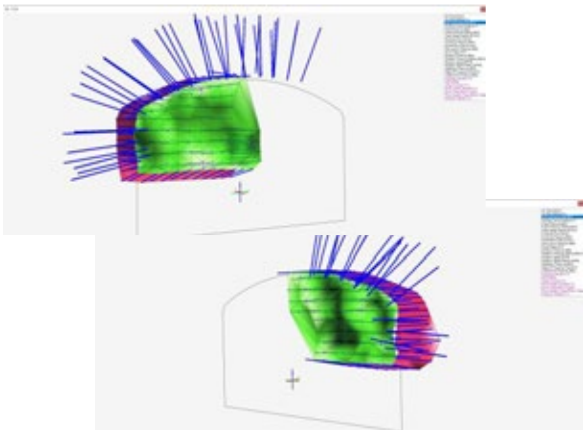

Figure 7. Graphical Output of As-built Blast in MWD

Pre-Blasting Check – Improve the Accuracy of Forecasting Rock Mass Condition ahead of Blasting Face

Our project team adopted MWD to improve the accuracy of forecasting the rock mass condition ahead of the blasting face. It can bridge the information gap between the early, somewhat uncertain geotechnical site investigation and the geological mapping done after excavation to optimise the tunnel temporary support design and enable a more prescriptive blast design. MWD provides a real time monitoring of geo-mechanical data in 3-dimension in real time in order to optimize the drilling and blasting cycle and achieve so-called “data driven productivity”. The key geo-mechanical data including penetration rate, percussion pressure, rotation pressure, flushing pressure, feed pressure is collected, which are shown in **Figure 8 – Figure 13**.

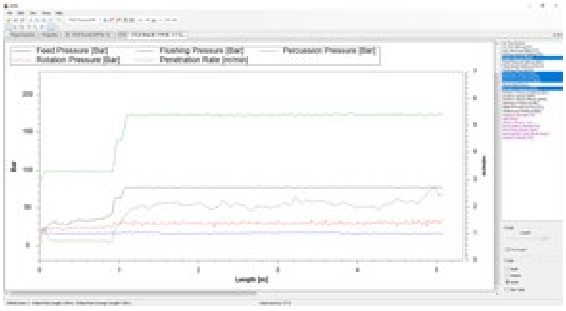

Figure 8. Variation of Key Geo-Mechanical Data along Drill Hole Depth

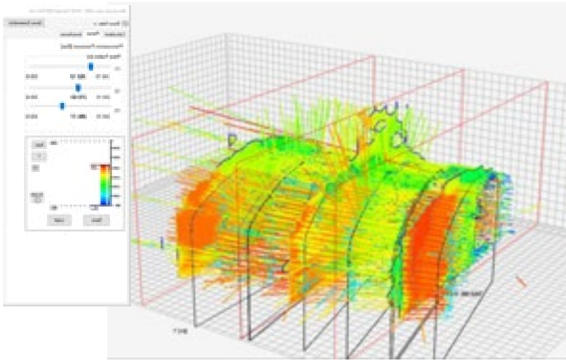

Figure 9. Layered View of Percussion Pressure in 3D Structural View

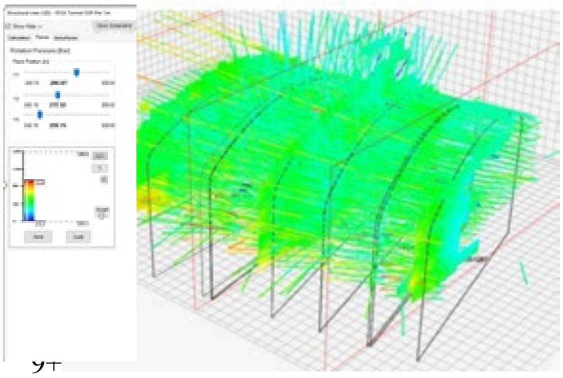

Figure 10. Layered View of Rotation Pressure in 3D Structural View

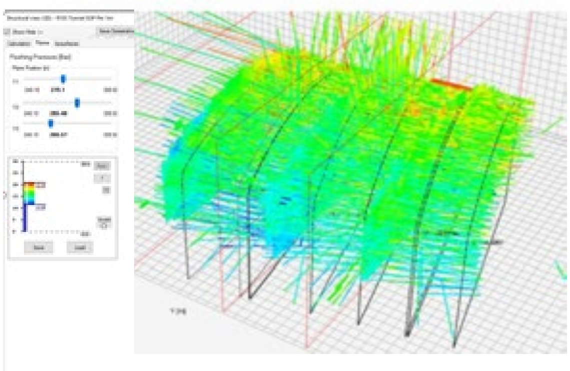

Figure 11. Layered View of Flushing Pressure in 3D Structural View

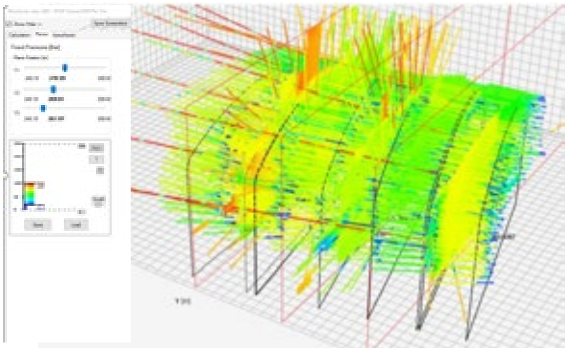

Figure 12. Layered View of Feed Pressure in 3D Structural View

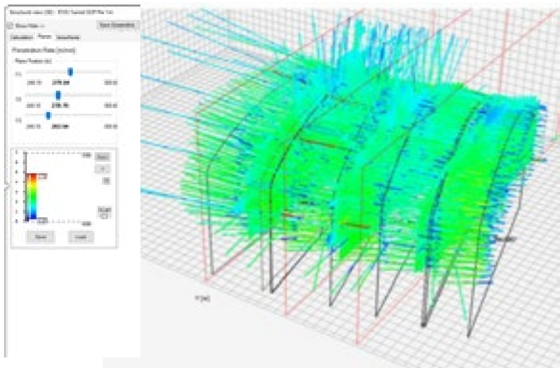

Figure 13. Layered View of Penetration Rate in 3D Structural View

The geo-mechanical data was analysed by MWD's extended function, which is called GeoSure, to normalize and filter the operational and machine influence to obtain the various geological indicators for the rock mass condition ahead of the blasting face. The geological indicators include Fracture Indicator, Rock Drilling Resistance, Water Indicator, Rock Quality Number.

Fracture Index (FI)

The FI is a ratio indicating the length of an encountered fracture with respect to the data sampling interval, which is a pre-set value of 2cm. The lower the value represents the smaller the size of the fracture at the respective sampling interval, which 0% implies no fracture while 100% implies the voids is bigger than the sampling interval. From the FI obtained in MAT-066, as shown in **Figure 14 – Figure 17**, the FI generally lies between 10% - 20% with only a small localized area with FI up to around 30%. Therefore, RSS anticipated that the size of fracture ahead the blasting face is small.

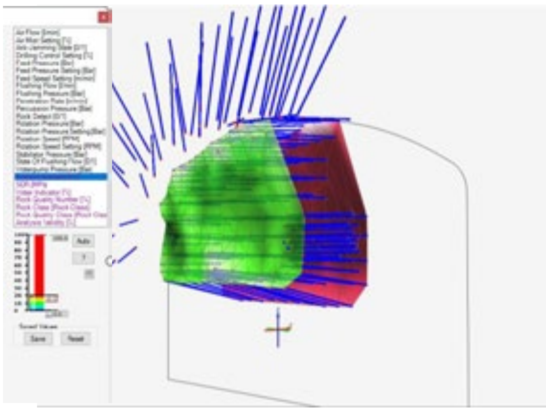

Figure 14. FI of MAT-066 in 3D

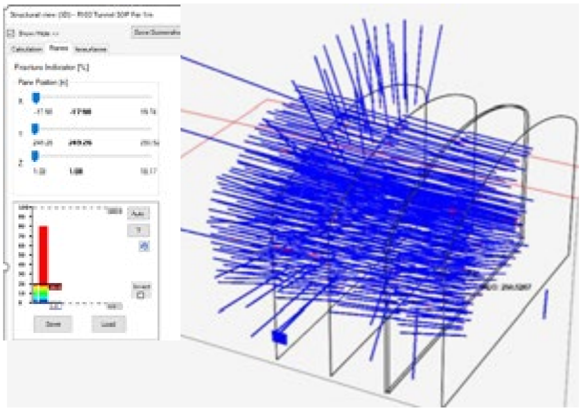

Figure 15. FI over a Tunnel Portion at MAT-066 in 3D

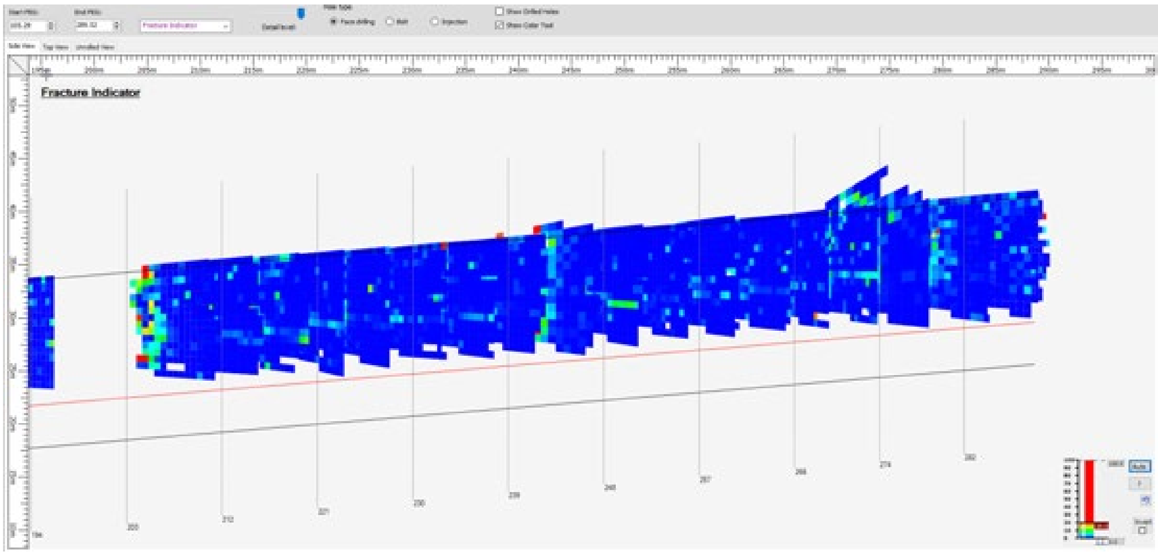

Figure 16. Overall Side View of FI across the Whole Tunnel

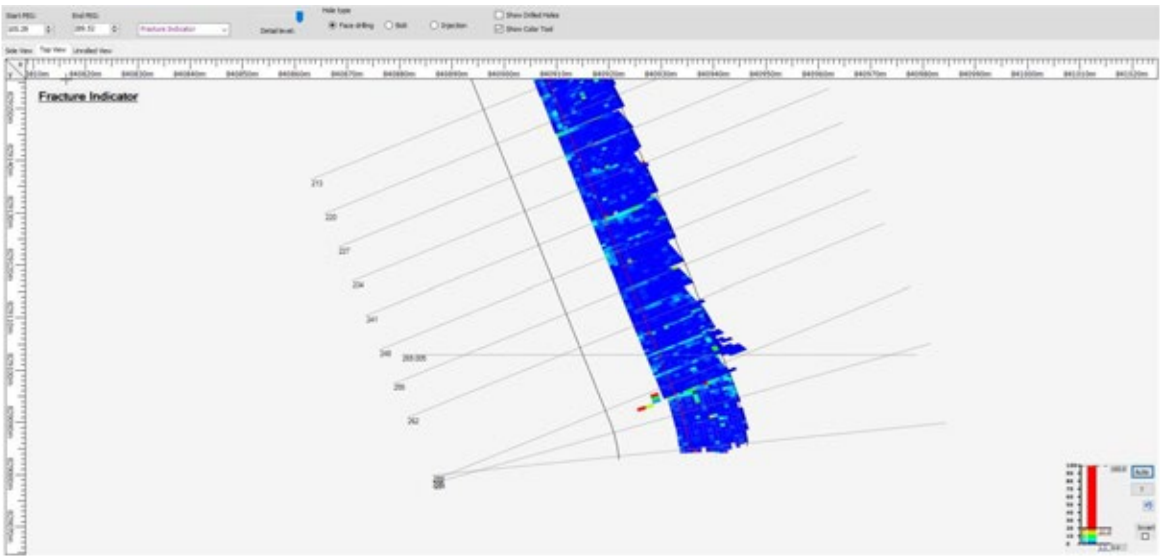

Figure 17. Overall Top View of FI across the Whole Tunnel

Rock Drilling Resistance (RDR)

The RDR indicates the rock's resistance to the drilling system, which is in direct proportion to the uniaxial compressive strength (UCS) of the rock with a site-specific coefficient. In order to correlate RDR obtained and the uniaxial compressive strength UCS of the rock mass, 3 nos. of rock core samples, as shown in **Photo 6 – Photo 8**, were retrieved across the tunnel and were sent to the laboratory for testing the UCS. The laboratory test results were then compared with the RDR recorded. The RDR results obtained from MWD at the retrieved rock core samples is shown in **Figure 18**. The results show that the UCS and DRD are in an approximate ratio of 1:1 and the detail of results are summarized in **Table 1**.

Sample No.	UCS (MPa)	RDR (Mpa)
1	136.4	~150
2	79.7	~80
3	124.3	~120

Table 1. Comparison of UCS and RDR

After the site-specific coefficient has been established, the RDR obtained can be used to anticipate the UCS of rock mass ahead of the blasting face. The results of RDR obtained for MAT-066 are shown in **Figure 19 – Figure 22**. The UCS of the rock mass was obtained between 50Mpa and 200Mpa. No localized weak zone was detected.

Photo 6 . Rock Core Sample No.1

Photo 7. Rock Core Sample No.2

Photo 8. Rock Core Sample No.3

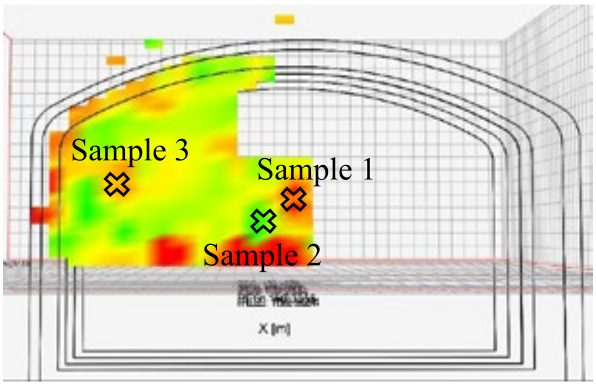

Figure 18. RDR results from MWD for Rock Core Samples Retrieved

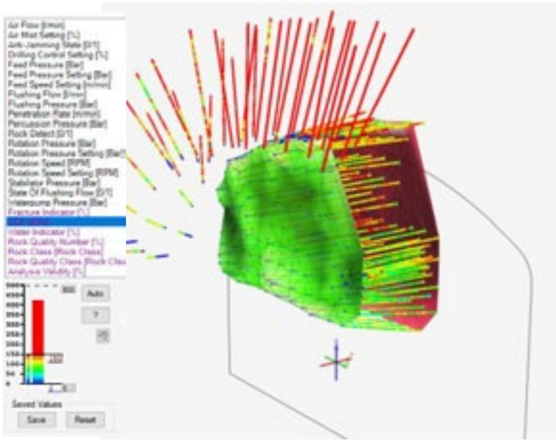

Figure 19. RDR of MAT-066 in 3D

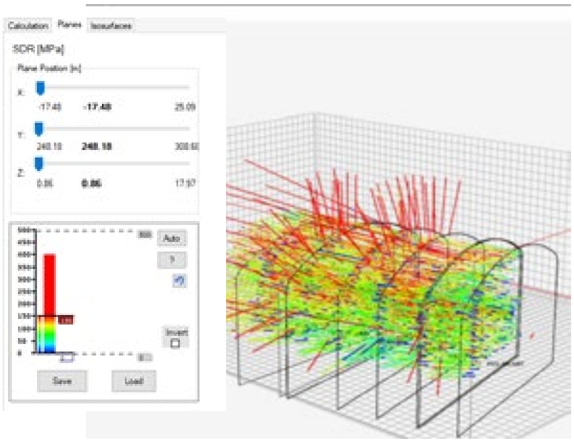

Figure 20. RDR over a Tunnel Portion at MAT-066 in 3D

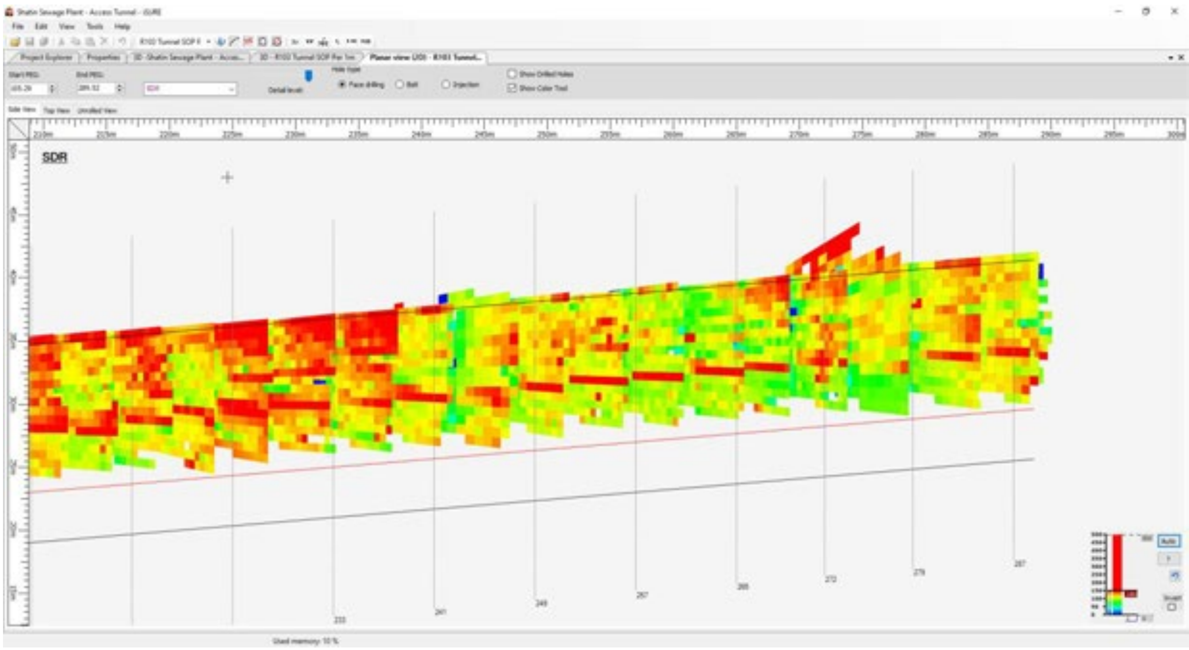

Figure 21. Overall Side View of RDR across the Whole Tunnel

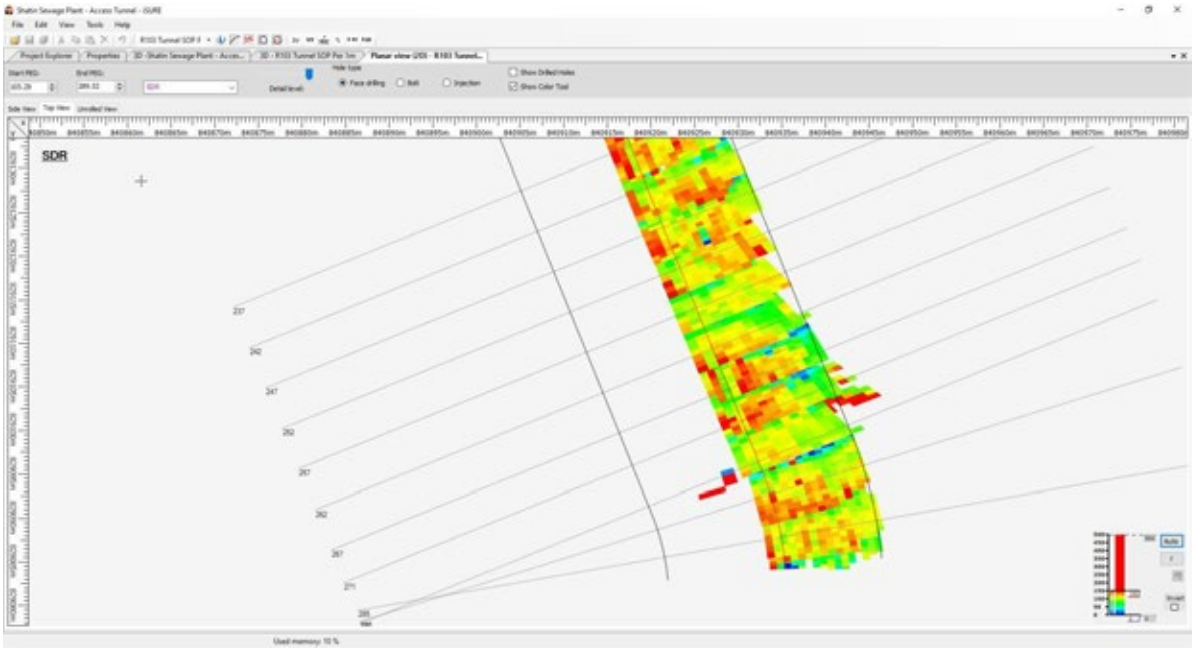

Figure 22. Overall Top View of RDR across the Whole Tunnel

Water Indicator

The water indicator is given at the positions where fracture is present and significant and characteristic changes in flushing flow and flushing pressure are detected. For water indicator equal to 0%, the presence of water is unlikely at the fracture. Water indicator equals to 100% meaning that there is presence of water is very likely at the fracture. The results of water indicator obtained for MAT-066 are shown in **Figure 23 – Figure 26**. The water indicator is generally below 5% indicating that the occurrence of groundwater inflow at fractures is negligible.

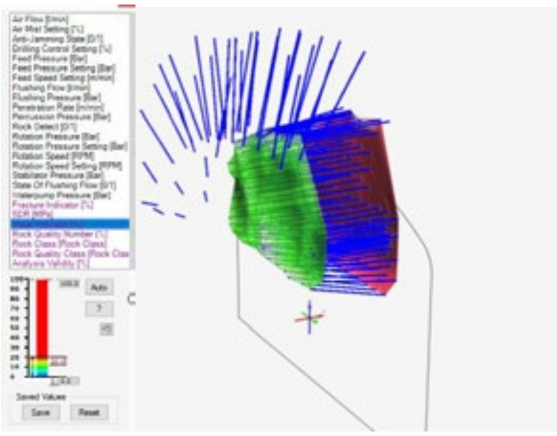

Figure 23. Water Indicator of MAT-066 in 3D

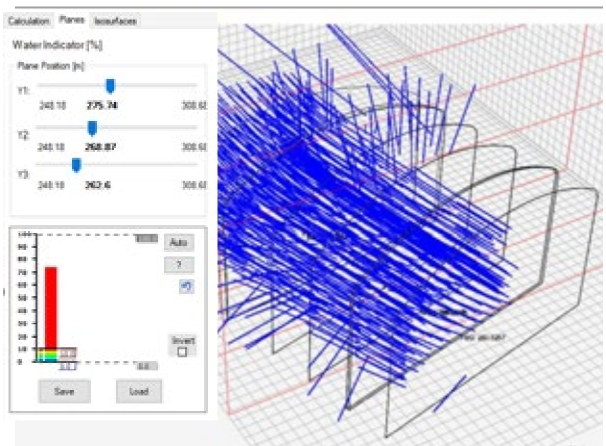

Figure 24. Water Indicator over a Tunnel Portion at MAT-066 in 3D

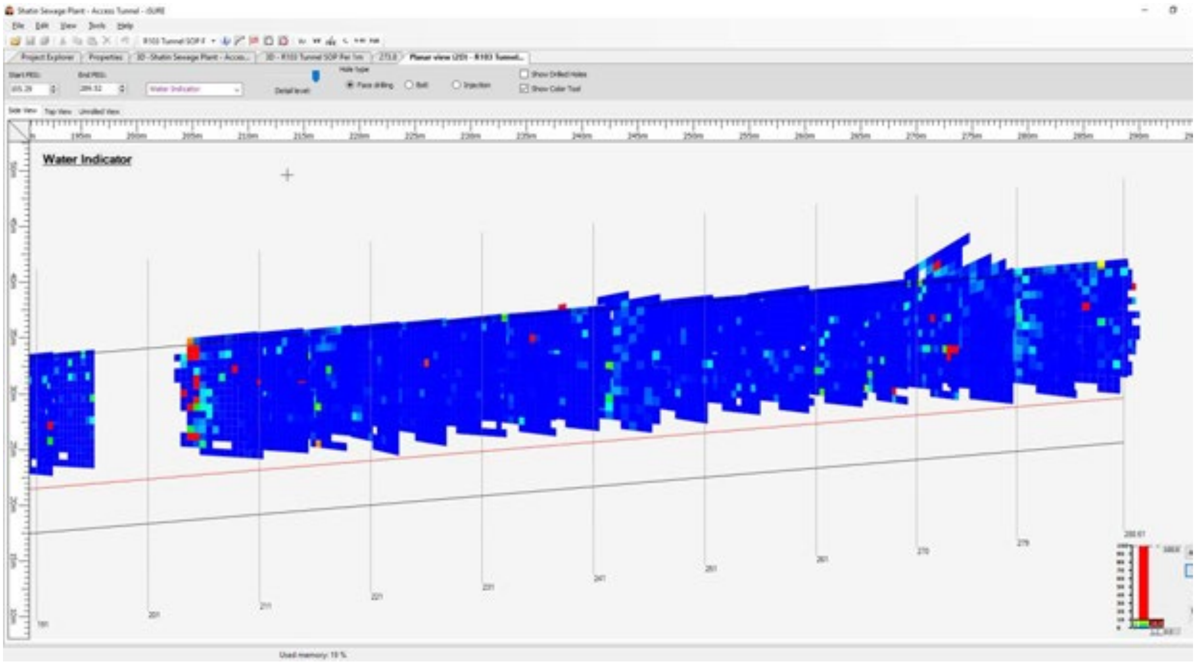

Figure 25. Overall Side View of Water Indicator across the Whole Tunnel

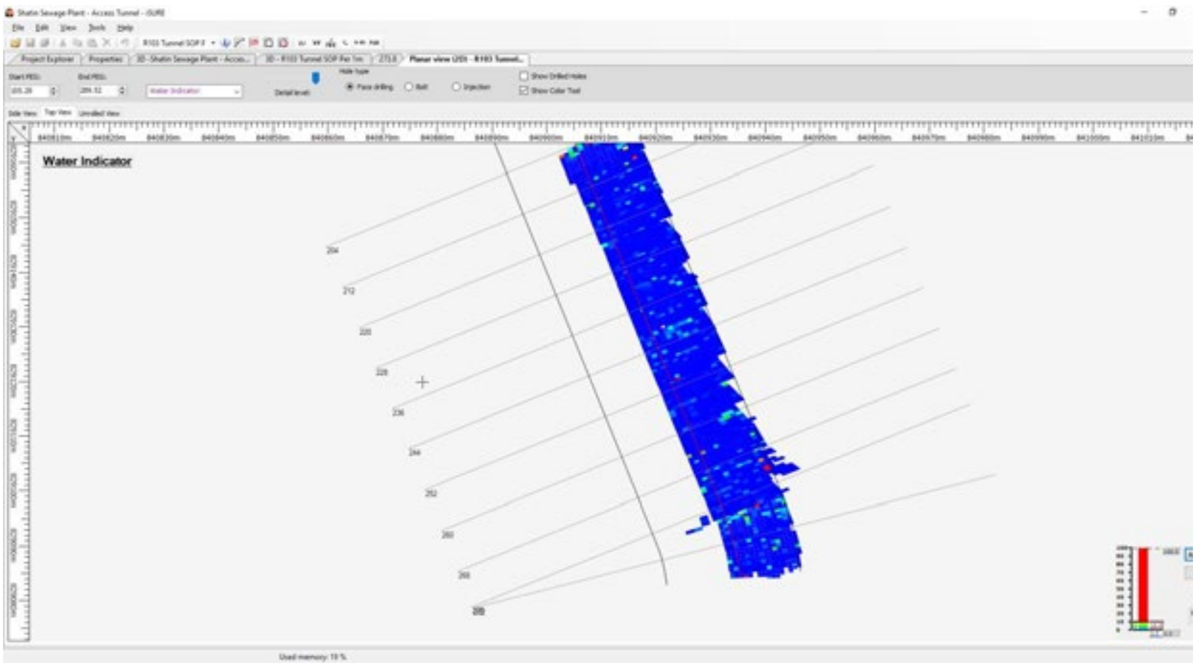

Figure 26. Overall Top View of Water Indicator across the Whole Tunnel

Rock Quality Number (RQN)

The RQN is defined as the total sum of intact rock over or equal to 10cm rock samples, which follow the same calculation principle of Rock Quality Designation (GEO 2017). The results of RQN obtained for MAT-066 are shown in **Figure 27 – Figure 30**. The RQN between 90% and 100% is generally obtained and the result is consistent with the FI obtained.

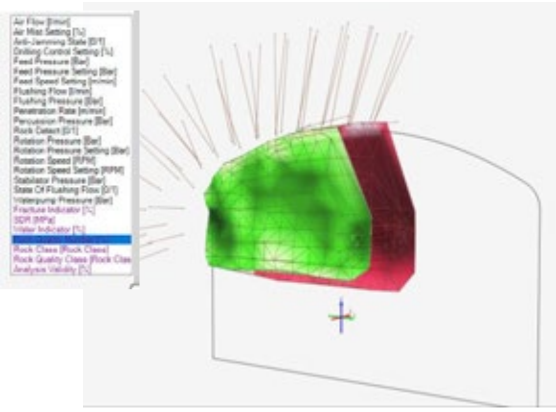

Figure 27. RQN of MAT-066 in 3D

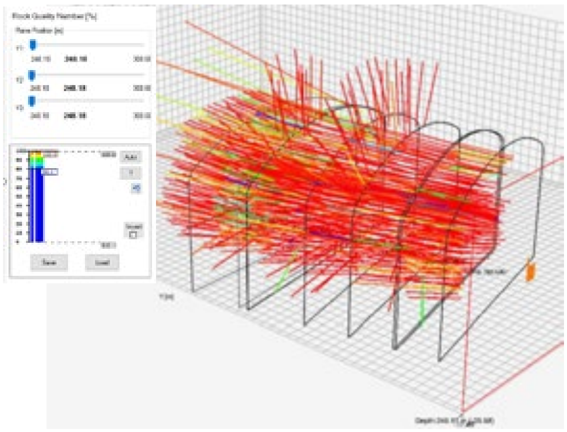

Figure 28. RQN over a Tunnel Portion at MAT-066 in 3D

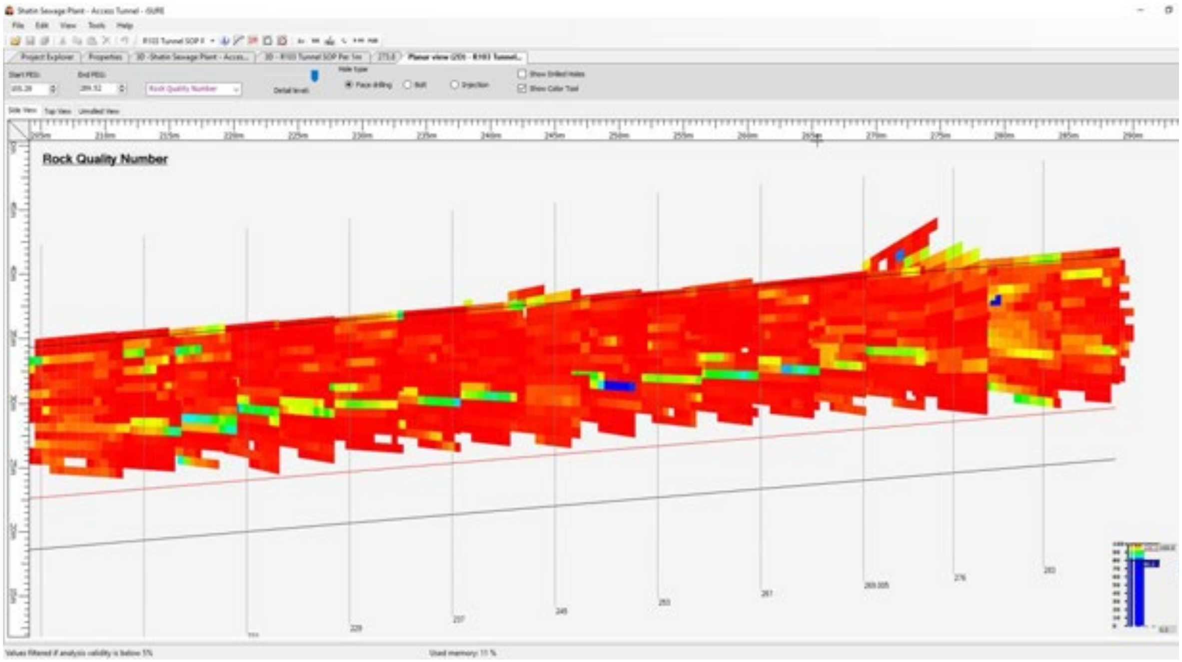

Figure 29. Overall Side View of RQN across the Whole Tunnel

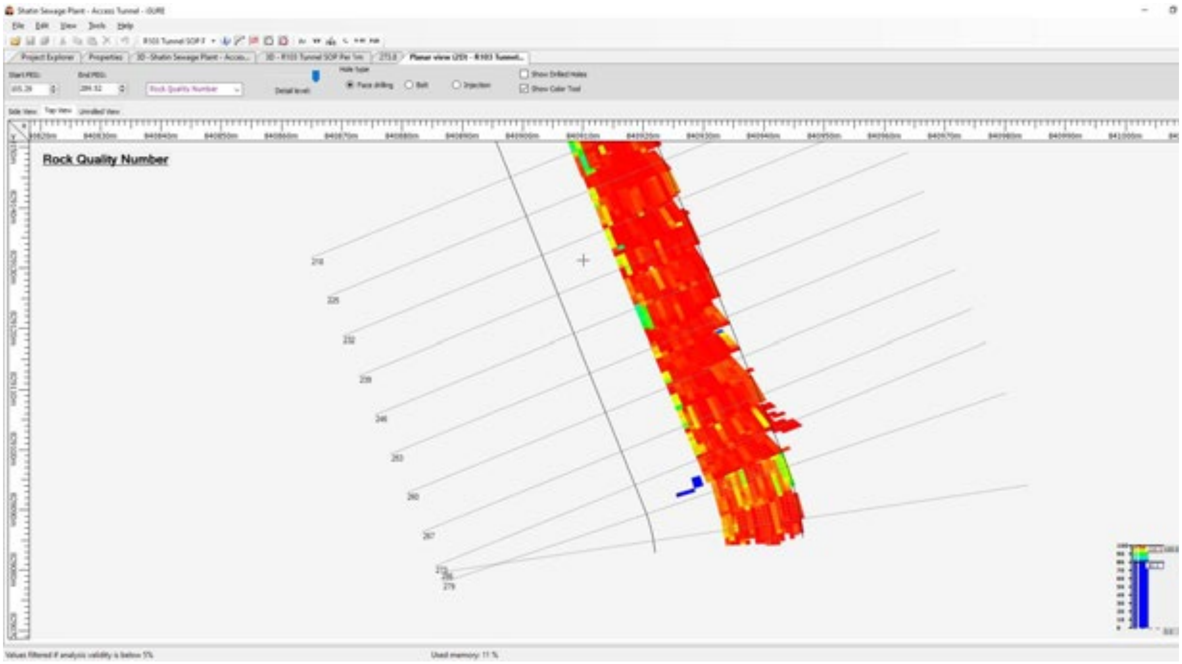

Figure 30. Overall Top View of RQN across the Whole Tunnel

6. Conclusion

According to Cavern Master Plan published by Hong Kong SAR government, the systematic use of rock caverns will be the long-termed options to increase the land supply. While Relocation of Sha Tin Sewerage Treatment Works to Cavern is a pilot public works project for cavern development in Hong Kong, our project team endeavours to adopt various innovative technologies in our project so as to lead the development of an industry culture that embraces change, innovation and new technologies to drive forward productivity, efficiency and enhanced project delivery outcomes. One of which we adopted was MWD and a case study for application of MWD on one of the blasting (MAT-066) has been discussed in this paper.

In MAT-066, our RSS carried out 100% three-dimensional live-checking of the as-built blast holes in real-time and provided a useful guidance to the contractor to implement immediate corrective actions to prevent the drilling of the blast holes from going any further in wrong alignment once the alignment is deviated from the designed profile. The quality supervision of the blast hole drilling by RSS has become more active and effective than ever before and the workmanship of the contractor was turned out to be improved substantially. The MWD provides a digitalized and quantitative way to the profile checking of the as-built blast holes such that greater than 90% and 99% of the as-built blast holes were found to be very slightly deviated from the designed profile and were longer than the designed drilling depth respectively in MAT-066. The good workmanship of the blast hole drilling laid a good basis for delivering good blasting outcomes.

The conventional approach for the underground infrastructure projects based on advanced site investigation and geological mapping during excavation could be benefit from the supplementing the instantaneous information on the rock mass condition ahead the blasting face. The RSS in this project adopted MWD to measure and collect various geo-mechanical data and produce several useful geological indicators including Fracture Index, Rock Drilling Resistance, Water Indicator and Rock Quality Number to facilitate a more prescriptive tunnel support design and blast design. Now that the Shatin Cavern Project team is adopting various technologies, the digital workflow and MWD is generating more data than ever before, leaving the team with tonnes of data and getting more ways to benefit from it and hopefully for the future cavern development in Hong Kong.

References

Peck RB, 1969, Advantages and limitations of the observational method in applied soil mechanics, Geotechnique 19(2): 171-187

CIC, 2020, Review Report on Quality Site Supervision Practices of the Hong Kong Construction Industry, Construction Industry Council, Task Force on Construction Industry Site Supervision Practice, P.23

GEO, 2017, Guide to Rock and Soil Description – Geoguide 3, 2017, Geotechnical Engineering Office, Civil Engineering and Development, HKSARG, P.27 – 28

Two Major Technical Solutions on the Lung Shan Tunnel – Pilot TBM Tunnel Enlargement and TBM U-turn in Cavern

X Monin, L Jeanne, V Tricot, R B Storry
Dragages Hong Kong Limited, Hong Kong, China

ABSTRACT

On the Liantang / Heung Yuen Wai Boundary Control Point Site Formation and Infrastructure Works – Contract 2 in Hong Kong SAR, Dragages Hong Kong Limited have proposed and implemented two major technical solutions and construction methodologies to overcome the programme constraints and the geotechnical challenges of the 4.8 km long Lung Shan Tunnels section.

1. Pilot TBM tunnel enlargement:
Due to a tight 350 m horizontal curve, the northern 500 m of the Liantang Lung Shan tunnels comprise mined tunnels of larger span (3m wider internally than the standard two lanes 14.1 m diameter TBM bored tunnel). For programme reasons it was not possible to wait for the 500 m long mined tunnel to be completed before the 14.1 m diameter TBM was launched in the southbound tunnel to bore the 2,400 m long segmental lining standard two lanes tunnel towards the Mid-Ventilation Junction Cavern.
Therefore the TBM was launched within the horizontal curve, at 200 m from the North Portal, and the 300 m long 14.1 m diameter TBM "pilot" tunnel within the curve had to be subsequently enlarged to its final size, using mined tunneling technique along with advanced construction methodology and temporary steel gallery.

2. TBM U-turn in Cavern:
In addition, to reduce the geotechnical risk of tunneling in faulted ground and to secure the Project programme, the TBM drive was significantly lengthened, from originally 1,000 m to 2,400 m per tunnel. Following the completion of the first TBM drive, the TBM was ripped over 100 m within the receiving southbound mined tunnel, from the TBM break-out face to the large size Mid-Ventilation Junction Cavern, where it did a U-Turn towards the short section of pre-excavated northbound mined tunnel for the break-in preparation of the second 2,400 m long TBM drive. Minimizing the extent of TBM dismantling and reassembly, and with the use of a turn table which was redesigned for the occasion, the overall operation took 3 months only, between the break-out date of the first drive and the break-in date of the second drive.

1 INTRODUCTION

1.1 The Project

The Liantang Heung Yuen Wai Boundary Control Point project comprises the site formation of about 23 hectares of land for provision of the Boundary Control Point (BCP) buildings and associated facilities, as well as the construction of about 11km long dual 2-lane Connecting Road between the BCP and Fanling Highway. Part of this Project, the Liantang / Heung Yuen Wai Boundary Control Point Site Formation and Infrastructure Works – Contract 2 constructed by Dragages Hong Kong Limited (DHK, a member of the Bouygues Construction Group) mainly consists of the design and construction of a 4.8 km long dual two-lane trunk road tunnel connecting the proposed Sha Tau Kok Road interchange and the Fanling Highway interchange, 49 cross passages, a 300 m long ventilation adit tunnel between the mid-Portal and the Mid-Ventilation Junction Cavern, three ventilation buildings, an administration building, and the site formation and slopes works at the South and North Portals. The project reduces the travel times from Fanling Highway to Ping Che area and Heung Yuen Wai, Ta Kwu Ling from 15 and 24 minutes, to 4 and 8 minutes respectively. The road tunnel was open to Public in May 2019.

The geology which consisted of Volcanic Ash Tuff Rock was found extremely variable during the works, from very strong rock (up to 200 MPa UCS) to Completely Decomposed Tuff (CDT), with many sections of faulted ground, geological structures and high-water inflow. A combination of a 14.1 m diameter Earth Pressure Balance Tunnel Boring Machine (EPB TBM), together with mechanical and drill and blast excavation techniques, was adopted to cope with the various ground conditions along the 4.8 km tunnel route. The EPB TBM was used for the construction of the tunnels in the northern section, where several fault zones and valleys were located, while drill and blast technique was mostly used in the more competent rock of the southern section, see Figure 1.

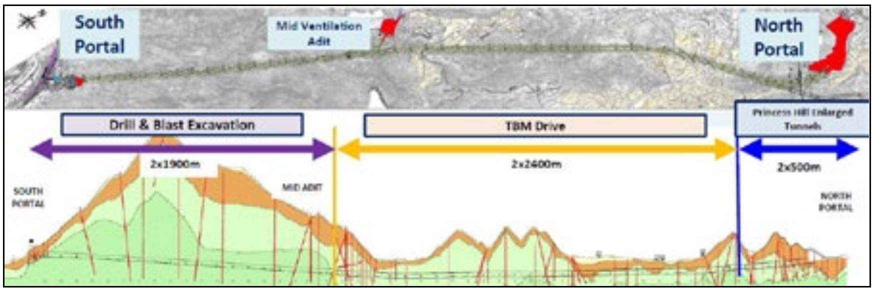

Figure 1 – Lung Shan tunnel geology and tunneling techniques

Due to land ownership constraints the northern 500 m section of the tunnels has a curved alignment with a 354 m radius which restricts the sight-line distance of the road users to below the minimum 110 m at 80 km/hr. To overcome this the internal span of the tunnels needed to be increased from 12.6 m, in the standard straight section, to 15.4 m in this curved section to accommodate a widened shoulder which provides the required sight-line distance. Therefore the 14.1m diameter TBM was not large enough to build the tunnel permanently in the first 500 m of the Project from the North Portal, see the blue section on Figure 2.

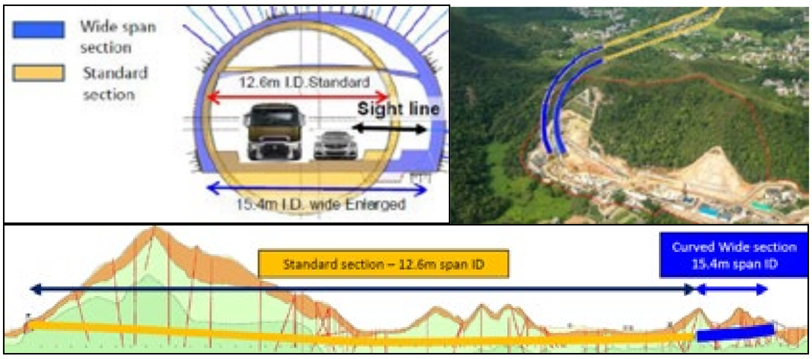

Figure 2 – Wider tunnel in the first 500 m long horizontal curve due to sight distance requirement

1.2 Challenging Programme and DHK's Alternative Scheme

Refer to Figure 3 below - in the conforming scheme the full 500 m length of the large span southbound tunnel was completed, before the TBM was launched, which resulted in a very late start of the TBM. Therefore, the TBM drive could only be short (approximately 1 km), could only address the crossing of the first valley, and had to be fully dismantled and reassembled for the second 1 km long drive in the northbound tunnel. Therefore, the second valley and faulted ground section were going to be excavated by traditional drill-and-blast or mechanical method, which DHK also identified as a very high risk for the Project. Finally, there was a programme risk to complete the Project meeting the Project completion date.

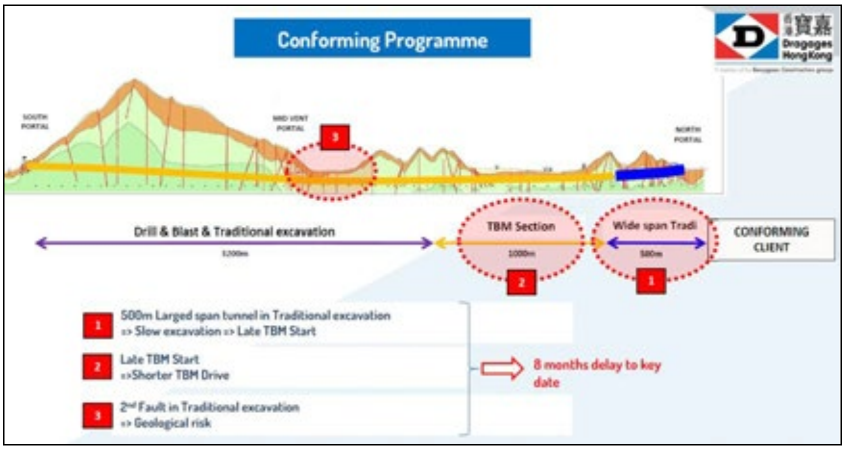

Figure 3 – Conforming scheme not meeting the Client's Project completion date

During the tender stage DHK identified three major objectives to deliver a successful Project to CEDD:

1. How to secure the Client's Project completion date?
2. How to optimize the use of the TBM?
3. How to reduce the geological risk?

As shown on Figure 4, to meet these objectives DHK developed and proposed the following alternative scheme in their tender submission:

a. The TBM was launched much earlier, as soon as it was getting ready to bore, after 200 m of large span tunnel excavation (instead of 500 m in the conforming scheme)

b. Therefore approximately 300 m of the 14.1 m diameter TBM tunnel became a pilot tunnel to be enlarged afterwards by 5 to 9 m

c. Thanks to the pilot tunnel enlargement methodology presented in the Section 2 below, the TBM could progress ahead along its drive southwards, while the pilot TBM tunnel was being enlarged behind, off the critical path

d. It was also decided to extend the EPB TBM drive from 1 km to 2.4 km length, thus mitigating the highest geotechnical risk of the project which would have consisted of crossing the 2nd valley and faulted ground section using mechanical or drill-and-blast technique in the conforming scheme

e. In addition, using the construction method presented in Section 3 below, the TBM was proposed to U-turn within the Mid-Ventilation Junction Cavern to minimize the time required to start the 2nd TBM drive northwards

f. Finally, thanks to this alternative technical scheme, DHK were able to advance the works by 8 months and to meet the Client's Project completion key date.

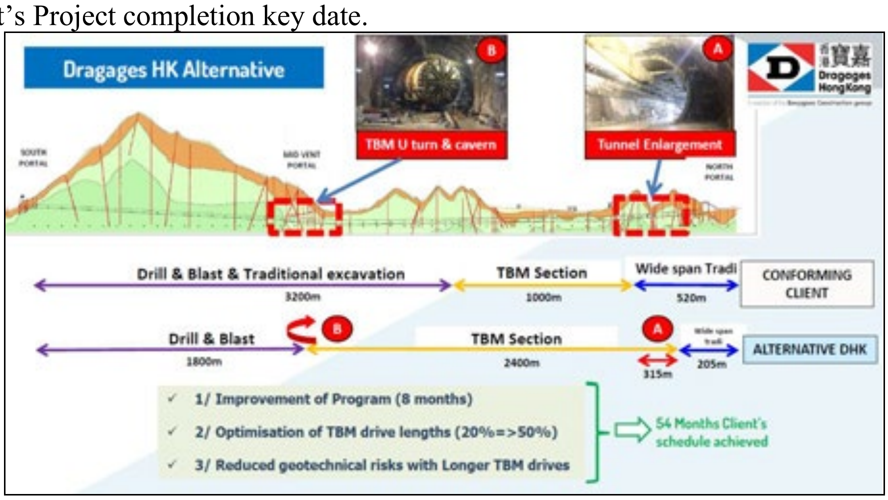

Figure 4 – DHK's alternative scheme with Pilot TBM Tunnel Enlargement and TBM U-turn in Cavern, meeting the Client's Project completion date

The Sections 2 and 3 below present the construction methodologies used for respectively the Pilot TBM Tunnel Enlargement works and the TBM U-turn inside the Mid-Ventilation Junction Cavern.

2 PILOT TBM TUNNEL ENLARGEMENT

2.1 Enlargement works and objectives of the construction method

As shown on Figure 5, the enlargement works of the pilot 14.1m diameter TBM tunnel are massive, in length (approx. 315 m) and in cross section. Considering all construction tolerances, where canopy vaults were required, the excavated span of the enlarged tunnel ranged from 21 m to 23 m and the height from 15.5 m to 16.5 m. With such large dimensions the total excavation area (235 m^2 to 275 m^2) was closer to the scale of a cavern rather than a standard tunnel.

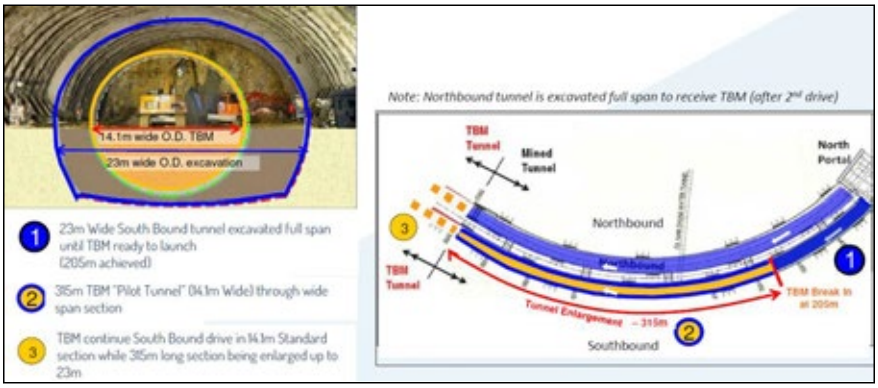

Figure 5 – Pilot TBM Tunnel Enlargement Works

A construction method had to be developed to enlarge the pilot TBM tunnel, while meeting the following objectives:

- To maintain 24 hours, 7 days a week, the TBM logistics traffic and utilities during the enlargement works, to continuously supply the 2,400 m long TBM drive ahead, particularly with temporary ventilation, precast segments and pipes delivery, EPB TBM mucking out conveyor belt, temporary utilities, workers' vehicle and pedestrian access
- No restriction to the TBM supply, the enlargement works having to adapt to the TBM cycle, and no stoppage of the TBM was allowed
- Ensure a safe environment, not only for the enlargement works but also to all other workers and plant transiting through the section of enlargement works, such as the TBM crew, maintenance teams, support teams (plant, survey, safety, quality, technical), drivers, MSV, site vehicles and plant, etc.

2.2 Proposed construction method and sequence

It was quickly identified that a temporary steel deck structure was required, on top of which the enlargement works of the tunnel top heading could be carried out, while the TBM logistics could flow underneath it. Several options were considered such as a tailor-made rolling gantry tool, a recyclable shorter temporary steel gallery, or a full-length temporary steel gallery. While the size required for the possible rolling gantry was found too large and unpractical, the option of recycling a short temporary steel gallery as the top heading enlargement works progress was found difficult logistics wise and likely unsafe. Finally, the project team selected the construction method using a full-length 315 m long temporary steel gallery.

Figure 6 shows an overall view of the site set up in the pilot TBM tunnel enlargement area, with the TBM progressing ahead towards the Mid-Ventilation Junction Cavern. The following Figures 7 to 14 illustrate the details of each step of the construction method and enlargement works sequence selected.

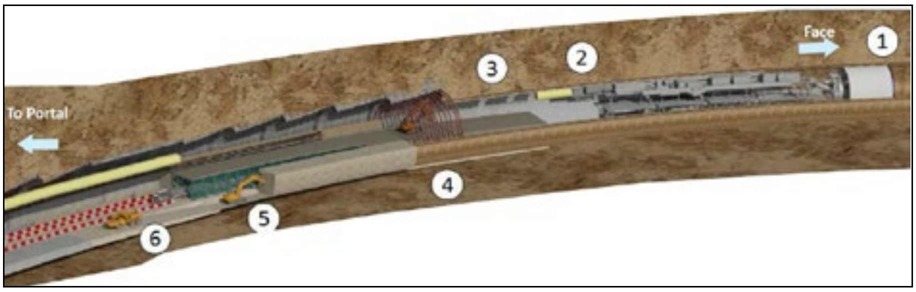

Figure 6 – Overall sequence of pilot TBM Tunnel Enlargement works

Step 1 – build the 315m long pilot 14.1 m diameter TBM tunnel, using steel fibre reinforced precast segments (to ease their subsequent demolition), which was a first of that size in Hong Kong. Three rings were indeed instrumented with strain gauges and crack meters to study the behaviour of large diameter fibre reinforced precast segmental rings in comparison with conventionally reinforced precast segmental rings.

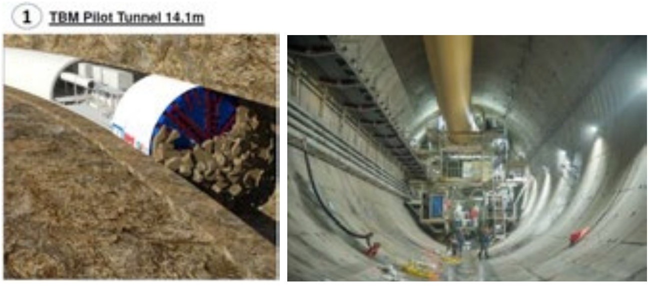

Figure 7 – 315m long pilot EPB TBM fibre reinforced segmental lining tunnel

Step 2 – install the arch ribs foundation of the future temporary steel access gallery, the temporary backfill and the temporary utilities required for the TBM (TBM mucking out conveyor, air and water supply pipes, 2.5m diameter ventilation duct and 22kVa electrical cables).

Figure 8 – Installation of temporary steel gallery foundation, backfill and utilities

Step 3 – install the 315 m long temporary steel gallery made of mostly universal columns, one bottom arch member and two vertical columns every 3.2m, as well as a deck made of universal columns and sheetpiles. The upper part of the structure is backfilled and dedicated to the top heading enlargement works, while its lower part hosts the conveyor and some utilities on one side, the TBM vehicular access in the middle, and a safe segregated pedestrian access, TBM ventilation duct and other utilities on the other side. The temporary steel gallery was designed by DHK's Designer Atkins China Limited, based on a series of load combinations defined from the detailed planning of the enlargement works.

Figure 9 – 315m long temporary steel gallery installation and backfill on the deck

A special section of steel gallery of approximately 80 m length is designed and installed at the start of the 315 m long gallery, including a steel ramp to the top side of the deck and an open side span for the traffic and logistics to be able to access underneath the deck of the gallery.

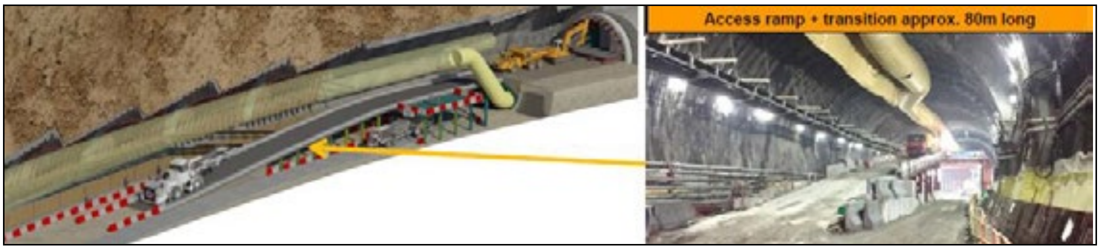

Figure 10 – Special gallery section at the start with access ramp and side span vehicle entrance into the gallery

Step 4 – carry out the tunnel top heading enlargement works consisting of a traditional excavation method:

- Pre-excavation probing and grouting to control the ground water inflow into the tunnel
- Installation of canopy vault in adverse ground conditions to strengthen the crown of the excavation
- Demolition of the temporary steel fiber TBM segments using breakers, by round of 1.6m advance being the width of a segment
- Installation of heavy temporary supports steel arch ribs, lattice girders, or rock dowels in better ground conditions, as well as shotcrete at the tunnel crown, walls and face
- At each 1.6 m advance, the cycle of excavation, breaking of segments, temporary support installation was repeated.

Figure 11 – Pilot TBM tunnel top heading enlargement works from the top of the temporary steel gallery

The dynamic force induced by the segment pieces falling onto the top of the technical gallery was expected to be significant. To reduce it an impact gantry was designed, fabricated and pulled below the segments being demolished. The impact gantry was composed of many longitudinal supporting beams, a receiving platform at the bottom, as well as sliding beams allowing movement of the whole gantry to its next position, Figure 12.

Figure 12 – Special impact gantry preventing the fall of large blocks and reducing the impact load on the steel gallery

Step 5 – following the top heading enlargement, it was then possible to relocate the utilities, the ventilation duct and the conveyor to the upper section of the tunnel, which allowed the partial dismantling of the right-hand side of the technical gallery, as well as the right-hand side bench enlargement, while the construction traffic remained in the middle part.

Figure 13 – Relocation of utilities, right-hand side bench enlargement and partial dismantling of the steel gallery

Step 6 – shift the construction traffic to the already enlarged bench on the right-hand side, complete the dismantling of the steel gallery and the bench enlargement on the left-hand side. The enlargement of the pilot TBM tunnel is now complete.

Figure 14 – Left-hand side bench enlargement and completion of the steel gallery dismantling

2.3 Enlarged tunnel temporary support

The geology in the section of pilot TBM tunnel enlargement was very variable, consisting generally of rock, partial rock 50/75, partial rock 10/30, or even CDT at crown, see Figure 15.

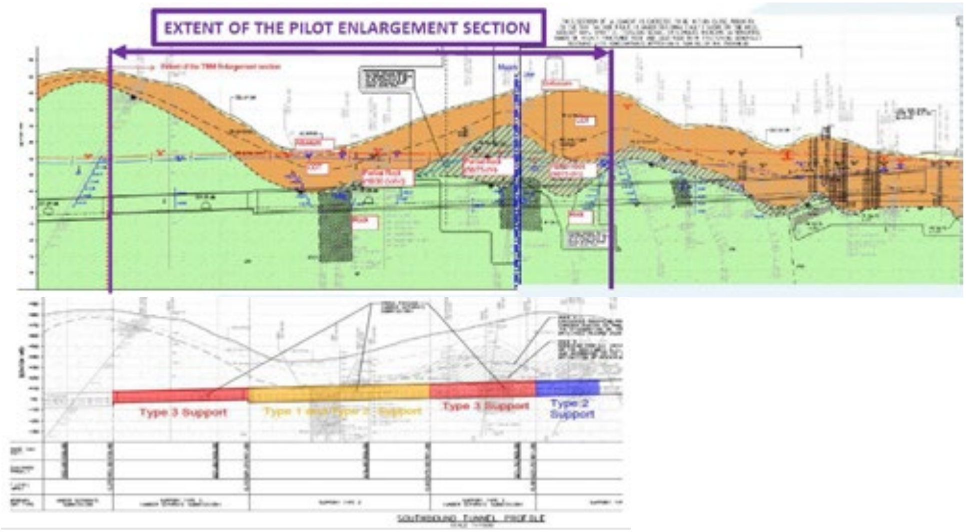

Figure 15 – Geology and temporary support types used for the pilot TBM enlargement works

See Figure 16, we developed 3 main types of temporary support designs, which were used alternately along the enlargement works, according to the ground conditions:

- Type 1 support was made of canopy tubes and steel arch ribs every 800mm, with 300mm shotcrete
- Type 2 support was of similar arrangement, however much lighter, with lattice girders instead of arch ribs
- Type 3 support was made of rock dowels and shotcrete

Pre-excavation probing and grouting were also included in the enlargement works cycle, following the same principles as in the standard mechanical excavation sequence.

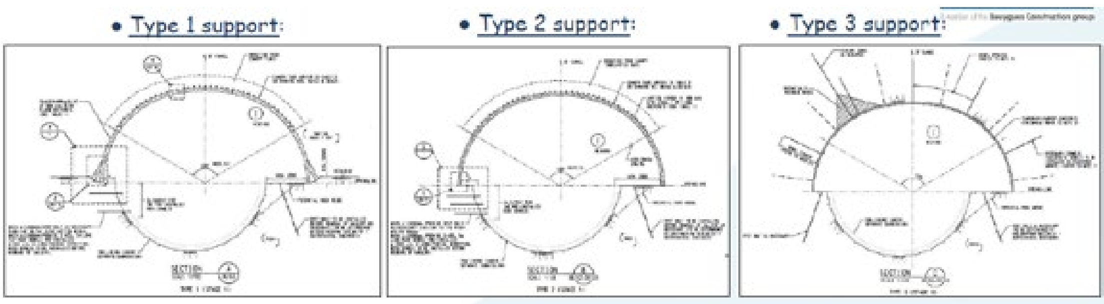

Figure 16 – Pilot TBM tunnel enlargement top heading temporary support designs

2.4 Achievement

The TBM pilot tunnel enlargement operation went better than anticipated: as shown on Figure 17, we managed to progress 1 ring per day for the top heading, 1.5 ring and 2.5 rings per day respectively for bench RHS and LHS enlargement. Overall, the enlargement of that 315 m long 14.1 m diameter pilot tunnel took 14 months instead of the 17 months anticipated. Most importantly we managed to carry out these very challenging enlargement works safely, without any disruption to the TBM progress ahead, saving about 5 months on the project critical path, in comparison with having waited for the completion of the 500 m long large span tunnel by traditional excavation means only.

We had also checked other possible TBM alternative schemes:

i. Two TBMs: one TBM of 17 m diameter to excavate the 500 m section of large span tunnels, and one TBM of 14.1 m diameter to do the rest of the drives, or

ii. One hybrid 17 m diameter TBM, which could change diameter to 14.1 m, after 500 m of excavation

Those alternative TBM schemes would have introduced more programme risks (risk of insufficient TBM torque of what would have been the largest TBM in rock in the world and in a tight horizontal curve; technical first of significantly modifying the cutter head and shield underground, with the need of a local cavern for the operation), would have been less cost effective, and less efficient for the Project critical path.

We trust that the 14.1 m diameter TBM pilot tunnel and its subsequent enlargement solution selected was the best technical scheme for the Liantang Project.

	Planned (month)	Actual (month)	Ratio Actual (Ring/day)
Top Heading	8 mths	7 mths	1 R/d
Bench RHS	5 mths	4 mths	1.5 R/d
Bench LHS	4 mths	3 mths	2.5 R/d
Overall	**17mths**	**14 mths**	

Figure 17 – Pilot TBM tunnel enlargement production rates

3 TBM U-TURN IN CAVERN

3.1 TBM U-turn methodology objectives and early engineering

As shown on Figure 18, three main TBM movements were required for the TBM U-turn operation across the Mid-Ventilation Junction Cavern, between the first and the second TBM drives:

- a longitudinal sliding in the southbound tunnel, from the break-out face to the cavern
- a rotation and lateral sliding within the cavern
- a longitudinal sliding in the northbound tunnel, towards the break-in position

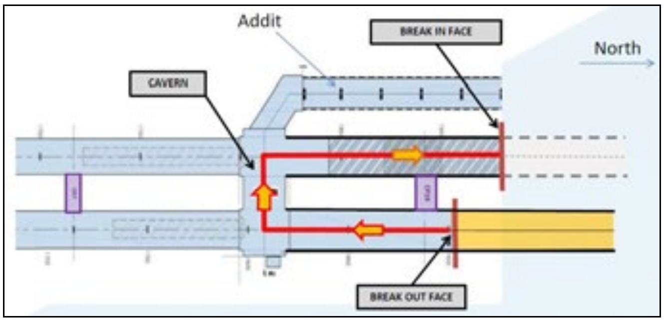

Figure 18 – TBM transfer underground between the two TBM drives incl. U-turn in the Mid-Ventilation Junction Cavern

The main objectives identified for the TBM U-turn methodology were:

- Ensure safety to the workers and to the TBM equipment throughout the operation
- Minimize the extent of TBM dismantling and reassembly to keep the overall operation to a minimum duration, with a target of 3 months
- Early planning and preparation of the civil works for the TBM break-in of the second drive

To meet these objectives the following actions were taken by DHK:

- Engage the specialist company VSL Hong Kong to prepare and operate the TBM sliding operations
- Reuse and refurbish the TBM Turn Table from our Port of Miami Tunnel Project
- Rationalize the geometry of the Mid-Junction Ventilation Cavern to ease the construction of its permanent works, while allowing sufficient space for the TBM U-turn operation, which was validated by detailed BIM coordination, see Figure 19 below
- Launch an early detailed design with our Designer Atkins China Limited to develop a fit-for-purpose break-in thrust frame scheme, compatible with the faulted ground conditions identified during the excavation of the ventilation adit from the Mid-Portal, see Section 3.3 below

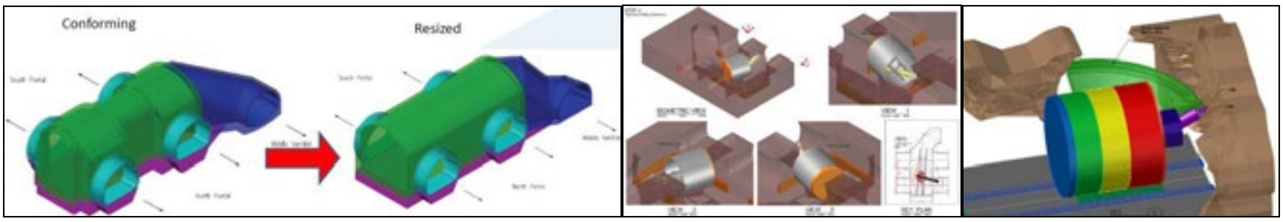

Figure 19 – Mid-Junction Ventilation Cavern early spaceproofing and sizing study for rationalized permanent works construction and TBM U-turn operation

3.2 TBM U-turn specific methods, technologies and operation

The TBM U-turn operation took place in the 22 m span x 23.5 m high x 50 m long Mid-Ventilation Junction Cavern and adjacent tunnels shown on Plate 1 below.

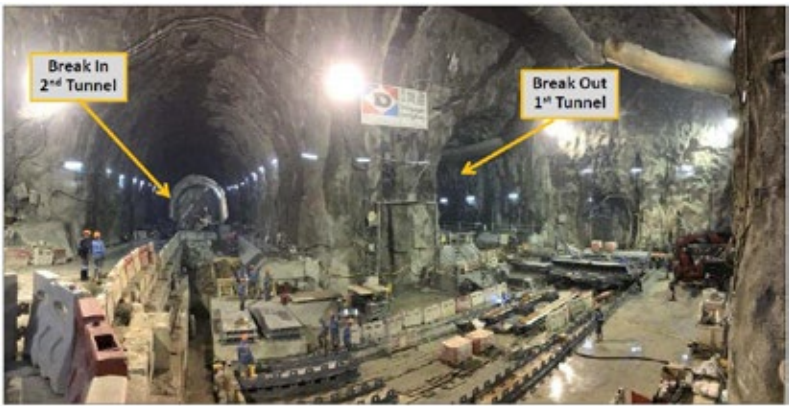

Plate 1 – Overall view of TBM U-turn preparation in the Mid-Ventilation Junction Cavern and adjacent tunnels

For the sliding of the TBM elements, the heaviest of which was the TBM shield (2,500 tons), VSL Hong Kong implemented a solution using 2 units of 330 tons strand jacks providing a total pulling capacity of 660 tons. The TBM shield was placed on skid shoes with steel against brass interface, Figure 20.

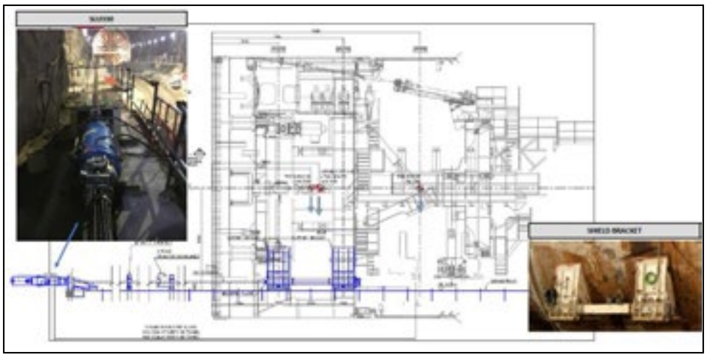

Figure 20 – VSL Hong Kong Ltd jacking system used for TBM sliding

To rotate and translate the TBM in cavern an automated hydraulic Turn Table was used with a limit capacity of 4,800 tons. This Turn Table consisted of a lower and an upper deck separated by a Teflon pad to allow a low friction rotation. 16 units of 300 tons jacks were used to lift the Turn Table, while 2 units of 300 tons jacks were used for the translation system, and the last 2 jacks ensured a rotation capacity of 1000 tm.

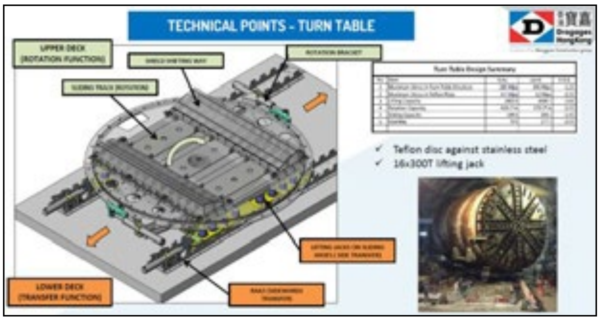

Figure 21 – Principles of the Turn Table used for the TBM U-turn and transfer operation

Plate 2 shows the transfer operation of the major TBM element including the cutter head, shield and screw. The same system was used for the transfer of all the TBM back up gantries which did not require to be dismantled.

Plate 2 – TBM U-turn and transfer operations within the Mid-Ventilation Junction Cavern

3.3 Innovative TBM Break-in methodology in adverse ground conditions

Following the excavation of the mid-ventilation adit from the Mid-Portal, it was found that the TBM break-in originally planned was located in faulted ground. The risk was considered not acceptable and the TBM break-in location was shifted northwards just passed the geological feature, see Figure 22.

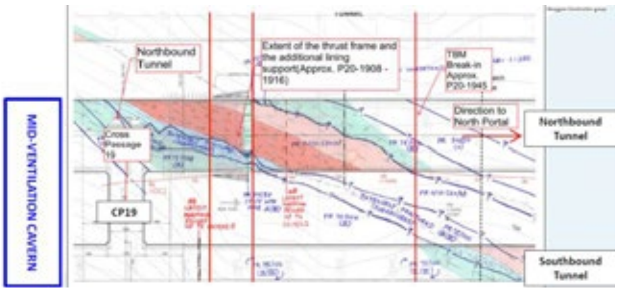

Figure 22 – Adverse geology in the TBM Break-in area of the 2nd northbound TBM drive

However, the TBM thrust frame behind had then to be designed for adverse ground conditions. In that context, based on 8 bar possible ground water pressure, we developed a hybrid thrust frame system made of:

1. A steel thrust frame connected to steel brackets embedded in a collar made of steel ribs and shotcrete above spring line / and supported by inclined steel struts to a reinforced concrete foundation at the bottom
2. A friction thrust frame, based on the mobilization by friction of the infill concrete between the tunnel segmental lining extrados over 8 rings and the arch ribs & shotcrete of the tunnel temporary support. T25 shear connectors were mounted at the segmental lining extrados to provide the required shear strength in the hatched areas indicated on the elevation of Figure 23 below.

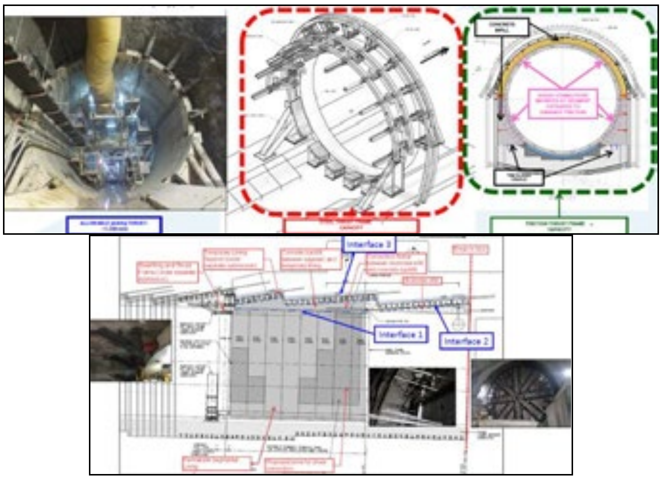

Figure 23 – Innovative hybrid thrust frame in adverse geology for the break-in of the 2nd TBM drive

3.4 Achievement

Thanks to a very detailed and early engineering of the Mid-Ventilation Junction Cavern spaceproofing, of the TBM U-turn operations, and of the TBM break-in system in the adverse ground conditions of the northbound tunnel, DHK managed to meet the objective of keeping the overall duration, between the break-out date of the first TBM southbound drive and the break-in date of the second TBM northbound drive, to 3 months only.

3 CONCLUSIONS

On the Liantang / Heung Yuen Wai Boundary Control Point Site Formation and Infrastructure Works – Contract 2, Dragages Hong Kong Limited proposed a series of advanced construction methodologies which benefited the Project:

- Use of a pilot 14.1 m diameter TBM tunnel in the tight horizontal curve from the North Portal, to reach the Mid-Ventilation Junction Cavern earlier and accelerate the progress of the excavation works
- Extend the TBM drives from 1,000 m to 2,400 m per tunnel to maximize the use of the EPB TBM
- Reduce the highest Project risk, by crossing the second valley and faulted ground area using the EPB TBM, instead of the mechanical or drill-and-blast technique of the conforming scheme
- Develop a safe methodology for the enlargement of the 315 m long pilot 14.1 m diameter TBM tunnel, off the critical path, and without any interruption of the logistics to the TBM operation ahead
- Implement very efficient TBM U-turn operation in the Mid-Ventilation Junction Cavern and preparation works for the innovative TBM break-in system developed for the adverse ground conditions of the northbound tunnel, which overall took 3 months only

These best-for-project technical solutions were implemented safely and resulted in an 8-month programme improvement.

ACKNOWLEDGEMENTS

The authors would like to express gratitude to the Civil Engineering and Development Department of the Hong Kong Special Administrative Region (CEDD) and its Engineer AECOM who supported the adoption of these best for project technical solutions.

REFERENCES

Storry, R.B., Altier, D., Tricot, V., *Advanced technical studies for tunnel enlargement in Hong Kong*. In Proceedings of the World Tunnel Congress, 2016. San Francisco, USA.

Novel Cementitious Materials for Geotechnical Applications – Vibration Resistant Sprayed Concrete for Rock Tunnel Lining and Self-compacting Backfill for Slope Upgrading Works

Martin M K Kwong, H G Zhu, Eric X R Chen, Ivan M L Sham
Nano and Advanced Materials Institute (NAMI), Hong Kong, China

Ivan H H Chan, Chris C W Chan, S N Goh
Geotechnical Engineering Office, Civil Engineering and Development Department, The Government of the HKSAR, Hong Kong, China

ABSTRACT

Innovations in material sciences create new opportunities to enhance the ways of construction in the geotechnical field. By streamlining the conventional construction procedures with the application of new materials, more efficient, more cost-effective and safer construction could be achieved. Two material development projects have been launched by the Geotechnical Engineering Office (GEO), Civil Engineering and Development Department, the Government of the Hong Kong Special Administrative Region, China, and the Nano and Advanced Materials Institute (NAMI) was commissioned to develop the vibration resistant sprayed concrete (VRSC) and the self-compacting backfilling material. This paper presents the development of the two novel materials with particular highlights on the benefits of their applications in rock tunnels and slope upgrading works respectively and addresses the potential development in further applications of the novel materials in the fields.

1 INTRODUCTION

Cementitious materials has a wide range of applications in geotechnical engineering, from structural support of tunnels, ground improvement to backfilling. Traditional concrete materials exhibit high compressive strength and stiffness. In combination with the use of steel reinforcements, reinforced concrete become an excellent material for many engineering applications. However, in order to meet the specific needs for applications in drill and blast rock tunnel lining support and fill replacement of slope upgrading works, extra performance in certain cementitious materials is required.

In drill and blast rock tunnelling, a two-pass concrete lining system, comprising one layer of sacrificial temporary sprayed concrete lining and another layer of permanent lining, is commonly adopted in Hong Kong for rock support. The first-pass lining (the temporary lining) is not considered as part of the permanent works as it could be damaged by blasting vibration in the tunnelling process. Potential damage of the fresh sprayed concrete is assumed in case when the allowable vibration limits, in terms of Peak Particle Velocity (PPV) based on the GEO Report No. 102, are exceeded. Experimental data and recommended limits in this report, however, were based on plain concrete and hence may not be directly applicable to fibre-reinforced sprayed concrete. Overseas examples from field and laboratory testing have demonstrated that sprayed concrete lining could sustain a PPV beyond 500 mm/s (Ansell, 2007; ITA Working Group n°12 & ITAtech, 2020), while the recommended PPV limit in the GEO Report No. 102 is only 70 mm/s at 24-hour after casting. This apparently conservative approach has added constraints to the optimisation of a drill and blast cycle in hard rock tunnelling and cavern excavation. To facilitate composite lining construction without discarding the structural capacity of the first-pass lining, a VRSC formula is being developed to improve the structural performance in vibration resistance and at the same time, enhance the flexural strength, toughness and residual strength. The VRSC development has shown promising interim results and brings insights on the enhancement of constructability, cost effectiveness and sustainability in the long-term strategic rock cavern development.

On the other hand, stabilization of loose fill slopes is always challenging in terms of constructability, cost and construction time of the works. Recompacting the top 3 m of loose fill is an acceptable solution, while pit-by-pit construction method is commonly adopted on sites with constraints, such as presence of mature trees and limited working area. However, manual operations inside pits with limited working space at steep terrain make pit-by-pit method very difficult and time consuming, not to mention the safety concerns of working in pits, difficulties in achieving an adequate degree of compaction and conducting the quality assurance test. To cope with such challenges, DM-4, a self-compacting backfilling material originally designed for trench backfilling for the Highways Department (HyD), was developed and found feasible in addressing the difficulties encountered in the pit-by-pit fill replacement works. This new material has a high flowability and short hardening time while exhibiting comparable properties to soil, such as strength and permeability. These characteristics make DM-4 an ideal alternative to compacting fill material in pits for enhanced constructability, cost effectiveness and safety in slope upgrading works.

2 THE DEVELOPMENT OF VIBRATION RESISTANT SPRAYED CONCRETE (VRSC)

2.1 Methodology

2.1.1 Theoretical analysis and simulation

To understand the blasting-based tunnel excavation process, numerical models for simulating the dynamic response in the tunnel environment were established to assess the blasting-induced vibration propagation in the sprayed concrete lining, maximum vibration velocity, the relation between explosive force impulse and surface vibration amplitude nearby, and the influence of explosive force impulse on the performance of the sprayed concrete lining.

2.1.2 Vibration resistant sprayed concrete formulation

Fibre was introduced to the VRSC formula for enhancing the tensile and flexural performance, residual strength, toughness and energy absorption capacity. Different fibre types may show different effects on VRSC's workability (including spraying capability) and mechanical performance. Various types of fibres with different geometry were evaluated, including synthetic macro fibre and steel fibre. Furthermore, polymer-modified cementitious material powder was introduced into the VRSC formula to enhance the bonding between the sprayed concrete lining and rock substrate and hence reduce the rebound during spraying and improving the water-tightness and durability.

Figure 1: The image and schematic drawing of SHPB

To assess the effects of blasting vibration on the performance of VRSC and determine the corresponding design acceptance criteria, a set of systematic evaluation procedures was designed. A dynamic material test will be conducted in the future with a Split Hopkinson Pressure Bar (SHPB) system as shown in Figure 1. In principle, a sprayed concrete lining is vulnerable to tensile stress that causes delamination or structural damage. A SHPB-based experiment simulates such scenarios by attaching a VRSC sample onto the end of the incident bar to simulate the effect of wave propagation on the sample. This experiment is also named the reflected-wave experiment. Finite element simulation of the SHPB test was conducted to correlate the dynamic stress and velocity fields in a sample for streamlining the complex testing and evaluation procedures. Further elaboration on the SHPB simulation is presented in Section 2.2.2.

2.2 Modelling and simulation

2.2.1 Simulation models

Two-dimensional and three-dimensional finite-element models of the tunnel were established based on Ansell's tunnel configurations and calculations (Ansell, 2004, 2007; Ahmed & Ansell, 2012, 2014) to determine the correlation between the mass of explosive charges, maximum impact on lining in term of stress and vibration speed in term of PPV. Soil and rock were simplified as an equivalent continuum material with the failure criterion following a pressure-sensitive model (e.g., the Drucker–Prager model). Material models for concrete and the sprayed concrete lining will be established based on the actual measured data from sites (or referred to the related literature) later. In the simulation, the detonation of the explosives in the cylindrical drill holes is simplified to being initial pressure impulses (e.g., a triangular impulse). The simulation was conducted by employing an explicit finite element solver, and the results were then interpreted as some snapshots of velocity and stress fields and the detailed velocity/stress variations with time at several concerned points after an explosion. The results helped us establish the relation between the pressure impulse—which may be related to the mass of explosives—and the maximum impact/vibration speed at the areas of sprayed concrete lining and determine the requirements of adhesiveness and strength of sprayed concrete lining under explosive force.

Based on the specific construction requirements for drill and blast tunnelling projects in Hong Kong, the analysis can be repeated to obtain the relation between tensile stress and distance from the explosion centre. A required safety distance of the sprayed concrete lining was established based on the data from the simulation. Figure 2 shows the constructed 3D model of a tunnel under the blast loading. Figure 3 shows the relationship between the distance from the explosive centre and PPV with different TNT equivalents after the simulation.

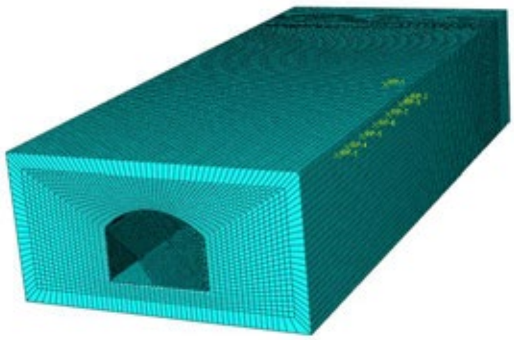

Figure 2: The 3D finite-element model of a tunnel under the blast load

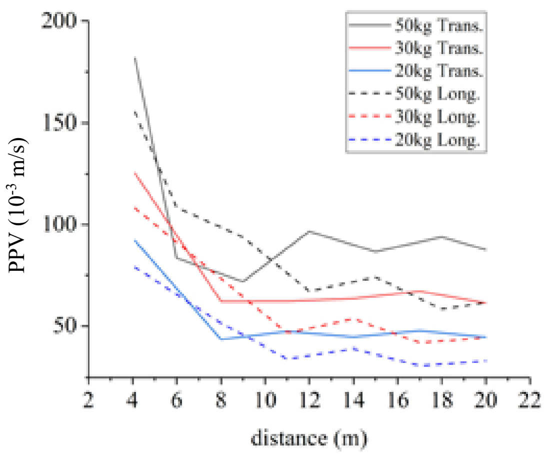

Figure 3: The simulation results of blasting radius versus measured PPV, with different TNT equivalent (kg)

2.2.2 *Split Hopkinson Pressure Bar (SHPB) simulation*

Before the SHPB simulation, it is critical to understand the nature of explosive waves generated by tunnel blasting. The explosive waves are initially isotropic pressure waves that propagate in all directions. However, the geometry of the tunnel complicates the wave propagation. For example, when a pressure wave reaches the tunnel wall, it results in compressive waves along and perpendicular to the wall. The compressive wave perpendicular to the wall bounces back when it hits the interface or surface, and this reflected wave from the surface becomes tensile. This is because the free surface is stress-free; an incident compressive wave must be balanced by a tensile wave to satisfy the stress-free state on the surface. Such a tensile wave induces the tensile stresses leading to delamination or spalling, which is a major concern in sprayed concrete lining, i.e., the sprayed concrete lining must resist a certain magnitude of tensile stresses normal to the interface. As such, a uni-directional SHPB test is adopted. In addition, it is noted that a wave has a wavelength or a duration of substantial stresses. Hence, static tests are not recommended because the action time of the tensile stresses is very short (e.g., within 1 millisecond). SHPB is therefore the tool to generate a stress wave with a finite duration, which suits the purpose.

The exact requirements of the dynamic strengths of concrete and concrete-rock bonding can only be determined based on the simulation results of tunnel blasting after the numerical model is validated by the on-site measurement of surface vibrations. To determine the dynamic properties of sprayed concrete and rock-concrete interface, SHPB experiments are necessary. Associated with the SHPB experiment to be done in the next phase of the project, SHPB simulations were conducted to assist our experimental design. Figure 4 shows the simulation results, indicating that the incident wave generated by the projectile was a uniaxial compression wave. The reflection from the interfaces and sample surface led to tensile waves; this phenomenon was in line with the stress wave propagation theory. Figure 5 (a) shows the simulation results on the interface between the sprayed concrete and rock. Figure 5 (b) shows the simulation results of tensile stresses measured on the same interface with different striker velocities of the aluminium (Al) striker.

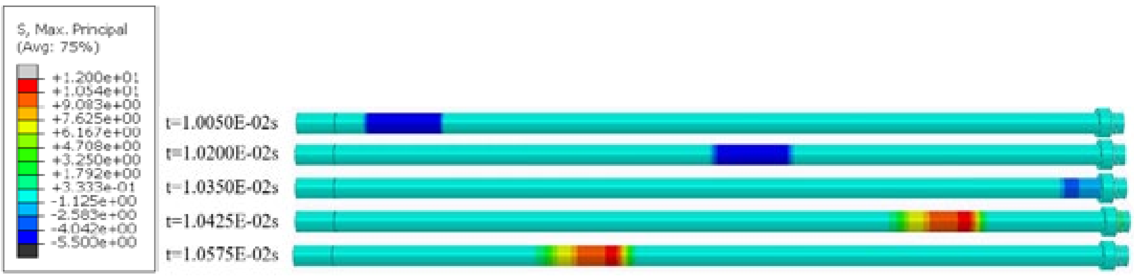

Figure 4: The propagation of stress wave in the SHPB (Positive as tensile)

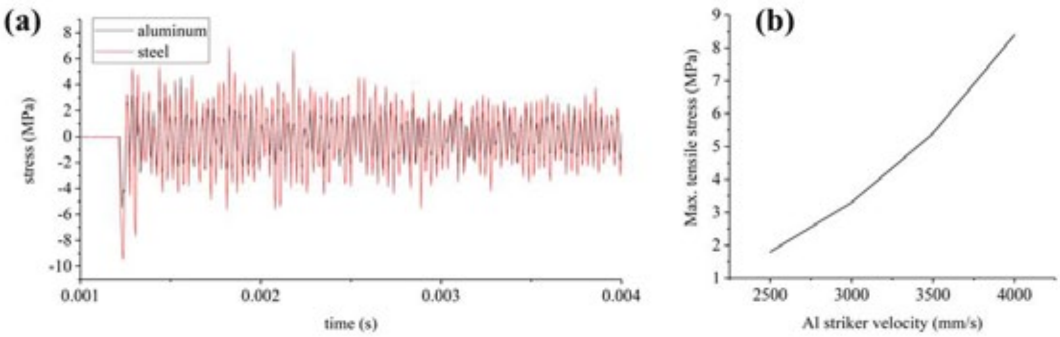

Figure 5: (a) The stress curves (Al and steel strikers, where positive and negative stresses are tensile and compressive respectively), & (b) the relations between Al striker velocity and maximum tensile stress measured on the sprayed concrete-rock interface

The SHPB simulations have shown that the actual measured PPV values during tunnel blasting together with the known quantities of explosives can be used to evaluate the relationship between PPV and tensile stresses that the VRSC lining has experienced. These numerical simulations provide useful and important information for the design of the SHPB test and give insights on completing and improving the SHPB setup. Moreover, they serve as a guideline for the VRSC mix design optimization such as the requirement on bond strength to the rock substrate at a specific distance away from the blast centre.

2.3 Site trial for scale-up production of VRSC

A site trial for scale-up production of VRSC was conducted for determining the mechanical properties and quantifying the performance of VRSC in a realistic construction process and environment. Laboratory testing such as flexural tests and direct pull-out tests were conducted. Flexural testing on beam specimens is important as it provides the fundamental significance of crack opening response when the concrete is under tensile loading; while plate or slab bending testing is more related to the energy absorption capacity, especially in the practical applications where the load-carrying capacity of concrete at large deformation is critical, and the design is primarily empirical. Direct pull-out testing examines the bond strength between the VRSC and the rock substrate, which is related to a typical failure mode of sprayed concrete lining.

2.3.1 Scale-up production

To verify the mechanical performance subject to transportation, the produced VRSC was transported from the concrete mixing plant at Yuen Long to the construction site located at Sha Tin, as shown in Figure 6. On site, flow table tests were conducted, and the temperature of the fresh VRSC were recorded. VRSC cubes, prisms and panels were also prepared for compressive strength tests, flexural strength tests, toughness and energy absorption capacity measurement respectively at specified ages, as shown in Figure 7.

2.3.2 VRSC performance

Table 1 shows the fresh VRSC performance which satisfies the requirements on workability, consistency and temperature both in the plant and on site. The produced VRSC showed a flow table value above 600 mm even at 2 hours after water addition, fulfilling the general concrete requirements. No bleeding was found in the fresh VRSC. The initial and final setting times of the produced VRSC were measured as 540 minutes and 625 minutes respectively. The temperature of fresh VRSC was around 26°C at the plant but raised to 29.9°C on site.

Figure 6: (a) The concrete truck arrived on-site, and (b) fresh VRSC was poured for testing

Figure 7: The fresh VRSC (a) prisms, and (b) cubes and panels

Table 1: Performance of the fresh VRSC

Fresh concrete properties	Condition	Results
Flow table value (FTV)	Initial	615 mm
	15 mins after addition of water	635 mm
	120 mins (on-site)	620 mm
Bleeding	At plant	No observed
	On-site	No observed
Setting time	Initial	540 mins
	Final	625 mins
Temperature	Initial	26.0 °C
	15 mins	25.9 °C
	120 mins (on-site)	29.9 °C

Table 2: Performance of the hardened VRSC

Testing Item	Age	Requirement	Results
Compressive Strength	24 hrs	≥ 14 MPa	18.5 MPa
	7 days	≥ 25 MPa	50.5 MPa
	28 days	≥ 35 MPa	63.1 MPa
Flexural Strength	28 days	≥ 5.0 MPa	7.0 MPa
Toughness Index I_5	7 days	≥ 3.5	3.8
	28 days	≥ 4.0	4.4
Toughness index I_{10}	7 days	≥ 5.0	7.0
	28 days	≥ 6.0	8.3
Residual Strength $R_{5.10}$	7 days	N/A	67.0
	28 days	≥ 60	78.7
Energy Absorption Capacity	28 days	≥ 700 J	1430 J

The values of measured compressive strength, flexural strength and toughness and the energy absorption capacity of the hardened VRSC are shown in Table 2, in which the requirements are also included. Although no accelerator was used, the 1-day compressive strength of the produced VRSC reached 18.5 MPa, fulfilling the requirements of 14 MPa. The 7-day and 28-day compressive strength reached 50 MPa and 63 MPa, respectively, both above the required values. The measured flexural strength, toughness index, residual strength and energy absorption capacity are all well-above the required values.

2.4 Current status of development and way forward

The formulation of VRSC has been characterized in the laboratory and plant trial. The results from the plant trial were found consistent with the result of the laboratory trial, which showed excellent mechanical performance. To test the sprayability, rebound and mechanical performance of VRSC on site, further site trials will be conducted in the next phase of the project where VRSC is applied to a rock substrate in the tunnel by mechanical spraying, as well as sprayed concrete panels for testing. To simulate the effect of blasting, the VRSC lining will be subject to blasting impacts where vibration monitoring will be done to measure the PPV experienced. The measured PPV data will be studied and used to calibrate the numerical simulation model.

3 SELF-COMPACTING BACKFILLING MATERIAL

3.1 Development of the DM-4 backfilling material

Facing the increasing need for frequent and rapid trench filling in roadworks, an universally applicable self-compacting backfilling material – DM-4 (hereinafter the DM-4 backfilling material) was developed by NAMI as initiated by the Highways Department (HyD). The development of the DM-4 backfilling material focused on the following aspects: high applicability, self-compacting ability and high flowability, making it a suitable backfilling material for trenches with congested pipe/cable networks. It also has a high thermal conductivity which fits the specific requirement for power cables. In terms of strength development, the DM-4 backfilling material was designed to gain strength rapidly after application, which increases the construction productivity and reduces the time of road reinstatement works. With these special characteristics, GEO launched a separate project on applying the DM-4 backfilling material on slopes as an alternative material for 'pit-by-pit' fill replacement for slope upgrading works under the Landslip Prevention and Mitigation (LPMit) Programme. More details of the site trials are presented in Section 3.3.

The DM-4 backfilling material has a high flowability (> 200mm slump) and a 28-day compressive strength lower than 1 MPa, designed for trench backfilling to allow easy manual excavation in the future. The formula verification and optimization for slope backfilling application was conducted in the NAMI laboratory. Plant trials were carried out in a local concrete plant to verify the scale-up producibility and consistency in mechanical properties of the DM-4 backfilling material. The volume of the proposed backfilling works, material discharge method and required laboratory and field testing details were also discussed and agreed with the relevant stakeholders before the site trials. The detailed arrangement and results of the site trials are presented in Section 3.3.

3.2 Formulation of the DM-4 backfilling material

The core part of the DM-4 formulation was the compatibility among cementitious materials, aggregates and admixtures. The DM-4 matrix was developed based on raw materials selected on their availability in the local market, such as Ordinary Portland Cement (OPC) and Pulverised Fuel Ash (PFA) as binders. In addition, different types of non-pozzolanic fine fillers, such as crushed rock fines (CRF), were also studied and applied in the formulation.

Among the major characteristics mentioned in Section 3.1, workability is the most important parameter to facilitate the backfilling application on-site. A high workability makes the DM-4 backfilling material highly pumpable and flowable. The mix formula was then optimized to achieve a balance between workability and compressive strength without causing segregation and bleeding but maintain a minimum slump loss. To lower the density, a nano-foam, which is an ultrastable and nano size foam developed by NAMI (Sun et al, 2019), was introduced into the mix. It also improved the workability and further reduced the risk of bleeding.

To verify the mechanical properties and performance of the DM-4 backfilling material, a series of laboratory and field tests on density, flowability, hardening time, initial strength and compressive strength were done, which are briefly presented in the sub-sections below.

3.2.1 Density

The wet density was measured on the site from two samples collected from the concrete truck by filling a 1 L volume cubic mould with the slurry of the DM-4 backfilling material. Figure 8 shows the wet density test carried out on site.

3.2.2 Flowability

The consistency of the slurry of the DM-4 backfilling material without segregation was checked upon delivery to the site by flowability testing in accordance with ASTM D6103. One sample of not less than 20 L was collected from the initial discharge of the batch, and the second sample of not less than 20 L was collected after half volume of the batch had been discharged for the flowability test. Figure 9 shows the flowability test carried out on site before placement.

Figure 8: Measurement of wet density on site

Figure 9: Measurement of flowability on site

3.2.3 Hardening time

Two samples of the DM-4 backfilling material of 2.65 L were collected from the first discharge of the concrete truck and tested in accordance with BS EN 13294 standard in the NAMI laboratory. Figure 10 shows the hardening time test carried out in NAMI laboratory for a sample casted on site.

Figure 10: Hardening time testing apparatus in NAMI laboratory

3.2.4 Initial strength

Before further works can be commenced on the surface of the backfilled area, the suitability for load application was tested according to ASTM D6024. A half-spherical weight was dropped five times from a height of 108-114 mm onto the surface of the backfilling material. The diameter of the resulting indentation was measured and compared to the established criteria. Figure 11 shows the initial strength test conducted on site by a “Kelly-ball” apparatus.

Figure 11: “Kelly-ball” test conducted on site

3.2.5 Compressive strength

To evaluate the compressive strength of backfilling material, 100 mm cube samples were collected on site. The samples were covered to eliminate water evaporation and kept at room temperature before drying to an oven-dry density and the compressive strength test at 3, 7 and 28 days with reference to Construction Standard CS1:2010. Figure 12 shows the compressive strength test in NAMI laboratory.

Figure 12: Sample for compressive strength testing

3.3 Site trials for slope upgrading works

After a series of site trials for trench backfilling of public utility works in 2020, NAMI successfully verified the production process and performance of the self-compacting backfilling material under practical situations. Since 2021, NAMI collaborated with the GEO and applied the DM-4 backfilling material in slope upgrading works under the LPMit Programme. The material has been used in both large and small scale backfilling operations since then. In smaller sites or areas inaccessible with a concrete truck, the DM-4 backfilling material was mixed on-site with a continuous mortar mixer and pumped into the pits. In larger operations starting from approximately 6 cubic meters, the material was pre-mixed in a concrete batching plant and delivered to the site by a concrete truck. During the site trials, the backfilling operation was tested by pumping the DM-4 backfilling material into a pit by a concrete pump. Specific arrangements should be taken into consideration before the pumping, such as checking the connection between pumping tubes and sealing of gaps between any formwork and soil to avoid leakage of the DM-4 backfilling material. Due to its high flowability, a single truckload of approximately 6 cubic meters of backfilling material can be pumped into the slope pits in less than 15 minutes. After the placement, the backfilled area was left to set before testing the initial load-bearing capacity of the hardened surface.

As a result of collaboration between NAMI and the GEO, over 500 m^3 of the DM-4 backfilling material has been successfully placed in various slope upgrading works sites since 2021. The use of the DM-4 backfilling material reduced significantly the manual handling and labour required for the fill replacement works for enhanced site safety. The availability of a dry-mix option and the feasibility to convey the material using concrete pump made the material particularly useful in overcoming site access constraints. The ease in placement and simple quality control of the material also led to a remarkable shortening of the construction duration. Having the successful results from the various site trials and conditions, additional slope sites involving the use of the DM-4 backfilling material are being arranged with a view to consolidating experience.

Figure 13: Overview of slope site at Lei Uk Tsuen, Shatin

Figure 14: Pumping backfilling material from concrete truck to the pit (Lei Uk Tsuen)

Figure 15: Slope works after placement of backfilling material (Lei Uk Tsuen)

3.4 Backfilling material in action

A pilot application of the DM-4 backfilling material was conducted at a site at Lei Uk Tsuen, Shatin as shown in Figure 13 to 15. Table 3 below shows the testing results which satisfy the acceptance criteria in terms of wet density, flowability, hardening time, initial strength and compressive strength. No segregation was found during the flowability test on site.

Table 3: Test results of backfilling material site trial at Lei Uk Tsuen, Shatin

Test items	Acceptance Criteria	Results
Flowability	> 200 mm (without segregation)	220mm without any segregation
Wet density	1900 kg/m^3-2100kg/m^3	2066kg/m^3
Hardening time	Reach 3.5 N/mm^2 within 24 hours	5.0 N/mm^2 at 23 hours
Initial strength	< 75 mm (indentation diameter)	64.0 mm at 21 hours
Compressive strength	0.3 - 1.0 MPa (28-day)	(0.54±0.03) MPa – 3-day (0.77±0.02) MPa – 7-day (0.95±0.05) MPa – 28-day

Other supplementary verifications carried out also confirmed that the shear strength and the permeability of the DM-4 backfilling material fulfilled the design requirements of typical compacted fill in slope upgrading works.

3.5 Current status of development and way forward

After a number of site trials, the feasibility about the use of the DM-4 backfilling material in slope upgrading works was successfully proven. In terms of supply of the material for use in the local construction industry, the DM-4 backfilling material has been licensed to four local companies for producing and selling the relevant products since 2021. Moving forward, the findings of the site trials on slopes are being consolidated for review and improvement. A standard material specification is intended to be prepared for promoting a wider use of such self-compacting backfilling material in slope engineering works in the near future.

4 CONCLUSION

4.1 The development of VRSC

The models for simulating tunnelling blasting and Split Hopkinson Pressure Bar (SHPB) experiments have been well established in the project. The simulation results provided very good insights on the corelation between PPV, tensile stresses and safe distances, which are very important for optimizing the design and construction requirements of sprayed concrete lining and concrete mix design. These models can also be extended for simulating a complete drill and blast cycle in a rock cavern and providing essential information that facilitates the sprayed concrete lining design.

Scale-up production of VRSC was successfully carried out in a ready mix concrete plant, with the performance of the produced VRSC fulfilling the currently in-use general requirements of sprayed concrete as permanent lining material in a rock cavern development project.

To conclude, the main objective of VRSC development is to streamline the construction cycle of drill and blast tunnelling, enhance overall cost-effectiveness and improve construction safety. Upon the completion of the project and its successful application in the field, a single pass tunnel lining can be assessed and verified to attain adequate resistance to blasting vibration without concerns about the damage on its structural integrity. First, this could assure a safe working environment by eliminating the risk of concrete fall (due to slow hardening and insufficient/loss of adhesion) during the construction stage within a shorter period after spraying. Second, the single pass lining could now be considered as a permanent lining or part of a permanent composite lining, which could result in a huge potential saving from the reduction in volume of rock excavation and the overall lining thickness.

4.2 The development of self-compacting backfilling material

The use of the novel material in the site trials completed so far has demonstrated that the construction time and the manual handling involved in the fill replacement works on slopes could be significantly reduced. In the future, more applications of the DM-4 backfilling material, in addition to trench backfilling for roadworks and fill replacement in slope upgrading works, will be explored. With the above background together with potential further development of a mix with higher permeability, lower density and shorter setting time, it is anticipated that the use of the DM-4 backfilling material will be further expanded in terms of quantity and scope of applications in view of the benefits to the Government departments, consultants and contractors in their projects.

ACKNOWLEDGEMENTS

This paper is published with the permission of the Head of the Geotechnical Engineering Office and the Director of Civil Engineering and Development, the Government of the Hong Kong Special Administrative Region, China. The authors would like to thank the GEO for steering and supporting the development and use of innovative materials for geotechnical applications. The funding supports on the development of DM-4 backfilling material from the Innovation and Technology Commission and the Construction Industry Council are also appreciated.

REFERENCES

Kwan, A.K.K., Lee, P.K.K. 2000. A study of the effects of blasting vibration on green concrete. *GEO Report No.102*. Geotechnical Engineering Office, Civil Engineering and Development Department, The Government of the Hong Kong Special Administrative Region.

Alejano, L.R., Bobet, A. 2015. Drucker-Prager Criterion. *The ISRM Suggested Methods for Rock Characterization, Testing and Monitoring: 2007-2014*: 247-252.

Ansell, A. 2004. In situ testing of young shotcrete subjected to vibrations from blasting. *Tunnelling and Underground Space Technology*, 19(6): 587-596.

Ansell, A. 2007. Shotcrete on rock exposed to large-scale blasting. *Magazine of Concrete Research*, 59.9: 663-671.

Ahmed, L., Ansell, A., 2012. Laboratory investigation of stress waves in young shotcrete on rock. *Magazine of Concrete Research*, 64(10): 899-908.

Ahmed, L., Ansell, A. 2014. Vibration vulnerability of shotcrete on tunnel walls during construction blasting. *Tunnelling and Underground Space Technology,* 42: 105-111.

ITA Working Group n° 12, ITAtech. 2020. ITA Report n° 24 - Permanent Sprayed Concrete Linings. *ITAtech Publications*: 55p.

Sun, G., Nissinen, T.P.B., Sham, I.M.L. 2019. Foam formulation and method of preparing solid porous materials with same. *United States Patent*, Patent No. US 10,442,734 B2.

Technical Developments Related to Deep Cement Mixing Method in Hong Kong

Philip Chung, Florence Chu
Geotechnical Engineering Office, Civil Engineering and Development Department, HKSARG, Hong Kong, China

Henry Cheung, C H Yan
Sustainable Lantau Office, Civil Engineering and Development Department, HKSARG, Hong Kong, China

Chris Cheung, Anthony Wong
AECOM Asia Company Limited, Hong Kong, China

ABSTRACT

In recent years, deep cement mixing (DCM) method, a non-dredged ground improvement technique, has been adopted in several local large-scale reclamation works. It is also a robust ground improvement solution and can expedite land formation. Currently, design and construction methods adopted in Hong Kong are mostly referred to the practice or guidelines developed in other countries. With more local experience gained and in view of the potential application in possible coming mega development projects which involve reclamation and ground treatment works, it is considered worthwhile and timely to conduct more detailed studies to understand the engineering properties of the materials improved by this technique and to harness the design and construction practice, with a view to enhancing the cost effectiveness of DCM works. This paper briefly introduces some on-going research related to DCM method covering several design and construction aspects including engineering properties, ground investigation and laboratory testing using laboratory mixed and field mixed cores. The objectives, potential application and preliminary results of the studies are presented and discussed in the paper.

INTRODUCTION

In recent years, deep cement mixing (DCM) method, a non-dredged ground improvement technique, has been adopted in several local large-scale reclamation works including the Three-Runway System project, the Tung Chung East reclamation project, and the Integrated Waste Management Facilities Phase 1 near Shek Kwu Chau. Soft deposit beneath the reclamation area is left in place and treated in-situ by DCM. The principle of DCM is to mix a cementitious agent with soft soils to produce either a column, a panel, or a mass block of improved materials with higher strength and enhanced stiffness characteristics within a short period of time. DCM is a robust ground improvement solution and can expedite land formation. Ground settlement can also be effectively controlled and the quantity of fill material for replenishing the settlement can be greatly reduced comparing with conventional drained ground improvement method using prefabricated vertical drains (PVD) and surcharging. Lastly, this method realizes the non-dredged reclamation more thoroughly that bulk removal and disposal of dredged materials, particularly for seawall construction, is no longer required. Potential impacts to surrounding water quality and marine ecology can be substantially reduced.

Currently, design and construction methods adopted in Hong Kong are mostly referred to the practice or guidelines developed in other countries such as Japan, Korea and United States. With more local experience gained and in view of the potential application of DCM in possible coming mega development projects which involve reclamation and ground treatment works like Lantau Tomorrow Vision and Northern Metropolis, it is considered worthwhile and timely to conduct more detailed studies to understand the engineering properties of the materials improved by DCM and to harness the design and construction practice, with a view to enhancing the cost effectiveness of DCM works.

This paper briefly introduces some on-going research related to DCM covering a number of design and construction aspects including engineering properties, ground investigation and laboratory testing using laboratory mixed and field mixed cores. The research includes reviewing the strength and stiffness characteristics of the treated soils under confining condition, evaluating tensile properties and compressibility of treated soils, evaluating the use of smaller diameter of cores for unconfined compression strength (UCS) test, developing correction factors for low aspect ratio specimens in UCS test, exploring alternative and supplementary test methods for DCM works, and proposing a standardized laboratory mixing test procedure. The objectives, potential application and preliminary results of the studies are presented and discussed in the paper.

2 ON-GOING RESEARCH

2.1 Strength and stiffness characteristics of DCM materials

The state of practice in Japan and United States is to use total stress friction angle of $\phi = 0$ and cohesion intercept of $c = 0.5*UCS$ for stability analyses (Bruce et al. 2013). Design parameters derived from UCS results without consideration of the effect of confinement of surrounding soils may be on the conservative side. In order to simulate the actual site conditions, to enable more rigorous analyses, and to review whether there are rooms to optimize the design of DCM works, consolidated undrained triaxial tests on field mixed cores were conducted. For each triaxial test, a corresponding UCS test was conducted on a sample selected along the same metre of the core. As such, all selected samples had the same diameter (approximately 100mm) and length (approximately 200mm).

Based on 21 triaxial test results, it was revealed that there was no significant difference between UCS and peak strength from triaxial test under the normal range of confining pressure (e.g. 50 to 400kPa). As presented in Figure 1, the peak shear strength from triaxial tests with respect to the corresponding UCS mainly ranged between 0.8 and 1.5. Comparing UCS test of which there is no residual strength in theory, residual strength with the presence of confining pressure, even under a low pressure of 45kPa, became evident (Figure 2). In triaxial tests, residual strengths were about 0.3 to 0.7 of the UCS.

As shown in Figure 3, the residual strength to UCS ratio appeared to decrease with increasing UCS. In other words, the drop of strength in the post peak stage under confining condition increased when DCM material possessed higher UCS. Figure 4 presents the relationship between the axial strain at failure (ε_f) and peak strength in triaxial test and UCS test. Overall, the magnitude of ε_f of DCM material determined from both tests was small (within 2%). However, in the case of confining conditions, the magnitude of ε_f, ranged between 0.4% to 1.8%, was about 1 to 4 times larger than those without confinement (about 0.4%). In addition, ε_f increased with the peak strength in triaxial test but relatively insensitive in UCS test. In view of this, the serviceability limit with reference to the strain from UCS tests can be considered as more robust.

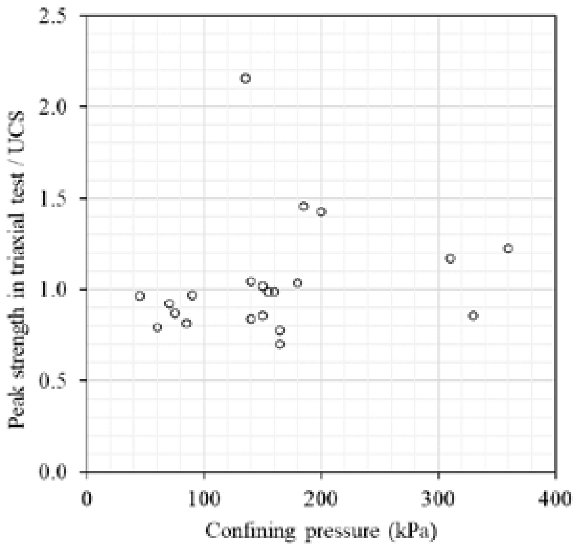

Figure 1: Relationship between peak strength in triaxial test to UCS of field mixed DCM material and confining pressure

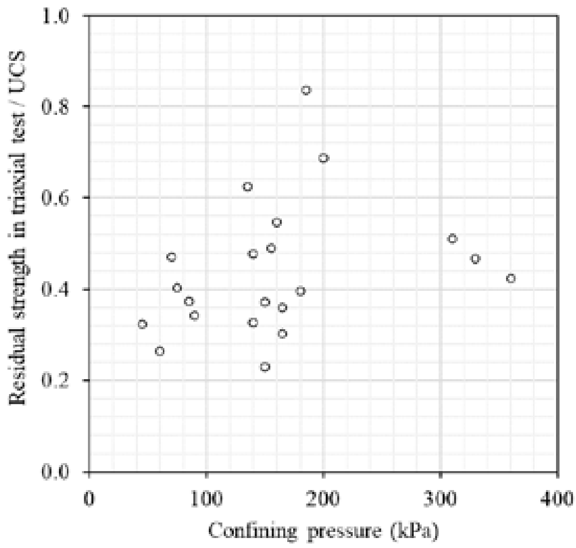

Figure 2: Relationship between residual strength in triaxial test to UCS of field mixed DCM material and confining pressure

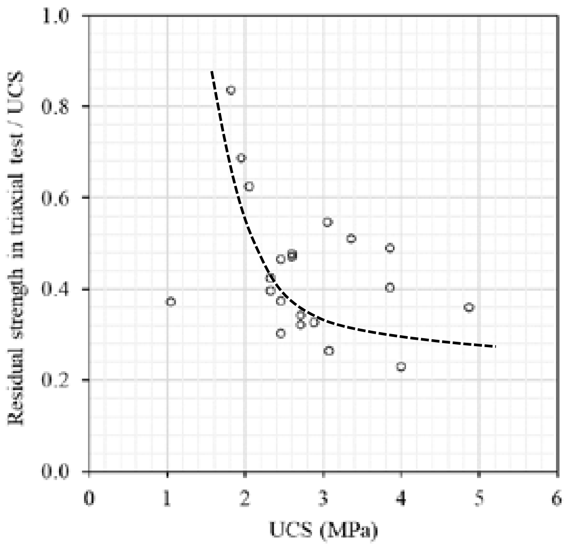

Figure 3: Relationship between residual strength in triaxial test and UCS of field mixed DCM material

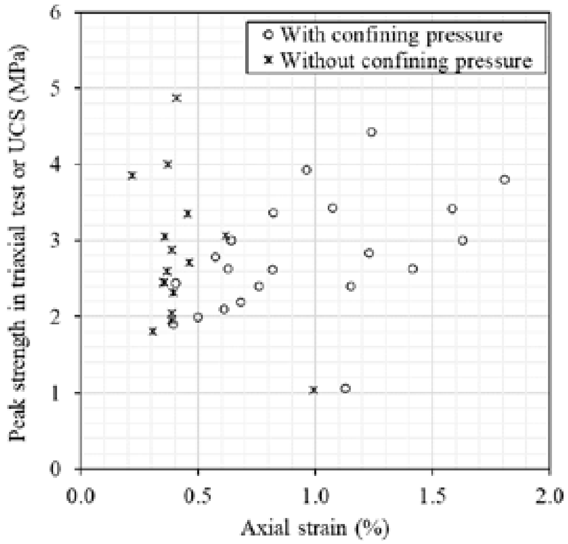

Figure 4: Strain at failure of field mixed DCM material with and without confining pressure

2.2 Tensile properties of DCM materials

Typical configuration of DCM materials includes column-pattern, wall-pattern, grid-pattern and block-pattern. Design in each pattern involves evaluation of external stability and internal stability under a variety of potential failure modes to ensure that the stress induced within and adjacent the treated soil do not exceed the material capacities like compressive strength, shear strength and tensile strength. Limited research has been conducted on the tensile properties of DCM material in Hong Kong (Cheung et al. 2021). This has limited the application of some configurations like column-pattern DCM material to support structures or control settlement. There is a lack of internationally testing standard for determining tensile strength of DCM material. Tensile strength of DCM material was evaluated by indirect tensile test (Brazilian test), simple tension test and bending test in previous studies (Bofinger 1970, Koseki et al. 2008, Consoli et al. 2010, Azneb et al 2021). However, the testing procedures were either inconsistent or not reported in detail.

A study aiming to review different testing methods and investigate tensile properties of DCM materials was carried out. Based on the results of laboratory mixed specimen, it was found that tensile strength determined by direct tensile test and Brazilian test are similar provided that the crack initiation process is cautiously monitored in the Brazilian test. For example, the crack should initiate from the centre of the specimen (Yanagidani et al. 1978). We found that the use of flat platen with plywood strip can prevent effectively premature failure in DCM specimens. The typical set up of a Brazilian test is presented in Figure 5. In the study, only test results from specimens with crack initiated from centre of the specimen were considered. Figure 6 shows an example of the crack development process in the specimen. Our results reveal that the tensile strength was about 17% to 21% of the UCS for laboratory mixed specimen with average UCS of 1.2 MPa; while for field mixed specimens with UCS ranged between 2.9 to 4.6 MPa, the tensile strength was about 9 to 18% of the UCS. The stress ratios (tensile strength / UCS) are generally consistent with the data in the literature (Bruce et al. 2013). The current design approach without considering tensile strength is on the conservative side. With improved knowledge on the tensile properties, potential beneficial effect in stability analysis for the application like DCM in column-type or DCM material as a retaining structure can be further studied.

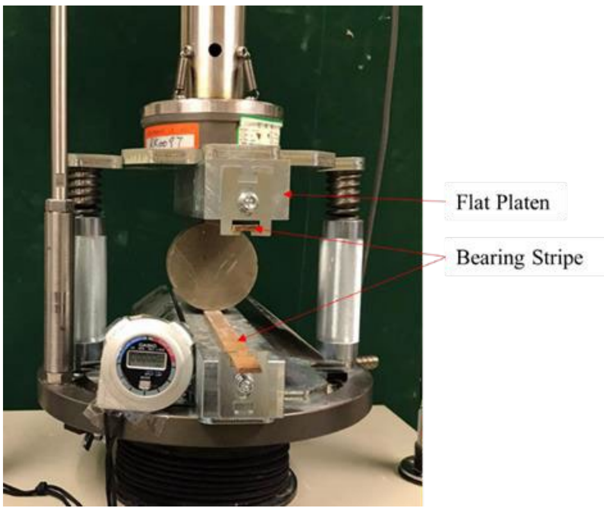

Figure 5: Set up of Brazilian test with the use of flat platen and plywood strip

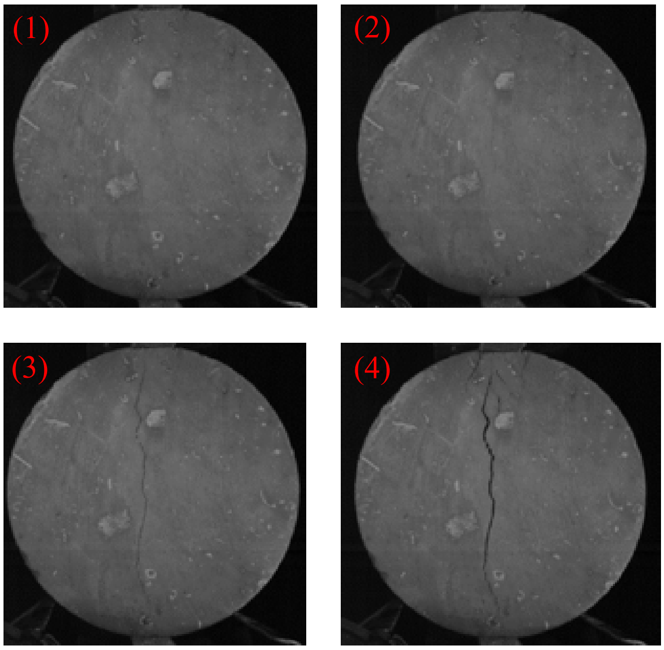

Figure 6: Crack development process of field mixed DCM materials (crack initiated from the centre of the specimen)

2.3 Compressibility of DCM materials

It has been documented in many literatures that the strength of DCM material continuously increases with time (Kawasaki et al. 1981, Saitoh 1988, Cement Deep Mixing Association 1999, Hwang et al 2004). However, there is not much information on its long-term creeping behavior. Although creeping is expected to be small, the intent of the study is to determine compressibility properties of DCM material for supplementing current design practice.

A series of oedometer tests were conducted on specimens trimmed from field DCM cores and cores of untreated marine deposit. The tests were carried out according to GEOSPEC 3 (2017). Coefficient of secondary compression (C_{sec}) of treated and untreated soil were determined at different applied pressures. C_{sec} is defined as $C_\alpha/(1+e_0)$ where C_α is the secondary compression index and e_0 is the initial void ratio. Figure 7 reveals that the magnitude of C_{sec} of DCM materials was about one order less than that of the untreated soil. After stabilized by DCM, C_{sec} of the treated material was not sensitive to the applied pressures (100 – 800kPa). It can be concluded that the treated material is unlikely a key player of the long-term deformation.

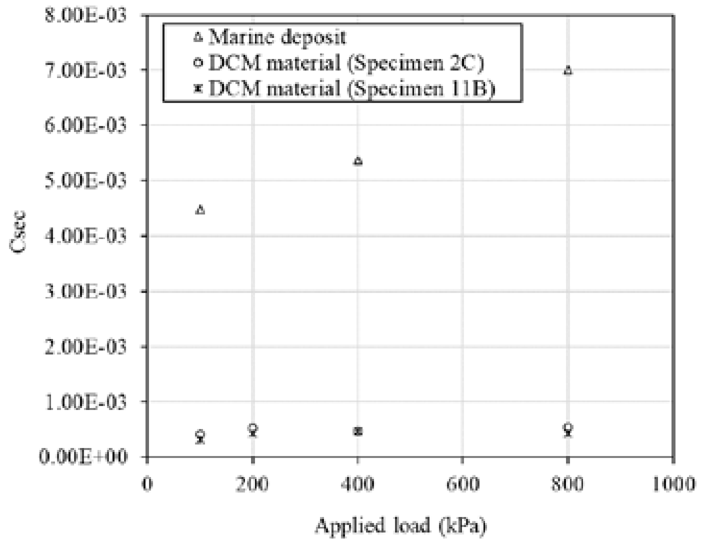

Figure 7: Coefficient of secondary compression of untreated and treated marine deposit by DCM

2.4 Use of smaller diameter of cores for unconfined compression test

In the current practice for UCS testing of DCM specimens, 50mm or 75mm diameter cores are used for laboratory mixed samples while 100mm diameter cores are adopted for field mixed samples. It is believed that specimens prepared under a laboratory-controlled environment possess far less potential variation as a consistent mixing method is applied. On the other hand, 100mm diameter specimens are considered less susceptible to localized ground variations and uncertainties during field mixing process. However, larger diameter specimens imply higher cost in coring and subsequent laboratory testing. A study is therefore conducted to investigate the credibility of adopting smaller diameter field mixed cores.

It is recommended in Federal Highway Administration Design Manual that the core diameter should be at least 64mm (Bruce et al. 2013). In this study, 100mm cores and 76mm or 64mm cores at adjacent locations were taken from field mixed DCM columns. Specimens were then selected along every metre from both the 100mm and 76mm or 64mm cores for UCS testing. As shown in Figure 8, a good correlation was observed between UCS of the 100mm diameter cores and the smaller 76mm or 64mm diameter cores, given the inherent variation of UCS results from field DCM cores. It was also noticed that smaller diameter cores were more susceptible to disturbance during core boring and fractures were found more frequently, resulting in less suitable specimens selected for test. The average success rate of specimen selection was 85% for smaller diameter cores (76mm or 64mm) and 95% for 100mm diameter cores. Based on available information, it is considered that both smaller core diameters are suitable for UCS test.

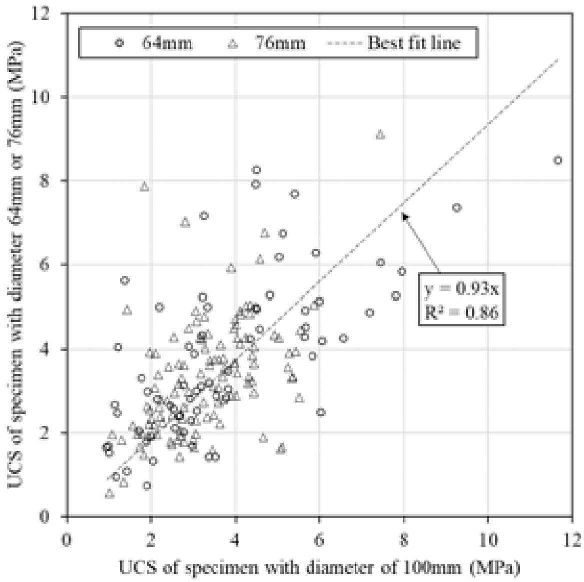

Figure 8: Relationship between UCS of 64mm/76mm diameter cores and UCS of 100mm diameter cores

2.5 Correction factor for shorter specimens in UCS test

Length to diameter (L/D) ratio affects the stress and strain distribution within the specimen during compression. The confinement effect due to the frictional force at the end surfaces would be insignificant if length to diameter ratio is sufficient. Specimen with smaller L/D ratio is typically able to resist higher loads. Currently, UCS test is carried out in accordance with HKIE Interim Guidelines on Testing of Unconfined Compressive Strength of Cement Stabilised Soil Cores in Hong Kong (HKIE, 2017). According to the Interim Guidelines, cylindrical specimen with L/D ratio of 2 is recommended for the test and specimen with L/D ratio between 1.5 (inclusive) and 2.0 can also be tested with lubricated ends and with the application of correction factor on the measured UCS. It is not uncommon to retrieve cores from DCM column with insufficient length (L/D < 1.5). To allow more flexibility in specimen selection for quality control, pilot tests were arranged on laboratory mixed specimens with different L/D ratios, ranging from 1.0 to 2.0, with an aim of determining a set of correction factors for shorter specimens.

Under the collaboration with the University of Hong Kong, laboratory mixed cores with target UCS ranged between 1MPa and 3MPa were prepared using kaolin or marine deposits as natural soil mixed with binder which included Portland cement or Portland blast-furnace cement. 250 specimens were then cut from these cores with different L/D ratios (1.0, 1.25, 1.50, 1.75 and 2). UCS was measured on the specimens cured for 21, 28 and 90 days. The data reported by Lin (2018) and Liu (2021) were consolidated and the correction factor under various L/D ratios were calculated using the following equation:

$$Correction\ factor = \frac{Average\ UCS\ of\ specimen\ with \frac{L}{D}\ of\ 2}{UCS\ of\ specimen\ with\ specific\ L/D} \quad (1)$$

Figure 9 presents the correction factors for specimens with different L/D ratios. As noted from the Figure, the mean and median of the correction factors for L/D ratio between 1 and 2 were both close to one. Although it is generally accepted that higher UCS will be resulted from shorter specimen, the result in this study indicated that the effect of L/D ratio on UCS was not significant. However, it should be noted that the data at various L/D ratios were scattered. The shaded area (bounded by a pair of black dash lines) covered about 80% of the data. The variation of correction factor was about ±0.1, ranged between 0.9 and 1.1. Based on the available test results, the correction factor recommended in Federal Highway Administration Design Manual (Bruce et al. 2013) for specimens with L/D ratio less than 1.5 can be considered as conservative.

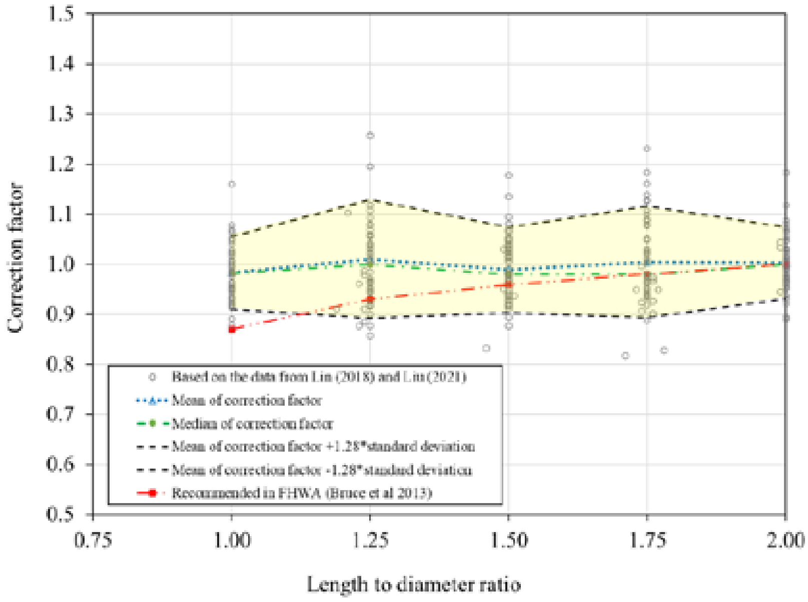

Figure 9: Relationship between correction factor and length to diameter ratio

2.6 Alternative and supplementary test methods for DCM works

The most commonly used engineering property for quality control is UCS. However, the requirement on the quality of field cores for UCS test is relatively high and the testing duration including the specimen preparation time is long. The study aimed to develop quick test methods, as alternative or supplementary tests, with less requirements on the specimens to facilitate early and fast testing on site. The applicability of two index test methods on DCM materials were studied.

2.6.1 Point load test

Point load test (PLT) is an index test for strength classification of rock materials. It is a form of "indirect tensile" test which is performed by loading the specimen between two steel conical platens to induce horizontal tensile stress until splitting failure occurs. The specimen can be loaded either diametrally or axially. Although ASTM D5731-16 suggests that PLT is applicable for medium strength rocks with UCS not less than 15MPa, some researchers suggested that this test method is applicable to brittle materials (Robins 1980, Levent & Gokce 2015). Considering the brittleness of DCM specimens and the advantages of PLT (such as simple testing procedures and less specimen preparation works), laboratory tests were arranged on laboratory and field mixed specimens to investigate the feasibility of using PLT to determine the UCS of DCM materials. According to ASTM D5731-16, point load strength index ($I_{s(50)}$) is calculated by following equation:

$$I_{s(50)} = (\frac{D}{50})^{0.45} \frac{P_f}{D^2} \quad (2)$$

where D is the diameter for diametrally loaded core specimen, or the equivalent core diameter ($D_e = \sqrt{\frac{4WD}{\pi}}$) for axially tested core specimen, W is the distance between loading points, and P_f is the failure load. Typically, a constant correlation (k) between UCS and $I_{s(50)}$ is proposed (UCS = $kI_{s(50)}$) for estimating UCS from PLT for rock testing. Laboratory mixed cement stabilized soil specimens with target UCS ranging from 1MPa to 30MPa were prepared to evaluate applicability of PLT to cement mixed material. As shown in Table 1, the coefficient of variation (CoV) of $I_{s(50)}$ for specimens with UCS less than 15MPa is slightly higher than that for specimens with higher strength. Overall, the CoV was less than 10% across specimens of all strengths. This magnitude of variation is comparable with the results from point load tests on rocks conducted by Bieniawski (1974). It seems that PLT can also be applied to cement mixed material with UCS below 15MPa without significant variation.

Table 1: Statistics of point load strength index for laboratory mixed specimens

Mix ID	Average UCS (MPa)	Diametral PLT				Axial PLT			
		No. of Test	Ave. $I_{s(50)}$ (MPa)	Std. dev. $I_{s(50)}$ (MPa)	CoV	No. of Test	Ave. $I_{s(50)}$ (MPa)	Std. dev. $I_{s(50)}$ (MPa)	CoV
PBFC-MD-1	0.9	8	0.08	0.006	7.9%	8	0.09	0.006	6.2%
PBFC-MD-2	3.8	5	0.19	0.014	7.4%	8	0.26	0.017	6.5%
PBFC-MD-3	4.9	5	0.27	0.029	10.7%	7	0.27	0.023	8.8%
PBFC-S-1-10	12.4	8	1.18	0.084	7.1%	8	1.22	0.099	8.2%
PBFC-S-2-20	22.5	8	1.73	0.095	5.5%	8	1.82	0.088	4.8%
PBFC-S-3-20	24.1	8	1.82	0.094	5.2%	8	1.93	0.090	4.6%
PBFC-S-4-30	36.3	7	2.02	0.122	6.0%	8	1.68	0.118	7.0%

Both diametral and axial PLT were carried out on field mixed DCM cores collected from a local project. However, correlation between UCS and $I_{s(50)}$ were scattered (Figure 10). This might be partly attributed to the heterogeneity of test specimens due to variability in soil conditions and mixing condition. In general, test results of axial PLT were more consistent than that of diametral PLT. Similar observation was noticed in the results of laboratory mixed specimen. For specimens which had similar UCS of field mixed cores (average UCS from 0.9MPa to 4.9MPa), axial PLT gave lower CoV of $I_{s(50)}$. Nevertheless, the lower bound values of k for two types of PLT were in similar order. Failure modes of specimen after PLT were briefly reviewed. It appeared that there is no significant relationship between $I_{s(50)}$ and the failure patterns. Potential use of the axial PLT to provide supplementary information to estimate UCS roughly will be carefully examined with the consideration of the distribution of data comparing with that in rocks from literatures.

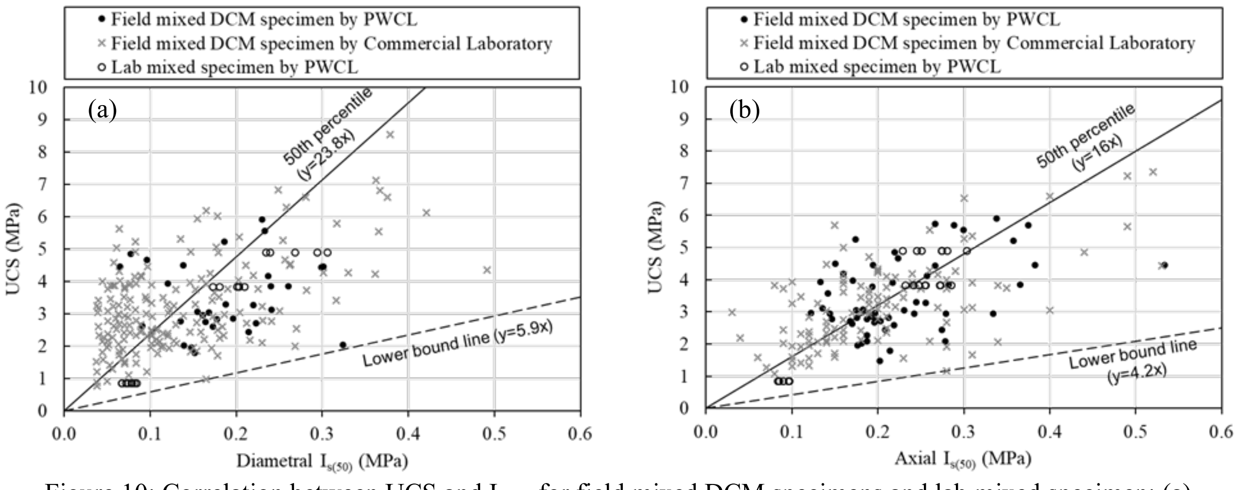

Figure 10: Correlation between UCS and $I_{s(50)}$ for field mixed DCM specimens and lab mixed specimen; (a) diametrally loaded; (b) axially loaded

2.6.2 Needle penetration test

Needle penetration test (NPT) is an index test for determining UCS of soft rock or stabilized soil through a correlation between needle penetration index (NPI) and UCS. Needle penetrometer, as shown in Figure 11, is a lightweight and portable device which utilizes a needle to penetrate the surface of the material to be tested. NPI is determined by following equation based on the measured load and the penetration of the needle:

$$NPI = F/D \tag{3}$$

where F is the measured load (N) and D is the measured depth of penetration (mm). The test is applicable to materials having UCS lower than 20 MPa (Ulusay et al. 2014). According to the ISRM Suggested Method for the NPT (Ulusay et al, 2014), the specimen is suggested to be greater than 15mm in thickness for cylindrical samples with diameter of 40 – 50mm. There are no special preparation requirements on the surface of the specimen.

Predicted UCS of DCM specimen can be determined based on a correlation between NPI and UCS proposed by Martuo Co. Ltd (2006) for artificial cement-based samples. Figure 12 presents the relationship between the measured UCS and the predicted UCS determined from NPI of DCM specimens. About 77% of the data had the difference between the measured and the predicted UCS within 1MPa. The analysis shows that UCS can be estimated from NPI based on the empirical relationships proposed by Maruto Co. Ltd. (2006):

$$\log(UCS) = 0.978\log(NPI) + 2.621 \tag{4}$$

where unit of UCS is kN/m^2 and NPI in N/mm. Considering that NPT has less requirements on the dimension and size of the specimen and can be carried out in laboratory or on site quickly, it may be used as a supplementary test method to estimate UCS when samples with sufficient length is limited or early knowledge of UCS of DCM specimens is required. Application of this test as a step of preliminary screening for determination of full coring and refining the testing programme can be explored. To further substantiate the correlation between the NPI and UCS and to develop the corresponding strength criteria, more test data can be collected from specimens with different soil types, binder dosages and binder types. However, when applying this test, practitioners should be aware of the uniformity of specimen in order to obtain a representative result from NPI.

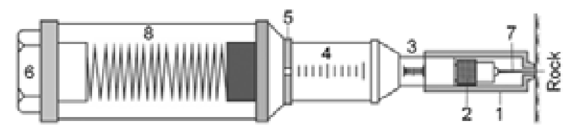

Figure 11: Needle penetrometer and its parts: 1 – presser, 2 – chuck, 3 – penetration scale, 4 – load scale, 5 – load indicating ring, 6 – cap, 7 – penetration needle and 8 – spring (Ulusay et al. 2014)

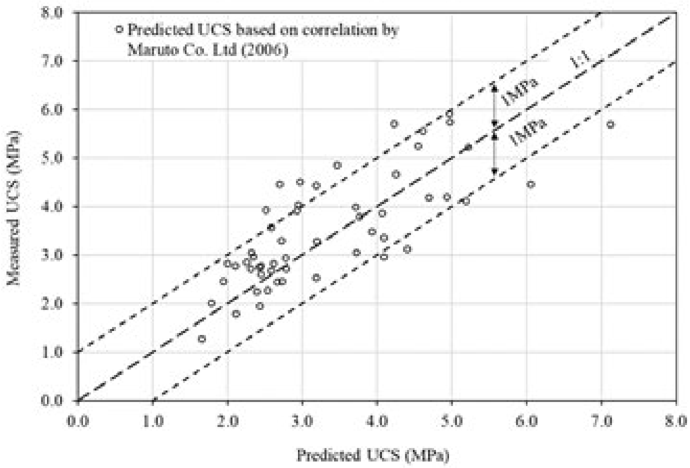

Figure 12: Relationship between measured UCS and predicted UCS based on NPI

2.7 Standardized laboratory mixing procedure

Laboratory mixing procedure is important for the mix design of DCM works as it greatly affects the strength and stiffness of the stabilized soils. Laboratory test results are used to establish design parameters for designers, and to determine operational parameters for construction. Jabban et al. (2020) reviewed various laboratory mixing procedures including ways to homogenize natural soil, blending time, mold types, molding techniques and curing conditions. They noted that molding techniques and curing conditions considerably influence more the properties of the stabilized soil. Tapping, rodding, static compaction and dynamic compaction are common molding techniques adopted in preparation of specimens in other counties. Previous research showed that molding techniques can greatly affect the magnitude and variation of UCS regardless of the soil type, type and amount of binder used (Kitazume et al. 2015).

In Hong Kong, a clear guideline for the selection of mixing and molding methods has not yet been established. Besides, there are no specified methods for evaluating the uniformity of the laboratory mixed specimens. In this context, several mixing methods from international testing standards and reported in literatures (e.g. BSI 1990a & 1990b, Bruce et al. 2013, Kitazume & Terashi 2013, Kitazume et al. 2015) were reviewed. Series of UCS tests on laboratory mixed specimens were conducted to study the applicability of two molding techniques available in local laboratories (the use of vibrating table and impact-type compactor). The variation of wet density and UCS of specimens were examined. Based on the review and laboratory test results, a mixing procedure with recommendations covering the preparation works on natural soil, soil and binder mixing, molding and curing are being prepared.

3 CONCLUSION

In view of the potential application of DCM in major reclamation projects, a series of studies related to material engineering properties of DCM material, ground investigation and laboratory testing were carried out using both laboratory prepared cores and field mixed cores collected from a local project. The objectives and preliminary results of the studies were presented in this paper. More works are in progress and all findings and recommendations will be consolidated later for further deliberation of the practitioners with the view to improve the practice and enhance the cost effectiveness of infrastructure works constructed by DCM method.

4 ACKNOWLEDGEMENTS

This paper is published with the permission of the Director of Civil Engineering and Development and the Head of the Geotechnical Engineering Office, the Government of the Hong Kong Special Administrative Region.

5 REFERENCES

ASTM (American Society for Testing and Materials. 2016. *Standard Test Method for Determination of the Point Load Strength Index of Rock and Application to Rock Strength Classifications*, D5731-16.

Azneb AS, Banerjee Subhadeep and RG Robinson. 2021. *Tensile strength of cement treated clay*, IOP Conf. Series: Earth and Environmental Science 727 (2021) 012005, 14th Baltic Sea Region Geotechnical Conference.

Bieniawski ZT. 1974. *The point-load test in geotechnical practice*, Engineering Geology, 9(1975), 1-11.

Bofinger HE. 1970. *The measurement of the tensile properties of soil cement*, Road Research Laboratory Report LR 365, Tropical Section, Road Research Laboratory, Ministry of Transport, Crowthorne, 12p.

Bruce MEC, Breg RR, Collin JG et al. 2013. *Federal Highway Administration Design Manual: Deep Mixing for Embankment and Foundation Support, Publication No. FHWA-HRT-13-046*. Offices of Research and Development, Federal Highway Administration, Washington, DC, USA.

BSI. 1990a. *BS 1924-1:1990: Stabilized materials for civil engineering purposes, general requirements, sampling, sample preparation and tests on materials before stabilization*, BSI, London, UK.

BSI. 1990b. *BS 1924-2:1990: Stabilized materials for civil engineering purposes, methods of test for cement-stabilized and lime-stabilized materials*, BSI, London, UK.

Cement Deep Mixing Association. 1999. *Cement Deep Mixing Method (CDM), Design and Construction Manual*. Japan.

Cheung CKW, Wong AHK, Cheung HKT, So STC. 2021. *Design of deep cement mixing treatment for non-dredged seawall in Hong Kong*. 2021 Deep Foundations Institute, 28-38.

Consoli NC, Cruz RC, Floss MF & Festugato L. 2010. *Parameters controlling tensile and compressive strength of artificially cemented sand*. J of Geotech and Geoenvironmental Engineering, ASCE, 136(5), 759-763

GEO. 2017. *GEOSPEC 3: model specification for soil testing*, Geotechnical Engineering Office, Civil Engineering and Development Department, HKSARG.

Hong Kong Institution of Engineers (HKIE). 2017. *Interim Guidelines on Testing of Unconfined Compressive Strength of Cement Stabilised Soil Cores in Hong Kong*, Geotechnical Division, the Hong Kong Institution of Engineers.

Hwang J, Humphrey A, Bobet A and Santagata M. 2004. *Stabilization and improvement of organic soils*, Report No. FHWA/IN/JTRP-2004/38 for the Joint Transportation Research Program, Purdue University, West Lafayette, Ind.

Jabban Al W, Laue J, Knutsson S and Al-Ansari N. 2020. *Briefing: Common laboratory procedures to prepare and cure stabilized soil specimens: a short review*, Geotechnical Research 7(1):3-10.

Kawasaki T, Niina A, Saitoh S, Szzuki Y and Honjyo Y. 1981. Deep mixing method using cement hardening agent, Proceeding of the 10th International Conference on Soil Mechanics and Foundation Engineering, Vol 3, 721-724.

Kitazume M & Terashi M. 2013. *The deep mixing method*, CRC Press, Boca Raton, FL, USA.

Kitazume M., Grisolia M., Leder E. et al. 2015. *Applicability of molding procedures in laboratory mix tests for quality control and assurance of the deep mixing method*, Soils and Foundations, 55(4): 761-777.

Koseki J, Tsutsumi Y, Namikawa T, Mihira S, Salas-Monge R, Sano Y, and Nakajima S. 2008. *Shear and tensile properties of cement-treated sands and their application to mitigation of liquefaction-induced damage*, Proceedings of 4th international symposium on deformation characteristics of geomaterials (IS-Altanta 2008), 1, 27-50.

Levent Selcuk and H. Suleyman Gokce. 2015. *Estimation of the Compressive Strength of Concrete under Point Load and its Approach to Strength Criterions*, KSCE Journal of Civil Engineering (2015) 19 (6): 1767-1774.

Lin MH. 2018. *Laboratory testing of unconfined compressive strength of cement stabilized soil cores*, Master of Science dissertation, The University of Hong Kong, 2018.

Liu YX. 2021. *Laboratory testing of unconfined compressive strength of cement stabilized soil cores*, Master of Science dissertation, The University of Hong Kong, 2021.

Maruto Co. Ltd. 2006. *Penetrometer for soft rock: Model SH-70 Instruction Manual*, Tokyo, Japan.

Robins P. J. 1980. *The point-load strength test for concrete cores*, Mag. Concrete Res. 32, 101-111.

Siatoh S. 1988. *Experimental study of engineering properties of cement improved ground by the deep mixing method*, Doctoral thesis, Nibon University, 317p.

Ulusay R et al. 2014. *ISRM suggested method for the needle penetration test*. Rock Mech Rock Eng (2014), 47: 1073-1085.

Yanagidani T, Sano O, Terada M and Ito I. 1978. *The observation of cracks propagating in diametrically-compressed rock discs*. Int J Rock Mech Min Sci Geomech Abstr, 15(5):225-235.

Pilot Use of Alternative Compliance Criterion for Cement-soil in a Slope Upgrading Works Project

Dominic O K Lo, Raymond S L Ng, Kian Y K Chiu
Geotechnical Engineering Office, Civil Engineering and Development Department
The HKSAR Government, Hong Kong, China

Victon W L Wong, Dennis K F Lau
AECOM Asia Co., Ltd., Hong Kong, China

ABSTRACT

Currently the General Specifications for Civil Engineering Works stipulates the use of in-situ density tests as compliance criterion for both compacted fill and cement-soil. However, the latter derives its strength from cementation between particles and could exhibit very high strength as opposed to the former whose strength closely relates to its density. Hence, the use of strength as a compliance criterion for cement-soil seems more direct and appropriate. This paper describes the pilot application of unconfined compressive strength as the compliance criterion for cement-soil in a slope upgrading works project. It details the field trial conducted prior to the production run to work out the mixing and placement procedures, the cement content to be adopted and identification of appropriate field control measure to augment the compliance criterion. It also covers the experience gained, the potential benefits of such application and areas where further optimisation could be achieved.

1 INTRODUCTION

Replacement of loose fill with suitable material is one of the engineering solutions to enhance the slope stability in Hong Kong. Fill replacement construction standard and compliance criterion are stipulated in the General Specification of Civil Engineering Works (GS). The compacted fill materials are required to achieve at least 95% relative compaction of compacted mixture and the moisture content to be within ± 3% of the optimum moisture content.

Mixing fill material with cement has sometimes been used to improve the existing fill engineering properties in slope upgrading works under the Landslip Preventive Measures (LPM) Programme (BBVL, 2002; Fugro 2009). Unlike compacted fill with strength closely related to its density and moisture content, the strength of a cement-soil mixture is due to cementation between soil particles resulting from the chemical reaction between soil and cement. The cement-soil could achieve relatively high strength and is generally designed to withstand the design load. Hence it will not contract resulting in an increase of pore water pressure during shearing and saturation, and liquefaction is generally not a concern in cement-soil. The behaviour of cement-soil is more akin to weak rock or soft soil treated with deep cement mixing which gains strength with time. As cement-soil behaves differently from compacted soil fill, it seems that in-situ density tests may not be appropriate for cement-soil. Furthermore, the relatively high strength of cement-soil also renders the in-situ density tests difficult to perform in the field.

In light of the foregoing, it seems more appropriate and direct to adopt strength tests as a compliance criterion for cement-soil. As cement-soil is similar to soft soil treated with deep cement mixing, unconfined compressive strength (UCS) was proposed as an alternative to in-situ density test as a compliance criterion for cement-soil at a fill slope at Pok Fu Lam Road. Prior to the production run, a field trial was carried out to:
(a) work out the mixing and placement procedures,
(b) determine the required cement content, and
(c) identify other appropriate tests as field control measures to augment the compliance criterion.

This paper describes the findings of the field trial and the experience gained in the production run. It also covers the potential benefits of the application of the alternative compliance criterion and areas where further optimisation could be achieved.

1.1 Background

This field trial was carried out at a large fill slope at the downslope side of Pok Fu Lam Road (see Plate 1). The fill slope was to be upgraded under the Landslip Prevention and Mitigation (LPMit) Programme managed by the Geotechnical Engineering Office, Civil Engineering and Development Department (CEDD) of the Hong Kong SAR. The maximum height of the fill slope is about 30 m, with an average slope angle of 30° and a length of 220 m along the crest.

Ground investigation records revealed that the slope comprised a thick layer of fill with a maximum thickness of 30 m. In-situ density tests indicated that the relative compaction of some of the fill samples at the slope was less than 75%. This precluded the use of soil nailing. Fill replacement with cement-soil at the top 3 m was proposed as a slope upgrading measure. Design assessment indicated that the cement-soil needed to exhibit a UCS of at least 0.07 MPa in order to have the upgraded slope meeting the prevailing standard.

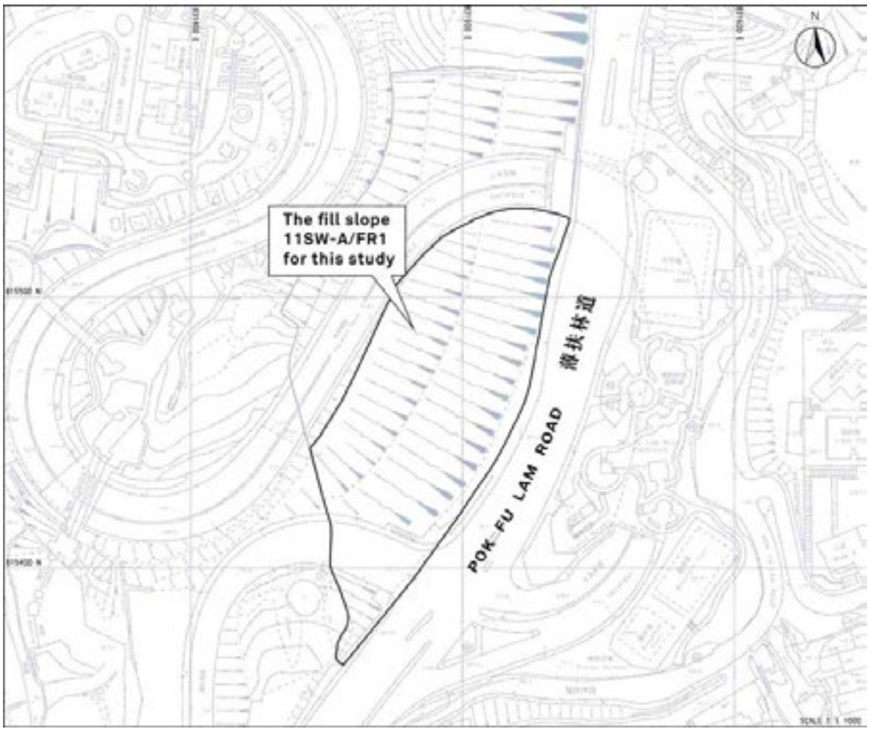

Plate 1: Location plan of the slope where the cement-soil study was conducted

2 CEMENT-SOIL MATERIAL COMPONENTS

2.1 Cement-soil composition

The GS stipulates that the cement-soil mixture shall comprise Portland cement, sand and inorganic soil. Soil material that is suitable for cement-soil mixture shall be free of organic matter and contains not more than 30% of soil particles passing a 63 µm British Standard test sieve. Portland cement and sand shall comply with BS EN 197-1 and BS 1200 respectively. The constituents of the cement-soil used in this project conformed with these requirements.

2.2 *Mixing and placement method*

Following the GS requirements, excavated fill material at the site was sieved to remove unwanted materials, including fallen foliage, roots, organic soil, construction debris and gravels with size larger than 20 mm before mixing with cement, sand and water.

The cement-soil mixture was prepared by first adding appropriate proportion of sieved fill material and sand to a pugmill mixer, then measured quantities of cement and water were added to the mixture and further mixing was performed until it was homogeneous in appearance. In view of the limited working space in most LPMit slope works sites, small plants and equipment were used. The pugmill mixer used was electric-powered with a 200 kg maximum loading capacity and consisted of a U-shaped trough in which a shaft fitted with pitched paddles to pulverise the cement-soil mixture (see Plate 2).

Plate 2: Mixing equipment

The cement-soil was placed in layers to the excavated pits/trenches within 30 minutes of mixing and compacted in lift thickness of 300 mm. Each layer was systematically tamped with a minimum of 8 passes by a mechanical rammer/tamper with a force output per 100 mm width in a range of 3.5 kN to 4.9 kN. Tamping operation was found necessary in order to ensure that the samples when extracted from the sampler would not disintegrate as discussed in Section 2.3.

2.3 *Cement content*

The cement content of cement-soil used in previous LPM projects ranged from 3% to 6%. In the field trial, the screened soil was mixed with cement content of 3% to 6% by weight of the soil. Samples were taken using open tube sampler for the determination of UCS.

Core samples of the cement-soil were delivered to the Public Works Central Laboratory (PWCL) of the CEDD for the determination of their UCS following the guidelines published by HKIE (2017).

After delivery to the PWCL, it was noted that some of the samples treated with 3% cement disintegrated when extracted from the sampler and could not be tested. Furthermore, some samples with 3% cement did not have uniform cross-sections or even surfaces (as shown in Plate 3) as required by HKIE (2017). Re-coring of samples was attempted in some cases to obtain better quality cement-soil samples for testing. Sometimes, this was not possible or not successful and no results were obtained for that particular batch.

Plate 3: Poor quality of core sample with 3% cement content

Figure 1 shows the average UCS obtained from about 200 samples with different cement contents. The compressive strength of the cement-soil increases with the cement content in the mixture. All individual samples met the project requirements of achieving a UCS of at least 0.07 MPa. It was noted that soil treated with 3% cement content yielded more varied UCS and exhibited lower consistency in sample quality. The uncertainty in the quality of samples with 3% cement content for laboratory testing described earlier renders it highly undesirable from a compliance testing perspective. Consequently, cement content of 3% was ruled out from further consideration.

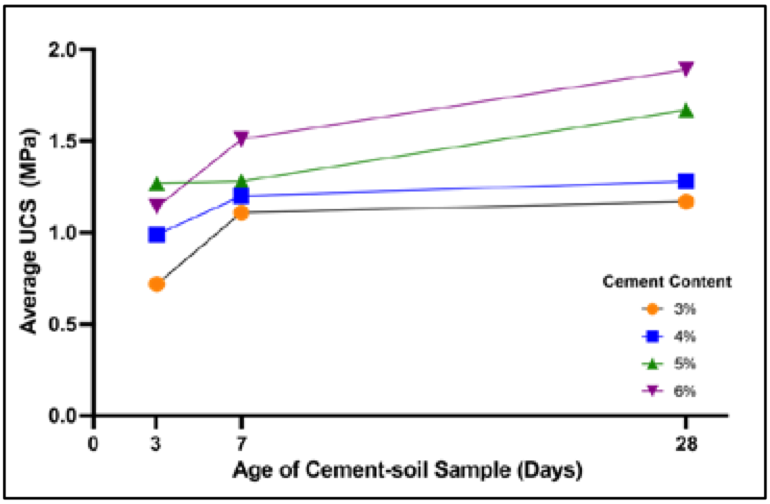

Figure 1: Average UCS of samples with different cement contents

Apart from the integrity of core samples, the opportunity for future landscaping of the cement-soil slope surface was taken into consideration in deciding on the cement content to be used. While high cement content in the mixture could yield higher strength and exhibit high reliability in meeting the compliance criterion, it also renders high pH value in the cement-soil which is less favourable to slope greening. To strike a balance amongst other things, the acceptable strength of cement-soil, the confidence level of core sample quality and the possibility of future slope greening, a cement content of 4% by weight of soil was selected for this project.

2.4 Sampling tools

Having an effective and practical means to recover good quality samples for testing was a challenging task and is critical to the practical application of the UCS as a compliance criterion. In principle, core samples should preferably be taken using ground investigation (GI) tools such as a double-tube or a triple-tube sampler driven by conventional GI drilling rig to minimise disturbance. In view of the limited working space in most LPMit slope works sites, mobilising such drilling rigs all over the slope could cause complications on site management and poses significant time and cost issues for sampling within the cement-soil. A portable sampler may be a viable option for this task. Due to the limited construction time, the LPMit contractor was unable to source a portable sampler and opted to devise a tailor-made sampling device. After several attempts of trying out different tailor-made core sampling methods in the field trial, a hand-held rotary coring machine using a 100 mm diameter core barrel was considered to be a viable means for procuring samples from the ground. It was noted that the friction developed between the core barrel and the surrounding cement-soil during coring could critically affect the quality of the core sample. The use of water as a flushing medium during the coring operation would damage the cement-soil structure and ruin the samples. As such, additional bits at the core barrel opening and additional auger-like blades were welded on the core barrel surface together with low pressure compressed air as a flushing medium (as shown in Plate 4) were used to improve the core recovery. The quality of a recovered sample is shown in Plate 5. This sampling method will no doubt inflict higher sample disturbance compared to that of sampling tools commonly used in geotechnical works. Given the relatively low UCS requirement in this project and the agility of such sampling method, it deemed to have met the project needs.

Electric hand-held coring machine connected with low pressure of compressed air

Additional welded bits and auger-like blades on core barrel

Plate 4: Tools for collecting UCS samples

Plate 5: Samples recovered using the tailor-made core sampling method

2.5 Field control

While 28-day UCS was used as compliance criterion, it is imperative to have some kind of early assurance that the cement-soil would meet the project strength requirement. Knowing that the strength of the cement-soil would increase with time, if its earlier UCS meets the project requirement, so will the 28-day strength (as shown in Figure 2). Hence, 3-day UCS and 7-day UCS of the samples were also determined in the field trial as possible early assurance indicators.

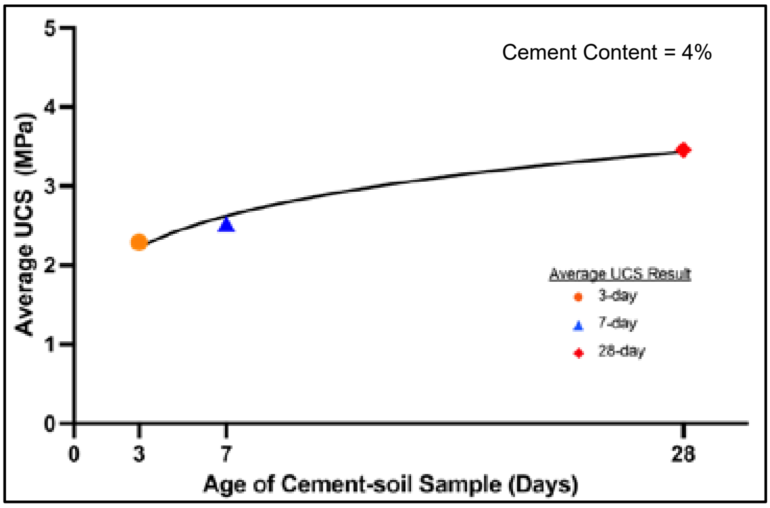

Figure 2: Correlation between average UCS and age of cement-soil samples

As the 3-day and 7-day UCS test results will only be available days after the placement of cement-soil, it is desirable to have a quicker means to give some indication on whether the in-place cement-soil meets the project requirement in order to expedite the works flow and minimise the need to carry out remedial works should the samples fail to meet the project requirement.

GCO probing was identified as a possible quick field control measure. During the field trial, it was conducted on cement-soil with different contents at hourly intervals for the first 4 hours after placement and then daily for the next 3 consecutive days to find out the optimum time to conduct such test. Figure 3 shows that GCO probe blow count increased gradually in the early stages and exceeded 40 at four hours after placement, thereafter there was a drastic increase.

To accommodate site workflow, GCO probe tests were conducted within 4 hours after the placement of a lift of 300 mm thick cement-soil. Following the practice of conducting a GCO probing for backfilling using pit by pit method, three GCO probe tests were conducted at each lift. Figure 4 shows that the 3-day UCS plotted against the minimum GCO blow count for the same lift in the field trial. All 3-day UCS exceeded 0.07 MPa and the minimum GCO blow count was 40.

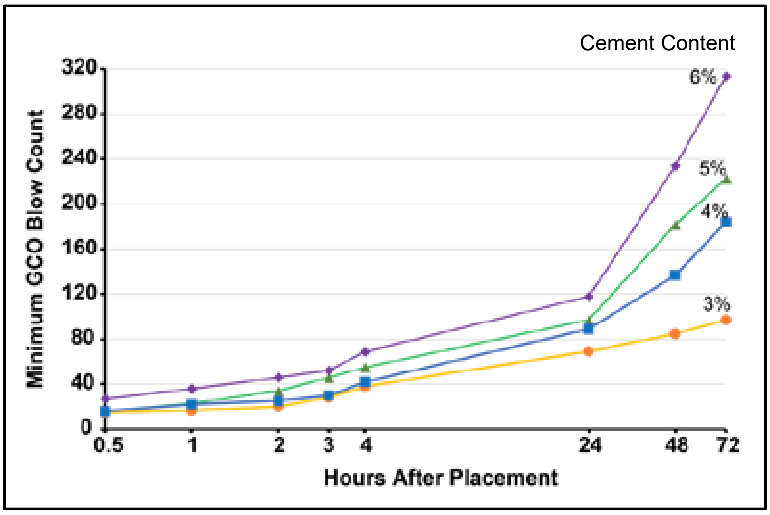

Figure 3: Field trial - GCO probe test results with different cement contents

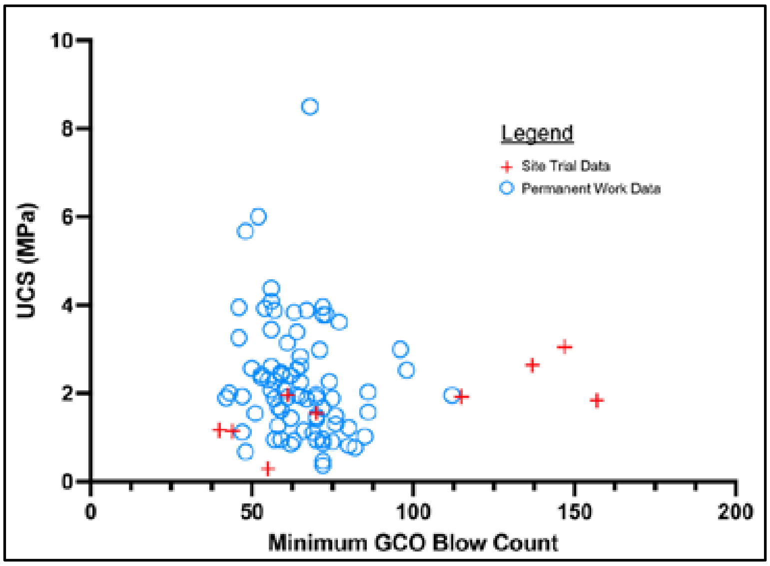

Figure 4: 3-day UCS vs GCO blow count

3 PERMANENT CEMENT-SOIL CONSTRUCTION

Upon the completion of the field trial, results of UCS tests and GCO probe tests substantiated the postulation of adopting alternative testing method for cement-soil. Consequently, these testing methods were implemented in the production run of placement of 4,200 m^3 of cement-soil at the study works site.

3.1 Mixing and placement

Following the GS requirements, excavated fill material was sieved as detailed in Section 2.2 in the field trial. To maintain the uniformity of the cement-soil fill and facilitate subsequent GCO probe tests, the excavated materials were further screened using 10 mm and 5 mm test sieves before adding into the pugmill for mixing.

In this study, cement content of 4% by weight of soil was adopted. The mixture consisted of Portland cement, sand and sieved fill material in the proportions of 1:4:20 by weight. Mixing and placement of the cement-soil followed the procedures outlined in Sections 2.2 and 2.3. Mixed cement-soil was backfilled in layers to the excavated trenches of 6 m long by 2 m wide within 30 minutes of mixing and compacted in lift thickness of 300 mm thick. As a common workmanship control on site, each layer was systematically tamped and the surface of the compacted cement-soil was then visually checked for any defects such as any cracks and dusting surface. If such circumstance occurred, water would be sprayed onto the compacted surface and the tamping procedure was repeated.

3.2 Field control and sampling frequency

To streamline the workflow in the production run, it was decided that GCO probe would be conducted within 4 hours after placement of three lifts of 300 mm thick cement-soil. Placement of cement-soil could be continued when the minimum GCO blow count for the previous 900 mm thick cement-soil exceeded 40. Figure 4 shows that such approach could speed up the production without compromising the reliability of the field control measure.

As the behaviour of cement-soil is akin to soft soil treated with deep cement method, the sampling frequency of cement-soil mixture in this study was devised with reference to that adopted in a recent CEDD reclamation project at Lantau Island using deep cement mixing. One continuous core sample would be taken at each 900 mm completed layer from a 3 m depth trench for every 50 m^2 of slope area treated with cement-soil for the compliance testing, i.e. determination of 28-day UCS. In this study, each 900 mm continuous core sample was split into three 300 mm core samples for 3-day, 7-day and 28-day UCS tests to furnish information on the early strength after placement. To allow for sufficient time for the cement-soil to gain some strength and for the contractor to cope with site workflow, sampling of cement-soil for UCS tests was conducted 24 hours after its placement. This arrangement took due account of the site works activities and also enabled sampling to be conducted after placement of every 3 lifts of cement-soil.

3.3 Optimised construction time

According to the GS, three in-situ density tests would be conducted for each batch of compacted fill. Table 1 shows the number of compliance tests required following the prevailing practice and the alternative proposed in this paper at the study work site. The proposed field control and compliance requirements, apart from entailing fewer tests, the time in relation to testing activities on site was also found to be shorter. As demonstrated in the production run, the time required for the excavation and placement of cement-soil and relevant field testing following the proposed field control and compliance requirements for a trench of 6 m long by 2 m wide by 3 m deep was completed in about 2 days. This considerably shortened the construction time and the works cycle was more effective and less affected by inclement weather. This is beneficial to site operation as it could reduce the risk of temporary slope instability and better utilise the limited storage area for mixing and storage of spoils.

Table 1: Number of in-situ tests for different compliance requirements at the study slope

	Compliance Criterion in GS for Soil-cement	**Tests for Field Control and Proposed Compliance Criterion for Cement-soil**	
	In-situ Density Test	UCS Test	GCO Probe Test
No. of test	1,650 approx.	348*	1,044

* 3-day, 7-day and 28-day UCS were determined for each 900 mm core sample

3.4 Experience gained

Adopting the alternative compliance criterion and field control for cement-soil permanent slope work would allow the contractor to have an early indication of the cement-soil strength condition in a short period of time. The time input for completing a 3 m depth trench of cement-soil backfilling was significantly reduced comparing with the use of the traditional in-situ density test for compacted fill. This allowed the backfilling operation to be carried out more efficiently and less affected by the weather conditions.

During the permanent works, attempts to further expedite the workflow was continued to be examined. For example, an attempt was made to increase the lift thickness to 500 mm while keeping the same number of passes of the tamper. However, it was found the quality of the samples deteriorated significantly when extracted for testing and was not pursued further. As the contractor gained more experience in the cement-soil backfilling operation and the use of the sampler in the latter phase of the permanent works, the core sampling depth for a 2.7 m deep cement-soil trench (excluding top 300 mm thickness for soft landscaping work) was relaxed from every 900 mm compacted thickness to a 2-phase coring of compacted thickness in 1.2 m and 1.5 m. This arrangement further improved the progress of work without sacrificing the quality of core samples.

The trial showed that both 3-day and 7-day UCS could be used as an early assurance indicator. However, as 3-day UCS was available sooner, it was preferred. Hence, the actual number of tests required to fulfil the proposed field control and compliance criterion would be less than that shown in Table 1. GCO probe seems to be a useful and agile field control tool giving early assurance once a correlation between the blow count and 3-day UCS was established.

A tailor-made sampler was used in this study because the contractor had difficulties in sourcing a portable sampler due to time constraints. While the tailor-made sampler seems to have served its purpose in this project partly because of the relatively low strength requirement of the cement-soil, it may not be adequate or efficient when higher cement content is adopted. Hence, the use of a portable sampler should be explored in future application in hope of standardising and making the sampling operation more efficient.

As this is a pilot application of the use of UCS as a compliance criterion, a conservative approach was adopted requiring all samples to meet the compliance criterion. While in principle, remedial works could be implemented if a specific layer failed to meet the compliance criterion, this would in reality pose much difficulty in doing so as that specific layer might already be covered by considerable thickness of cement-soil and would have a significant impact on the works programme. This may be circumvented with the choice of a more conservative GCO blow count as field control to minimise such occurrence or it is worth exploring the possibility of accepting a small percentage of samples not complying with the criterion. As the slope stability is governed by the strength of the soil mass, the impact of having discrete locations of slightly lower strength can be assessed by means of slope stability assessment to see if this can be accommodated or whether appropriate remedial measures are needed.

The requirement of adding sand to the cement-soil mixture as stipulated in GS is worthy of further examination. If the sand is substituted by the original sieved soil, this could, in some cases, minimise the transport of surplus excavated soil offsite and better utilise the in-situ material.

4 CONCLUSION

The GS adopts the same compliance criterion for both compacted fill and cement-soil. The strength of cement-soil derives from cementation resulting from chemical reaction between cement and the soil while that of the compacted fill closely relates to its density. Hence, the use of strength rather than density seems to be a more direct and appropriate parameter for compliance criterion of cement-soil. This paper describes the pilot use of UCS as an alternative compliance criterion for cement-soil used in a slope upgrading works project. It details the findings of a field trial prior to the production run to work out the mixing and placement procedure. It identifies that GCO probing could be a useful field control measure to augment the use of UCS as compliance criterion.

Furthermore, in the prevailing practice, in-situ density tests are generally performed on cement-soil at least 24 hours after its placement. Figure 3 shows that 24 hours after its placement, the cement-soil could have gained significant strength as reflected by the high GCO blow counts. It can be easily envisaged that use of conventional hand tools to excavate the cement-soil for in-situ density tests could be a daunting task.

The pilot application indicated that the adoption of the proposed alternative compliance criterion could lead to optimisation of the work flow in placement and sampling of cement-soil. This allows more efficient site operation resulting in potential time and cost saving. The filling operation would also be less affected by inclement weather.

As this is a pilot application, the work procedure had been concocted in a cautious manner. There is room for further improvement/optimisation, some of which are outlined in this paper for consideration.

ACKNOWLEDGEMENTS

This paper is published with the permission of the Head of the Geotechnical Engineering Office and the Director of Civil Engineering and Development, Government of the Hong Kong Special Administrative Region.

The authors would like to express their appreciation to the project team who participated in this study, in particular, Ir. Florence L. F. Chu, Ir. Edward K. C. Lam, Ir. Raymond L. M. Yim, Ir. Max C. N. Cheung, Ir. Charles K. L. Tang and the LPMit specialist contractor – Dix Construction & Transportation Ltd. for their valuable works experience and advice on laboratory testing, field testing and works operation.

REFERENCES

BBVL. 2002. Review of Upgrading of Loose Fill Slope in Hong Kong.

Construction Standard CS1:2010 Testing Concrete. 2010.

Fugro. 2009. Study on Soil Cement Used in Slope Works.

General Specification of Civil Engineering Works. 2006.

HKIE. 2017. Interim Guidelines on Testing of Unconfined Compressive Strength of Cement Stabilised Soil.

Bridging the Micro and Macro Mechanical Behaviour of Granular Materials

Q Zhao[1]
The Hong Kong Polytechnic University, Hong Kong, China
Y Chen
Changjiang Survey, Planning, Design and Research Co., Ltd., Wuhan, China
G Ma
Wuhan University, Wuhan, China

ABSTRACT

Understanding the underlying physics and mechanisms responsible for the loss of stability of granular systems is crucial to the mitigation of geohazards such as landslides and earthquakes. We use a combination of in situ testing under X-ray micro-computed tomography (micro-CT) and the hybrid finite and discrete element method (FDEM) to investigate the mechanical behaviours of granular materials from the microscopic to the macroscopic scales. We conduct a miniature triaxial test on a granular column sample that is imaged with X-ray micro-CT at incremental strain steps. Then, spherical harmonic (SH) analysis is performed to characterize and reconstruct the multi-scale morphological characteristics of particles, which was used to create the digital twin of the tested sample. FDEM simulation quantitatively agrees with the overall response observed in the experiment. We find that the granular material deforms plastically through spatially localized zones of large nonaffine displacements, and the spatiotemporal evolution of these zones controls the macroscopic responses of the system. Our method sheds light on bridging length scales from microscopic scale to macroscopic granular systems.

1 INTRODUCTION

Mechanical behaviour of granular materials in nature is related to geohazards such as landslides, soil foundation instability, and earthquakes. The granular system responds to the mechanical perturbation through the spatial rearrangement of particles and the dynamics of force transmission network (Majmudar & Behringer, 2005). Therefore, it is crucial to understand the underlying physics and mechanisms responsible for the loss of stability of granular systems.

X-ray micro computed tomography (micro-CT) is a non-destructive approach of examine material internal structures. Micro-CT have been successfully used to characterize the structural properties and microscopic scale dynamics of different materials (e.g., Andò et al., 2012; Weis & Schröter, 2017; Q. Zhao et al., 2018; Q. Zhao et al., 2020). X-ray computed tomography aided laboratory test allows for the investigation of granular materials from microscopic to macroscopic scales (e.g., Karatza et al., 2017; Afshar et al., 2018; Cheng & Wang, 2018; Kong & Fonseca et al., 2019; Chevalier et al., 2019), making it a promising tool in studying the behaviour of complex granular systems. This technology was used to measure contact forces among particles (e.g., Saadatfar et al., 2012; Andrade & Avila, 2012). However, it was only applied to granular systems with small number of particles. Tracking the trajectory of large number of moving particles and evaluating their interactions remains a challenging task, especially for the granular systems that experience large deformation.

The particle based numerical simulation methods provide a different perspective to examine the behaviour of granular systems. Previous studies suggested that particle shape has profound influences on granular dynamic behaviour, which promoted the development of advanced modelling techniques (Alshibli et al.,

[1] E-mail: qi.qz.zhao@polyu.edu.hk

2016; Murphy et al., 2019), such as the discrete element method (DEM) (e.g., Wu et al., 2020), the hybrid finite and discrete element method (FDEM) (Ma et al., 2014; Ma et al., 2016; Chen et al., 2021), and the level set DEM (LS-DEM) method (Kawamoto et al., 2016; Kawamoto et al., 2018).

In this study, we investigate the microscopic and macroscopic behaviour of granular materials by combining in situ testing under X-ray micro-CT and FDEM modelling. With this novel combination of technologies, we achieved a quantitative description of the macroscopic responses and microscopic dynamics of the granular system during the whole deformation process.

2 MATERIAL and METHODS

2.1 In situ testing under X-ray micro-CT

The experiment was carried out using the in situ testing apparatus under micro-CT (ERDμ) developed by Q. Zhao et al. (2017) (Figure 1). The apparatus consists of a control panel and an X-ray transparent loading vessel (Figure 1a). Data acquisition equipment and drivers of the step motors are mounted on the control panel. During an in situ testing, the whole system is placed inside the cabinet of the micro-CT (Figure 1 b&c). This apparatus can conduct unconfined (uniaxial) compression tests, confined compression tests, and rotary shear tests.

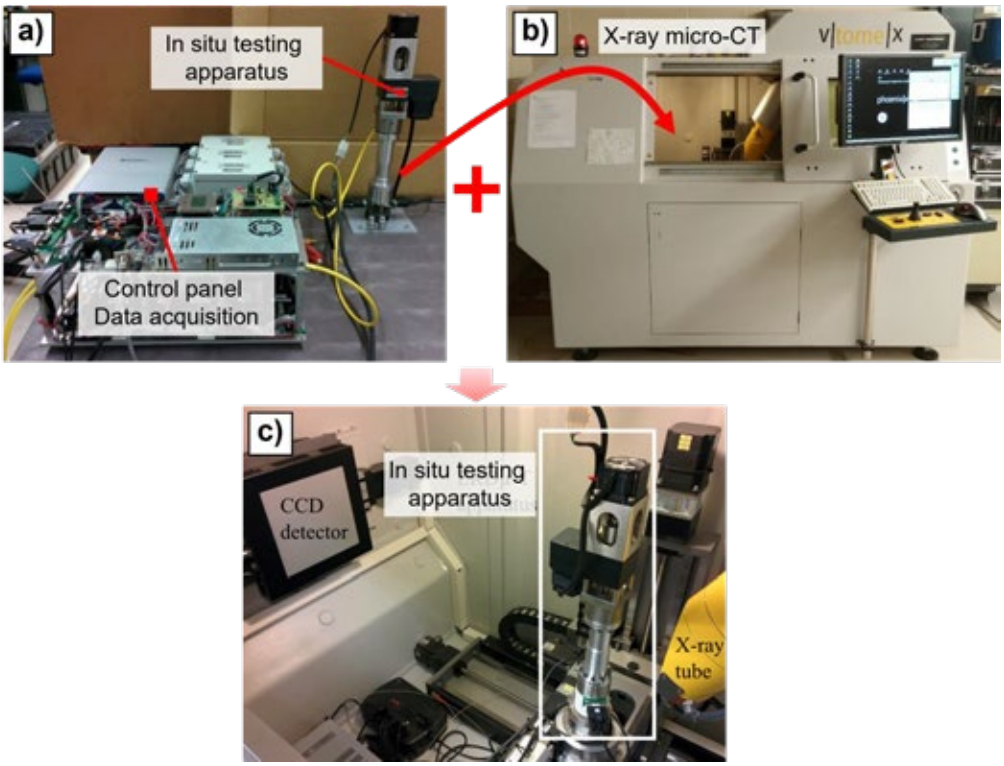

Figure 1. The in situ testing apparatus under X-ray micro-CT. (a) the control panel and the X-ray transparent loading vessel, (b) the X-ray micro-CT machine, and (c) the testing apparatus seated inside the micro-CT during the test.

2.2 Sample preparation and testing procedure

The sample is made of Ottawa sand and has an initial diameter of approximately 12 mm and a height of 25 mm. It is prepared using the dry pluviation method and subjected to vibration and tapping until a dense packing is achieved. The sample is confined by a 0.3 mm thick flexible latex membrane, providing the flexible boundary condition while allowing for the application of confining pressure. Then, the sample is placed inside the ERDμ apparatus that is mounted on the rotation table inside the X-ray micro-CT (Figure 2a).

During the experiment, the specimen was first isotropically compressed to the confining pressure (σ_3) of 300 kPa and then the axial stress (σ_1) is increased by the downward movement of the top loading platen at a constant strain rate of 0.1%/min (Figure 2b).

Three dimensional (3D) micro-CT scans of the sample were acquired at 15 strain levels. The first scan was conducted after the application of the confining pressure. During each 3D scan, 1080 two dimensional (2D) radiographic projections with a pixel size of 27.5 μm were acquired, while the ERDμ apparatus was rotated 360° around the vertical axis. The loading platen was kept stationary during scans and the confining pressure was maintained constant throughout the experiment. The imaging of the incrementally strained sample allowed us to investigate the gradual variation of the sample internal structures.

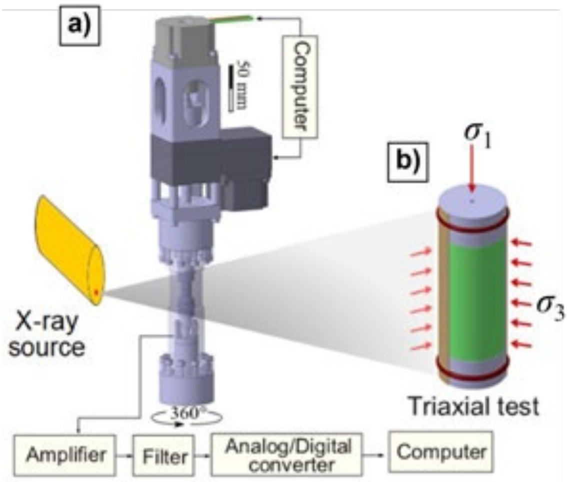

Figure 2. Schematic diagram of the experimental setup. (a) The ERDμ X-ray transparent testing vessel. (b) The sample assembly and loading conditions in the experiment test.

2.3 Image processing

The 2D radiographic projections were reconstructed into a 3D digital volume of the sample, with the greyvalues of the voxels directly related to the density of the sample at the corresponding spatial coordinates (Figure 3 a-b). Then, the digital volume was divided into two phases: air and solid, based on global thresholding. In the binarized image, contacting grains are connected due to the partial volume effect, and a mark-controlled watershed segmentation was used to separate the grains. This watershed algorithm uses the image morphology to identify the grains and separate them from each other. Finally, the separated grains are labelled for further tracking and analysis (Figure 3c). Contacts between neighbouring particles can be identified by subtracting the watershed segmented data from the binarized data.

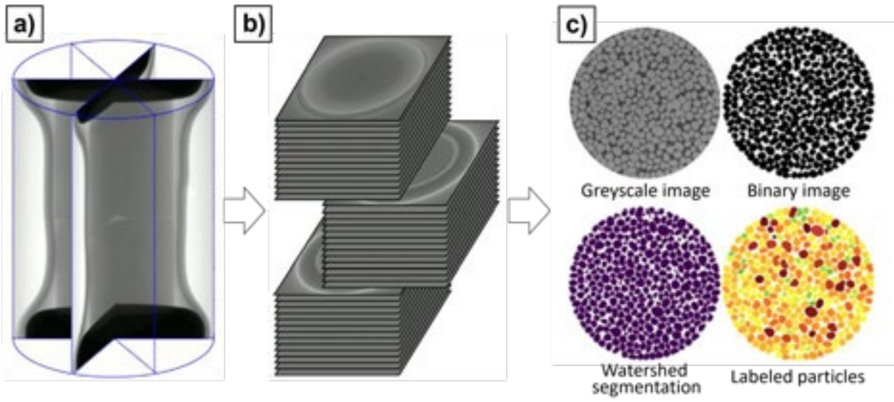

Figure 3. Image processing procedure. (a) Raw radiographic projection images, (b) horizontal image stack after reconstruction, and (c) image thresholding, watershed segmentation, and labelling.

Particle morphological features such as the particle volume, surface area, and principal axis lengths of the particle are used in particle matching and tracking algorithms. These morphological quantities are sensitive to the X-ray CT imaging quality. One promising approach of improving the matching accuracy is to use more morphological features ranging from particulate size to surface texture. Spherical harmonic (SH) analysis mathematically describes the general conformation of the particle shape at different scales. SH analysis is capable of characterizing and quantifying the multiscale morphological features of irregularly shaped particles (Garboczi, 2002; Zhou et al., 2015; Wei et al., 2018). The SH invariants, independent of particle translation and rotation, are adopted in evaluating the similarities of particles to track particles across multiple loading steps (Kazhdan et al., 2003; B. Zhao et al., 2017; B. Zhao et al, 2018).

We use SH function to represent the surfaces of particles extracted from image data:

$$r(\theta,\varphi)=\sum_{n=0}^{\infty}\sum_{m=-n}^{n}c_n^m Y_n^m(\theta,\varphi) \tag{1}$$

$$Y_n^m(\theta,\varphi)=\sqrt{\frac{(2n+1)(n-m)!}{4\pi(n+m)!}}P_n^m(\cos\theta)e^{im\varphi} \tag{2}$$

where $r(\theta,\varphi)=\sqrt{\sum_{x,y,z}(\kappa-\kappa_0)^2}$ is the polar radius from particle centroid (x_0, y_0, z_0), $\theta\in[0,\pi]$ and $\varphi\in[0,2\pi]$ are the spherical coordinates, and c_n^m is the corresponding SH coefficient. Taking $r(\theta,\varphi)$ as the input on the left side of Eq. (1), a linear equation system with $(n+1)^2$ unknowns can be obtained to determine coefficients c_n^m . $P_n^m(\cos\theta)$ is the Legendre function of degree n and order m , expressed by Rodrigues's formula:

$$P_n^m(x)=(1-x^2)^{|m|/2}\cdot\frac{d^{|m|}}{dx^{|m|}}\left[\frac{1}{2^n n!}\cdot\frac{d^n}{dx^n}(x^2-1)^n\right] \tag{3}$$

We define a set of SH frequencies as $R_n(\theta,\varphi)=\sum_{m=-n}^{n}c_n^m Y_n^m(\theta,\varphi)$, which exhibit rotational invariant properties independent of particle translation and rotation (Kazhdan et al., 2003), and the modulus of the SH frequency, that is, the SH rotation-invariant is calculated as:

$$\|R_n(\theta,\varphi)\|=\sqrt{\int_0^{2\pi}\int_0^{\pi}R_n(\theta,\varphi)^2\,d\theta d\varphi}=\sqrt{\sum_{m=-n}^{n}\|c_n^m\|^2} \tag{4}$$

The SH coefficients describe the general conformation of the particle shape at different scales. While a high SH degree can represent the shape of the grains with fine details, it was found that an SH degree of 15 is sufficient to describe the grains in this study. For natural sand, there are no two particulates with completely identical morphological features; therefore, the unique set of SH rotation-invariants can be used as the geometrical DNA for matching particles.

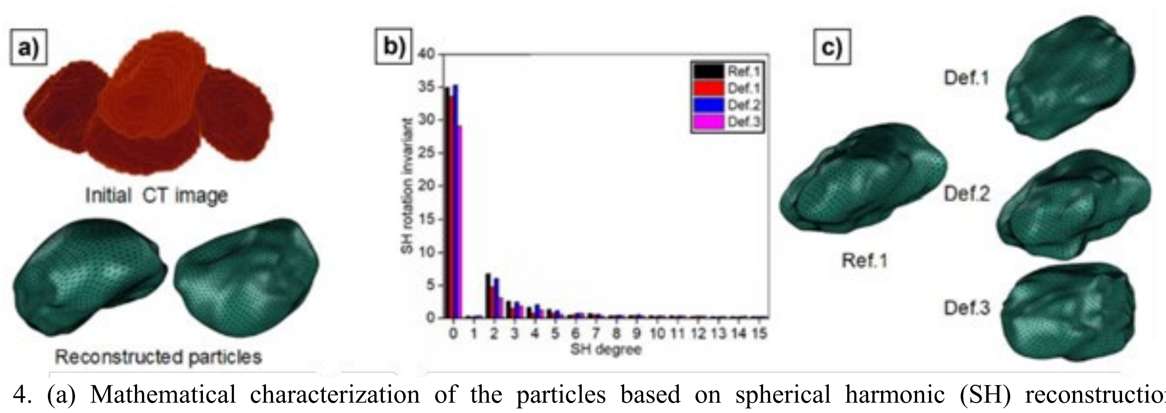

Figure 4. (a) Mathematical characterization of the particles based on spherical harmonic (SH) reconstruction. (b) Statistical difference of the derived spherical harmonic rotation-invariants at different SH-degrees. Comparison is shown

between one particle from the Reference configuration (Ref.) and three particles from deformed configuration (Def.). (d) Examples of the digital reconstruction and matching results.

Lastly, we can identify the matching particles between adjacent loading states by evaluating the minimum L^2- *norm* difference between the corresponding vectors $\mathbf{R}_n$ (B. Zhao et al., 2018), measured by

$$\left\| R_n^k(\theta,\varphi) - R_n^{k+1}(\theta,\varphi) \right\| = \sqrt{\sum_{n=0}^{\infty}\left(\left\|R_n^k\right\| - \left\|R_n^{k+1}\right\|\right)^2} \quad (k = 1, 2, \ldots, N_S) \tag{5}$$

where k is the loading states and N_S is the total number of micro-CT scans. With this particle characterization and matching method, we successfully tracked the movement of almost all the particles and created a library of the multiscale morphological information of the granular material tested in the experiment (Figure 4).

2.4 Creation of the digital twin

We built a digital twin of the laboratory sample using the FDEM method. A typical FDEM model utilizes the cohesive crack model to achieve simulation of the fracturing process, however, in this study, we did not observe grain breakage from the experimental results, which is supported by the particle size distribution (PSD) of the grains from the first and last micro-CT scan image data (Figure 5). Thus, the FDEM model we implement considers only the interaction of grains and no grain breakage is simulated.

The digital twin of the tested sample is configured to statistically resemble the laboratory sample, in terms of, grain numbers, grain size distribution, and grain morphological features. Each grain was meshed into many second-order tetrahedral finite elements (Figure 6). In addition, a typical FDEM model involving fracturing requires an iterative calibration process (Tatone & Grasselli, 2015); however, in this study, no calibration was conducted, and the basic material parameters are assigned to the grains (Table 1).

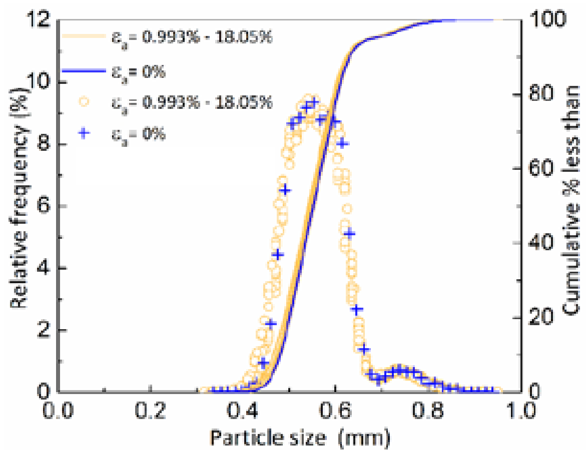

Figure 5. Particle size distribution (PSD) of the laboratory sample at the first and last micro-CT scan data.

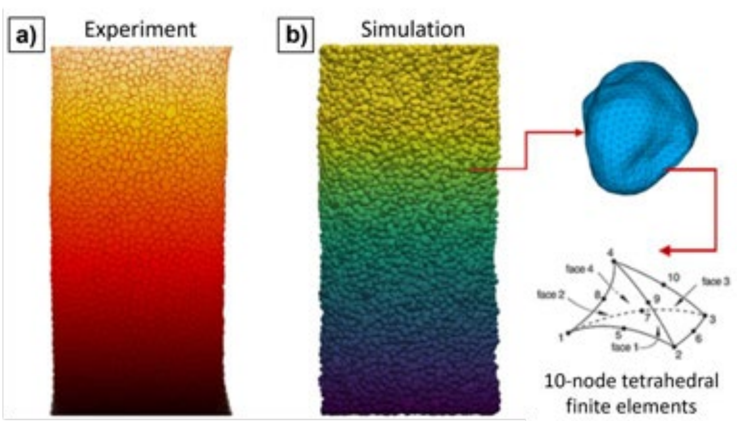

Figure 6. Creation of the digital twin of the laboratory sample.

Table 1: Material parameters used in the FDEM simulation (from Chen et al., 2021).

Parameter (unit)	Value
Density (kg/m^3)	2650
Young's modulus (GPa)	92.1
Poisson's ratio (-)	0.118
Friction coefficient (-)	0.5
Normal and tangential penalty (N/m^3)	92.1×10^{11}
Damping factor (0.03)	0.03

3 RESULTS AND DISCUSSION

3.1 Macroscopic stress-strain behaviour

The FDEM model, without calibration against the experimental results, reasonably reproduces the macroscopic behaviours of the laboratory sample including the stress-strain and dilation behaviours (Figure 7). The simulation shows an earlier peak stress ratio σ_1/σ_3 than the experiment, which may be related to the micro-CT scans conducted before the peak.

The overall consistency suggests that the critical information needed in the modelling of granular material are particle shape and packing properties, which is confirmed by other researchers (Kawamoto et al., 2018). Note that, the drop in stress ratio during each scan is due to the stress relaxation caused by the loading pause during each X-ray imaging.

We choose six strain intervals (I-VI) for further analyse: 0.00% – 0.99%, 0.99% – 5.03%, 5.03% – 8.06%, 8.06% – 11.06%, 11.06% – 14.06%, and 14.06% – 18.06%, which are divided by five strain states marked A-E in Figure 7.

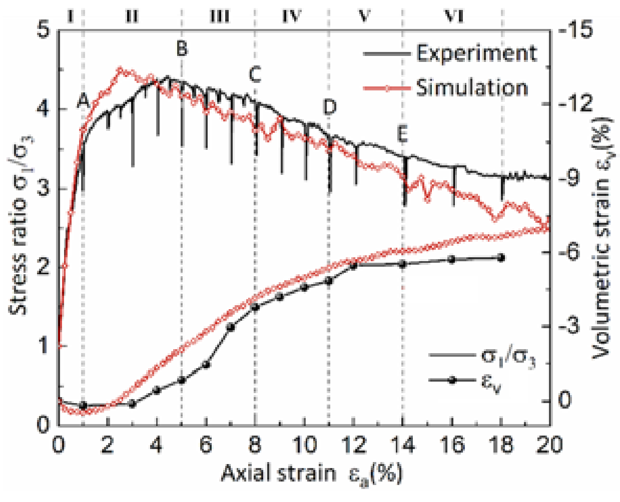

Figure 7. Stress-strain and dilation curves of the experimental and numerical simulated results. Strain point A-E divides the loading process into six incremental strain steps (I-VI) that are further evaluated.

3.2 Microscopic particle dynamics

We identified 15961 individual particles in the tested sample. We further compare the incremental particle displacements at six strain states to examine the particle kinematics obtained from the experiment and the FDEM simulation (Figure 8). The FDEM simulated particle displacement field is in good agreement with that obtained in the experiment. The magnitude of particle displacement increases with the shearing process and bulging are shown in all the steps. Two cone-shaped dead zones are developed at the top and bottom of the sample at the post-peak softening stages. While in the middle of the sample, a zone of intensive shearing localizes into an X-shaped shear band.

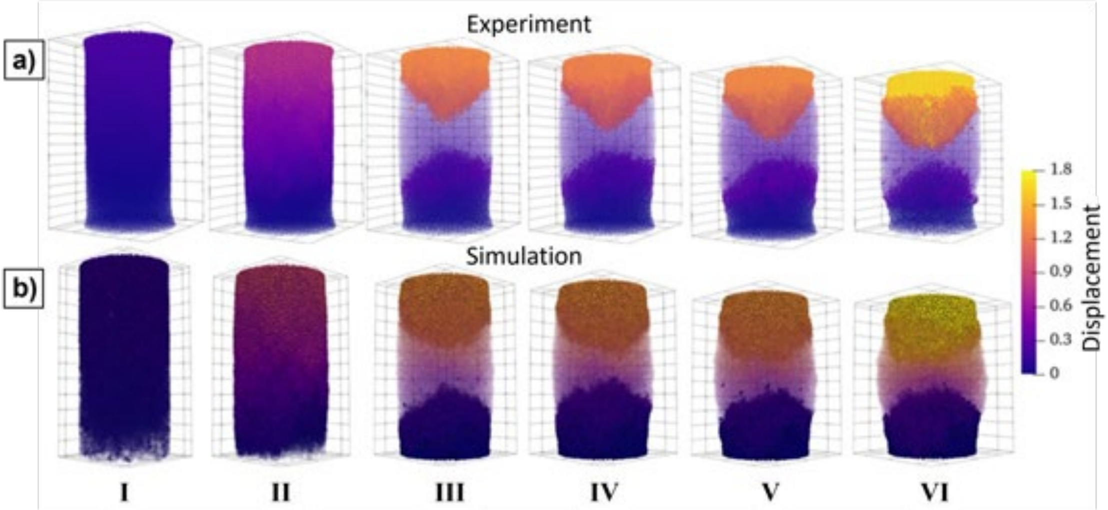

Figure 8. Particle displacements at incremental strain steps for (a) experimental test and (b) FDEM simulation.

At the microscopic scale, the grains rearrange themselves in response to the shear deformation, and the varying local structures of particles creates highly heterogeneous particle motion. As a result, granular materials deform in a nonaffine form (Ma et al, 2018), that is, non-uniform rotation, deformation and rearrangement of particles. The micro-CT image data and FDEM simulation allow us to quantify the nonaffine motion of particle using the local minimum nonaffine displacement $D^2_{\min}$ that measures the mean square deviation of the particle's position from the best-fit affine transformation of its neighbourhood over the strain interval $\delta\varepsilon$ (Falk & Langer, 1998; Ding et al., 2014; Cubuk et al., 2017):

$$D^2_{\min}\left(\varepsilon, \varepsilon+\delta\varepsilon\right) = \frac{1}{N_i}\sum_{k}^{N_i}\left[\boldsymbol{\mu}_{ki}(\varepsilon+\delta\varepsilon) - \boldsymbol{\Lambda}_i(\varepsilon)\boldsymbol{\mu}_{ki}(\varepsilon)\right]^2 \tag{6}$$

where $\boldsymbol{\Lambda}_i(\varepsilon)$ is the best-fit affine deformation tensor of particle i extracted by minimizing the $D^2_{\min}\left(\varepsilon, \varepsilon+\delta\varepsilon\right)$ (Chikkadi & Schall, 2012; Guo & Zhao, 2014):

$$\boldsymbol{\Lambda}_i = \mathbf{X}\cdot\mathbf{Y}^{-1} \tag{7}$$

$$\mathbf{X} = \sum_{k}^{N_i}\boldsymbol{\mu}_{ki}(\varepsilon+\delta\varepsilon)\otimes\boldsymbol{\mu}_{ki}(\varepsilon) \tag{8}$$

$$\mathbf{Y} = \sum_{k}^{N_i}\boldsymbol{\mu}_{ki}(\varepsilon)\otimes\boldsymbol{\mu}_{ki}(\varepsilon) \tag{9}$$

where $\boldsymbol{\mu}_{ki}(\varepsilon)$ is the displacement vector between the reference particle i and its neighbour k at strain state ε. Note that the nonaffinity measure depends on the size of the neighbourhood. Here, we take the first minimum of the pair-correlation function as the cutoff distance (Chikkadi & Schall, 2012; Chen et al., 2021). Our results showed that probability distribution functions of the local minimum nonaffine displacement $D^2_{\min}$ exhibits a power-law decay, which implies that particles with large nonaffine displacements are collectively organized, and particles with similar nonaffine displacements tend to form compact clusters (Kou et al., 2018; Chen et al., 2021).

The local strain tensor is determined based on the affine tensor $\boldsymbol{\Lambda}$ using: $\boldsymbol{\varepsilon}^L = -\left(\boldsymbol{\Lambda}+\boldsymbol{\Lambda}^T\right)/2$, and the local deviatoric strain for each particle can be calculated as $\varepsilon_q^L = \sqrt{\frac{2}{3}\boldsymbol{\varepsilon}^L_{dev}:\boldsymbol{\varepsilon}^L_{dev}}$. The local deviatoric strain ε_q^L are evaluated at strain intervals I-V (Figure 9).

Similar spatial distribution and temporal evolution of the granular system are observed in the experimental and numerical results. At 1.0% axial strain, a few localized plastic zones appeared randomly in the elastically deformed surroundings. After the onset of yielding, particles rearrange themselves to accommodate the increased strain, and many activated plastic zones appeared. These zones are characterized by close-packed particles with high local strain magnitude. Eventually, those plastic zones coalescence into a conjugate X-shaped shear band spanning the granular system. Once the shear band is formed, the subsequent plastic activity is essentially dominated by the evolution of the shear band through thickening and sliding.

Although the evolution patterns of the granular systems observed in experiment and simulation show great similarities, the thickness and spanning region of the shear band are slightly different. This may be related to the fact that the FDEM simulation lacks the consideration of multiscale contacting behaviour of particles. The FDEM contact model assumes the contact point is fully sticking before reaching the Column frictional resistance. For real particles with multiscale morphological characteristics may experience relative motion even under tiny perturbation and affect the local rearrangement of particles (Kou et al., 2017). In addition, a constant sliding friction coefficient is applied to the FDEM model, which ignores the variable friction conditions in actual particle surfaces.

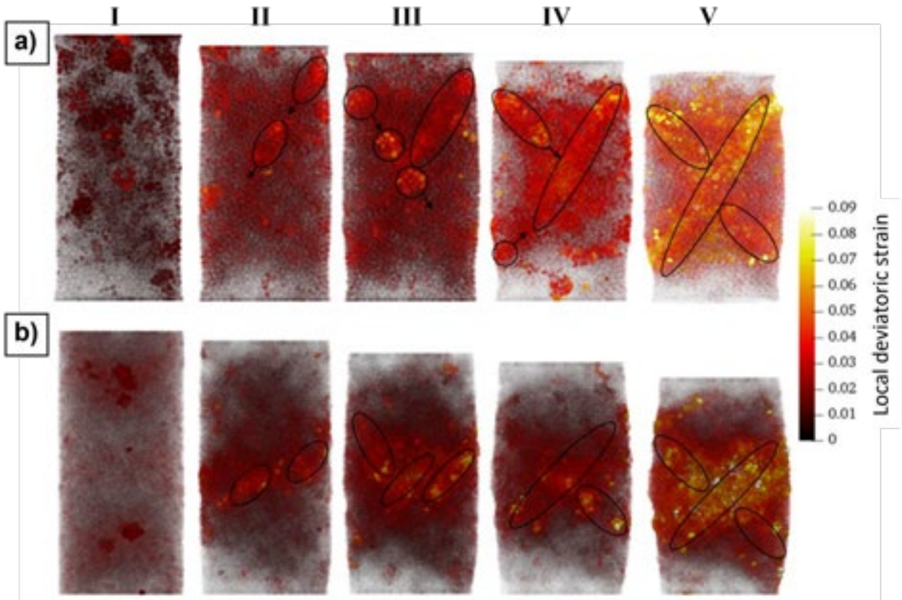

Figure 9. The spatial distribution of local deviatoric strain at strain states I-V for both (a) experiment and (b) numerical simulation. The yellow and red indicate particles subjected to large local deviatoric strain, and particles with small are coloured black and are transparent.

In this study, the grain size is relatively large at the millimetre scale, and with the high resolution micro-CT scan, almost all the grains were captured with high image quality. In some cases, for example, when clay samples are examined, the grain size may be at the micrometre scale that the micro-CT imaging may not be able to resolve each individual grain. In those cases, segmentation-based image analysis would not be applicable. Instead, a direct estimation of the spatial variation of density can be achieved through a correlation between grayvalues and density.

4 CONCLUSIONS

In this work, we investigate the mechanical behaviour of granular materials by combining the merits of the in situ testing under X-ray micro-CT and FDEM numerical modelling. We perform spherical harmonic analysis to characterize and reconstruct the multiscale morphological characteristics of irregularly shaped particles, which enables accurate matching of particles even at the large strain intervals. Relying on the detailed spherical harmonic reconstruction, we establish high fidelity numerical model with the consistent particle morphology and disordered structure. The FDEM simulation results quantitatively agree with the overall response recorded in the experiment test. The particle scale dynamics including the nonaffine particle displacements and particle clustering behaviour show a remarkable quantitative agreement between simulation and experiment. Our results demonstrated that the spatiotemporal evolution of localized microscopic scale plastic deformation controls the macroscopic responses of the granular system. The proposed tool in this study sheds light on bridging the microscopic and macroscopic mechanical behaviour of granular materials by 3D visualization and quantitative analysis. This providing us with a better understanding of the physical mechanisms behind the failure of granular systems, such as failure of soil slopes and weakening of gouge filled fault zones.

ACKNOWLEDGEMENTS

Q. Zhao is supported by the FCE Start-up Fund for New Recruits at PolyU (Project ID P0034042) and the Early Career Scheme of the Research Grants Council of the Hong Kong Special Administrative Region, China (Project No. PolyU 25220021).

REFERENCES

Afshar, T., Disfani, M. M., Narsilio, G. A., & Arulrajah, A. (2018). Post-breakage changes in particle properties using synchrotron tomography. *Powder Technology*, 325, 530-544.

Alshibli, K. A., Jarrar, M. F., Druckrey, A. M., & Al-Raoush, R. I. (2016). Influence of particle morphology on 3D kinematic behavior and strain localization of sheared sand. *Journal of Geotechnical and Geoenvironmental Engineering*, 143(2), 04016097.

Andrade, J. E., & Avila, C. F. (2012). Granular element method (GEM): linking inter-particle forces with macroscopic loading. *Granular Matter*, 14(1), 51-61.

Andò, E., Hall, S. A., Viggiani, G., Desrues, J., & Bésuelle, P. (2012). Grain-scale experimental investigation of localised deformation in sand: a discrete particle tracking approach. *Acta Geotechnica*, 7(1), 1-13.

Chen, Y., Ma, G., Zhou, W., Wei, D., Zhao, Q., Zou, Y., & Grasselli, G. (2021). An enhanced tool for probing the microscopic behavior of granular materials based on X-ray micro-CT and FDEM. *Computers and Geotechnics*, 132, 103974.

Cheng, Z., & Wang, J. (2018). Experimental investigation of inter-particle contact evolution of sheared granular materials using X-ray micro-tomography. *Soils and Foundations*, 58(6), 1492-1510.

Chevalier, B., Tsutsumi, Y., & Otani, J. (2019). Direct shear behavior of a mixture of sand and tire chips using X-ray computed tomography and discrete element method. *International Journal of Geosynthetics and Ground Engineering*, 5(2), 7.

Chikkadi, V., & Schall, P. (2012). Nonaffine measures of particle displacements in sheared colloidal glasses. *Physical Review E*, 85(3), 031402.

Cubuk, E.D., Ivancic, R.J.S., Schoenholz, S.S., Strickland, D.J., Basu, A., Davidson, Z.S., Fontaine, J., Hor, J.L., Huang, Y.R., Jiang, Y. and Keim, N.C. (2017). Structure-property relationships from universal signatures of plasticity in disordered solids. *Science*, 358(6366), 1033-1037.

Ding, J., Patinet, S., Falk, M. L., Cheng, Y., & Ma, E. (2014). Soft spots and their structural signature in a metallic glass. *Proceedings of the National Academy of Sciences*, 111(39), 14052-14056.

Falk, M. L., & Langer, J. S. (1998). Dynamics of viscoplastic deformation in amorphous solids. *Physical Review E*, 57(6), 7192.

Garboczi, E. J. (2002). Three-dimensional mathematical analysis of particle shape using X-ray tomography and spherical harmonics: Application to aggregates used in concrete. *Cement and concrete research*, 32(10), 1621-1638.

Guo, N., & Zhao, J. (2014). Local fluctuations and spatial correlations in granular flows under constant-volume quasistatic shear. *Physical Review E*, 89(4), 042208.

Karatza, Z., Andò, E., Papanicolopulos, S. A., Ooi, J. Y., & Viggiani, G. (2017). Evolution of deformation and breakage in sand studied using X-ray tomography. *Géotechnique*, 68(2), 107-117.

Kong, D., & Fonseca, J. (2019). On the kinematics of shelly carbonate sand using X-ray micro tomography. *Engineering Geology*, 261, 105268.

Kawamoto, R., Andò, E., Viggiani, G., & Andrade, J. E. (2016). Level set discrete element method for three-dimensional computations with triaxial case study. *Journal of the Mechanics and Physics of Solids*, 91, 1-13.

Kawamoto, R., Andò, E., Viggiani, G., & Andrade, J. E. (2018). All you need is shape: Predicting shear banding in sand with LS-DEM. *Journal of the Mechanics and Physics of Solids*, 111, 375-392.

Kazhdan, M., Funkhouser, T., & Rusinkiewicz, S. (2003, June). Rotation invariant spherical harmonic representation of 3 d shape descriptors. In Symposium on geometry processing (Vol. 6, pp. 156-164).

Kou, B., Cao, Y., Li, J., Xia, C., Li, Z., Dong, H., Zhang, A., Zhang, J., Kob, W. & Wang, Y. (2017). Granular materials flow like complex fluids. *Nature*, 551(7680), 360-363.

Kou, B., Cao, Y., Li, J., Xia, C., Li, Z., Dong, H., Zhang, A., Zhang, J., Kob, W. and Wang, Y. (2018). Translational and rotational dynamical heterogeneities in granular systems. *Physical review letters*, 121(1), 018002.

Murphy, K. A., Dahmen, K. A., & Jaeger, H. M. (2019). Transforming Mesoscale Granular Plasticity Through Particle Shape. *Physical Review X*, 9(1), 011014.

Ma, G., Zhou, W., & Chang, X. L. (2014). Modeling the particle breakage of rockfill materials with the cohesive crack model. *Computers and Geotechnics*, 61, 1320–1143.

Ma, G., Zhou, W., Chang, X.-L., & Chen, M.-X. (2016). A hybrid approach for modeling of breakable granular materials using combined finite-discrete element method. *Granular Matter*, 18(1), 7.

Ma, G., Regueiro, R. A., Zhou, W., Wang, Q., & Liu, J. (2018). Role of particle crushing on particle kinematics and shear banding in granular materials. *Acta Geotechnica*, 13(3), 601–618.

Majmudar, T. S., & Behringer, R. P. (2005). Contact force measurements and stress-induced anisotropy in granular materials. *Nature*, 435(7045), 1079.

Saadatfar, M., Sheppard, A. P., Senden, T. J., & Kabla, A. J. (2012). Mapping forces in a 3D elastic assembly of grains. *Journal of the Mechanics and Physics of Solids*, 60(1), 55-66.

Tatone, B. S., & Grasselli, G. (2015). A calibration procedure for two-dimensional laboratory-scale hybrid finite–discrete element simulations. *International Journal of Rock Mechanics and Mining Sciences*, 75, 56-72.

Wei, D., Wang, J., & Zhao, B. (2018). A simple method for particle shape generation with spherical harmonics. *Powder technology*, 330, 284-291.

Weis, S., & Schröter, M. (2017). Analyzing X-ray tomographies of granular packings. *Review of Scientific Instruments*, 88(5), 051809.

Wu, M., Wang, J., Russell, A., & Cheng, Z. (2020). DEM modelling of mini-triaxial test based on one-to-one mapping of sand particles. *Géotechnique*, 1-14.

Zhao, B. D., Wei, D. H., & Wang, J. F. (2017). Particle shape quantification using rotation-invariant spherical harmonic analysis. *Géotechnique Letters*, 7(2), 190-196.

Zhou, B., Wang, J., & Wang, H. (2018). A novel particle tracking method for granular sands based on spherical harmonic rotational invariants. *Géotechnique*, 68(12), 1116-1123.

Zhao, Q., Tisato, N., & Grasselli, G. (2017). Rotary shear experiments under X-ray micro-computed tomography. *Review of Scientific Instruments*, 88(1), 015110.

Zhao, Q., Tisato, N., Kovaleva, O., & Grasselli, G. (2018). Direct Observation of Faulting by Means of Rotary Shear Tests Under X-Ray Micro-Computed Tomography. *Journal of Geophysical Research: Solid Earth*, 123(9), 7389-7403.

Zhao, Q., Glaser, S. D., Tisato, N., & Grasselli, G. (2020). Assessing energy budget of laboratory fault slip using rotary shear experiments and micro-computed tomography. *Geophysical Research Letters*, 47(1), e2019GL084787.

Zhou, B., Wang, J., & Zhao, B. (2015). Micromorphology characterization and reconstruction of sand particles using micro X-ray tomography and spherical harmonics. *Engineering geology*, 184, 126-137.

Geosynthetics – A Sustainable Construction Material

S T G Ng
G and E Company Limited, Hong Kong, China

ABSTRACT

Geosynthetic is a broad term given to geotextile, geomembrane, geogrid, geocell etc. It's provenance in the 60's was primarily the cut of construction cost and time. Ubiquitous savings were evidenced over the years. Several decades later, a new age of sustainable construction is dawning, in preserving resource, mitigating climate change and reducing greenhouse gas (GHG) emission, the best of both worlds in cost effectiveness and sustainability. But how sustainable is with the use geosynthetics. Carbon footprint assessment has been introduced to quantify any hindsight. From resin production, to manufacturing, to shipment and from site installation, to operation, to maintenance and eventually to dismantling and disposal, equivalent CO_2 emission can be traced and calculated. This paper reviews some of the trends and studies on this emission benchmark development, and therefore the comparison of CO_2 emission between different methods of construction with geosynthetic and that of the conventional. The picture, indeed, underpins cogent discussion. It is hoped that a change of local mind set to appreciate geosynthetic, to accept its design, to review construction rule and regulation and to educate the next generation can be way forward to underline geosynthetic as a viable sustainable construction material.

From the beginning - Geotextile debut in Europe in the 60's as a man-made granular filter. The innovation took the construction industry to enjoy high efficiency, financial benefit, readily availability and predictable performance enhancement. Application exponentiated, largely the drive and espouse of textile company (Tencate, Nicolon) and chemical companies (ICI, Dupont, Amoco). Soil reinforcement geogrid, barrier geomembrane, erosion control geocell received similar zeal and the generic term 'geosynthetic' to represent this group of material was officially coined in 1977. What was not realized then was the contribution to sustainability, the avoidance of the depletion of natural resource to maintain an ecological balance for the future generation in a world we are living beyond our means. United Nation Program 2016 establishes 17 sustainable development goals (SDG), geosynthetic excels in goals 6, 9, 12, 13 & 17, preserve resources, access clean water, reduce GHG emission, control climate change, safeguard from contamination and protect the environmental. These are very macro goals pillared by environmental, economic and social considerations. This paper focuses only on the environmental impact, in terms of GHG, on using geosynthetic in construction.

Carbon footprint - In 1988, at the UN initiatives, European Commission put forward GHG policy that heralded Intergovernmental Panel on Climate Changes (IPCC) report 2014 on controlling 'GHG emission'. The term becomes the marker of sustainability used by international treaties, agreements and targets. Since over 76% of world's GHG is CO_2 (along with methane, nitrous oxide, hydrofluorocarbon, perfluorocarbon & sulphur hexafluoride), CO_2 emission was consolidated and adopted to ascertain the level of sustainability.

CO_2 emission can be presented as a quantitative measurement of GHG emission over the whole life for a specific product or service or solution or event expressed in tonnes of carbon dioxide equivalent (tCO_2e), It is derived from the total embodied energy (EE) (J/kg) consumed in each key source of the entire supply chain and operation of, in our case, a specific construction activity. EE is then converted to EC through knowledge of CO_2 emitted during generation of the energy used (oil, fossil fuel, wind, solar, nuclear, renewal etc). This associated total gas emission, embodied carbon (EC), sums up the carbon footprint of any unique construction method, solution or project. It allows comparison between different construction scenario - less emission leads to better sustainability.

Sustainability assessment - Sustainability is gauged to satisfying and balancing three sets of requirements, environmental, economic and societal/functional/equity criteria. Methods can be by means of qualitative method using colour coded chart and figure or quantitative method using rating system or sustainability metrics using EC accumulation based on a defined life cycle. EC interpretation is the simplest and most widely used in construction. Economic consideration such as financial impact and direct cost, and social equity such as resource depletion, climate change (GWP), photochemical, desertification, deforestation, ozone creation, acidification, eutrophication, toxicological effect, land competition, water use, air pollution, modification of ecosystem, even road congestion, noise & air pollution and aesthetics are much wider scope beyond construction activities. Economic and social issues are not adduced here.

Life cycle assessment (LCA) – LCA is a method to determine EC emission. There are several boundary conditions, acquisition of raw material and production processes of a construction material, eg geosynthetic (cradle to gate CTG), transportation of material to site (cradle to site CTS), use of the material for construction (cradle to construction CTC) and operation, maintenance and final dismantling, disposal and recycling at the end of the life (cradle to grave CTGr). The method generally takes reference to ISO 14040, 44 and 49, environmental management LCA principles; PAS 2050:2011 UK carbon footprint standard, EU international Life cycle data handbook, BPX 30-323 French footprint guideline and USA EPA life cycle assessment, principle and practice; or other countries' specific requirement. These are well document, transparent, repeatable guideline to conduct and report LCA.

To establish comparative life cycle analysis, same scope of use, technology and functions are essential. Boundary condition and scope of emission analysis, solution, or design in which the basis for comparison must be defined, inventory of material must be quantitated, each source of material must be determined, transportation, installation and construction activities must be recorded, end of life duty are to be known and finally the accumulated EC can be calculated and compared. A low carbon alternative can then be concluded. Since the relative reduction is often sought, some common denominations, activities and material to both solutions are balanced out, such exercise can be excluded. Geographic location, culture, local practice, resources differ from place to place, constant evolution to encompass different approach, priority and stakeholder's interest can compound any analysis. As such, every LCA has its unique characteristics, hence its footprint or "the carbon footprint".

The cumulated energy demand (CED) is first calculated by iterate approach, summing up the actual energy consumed of all items in the supply chain for each cycle; excavation of raw material (soil, gravel, clay, ore, crude oil, resin); transportation of raw material to site or factory; production of primary product (cement, lime, iron ore, polymer); transportation of primary product to manufacturer or contractor; manufacturing of product (concrete, steel, geosynthetics); transportation of product to site; integration of the product at site; realization of installation and construction; using of product and maintenance until end of life; dismantling, re-using, recyclingmethod, energy recovery and ultimate waste disposal. CED can then be converted to EC. Table 1 expatiates the framework of LCA, mapping out the typical supply chain, EC data sourcing, material inventory and calculation of total EC emission of any particular construction method, solution or project.

There are open sources of international EC value database for calcualtion (Inventory of carbon & energy, Harmmond & Jones at Bath University (2011); European life cycle analysis database 'Ecoinvent v3.3' (2016); International reference life cycle handbook (ILCD 2010); Germany Institute FFR in house calculator from manufacturers; US EPA, inventory of US greenhouse gas emission and sinks (2008); Chinese life cycle database 2013. However, none of these cover geosynthetic product as yet, only that of generic polymer type of which the geosynthetic is made from or that provided by some manufacturers can now be used for analysis.

CTG is relatively straight forward because of the abundance of EC data, CTS is geographical location dependent and has dramatic variations, CTC adds on the reliance of local experience, site record and staunch construction data. CTGr is complicated by the fact that civil engineering works tend to have little energy consumption in operation and maintenance (except disaster repair) and indeed many structures have not come to an end of life, let alone dismantling and disposal. Therefore, most of the geosynthetic LCA studies focus on CTG, CTS and CTC.

Typical Framework of Life Cycle Assessment	Parameter	Embodied CO_2 Emission
Comparative CO_2 study purpose & scope	Project information	
LCA boundary conditions	Criteria identification	
Comparable solution & designs scheme	Solution & design details	
Preparation and Setting up		
Raw material extraction (i.e. iron ore, aggregate, crude oil)	Material inventory quantitates, EC data soruce	Calculate Embodied
Transport raw material to factory (i.e. method, load and fuel)	Distances & fuel	Conversion to carbon emission
Primary production (i.e. cement, resin, concrete, steel)	Material inventory quantitates, EC data soruce	Calculate Embodied
Transport primary product to manufacturing (i.e. method, load and fuel)	Distances & fuel	Conversion to carbon emission
Product production (i.e. concrete, steel , geosynthetics)	Material inventory quantitates, EC data soruce	Calculate Embodied
Cradle to Gate (CTG)		$\sum$ **Embodied CO_2 Emission**
Material (i.e. soil, stone, concrete steel, geosynthetics)	Material inventory quantitates, EC data soruce	Calculate Embodied
Transport of material to site (i.e. method, load and fuel)	Distances & fuel	Conversion to carbon emission
Cradle to Site (CTS)		$\sum$ **Embodied CO_2 Emission**
Plant & equipment (i.e. installation, construction, material integration)	Distances & fuel	Conversion to carbon emission
Cradle to End of Construction (CTC)		$\sum$ **Embodied CO_2 Emission**
Plant & equipment i.e. (use of material, operation, maintenance)	Distances & fuel	Conversion to carbon emission
End of life (i.e. demolish, dismantling, disposal)	Distances & fuel	Conversion to carbon emission
Cradle to Grave (CTGr)		$\sum$ **Embodied CO_2 Emission**
		Total Accumulated Embodied CO_2 Emission

Table 1 - Framework of Life Cycle Assessment (LCA)

Beauty of using geosynthetic - For many years, economical advantage of construction incorporating geosynthetics are acknowledged. Some obvious countenances are pinpointed on more efficient use of natural resources, improvement of performance of scarce material, less excavation and quarrying, less use of concrete and steel, less transportation and haulage, less manoeuvring on site and less wastage, streamlining construction activities, allowing the use of lower grade granular material at the same time. Indeed, geosynthetics shred granular use, optimise difficult design, extend service life, minimize land disturbance and erosion, enhancing resilience to coastal protection, safeguard marine engineering destruction and generate green power. Innovations put in practice are evolved time and again.

Classic examples are geogrid in reinforced fill construction, geomembrane in containment barrier, geocomposite in drainage and harvest biogas, geotextile in road paving stability. Several manufacturers claim palatable merit of geosynthetic - 300-500 mm stone layer can be replaced by a 4-25 mm drainage geocomposite, one truck load stabilization geogrid saves 200 truck load of aggregate, 150 truck of clay is equivalent to 1 truck of GCL and 1 pallet of geosynthetic cementitious composite mat (GCCM) can be used when 6 trucks of shotcrete are needed.

LCA Research and Case History – With these beauties, a great many studies on comparative LCA involving the use of geosynthetic have been published. Earlier reports are from WRAP (table 2) and EAGM (table 3). Together with this prominent research, a collection of LCA from geosynthetic manufacturers (table 4) and that from the academics (table 5) are enumerated for reference.

WRAP (Waste & Resources Action Programme, UK) - WRAP is a published geosystem report “Sustainable geosystems in civil engineering applications” authored by 16 UK organizations (one third was involved with geosynthetic) in February 2010. It showcases the potential in EC reduction, adding element of cost, time, and material wastage savings through detailed calculation of six cases of civil engineering projects, comparing the carbon emission in each case with the use of geosynthetic against that of the conventional. Unambiguous conclusion was drawn to the significance of CO_2 reduction (from 31% to 87%). See table 2.

Construction and Design		Carbon Emission (ton CO_2e)		Reduction
Enbankment bund - 9.5 ht x 350 m	CTC	Gabion system 143.17	Reinforced soil 19.21	87%
Bridge approach 1V:2H - 40,000 m^3 fill	CTC	Gravel fill 454.12	Geogrid with cohesive soil 314.02	31%
Rebuilding collapsed retaining wall - 20 m	CTC	Reinforced concrete 32.26	Geogrid crib wall 9.55	70%
Interlock steel pile wall - 112 ton pile	CTC	Sheet pile wall 393.42	Steel strip RE precast wall 72.78	82%
Retaining concrete wall - 230 m^3 reused fill	CTC	Reinforced concrete 96.95	Modular block wall 42.46	56%
Retaining wall drainage layer - 2.5 km	CTC	Hollow block drainage 171.93	Geocomposite 29.01	83%

Table 2 - Waste & Resource Action Program (WRAP) Geosystem Report February 2010 [5]

EAGM - European Association of Geosynthetic Manufacturer (EAGM) did a study titled “comparative life cycle assessment of geosynthetic versus conventional construction material” between 2009-2011 to promote the knowledge of high quality geosynthetic and to underline the benefits when applying these products. Four exemplary models of common and frequent construction applications where geosynthetic and conventional solutions with technically equivalent function were chosen. Apart from carbon footprint, eight economic and social impact indicators were assessed, adhered to ISO 14040 and 14044. The results were shown as CTGr but the report centered on CTC when operation and maintenance were omitted citing too little impact. Geosynthetic does offer “advancing sustainability”. A subsequent critical review was performed by three independent experts in 2018. The report was re-presented in 2019 and the reduction of carbon emission (from 11% to 90%) concluded in 2011 remains consistent, sound, and valid. See table 3.

Construction and Design		Carbon Emission (Kg CO_2e/m2)		Reduction
Foundation & subgrade filter separation layer	CTGr	Gravel base 7.80	Geotextile base 0.81	90%
Road foundation on weak soil 1 km x 12 m width	CTGr	Conventional fill base 730.00	Geogrid base 650.00	11%
		Cement/lime base 950.00	Geosynthetics base 650.00	32%
Landfill drainage system	CTGr	Gravel base drainage 10.90	Geocomposite 3.60	67%
Retaining wall 3 m height	CTGr	Reinfoced concrete wall 1300.00	Geogrid reinforced wall 200.00	85%

Table 3 - Comparative Life Cycle Assessment EAGM Report 2019 [1]

Research around the world – A wide spectrum of similar comparative studies covering different type of construction method and solution, protean design with a variety of geosynthetic are described in case history literatures from geosynthetic manufacturers (table 4) and journalized by savants and practitioners (table 5). Substantial carbon reductions are reported across the board.

	Construction and Design		Carbon Emission (ton CO_2e)		Reduction
ACE Geosynthetics Taiwan 2013	Road rehabiliation 150 m length 10 m height	CTS	Retaining wall 3167.00	Reinforced soil slope 670.00	79%
Huesker Germany 2015	Lining protection trial 10,000m2	CTC	Clay ballast liner 506.30	Geosynthetic mattress 20.70	96%
Maccaferri Italy case study 2014	River revetment	CTC	Gravity wall 54.00	Gabion 18.00	67%
	Gavity wall	CTC	large stone riprap 160.00	Reno mattress 80.00	50%
Maccaferri Italy techncial note	Retaining structure 8 m ht 10 m	CTC	Concrete wall 52.00	Gabion wall 7.50	86%
	River bank protection 5,400 m^2	CTC	Riprap 160.00	Reno mattress 80.00	50%
Tensar USA Research 2016	Optimized pavement design 1 km x 20 m	CTC	Primary pavement 4977.00	Geogrid pavement 3822.00	23%
Pietrucha Poland study 2019	Sheet pile 1 km 5 m depth	CTC	Steel sheet pile 1830.00	PVC sheet pile 200.00	89%
Solmax Canada techncial notes	Impermeable lining, 4,047 m^2	CTC	Clay/HDPE/granular 250.00	GCL/HDPE/geocomposite 68.00	73%
ABG UK Production	Drainage core with recycled HDPE	CTG	100% virgin resin 2.13	80% recycled 1.24	42%
ABG UK technical note	Landfill slope drainage 22,500 m^2	CTC	Gravel with geotexitle 600.00	Geocomposite 318.00	47%
ABG UK technical note	Retaining Wall drainage 55 m2	CTG	Hollow drainage block 1.79	Geocomposite 0.15	92%
		CTG	No fine concrete 4.31	Geocomposite 0.15	97%
Concrete Canvas UK techncial note	Slope erosion protection 100 m2	CTG	150 mm concrete 3.60	8 mm GCCM 1.61	55%

Table 4 - Life Cycle Assessment from Manufacturers' literature

	Construction and Design		Carbon Emission CO_2		Unit	Reduction
Herteen	Retaining Structure 150 m x 5.5 m ht	CTC	Retaining wall 542.00	Green slope 101.00	ton	81%
	Road improvement	CTC	Lime /cement milling 1325.00	Geogrid 49.00	ton	96%
Viktor Toth 2018 [21]	Terrace wall, 6 m height		Retaining wall	Face panel		
	Extract raw material		75.00	10.00	kg/m	87%
	Import material and construction		33.00	16.80	kg/m	49%
	Operation, removal and disposal		9.80	6.00	kg/m	39%
		CTGr	117.80	32.80	kg/m	72%
	Terrace wall, 6 m height		Retaining wall	RE steep slope		
	Extract raw material		75.00	3.50	kg/m	95%
	Import material and construction		33.00	16.90	kg/m	49%
	Operation, removal and disposal		9.80	5.00	kg/m	49%
		CTGr	117.80	25.40	kg/m	78%
Geosyntheitcs	Landfill capping barrier 9,572 m^2	CTC	1,000 mm clay 111.37	Geomembrane / geotextile 32.20	ton	71%
ICE Publishing 2016 [2]	Hypothetical Retaining wall 15 m ht	CTC	Gravity wall 28.00	Geogrid MSEW 3.00	t/m	89%
		CTC	Gravity wall 28.00	Steel strip MSEW 4.00	t/m	86%

Table 5 - Life Cycle Assessment Research Summary

24th Geosynthetics Research Institute Conference March 2011 [12]	Levee after Katrina, New Orleans	CTS	Compact concrete 0.53	Turf reinforced mat 0.09	t/sy	84%
		CTS	Articulating concrete block 0.59	Turf reinforced mat 0.09	t/sy	85%
	Erosion control, California 8,890 m^2	CTC	Concrete swale 246990.00	RECP channel 75622.00	MJ	69%
	Flood control dyke, Taiwan, 961 m	CTC	Concrete Slab 704.00	Erosion mat 235.20	ton	67%
	Stormwater retention 10,000 m^3	CTG	Corrugated steel pipe 571.23	Plaster Modular system 29.34	ton	95%
		CTG	Corrugated steel pipe 571.23	Corrugated plastic pipe 186.17	ton	67%
		CTG	Corrugated steel pipe 571.23	Geostorage 25.47	ton	96%
	Containment berm, 40 ft height	CTS	Unreinforced berm 3H:1V 200.30	MSE berm 0.5H/1V 133.90	kg/ft2	33%
	Hypothetical landfill bottom lining	CTS	0.6m CCL 165.00	GCL 122.00	t/ha	26%
	California Landfill closure	CTC	Soil /geomembrane 652.40	Exposed geomembrane cover artifical grass 132.20	t/ha	80%
Geosynthetic Institute white paper 41 2019 [17]	1,160 kN working platform	CTS	Conventional gravel 16.68	Polyester geotextile 9.53	kg/m2	43%
Geosynthetics Institute white paper 44 2020 [19]	Unpaved road 800 m x 4 m	CTG	Gravel strength sub-base 94.00	Woven geotextile 25.00	ton	73%
	Reflective crack prevention 100 m x 9 m road	CTG	Bituminous overlay 18.60	Paving geotextile 10.90	ton	41%
	Paved road 1.6 km x 9 m	CTG	Aggregate Asphalt 536.00	Tri-axial geogrid 396.00	ton	26%
	3H:1V slope 10 m long 5 m section	CTG	460 mm Rip rap 4360.00	Turf reinforcement mat 356.00	ton	92%
MDPI Journal Sustainability 2021 [18]	Dyke, Germany, external sealing	CTC	Clay 122.30	GCL 70.80	kg/m^2	42%
		CTG	9.90	4.00	kg/m^2	60%
Master thesis University of Toledo 2015 [23]	Hypothetical retaining wall 35 ft height	CTG	Gravity retaining wall 1680.00	MSEW 620.00	kg/ft^2	63%
		CTG	Gravity retaining wall 1680.00	Geotextile wrap around wall 100.00	kg/ft^2	94%
		CTG	Gravity retaining wall 1680.00	Gabion wall 100.00	kg/ft^2	94%
Geoamerica 2016 Proceeding [14]	Bridge Abutment 4.7 m ht x 11.7 m	CTG	Geosynthetic MSPW 49.84	Geosynthetic reinfoced block 30.80	ton	38%
Handbook of Geosynthetic Engineering 2012 Chapter 18 [24]	Retaining wall 4.6 m ht x 131 m	CTG	Gravity wall 420.00	MSEW 99.00	ton	76%
	Landfill drainage	CTC	Mineral drain 192.00	Geocomposite 137.00	MJ	29%
Geotextile from Design to Applications 2016 Chapter 26 [10]	Filter layer	CTG	100 mm sand 1.02	Non woven geotextile 1.18	kg/m^2	-16%
	50 km away	CTS	1.78	1.18	kg/m^2	34%
	100 km away	CTS	2.56	1.18	kg/m^2	54%
	Working platform	CTS	1.2 m aggregate 16.68	0.6 m aggregate/geotextile 9.53	kg/m^2	43%
	Landfill capping	CTC	1,000 mm cohesive soil 47.22	1.0 mm LLDPE / geotextile 32.03	t/ha	32%
GeoAmerica 2020 Proceeding [29]	Waterproofing 10,000 m^2	CTG	Compacted clay 109.59	1.5 mm geomembrane 30.84	ton	72%
GeoAmerica 2020 Proceeding [28]	Primary leachate collection system 6,000 m^2	CTG	800 mm granular layer 6.40	7 mm geocomposite 4.60	ton	28%

Table 5 - Life Cycle Assessment Research Summary

In all these quests, the outcome of low carbon footprint is no surprise, with remarkable saving of up to 97% in certain application. Table 6 wraps up the carbon reduction of all these forty-eight LCA analysis. Typical constructions are categorized into retaining structure, ground stabilization, containment, erosion control and drainage. In figure 1, comparative construction schematics are put side by side with the corresponding reduction percentage. The ceiling of an upside (80 - 97%) is to be proud of, even the bottom line (28 - 50%) cannot be slighted.

Construction and Design	Cases	CO_2 Reduction Ceiling	Bottom line
Retaining structure vs reinforced structure	15	94%	33%
Granular formation vs geotextile stabilization	7	96%	23%
Containment barrier vs geomembrane and Geosynthetic Clay Liner GCL	7	80%	26%
Embankment structure vs erosion geosynthetic	9	96%	50%
Granular drainage vs geocomposite	9	97%	28%
Recycled polymer vs virgin material	1	55%	-

Table 6 - Summary of Carbon Emission Reduction

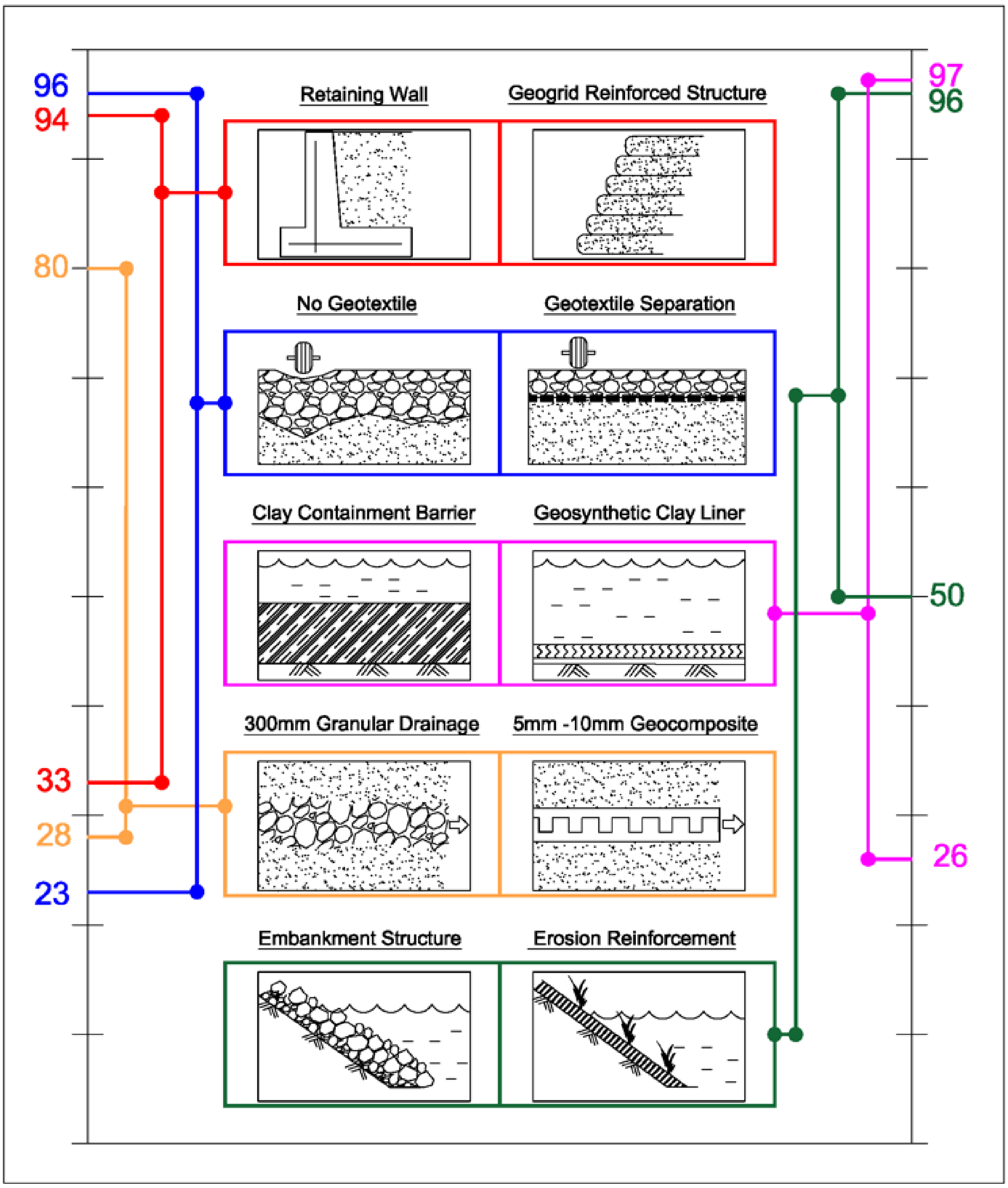

Fig 1. Percent of CO_2 Emission Reduction - Geosynthetic VS Conventional

Reliable embodied carbon database – LCA methodologies employed are relatively consistent, despite the fact that geosynthetic EC data base is not available. Dixon [4] coordinated with manufacturers in 2015 to collect raw material source, logistic data and energy consumption in geotextile and geogrid production process to come up with specific CO_2 emission. The actual measured energy is then converted to CO_2 by UK greenhouse gas reporting conversion factors (DEFRA 2013). First-hand calculation of non-woven PP geotextile give an EC value of 2.28 – 2.42 tCO2e/t (EC of PP film grade resin is 3.43 – 4.49 from ICE polymer data base), that of extruded PP geogrid is 2.97 tCo2e/t and PET woven geogrid is 2.36 tCO2e/t (EC of PET granule is 2.70–2.90 from EcoInvent polymer data base). Since current LCA studies rely mostly on open-source polymer data base which are considerably higher than that calculated from Dixon, EC is therefore generally overestimated, or current LCA tends to be conservative. There is a strong motivation to apprehend a more realistic comprehensive geosynthetic data base.

Recycling dilemma – Used of regrind and offcut material is an option to reduce carbon emission. In Europe, CE marking Declaration of Performance under the EN harmonized standards for geosynthetic allows manufacturers to declare a service life of 5 years with inclusion of any post-industrial or post-consumer polymer (PIM or PCM) and only for non-reinforcing functions. As most manufacturers could not guarantee a sufficient consistency of supplying recycled to ensure reliable durability prediction, resetting these rules will be long and hard. In any case, Geofabric in Australia has made non-woven paving fabrics from recycled plastic bottle in May 2020. Kaytech in South Africa did not use virgin resin for geotextile since early 2000s. In Brazil, run off drain uses compressed plastic bottle encased in geotextile. Rework, regrind and multi processed polymer is very well manipulated in China to compensate price concession. In USA, off spec material is at steep discount. However discordant, manufacturing geosynthetic, by and large polymer chemistry, stimulates and encourages recycle and reuse. The ambivalence appears to be identifying the balance and compromise when entrenched quality assurance associated with virgin resin and sustainability supported by recycling are treasured at the same time.

International Geosynthetics Society (IGS) enthusiasm- the prestigious association shares the UN's SDGs blueprint and is committed with a sustainability mission which will engage members, suppliers and stakeholders to improve, report, disclose sustainability performance through webinar, conference and lecture. A special committee kick started a task force in October 2019 spearheading the understanding and adoption of geosynthetic as a key component in creating more sustainable actions, such as promoting the swap of geosynthetics solution for less sustainable construction techniques, reintroducing production waste to feed stock, designing application with better performance and perfecting carbon emission data base. These are positive directives.

Manufacturer dedication - Geosynthetic manufacture's impetus of rolling out green measures to join force in corporate social responsibility (CSR) and environment, social & governance (ESG) program, and to capitalize on sustainability. In the spring 2021 IGS survey, most prominent manufacturers have environmental policy or are planning one. Many are carving out ways to enhance product and performance, to formulate requirement to upstream supplier, to provide more unbiased EC database regardless of commercial confidentiality and to cap production energy.

Some examples: Solmax's heat recovery realizes 90% natural cost from 2019 by pit thermal energy storages; TRI's foul water management slashes water use by 70%; RE-Gen Enterprise supplies regrind from used containment liner; Maccaferri's new steel coating extends service life, Agru's closeturf integrates impermeable high friction barrier with artificial turf; Tencate glacier's geotextile slows snow melting; Concrete Canvas's GCCM replaces permanent shotcrete; ABG's geocomposite retains soil moisture on roof garden; drainage cell improves storm drain storage capability; geofoam lightweight backfill substitutes import fill; electrokinetic speeds up stability equilibrium; geocell improves resilience of coastal protection and the list goes on. Outrageous ideas not too long ago are now on stream. Thanks to the persistence of manufacturers and the understanding of engineers.

Carbon Credit - Following the Kyoto Protocol, carbon credit investment market has been established to mitigate the environmental crisis. A polluter (organization that consumes energy) can buy carbon credit to reduce their carbon footprint at a price and gain permission to generate CO_2 from those who have excess credit. This offset reconciles the continuous emission escalation. Construction industry is welcome to participate in this ‘cap and trade’ charter.

Peroration - Geosynthetics does broadened sustainable construction and provide a means to achieve long term targeted carbon emission commitment. LCA is justifiable to quantify the potential. But such analysis is sometimes a subjective interpretation and has shortcomings. With the absence of actual EC of geosynthetic and therefore the underestimation of reduction, it is discernible that any CO_2 emission reduction may not be an absolute representation. Nevertheless, reports of flying colour from most studies are continuously filed. With the recyclers’ incentive, IGS’s enthusiasm, geosynthetic manufacturers’ persistence and carbon credit market players’ interest, LCA can become a firm basis to advance geosynthetic application. There is unprecedented worldwide sustainability commitment, it is hoped that geosynthetic can play a heavier role.

Closer to home, the government leads the initiative to look at low carbon construction. The Construction Industry Council (CIC) put focus on sustainability in 2007 supporting HK climate change action plan 2030+, launched the CIC carbon labelling scheme on intensive construction material in 2013 and devised a life cycle carbon assessment tool in 2019, in line with the international approach. This refers primarily to building construction since consumption of energy with running building and human activities are far more significant. The geosynthetic community craves to see that their product would find its position, however trifling, in construction sustainability.

Climate change is sadly depicted as anthropogenic. Stronger awareness of reducing carbon emission may stimulate moral thinking to bring about sustainable construction. Transforming the mind set of placing more attention to accepting solution with geosynthetic is sought. The defiance becomes the drive of having an open mind to step aside from traditional, conformable and comfortable design, to make more adaptation to integrate geosynthetic into construction design, rule, regulation, code of practice and shrewd legislation. Indeed, the status quo seems to have remained unchanged; if something has not been used here, do not use it.

Geosynthetic is not novel and untested, as Neil Dixon professed in Geoamerica 2016 - “geosynthetic is framed as a forever new technology”. It is not. Perhaps geosynthetic is too small an item in most construction, perhaps product knowledge has not been popularised, perhaps our education curriculum has minimal coverage. Early training can be brought forward to show the rope to the younger generation. Decarbonising the world is likely to toil for donkey’s year, only achievable in the coming generations, in the meantime, every minute effort counts, slather geosynthetic in construction will hopefully step up the momentum.

REFERENCES

1. Frischknecht, R., Stucki, M.; Büsser, S., Itten, R., and Wallbaum, H. Comparative Life- Cycle Assessment of Geosynthetics versus Conventional Construction Materials. EAGM Report 2019
2. Damians, I.P., Bathurst, R.J., Adroguer, E.G., Josa, A., and Lloret, A. Sustainability assessment of earth-retaining wall structures, 2016, ICE Publishing.
3. Heerten, G. Reduction of Climate-damaging Gases in Geotechnical Engineering by Use of Geosynthetics, 2009 Naue Gmbh & Co.
4. Raja, J., Dixon, N., Fowmes, G., Frost, M., and Assinder, P. Obtaining reliable embodied carbon values for geosynthetics, 2015, Geosynthetics International.
5. Corney, N., Cox, P, Norgate, S., and Thrower, A. Sustainable geosystems in civil engineering applications, Geosystems Report, WRAP report, February 2010.
6. Jones, D.R.V. Using Geosynthetics for Sustainable Development, 2015, the 2nd International GSI-Asia Geosynthetics Conference.
7. Jones, R. and Dixon, N. Sustainable development using geosynthetics: European perspectives. GRI-24, March 16, 2011.

8. Ng, S. T. Reducing the embodied carbon of construction projects through a carbon emission encompassed tender, 2011, WIT Transactions on Ecology and the Environment, vol 195, WIT Press .
9. Ng, T., Lo, I. M.C. and Cheng, J. C.P. A comprehensive Hong Kong based carbon labelling scheme covering emission intensive construction materials. CIC Research Report No. CICRS_023, 2018.
10. Raja, J., Dixon, N., Fowmes, G., Frost, M.W. and Assinder, P. Chapter 27: Sustainability Aspects of Using Geotextiles.
11. Dixon, N., Fowmes, G. and Frost, M. Global challenges, geosynthetic solutions and counting carbon, Geosynthetics International, 2017, 24, No. 5
12. Koerner, G. R., Koerner, R. M., Ashley, M. V., Hsuan, Y. G., and Koerner, J. R. Optimizing Sustainability Using Geosynthetics, Conference Proceedings, GRI-24th annual Conference, March 16, 2011.
13. Basu, D., and Lee, M. ICE Handbook of Geosynthetic Engineering: Geosynthetics and their applications, Chapter 21, Sustainability considerations in geosynthetic applications, 2021, ICE Publishing.
14. Kelsey, C. Life Cycle Assessment of Geosynthetic Reinforced Bridge Abutment Designs, Geosynthetics Magazine, April 21, 2020.
15. Koerner. R. M. Designing with Geosynthetics. 6th Edition Vol. 1. 2012.
16. Palmeira, E. M., Araújo, G. L. S. and Santos, E. C. G. Sustainable Solutions with Geosynthetics and Alternative Construction Materials – a Review, 2021, MDPI.
17. Koerner, R. M., Koerner, J. R. and Koerner, G. R. Relative Sustainability (i.e., Embodied Carbon) Calculations With Respect to Applications Using Traditional Materials Versus Geosynthetics. GSI paper #41, April 10, 2019
18. Rimoldi, P., Shamrock, J., Kawalec, J. and Touzze, N. Sustainable Use of Geosynthetics in Dykes. Sustainability 2021, 12, 4445, MDPI.
19. Whitty, J. E, Koerner, J. R. and Koerner, G. R. Relative Sustainability of Road Construction/Repair: Conventional Materials versus Geosynthetic Materials. GSI White Paper #44. March 16, 2020.
20. Fraser, I. The use of recycled polymers in geosynthetics and implications for durability statements made under the European Harmonised Standards and CPR. TCS Geotechnics Ltd, March 13, 2019.
21. Tóth, V., Paločko, P. and Bakoš, M. Carbon footprint in geotechnical constructions and geosynthetics impact on the environment, proceeding 11th International Conference on Geosynthetics, 2018
22. The GSI Newsletter/Report. Vol. 33, No. 1, March 2019.
23. Chulski, K. D. Life Cycle Assessment and Costing of Geosynthetics Versus Earthen Materials. The University of Toledo. Abstract of Master Thesis, May 2015.
24. Bouazza, A. and Heerten, G. Geosynthetic applications – sustainability aspects. Handbook of Geosynthetic Engineering. Second Edition, 2012. Chapter 18, ICE Publishing.
25. Raja, J., Dixon, N., Fowmes, G., Frost, M., and Assinder, P. Proceedings of the Institution of Civil Engineers. Engineering Sustainability 167, October 2014 Issue ES5 Pages 197 – 207, ICE Publishing.
26. Dixon, N., Postill, H., and Fowmes, G. Global challenges, geosynthetic solutions, counting carbon and climate change impacts. Proceedings of the 11th International Conference on Geosynthetics. 16 – 21 September 2018.
27. Ehrenberg, H. Sustainable Geosynthetics or Sustainable Constructions with Geosynthetics. Invited lecture, IGS UK Chapter. March 10, 2022.
28. Gutiérrez, J. and Conesa, S. Performance of High-quality drainage geocomposites and analysis of the carbon footprint vs. conventional solutions. 4th Pan American Conference on Geosynthetics. 26 – 29 April 2020, Rio de Janeiro, Brazil.
29. Muňoz, J.M. Carbon Footprint of Geomembrane HDPE vs Traditional Waterproofing Barrier. 4th Pan American Conference on Geosynthetics. 26 – 29 April 2020 Rio de Janeiro, Brazil.

Application of Low Carbon Concrete on Reinforced Earth Wall

Norman M H Lee, Yassine Bennani Braouli
Reinforced Earth Pacific Limited, Hong Kong, China

ABSTRACT

Global warming is one of the big issues all over the world. Continued global warming could bring a series of damaging effects. Many countries are now pursuing a broad range of strategies to reduce emissions of greenhouse gases, such as reducing the vehicle use, development of renewable energy etc. Minimize the use of cement is one the method to reduce the emission of carbon dioxide. Comparing the concrete volume used between Reinforced Earth Wall and traditional R.C. wall, Reinforced Earth Wall is an environmental friendly and more economical solution with less concrete consumption. Apart from this, the carbon dioxide emission can be reduced by minimizing the cement ratio in concrete.

Low carbon concrete consists of industrial cement combined with mineral compounds, such as ground-granulated blast furnace slag, calcined clay and fly ash. With only 12% dosage in weight of concrete, the cement is responsible for 85% of carbon dioxide emission. By using the low carbon concrete, there will be a high possible reduction of carbon dioxide emission. Concrete facing panel is one of the three main components of Reinforced Earth Wall. The emission of carbon dioxide is mainly caused by the production of concrete panel. Using low carbon concrete can help to minimize the carbon dioxide emission.

1 INTRODUCTION

Over the past few centuries, the world has been moving towards urbanization as human beings have advanced and developed technologically and economically. The global population is growing every year. More and more people are migrating from rural and suburban areas to cities, so the size and the number of cities is expanding and increasing and many countries having most of their population living in cities increasing the various environmental problems associated with urban living. We have been paid for the price of the environment and creating a lot of pollution due to the rapid development.

Climate change is one of the big issues for environment due to the rapid development. The emission of greenhouse gases into the earth's atmosphere produces a greenhouse effect and thus contributes to global warming which has caused many problems such as more frequent heat waves, changes in rainfall, rising sea levels, reduced agricultural production, spread of diseases, depletion of water resources, environmental and ecological imbalances etc. Greenhouse gas emissions from human activities strengthen the greenhouse effect and the major sources of greenhouse gas emissions from human activities in Hong Kong are electricity generation, transportation and waste management. The Paris Agreement entered into force on 4 November 2016 and is applicable to the Hong Kong Special Administrative Region. The parties to the agreement will work to promote carbon reduction policies that will limit global temperature increases to no more than 2 degrees Celsius this century, set a more ambitious target of 1.5 degrees Celsius and achieve carbon neutrality by 2050.

Apart from the climate change, another environmental issue is finite resources. Besides water, sand is the most widely used natural resource by humans on the planet. Sand is an important ingredient in most construction projects. The main reason for the sand supply crisis is the rapid global urbanization. Building high-rise buildings and construction for road works for the world's growing urban population requires huge amounts of sand and other construction materials. The sand we need is relatively coarse and dry sand mined which is from riverbeds, riverbanks, and shores. The demand for this sand material become higher and higher that the world's riverbeds and beaches are being mined out of sand. Most of the sand mined by humans is used to make concrete.

There are two ways to minimize the impact. 1. Consuming less construction material or minimize the usage of machine is one of the methods to minimize the greenhouse gas emission. 2. Using the materials that are less emissive. (e.g. low carbon concrete).

2 CONCRETE

2.1 Advantages of using concrete

Concrete is the most common material used for infrastructure purposes. It is a mixture of several other materials like cement, water, sand and gravel. Ready-mix concrete has become popular in recent years to accelerate the construction process and make it more reliable.

Concrete is used to provide strength, durability, and versatility during the construction of a structure. These excellent properties have made concrete a reliable and long-lasting choice of construction companies for both commercial and domestic types of constructions.

Different types and qualities of concrete are available on the market and some of the properties of concrete that make it important in construction are:

2.1.1 Strength

Concrete is a solid material that can withstand tensile and compressive stresses easily without getting affected. The strength of concrete has made it essential in the infrastructure, construction of buildings, foundations, civil works and many other types of structures for many years. The strength of the concrete is adaptable to the specific requirements of the construction project by making changes in the mixture, for example, by increasing or decreasing the ratio of the quantity of water, cement and crushed stone. Moreover, concrete can increase in strength over time.

2.1.2 Durability

Concrete can last for ages as it can survive harsh weather conditions and natural disasters and it is resistant to abrasion, rusting, chemical reactions, fire and any other deterioration and will retain its original form, quality and serviceability when it is exposed to the environment. As a result, the structural integrity of the concrete will not be undermined for an extended period which makes it suitable for every other place in the world.

Some concrete structure which was built in ancient times are still found. The longevity of this popular material has made it important for the construction of permanent buildings and strong structures like bridges and dams.

2.1.3 Versatility

Concrete is one of the most versatile materials used for construction of many structures due to its strength and ability to modify its according to the construction requirements, shape and size and its high durability and fire resistance.

2.2 Environmental Impact of using concrete

The advantages of the concrete are undeniable. However, some environmental impacts are given out by manufacturing concrete cannot be ignored.

2.2.1 Shortage of natural resources

Concrete is a mixture of cement, water, sand and aggregates. Sand is one of the most versatile natural materials used in construction. In addition to construction, sand is highly used in land reclamation, water filtration and glass making. According to the data from United Nation, the demand of sand resources is rising and we are now need 50 billion tons per year, an average of 18kg per person per day. And another problem is we are running out of sand at a much faster rate than its natural renewal. Sand takes thousands of years to form through erosion.

At the same time, the loss of sand threatens the fragile ecosystem. Most of the sand is dredged from the river and it will harmful the fisheries, aquifers and protected areas. Uncontrolled mining can greatly threaten biodiversity. Moreover, sand carriers can carry invasive species and placing a huge burden on species habitats and ecological communities. Over exploitation can lead to an unstoppable decline in the ability of eroded coasts to defend and repair themselves from natural disaster. It can also exacerbate drinking water and food problems and there will be the risks for human health and regional security.

2.2.2 Emission of greenhouse gas

The manufacturing process of cement produces about 5% to 8% of global man-made carbon dioxide. The production of cement releases greenhouse gas emissions both directly and indirectly. Approximately 50% of these emissions come from a chemical process called calcination. Calcination occurs when limestone is heated and breaking down into calcium oxide and CO_2. Around 40% comes from the energy by burning fossil fuels to heat the kiln which is usually heated by coal, natural gas, or oil. The final transportation of cement represents another 5-10 percent of the industry's emissions. (Madeleine Rubenstin, 2012)

Around 30 billion tons of concrete are produced worldwide every year and this production is not expected to slow down in the near future. Therefore, modification on the concrete mix may be a powerful solution to prevent the greenhouse gas to entering the atmosphere.

2.2.3 Low carbon concrete

Low carbon concrete consists of the cement combined with mineral compounds such as fly ash, slag etc to minimize the carbon footprint. In order to reduce the carbon footprint from concrete, reduce the ratio of the cement in concrete and replaced by supplementary cementitious materials is one of the solutions. The composition and CO_2 emission are shown in Figure 1.

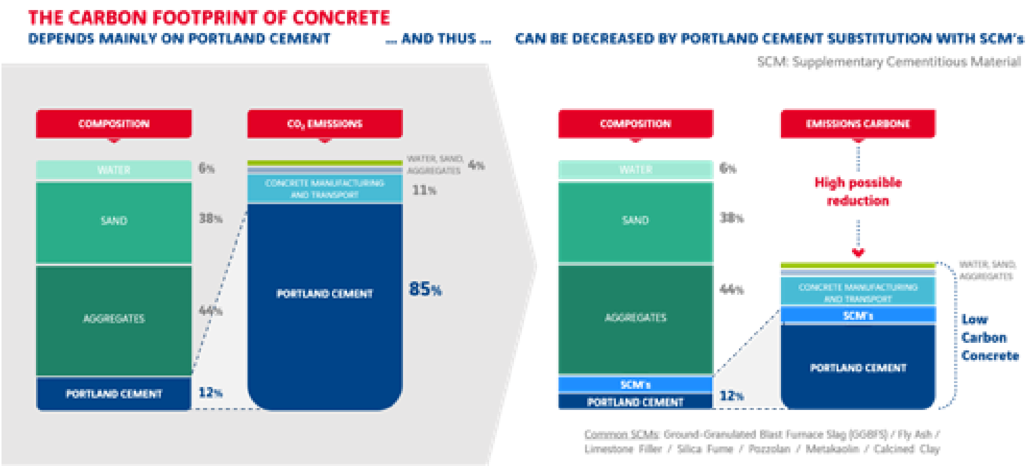

Figure 1: Carbon footprint of concrete

With only 12% dosage in weight in concrete, cement is responsible for 85% of CO_2 emissions. By reducing around 50% of usage of Portland cement, more than 40% CO_2 emissions can be reduced.

VINCI Construction evaluate and classify a concrete formulation according to their emissions (kg $CO_2e/m3$) and compressive strength (MPa). They evaluate the concrete with the prism of environmental performance and to classify it into three levels: low carbon, very low carbon, ultra low carbon which is shown in Figure 2.

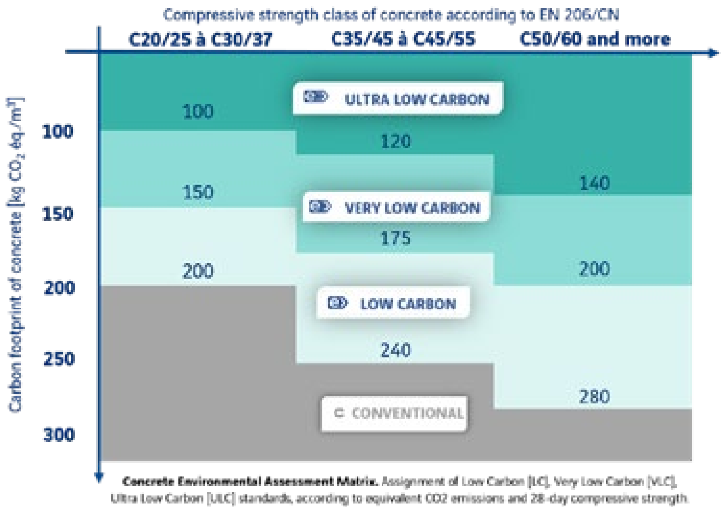

Figure 2: Concrete Environmental Assessment Matrix

The pros of using low carbon concrete is easy and practical and some trials by using around 50% SCM had been done. But the cons is the early strength of the concrete is reduced. It may limit the use for the site work. But for the Reinforced Earth wall, the concrete panel is precast and it will minimize the influence of the early strength.

3 APPLICATION OF CONCRETE ON RETAINING WALL

3.1 Comparison of material used between the Reinforced Concrete Wall and Reinforced Earth Wall

In order to minimize the embodied carbon of concrete, reduce the volume of concrete using is one of the methods to reduce the carbon footprint. The benefit of using the Reinforced Earth retaining wall by comparing with the R.C. retaining wall is not only the cost saving, but also the environment friendliness. Figure 3 shows the ecological parameters for a typical 6m high Reinforced Earth Wall and an equivalent reinforced concrete retaining wall. Even though it is an optimized design of the reinforced concrete retaining wall, the different of the efficiency in ecological terms of both walls is significant (Geoguide 6, 2002).

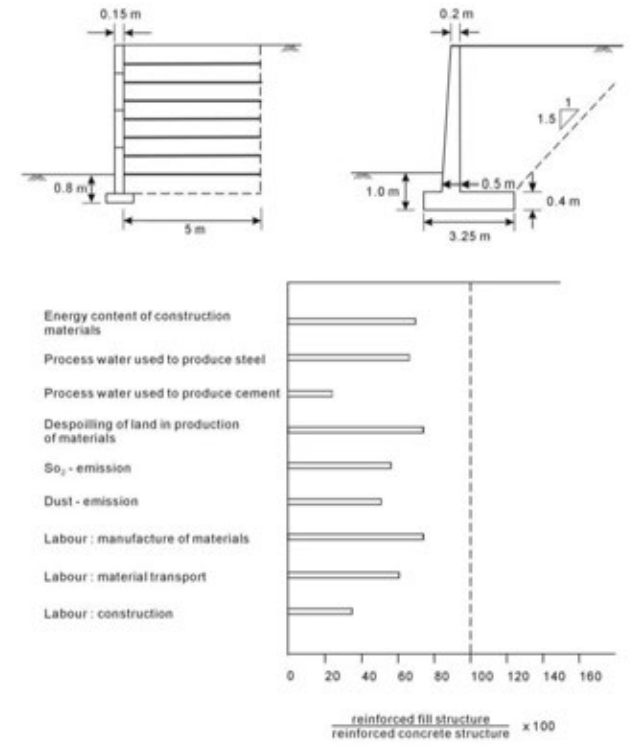

Figure 3: Ecological Parameters for a 6m High Reinforced Earth wall and an equivalent Reinforced Concrete Retaining Wall

Below is an example showing the difference of the material and greenhouse gas emission between two different types of retaining wall. The original design of abutment is a Reinforced Concrete (R.C.) retaining wall supported by socketed H-pile with 1.5m combined pile cap (Figure 4). The design has been revised to Reinforced Earth True abutment with a L-shape R.C. seating as an alternative (Figure 5).

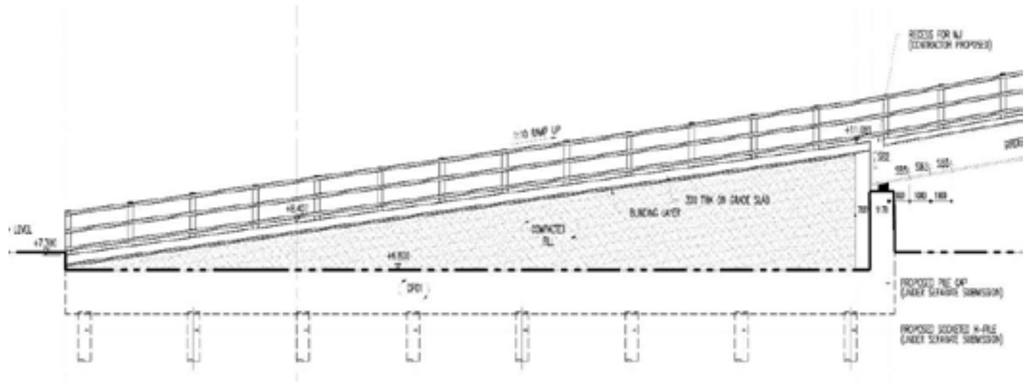

Figure 4: Original Design

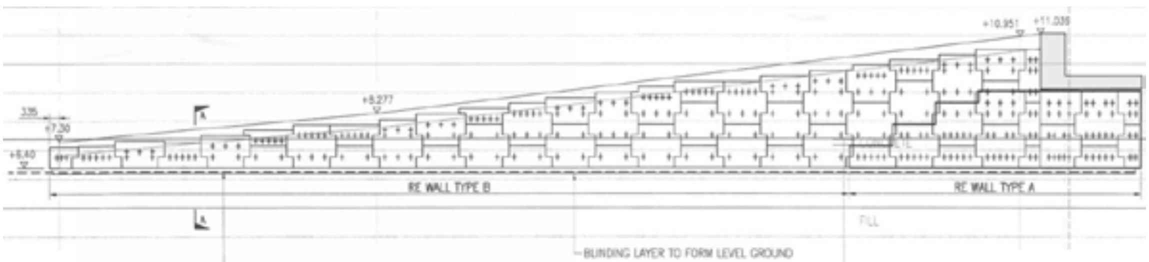

Figure 5: Reinforced Earth Wall Design

The summary of the material used on both schemes are illustrated in Table 1.

Table 1: Comparison of Material Used

Scheme	Element	No. of pile (nos.)	Concrete (m^3)	Structural Steel / Rebar / Strip (ton)
Reinforced Concrete wall with Piling Scheme	Foundation	24	-	245
	Cap	-	535	130
	Wall	-	100	6
Total		**24**	**635**	**381**

Scheme	Element	No. of pile (nos.)	Concrete (m^3)	Structural Steel / Rebar / Strip (ton)
Reinforced Earth Wall Scheme	Panel	-	33	2
	Levelling Pad	-	6	0
	L-shape RC wall	-	35	4
Total			**74**	**6**

The table above reveals that the consumption of concrete, structural steel, and reinforcement / steel strip of Reinforced Earth retaining wall with L-shape R.C. seating is far below than the original piling and pile cap with R.C. retaining wall scheme. Carbon footprint could be reduced by this proposal. By eliminating the piling, construction waste can further be reduced and clean underground could be allowed for future development in case.

3.2 Life Cycle Analysis of the Reinforced Concrete Wall and Reinforced Earth Wall

Life cycle analysis is a method to access the environmental impacts of all stages of the work (from material production, construction, use and maintenance and end of usage/reconstruction) and the life cycle assessment of CO_2 emission of this project is shown in Figure 6.

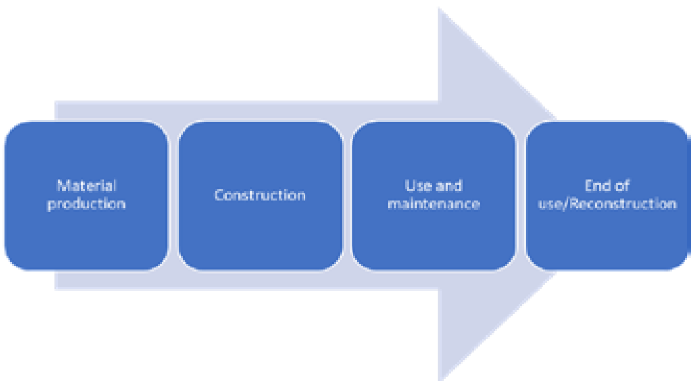

Figure 6: Life Cycle Analysis

In this study, the first two stages which are related to the construction process (material production and construction) of CO_2 emission will be compared. Table 2 shows the CO_2 emission from the material production and also for the equipment of construction.

Table 2: Comparison of CO_2 emission between R.C. wall and Reinforced Earth Wall

Scheme	kg of CO_2 emission			
	Concrete	Steel	Operation equipment	Total
Reinforced Concrete wall	260,350	724	7,770	268,844
Reinforced Earth Wall	30,340	11	2,590	32,411

For the analysis, the production process of concrete had the big influence on the emission of CO_2, the difference is significant since the volume of concrete usage on the reinforced concrete wall is much higher than that for the reinforced earth wall. Moreover, due to the duration of work is longer and the number of construction machine are more than reinforced earth wall. The high consumption of fuel leads to the high emission of CO_2.

3.3 Life Cycle Analysis of Reinforced Earth Wall with GGBS used in the precast concrete panel

Design the concrete with the addition of an appropriate proportion of Ground-Granulated Blast Furnace Slag (GGBSS) can help to reduce carbon footprint. The cement content of the panel is around 400kg per m3 of concrete and the cement content can be reduced to 220kg by mixed with GGBS. Table 3 shows the emission of CO_2 by using GGBS in the concrete mix.

Table 3: Comparison of CO_2 emission between R.C. Wall and Reinforced Earth Wall (with and without using GGBS)

Scheme	kg of CO_2 emission			
	Concrete	Steel	Operation equipment	Total
Reinforced Concrete wall	260,350	724	7,770	268,844
Reinforced Earth Wall	30,340	11	2,590	32,410
Reinforced Earth wall with GGBS	25,142	11	2,590	27,212

Although the characteristic strength of the concrete made by mixing the cement with GGBS is low in early stage. It does not mean that we have to sacrifice the strength, on the contrary, the strength is much higher on 28 days and it is more durable and environmental friendly. The typical example of the strength of the concrete up to 150 days is shown in Figure 7 (source by Greentex Construction Materials Ltd).

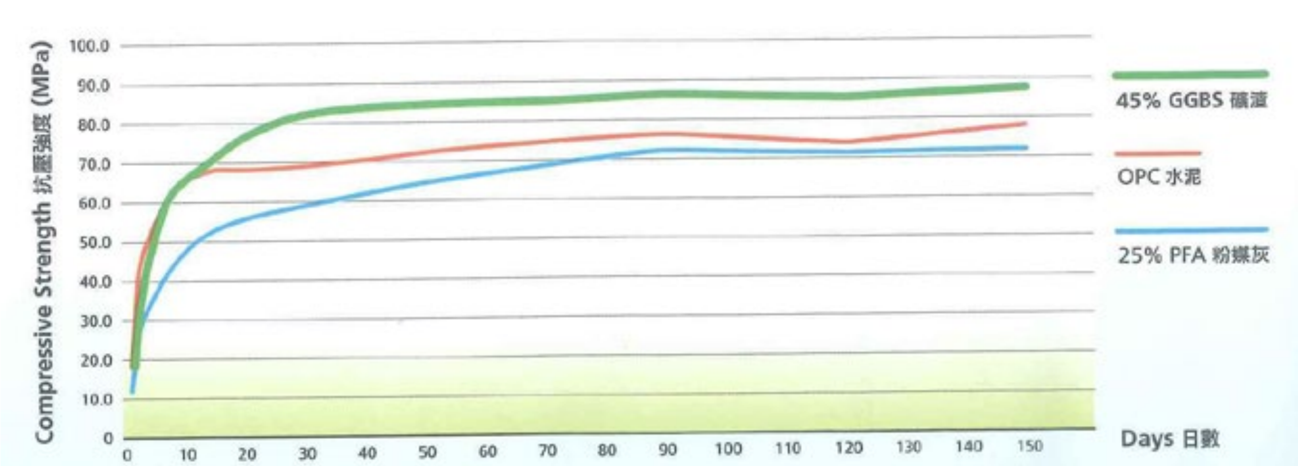

Figure 7: Typical example of concrete strength

3.4 Advantages on construction of Reinforced Earth Wall

From the ecological point of view, the construction method of Reinforced Earth Wall has its significant advantages. First of all, formwork is eliminated as the precast concrete panels interlocked each other. Formwork is not required since the installation and the backfilling are all on the inner side of the structure. No scaffolding and moulds mean that the site space require for the construction can be reduced significantly and can be constructed to the existing structure closely. Likewise, trees and vegetations can be retained in front of the Reinforced Earth Wall.

Construction sequence of R.C. wall including setup of formwork and scaffolding, fixing up the rebar, concrete pouring, demoulding and backfilling. Different from the traditional method, construction time of the Reinforced Earth Wall is based on the time for the backfilling. Therefore, the construction time of the Reinforced Earth Wall is much less than the R.C. wall and easier to control. On the other hand, construction of Reinforced Earth Wall requires neither scaffolding nor heavy weight machine. By comparing to the traditional method, only a light crane and a roller is necessary for the panel installation and compaction. It also a great advantage in terms of safety since less machine will be used.

In terms of economical benefit, Reinforced Earth wall have been found on the sloping ground without using the pile foundation. When constructed on sloping ground, the relatively rigid reinforced concrete retaining wall generally imposes higher bearing stress at the wall toe and may require piles for support. The alternative solution involving the use of the reinforced fill technique could be much more economical and environmental friendly. An example is shown in Figure 8. Another example to show the Reinforced Earth wall offer technical and economical benefits over the conventional concrete viaducts which have been used in some projects in Hong Kong (Geoguide 6, 2002). The major saving is the viaducts are generally sensitive to differential settlement and are usually supported on piled foundations, whilst reinforced fill structures can accommodate differential settlements and do not require expensive foundation support (Figure 9).

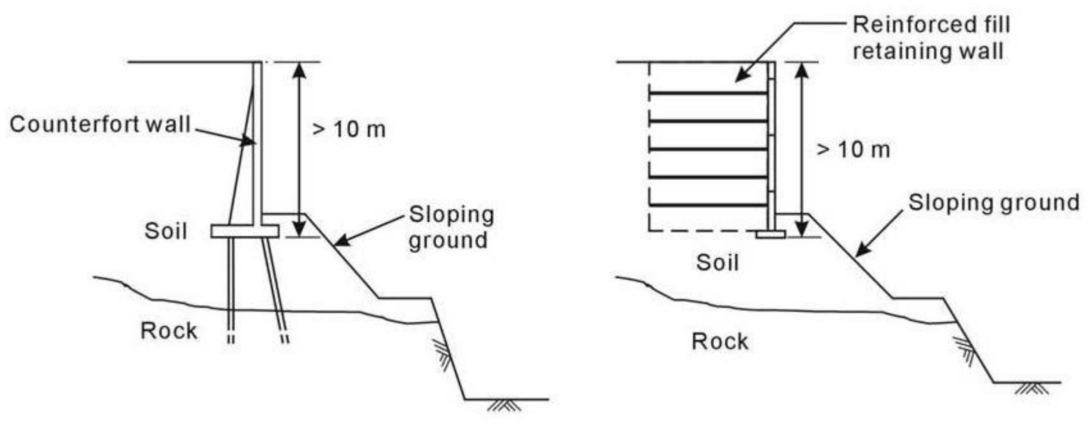

Figure 8: Example of the retaining wall on sloping ground

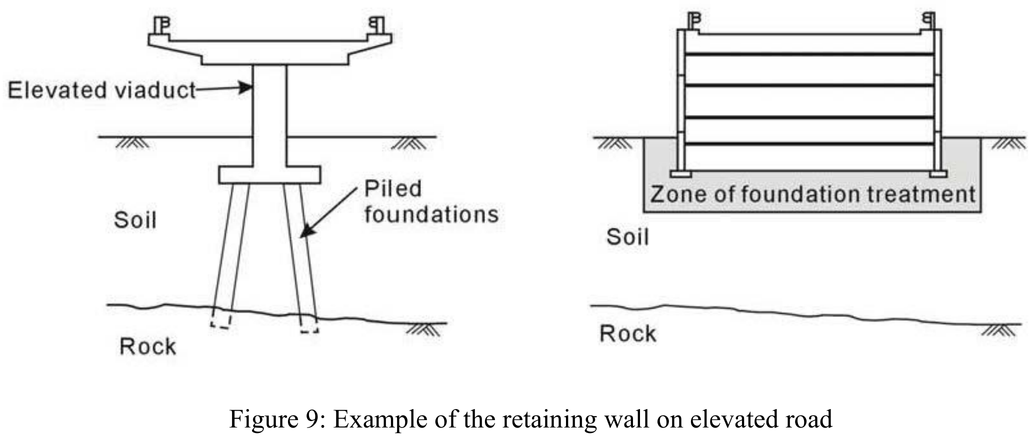

Figure 9: Example of the retaining wall on elevated road

4 CONCLUSION

Concrete works is playing an important role in the construction industry. At the same time, it will be a very heavy burden to the society in the future. Reinforced Earth structures provide great strength and flexibility. Moreover, the ecological advantages of Reinforced Earth retaining wall are undeniable. The use of the technique results in saving materials and energy, reducing nuisance associated with the construction of a structure such as air pollution and traffic congestion and also reducing disturbances to the foundation soil. By using the GGBS in the reinforced concrete panel, the content of the cement will be decreased and the emission of greenhouse gas will be further reduced. Nowadays, one of the development directions of concrete is high performance mix concrete, and its basic feature is its durability. The strength and durability of the concrete will be improved by mixing with GGBS. The use of GGBS can be used rationally to replace part of the cement and will be the future “green” material.

REFERENCES

GEO, CEDD, 2002, Geoguide 6 Guide to Reinforced Fill Structure and slope design
Madeleine Rubenstin, 2012. Emissions from the Cement Industry

Composition and Strength of Middle Pleistocene till in Lithuania

Ieva Lekstutytė, Gintaras Žaržojus, Saulius Gadeikis, Gisela Domej
Department Hydrogeology and Engineering Geology, Vilnius University, Vilnius, Lithuania

Šarūnas Skuodis
Department of Reinforced Concrete structures and Geotechnical Engineering, Faculty of Civil Engineering, Vilnius Gediminas Technical University, Vilnius, Lithuania

ABSTRACT

In Lithuania, the upper part of the Earth's crust was formed during the Pleistocene. Only a small part of Lithuania is a relic of the previous Medininkai stage (Lonian) glaciation in the Middle Pleistocene (Chibanian Age), which occur on the surface only in the southeastern area. Medininkai glacial period till soils are an almost unstudied soil type in Lithuania. Due to geotechnical investigations on new construction sites, an opportunity appeared to provide experimental investigations with Medininkai glacial period till soils.

One of the main challenges of this research is to collect a perfectly undisturbed sample that would reflect the in-situ conditions. The Medininkai glaciation till soil is a mixture of different portions of clay, sand, and gravel and are different from other detectable till soils globally and unique.

The main purpose of this study is to explore and review the strength and deformation properties of till soils of the Medininkai glacial period. Triaxial testing and oedometer tests were used for soil investigation in order to achieve the aim of the study. During the in-situ tests, cone penetration tests were performed as well as the borehole data was described.

In this paper, the most important researches were achieved due to comparison single-stage triaxial (SST) and multi-stage triaxial (MST) test methods applying different soil testing conditions. It was concluded that there are no significant differences, only small due to moisture content and drainage conditions. Also, based on different calculate method for OCR evaluation was determined that this till soil is overconsolidated.

1 INTRODUCTION

1.1 Geology and investigated site

The upper part of the Earth's crust in Lithuania, as well as the geological environment, which is interesting from an engineering point of view, was formed during the Pleistocene glacial period (2588–12 thousand years BP) – i.e., during the longest Quaternary glacial period. Glacial and interglacial periods make the Quaternary period exceptional, as, during that time, Lithuania was covered several times by glaciers whose deposits cover the entire surface of Lithuania today. The average thickness of these deposits amounts to approximately 100 m, and the maximum thickness reaches more than 315 m (Bičkauskas, et al., 2011).

Generally, glacial deposits are very diverse, and their characteristics depend on the conditions of formation. Usually, most glaciogenic environments are mainly occupied by till deposits formed at the edges of sliding glaciers and beneath them. Available data shows that till soils formed throughout glacial periods are the most predominant across Lithuania; they make up 70% by volume and 41.3% of the prevalent Qaternary stratum (Putys, et al., 2010)

According to the stratigraphic scheme of the Lithuanian Quaternary period (Satkūnas, 2009), which is based on the age of soil formation, the largest geomorphological complexes of the country's relief were formed during the Upper Pleistocene Nemunas stage (Tarantian) glacial period. Only a small area of the Lithuanian relief is formed during the Middle Pleistocene Medininkai glacial period (Lonian; Figure 1).

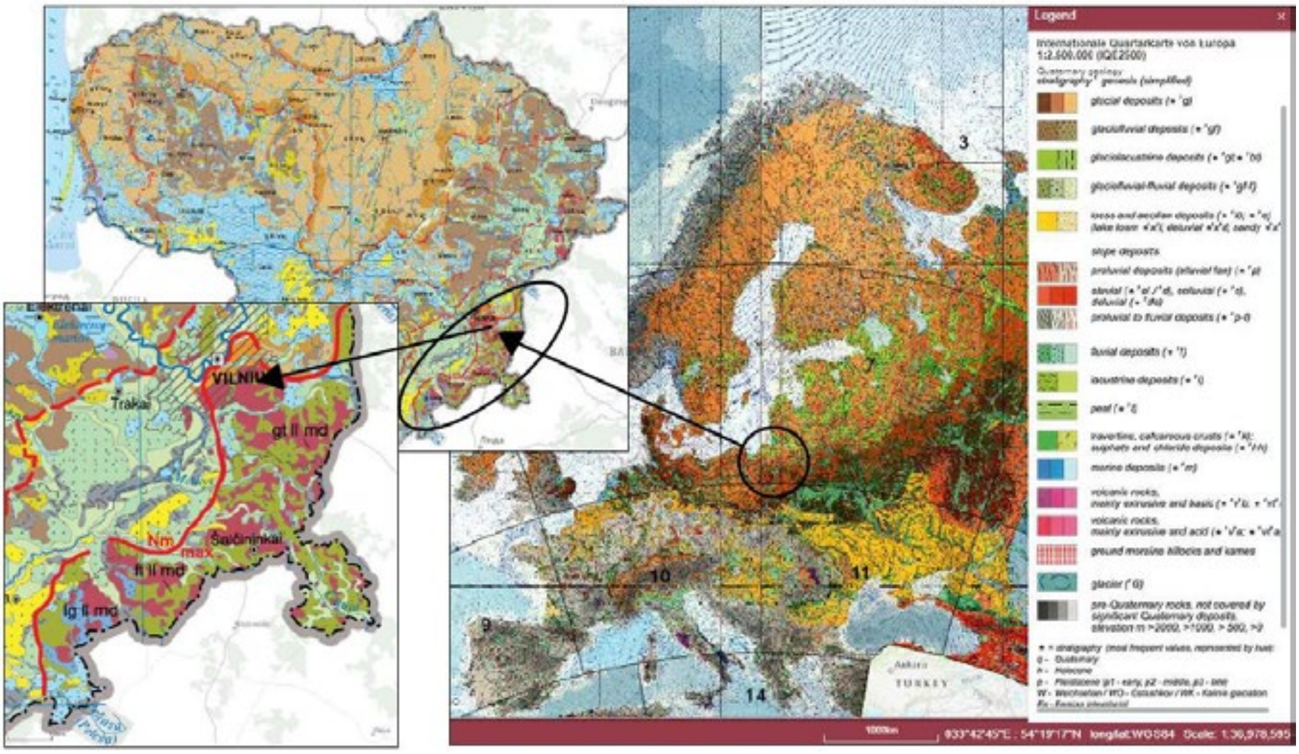

Figure 1: Middle Pleistocene Medininkai glacial (Lonian) in Lithuania and the site of the investigated soil (Guobytė, 1999; Geoviewer at https://geoviewer.bgr.de)

The Medininkai glacial period (195–128 thousand years BP) formed deposits with an average thickness of 30–40 m. The maximum thickness amounts to 50–100 m (Kavoliutė, 2012); however, the predominant layer is about 10–30 m thick (Grigelis, et al., 1994). In Lithuania, deposits from the Medininkai glacial period are widespread throughout the territory; but only in the southeastern part of the country, they outcrop across about 1459.6 km² – i.e., across 2.25% of the territory of Lithuania (Satkūnas, et al., 2007).

In this region, the glacial till soils of the Medininkai glacial period consist mainly of sandy clay and sandy silt. The mineral content shows that these deposits contain a high amount of cluster elements (Zr, Mn, Ti, Y, Yb, Pb), which are associated with weathering-resistant minerals. In contrast, the till deposits in other regions of Lithuania mainly contain lithogenic elements (Ga, Cr, Co, V, Ni), which are related to clay minerals (Bitinas, 2011).

The deformation and strength properties of the glacial till soils of the Medininkai glacial period have not been studied extensively, and, therefore, they are often characterized by properties of soils of different genesis. As these glaciogenic soils in question do not only cover a large area throughout Lithuania but also are often used as a medium for buildings, their structural parts, commercial deposits, etc., the study of the properties of these soils is essential for the country's economy. Also, on an international level, the results of this study are significant as glacial soils are difficult to study all over the world due to their property particularities.

1.2 Engineering challenges

One of the major challenges of this study is to collect high-quality undisturbed samples which would reflect the real in-situ conditions. Usually, many problems arise at collecting high-quality samples from stiff and overconsolidated soil. The size of the sample, the sampling method, sample storage, and the transport methods have a major influence on the physical and mechanical soil properties, which are to be determined. Due to the distinctive structure of the till soil of interest in this study and the effect of sampling methods, it may be difficult to determine the exact properties of the soil. In geotechnical studies involving very stiff and overconsolidated cohesive soils, the most common problem relating to result accuracy is the occurrence of cracks in the soil sample and its potential for swelling. Geotechnical literature provides a variety of references on optimized soil sampling practices (Gaoshan, et al., 2019), but the impact of sampling on measured soil properties is still an issue that remains to be addressed.

1.3 Problem statements

A typical problem with sampling is that the sampling itself disturbs the soil. Deep penetration into layers during soil sampling distorts the surrounding soil and engenders shear deformations. This disturbance can be so tremendous that the soil behavior in the laboratory differs significantly from in situ. Disturbances due to sampling in very stiff and overconsolidated cohesive soils are also thought to be due to microstructural damage (i.e., due to composition and bonding) and a result of effective stress variation compared to geostatic conditions (Tanaka, et al., 2006). As geostatic stresses are reduced to zero during sampling in situ, soil samples could potentially swell, resulting in a weaker soil structure. Moreover, the sample tends to lose a significant amount of its residual effective stresses instantly, so – as mentioned above – the sample may swell (Amundsen, et al., 2017; Berre, 2014). These processes start during drilling and continue while penetrating the soil and collecting samples as well as during the transportation of the sample to the laboratory, storing, preparing, and placing into testing apparatus (Tanaka, et al., 2006; Rocchi, et al., 2013). Therefore, disturbing the soil due to the entire sampling process is a considerable problem, resulting in difficulties while obtaining parameters of the soil reflecting reality. Many researchers have attempted to evaluate the effect of sampling disturbance on the mechanical properties of both intact soils in situ and laboratory-prepared normal and overconsolidated soils (Georgiannou, et al., 1994; Rahman, et al., 2010).

There are several studies for very stiff overconsolidated clays (Rahman, et al., 2010). Their results show that, due to disturbances created by sampling, initial effective stress (σ'_i), undrained shear strength (c_u), initial tangent modulus (E_i), and secant modulus (E_{50}) all decrease. Also, in the disturbed soil samples, lower pore pressure (u_0) and a higher value of axial strain (ε) are observed at the peak value of the deviator (Rahman, et al., 2010), changes related to the formed stresses are noticed in the overconsolidation ratio (OCR). Rahman, et al. (2010) and Krage, et al. (2016) suggest that in poorly collected soils, effective stress and the Skempton Pore Pressure Parameter at the peak deviator value (A_p) decreases proportionally with the increase of the OCR.

The correct results of the tested soil depend not only on the factors engendered during the sampling but also on the sensitivity, strength, porosity of the soil, its mesostructure (i.e., its cracks), the soil location environment, depth, aquifer, soil composition, amount of trace elements and their type.

The till soils of the Medininkai glacial period in the southeastern part of Lithuania are very stiff, overconsolidated, and widely known for their heterogeneous properties and complex soil structure. Sand inclusions, gravel, pebbles, and occasional larger gravel interlayers can affect the strength of the entire soil mass. Also, worth to mention that this soil due to its strength, low porosity and overconsolidation has low sensitive to pore pressure.

Therefore, when evaluating results, it is crucial to consider the influence of disturbances caused by soil sampling. Laboratory testing of soil samples requires a quantitative evaluation of the sample quality in order to evaluate the effectiveness of the test results in representing the in-situ soil properties. Empirical corrections, models, and simulations are proposed that "adjust" obtained results (Rocchi, et al., 2013; Nagaraj, et al., 2003). In this study, no corrections to results were applied yet. However, distortions in the results obtained from a potentially low-quality sample were taken into account, and the inaccurate results were eliminated.

The main purpose of this study is to explore, review and compare the strength and deformation properties of an almost unstudied till soil type in Lithuania. Taking into account main challenges like-complex till soil structure and composition as well as to collect a high-quality undisturbed sample that would reflect the in-situ conditions.

2 INVESTIGATION SITE

The investigated soil is located in eastern Lithuania (Figure 2). Medininkai glacial period deposits are found superficially only in this part of the country; these deposits consist solely of glacial (g II md) and fluvioglacial (f II md) formations.

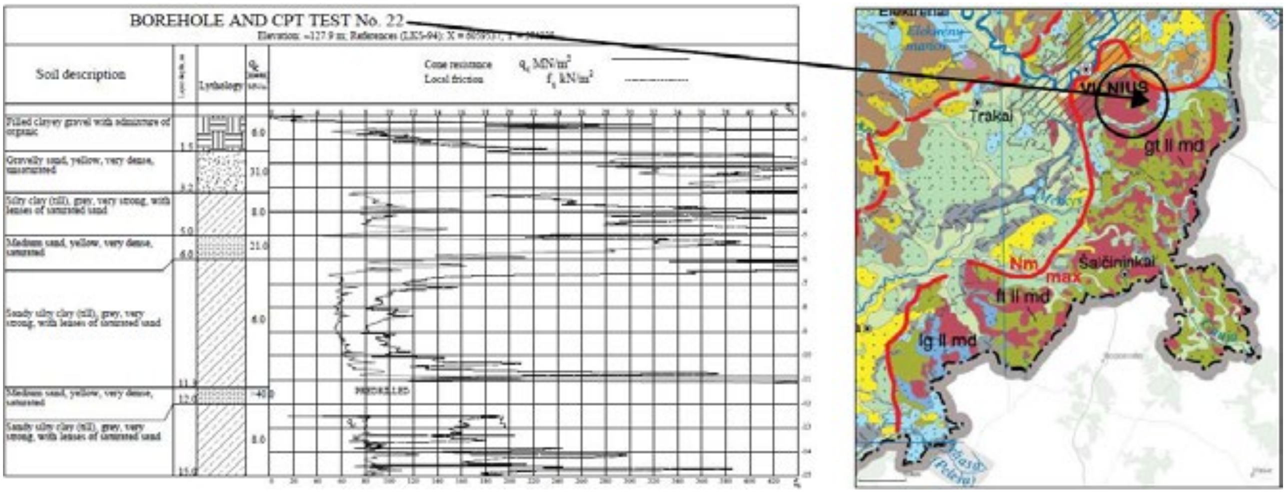

Figure 2: The site of the investigated soil and borehole and CPT test of sampling place (Gadeikis, et al., 2017)

Several field tests were performed in the research area: borehole drilling and cone penetration tests (Figures 2 and 3). Disturbed and undisturbed soil samples were taken for laboratory testing of physical and mechanical properties during drilling. The maximum depth reached with these surveys was 15 m. Hence, almost the entire depth of the Medininkai stratum layer was covered at this study site.

In order to obtain high-quality, undisturbed samples were used-Shelby tube sampling. This technic was used in order to recover intact samples that represent the in-situ soil density and moisture content. These two factors are obligatory to evaluate the most important soil engineering properties-strength, compressibility and density. The sample was subsequently extruded from the Shelby tube using an appropriately-sized hydraulic extruder and extrusion platen. There was sealed the top and bottom of the tube to prevent moisture loss, by spooning wax over the ends. Samples were kept in a container to avoid impacts of jarring or vibration until ready for testing.

Following the borehole information (Figure 3), glacial till (g II md) deposits predominate in the area under the fluvioglacial sediment (gravely sand; f II md). Most common are till-low plasticity sandy clays with medium sand interlayers and inclusions.

3 METHODOLOGY

Based on borehole drilling and cone penetration tests (CPT; Figures 2 and 3), the investigated glacial till soil from the Medininkai glacial period is encountered below 6.0 m of depth. Thus, samples with Shelby tubes for laboratory tests were taken from depths between 8.0 m and 15.0 m. According to CPT data, the studied soil is classified as very strong soil with cone resistance (q_c) > 4 MPa (LST EN 1997-2:2007).

Samples collected from depths between 8.0 m and 10.7 m have a q_c of about 6.0 MPa, whereas samples collected from deeper depths up to 15.0 m have a $q_c \sim 8.0$ MPa. The physical and mechanical properties of the soil were investigated during the research.

It is very important to mention that investigated Lithuanian till soil is poorly permeable and considered as partially saturated soil. In this case the principles of unsaturated soil mechanics are not studied. After the test B, it was obtained that the samples were not completely saturated. B value was from 0.65 to 0.70. This is the maximum values for these soil types. These values were achieved after three weeks of saturation process.

3.1 Investigation of physical properties

The following physical properties of the soil were determined for the studied soil: natural density, moisture content, plasticity, and liquid limits. Also, a grain size distribution analysis was conducted (Figure 4, Table 1).

Laboratory tests were performed according to predefined standards (CEN ISO/TS 17892-12:2004; CEN ISO/TS 17892-4:2004).

3.2 Investigation of mechanical properties

Soil strength properties were determined by triaxial testing (LST EN ISO 17892-9:2018) using single-stage triaxial (SST) and multi-stage triaxial (MST) setups (Hormdee, et al., 2012; Shahin, et al., 2011) (Figure 3). The main differences in SST and MST tests are that in the SST test a constant confining (cell) pressure is applied for difference soil samples and the axial stress is increased until the sample achieve a failure. Considering the multistage triaxial test, where procedure uses one soil specimen that is consolidated under different confining pressures. Test include consolidation of the soil specimen and then stress deviator increase with constant vertical strain ramp until the soil specimen deforms plastically. This procedure is repeated for a second and third time under increased confining pressure. (Alsalman, 2015; Shahin, et al., 2011). In the SST test we can measure peak and residual values in the meantime, in MST test only peak shear values.

Within the SST test, all samples had a height-to-diameter-ratio of 2 (H = 100 mm, D = 50 mm). Here, two test series were performed by applying different testing methodologies. The first test series was performed in unsaturated consolidated undrained (UCU) triaxial conditions the confining pressure in this test were 160 kPa, 260 kPa, and 360 kPa. The second test series was performed in saturated consolidated drained (SCD) triaxial conditions, and consolidation stress was 200 kPa, 300 kPa, and 400 kPa. In the unsaturated condition test pore pressure was measured. Also, in both unsaturated and saturated test conditions water content was captured before test and after test in the dry soil. The test loads were selected to reflect the natural soil location conditions, considering that the soil can be loaded or unloaded by 100 kPa. The vertical axial deformation velocity in both SST test series was 0.002%/min (reaching a maximum of 15% vertical axial deformation).

Within the MST tests, samples of different height-to-diameter-ratio were analyzed using different test methodologies. The first test series was performed on samples with ratios H/D = 2 (H = 100 mm, D = 50 mm) and H/D = 2 (H = 200 mm, D = 100 mm) in unsaturated consolidated drained (UCD) triaxial conditions; the confining pressurein this test were 150 kPa, 250 kPa, and 350 kPa. The second test series was performed as well for samples with rations H/D = 2 (H = 100 mm, D = 50 mm) and H/D = 2 (H = 200 mm, D = 100 mm), but in unsaturated consolidated undrained (UCU) triaxial conditions. The loads in the UCU tests were 200 kPa, 300 kPa, and 400 kPa. Again, the test loads were selected to reflect the natural soil location conditions, considering that the soil can be loaded or unloaded by 100 kPa. The vertical axial deformation velocity in both MST test series was 0.027%/min (reaching a maximum of 15% vertical axial deformation).

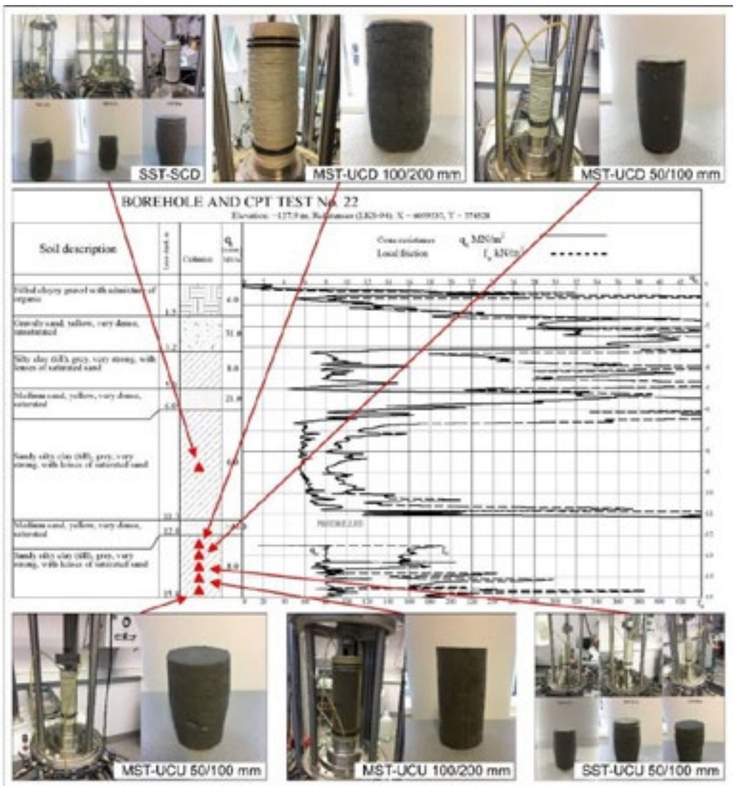

Figure 3: Borehole and CPT test of sampling place and triaxial test samples

Soil strength properties were estimated and calculated by applying several methodologies (LST EN ISO 17892-9:2018; Šimkus, 1987; Dirgėlienė, 2013; Dirgėlienė, 2007; Ho Chi Minh City University of Technology, 2016) using corrections of these methodologies as suggested Amšiejus, et al. (2010).

Soil deformation properties were estimated by performing oedometer (OED) tests applying additional compression on the samples (CEN ISO/TS 17892-5:2004). The tests were performed on undisturbed soil samples with heights of 20 mm and diameters of 70 mm. Loads used in the tests were 50 kPa, 160 kPa, 360 kPa, 780 kPa, and 1610 kPa. The additional load was added every 24 hours (Table 3).

Based on the obtained results, OCR and secant moduli E50 were calculated by examining the deformation and strength properties. The secant modulus E50 is given by the ratio of the peak normal stress deviator to the corresponding deformation (Varga, et al., 2004; Hatanaka, et al., 2003); it was calculated from stress dependence on strain obtained from the single-stage triaxial and multi-stage triaxial tests.

OCR were calculated from the OED tests implying gradual soil loading. Overconsolidation pressures were identified using the Casagrande graphical procedure (Jozsa, 2013; L'Heureux, et al., 2016) as well as results obtained from the oedometer moduli (E_{oed}) under different stresses (Józsa, 2016).

Additionally, the OCR were calculated from the results obtained from SST and MST tests. The OCR calculation was based on the calculated secant modulus E50 values (Józsa, 2016) and applying the SHANSEP methodology with different coefficient values to evaluate the minimum and maximum values (Mayne, 1988; StroLyk, et al., 2014; Tankiewicz, et al., 2021).

The OCR was also calculated based on CPT data by applying a calculation methodology for cohesive soils (Lunne, et al., 1997). This calculation methodology is based on the soil type and the plasticity index. To adapt it to Lithuanian till soils, the calculation corrections were introduced (Urbaitis, et al., 2016).

The results for strength properties calculated from SST and MST tests are compared with those values given in the literature (Bucevičiūtė, et al., 1997) that are often used and treated as appropriate. Deformation properties (E_{oed}) obtained from tests gradually loading the soil were compared with those calculated according to defined standards (CEN EN 1977-1:2004) and those given in the literature (Bucevičiūtė, et al., 1997).

4 RESULTS AND DISCUSSION

4.1 Physical properties from laboratory tests

Based on grain size distributions (Figure 4) and the results from the consistency limit identification in the laboratory (Table 1), the investigated soil is sandy low plasticity clay (saClL) (EN ISO 14688-1:2018; EN ISO 14688-2:2018).

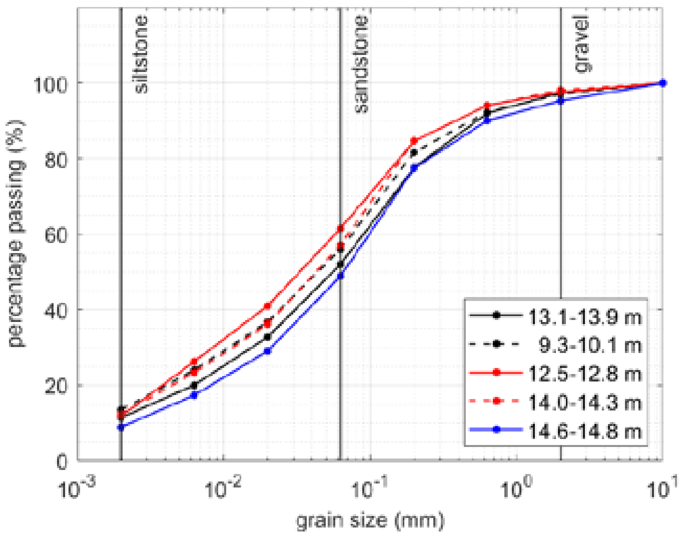

Figure 4: Grain size distributions for five samples from different depths

Table 1: Minimum/ maximum values of the different physical properties.

Bulk density (min/max)	Particle density	Moisture content	Void ratio	Plasticity index			
ϱ, g/cm^3	ϱ$_s$, g/cm^3	w (min/max) -	e (min/max) -	w_L (min/max) -	w_P (min/max) -	I_P (min/max) -	I_L (min/max) -
2.27/2.40	2.72	0.09/0.11	0.24/0.33	0.211/0.245	0.125/0.139	0.111/0.100	-0.118/-0.215

4.2 Mechanical properties from laboratory tests

Soil strength properties were analyzed by single (conventional) stage triaxial (S(C)ST) tests on samples with a depth-to-height-ratio of 50/100 mm and multi-stage triaxial (MST) tests on samples with different sizes (D/H = 50/100 mm and D/H = 100/200 mm) (Hormdee, et al., 2012; Shahin, et al., 2011).

Unsaturated consolidated drained (UCD) (Trinh, et al., 2006), unsaturated consolidated undrained (UCU) (Ding, et al., 2018) and saturated consolidated drained (SCD) (Lipinski, et al., 2010) test conditions were applied (Table 2).

Table 2: Comparison of shear strength in terms of peak friction angle (φ) and peak cohesion (c) obtained from multi-stage triaxial (MST) tests and single-stage triaxial (SST) tests.

	Triaxial test method	Sample size D/H, mm	ϕ_{peak}, °	c_{peak}, kPa
MST	UCD	50/100	25.53–28.40	36.57–37.03
		100/200	23.00–29.25	48.24–53.20
	UCU	50/100	19.87–21.29	35.40–35.88
		100/200	22.11–25.33	42.47–53.84
SST	UCU	50/100	23.50–25.81*	27.52–30.59*
	SCD	50/100	23.58–25.88*	22.67–28.03*
From literature	(Bucevičiūtė, et al., 1997)		35.00**	26.00**

*In this work and average values (**) obtained by Bucevičiūtė, et al. (1997). Data marked with one asterisk (*) are taken from Lekstutytė, et al., (2019) with added calculation method from (LST EN ISO 17892-9:2018).

Comparing the results of the strength properties obtained from the SST and MST tests of the uniform scale samples (i.e., D/H = 50/100 mm; Table 2), it can be seen that the mean cohesion values obtained from the MST test are higher by about 9 kPa (i.e., ~ 15%). However, the difference between the mean values of the internal friction is very small and, therefore, evaluated. Similar differences between the results obtained from the SST and MST tests were found in other works (Shahin, et al., 2011). The reasons for these higher values are the stresses and strains acting on the sample during the previous load steps (Choi, et al., 2018). The transformed Kondner's Hypothesis is proposed to be used to correct the difference (Sridharan, et al., 1972). As well as influence had different vertical axial deformation velocity (Barahona, et al., 2021). There in SST test velocity is 0.002%/min and in MST 0.027%/min. The peak deviatoric stress in MST is higher than in SST test. Consequently, and strength properties obtained in MST is slightly higher. Differences between values obtained in this work are not corrected because they are not significant. Therefore, after analyzing more samples and comparing values obtained from uniform triaxial tests, it can be stated that SST and MST test results are correlated. It can also be concluded that the MST testing method is suitable because it requires only one sample, which reduces the risk of errors and inaccurate results when collecting and preparing samples at different loads (Hormdee, et al., 2012).

In addition, the effect of excess pore water pressure is worth a relevant consideration. Elevated excess pore water pressure records a higher soil deformation that is mean that reducing overall soil shear strength properties. (Thu, et al., 2006). The amount of generated excess pore pressure increases as the degree of saturation increases. Excess pore pressure is very similar between the sample, which has a degree of saturation of 0.12–0.40. Strength parameters decreases as the degree of saturation increases. That decrese is noticeable within the range of degree of saturation between 0.80 and 1.0. (Kuwano, et al., 1988). As was mentioned before investigated soil is considered as partially saturated and that mean there is no significant influence for soil strength properties due to saturation.

Within the MST test series, samples in UCD and UCU conditions were analyzed, having ratios of D/H = 50/100 mm and D/H = 100/200 mm were analyzed (Table 2). A general review of the results between the UCD and the UCU shows that the results obtained during the UCD test are higher than those of the UCU. It must be emphasized that shear strength parameters are slightly influenced by moisture conditions. In referenced literature (Bláhová, et al., 2013) it can be found that overall shear strength decreases with increasing water content. In this study, the water content of the UCD samples is higher about 2%. Either the differences can be described due to different test methodologies - i.e., due to drained and undrained conditions. When in a drained test condition, pore pressure does not occur and does not reduce values. In SST test series soils moisture is almost the same.

The results from the UCD tests (Table 2) show that the mean values ($\varphi°$) studied in the soil samples of different sizes by different methods are very similar, and the differences are small. Comparing to the $\phi°$ values obtained from the 50/100 mm samples analyzed in UCD conditions, it can be seen that they are slightly higher by about 0.8° than in the 100/200 mm samples. This indicates that the effective peak values used to determine the friction angle decrease with increasing sample size (Skuodis, et al., 2019). However, the opposite result was obtained from the UCU tests, where the mean value ($\varphi°$) in the 100/200 mm samples is higher by 3.2° than in the 50/100 mm samples. This difference can be explained due to moisture content. In UCU 100/200 mm sample moisture is slightly higher than in 50/100 mm.

The evaluation of the cohesion values for samples of different dimensions (Table 2) shows the same regularity of results as the values increase for samples with higher specimen ratio. In the 50/100 mm samples, this value is smaller by 3–4 kPa than in 100/200 mm samples, regardless of the drainage conditions. Here, the effective peak values decrease with increasing sample size.

Comparing values from literature (Table 2) with the values obtained in our tests, the strength values of the Medininkai glacial period till soil were taken from the Engineering Geological Map of Lithuania (Bucevičiūtė, et al., 1997). Evaluating these results, we see that the mean value of the cohesion falls within the mean values obtained in the laboratory tests when evaluating the SST test applying SCD and UCU conditions, and the difference varies only about 3 kPa. Compared to the results obtained from the MST triaxial tests in UCD and UCU conditions, the cohesion in literature is smaller by 9.0–27.0 kPa than in our laboratory tests. However, the internal friction angle is greater than those obtained from the triaxial tests. Theoretical values are higher by 6°–16°. From the comparison with the results reported in the literature, it can be concluded that the results presented are not reliable and do not always correlate with the values determined in the laboratory.

Soil deformation properties were investigated via the oedometer (OED) test, where samples were gradually subjected to additional loads (CEN ISO/TS 17892-5:2004) (Table 3). As was mention before due to complex soil structure and composition this soil is considered as partially saturated.

Table 3: Comparison of deformation properties in terms of secant modulus (E_{50}) calculated from multi-stage triaxial (MST) tests and single-stage triaxial (SST) tests.

	Triaxial test method	Sample size D/H, mm	E_{50}, MPa		
MST	UCD	50/100	13.37 ^{150*}	8.94 ^{250*}	6.48 ^{350*}
		100/200	29.89 ^{150*}	15.75 ^{250*}	9.20 ^{350*}
	UCU	50/100	8.94 ^{200*}	5.87 ^{300*}	5.20 ^{400*}
		100/200	20.73 ^{200*}	11.21 ^{300*}	6.75 ^{400*}

SST	UCU	50/100	7.75 [160*]	7.56 [260*]	10.78 [360*]
	SCD	50/100	10.92 [200*]	8.37 [300*]	13.25 [400*]

E_{oed}, MPa	
OED test	5.20 - 7.95 [160*]
	11.48 - 15.53 [360*]
CPT test (LST EN 1997-2:2007)	63.08 - 94.60
CPT test (LST EN 1997-2:2007) (TAR, 2015-11-16, Nr. 18162)	60.00 - 80.00
From literature (Bucevičiūtė, et al., 1997)	49.00**

*Deformation modulus (E_{oed}) obtained from oedometer (OED) tests in this work and average values (**) obtained by Bucevičiūtė, et al. (1997). Values marked with one asterisk (*) indicate the pressure in kPa loaded on each sample.

After analyzing the data obtained from the OED tests, only the results from those samples are given that underwent similar pressures during triaxial testing. To assess the deformation properties of the soil, E_{oed} values (tangent modulus values from primary oedometer loading) are compared with E_{50} (elastic modulus - secant modulus values calculated from the triaxial tests) (Table 3). On a global view, the larger differences are only visible when comparing E_{oed} with values of E_{50} calculated from MST tests and 100/200 mm samples. When a sample experience 150 kPa and 200 kPa cell pressures, the E50 values are 3–4 times higher than E_{oed} values at similar pressures. When analyzing E_{50} and E_{oed} values at different pressures and test conditions, the results are close without significant differences. Small differences can be explained by heterogeneous soil composition – i.e., when more prominent sand inclusions, gravel, and pebbles are present in the samples. Therefore, the results are distorted.

When comparing E_{oed} values obtained from OED tests with E_{oed} values calculated from CPT, geostatic pressure, and plasticity index (LST EN 1997-2:2007). Large differences in the results is seen with values which are calculated from CPT. Result from CPT are more than 5–10 times greater than the Eoed values. A similar difference between results is noticed likewise while comparing them with the theoretical results presented in the literature (Bucevičiūtė, et al., 1997). We emphasize that (LST EN 1997-2:2007) the presented calculation is not adapted to till soil genesis and soil property characterization. Therefore, when evaluating the deformation properties of such soil based on theoretical charts or by calculation from the cone resistance (qc) alone, it is necessary to do so with great care and without relying solely on obtained results.

Focusing only on the E50 values (Table 3), it can be seen that the higher values are found in the 100/200mm samples (differences ranging from ~ 1.5–2.0 times). This tendency for higher results is seen in all analyzed data when evaluating the deformation and strength properties of the soil. Only with increasing acting stresses the results become more uniform. This trend can also be seen in other works (Ranjan, et al., 2000), which explains that E50 values decrease with increasing stresses (Figure 5) because the values are determined from the stress-strain curve, whose curvature goes down.

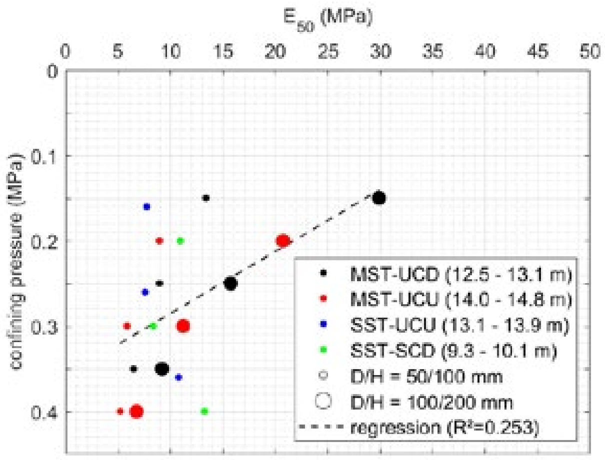

Figure 5: Secant modulus (E_{50}) versus confining pressure

When evaluating the OCR, it should be emphasized that it is particularly important for Lithuanian soils to understand their degree of consolidation, cracks, formation, and resistance to shear stresses. Typically, the OCR is calculated from the qc values obtained from CPT (Figure 6). Here, the OCR values, excluding the peaks, ranging from 20 to 9. This indicates that the soil is overconsolidated, and the degree of overconsolidation decreases with depth.

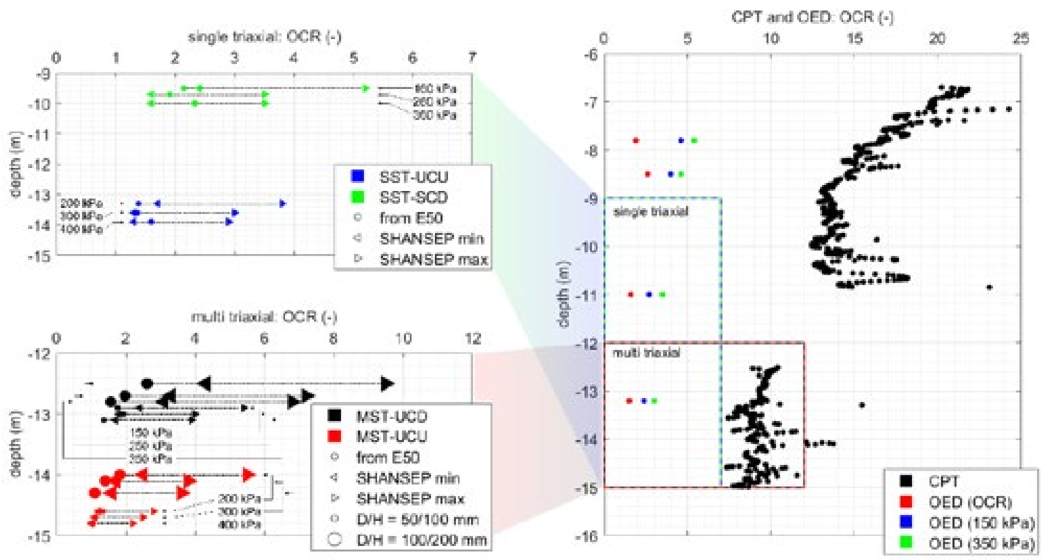

Figure 6: Overconsolidation ratio (OCR) values versus depth

The most accurate method of estimating OCR is considered to be (Urbaitis, et al., 2016) the overconsolidation pressure ratio with effective geostatic stresses σ'_p/σ'_{vo} calculated or estimated from the results of OED testing. It is seen (Figure 6, Table 4) that OCR values range from 1.5 to 2.6. OCR values from OED testing show that the soil is overconsolidated. These values are significantly lower than the values calculated from CPT. OCR values obtained from CPT are much larger (about 3 times) due to improper calculation formulas to Lithuanian till soil. Due to the exceptional properties of these soil we cannot directly apply these formulas as submitted Urbaitis, el. al. (2016) and properly compare with other OCR results.

Table 4: Overconsolidation ratio (OCR) values calculated with different methodologies.

Triaxial test			OCR (E_{50})			OCR (SHANSEP)		
						Min-Max	Min-Max	Min-Max
MST	UCD (12.5–13.1m)	50/100	1.8^{150*}	1.9^{250*}	1.4^{350*}	$2.4\text{-}5.4^{150*}$	$1.8\text{-}4.0^{250*}$	$1.7\text{-}3.9^{350*}$
		100/200	2.6^{150*}	2.0^{250*}	1.6^{350*}	$4.3\text{-}9.5^{150**}$	$3.3\text{-}7.2^{250}$	$3.1\text{-}6.8^{350*}$
	UCU (14.0–14.8m)	50/100	1.3^{200*}	1.1^{300*}	1.1^{400*}	$1.2\text{-}2.8^{200*}$	$1.1\text{-}2.5^{300*}$	$1.0\text{-}2.2^{400*}$
		100/200	1.8^{200*}	1.4^{300*}	1.1^{400*}	$2.5\text{-}5.5^{200}$	$1.7\text{-}3.8^{300*}$	$1.6\text{-}3.6^{400*}$
SST	UCU (13.1–13.9m)	50/100	1.4^{160*}	1.4^{260*}	1.6^{360*}	$1.7\text{-}3.8^{160*}$	$1.3\text{-}3.0^{260*}$	$1.3\text{-}2.9^{360*}$
	SCD (9.3–10.1)	50/100	2.1^{200*}	1.9^{300*}	2.3^{400*}	$2.4\text{-}5.2^{200*}$	$1.6\text{-}3.5^{300*}$	$16\text{-}3.5^{400*}$

OCR (OED test)		
Depth, m	OCR = σ'_p/σ'_{vo}	OCR (E_{oed})
7.7–7.8	1.9	4.6^{150} - 5.4^{350**}
8.4–8.6	2.6	4.0^{160} - 4.6^{360**}
11.0–11.3	1.6	2.7^{150} - 3.5^{350**}
13.2–13.4	1.5	2.4^{150} - 3.0^{350**}

*Values marked with one asterisk (*) indicate the pressure in kPa loaded on each sample. Values marked with two asterisks (**) show pressure chosen from OED tests regarding pressures during the triaxial tests.

E_{oed} values were used to estimate OCR values from OED tests (Figure 6, Table 4). When comparing these E_{oed} results with OCR= σ'_p/σ'_{vo} (Figure 6), similar results of increasing-decreasing tendencies are seen (i.e., decrease with depth). Here, OCR values are about 1.5–2 times higher than in the laboratory tests, but the difference is as significant as it was with values from CPT. Here, results are closer to the laboratory tests and show that this soil is also overconsolidated. In this calculation method, OCR values were calculated from selected E_{oed} results with the same pressures as for the triaxial tests.

OCR were calculated and evaluated from the results obtained from triaxial tests using various testing methodologies (Table 4) mentioned before. OCR (E_{50}) values calculated from the secant modulus are very close to the values obtained from OCR= σ'_p/σ'_{vo} (Figure 6). Although values are close, but using UCU test conditions to investigate 50/100 mm sample it can be seen that the soil is normally consolidated according to the OCR value (OCR > 1.5). However, when evaluating the obtained mean OCR value from different pressures, the soil is nonetheless overconsolidated-except for MST and SST 50/100 mm tests in UCU conditions, in which it stays normally consolidated. However, we emphasize that this normally consolidated sample was collected from a different depth, where no OED test was performed.

Also, an OCR (SHANSEP) calculation (Figure 6, Table 4) was performed for the data from the triaxial tests. The minimum and maximum values calculated with the SHANSEP formula according to different coefficients at specific pressures show that the soil is overconsolidated. OCR obtained using this method are close to the OCR (E_{50}), OCR= σ'_p/σ'_{vo} and OCR(E_{oed}) values. It is also observed that minimum values obtained in the MST and SST triaxial test by UCU conditions and in 50/100 mm sample sizes show that the soil is normally consolidated.

5 CONCLUSIONS

Deformation and strength properties of Middle Pleistocene Medininkai glacial period till soils are very poorly investigated. However, the soils of this period and composition do not only cover the surface of Lithuania but are often subjected to human economic activity (i.e., as medium for buildings or commercial deposits, etc.).

Strength properties of the soil were investigated via single (conventional) stage triaxial (S(C)ST) tests with 50/100 mm size samples and via multi-stage triaxial (MST) tests having soil samples of different sizes (50/100 mm, 100/200 mm) by applying unsaturated consolidated drained (UCD), unsaturated consolidated undrained (UCU) and saturated consolidated drained (UCD) conditions. Deformation properties of the soil were investigated in oedometer (OED) tests, during which the soil gradually underwent additional load cycles.

The analysis of the results obtained from the different SST and MST test methods suggests that the MST test method is suitable as it requires only one sample, which reduces the risk of errors and inaccurate results when collecting and preparing samples at different loads.

When comparing the strength and deformation properties of the soil determined by different test methods, no significant differences in the results were observed. However, a large gap in the results has been observed compared to those widely published in the literature and used in our study.

The calculation of the OCR for Medininkai glacial period till soils shows that these soils are overconsolidated (OCR > 1.5).

6 REFERENCES

Alsalman, M., 2015. *Comparison and Correction Of Multistage Triaxial Tests To Single Stage Truaxial Test For The Rock Mechanical Testing*, Houston: University of Houston.

Amšiejus, J., Dirgėlienė, N. & Norkus, A., 2010. *Analysis of methods for evaluation of soil shear strenght parameters.* Vilnius, Lithuania, Vilnius Gediminas Technical University, pp. 1077 - 1082.

Amundsen, H. A., Dang, H., Adamson, M. & Emdal, A. T. V., 2017. A New Laboratory Procedure to Study Stress Relief in Soil Samples. In: J. L. A. L. Vikas Thakur, ed. *Landslides in Sensitive Clays.* s.l.:Springer International Publishing.

Barahona, C. et al., 2021. *Loading rate effect on mechanical properties of an unsaturated silty sand*. s.l., EDP Sciences.

Berre, T., 2014. Effect of sample disturbance on triaxial and oedometer behaviour of a stiff and heavily overconsolidated clay. *Canadian Geotechnical Journal*, 16 June, 51(8).

Bláhová, K., Sevelov, L. & Pilařová, P., 2013. Influence of water content on the shear strength parameters of clayey soil in relation to stability analysis of a hillside in Brno region. *Acta Universitatis Agriculturae et Silviculturae Mendelianae Brunensis*, 61(6), pp. 1583-1588.

Bičkauskas, G., Brazauskas, A., Kleišmantas, A. & Motuza, G., 2011. *Bendrosios geologijos pratybos.* Vilnius: Vilniaus universiteto leidykla.

Bitinas, A., 2011. *Paskutinis ledynmetis Rytinės Baltijos regione.* Klaipėda: Klaipėdos universiteto leidykla.

Bucevičiūtė, S., Marcinkevičius, V. & D, D., 1997. *Lietuvos inžinerinis geologinis žemėlapis, M 1:500 000.* :Lietuvos Geologijos Tarnyba.

CEN EN 1977-1:2004. Eurocode7: Geotechnical design-Part 1:General rules.

CEN ISO/TS 17892-12:2004. Geotechnical investigation and testing - Laboratory testing of soil - Part 12: Determination of Attenberg limits.

CEN ISO/TS 17892-4:2004. Geotechnical investigation and testing - Laboratory testing of soil - Part 4: Determination of particle size distribution.

CEN ISO/TS 17892-5:2004. Geotechnical investigation and testing — Laboratory testing of soil — Part 5: Incremental loading oedometer test.

Choi, J.-H., Dai, S., Lin, J.-S. & Seol, Y., 2018. Multistage Triaxial Tests on Laboratory-Formed Methane Hydrate-Bearing Sediments. *Journal of Geophysical Research: Solid Earth*, 123(5), pp. 3347-3357.

Ding, J. et al., 2018. Consolidated Undrained Triaxial Compression Tests and Strength Criterion of Solidified Dredged Materials. *Advances in Civil Engineering,*, pp. 1-10.

Dirgėlienė, N., 2007. Grunto stipruminių ir deformacinių savybių tyrimas triašio slėgio aparate bei jų tikimybinis vertinimas [Research of soil strenght i triaxal tests and probabilistic assessment of results].

Dirgėlienė, N., 2013. *Grunto tyrimai triašio slėgio aparatu: metodikos nurodymai.* Vilnius: Vilniaus Gedimino Technikos Universitetas.

EN ISO 14688-1:2018. *Geotechnical investigation and testing - Identification and classification of soil - Part 1: Identification and description.*

EN ISO 14688-2:2018. *Geotechnical investigation and testing - Identification and classification of soil - Part 2: Principles for a classification.*

Gadeikis, S. & Žaržojus, G., 2017. *Cogeneration power station at Jocioniu str. 13,* Vilnius: JCS Geotestus.

Gaoshan, L., Yongjian, P. & Xuhua, M., 2019. Comparative experimental analysis of physical and mechanical properties of saturated soft soil under different sampling methods. *Journal of Engineering Geology,* 27(3), pp. 550-558.

Georgiannou, V. N. & Hight, D. W., 1994. The effects of centerline tube sampling strains on the un-drained behavior of two stiff over-consolidated clays. *Geotechnical Testing Journal,* 17(4).

Grigelis, A., Gailius, R. & Kadūnas, V., 1994. *Lietuvos geologija: monografija.* Vilnius: Mokslo Ir Enciklopediju Leidybos Institutas.

Guobytė, R., 1999. *Lithuanian quaternary geological map M 1:200 000,* Vilnius: s.n.

Hatanaka, M., Yuji, T. & Uchida, A., 2003. *Effect of anisotropy on drained and undrained shear behavior of in-situ sandy soils.* Lyon, France, s.n.

Ho Chi Minh City University of Technology, 2016. hapter 11: Shear Strength of Soil . In: *Ho Chi Minh City University of Technology.*

Hormdee, D., Kaikeerati, N. & Angsuwotai, P., 2012. Evaluation on the Results of Multistage Shear Test. *GEOMATE Journal*, 2(1), pp. 140-143.

Jozsa, V., 2013. *Empirical correlations of overconsolidation ratio, coefficient of earth pressure at rest and undrained strength.* Hungary, Budapest, s.n., pp. 88-92.

Jozsa, V., 2016. Estimation and Separation of Preconsolidation Stress Using Triaxial,- and Oedometer Test in Kiscelli Clay. *Periodica Polytechnica Civil Engineering*, Januray, 60(2), pp. 297-304.

Kavoliutė, F., 2012. *Lietuvos Gamtinis Pamatas, I dalis - Gelmės ir paviršius.* Vilnius: Vilniaus Universitetas.

Krage, C., Albin, B., Dejong, J. & DeGroot, D., 2016. *The Influence of In-situ Effective Stress on Sample Quality for Intermediate Soils.* Brisbane, AUS, s.n., pp. 565-570.

Kuwano, J., Yoshida, Y. & Ishihara, K., 1988. *Change in the Stability of Slopes with degree of Saturation*. Sydney , s.n., pp. 465-469.

Lekstutytė, I., Gadeikis, S., Žaržojus, G. & Skuodis, Š., 2019. Engineering geological and geotechnical properties of till soil of the Middle Pleistocene glacial period. *Estonian journal of earth sciences,* 68(2), pp. 101-111.

L'Heureux, J.-S., Yang, S. & Lunne, T., 2016. *Study on the practices for preconsolidation stress evaluation from oedometer tests.* s.l., s.n.

Lipinski, M. J. & Wdowska, M., 2010. Saturation criteria for heavy overconsolidated cohesive soils. *Land Reclamation*, 42(2), pp. 295-302.

LST EN 1997-2:2007. *Eurocode 7: Geotechnical design - Part 2: Ground investigation and testing.*

LST EN ISO 17892-9:2018. *Geotechnical investigation and testing. Laboratory testing of soil. Part 9: Consolidated triaxal compression test on water saturated soils, 27pp.*

Lunne, T., Powell, J. & Robertson, P., 1997. *Cone Penetration Testing in Geotechnical Practice.* London: s.n.

Mayne, P. W., 1988. Determining OCR in Clays from Laboratory Strength. *Journal of Geotechnical Engineering*, 114(1).

Nagaraj, T., Miura, N., Chung, S. & Pasad, K., 2003. Analysis and assessment of sampling disturbance of soft sensitive clay. *Ge´otechnique*, January, 53(7), pp. 679-683.

Putys, P., Satkūnas, J. & Jusienė, A., 2010. Lietuvos kvartero storymės geologinių struktūrų tūrio įvertinimas. *Geologijos akiračiai,* Volume 3 - 4, pp. 20-30.

Rahman, M. M. & Siddique, A., 2010. Effects of Sampling Disturbance and its Minimization in Reconstituted over-consolidated Dhaka Clays. *Dhaka University of Engineering & Technology Journal,* 1(1), pp. 18-26.

Ranjan, G. & Rao, A. S. R., 2000. *Basic and applied soil mechanics.* s.l.:New Age International Pvt Ltd Publishers.

Rocchi, G., Vaciago, G., Fontana, M. & Prat, M. D., 2013. Understanding sampling disturbance and behaviour of structured clays. *Soils andFoundations*, 53(2), pp. 315-334.

Satkūnas, J., 2009. *Lietuvos Kvartero stratigrafijos schema.* Vilnius: Lietuvos geologijos tarnyba.

Satkūnas, J., Grigienė, A. & Bitinas, A., 2007. Lietuvos Kvartero stratigrafinio suskaidymo būklė. *Geologijos akiračiai*, Volume 1.

Shahin, M. A. & Cargeeg, A., 2011. Experimental Investigation into Multistage versus Conventional Triaxial Compression Tests for a C-Phi Soil. *Applied Mechanics and Materials*, Volume 90-93, pp. 28-32.

Šimkus, J., 1987. *Gręžtinių pamatų projektavimas ir statyba. Gruntų tyrimas statiniu zondavimu. Metodikos nurodymai..* Vilnius: s.n.

Skuodis, Š., Dirgelienė, N. & Lekstutytė, I., 2019. Change of soil mechanical properties due to triaxial sample size. *13th International Conference MODERN BUILDING MATERIALS, STRUCTURES AND TECHNIQUES*, pp. 470-474.

Sridharan, A. & Rao, S. N., 1972. New Approach to multistage triaxial test. *Journal of Soil Mechanics and Foundations Division*, 98(11), pp. 1279-1286.

StroLyk, J. & Tankiewicz, M., 2014. The Undrained Shear Strength of Overconsolidated Clays. *Procedia Engineering*, pp. 317-321.

Tanaka, H., Udaka, K. & Nosaka, T., 2006. Strain rate dependenc yof cohesive soils in consolidation settlement. *Soils and Foundations*, 46(3), pp. 315-322.

Tankiewicz, M., Stróżyk, J. & Zięba, Z., 2021. *Undrained Shear Strength cu and Undrained Elastic Modulus Eu of Anthropogenic Soils from Laboratory Tests.* s.l., s.n.

Thu, M. T., Rahardjo, H. & Leong, E.-C., 2006. Shear Strength and Pore-Water Pressure Characteristics during Constant Water Content Triaxial Tests. *Journal of Geotechnical and Geoenvironmental Engineering*, 132(3), pp. 411-419.

Trinh, M. T., Rahardj, H. & Leong, E.-C., 2006. *Effects of Hysteresis on Shear Strength Envelopes from Constant Water Content and Consolidated Drained Triaxial Tests.* Carefree, Arizona, United States, s.n., pp. 1212-1222.

Urbaitis, D., Lekstutytė, I. & Gribulis, D., 2016. *Overconsolidation Ratio Determination of Cohesive Soil.* Vilnius, s.n., pp. 108-113.

Varga, G. & Czap, Z., 2004. Soil Models: Safety factors and settlements. *Periodica Polytechnica Civil Engineering,* 2 November, 48(1-2), pp. 53-63.

Quick Methods of Measurement of Relative Compaction and Moisture Content

Philip W K Chung, Florence L F Chu
Geotechnical Engineering Office, CEDD, HKSARG, Hong Kong, China

ABSTRACT

The need of compaction control is well-recognized to ensure safety and satisfactory performance of fill body. Minimum relative compaction is commonly used in the end-product specification for earthworks. The Hilf method is a way to determine the relative compaction and deviation from optimum moisture content without the need to know the moisture content of soil. Infrared with convection heating is a drying method to dry soil rapidly (within 3.5 hours for common fill materials in Hong Kong). These two methods facilitate the quick determination of the relative compaction. This paper examines these two quick methods. It also presents the review of the applicability of the Hilf method in fill compaction control based on 271 pairs of results conducted in public works projects and the effectiveness of the infrared with convection drying in measuring moisture content of soil based on 167 sets of test results. The results showed that there is a reasonably good correlation between the relative compaction determined from the Hilf method and sand replacement test, with an absolute difference in relative compaction mainly within 3%; while the moisture content obtained from the infrared with convection drying and the conventional oven drying method are statistically identical with majority of the results having differences less than 0.4% which is considered practically insignificant for geotechnical engineering applications.

1 INTRODUCTION

1.1 Background

The need of compaction control is well-recognized to ensure safety and satisfactory performance of fill body. Minimum relative compaction (RC), which is a ratio of field dry density (ρ_d) to maximum dry density (ρ_{dm}) of the compacted soil, is commonly used in the end-product specification for earthworks. Field moisture content (w_f) within a specific range from the optimum moisture content (w_o) (also called optimum water content) may also be specified in compaction control of fill materials. In Hong Kong, ρ_{dm} is determined using Proctor compaction test method in laboratory while ρ_d is calculated using the equation "$\rho_d = \rho_w /(1 + w_f)$", where field wet density (ρ_w) (also known as in-situ bulk density) and w_f are measured by sand replacement test (SRT) and conventional oven drying method, respectively. SRT has been used for many decades, which is a reliable and economic method. Conventional oven drying method for measuring moisture content usually takes at least 24 hours to complete. In practice, Additional time is required due to following reasons: (i) delivering samples from field to the laboratory; (ii) non-operating hours of laboratory; and (iii) administrative procedures and quality control process in the laboratory, such as checking of all relevant test results. Consequently, the information on RC may only be available at least 2 days after the SRT, which is highly undesirable to construction works especially during the wet seasons. It is imperative if the field compaction results could be obtained as soon as possible, in particular for large-scale backfilling works such as fill reclamation.

Hilf (1957 and 1961) proposed a method to determine the RC and the deviation of w_f from w_o without the need to determine w_f of the soil. Usually, the results of only three additional Proctor compaction tests are required after the SRT and these can be completed in less than two hours. The Hilf method has been widely used in the

USA since its development in 1957. Subsequently, it has been codified as testing standard in Australia (AS, 2006), Brazil (ABNT 1991) and the USA (USBR 1990 & 2012; ASTM 2017). Historically, the method was introduced for cohesive soil and was used in compaction control on such soil satisfactorily (Hilf 1961). As specified in some testing standards, the method is applicable on wider range of soils. For example, in ASTM (2017), the test method is normally performed for soils containing more than 15% fines. In Hong Kong, the Hilf method has been included in General Specification for Civil Engineering Works (GS) (HKG 1992) as an alternative method to determine RC, ρ_{dm} and w_o of compacted fill with particles retained on 37.5 mm BS test sieve not exceeding 20%. However, the Hilf method receives little attention in local construction industry. The reason of not adopting the method in the past three decades by the practitioners is not known.

Another way to determine RC quickly is to shorten the duration to obtain w_f. Convection heating is adopted in conventional oven drying method. Heat is transferred through air inside the oven to soil specimens and this takes relatively long period to supply enough thermal energy to extract moisture out of the specimens. While for infrared (IR) heating, radiation is transmitted to soil specimens and water inside directly without the presence of a heating medium (e.g. air). Since there is no significant loss of energy to the ambient, the efficiency of energy transfer can be maximized, in particular if the peak output wavelength of the IR source matches with the absorption band of the material being heated. Natural wavelength of water molecule is close to that of intermediate and far IR (i.e. 1 μm to 10 μm), indicating that IR is an effective heat source for water heating. IR heating has an extensive application in manufacturing sectors, such as food, polymer and mineral processing industry. Drying of materials by combined convection and IR heating has also been studied (Masanobu et al 1988, Mortaza 2016). The drying rate is found to be remarkably increased under hybrid heating method comparing to those by convection heating alone. The use of convection heating with IR heating enhances the IR drying rate as the diffusion rate of the water vapor and the heating rate of the material would be increased (Tiller and Garber 1942). It is considered that a more stable and uniform temperature distribution and energy efficiency of IR drying process can be elevated by combined use of convection oven with IR heating source.

This paper examines the above two quick methods. It also presents the review of the applicability of the Hilf method in compaction control based on the tests conducted in public works projects and the effectiveness of the IR with convection drying in measuring moisture content of local soils.

2 THE HILF METHOD

2.1 The theory

RC can either be expressed as a function of wet density or dry density, see Figure 1.

$$RC = \frac{\rho_d}{\rho_{dm}} = \frac{\rho_d(1+w_f)}{\rho_{dm}(1+w_f)} \tag{1}$$

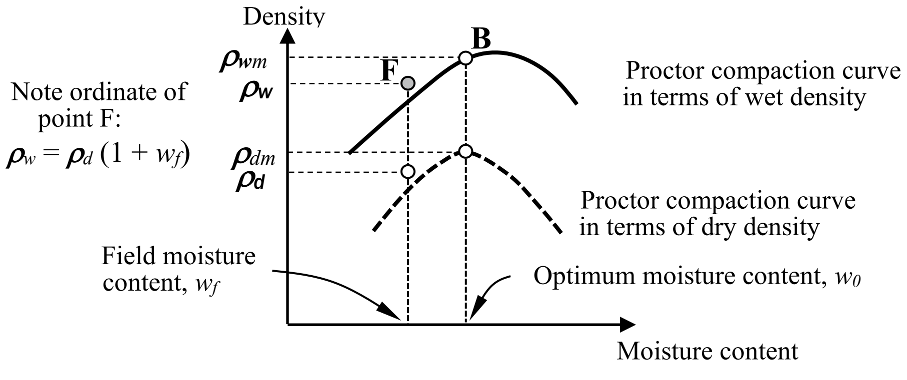

Figure 1: Proctor compaction curve

After the SRT in the field, additional soil samples surrounding the SRT spot are taken. When the soils are transported back to the laboratory, typically three compaction tests using Proctor equipment are conducted on the soil samples to obtain the wet densities. The moisture content of the three specimens for the compaction tests is normally pitched at z = 0, ±2%, ±4%, where z is defined as the added/removed water in reference to w_f in percentage of soil wet mass before adding any water in laboratory (see Equation (2)). The "±" sign depends on whether w_f is estimated to be less than or greater than w_o. For example, if w_f is estimated to be less than the w_o, then the three moisture contents could be z = 0, +2% and +4%.

$$z = \frac{wM_s - w_f M_s}{M_s(1+w_f)} = \frac{w-w_f}{1+w_f} \qquad (2)$$

where M_s is the dry mass of soil and w is the moisture content of soil. Rearranging Equation (2) gives 1 + z as shown below:

$$1 + z = \frac{1+w}{1+w_f} \qquad (3)$$

Each soil compaction test on the additional soils taken from the field gives a point on a plot with wet density as ordinate and z as abscissa (see P1, P2 and P3 in Figure 2, assume positive z). For each of these three points, the ordinate is divided by (1 + z) to obtain a so-called converted wet density (also known as converted bulk density). A parabola may be fitted to the three converted wet density data points. The maximum value of this parabola can then be obtained (see point A in Figure 2). The converted wet density (CWD) is calculated from dividing the wet density of soil by (1 + z),

$$\mathrm{CWD} = \frac{\text{wet density}}{1+z} = \frac{\rho_d\,(1+w)}{1+z} = \frac{\rho_d(1+w)}{\frac{1+w}{1+w_f}} = \rho_d\,(1+w_f) \qquad (4)$$

Since w_f is a constant, the maximum value of the CWD (i.e. the vertex of the parabola, MCWD) must be $\rho_{dm}(1+w_f)$, i.e. point A in Figure 2. Equation (4) also shows that when $w = w_o$,

$$\frac{\rho_{dm}\,(1+w_o)}{1+z_m} = \rho_{dm}(1+w_f) \qquad (5)$$

where z_m is the abscissa of point A.

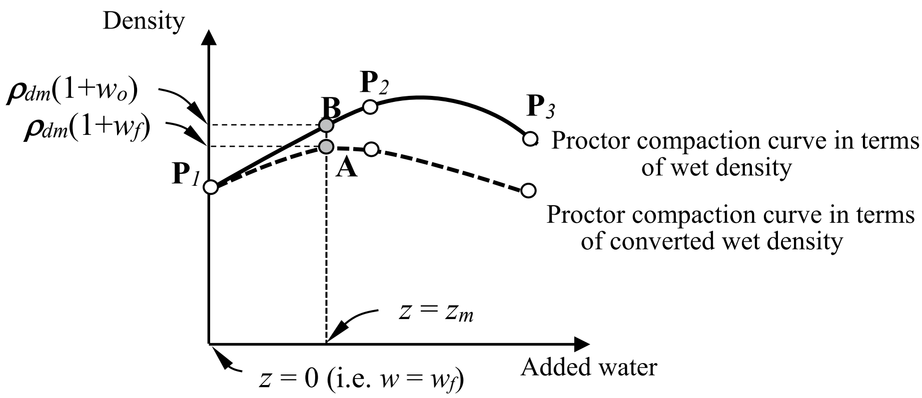

Figure 2: The Hilf method compaction curve

RC (also known as ratio D in Hilf method) can now be obtained from ordinates of Point F in Figure 1 and Point A in Figure 2:

$$\text{RC or D} = \frac{\rho_d}{\rho_{dm}} = \frac{\rho_d\,(1+w_f)}{\rho_{dm}\,(1+w_f)} = \frac{\text{ordinate of Point F (Figure 1)}}{\text{ordinate of Point A (Figure 2)}} \tag{6}$$

As far as density control of fill compaction is concerned, in addition to a specified minimum RC, many specifications also require w_f be close to w_o, for example, a tolerance of ± 3% of w_o. The Hilf method provides information of the difference between w_f and w_o (i.e. $w_f - w_o$) without the determination of the w_f of the compacted fill material. Refer to the converted wet density curve in Figure 2, the z value corresponds to the peak point (A) is z_m. Rearrange Equation (5) and from the definition of z_m to give:

$$w_o - w_f = \frac{z_m}{1+z_m}(1+w_o) \tag{7}$$

The right-hand side of Equation (7) cannot be evaluated unless w_o is known or estimated. Hilf then made use of about 1,300 data set compiled by the Bureau of Reclamation of US to establish a correlation between the maximum wet density (ρ_{wm}) and w_o. As Point B (i.e. ρ_{wm}) shown in Figure 1 and Figure 2 are known, the corresponding w_o can be estimated from the correlation. The correlation between ρ_{wm} and w_o can also be developed based on the results of Proctor tests in Hong Kong (see Figure 6). The difference between w_f and w_o (i.e. w_o - w_f) is then calculated from Equation (7).

2.2 Test programme

A total of 102 field trials were conducted in 40 different construction sites. Amongst the field trials, 77 of them used 2.5 kg rammer in Proctor compaction test while the remaining adopted 4.5 kg rammer. Usually, more than one SRT is carried out for one batch of fill compaction works according to GS (HKSAR 2020). Therefore, in total, 271 pairs of results were obtained from these trials to compare the RC values calculated from the Hilf method with that determined from SRT. Analysis of the difference between w_f and w_o determined from the Hilf method and conventional oven drying method was also carried out.

Distribution of the data set collected from the trials in terms of soil types and compaction efforts in Proctor tests is presented in Table 1. The fill materials covered in the study were mainly coarse-grained soils and classified as sandy GRAVEL or gravelly SAND. The distribution of ρ_{dm} and the corresponding ρ_{wm} at w_o against w_o are presented in Figure 3. As shown in the Figure, fill material in this study had ρ_{dm} and w_o close to the relationship between ρ_{dm} and w_o (i.e. $\rho_{dm} = 3.703\ w_o^{-0.266}$) for sandy GRAVEL, gravelly SAND and silty/clayey SAND proposed by Chung & Chu (2020).

Table 1: Distribution of Soil Types in Field Trial

Soil Type	Compaction Effort Used in Proctor Test	Number of Data Set Collected from Trials	Percentage in Entire Set of Data
sandy SILT/CLAY	2.5 kg	22	8.1%
silty/clayey SAND	2.5 kg	18	6.6%
gravelly SAND	2.5 kg	128	47.2%
sandy GRAVEL	2.5 kg	46	17.0%
sandy GRAVEL	4.5 kg	57	21.0%
Total number of data set		271	100%

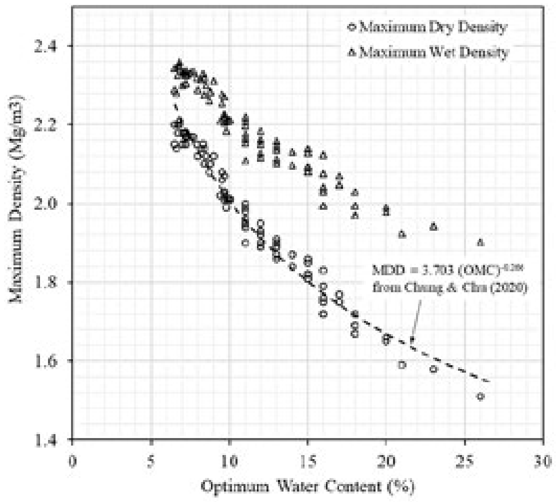

Figure 3: Maximum density versus optimum moisture content of soils in the study

For each trial, sufficient soil from the compaction layer near one of the locations of SRTs was collected for the additional Proctor compaction tests under the Hilf method. The soil was kept in a sealed plastic bag to preserve its field moisture content, w_f. Upon returning to the laboratory, the soil was screened over 20 mm BS test sieve and subdivided into equal portions. First portion of the soil was compacted at its w_f in a standard cylindrical mould according to the procedure of the Proctor test. The rammer used in the Hilf method followed the one used to determine ρ_{dm} through Proctor test for the calculation of RC.

Specific amount of water which equaled to certain percentage of the wet mass of the soil was added to or removed from other portions of the soil (e.g. z = ± 2%). The soil with adjusted water content was compacted in the same way. Converted wet density was then calculated from the wet density divided by (1 + z). For each trial, the w_f was also determined from oven drying method so that assessment on the applicability of the Hilf method in prediction of the difference between w_f and w_o can be made. In general, 3 to 4 compaction tests were carried out for each trial. It took about 2 hours to complete sample preparation and additional compaction tests in the laboratory. With the use of Hilf method, the information on RC may be available within 0.5 to 1 day after the SRT.

2.3 Density control by the Hilf method

Relative compaction value (D) obtained from the Hilf method was compared with the RC value obtained from SRT (Figure 4). In general, D value increased with the increase of RC value. Regression analysis was conducted. A linear relationship between D and RC values with the R-squared of 0.71 was determined. Most of the results had the absolute difference between D and RC values within 3% (84% of the data). The mean of the difference ($\overline{X}_{D\text{-}RC}$) and the standard deviation of the difference ($S_{D\text{-}RC}$) were 0.32% and 2.22% respectively.

The distribution of the difference between D and RC values was further evaluated based on soil type and compaction effort used in the compaction test. As shown in Figure 5, the differences were concentrated within ± 3% irrespective of soil type and level of compaction effort used (i.e. 2.5 kg and 4.5 kg). The trend of the relationship between D and RC values for different soil types and compaction efforts were similar to the data considered in one single group. If RC ≥ 95% is adopted as the compliance criterion in fill compaction control, only a very small proportion of data (about 2.9% bounded by the red dashed box) was interpreted as compliance results based on the Hilf method but non-compliance in accordance with the SRT results.

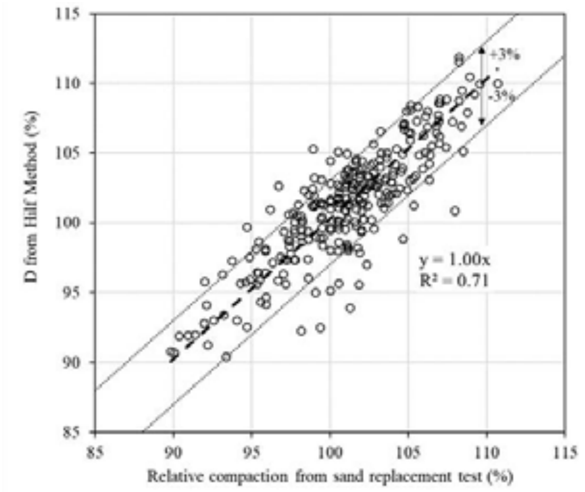

Figure 4: D values versus RC values

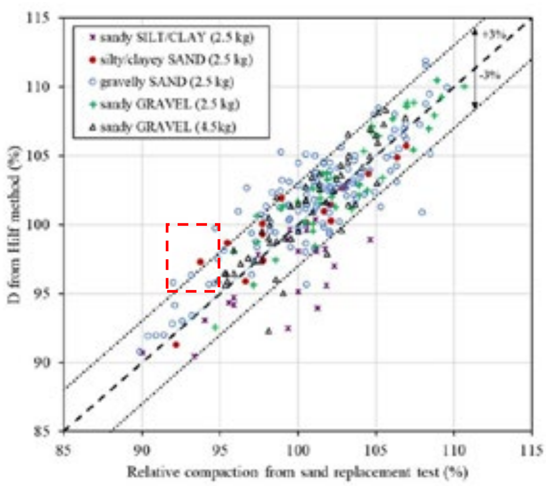

Figure 5: D values versus RC values for different soil types and compaction efforts

2.4 Moisture content control by the Hilf method

The applicability of the Hilf method for moisture content control was evaluated. In the Hilf method, the deviation of w_f from w_o is estimated based on a relationship between ρ_{wm} and w_o without knowing w_f or w_o for each in-situ density test. Local ρ_{wm} - w_o relationships were used in this study. The relationships were determined from a review of 15,952 results of Proctor tests conducted between 2014 and 2018 under public works projects in Hong Kong. Relationships between ρ_{dm} and w_o were first established for 4 different soil types and 2 different compaction efforts. Then the relationships between ρ_{wm} at w_o and w_o with the highest R-squared were determined. The relationships are presented in Table 2. Figure 6 shows the distribution of data for four soil types in two different compaction efforts. With the measured ρ_{wm}, w_o was calculated based on these relationships. (w_f - w_o) was then determined using Equation (7) based on z_m and w_o.

Table 2: Local Relationships between ρ_{wm} at w_o and w_o

Soil Type	Rammer Used in Proctor Test	Best-fit Relationship	R-squared	Number of Proctor Test
sandy SILT/CLAY	2.5 kg	ρ_{wm} = -0.021 (w_o) + 2.399	0.789	965
silty/clayey SAND	2.5 kg	ρ_{wm} = 2.385 e $^{-0.009\, wo}$	0.752	2626
gravelly SAND	2.5 kg	ρ_{wm} = 2.996 (w_o) $^{-0.134}$	0.756	8084
sandy GRAVEL	2.5 kg	ρ_{wm} = 2.514 e $^{-0.012\, wo}$	0.691	1487
sandy GRAVEL	4.5 kg	ρ_{wm} = 2.491 e $^{-0.01\, wo}$	0.467	2790

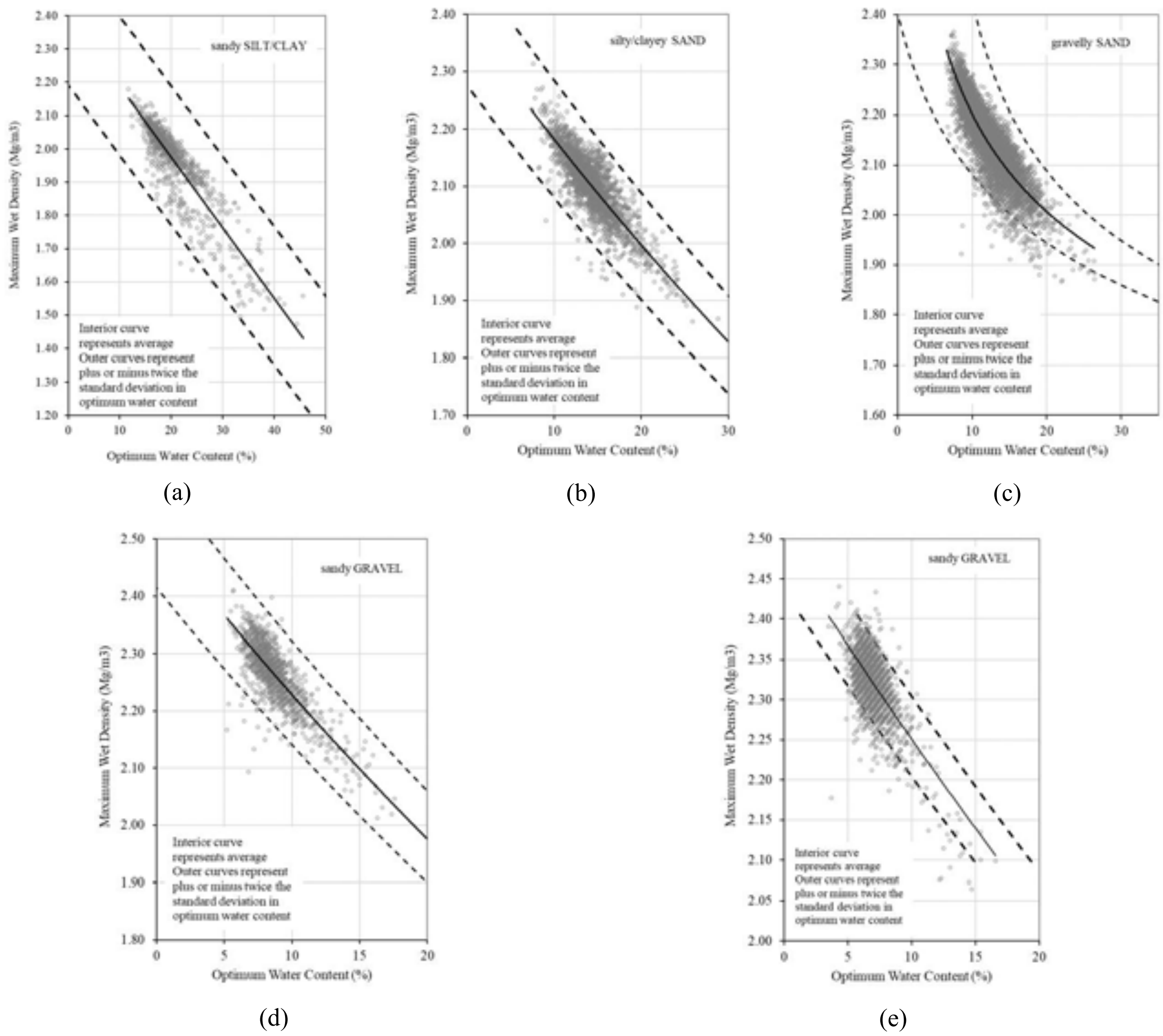

Figure 6: ρ_{wm} - w_o Relationship for (a) sandy SILT/CLAY (2.5 kg); (b) silty/clayey SAND (2.5 kg); (c) gravelly SAND (2.5 kg); (d) sandy GRAVEL (2.5 kg); and (e) sandy GRAVEL (4.5 kg)

The values of (w_f - w_o) determined from the Hilf method based on local ρ_{wm}-w_o relationships were plotted against the values of (w_f - w_o) with w_f determined from oven drying method and w_o from Proctor test (see Figure 7). The values of (w_f - w_o) determined from the Hilf method and oven drying method showed a linear relationship. Regression analysis showed that more that 90% of the data (w_f - w_o) were negative indicating that w_f at the time of carrying out SRT was mostly on the dry side of the w_o. About 50% of the data had w_f less than w_o more than 3%. This observation matched with the review carried out by Chung & Chu (2020) which showed that about 37% of 42,191 SRTs conducted under public works projects had w_f less than w_o more than 3%. The best fit curve established between (w_f - w_o) from the Hilf method and (w_f - w_o) from oven drying method and Proctor test attained a high R-squared of 0.844.

Similar to the comparison between D and RC values, the data of (w_f - w_o) from the Hilf method and oven drying method was re-analyzed based on soil types and compaction efforts used in the compaction tests. As shown in Figure 8, the differences were concentrated within ± 3% for all soil types and compaction efforts. About 11% of the data (as highlighted in red dash box) indicated that the compacted fill had w_f meeting the requirement in GS (i.e. w_f within ± 3% from w_o) while the compaction did not meet the requirements based on the results from oven drying method (i.e. $w_f < w_o$ -3%).

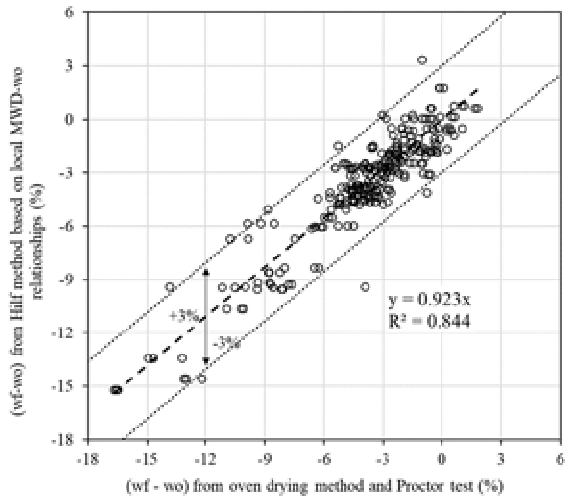

Figure 7: (w_f - w_o) determined from the Hilf method (based on local ρ_{wm} - w_o relationships) and oven drying method

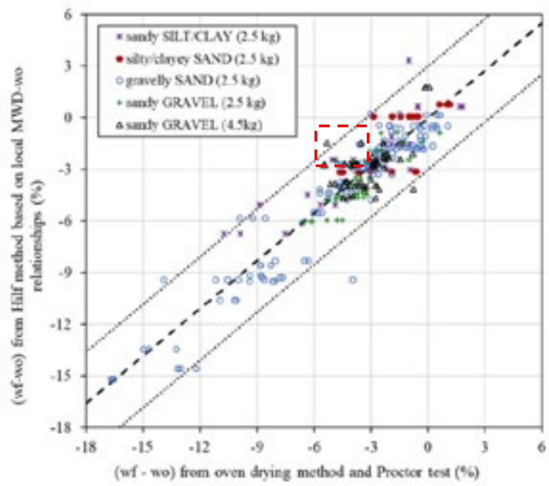

Figure 8: (w_f - w_o) determined from the Hilf method (based on local ρ_{wm} - w_o relationships) and oven drying method in different soil types

2.5 Review on the use of the Hilf method

The results show that there is a reasonably good correlation between “degree of compaction” from the Hilf method and SRT. There is also no significantly difference in “deviation from optimum moisture content” determined from the Hilf method and oven drying method. The findings suggested that the Hilf method can provide an alternative option for density control and moisture content control in compaction works should quick results are required. The use of the Hilf method may increase certain uncertainty of the compaction works and hence the engineer’s risk. Therefore, it is suggested that the Hilf method should not replace all the compaction control tests using RC and oven drying method as routine procedure. The Engineer/designer may decide an appropriate frequency of using the Hilf method taking into consideration of (a) the acceptance level of the uncertainty in compaction works; and (b) the calibration results of D (from Hilf method) and RC (from SRT) in the course of construction.

3 INFRARED WITH CONVECTION DRYING METHOD

3.1 Heating mechanism and performance of the oven with hybrid heating

The oven to be reviewed in the study adopts hybrid heating method with mid to far-IR radiation and convection heating. 16 pieces of IR panels are installed at top and bottom sides. Each IR panel is 0.2 kW and the total power of all panels is 6.4 kW. The interior of the oven is shown in Figure 9. There are two K thermocouples for the IR heater built in the center and one double K thermocouple for unit body temperature control using Proportional-Integral-Derivative (PID) controller. PID controller uses a control loop feedback mechanism to control process variables. It receives information from temperature sensors as input and compares the actual temperature to the target temperature, then provides output to control the heating sources. In this study, the target temperature of the convection heating source and IR panels were both set at 105ºC. Distribution of temperature inside the hybrid oven was reviewed based on the method of calculating the temperature deviation of the oven following a method suggested by Hong Kong Accreditation Service (HKAS) (HKAS 2019). The temperature deviation was found to fell within 1.79ºC and 2.17ºC with 60 minutes of pre-heating time; while ranged between 1.12ºC and 1.36ºC with 90 minutes of pre-heating time. These deviations well satisfy the requirement of ± 5ºC from 105ºC as specified in GEOSPEC 3 (GEO 2017).

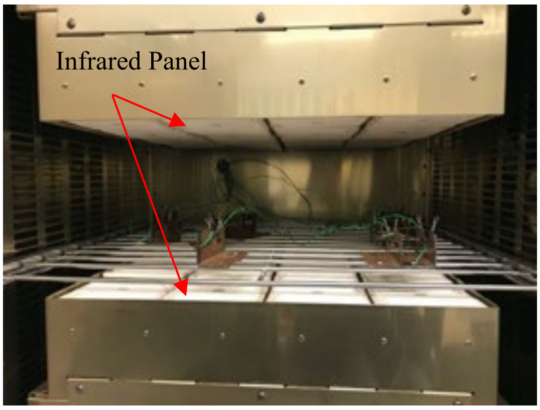

Figure 9: Internal Space of Hybrid Oven

Efficiency of the oven was also reviewed based on its ability to evaporate water. Following the Public Works Laboratories (PWL) Checking Procedure for Oven (PWL 2013), the average evaporation rate of the hybrid oven with convection and IR heating was about 50% to 57% higher than that of conventional oven with average measured temperature at 105.5ºC. Besides, dry uniform sand with particle size between 63 µm and 600 µm was used to review the capability of the oven to maintain the soil temperature without overshooting above 110ºC. As shown in Figure 10, temperature of all sand specimens achieved a mean temperature of about 105 ºC after 100 minutes then levelled off.

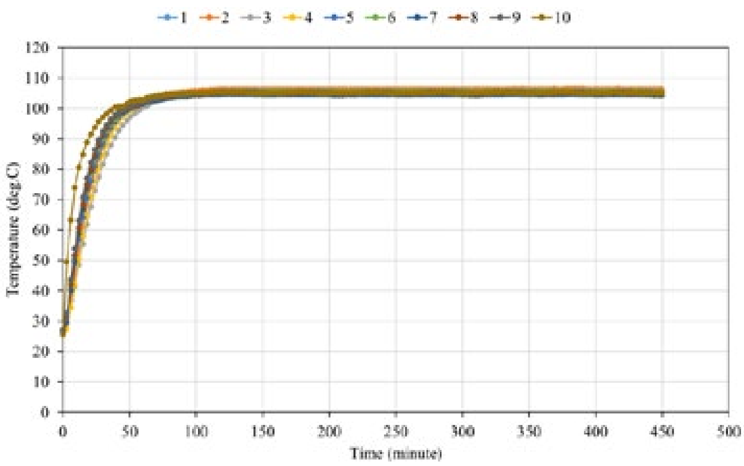

Figure 10: Temperature of dry uniform sand during drying period in hybrid oven

3.2 Test programme

Ten soil types, ranged from fine-grained to coarse-grained, were prepared for the study. The finest soil had 100% of particles passing 63 µm test sieve whereas the coarsest soil has 10% of particles larger than 37.5 mm with the maximum particle size limited to 50 mm. Fine soil with all particles passing 63 µm test sieve is considered rarely in use for fill compaction works in Hong Kong and this soil type probably represents a worse composition of materials in local filling works in practice. All soils were mixed with a specific amount of water to achieve a moisture content of about 3% above OMC in this study. Each specimen was prepared with a minimum mass of soil according to GEOSPEC 3 (GEO 2017) based on its particle size distribution.

The successive masses of the specimens after 3 hours and 3.5 hours under hybrid heating (with IR and convection heating at the same time) were measured and the mass of specimen after 3.5 hours of drying was used to determine the moisture content of the specimens. Afterwards, the specimens were transferred to conventional oven with temperature set at 105 ± 5ºC for further drying of 24 hours. In this period of time, the specimens were subject to convection heating solely which was same as that in routine moisture content test according to GEOSPEC 3 (GEO 2017). Moisture content of the specimens after drying in conventional oven was determined. Hybrid heating is considered acceptable for rapid moisture content determination with drying time of 3.5 hours if there is no significant difference between moisture content values obtained from hybrid heating and subsequent conventional heating. The drying criterion of hybrid heating (i.e. difference in any two successive weighings of the specimens, taken after 3 hours and 3.5 hours of drying, less than 0.1% of the initial soil mass) was examined as well.

3.3 Test results

Three fine-grained soil types, with a total of 54 specimens, were tested. For specimens with initial mass of at least 30 g, the differences in successive weighings of most specimens after hybrid oven and conventional oven drying ranged between -0.09 g to 0.07 g, except one with value of 0.24 g. The differences led a small variation of less than 0.4% in moisture contents between two drying methods for most of the specimens (about 93% of the specimens). The small variation in moisture content indicated that moisture in fine-grained soils were successfully removed within 3.5 hours using hybrid drying method. 7 out of 54 specimens (about 13% of specimens) did not meet the drying criterion for hybrid oven drying. The difference in successive weighings was more than 0.1% of the initial soil mass with the largest value of 0.42% (equivalent to 0.13 g).

Five medium-grained soil types, with a total of 105 specimens, were tested. The differences in successive weighing of specimens after hybrid oven and conventional oven drying fell within a range of 0.01 g to 0.92 g for specimens with minimum initial mass of 300 g. The differences resulted in changes of less than 0.4% in moisture contents determined from two oven drying methods for most of the specimens. The small changes revealed that moisture in medium-grained soils were successfully removed within 3.5 hours using hybrid drying method. Similar to fine-grained soil, small proportion of specimens (about 17%) had successive mass difference between 3 hours and 3.5 hours of drying more than 0.1% of the initial soil mass, with highest value of 0.6% (equivalent to 1.8 g).

While for coarse-grained soil, 8 specimens in three soil types were tested. The changes in successive weighting of specimens after drying in two ovens were between -0.9 g and 5.3 g for specimens with minimum initial mass of 3000 g. These changes caused the differences were less than 0.3% in moisture contents determined from two oven drying methods. The test results indicated that moisture in coarse-grained soil was also successfully removed by hybrid drying method. Only one specimen slightly deviated from the drying criterion for hybrid oven with value of 0.16% (equivalent to 4.8 g).

Throughout the drying process, temperature of all specimens were well controlled below 110 ºC.

3.4 Discussions

Based on the experimental test results, the oven with hybrid drying method (IR with convection heating) was capable to maintain the target temperature with a deviation less than that required in conventional drying method stipulated in GEOSPEC 3 (GEO 2017). The higher evaporation rate of about 50% more than that of conventional oven indicated that the performance of the hybrid oven was elevated in terms of the efficiency of removing water. The requirement of maintaining soil temperature without exceedance of 110ºC was also satisfied.

Drying method with the adoption of both IR and convection heating was applicable to determine moisture content of fine-grained to coarse-grained soil rapidly, within 3.5 hours of drying, if soil has a moisture content 3% above the OMC. Figure 11 shows the moisture content determined from hybrid oven drying and subsequent convection oven drying for all soils in this study. A linear relationship between moisture content from two drying methods with the R-squared of 1 was determined. The mean and the standard deviation of the difference between two moisture contents were only 0.01% and 0.17% respectively. The test statistic was 0.837 which was lower than the critical value of 1.974 for significant level of 0.05 and with degree of freedom of 166. The null hypothesis for no difference in moisture content determined from two drying methods could not be rejected. In other words, the moisture contents determined from these two drying methods could be considered as statistically identical for a significant level of 5%. Besides, the difference between the moisture content determined from hybrid oven and conventional oven drying was in general less than 0.4% for different soil types. The difference is considered practically insignificant for geotechnical engineering applications.

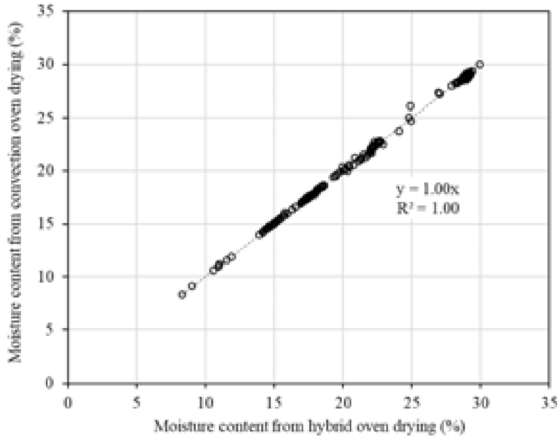

Figure 11: Moisture Content Determined from Hybrid Oven Drying versus Moisture Content Determined from Convection Oven Drying

Regarding the termination criterion for IR and convection heating method, the comparison illustrated that soil could be deemed to be dried if the successive weights of specimens taken half-hourly after 3 hours of drying with IR and convection heating was less than 0.1% of the original mass of the specimen. For some specimens which cannot meet this drying criterion, it is recommended that the specimens to be returned to the hybrid oven for successive drying and weighted at half-hourly intervals until the drying criterion is satisfied. It is expected that the difference in moisture contents between two oven drying methods would be further reduced, less than 0.4%.

To provide more effective drying, it is suggested that soil specimen should be crumbled and placed loosely in the container. As the temperature during drying process is up to 110ºC, the method is considered not suitable for soils containing gypsum, calcareous or organic matter. Drying by other means (e.g. in convection oven at 45ºC) is considered more appropriate.

4 CONCLUSION

This paper examined two quick methods in measuring RC and moisture content. 271 pairs of results from 102 field trials conducted in public works project showed that there is a reasonable good correlation between “degree of compaction” from the Hilf method and sand replacement test. There is also no significant difference in “deviation from optimum moisture content” determined from the Hilf method and oven drying method. The findings of the review suggested that the Hilf method can provide an alternative option for density control and moisture content control in compaction works for fine to coarse-grained soil should quick results be required.

There was practically no difference in the moisture content results determined from the hybrid oven and conventional oven based on 167 test results on 10 soil types from fine to coarse-grained soils. The results also showed that moisture content test with hybrid drying could be completed within 3.5 hours for soils with moisture content of about 3% above optimum moisture content. The study demonstrated that hybrid drying with IR and convection heating is a reliable and quick alternative method to determine moisture content for most of the soils encountered in compaction works in Hong Kong.

ACKNOWLEDGEMENTS

This paper is published with the permission of the Head of the Geotechnical Engineering Office and the Director of Civil Engineering and Development, the Government of the Hong Kong Special Administrative Region.

REFERENCES

ABNT. 1991. *Solo - Controle de Compactação Pelo Método de Hilf.* Rio de Janeiro: ABNT (MB-3443).

ASTM. 2017. *Standard Test Method for Rapid Determination of Percent Compaction*, ASTM - D5080, ASTM International.

AS. 2006. *Methods of Testing Soils for Engineering Purposes - Method 5.7.1: Soil Compaction and Density Tests – Soil Compaction and Density Tests – Compaction Control Test – Hilf Density Ratio and Hilf Moisture Variation (Rapid Method) - Standard Method*. AS 1289.5.7.1-2006.

Chung, P.W.K. & Chu, F.L.F. 2020. *Review of Quality Control of Fill Compaction Works in Hong Kong*. Proceeding of HKIE Geotechnical Division Annual Seminar 2020, Hong Kong Institution of Engineers - Geotechnical Division, 2020.

GEO. 2017. *GEOSPEC 3 - Model Specification for Soil Testing*, Geotechnical Engineering Office, Civil Engineering and Development Department, HKSAR.

Hilf, J.W. 1957. *A Rapid Method of Construction Control for Embankments of Cohesive Soil*. American Society for Testing and Materials, Philadelphia. Special Technical Publication 32.

Hilf, J.W. 1961. *A Rapid Method of Construction Control for Embankments of Cohesive Soil* (Revised in September 1961). Engineering Monographs, (26). United States Department of the Interior, Bureau of Reclamation.

HKAS. 2019. *Guidance on Calibration and Performance Verification of Temperature Chambers (Informative)*, HKAS Information Notes No. 3, Issue No. 3.

HKG. 1992. *General Specification for Civil Engineering Works (1992 Edition)*. The Hong Kong Government.

HKSARG. 2020. *General Specification for Civil Engineering Works (2020 Edition)*. The Government of the Hong Kong S.A.R.

Masanobu Hasatani, Yoshinori Itaya and Kouji Miura. 1988. *Hybrid Drying of Granular Materials by Combined Radiative and Convection Heating*, Drying Technology, 6(1): 43-68 (1988).

Mortaza Aghbashlo. 2016. *Exergetic Simulation of a Combined Infrared-convection Drying Process*, Heat Mass Transfer, Vol. 52, No. 4: 829-844.

PWL. 2013. *Checking of Oven - PWCL Checking Procedure No. 22*, Issue 3, 2013.

Tiller, F.M. and Garber, H.J. 1942. *Infrared radiant heating*, Ind. Eng. Chem., 34: 773 - 781.

USBR. 1990. *Procedure for Preforming Rapid Method of Construction Control*. USBR 7240, Earth Manual, Part 2, Third Edition, US Bureau of Reclamation (USBR).

USBR. 2012. *Design Standards No. 13, Embankment Dams, Chapter 10: Embankment Construction.* The Bureau of Reclamation. 91 p.

Laboratory Studies on the Characteristics of Public Fill used in Reclamation Project in the Deep-sea Area

Z X Cao, Y Chen, J Chen, Q Xu
China Harbour Engineering Company Ltd, Hong Kong, China

ABSTRACT

To reduce solid wastes and recover useful resources, an artificial island in the deep-sea area was built and it was planned to use the sorted public fill as the replacement of sand in the land reclamation. The use of the public fill as the replacement of sand not only reduced the CO_2 emission, but also shortened the construction period. Although the use of public fill gives benefits to environmental sustainability, the public fill is rarely used in Hong Kong for reclamation in the deep-sea artificial island. Furthermore, the short-term and long-term post-construction settlement due to surcharge load is a key issue in the reclamation work, while limited information of the physical and mechanical properties of the public fill could be found in the past engineering projects. In addition, there are many uncertainties and influencing factors in the construction site such as the surcharge load magnitudes, modes of the loading process, and the variability of geotechnical parameters. How these factors influence the mechanical behavior of the public fill is an interesting issue. This paper gives first-hand laboratory test results accompanied by theoretical analysis to address the mentioned issues. After a comprehensive and careful measurement of several basic engineering properties, such as bulk density, particle size distribution, and Atterberg limits, large-scale oedometer tests were systematically conducted to study the compressibility of the public fill. It is found both volume compressibility and consolidation coefficient decrease with an increasing axial effective stress. An interesting finding is that an increasing fines content with a certain range will lead to an increase in the compressibility of the public fill, indicating the fines content may need to be considered in the land reclamation works. In addition, remarkable creep could be observed if the current vertical stress is lower than the preloading pressure. After obtaining design parameters and ensuring allowable settlement through both in-house laboratory tests and in-situ field tests, the project in the technical paper may be a good reference for future land reclamation design and construction cases.

1 INTRODUCTION

The project was constructed to substantially reduce the bulk size of mixed waste and to recover useful resources. The project was built on an artificial island in the deep sea. In this project, it was planned to use the sorted public fill as the replacement of sand in the land reclamation. Although the use of public fill gives benefits to construction cost and environmental sustainability development compared to sand, the public fill is rarely used in Hong Kong for reclamation in the deep-sea artificial island. Furthermore, the short-term and long-term post-construction settlement due to surcharge load is a key issue in the reclamation work. Accurate estimation of consolidation settlement is very important during design of reclamation structures. In geotechnical engineering, standard oedometer tests are conducted to investigate compressibility of soils due to applied loading. The tests are performed by adding constraint of zero radial strain and applying axial stress under saturated conditions, in which the excess pore-water pressure dissipates with time, leading to deformation. Terzaghi (1943) was the first one who proposed mathematical theory of one-dimensional consolidation. However, Terzaghi's theory did not consider the creep effect of clayey soils. In reclamation projects in Hong Kong, ground settlements are mainly due to creep, water level change, and surcharge. This implies the creep behaviors of clayey soils are very important in HK local practice. Yin and Graham (1996) proposed an elastic visco-plastic (EVP) constitutive model to calculate settlements and excess pore water pressures in clays under multi-stage constant vertical loads. The EVP model was used to study the influence of soil thickness on settlements, pore water pressure dissipation, stress and strain. It was concluded the model was capable to simulate the viscous nature of soils and the predicted results were in good agreement with the test data. The framework gives simple and helpful way to estimate creep behavior in reclamation work (Nash and Ryde, 2001; Feng *et al*., 2017).

This paper gives first-hand laboratory test results accompanied by theoretical analysis to explore the mechanical behavior of the public fill used in the deep-sea area. After a comprehensive and careful measurement of several basic engineering properties, such as bulk density, particle size distribution, and Atterberg limits, large-scale oedometer tests were systematically conducted to study the compressibility of the public fill. It is found both volume compressibility and consolidation coefficient decrease with an increasing axial effective stress. An interesting finding is that an increasing fines content with a certain range will lead to an increase in the compressibility of the public fill, indicating the fines content may need to be considered in the land reclamation works. In addition, remarkable creep could be observed if the current vertical stress is lower than the preloading pressure. After obtaining design parameters and ensuring allowable settlement through both in-house laboratory tests and in-situ field tests, the project in the technical paper may be a good reference for future land reclamation design and construction cases.

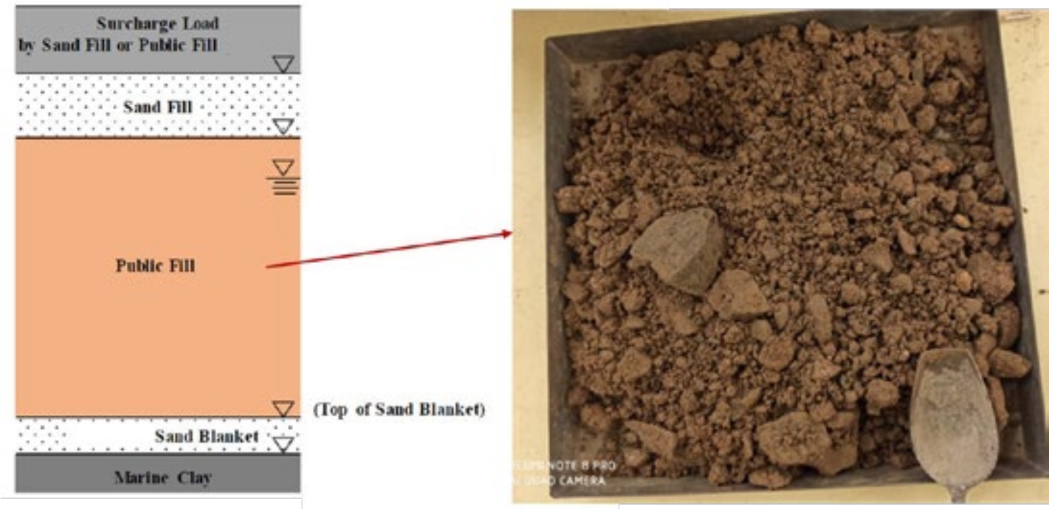

Figure 1 Simplified soil profiles and public fill used in the tests

2 TEST ARRANGEMENTS

2.1 Test for basic physical properties

The tests were conducted in the laboratory in the Hong Kong Polytechnic University and detailed summary of the test procedures and test data analysis was conducted by Liu *et al.* (2020). Before conducting oedometer test, the basic physical properties of the public fill (e.g. particle size distribution, moisture content, relative density, and Atterberg limits) was determined in the soil laboratory. It should be noted the test procedures of maximum dry density test, PSD test, Atterberg limits test were in accordance with GeoSpec. 3 (2017). The minimum dry density test was conducted based on BS 1377-4 (2002). Figure 2 shows the PSD curve of the public fill. Table 1 summarizes the basic properties of the public fill in the test No. LOT-2, LOT-4, LOT5.

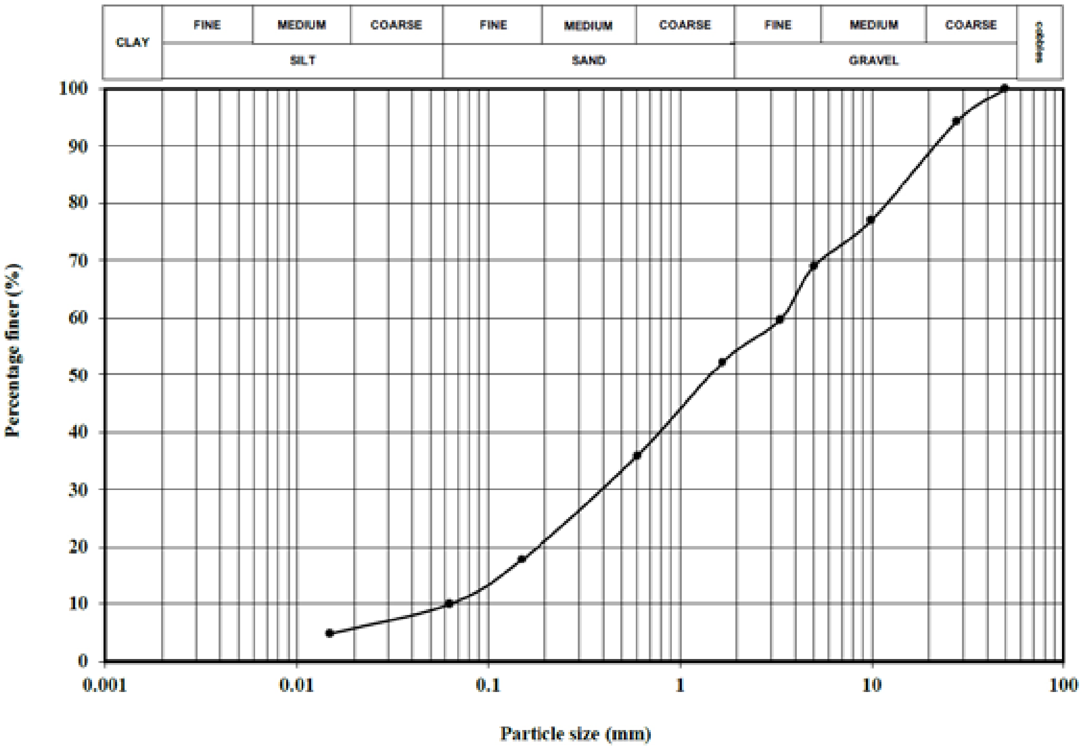

Figure 2. Particle size distribution of test No. LOT-2

Table 1. Summary of PSD, Atterberg limits, optimum water content, and maximum dry density

Test Items	LOT-2	LOT-4/LOT5
Particle Size Distribution:		
D_{60} (mm)	3.35	1.5
D_{10} (mm)	0.063	0.018
C_u (mm)	53.17	83.33
Atterberg Limits:		
Plastic limit (%)	-	28.3
Liquid limit (%)	-	43.2
Plasticity index (%)	-	14.9
Optimum Water Content and Maximum Dry Density:		
Optimum water content (%)	12.3	16.8
Maximum dry density (g/cm^3)	2.256	2.161

2.2 Multi-staged large-scale oedometer test

Figure 3 shows the arrangements of the large-scale oedometer test. Specifically, a steel-made cylinder model with a diameter of 300 mm and a height of 450 mm was used to conduct the large-scale oedometer tests. A pore water pressure transducer was placed in the large-scale oedometer test to monitor the changes of pore water pressure. The axial effective stress, vertical displacement, pore water pressure, and time were measured during the test process. There are three test schemes LOT-2, LOT-4, and LOT-5, which were conducted under various initial void ratios, fines content, and loading sequence. For test scheme LOT-2, the moisture content and relative density at 25kPa effective stress are 34.2% and 52.8%. The void ratio after sample preparation is 0.742 and the void ratio after test is about 0.534. The detailed procedures of the multi-stages oedometer test is summarized as follows:

(a) (b)

Figure 3. Multi-staged large-scale oedometer test:
(a) 25kPa stage; (b) 200 kPa stage

(a) Calibrate the displacement and pore water transducers.
(b) Set up the cropped permeable geotextile membranes and filter paper at the bottom. Weigh and place the public fill in the cylinder model. Place filter paper, permeable geotextile membrane, and punched steel plate on the soil surface.
(c) Apply an initial loading.
(d) Weigh and place the public fill by controlling a constant height. Place a pore water pressure transducer in the middle of the second layer.
(e) Conduct multi-stages oedometer tests with various loading sequence. For example, LOT-2 test was conducted by increasing axial stress from 25kPa to 400kPa. An unloading stage was performed by reducing axial stress from 400kPa to 200kPa. A one-week creep test was conducted by keeping axial effective stress of 200kPa for one week. Measure the settlement and pore water pressure at all test stages.
(f) Measure the moisture content after completion of test.

3 RESULTS AND DISCUSSION

In this part, detailed discussion of the test results will be conducted, particular emphasis is given to explore the compressibility and time-dependent behavior of the public fill.

3.1 Compressibility parameters of the public fill

The public fill is the inert material arising from construction and demolition activities which was used in the reclamation and building of artificial island in deep sea, the compressibility of the material is an important factor in the deformation prediction. In this study, some compressibility parameters are introduced and calibrated based on test results, which may improve and complete the test database of the soils in this project. To evaluate the compressibility of the public fill, the variation of the axial strain with the axial effective stress is plotted in Figure 4. During data analysis, the compression parameter (λ/V), which is defined as the slope of the consolidation path in the ε_z and $\ln(\sigma_z)$ plot, is proposed to measure the engineering properties of the public fill:

$$\frac{\lambda}{V} = \frac{\Delta \varepsilon_z}{\Delta \ln \sigma_z} \quad (1)$$

where $\Delta\varepsilon_z$ = change of the axial strain, $\Delta\ln\sigma_z$ = change of the axial stress, $V = 1 + e_0$ is the initial specific volume, e_0 is the initial void ratio. The compression ratio (CR) and the recompression ratio (RR) are introduced to evaluate soil behaviors under normal consolidated and over-consolidated conditions.

$$CR = \frac{C_c}{V} = 2.3\frac{\lambda}{V} \tag{2}$$

$$RR = \frac{C_r}{V} = 2.3\frac{\kappa}{V} \tag{3}$$

where κ = the slope of the unloading or reloading path in the ε_z and $\ln(\sigma_z)$ plot of soils under over-consolidated conditions. The volume compressibility (m_v) is defined as follows:

$$m_v = \frac{\Delta\varepsilon}{\Delta\sigma} \tag{4}$$

where $\Delta\varepsilon$ = the change of the strain, $\Delta\sigma$ = the change of effective stress. In this study, the coefficients of consolidation are evaluated using Casagrande Logarithm of Time Method (CA) and Taylor Square Root of Time Method (TA) (Olek, 2019). Specifically, the coefficient using CA method is defined as $C_v = 0.197H^2 / t_{50}$, and TA method gives $C_v = 0.848H^2 / t_{90}$, where Cv is coefficient of consolidation, t_{50} is time period for 50% consolidation, t_{90} is time period for 90% consolidation.

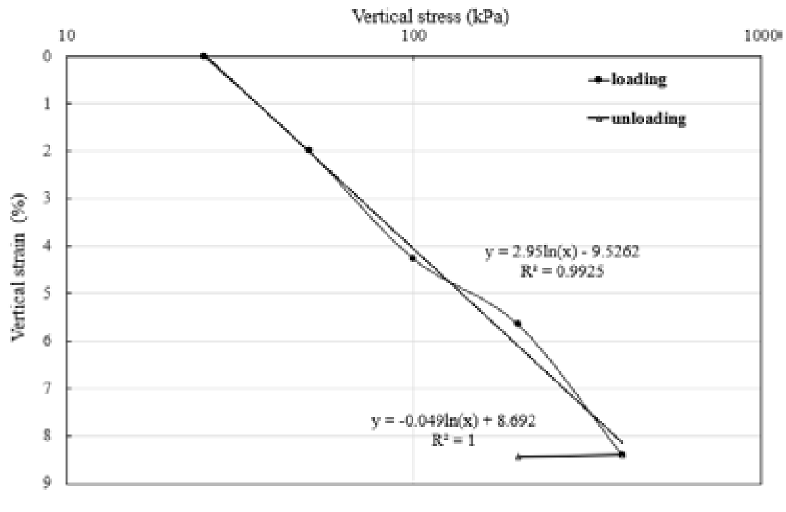

Figure 4 The variation of axial strain with axial effective stress in No. LOT-2 test

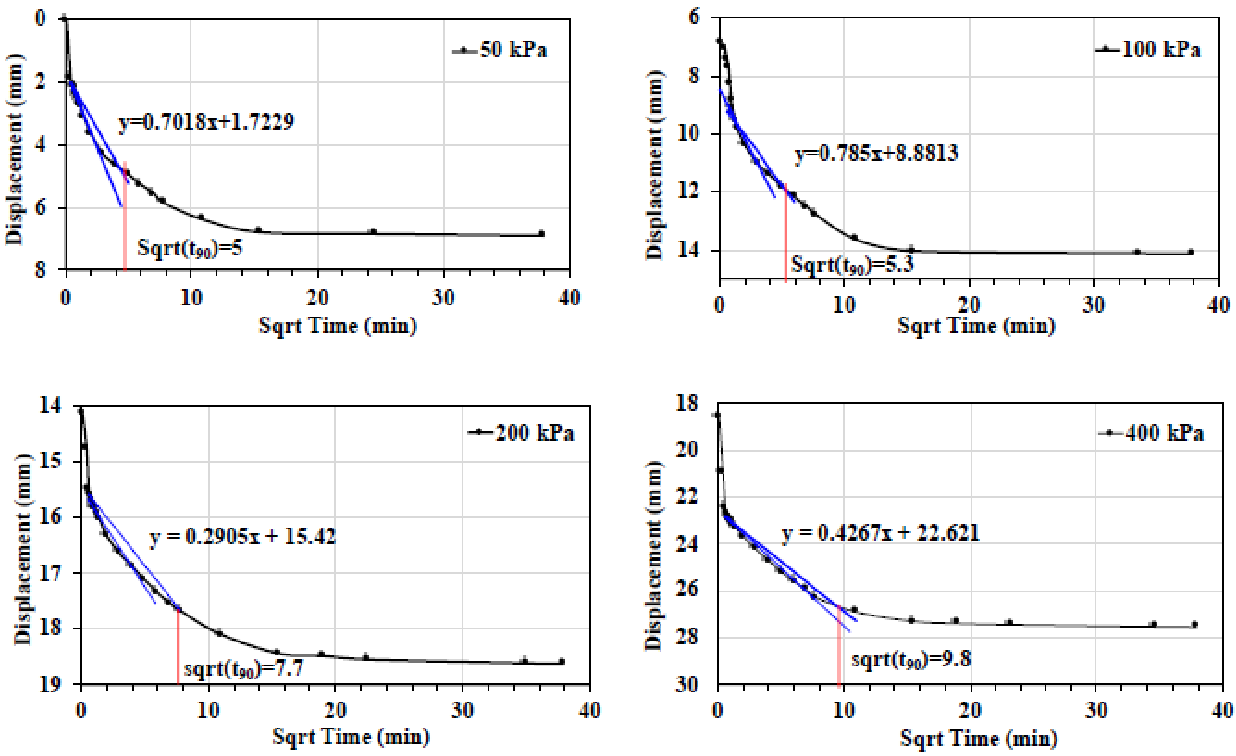

Figure 5 The coefficients of consolidation evaluated using Taylor Square Root of Time Method (TA) in No. LOT-2 test

Figure 4 shows the relationship between axial/vertical strain and axial/vertical effective stress of the public fill in No. LOT-2 test. There are two test stages, namely, loading and unloading. The compression parameter, compression ratio, recompression ratio, volume compressibility could be directly or indirectly obtained from the data points after conducting data analysis. Figure 5 gives detailed procedure of evaluating consolidation coefficients of the soil sample subjected to various axial effective stresses. Table 2 gives a comprehensive summary of compressibility parameters of LOT-2, LOT-4, LOT-5 tests with various axial effective stress and void ratio. It can be found the compression parameters (λ/V) of LOT-2, LOT-4, LOT-5 are 0.0295, 0.0433, and 0.0420, respectively. The compression ratios (CR) of these samples are 0.07, 0.10, 0.10. The recompression ratios (RR) are 0.00113, 0.00873, 0.00562. It can be observed that the volume compressibility (m_v), the coefficients of consolidation based on CA and TA methods are sensitive to the axial effective stress, and those mechanical coefficients decrease with an increasing axial effective stress. It should be noted different compressibility parameters of the public fill of LOT-2, LOT-4, LOT-5 may be due to different particle size distribution, particle minerology, fines content of test materials.

Table 2. Summary of compressibility parameters of the test materials

Test No.	Axial effective stress (kPa)	Void ratio (-)	λ/V (-)	κ/V (-)	CR (-)	RR (-)	m_v (kPa^{-1})	C_v based on CA (m^2/year)	C_v based on TA (m^2/year)
LOT-2	50	0.644	0.0295	0.00049	0.07	0.00113	0.00080	304.01	418.76
	100	0.606					0.00045	262.53	362.08
	200	0.583					0.00014	139.13	161.62
	400	0.536					0.00014	138.88	99.60
LOT-4	50	0.793	0.0433	0.00379	0.10	0.00873	0.00176	110.97	83.07
	100	0.751					0.00058	48.30	47.14
	200	0.705					0.00023	46.07	57.50
	400	0.650					0.00014	43.58	54.39
LOT-5	50	0.838	0.0420	0.00244	0.10	0.00562	0.00135	79.06	82.57
	100	0.791					0.00058	60.91	40.01
	200	0.741					0.00025	59.07	38.45
	400	0.683					0.00016	58.11	38.39

The fines content can influence the mechanical behavior of soils (Yang and Wei, 2012). To validate the effect of fines content on the compressibility of the public fill, the fines contents of three samples of LOT-2, LOT-4, LOT-5 were quantified using the results from particle size distribution (PSD) tests, and the fines contents of LOT-2, LOT-4, and LOT-5 are 11%, 26%, and 26%. Figure 6 shows the influence of the fines content on the compressibility (m_v) of the public fill. Clearly, it can be observed that an increase of the fines content from 11% to 26% could lead to an increase of m_v of materials subjected to various axial effective stress, which means an increasing fines content with a certain range will lead to an increase in the compressibility of the public fill and the fines content may need to be considered during design and construction of the land reclamation works.

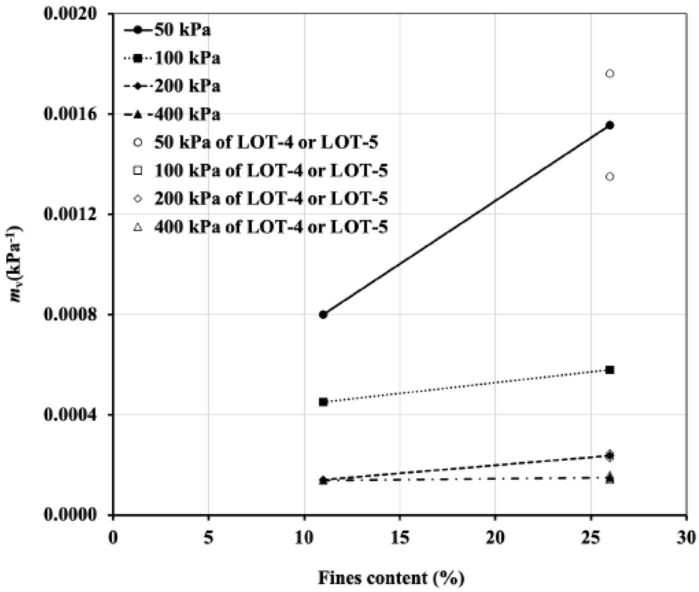

Figure 6 The effect of fines content on m_v

3.2 Creep behaviour

The time-dependent mechanical behavior of soils is very important to estimate the long-term settlement of ground in the land reclamation works. Feng *et al*. (2017) studied the long-term non-linear creep and swelling behavior of marine deposits by doing oedometer tests. Detailed interpretation and discussion of creep/swelling behaviors and the mechanism of granular particles was made, contributing to in-depth understanding of long-term non-linear creep and swelling behavior of HK Marine Deposit. In this study, the creep behavior of the public fill will be summarized using the test results from Liu *et al*. (2020).

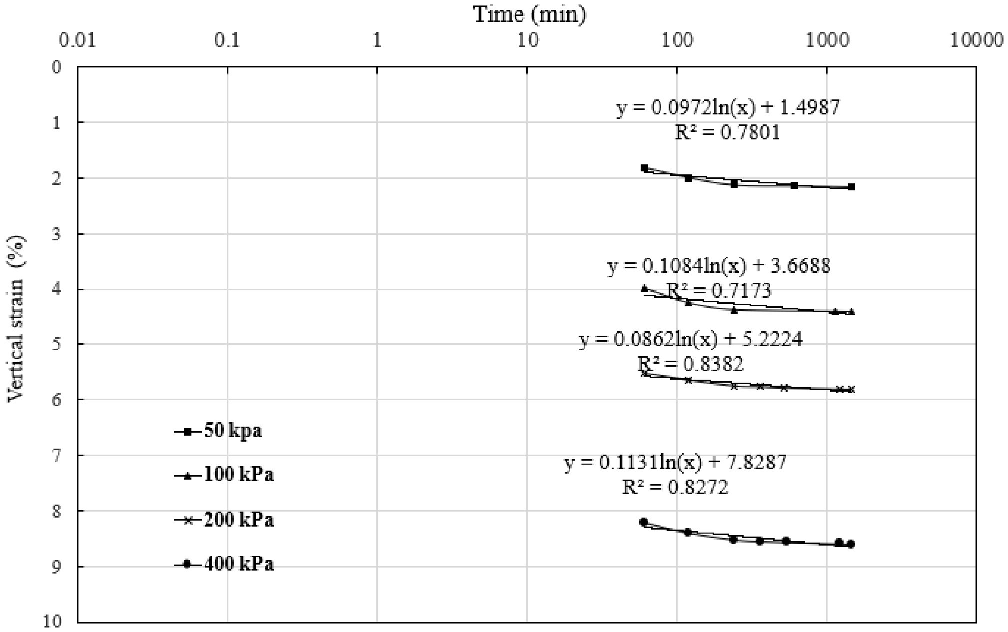

Figure 7 The relationship between axial/vertical strain with time of LOT-2 samples in the oedometer test

Figure 7 shows the relationship between axial/vertical strain with time of LOT-2 samples in the oedometer test. The creep parameter (ψ/V) in defined as follows:

$$\varepsilon_z = \varepsilon_{z0} + \frac{\psi}{V} \ln\left(\frac{t_0^c + t_e^c}{t_0^c}\right) \tag{5}$$

where t_e^c = creep equivalent time proposed by Yin and Graham (1994); t_0^c = time parameter corresponding to the beginning of creep time; ε_{z0} = strain when $t = t_0^c$. After knowing the creep parameter (ψ/V), the logarithmic creep compression rate (α) is defined as follows:

$$\alpha = 2.3\frac{\psi}{V} \tag{6}$$

Table 3 summarizes the creep parameter (ψ/V) and creep compression rate (α). It can be found these creep parameters are sensitive to the axial stress level, loading type, and material characteristics such as fines content and particle size distribution (Feng *et al*., 2017). Specifically, the loading history, which covers loading, unloading, and reloading process during oedometer test, has significant influence on the creep behavior of sandy soils. It can be found creep parameters (ψ/V) of LOT-4 in the reloading process are smaller compared to creep behavior in the loading process. This means creep behavior is minor if the public fill was subjected to large preloading pressure and the preloading process with reasonable axial stress level should be carefully considered during design and construction of embankment works. It should be noted large preloading pressure is the larger axial effective stress applied at loading stage in the lab test, and it is an observation from the lab test results of LOT-4. When 400kPa axial effective stress is applied at the loading stage, the creep parameter and the logarithmic creep compression rate for axial effective stress 50kPa, 100kPa and 200kPa are very small at reloading stage compared with the same axial effective stresses at loading stage. The reduction of the creep behavior if the public fill was subjected to preloading history may be due to loading-history induced particle rearrangement or particle crushing (Liu *et al*., 2020), and more detailed studies such as imaged-based micro-scale analysis or DEM analysis may be needed to further explore the mechanism of loading-history dependent creep behavior. As for the effect of axial stress on the creep behavior during loading stage, it is found that the creep parameter (ψ/V) decreases (despite some deviation) with an increasing axial effective stress. In summary, the test results show that the creep behavior of the public fill is significantly influenced by the preloading history.

Table 3. Creep parameters of the public fills

Test No.	Axial effective stress (kPa)	Loading type	ψ / V (-)	α (%)
LOT-2	50	Loading	0.00097	0.224
	100	Loading	0.00108	0.249
	200	Loading	0.00086	0.198
	400	Loading	0.00113	0.260
LOT-4	50	Loading	0.00400	0.920
	100	Loading	0.00203	0.468
	200	Loading	0.00216	0.497
	400	Loading	0.00196	0.452
	50	Reloading	0.00001	0.001
	100	Reloading	0.00008	0.019
	200	Reloading	0.00012	0.028
LOT-5	50	Loading	0.00299	0.687
	100	Loading	0.00185	0.426
	200	Loading	0.00243	0.559
	400	Loading	0.00096	0.221
	50	Reloading	0.000004	0.001
	100	Reloading	0.000033	0.008
	200	Reloading	0.00005	0.012

It should be noted this technical paper summarizes the compressibility and creep behavior of the public fill in the land reclamation work in the deep sea using in-house laboratory test data. The large scale oedometer tests were conducted using distilled water during the laboratory investigation. Secondly, there are many uncertainties in the construction site such as relative densities, fines content, surcharge load magnitudes and loading history, depth of the public fill, fabric anisotropy, making it challenging to represent and predict short-term and long-term settlement using analytical methods, constitutive models, and FEM software. This means in practice, the ground profiles, material behaviors, performance of constitutive models, model input parameters should be carefully studied and interpreted based on empiricism. In addition, there are many construction activities in the construction site such as excavation and lateral support, bored pile and steel H pile installation, machine foundation design and construction. More detailed numerical and laboratory studies on the drained and undrained shear strength, soil-structure interaction, dynamic properties, liquefaction resistance may need to be further explored in the future.

4 CONCLUSIONS

This paper gives first-hand laboratory test results accompanied by theoretical analysis to address the compressibility and the creep of the public fill used in a reclamation work of an artificial island. After a

comprehensive and careful measurement of several basic engineering properties, such as bulk density, particle size distribution, and Atterberg limits, large-scale oedometer tests were systematically conducted with different confining pressures and fines contents to study the compressibility of the public fill. It can be found that:
(1) Both volume compressibility and consolidation coefficient decrease with an increasing axial effective stress.
(2) An increasing fines content with a certain range will lead to an increase in the compressibility of the public fill, indicating the fines content may need to be considered in the land reclamation works.
(3) Remarkable creep of the public fill could be observed if the current vertical stress is lower than the preloading pressure.

ACKNOWLEDGEMENTS

The authors would like to thank Prof. Jianhua Yin, Dr. Kai Liu, and Dr. Weiqiang Feng for sharing test data. The authors would like to express gratitude to colleagues in the China Harbour Engineering Corporation forsupport during paper preparation. The authors would like to thank the Geotechnical Division Committee of the HKIE for giving this opportunity.

REFERENCES

BS 1377-4 (2002). Method of test for soils for civil engineering purposes. *British Standards Institution*, UK.
BS EN ISO 17892-2 (2014). Geotechnical investigation and testing-Laboratory testing of soil. Part 2: Determination of bulk density. *British Standards Institution*, UK.
Yang, J., Wei, L.M. (2012). Collapse of loose sand with the addition of fines: the role of particle shape. *Geotechnique*, 62(12), 1111-1125.
Yin, J. H., Graham, J. (1994). Equivalent times and one-dimensional elastic viscoplastic modeling of time-dependent stress-strain behaviour of clays. *Canadian Geotechnical Journal*, 31(1), 42-52.
Yin, J. H., Graham, J. (1996). Elastic visco-plastic modelling of one-dimensional consolidation. *Geotechnique*, 46 (3), 515-527.
Nash, D.F.T., Ryde, S. J. (2001). Modelling consolidation accelerated by vertical drains in soils subjected to creep. *Geotechnique,* 51 (3), 257-273.
Feng, W. Q., Lalit, B., Yin, Z. Y., Yin, J. H. (2017). Long-term Non-linear creep and swelling behavior of Hong Kong marine deposits in oedometer condition. *Computers and Geotechnics*, 84, 1-15.
Liu, K., Feng, W. Q., Yin, J. H. (2020). The laboratory tests for the compressibility of public fill, Department of civil and environmental engineering, *The Hong Kong Polytechnical University*.

Digital Classification of Anthropogenic Features for Natural Terrain Hazard Assessment in the Quasi-natural Heritage Landscape of the Lin Ma Hang Lead Mine

Petra Lee, Collette Tse, Francis Lee, Geoffrey Pook, Kevin Styles
Meinhardt Infrastructure and Environment Ltd., Hong Kong, China

ABSTRACT

Much of the Hong Kong landscape consists of densely vegetated steep hillside and may give the impression of natural terrain untouched by man-made activities. However, much evidence of old human activities occurs in our vegetated landscape. The old lead mine workings in the Lin Ma Hang district of the northeast New Territories form a significant industrial heritage site now hidden by dense vegetation. Extensive old anthropogenic activities are seen in site reconnaissance. Most of the man-made features were formed during the mining period (1860-1960) and the WWII (1941-45) occupation of the mine site. Some features have more obscure origins associated with cycles of agricultural activity and settlement of more than 1000 years.

The unique and diverse nature of the Lin Ma Hang hillsides provides an ideal case study to demonstrate the benefits of systematic assessment of anthropogenic features in Natural Terrain Hazard Assessment. Some of these man-made features may create impacts as potential adverse Hillside Pocket scenarios and require inventory and classification during natural terrain hazard and other geotechnical studies (Ho & Roberts, 2016).

Over the past decade, the application of airborne LiDAR data for site characterization has grown significantly, in part due to advances in handling of very large data sets. Through 3D topographic models using LiDAR in combination with visual data, landforms are revealed and terrain classification is enhanced allowing identification of anthropogenic features of varying scale and origin within their geomorphological setting. The authors discuss the application of a digitally aided approach for terrain mapping with emphasis on the identification and classification of anthropogenic features based on size, type, origin, material, extent and location. These are classified within a Hong Kong-based framework of an 80 class classification following from Styles & Law (2012).

1 INTRODUCTION

1.1 Site description

The Lin Ma Hang Lead Mine is an abandoned mine site operated intermittently from 1860s until 1962. The site is located in the Sha Tau Kok area of Hong Kong and north of the Robin's Nest (Hung Fa Leng, +492mPD). The lower slopes abut the Lin Ma Hang and Sha Tau Kok Closed Frontier Roads on the border with Shenzhen. The Lead Mine is a significant historical mining site with a rich heritage linked with the local villages and a legacy of military conflict prior to and during WWII. The Natural Terrain Hazard Study Area (NTHSA) is the catchment above the entrance to the Mine Cavern Atrium to the north and south. The NTHSA has an area of some 4.5 ha and rises from an elevation of about +184mPD in the Cavern Atrium at the toe to +328mPD at the summit some 280m upslope (Figure 1).

Mining at the Lin Ma Hang can be traced back to the 1860s in the area of the Portuguese Workings adjacent to the Frontier Closed Road to Sha Tau Kok. The main mining activities commenced in 1913 operating intermittently under the control of several mining companies until 1958. Small-scale working by the Japanese occurred from 1941 to 1945 during WWII. In 1962, the Government rescinded the mining lease and the mine was abandoned.

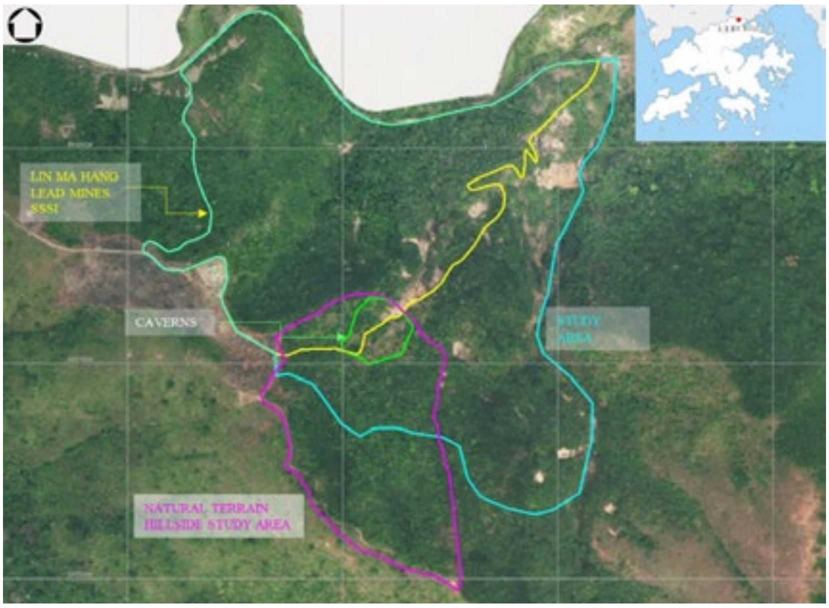

Figure 1: Site Layout (Cyan is the Project Study Area; green is the Mine Cavern; magenta is the NTHSA boundary; yellow is the SSSI boundary)

While the terrain in the NTHSA is generally masked by moderate to dense vegetation, extensive old anthropogenic features associated with cycles of agricultural activity, past mining, prospecting and military activity are seen during site reconnaissance. They consist of remnants of mining works including rubble walls, concrete platforms, building ruins, adits and shafts, open-cuts, water tanks, prospecting, military trenches and associated features. Remnants of very old agricultural practices also exist with rubble wall terraces and earthen step-form terraces. Together, the old anthropogenic features form a 'palimpsest' imprinted on the generally '*quasi-natural*' terrain settings across the Lin Ma Hang hillsides (Ho & Roberts, 2016).

1.2 Review of terrain classification

Regional and district scale systematic terrain classification in Hong Kong commenced in the late 1970s as part of the Geotechnical Area Studies Programme (Styles & Hansen, 1989). Over the following decade regional studies continued apace with many applications including computer generated maps (GEOTECS). The purpose of the GASP was to:

1. form a terrain classification inventory of physical land attributes (slope gradient, aspect, superficial / in situ geology, man-made slope features, developed/undeveloped land, erosion and instability using the geomorphological mapping techniques of aerial photograph interpretation (API) and field mapping; and
2. better understand the nature and distribution of landforms and instability using a variety of user-oriented derivative maps for planning and land management purposes.

In the 1990s and early 2000s terrain related studies in Government (GEO) focused more on targeted investigation with a departure from systematic area-based multi-attribute terrain classification approach to more conventional data capture. Having reduced landslide risk associated with much of the registered man-made slope features in the Territory, attention transferred to landslide hazards and instability on natural terrain. The 2400 natural terrain landslides on Lantau in June 2008 reinforced the need for study and mitigation. Many of the early Natural Terrain Hazard Studies in the mid-2000s and the 1963-based relict landslide mapping in the ENTLI in 2006-08 further confirmed the first API-based Site Histories in 1978 revealing old anthropogenic activities on undeveloped hillsides. Styles & Law (2012) highlighted some features and impacts on slope stability ranging from adverse, benign to beneficial depending on the engineering geological settings.

A shift in policy to remove Registered Disturbed Terrain features from the Catalogue of Slopes, coupled with a growing acceptance of the need to integrate old anthropogenic features on natural terrain led to a Hillside Pocket (HP) approach being included in Natural Terrain Hazard Assessment with the revision of GEO 138 (Ho & Roberts, 2016). Inventory of anthropogenic features in NTHA provided a potential method of applying the

HP-Pocket approach in a systematic manner. Digital methods enabled by airborne LiDAR integrated with API and field reconnaissance became a pragmatic method for mapping and identification of adverse settings.

Parry & Jonas (2007) discussed the use of LiDAR pilot study work for landslide hazard assessment in Hong Kong. With the first Territory-wide airborne Light Detection and Ranging (LiDAR) survey in 2010 (Lai et al, 2012) digital data became readily available for NTHS and streamlined systematic site characterization. Opportunities for automated mapping however, were limited by the restricted ability to process and manipulate very large data sets.

Application of LiDAR-derived DEM-based terrain classification has been discussed by others in terms of different data processing methodologies. Sas et al. (2012) described the identification of old agricultural terraces using Topographic Position Index (TPI) applied to LiDAR-derived Digital Elevation Models (DEM). Tam et al. (2017) integrated TPI and slope gradient and morphological data in GIS for automated geomorphological mapping in an Automated Integrated Mapping System (AIMS).

With the ever improving ability for hi-resolution LiDAR penetration of surface vegetation, detailed ground information can be captured as point clouds. High resolution capture and processing enable quality DEMs. Many approaches are available given advances in software and large data management. The DEM enable indirect mapping in software such as Geographic Information System (GIS) with derivation of topographic data of slope angle, aspect and detection of landform changes and man-made features.

With the improvement in LiDAR data resolution reflected in the 2020 Territory-wide survey, advances in data collection techniques coupled with processing enable a range of presentations. The concept of automated DEM-based terrain classification can be applied to the systematic identification and characterization of anthropogenic features of different size and origins. Classification of man-made features is important in assessing the potentially “adverse” Hillside Pocket scenarios during NTHS and join the five hazards (OHL, CDF, RF, BF & DS) for consideration (Ho and Roberts, 2016).

2 METHODOLOGY

2.1 Source of data

The most recent Territory-wide aerial LiDAR survey was conducted from December 2019 to February 2020 by the GEO (Wong, 2021) to obtain an airborne-LiDAR point cloud dataset. Processed ground return LiDAR data was used to generate high resolution DEM for the site. DEM can be interpolated in ArcGIS Desktop 10 using various spatial interpolation algorithms such as Inverse Distance Weighted (IDW), Triangulated Irregular Network (TIN) and Kriging. TIN model was used which generally provides higher resolution in areas that are highly variable and preserves precision of the input data.

A 0.25-m node distance in relation to the 0.25-m maximum point spacing for the 2020 LiDAR dataset was adopted. The choice of DEM cell size depends on the density of point cloud data and the scale of the study. A finer cell size was adopted in this study in order to identify anthropogenic features which are often around 0.5m in elevation.

2.2 Digital terrain mapping

GIS interprets land surface morphology in uniform grid squares, each grid is referred to as a “cell” of a raster surface. In a raster, every cell is given a value. A digital topographic model that stores raster values for terrain elevation is a Digital Terrain Model (DTM). ArcGIS software is capable of harnessing geospatial information of a DTM by mathematical abstraction to produce maps for visualisation, modelling and analysis.

Slope gradient is a major mobilisation factor associated with slope processes. Slope gradient data is a primary input in terrain classification derived from the DEM. Slope parameters are identified by steepness in each cell. In relation to slope raster, the lower the slope value, the flatter the terrain; the higher the slope value, the steeper the terrain. Slope gradient can be combined with morphology and aspect to refine determination.

2.3 Natural terrain hazard assessment

The site is considered as ‘densely-used open space’ and public waiting area - a Group 3 facility according to GEO Report No, 138 (2nd Ed.) (Ho & Roberts, 2016), and route upgrading will occur as part of the proposed mine cavern enhancement. Information boards and educational facilities will be constructed within and along walkways. The large mine cavern will be used for some educational display and shelter in adverse weather.

The NTHA is predominantly north-facing hillside, with slope gradients exceeding 15° within some 100m upslope from the Caverns. In accordance with GEO Report No. 138 (2nd Ed.) (Ho & Roberts, 2016), the guidelines for "Inclusion" and further screening in respect of natural terrain hazards are fulfilled.

3 APPLICATIONS IN LIN MA HANG

3.1 NTHS in Lin Ma Hang

The Natural Terrain Hazard Study Area (NTHSA) is quasi-natural hillside, predominantly underlain by coarse ash crystal tuff of the Tai Mo Shan Formation. Desk study involving a review of elevation data and Aerial Photograph Interpretation (API) reveals extensive evidence of old anthropogenic activities within the terrain.

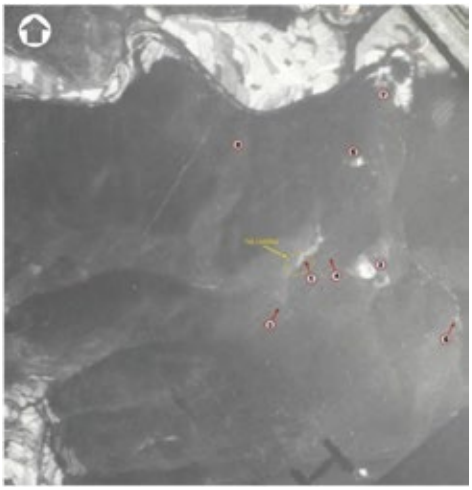

Plate 1: Aerial photograph in 1924. The cavern atrium, tailings dumps, open cast and numerous shafts and remnants of old terraces are evident.

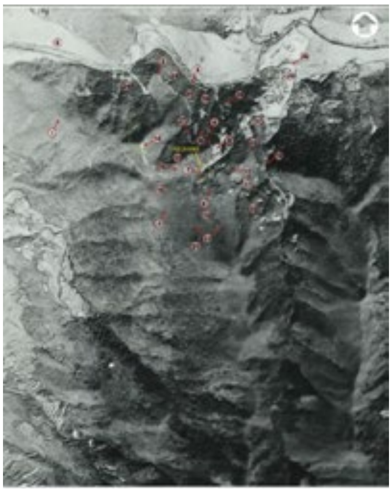

Plate 2: Aerial photograph in 1945. The cavern atrium, many tailings deposits, shafts, mine workings, military trenches and associated activities occur.

Plate 3: Aerial photograph in 1986. The last year that most of the old workings and remnants of terraces are evident before being masked by vegetation.

The "conceptual" geomorphological model is based on detailed API integrated with the 2010 and 2020 LiDAR and field reconnaissance as part of the traditional NTHA approach. As the information collection developed, the need for a more comprehensive systematic approach to better classify the terrain model was necessary. Due to the diversity and quantity of the anthropogenic features present, an automated approach was explored. The 1924 (Plate 1), 1945 (Plate 2) and 1986 (Plate 3) aerial photographs show the diverse range of anthropogenic features. In 1986 in particular, areas of bedrock, drainage lines, and zones of colluvial deposition are evident. After 1986 the NTHA becomes progressively more densely vegetated "quasi" natural terrain. The area largely consists of the moderately steep north-facing triangular-shaped hillside catchment, maximum elevation +330mPD, with a small section of southeast-facing open hillside catchment on the upper terrain, rising to +220mPD. A circular basin-like catchment is northeast of the mine. The lower sections of the three catchments meet along an east-west trending incised valley at about +185mPD. The mine atrium is at the toe. From the early 1990s, the ground surface, and with it most evidence of the past mine activity, has been almost completely obscured by the ever increasing density of vegetation. Recent aerial LiDAR surveys in 2010, and 2020 in particular, has enabled improved systematic characterization of the terrain surface revealing the morphology of the quasi-natural ground surface.

Field mapping was in July to August 2021 to verify API, LiDAR and desk study findings, and determine the geological, geomorphological and hydrological conditions. Field work focused on mapping the regolith, landslide features, topographic depressions, drainage lines, prominent rock outcrop, boulders, water inflow, traces of seepage and the extensive impacts of mining related and other anthroprogenic activity. The overall geomorphological characteristics of the mine are consistent with those identified in API integrated with the 2020 LiDAR data.

3.2 Digital terrain mapping in Lin Ma Hang

Utilizing the DTM patterns derived from LiDAR, hillshade models are derived (Figure 2), including slope angle, morphology, drainage patterns and catchment zones. These data layers form the foundation of the ground model for terrain classification, as well as the broader geomorphological assessment. The concept of digital terrain mapping system can be illustrated by highlighting features in Lin Ma Hang using GIS related tools for automated spatial analysis.

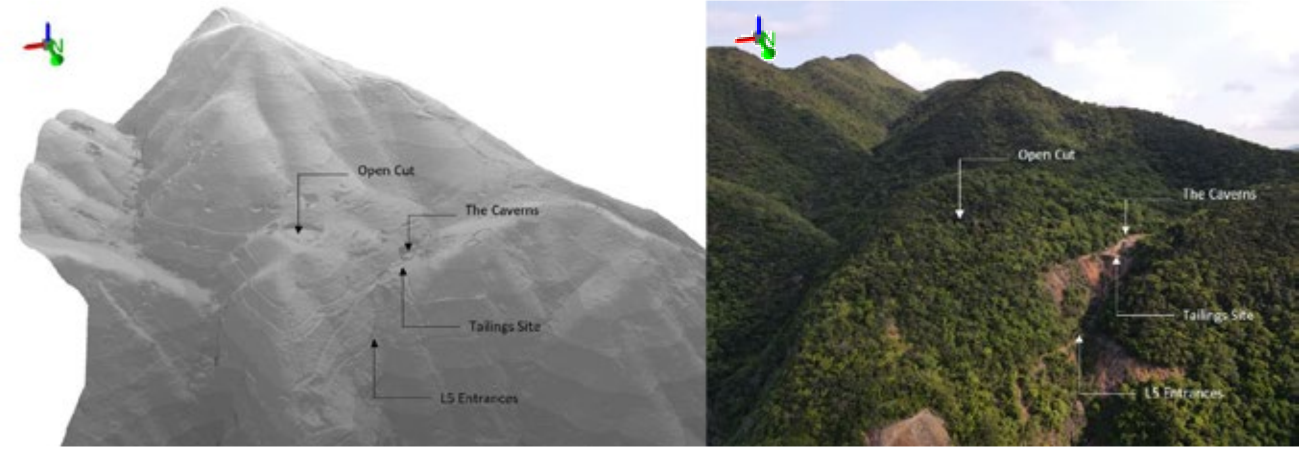

Figure 2: Hillshade model derived from 2020 LiDAR. Numerous platforms, terraces, tailings/spoil deposits, excavations, adits, shafts, military trenches, pathway networks and slope failure.

The first aspect is break-in-slope (BiS). From the DTM, slopes are represented by percentage rise. To identify breaks-in-slope, percentage change between adjacent slope planes are observed. The concept of the tool is to distinguish conditions where adjacent slope planes are at least a 70% change to produce breaks-in-slope on the raster surface. The tool is based on the [SLOPE (Spatial Analyst)] geoprocessing tool modelled in ArcGIS Pro. Slope gradient of the DTM is calculated in terms of percentage rise. Where rise equals run, the percentage would be 100%; situations greater than a 45-degree slope will be greater than 100%; and the percentage decreases as the slope flattens. A slope raster is formed in the same extent as the original DTM. Where the percentage rise is larger than 70%, the raster will flag to indicate BiS. This results in a raster with binary values: 1 is BiS; 0 is not. To optimise visualisation, the results can be modified to show only BiS (value: 1). An extract of the outcome is illustrated against the hillshade (Figure 3) to verify the accuracy of the result. Site reconnaissance was conducted to identify BiS and results were documented in Figure 3b. A comparison of the same extent against the BiS tool results (image in Figure 3a) suggests that the tool produces comparable, or finer detail.

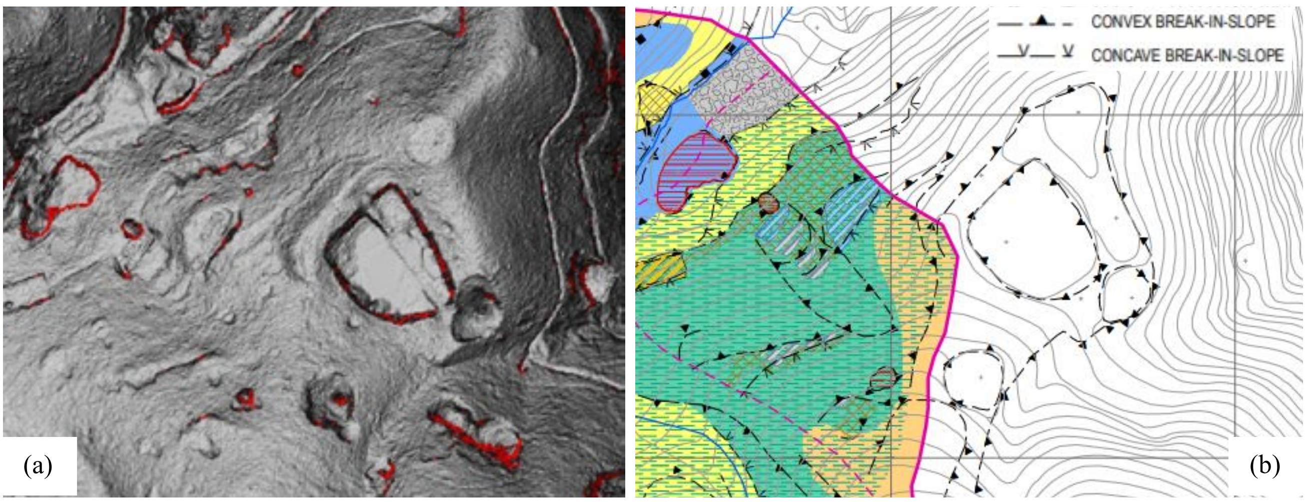

Figure 3a & b: Comparative analysis of BiS detection. a. BiS identified by BiS tool based on 2020 LiDAR data; b. BiS identified in site reconnaissance.

The second feature is shaft detection. Site reconnaissance identified shafts on some terrain mostly hidden by tree canopy. These shafts are generally shallow (~2m) with wide opening; or deep (~10m) with small openings. The study recognised them as historical shafts for mines or subsidence sinks, some possibly from collapsed mine roof or leads. When viewed with hillshade, the shafts are easily visible by eye. However, the output is in raster graphics that displays a 3D representation of the shafts by shaded relief. In further analysis, separate layers will be exported to depict the outline of the shafts. A tool is developed to outline these shaft features in the terrain. Naturally, each cell in the DTM raster has 8 neighbouring cells. Based on the gridded terrain, the tool identifies the elevation value of each adjacent cell. Once adjacent cells are identified, the corresponding elevation of the middle cell is compared against that of all neighbours. "Sinks" are identified by digitally searching through every cell of the DTM for ones where no neighbouring cells have lower elevation. A smoother new surface raster with no sink is created.

This new surface is envisaged as a piece of cloth draped over the terrain. This surface will have artificially removed topographic features such as subsidence sinkholes and extrapolate them into a smooth facade. The elevation value of the original DTM (representation of the actual landform) will be subtracted by that of the smooth surface. By doing so, not only can sinks be identified, the subtraction also produces a difference in elevation between the 2 surfaces and yields the depth. The tool is based on the [FILL (Spatial Analyst)] geoprocessing tool modelled in ArcGIS Pro. The original DTM is filled. An algorithm was used to locate and fill or remove all depressions or sinks in the DEM, where there is no flow from one cell to another within a conceptual hydrological system. The DTM surface is processed such that any sinks or peaks are removed by iteration until the surface is smoothed. This tool acts as a first-pass to identify shafts in which precision can be adjusted to fit the uniqueness of each terrain. One of our models is shown in Figure 4.

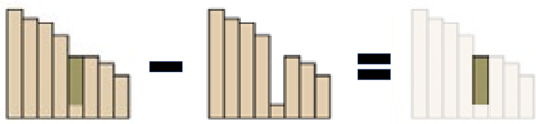

Figure 4: Sink and peak detection

Cell values of the filled-DTM are compared against the original DTM on a cell-by-cell basis. A map algebra will calculate the difference between the filled and original DTM to find areas were fill occurred, by how much, and which should correspond to locations and depth of these sinks. The result of the tool is a raster registered with attribute indicating the depth (Figure 5). The tool result is verified against the hillshade. Key sinks and depressions are outlined to reveal some very fine detail including depth.

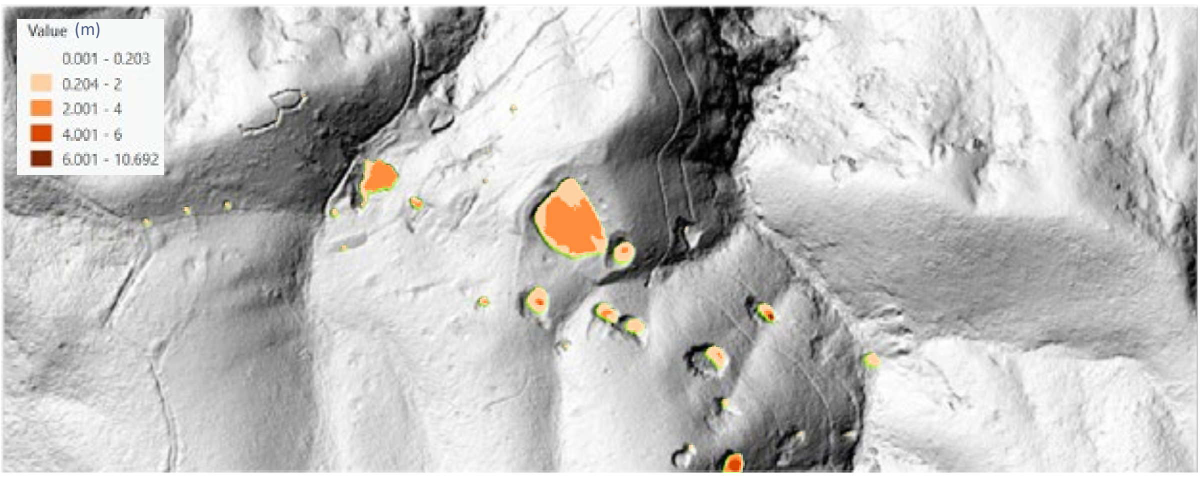

Figure 5: Depth analysis of sinks and excavations, only those sinks that are defined by the input parameters are shown.

The third feature addresses traces of other anthropogenic activity that are apparent based on slope gradient. For example, slopes with gradient more than 5 but less than 60 degrees could be conceived as natural terrain and quasi-natural terrain; or less than 5 degrees, as platforms. Similar to the BiS tool, a procedure is formulated based on the [Slope (Spatial Analyst)] geoprocessing tool in ArcGIS Pro. Instead of the percentage rise, slope angle in degree is calculated from the DTM by the steepness of the elevation value of the raster: the lower the flatter, and vice versa. A customised range of slope angle is then set to display potentially corresponding anthropogenic features in map form. A plate overlaying the tool result on the terrain is verified against photographs in site reconnaissance (Figure 6).

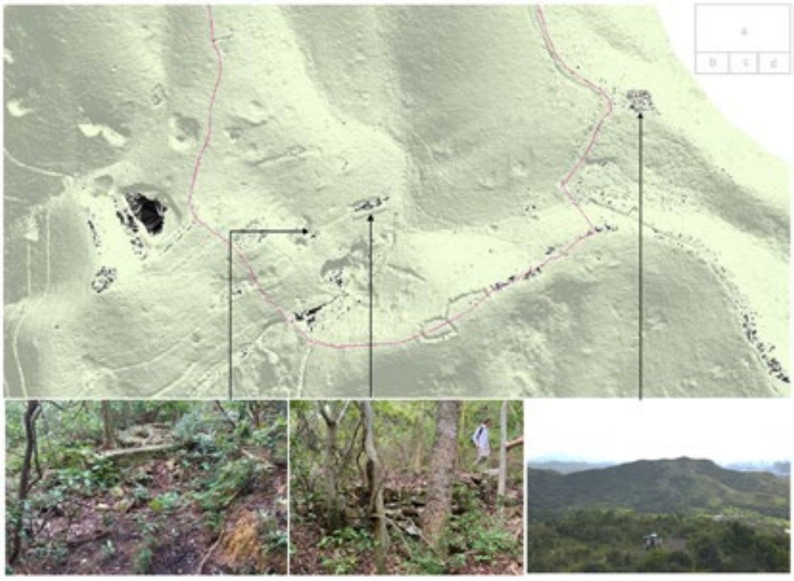

Figure 6: Site verification of the ‘platform’ features. a. Platform features identified by ‘Automated Spatial Analysis Approach’ in black clusters; b. Platform with building foundation; c. Rubble wall platform; d. Helicopter pad.

3.3 Classification of anthropogenic features

Extensive evidence of anthropogenic activities occurs within the NTHSA. These include:

a) remnants of earthen-step and rubble wall terraces associated with past cycles of old agricultural activity;
b) excavations related to the mine cavern, shafts, adits;
c) deposits of spoil/ tailings;
d) cut and fill slopes associated with mining activities;
e) military trenches and platforms;
f) cut platforms associated with other military security activity; and
g) footpaths and other man-made cuts and channels.

The environs of the mine have been extensively disturbed by mining and military activity with numerous anthropogenic features identified through API integrated with 2020 LiDAR and field mapping.

There is also evidence of older extensive remnants of earthen-step form agriculture and some rubble terraces. Some of these old anthropogenic features resemble landslide scars and tension crack-like breaks-in-slope which in API, and sometimes in the field, are difficult to distinguish. According to Styles & Law (2012) similar features are quite common on natural terrain in Hong Kong and need to be considered on a case by case basis. The impacts on slope stability may be beneficial, benign or adverse depending on the geomorphological setting.

According to the observations from the API, the majority of the hillsides near the mine have been disturbed by the anthropogenic activity in the past with impacts on the current landforms creating much “quasi-natural” terrain. The main types of anthropogenic activity are based on the observations from the API integrated with 2010 and 2020 LiDAR and reconnaissance field mapping. There is much evidence of Hillside Pocket (HP) Settings GEO Report 138 (GEO, 2016). The anthropogenic classification provides an inventory of the main forms encountered in the area (Table 1 & Table 2). The classification scheme arises from Styles & Law (2012).

The classification will be further refined with ongoing field work related to the project GI. Some of these features are described below based on information collected through the automated tools integrated with API and field mapping.

Table 1: Observed anthropogenic features

i.	A rock adit tunnel southeast of the mine (Plate 4) the portal cutting into a northwest facing natural slope. The adit leads to two dead-ends some 16m long. Three stepped cut platforms, each of them around 1m high, are adjacent to the portal whilst local subsidence is noted near the platforms. The steep portal cut is indicated by slope gradient >60°.
ii.	A rock cut vertical shaft (Plate 5) to the southwest of the atrium, adjacent to the man-made channel about 2m by 2m opening and some 8m in depth. The shaft is connected to an adit inside the mine.
iii.	A platform with a rubble wall about 1m high and 18m long was identified adjacent to a drainage line. Another cut platform, about 2.5m high with remnants of a pad foundation was identified slightly northeast of the stepped platform at the eastern edge of the site. The terrain is marked as being <20m in length and with a gradient of <5°.
iv.	Remnants of earthen step-form terraces and old rubble wall terraces on the planar hillslope between drainage lines were observed in API and were confirmed during field mapping. The terrain is characterised by remnants of a contour-like stepped profile formed by very old terraces. The platforms are small and linear, and are about 0.5m high and less than 2m wide.
v.	A military trench system occurs at the crest of slope north of the mine. The trench is about 0.5m wide and 1.5m deep circular in nature and is clearly evident in 1945 aerial photographs and the 2020 LiDAR. Further trenches or cuts about 0.5m wide and 0.3m deep were recognised downslope and may be associated with military activity. The small scale of the cut, <5m, and shallow depth mean it is difficult to detect in automated tools. The steep cut slopes, > 60°, are easily identifiable as breaks-in-slope.
vi.	Man-made feature no. 3NE-A/C78 is a concave depression characterised by a landslide-like scarp break-in-slope probably associated with man-made cutting and disturbance.
vii.	Three old potential water storage excavations identified near the mine. Two are adjacent to a drainage line whilst one is in a rubble wall platform.
viii.	A U-channel at the edge of the tailings site. At present, water flows from the man-made channel into the mine and via an adit towards the tailings site. Flows are collected by an old U-channel on the tailings before discharging into the natural drainage line to the northeast.
ix.	Barbed wire traversing the hillslope southwest of the mine was apparent in the API. During the field mapping, remnants of the barbed wire and associated gates are scattered around the terrain generally consistent with the API observations.

Plate 4: Adit identified by LiDAR integrated with API and field mapping.

Plate 5: Shaft identified by LiDAR integrated with API and field mapping.

The automated spatial analysis tool is able to identify most features and forms an initial layer for terrain mapping analysis. Remnants of rubble wall/concrete platforms with building ruins, tailings/ spoil deposits (Plate 6), mine adits and shafts, open-cuts (Plate 7), water tanks and other workings, together with military trenches and associated activity, fortuitous prospecting, as well as very old remnants of agricultural practices with rubble walls and earthen step-form terraces are all observed. The definitions and general descriptions of anthropogenic features in the Lin Ma Hang area are contained in Table 2. The classification forms part of an overall 80 class system for the territory (Styles & Pook, in prep.). These are further subdivided based on dimensions to enable a systematic assessment of the hazard susceptibility of various features within the natural terrain.

Plate 6: Tailings / spoil deposits identified by LiDAR integrated with API and field mapping.

Plate 7: Open cut identified by LiDAR integrated with API and field mapping.

Table 2: Anthropogenic features identified at Lin Ma Hang

Class	Type / Nature / Description (after Styles & Law, 2012)	
A – Agricultural terraces & associated activities	A1 – Old Remnants walled terraces	Presence of wall e.g., stone, rubble wall agricultural terraces. Previously formed for cultivation
	A2 – Old walled terraces (herringbone)	Presence of walls e.g., stone, rubble in herringbone pattern - formed for cultivation. Usually associated with tea production
	A3 – Old earthen step form terraces	No walls Series of small cut slopes usually on steep slopes on deeply weathered terrain Previously formed for cultivation
	A4 – Remnants of old step form terraces	No walls Intermittent remnants of eroded & degraded terraces
	A9 – Old ruins / rubble wall terraces / undetermined	Presence of ordered layout of very old structures or rubble terraces. May be single layer or intermittent parts of ruins
B – Military & associated activities (cut & fill generally associated)	B1 – trenches	A narrow, linear excavation used in military defences
	B2 – Foxholes, some trenches & other minor excavations	A shallow pit or shallow excavation dug by military for defensive refuge & as firing locations
	B5 - Battlefield / Conflict Zone (general locations)	An area of previous military combat.
	B7 – Undetermined military disturbance	Disturbance caused by unknown military activities
	B9 – Observation Post	Military or Police look out location

Class	Type / Nature / Description (after Styles & Law, 2012)
	Disturbed area caused by the processes of extracting ore or minerals, adits, platforms, spoil & tailings deposits
C1 – Mining Large Scale Mechanised Industrial	1 – Tailings/Spoil (Fill)
	2 – Cut
	3 – Retaining Structure
	4 – Retaining Structure – Fill Platform
C2 - Prospecting & opportunistic mining (labour intensive)	Disturbance caused by labour intensive prospecting - usually single man operations
I – Other man-made disturbance (cut and fill generally associated)	I1 – Cut off drain – U channel
	I2 – Pipeline
	I4 – Paths, tracks & roads
K – Registered cut & fill features	K1 - Registered Retaining Wall Feature
	K2 - Registered Cut slope Feature
	K3 - Registered Fill slope Feature

3.4 Hazard assessment

By applying an automated spatial analysis tool approach to identify anthropogenic features, such as shafts or breaks-in-slope, it is possible to overlay these with various data layers for hazard analysis. The first stage, in an area so densely affected by anthropogenic features, is inventory of occurrence, and then to determine where a hillside pocket scenario is susceptible to an "adverse" geomorphological scenario or setting (Figure 7). By identifying drainage lines, catchment basins, clusters of disturbance or fill deposits with an appropriate buffer, a data layer of potential adverse anthropogenic features can be obtained based on the dimensions and nature of the anthropogenic feature using a fast and efficient automated system. This provides a platform for more detailed analysis through traditional methods including site verification. Use of GIS tools to detect and determine the breaks-in-slope and shafts/ excavations and other features is vital. Part of the scope of the project was to determine the extent and layout of shafts, adits and related excavated features that could potentially pose a hazard to the public after the enhancement scheme.

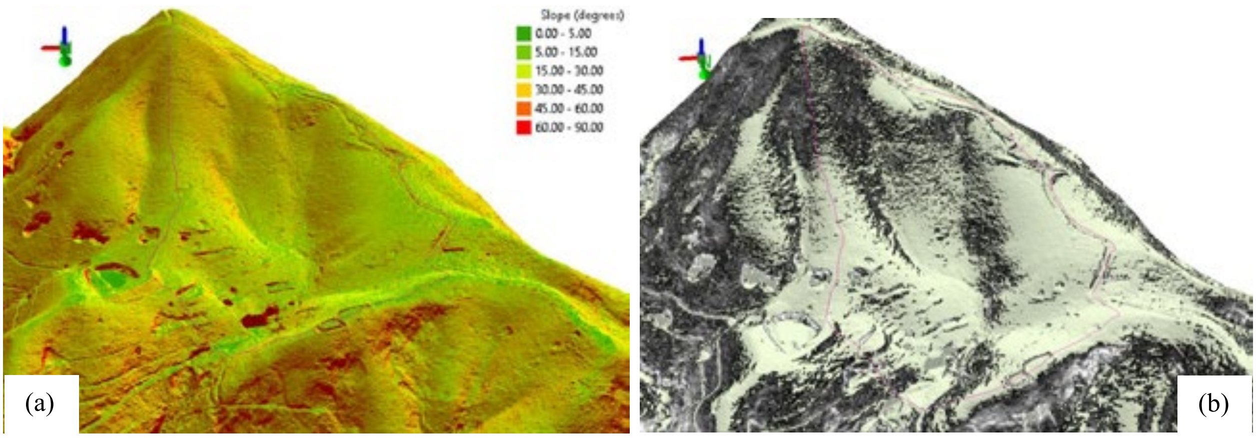

Figure 7: (a) Slope angle map derived from 2020 LiDAR-based DTM – anthropogenic features such as caverns and open cut are clearly visible, (b) Terrain surface heterogeneity.

3.5 Field verification and discussion

A classification system for anthropogenic features is being developed with reference to the diversity of features associated with the mine and hillside terrain. The automated spatial analysis tools applied to date have had initial success, with further refinement and applications likely. The LiDAR data and field mapping observations were generally reflected in the output. The advantages are that an initial shape file with key dimensions is derived from the terrain features which can aid in early hazard analysis. These can be verified and modified from site observations to form an integrated ground model. The approach provides an important first step in screening for features that require investigation.

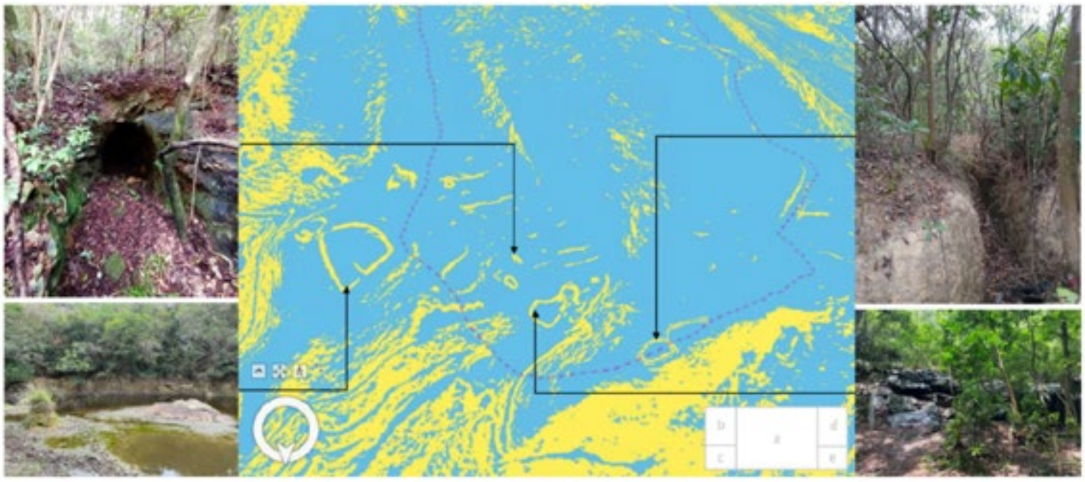

Figure 8: Site verification of 'break-in-slope (BiS)' features identified by automated spatial analysis approach – remnants of terracing and platforms are visible

The principle of utilizing automated spatial analysis tools is to define Terrain Unit Elements (TUE) based on extent and position relative to contours (Table 3). These are then subdivided by gradient of slope and classified according to morphology as planar, concave or convex. Breaks-in-slope are identified and differentiated as convex or concave to distinguish areas of homogeneity (Figure 8). Vertical features can be further classified based on depth/ height. This initial stage of automated spatial analysis tools is for terrain inventory classification. Derivative maps can be produced using a variety of buffer and overlay functions to display the data for specific requirements, such as proximity to natural drainage lines; man-made drainage lines; slopes >30 degrees in gradient and 3m in height/depth; and platforms >3m in height. As an example, the large anthropogenic fill features are shown in relation to drainage lines to determine the potential for adverse hillside pocket scenarios in NTHA of the quasi-natural terrain.

Table 3: Terrain Unit Element (TUE) Classification

TUE	Attribute			Possible Anthropogenic Feature
	Length	Slope Gradient	Depth	
Normal to contour & planar	<20m	<5°	-	Platforms
Normal to contour & planar	<20m	>60°	-	Masonry walls & steep cuts
Normal to contour	>20m & <60m	>30° & <60°	-	Large tailings & spoil dumps
Normal to contour	<20m	>30° & <60°	-	Smaller tailings, spoil dumps & fill slopes
Normal to contour	<5m	>60°	-	Military trenches
Any location	<10m	-	>3m	Vertical shafts
Any location	>40m	-	>3m	Open cut

4 CONCLUSION & FURTHER STUDIES

Well established principles of API 4D analysis integrated with LiDAR and field verification underpin an automated spatial analysis tool approach. Techniques based on digital data inputs of slope gradient, size, shape, extent and aspect of features to help delineate anthropogenic activity on the quasi-natural landscape. With the aid of digital classification, potentially adverse Hillside Pocket settings can be systematically highlighted for field review and modelling in Natural Terrain Hazard Assessment.

The success of automated spatial analysis tools are tempered by the knowledge that to get the most accurate result for feature location, such as shaft identification, scripting and machine learning techniques are required. Flow direction tools can be further explored as an option where Terrain Unit Element (TUE) lengths are normal to the contours. Further work will be conducted on ways to enable extraction of BiS and to convert raster results into line features. Throughout the process the need to build a statistical model to determine the geomorphometric characteristics of a large number of anthropogenic features is recognised to refine the parameters for identification in the LiDAR derived DTM.

Further works will aim to incorporate a spatial tool kit approach for anthropogenic features into an automated systematic terrain classification for NTHS.

ACKNOWLEDGEMENTS

The 2020 LiDAR survey data has been used with the consent of the Geotechnical Engineering Office of the Civil Engineering and Development Department, of the Government of the Hong Kong SAR

REFERENCES & BIBLIOGRAPHY

Chu, J., & Chan, J. 2015. Hong Kong Mining History (1st ed., pp. 19-41). ProjecTerrae.

Davis, S. G., & Snelgrove, A. K. 1956. Geology of the Lin Ma Hang Lead Mine, New Territories, Hong Kong.

Davis, S. G. 1964. Symposium on Land use and Mineral Deposits in Hong Kong, Southern China and South East Asia – Proceedings, HKU, pp. 263

GEO 2004. Guidelines on Geomorphological Mapping for Natural Terrain Hazard Studies. GEO Technical Guidance Note No. 22 (TGN 22). Geotechnical Engineering Office, Civil Engineering Department, Hong Kong, 8 p.

Geotechnical Engineering Office 1991. Hong Kong Geological Survey (HKGS) Map Sheet 3, Solid and Superficial Geology, Sheung Shui, 1:20,000 – scale, HGM20 series.

Geotechnical Engineering Office 2016. Supplementary Guidelines on Natural Terrain Hazard Studies for Hillside Pockets. GEO Technical Guidance Note No. 46 (TGN 46). Geotechnical Engineering Office, Civil Engineering and Development Department, Hong Kong.

Ho, H.Y. & Roberts, K.J. 2016. Guidelines for Natural Terrain Hazard Studies. GEO Report No. 138 (2nd Edition), Geotechnical Engineering Office, Civil Engineering and Development Department, Hong Kong.

Lai, A.C.S., So, A.C.T., Ng, S.K.C. & Jonas, D. 2012. The territory-wide airborne light detection and ranging survey for the Hong Kong Special Administrative Region. The 33rd Asian Conference on Remote Sensing, Pattaya, Thailand.

Parry, S. & Jonas, D.A. 2007. The use of LiDAR for Landslide Hazard Assessments: Hong Kong Case Studies. Conference on Engineering Geology in Geotechnical Risk Management, pp 151-161. Hong Kong Regional Group of the Geological Society of London.

Sas Jr., F.J., Yu, J.P., Pau, Y.Y. & Styles, K.A. 2012. Detection of Old Agricultural Terraces in Steep, Vegetated Terrain Using Airborne LiDAR: Case Studies from Hong Kong. 33rd Asian Conference on Remote Sensing (ACRS 2012) Pattaya, Thailand. 10p.

Styles, K.A. & Hansen, A. 1989. Geotechnical Area Studies Programme – Territory of Hong Kong (GASP Report XII). Geotechnical Control Office, Hong Kong, 346p plus 14 maps.

Styles, K.A. & Law, M.H 2012. Some Observations about Man-made Features on Natural Terrain in Hong Kong. The Quarterly Journal of Engineering Geology and Hydrology, 45, The Geological Society, London, p. 131 – 138.

Styles, K.A & Pook, G (in prep). A Classification System for Anthropogenic Features with Potential Impacts for Slope Stability Assessment on Steep Natural Terrain in Hong Kong.

Tam, H.T., Yeung, K.W., Yu, P., Hu, S.L. & Styles, K.A 2017. Application of an Automated LiDAR-based Mapping System in Natural Terrain Hazard Studies in Hong Kong. The HKIE Geotechnical Division Annual Seminar 2017. 7p.

Wong, J. 2021. Detector in the Air – 2020 Airborne LiDAR Survey. Joint Technical Symposium on Digital Geosciences & Geotechnology. 16 September 2021.

阮志 2012.《中港邊界的百年變遷：從沙頭角蓮蔴坑村說起》。香港：三聯書店（香港）有限公司。

Deep Cement Mixing –The Experience in Tung Chung East Reclamation and Challenges Ahead

Henry Cheung, C H Yan
Sustainable Lantau Office, Civil Engineering and Development Department, HKSARG, Hong Kong, China

Chris Cheung, Anthony Wong
AECOM Asia Company Limited, Hong Kong, China

ABSTRACT

Reclamation has been the most tenable land supply in the interest of the public. Today, around 27% of Hong Kong people are living on reclaimed land formed in the past decades. Over the past few decades, reclamation methods and ground treatment techniques have been advanced to meet the technical requirements and social acceptance at different times. In response to the increasing environmental awareness of the public, non-dredged reclamation methods in association with Deep Cement Mixing (DCM) has been introduced in Hong Kong. Tung Chung East (TCE) reclamation, as one of the ongoing projects adopting this novel technology, has showcased a role model on assimilation and adaptation of this new technology in tackling ever changing challenges in the construction industry. The success of the project markedly attributes to the application of this new ground treatment technique.

In this paper, some background and geotechnical considerations for the adoption of DCM method and design approach in TCE reclamation will firstly be discussed. To date, majority of the DCM works have been completed and the reclamation works have been proceeding well. With the experience acquired and construction data collected at the site specific DCM trial embankment as well as during the construction stage, the merits and benefits of DCM method, in terms of both stability and settlement control, will be highlighted. More importantly, there has been a lot of precious experience upon construction and the project team has ironed out all these hurdles through adaptation of this technology on site. There is no doubt that the documentation of all the experience in TCE reclamation could become a great reference for the development of a local guidance for practitioners in Hong Kong and upcoming mega development projects.

1 INTRODUCTION

1.1 Reclamation in Hong Kong

In the last century, there was a rapid and continuous growth in population in Hong Kong, from less than 2 million in the 1950s to over 7.4 million in 2020. The stable growth of population at the same time drove a substantial economic growth and transformed Hong Kong from a re-export port with GDP per capita of less than HK$2,400 in 1961 to an international metropolitan with GDP per capita of over HK$340,000 in 2020. The unremitting growth of economy in Hong Kong would not have been possible without the provision of sufficient land to meet the development needs. Out of the numerous land supply options, land reclamation has been the most tenable supply in the interest of the public. Today, around 27% of Hong Kong people live on reclaimed land formed in the past decades.

In the 20th century, there were different land reclamation projects, for example Kai Tak Airport Extension (1957 - 1974) and new town developments. Formation of land by reclamation for new town development in Hong Kong was initiated in the 1970s, including Tsuen Wan, Shatin, Tai Po, Ma On Shan, Tseung Kwan O and Tung Chung etc. (1973 – 2003). Other notable reclamation projects include the Disneyland development at Penny's Bay, Hong Kong International Airport at Chek Lap Kok, and artificial island for Hong Kong Port of Hong Kong-Zhuhai-Macao Bridge. Currently, reclamations for the Three Runway System (3RS) at the Hong Kong

International Airport (commenced in 2016), TCE and Integrated Waste Management Facilities (IWMF) (both commenced in 2017) projects, with a total reclaimed area of about 796 ha, are in progress.

1.2 Tung Chung East (TCE) Reclamation

The planning and engineering study for Tung Chung New Town Extension commenced in 2012 and the reclamation works, Contract No. NL/2017/03 for the reclamation of about 130 hectares at TCE (Figure 1), started in end 2017 seizing a record of less than 6 years from planning to commencement of works for projects of similar scale. Land formation is completed by phases and and is scheduled for completion in 2023. The first phase involving around 7 hectares of land was completed and handed over for housing development in Q1/2020, that was 27 months from the commencement.

Figure 1: Tung Chung New Town Extension

Concerns over impact of land reclamation on its surrounding environment and ecology are appreciated. While with proper investigation, planning and mitigation measures, it is possible to work out some environmentally friendly solutions to strive for a balance between development and conservation. Over the past few decades, reclamation methods and ground treatment techniques have advanced considerably to meet the technical requirements and social acceptance. In the TCE reclamation project, a new sustainable ground treatment method. i.e. the deep cement mixing (DCM) method has been adopted in non-dredged reclamation.

2 GEOLOGY OF TUNG CHUNG EAST

The marine environment in TCE is generally covered by very soft to soft marine deposit of silty to clayey material. The marine deposit is classified as Holocene Hang Hau Formation and the thickness of the marine deposit is generally in the range of 10m to 16m. It is locally about 17m to 18m thick near western flank of the reclamation area. Underlying which is an alluvial layer of Chek Lap Kok Formation, and it is typically between 15m and 20m thick.

Based on results from vane shear tests and unconsolidated undrained triaxial tests, the undrained shear strength (Su) of marine deposit is found to be from 3kPa to 25kPa (Figure 2) and it exhibits an increasing trend with depth as revealed from cone penetration tests. The trend can be expressed as $S_u/\ \sigma_i = 0.11 + 0.0037\ I_p$ with reference to the empirical relationship between undrained shear strength, effective overburden pressure and plasticity index as given by Skempton (1957). Oedometer tests have been carried out to determine the compressibility of marine deposit and the compression index (Cc) of marine deposits is around 1.0. The over-consolidation ratio (OCR) is generally close to 1.0, whereas OCR is slightly higher, up to 1.5, close to the original seabed level.

The underlying unit is Chek Lap Kok Formation (Strange & Shaw, 1986) which comprises a 10 to 20m thick highly heterogeneous mix of sands, gravels, silts and clays interbedded with each other. The thickness of the formation is typically between 10m and 20m. Cohesive alluvial layers are generally described as firm to stiff, light grey or dark red with orange or red mottling slightly sandy clayey silts, and these softer layers normally have a high moisture content. The plasticity index of cohesive alluvial silts/clays is around 30% with a corresponding liquid limit of around 50%. The undrained shear strength of cohesive alluvial silts/clays is estimated to range from 20kPa to over 80kPa. Stiffer layers generally lie at a deeper depth. Based on laboratory test data, the compression index is from 0.2 to 0.5 that is markedly less compressible as compared with marine deposit. According to previous local experiences such as Endicott (1992) and Koutsoftas et al. (1987), OCR of alluvium can be in the range from 2 to 3. Granular lenses of silty sand with occasional fine to coarse gravels are interbedded with alluvial clays/silts layers. In some areas, dense cobble sized granular layers are present overlying cohesive alluvial layers.

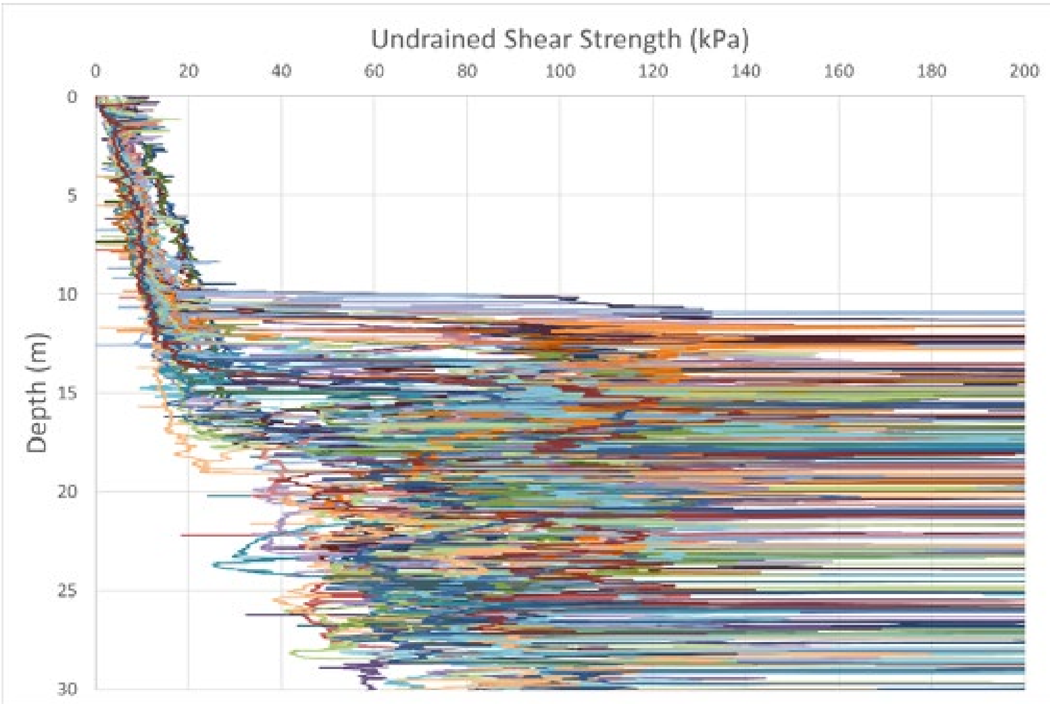

Figure 2: Variation of Undrained Shear Strength

3 CONSIDERATIONS OF GROUND TREATMENT METHOD

The low shear strength and high compressibility of soft marine deposit and alluvial layers renders reclamation and construction of revetment structures difficult. The major challenges involve stability and settlement control in the course of seawall construction and filling. The soft marine sediment is highly compressible and would exhibit large settlement or even shear failure under the weight of the reclamation fill, if suitable ground treatment is not carried out. In evaluating ground treatment options, a basket of factors including cost, time, robustness, safety and environmental etc. are considered. For soft clay, it is the major challenge to develop a suitable solution to safeguard stability and avoid excessive deformation affecting the functional performance of the structures/utilities etc. during and/or after construction. Three approaches namely, (a) fully dredged method to replace soft sediment with granular soil; (b) conventional drained method to improve soil properties through consolidation, and (c) deep cement mixing method to reinforce soft soil to form a composite material, have been considered.

3.1 Fully Dredged Method

In the old days, soft marine deposit was completely dredged and subsequently filled with sand fill or general fill. While dredging eliminates the engineering problems arising from these soft strata, there is a substantial implication to the environment and society. Disposal of dredged sediment may use up the capacity of disposal sites. In addition, it would generate substantial marine vessel trips for transportation of dredged sediment to disposal pits and import of fill material for backfilling that results in significant carbon footprint. Coupled with the increasing social awareness on environment, it is preferable to adopt non-dredged methods and treat the soft marine sediment in-situ.

3.2 Conventional Drained Method

Conventional drained method has been adopted for decades. Instead of fully removal of the marine sediment, prefabricated vertical drains (PVDs) are installed through the soft compressible soil stratum to facilitate drainage and consolidation. Together with surcharge loading on top, the soft marine sediment layer is compressed to eliminate primary consolidation within design timeframe. Based on the experience in TCE, the estimated consolidation period is normally in the range of 9 months to 12 months that results in a relatively longer construction period. Apart from a longer construction time, previous experience revealed that the performance of PVDs is relatively uncertain in some circumstances, e.g. under substantial ground settlement. Construction time and quality control pose critical factors to the option assessment.

3.3 Deep Cement Mixing

Amongst the approaches considered, in-situ deep cement mixing has the advantage of which it can quickly solidify soft sediment as compared with conventional drained method, whilst removal of sediment is not required. The merits and considerations are further presented in the following paragraphs.

4 DEEP CEMENT MIXING METHOD

DCM method involves in-situ solidification of marine sediment by mixing with stabilization agent or binder such as lime, cement, or a combination of different binders. Research and development of modern mixing technique commenced in late 1960’s using lime as the principle binder. DCM method was put into practice in Nordic countries and Japan in mid-1970’s. The technique has been recognized worldwide as an effective ground treatment method of soft marine sediment. Major infrastructure project like Haneda Airport at Tokyo in Japan has adopted DCM method as part of its runway extension.

4.1 Design Considerations

The deep mixing technique has been well-established. Factors governing the performance of DCM method can be categorised into 4 key groups (Kitazume & Terashi, 2013) (i) characteristics of in-situ soil, which include physical and chemical properties, organic content, pH value and moisture content; (ii) characteristics of binder, which include binder type, binder dosage and water to binder ratio; (iii) mixing conditions, which include blade rotation number and type of mixing tool; and (iv) curing conditions, which include curing time, temperature and confining pressure along a DCM element. All the above factors can affect the performance of DCM works, which is usually assessed in term of Uniaxial Compressive Strength (UCS) in laboratory. The design UCS is the principle parameter in the determination of the treatment pattern, or the replacement ratio in the design.

4.2 Ground Investigation

Like other geotechnical engineering projects, thorough understanding of geological setting and ground conditions is essential for reclamation. Ground investigation for detailed design of reclamation and ground treatment works was carried out in 2017. Geophysical survey was first conducted to reveal the general conditions of the ground and identify anomalous features on the seabed that might pose potential obstructions to the ground treatment works. Apart from geological units, site history and authropogenic features are also of interest for the design and construction ground treatment works. Granular soils of cobble / boulder-sized with thickness exceeding 1m embedded within sediment / deposits could pose significant difficulties to the penetration of ground treatment equipment and mixing shaft. The persistence of such obstructions is warranted to be identified during ground investigation as far as practicable, so that the subsequent ground treatment design could cater for such hard crust.

In addition to marine boreholes, in-situ field tests such as cone penetration tests (CPT) and vane shear tests were particularly important for acquiring in-situ engineering properties of the sediment. CPT provided continuous data for evaluating soil profile and properties, which were essential for the design and construction of DCM works. To prepare for reference data for DCM design, a series of laboratory trials were conducted in addition to conventional laboratory tests.

Water content is a prime factor for the chemical reaction of cement-based binder. As revealed from site-specific ground investigation, moisture content of marine deposit is generally from 60% to 108% with an average of around 86% and a higher moisture content near the seabed as shown in Figure 3. For alluvium, moisture content is generally from 16% to 50%, with some outliers up to 84% as shown in Figure 4.

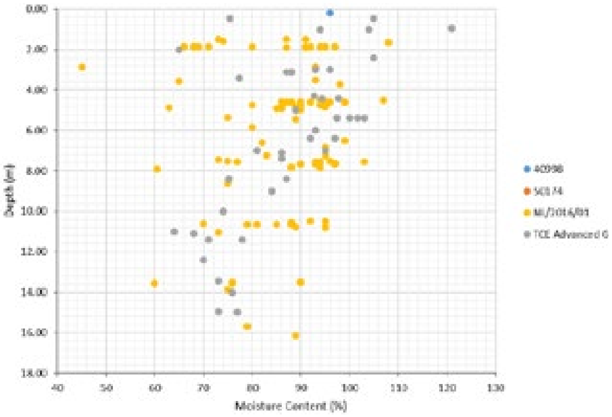

Figure 3: Moisture Content of Marine Deposit

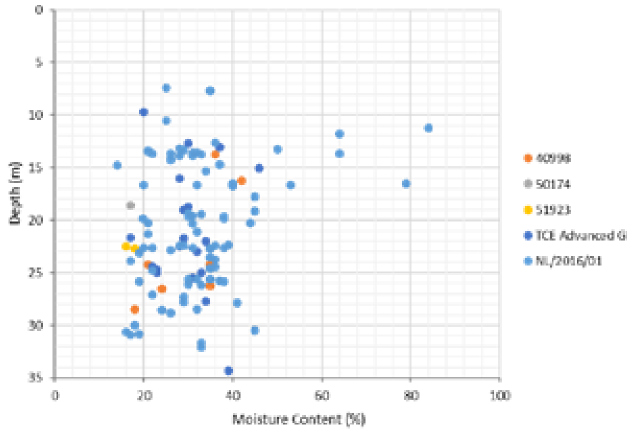

Figure 4: Moisture Content of Alluvium

In terms of chemical properties, the key parameters of interest are the pH value and the organic content of the in-situ soil. The effects of pH value and organic content of in-situ soil have on cement stabilisation are well documented in various literatures (Babasaki et al., 1996). For optimal results, the pH value of the in-situ soil should not be lower than 5, and the ignition loss should not be greater than 15%. Based on laboratory testing results, marine deposit at Tung Chung East are slightly basic with an average pH value of around 8.0 and the ignition loss is around 6%. The chemical properties reveal that treatment with cement-based binder should be effective.

4.3 DCM Laboratory Mixing and Field Trials

The performance of DCM treatment attributes to soil properties, binder dosage and workmanship despite a robust quality assurance and quality control framework. All these mixing parameters shall be developed based on laboratory testing which provides an indication of required dosage and mixability. With the results of laboratory testing, field trial shall be carried out to verify the mixing parameters including the required dosage and cycle diagram etc.

A series of laboratory mixing tests were carried out using the undisturbed soil samples of marine deposits and alluvial clay to develop the mixing parameters. The testing procedures followed the recommendations in Practice for Making and Curing Stabilized Soil Specimens without Compaction (JGS 0821-2009), by Japanese Geotechnical Society.

Ordinary Portland Cement (OPC) is commonly adopted as the binder for modern DCM works but it has an intrinsic drawback for its high carbon footprint. Ground Granulated Blast furnace Slag (GGBS) is a by-product of steel industry and thus it is not only environmentally friendly for beneficial reuse of this by-product, but also improves overall durability that upholds the end-product resistance to alkali-silica, sulphate and chloride reactions. As an alternative, Portland Blast Furnace Cement (PBFC) has been adopted as the binder for DCM works in TCE reclamation. Specimens were prepared for these two different cement-based binders. The PBFC comprised 40% OPC and 60% GGBS. The reduction in greenhouse gas emission, in terms of carbon-dioxide (CO_2), is remarkable. The carbon emission in the course of production for GGBS is only 6~7% of that for OPC (Higgins, D. 2007).

Over 1400 in-situ soil samples of marine deposits and alluvial clays were mixed in laboratory with OPC and PBFC. Five different binder dosages were tested: 140, 160, 180, 200 and 220kg/m^3 for PBFC, and 160, 180, 200, 220 and 240kg/m^3 for OPC respectively. To evaluate the strength variation of the mixed specimens with respect to binder type and binder dosage, moisture contents of the marine deposit and alluvial clay specimens have been controlled and adjusted to the average value of the respective soil (by addition of water to the in-situ soil). The unconfined compressive strength (UCS) of these laboratory mixed specimens were tested on the 28th day. The results are presented in Figures 5 and 6. It is revealed that for a required strength, the required cement content and thus, embodied carbon, could be reduced considerably using PBFC. For the application at TCE reclamation, using PBFC as the binder for DCM works in this project reduced around 600,000 tonne CO_2 equivalent greenhouse gas emission.

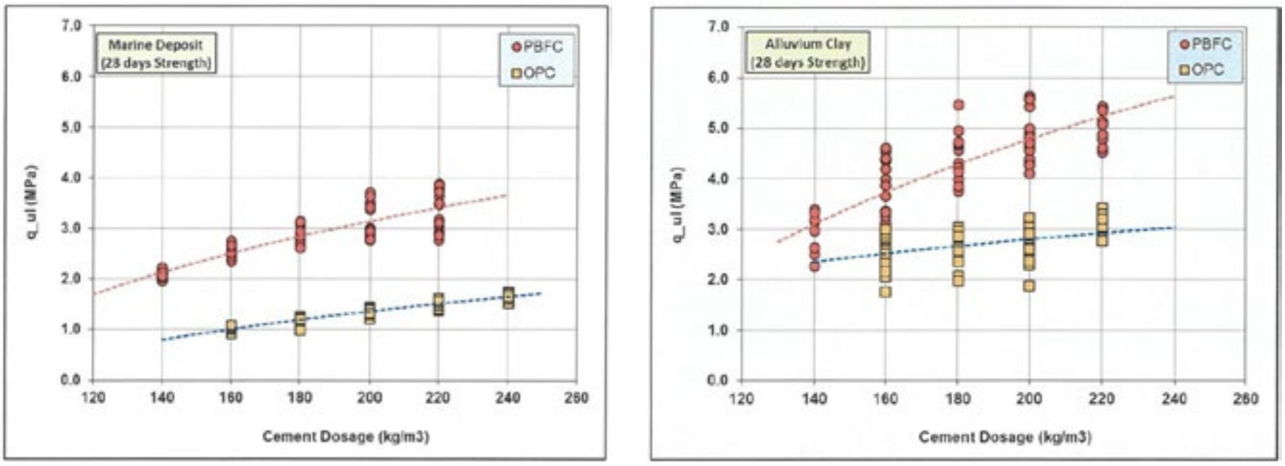

Figures 5 & 6: Relationship between 28th day UCS and Binder Type for Marine Deposit and Alluvium

4.4 Binder Dosage and Water Content

Binder dosage is another important parameter as well as cost component to ground treatment works. Considering the particular shallow water depth site constraint at TCE, it is desirable to adopt a suitable binder and optimise the dosage that can minimise heaving of seabed, whilst the required quality and cost effectiveness can be maintained.

Figure 7 compares the UCS results of marine deposits and alluvial clays mixed with PBFC. The testing moisture contents of marine deposits and alluvial clays were 85% and 40% respectively. The specimens mixed with alluvial clay exhibited higher UCS than those mixed with marine deposit at the same binder dosage. The results attribute to a higher total water-to-binder ratio in marine deposit than alluvium. These results suggest that it is desirable to control binder dosage across different soil stratigraphy to enhance cost effectiveness of the design.

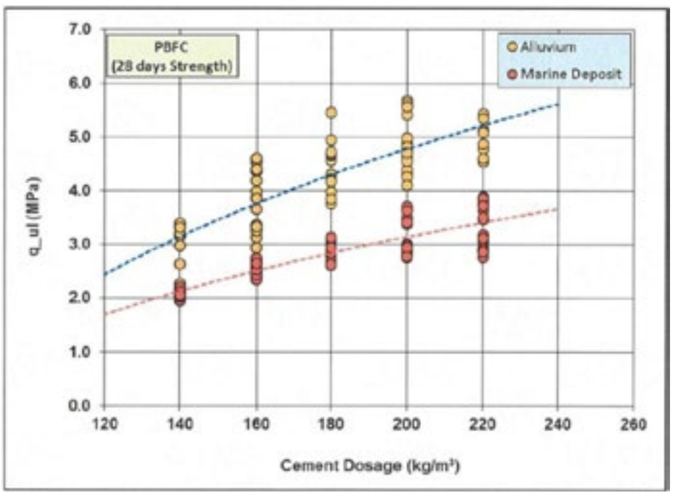

Figure 7: Relationship between 28th day UCS and In-situ Soil mixed with PBFC

5 DESIGN APPROACH

5.1 Design Concept and Approaches

DCM method is an in-situ ground treatment technique to mix soil and binder using mechanical tools to form DCM clusters. For seawall and revetment structures, DCM clusters are commonly overlapped to form wall, grid or block to enhance shear resistance, Figure 8 (Kitazume & Terashi, 2013). In between the DCM wall, cross walls may be constructed to provide lateral restraint and to prevent extrusion failure of soft soil in between two DCM walls. Where stress concentration is identified, short DCM clusters may be constructed as block type locally to enhance the resistance.

The current design practice of DCM treatment in Hong Kong have made reference to both US and Japanese standards (FHWA, 2013 and Kitazume & Terashi, 2013) which follow the limit state approach. Taking into account the uncertainties, partial factors are applied to material strength properties. For the ultimate limit state, both external and internal stability have to be considered. Potential failure modes including sliding, overturning, bearing capacity and shearing along other potential slip surfaces underneath the DCM treatment have to be studied, whereas crushing of DCM clusters under vertical load, crushing of shear wall panels at the outer treatment toe, vertical shearing between overlapped columns within a shear wall panel, shearing along other potential slip surfaces within the DCM treatment and extrusion failure of untreated soil between shear wall panels are considered in the internal stability check. For serviceability limit state, ground settlement and deformation are assessed.

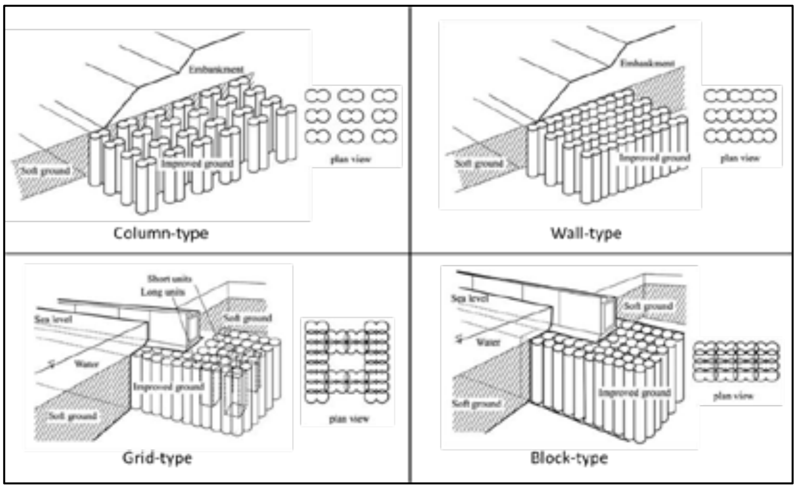

Figure 8: Typical DCM Treatment Pattern

5.2 Grid-type Treatment as Seawall Foundation

Grid-type DCM treatment has been adopted for seawall foundation (Figure 9) to improve lateral rigidity and robustness at TCE reclamation. In most of the design cases, overall stability in form of shear failure governs, especially during temporary loading stages of reclamation filling and surcharging, and the treatment extent shall be adjusted. The required treatment depths have strong correlation with the shear strength of the soil profile and is generally around 20m given the offshore stratigraphy in Tung Chung East.

In regions with high stress concentration, such as the base of a vertical seawall, localized higher replacement ratio has been adopted to facilitate the distribution of large stresses. Additionally, a DCM transfer slab consisting of short clusters is provided to prevent local failure of unimproved soft clays between DCM grids and to limit differential settlement. Evaluation of internal stability for vertical shearing between long and short clusters has been performed to assess the required thickness of the DCM slab.

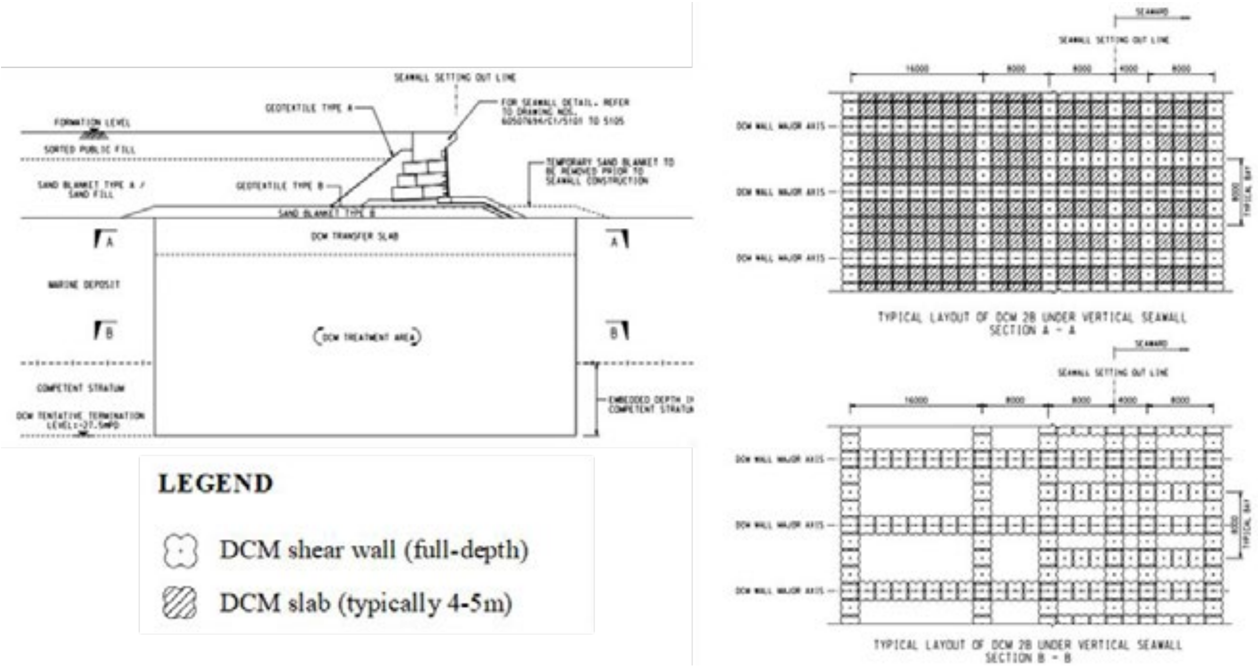

Figure 9: Typical Sections of DCM Treatment as Foundation of a Vertical Seawall

5.3 Finite Element Analysis

A more rigorous approach using finite element analysis with the input parameters properly evaluated is recommended throughout the design process to identify stress distribution and deformation, instead of solely relying on conventional limit equilibrium approach. The DCM treatment has been modelled with an undrained Mohr-Columb constitutive model. By assuming that the treated soil mass behaves as a composite material, parameters such as the undrained shear strength and Young's modulus have been derived using the concept of area replacement ratio. Figure 10 shows an example of a design case. It is noted that overall stability may be of concern when the surcharge height reaches 6m from the formation level. To prevent local failure behind the DCM treatment, reclamation filling is required to be carried out layer by layer to allow sufficient pause periods for consolidation at each loading stage. Additional sensitivity analysis has revealed that due to the relative stiffness between DCM treatment and in-situ soil, the design is governed by the extent of the DCM treatment and the properties of in-situ soils.

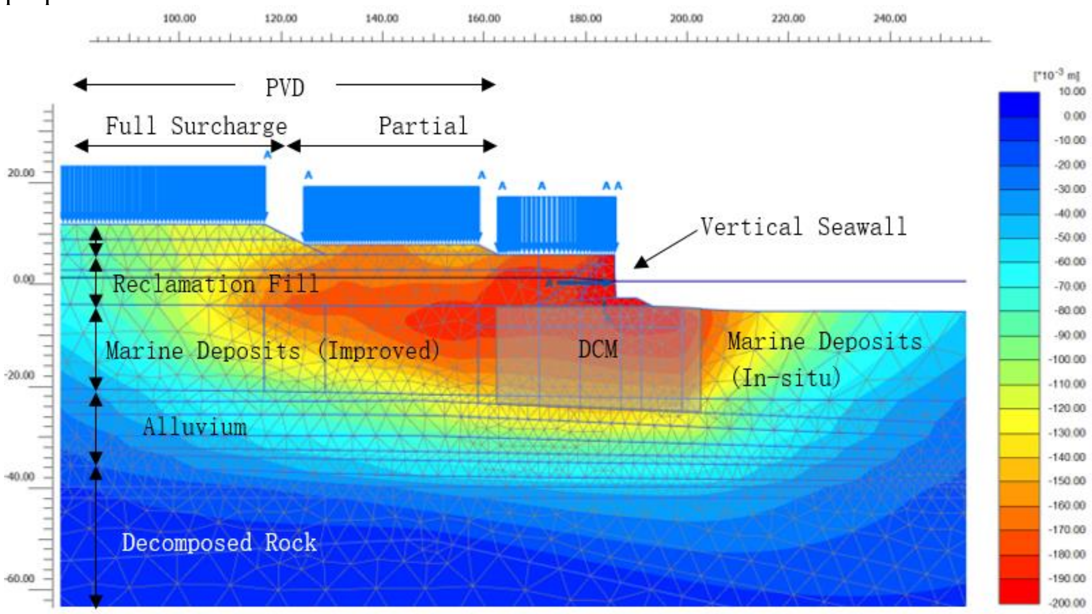

Figure 10. Finite Element Analysis – Lateral Deformation

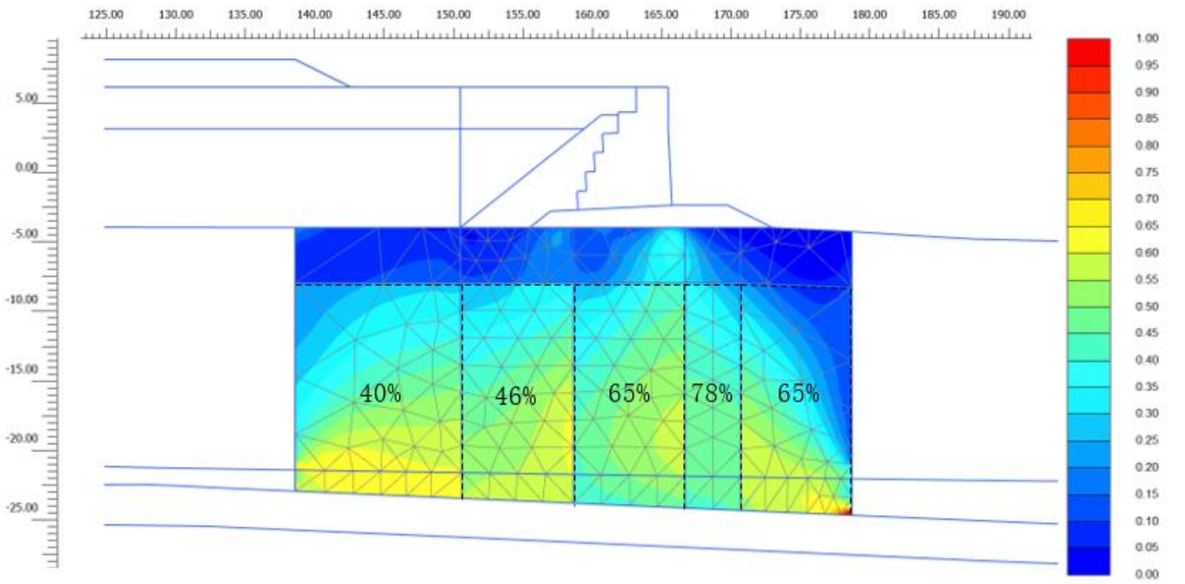

Figure 11: Finite Element Analysis Result – Ratio of Mobilised Shear Stress to Available Shear Strength of DCM

Finite element analysis has provided the insight for evaluating internal stability of DCM design. The analysis allows the designer to examine stress distribution of design model and optimise the treatment replacement ratio. The example as given in Figure 11 shows that there is a relatively high stress concentration directly underneath the vertical seawall and at the outer toe of the DCM treatment. Accordingly, a higher replacement ratio of DCM treatment is assigned near the regions of high stress concentration to evenly distribute the stress for a robust foundation. Although finite element analysis is versatile and power, it is of paramount importance to validate the input parameters and numerical model for better understanding of physical behaviour and meaningful results. One of the validation approaches is physical modelling in geotechnical centrifuge facilities (Ng, 2014). The recent collaboration project with HKUST has enabled the project team to acquire insightful knowledge of modelling parameters, and subsequently the reclamation design can be optimised for cost effectiveness (Figure 12).

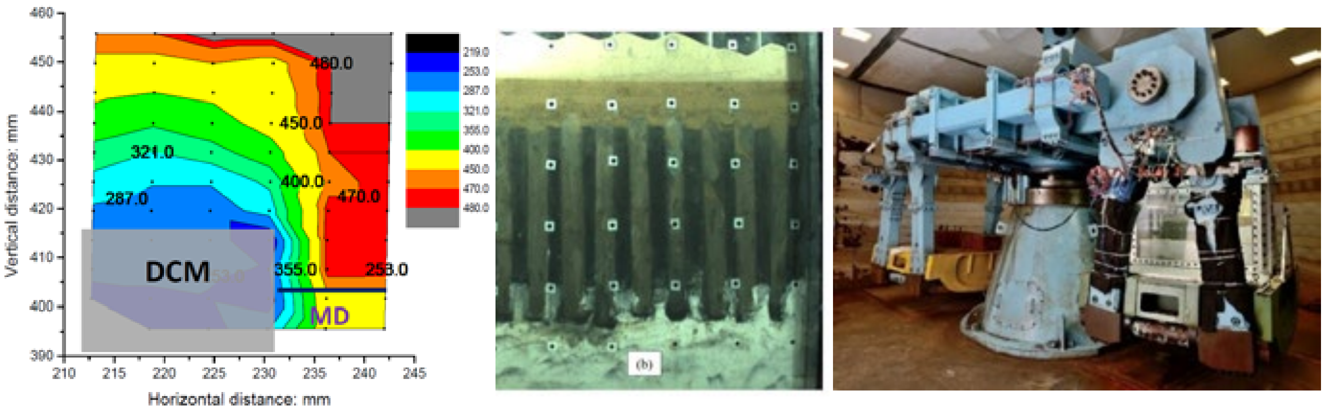

Figure 12. Physical Modelling of DCM Ground Treatment in the Geotechnical Centrifuge Facility at HKUST

6 PERFORMANCE OF DCM METHOD

6.1 Monitoring at Trial Embankment

At the time of drafting this paper, reclamation was in progress and monitoring stations were installed progressively. Notwithstanding, based on the monitoring data at the trial embankment and completed site areas, the performance of DCM ground treatment method has been found promising and the recorded ground settlement and deformation are within the design prediction.

The robustness of DCM method can be demonstrated from a fully instrumented trial embankment. At the early stage of reclamation works contract, a trial embankment was first constructed with a view to ascertaining the performance of DCM design and construction. The trial embankment consisted of a concrete blockwork seawall that was supported by DCM treated foundation. Earth filling was carried out behind the seawall to simulate permanent loading conditions in the future.

Intensive monitoring at the trial embankment was implemented. For the sake of clarity, only a selection of instruments will be discussed in this paper. The selected instruments were located in 3 different points namely Points A, B and C as shown in Figure 13. Point A was placed on top of the sand blanket situated within the PVD treatment at 25m from the edge of the DCM treatment zone. Points B and C were situated on the surface of the blockwork seawall, which in turn was founded on the DCM treatment. The monitoring data at these 3 locations are discussed in depth in the following sections.

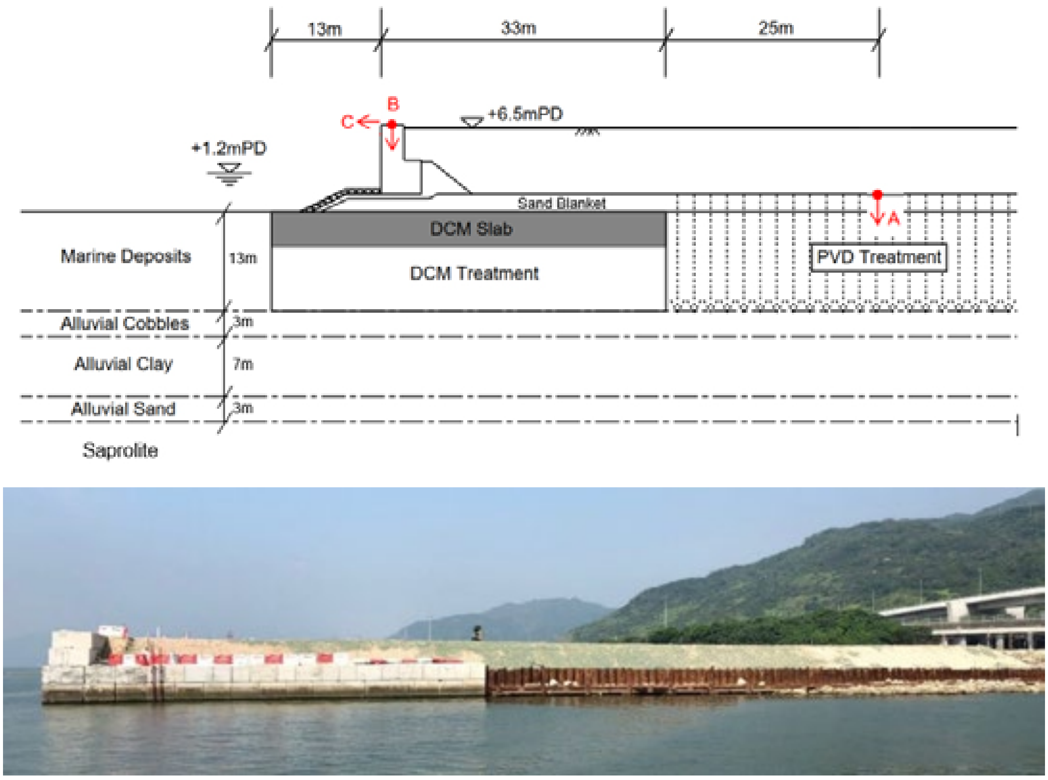

Figure 13: Section of the Trial Embankment

6.2 Settlement monitoring

Ground settlement recorded from settlement markers at Points A and B are plotted in Figure 14. At Point A, the ground settlement profile exhibits an exponential trend upon loaded with reclamation fill. The recorded settlement at Point A was roughly 2.3m after about 7 months.

At Point B, the ground settlement trend reached a steady state soon after loading. It should be noted that the settlement magnitude at Point B was a hundredfold smaller as compared with the settlement magnitude at Point A. The recorded settlement at Point B was roughly 25mm.

The settlement profile at Point B has been examined further with respect to depth by analysing data from magnetic extensometers. Settlement contributed by the fill layer could be obtained from the difference between settlement at the ground level and settlement at the top of DCM treatment zone. Settlement due to compression of DCM clusters could be obtained from the difference between settlement at the top and bottom levels of the DCM treatment zone. Based on the extensometer data (Figure 15), it could be concluded that the DCM treated marine clay layer was nearly incompressible at the trial embankment. Most ground settlement attributed to the overlying fill layer and the underlying alluvium.

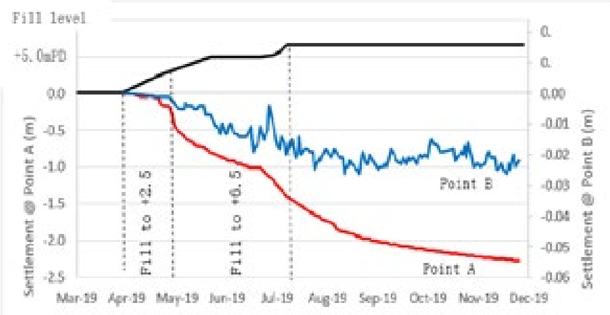

Figure 14: Ground Settlement measured from Settlement Markers at Points A and B

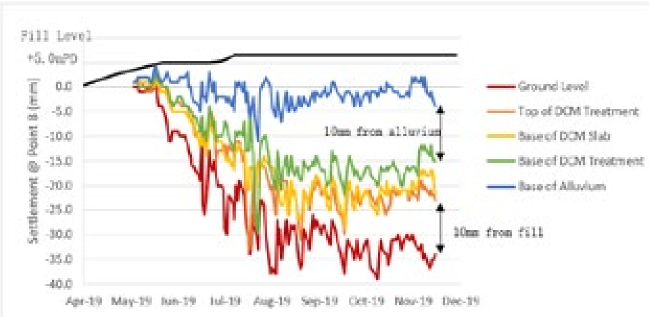

Figure 15: Ground Settlement measured from Magnetic Extensometer at Point B

6.3 Seawall Lateral Movement

Lateral seawall movement was measured by multiple surface movement markers installed along the seawall. Figure 16 shows the measurement from one of such markers. The general trend of the recorded lateral movement was consistent with filling activities, as spikes of lateral movements were observed when major filling works were taking place. Lateral movement stalled after filling reached the final formation level at +6.5mPD. After 7 months, the recorded seawall lateral movement was roughly 50mm. This lateral movement magnitude was within the predicted range of around 60mm. It could be concluded that the DCM treatment was very effective in controlling seawall lateral movement.

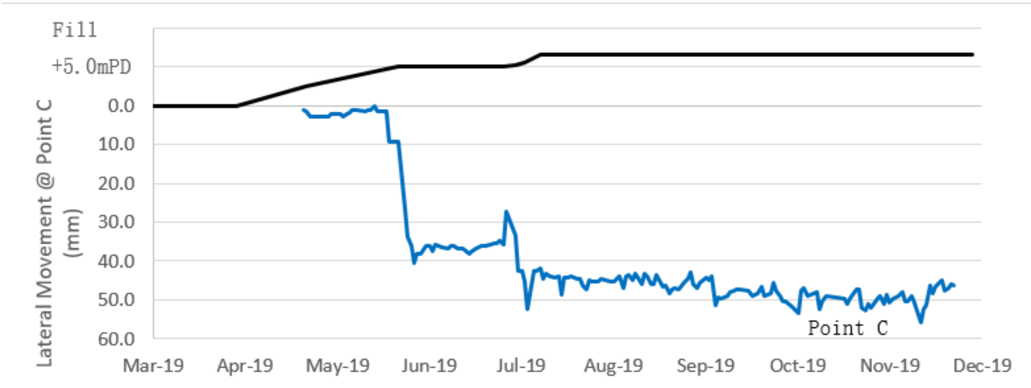

Figure 16: Seawall Lateral Movement measured from Surface Movement Marker at Points C

The above monitoring data demonstrates the effectiveness of settlement control. By reinforcing soft sediment to form a composite, ground settlement arising from the weight of reclamation fill can be effectively managed. As a result, the demand for fill material for replenishing settlement can be reduced significantly. In TCE reclamation, the saving of fill material was about 25%. This not only eased the demand of fill material but also reduced 3,000 vessel trips passing through the north Lantau water channel near Brothers Marine Park. The reduction in vessel trips would bring benefit in reducing the noise and air impacts and minimizing the disturbance of marine habitat. The reclamation works have been proceeding at a very promising pace with comparatively less impact on the environment. All these attribute to the adaptation of DCM method in the reclamation works.

7 CONCLUSIONS

A new technology – deep cement mixing (DCM) method, has been introduced in TCE reclamation materialising sustainable land reclamation. Through mechanical blending and mixing of binder slurry, soft marine sediment can be effectively reinforced and strengthened in-situ, and a composite material is formed quickly. This method fast-tracks the ground treatment process considerably as compared with conventional drained method and offers a robust solution for non-dredged reclamation.

Like many other geotechnical designs, a thorough understanding of ground conditions is vital for the DCM design and construction. A well-planned ground investigation and instrumentation monitoring programme and precise ground investigation data are the keys for the determination of mixing parameters, including binder type, dosage, and treatment pattern etc. In particular, the knowledge of in-situ water content and chemical composition within soft sediment are critical to the ultimately performance of DCM method, and cost effectiveness. The presence of obstructions, either natural or artificial, will affect the penetration of mixing shaft and constructability, that warrant to be attended during the planning and design stages.

Like other ground treatment methods, DCM method also involve certain embodied carbon, the choice of suitable binder augments the sustainability of DCM method, when applied in a large scale. The successful application of sustainable binder PBFC in TCE reclamation forms a model case for wider applications in future reclamation projects.

DCM is an effective and sustainable ground treatment method. The current design and construction contract specifications at TCE reclamation made reference to the FHWA design guidelines, (FHWA, 2013), but there is no doubt that the reference book is not fully applicable to local site conditions and practice in terms of design, construction and quality control. While the experience at TCE reclamation and ongoing site monitoring data are precious assets, the documentation of experience and collaboration amongst the industry, academies and the Government would definitely facilitate the technological advancement of the local construction industry to overcome the future challenges in upcoming reclamation projects.

8 ACKNOWLEDGMENT

The authors would like to thank the Director of Civil Engineering Development (CEDD) and Head of Sustainable Lantau Office of CEDD, AECOM design and construction teams and HKUST for their supports.

9 REFERENCES

Babasaki, R., Terashi, M., Suzuki, T., Maekawa, A., Kawamura, M. and Fukazawa, E. 1996. *Japanese Geotechnical Society technical committee reports: factors influencing the strength of improved soil*. Proceedings of the 2nd International Conference on Ground Improvement Geosystems, Vol. 2, 913-918

Endicott, L.J. 1992. *Evidence from engineering properties*. Proceedings of the Workshop on the Logging and Interpretation of Transported Soils in Offshore Boreholes, Hong Kong, pp. 39-48.

FHWA. 2013. "*Federal Highway Administration Design Manual: Deep Mixing for Embankment and Foundation Support*." Report No. FHWA-HRT-13-046, October 2013.

Higgins, D. 2007. *Briefing: GGBS and Sustainability*. Proceedings of the Institution of Civil Engineers Construction Materials 160 August 2007. Issue CM3, pp 99-101.

JGS 0821-2009. Practice for Making and Curing Stabilised Soil Specimens without Compaction, Japanese Geotechnical Society.

Kitazume, M. and Terashi, M. 2013. *The deep mixing method*. CRC Press/Balkema, Leiden, 405 p.

Koutsoftas, D.C., Foott, R. and Handfelt, L. 1987. *Geotechnical investigations offshore Hong Kong*. Journal of Geotechnical Engineering, ASCE, 113(2), pp. 87-105

Ng, C.W.W. 2014. *The state-of-the-art Centrifuge Modelling of Geotechnical Problems at HKUST*. J. Zheijang Univ.-Sci. 15, 1-21.

Skemption, A.W. 1957. *Discussion of the planning and design of new Hong Kong airport*. Proceedings of the Institution of Civil Engineers, 7 (1957). pp. 305-307

Strange, P.J. and Shaw, R. 1986. *Geology of Hong Kong Island and Kowloon*. Hong Kong Geological Survey Memoir No. 2, Geotechnical Control Office, Hong Kong, 134 p.

Marine Deep Cement Mixing (Cutter Soil Mixing Technique)

Derek Yung[1], Ricky Pang[2], Alex Chan[3]
Bachy Soletanche Group Limited, Hong Kong

ABSTRACT

In recent years, marine deep cement mixing was widely adopted in Hong Kong as the ground treatment method for many mega reclamation projects. Compared to the traditional dredging method, the deep cement mixing method is renowned for its environmentally friendly and high-quality standard. The installation of the deep cement mixing works will generate less vibration to the surrounding and prevents bringing the toxic material into the open water. Also, the deep cement mixing can provide a stable foundation for the land formation and comparatively less settlement is expected. The Cutter Soil Mixing technique is a type of deep cement mixing method. It is developed based on the Hydrofraise Cutter technology, crushing the soil through two counter-rotary cutters, and simultaneously mixed with a slurry binder to achieve the contract required strength. This paper presents a recent ground improvement project in Hong Kong with the application of marine Cutter Soil Mixing technique. Several essential working parameters such as mixing factor, dosage design and the criterion to achieve the top of competent stratum for the Cutter Soil Mixing installation are discussed. In addition, real time supervision and monitoring system by using a set of sophisticated instruments are introduced. The environmental considerations and measures of the project are also presented in this paper.

1. INTRODUCTION

Deep cement mixing (DCM) technique is being used over decades to improve the properties of in-situ soil. Unlike other replacement or displacement methods, DCM mixes cement into the ground without generating large volume of spoil. The three critical success factors are efficiency of mixing, reliability of the mixed soil and sustainability.

Bachy-Soletanche, as a specialist geotechnical solution provider, has developed its patented DCM system (namely GEOMIX®). It is a deep cement mixing process using Hydrofraise Cutter technology which is also called Cutter Soil Mixing (CSM). Geomix has been used worldwide in various geotechnical applications such as retaining walls, cut-off walls, mitigation of liquefaction hazards and soil improvements. Since 2014, the first deep cement mixed soil block was constructed in Hong Kong by Bachy Soletanche Group Limited (BSG) to strengthen the soft soil as a plug in front of the launching shaft for two large diameter (remarkably 14m and 17.6m) Tunnel Boring Machines (TBM) to break-in. In the following years, DCM has been used extensively in the reclamations in Hong Kong and is recognized as one of the most environmentally friendly choices for ground improvement. It not only avoids the disturbance to the marine environment induced by dredging marine clay, but also shorten the time taken for the stabilization of newly reclaimed lands. This paper presents a recent Hong Kong project in which BSG has successfully completed the biggest size of CSM project ever, with over 92,000 nos. of marine CSM panels (over 5.1 million m^3 of CSM treatment), without exceeding the low head room limits set by adjacent operating airport. The team worked 24hours/7days in 33 months, started with 2 barges from Oct 2016 and increased to 16 barges at the peak production period.

2. BACKGROUND OF THE PROJECT

The project presented in this paper is the soil improvement works using CSM technique to strengthen and stabilize the in-situ soft marine clay without dredging them away from the seabed. Avoiding any dredging prevented the adverse disturbance to the ecology of the sea environment in particularly the dolphins living close to the area of the proposed reclamation. Part of the proposed reclamation area had been used as the dump site

[1] E-mail: Derek.yung@soletanche-bachy.com
[2] E-mail: Ricky.pang@soletanche-bachy.com
[3] E-mail: Alex.chan@soletanche-bachy.com

for dredged marine clay which were packed in geotextile and known as Contaminated Mud Pit (CMP) in the past. This CMP may also be hazardous to the ecology. A protective system of silt curtain together with a real-time monitoring system of the appearance of dolphins have been adopted to achieve the environmental protection standard.

With respect to the headroom limitation (as low as 6.8m from the design highest sea level) in related to the aviation operation of the adjacent airport, all machines working on barges had been monitored by the tailor-made digital devices which were able to send alert and alarm warnings to the control teams if any booms of cranes or any parts excesses the height limit at the specific controlled locations.

Figure 1: Marine CSM working in low headroom condition

In order to shorten the stabilization time period as well as to reduce the residual settlement of the proposed reclamation to facilitate earliest commencement of the construction of seawalls and other permanent structures, CSM had been designed in pattern of individual rectangular panel of size of 2.8m x 1.2m (with cross sectional area of 3.36m^2) with different replacement ratio or in groups of overlapping panel walls to suit the corresponding load bearing and deformation performance requirements at different zones. Figure 2 below shows those different panel arrangements. The typical CSM treatment started from a thin layer of sand banket overlaid above the soft marine clay (from -6mPD to -15mPD, moisture content 75% to 95%), and penetrated through the soft Alluvium (soft to firm silt/clay, moisture content 30% to 75%). The termination criteria of CSM in the project was in general about 2m penetration of competent alluvium stratum (firm and stiff silt/clay, cone end resistance q-c of 1MPa to 2MPa), with a CSM treatment depth averaging 17m below the existing seabed.

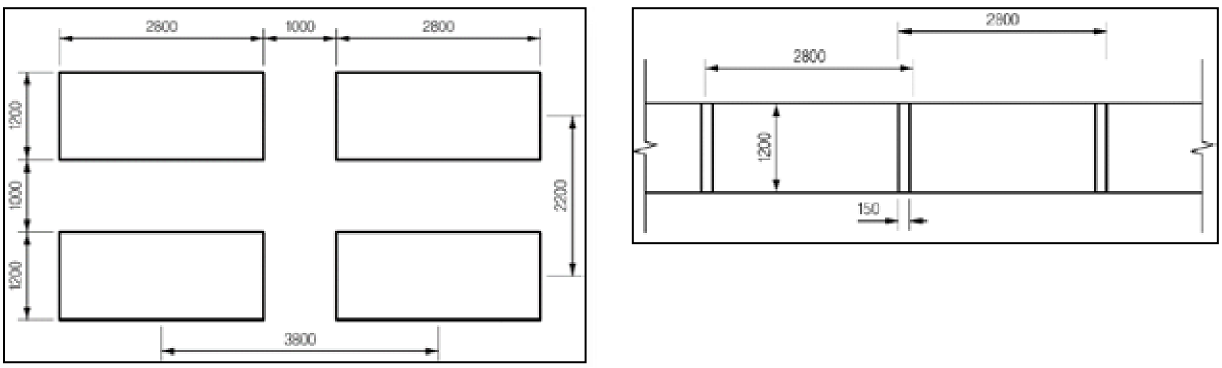

Figure 2 : Typical CSM panel: Individual Panel (left) and Panel Wall (Right)

The predicted properties of the CSM are measured and controlled under the contract quality plan by the Contract Required Unconfined Compressive Strength (CRUCS). In the project, 90% of the tested samples were required to achieve the minimum CRUCS of 0.8MPa to 1.2MPa, depending on the design requirement at various zones.

3. MARINE CUTTER SOIL MIXING TECHNIQUE

3.1 Introduction of CSM

The Cutter Soil Mixing (CSM) technique is a type of deep cement mixing method. It was developed by Bachy Soletanche derived from the Hydrofraise Cutter technology used in the construction of diaphragm walls. Figure 3 shows the Low Headroom Deep Cement Mixing tool (LHDCM) used on this project. On this equipment, the two counter rotary cutters disaggregate the in-situ soil, and simultaneously mix this soil with a slurry binder to produce a cemented compound with higher strength and stiffness than the original in-situ soil.

The cutter drums and the hydraulic motors were designed to optimize the mixing of ground in place with grout injected to reinforce the ground. As the hydraulic motors are embedded into the cutter drums and to be lowered to the treatment layer during mixing, it gives out direct power to the mixing operation and guarantees a very homogeneous material to be obtained under a relatively low cement consumption. In addition, as the mixing tool is mounted on the cable wire together with the Kelly bar, its center of gravity ensures very low deviation with good verticality and offset control.

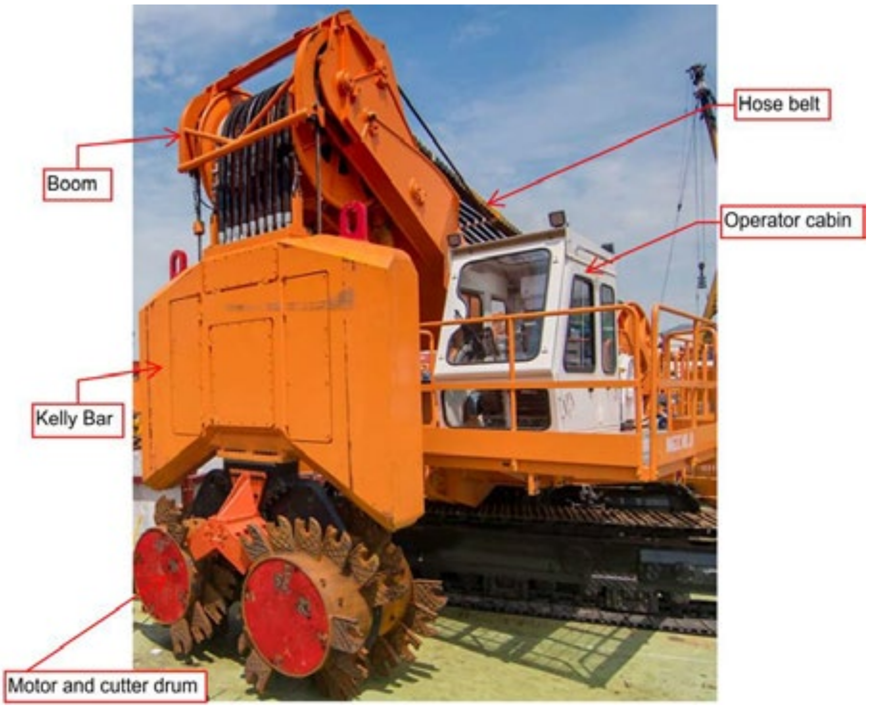

Figure 3 : CSM Type Low Headroom Rig

In this project, with respect to the specific site condition, the marine base CSM rig was designed by Bachy Soletanche to work in a low headroom condition of as low as 6m in height, with the reachable depth of around 40m below deck. Moreover, based on the real situation, by extending the length of the hose belt and cable wires, the capacity of the CSM rig can reach a depth of 60m or over, while maintaining the same low headroom condition. The rig was flexible in height and compact in size, and fast in production as no connecting of drill rods was required throughout the entire CSM panel installation.

Each equipment was installed on a barge, together with a set of grout batching plant and horizontal silos, as shown on figure 4. Each barge was positioned with a system of winches and anchors with the assistance of a GPS positioning.

Figure 4 : CSM Type Low Headroom Barge

On this project, the installation of a CSM panel was divided into two following phases:

a. Penetration Phase

The purpose of the penetration phase was to pre-mix the soil thoroughly and get ready for the withdrawal phase of the CSM operation. Once the CSM rig has been set up at the desired treatment location, the cutter started to penetrate and mix the in-situ soil with water injection. The incorporation of water was aimed to facilitate the mixing of the in-situ soil into a relatively homogeneous state, especially for the stiffer soil layer such as stiff alluvium. Thus, it was important to control the amount of water injection during this stage; too less water would make the soil difficult to mix with cement and hence decrease the degree of homogeneity, however, excessive water injection would weaken the final strength of the treatment.

b. Withdrawal Phase

After the cutters have reached the required bottom level of the CSM panel, the withdrawal phase began. During this phase, a cement binder grout was injected between the counter-rotating wheels and mixed with in-situ soil. The volume of cement grout delivered was determined to achieve the required strength. An extra volume of grout was required at particular depth in case excessive water volumes were introduced during the penetration phase. Same as the penetration phase, rotation speed, advancement rate of the cutters, together with the dosage design were pre-determined before commencement of the permanent works installation.

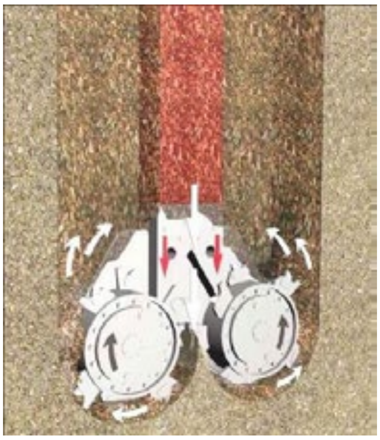

(1) Penetration Stage
Cutter goes DOWN
+
Incorporation of WATER
+
Premixing soil Downwards

(2) Withdrawal Stage
Cutter goes UP
+
Incorporation of BINDER
+
Mixing soil upwards

Figure 5 : Mechanism of CSM operation

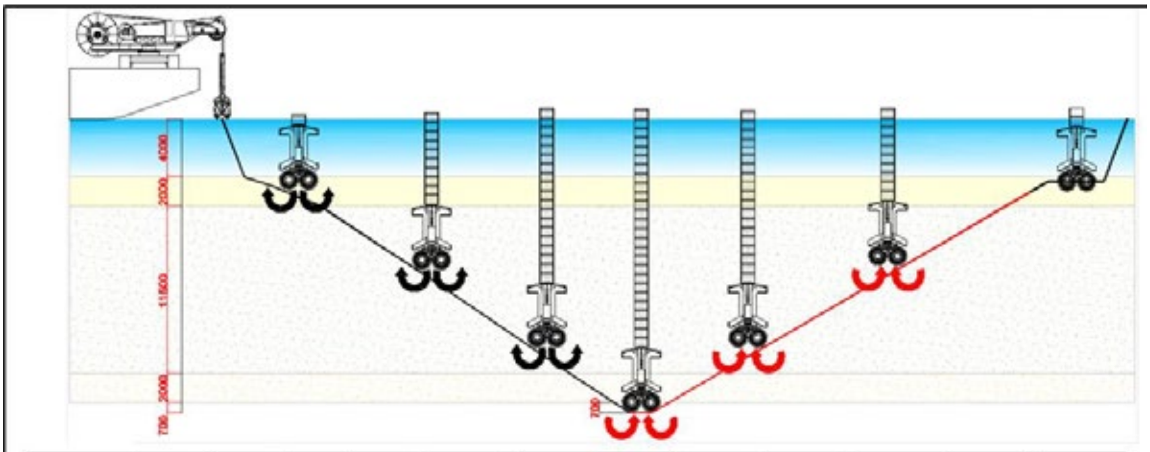

Sequence	1 Positioning	2 Penetration of soft layer	3 Penetration of stiff layer	4 Bottom cement slurry injection	5 Withdrawal with cement slurry	6 Rotate mixing wheels within sand blanket
Procedure	Set mixing wheels to the exact position and confirm the vertical stability	Penetration by mixing wheels with normal rotation and moving speed	Cutter penetration until the Hydraulic pressure reaches Required bars for continuous 10 seconds. Go further 2m down to achieve the panel toe level	After confirm founding level, start cement slurry injection for replace seawater inside hose system. (30s ~)	After bottom cement slurry injection, withdrawal of mixing wheels with reverse rotation and injection of cement slurry until 1m below top of sand blanket	Upon completion of the LHDCM panel, lift up and rotate mixing wheels within sand blanket before raising into the water
	Mixing-down phase (seawater injection)			Mixing-up phase (cement slurry injection)		

Figure 6 : Standard Installation Procedure of CSM

3.2 Working Parameters

Several working parameters were essential for the success of this operation and needed to be closely followed. In the below sections, these working parameters are presented and discussed.

a. Mixing Factor

The CSM tool is mainly composed of 3 main elements: cutting drums powered by the hydraulic motors, cutter blades and the scrappers. When a drum rotates, the scrappers fixed below the Kelly Bar interact with cutter blades and shear the soil to facilitate the mixing process. During one single rotation of each drum, the mixing effect by shearing occurs several times as each cutter drum carries several rows of 3 mixing blades each.

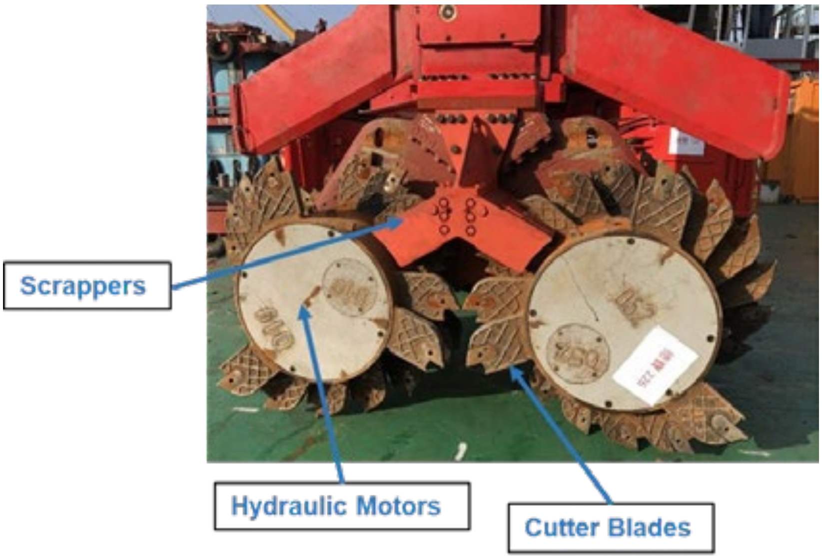

Figure 7 : Configuration of a CSM tool

Unlike the standard auger-based DCM tools, the mixing factor with CSM equipment is not directly related to the quantity of blades used. Instead, based on Bachy Soletanche's experience in CSM works, the controlling criteria was the percentage of coverage of the cutter drum surface by sufficient cutter blades. The degree of mixing equation is given on Figure 8. The formula takes into account the advancement rates and the corresponding cutter rotational speeds.

$$T_{LHDCM} = \left(\frac{Nu}{Vu} + \frac{Nd}{Vd}\right)$$

Where,

T_{LHDCM}: mixing factor for LHDCM works

N_u: Rotation speed in rpm of the blades during withdraw

V_u: Mixing blade withdrawal velocity

N_d: Rotation speed in rpm of the blades during insertion

V_d: Mixing blade insertion velocity

Figure 8 : Mixing Factor equation for CSM works

As the in-situ soil represents a significant part of the final mixture, the homogeneity of the deep cement mixed material may follow a log-normal statistical distribution of compressive strength driven by a ratio between standard deviation and average value, also called Coefficient of Variation (COV). As reported in the *Design of*

Deep Mixing for Support of Levees and Floodwalls[1], the strength of the deep mixed ground has relatively high variability, with coefficient of variation ranging from 34% to 79%, with an average value of 56%.

Classically, any COV should be linked to a given value of mixing factor.

However, based on the experience of Bachy Soletanche's previous projects, the coefficient of variation for CSM works generally lies between 30% to 40%, with a corresponding mixing factor being achieved at various soil condition. The relatively lower COV credits to the mixing mechanism of the CSM tool, which is in direct contact with the soil and does not allow any soil particle to stay in place. This enhances the quality and homogeneity of the treated soil when treated with CSM.

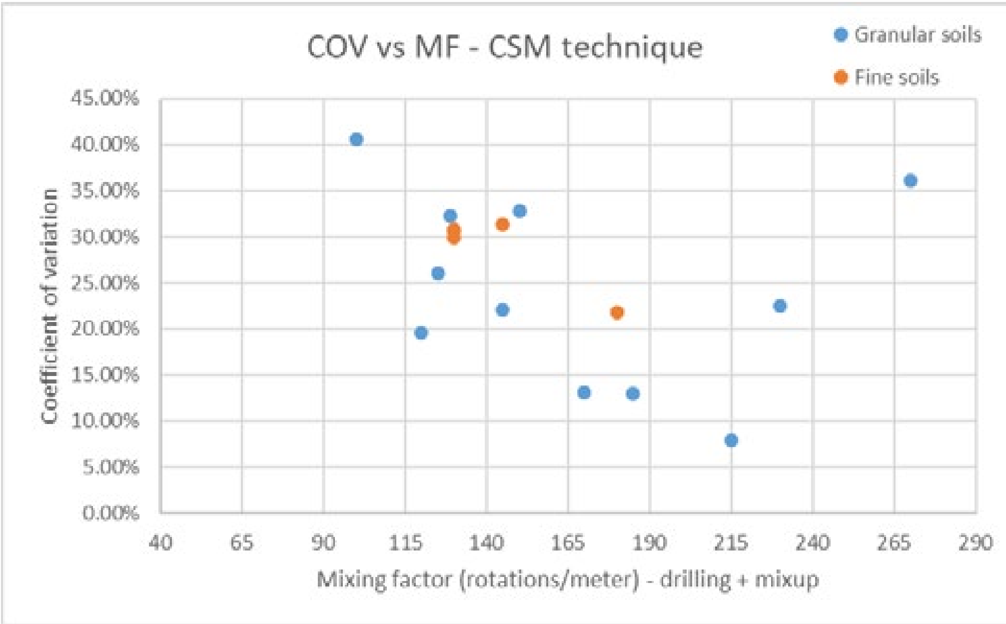

Figure 9 : Few examples of COV vs Mixing Factor with CSM

b. Dosage Design

Dosage design is usually defined by the ratio between the dry binder mass incorporated into one cubic metre of DCM element. In practice, this value is related to the injection volume of binder to the treatment and will have a great impact on the final product strength.

Basically, the cement dosage depends on: (i) Type of cement and quantity of cement, (ii) Type of in-situ soil and its properties, (iii) the method of mixing treatment.

Few additional factors were considered when designing the cement dosage, such as the natural water content of the soil, organic content of the soil, water/cement ratio of the grout, level of confidence of the contract requirement uniaxial compressive strength to be achieved, the coefficient of variation of the mixing and the factor between the laboratory strength and the field strength.

A balance between all these factors was made to obtain the most appropriate dosage. As the dosage design is sensitive to site-specific factors, it was required to start with a laboratory test and to be followed by a site field trial.

In this project, various soil samples along the site area were obtained by Vibrocore at different depth. Properties tests such as Atterberg Limits, natural moisture content, bulk density, particle size distribution, pH value, organic matter content, etc. were performed. According to the ground investigation report, the soil samples were classified into 3 main categories: high moisture content marine deposit, low moisture content marine deposit and alluvium. Then various preset volume of seawater and binder grout were mixed with these soil samples to simulate the real mixing situation on site. According to the specification, 5 nos. of proposed dosages with different binder types were tested for a given Contract Required Unconfined Compressive Strength (CRUCS).

According to *The Deep Mixing Method*[2], Kitazume mentioned that "*usually the in-situ stabilized soil column has smaller average strength and larger strength deviation than those of the laboratory specimen*" and in the case of the land DCM, the field strength is generally about one-half to one-fifth for clay and about two-third for sand of the lab strength; while in the case of marine constructions, the UCS of in-situ stabilized soil is almost the same order with the laboratory strength.

A further coefficient of 15% was adopted in this project on the laboratory strength when designing of the cement dosage for the start of permanent works.

Field trials shall be carried out before the commencement of the permanent works to test the capability of the machine and to justify the design working parameters assumptions. Figure 10 below compares the unconfined compressive strengths (UCS) taken from cores samples inside one panel together with the UCS measured during the laboratory trials.

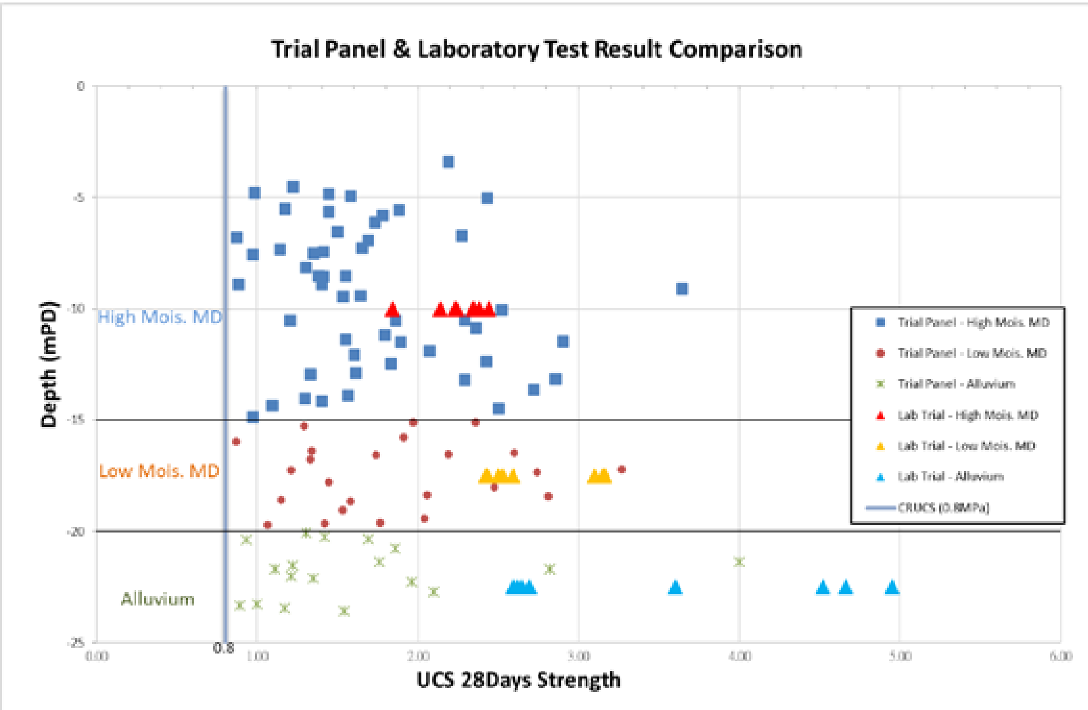

Figure 10 : Test Result of laboratory test and field trial for a cement dosage

c. Top of Competent Stratum

In this project, all CSM panels were required to have a 2m embedment into the competent stratum, mainly classified as stiff alluvium with minimum CPT's cone end resistance > 1MPa.

Before commencement of the CSM panel installation, a site mapping of about 100nos. pre-CPT with approximately 100m distance apart from each other was conducted to determine of the design founding levels for each CSM panel. A contour plan with all the analyzed CPT results was then generated for construction purpose.

Besides, during the course of the CSM works, a test called trial insertion was conducted periodically to re-calibrate the performance of the CSM rigs and to justify the depth of each CSM panel to be or being constructed. The trial insertion system consisted of a CPT being performed at the test panel to compare with the CSM rig's response when encountering the top of the competent stratum. It was understood that the cutter wheels of the CSM machine would have a significant change of hydraulic pressure when encountering a comparatively stiffer material. With various trials at different locations on site, the relationship between hydraulic pressure with time and ground condition at the competent stratum could be established. This was a site-specific criterion and shall be assessed on each project.

3.3 Environmental

Compared to the traditional dredging method, CSM method was a more environmentally friendly method where the soil was mixed in-situ preventing toxic material of the contaminated soil being exposed into the water.

During the CSM installation, few environmental measures were implemented.

a. Sand blanket
A layer of 1m to 2m thick sand blanket was placed on top of the existing seabed as an insulating capping layer. The purpose of the sand blanket treated as a capping layer was to prevent any excessive toxic material being released into the open water. Upon completion of each CSM panel, the cutter spent at least 5 minutes to rotate within the sand blanket to wash out and to remove the muddy mixture on the cutter before retrieving back on the deck. In addition, this capping layer helped to ensure the treatment quality for the top few meters of the soil as it prevented any excessive seawater being introduced into top of the treatment.

b. Silt Curtain
Primary silt curtain was equipped on each CSM barge. The primary silt curtain system was treated as the major protection. It was surrounding the CSM cutter and was lowered down to the top of sand blanket during each CSM operation. In case there was any exceedance of water quality level during the real-time water monitoring process, the woven geotextile fabric secondary silt curtain enclosing the barge itself was deployed.

c. Water quality monitoring
Apart from the silt curtain deployment, real time water quality monitoring is adopted for each CSM barge with in-situ continuous and on-site water quality monitoring data during the CSM works throughout the duration of the Contract. Monitoring locations are set up outside the boundary of the primary silt curtain. Sondes are used for continuous monitoring. Data such as salinity, pH value, dissolved oxygen, turbidity will be recorded every 5 minutes throughout the project.

d. Use of slag cement

The use of slag cement replacement was more sustainable to the environment as it had significantly reduced the amount of clinker, a major component of Ordinary Portland Cement. This lead to consume less energy for production and reduced by 380,000 tonnes the carbon footprint of the whole project. Moreover, as the strength achievement of slag cement was higher than that of OPC with the same dosage, we further managed to use less cement binder in the CSM treatment for the same final quality.

e. Mammal Observation

This project adopted and maintained 24-hour stations for implementing the Dolphin Exclusion Zone (DEZ) to minimize the impact on the Chinese White Dolphin. DEZ of 250m distance from the boundary of the works area was established during the CSM works. An innovative CCTV system was set up on the CSM barge to cover all sea surfaces within the DEZ as the monitoring stations. A group of minimum 2 numbers of well-trained dolphin observers were monitoring the process through a high resolution and zoomable network camera at a centralized monitoring office.

3.4 Supervision and monitoring

As each low headroom barge working on sea was far away from the central site office, they were treated as a single remote site. A set of sophisticated instruments with the software developed by the team were installed on each CSM rig for data recording and monitoring to ensure the quality of the CSM works shall achieve the contract requirement.

Figure 11 : Instruments on CSM rig

On each CSM rig, a customized interface with all necessary parameters presented in graphical format were displayed on screen and enabled the operator to keep track of the current working status and have a full control of the CSM installation. These displayed graphs and figures were designed in accordance with the working parameters in the contract requirement and specification. During the CSM operation, these visualized graphs and figures were shown in eye-catching color. In case of any requirement that are not being achieved, warning messages appeared on the screen to alert the operator for immediate corrective actions accordingly.

Figure 12 : Graphs/figures during Penetration stage (left) and Withdrawal stage (right)

At the same time, the data was automatically transmitted to the Cloud where the whole installation process was recorded and saved. Real-time supervision works of all working rigs was centralized and monitored through the software at the remote main office. In addition to the front-line engineers, a team of monitoring engineers managed and supervised 24 hours per day to ensure the CSM works were in full compliance to the contract requirements. Hundreds of completion reports were automatically generated from the Cloud storage and cross checked before submission to the client within 24 hours after completion.

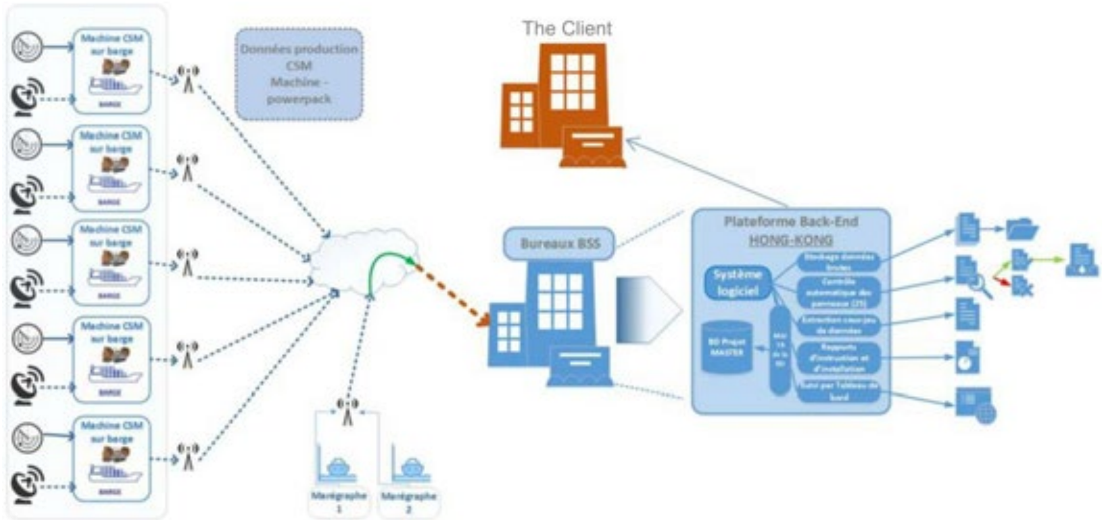

Figure 13 : Transmission of data

In terms of analysis, data were retrieved from the Cloud for big data analysis. Throughout the CSM installation process, one line of data was recorded for every 1 second or 2 centimeters of the cable wire movement. The huge amount of data will be handled and organized by a database which allowed stability of data processing and provided a clear and structured organization of the data.

3.5 Quality

Upon completion of the CSM panels, testing works consisted of full depth core and post-CPT were carried out to justify the quality of the treated panel in terms of strength and embedment depth requirement.

a) Coring

Coring was performed to test the strength of the treatment installed by CSM. For the continuous CSM panel wall under the seawall footprint, continuous core sample was conducted at the 150mm overlapping joint of two panel walls; while the core was taken near the center of the CSM panel for those outside the seawall footprint. Under this project, the requirement of the full depth coring was required to carry out according to the following criteria:

Panel Location	**Testing Frequency of Full Depth Core**	
Seawall footprint	1 test for every 2 panels wall along the seawall chainage	1 specimen for each meter length of core
Outside seawall footprint	~1 core for every 250 CSM panels	10 specimens selected evenly per core

Table 1: Contract requirement on coring frequency

Around 1,300nos. of core holes were conducted in this project. One of these coreholes is shown on Figure 14. About 95% of the overall UCS tested samples were over 0.8MPa at 28-day strength, which met the CRUCS of 0.8MPa with level of confidence of 90%. A view of the UCS measured on samples in given in Figure 15.

For the Coefficient of Variation, it was observed that at the upper and lower marine deposit, the COV were in the range of 30% to 40%, while the COV in the competent stratum was between 40% to 50%.

Figure 14 : Corebox photo of a CSM treated panel

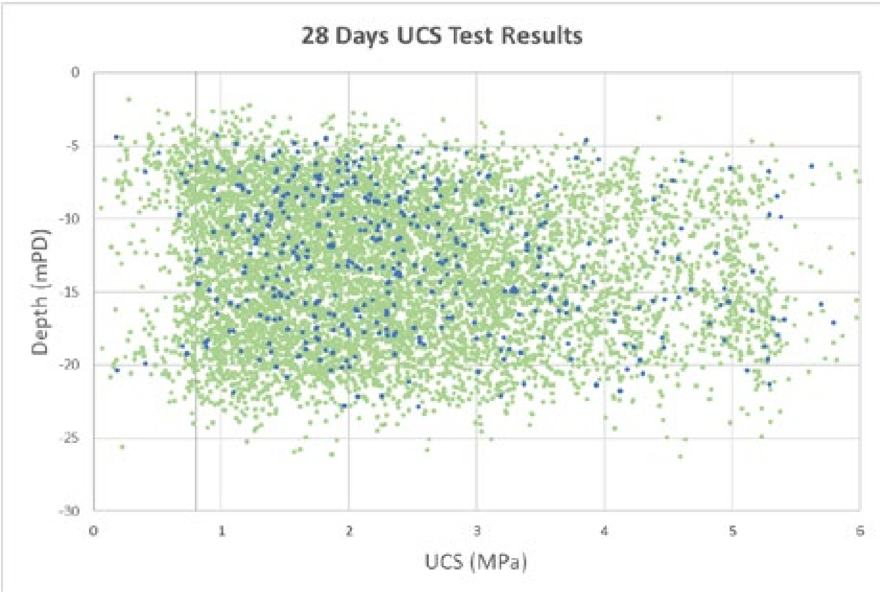

Figure 15 : UCS test results

b) Post CPT

Post CPT was carried out at 600mm away from a constructed CSM panel as the proofing test of sufficient embedment into the competent stratum according the contract requirement. Under the contract requirement, the testing frequency is indicated in Table 2 below.

Panel Location	Testing Frequency of Post Cone Penetration Test (CPT)
Seawall Panel	1 test for every 2 panels wall along the seawall chainage
Load Transfer Plate Panel	~1 core for every 100 CSM panels

Table 2: Contract requirement on Post CPT frequency

Around 1,450nos. of post CPT were carried out and all of them were found deep enough with minimum 2m embedment into the competent stratum. In fact, the average toe level between the pre-CPT results, the as-built CSM panels and the post-CPT results were consistent. It further proved the effectiveness of the trial insertion system and the appropriateness of the criterion using the hydraulic pressure of the cutter to define the top of competent stratum.

Figure 16 : CPT Test unit

4. CONCLUSION

The largest marine CSM project ever constructed in Hong Kong containing more than 92,000 panels have been completed. In this benchmarking project, not only the excellent safety performance of the team as continuously appreciated by Client via various safety prizes, but also the quality and environmental management systems are demonstrated to be successful.

The CSM barges and its supporting facilities are all tailor-made designed and fabricated to suit the low headroom requirement of the project.

All the data collected by the digitization monitoring system will flourish our database of Geomix CSM and become our valuable assets for future development of the technology in Hong Kong and worldwide.

The contract arrangement, quality assurance framework and testing procedure developed for and improved throughout the project will form good example for the further reclamation projects.

REFERENCES

[1] George Filz, Tiffany Adams, Michael Navin, A.E. Templeton

Design of Deep Mixing for Support of Levees and Floodwalls

In: Grouting and deep Mixing 2012

[2] Masaki Kitazume

The Deep Mixing Method: pp 128-130, 373

[3] Fabrice Mathieu, Jean-Francois Mosser, Nicolas Utter, Sabine Darson-Balleur

Deep soil mixing with Geomix method: Influence of dispersion in UCS values on design calculations

Use of Smart Devices in Civil and Geotechnical Works for Vibration, Noise and Temperature Measurement

Thomas S K Lam, Kathy Lau
Construction Industry Council, Hong Kong, China
Songye Zhu
Department of Civil & Environmental Engineering, The Hong Kong Polytechnic University, Hong Kong, China
Goman Ho
Arup, Hong Kong, China

ABSTRACT

The Construction Industry Council (CIC) was set up with a vision to drive for excellence of the construction industry in Hong Kong. The CIC encourages and facilitates research activities and the use of innovative techniques for the construction industry, as one of the many functions. The CIC engages consultants, academic institutions, in-house resources, etc., to carry out study and research work on practical construction problems in response to the needs of the construction industry.
Recently, work on the development of an App for iPhones for real-time monitoring and assessment of construction-induced vibration and noise, and the application of the maturity method for estimation of concrete strength in concrete structures was completed.
In this paper, a detailed description of the laboratory calibration and site validation of the App developed for iPhones for vibration and noise monitoring, and the results obtained, including the setting-up requirements, are presented. This is followed by a discussion of the use of the maturity method for concrete strength measurement. The application of the maturity method to a case, involving installation of temperature sensors to measure the temperature development in a retaining wall structure to estimate the gain in strength, and a detailed interpretation of the results, are given.

1 INTRODUCTION

In civil and geotechnical works, there is a requirement for vibration and noise monitoring to check that the effect of vibration and noise as a result of the works will not produce any adverse effects on the structures and geotechnical features in the vicinity of both private and public project works. It is a practice that commercial seismograph/sound level meter units are used. These units are expensive, so usually only one to two units are kept on site at most. This makes vibration and noise monitoring an expensive and inconvenient exercise. The use of a smartphone, such as an iPhone, with a built-in App has made the vibration and noise monitoring a simple and inexpensive exercise.

In construction, in-place concrete strength is determined by performing compression tests on concrete test cube or cylinder samples collected on site in laboratory. Concrete samples are made on site as the concrete arrives on site. There is a waiting time for these test samples to gain strength before they can be tested. Using the maturity method and by measuring the temperature in the concrete in the structures, concrete strength can be evaluated in real-time. This will cut away the time needed for performing compression tests on the samples at the specified times. The number of the test samples required for quality control/quality assurance will also decrease. This method will enhance construction productivity, because by knowing the concrete strength early, many construction works that follow, such as stressing of tendons in pre-stressed concrete structures, stripping and removal of formworks and shoring, application of loads, etc., can move ahead of the construction schedule.

In this paper, a detailed description of the laboratory calibration and site validation of the App developed for iPhones for vibration and noise monitoring, and the results obtained, including the setting-up requirements, is given. A comparison of the vibration and noise results as obtained from iPhones from a site with those obtained from a seismograph/sound level meter is given and discussed. This is followed by a discussion of a case using temperature sensors to measure the temperature development in a retaining wall structure to estimate the gain in strength. The procedures of laboratory calibration and site validation for the method and a detailed interpretation of the results obtained are presented.

2 USE OF V&N APP FOR MEASUREMENT OF VIBRATION AND NOISE

2.1 Background

In 2019, the CIC engaged Prof. Songye Zhu of the Hong Kong Polytechnic University (PolyU) to develop a new method for construction-induced vibration and noise monitoring, making use of the latest smartphone technology (CIC, 2021a). There are three main tasks of investigation under the study: (1) laboratory calibration; (2) App development; and (3) site validation. In this study, focus was put on the App development for iPhones (iOS environment) only. The App developed is called V&N App. User guidelines and details of the data input and output for the V&N App are given in CIC (2022). This paper focuses on the procedures and findings of Tasks (1) and (3).

2.2 Data Interpretation

(a) Peak particle velocity (PPV)

PPV is defined as the maximum velocity of the measured surface during a time interval (BSI, 1993) in mm/s. The V&N App measures the acceleration signal ($a(t)$), and then converts it to a velocity signal v(t) by integrating $a(t)$. PPV limits are set as a requirement in most civil and geotechnical works. The V&N App measures and reports PPV in three perpendicular directions (PPVx, PPVy, and PPVz) every 5 seconds. The resultant PPV is given by the peak vector sum, which is given by the square root of the sum of the squares of the individual PPV values in the three directions.

(b) Root-mean-square (RMS) velocity

The evaluation of vibration impact on sensitive equipment is based on the RMS velocity in the 1/3 octave band spectrum, in accordance with BS 5228-2 (BSI, 2009). The V&N App provides the RMS velocity in the 1/3 octave band spectrum in both the time and frequency domains. The transformation from the time domain to the frequency domain is conducted through the fast Fourier transform (FFT).

(c) A-weighting noise level

In the A-weighting scale, the sound pressure levels for the low-frequency bands and high-frequency bands are reduced by certain amounts before they are combined together to give one single sound pressure level value. This value is designated as dB(A). The dB(A) is used for environmental noise measurement as it reflects more accurately the frequency response of the human ear (see EPD (2022)). The V&N App provides this noise level, including the instantaneous level.

2.3 Laboratory Calibration

2.3.1 Vibration Calibration

Most iPhones and Android phones are equipped with a six-axis MEMS vibration sensor (triaxial accelerometer and triaxial gyroscope) and an internal microphone. These sensors can be used for vibration and noise monitoring.

To check the accuracy of the vibration measurements from the smartphones, laboratory calibration tests were carried out. The test set-up is shown in Plate 1. A high-fidelity triaxial accelerometer (PCB 356b18) was used. The smartphones, together with the PCB accelerometer, were mounted on a steel cube on an exciter. The smartphones were attached to the steel cube by a strong magnet. Harmonic sinusoidal excitations were provided to the exciter by a signal generator and a power amplifier at a specific frequency and amplitude respectively.

The smartphones tested included iPhone 6, iPhone 7, iPhone 8, iPhone X, iPhone 11 Pro Max, Samsung Note 9 and VivoNex, as shown in Plates 1 & 2. The frequencies of the harmonic sinusoidal excitations applied were 4 Hz, 6 Hz, 8 Hz, 10 Hz, 16 Hz, 20 Hz and 25 Hz, which covered the common range of the construction-induced vibrations. Different amplitude levels were applied. The sampling frequency of the measurement was set at 100 Hz.

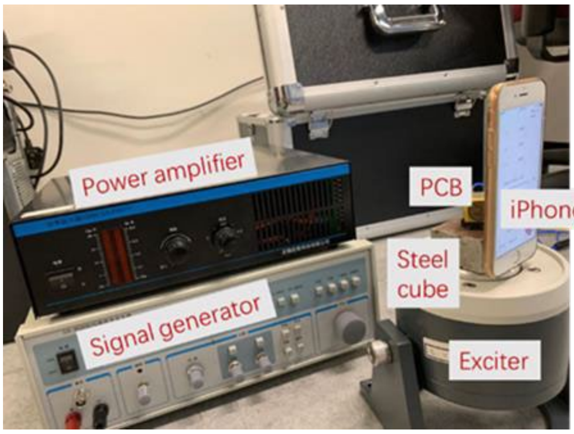

Plate 1: Set-up for vibration calibration

Plate 2: Calibration test of various smartphone models on a shaking table

A typical comparison of the acceleration time histories at 4 Hz harmonic sinusoidal excitation recorded by iPhone 8 and the PCB accelerometer is shown in Figure 1. The measurement results from iPhone 8 coincide well with those from the PCB accelerometer over the time domain examined.

A typical comparison of the RMS velocity in the 1/3 octave band spectrum is given in Figure 2. The results obtained from iPhone 8 and the PCB accelerometer were almost the same in the frequency domain. The location and the amplitude of the peaks coincide well, and the variation trend over the frequency range is the same.

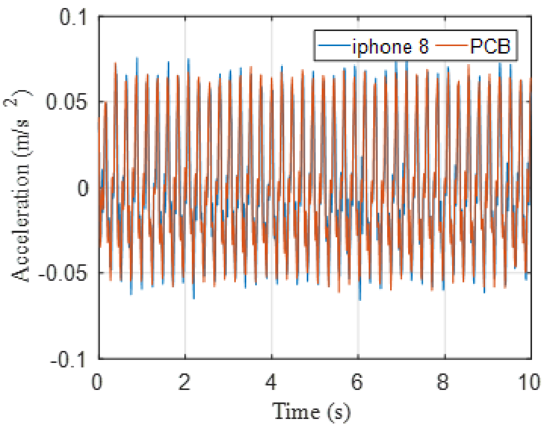

Figure 1: Comparison of acceleration at 4 Hz excitation between iPhone and PCB accelerometer

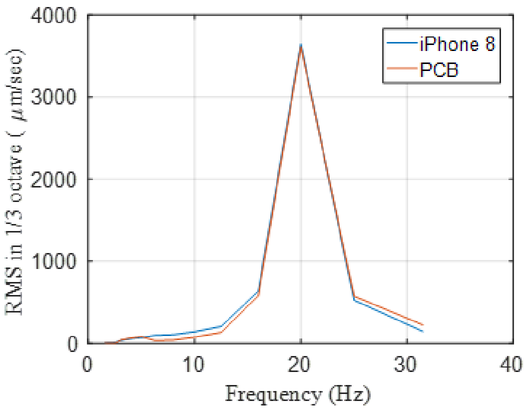

Figure 2: Comparison of RMS velocity in 1/3 octave band spectrum at 20 Hz excitation between iPhone and PCB accelerometer

The performance of the different iPhone models used was examined, in terms of the relative difference (RD) between the measurement results of the smartphones and the PCB accelerometer, as follows:

$$\mathrm{RD}(\%) = \left|\frac{\mathrm{A-B}}{\mathrm{A}}\right| \times 100\% \qquad (1)$$

where A is the measurement recorded by the PCB accelerometer, in terms of acceleration, PPV or RMS velocity in the 1/3 octave band spectrum, and B is the corresponding measurement recorded by the smartphone.

A direct comparison of the measurement results, in terms of PPV every 10 sec and RMS velocity in the 1/3 octave band spectrum under different vibration amplitudes at 25 Hz excitation, between those obtained by iPhone 8 and the PCB accelerometer, is shown in Figures 3 and 4. The measurement results coincide very well.

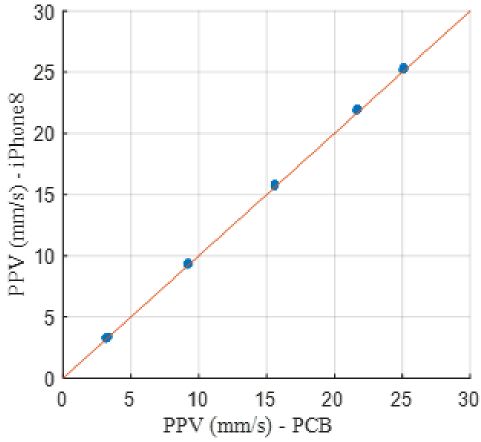

Figure 3: Comparison of PPV at 25 Hz excitation between iPhone 8 and PCB accelerometer

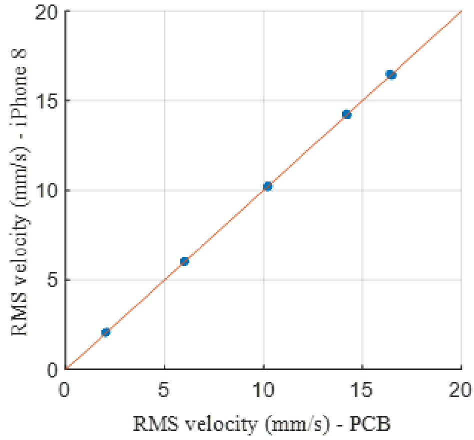

Figure 4: Comparison of RMS velocity at 25 Hz excitation between iPhone 8 and PCB accelerometer

In general, the RD is less than 3%, except at the lowest vibration level where the maximum RD could reach 5%. The lowest vibration level is defined as the acceleration level at 0.1 to 0.15 m/s^2, the PPV level of less than 0.5 mm/s, and the RMS velocity in the 1/3 octave band spectrum of 100 to 150 µm/s. This small value of RD is considered accurate enough for the purpose of construction monitoring.

Two Android smartphones (Samsung Note 9 and VivoNex) were tested for parallel comparison, as shown in Plate 2. Excitation frequencies of 2 Hz, 4 Hz, and 6 Hz were applied.

The results indicated that Samsung Note 9 had acceptable accuracy, while the performance of VivoNex was not stable.

The iPhone series was found more suitable for vibration monitoring, as compared with the Android smartphones, due to the consistency in performance.

2.3.2 Noise Calibration

The noise data were acquired using the internal microphone built inside the iPhones and were compared with those obtained by a sound level meter (BSWA 308). For this calibration, iPhone 8 and iPhone 11 were used. The test set-up is shown in Plate 3. Both the slow-time weighting and fast-time weighting measurements were tested (fast corresponds to a 125 ms time constant whereas slow corresponds to a 1 second time constant). Figure 5 shows the noise level recorded by iPhone 11 using fast-time weighting measurement, in terms of dB(A) and the RD computed. The difference in the sound level recorded is less than ±2 dB(A).

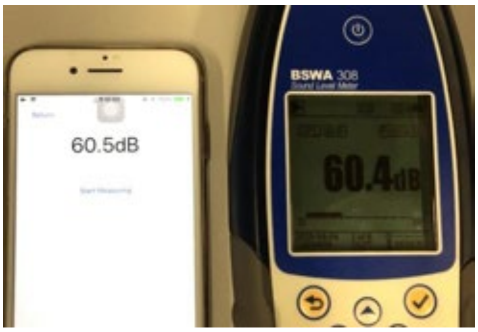

Plate 3: Set-up for noise calibration

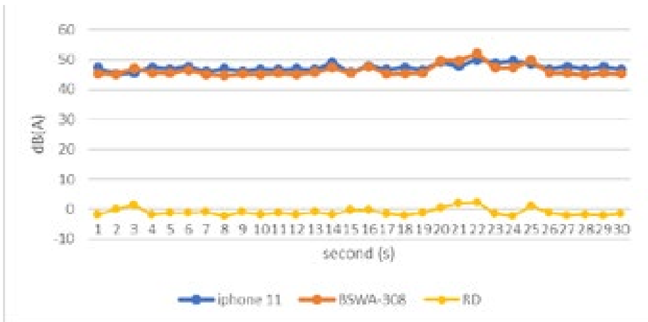

Figure 5: Comparison of noise level recorded by iPhone 11 and sound level meter

2.4 Site Validation

To validate the V&N App developed for measuring the construction-induced vibration and noise, eight field measurements were carried out, as shown in Table 1, for various construction activities, including socketed H-piling, sheet piling, mini-piling and rock excavation works.

Table 1: Field measurement project information

Co-ordinator	Project	Location	Type of works
QMH	Queen Mary Hospital Expansion Project	Pok Fu Lam	Rock excavation
Chevalier Group	Tuen Mun Hospital Expansion Project	Tuen Mun	Concrete breaking
Chevalier Group	Kwun Tong Preliminary Water Treatment Works	Kwun Tong	Sheet piling & Mini-piling
CEDD	Contract No. ND/2019/04 - Fanling North New Development Area, Phase 1: Fanling Bypass Eastern Section (Shek Wu San Tsuen North to Lung Yeuk Tau)	Fanling	Pre-bored socketed H-piling
CEDD	Contract No. NE/2017/05 – Tai Po Road, Sha Tin Section	Sha Tin	Sheet piling
CEDD	Contract No. ND/2018/01- Kong Nga Po construction site	Fanling	Sheet piling
ArchSD	Contract No.SSH502 -Design and Construction of Joint-user Government Office Building in Area 67	Tseung Kwan O	Bored piling
HD	Sheung Shui Areas 4 & 30, Site 1 Phase 1	Sheung Shui	Pre-bored socket H-piling

In the test set-up, two or more strong magnets were attached to the back of the smartphones using strong tapes, and a steel soil nail, steel block or steel plate was used for vibration monitoring on soil surface, rock or ground surface or vertical structural surface respectively, as shown in Plate 4.

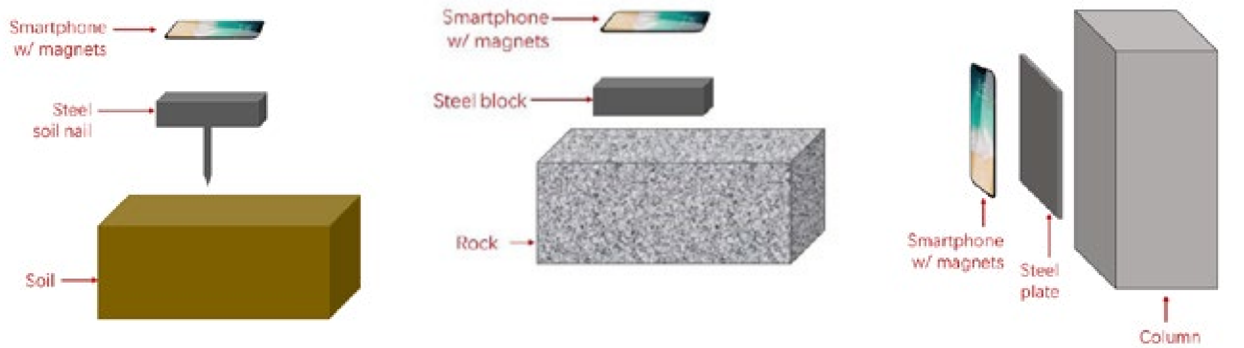

(a) On soil surface (b) On rock or ground surface (c) On vertical structural surface

Plate 4: Set-up for smartphones on different types of surfaces

In the site validation, the operational performance of the V&N App was tested. The vibration and noise measurements were acquired and processed by the V&N App installed in the iPhones, and the data, including photo, text remarks, etc., were uploaded to the cloud (Google Firebase in this case), and test emails were sent.

The results obtained from the monitoring the Sheung Shui site involving socketed H-piling works are presented herein.

Two smartphones (iPhone 8 and iPhone 12) were used, and they were installed at different locations for vibration measurement. Soil nails were first inserted into the soil ground at the monitoring locations. The distances from the socketed H-pile to iPhone 8 and iPhone 12 were 3.3 m and 10.8 m respectively, as shown in Plate 5. An accelerometer (PCB 356b18) was used to measure the vibration at the iPhone 12 location.

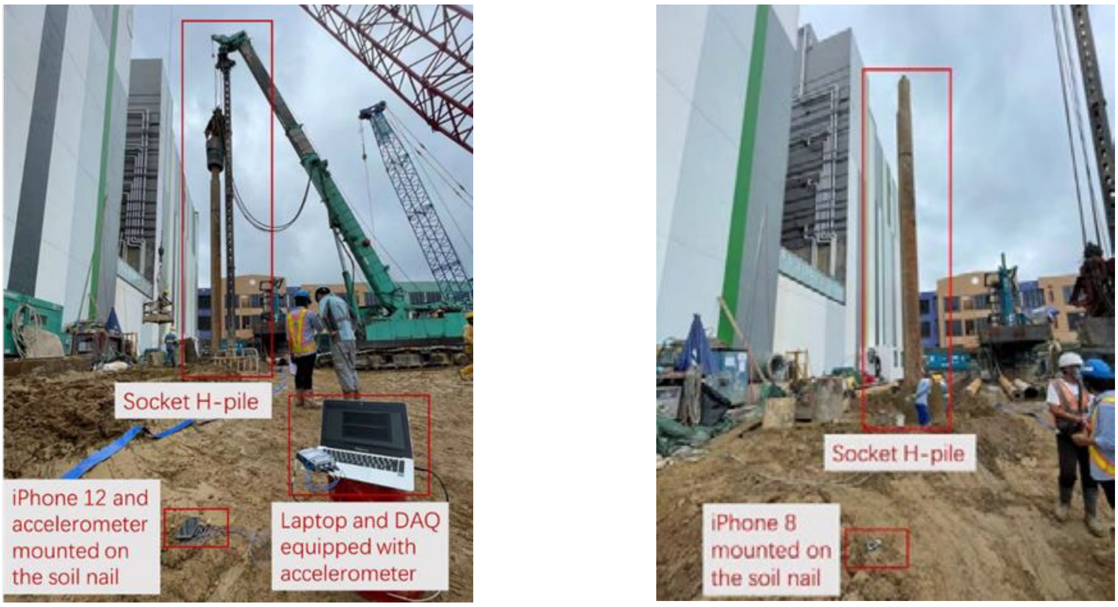

(a) Set-up for iPhone 12, accelerometer and soil nail (b) Set-up for iPhone 8 and soil nail

Plate 5: Set-up for site validation

The V&N App operated normally during the whole measurement process. The acceleration time history, velocity time history, and RMS velocity in time domain recorded by iPhone 8 are given in Figure 6.

The acceleration measured by iPhone 12 ranges from -0.231 m/s^2 to 0.192 m/s^2, whereas that measured by iPhone 8 ranges from -0.381 m/s^2 to 0.251 m/s^2. The vibration attenuates with distance.

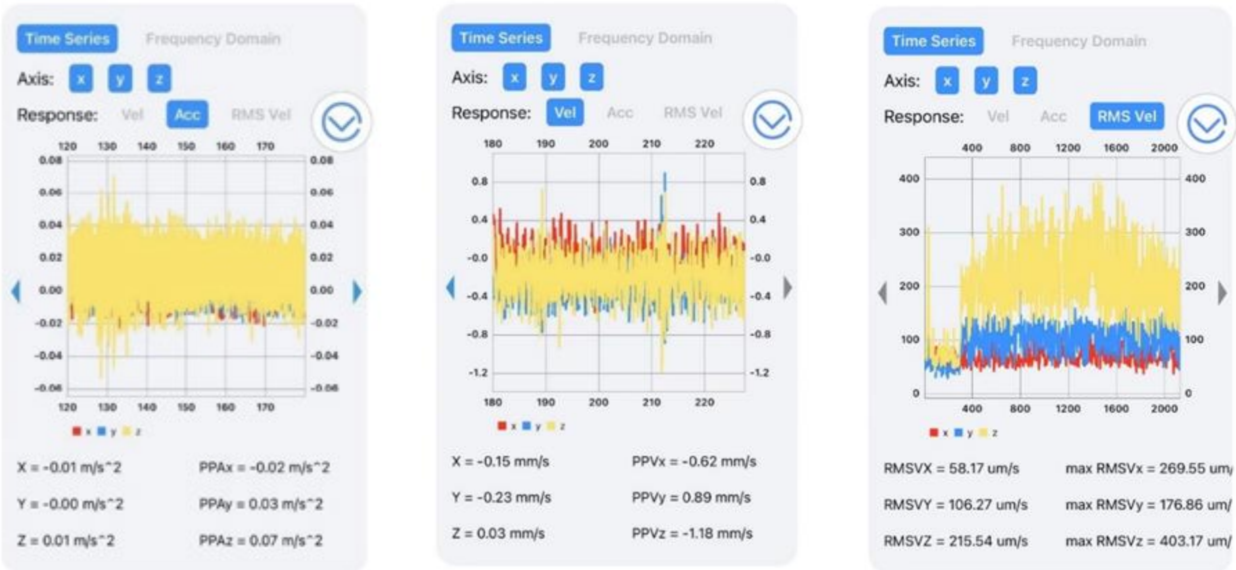

(a) Acceleration time history (b) Velocity time history (c) RMS velocity in time domain

Figure 6: Screen shots of vibration results from V&N App

A comparison of the PPV values recorded by iPhone 12 and the accelerometer (PCB 356b18) is shown in Figure 7. The green dashed lines show the 10% difference bounds. The average RD of PPVx, PPVy and PPVz is 5.27%, 5.86%, and 4.87% respectively. The measured PPV ranges from 0.493 to 3.175 mm/s. In general, there is good comparison between the PPV values measured by iPhone 12 and the accelerometer. The dominant frequencies recorded by iPhone 12 in x, y and z directions were 32.01 Hz, 33.53 Hz, and 32.73 Hz respectively, whereas those by iPhone 8 were 24.46 Hz, 24.91 Hz, and 24.64 Hz.

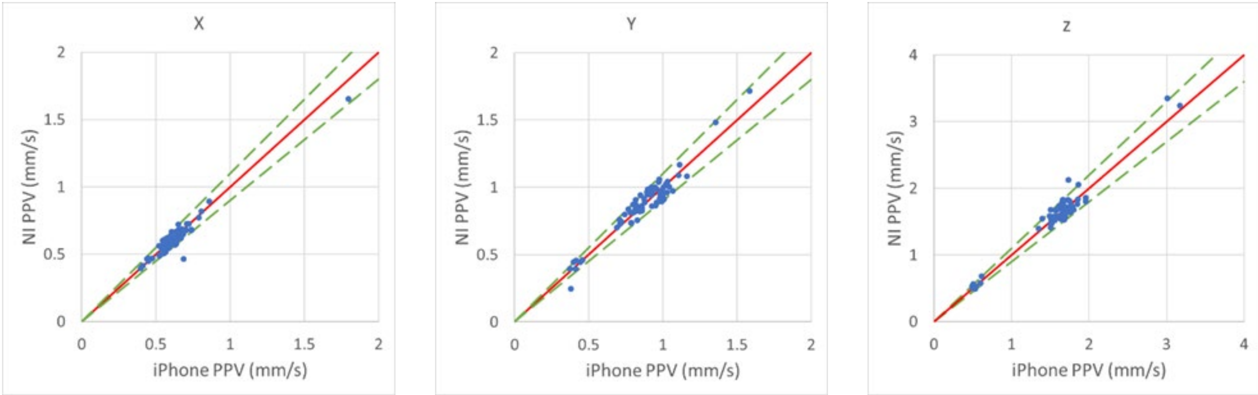

(a) PPVx b) PPVy (c) PPVz

Figure 7: Comparison of PPV between iPhone 12 and accelerometer

Noise was also measured. A sound level meter (BSWA 309) was used, as shown in Plate 6. A comparison of the noise levels obtained by iPhone 12 and iPhone 11 with that obtained by the sound level meter is shown in Figures 8 and 9. The noise levels measured by iPhone 12 ranged from 89.47 to 93.10 dB, whereas those by iPhone 11, ranged from 89.49 to 96.29 dB. There is good agreement between the noise levels recorded by the iPhones and the sound level meter.

Plate 6: Noise measurement by iPhone 11 and sound level meter

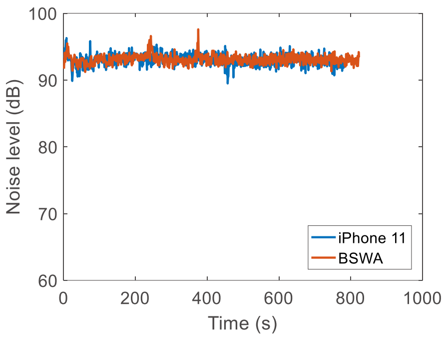

Figure 8: Noise level recorded by iPhone 12 and sound level meter

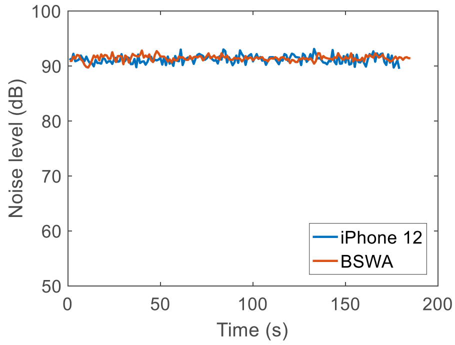

Figure 9: Noise level recorded by iPhone 11 and sound level meter

3 USE OF MATURITY METHOD FOR CONCRETE STRENGTH ESTIMATION

3.1 Background

In 2020, the CIC engaged Ove Arup & Partners Hong Kong Ltd. (Arup) to prepare a Practical Guideline on the use of maturity method to estimate early concrete strength (CIC, 2021b). The maturity method has been used commonly in other parts of the world, and the procedures are given in ASTM (2011) and Carino & Lew (2001). In the Arup's research project, 5 site trials to test the maturity method had been carried out (HyD Central Kowloon Route (Trial nos. 1 and 3), DSD Shek Wu Hui (Trial no. 2), ArchSD Kai Tak Station Square (Trial no. 4) and CEDD Kwu Tung North Retaining Wall (Trial no. 5)). The procedures of laboratory calibration and site validation for the maturity method for Trial no. 5 and a detailed interpretation of the results obtained are presented herein.

3.2 Maturity Functions

The two maturity functions that are commonly used for computing the maturity are:
(a) Nurse-Saul method

$$M(t) = \Sigma\,(Ta - To)\Delta t \tag{2}$$

where M(t) = temperature-time factor at age t (°C-day or °C-hr), Ta = average concrete temperature during time interval Δt (°C), To = datum temperature (°C) (the temperature below which strength development ceases) and Δt = time interval (day or hr).

(b) Arrhenius method

$$t_e = \Sigma\,[\,e^{-Q\left(\frac{1}{Ta}-\frac{1}{Ts}\right)}\,]\,\Delta t \tag{3}$$

where t_e = equivalent age at a specified temperature T_s (day or hr), Q = activation energy (Ea) divided by the gas constant (R) (=8.3114 $Jmol^{-1}K^{-1}$) (in K), T_a = average concrete temperature during time interval Δt (in K), T_s = specified temperature (in K), taken as 25°C (298°K) and Δt = time interval (day or hr).

The Arrhenius method is in most cases better than the Nurse-Saul method because the rate of strength development is assumed to vary exponentially with temperature in the method, which is considered more realistic. In the interpretation that follows, focus is placed on the Arrhenius method.

3.3 Laboratory Calibration

3.3.1 Testings

For the Kwu Tung North retaining wall, a Grade 30/20D concrete with a water/cement ratio of 0.49 and a slump of 75 mm was used. The mix design is given in Table 2.

Table 2: Mix design

Materials	Mass (kg/m^3)
Cement	285
PFA	95 (25%)
20 mm aggregate (crushed rock)	671
10 mm aggregate (crushed rock)	281
Stone fines (crushed rock)	807
Water	187
Admixture: water-reducer and set retarder	3.31

Concrete cubes were made on site and delivered to the laboratory for curing in three water tanks at 25°C, 40°C and 55°C, as shown in Plates 7 sand 8. Alternatively, a temperature matched curing (TMC) system, as shown in Plate 9, can be used. In the system, concrete cubes are stored in the box on the left and the temperature is controlled by the data logger/transmitter on the right in Plate 9, which is received from cloud.

Plate 7: Water curing of concrete cubes in temperature control tank

Plate 8: Maturity equipment

Plate 9: Set-up of temperature matched curing (TMC) system

Maturity sensors were installed in two concrete cubes placed in each water tank to monitor the temperature development. Compression tests on the concrete cubes taken from the three water tanks were carried out at 6-hour, 12-hour, 1-day, 2-day, 3-day, 7-day, 14-day and 28-day intervals.

The following exponential equation, as proposed by Freiesleben Hansen & Pedersen (1985), was used to fit the average cube compression test results as a function of time of testing to determine the Q value, as used in the Arrhenius method, for the three curing temperatures:

$$S = S_u e^{-\left(\frac{\tau}{t}\right)^{\alpha}} \tag{4}$$

where S = average cube compressive strength at age t (MPa), t = test age (day or hr), S_u = limiting strength (MPa), τ = characteristics time constant (day or hr) and α = shape parameter (taken as 1).

Initial values of τ and Su were first assumed in the computation of the compressive strength values. By minimizing the sum of the square of errors (SSE) of the actual and computed compressive strength values for the three curing temperatures, the parameters that give the minimum SSE were determined. The solver function in the Microsoft Excel was used to determine the best fit parameters.

The parameters established to best fit the compressive strength values for the three curing temperatures are given in Table 3.

Table 3: Parameters for exponential equations

Curing temperature (Tc) (°C)	Su (MPa)	τ (hr)	α
25	46.27	28.83	1
40	57.26	22.85	1
55	51.42	17.60	1

The best fit lines, given by the parameters established for the exponential equations, are given in Figure 10. By plotting the natural logarithm of the τ values and the inverse of the curing temperature, the Q value, given by the gradient of the line, is evaluated. A Q value of 1605 K, as shown in Figure 11, was established.

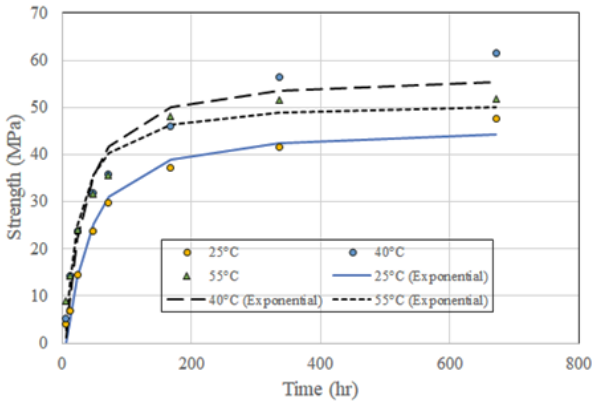

Figure 10: Comparison of actual and computed compressive strength

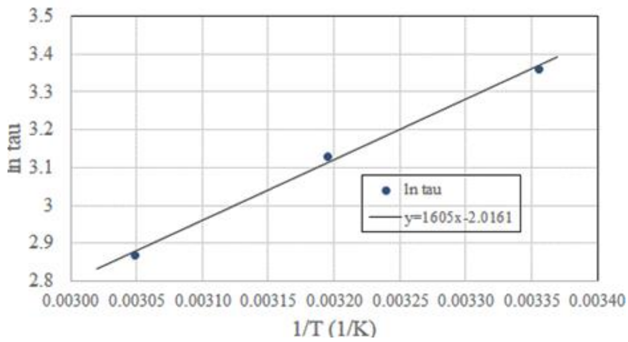

Figure 11: Plot of natural logarithm of τ values versus inverse of curing temperature

3.3.2 *Maturity Functions*

The maturity function based on the Arrhenius becomes

$$t_e = \Sigma\left[e^{-1605\left(\frac{1}{Ta}-\frac{1}{298}\right)} \right] \Delta t \tag{5}$$

The strength-maturity relationship for the curing temperature of 25°C is then given by

$$S = 46.27\, e^{-\left(\frac{28.83}{te}\right)^{1}} \tag{6}$$

The development of t_e with time is given in Figure 12, and the strength-maturity relationship for the curing temperature of 25°C is shown in Figure 13. This temperature is used because this is close to the curing temperature in the field. At the curing temperature of 25°C, the Su, τ and α values used are 46.27 MPa, 28.83 hrs and 1 respectively (see Table 3).

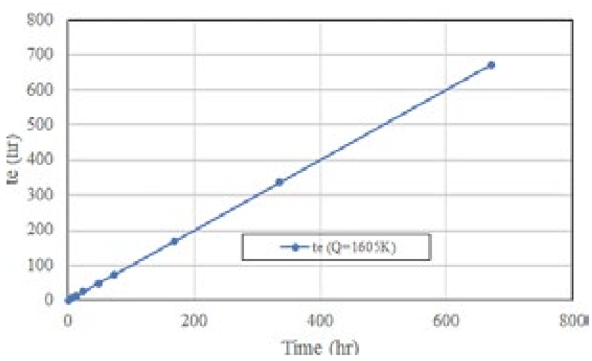

Figure 12: Development of te with time

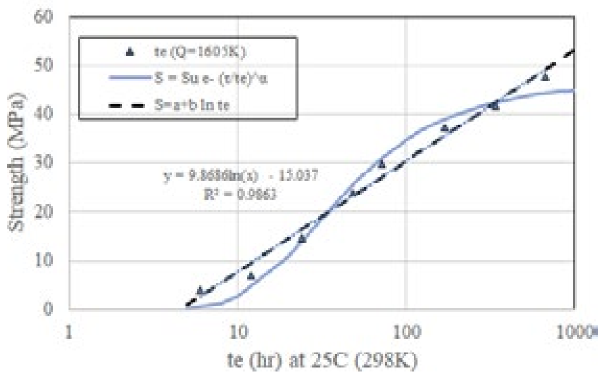

Figure 13: Strength-maturity (te) relationship

3.4 *Site Validation*

Sensors were installed in a retaining wall structure for a CEDD project at Kwu Tung North (Plate 10). Four brands of sensors were used for result comparison, as shown in Plate 11. Two locations A and C have been selected for sensor installation in the retaining wall, as shown in Figure 14, based on the locations of the highest expected stress level and coldest temperature development. Locations B and D are the designated redundant locations in case of sensor data loss at Locations A and C.

Plate 10: Construction of a retaining wall at Kwu Tung North

Plate 11: Four brands of temperature sensors used (top left: Command Center; top right: LumiCon; bottom left: SmartRock; bottom right: Converge)

For this paper, focus is put on the temperature data collected at Location C by Command Center sensors, as shown in Figure 15. The Arrhenius method was used by Command Center in the analysis.

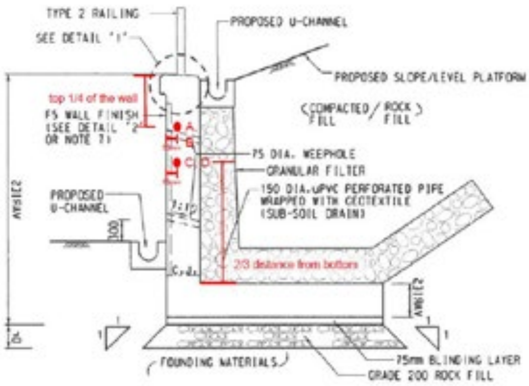

Figure 14: Maturity sensor installation locations

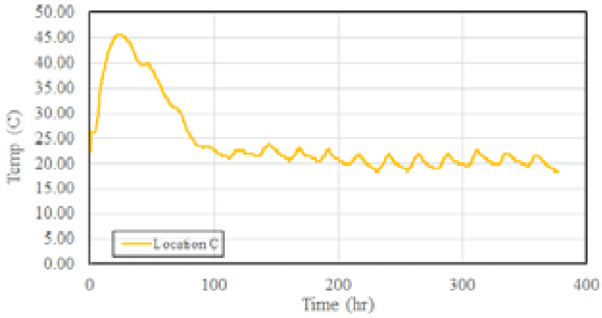

Figure 15: Temperature development profile at Location C recorded by Command Center sensors

Based on this temperature profile, t_e was evaluated, as shown in Figure 16. The strength development corresponding to the curing temperature of 25°C, computed using Equation (6), is shown in Figure 17.

Compression tests on TMC concrete cubes were carried out for conformity check. The results are included in Figure 16. A good comparison is obtained between the TMC results and the compressive strength obtained from the temperature development profile. The ratio of the compressive strength obtained to the TMC value at the time of testing is within the allowable limits. The time duration of concern is from 12 hrs onwards to less than 100 hrs.

The criteria for removal of the formwork is the attainment of concrete strength of 30 MPa. From Figure 17, it can be seen that the time allowed to remove the formwork is 51.75 hrs (2.16 days), as compared with 7 days as specified in the Code of Practice for Structural Use of Concrete 2013 (BD, 2020). There was a gain of 4.84 days in the works progress, based on the maturity method for determining the gain in strength in the concrete.

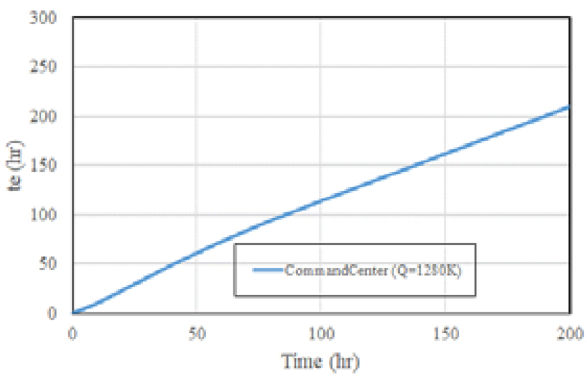

Figure 16: Development of te with time for the temperature profile at Location C

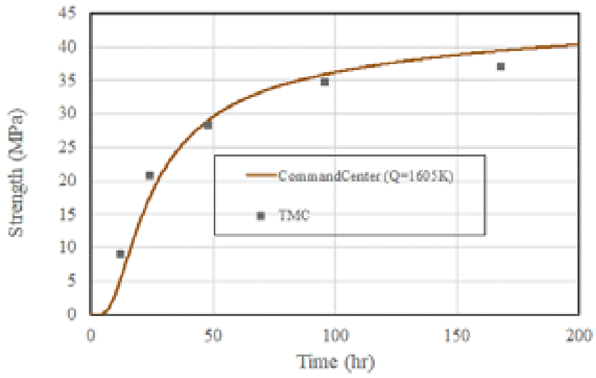

Figure 17: Development of compressive strength with time at Location C

4 CONCLUSIONS

The following conclusions can be made from the above studies:

(a) The CIC engaged PolyU to develop a new method for construction-induced vibration and noise monitoring, making use of the latest smartphone technology. The work was completed satisfactorily. A reference material on the method was published on the CIC website and the V&N App is already available for download in the Apple App Store.

(b) The iPhones and the V&N App developed had been calibrated in laboratory and validated on site. It was shown that there was good comparison between the measurement results, in terms of vibration and noise levels, from the iPhones tested and the commercial units. The V&N App developed for iPhones was able to acquire, process and analyse the data accurately for use and reporting. The following iPhones have been checked and verified as acceptable for use with the V&N App (iPhone 12 Pro Max, iPhone 12 Pro, iPhone 12, iPhone 12 mini, iPhone 11 Pro Max, iPhone 11 Pro, iPhone 11, iPhone SE (2nd gen.), iPhone XS Max, iPhone XS, iPhone XR, iPhone X, iPhone 8 Plus and iPhone 8).

(c) The iPhones and the V&N App developed provide a good and accurate method for construction-induced vibration and noise monitoring, as an alternative to the commercial units available. They have edges over the commercial units in that they are cheaper, and they can be installed and operated easily and conveniently. They could provide continuous and stable data measurement, with no data loss or crashes during the measurement process.

(d) The CIC engaged Arup to investigate the application of maturity method for concrete strength estimation in Hong Kong. The work was completed satisfactorily and a practical guideline on the use of maturity method to estimate early concrete strength was issued.

(e) Five site trials to test the maturity method had been carried out. The procedures of laboratory calibration and site validation for the maturity method and a detailed interpretation of the results obtained for Trial no. 5 for a retaining wall structure at Kwu Tung North are presented. The development of strength in the concrete, and hence the time for removal of the formwork was established. There was a gain of 4.84 days in the works progress in this case, based on the maturity method for determining the gain in strength in the concrete.

ACKNOWLEDGEMENTS

The authors would like to thank the CIC, PolyU and Arup for their consent to present and publish the results and findings given in the paper. Thanks are due to PolyU and Arup for conducting the studies and preparing the reference material and practical guideline on the subjects for use by the construction industry.

REFERENCES

ASTM (2011). Standard Practice for Estimating Concrete Strength by the Maturity Method C1074-11.
BD (2020). Code of Practice for Structural Use of Concrete 2013. Government of the HKSAR, Hong Kong, China.

https://www.bd.gov.hk/doc/en/resources/codes-and-references/code-and-design-manuals/CoP_SUC2013e.pdf

BSI (1993). Evaluation and measurement for vibration in buildings – Part 2: Guide to damage levels from groundborne vibration (BS 7385-2: 1993). British Standards Institution, London.

BSI (2009). Code of Practice for Noise and Vibration Control on Construction and Open Site – Part 2: Vibration (BS 5228-2: 1993). British Standards Institution, London.

Carino, H.J. & Lew, H.S. (2001). The Maturity Method: From Theory to Application. *Proc. of the 2001 Structures Congress & Exposition.* ASCE.

CIC (2021a). Research Summary - Smartphone as Next-generation Monitoring Devices for Construction-induced Vibrations and Noise. Hong Kong, China. http://www.cic.hk/files/page/51/CIC%20Maturity%20Method%20Practical%20Guideline.pdf

CIC (2021b). Reference Materials - Maturity Method for Estimation of Concrete Strength Practical Guideline. Hong Kong, China. http://www.cic.hk/files/page/51/CIC%20Maturity%20Method%20Practical%20Guideline.pdf

CIC (2022). Reference Materials V&N App Installation and User Guide (for Measurement of Vibration and Noise). Hong Kong, China. https://www.cic.hk/files/page/10389/CIC%20VN%20App%20User%20Guide.pdf

EPD (2022). Environmental Noise. Environmental Protection Department, Government of the HKSAR, Hong Kong, China. https://www.epd.gov.hk/epd/noise_education/web/ENG_EPD_HTML/index/index.html

Freiesleben Hansen, P. & Pedersen, J. (1985). Curing of Concrete Structures. *CEB Information Bulletin 166, May, 42 p.*

GIS-BIM Adoption for Construction Digitalization

Paul Tsui, Vincent Leung, Simon Leung, Kevin Chan, Anthony Hui
Esri China (Hong Kong) Limited, Hong Kong, China

ABSTRACT

GIS is assisting architecture, engineering, and construction (AEC) companies build smart assets and communities for the future. The fusion of GIS and BIM enables stakeholders to put their projects, issues, and assets on a map, while gaining a deeper understanding of their interaction within the geographic context. Cited with examples and applications of adopting GIS-BIM integration technology in Hong Kong, we will examine how construction digitalization can supercharge projects collaboration and to build smarter, more resilient infrastructure for our city. It is worth taking an in-depth look at the GIS-BIM integration in geotechnical engineering in Hong Kong, 3D voxel for visualization of the geological condition underground, and other latest development in construction digitalization.

1 INTRODUCTION

The integration of Geographic Information Systems (GIS) and Building Information Modeling (BIM) has led to a transformative technological advancement in the architecture, engineering, and construction (AEC) industry, including geotechnical engineering projects. GIS and BIM have a beneficial relationship that complements one another. GIS offers a geographical context that supports geospatial visualization-based decision making and geospatial modeling in a geographical context, while BIM provides rich geometric with semantic information through the construction life cycle (Song et al. 2017). Both GIS and BIM offer unique and essential roles in every phase of the life cycle of construction projects. However, there are significant needs for GIS and BIM integration to maximize their capabilities and benefits.

The capabilities of GIS allow users to create, manage, analyze and map many different types of geospatial data, including but not limited to raster data from imagery, vector data like point, line, and polygon, and 3D data such as point cloud, 3D mesh model and BIM data. The integration of GIS and BIM is an emerging research area (Ma and Ren, 2017). In Hong Kong, such integration has been gradually applied in different stages of the project life cycle, from planning and design, and construction, to operation and maintenance phases.

The objective of this paper is to illustrate the conceptual framework of GIS and to discuss the latest technological development of GIS and BIM applications supported by six Hong Kong examples. These examples are 3D slope visualization, GIS-BIM integration for Smart Barrier System, 3D GIS voxel for geological condition visualization, GIS-BIM-IoT integration for real-time slope safety monitoring, 3D landslide simulation, and Common Operational Picture.

2 CONCEPTUAL FRAMEWORK OF GIS

2.1 What is GIS?

In a classic definition, GIS is a computer system with a graphical user interface software for capturing, storing, querying, analyzing, and visualizing geographically referenced data. Geographically referenced data also called geospatial data, which describes the location and characteristics of spatial features such as a house, street, road, vegetation, or forest (Chang, 2006).

From a system perspective, GIS supports three fundamental systems: a system of record for transactional data management, a system of insight for analytics, and a system of engagement through apps and maps that connect people to the organization's project and help them communicate and share information.

System of record is the foundation of GIS. Analysis and engagement cannot be done without the system of record. The ability of GIS to store and process spatiotemporal data with other 2D and 3D datasets distinguishes GIS from other systems. It makes GIS imperative for a broad-range variety of applications. Spatial statistical analysis, GeoAI or open-science AI algorithms can be applied to the data to find insightful results. Users can share the findings with stakeholders, colleagues, or the public via GIS.

From an application perspective, GIS provides tools for mapping, measurement, geospatial data visualization, modeling and analysis, planning and design. Therefore, an action plan can be generated through a geographic approach with location intelligence.

Nowadays, the capability of GIS is expanding. The modern GIS platform can process a large amount of heterogeneous spatial data from different technologies, such as orthophoto map and 3D Mesh from drone mapping, Lidar point cloud, real-time data from IoT sensors, CCTV feed, BIM models, CAD drawings, 3D map, etc. GIS can integrate all these data in a unified platform.

For the platform choices, traditionally, GIS is a desktop-based system for storing and analyzing geospatial data. Over the past decade, mobile devices are becoming more and more popular. Meanwhile, cloud platforms are playing a significant role in boosting this transformation. Hence, GIS platforms are developed and deployed on computers, servers, mobile phones, and tablets for various purposes.

2.2 GIS BIM Integration

As discussed in the previous sessions, GIS allows many different types of data to be integrated with various operation systems. BIM is one of the data types that can be integrated with GIS.

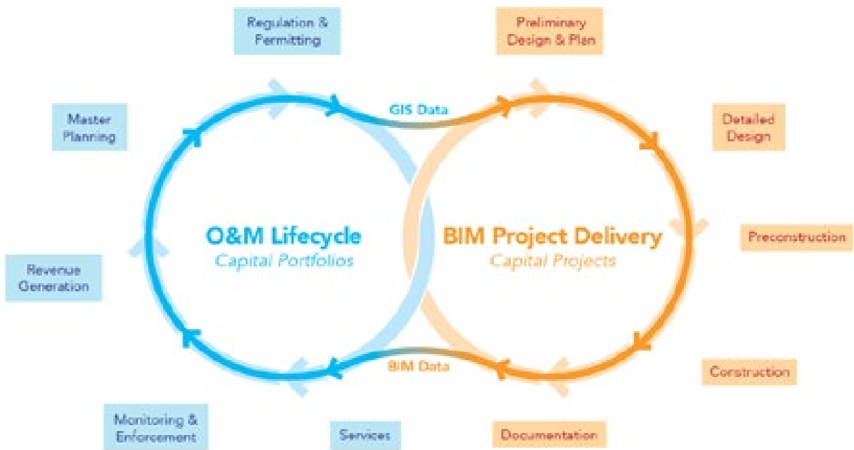

Figure 1: The GIS and BIM workflows (Andrews, 2018).

In a construction project life cycle, BIM supplies detailed information about assets, while GIS provides information about assets in the context of the built and natural environment. GIS and BIM workflows are happening continuously and complement each other perfectly. Figure 1 shows that GIS focuses on master planning, regulation and permitting, monitoring and enforcement, and revenue generation. BIM, on the other hand, plays a role in the preliminary design and plan, detailed design, preconstruction, construction, and documentation.

The Construction Industry Council released the "Construction Digitalisation Roadmap for Hong Kong" in November 2021. The Roadmap emphasized the integration of GIS and BIM, Common Spatial Data Infrastructure and Common Data Environment, form the core of construction digitalization for smart data sharing, "which can facilitate collaboration among all stakeholders on a city or project level" (Construction Industry Council, 2021).

Furthermore, there are enormous advantages from the GIS-BIM integration in every phase of the construction project life cycle. 3D geospatial and BIM data can leverage the digital planning and design phase through a series of environmental and engineering analysis tools. Better situational awareness can be provided with the use of design and construction data under a geographical context. More efficient planning can be achieved through a broader analysis of environmental, demographic, and economic factors surrounding the new development areas. (Construction Industry Council, 2021). In the construction phase, the GIS-BIM integration provided a modernized project delivery that enables collaborative workflows. A Common Data Environment (CDE) supported by web GIS technology also serves as a common platform for the project stakeholders to collaborate and communicate with each other securely. Hence, AEC companies can make well-informed decisions to speed up project delivery.

2.3 Digital Twin

GIS builds digital twins of both the natural and built environments. A digital twin is a virtual representation of physical objects, processes, relationships, and behaviors. A digital twin can be created with the integration of Landscape Information Modeling (LIM), Building Information Modeling (BIM), Network Information Modeling (NIM), and Cities Information Modeling (CIM). It is abstracting and modeling everything. Digital twin provides a framework for real-time visualization, analysis for future prediction, and information sharing and collaboration for solving real-world challenges.

3 Hong Kong Examples of Geotechnical Engineering Projects with GIS and BIM integration

3.1 PoC study of 3D Web GIS for Slope Visualization and Analysis

To grasp the trend of 3D GIS development, a Proof of Concept (PoC) study was carried out to develop a 3D Web GIS for slope visualization and analysis. It was a feasibility study of turning a 2D slope information system into a 3D GIS web platform. The 3D GIS web platform was constructed with two major components – 3D slope visualization and a landslide detection system for smart barriers. In this project, the study area was located at the western part of Hong Kong Island, approximately 5km x 5km in a 3D scene. The platform provided visualization of the 3D boundary of not more than 600 nos. of man-made slope features with the labeling of their feature numbers. The slope data are provided by the Geotechnical Engineering Office (GEO) of Civil Engineering and Development Department (CEDD).

This 3D slope visualization was integrated with layers of a 3D mesh model, a 3D digital terrain model with 3D building and infrastructure objects in a 3D scene. Three types of data have been applied (Table 1), and each data is converted to GIS format and integrated into the 3D GIS web platform with World Geodetic System 1984 (WGS 84) coordinate system. All converted data are uploaded and integrated into the 3D GIS web platform for assessment.

Table 1: Three Types of Data Applied for the 3D Slope Visualization

Data Type	Extension	Area	Usage
Mesh Data	.osgb	Conduit Road Victoria Road Queen Mary Hospital	Mesh data in tiles to be converted to Integrated Mesh Scene Layer and modified by the footprint of the BIM data.
Lidar data	.las		Provides elevation information is converted to Raster for ArcGIS to custom an Elevation Service.
3DS data	.3DS	Conduit Road Victoria Road Queen Mary Hospital Tung Chung	Provides 3D spatial data of Digital Terrain Model (DTM) and buildings and is converted to ArcGIS 3D model, that is the Multipatch feature layer.

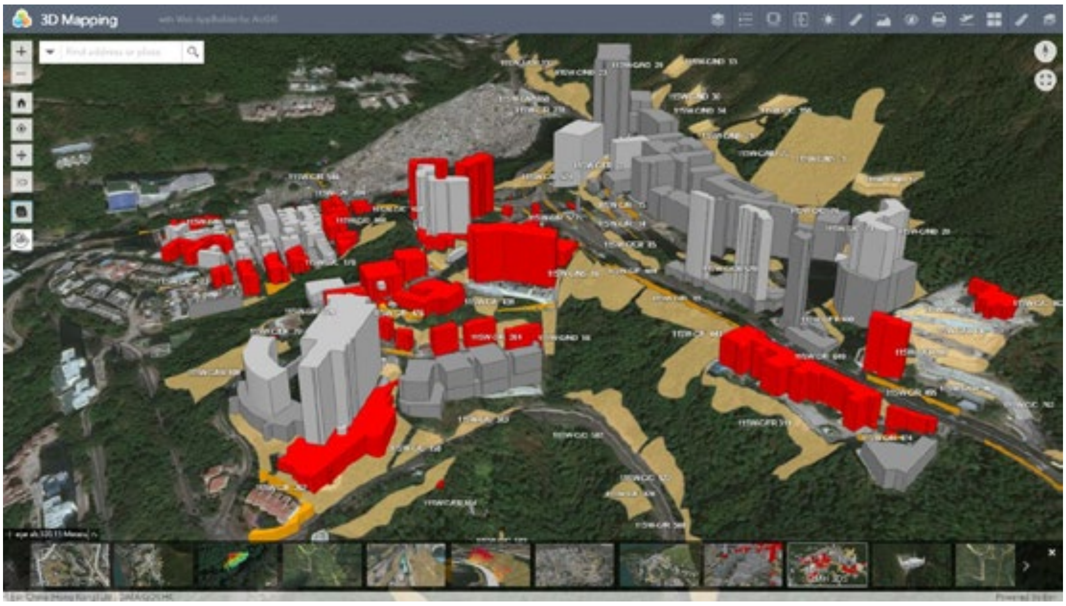

Plate 1: In the PoC study, the 3D visualization of the slope data and 3D buildings are shown in the study area.

In plate 1, the 3D GIS Web Platform using ArcGIS Pro and ArcGIS Enterprise was established, which offers a visualization of 3D slope and landslide data. The platform allowed an effective, efficient, and user-friendly storage, retrieval and update of slope data, GIS data, BIM model data, satellite images, 3D spatial data, 3D mesh models, and laser scanning point cloud data in one single platform.

ArcGIS Pro, ArcGIS Online, and ArcGIS Enterprise have been adopted in the project.

3.2 GIS-BIM-IoT Integrated Smart Barrier System

CEDD developed the Smart Barrier System with BIM and GIS integration and an internet-of-things (IoT) sensor system, to detect the impact of landslide debris on debris-resisting barriers to transmit real-time alerts to relevant officers for immediate follow-up (Civil Engineering and Development Department, 2019).

To construct the Smart Barrier system, the BIM model data (Table 2) representing the smart barriers is imported to the GIS platform together with other 3D geospatial data mentioned in Table 1. The smart barriers are located in the western part of Hong Kong Island. The point data of its IoT sensors includes two depth gauge sensors, three impact switches, and two cameras.

Table 2: Data Applied for the Smart Barriers

Data Type	Extension	Area	Usage
BIM Model Data (Revit)	.rvt	Conduit Road Victoria Road Queen Mary Hospital	Representing the smart barriers converted to 3D format

The Smart Barrier System integrated with a 3D mesh model, 3D digital terrain model, 3D building, and infrastructure objects in a 3D scene, which formed the landscape information model. The Smart Barrier System displays the real-time and dynamic monitoring data captured from the smart barriers, including numeric data of debris depth in graphical format and photos captured for a specified period by connecting to on-premises SQL Server databases. Conspicuous alert signals such as flash warning symbols will be popped up when the impact switches detect impact from landslide debris.

Plate 2: Integrated with BIM data, IoT sensors, 3D mesh model, and 3D digital terrain model with 3D building and infrastructure objects, the smart barrier 11SW-C/ND 32 was shown in the Smart Barriers System.

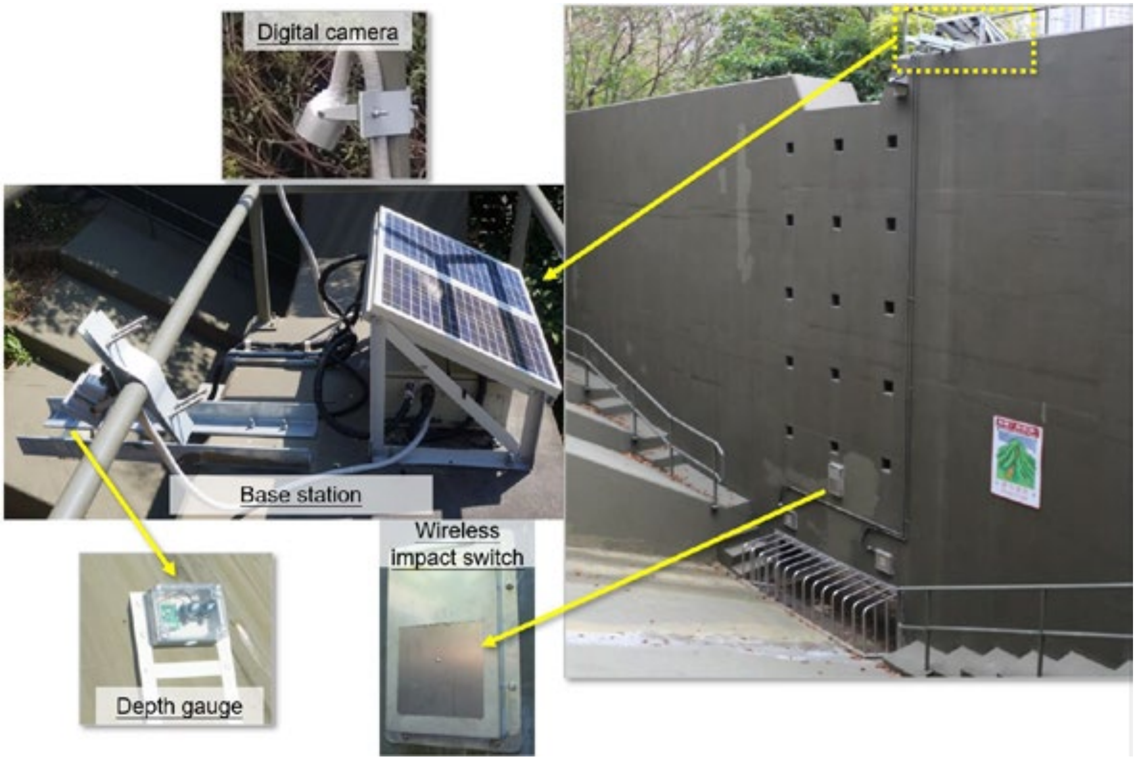

Plate 3: The smart barrier 11SW-C/ND 32 was installed with the depth gauge sensors, impact switches, and cameras. All sensors and cameras were connected to the Smart Barrier System for real-time monitoring.

ArcGIS Pro, ArcGIS Online and ArcGIS Enterprise have been implemented in the Smart Barriers System.

3.3 GIS Voxel for Geological Condition Visualization

The 3D GIS voxel layer for the visualization of the geological condition is an enhancement project based on the demo 3D GIS Web Platform discussed in sessions 4.1 and 4.2. Voxel is a 3D visualization of an objection constructed by 3D pixel cubes representing its characteristics. In the following PoC, the study area was a 59,000m^2 site area in Tung Chung.

To establish a GIS voxel layer for the 3D geological underground model, different types of data were integrated including six main geological layers of superficial deposits and in situ weathered materials which are stored in TIN format.

The geological layers will be geo-referenced and converted to a netCDF layer through a data conversion process in GIS. Based on the spatial information (X, Y, Z) stored in the netCDF, it can be visualized in the GIS voxel layer, and the spatial relationships with different 3D models can be assessed.

For instance, an underground geological model visualized as a 3D GIS voxel layer can be viewed together with multiple boreholes or construction that is planned in a development area.

Fitting of BIM data with surrounding topography – it also provides practical solutions for locally adjusting/modifying the 3D mesh model and the 3D digital terrain model such as elevation layer in tile package generated by LiDAR data by using ArcGIS software.

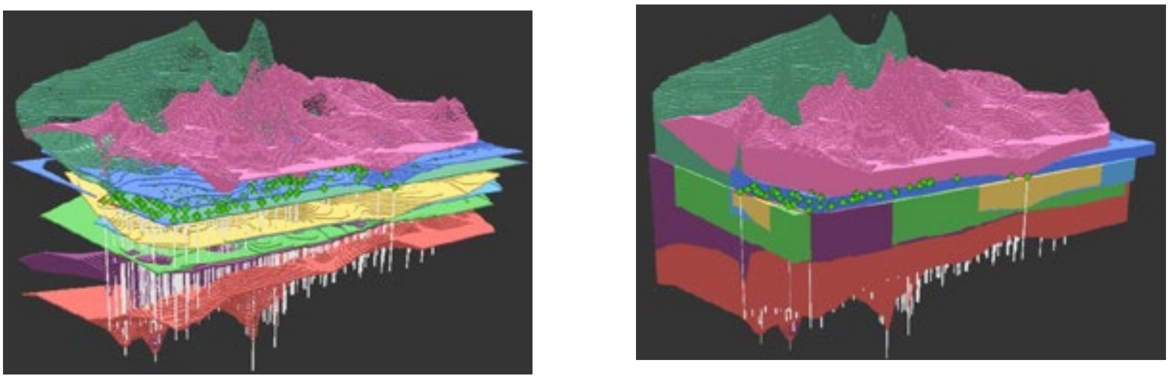

Plate 4: The GIS voxel layer showcases the surface type (left) and volume type (right) of the full model visualization of the geological conditional in the study site.

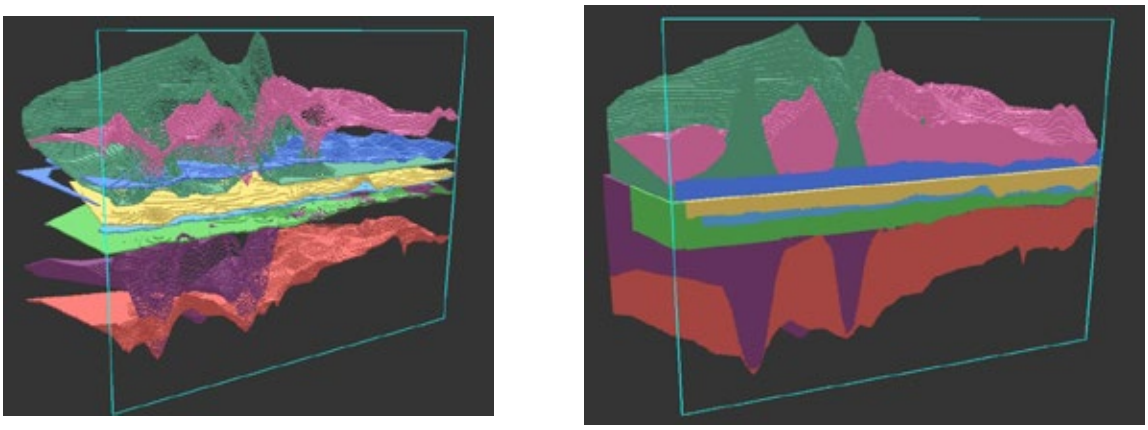

Plate 5: The slice view of the voxel layer in surface type (left) and volume type (right).

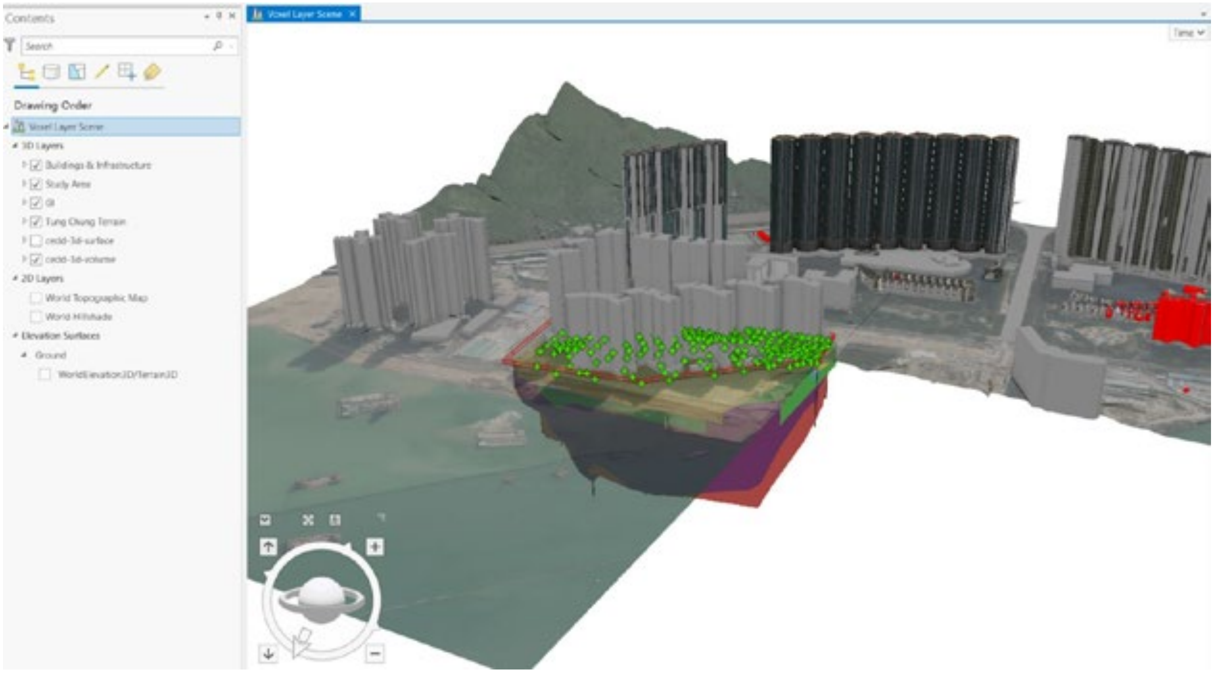

Plate 6: In the Tung Chung study site, the integration of voxel layer, boreholes, 3D digital terrain model, 3D building, and infrastructure objects were displayed in ArcGIS Pro.

3D GIS voxel layer provides various forms of applications for construction digitalization. The Netherlands has been developing a 3D voxel model to visualize the soil types underneath her territories. According to Seler (2020), a GIS voxel layer was created to visualize different soil types in the Netherlands. Peat soil is one of the soil types found within the territories. It is a soft substance and would cause higher construction costs. By early detection of peat soil via the 3D voxel information system, AEC sectors can make a better decision before the project starts.

ArcGIS Pro and ArcGIS Enterprise have been used in the 3D GIS voxel project in Tung Chung, Hong Kong.

3.4 GIS-BIM-IoT Integration for Real-Time Slope Safety Monitoring

With the adoption of GIS-BIM integration and IoT technologies, the landslide prevention and mitigation system at Po Shan, Mid-levels was built by the GEO of CEDD. The innovative regional groundwater regulation system provides real-time groundwater monitoring and regulation to maintain slope stability, therefore, protecting lives and property.

The Po Shan Drainage Tunnels were constructed to regulate the regional groundwater level and reduce the potential landslide risk in the Po Shan area. The drainage tunnels comprise a network of 172 sub-vertical drains for controlling the groundwater level in the soil mass (Civil Engineering and Development Department, 2021a). The groundwater level is continuously monitored by the pressure gauges installed on the sub-vertical drains and the piezometers in the slope.

The monitored data are fed to a pressure relief system with automatic valves mounted at the ends of the vertical drains and they would open and close in order to keep the groundwater level within a pre-defined range. Given the slope stabilization nature of the system and availability of real-time monitoring data, a pilot digital twin for the Po Shan Drainage was prepared by GEO on GEO's 3D Mapping System. The 3D mapping System can directly incorporate the BIM model of the tunnel structures with the automated instrumentation system. The digital twin can assist the project team to monitor the groundwater level in the Po Shan area and allow them to carry out regular reviews for the performance of the drainage system.

For the development of the BIM model, the alignments of the drainage tunnels, 172 sub-vertical drains, associated water flow controlling valves, pipelines and standpipes/piezometers were generated in the 3D BIM platform based on the as-built records (Plate 7). The digital twin would send alert message to notify the project team when the readings of sub-vertical drains and piezometers exceed the pre-defined range and the respective location of the exceedance will be highlighted in the BIM model.

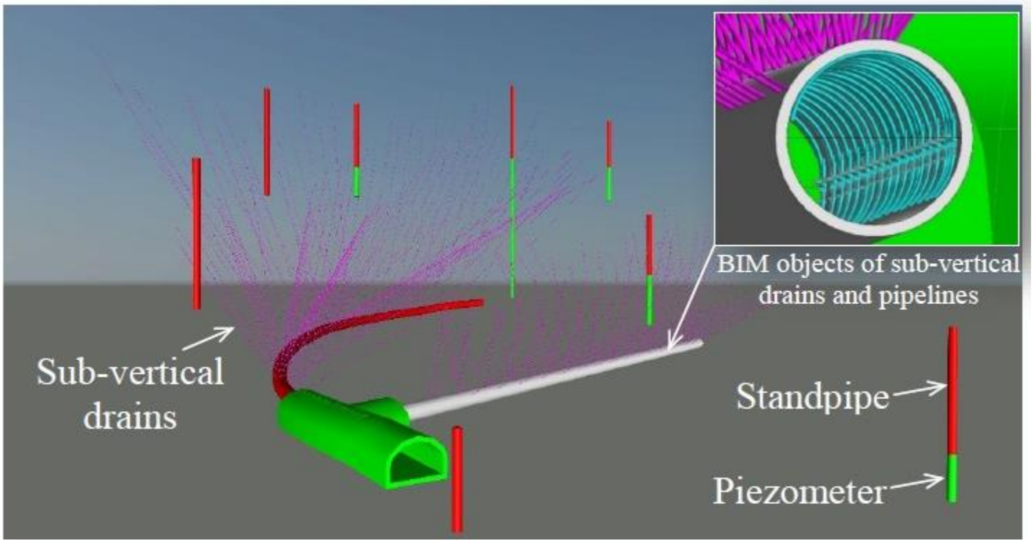

Plate 7: Po Shan Drainage Tunnels displayed on the BIM platform.

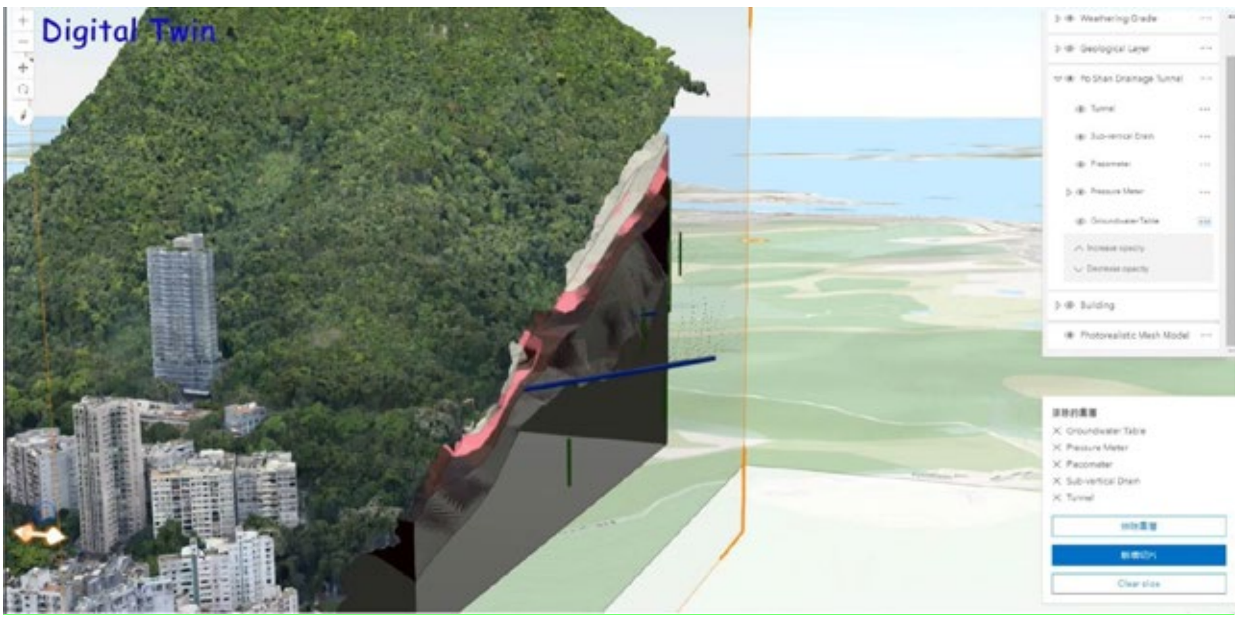

Plate 8: 3D photogrammetry and BIM model coupled with real-time monitoring sensors are integrated into a GIS system to create a digital twin for data and as-built records visualization.

The digital twin allows 3D visualization of the site environment and the underground geological profile, as well as the simulation of the temporal groundwater regime based on interpolation of site-specific piezometric readings. Users can examine the water pressure at individual sub-vertical drain and piezometer to promptly retrieve their real-time and historical data in tabular and graphical format.

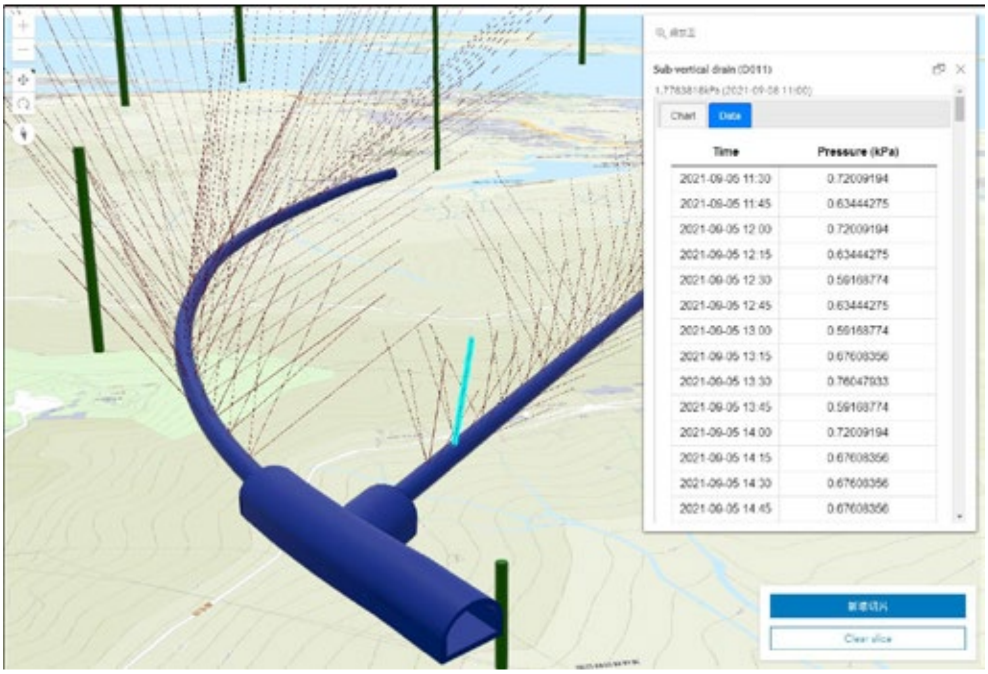

Plate 9: Equipped with real-time BIM visualization of data, the Po Shan Drainage Tunnels allow the operators to react promptly to the changing situation with a much better quality of the information available.

The benefits of adopting GIS BIM integration Web platform for Po Shan Groundwater Regulation System are numerous. The quality of the information presented to the operators is greatly improved. It allows immediate access and preliminary analysis of real-time data for both automatic groundwater monitoring devices and sub-vertical drains on computers or mobile devices with internet connection. The system is equipped with real-time BIM visualization of data, which allows the operators to react promptly to the changing situation with better quality of the information available. In addition, the key information would be acquired in real-time for preliminary analysis and decision-making.

ArcGIS Pro, ArcGIS Enterprise, and ArcGIS GeoEvent Server have been adopted in the Po Shan Drainage Tunnels use case.

3.5 Landslide Debris Simulation

Two-dimensional modeling of landslide motions has routinely been used to assess landslide mobility in natural terrain hazard studies in Hong Kong. With the advance in digital and computer technology, 3D debris mobility assessment can be carried out on a GIS platform with GEO's data. In this example, a GIS application that incorporates the Smoothed Particle Hydrodynamics (SPH) module for 3D debris mobility assessment of landslides was developed.

Smoothed Particle Hydrodynamics (SPH) is a computation modeling for simulating the flow of fluid or solid mechanics. Landslide debris is one of the applied areas. A landslide simulation system was developed in a GIS platform to interact and integrate with the SPH program provided by the GEO so that 3D debris mobility assessment of landslides can be undertaken in a GIS environment.

Identification of design flow path through batch analysis can be delivered in a GIS platform through the integration with GEO's SPH program. The flow path is determined according to the steepest path of the topography. In case of a flat path encountered, continue the path in a straight line when the flow path met the Area of Interest (user-defined boundary) in GIS. A developed application shall allow users to amend the flow path by manually editing.

For identification of the flow path with the highest runout, users can choose the source location from the source region (defined debris area), in grid form to allocate the source location within the source region (boundaries of source groups). The individual runout analysis is using the same set of input parameters and it could provide an environment to integrate with 2D debris mobility assessment analysis. The parameters shall be given in batch run for example (friction angle = 15º, 20º, and 25º), volume, and channel width.

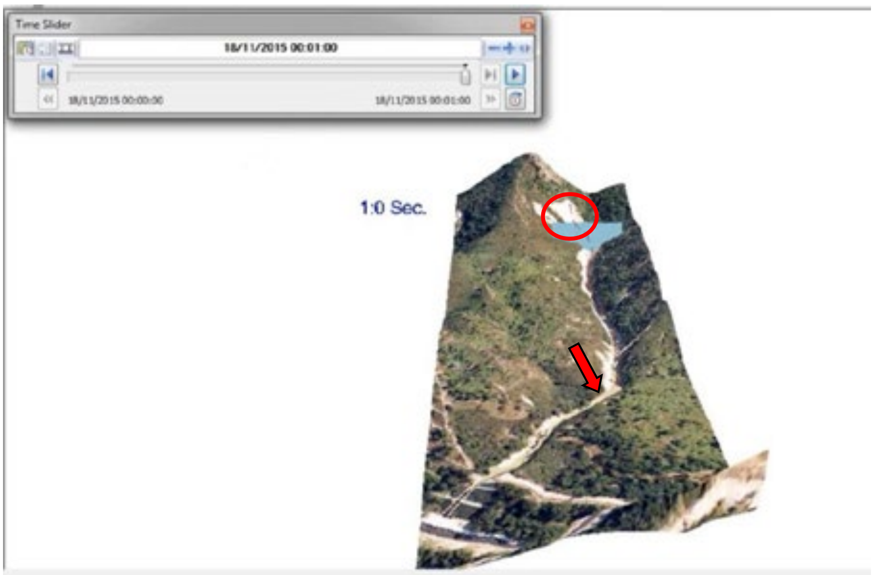

Plate 10: The simulated landslide occurred on the slope (circled). The debris flow simulation (arrowed) was computed by application of the Smoothed Particle Hydrodynamics.

The source region can be drawn by the user in a GIS system and manually amendable. The flow path with the steepest path analysis shall be automatically generated by selecting a single source location and multiple source locations. The flow path (steepest path) also can be easily amended by the user via the editing function.

ArcGIS Desktop has been implemented in the landslide debris simulation project.

3.6 Common Operational Picture for Natural Disaster-related Intelligence Sharing

Common Operational Picture is an example of a GIS-based information sharing platform for emergency response. Climate change is one of the factors to worsen extreme weather in terms of intensity, frequency, and impacts. Such adverse weather condition brings Hong Kong unforeseen work incidents and economic loss. For instance, on the North Lantau Highway (NLH) natural terrain in June 2008, some 35 landslides were initiated on a natural hillside above the NLH. As a major transportation corridor to the Hong Kong International Airport, the NLH was closed for 16 hours (Civil Engineering and Development Department, 2021b). Another extreme weather event was Super Typhoon Mangkhut battered Hong Kong in 2018. Severe weather causes interruptions in our city that required emergency responses through collaboration with different parties. Common Operational Picture (COP) was developed in 2017 and launched in 2020 for better communication, collaboration, information sharing, and enhancing situational awareness in natural disasters.

Developed by CEDD, COP is a common GIS platform for real-time incidents information sharing including landslides, flooding due to heavy rain, storm surge inundation, and major road incidents with “supporting information” such as weather and traffic condition. The Lands Department, Hong Kong Police Force, Fire Services Department, Hong Kong Observatory, Government Flying Service, Hospital Authority, Civil Aid Service, Auxiliary Medical Service contribute input to the databank of “supporting information” in the COP when natural disasters occur (Security Bureau, 2018).

The COP aims to enhance the existing communication channel among bureaus and departments to share emergency information. The COP is a Web GIS-based cloud platform to ensure its availability at anytime and anywhere with an internet connection. High-resolution territory-wide maps with accurate mapping data would be useful for field workers to collect data and update the COP in real-time under severe weather conditions for formulating contingency plans (Lam et al., 2021). When COP was launched in 2020, six government works departments including CEDD, Buildings, Highways, Housing, Drainage Services, and Lands Department collaboration on sharing emergency incidents like landslides, flooding, and major road blockages, and structural incidents (Tang 2022).

Plate 11: The Common Operational Picture (COP) is shown in the interactive map dashboard for government bureaus and departments' cross-collaboration.

The COP is expanding the data integration with more bureaus and departments. Home Affairs, Transport, Census and Statistics, Environmental Protection, Marine Department, and with Tree Management Office share "supporting information" such as temporary shelters, traffic, landfill information, tidal, past tree failure incidents respectively. Meanwhile, the Independent Checking Unit of Transport and Housing Bureau, Water Services Department, and Architectural Services Department report emergency incidents information to the COP directly.

ArcGIS Pro and ArcGIS Enterprise have been adopted in the COP use case.

4 CONCLUSIONS

The GIS-BIM integration for construction digitalization provides a geographical context for project visualization and management. By integrating with the latest technologies such as IoT sensors, advanced computer simulation, and 3D data modeling, the GIS-BIM integrated environment can be further empowered. Collaboration with stakeholders and public engagement can be achieved through web-based applications and dashboards. The examples cited in this paper also demonstrated GIS is a system of record, insights, and engagement. All in all, GIS is one of the driving forces for smart city development.

ACKNOWLEDGEMENT

The authors would like to give sincere gratitude to the Geotechnical Engineering Office (GEO) of Civil Engineering and Development Department (CEDD) for their generous support in authorizing the use of the examples of GIS and BIM integration for Hong Kong construction digitalization and other relevant applications.

REFERENCES

Andrews, C. (2018). GIS and BIM Integration Leads to Smart Communities. *ArcUser*, 16–19. https://www.esri.com/content/dam/esrisites/sitecore-archive/Files/Pdfs/news/arcuser/0518/arcuser-spring-2018.pdf

Chang, K.-T. (2006). *Introduction to geographic information systems*. Mcgraw-Hill.

Civil Engineering and Development Department. (2019). *Emergency Preparedness for Climate Change on Slope Safety*. HONG KONG SLOPE SAFETY SYSTEM; Civil Engineering and Development Department. https://www.ceddreport201519.gov.hk/en/projects-services-detail/slope

Civil Engineering and Development Department. (2021a). *Landslip Prevention and Mitigation Works at Po Shan, Mid-levels*. https://www.cedd.gov.hk/filemanager/eng/content_454/IN_2021_05E.pdf

Civil Engineering and Development Department. (2021b, October 26). *Past Notable Landslides*. Hong Kong Slope Safety; Civil Engineering and Development Department. https://hkss.cedd.gov.hk/hkss/en/facts-and-figures/past-notable-landslides/index.html

Construction Industry Council. (2021, November 1). *Construction Digitalisation Roadmap for Hong Kong: A Path Way Towards Smart Construction*. Bim@Cic.hk; Construction Industry Council. https://www.bim.cic.hk/en/resources/publications_detail/95?cate=53&back=%2fen%2fresources%2fpublications%3fcate%3d53

Lam, F., Wong, E., Tang, A., & Cheng, D. (2021, May). Creating a disaster resilient built environment. *Surveyors Times*, 8–11. https://www.hkis.org.hk/archive/materials/category/ST05_Med.pdf

Ma, Z., & Ren, Y. (2017). Integrated Application of BIM and GIS: An Overview. *Procedia Engineering*, *196*, 1072–1079. https://doi.org/10.1016/j.proeng.2017.08.064

Security Bureau. (2018, June). *Government's preparedness for the approach of typhoon season and related natural disasters and emergency response*. Legislative Council Panel on Security; Legislative Council. https://www.legco.gov.hk/yr17-18/english/panels/se/papers/se20180605cb2-1480-7-e.pdf

Seler, I. (2020, July 14). *ArcGIS Pro 3D Voxels*. Www.youtube.com; Esri Events. https://www.youtube.com/watch?v=JF7Z1xjZx-0

Song, Y., Wang, X., Tan, Y., Wu, P., Sutrisna, M., Cheng, J. C. P., & Hampson, K. (2017). Trends and Opportunities of BIM-GIS Integration in the Architecture, Engineering and Construction Industry: A Review from a Spatio-Temporal Statistical Perspective. *ISPRS International Journal of Geo-Information*, *6*(12), 397. https://doi.org/10.3390/ijgi6120397

Tang, W. (2022). *SMART CITY 4.0* (pp. 220–224). Esri China (Hong Kong) Ltd. https://winnietang.hk/ebook/SmartCity4.0_Eng.pdf (Original work published 2021)

Monitoring of a Peanut-shaped TBM Launching Shaft Excavation using Fibre Optics and Remote Sensing Techniques

I Li, E H Y Sze, F L C Lo
Geotechnical Engineering Office, Civil Engineering and Development Department, Hong Kong SAR, China

S Q Lin, D Y Tan, A Y F Leung
The Hong Kong Polytechnic University, Hong Kong SAR, China

A W Y Chan, T C W Wong, E Y M Chan
East Development Office, Civil Engineering and Development Department, Hong Kong SAR, China

ABSTRACT

The trial application of fibre optics and remote sensing techniques for monitoring a peanut-shaped tunnel boring machine (TBM) launching shaft in the Trunk Road T2 and Cha Kwo Ling Tunnel project has recently been completed. This is the first time in Hong Kong that these techniques are deployed to systematically monitor the entire excavation process of the peanut-shaped shaft. In particular, distributed fibre optic sensing (DFOS) technique based on optical frequency domain reflectometry (OFDR) was used to capture the continuous profiling of the strain measurement by fibre optics installed in the diaphragm wall panels, thus enabling the development of hoop strain to be revealed. To facilitate data interpretation, the excavation process was regularly recorded by the handheld light detection and ranging (LiDAR) scanning technique. This paper reports the background and key findings of the monitoring work as well as the results of the data analysis. The monitoring work provides valuable field data, which could not be easily obtained on site in the past. The data may be of use for numerical back-analysis to better understand the behaviour of shaft excavation. Insights gained in this study could also be useful to future design and construction of similar excavation works.

1 INTRODUCTION

The use of circular excavation has become increasingly common for resisting the earth and groundwater pressures by mobilizing hoop compression. Pappin (2011) reported a series of case histories of circular excavations using diaphragm walls as earth retaining structure, including a case in Singapore using dual circular excavation, also known as “peanut-shaped” excavation. Similar peanut-shaped configuration as excavation support has been adopted in the Trunk Road T2 and Cha Kwo Ling Tunnel (collectively “the T2”) project in Hong Kong for the launching of the TBMs in order to enhance construction flexibility by eliminating steel struts, facilitate faster shaft excavation, assembly of the TBMs and construction of the permanent tunnel box structure, and significantly reduce impacts on adjacent structures and environment. However, the performance of such an innovative scheme, in particular the mobilisation of hoop action, has not been systematically monitored and reviewed in Hong Kong. Therefore, a comprehensive monitoring scheme was deployed to understand the performance of the peanut-shaped shaft excavation of the T2 project. Fibre optic sensing was proposed as the primary sensing technique for the monitoring scheme to monitor the structural performance of the shaft, supplemented by remote sensing technique using handheld LiDAR scanner to monitor the progression of excavation.

Various literature has reported a wide range of application of fibre optics on geotechnical engineering over the last decade such as the detection of slope and ground surface movements (e.g. Zhu et al. 2012, Kechavarzi et al. 2016 and Schenato et al. 2017), earth pressures measurements (e.g. Xu et al. 2017) and determination of soil nail forces (e.g. Zhu et al. 2012 and Kechavarzi et al. 2016). Hoop action in circular excavation was studied by Schwamb et al. (2014) and Torisu et al. (2019) using distributed fibre optic sensing (DFOS) technique based on Brillouin optical time domain reflectometry (BOTDR) with a spatial resolution of 1.0 m. However, the behaviour of non-conventional circular shafts such as peanut-shaped excavation has not been studied in detail using such technology. In this study, the peanut-shaped shaft of the T2 project was instrumented with DFOS system based on optical frequency domain reflectometry (OFDR), which enables an improved spatial resolution of 5 cm.

Application of remote sensing techniques has also gained its popularity in geotechnical engineering over the last decade. In Hong Kong, the Geotechnical Engineering Office (GEO) of the Civil Engineering and Development Department (CEDD) has been applying various remote sensing techniques such as light detection and ranging (LiDAR), Interferometric Synthetic Aperture Radar (InSAR) and photogrammetry for acquisition of geospatial data to support geotechnical studies on landslide hazard. Amongst different techniques, LiDAR was considered the most effective for the unique terrain setting of Hong Kong (So et al. 2021). Comprehensive reviews on the application of different LiDAR equipment including terrestrial, airborne, mobile and handheld devices were given by Leung & Ho (2020). The use of handheld LiDAR scanner was found the most suitable for the remote, cramped and complicated site setting in Hong Kong due to its compactness, simple operation, and short mobilisation time while maintaining high accuracy. To date, most applications of handheld LiDAR devices were on slope stability and emergency landslide inspection. In this study, their application is extended to the monitoring of the excavation and lateral support works at the peanut-shaped shaft of the T2 project with an aim to assist the interpretation of fibre optics monitoring.

2 PROJECT BACKGROUND

The T2 project comprises 3.4 km of dual-two lane trunk road connecting the Central Kowloon Route on the West and the Tseung Kwan O-Lam Tin Tunnel on the East. Together they constitute Route 6. In this project, two 2.4 km sub-sea tunnels will be constructed mainly using two 14 m diameter TBMs drilling concurrently from Kai Tak through Kwun Tong Typhoon Shelter to Lam Tin. The TBM launching area comprised a conventional rectangular cut-and-cover tunnel and a peanut-shaped shaft as shown in Plate 1 and Figure 1. Both tunnel and shaft were constructed by diaphragm walls as vertical support elements. In this study, fibre optic cables were installed in three selected diaphragm wall panels as shown in Plate 1. Two panels, C1-01 and C2S-03 were located at the peanut-shaped shaft. The third panel, DN-03, was located at the cut-and-cover tunnel. As shown in Figure 1(b), the site is generally underlain by 14 m of fill and 5 m of marine deposits which overlaid 18 m of alluvium followed by 24 m of Completely Decomposed Granite (CDG) above the bedrock at around 60 m below ground. In general, the diaphragm wall panels in the cut-and-cover tunnel and the Y-shaped wall panels in the peanut-shaped shaft were founded on Grade III or better rock while the other panels in the peanut-shaped shaft were founded in CDG.

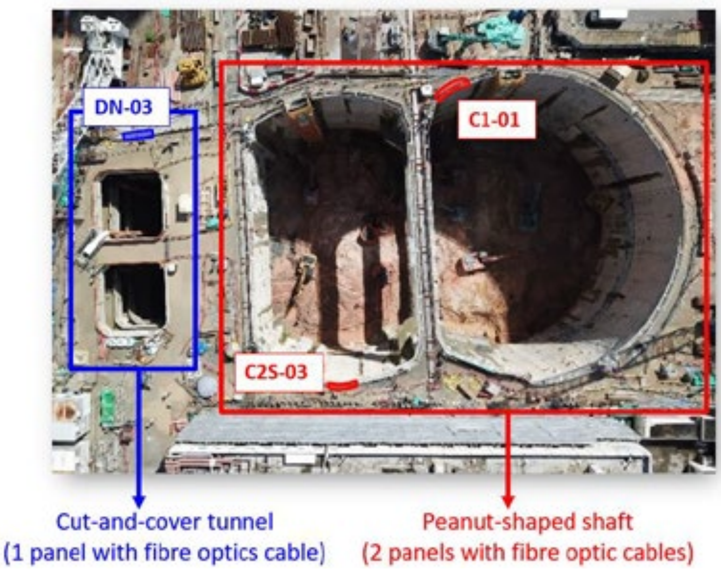

Plate 1: General view of the TBM launching area showing diaphragm wall panels with fibre optics cables instrumented

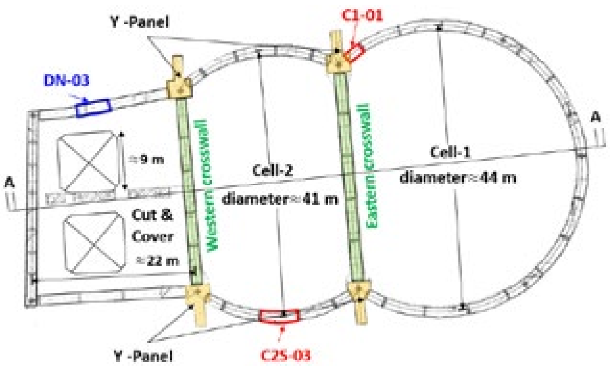

(a)

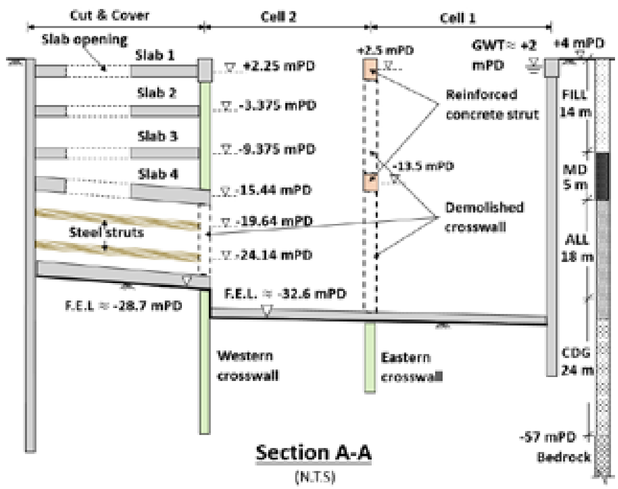

(b)

Figure 1: (a) General layout of the TBM launching area and (b) Cross section of the TBM launching area

The rectangular cut-and-cover tunnel was approximately 22 m long and 30 m wide on plan with a maximum excavation depth of about 32 m. The lateral support system included four layers of concrete slab and two layers of steel struts as shown in Figure 1(b). The peanut-shaped shaft was mainly constructed from two circular shafts, namely, “Cell 1” and “Cell 2”, with diameters of approximately 44 m and 41 m respectively. The maximum excavation depth was approximately 38 m. Cell 1 and Cell 2 were connected by four Y-shaped wall panels and two crosswalls, namely, the eastern crosswall and western crosswall as shown in Figure 1(a). The peanut-shaped shaft was further supported laterally by two reinforced concrete beams installed at +2.5 mPD and -13.5 mPD spanning across the northern and southern side of the cofferdam as shown in Figure 1(b). The peanut-shaped cofferdam resisted the lateral earth and water pressure by developing compressive hoop forces which were then transferred to the Y-shaped wall panels, the reinforced beams and the two crosswalls.

The fibre optics and handheld LiDAR monitoring period was approximately 6 months, covering the pumping test, bulk excavation, lateral support and base slab installation works. It also captured the effect of the concurrent demolition of the crosswalls as the excavation proceeded. The construction sequence is mainly divided into six stages and they are plotted with the change in general excavation levels in the peanut-shaped shaft as shown in Figure 2.

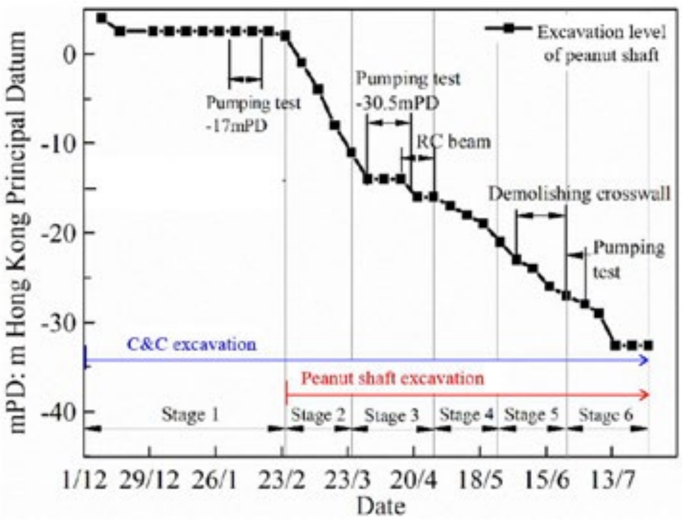

Figure 2: Construction sequence and general excavation levels in the peanut-shaped shaft

3 DISTRIBUTED FIBRE OPTIC SENSING (DFOS)

3.1 Working Principle

The basic working principle of using optical fibres for vibration, strain or temperature measurement is based on light scattering. Light, being a transverse electromagnetic wave, when being transmitted through the core of the optical fibre, interacts with the constituent atoms and molecules of the core. Local impurities within the cable will cause back-scattering of the light (Soga & Luo 2018). If the fibre is subjected to temperature or strain changes, the characteristics of the back-scattered beam and thus the scattered signal in the fibre will be modulated by these physical changes. By measuring the changes of the modulated signal, the corresponding changes in strain and temperature can be correlated (Bao & Chen 2012). There are three different mechanisms of back-scattering – Rayleigh, Brillouin and Raman scattering as shown in the typical back-scattered light spectrum in Figure 3. A detailed account of different DFOS systems was given by Soga & Luo (2018), which are mainly categorised based on the technique used for detection of various forms of back-scattering and hence the measurement of vibration, strain or temperature.

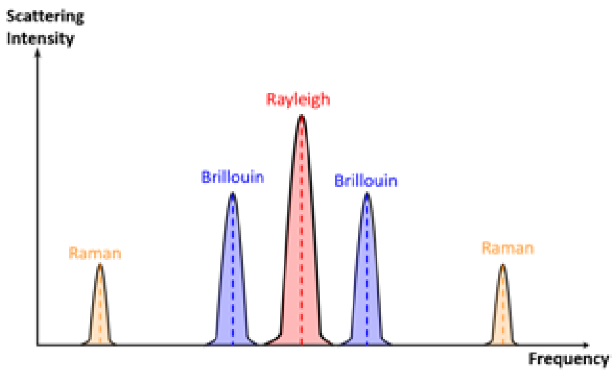

Figure 3: Typical spectrum showing three modes of back-scattering

In this study, the DFOS system adopted is based on optical frequency domain reflectometry (OFDR) for Rayleigh scattering detection. The typical set-up is shown in Figure 4. Similar set-up was also reported by Wu et al. (2020). The incident light from a tunable laser source is divided into the reference light and measurement light by an optical coupler. Once the measurement light is back-scattered, the back-scattered light will be mixed with the reference light by the optical coupler and subsequently demodulated by the photoelectric detector to obtain the strain and temperature measurement. The changes in strain and temperature can be correlated with the spectral shift by Equation (1):

$$\Delta v = C_\varepsilon \Delta\varepsilon + C_T \Delta T \qquad (1)$$

where Δv = Rayleigh spectrum shift, $\Delta\varepsilon$ = strain changes in the fibre optic cable, ΔT = temperature change for the fibre optic cable, C_ε = strain change constant and C_T = temperature change constant

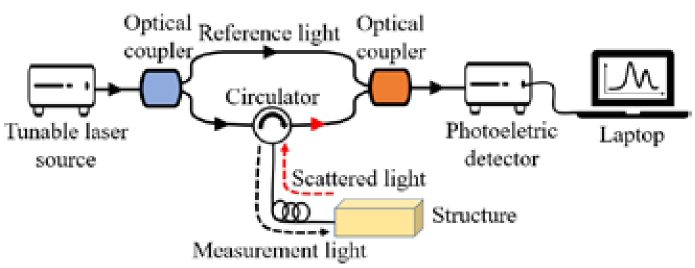

Figure 4: Typical set-up of OFDR for Rayleigh scattering detection

3.2 Field installation and monitoring

Two types of fibre optic cables, namely, strain sensing cable and temperature sensing cable, were installed in the three selected diaphragm wall panels for monitoring. The strain sensing cable is fabricated using tight-buffered, steel strand-reinforced and medium-density polyethylene (MDPE) with a diameter of 5.0 mm (Figure 5(a)). Strain is therefore transferred effectively due to the tight buffering while the cable is well protected by the steel strand reinforcement against damage during reinforcement cage transportation and tremie concreting. The temperature sensing cable is a loose tube cable of diameter of 5.0 mm. An annulus is maintained between the loose cable and the outer protective layer which comprises spiral armour, Kevlar, metal mesh and a low smoke halogen (LSZH) sleeve (Figure 5(b)). The annulus enables the loose cable to be free from mechanical strain and thus the strain changes due to temperature alone can be measured to compensate the strains measured by strain sensing cables.

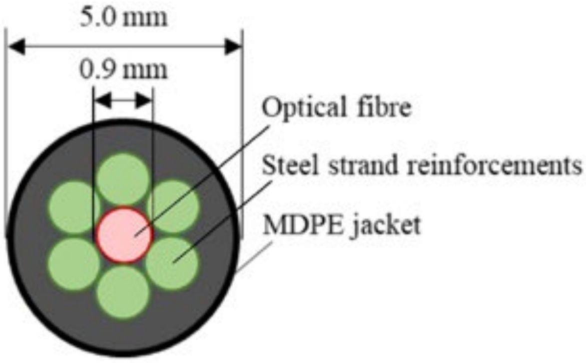

(a)

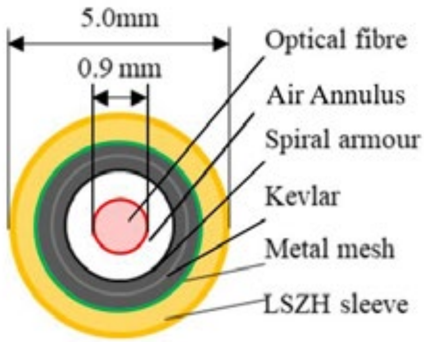

(b)

Figure 5: (a) Strain sensing cable and (b) temperature sensing cable

Strain and temperature sensing cables were installed on both the retained side and excavated side of the diaphragm wall panels. The typical arrangement of the cables is shown schematically in Figure 6(a). The strain sensing cables were arranged in two different configurations. One was aligned vertically along the wall panel for bending strain measurement for all three panels. The other was a zig-zag layout for hoop strain measurement at 6 different elevations (H1 to H6) for panels C1-01 and C2S-03. Meanwhile, temperature sensing cables were aligned vertically along all three wall panels to measure temperature induced strain at different elevations. The fixing details of the cables are shown in Figure 6(b). During the fabrication of the reinforcement cage, the cables were fixed to the steel bars of the reinforcement cage by hose clips and rubber sheets. Pre-tensioning was applied to both bending and hoop strain sensing cables using a tensioning device to achieve a pre-tensile strain of about 1000 $\mu\varepsilon$. Pre-tensioning enables easy identification of the measuring sections interested due to the exhibition of peak strain at the pre-tensioned sections of the cables (Schwamb et al. 2014). No pre-tensioning was applied to the temperature sensing cables. Due consideration and attention should also be given to the future construction activities near the instrumented panels. In panel C1-01, for instance, breaking of concrete cover was necessary as part of the construction to expose the couplers for connecting the lateral support beams. Based on experience gained, since the cables were placed very close to the concrete cover, extreme care must be exercised in installing cables and breaking concrete cover in panels of this type to avoid accidental exposure and physical damages to the cables.

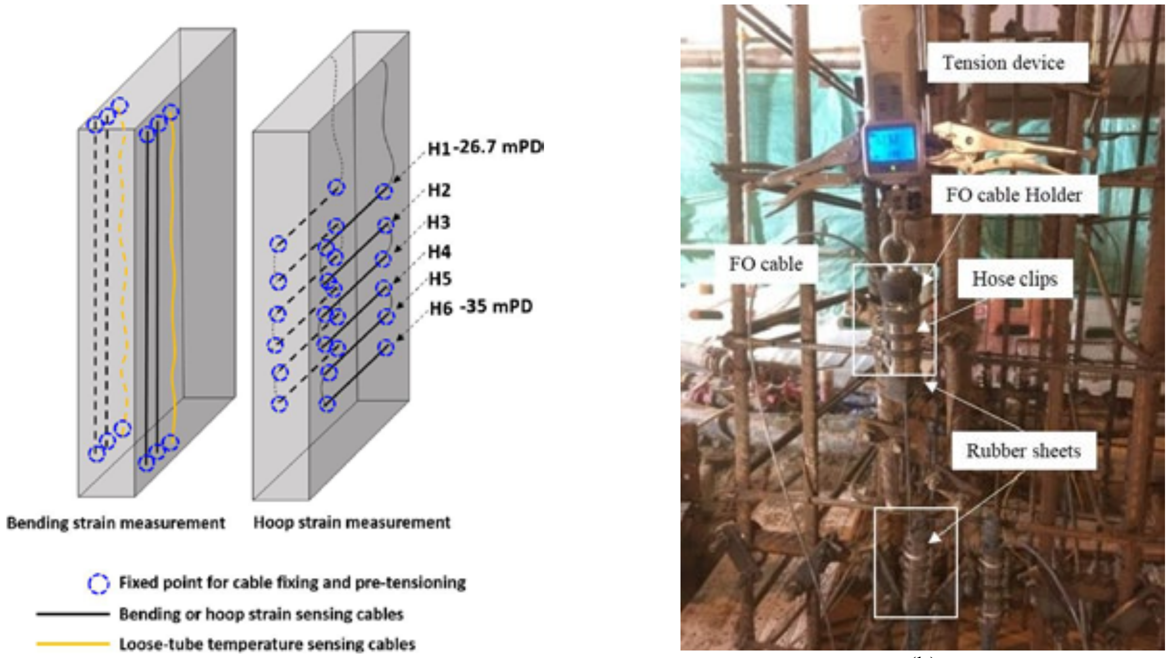

(a) (b)

Figure 6: (a) Typical arrangement of fibre optic cables and (b) fixing details of fibre optic cables on reinforcement cages

DFOS data was collected using an OFDR-based interrogator (OSI-S). The device can produce a spatial resolution of 1 cm in a sensing range of 100 m with a measuring accuracy of $\pm$ 1 $\mu\varepsilon$. In this study, given the signal to noise ratio and the length of the fibre optic cables, a spatial resolution of 5 cm was achieved.

3.3 Data analysis

3.3.1 Curvature and lateral wall movement

Wall curvature can be computed from the strain measurement obtained from the retained side and excavated side using Equation (2):

$$k(z) = \frac{[\varepsilon_r(z) - \varepsilon_e(z)]}{\Delta d} \tag{2}$$

where $k(z)$ = curvature at depth z, $\varepsilon_r(z)$ = strain at the retained side at depth z, $\varepsilon_e(z)$ = strain at the excavated side at depth z and Δd = horizontal distance between the cables on the retained side and the excavated side

Lateral wall deflection is then computed by double integration of the curvature obtained from Equation (2) above. Inclinometers were installed at or near the three instrumented wall panels for establishing the two boundary conditions for integration. The top deflection could therefore be derived directly from the measured top movement from inclinometer. The bottom deflection is taken as zero, which is the same assumption used for inclinometers.

The reliability of using fibre optic sensing to obtain wall curvature and deflection profile is best investigated using data obtained from wall panel no. DN-03 in the conventional multi-propped rectangular excavation, in which the results can be easily interpreted. Figure 7(a) and Figure 7(b) shows a comparison between the results obtained from inclinometers and fibre optic sensors on accumulative curvature and wall deflection of DN-03. The data shows the change from Stage 3 to Stage 5 where concurrent excavation and support installation took place in the rectangular tunnel. It can be seen that while the general trend of curvature was comparable between the two instruments, the fibre optic sensors registered a more reasonable curvature characteristic below the excavation depth with less fluctuation. Regarding wall deflection, a more consistent and comparable trend was observed. In particular, both optic fibre sensor and the inclinometer recorded a maximum deflection of about 28.4 mm and 37.2 mm respectively near the excavation depth at -25 mPD.

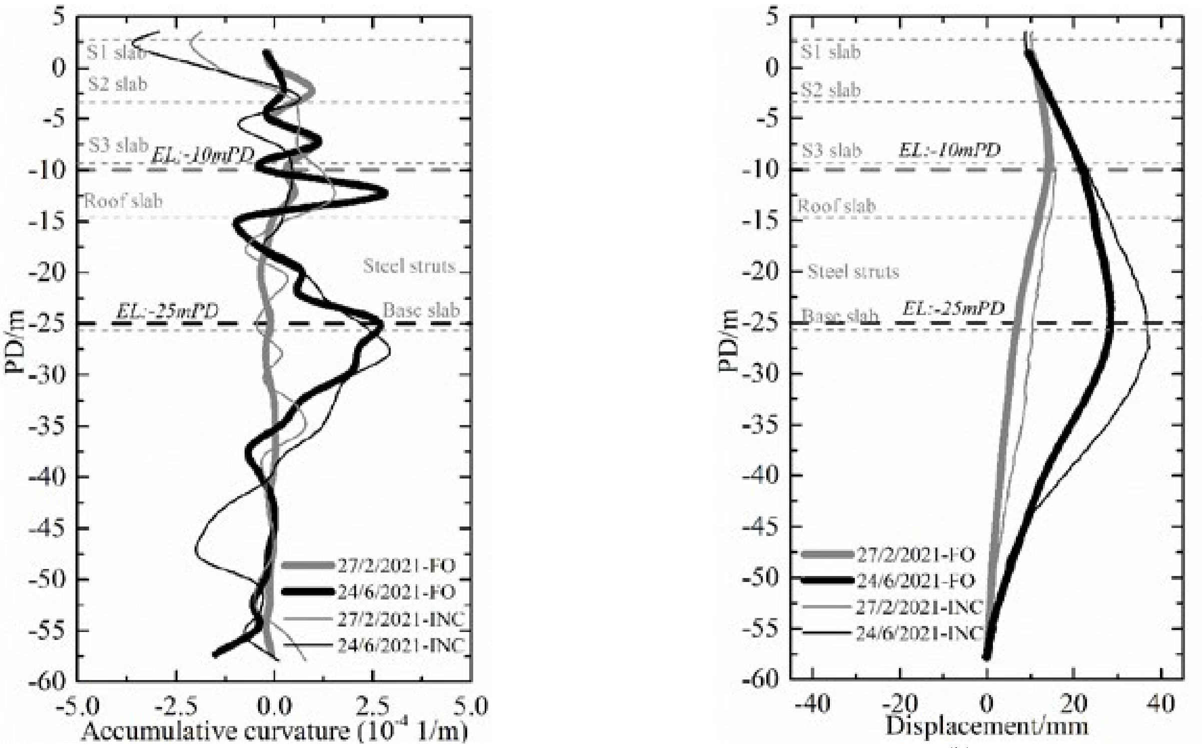

(a) (b)

Figure 7: Comparison between fibre optics sensing and inclinometer on (a) accumulative curvature and (b) wall deflection on DN-03

3.3.2 Hoop force and circumferential bending moment

In this paper, the results from C2S-03 will be presented as an example to demonstrate the use of fibre optics sensing technology for studying hoop force and circumferential bending moment development in the peanut-shaped shaft. As mentioned in Section 3.2, hoop strains were measured at six different elevations from -26.7 mPD to -35 mPD across the wall panel indicated as H1 to H6. For better visualisation, hoop strains from the top (H1), middle (H3) and bottom (H6) sections are presented as shown in Figure 8(a) and Figure 8(b) (tensile strain as positive and compressive strain as negative). The hoop strains indicated here were averaged out per 1 m cable length at each elevation and plotted against the construction stages Stage 1 (S1) to Stage 6 (S6). In general, both retained side and excavated side of the peanut-shaped shaft developed compressive hoop strain as the excavation works proceeded, with a larger hoop strain increase at the retained side, which is reasonable.

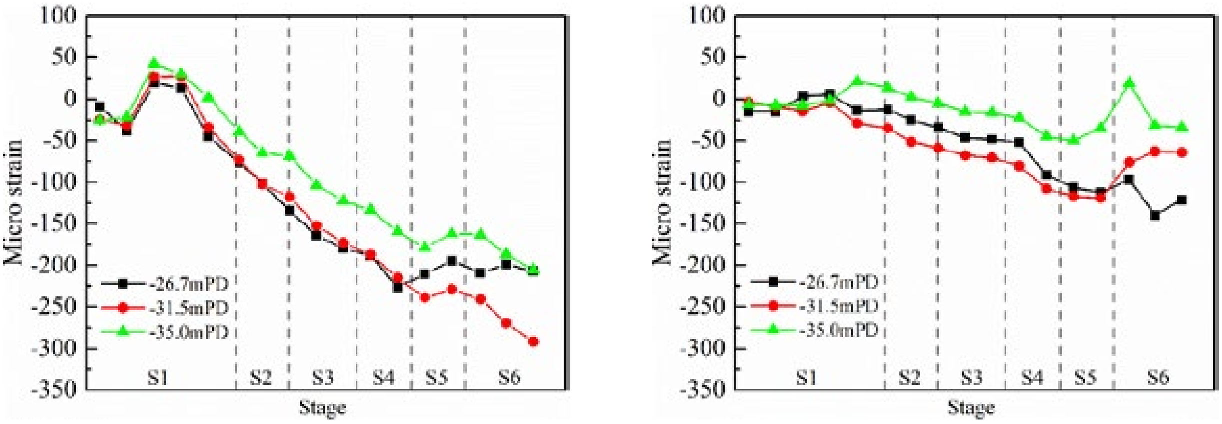

(a) (b)

Figure 8: (a) Hoop strains development on retained side and (b) hoop strains development on excavated side of C2S-03

To better understand the behaviour of the peanut-shaped excavation, the hoop force and circumferential bending moment of C2S-03 are presented in Figure 9(a) and Figure 9(b) respectively. During Stage 1, before excavation in Cell 1 and Cell 2, the positive hoop force and negative bending moment induced in C2S-03 were likely attributed by the partial lateral pressure release due to the excavation of the adjacent cut-and-cover tunnel. During Stage 2 to Stage 4, the combined effect of the dewatering and excavation works at the peanut-shaped shaft induced a progressive increase in compressive hoop force and hence an increase in circumferential bending moment. When the excavation level reached about -27 mPD at Stage 5, the western crosswall was concurrently demolished from -15.0 mPD to -25 mPD as shown in Figure 1(b). The release of the compressive hoop force and circumferential bending moment due to this crosswall demolition was successfully captured by the fibre optics sensors as highlighted in grey in Figure 9(a) and Figure 9(b). Once the excavation works proceeded beyond -25 mPD, both the compressive hoop force and circumferential bending moment increased again until they were generally stabilised when the final excavation level at about -32.6 mPD was reached during Stage 6.

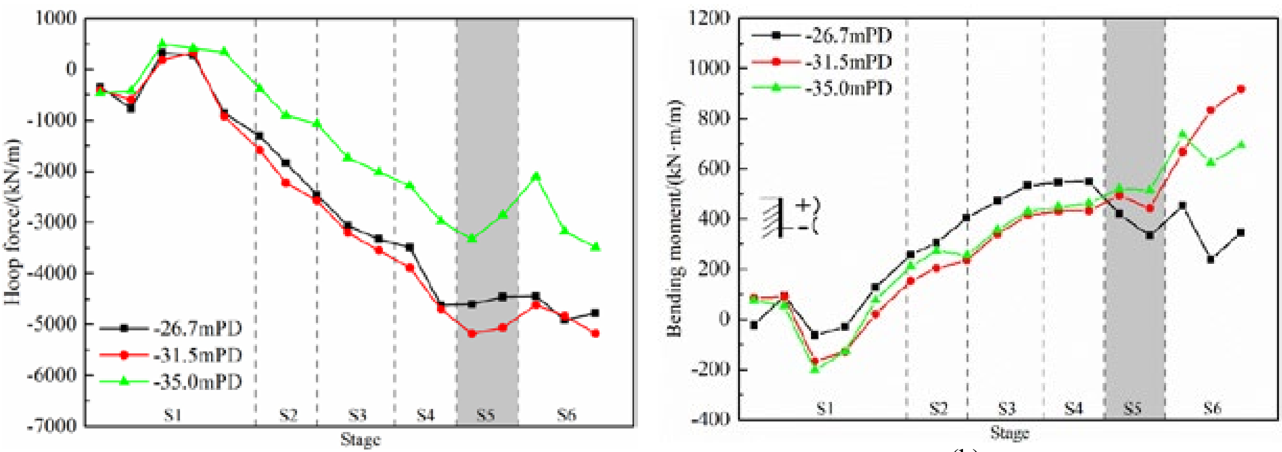

(a) (b)

Figure 9: (a) Hoop force development and (b) circumferential bending moment development of C2S-03

From the data analysis, it can be seen that DFOS technology offers an innovative and reliable solution in investigating the performance of the peanut-shaped excavation with partial crosswall demolition. In particular, the capability of producing continuous profiling of hoop forces and circumferential bending moment development is a clear advantage over other traditional instrumentations such as inclinometers and vibrating wire strain gauges, which only provide discrete measurement points.

4 REMOTE SENSING USING HANDHELD LiDAR SCANNER

4.1 Methodology

Remote sensing using LiDAR technique was carried out as part of the monitoring scheme of the peanut-shaped excavation in the T2 project to obtain 3D geospatial information (point clouds) of the site. Given the cramped setting of the construction site with much plant and machinery that operated around the clock, handheld scanning devices were considered the most suitable where portability and efficiency were the main considerations such that impact to the construction progress could be minimised. In order to compare the 3D information with the actual site conditions and measurements, the point clouds obtained were transformed to the Hong Kong coordinate system HK80 by geo-referencing. A combination of fixed control points using existing structures coordinates and mobile control points using survey spheres was established on site to ensure sufficient control points could always be maintained within the line of sight throughout the monitoring period. In order to minimise cumulative error due to drift, a “closed loop” survey path was maintained in every scan to ensure the compounded error could be distributed within the loop. The scanning covered the entire TBM launching area at the T2 including both the cut-and-cover tunnel and peanut-shaped shaft.

4.2 Equipment and Data Acquisition

The portable scanning device adopted in this study was the ZEB Horizon. It mainly consists of a 2D laser range scanner head and a built-in inertial measurement unit (IMU) mounted on a rotary motor drive (Figure 10). The rotary action of the scanner provides the third dimension required to generate 3D information. The scanner head emits laser pulse and subsequently detects reflected pulses to determine the distance between the scanner and the objects being measured (Leung & Ho, 2020). Data received from the scanner head is then combined with the IMU data using the simultaneous localisation and mapping (SLAM) algorithm for acquisition of 3D point clouds (GeoSLAM Limited, 2020). The total weight including the battery and data-logger is only about 3 kg. The maximum scanning range is 100 m with a scanning rate of 300,000 points per second. A complete scan including set-up time required about 1.5 hour, which is considerably quicker than conventional land surveying, which normally takes at least half a day to cover a site of comparable size.

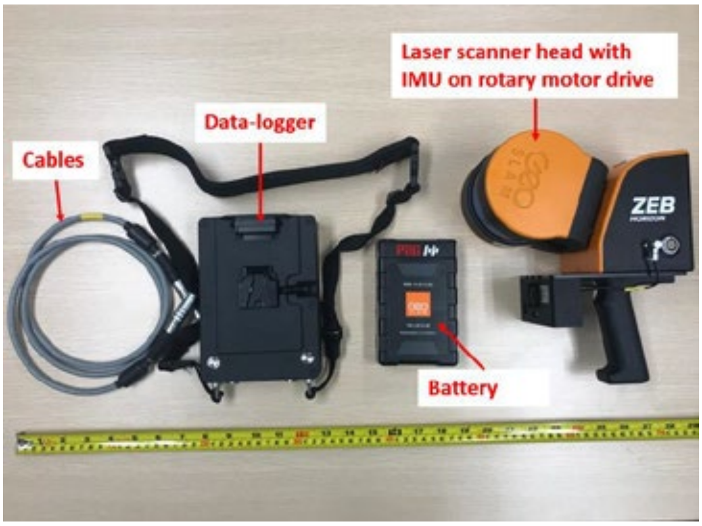

Figure 10: Main components of the handheld laser scanning device

4.3 Data processing

The common data processing included noise removal, sub-sampling, geo-referencing and merging datasets, etc. Noise was mainly contributed from moving objects, which generated redundant signal and should be removed.

In order to enhance the level of detail obtained from the cut-and-cover tunnel where multiple lateral supports were constructed, separate scanning was performed at close range at different support levels within the cut-and-cover tunnel. After geo-referencing, these individual sub-sample datasets could be easily merged to supplement the geospatial information of the main model. In this study, data processing was carried out using an open-source freeware CloudCompareV2 (CloudCompare 2015). Figure 11 shows the typical work flow outlining the processing tasks to produce a 3D model of the TBM launching area.

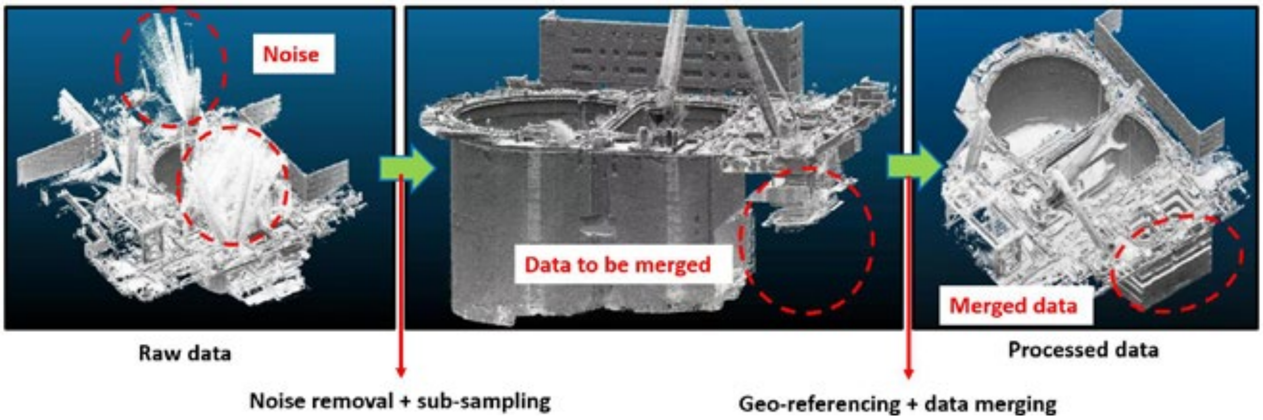

Figure 11: Typical workflow of data processing

4.4 Data analysis

The processed data, being geo-referenced, enable useful analysis like cutting cross-sections, dimension measurement and estimation of excavation extent, etc. By way of an example, Figure 12(a) shows the measurement of excavation depth of a typical cross-section extracted from the cofferdam using CloudCompareV2. Throughout the construction, a trial location was selected and a comparison was made between LiDAR measurement and site records on excavation level as plotted in Figure 12(b). It demonstrates that LiDAR measurement can provide reasonably comparable results. The use of LiDAR technique offers an added advantage of capturing the entire profile in the space as compared with integrating single measurement points manually based on the conventional survey method.

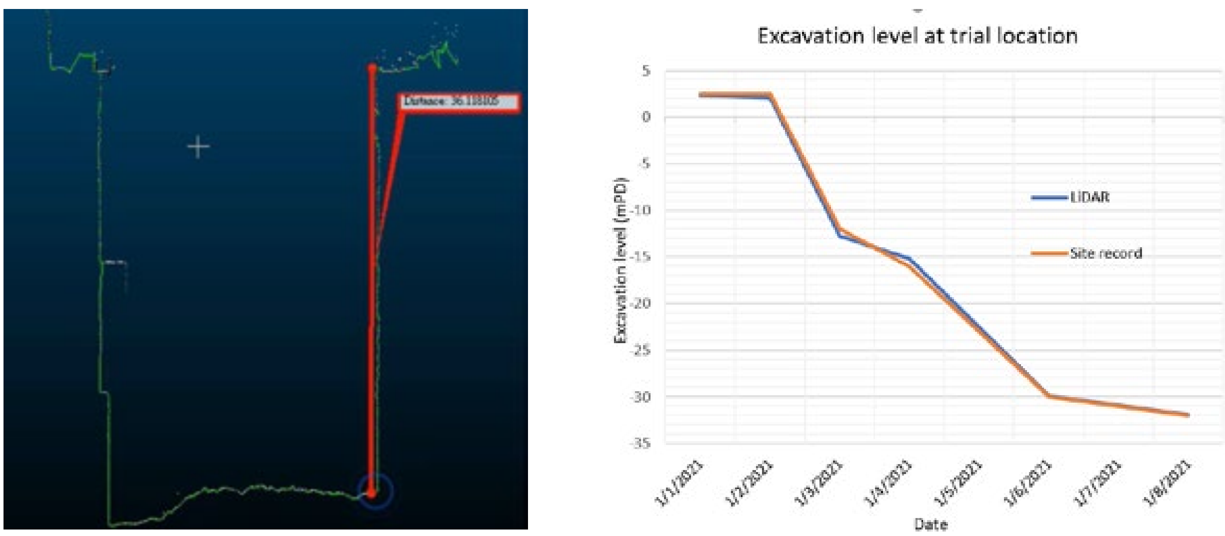

(a) (b)

Figure 12: (a) Typical cross section extracted from 3D LiDAR model and (b) comparison between LiDAR measurement and site measurement

Previous LiDAR studies undertaken on natural hillsides or landslide sites seldom involved frequent and periodic scanning. Their data analysis was largely based on a single model. Change detection application reported by So et al. (2021) was based on 3 different LiDAR datasets that were few to ten years apart for assessing change of ground profile due to landslide. However, a higher monitoring frequency is more suitable for excavation and lateral support works. In this study, frequent scanning on a weekly basis was carried out throughout the entire monitoring period. Over 30 complete datasets were acquired. The geo-referenced 3D information can be integrated against time for a complete 3D visualisation of the construction sequence. Figure 13 shows some extracted dataset which are correlated with the construction sequence Stage 1 to Stage 6 mentioned in Figure 2.

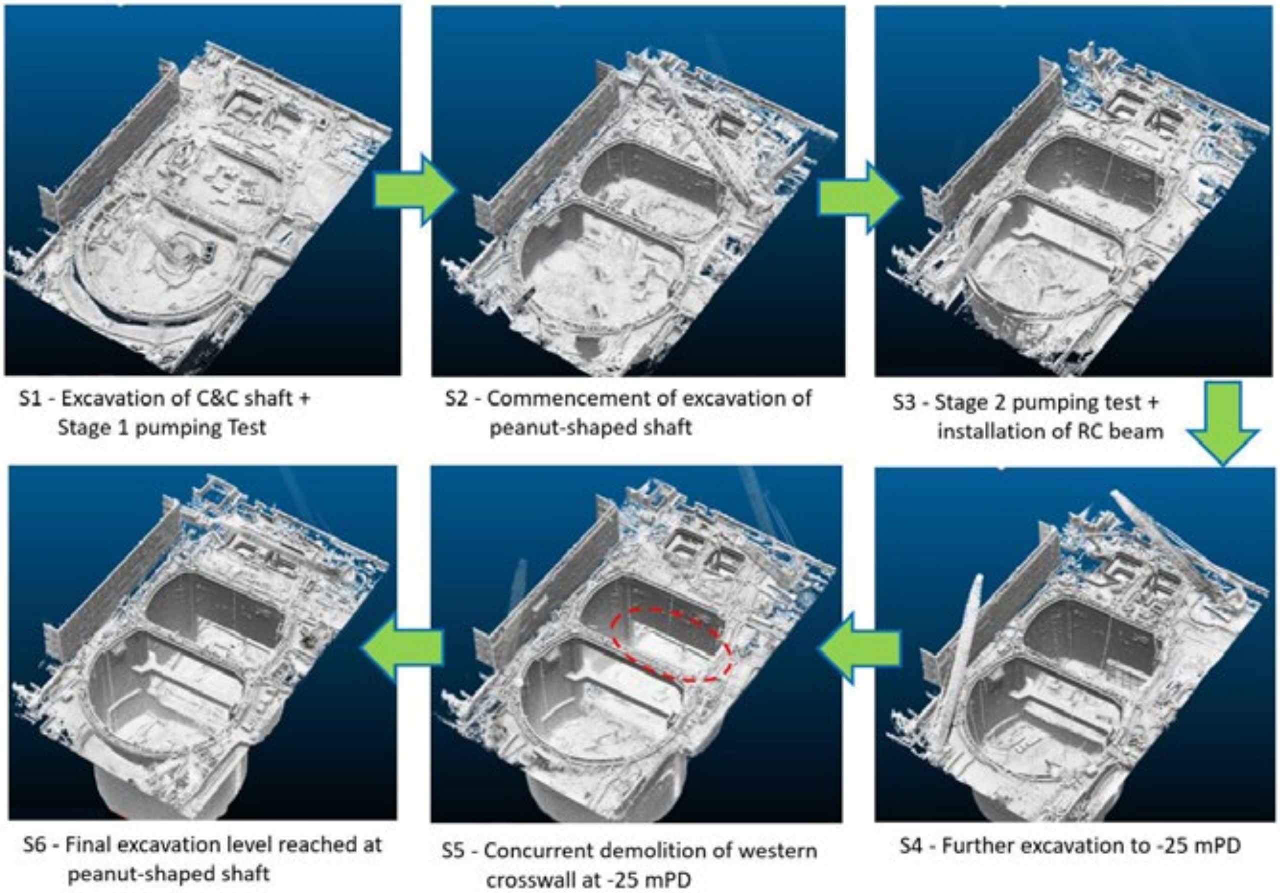

Figure 13: 3D visualisation of construction sequence from LiDAR dataset showing key construction stages S1 to S6

Given the complex site setting and construction sequence of the T2 project, the 3D construction sequence visualisation served as a useful tool for prompt cross-checking of the actual construction progress against the design scheme. The LiDAR data successfully captured the critical activities such as excavation, installation of lateral supports and crosswall demolition. Clearly, the information obtained further reinforced the interpretation of the fibre optics results presented in Section 3 above.

5 CONCLUSIONS

This paper presented the state-of-the-art monitoring techniques employing fibre optics sensing and handheld remote sensing devices using LiDAR to study the behaviour of a peanut-shaped excavation, which is first of its kind being implemented in Hong Kong. Fibre optics sensing offers superior capability over traditional monitoring instruments in terms of producing continuous profiling of hoop strains, hoop forces and circumferential bending moment, which are essential in assessing the soil-structure interaction of non-conventional circular excavation. Wall deflection profiles obtained are comparable with those obtained from inclinometers. Potential further work including using the fibre optics data for numerical back-analysis can be explored to facilitate the future design and construction of excavation and lateral support works of a similar nature. The simple operation of handheld LiDAR scanner also greatly reduces the surveying time and minimises disturbance to the site works. Digitisation of actual site conditions allows quick data analysis to assist the verification of design and monitoring of construction progress. Further application is envisaged to incorporate the 3D dataset into the Building Information Modelling (BIM) system to facilitate design optimisation and assets management.

ACKNOWLEDGEMENTS

This paper is published with the permission of the Director of Civil Engineering and Development, the Head of the Geotechnical Engineering Office, the Project Manager of the East Development Office and the Hong Kong Polytechnic University of the Hong Kong Special Administrative Region, China.

REFERENCES

Bao, X. & Chen, L. 2012. Recent progress in distributed fiber optic sensors. *Sensors 2012, 12(7)*: 8601-8639.

CloudCompare 2015. *CloudCompare Version 2.6.1: User Manual*. CloudComapre.

GeoSLAM Limited. 2020. *ZEB-Horizon User's Manual v1.3*. GeoSLAM Limited.

Kechavarzi, C., Soga, K., de Battista, N., Pelecanos, L., Elshafie, M.Z.E.B. & Mair, R.J. 2016. *Distributed Fibre Optic Strain Sensing for Monitoring Civil Infrastructure-A practical guide*. ICE Publishing.

Leung, W.K. & Ho, Y.K. 2020. A New Generation of Handheld Laser Scanning for Quality Enhancement in Geotechnical Studies. *Proceedings of HKIE Geotechnical Division Annual Seminar 2020*: 50-61.

Pappin, J.W. 2011. Circular excavations using diaphragm walls. *APEC Seminar on the State-of-the-Practice of Deep Excavation Works in Malaysia*, *Taiwan and Hong Kong 2011*: 111-120.

Schenato, L., Palmieri, L., Camporese, M., Bersan, S., Cola, S., Pasuto, A., Galtarossa, A., Salandin, P. & Simonini, P. 2017. Distributed optical fibre sensing for early detection of shallow landslides triggering. *Scientific Reports 7*: 14686. DOI: 10.1038/s41598- 017-12610-1.

Schwamb, T., Soga, K., Mair, R. J., Elshafie, M.Z.E.B., Sutherden, R., Boquet, C., & Greenwood, J. 2014. Fibre optic monitoring of a deep circular excavation. *Proceedings of the Institution of Civil Engineers - Geotechnical Engineering*, 167(2): 144-154. ICE Publishing.

So, A.C.T., Ho, T.Y.K., Wong, J.C.F., Lai, A.C.S., Leung, W.K. & Kwan, J.S.H. 2021. Advancing the use of LiDAR in geotechnical applications in Hong Kong – A 10-year overview. *The 42nd Asian Conference on Remote Sensing (ACRS2021), Vietnam, 22-24 November 2021*: pp 11.

Soga, K. & Luo, L. 2018. Distributed fiber optics sensors for civil engineering infrastructure sensing. *Journal of Structural Integrity and Maintenance*, 3(1): pp 21.

Torisu, S.S., Faustin, N.E., Elshafie, M.Z.E.B., Black, M., Soga, K., & Mair, R.J. 2019. Monitoring of Shaft Excavations in Clay. *International Conference on Smart Infrastructure and Construction 2019 (ICSIC)*: 655-664. ICE Publishing.

Wu, H., Zhu, H.H., Zhang, C.C., Zhou, G.Y., Zhu, B., Zhang, W. & Azarafza, M. 2020. Strain integration-based soil shear displacement measurement using high-resolution strain sensing technology. *Measurement*, 166: pp 12.

Xu, D.S., Dong, L.J., Borana, L. & Liu, H.B. 2017. Early-warning system with quasi-distributed fiber optic sensor networks and cloud computing for soil slopes. *IEEE Access*, vol. 5: 25437 – 25444. DOI: 10.1109/ACCESS.2017.2771494.

Zhu, H.H., Ho, A.N.L., Yin, J.H., Sun, H.W., Pei, H.F. & Hong, C.Y. 2012. An optical fibre monitoring system for evaluating the performance of a soil nailed slope. *Smart Structures and Systems* 9(5): 393-410.

Are We Ready to Use AI Technologies for the Prediction of Soil Properties?

Ryan Yan
AECOM Asia Co. Ltd., Hong Kong, China

ABSTRACT

Artificial intelligence (AI) has become a hot topic for different professions in which geotechnical engineering is no exception. It is anticipated that AI could perform tasks, solve complex problems and make decision by mimicking intelligence or behavioral pattern of humans or any other living entities. Attempts have been made to study and adopt AI technologies in geotechnical engineering. In this paper, a dataset of marine soil in South Korea is re-analyzed using different commonly adopted AI algorithms. The soil's compressibility is considered as the dependent variable (i.e., to be predicted) while other soil index and physical properties are regarded as the independent variables. The data are split into the training and validation set. While an algorithm learns from the training set, its prediction performance is examined using the validation set. Then, the Bayesian model class approach has been used to explain the potential problem of the use of AI algorithm to predict soil properties. At the end, by using this study as an example, the author discusses from a partitioner's perspective how AI could affect our professions. In particularly, the question "are we ready for using AI to predict soil properties" is addressed.

1. INTRODUCTION

1.1 Overview

Artificial Intelligence (AI) can be referred to as the intelligence exhibited by machines or software capable of performing tasks, solving complex problems or making decision by mimicking intelligence or behavioral pattern of humans or any other living entity. There are many AI-related terminologies in which people often find confusing. Figure 1 shows a simple diagram to illustrate the relations among these terminologies. Machine Learning (ML), a subset of AI, is a technique by which a computer program can perform prediction without the use of any prescribed set of rules including mainly for instance statistical theories. This approach trains a predictive model from data. In a layman's term, the data will tell you the underlying pattern or governing rules, if any. Neural Network (NN) or in many studies people call this Artificial Neural Network (ANN), a subset of ML, is a technique to perform machine learning inspired by our brain's own network of neurons. In the case when multiple layers of neurons are used, it is called the Deep Neural Network (DNN).

In general, a key concept of AI is to convert data into value. AI has been embedded in our daily lives. Examples include Siri, automates driving, robot-advisors, email spam filtering, Netflix recommendations, facial detection and recognition, etc. It is believed that soon or later AI will dominate the area of data analytics.

1.2 Applications of AI technologies to Geotechnical Engineering

AI technologies appear very appealing, and attempts have been made by geotechnical engineers to employ the techniques to solve engineering problems. Generally speaking, the development of an AI application involves the following key stages:

- Collection of data which can be structured, unstructured, or both;
- Data conditioning including for example dimensionality reduction, outlier detection, looking for biases in the collection, highlighting incomplete data, etc;
- Learning via algorithm;
- Validation and prediction;
- Publishing.

The applications of AI to geotechnical engineering can generally be divided into 4 categories. They are material behavior, system performance, classification, and automation. Material behavior refers to as the prediction of geomaterial properties using predominantly ML and ANN algorithms. System performance refers to the use of AI technologies to examine/predict the performance of an engineered or natural system, for example the prediction of damages due to natural disasters such as earthquakes and landslides. Classification refers to the categorization of features, profiles and systems. Typical examples include cracks and landslides recognition from images, classification of soil type and geological profile, etc. AI automation refers to the decision making based on defined rules and experience. In Hong Kong, AI automation has been applied mostly to site safety monitoring. Over years, increasing efforts have been spent to apply AI technologies in particularly ML and ANN to geotechnical engineering (Shahin, 2016; Ebid, 2021; Jaksa and Liu, 2021; Jong et al., 2021; Zhang et al., 2021a,b; and many more).

This study first presents the use of various AI algorithms to predict the soil compressibility of marine soils based on a database compiled from literature. Performance of the prediction is discussed. Based on the findings, the author then shares his thoughts on whether AI-based prediction of soil properties should be widely adopted in the profession.

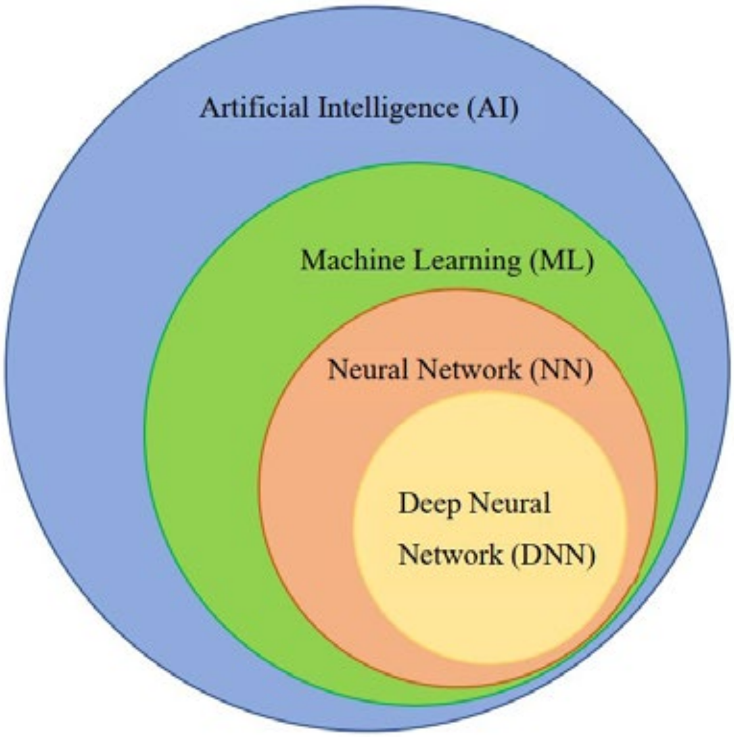

Figure 1: Relations among different terminologies in the family of AI.

2 PREDICTION OF SOIL COMPRESSIBILITY

2.1 Database

A comprehensive dataset containing the compression index C_c and other soil properties including the in-situ water content w_n, initial void ratio e_0, liquid limit LL, plasticity index PI, specific gravity G_s, and soil dry density ρ_d of marine clays in the coasts of South Korea is re-examined. The dataset contains 223, 274 and 298 complete sets of records from the east, south and west coast of South Korea, respectively. Figure 1 shows the variation of C_c with each soil parameter. Clearly, a large range of soil compressibility can be identified in the east and south coast data while that in the east coast covers a smaller range. More details of the sites and soils can be found in Yoon et al., (2004). In the following prediction analysis, the compression index is considered as the dependent variable while the remaining soil properties are considered as independent variables. In other words, the compression index will be predicted using the independent soil properties.

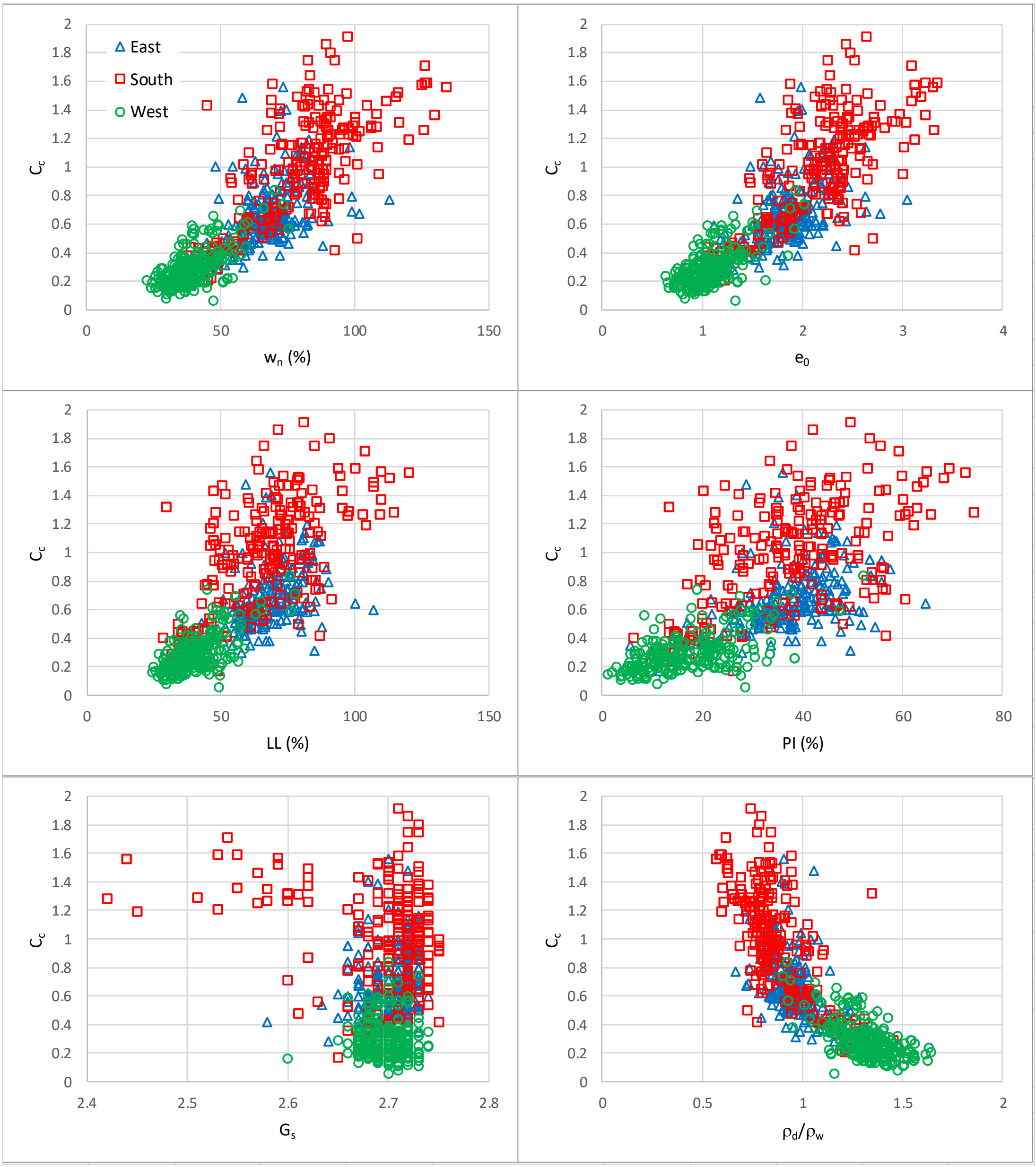

Figure 2: Variation of compression index with soil properties.

2.2 Readily Available Solutions using Microsoft Machine Learning Studio (classic)

Released in 2015, Microsoft Machine Learning Studio (classic), refers to as ML Studio hereafter, was the first drag-and-drop machine learning model builder in Microsoft Azure. It is a standalone service that offers a visual experience of ML. Microsoft Azure Machine Learning, however, is a separate service that delivers a complete data science platform. It is a cloud-based service to manage machine learning projects from model development, training, deployment and managing Machine Learning Operations (MLOps). Users can create a model in Azure Machine Learning or use a model built from an open-source platform. The Azure Machine Learning Studio is a graphical user interface for a project workspace. In this study, ML Studio is employed to develop readily-to-be-used ML solutions for the prediction of soil compressibility.

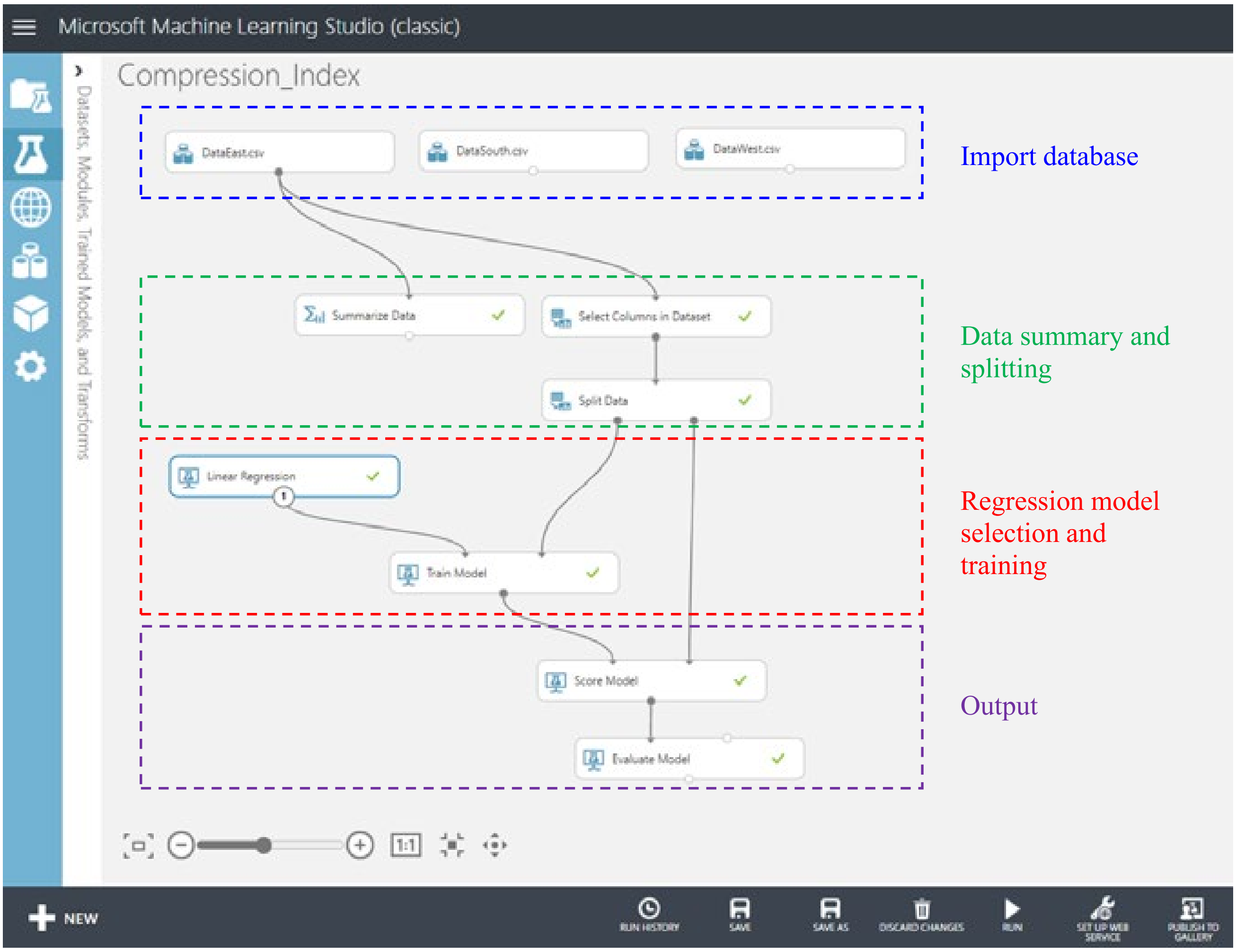

Figure 3: An example workflow in ML Studio.

The prediction of compression index falls into the regression category in ML. Many readily available regression models have been deployed in the ML Studio. For example:

- Linear Regression
- Bayesian Linear Regression
- Boosted Decision Tree Regression
- Decision Forest Regression
- Neural Network Regression
- Poisson Regression

The above regression models are used in this study to predict compression index from the independent soil properties. The dataset is divided into 2 groups: namely the training set which contains 70% of the entire dataset and the validation set containing the remaining 30%. This ratio of splitting is a common practice in ML. In most cases, default setting of the built-in models is adopted. It aims to mimic users with little experience or understanding of each ML algorithm. Its impact and implication will be discussed later in this paper. Figure 3 shows how the ML Studio graphic interface looks like. The drag-and-drop nature of the platform can be readily seen. As illustrated, the workflow can be divided into 4 parts: (i) import database, (ii) data summary and splitting; (iii) regression model selection and training; and (iv) output. It is worth noting that the use of ML studio requires nearly no experience of program coding.

In this study, the ordinary least squares method is adopted as the solution scheme for the linear regression model. This method attempts to minimize the sum of the squared residuals to evaluate the values of the fitting coefficients. The Bayesian linear regression method in this study refers to the use of Bayesian inference to evaluate the model fitting parameters. It is assumed that the errors of regression model possess a normal distribution and the posterior probability distributions of the model parameters are evaluated based on a prior distribution of the parameters. Weight regularization is used to reduce overfitting. Boosted decision tree method builds a series of trees in a step-wise fashion and then selects the optimal tree using an arbitrary differentiable loss function. Decision forest regression is a non-parametric approach that perform a sequence of simple tests traversing a binary tree data structure until a decision is reached. In this study, the bagging resampling method and a single parameter training method is adopted. Neural network regression is a multiple interconnected node approach. In this study, the min-max normalizing approach is used. Poisson regression assumes the output follows a Poisson distribution and the logarithm of its expected value can be modeled by a linear combination of the independent variables. Details of each algorithm is beyond the scope of this paper and readers are recommended to read corresponding learning materials which can be easily found in textbooks and/or from the internet.

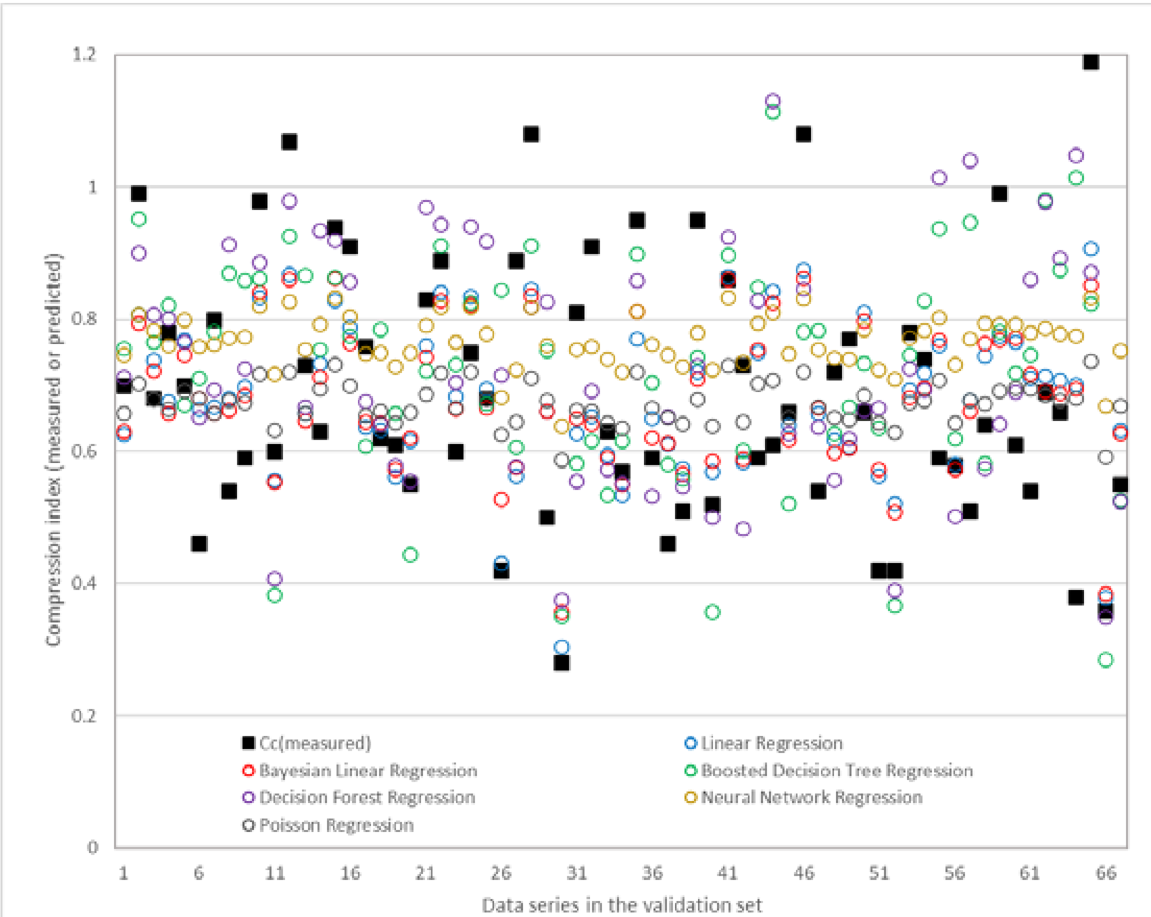

Figure 4: Prediction from different ML models (data from validation set of East Coast).

Figure 4 shows the comparison of prediction made using different ML algorithms for the East Coast validation dataset. There are 67 sets of date in this validation set (i.e., 30% of 223). The square symbol denotes the measured compression index and the circles having different colors represent prediction obtained from different algorithms. One can see clearly that the difference among the model predictions is noticeable.

Equation (1) is used to quantify the prediction error of the validation set where E denotes the mean absolute percentage error, y_i^m and y_i denote the measured C_c and corresponding prediction of entry i, respectively, N is the total number of data in the validation set.

$$E = \frac{1}{N}\sum_{i=1}^{N}\left|\frac{y_i - y_i^m}{y_i^m}\right| \tag{1}$$

The larger the E, the more discrepancy between the measurement and the prediction is. Figure 5 summarizes the results for different algorithms at different location groups of the data. In generally, the linear and Bayesian regression algorithm give the smallest prediction discrepancy among other algorithms. They give an average absolute error of about 20%.

It is worth noting that fitting error is only one of the criteria to judge whether a prediction is good or not. Robustness of the fitting formula, for example, would also tell if the prediction is worth to be adopted. Overfitting is a common problem to observe. More details will be elaborated next.

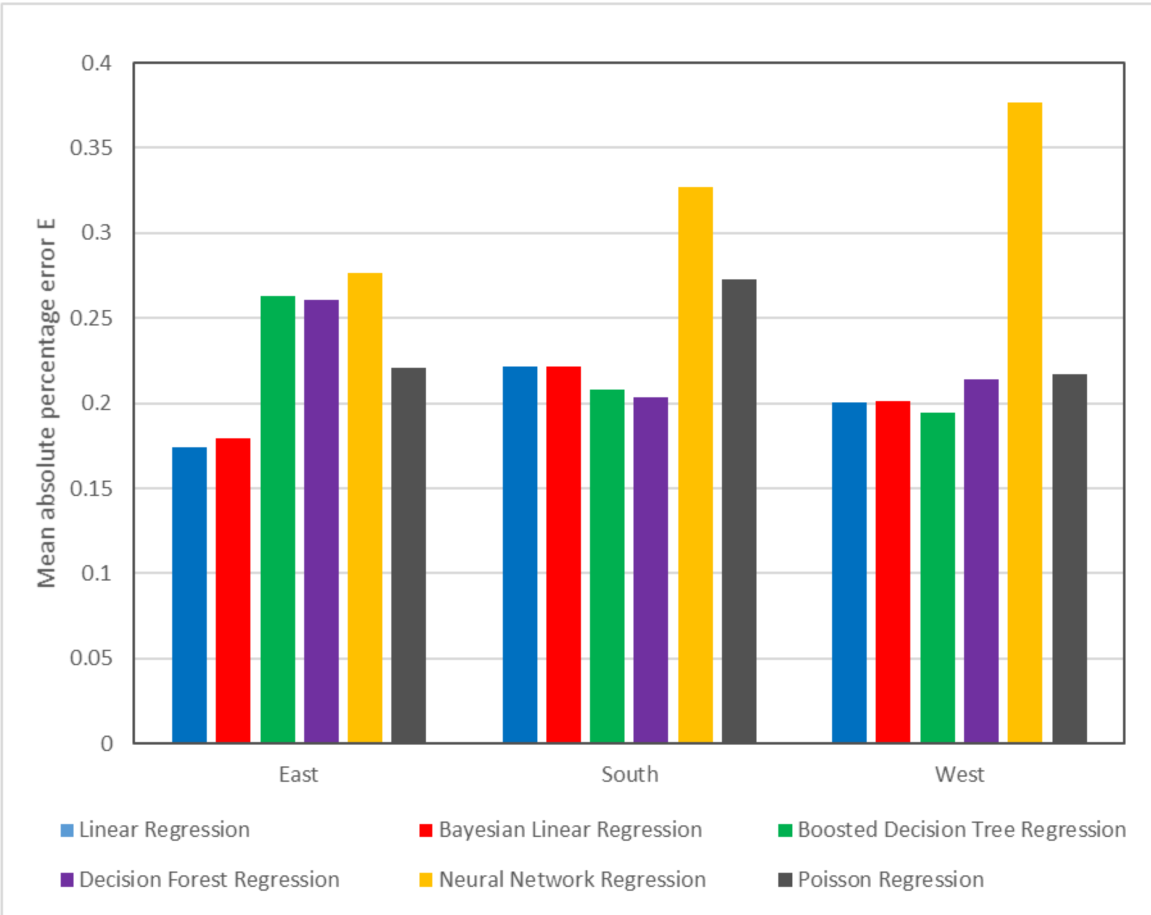

Figure 5: Mean absolute percentage error of each ML algorithm.

2.3 Parametric Bayesian Probabilistic-based Model Class Selection

Yan et al. (2009) presented a Bayesian probabilistic-based parametric approach to predict the soil's compression index. This approach has two major merits. First, by using the Bayesian probabilistic model class approach the most probable empirical prediction formula form is selected by achieving a balance between data fitting capability (i.e., likelihood) and sensitivity to modeling noise. This would mitigate the problem of overfitting. Second, an explicit form of empirical formula showing the optima fitting parameters is obtained which allows the formula to be examined or verified in the context of geomechanics. Though AI terminologies were not mentioned in their paper, the analysis was indeed falling into the family of ML according to the classification as presented in Section 1 of this paper. Based on their findings, the soil's compression index C_c can be expressed as

$$C_c = c_0 + c_1 e_0 + c_2 LL \tag{2}$$

where = c_0, c_1 and c_2 are fitting parameters calibrated from the dataset.

By using the parametric Bayesian probabilistic-based model class approach, the most probable empirical formula can be found. First, the problem of overfitting can be resolved using the data themselves. The most complex formula is not always the most probable one due to the problem of overfitting. Indeed, an over-complex prediction formula could bring in too much modelling noise. Second and more importantly, the formula offers geomechanics insights into the problem. In this compressibility prediction, for instance, the formula explicitly states that the soil compressibility would depend on a soil intrinsic index, the liquid limit, and another soil physical property, the initial void ratio. From a geomechanics perspective, the liquid limit quantifies the water content of a remolded soil for a specified undrained shear strength. Therefore, it is linked to the nature and the mineralogical composition of the soil and thus governs the compressibility. Besides, compressibility is affected by the soil structure which depends on its geological history. The initial void ratio is a suitable indicator to address this effect. A proper fundamental understanding of the rationale of the prediction formula helps to provide confidence when the formula is being used.

3 OBSERVATIONS AND LESSON LEARNT

Commercially available ML platforms offer a catalyst for the adoption or application of AI to our profession. The ML studio is adopted in this study. There are many built-in algorithms in the platform and simple drag-and-drop interface has been developed to facilitate the ML applications. On the one hand, different from the traditional structural coding/programing approach, this visual programming offers a mostly painless environment to develop the ML applications. On the other hand, users may overlook the default setting of each mathematical algorithm and make unintentional mistakes

This study has clearly demonstrated that various algorithms could give essentially "promising" or "non-promising" predictions. Adopting the ML algorithm like a black-box appears to give prediction without too much physical support. As shown in this study, noticeable difference in prediction could be obtained from various ML algorithms. Without going into details of the solution scheme one could not resolve the problem of overfitting and would be very difficult to judge which algorithm(s) outperforms the others. In the data science discipline, people believe that only a massive amount of good quality data could provide us more confidence on the results. Unfortunately, in geotechnical engineering massive amount of data is often impossible. Nevertheless, how to deal with sparse geotechnical data, particularly for modeling spatial variability of soil properties (e.g., Wang and Zhao 2017) and subsurface stratigraphy (e.g., Shi and Wang 2021), has been an active research area in recent years. The uncertainties associated with ML results of sparse data can be quantified using Bayesian methods and stochastic simulations (e.g., Wang et al. 2022). Promising development in this area is expected.

An independent study of Bayesian-based model class selection has demonstrated the importance of avoiding over-complex formula. Besides, physical significance of any prediction formula should be examined which could shed light on its validity.

To answer the statement "are we ready to use AI technologies for the prediction of soil properties", the author believes that we are still at the starting point of the race. Collaboration between data scientists and geotechnical engineers would be required to bring forward this idea. Predicting soil properties should not be considered a purely mathematical issue but would need the knowledge of geomechanics.

4 CONCLUDING REMARKS

This paper presents the performance of predicting the compression index of marine clays found in different areas of South Korea using various built-in ML algorithms available in a commercial ML platform. The prime aim of this study is by using the above application as an example to examine if the use of ML for soil properties prediction can be readily adopted in the industry without much a concern. It is concluded that without a proper understanding of the basics of these algorithms any prediction might be misleading and dangerous. Fundamental geomechanics still plays a key role in geotechnical engineering applications and any advanced tools or algorithms should be used with caution.

REFERENCES

Ebid, A.M. 2021. 35 years of AI in geotechnical engineering: state of the art. *Geotechnical and Geological Engineering,* 39: 637-690.

Jaksa, M., Liu, Z. 2021. Editorial for special issue "application of artificial intelligence and machine learning in geotechnical engineering". *Geoscience*, 11(10): 399.

Jong, S.C., Ong, D.E.L., Oh, E. 2021. State-of-the art review of geotechnical-driven artificial intelligence techniques in underground soil-structure interaction. *Tunnelling and Underground Space Technology*, 113: 103946.

Shahin, M.A. 2016. State-of-the-art review of some artificial intelligence applications in pile foundations. *Geoscience Frontiers*, 7: 33-44.

Shi, C., Wang, Y. 2021. Development of subsurface geological cross-section from limited site-specific boreholes and prior geological knowledge using iterative convolution XGBoost. *Journal of Geotechnical and Geoenvironmental Engineering*, 147(9): 04021082.

Wang, Y., Hu, Y., Phoon, K.K. 2022. Non-parametric modelling and simulation of spatiotemporally varying geo-data. *Georisk: Assessment and Management of Risk for Engineered Systems and Geohazards*, 16(1): 77-97.

Wang, Y., Zhao, T. 2017. Statistical interpretation of soil property profiles from sparse data using Bayesian Compressive Sampling. *Géotechnique*, 67(6): 523-536.

Yan, W.M., Yuen, K.V., Yoon, G.L. 2009. Bayesian probabilistic approach for the correlations of compression index for marine clays. *Journal of Geotechnical and Geoenvironmental Engineering ASCE*, 135(12): 1932-1940.

Yoon, G.L., Kim, B.T., Jeon, S. S. 2004. Empirical correlations of compression index for marine clay from regression analysis. *Canadian Geotechnical Journal*, 41(6): 1213-1221.

Zhang, P., Yin, Z., Jin, Y. 2021a. Machine learning-based modelling of soil properties for geotechnical design: review, tool development and comparison. *Archives of Computational Methods in Engineering*, 29(2): 1229-1245.

Zhang, W., Li, H., Li, Y., Liu, H., Chen, Y., Ding, X. 2021b. Application of deep learning algorithms in geotechnical engineering: a short critical review. *Artificial Intelligence Review*, 54: 5633-5673.

An Unprecedented Land Supply Means in Hong Kong: Underground Quarrying-cum-Cavern Development

W H Tsang
Geotechnical Engineering Office, Civil Engineering and Development Department, Government of the HKSAR of the People's Republic of China, Hong Kong, China

Y K Ho
Development Bureau, Government of the HKSAR of the People's Republic of China, Hong Kong, China

Clayton Y K Chan
AECOM Asia Company Limited, Hong Kong, China

ABSTRACT

Cavern development is a viable source of land supply, which can provide solution space for a broad variety of land uses and preserve the valuable ecology and green environment at the ground surface. While most of the caverns are purposely built to house various facilities, underground quarrying-cum-cavern development at suitable sites is a viable means of creating a valuable cavern land bank. With thoughtful planning and prudent site selection, the operation of an underground quarry associated with concrete batching and asphalt production operations can be a self-financing or even profitable business in the short to medium term, while the cavern space created can be utilized for other strategic uses in the long term. To take forward this initiative, the Civil Engineering and Development Department has completed a technical study to establish the technical feasibility and possible implementation arrangement of underground quarrying-cum-cavern development in Hong Kong. A prototype reference design based on the site setting of the Lam Tei Quarry has been produced, considering factors including technical, operational and logistic considerations. This paper presents the findings of the study, including the reference design and implementation model, and discusses the prospect of the underground quarry-cum-cavern development as a land supply means in Hong Kong.

1 INTRODUCTION

The hilly terrain with strong rocks in Hong Kong is highly suitable for developing rock caverns. Ho et al. (2020) provided a comprehensive overview of the prospect of cavern development in Hong Kong. Relocation of suitable existing facilities to rock caverns can release surface sites for other development uses and remove incompatible land uses by placing 'not in my backyard' ('NIMBY')-type facilities in caverns. Rock caverns can also provide space to accommodate suitable new facilities, thereby lessening the high demand for surface land in Hong Kong. These benefits, however, have not been actively reaped in the past.

To unleash the potential of cavern development, Civil Engineering and Development Department (CEDD) completed a strategic study for cavern development (Arup 2018) and implemented a suite of facilitating measures, including the promulgation of the Cavern Master Plan (CEDD 2017). The strategic study identified many successful examples of underground quarrying in other countries, such as the Schollberg Underground Quarry in Switzerland (Plate 1) (Chan et al. 2017). In addition, there are other cases where the caverns formed by underground quarrying were subsequently utilized for a wide range of uses, such as cold storage, warehousing and archive facilities in the USA (Pelizza and Peila 1995), and also data centres in Norway (Saunavaara et al. 2022). These examples indicated that the underground quarrying-cum-cavern development could be a viable and cost-effective means of providing sustainable cavern space. Given that land is a scarce resource in Hong Kong and there is a pressing need for increasing land supply to sustain the city's development, this development model is of high reference value to Hong Kong.

Plate 1 – Schollberg Underground Quarry in Switzerland;
(left) rock processing plant; (right) underground quarry excavation

Despite the conceivable potential of cavern land supply by underground quarrying-cum-cavern development, this development model is unprecedented in Hong Kong. With this in mind, the CEDD has carried out a study to establish the technical feasibility and possible implementation arrangement of underground quarrying-cum-cavern development in Hong Kong. This paper aims to provide an overview of the prospect and technical issues of underground quarrying-cum-cavern development, focusing on a prototype reference design based on the site setting of the Lam Tei Quarry.

2 BENEFITS OF UNDERGROUND QUARRYING

2.1 Green and sustainable cavern land bank

The main benefit of underground quarrying is the green and sustainable supply of cavern land bank. Hong Kong has a long history of quarrying, which supports the local construction industry through the production of aggregates and, at the same time, provides valuable surface land for development uses in the long term. With less environmental disturbance, the underground quarrying could be operated deep underground while preserving the valuable ecology and green environment at the ground surface. In addition, the caverns formed by underground quarrying can accommodate a wide range of uses in the long term, thereby realizing the full potential of the underground resource in different periods of time. The most prominent example is the underground quarry in SubTropolis, USA. The underground quarrying created over 5,000,000 sqm of cavern space involving a wide range of business and industrial activities, such as warehousing, light manufacturing, office and retail, run by more than 55 companies and over 2,000 employees (Plate 2).

Plate 2 – Underground quarry turned into a business and industrial complex in SubTropolis, USA

2.2 Housing rock processing, concrete batching and asphalt production plants in caverns

The land shortfall in Hong Kong has led to intense competition for land between the construction industry and other different sectors of industry. As construction-related activities involving rock processing, concrete batching and asphalt production could potentially cause adverse environmental nuisances such as dust and noise, it is challenging to locate suitable sites for these operations because of the potential environmental and visual impacts to the nearby sensitive receivers.

As the underground quarrying would typically be bundled with rock processing, concrete batching, and asphalt production, it can provide stable sites for these activities. In addition, there are several successful overseas examples of accommodating construction-related facilities inside caverns, such as the rock processing plants at Stendafjellet Rock Quarry and Ytre Arna Quarry, and also concrete batching plants at Hagerbach Test Facility (Plate 3) (Sum et al. 2018). These ancillary operations can be operated at the surface portal at the initial phase of the underground quarrying and then move into the caverns created by quarrying excavation at the later phase or even after the quarrying operation. As the quarrying period is normally 10-20 years, this creates an opportunity to provide long-term and stable sites for rock processing, concrete batching and asphalt production while reducing the environmental nuisance to the nearby sensitive receivers.

Plate 3 – Underground concrete batching plant at the Hagerbach Test Facility in Switzerland

2.3 Supplement to local rock production

Another add-on benefit is the potential to supplement the local rock production. Before the 1980s, the demand for rock materials by the Hong Kong construction industry was entirely met by local quarries. Since then, with the progressive closure of local quarries and the increasing demand for rock materials to meet development needs, the main source of rock material has been imported from Mainland China. Therefore, underground quarrying in Hong Kong can supplement the surface quarrying by supplying various rock products (Plate 4).

Plate 4 – Example of rock products: marine works, railway ballast, concrete, asphalt

3 SITE SELECTION CONSIDERATIONS

In a congested city like Hong Kong, the selection of a suitable site for underground quarrying is a challenging task. Therefore, the site selection process should carefully balance the below considerations.

3.1 Geotechnical considerations

Sites with sizable rock reserves and good rock mass quality would be considered favourable for underground quarrying. This would generally apply to large volcanic or intrusive igneous bodies that have not been affected by faulting or dyke intrusion, and therefore less or even no rock reinforcement and grouting is required for cavern stability and groundwater ingress. Other geotechnical works unrelated to quarry production, i.e. site formation, natural terrain hazard mitigation and soft ground tunnelling, should also be kept minimal. Therefore, sites with available surface land immediately adjacent to the existing rock face would be highly preferable.

The suitability of the rock to be used as aggregate is also an important consideration. The sedimentary rocks in Hong Kong have been screened out primarily due to their lower rock strength and, thus, only intrusive or volcanic rocks should be considered further. Recognizing that there are measures that can be undertaken to counteract the impact of Alkali-Silica Reaction (ASR), the presence of rock that is potentially reactive has not been adopted as a fundamental criterion to rule out the feasibility of a site, although it is not as favourable as those sites with non-reactive rocks.

As the underground quarry and access tunnels would be excavated by the drill and blast method, lower explosive quantities per blast hole may be required if there are sensitive receivers within the blasting influence zone. This would result in a less efficient quarry operation and would therefore be considered less favourable.

3.2 Quarry operational requirements

At the commencement of the quarrying operation, rock processing plants, concrete batching plants and asphalt production plants have to be established on surface land in combination with offices and other ancillary facilities, which will enable the revenue earning facilities to be operational earlier. If there is sufficient surface area that can accommodate these associated facilities, the initial capital investment and overall operational costs can be reduced. Nevertheless, given the difficulty of finding an existing available surface land, an operational plant comprising rock crushing, concrete batching and asphalt production could be set up on a site as small as 2ha to 3ha. This could be considered as the minimum desirable surface land area.

3.3 Environmental considerations

Although the quarrying operation deep underground should generally result in minimal environmental impact, there are inevitability some residual impacts to the surroundings due to the operation at the surface portal site. These impacts include air, noise, water, waste, ecology, land contamination, fishery, cultural heritage, landscape and visual impact. Therefore, the portals of the underground quarry should avoid being located close to the environmentally sensitive areas.

3.4 Planning and land use compatibility

The planning compatibility between the underground quarrying-cum-cavern development and the surrounding area has to be taken into account. While the after-use of the caverns created by quarrying could be finalized toward the end of the underground quarrying period, the conceptual after-use of the caverns should be preliminarily formulated with flexibility reserved for various other uses. The long-term use of the created cavern space is considered one of the benefits to the local community in terms of providing land for relocating some existing NIMBY-type facilities into caverns and thereby releasing land for other community welcome facilities. Careful selection of the underground quarry site and planning of the long-term use are required to foster public support for smooth implementation and operation of the quarry site. This would include sites that are remote from residential areas and sites with existing NIMBY-type facilities nearby that are suitable for relocation into the underground space formed by the quarrying operation.

3.5 Traffic conditions

The underground quarry development will generate road traffic due to the transportation of raw materials to the site (e.g. imported rock, cement and bitumen) and the delivery of manufactured products to other construction sites (e.g. aggregates, concrete and asphalt). The transport route to and from the quarry should not affect roads that suffer from high peak traffic flow, which may restrict the allowable transportation hours of quarry products. Sites with good connectivity to road networks or waterfront with suitable barging facilities would be considered favourable.

4 REFERENCE DESIGN AT LAM TEI QUARRY

4.1 Site selection for reference design

As underground quarrying is unprecedented in Hong Kong, a prototype reference design was produced for the purpose of investigating the operation parameters and establishing the technical feasibility of underground quarrying. The reference design was carried out based on the actual site setting of the Lam Tei Quarry (Figure 1), which has been operated for many years as a surface quarry and has proven to be suitable for quarrying operation. This site possesses a number of essential features for underground quarrying: sufficient surface area for ancillary operation, availability of sizable rock face and rock reserve; good rock quality suitable for concrete production; direct connection to existing road network; known local demand for rock products and the limited population at the surrounding area. This reference design can serve as a model that can generally be applicable to other similar underground quarry sites as identified in the territory.

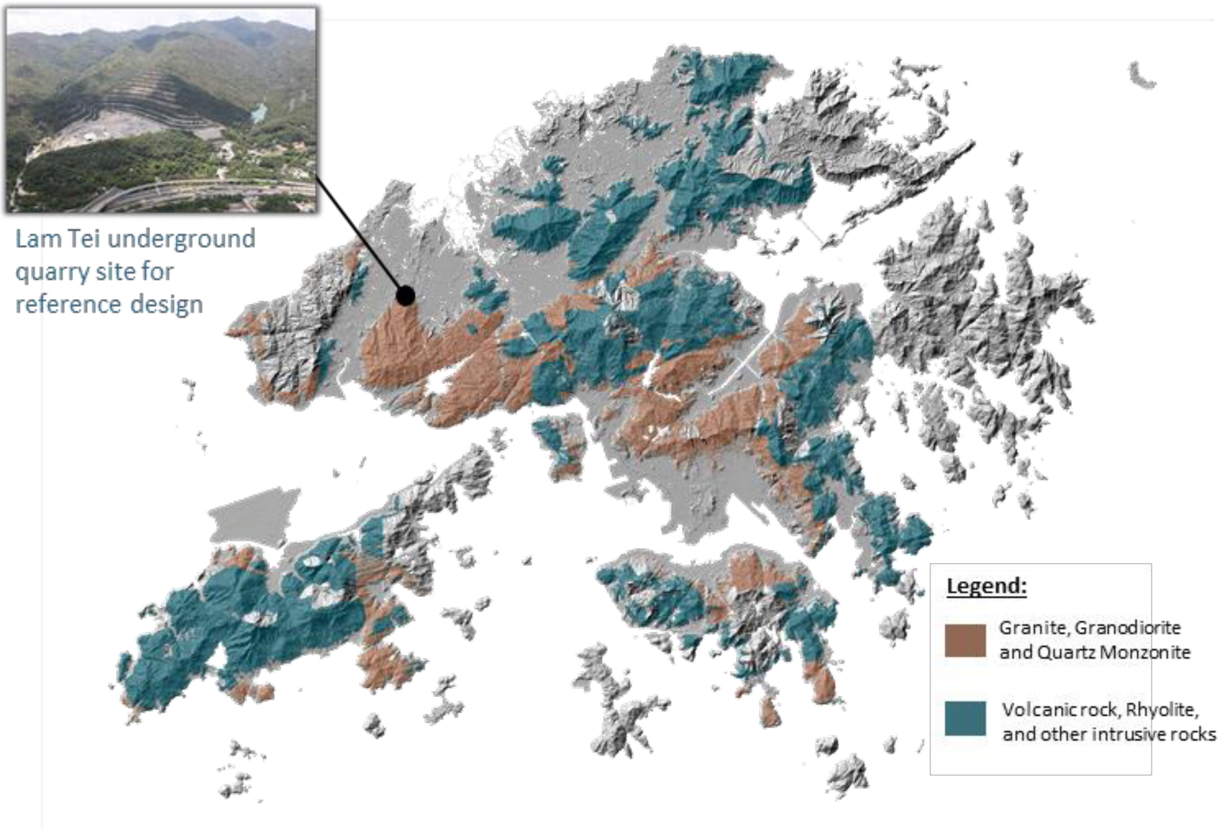

Figure 1: Selected site for reference design

4.2 Design considerations

Operational and logistical arrangement
To facilitate a streamlined production with high efficiency, upstream procedures should be located near the rock reserve, while downstream procedures should be located close to the public road network. The portals of the underground quarry should be directly connected to the surface works area. The operation cost of an underground quarry should be optimized by providing a logistics-friendly overall layout, minimizing the reinforcement needed for underground excavation, using aggregates from its own production, minimizing the provision of the groundwater drainage system and avoiding excessive provisions for fire safety and ventilation systems.

The layout of underground quarry
Bord and pillar quarrying layout is proposed for the underground quarry. The main access tunnel surrounds the perimeter of the underground quarry and connects to two portals. The production caverns of various lengths are located further away from the portals. Adjacent production caverns are linked with connection adits at typically 50m spacing. All production caverns can be accessed at both ends via a sub-perpendicular main access tunnel. The formation level of the portals should match the level of the surface works area. A 1 in 100 longitudinal fall is assigned towards the portals to allow for the gravity drainage of groundwater seepage.

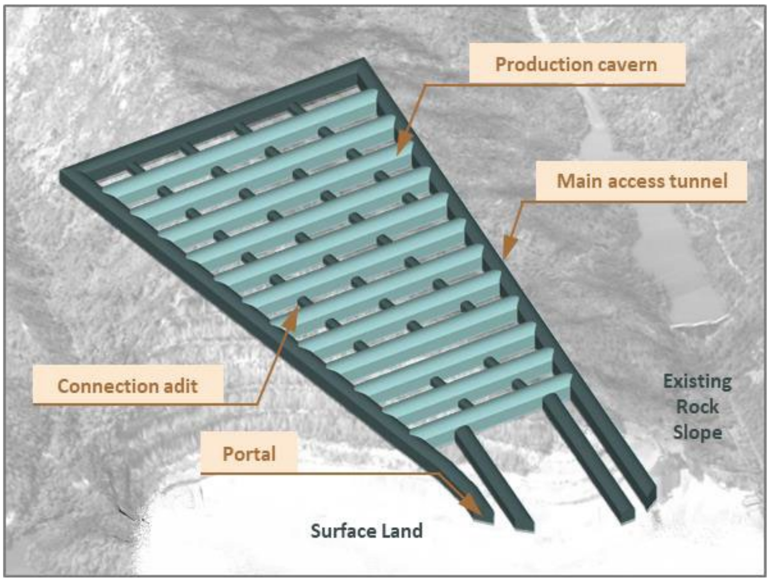

Figure 2: Layout of underground quarry

Spatial requirements
The dimensions of the underground space created by the underground quarrying should take account of the potential types of after-use of the caverns to minimize any further modification works required. The dimensions of the main caverns were designed to be 20m (W) and 20m (H). Considering the space required for the installation of ventilation systems, utilities, fire safety provisions, structural slab and ceilings for the after use, the clear headroom of the caverns would be 10m to 15m, subject to the detailed design of the cavern usage. With the flexibility of further division into compartments, this size is generally sufficient for the operation of various potential after-uses such as logistics warehouses and data centres.

Geotechnical stability
The preliminary design of the rock pillars and cavern reinforcement is according to the Geoguide 4 (2nd Edition) (GEO 2018). The orientation of production caverns is chosen to minimize any instability due to rock joints and rock stress. The rock pillar width is conservatively assumed to be equal to the cavern span (i.e. 20m), which can be further optimized when there is more available information about the rock mass properties. The roof and wall reinforcement should be generally derived from NGI Q-system (NGI 2015) and verified by design

analysis. The support classes should be designed based upon the estimated Q-values and eventually assessed on-site based on face mapping. With a balanced excavation size and careful site selection for competent rock mass, the caverns should be formed with only minimal or without reinforcement elements in general.

4.3 Housing ancillary facilities in caverns

While the ancillary facilities can be operated on the surface land at the portal of the underground quarry, a variation of this typical reference design was also developed to examine the details of housing rock processing, concrete batching and asphalt production plants inside the formed caverns. Such configuration is a very effective use of cavern land resources and is suitable for later stages or even after the quarrying operation. The three production caverns formed near the portal can be used for rock processing, stockpiling and concrete batching. The asphalt production plant should be placed in a separate cavern to cater for the operational need of asphalt production. The dimensions and functions of different types of caverns, tunnels and adits are summarized in Table 1.

Table 1: Summary of Caverns, Tunnels and Adits

Types of Caverns, Tunnels and Adits	Span (m)	Height (m)	Functions
Main access tunnel	16	20	Primary access and evacuation route of the entire underground quarry
Production caverns	20	20	Where main rock extraction takes place; the main venue for after-use development
Connection adits	9	9	Evacuation route from production caverns
Concrete batching plant access tunnels	16	16	Separate access to the concrete batching plant
Rock processing cavern	20	20	Placement of the rock processing facilities
Stockpiling cavern	20	20	Stockpiling area
Concrete batching cavern	20	20	Placement of concrete batching plant
Asphalt production cavern	12	12 and 20	Placement of asphalt production plant

Rock processing and stockpiling

The rock processing equipment for the concrete batching can be housed in a production cavern with a size of 20m (W) x 20m (H). The stockpiling cavern is positioned next to the rock processing cavern and set up for the temporary storage of crushed rock and aggregates produced from the rock crushers before they are sent to the concrete batching plant. The crushed rock/aggregates products are transferred from the rock processing cavern to the stockpile cavern via conveyor belts through the connection adits.

Concrete batching

The concrete batching plant can also be housed in the completed production cavern near the portals and next to the stockpiling cavern. Aggregates should be delivered to the concrete batching plant by conveyor belts and stored in different aggregate bins. Water should be supplied by pipeline and pumped to water tanks inside the cavern. Cement should be transported by trucks and transferred to the cement storage silos by pipeline. Each of the raw materials would be fed through weight hoppers to the concrete mixer for concrete mixing. An ice plant would be available for ice production if necessary. Such a layout arrangement aims to minimize vehicular traffic inside the caverns.

Considering there will be a relatively high traffic flow generated from the operation of the underground concrete batching plant, separate vehicular access tunnels should be provided. Two access tunnels independent from the quarry operation can form a one-way designated circulation of concrete truck traffic to and from the underground concrete batching plant. They connect the concrete batching cavern to the portals for the delivery of concrete produced. In addition, comprehensive dust control measures, such as materials delivery and storage by enclosed conveyor belts and tankers, together with an effective ventilation system, should be designed to mitigate the potential environmental and; occupational health and safety problems.

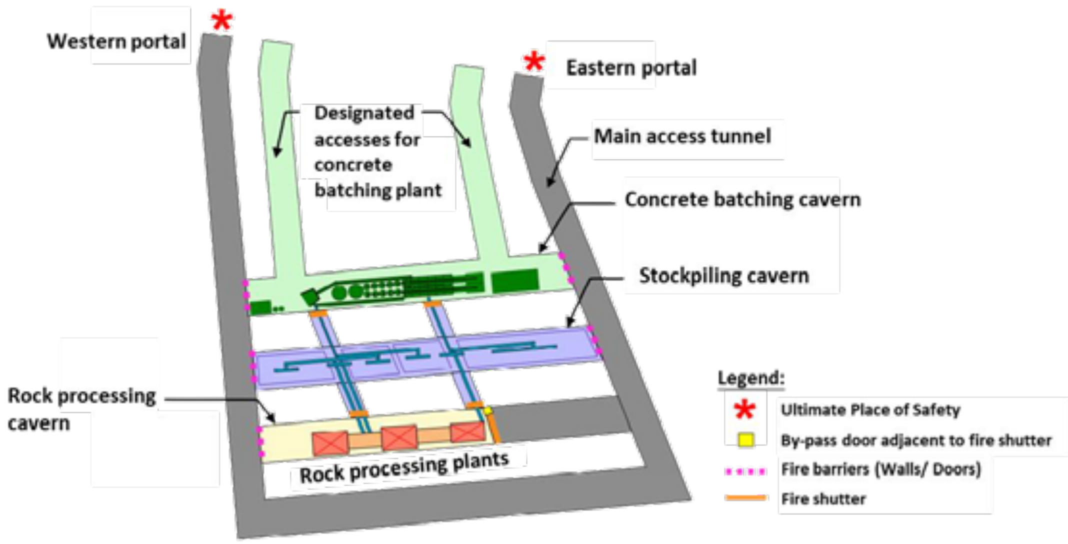

Figure 3: Layout of housing rock processing and concrete batching plant in caverns

Asphalt production

For the asphalt production plant, it is placed in a separate cavern with a limited length from the portal (< 30m) to allow for good ventilation, which is required to mitigate the heat generated from bitumen processing and the potential hazards due to the fume emission during the production process. Bitumen is stored in heated tanks while awaiting delivery to the drum. When the hot asphalt mix is required, bitumen should be delivered to the asphalt drum by pipeline for mixing with the aggregate, which is first heated in the dryer drum. The output of hot mix asphalt is discharged to the storage silos for final loading onto trucks. During the production of the asphalt mix, a baghouse should be provided to remove fine particulate matter from the dryer exhaust gases, and additional silos should also be provided for storing mineral filler or special additives that are added to the hot mix.

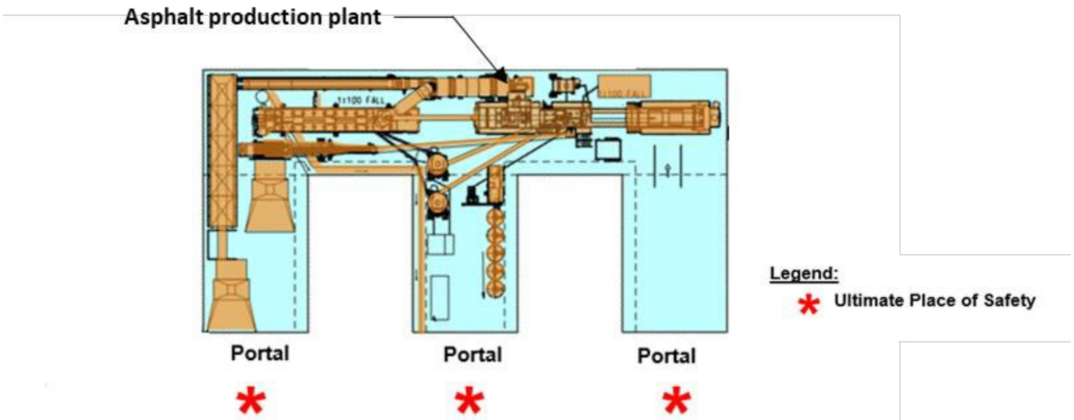

Figure 4: Layout of housing asphalt production plant in cavern

4.4 Fire engineering

A comprehensive fire safety design has been devised with reference to the Guide to Fire Safety Design for Caverns 1994 and the fire engineering approach to suit the special nature and functional requirements of the caverns. Computational fluid dynamics have been conducted to verify the key performance of the design. The key features of the fire safety strategy for fire resisting construction, means of escape/access, smoke control strategy and fire service installations (FSI) for the proposed caverns housing the rock processing plant, concrete batching plant and asphalt production plant are summarized as follow:

Fire resisting construction
Each of the rock processing caverns, stockpiling cavern and concrete batching cavern should form a single compartment with a compartment area limited to 10,500m^2. All elements of construction should have a fire resistance rating (FRR) of 240/240/240. Fire barriers and fire shutters should have FRR not less than -/120/120.

Means of escape/access
In case of fire in one of the main caverns, occupants should be evacuated to the Place of Safe Passage (i.e. main access tunnel) and proceed to the Ultimate Place of Safety (Figure 3). The travel distance to the Place of Safe Passage is limited to 72m. In case of fire at the main access tunnel, occupants will evacuate from the incident smoke zone to the non-incident zone within 72m and further proceed to the Ultimate Place of Safety. The main access tunnel is designed as Emergency Vehicular Access (EVA) route so that the areas within the caverns can be reached directly by the emergency vehicles. A clear space of 7.3m (W) x 4.5m (H) should be designed along with the EVA, which allows passage of the emergency vehicles.

Smoke control and fire service installations
A smoke control system should be provided to the main access tunnel, concrete batching, and rock processing/stockpiling caverns in order to limit the smoke spread and help to maintain a tenable environment for evacuation and firefighter's access. A linear heat detection system, water spray system, and other FSI should be provided at designated locations to detect and control the fire.

Fire safety management plan
A comprehensive fire safety management plan has been developed to mitigate the inherent fire risk associated with the nature of the underground quarry (e.g. checking of vehicle engine temperature before entering the caverns, a limited number of workers inside the caverns, proper fire safety training to the workers, etc.)

4.5 Quarrying method and sequence

Quarrying method
Similar to traditional surface quarrying, drill and blast is the most productive and cost-effective excavation method for hard rock. Before the blasting, probing and grouting would be carried out if necessary. The blasting operation starts with marking up the blast pattern on the tunnel face and reviewing the rock characteristics. Then the blast holes should be drilled in accordance with the blast design in terms of hole depths and locations. Explosives would then be delivered to the site, and the blast holes would be charged and connected up. Following the blast, the shotfirer would check to confirm that there have been no misfire and site activities around the blast area can recommence in a safe condition. The excavated rock can be mucked out by truck loaders and backhoes.

Due to the considerable height of the tunnels and caverns to be excavated, a heading and bench sequence of excavation is necessary for the underground quarry. Top heading excavation should commence first at the upper half of the caverns, followed by lower bench excavation. The cross-section of excavation with top-heading and bench is shown in Figure 5.

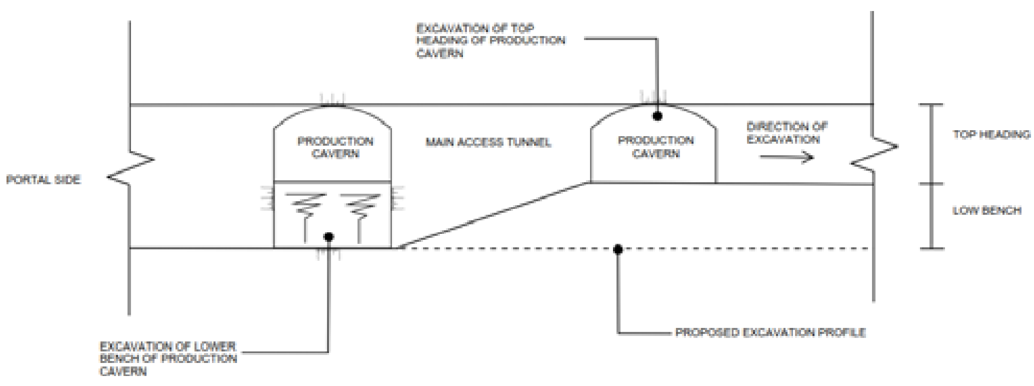

Figure 5: Excavation sequence of top heading and lower bench

After every round of excavation, geological mapping of the exposed rock face is conducted by geologists to assess the rock quality around the excavation. Reinforcement elements in the form of sprayed concrete and rock dowels are installed if necessary, corresponding with the rock quality. The next excavation cycle follows when all reinforcement elements to the excavation are installed as required.

Quarrying sequence
Before any production from rock excavation, the initial set-up phase would take typically one to two years, including the period required for procurement, delivery, installation and license application for plants. The top heading of the main access tunnel is excavated first to provide utilities and services. Then the excavation of the top heading proceeds to caverns from the near end to the far end of the portal. The excavation of the low bench of access tunnel and caverns follows the top heading excavation at a distance. An inclined floor to the low bench will be provided at the transition of top heading and lower bench excavation for access. This sequence offers fast access and fast delivery of excavated rock. Each quarrying area shall be further divided into portions for excavation to limit the active working area within the quarry. Excavation portion by portion can prevent recirculation of air and maintain the required airflow along the main access tunnel during the excavation stage of the quarry. There should be two to three excavation faces at each time within an active working area. A typical excavation rate is estimated to be about 5 blasts per week with an average production rate of $500m^3$ to $600m^3$ per blast based on the site setting of Lam Tei Quarry.

5 POSSIBLE IMPLEMENTATION MODEL

Based on the operation parameters of the reference design, a possible implementation model is broadly examined. The underground quarrying-cum-cavern development can be implemented in 2 stages: (1) underground quarrying by an operator; and (2) long-term use of cavern space by end-users.

5.1 Underground quarrying stage

The first quarrying stage can be operated by a revenue-earning quarrying contract, which should be sufficiently long to provide a stable site for operation. The underground quarrying should be bundled with the revenue-earning business of rock processing, concrete batching and asphalt production, as well as recycling of imported rock. The establishment of ancillary operations on surface land (Figure 6) at the beginning can enhance the business model of the underground quarry by starting up these revenue-earning facilities to be operational as early as possible. With a compact site set up, a surface area of about 2ha to 3ha at the portal location is considered necessary for setting up facilities, including ancillary operations to support the underground quarrying operations. The reference design also demonstrated that these ancillary operations could be moved into the caverns at the later stage of the underground quarry period.

Figure 6: Typical ancillary facilities at surface portal site for underground quarrying

Rock reinforcement costs will be kept to a very nominal level by carefully sizing the excavations and prudent site selection. For the operation cost, the quarry layout should be designed to allow for multiple and flexible work fronts to optimize the blasting operation and the utilization of plants and equipment. During the quarrying stage, the quarry operators should also be allowed to use the cavern space for other revenue-earning activities to optimize the use of the space formed in the interim term, provided that the regulations and contractual obligations of the underground quarry are not be compromised. The operation of an underground quarry associated with concrete catching and asphalt production can be a self-financing or even profitable business.

5.2 Long-term use of cavern space by end-users

After the completion of the quarrying stage, the cavern space should be handed over to the government for construction of public facilities or disposed of/leased to the private sector for private development, depending on the nature of the future land uses of the cavern space. As the major excavation works would already be completed in the quarrying phase, the underground quarrying-cum-cavern development is a very cost-effective means for cavern land supply for various uses. According to many overseas experiences, the uses of underground spaces are often an afterthought development after the formation of underground spaces. A recent example includes the Lefdal Mine Data Centre in Norway (Saunavaara et al. 2022), which was converted from an abandoned olivine mine. Conversion works on the site started in mid-2015 and the data centre was officially opened in May 2017. The layout and dimensions of the caverns can be developed based on a conceptual after-use, with flexibility reserved for various other uses to minimize any modification works of cavern development required in the future.

6 CONCLUSION

This paper presents the concept of underground quarrying-cum-cavern development. This development mode can supplement the local rock products supply, accommodate various construction-related activities in the interim term and provide green and sustainable cavern space in the long term. The site selection for underground quarrying should carefully balance the considerations of geotechnical, operational, environmental, traffic, planning and land use compatibility. The prototype design presented in this paper established the technical feasibility of this unprecedented land supply means in Hong Kong. A viable implementation model based on the referenced design is also devised for future reference.

With proper planning and design, the underground quarrying-cum-cavern development could be a self-financing or even profitable business in the short to medium term, while the created cavern space can be utilized for a wide range of strategic use in the long term, thereby realizing the full potential of the underground resource to support the development of Hong Kong.

ACKNOWLEDGEMENTS

This paper is published with the permission of the Head of the Geotechnical Engineering Office and the Director of Civil Engineering and Development Department of the Government of the Hong Kong Special Administrative Region. More information on the cavern development mentioned in this paper can be found on the website (www.cavern.gov.hk).

REFERENCES

Arup 2018. *Executive Summary on Long-term Strategy for Cavern Development – Feasibility Study*. Ove Arup and Partners for Geotechnical Engineering Office, Civil Engineering and Development Department, Government of the Hong Kong Special Administrative Region, Hong Kong, China.

Building Authority and Fire Services Department 1994. *Guide to Fire Safety Design for Caverns*, Building Authority and Fire Services Department, the Government of Hong Kong Special Administrative Region, Hong Kong, China.

CEDD (Civil Engineering and Development Department) 2017. *Cavern Master Plan*. CEDD, Government of Hong Kong Special Administrative Region, Hong Kong, China. See https://www.cedd.gov.hk/eng/topics-infocus/index-id-27.html

Chan H.K.K, Mills S.W., Wallace M.I. and Hung K.C. 2017. Hong Kong's Hidden Aggregate Resource: The Potential for Underground Quarrying, *Proceedings of the 37th Annual Seminar, Hong Kong.* Geotechnical Division, The Hong Kong Institution of Engineers, pp. 34-44

GEO (Geotechnical Engineering Office) 2018. *Geoguide 4 – Guide to Cavern Engineering, 2nd edition*. Geotechnical Engineering Office, Civil Engineering and Development Department, Government of the Hong Kong Special Administrative Region, Hong Kong, China.

Ho Y.K., Tsang W.H. and Chan C.C. 2020. Rock cavern development in Hong Kong: past, present and future. *Proceedings of the Institution of Civil Engineers – Civil Engineering* 173(5): 25–31, See https://doi.org/10.1680/jcien.19.00031

NGI (Norwegian Geotechnical Institute) 2015. *Handbook Using the Q-system – Rock Mass Classification and Support Design*. Norges Geotekniske Institutt, Oslo, Norway.

Saunavaara J., Laine A. and Salo M. 2022. The Nordic societies and the development of the data centre industry: Digital transformation meets infrastructural and industrial inheritance. *Technology in Society* 69, See https://doi.org/10.1016/j.techsoc.2022.101931

Sum D.T.C., Ho Y.K., Chan C.Y.K. and Lo L.K.W. 2018. Exploring underground solution for accommodating concrete batching and asphalt production plants. *Proceedings of the 16th World Conference of the Associated Research Centers for the Urban Underground Space, Wanchai, Hong Kong.* Elsevier, Amsterdam, the Netherlands, pp. 463–473.

Peila D. and Pelizza S. 1995. Civil reuses of underground mine openings: a summary of international experience. *Tunnelling and Underground Space Technology.* 10. 179-191. 10.1016/0886-7798(95)00006-K.

Rock Breaking Using Supercritical Carbon Dioxide (SC-CO_2) Technology – A Safe, Efficient, and Sustainable Approach

G X Guan
G & K Consultancy Limited, Hong Kong, China

X Wang, Weyman C T Ngai
SHTD, China Energy Engineering Group Co. (CEEC), Hong Kong & Mainland China

P L Ng, A K H Kwan
The University of Hong Kong, Hong Kong, China

ABSTRACT

Rock breaking by drill and blast using chemical explosives has been a dominant method in construction. However, blasting is hazardous and risky in nature: it involves the use of Category 1 Dangerous Goods; and it induces ground vibration and risks of fly rocks and air over pressure. Mechanical rock breaking, chemical expansion agent, and hydraulic fracturing techniques, complemented with hole drilling, wedging or splitting, are sometimes used as alternatives to drill and blast for rock breaking. However, these methods are extremely slow to match with construction progress and are also costly. In particular, mechanical rock breaking brings about continuous noise, dust and nuisances to the surroundings. As more and more construction works nowadays are in congested urban region, the construction industry needs to adopt a safe, efficient, and sustainable rock breaking approach. In view of this, rock breaking using supercritical carbon dioxide (SC-CO_2) technology has been developed recently, and it has successfully been applied to numerous real projects.

1 INTRODUCTION

1.1 Conventional rock breaking

Rock breaking is commonly practiced in mining as well as civil and building engineering for site formation, tunnelling, cofferdam excavation, and foundation construction. There are various methods of rock breaking, such as drill and blast, mechanical breaking, the use of chemical expansion agents, and hydraulic fracturing techniques. Drill and blast involves drilling of holes into the rock mass for placing chemical explosives. It is a highly effective method of rock breaking. In Hong Kong, explosives are classified as Category 1 Dangerous Goods under the Law Cap. 295 Dangerous Goods Ordinance, and the storage and transportation are subjected to stringent control. Besides, in view of the engineering risks of explosives, comprehensive precautionary and preparatory measures must be implemented before the execution of blasting works, such as identifying sensitive receivers, conducting blast assessment, planning delivery schedule and route of explosives, devising instrumentation and monitoring plan, determining alert-action-alarm levels of ground vibrations, assessing the risk of fly rock and air over pressure, designing and erecting blast doors and blast covers etc. Adequate time and resources have to be allowed for these measures.

Mechanical rock breaking is comparatively simple, it involves the use of hydraulic breaker and wedge splitter or piston splitter. The hydraulic breaker is often mounted on backhoe (Figure 1). During breaking, high level of noise in the range of 95 to 105 dB(A) would be generated. Labourers exposed to continuous noise over long-term may suffer from hearing impairment, and the noise would also cause nuisance to the public in surroundings. Wedge and piston splitters rely on splitting stresses for rock breaking. Figure 2 shows a wedge splitter mounted on backhoe; whereas Figure 3 depicts rock splitters which exert pressure on rock by pistons (Figure 3(a)) and by wedging (Figure 3(b)), both powered by hydraulic power unit, i.e. power pack. Unlike backhoe-mounted wedge splitter, these rock splitters need to be relocated from one place to another by lifting plants. Another alternative method of rock breaking involves the use of chemical expansion agents which are non-explosive nor blasting agent. The expansion agents are usually proprietary products and different choices are available. For example, a product described as cracking agent uses an electric shock to induce gas expansion, and a product described as demolition agent comprises inorganic compounds and make use of solid expansion of calcium hydroxide hydrates. It should be noted that the use of wedge splitter, piston splitter, and chemical expansion agents requires prior drilling of holes for insertion of splitter or filling of chemical agent. Overall speaking, the productivity, i.e. the rate of rock breaking by mechanical method or by chemical expansion agents is rather low, and this often becomes the constraining factor to the construction progress.

Figure 1: Hydraulic breaker mounted on backhoe


Figure 2: Wedge splitter mounted on backhoe

(a) (b)
Figure 3: (a) Piston-type rock splitter & (b) wedging-type rock splitter

1.2 Hydraulic fracturing

The hydraulic fracturing technique is commonly used in rock drilling for petroleum extraction. Basically, this technique is to inject a pressurized hydraulic fluid into the end of the borehole, which may be at a depth greater than 1000 m, to fracture the rock. The hydraulic fluid (also called fracturing fluid) serves two purposes: (a) to wedge-open and extend a fracture hydraulically; and (b) to transport and distribute the proppant along the fracture (Ishida et al. 2004). Hydraulic fluids used include oil-based fluids, water-based fluids and alcohol-based fluids. In recent years, liquefied and pressurized carbon dioxide, especially supercritical carbon dioxide, has become popularly used as the hydraulic fluid due mainly to its much lower viscosity (Kizaki et al. 2012; Liu et al. 2014; Bennour et al. 2015).

Ishida et al. (2004) had studied the influence of fluid viscosity on the hydraulic fracturing mechanism by fracturing granite blocks using viscous oil or water, and found that viscous oil tends to generate thick and planar cracks with few branches while water tends to generate thin and wavelike cracks with many secondary branches. Hence, a less viscous fluid would penetrate more deeply to produce thinner cracks with more secondary branches. Bennour et al. (2015) later compared viscous oil, water and liquid carbon dioxide (L-CO_2) as hydraulic fluids in fracturing of shale, and observed that with the use of L-CO_2, which has the lowest viscosity, the cracks formed tend to be widely extended with many branches. The effects of using supercritical carbon dioxide (SC-CO_2), which has an even lower viscosity, will be explained later in this paper.

The hydraulic fracturing technique is also being applied to rock breaking for excavation (Ishida et al. 2012; 2013; Zhang et al. 2018), although the rock blasting technique of using a chemical explosive is still dominant. It may appear at first sight that hydraulic fracturing may not be powerful enough to break strong rocks like granite and volcanic tuff. But actually, the breaking power is just a matter of the quantity of hydraulic fluid injected into the borehole, the pressure applied to the hydraulic fluid, and the penetrability of the hydraulic fluid into fine cracks to wedge-open and extend the cracks (i.e. to extend the fracture). In the case of using liquefied and pressurized gas (e.g., CO_2) as the hydraulic fluid, the breaking power is dependent also on the amount of heat applied to gasify and cause rapid expansion of the gas in the borehole.

1.3 Overview of the study

As will be explained later, with SC-CO_2 used as the hydraulic fluid, the rock breaking can be accomplished at a much lower breakdown pressure (also called fracturing pressure or explosion pressure), meaning that much less shock would be generated during rock breaking. In theory, the hydraulic fracturing technique without using any explosive should be much safer to use than the rock blasting technique using an explosive.

At the outset, it should be pointed out that SC-CO_2 is not solid, liquid or gas, but has certain properties favouring rock drilling and rock breaking. In the following, it will be explained how and why liquid L-CO_2 used in rock drilling for petroleum extraction is being replaced by SC-CO_2. Then, it will be discussed how SC-CO_2 could be applied to rock breaking for excavation. For rock breaking, SC-CO_2 is used like a chemical explosive, but actually is not an explosive and thus is safer to use. Lastly, the advantages and disadvantages of using SC-CO_2 will be discussed and application examples will be presented.

2 SUPERCRITICAL CARBON DIOXIDE

2.1 Basic properties of supercritical CO_2

For most materials, its phase transforms between solid, liquid or gas as the temperature and/or pressure changes. However, for some materials, there could be the fourth phase. For instance, supercritical carbon dioxide (SC-CO_2) is not solid, liquid or gas, but is of the fourth phase. Carbon dioxide will be transformed into a supercritical state when its temperature and pressure exceed those at the critical point (critical temperature = 31.1°C and critical pressure = 7.38 MPa), as shown in Figure 4 (Roland & Wagner 1996; Lv et al. 2013).

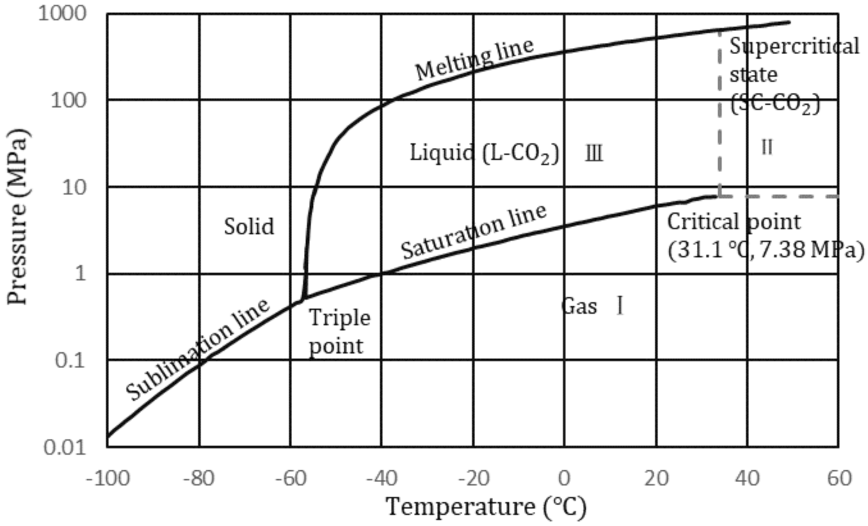

Figure 4: Phase diagram of CO_2

In the supercritical state, CO_2 has a relatively high density like liquid but a very low viscosity close to gas, thus allowing a large quantity of CO_2 to be filled into the container or borehole and the CO_2 to penetrate into very fine gaps (Kizaki et al. 2012). In fact, the very small inter-molecular forces, zero surface tension and very strong mobility of SC-CO_2 (these are the properties causing the SC-CO_2 to have a very low viscosity) would enable the SC-CO_2 to penetrate into any space larger than the size of CO_2 molecules (Liu et al. 2014; Wang et al. 2017). Therefore, SC-CO_2 can penetrate into micro-fractures that most other hydraulic fluids, including L-CO_2, cannot. This allows the SC-CO_2 to penetrate into the very fine crack tips to keep on wedge-opening the cracks and extending the fracture once initiated.

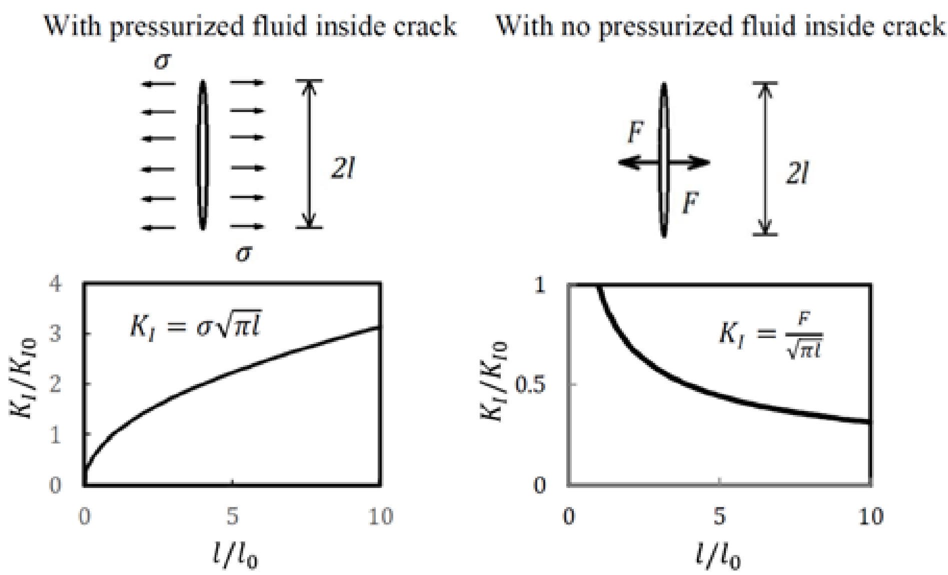

Figure 5: Stress intensity factor at crack tip

To better understand the importance of the hydraulic fluid penetrating into fine cracks, it should be noted that the hydraulic fluid does not just fracture the rock by exerting pressure onto the borehole wall. Ishida et al.

(2004) fractured granite blocks by injecting a pressurized fluid (water or oil) directly into the borehole or inflating a urethane sleeve inserted into the borehole, and found that with direct fluid injection, the cracks formed propagated away from the borehole but with pressurization via the urethane sleeve (no fluid penetrating into the fracture), cracks were only formed in the vicinity of the borehole. Moreover, the breakdown pressure due to pressurization via the urethane sleeve was about three times that due to direct fluid injection. Ishida et al. (2004) explained this phenomenon by considering the stress intensity factor at the crack tip, as depicted in Figure 5. With a pressurized fluid inside the crack (direct fluid injection), the stress intensity factor increases with the crack length and thus the crack would propagate once formed. With no pressurized fluid inside the crack (pressurization via urethane sleeve), the stress intensity factor decreases with the increase in crack length and thus the crack would not propagate.

Moreover, Ishida et al. (2012) had conducted hydraulic fracturing experiments using SC-CO_2 (at temperature higher than the critical temperature) and L-CO_2 (at temperature lower than the critical temperature) in granite blocks, and revealed that SC-CO_2 tends to generate cracks extending more three dimensionally while L-CO_2 tends to generate cracks along a flat plane. More importantly, the breakdown pressure with the use of SC-CO_2 is lower than that of L-CO_2. They attributed such differences to the lower viscosity and higher compressibility of SC-CO_2 compared to L-CO_2. Ishida et al. (2013) had also conducted hydraulic fracturing experiments using SC-CO_2 and water in granite blocks under triaxial stresses, and revealed that the lower viscosity SC-CO_2 (viscosity of SC-CO_2 is only 5% of that of water) would induce more three dimensionally and widely spreading cracks under lower breakdown pressure than water. Putting these results together with their previous results, they concluded that the breakdown pressure is higher when the viscosity of the hydraulic fluid is higher and lower when the viscosity of the hydraulic fluid is lower.

2.2 Utilisation of SC-CO_2 in rock drilling

In rock drilling, the hydraulic fluid is pumped into the bottom of the borehole to pressurize the borehole at the bottom end and fracture the rock there. The hydraulic fluid is continuously injected into the bottom of the borehole through a packer with a seal to confine the hydraulic fluid for building up the pressure needed to fracture the rock. As the hydraulic fluid is injected through the packer, the pressure of the hydraulic fluid increases until it reaches the breakdown pressure at which the rock is fractured and then due to expansion of the hydraulic fluid into the cracks and voids formed, the pressure rapidly drops, as shown in Figure 6 (Kizaki et al. 2012).

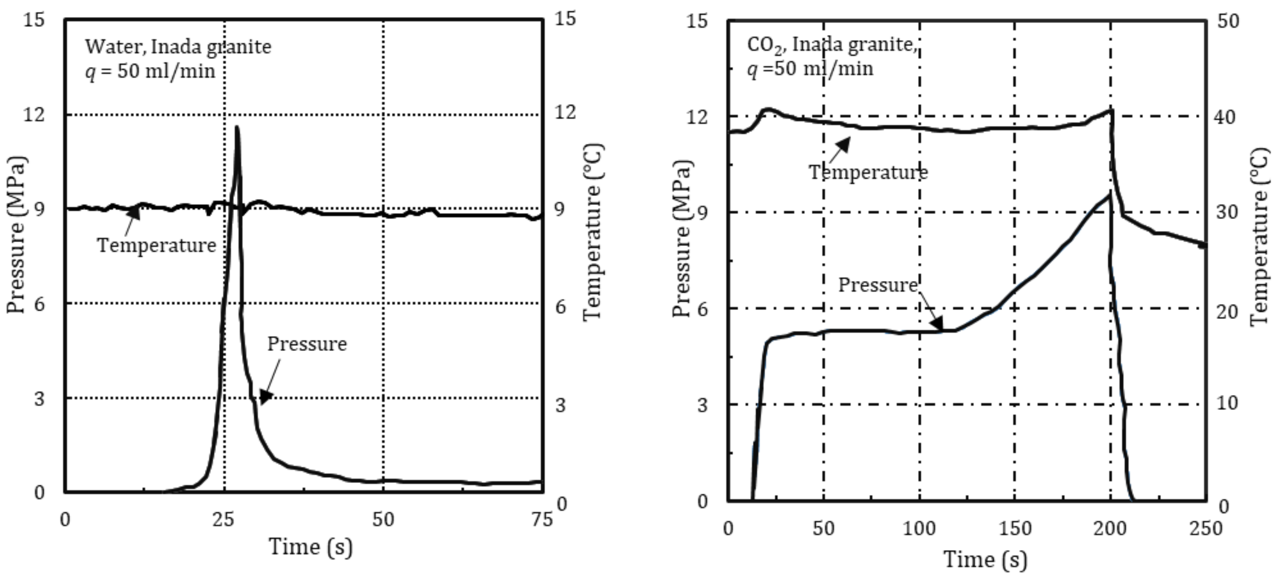

Figure 6: Temperature and pressure during hydraulic fracture of Inada granite

Kizaki et al. (2012) suggested that since SC-CO_2 has lower viscosity compared to that of L-CO_2, the SC-CO_2 has a higher tendency to permeate into fine pores and micro-cracks and is thus a better fracturing fluid in the making of a fractured reservoir with a high fracture density for applications such as carbon sequestration, geothermal energy extraction and recovery of oil and gas from depleted reservoirs. Liu et al. (2014) pointed out the problem that in deep wells, the CO_2 can usually reach the critical temperature to become supercritical, but in shallow wells, the CO_2 may not reach the critical temperature and thus heating may be required to transform the CO_2 to the supercritical state. They also mentioned that compared with the use of L-CO_2, the use of SC-CO_2 as the fracturing fluid can decrease the fracturing pressure and thus reduce the treatment cost. Wang et al. (2015) cited previous researches revealing that the use of SC-CO_2 jets to cut rock needs much shorter time and much lower threshold pressure, and to be specific, the threshold pressure for SC-CO_2 jet is just 2/3 of that for water jet when breaking granite and even less than one half of that for water jet when breaking shale. And, in oil drilling, SC-CO_2 will enhance single well production and recovery after entering the reservoir.

Apart from the above, the use of CO_2 also has the following advantages (Du et al. 2012): superior hole-cleaning performance, little formation damage, no reaction with clay to cause swelling of clay, can dissolve hydrocarbons and other chemicals to remove them in near-well formation etc. Added all up, there is a tendency of replacing other fracturing fluids by SC-CO_2.

3 USE OF SC-CO_2 FOR ROCK BREAKING

Currently, one the dominant methods of rock breaking for excavation is the drill and blast method (Persson et al. 1993; Lucca 2003). Basically, boreholes are drilled into the rock, a chemical explosive is filled into each borehole and then the explosive is detonated to trigger an explosion by which the explosive is instantaneously transformed into a hot and high-pressure gas. The sudden expansion of the explosive within a confined space produces an extreme gas pressure and imparts very large dynamic stresses to the surrounding rock. The extreme pressure exerted by the gas may exceed 1 GPa. After blasting, the borehole would be enlarged by the high pressure gas, the rock right at the borehole wall would be crushed, and the rock further away would be fractured as shown in Figure 7. Along with the violent rock fracturing, stress waves are produced, causing intensive deformation and vibration of the ground, and possibly damages to the nearby structures. There also may be air-blast and fly-rock, if the explosive was over-charged and/or the blasting area was not adequately covered. Hence, rock blasting, i.e. rock breaking using the drill and blast method, is a dangerous operation, and has to be very carefully controlled, especially in urban areas or in close proximity to sensitive receivers or green concrete, i.e. freshly cast concrete (Kwan & Lee 2000).

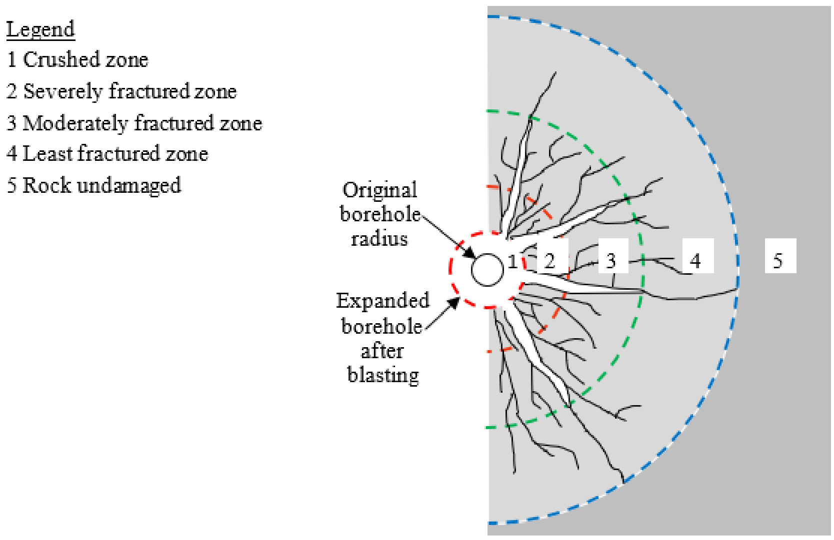

Figure 7: Rock mass damage after blasting

The success of hydraulic fracturing in rock drilling for petroleum extraction has gradually led to the extension of its applications to rock breaking for excavation, although some engineers are still skeptical about its ability to break strong rocks like granite and volcanic tuff. Ishida et al. (2004) applied the hydraulic fracturing technique to break granite under horizontal confining stresses of 3 MPa and 6 MPa, and found that with water or oil directly injected into the borehole, the breakdown pressure was only about 17 to 18 MPa. Kizaki et al. (2012) used water or SC-CO_2 as the hydraulic fluids to break granite and volcanic tuff under triaxial confining stresses of 1 MPa, 3 MPa and 5 MPa, and found that the breakdown pressure was only about 11 MPa when water was used and about 10 MPa when SC-CO_2 was used. Ishida et al. (2012) used SC-CO_2 and L-CO_2 to break granite under triaxial confining stresses of 1 MPa in each direction, and measured that the breakdown pressure was only 8.44 MPa when SC-CO_2 was used and 10.56 MPa when L-CO_2 was used.

Putting all the above results together, it seems that the breakdown pressure is dependent on the type of rock, the confining stresses and of course the type of hydraulic fluid used. Evidently, the use of SC-CO_2 as the hydraulic fluid would lead to the lowest breakdown pressure, which seems to be about 10 MPa. Compared to the extremely high gas pressure of the order of 1 GPa during blasting, which crushes the rock at the borehole wall and generates a huge shock to the ground, such a breakdown pressure during hydraulic fracturing of the order of 10 MPa is only about 1%. With the very much reduced explosion pressure (breakdown pressure) and shock produced, the ground deformation and vibration induced should be much smaller and thus the hydraulic fracturing technique using SC-CO_2 as the fracturing fluid should be much safer to employ than the blasting technique using a chemical explosive. Moreover, with the hydraulic fracturing technique employed, there is no explosive (which is Category 1 Dangerous Goods under the relevant Laws of Hong Kong) to be stored and delivered to the construction site. During transportation and storage, the carbon dioxide exists as liquefied CO_2 (which is Category 2 Class 2 Dangerous Goods (i.e. liquefied gas) under the Laws of Hong Kong), and it reaches supercritical state to become SC-CO_2 only during rock fracturing. Particularly, for close-in blasting (blasting within 20 feet or 6 metres as per Lucca (2003)), where there is less margin for error because of the proximity of structures affected by fly-rock and vibration effects, immediate considerations should be given to changing over to hydraulic fracturing using SC-CO_2.

4 ADVANTAGES AND DISADVANTAGES

4.1 Advantages of using SC-CO_2 in rock breaking

The hydraulic fracturing technique for rock breaking has the main advantages as listed below:

i) No chemical explosive is used and thus there is no need to store and deliver the explosive to the construction site, which can be very dangerous, especially if the site, storage area or route of delivery is close to any fuel tanks, densely populated areas or sensitive receivers.

ii) The breakdown pressure and shock produced are much smaller and thus the ground deformation and vibration induced would be much smaller. This would help to avoid causing damages to nearby structures, utilities and sensitive receivers, and in urban areas, also reduce the number of complaints.

iii) With the pressure of the fracturing fluid rapidly decaying as the fracturing fluid expands into the fractures and voids, there should be little risk of air-blast and fly-rock (nevertheless, for added safety, it is still recommended to provide some overburden to cover the rock breaking area).

iv) Overall, for rock breaking, the hydraulic fracturing technique using a fracturing fluid should be much safer than the blasting technique using a chemical explosive.

The use of liquefied and pressurized CO_2 as the fracturing fluid in hydraulic fracturing has the following additional advantages:

i) CO_2 is by nature a gas. As the pressure drops after the initiation of rock fracture, some of the CO_2 would be gasified to expand up to 600 to 700 times its original liquid volume, and thus would squeeze the CO_2 to penetrate into fine cracks to wedge-open the cracks and thereby extend the fracture.

ii) The breakdown pressure is lower when CO_2 is used as the fracturing fluid than when water or oil is used as the fracturing fluid.

iii) After the rock fracturing, the CO_2 would return to its gaseous state and thus simply escape without leaving behind any un-detonated explosive or chemical residues that might cause any danger or contamination.

The use of SC-CO_2 instead of L-CO_2 as the fracturing fluid in hydraulic fracturing has the following additional advantages:

i) SC-CO_2 has lower viscosity and stronger mobility than L-CO_2, and thus is more able to penetrate into very fine cracks to wedge-open the cracks and thereby extend the fracture. As a result, the breakdown pressure is even lower when SC-CO_2 is used instead of L-CO_2 as the fracturing fluid.

ii) Both SC-CO_2 and L-CO_2 are 100% CO_2. The only process needed to convert L-CO_2 to SC-CO_2 is to apply heating to raise its temperature to well above the critical temperature of 31.1°C. Actually, the pressurization of the CO_2 would already slightly increase the temperature through adiabatic compression.

4.2 Disadvantages of using SC-CO_2 in rock breaking

Regarding the disadvantages, the major disadvantage is that the use of SC-CO_2 in the construction industry in Hong Kong is still new and is not supported by abundant field data. Most construction professionals are not familiar with this new rock breaking technology, albeit the use of SC-CO_2 in the petroleum industry is already quite common. Construction professionals are by training extremely careful and very conservative in employing any new technology, which at the beginning, does not have any job reference. In this regard, it is recommended to carry out some field trials, with the temperature and pressure of the CO_2, borehole pressure, shock vibration, extent of rock fracture, any air-blast and any fly-rock etc. recorded for detailed study and analysis. More basic research on this new technology, especially on the data collection and safety related issues, should also be carried out to develop guidelines so that eventually, this newer, more advanced and theoretically safer technology could be adopted in a larger scale.

5 APPLICATIONS IN CONSTRUCTION PROJECTS

The SC-CO_2 technology has been successfully applied to numerous construction projects in real-life, as exemplified in the following. Figure 8 illustrates the application to site formation works for Zhanghua Highway construction in Hunan Province, China in year 2017-2018. The volume of rock breaking was approximately 0.2 million m^3 and the rock type was mainly shale. Figure 9 illustrates the application to basement excavation for a building project in Loudi, Hunan Province in 2019, with the volume of rock breaking of approximately 50000 m^3. Pioneering applications to special cases have been carried out and proven successful. For example, tunnel portal excavation with very limited rock overburden for Bailushi Tunnel in Yiyang, Hunan Province (Figure 10) in 2018; as well as underwater rock fracturing in Guangxi Province (Figure 11) in 2020. For the latter case, fish survey was conducted in the vicinity of works and the results demonstrated that the fishes were not harmed by the works. The experience gained from the past construction projects provides confidence and serves useful reference for extending the application of SC-CO_2 technology to wider project settings. After the turn of year 2020, two large-scale mining projects in Yunnan Province, China with the employment of SC-CO_2 technology have been ongoing.

Figure 8: Site formation for highway project using SC-CO_2

Figure 9: Basement excavation for building project using SC-CO_2

Figure 10: Tunnel portal excavation using SC-CO_2

Figure 11: Underwater rock fracturing using SC-CO_2

6 CONCLUSIONS

Rock breaking for excavation by blasting using a chemical explosive, i.e. by the drill and blast method, is potentially dangerous and risky by nature. The shock, vibration and air-blast generated during blasting may cause damages to nearby structures and sensitive receivers, and arouse complaints because ground shaking and loud noise could be scary to some people. This situation is not entirely satisfactory and sustainable. It is now about time to explore and develop a more advanced and safer method of rock breaking for excavation.

On the other hand, hydraulic fracturing using L-CO_2 (liquid carbon dioxide) or SC-CO_2 (supercritical carbon dioxide) as the hydraulic fluid has been successfully applied to rock drilling for petroleum extraction and is already quite common in the petroleum industry. This hydraulic fracturing technology has also been proven to be powerful enough to break strong rocks like granite and volcanic tuff. Hence, this hydraulic fracturing technology may also be applied to rock breaking for excavation. Relatively, the use of SC-CO_2 would lead to a lower breakdown pressure and more extensive fracture, and thus should be a better hydraulic fluid to use. Overall, since no explosive is used and the breakdown pressure is only a very small percentage of the extremely high gas pressure of around 1 GPa during blasting, this hydraulic fracturing method should be much safer than the conventional rock blasting method. It is thus advocated here that it is time to change to adopt the more advanced and safer method of hydraulic fracturing using SC-CO_2. To promote the use of this new technology, it is recommended to carry out field trials in Hong Kong to gain confidence and more basic research to develop guidelines for the local industry to follow.

REFERENCES

Bennour, Z., Ishida, T., Nagaya, Y., Chen, Y., Nara, Y., Chen, Q., Sekine, K. & Nagano, Y. 2015. Crack extension in hydraulic fracturing of shale cores using viscos oil, water and liquid carbon dioxide. *Rock Mechanics and Rock Engineering*, 48(4): 1463-1473.

Du, Y.K., Wang, R.H., Ni, H.J., Li, M.K., Song, W.Q. & Song, H.F. 2012. Determination of rock-breaking performance of high-pressure supercritical carbon dioxide jet. *Journal of Hydrodynamics*, 24(4): 554-560.

Ishida, T., Chen, Q., Mizuta, Y. & Roegiers, J.C. 2004. Influence of fluid viscosity on the hydraulic fracturing mechanism. *Transactions of the ASME*, 126: 190-200.

Ishida, T., Aoyagi, K., Niwa, T., Chen, Y., Murata, S., Chen, Q. & Nakayama, Y. 2012. Acoustic emission monitoring of hydraulic fracturing laboratory experiment with supercritical and liquid CO_2. *Geophysical Research Letters*, 39: L16309.

Ishida, T., Nagaya, Y., Inui, S., Aoyagi, K., Nara, Y., Chen, Y., Chen, Q. & Nakayama, Y. 2013. AE monitoring of hydraulic fracturing experiments conducted using CO_2 and water. In M. Kwaśniewski & D. Łydżba (ed.), *Rock Mechanics for Resources, Energy and Environment*. Taylor & Francis, 957-962.

Kizaki, A., Tanaka, H., Ohashi, K., Sakaguchi, K. & Matsuki, K. 2012. Hydraulic fracturing in Inada granite and Ogina tuff with super critical carbon dioxide. *Proceedings*, *7th Asian Rock Mechanics Symposium*. *Seoul*, *Korea*, 1-8.

Kwan, A.K.H. & Lee, P.K.K. 2000. *GEO Report No. 102: A Study on the Effects of Blasting Vibration on Green Concrete*, Geotechnical Engineering Office, Hong Kong Government.

Liu, H., Wang, F., Zhang, J., Meng, S. & Duan, Y. 2014. Fracturing with carbon dioxide: Application status and development trend. *Petroleum Exploration and Development*, 41(4): 513-519.

Lucca, F.J. 2003. *Effective Blast Design and Optimization*, Terra Dinamica L.L.C.

Lv, Q., Long, X.P., Kang, Y., Xiao, L.Z. & Wu, W. 2013. Numerical investigation on the expansion of supercritical carbon dioxide jet, *IOP Conference Series: Materials Science and Engineering*, 52: 072011.

Persson, P.A., Holmberg, R. & Lee, J. 1993. *Rock Blasting and Explosives Engineering*, CRC Press.

Roland, R. & Wagner, W. 1996. A new equation of state for carbon dioxide covering the fluid region from the triple-point temperature to 1100 K at pressures up to 800 MPa. *Journal of Physical and Chemical Reference Data*, 25(6): 1509-1596.

Wang, H., Li, G., He, Z., Shen, Z., Wang, M. & Wang, Y. 2017. Mechanism study on rock breaking with supercritical carbon dioxide jet. *Atomization and Sprays*, 27(5): 383-394.

Wang, H., Li, G., Shen, Z., Tian, S., Sun, B., He, Z. & Lu, P. 2015. Experiment on rock breaking with supercritical carbon dioxide jet, *Journal of Petroleum Science and Engineering*, 127: 305-310.

Zhang, Y., Deng, J., Ke, B., Deng, H. & Li, J. 2018. Experimental study on explosion pressure and rock breaking characteristics under liquid carbon dioxide blasting. *Advances in Civil Engineering*, 2018: Article 7840125.

Evaluation of Digital Rock Mass Discontinuity Mapping Techniques for Applications in Tunnels

P K K Wu, J Chin, R Tsui, C Ng
Aurecon Hong Kong Limited, Hong Kong, China

ABSTRACT

High-quality coloured 3D point clouds can now be readily generated by digital surveying techniques such as structure from motion (SfM) photogrammetry and terrestrial laser scanning (TLS). Point clouds allow discontinuities to be mapped digitally on rock slopes and this has been widely studied in Hong Kong. In comparison, few similar applications have been reported in tunnels in Hong Kong. To extend the application of this technology for tunnel excavation, we carried out three site trials in two drill-and-blast hard rock tunnels in Hong Kong. Both SfM photogrammetry and TLS were used to generate point clouds for the exposed rock tunnel surfaces. The generated point clouds were then tested for semi-automatic extraction of rock mass discontinuities using DRM2.0, Aurecon's in-house developed software. This paper provides detail accounts of data acquisition, data processing, present the findings on the performance of semi-automatic identification of discontinuities, and the comparison between SfM and TLS techniques. The paper also discusses the challenges in digital mapping inside tunnels and provide useful suggestions on conducting laser scanning and photogrammetry in tunnels.

1 INTRODUCTION

Tunnel face mapping is a vital step in tunnel excavation process that is traditionally carried out by an engineering geologist. One of the main purposes of tunnel mapping is to determine the quality of the rock mass through observation of rock discontinuities such as orientation, spacing, persistence and roughness as part of rock mass quality parameters. The task of face mapping itself consists of two major challenges: the first being that mapping must be completed within very limited timeframe between scaling and temporary support installation; and second, when the same exposed tunnel face is mapped by different geologists, the result could potentially vary due to the degree of skill and experience of the geologist (as much as the estimation of the characteristics of rock discontinuities from some distance of the tunnel face due to the unsupported zone, underlying personal judgment, human error or bias).

Point cloud data has been widely used in the construction industry thanks to the recent rapid growth of digital surveying technology. As high-quality coloured 3D point clouds can now be readily generated, the new technology further diversified the application of point clouds. And it can now be applied to geotechnical engineering such as rock mass discontinuity mapping. Between December 2019 and March 2021, the GEO organized a benchmarking exercise on digital rock mass discontinuity survey for rock slopes, which formed part of the Innotech Forum on Geotechnology 2021 in March 2021. We were invited to this Forum and presented the findings of digital rock mass discontinuity survey.

While digital rock mass discontinuity mapping has been applied to rock slopes in Hong Kong (Gibbons et al. 2019; Wong et al. 2019; CEDD 2021), few similar studies have been conducted in tunnels in Hong Kong (e.g. Chan et al. 2019). We carried out three site trials in tunnels to extend the application of this technology for tunnel excavation. These site trials were conducted in two drill-and-blast hard rock tunnels in

Hong Kong. Two remote sensing techniques, namely structure from motion (SfM) photogrammetry and terrestrial laser scanning (TLS), were used to generate point clouds for the exposed rock tunnel surfaces. The point clouds were then tested for semi-automatic extraction of rock mass discontinuities using DRM2.0 (Aurecon's in-house developed software) and Facet.

2 SITE DESCRIPTION

The two drill-and-blast tunnels (Tunnel A and Tunnel B) where trails were carried out are located in Hong Kong. Trial 1 and 2 were carried out in Tunnel A, while Trial 3 in Tunnel B. The tunnel faces of Trial 1 and 3 were excavated by drill and blast method while the tunnel face of Trial 2 was excavated by drill and break method. Figure 1 summarizes the excavated dimensions of the tunnel face, the tunnel depth and the rock mass characteristics at the three site trials. The rock mass characteristics were estimated by the mapping geologists and were agreed by the authors.

For Trial 1, the tunnel face is formed in strong to very strong Grade II medium-grained granite with massive rockmass. The Q' value was estimated to be 5.6. For Trial 2, the tunnel face is formed in strong to very strong Grade II/III fine-grained granite, with an estimated Q' value of 3.35. For Trial 3, the tunnel face comprises strong Grade II lapilli-bearing fine ash tuff, with an estimated Q' value of 2.89. Based on the observation on site, the rock mass overall becomes blockier from Trial 1 to Trial 3. It is also consistent with the factor of RQD / Jn which describes the degree of jointing (or block size). It should be noted that Q' differs from Q in that Q' is obtained from RQD, Jn, Jr, and Ja while Q is obtained with Jw and SRF in addition to the aforementioned four parameters.

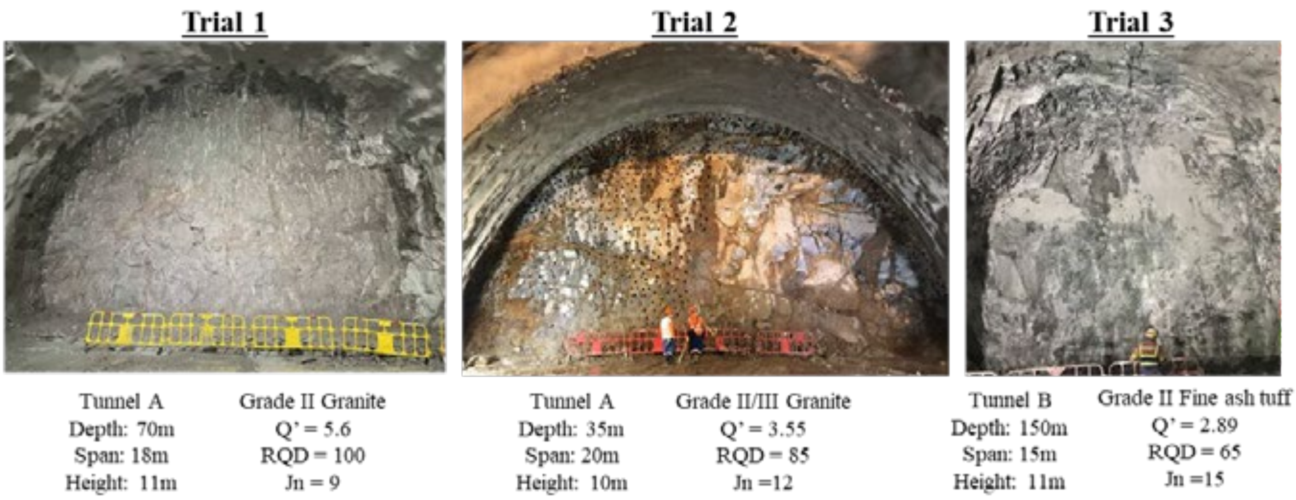

Figure 1: Photos of the tunnel faces in Trial 1 to Trial 3, with dimensions and ground conditions at the bottom.

3 DATA ACQUISITION AND PROCESSING

The data acquisition, including laser scanning and photo-taking, was completed within a short timeframe during the mapping and surveying time after mucking out. The data acquisition procedures require minimal additional arrangements in the tunnel except for the preparation of ground control points. Back in the office, the raw data were readily converted into point clouds by sophisticated commercial software. Details of the data acquisition and data processing are provided below.

3.1 Terrestrial laser scanning (TLS)

The TLS in Trial 1 to Trial 3 were carried out by a Leica BLK360 Imaging Laser Scanner. The scanner is equipped with a 15 megapixel 3-camera system for spherical imaging, therefore coloured point clouds can be produced. In the site trials, the scanner was positioned approximately 10 to 15m away from the tunnel face. To minimize occlusions (areas of lack of point cloud data, usually at the shadow of a protruding object which cannot be captured by laser scanner / camera, e.g. a horizontal discontinuity plan facing upward and located at higher level), two laser scans were taken at different positions to generate the point cloud. The scan locations in Trial 2 are shown as an example in Figure 2.

The scanner was carefully levelled prior to scanning. In Trial 1, the scans were in taken in medium-resolution mode. In Trials 2 and 3, the scans were in taken high-resolution mode. Each scan took 4-7 minute. No spherical / black and white targets were needed.

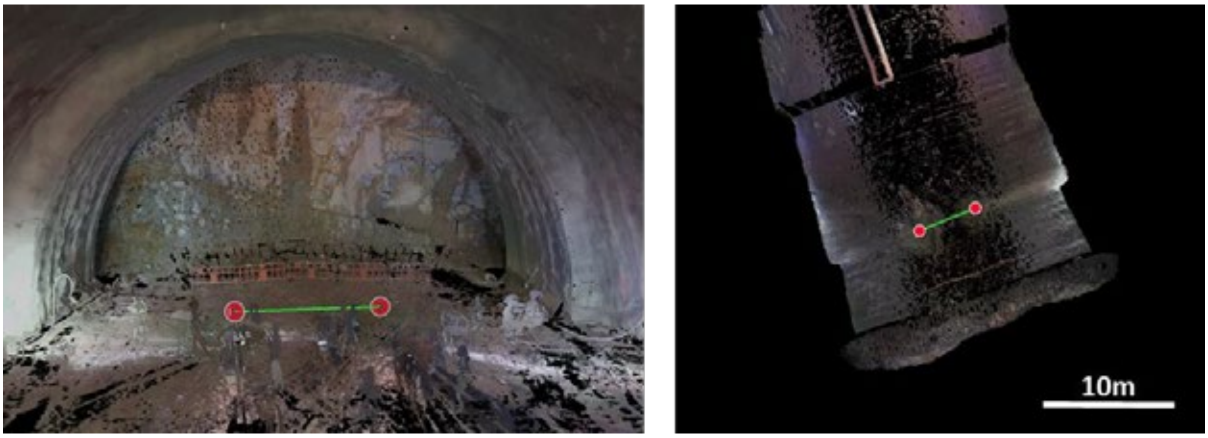

Figure 2: Laser scanner locations (red dots) in Trial 2

Back to office, the scans were registered automatically without any targets with Leica's software, Cyclone Register 360. The registration error was approximately 2 to 3mm. The resultant point clouds generated are approximately 30 to 40m in range. The subsequent data processing is discussed in Section 3.3.

3.2 Structure-from-motion (SfM) Photogrammetry

We carried out SfM and TLS simultaneously in Trials 1 and 2. The SfM technology works by extracting and matching feature points across photos, estimating the camera orientations, calculating the 3D locations of feature points, and finally constructing a dense point cloud.

In a review on using SfM technology for geomorphological research, Micheletti et al. (2015) provided a list of suggestions on taking photos for SfM technology. These include maintaining a static scene, using consistent lighting, taking photos from different positions and orientations, and avoiding different zoom settings and flashlights, among others. These suggestions are generally followed in our site trials.

In our trials, the photos were taken by a 24.2 Megapixel full-frame mirrorless camera equipped with a 24mm f/1.8 prime lens. The camera must be mounted on a tripod for stability since the exposure time was relatively long. Consistent camera settings were used throughout each trial, as summarized in Table 1.

Table 1: Camera settings used in Trial 1 and Trial 2

Trial #	Shutter speed (s)	Aperture	ISO
Trial 1	1/8	f/7.1	1000
Trial 2	1/6	f/7.1	1000

The photos were taken at approximately 15m from the tunnel face. Roughly one-third of the photos were taken orthogonal to the tunnel face; the remaining two-third were taken at an oblique angle approximately 45° to the tunnel face (in both directions). Each photo was taken at a different location, with at least 60% overlap with prior photo.

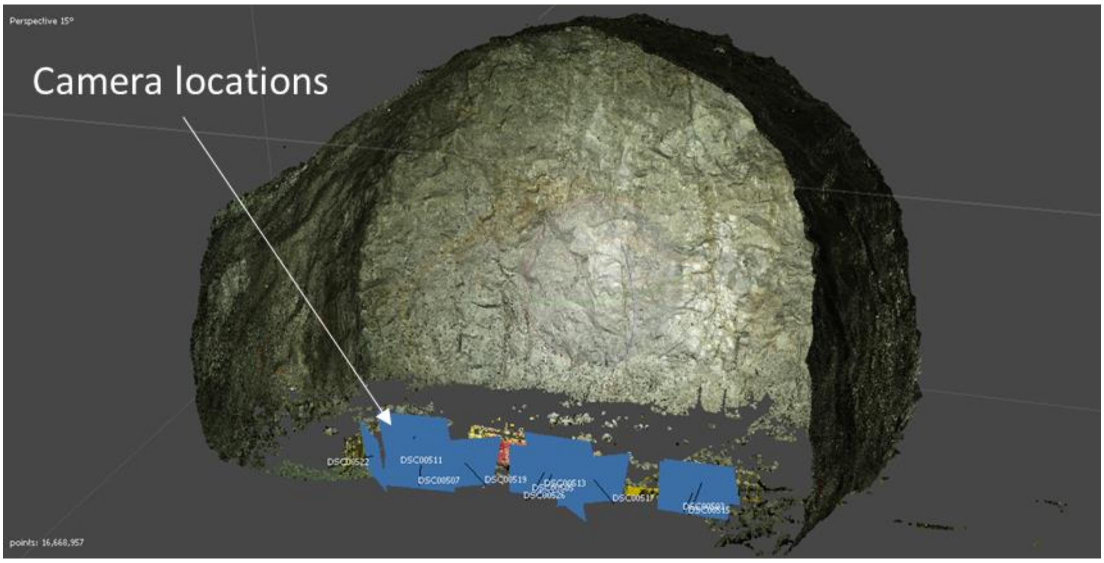

Figure 3: Camera locations and orientations for the 10 photos used for constructing the point cloud in Trial 2

A total of 58 and 39 photos were taken in Trial 1 and Trial 2 respectively. The 3D photogrammetry models were only generated by 10 selected photos in each trial, using the software Agisoft Metashape, which automatically generate point clouds from plain photos by SfM photogrammetry.

3.3 Data Processing

Initially, both the TLS- and SfM-derived point clouds were not orientated properly. In addition, the SfM-derived point clouds were not scaled properly. To correct the orientation and the scale, the point clouds were georeferenced using 5 to 7 ground control points (GCPs) sprayed by paint on two sides of the supported tunnel side walls (locations and close-up photo shown in Figure 4). As shown in the close-up screenshot in Figure 4, the GCPs can be easily identified on the colored point clouds. With real-world coordinates of the GCPs, the point clouds were georeferenced in the software CloudCompare (CloudCompare 2017). It is noted that a minimum of 3 GCPs are needed for georeferencing the point clouds and these should not be colinear.

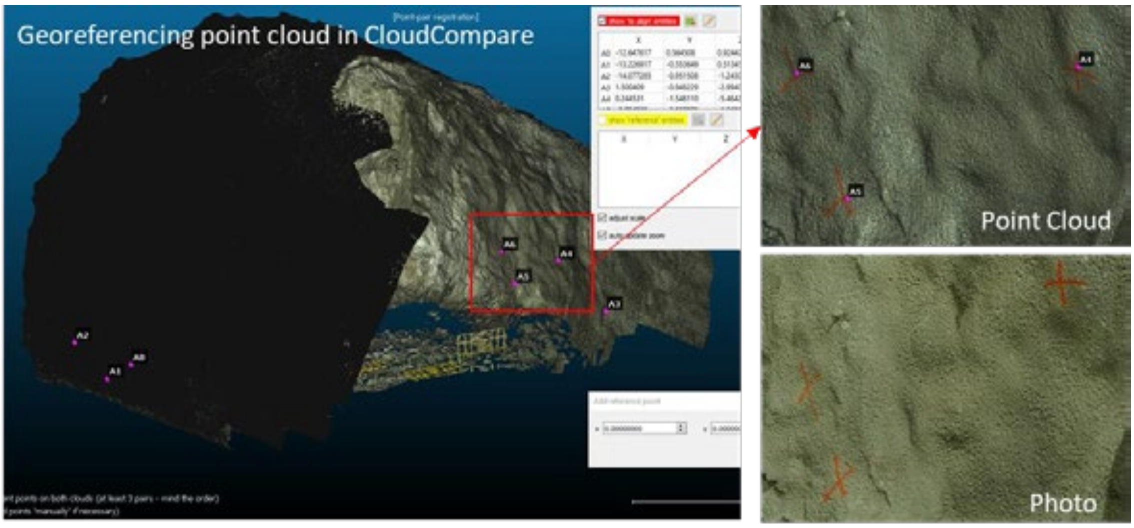

Figure 4: Ground control points – locations, close-up screenshot of the point cloud, and a photo for comparison

The point clouds are then further processed in CloudCompare to crop out the areas of interest, i.e. the tunnel face (Figure 5). The quality of the point clouds is further discussed in Section 5.1.

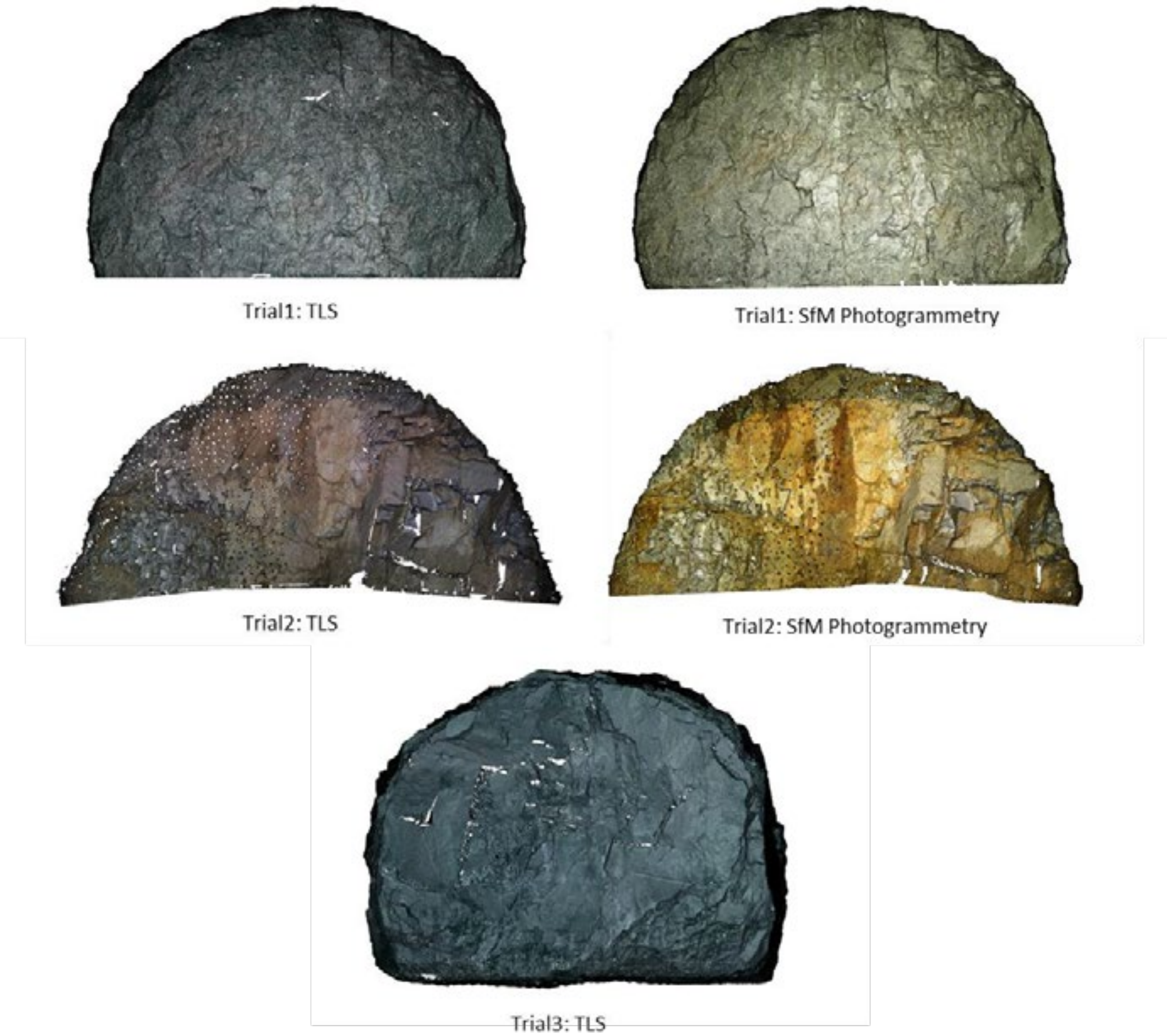

Figure 5: Point clouds of each tunnel faces in Trial 1 to Trial 3 after cleaning

4 AUTOMATIC IDENTIFICATION OF DISCONTINUITY PLANES

4.1 Digital rock mapping with DRM2.0

Automatic identification of discontinuity planes was carried out with DRM2.0 developed by Aurecon Group (Gibbons et al. 2019) and FACETS (Dewez et al. 2016), a widely used plugin in CloudCompare. For comparison purpose, in all three trials, the TLS-derived point clouds were used, although as we will discuss in Section 6.1, the quality for SfM-derived point clouds are also sufficient for digital rock joint mapping.

DRM2.0 is integrated with the discontinuity analysis software DIPS developed by Rocscience. The extracted planes from DRM2.0 were analyzed in DIPS and subsequently classified into different joint sets. The classified results were then imported back to DRM2.0 and are shown with different colors for easy visualization (Figure 6). The spacing and persistence of each joint sets can also be computed, which will not be discussed in this paper. Interested readers can refer to Aurecon's submission on the Benchmarking

Exercise 2021 (CEDD 2021) and the presentation (Aurecon 2021) for a demonstration of DRM2.0's spacing and persistence function.

DRM2.0 also contains a convenient "virtual scanline" function. The user can place a "cube" inside the 3D model with specified dimensions to sample extracted planes intersecting with the cube (Figure 6). In Trial 1 to Trial 3, a virtual scanline of 1m × 1m × 1m were used. RQD (rock quality designation), one of the six parameters in Q-value (NGI, 2015), were estimated based on planes intersecting the cube along three different axes. The locations of the scanlines used in each trial are shown in Figure 7.

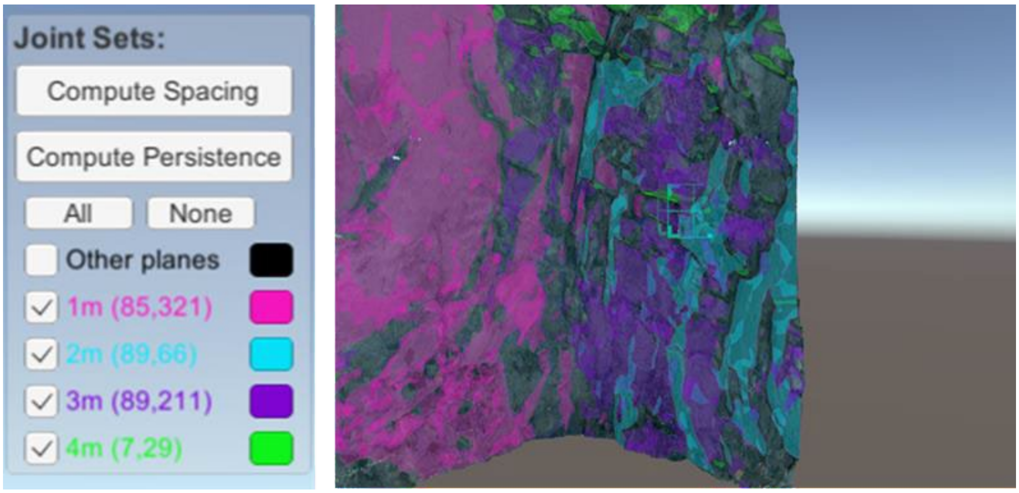

Figure 6: Functions in DRM2.0

(Left: Visualization of classified joint sets; Right: virtual scanline function using the sampling code)

FACETS was also used on the same data, in addition to DRM2.0, to explore the application of automatic extraction of discontinuities for tunnel mapping.

4.2 Results

In general, the performance of the discontinuity extraction increases from Trial 1 to Trial 3. The results of the discontinuity extraction and the contoured stereoplots (plotted in DIPS) are shown in Figure 7. A summary of the results is provided in Table 2.

Table 2: Results of automatic identification of discontinuity planes

Trial #	Planes identified		Major joint sets from DRM2.0 (Dip / Dip Direction)				Estimated RQD from DRM2.0
	DRM2.0	FACETS	J1	J2	J3	J4	
Trial 1	954	1707	(not classified)				91-96
Trial 2	1785	1707	86°/244°	84°/262°	48°/062°	-	73-97
Trial 3	2389	2362	85°/321°	89°/066°	87°/211°	07°/029°	55-72

Overall, both software identified similar discontinuity patterns in the three trials, except the density of the discontinuity sets may differ.

For Trial 1, as shown in the stereoplot in Figure 7, the planes identified in DRM are predominantly subparallel to the tunnel face. A small proportion are along the tunnel side wall and crown. Closer inspection reveals that a lot of these identified planes are induced fracture surfaces (caused by blasting or breaking) instead of natural discontinuities. Since the identified natural discontinuities are masked by the fracture surfaces caused by the blasting or breaking works, joint sets were not classified in DRM for Trial 1. The results in FACETS for Trial 1 are similar, where blast/breaking-induced fracture surfaces dominate the extracted planes. The results are expected as the tunnel face in Trial 1 is massive with visually limited exposed discontinuity surfaces.

For Trial 2 and Trial 3, three to four joint sets could be classified based on the stereoplots in both DRM and FACETS. The results are expected as the tunnel faces in Trial 2 and Trial 3 are blockier and with more exposed discontinuity surfaces than tunnel face in Trial 1.

The results show consistent increase of identified planes from Trial 1 to Trial 3, as the rockmass become blockier from Trial 1 to Trial 3. And the estimated RQD decreases accordingly.

Another observation is that the reliability of the results could be affected by operational artifacts. Half of the tunnel face in Trial 2 was covered with split holes needed for drill and break excavation, where the internal profiles of which were picked up by the TLS. These were being shown as long 'spikes' behind the point cloud (Figure 8). Results show that the extraction of planes holding the split holes was unaffected in both software. However, FACETS identified a number of false planes associated with these split holes (Figure 8), which correspond to the plane cluster of approximately 45°/320° in the stereoplot. On the other hand, DRM2.0 was less affected (Figure 8).

In Section 5.2, we will further compare the results from digital rock mapping with the manual mapping records.

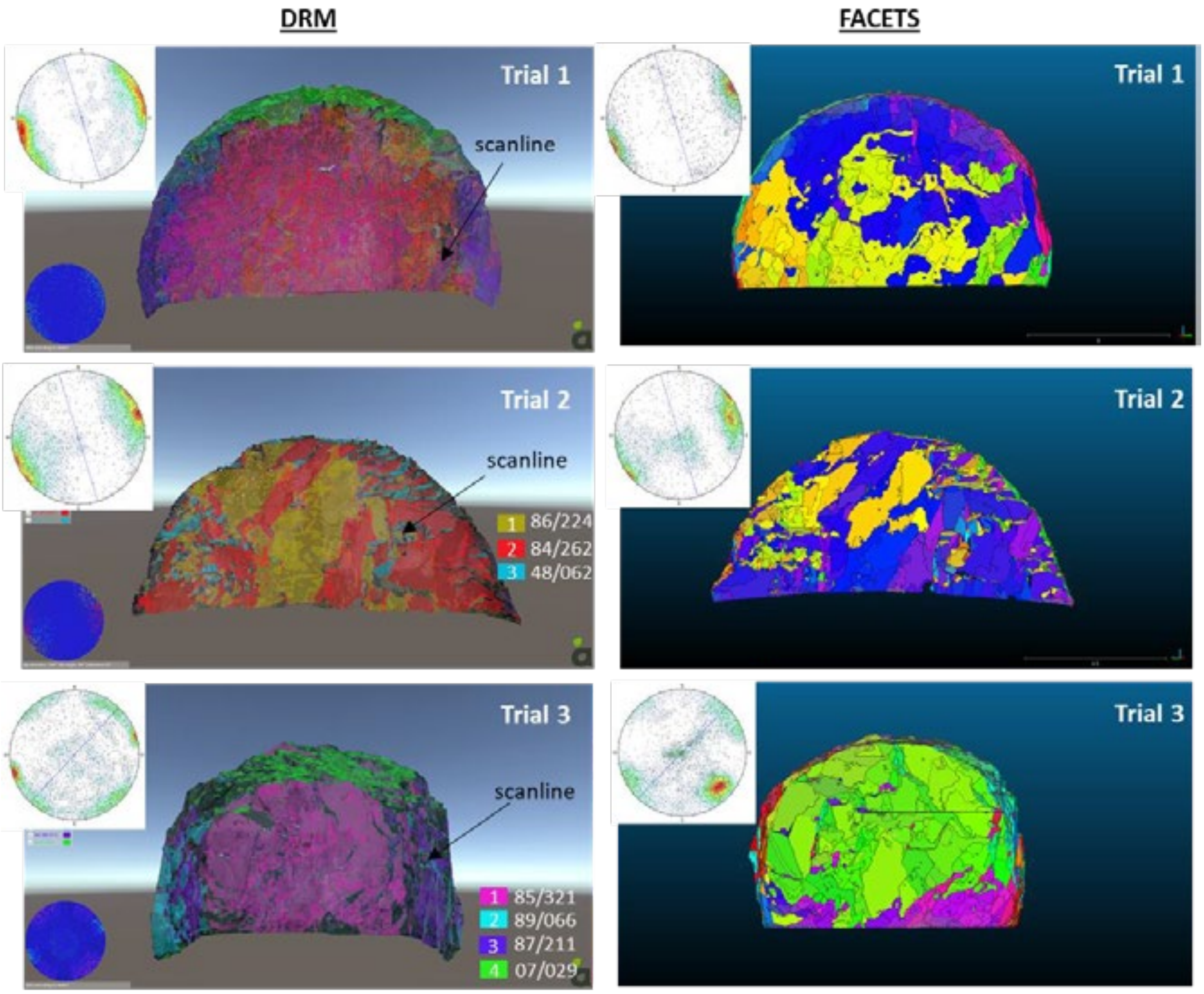

Figure 7: Results of the semi-automatic joint extraction
(Left column: results from DRM. Right column: results from FACETS as reference)

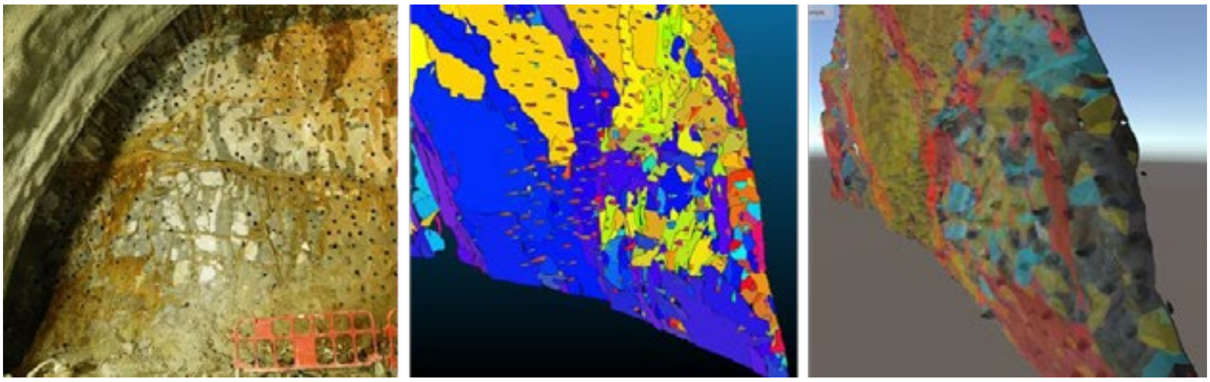

Figure 8: Effect of split holes on semi-automatic discontinuity extraction
(Left: Photo of the tunnel face in Trial 2 showing the split holes;
Middle: Automatic discontinuity extraction in FACETS;
Right: Automatic discontinuity extraction in DRM2.0)

5 COMPARISONS AND VERIFICATIONS

5.1 Point Cloud Quality

One of the goals of this study is to evaluate the difference between acquisition methods on digital rock mapping in tunnels. We will compare the quality of point clouds from TLS and SfM photogrammetry and discuss the number of photos needed for SfM photogrammetry.

The accuracy of the point clouds was checked against the survey points on the excavation profiles measured using typical survey method with a total station. The accuracy is reported below as the RMS error of the differences between the point clouds and the 20 to 80 check points extracted from the corresponding 3D profile. The accuracy includes georeferencing errors.

5.1.1 TLS vs SfM photogrammetry

In general, the quality of the SfM-derived point clouds (derived from 10 photos) is comparable to the TLS-derived point clouds, although the former have lower accuracies (Table 3).

As expected, the accuracy of the TLS-derived point clouds (4 – 10mm) are better than that of the SfM-derived point clouds (21 – 25mm) in both Trial 1 and Trial 2 but both are considered sufficient for rock joint mapping purpose as part of the tunnel excavation process. While the resolutions of the generated point clouds are dependent on the laser scanner settings or settings in the photogrammetry software, comparable resolution up to 4-5mm can be achieved.

Table 3: TLS VS SfM photogrammetry in Trial 1 and Trial 2

Trial #	Accuracy (mm)		Resolution (mm)	
	TLS	SfM-Photogrammetry	TLS	SfM-Photogrammetry
Trial 1	10	21	12 (medium-resolution scan)	5
Trial 2	4	25	5 (high-resolution scan)	4

In terms of occlusions, sub-horizontal discontinuities at higher elevations on the tunnel faces may be under-sampled as these may not be reached by the angle of incidence from the laser scanner, or the camera in the case of photogrammetry. An example of such sub-horizontal discontinuity is indicated in Figure 8 with a red arrow. In addition, occlusion can be from the lateral direction. Since the laser scans were taken at a further distance to the tunnel side walls, some of the discontinuities facing and close to the tunnel side walls may be missed. An example is shown in Figure 9 by a yellow arrow. In contrast, SfM-derived point clouds miss fewer of these discontinuities as the camera stations are closer to the side walls.

In terms of visualization, SfM-derived point clouds have more vibrant colors, which can aid geologists to better visually identify possible features on the tunnel faces.

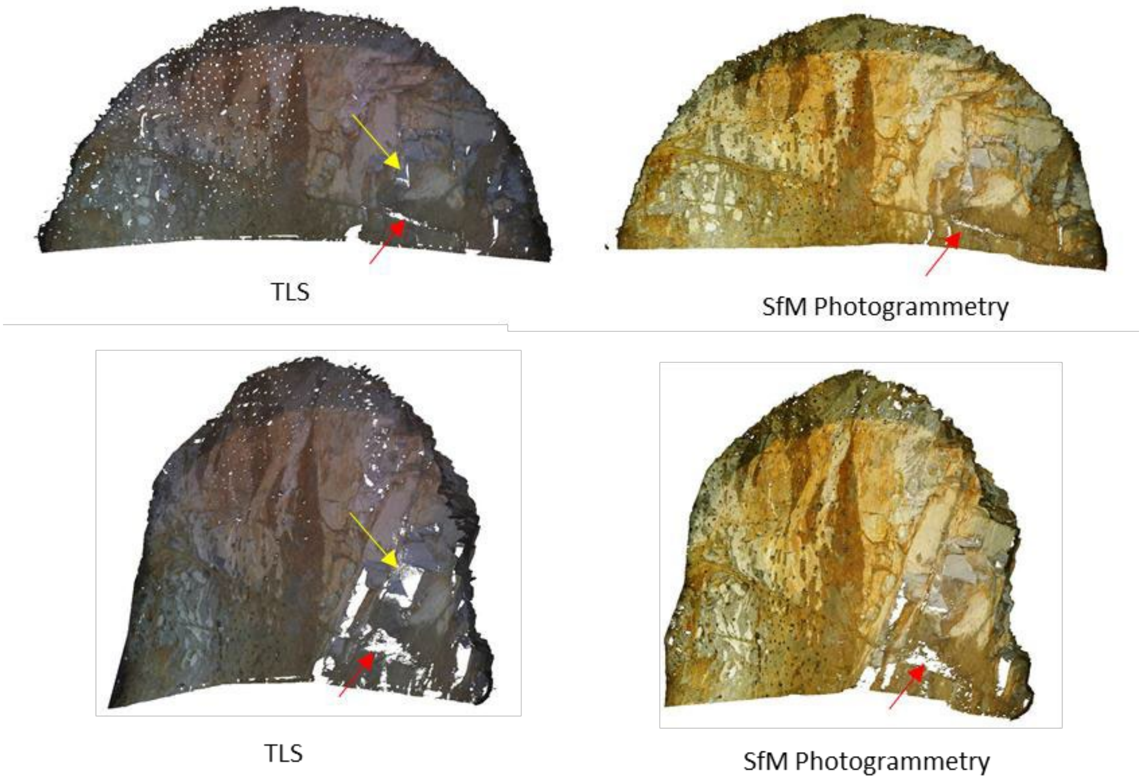

Figure 9: Occlusion in the point clouds produced by TLS and SfM photogrammetry

5.1.2 Number of photos required for SfM photogrammetry

In Trial 1 and Trial 2, we found that when the number of photos used in SfM photogrammetry is reduced from over 30 to 10, the quality is more or less comparable.

Micheletti et al. (2015) suggested using 10 to 100 photos for 3D models at close scale (i.e., cm to 10s of m). They also pointed out that accuracy generally improves as more photos are used. However, as taking more photos also means longer surveying time in the tunnel, it is useful to know the minimum number of photos required to generate the same level of accuracy.

Garcia-Luna et al. (2019) has carried out systematic analysis on the effect of using different number of photos in SfM photogrammetry for tunnel mapping by Discontinuity Set Extractor (Riquelme et al. 2014), another popular software for automatic discontinuity extraction. Garcia-Luna et al. (2019) conclude that around 15 good quality photos are sufficient for a tunnel face with area of 50m^2.

We experimented with using only 10 photos to build the photogrammetry models. As indicated in Table 4, comparing to the models built from the maximum photos we took (i.e. 58 photos in Trial 1 and 39 photos in Trial 2), the accuracy of point clouds built from 10 photos are indeed lower. However, when the number of photos was reduced to 10, occlusion problem does not worsen significantly (Figure 10). The texture of the rock surfaces is also almost unaffected by reducing number of photos to 10 (Figure 11).

Table 4: Comparison of accuracy using different number of photos in Trial 1 and Trial 2

Trial #	Accuracy (mm)		Resolution (mm)	
	10 photos	58 photos (Trial 1) 39 photos (Trial 2)	10 photos	58 photos (Trial 1) 39 photos (Trial 2)
Trial 1	21	11	5	5
Trial 2	25	8	4	4

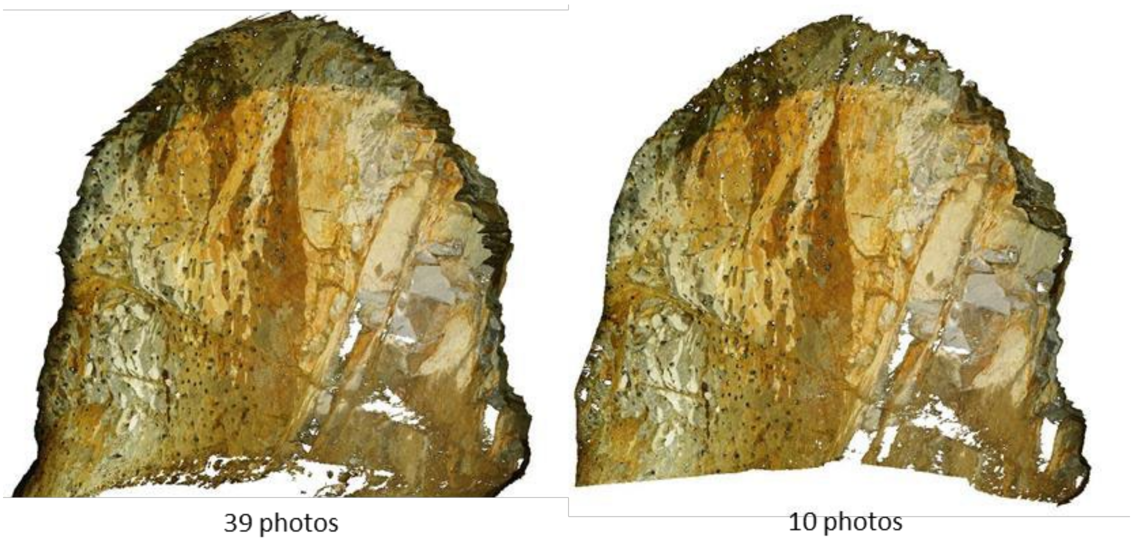

Figure 10: Occlusions in SfM-derived point clouds generated by different number of photos

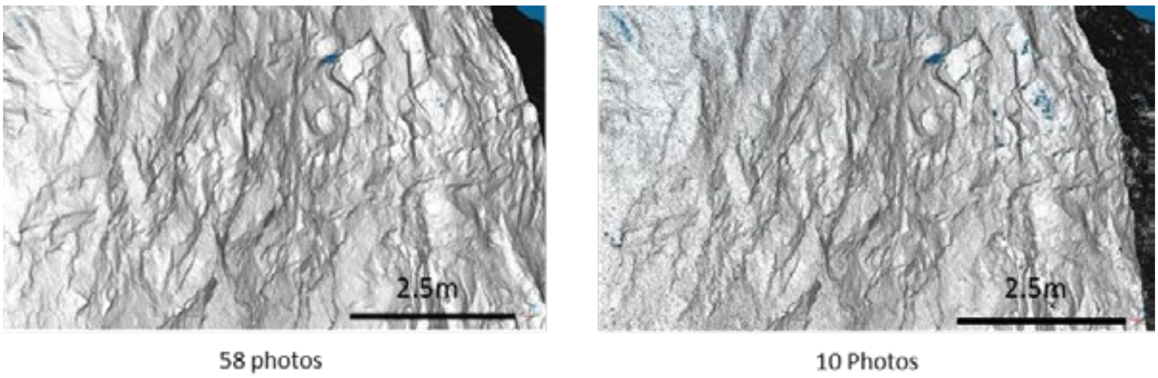

Figure 11: Textural comparison in the SfM-derived point clouds produced by different number of photos

5.2 *Comparison with manual mapping*

In general, the digital mapping results (Section 4.2) are found to be in good agreement with manual mapping in Trial 2 and 3, and to a lesser extent in Trial 1. However, the results also reveal limitations of current automatic discontinuity extraction techniques.

In the massive rock mass in Trial 1, while major joint sets cannot be effectively classified among the data with high noise ratio shown in the stereoplot (i.e., a large number of non-discontinuities being identified), the individual joint planes, especially the persistent ones, are still observed to be accurately extracted and their dip and dip directions are in line with the major joint sets in the manual mapping records. This is checked within DRM2.0, as DMR2.0 can display the orientation of the identified planes and the corresponding stereoplot location when the user clicks a plane on screen, providing a convenient and interactive experience.

Automatic discontinuity extraction in Trial 1 failed to identify two joint sets (i.e., 60-80°/340° and 15°/220°). The result is expected as these two sets have very limited areal exposure on the tunnel face. Rather, these sets just appear as trace lines on the tunnel face. Same problem is also faced by FACETS (Figure 7).

For the blockier rock mass in Trial 2, the subvertical joint sets J1 and J2 (86°/224° and 84°/262°) identified can only be roughly matched with the manual mapping record (80°/245-265° and 70°/280-320°). As these two sets are roughly subparallel to the tunnel face, they are also susceptible to being masked by noises created by the non-discontinuities. As a result, the spread of the clusters are large and the corresponding density peaks are not well defined.

In the blocky rock mass in Trial 3, the subvertical joint sets identified are in general rather close to the manual mapping record, with around 5° to 10° difference.

Due to shallower dip angles, the moderately inclined to sub-horizontal joint sets are not identified with high certainty in Trial 2 (J3: 48°/062° vs 10-20°/100-130°) and Trial 3 (J4: 07°/029° vs 10-20°/050°).

Overall, the results are consistent in that as the rockmass becomes blockier from Trial 1 to Trial 3, the number of identified planes increases with increasing accuracy. In addition, while the range of the estimated RQD is large, it is in general consistent with manual mapping in all three trials (Figure 1 and Table 2).

6 DISCUSSIONS

6.1 TLS vs SfM photogrammetry for tunnel mapping

As discussed in Section 5.1.1, the quality of the SfM-derived point clouds is comparable to the TLS-derived point clouds. Considering the much cheaper cost of SfM photogrammetry (Table 5) and its ease of use, it is a good alternative to TLS (or even more preferable) when accuracy in the magnitude of 10^{-3}m is not required.

As for the data acquisition time, both methods are similar – less than half an hour (Table 5). Time needed for levelling the tripods for the TLS and for tuning the camera settings have been considered. As the data acquisition time is relatively short, these can be comfortably squeezed into the mapping / surveying time in the tunnel site schedule.

Back in office, data processing for data acquired with both methods (including processes such as scan registration, SfM photogrammetry, georeferencing and data cleaning) can be completed within an hour. Much of the time spent on the raw point cloud generation can be processed in background. Using DRM2.0, the digital rock mapping can be completed within 40 minutes.

Table 5: Comparison on cost and time for TLS and SfM photogrammetry

Data acquisition methods	Cost	Data Acquisition Time (Site)	Data Processing Time (Office)	Digital rock mapping with DRM2.0 (Office)
TLS	> 100,000 HKD (Scanner and accessories)	~24 minutes (2 high-resolution scans)	<1 hour	<10 minutes (calculation) + 30 minutes (interpretation and fine-tuning)
SfM photogrammetry	20,000 HKD (Camera + Lens + Agisoft Metashape)	~ 15 minutes (10 photos)	<1 hour (high accuracy settings)	

SfM photogrammetry has the additional advantages of being capable of producing point clouds with sharper colors, and less susceptible to occlusion problems from the sides. Therefore, from the authors' point of view, SfM photogrammetry is a preferrable data acquisition method for automatic discontinuity identification for tunnel mapping based on the common tunnel excavation practice in Hong Kong.

The authors would highlight that some of the smart phones (e.g. iPhone 13 Pro) is incorporated with LiDAR scanner nowadays. A testing was carried out for the same tunnel face in Trial 2 using the LiDAR Scanner of iPhone 13 Pro. As shown in Figure 12, the quality of the 3D model is quite good and the details of the rock joint surface can also be seen. A key limitation for iPhone 13 Pro is the range of the LiDAR scanner – it is only up to 5m and therefore the tunnel face with a height of 12m could not be completely scanned in the testing.

Figure 12: 3D model generated by iPhone 13 Pro for the tunnel face of Trial 2

6.2 Advantages of digital rock mapping in tunnels

Undoubtedly, digital rock mapping cannot replace manual tunnel mapping based on the current technology, and additional time and effort will be required if both digital and manual mapping have to be carried out (however it is considered achievable for both digital and manual mapping to carried out between the limited time of scaling and subsequent temporary support installation). Instead, digital rock mapping can supplement the traditional tunnel mapping work by providing much richer and more objective data.

In traditional tunnel mapping, the geologist can only observe the rock mass and measure the orientation of the discontinuities from a distance of tunnel face. And due to extreme time constraint, the geologist can only identify and record a small portion of all visible joints which he / she considers representative. Compare with rock slope mapping that can always afford much longer time for mapping, not many measurements of the discontinuities in tunnel mapping can be done and it is one of the reasons that only orientations of the major joint sets are recorded. The quality of the data collected is also highly dependent on the skill and experience levels of individual geologists. The mapping results are often not repeatable and reproducible for the same purpose.

In the case of digital mapping, if the point clouds are properly georeferenced, the dip and dip direction of individual discontinuity planes are, in theory, much more accurate and objective as the best-fit planes will be computed. Associated joint characteristics such as persistence can also be quickly and easily computed. Better data consistency can be maintained throughout the tunnel. In addition, in a blocky rock mass such as Trial 3, automatic extraction of discontinuity will be able to provide data on almost all the exposed joints, instead of only a few selected ones from traditional mapping. The RQD can also be estimated more objectively with a virtual scanline. With more robust statistics and more accurate data, a database of rock mass discrete fracture network (DFN) can be developed and hence more reliable and representable parameters of DFN can be developed in the detail design work (Figure 13). This database can definitely help the designer improve the underground support design. It is particularly useful for the extensive tunnels and caverns development in Hong Kong.

In digital rock mapping, a 3D record can be preserved for future use. The point clouds can be "revisited" in the future if needed, which improves quality control and cost saving. 3D records also communicate the findings better than using sketches, as 2D lines in rock mapping records often cause confusion. This makes it easier to communicate risks to client and stakeholders. This is particularly useful in tunnel and cavern construction involving scenarios with higher geometric complexity (e.g. tunnel/adit intersection and multiple stages / headings of excavation, especially for large span of excavation), and requiring more detailed record and study related to excavation profile (i.e. overbreak / underbreak) which could be affected by geological factors.

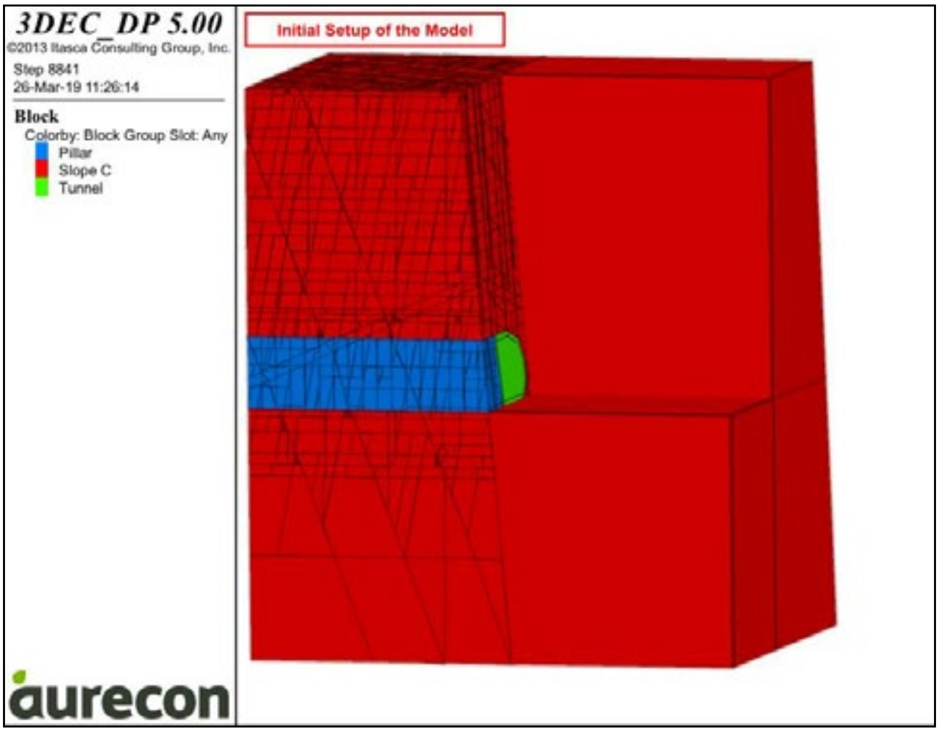

Figure 13: An example DFN developed for a rock tunnel support design

6.3 Limitations, potential solutions, and further investigations

While digital rock mapping in tunnel can supplement the traditional way to map tunnel face, there are various limitations to overcome. Some of the major limitations and possible solutions are listed below.

(1) Trial 2 (Figure 9) shows occlusions on the tunnel face at several subvertical joints close to and facing the tunnel side walls, and also at several sub-horizontal joints at higher elevations. While the former type of occlusion is generally hard to avoid as it is impossible to get too close to the tunnel face beneath unsupported ground, the camera / laser scanner locations can be placed closer to the tunnel walls to alleviate the effect. For the latter type of occlusion, a possible way is to deploy unmanned aerial vehicles (UAV) in tunnels, as UAVs can take photos at higher elevation to cover the sub-horizontal joints. However, it is expected that the occlusion effect become less significant for smaller tunnels (e.g. water-carrying or drainage tunnels of smaller typical cross-section) as the tunnel size becomes smaller.

(2) It is challenging for semi-automatic discontinuity extraction software (even for experienced geologists) to distinguish fractures formed by blasting or breaking from discontinuities. This is particularly relevant if the rockmass is massive (like Trial 1) where the automatically extracted planes may be masked by a large number of non-discontinuities (fractures and rock surfaces). At the current stage, for massive rock mass, or when only a few protruding rock joints are present, the best way is to just check the orientation of selected discontinuities by virtual manual measurements using software like the qCompass in CloudCompare.

(3) Discontinuity traces cannot be extracted (i.e. discontinuity without a protruding surface but rather appear as a "line" on the rock surfaces). This may lead to a whole joint set being missed out statistically. Currently, while automatic extraction of traces based on curvature or color is being actively researched (e.g. Umili et al. 2013; Guo et al. 2019; Zhang et al. 2020), it appears that no software is available for trace extraction yet, except the Trace Tool in CloudCompare (Thiele et al. 2017), which is a tool to aid manual digitization of traces. Our team is currently in active collaboration and research with other professionals in this industry to develop ways for trace and block extraction (Figure 14).

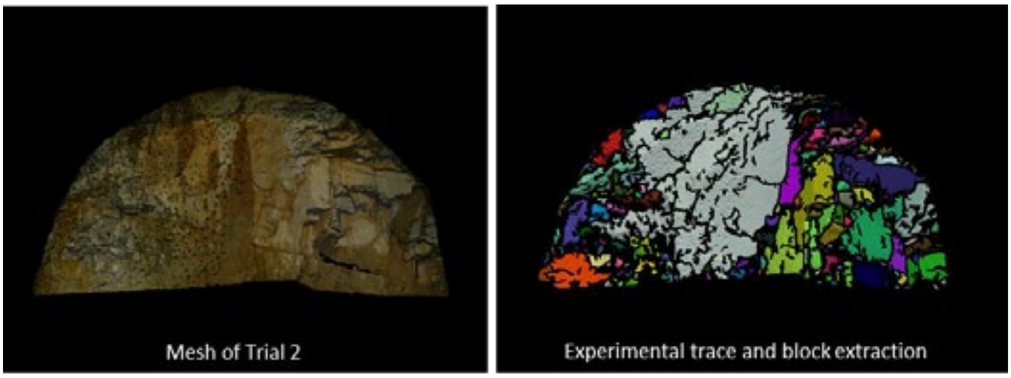

Figure 14: Experimental trace and block extraction (partial script developed by GeoRisk Solutions Ltd)

(4) Some artifacts, such as the split holes in Figure 8, are difficult to clean. The results should be checked against actual field conditions and manually removed from digital results.

(5) Roughness, alteration, infilling of the discontinuities cannot be reliably assessed from point clouds. These correspond to the Jr and Ja parameters in Q-value and control the discontinuity shear strengths. While there are not a lot of research on digital extraction of infilling and alteration, several attempts have been made on estimating the roughness, such as by calculating discontinuity roughness angle at different scales (Gigli and Casagli 2011), or correlating the RMS of the discontinuity profile to the Joint Roughness Coefficient (JRC) (Li et al. 2019). These may become part of digital rock mapping workflow in the future.

6.4 Other potential uses

Other than rock mapping, other uses of point clouds in tunnels include checking shotcrete thickness by comparing the pre-shotcrete and the shotcreted 3D models (Fekete et al. 2009), automatic extraction of steel arches (Zhang et al. 2019), automatic identification of roof bolts (Singh et al. 2021) and generating smooth and continuous 3D tunnel profile for overbreak and underbreak study (instead of using typical method by linking the limited number of individual survey points taken for each chainage for generating 3D tunnel profile).

7 CONCLUSIONS

We carried out three site trials at two drill-and-blast tunnels with two data acquisition methods: TLS and SfM photogrammetry. We find that if a magnitude of 10^{-3}m level of accuracy is not required, the quality of the SfM-derived point clouds is comparable with, or even better than, the TLS-derived point clouds. We find that 10 photos are sufficient to produce point clouds with good quality by SfM. Given the much cheaper cost, SfM photogrammetry is more preferable for digital mapping in tunnel. We analyzed the point clouds using Aurecon’s in-house developed software DRM and another free software FACETS. Both results are in good agreement with traditional mapping in blocky rock mass but less so when the rock mass is massive where joints appeared as “lines” instead of planes on the tunnel face. While at this stage digital rock mapping may not be able to save time and replace human judgement in some mapping-related activities (e.g. identifying potentially unstable blocks that warrant spot bolting), the technique can supplement traditional mapping by providing massive objective and consistent data, help to build up useful DFN database for underground development, and by providing 3D records for better quality control, cost saving and communication. Although this technology cannot replace traditional tunnel mapping at the moment, it is being continuously refined.

ACKNOWLEDGEMENTS

The authors would like to thank the support from Johnathan Hart of GeoRisk Solutions Limited to the development of the scripts used in the experimental trace and block extraction in the initial stage.

REFERENCES

Aurecon Hong Kong Limited. 2021. Benchmarking Exercise on Digital Rock Mass Discontinuity Survey. https://hkss.cedd.gov.hk/InnoTech2021/materials/presentation/13%20BM4-(Aurecon).pdf

CEDD. 2021. Review of Benchmarking Exercise on Digital Rock Mass Discontinuity Survey 2020. Hong Kong.

CloudCompare 2017 CloudCompare (version 2.9). 2017. Retrieved from http://www.cloudcompare.org/

Chan, T.H, Woodmansey, P., Suen, H.Y., Lee, S.W., Henderson, T. 2019. Application of Digital Engineering to Geotechnical Tunnel Design, *Proceedings of HKIE Geotechnical Division Annual Seminar 2019.*

Dewez, T.J., Girardeau-Montaut, D., Allanic, C., & Rohmer, J. 2016. Facets: A CloudCompare Plugin To Extract Geological Planes From Unstructured 3d Point Clouds. Int. Arch. Photogramm. Remote Sens. Spatial Inf. Sci., XLI-B5: 799-804.

Fekete, S., Diederichs, M. and Lato, M., 2009. Geotechnical applications of Lidar scanning in tunnelling. RockEng. Diederichs and Grasselli, Toronto, pp.1-12.

Gibbons, C., Hoel, O., Lo, K.P., Chiu, S.L., Yan, K.W., Lau, C.F., 2019. On The Application Of UAVs For Rock Joint Mapping – A Case Study. In HKIE, *Proceedings of HKIE Geotechnical Division Annual Seminar 2019.*

Gigli, G., & Casagli, N. .2011. Semi-automatic extraction of rock mass structural data from high resolution LIDAR point clouds. *International Journal of Rock Mechanics and Mining Sciences*, 48(2), 187-198.

García-Luna, R., Senent, S., Jurado-Piña, R., & Jimenez, R. 2019. Structure from Motion photogrammetry to characterize underground rock masses: Experiences from two real tunnels. *Tunnelling and underground space technology*, 83, 262-273.

Guo, J., Liu, Y, Wu, L., Liu, S., Yang, T., Zhu, W. & Zhang, Z. "A geometry-and texture-based automatic discontinuity trace extraction method for rock mass point cloud." *International Journal of Rock Mechanics and Mining Sciences* 124 (2019): 104132.

Li, X, Chen, Z., Chen, J., and Zhu, H. 2019. Automatic characterization of rock mass discontinuities using 3D point clouds." *Engineering Geology* 259: 105131.

Micheletti, N., Chandler, J.H., Lane, S.N., 2015a. Structure from motion (SFM) photogrammetry. In: Clarke, L.E., Nield, J.M. (Eds.), Geomorphological Techniques (Online Edition). British Society for Geomorphology, London Chap. 2, Sec. 2.2. https://dspace.lboro.ac.uk/2134/17493.

NGI. 2015. Using the Q-system: Rock Mass Classification and Support Design (handbook). Norwegian Geotechnical Institute, Oslo.

Riquelme, A. J., Abellán, A., Tomás, R., & Jaboyedoff, M. 2014. A new approach for semi-automatic rock mass joints recognition from 3D point clouds. *Computers & Geosciences*, 68: 38-52.

Singh, S.K, Raval,S & Banerjee,B. 2021. A robust approach to identify roof bolts in 3D point cloud data captured from a mobile laser scanner. *International Journal of Mining Science and Technology* 31, no. 2: 303-312.

Thiele, S.T., Grose, L., Samsu, A., Micklethwaite, S, Vollgger, S.A. and Cruden A.R. 2017. Rapid, semi-automatic fracture and contact mapping for point clouds, images and geophysical data. *Solid Earth* 8, no. 6: 1241-1253.

Umili, G, Ferrero, A. & Einstein, H. H. 2013. A new method for automatic discontinuity traces sampling on rock mass 3D model." Computers & Geosciences 51: 182-192.

Wong, D., Chan, K., Millis, S., 2019. Digital Mapping of Discontinuities. In HKIE, *Proceedings of HKIE Geotechnical Division Annual Seminar 2019.*

Zhang, Wenting, Wenjie Qiu, Di Song, and Bin Xie. "Automatic tunnel steel arches extraction algorithm based on 3D LiDAR point cloud." *Sensors* 19, no. 18 (2019): 3972.

Zhang, Keshen, Wei Wu, Hehua Zhu, Lianyang Zhang, Xiaojun Li, and Hong Zhang. "A modified method of discontinuity trace mapping using three-dimensional point clouds of rock mass surfaces." *Journal of Rock Mechanics and Geotechnical Engineering* 12, no. 3 (2020): 571-586.

Rock Load Transfer Mechanisms and Interactions at Cavern Junctions

Andrew K W Seto, Alan K L Kwong
AECOM Asia Company Ltd., Hong Kong, China

Joel Y F Wong
Drainage Services Department, HKSARG, Hong Kong, China

ABSTRACT

Rock at depth is subjected to stresses resulting from the weight of the overlying strata. When an underground opening is excavated, the stress field in this rock mass is locally disrupted and induces a new set of stresses surrounding the new opening.

At tunnel and cavern associated junctions, the re-distributed stresses will alter the stress fields of adjacent openings. For example, loadings from a taller cavern will be transferred through the rock arch and concentrated as additional vertical stress above the crown of the shorter cavern.

The load transferring mechanisms in this paper refer to the construction of the cavern complex, which involves developing new sewage treatment works in caverns to be constructed at Nui Po Shan, A Kung Kok, Sha Tin, to replace the existing Sha Tin Sewage Treatment Works (STSTW). Upon functioning of the new STSTW, the existing site will be released for other uses beneficial to the development of Hong Kong.

The works at the new STSTW occupies about 14 hectares in the area comprising of Main Access Tunnel (MAT), Secondary Access Tunnel (SAT), fifteen Process Caverns, the Main Driveway (MD), Secondary Driveway (SD), four Branch Driveways, Ventilation Shaft, Ventilation Adit, two Effluent Pipelines, and lining and portal structure of MAT and SAT. These structures are excavated mainly by the drill-and-blast method in hard rock, with rock covering more than half of the excavation span/height above the crown. They are designed as drained and are primarily supported by the rock arch, reinforced by systematic permanent rock bolts with permanent sprayed concrete. In addition, drained cast-in-situ reinforced concrete lining is proposed for poor ground conditions.

For the proposed cavern complex, most of the Branch Driveways are taller than Process Caverns and MD/SD except for the middle cavern for sludge treatment (STC) purposes. STC's design span and height are 30 m and 35 m, respectively. Therefore, additional stresses are expected to transfer from Branch Driveways and STC to other Process Caverns and MD/SD. Numerical modeling using finite element methods has been established, where two-dimensional design models and three-dimensional verification models in accordance with the varying excavation profiles, overburden depth, and rock mass quality have been carried out. By observing the stress redistribution from the taller STC to other Process Caverns, the two-dimensional and three-dimensional models aim to study the stress concentration zones and the extent of the influence zone at tunnel and cavern associated junctions. The maximum deformation is located along with the crown of STC and intruding corners at the associated junctions, in which the Process Caverns with the largest excavation span and height are proposed.

This paper provided a detailed description of the geology, cavern complex geometrical arrangements, rock mass properties for the modeling, methodology of modeling, and mechanism of load redistribution observed at the junctions.

1 INTRODUCTION

1.1 Background

To enhance the land supply strategy in Hong Kong to support the rapidly growing social and economic development, an initiative was put forward by the Development Bureau (DevB) to launch strategic planning and technical studies as part of their 2009-10 Policy Agenda. The initiative aims at promoting the enhanced use of rock caverns as part of Hong Kong's pursuit of sustainable development to build up sufficient land reserves to meet future social, environmental, and economic needs. As part of this initiative, the Drainage Services Department (DSD) proposed relocating the Sha Tin Sewage Treatment Works (STSTW) to caverns to release the existing site of approximately 28 hectares for other beneficial uses.

The works at the new STSTW occupies about 14 hectares in the area comprising Main Access Tunnel (MAT), Secondary Access Tunnel (SAT), five chains of Process Caverns, Main Driveway (MD), Secondary Driveway (SD), four Branch Driveways, Ventilation Shaft, Ventilation Adit, Effluent Tunnel, as well as the portal structure at Main Portal and Secondary Portal. In this paper, all these caverns/driveways holding the sewage treatment facilities are collectively referred to as Cavern Complex. STSTW is to be constructed at Nui Po Shan, A Kung Kok, Sha Tin, and the layout plan of the site area with an isometric view is presented in Figure 1.

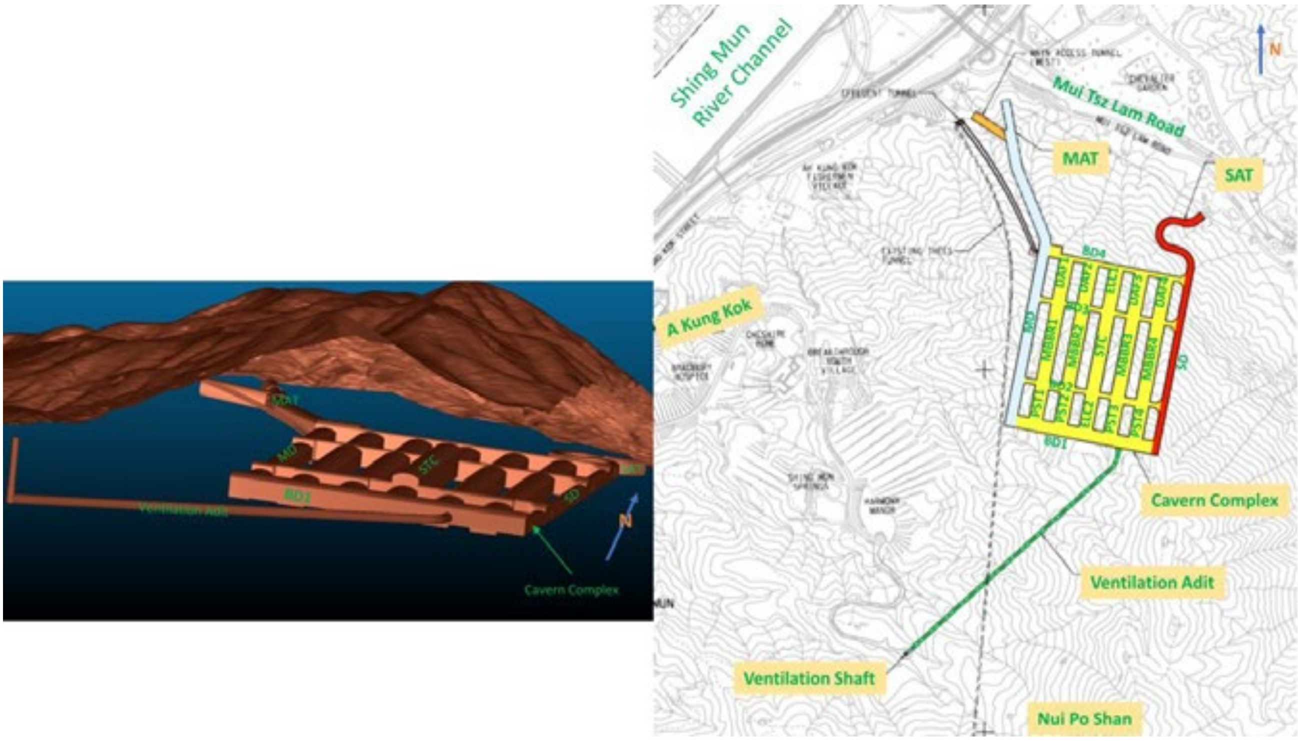

Figure 1: Layout Plan of STSTW (with Isometric View)

1.2 Geological Conditions

The proposed Cavern Complex is situated beneath the natural hillslope, where the existing ground level ranges from +87 mPD at the end of the proposed SAT to +312 mPD at the southeastern edge of the Cavern Complex. The general topography increases towards the southeast, and the steepest gradient is noted on the northeast facing hillslope above the eastern part of the Cavern Complex. The majority of the Cavern Complex is located beneath north to northeast-facing hillslope, where an east-facing hillslope is encountered above the southeastern part of the Cavern Complex.

The solid geology of the site area is predominantly equigranular medium-grained Granite with some porphyritic fine-grained Granite of the Shui Chuen O Granite of the Early Cretaceous age. The proposed Cavern Complex is well below the engineering rock head, which is inferred from borehole data based on the criterion of at least 5 m penetration by boreholes into the moderately strong or better rock of weather Grade III or better with at least 85% core recovery to the length of 1.5 m core run. The engineering rock head within the site generally follows the topography and ranges from +28 mPD at the Secondary Portal to +285 mPD at the southeastern corner of the Cavern Complex.

The rock cover (the vertical distance between the underground structures and engineering rock head) of the Cavern Complex ranges from 45 m to 169 m approximately. A generalized geological section A-A is presented in Figure 2 to illustrate the rock cover above the cavern's roof is well above one excavation span, depending on its physical location. On top of the rock head, it is overlaid by a layer of saprolite which comprises highly (Grade IV) to completely (Grade V) decomposed rock with a thickness of up to 20 m. Colluvium is mainly found above the saprolite on the lower slopes close to Mui Tsz Lam Road and locally on the slopes over the Cavern Complex and other structures. The typical thickness of colluvium is 0.5 m to 3 m.

Local and minor occurrences of basalt dykes, pegmatite, quartz monzonite, and quartz synenite may be encountered within the Cavern Complex, but their effects on the excavation are considered insignificant. A few minor faults are expected crossing the Cavern Complex. Groundwater can be assumed to be close to the ground surface; however, it is not significant to the analysis results as the proposed Cavern Complex is designed to be drained except for the local portions near Main Portal and Secondary Portal.

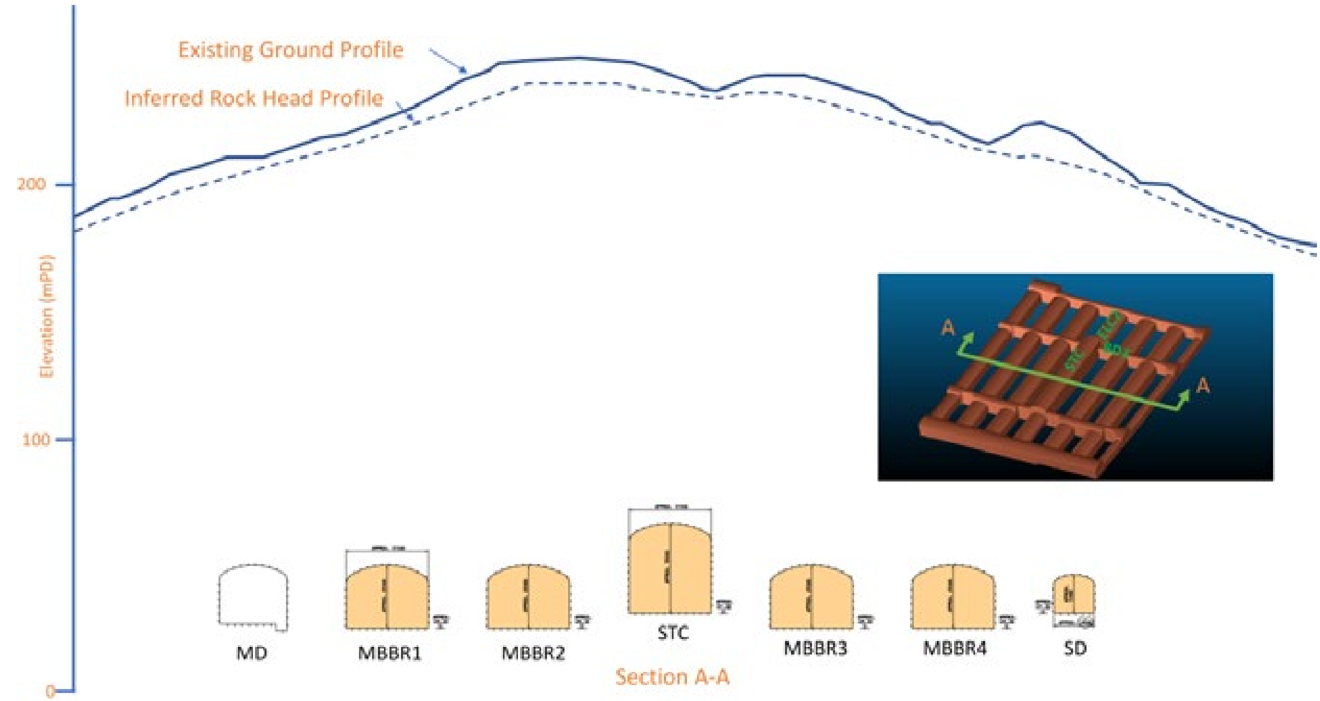

Figure 2: Geological Section A-A

2 GEOTECHNICAL PARAMETERS

2.1 Rockmass Properties

Using the available relevant field and laboratory test data, the adopted design parameters of rock mass used explicitly in this study as a framework for the analysis are taken in the middle range, as shown in Table 1.

A detailed assessment of the rock mass quality "Q index" has been carried out based on the borehole records from the project-specific deep boreholes drilled in vicinity of the site area during feasibility study and detailed design stages as well as the archived ground investigation results which are available, and their associated core photographs, and the interpretation of the stereonets and assessment of the lineaments.

For the Q-logging of the borehole records, the J_n values within Granitic bedrock typically range from 6 to 15 but may increase further where features such as core loss or weakness are indicated.

The J_w parameter has generally been taken as 1, but a value of 0.66 has been assigned where the rock mass shows adverse geological features such as core loss or weakness, which may likely increase groundwater inflow into the tunnel.

A minimum SRF value of 10, 7.5, 5, or 1 has been assigned for zones of competent rock depending on the depth below the engineering rock head level. However, the value would be increased to 2.5, 5, or 10, where the core loss or weakness zones were recorded in boreholes.

The ranges of the Q index around the Cavern Complex were assessed as shown in Table 1.

In Table 1, the Generalized Hoek-Brown parameters are derived from the Geological Strength Index (GSI), which is correlated to the Q index and the intact rock strength. The parameters in this table are not considered for design purposes as large variations will occur on-site, which can only be apparent after the excavation has been carried out and the rock face has been mapped.

Table 1: Rock Mass Properties

Parameter	Bulk Unit Weight (kN/m^3)	UCS (MPa)	Tensile Strength (MPa)	Young's Modulus E (GPa)	Poisson's ratio υ	Shear Modulus (GPa)			
MDG	25.5	75	5	15	0.3	10			
Rock Mass	Q	m_i	E_i (MPa)	MR	GSI	E_m (MPa)	m_b	s	A
	5.9>Q>1.9	32	27524	367	54	10370	6.08	0.00571	0.504

2.2 Rock Joint Parameters

Optical and acoustic televiewer tests were carried out in the vertical, inclined, horizontal boreholes, and horizontal directional coring. Major joint sets in different sub-areas have been identified from stereographic analysis in Table 2 for the Cavern Complex.

Table 2: Rock Joint Parameters

Area	Major Joint Set 1	Major Joint Set 2	Major Joint Set 3	Major Joint Set 4	Major Joint Set 5
Cavern Complex	245°/81°	053°/82°	343°/85°	320°/18°	221°/81°

Based on all the rock joint shear test results conducted, the typical values of peak friction angle, residual friction angle, and cohesion for estimating rock joints shear strength are 40°, 30°, 0 kPa, respectively, with an estimated JRC of 5 and JCS of 25% of UCS.

2.3 In-situ Stress Assumptions

Based on the over-coring and hydraulic fracturing tests, the ratio of the maximum principal horizontal stress to the vertical stress and the ratio of the minor principal stress to the vertical stress is taken as 2.1 and 1.0, respectively, in the following analysis. These site-specific data generally give a higher ratio of the maximum principal horizontal stress to the vertical stress than other projects, which implies a more favorable condition for large rock cavern development. Therefore, again, these ratios are explicitly adopted in this study for the purpose of analysis only.

3 DEVELOPMENT OF ROCK ARCHES

3.1 Rock Reinforcement

Drill-and-blast is proposed for the Cavern Complex, where the engineering rock cover is more than one excavation span/height above the crown of the cavern. They are primarily supported by the rock arch reinforced by systematic rock bolts with permanent sprayed concrete. The support classes shall be determined based on the mapped Q values by the engineering geologist after excavation.

The envisaged construction sequence for the permanent systematic rock bolts and permanent sprayed concrete is shown as follows:

1. Drill probe holes in front of the tunnel face and carry out pre-excavation grouting in case of excessive groundwater inflow;
2. Excavate the caverns/tunnels by drill-and-blast method;
3. Carry out geological mapping to determine the support classes according to the mapped Q-values;
4. Survey to identify any overbreak/underbreak and the associated remedial works;
5. Install temporary sprayed concrete, smoothing sprayed concrete layer (as required), and permanent rock bolts;
6. Install the drainage strips and permanent sprayed concrete, and
7. Repeat the above procedures to advance the construction of a permanent rock support system.

Top-heading and bottom-benching methods are anticipated considering the cavern profiles, logistic construction flow, blasting operations, pull length, mucking out, and excavation cycle-time etc.

3.2 Rock Load Transfer Mechanisms

Rock at depth is subjected to stresses resulting from the weight of the overlying strata. When an underground opening is excavated, the stress field in this rock mass is locally disrupted and induces a new set of stresses surrounding the new opening.

At tunnel and cavern associated junctions, the re-distributed stresses will alter the stress fields of adjacent openings. For example, loadings from a taller cavern will be transferred through the rock arch and concentrated as additional vertical stress above the crown of the shorter cavern. An illustrative sketch of the stress transfer mechanism is shown in Figure 3.

For the proposed Cavern Complex, most of the Branch Driveways are taller than the Process Caverns and MD/SD except for the middle cavern STC for the Sludge Treatment purposes. Therefore, additional stresses are expected to transfer from Branch Driveways and STC to the Process Caverns and MD/SD at those localized junctions. Different sewage treatment facilities are housed in different caverns/tunnels, and they are collectively given the term Process Caverns. For illustration purposes, in this paper, the study focuses only on the junctions of STC, the Process Cavern called ELC2, and the Branch Driveway called BD3.

The load transferring mechanisms in this paper will refer to the construction of the Cavern Complex at the junctions of the Sludge Treatment STC, ELC2, and BD3 with their locations, as shown in Figure 2. The internal span and height of STC are 30 m and 35 m, respectively. For ELC2, its internal span and height are 30 m and 13 m, respectively, whereas BD3's internal span and height are 10 m and 23 m, respectively. Numerical modeling using finite element methods has been established, where two-dimensional design models and three-dimensional verification models in accordance with the varying excavation profiles, overburden depth, and rock mass quality have been carried out. By observing the stress redistribution from STC to BD3/ELC2, the two-dimensional and three-dimensional models aim to study the stress concentration zones and the extent of the influence zone at tunnel and cavern associated junctions. Within the context of this paper, continuum mechanics is assumed for the analysis where the rock mass behavior is considered homogeneous and isotropic without adverse weakness and blocky rock mass influence.

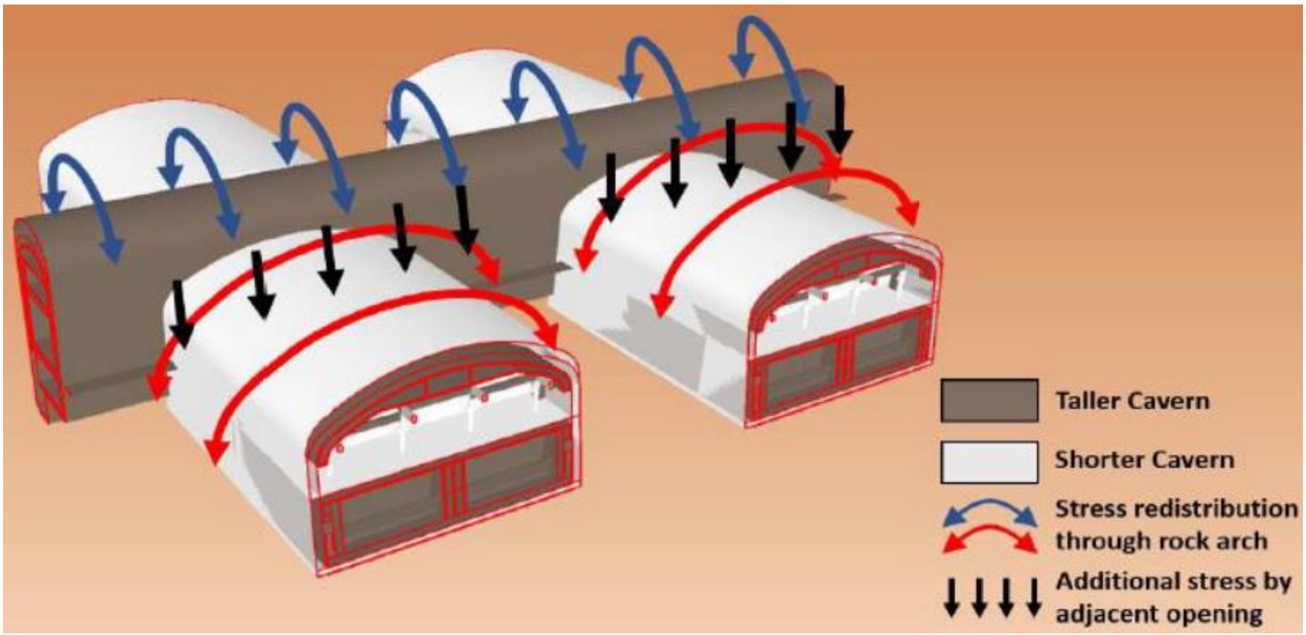

Figure 3: Rock Load Transfer Mechanisms at Junctions

4 FINITE ELEMENT MODELLING

4.1 Verification Model for Full Cavern Complex

A three-dimensional analysis can provide clear indications of stress concentrations due to the stress interactions of three-dimensional geometry. Therefore, an elastic analysis was first carried out by a three-dimensional finite element program 'RS3 Version, 2.023'developed by Rocscience Inc., to assess whether the zone of influence at the intersections is limited to about one diameter of the smaller openings. As a result, the maximum deformation of a few millimeters is located along with the crown of STC and intruding corners at the associated junctions, in which the Process Cavern with the largest excavation span and height is proposed. Figure 4a shows the major principal stress contour, σ_1, where stresses redistributions are found at the transition from crown to wall/pillar, but no sign of excessive stress concentration is observed. Also, the vertical stress contour plot shows no sign of excessive vertical stress observed at the junctions intersecting Branch Driveways. It is because the proposed Cavern Complex involves seven parallel large-span openings with closely-spaced rock pillars, and the in-situ stress field has been greatly disrupted. A longitudinal section showing the vertical stress contour intersecting the Branch Driveways along STC is shown in Figure 4b.

Initially, the in-situ stress within the rock mass follows the ground profile of the overlying stratum. After excavating the Cavern Complex, the stress is re-distributed through the rock arch to the wall/pillar along STC. The zone of stress redistribution decreases at approximately 45° until reaching the excavation boundary at the end of the excavation. After further excavating the Branch Driveways, the stress at junctions is further re-distributed. As a result, the extent of the influence zone is slightly less than one excavation span of the Branch Driveways. Based on this observation, it is practical to simplify the problem into two-dimensions by considering the additional vertical stresses at critical sections to verify the maximum forces on permanent rock bolts at all junctions.

4.2 Two-dimensional Plastic Model

The finite element program, PHASE2 Version 8.0, developed by Rocscience Inc., was used to check the permanent rock bolt supports due to the additional vertical stresses with the Generalised Hoek-Brown failure criteria. In addition, the convergence-confinement method was used to model the relaxation of ground loading during the blast face advances following the methodology by Kersten Lecture (2008) and Vlachopoulous and Diederichs (2009). The blast face advancement is modeled by decreasing face support pressure from full to zero in multiple stages without installing any rock reinforcement or support. The deformation is measured for all stages.

The equivalent support pressure versus distance from the blast face of the tunnel is then calculated. This deformation versus face support pressure relationship will determine the amount of ground relaxation behavior of the rock mass when unsupported and imply the amount of loading sustained by the rock bolts and the temporary or permanent supports to the tunnel/cavern when installed accordingly. In the model, sprayed concrete and rock bolts were activated sequentially in pace with the relaxation of ground loading during blast face advances. Stage factors are available in PHASE2 Version 8.0 for simulating the relaxation of ground loading as a function of the excavation stage. In the numerical model stage, the ground loading is relaxed by changing the ground stiffness at the initial stage from 1E to 0.5E for first blast face advancement, 0.3E for second blast face advancement and installation of permanent supports, and full excavation for further blast face advance. A 1 m blast disturbed zone was set up around the excavation to simulate the damage and strength loss in rock mass caused by blasting. A disturbance factor D=0.2 was applied to the blasting damage zone.

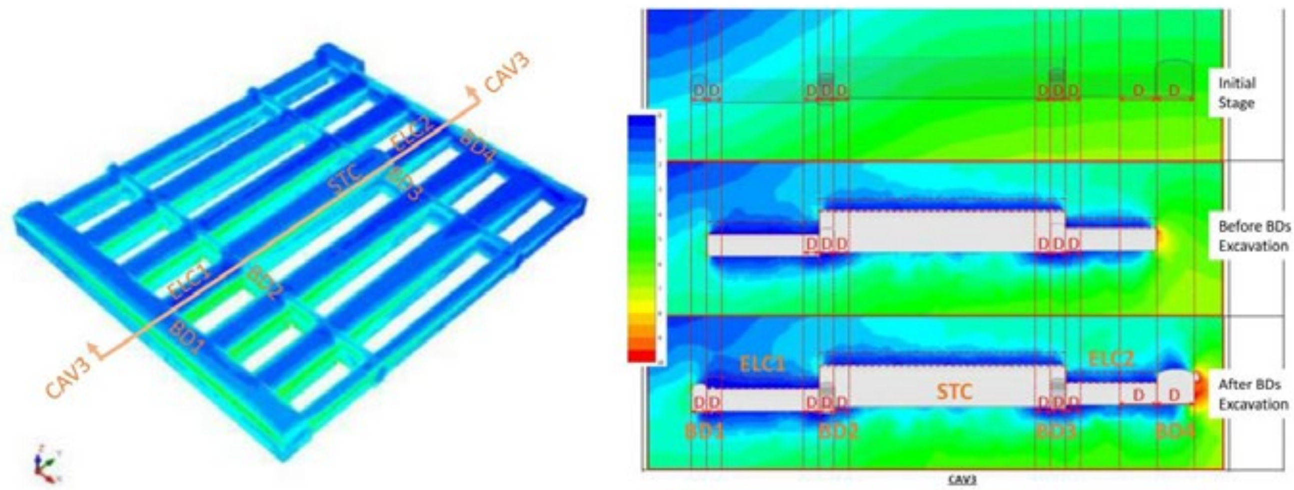

Figure 4: a) Major Principal Stress at Full Cavern Complex Model, b) Change of Vertical Stress along STC

An example of a design checking model along STC is presented in Figure 5. It assesses the ground interactions due to multiple openings at junctions. In addition, it determines the additional vertical stresses to be transferred from Branch Driveways through the rock arch and concentrated at the crown of Process Caverns and MAT/SAT. The additional stress is determined based on the difference in vertical stress before and after excavation.

Uniform distributed loadings are incorporated in the models to simulate the effect of additional loadings at junctions, as illustrated in Figure 6. The magnitude of the uniform distributed loadings was assigned a range of 100 kPa to 300 kPa, at a location above the roof of the short caverns.

The induced stresses of the permanent rock bolts are well within the structural capacities, as demonstrated by the plot of axial forces in Figure 6.

5 CONCLUSIONS

Numerical modeling using finite element methods has been established, where two-dimensional design models and three-dimensional verification models in accordance with the varying excavation profiles, overburden depth, and rock mass quality have been carried out. It is observed that the maximum deformation is located along with the crown of STC and intruding corners at the associated junctions, in which the Process Cavern with the largest excavation span and height is proposed. Furthermore, the vertical stress contour plot shows no sign of excessive stress concentration observed at the junctions intersecting Branch Driveways. The extent of the influence zone is slightly less than one excavation span of the Branch Driveways. Based on this observation, it is practical to simplify the problem into two-dimensions by considering the additional vertical stresses at critical sections to verify the maximum forces on permanent rock bolts at all junctions. The induced stresses of the permanent rock bolts are well within the structural capacities, as demonstrated by the plot of axial forces.

The analysis within the context of this paper is based on continuum mechanics, where the rock mass behavior is considered homogeneous and isotropic without adverse weakness and blocky rock mass influence. This could be another topic interesting for further investigations and studies.

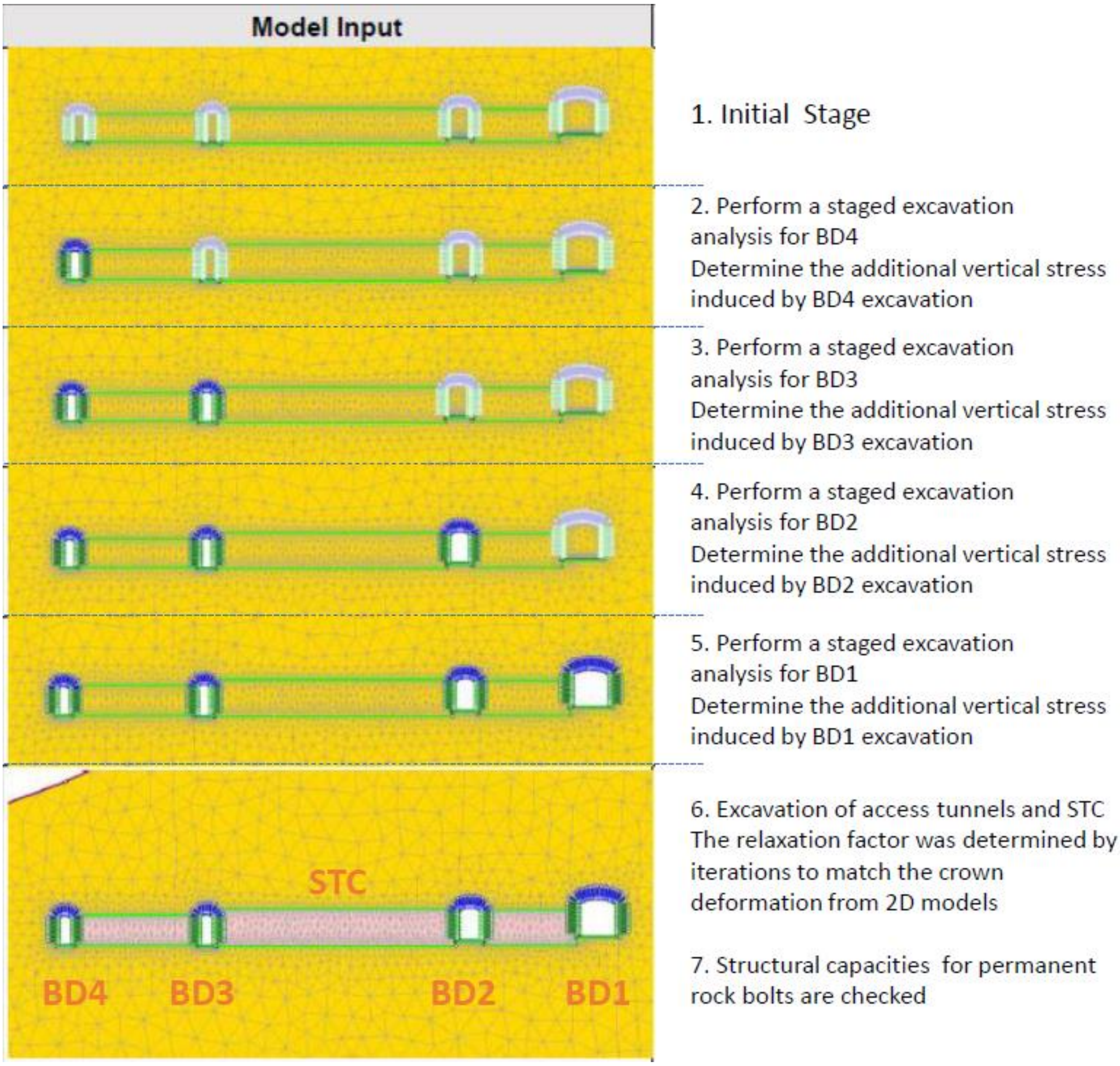

Figure 5: Methodology to Determine Additional Vertical Stresses Acting from a Taller to Shorter Cavern

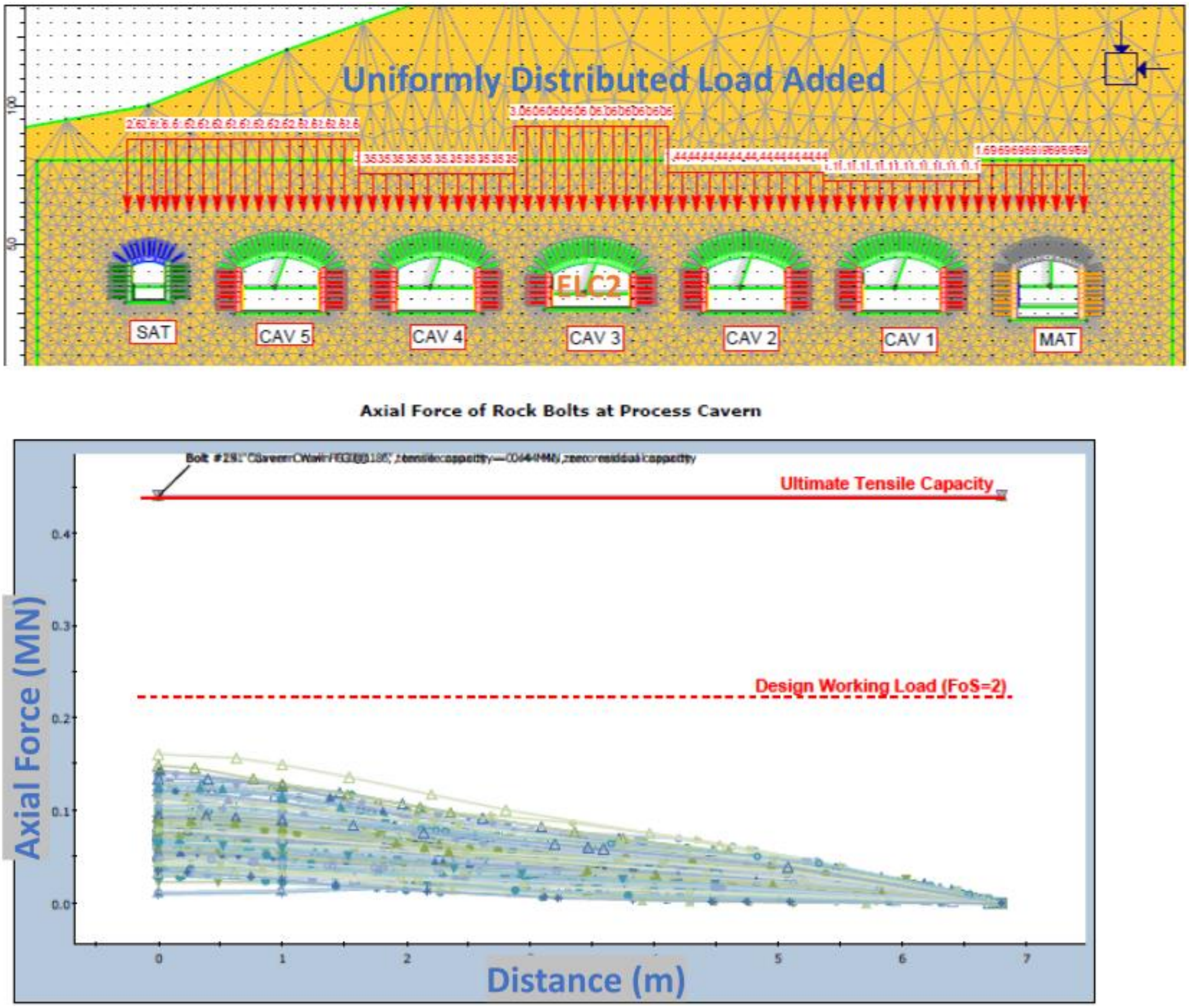

Figure 6: Additional Loadings at Junctions from STC to ELC2

ACKNOWLEDGEMENTS

The writers are grateful for the support of the Drainage Services Department, HKSARG. Their support contributed to expediting the approval process. However, the contents of this paper do not necessarily reflect the views and policies of these supporting organizations, nor does the mention of trade names and commercial products constitute endorsement or recommendation for use.

REFERENCES

Hoek, E., Carranza-Torres, C., Diederichs, M. S. and Corkum, B. 2008. *The 2008 Kersten Lecture – Integration of geotechnical and structural design in tunneling.* Proceedings University of Minnesota 56th Annual Geotechnical Engineering Conference, Minneapolis, pp. 1-53.

PHASE^2 Version 8.0. Rocscience Inc., *https://www.rocscience.com.*

RS3 Version 2.023. Rocscience Inc., *https://www.rocscience.com.*

Vlachopoulous, N. and Diederichs, M. S. 2009. *Improved Longitudinal Displacement Profiles for Convergence Confinement Analysis of Deep Tunnels*. Journal of Rock Mechanics and Rock Engineering, Volume 42, Number 2, April 2009, pp. 131-146.

Observational Method for Ground Treatment of Tunnel Cross Passages in Complex Ground Conditions

T M S Sacadura, N Taylor, J Gaudon, K Sevecek
Intrafor Hong Kong Limited, Hong Kong, China

R B Storry, X Monin
Dragages Hong Kong Limited, Hong Kong, China

ABSTRACT

This paper focuses on the design and review of the ground treatment and rock fissure grouting required to excavate tunnel Cross-Passages in the Liantang / Heung Yuen Wai Boundary Control Point Site Formation and Infrastructure Works – Contract 2 in Hong Kong SAR. The Cross-Passages were expected to go through Tuff in various degrees of weathering (Grade V to Grade III/II). The Site Investigation, SI, showed that SPTs numbers generally ranged from 30 to 50 for the Completely to Highly Decomposed Tuff, CDT / HDT, with localised values as low as 6. Ground Treatment consisting of permeation and rock fissure grouting as well as 120° pipe roof / canopy tubes, was required to ensure not only the stability during excavation but also limit the groundwater inflow. The SI determined *in-situ* permeabilities ranging from $1x10^{-5}$ to $1x10^{-6}$ m/s for the CDT and a 21m long probe hole recorded a water inflow in excess of 60 l/minute. A discussion relative to the methods employed for drilling, e.g. pressure balance drilling system, drilling alignment tools used, and grouting techniques, e.g. microfine cement, chemical grout is presented in this paper. The use of drilling survey tools integrated with 3D representation models of the cross-passage and the ground treatment is discussed. A review of the overall performance of the Cross-Passage, e.g. groundwater inflow, stability, is undertaken.

1 INTRODUCTION

The Liantang Heung Yuen Wai Boundary Control Point project mainly comprises of site formation of about 23 hectares of land for provision of Boundary Control Point (BCP) buildings and associated facilities. As well as construction of about 11km long dual 2-lane Connecting Road linking up the BCP with Fanling Highway. Integrated in the main project was the Site Formation and Infrastructure Works – Contract 2. This contract comprises the design and construction of a dual two-lane trunk road. This includes an approximately 4.8km long tunnel linking up the proposed Sha Tau Kok Road interchange and Fanling Highway interchange, three ventilation buildings, and an administration building. The project reduced travel times from Fanling Highway to Ping Che area and Heung Yuen Wai, Ta Kwu Ling from 15 and 24 minutes, to 4 and 8 minutes respectively. A combination of Tunnel Boring Machine (TBM), and drill and blast solutions were adopted, to cope with various ground conditions along the 4.8km tunnel route. A dual mode Earth Pressure Balanced TBM was used for the construction of the tunnels in the northern section, where various fault zones were located. Meanwhile, drill and blast techniques were implemented in rock zones in the southern section.

A total of 49 Cross Passages (CPs) were required at maximum 100m intervals to comply with local regulations in Hong Kong. Of all the tunnel CPs four of them were expected to be the most challenging to build due to the ground conditions. These CPs were expected to go through Tuff in various degrees of weathering (Grade V to Grade III/II). CP No. 35, 37 and 40 were expected to be in mixed ground conditions (soil / rock) whereas CP42 was expected to be fully in Completely to Highly Decomposed Tuff, CDT / HDT. The ground investigation determined permeabilities ranging from $1x10^{-5}$ m/s to $1x10^{-6}$ m/s within the CDT while the HDT recorded permeabilities in the range of $3x10^{-5}$ m/s and $2x10^{-7}$ m/s. The Particle Size Distribution analysis from samples collected at CP42 determined that the CDT / HDT was classified mainly as sandy Silt with fine content ranging from 39% to 55%. Traditionally these ground conditions are not suited for permeation grouting and designers and contractors are led down the path of more expensive ground treatment techniques. These techniques usually range from jet grouting done from the surface or ground freezing if the works are done from within the tunnel. Considering that the CPs were 35m to 50m deep it was decided that the ground treatment would be undertaken from within the South-bound tunnel towards the second TBM drive, North-Bound. This influenced the geometry of the treatment since it would not follow the more common approach of drilling from both tunnels towards the middle of the CP. The programme of works was also stringent since the ground treatment works would have to be completed before the second TBM drive. This meant that the last accessible CP from the first TBM drive would be the first CP the North-Bound tunnel drive would encounter. The internal diameter of the tunnel was 12.6m and an approximately 4.0m wide permanently open lane was required to ensure that the other associated tunneling works could continue without disruption. Therefore, the available working space for the ground treatment works was greatly limited.

An innovative observational approach for these ground and site conditions was envisaged as the ground treatment solution. The ground treatment consisted of permeation grouting in soil and rock fissure grouting as well as a 120 degrees pipe roof / canopy tubes.

2 SITE DESCRIPTION AND GROUND CONDITIONS

2.1 Site Description

The site is located in the upper Northeast of the Hong Kong SAR near the border with Shenzhen close to the town of Sha Tau Kok. This location is the most northern on the project and where the TBM is launched from and received for the 2 main drives. Additional drill and blast excavation occurred from the Southern portal and at Mid-vent portal to excavate a cavern for TBM turnaround. The approximately 4.8km tunnel was at the time of construction the longest land-based road tunnel in Hong Kong.

The ground treatment for the four CPs was carried out from inside the South Bound tunnel and completed ahead of the North Bound tunnel drive. The CPs were 35m to 50m deep and their length varied from approximately 16m to approximately 18m. The works were completed concurrently with the ongoing tunneling works for the South Bound, which required an approximately 4.0m wide permanently open lane. The tunnel had an internal diameter of 12.6m and therefore the working space was greatly limited.

2.2 Ground Conditions

Site investigation campaigns identified that the four CPs would go through Tuff in various degrees of weathering (Grade V to Grade III/II). The Completely to Highly Decomposed Tuff, comprised of medium dense to dense silty / clayey Sands and stiff to hard sandy Silts / Clays, generally recorded Standard Penetration Tests, SPT, ranging from 30-50. However, localized SPT values as low as 6 were recorded indicating that less dense / softer pockets of material existed along some of the CP's alignment. Figure 1 shows the Particle Size Distribution, PSD, of samples collected at CP42. The PSD determined that the CDT / HDT was mainly sandy Silt, slightly gravelly at some of the samples, and with fine content ranging from 39% to 55%.

CPs Nos. 35, 37, and 40 were in mixed ground conditions, soil / rock, with estimated percentages of soil vs rock varying from 15% to 30% at CP37 and CP40, respectively. During the South Bound TBM drive the geological inspections confirmed the absence of grade V Tuff, CDT. Therefore, the ground treatment for these CPs would consist of rock fissure grouting only. The grade IV Tuff, Highly Decomposed Tuff, is not considered rock for structural design purposes; however, for grouting works it's expected that the grout injection will displace the water through fissures rather than through the soil mass. Therefore, from an injection / grouting point of view the HDT was expected to behave as a weak rock. CP42 was expected to be located completely within the CDT / HDT zone, see Figure 2, and the groundwater table was 25m above the crown of the CP.

Falling head tests undertaken at the crown of the CPs, within the CDT, determined permeabilities ranging from $1x10^{-5}$ m/s to $1x10^{-6}$ m/s while complementary ground investigation recorded permeabilities in the range of $3x10^{-5}$ m/s and $2x10^{-7}$ m/s for the HDT. A 21m long probe hole was performed at CP42 prior to the ground treatment and a water inflow larger than 60 l/min was recorded.

These ground conditions usually lead designers and contractors to either ground freezing or ground mixing techniques from the surface, e.g. jet grouting. This is due to the difficulty of employing permeation grouting techniques in a satisfactory manner.

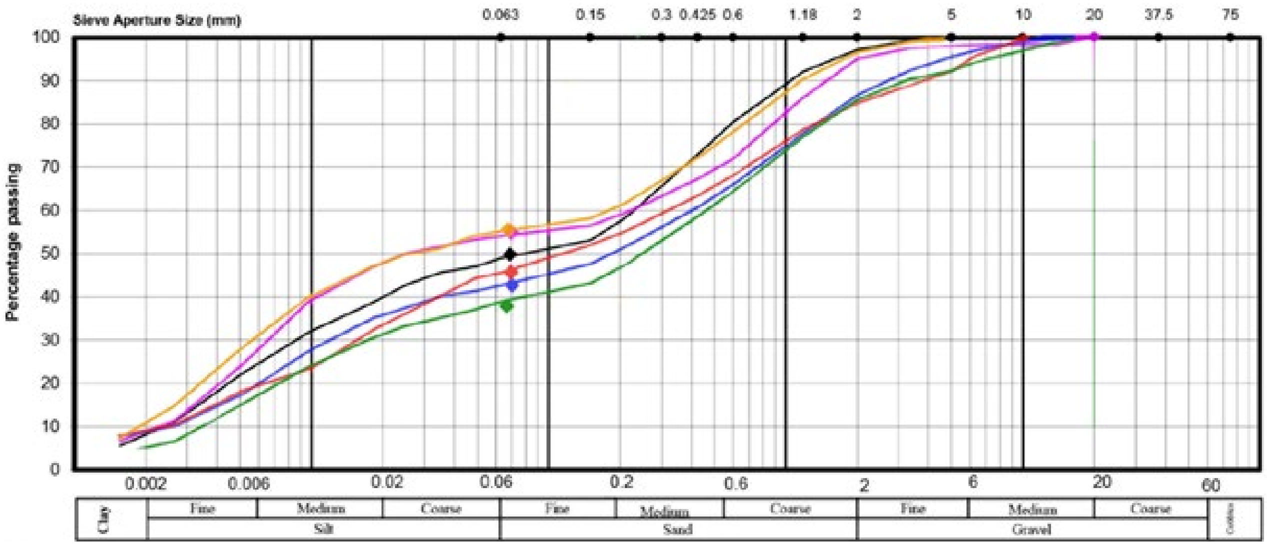

Figure 1 – Particle Size Distribution from Samples at CP42

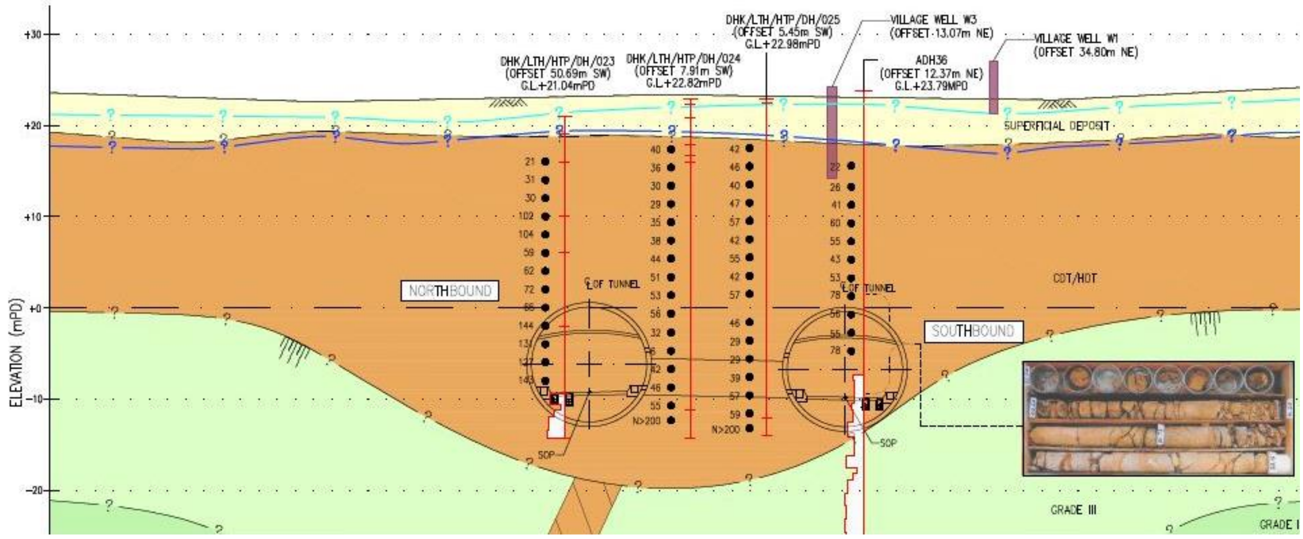

Figure 2 – CP42 Geological Section

3 GROUND TREATMENT DESIGN

Considering the size of the tunnel, internal diameter of 12.6m, and the depth of the Cross Passages, from 35m deep to 50m, it was decided that the most effective option was to carry out the ground treatment from within the tunnel, South-bound tunnel towards the North-Bound. This influenced the geometry of the treatment since it would not follow the more common approach of drilling from both tunnels towards the middle of the CP. However, it had the programme advantage of allowing the CP excavation to start right after the second TBM drive. CP's length varied from approximately 16m to approximately 18m while drilling lengths and correspondent ground treatment varied from 20m to 23m long. Two types of grouting were envisaged, permeation grouting for the soil and rock fissure grouting. Considering the insitu permeability results as well as the PSD curves the ground treatment was designed as a combination of Microfine Cement and Chemical Grout, grouted at pressure using the Tube a Manchette, TAM, grouting method with double packers. The Microfine Cement was envisaged to fill the voids in the soil mass while the Chemical Grout was meant to displace air / water from the inter particle pores. The Chemical Grout mix was designed to achieve a viscosity similar to water so that its penetration radius could be increased. This was achieved by reducing the amount of sodium silicate favoring the ability of the treatment to reduce permeability by sacrificing strength. The mix was tested with soil collected from SPT samplers from boreholes undertaken in the vicinity of CP42 and adjusted to meet optimum results. Chemical Grout mix was only required at CP42 due to its geological / geotechnical conditions. The ground improvement for the other CPs was undertaken with MFC only.

There were two discrete parts to the treatment, the "plug" (Stage 1 & 2), see Figure 3 and Figure 4 and the "tube" (Stage 3a & 3b), see Figure 5 and Figure 6. The future North-Bound Tunnel, second TBM drive, is shown to indicate the relative position of the ground treatment. The purpose of the "tube" is to encapsulate the CP while the "plug" is meant to seal the distal end. The "plug" was designed to act as a bulkhead providing a seal from water ingress and stabilizing the ground mass against collapse whilst securing the formwork for the concrete bulkhead for TBM passage. Meanwhile the southbound permanent opening remains open for excavation.

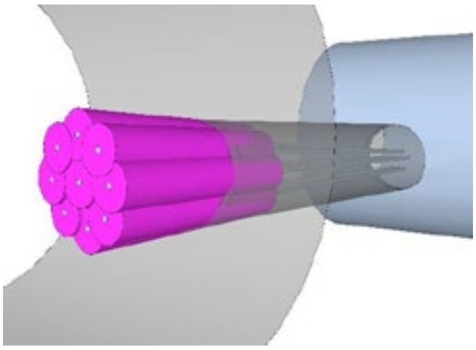

Figure 3 – Stage 1 (inner plug)

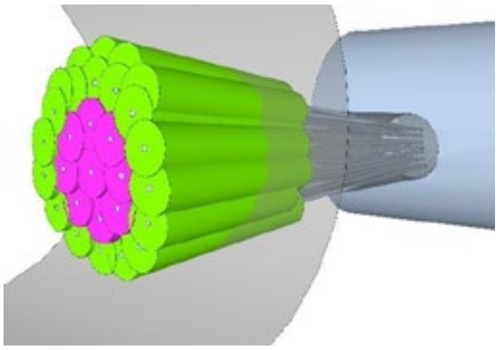

Figure 4 – Stage 1 (outer plug)

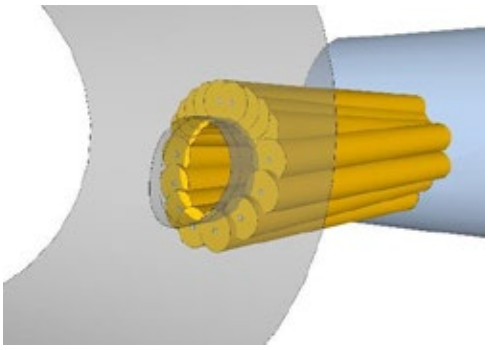

Figure 5 – Stage 3a (inner tube and canopy tube / roof)

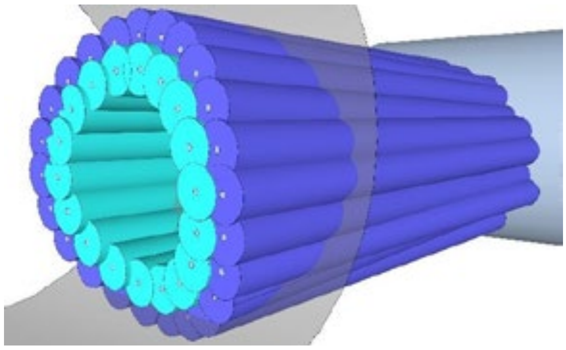

Figure 6 – Stage 3b (Ring 2 and 3) (outer tube)

The combined treatment meant to create a 3m thick effective grout envelope around the whole excavation with a 120° pipe roof / canopy tubes crown. The later meant to ensure the stability of the ground during the excavation stage while the grouting works main objective was to limit groundwater inflow to the excavation. The canopy tubes were designed to terminate at least 1.0m away from the future position of the Northbound tunnel lining. Stages 1 and 2 were designed to depart from the permanent CP opening and radiate outwards towards the North-bound tunnel. Stages 3a and 3b were designed approximately parallel to the CP alignment subject to the segment drilling limitations. As discussed in Point 2.2 above it was assumed that grouting in grade IV or better rock (HDT) would behave like Rock Fissure Grouting. A triangular pattern was designed spaced at 2.4m center to center and assumed that the grouting could penetrate a radius of 1.6m. The pattern assumed that each drill hole would achieve a 800mm grout overlap with the adjacent holes, see Figure 7. For grade V rock (CDT) the triangular pattern spacing was reduced to 1.2m with a grout penetration radius of 0.8m per hole, see Figure 8. The assumed grout overlap between adjacent drillholes would be of 400mm. The ground treatment design is highly dependent of the assumed grout penetration radius as this drives the ground treatment pattern.

At an initial stage the design assumed a certain degree of conservatism into the grouting pattern that was to be validated by site trials.

The segment coring / drilling was set out with the objective of creating the least damage to the permanent segmental concrete lining. To achieve this "no drill zones" were specified by the main contractor's designer in view of maintaining both the watertightness of the tunnel and the structural integrity of the lining. In addition, it was specified that the drill holes maximum diameter was limited to 125mm and that they could not be spaced less than 300mm in any direction to ensure that no consecutive steel reinforcement bars were damaged. These requirements increased the drillholes spacing, which then caused extra drillholes to be added to the initial scheme so that the ground treatment envelope could be ensured.

The criteria for grouting was based on an observational approach, which depended on volume and pressure, and was verified using the methodology described in Point 5.1. Table 1 summarises the grouting criteria where the volume represents a percentage of the treated ground envelope. In soil the assumed grout intake is the sum for both Microfine Cement and Chemical Grout.

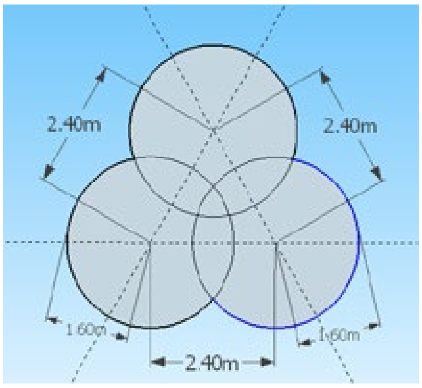

Figure 7 – Ground Treatment Pattern for Grade IV or better Tuff

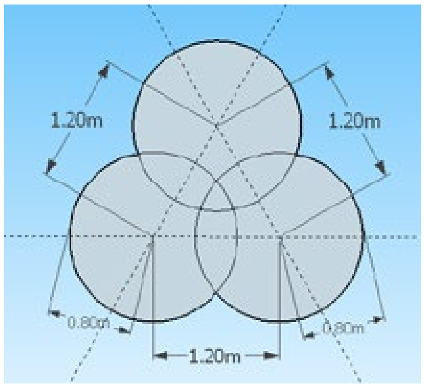

Figure 8 – Ground Treatment Pattern for Grade V Tuff

Table 1 – Grouting Criteria per Treatment

Grouting Method	Grout Type	Pressure (bar)		Treated Volume (%)
		< 5.0m behind tunnel lining	≥ 5.0m behind tunnel lining	
Rock Fissure Grouting	Microfine Cement Mix	15	25	10.6
Permeation Grouting (TAM)	Microfine Cement Mix	10	15	17.4
	Chemical Grout Mix	10	20	18.3

The grouting sequence was planned from the bottom of the CPs to the top and from the inside out with the inner rings being grouted before the outer rings. This was meant to push the water away from the future alignment of the CP / future excavation zone. The last stage of grouting was done through the canopy pipes at the top of the excavated CP crown. Canopy steel pipes with 70mm outer diameter and 20mm thick were installed in all CPs (35, 37, 40 and 42). The PVC TAM pipes were smaller in diameter with only 60mm but maintained the same inner diameter of the steel pipes since they were only 10mm thick.

Prior to the execution works a site trial consisting of 3 nos. of 4.0m long holes were drilled and grouted to confirm the suitability of the ground treatment and the Chemical Grout mix. A verification hole was carried out in the middle of the treatment to validate the suitability of the grout pattern to limit the groundwater inflow. From the trials it became apparent that the high temperatures, both ambient temperature inside the tunnel and the temperature of water being supplied, were negatively impacting the gel time of the mix. Therefore, new tests were done using an alternative supply of water, that was chilled before use and with a temperature of approximately 7°C, and using a refrigerated container to store the other mix constituents. The results from the trial were satisfactory at increasing the gel time and both measures, cooled water and refrigerated container for the Silicate and hardener, were implemented.

4 SITE IMPLEMENTATION

All drilling and grouting were completed from the South-bound tunnel towards the Northbound tunnel, while keeping circulation in the South-bound tunnel for its other tunneling associated works. This required advance planning for the site layout and testing of different configurations using 3D models, see Figure 9. The works were carried out from July 2016 to July 2017. The treatment envelope required the drilling to be both executed from the backfilled tunnel invert level and using an elevated platform, see Plate 1 and Plate 2.

Figure 9 – Planning Stage of Site Layout

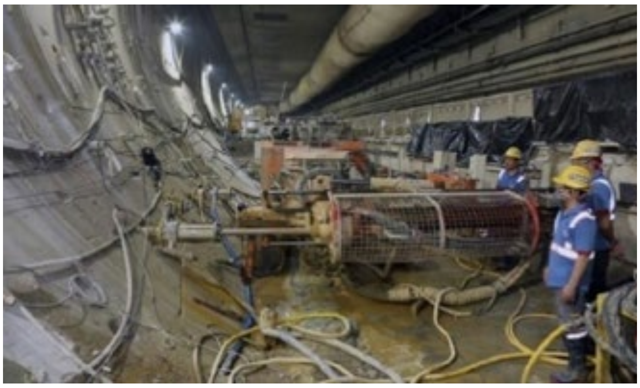

Plate 1 –CP42 Drilling Works from Tunnel Invert Level

Plate 2 –CP42 Drilling Works from Elevated Platform

Variations in ground conditions throughout the Cross Passage would impact the grouting design assumptions and the grouting technique (Permeation Grouting or Rock Fissure Grouting) as detailed in Point 3. Therefore, the drilling operations were continuously monitored to access the drilling spoil and drilling parameters, e.g., drilling speed, drill bits abrasion, and verify if the assumed geology was correct. For CP42 bentonite was used for drilling stability, generally up to 4m before the end of the envisaged drilling hole when it was replaced by a sleeve grout mixture. For the other CPs the drilling medium was water since the drilling did not encounter Grade V Tuff. Once the sleeve grout was applied and drilling finished the rods would be extracted and the Tube a Manchette installed. The sleeve grout mix contained bentonite to ensure its reduced strength when compared to the MFC and therefore, not impart the grouting activities. Grouting using a double packer in either PVC, Plate 3, or Steel TAM pipes with sleeves at 0.33mm centers would then be carried out, with the latter only used for the canopy.

Investigation holes were drilled under Blow Out Preventors, BOP, Pressure Balance Drilling for CPs 35, 37 and CP40 to confirm that there was no adverse impact to existing ground conditions. The existence of grade V Tuff had been ruled out through geological inspection during the Southbound TBM drive and therefore, the rock fissure grouting technique was validated for these three CPs ground treatments.

For CP42 where drilling was expected to be within Grade V Tuff drilling was done in a similar fashion to what was employed at other CPs, using the BOP. At some discrete locations, mainly during the drilling in the upper half of the CP face, drillholes were found to be collapsing before the TAM pipe could be installed. As a remedial measure the drillholes were re-drilled to clear the obstruction and backfilled with a BC grout mix with pressure locked in to seal loose blocks on the borehole wall. The drillholes were then re-drilled, if the pipe could not be inserted then the process was repeated but in telescopic sequence with 5m stages which was largely successful. The use of this technique also served to limit deviations.

Plate 3 – TAM Grouting Pipes

Plate 4 – Grouting Dialog

4.1 Pressure Balance Drilling

To mitigate the risk of groundwater drawdown, groundwater inflow and washout / erosion of fine soil particles during drilling a pressurised drilling system, Figure 10, was deemed required. Using a pressurised system with a pressure vessel containing a compressed outflow pipe, Blow Out Preventor, allowed for the borehole pressure to be maintained, see Plate 5. Once the drilling fluid pressure mirrors the insitu pressure the inflow of water into the bore is prevented. If this pressure is held slightly above the formation pressure, then it allows a filter cake to form on the borehole walls, which improves the stability of the drillhole. This system facilitated the installation of the Tube-a-Manchette, TAM by maintaining the grout pressure during its installation.

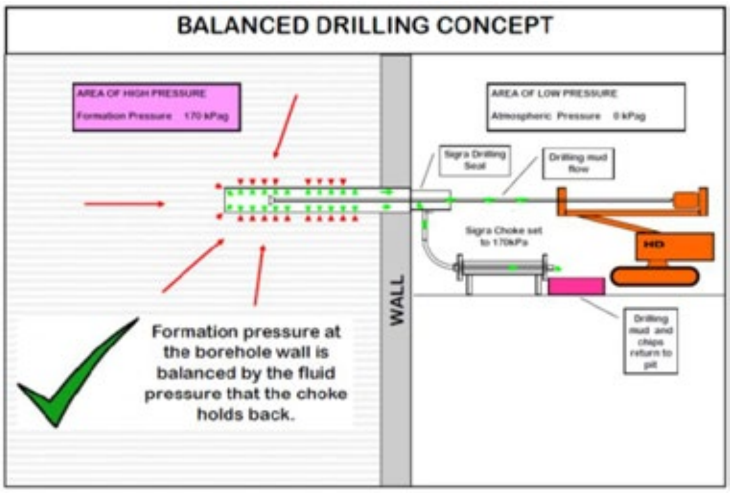

Figure 10 – Pressurised Drilling System Schematics, courtesy of Sigra Lt

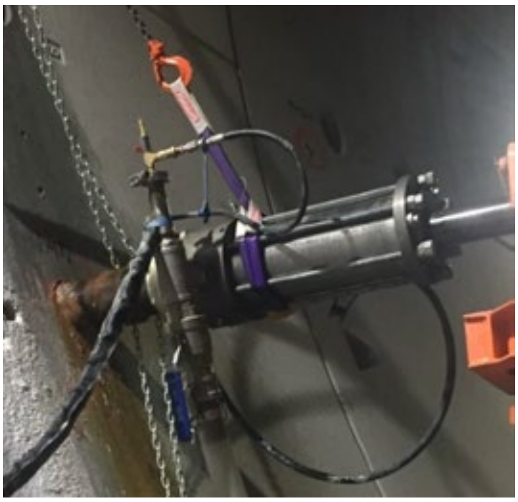

Plate 5 – Blow out Preventor

Blow out preventors are usually only used in specific drilling applications, and therefore, most drilling staff needs to be thoroughly briefed on how to use the equipment to ensure proper utilization and minimize wear and tear. It was specified that the system would be used for all drilling holes of all CPs, which proved to be counterproductive. When used in Grade III/II rock the Blow Out Preventor was not really required since the risk of drillhole collapse was minimum and water inflow was manageable. Therefore, using the equipment in these geological conditions led to improper use and an underappreciation of the equipment's capability. Since maintaining the pressure was not required for stability, the choke was being continually balanced as it benefited production. Afterwards when the drilling progressed to the Grade V Tuff the habit of continually balance the choke pressure was carried on. This behavior watered down the drilling fluid, bentonite, causing drillhole collapses, which would have been avoided with proper use. Stricter quality controls were required, as well as re-training staff regarding the proper use of the Blow Out Preventor.

4.2 Alignment Tool

Correctly setting up the accurate dip and azimuth for each drillhole prior to drilling is increasingly challenging underground. Normally this process is conducted by a surveyor with a total station, a process that can take up to 90 minutes, and that can create extensive standing time whilst the drilling team waits for the survey team to be mobilized. A proprietary system, which was developed for underground mining exploration in Australia, known as the Azimuth Aligner™, Plate 6 and Plate 7, was used in this project.

Plate 6 – Aligner unit, clamped to leading drill rod

Plate 7 – Azimuth Aligner Readout Unit

The unit is clamped to the lead rod and provides a real time readout of the current dip and azimuth whilst providing the closure distance to the planned / design dip and azimuth. This works by measuring the divergence of a laser beam by background magnetism and unaffected by ferrous objects. On site this was used for the alignment of the core barrel for concrete coring and for the alignment of the drilling rig. The tool provided accuracy to 0.2°, which equated to 60mm at 15m length.

The use of this alignment tool was an innovation that proved to be a very reliable and effective with the advantage of allowing for periodic checks in case the drilling mast is pulled out of line for any reason.

5 CROSS PASSAGE TREATMENT PERFORMANCE REVIEW

5.1 Grouting Cartography

The Grouting Cartography is a Visual Management Tool, which was implemented to track the grouting progress, ensure a proper grouting strategy, and guarantee the performance of the grouting treatment, see Figure 11. The Grouting Cartography consists of spatial mapping of the treatment zone displaying the intake of grout and grouting pressure achieved at each grouting stage. The grouting cartographies supported the technical decisions and were reviewed on a bi-monthly basis. Firstly, they were used to define the re-grouting strategy, e.g. where the grout intake and / or pressure were not satisfactory. For example, the zones in which the manchettes did not achieved a minimum of 2.5 bars were re-grouted. Secondly, the cartographies were key to decide when to transition from the Microfine Cement Stage to the Chemical grout. When it could be observed that the MFC already filled in the voids and increases of pressure did not result in further intake it meant that the treatment could be switched to the next stage with the Chemical Grout. Finally, the grouting cartography was also used to monitor the grouting performance in zones where drillholes had recorded non-compliant deviations. The grout intake of adjacent holes would be reviewed and re-assessed to ensure that the volume of soil to be treated could be achieved despite the deviations.

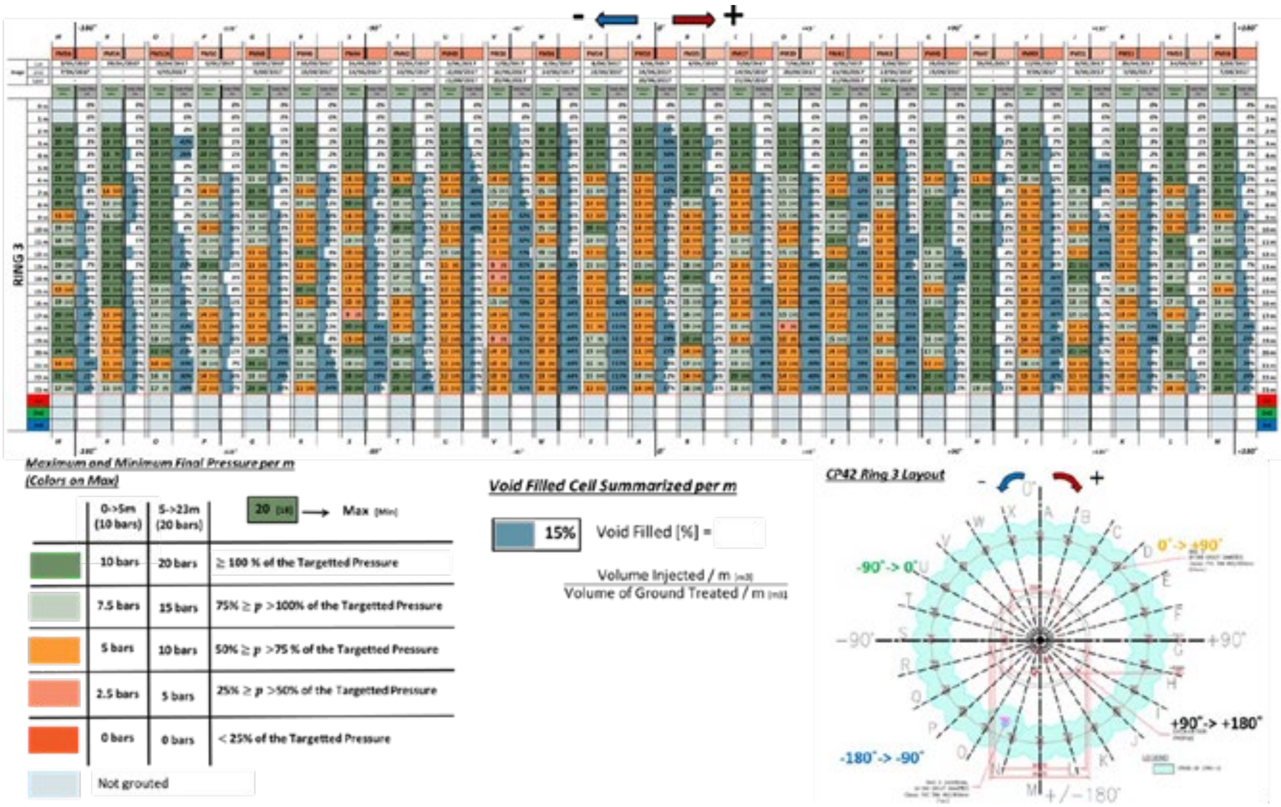

Figure 11 – Chemical Grouting Cartography CP42 Ring 3

5.2 Drillhole Deviation and 3D Model

All the drillholes were surveyed after TAM installation using a Reflex Gyro™ system. The Gyro™ has an integrated GPS based compass, unaffected by magnetic interference, which measured azimuth and dip at 1.0m intervals. After analysing the data from 169 surveys it was observed that the trend of deviation showed a downward fall to the right-hand side most likely due to gravity and the rotational bias of the tricone drill bit (clockwise direction). This can be explained by the weight of the non-return valve and the leading rod, which causes the drill string to sit on the invert of the borehole, and the anulus gap between the drill bit and the leading rod. Based on this data the theoretical position of the drillholes was adjusted to terminate 200mm above their previous position so that some of the drilling deviations impact could be minimized. While the trend was expected the magnitude of the deviation was unknown and therefore could only be corrected once there was enough data to support it.

At tender stage the deviation criteria were 2% for drillholes and 1% for canopy tubes. While these are generally achievable when drilling sub horizontal drillholes in homogeneous soil the varying strength and deformability characteristics of the residual soil found at CP42 exacerbated the drilling deviations. Special consideration for the heterogeneous nature of the soil should have been exercised and the deviation criteria re-accessed. The data showed that 22%, 42%, 51% and 58% of the drillholes at CP42 were out of tolerance respectively at 5m, 10m, 15m and 20m length. To ensure that the drilling deviations recorded did not impact the effectiveness of the ground treatment a 3D model with the respective as-built coordinated was created. In Figure 12 the design drillholes are shown in grey while the as built drillholes are shown in red.

The theoretical grout penetration, as detailed in Point 2 above, was then centered along the as built drilling alignment in order to determine possible gaps to the 3m ground treatment envelope, Figure 13 and Figure 14. Gaps in the ground treatment were either corrected by adding additional drillholes with associated grouting or increasing the volume stop criteria, discussed in Point 5.1.

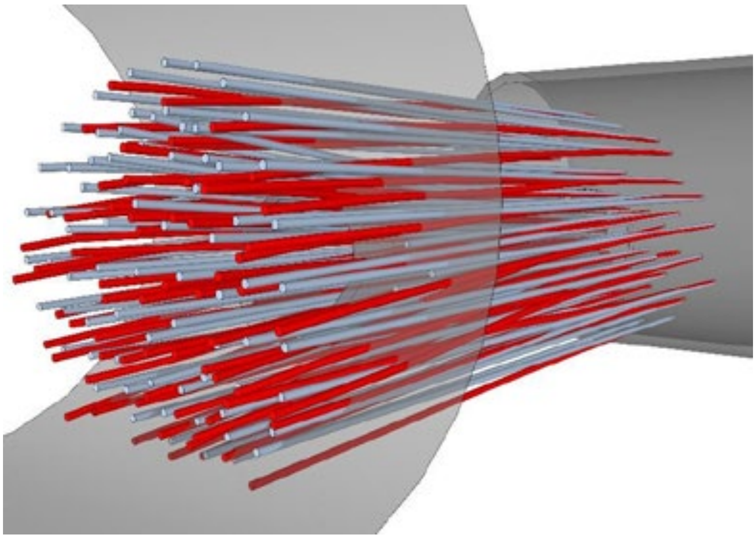

Figure 12 – Drillholes Alignment: Design, grey, vs As Built, red

Figure 13 – Stage 1 and 2 Design vs As-build Treatment Envelopes

Using CP42 as an example a total number of 11 additional drillholes, 7 in Stage 2 and 4 in Stage 3, were added to compensate for the recorded deviations and maintain an effective ground treatment envelope. There was a considerable improvement in the magnitude of deviations when comparing the early stages with the later ones.

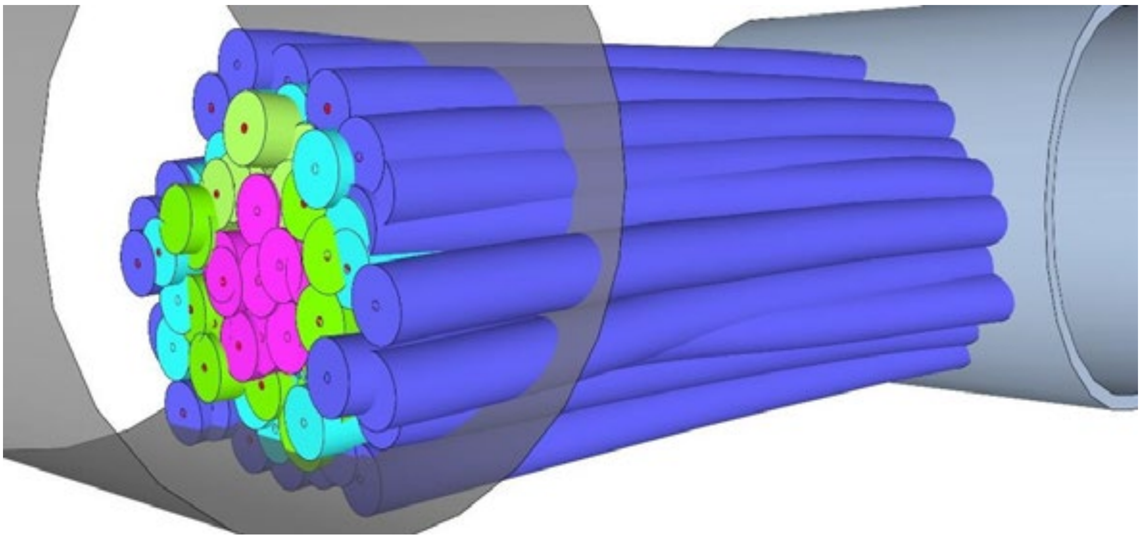

Figure 14 – Theoretical Ground Treatment Envelope, Adjusted with drilling As Built Information

5.3 Verification Drill Holes and Cross Passage Excavation

Probing was conducted in CP42 prior to the start of production drilling. Drillhole PB01 was drilled on the 19th of September 2016 and recorded 60.33 l/min across its 21m length.

Upon completion of the ground treatment at CP42 a total of 4 no. post grouting probes were drilled, orientated to terminate within the grouted envelope. CTR-001 to CTR-004 were drilled on the 23rd & 24th of June 2017 with a length of 15m each. The recorded inflow is summarised in Table 2.

Table 2: Recorded Inflow in both Pre-Treatment and Post-Treatment Probes

	Probing	Post-Treatment Confirmation			
DH ID	PB-01	CTR-001	CTR-002	CTR-003	CTR-004
Flow (l/min)	60.33 (43.09)*	0.15	0.19	0.22	0.21

* Pro-rata flow at 15m length

From Table 2 the expected groundwater inflow to the excavation was greatly reduced due to the ground treatment. The post grouting probes were used to determine the acceptability of the ground treatment by both the main contractor and its designer.

The excavation progressed in a dry and stable manner, Plate 8 and Plate 10, and without additional grouting being required. Plate 9 shows an excavated grouted soil block where it is visible that the Microfine cement penetrated through the sleeve grout. Lattice girders and shotcrete were used as the primary lining of the Cross Passages and was placed during the excavation as planned and prior to the permanent structural lining, Plate 11. The ground treatment allowed for an efficient excavation that was able to meet the planned programme and without adverse impact, e.g. water drawdown outside the CP.

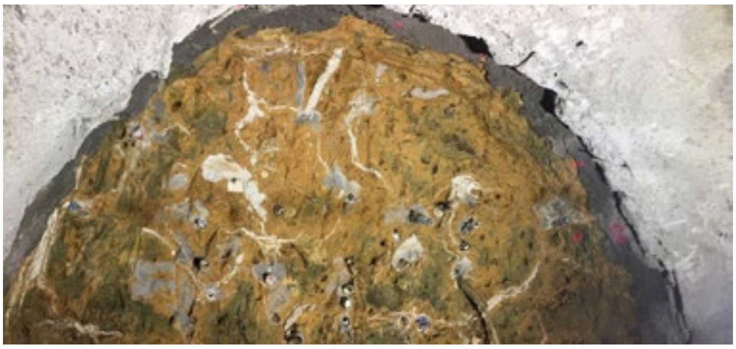

Plate 8 – CP Excavation within the "Tube" and prior to the "Plug"

Plate 9 – Treated Excavated Soil Block

Plate 10 – Cross Passage Excavation (View from Permanent Opening

Plate 11 – Cross Passage with Permanent Structural Lining

6 CONCLUSIONS

The observational approach used when designing the 3.0m thick grouting envelope to the CP's allowed the design to be flexible and efficient. When changes where encountered, e.g. grout intake, drilling deviations, the design was able to adapt and remain efficient. The ground conditions required the permeation grouting to be divided into two stages, with a first stage with Microfine Cement and the second with Chemical Grout. This ground treatment solution was more favorable in terms of programme and cost when comparing to typical solutions adopted in similar ground conditions, e.g. ground freezing and jet grouting from the surface. The 3D model and the Grouting Cartography were paramount to the review and implementation of the ground treatment.

The as-built survey of the drillholes using the Reflex Gyro™ system revealed the magnitude of the deviation, which exhibited a downward fall to the right-hand side trend. The ground treatment design was then adjusted to compensate for this deviation. To ensure that the recorded drilling deviations did not impact the effectiveness of the ground treatment a 3D model with the respective as-built coordinates was created. Where gaps on the ground treatment due to the deviation were considerable, additional drillholes with associated grouting were specified. For CP42 a total of 11 additional drillholes were specified to compensate for the recorded deviations. When these gaps were marginal the volume stop criteria of adjacent holes was adjusted to ensure the grout treatment was sufficient.

The grouting progress was tracked using the Grouting Cartography, which consists of the special mapping of the treatment zones displaying intake of grout and pressure. The Grouting Cartography was reviewed bi-monthly and was used to define where to re-grout, when to transition from Microfine Cement to Chemical grouting and if minor deviations could be compensated by increasing the intake at adjacent drillholes.

The Pressure Balance Drilling tool, Blow Out Preventor, helped minimize drilling hole collapses, groundwater drawdown / inflow and washout and facilitated the installation of the TAM, pipes. However, the use of the BOP in less adverse soil conditions let to an improper use of the tool that required enhanced quality controls and staff training. It would have been preferable to specify the use of the tool only in soil or mixed soil conditions where it could bring the most value. The Azimuth Aligner proved to be a very reliable and effective tool specially to set out the drilling positions from inside the tunnel. When compared to the traditional process of setting out with a surveying team the alignment tool greatly minimized standing times and allowed for period checks to ensure the dip and azimuth were maintained.

A total of 4 no. post grouting probes were drilled upon completion of the ground treatment at CP42, which were orientated to terminate within the grouted envelope. The maximum recorded inflow was 0.22 l/min, testament to the effectiveness of the ground treatment when compared with the initial inflow of 43.09 l/min. The excavation of CP42 progressed in dry and stable manner until completion, which allowed the main contractor to meet the planned programme of works, with no adverse impact.

REFERENCES

Littlejohn, G.S., 1985. Chemical grouting. Ground Engineering, 18, Part1, No. 2, 13–18; Part2, No. 3, 23–28; Part3, No. 4, 29–34

Rawlings, C.G., Hellawell, E.E., Kilkenny, W.M., 2000, Grouting for Ground Engineering: C514, Construction Industry Research & Information Association

Wall-Soil Interaction Effects on Ground Movements Adjacent to Excavations

L W Wong
SMEC Asia Limited, Hong Kong, China

ABSTRACT

Accurate prediction of ground movements is essential for assessing the potential risk of damaging structures adjacent to deep excavations. Numerous studies have previously been conducted to estimate the magnitudes and the distributions of ground movements. However, the wall-soil interaction effects have not been fully explored. Particularly, the soft toe condition, the effects of vertical loading on walls and the effects of the excavation widths have seldom been discussed. Presented herein is a parametric study conducted to quantify the influence of wall movements on vertical ground movements. A case history of the excavation in soft ground in the Taipei basin is collected for the studies. The excavation was retained by diaphragm walls of 31.5 m in length. Six cases with excavation widths of 11.2 m and 41.2 m with and without soft toes have been analyzed. The non-linear Hardening-Soil with Small Strain constitutive soil model is adopted. The stiffness parameters for the HSS soil model are validated by comparing the results of analyses with the observed ground movements.

Keywords: Deep Excavation, Surface Settlement, Heave, Hardening Soil, Wall Settlement

1. INTRODUCTION

Estimation of ground movements induced by excavation has been a challenging task for geotechnical engineers, particularly if the settlement of the retaining wall is to play a vital role. In the old days, excavations were generally shallow, say, up to 30 m in depth, so the retaining walls were rather stable and the settlements of walls were small. In recent years, as the demand for underground spaces keeps on growing, excavations tend to become deeper and deeper. For example, metro systems are being constructed in many major cities and excavations frequently exceed 30 m in depths for constructing stacked tunnels, river crossings and interchange stations and so on. As such, the settlements of retaining walls could have significant influences on ground movements and should be included in consideration in designs.

Retaining walls are dragged downward by the settling soils behind the walls and dragged upward by the heaving soil inside the pits. The interaction between the upward and the downward movements along both sides of the walls is rather complicated. As an excavation proceeds, the earth in the pit is removed stage by stage and the overburden pressures are reduced accordingly. As a result, the upward resistance on the inner face of the wall is reduced and the wall tends to settle. This is particularly true if the wall is used to support vertical loads such as those from the floor slabs of the top-down construction or ground anchors. In such cases, the settlements of the wall due to the vertical loads could be significant and should not be overlooked. Such complex soil-wall interaction effects can only be analyzed by using non-linear finite element methods.

To investigate the factors which affect the performance of retaining walls (i.e., diaphragm walls for deep excavations), hence, the ground movements, a parametric study has been conducted for this purpose and the results are presented herein.

2 CASE STUDIED

A hypothetical case resembling a section of the cut-and-cover tunnel in Taipei Metro was adopted as the subject of the study. The excavation was carried out by using the bottom-up method of construction to a depth of 16.5 m in 6 stages and was retained by diaphragm walls of 31.5 m in length and 0.8 m in thickness. A preliminary study on the case was previously reported in Wong and Hwang (2021) and the results of the supplemental analyses are available in an accompanying paper included in this volume of the proceedings (Wong 2022). Readers are encouraged to read these two papers to have a basic understanding of the case.

2.1 Ground conditions

The site is located in the T2 Geological Zone of the Taipei Basin. Figure 1 depicts the soil strata at the sites and the excavation scheme. The Songshan Formation at the surface comprises six alternating sand (SM) and clay (CL) layers. Sublayers I, III and V are sandy soils with the N values increasing from 5 at 6 m depth to 30 at 44 m depth. Sublayers II, IV and VI are clayey soils. Due to extraction of groundwater in the underlying gravelly Jingmei Formation, significant reduction in water pressures in Songshan Formation and substantial ground settlements as a results. The piezomteric levels in the Jingmei Formation did not recover until mid-1790s. The subsoils in the Songshan Formation in the Taipei Basin are substantially over-consolidated. The hardening soil model with small strain is adopted to simulate the non-linear relationship between stresses and strains of soils. Readers are urged to read Wong (2022) for soil properties and groundwater conditions.

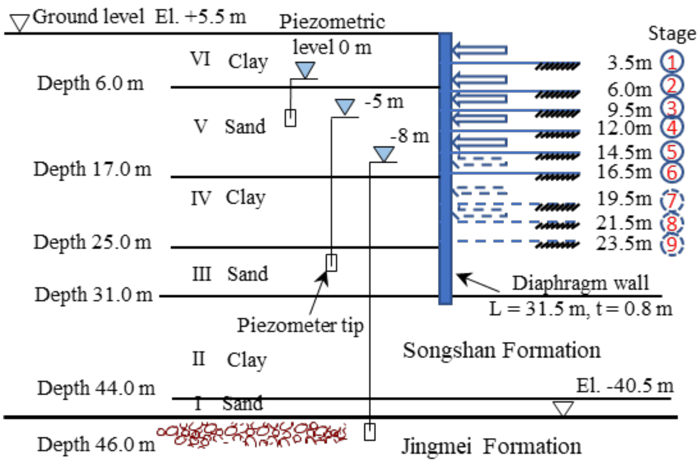

Figure 1: Soil profile of the Cross-over tunnel and excavation scheme

2.2 Parameters studied

As depicted in Table 1, numerical analyses were carried out for 6 cases to study the influences of the toe condition, loading on the wall, and the width of the pit on wall settlements and ground movements. It is a well-known fact that sludge at the bottoms of bored piles is difficult to be completely removed and is likely to reduce the tip resistance of the piles upon loading. This is the so-called soft-toe condition.

Table 1: Scenarios analyzed

Scenario	Wall length L, m	Excavation width, B, m	Toe stiffness E_{ref-50}, MPa	Toe condition	Vertical load on wall, P_v, kN/m
Case 1	31.5	11.2	13.4	Normal toe	0
Case 2	31.5	11.2	0.134	Soft toe	0
Case 3	31.5	11.2	13.4	Normal toe	63
Case 4	31.5	11.2	0.134	Soft toe	63
Case 5	31.5	11.2	13.4	Normal toe	160
Case 6	31.5	41.2	13.4	Normal toe	0

Diaphragm walls are, in a sense, rectangular bored piles and would be in the same situation. In fact, barrettes, installed by using the diaphragm walling technique, are frequently adopted as foundation piles. Therefore, it is reasonable to expect that the tip resistance at the diaphragm wall toes will be minimal. Cases 1 and 2 simulate the conditions of the walls without and with soft toes. Case 1 is the benchmark case for comparison with the rest of the cases. Cases 3 to 5 are conducted to evaluate the effects of vertical loads on the walls without and with soft toes, and Case 6 is conducted to evaluate the effects of the width of the pit on the ground movement.

2.3 Finite element model

The finite element mesh for the excavation cases with a wall length of 31.5 is presented in Figure 2. Readers are urged to read Wong (2022) for the structural properties of the wall and the steel struts. Although the excavation was carried out to a depth of only 16.5m in 6 stages, analyses were conducted to a depth of 23.5m by adding 3 more stages to investigate the stability of the wall if the excavation were continued.

Since the underlying gravelly Jingmei Formation is very stiff and can be assumed as the competent formation with minimal ground movements, conventionally, the bottom of finite element models is placed at the top of the Jingmei formation. However, a Jingmei Formation layer of 15 m in thickness is included in this study to account for some of the contribution from this formation to the ground movements.

The wall is simulated by a plate element that has the zero thickness and by soil clusters of 0.4 m in width on both sides of the wall to achieve the wall thickness of 0.8 m. The soft toe condition for Cases 2 and 4 is simulated by a soil cluster of 0.8 m in width and in thickness at the depths between 31.5 m and 32.3 m. The stiffness for the soft toe is taken as 1/100 of that for the surrounding soil stratum to see if it makes differences.

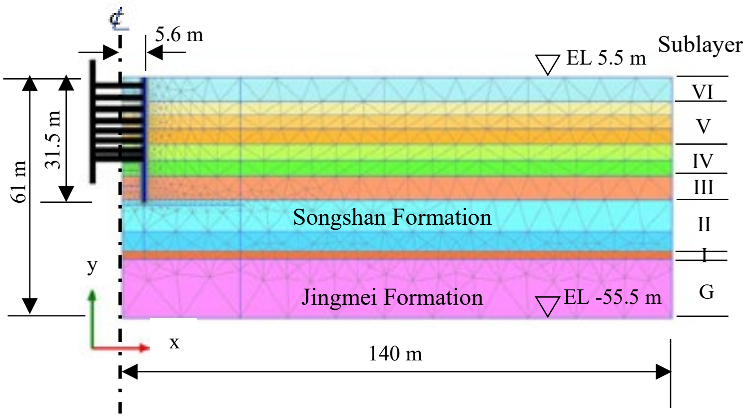

Figure 2: Finite element mesh for Cases 1 to 5

3 LATERAL WALL DEFLECTIONS AND SURFACE SETTLEMENTS

The computed wall deflections and ground settlements for the various stages of excavations in Case 1 and Case 6 are presented in Figure 3 and Figure 4 respectively. As the wall toe is located at 31.5 m depth, the portions of the profiles above the toe level are wall deflection profiles and those below the toe level are horizontal ground movement profiles. The graphic presentations of the results obtained in Cases 2 to 5 are similar to those for Case 1 and are thus omitted. Instead, the maximum movements are given in Table 2.

3.1 Effects of depth of excavation

As can be noted, there is a general trend that the deeper the excavation, the larger wall deflections and ground settlements would be. The wall deflections and surface settlements for Case 1 and Case 3 are similar to each other at the excavation depths all the way down to 23.5 m. Table 2 summarized the computed maximum wall deflections and maximum surface settlements for the excavation depths of 16.5 m and 23.5 m.

As can be noted, as the depths of excavation increase from 16.5 m to 23.5 m, the maximum wall deflections increase from 33.1 mm to 35.3 mm, or roughly by 6.6 %, and the maximum settlements increase from 22.9 mm to 29.1 mm, or roughly by 27 %. The percentages of increases are of similar magnitudes in the other 3 cases. It appears that the surface settlements are more sensitive to the increase in the depth of excavation than wall deflections. This means, the ratios between the maximum surface settlement and the maximum wall deflection are not constant, but increase as the excavation depths increase. Take Case 1 as an example, this ratio is 22.9/33.1= 69 % for a depth of excavation of 16.5 m and increases to 83 % for a depth of excavation of 23.5 m.

Table 2 shows that differences in wall deflections and surface settlements are insignificant between Case 1 and Cases 2 to 5. For the cases with normal toes and with soft toes, and for the cases with the vertical loads on wall varying from 63 kN/m to 160 kN/m, the wall deflections are virtually the same. The differences in surface settlements are negligible, within 1 mm for the cases with and without vertical loads.

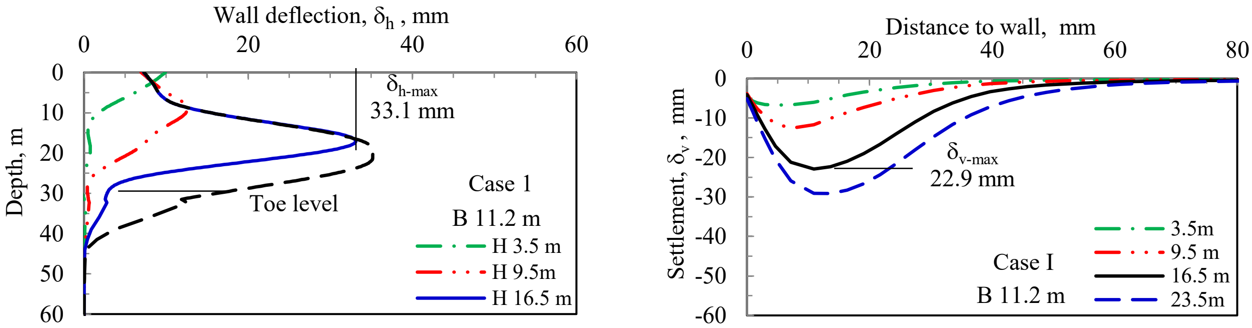

Figure 3: Computed wall deflections and surface settlements for Case 1

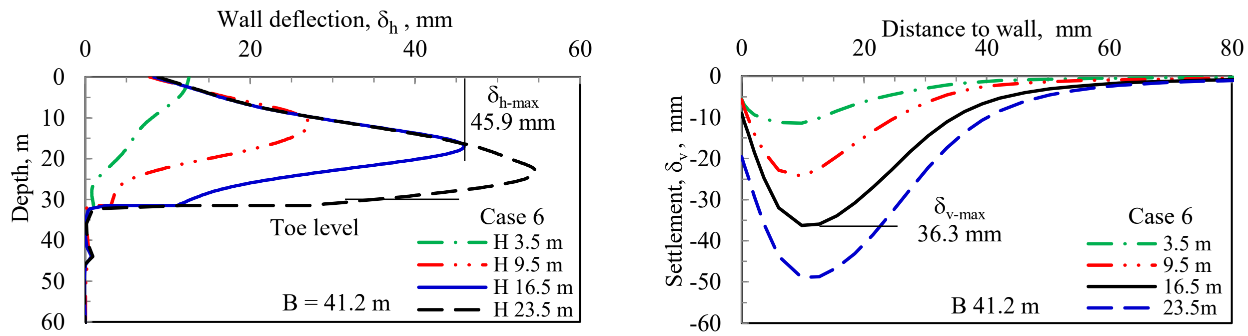

Figure 4: Computed wall deflections and surface settlements for Case 6

Table 2: Computed wall and ground movements for the excavation depths 16.5 m and 23.5 m

Studied Case	Vertical load on wall, P_v, kN/m	Excava-tion width B, m	Toe condition	Excava-tion depth, H m	Maximum deflection		Maximum settlement	
					Wall deflection $\delta_{h\text{-max}}$, mm	Incre-ment %	Surface settlement $\delta_{v\text{-max}}$, mm	Incre-ment %
Case 1	0	11.2	Normal	16.5 23.5	33.1 35.3	6.6	22.9 29.1	27
Case 2	0	11.2	Soft	16.5 23.5	33.2 35.3	6.5	23.2 29.6	28
Case 3	63	11.2	Normal	16.5 23.5	33.1 35.2	6.6	23.2 29.5	27
Case 4	63	11.2	Soft	16.5 23.5	33.1 35.3	6.6	23.4 30.0	28
Case 5	160	11.2	Normal	16.5 23.5	33.1 35.3	6.4	23.4 29.9	27
Case 6	0	41.2	Normal	16.5 23.5	45.9 54.6	18.9	36.3 48.9	35

3.2 Effects of excavation width

Larger excavation widths would likely cause larger wall deflections and surface settlements. The comparison between Figures 3 and 4 shows that for the wider excavation in Case 6, the computed maximum wall deflection for the excavation depth of 16.5 m is 45.9 mm, which is 39 % larger than the maximum wall deflection of 33.1 mm for the narrower excavation in Case 1. Similarly, the maximum surface settlement for Case 6 is 36.3 mm, which is 59 % larger than the maximum wall deflection of 22.9 mm obtained in Case 1.

Table 3 summarizes the maximum wall deflections near the excavation levels, the toe deflections at 31.0 m and at 31.5 m depths and the horizontal ground movements occurring at 32.3 m depth for Case 1 and Case 6. It can be noted that the wall deflections for Case 6 above the toe level for various excavation depths are larger than those for Case 1. The ratio in maximum deflections between Case 6 and Case 1 is 1.39 for the excavation depth of 16.5 m. The toe deflections occurring at 31.5 m depth are identical between Case 1 and Case 6.

The trend for the wider excavation to cause larger wall deflection reverses for the horizontal ground movements beneath the wall toe. Table 3 summarizes that the lateral ground movements occurring at 0.8 m below the toe level are 0.6 mm for the excavation depth of 16.5 m for Case 6, which is less than the value of 2.8 mm for Case 1. For the excavation depth of 23.5 m, the lateral ground movement at that depth for Case 6 is 1.2 mm, which is less than 12.5 mm for that of Case 1. The ratios in ground deflection at that depth between Case 6 and Case 1 vary from 0.1 to 0.2 for the excavation depths larger than 16.5 m.

The normal trend of the wider excavation width resulting in larger wall deflection could be partially attributable to the stiffness of the propping system, which uses the elastic steel struts as the primary lateral supports. The reverse trend in ground movements below the wall toe level could be attributed to the nonlinearity of soil. With the wider excavation width, the ground would be in smaller strain levels and the soil stiffnesses would be larger. As a result, less ground movements would occur in Case 6 than those in Case 1.

Table 3: Horizontal wall and ground movements along the wall for Case 1 and Case 6

Scenario	Excavation depth H, m	Wall deflection, mm			Ground deflection, mm	Ratio of Case 6/Case 1	
		Maximum	0.5 m above toe level	At toe level	0.8 m below toe level (at 32.3 m depth)	Maximum deflection	0.8 m below toe
Case 1	16.5	33.1	2.8	2.6	2.8	-	-
	23.5	35.3	13.4	11.9	12.5	-	-
Case 6	16.5	45.9	11.7	2.6	0.6	1.39	0.21
	23.5	54.6	29.8	11.9	1.2	1.55	0.10

4 WALL SETTLEMENTS

4.1 Soft toe effects

The settlements of the walls in Case 1 to Case 6 are summarized in Table 4 and depicted in Figure 5. For excavation depths down to 23.5 m, the settlements at wall tops would be 4.6 mm and 5.8 mm for the walls without (Case 1) and with soft toes (Case 2) respectively. The soft toe condition would increase the settlements of the walls by only 1.2 mm.

4.2 Effects of vertical loading on wall settlements

To study how vertical loads on diaphragm walls would affect the settlements of the wall and the ground, analyses were conducted in Cases 3 to 5. Ideally, loads should be applied stage by stage to account for the vertical components of strut loads and loads from superstructures, if any. However, such a process would raise numerous questions regarding how the magnitudes of loads are determined and how the loads should be applied. Since this is a qualitative study, the unnecessary complication will cause confusion and defeat the purpose of the study. For simplicity, in the finite element models for Case 3 (with normal toe) and Case 4 (with soft toe), a vertical load, P_v, of 63 kN/m is applied along the entire length of the wall to simulate the loads from 5 levels of struts and waling and 10 kPa from the traffic deck for the bottom-up construction. In Case 5, this vertical load is increased to 160 kN/m to account for the weight of 5 levels of concrete slabs of 0.25 m in thickness, supported on king posts of 8 m span aligned along the transverse direction in top-down constructions and loads of 10 kPa on the uppermost slab. The toe stiffnesses and the loads applied for Case 3 to Case 5 are summarized in Table 1.

Table 4: Wall settlements for the excavation depths of 16.5 m and 23.5 m

Scenario	Excavation width, B, m	Toe condition	Vertical load on wall, P_v, kN/m	Excavation depth, H, m	Wall settlement, mm		Wall shortening, mm
					Wall top	Wall toe	
Case 1	11.2	Normal	0	16.5	-3.5	-2.8	0.7
				23.5	-4.6	-3.6	1.0
Case 2	11.2	Soft	0	16.5	-4.0	-3.4	0.7
				23.5	-5.8	-4.8	1.0
Case 3	11.2	Normal	63	16.5	-4.6	-3.8	0.8
				23.5	-6.3	-5.2	1.1
Case 4	11.2	Soft	63	16.5	-5.2	-4.4	0.8
				23.5	-7.5	-6.5	1.0
Case 5	11.2	Normal	160	16.5	-5.3	-4.5	0.6
				23.5	-7.4	-6.3	1.1
Case 6	41.2	Normal	0	16.5	-8.3	-7.5	0.8
				23.5	-19.0	-18.1	0.9

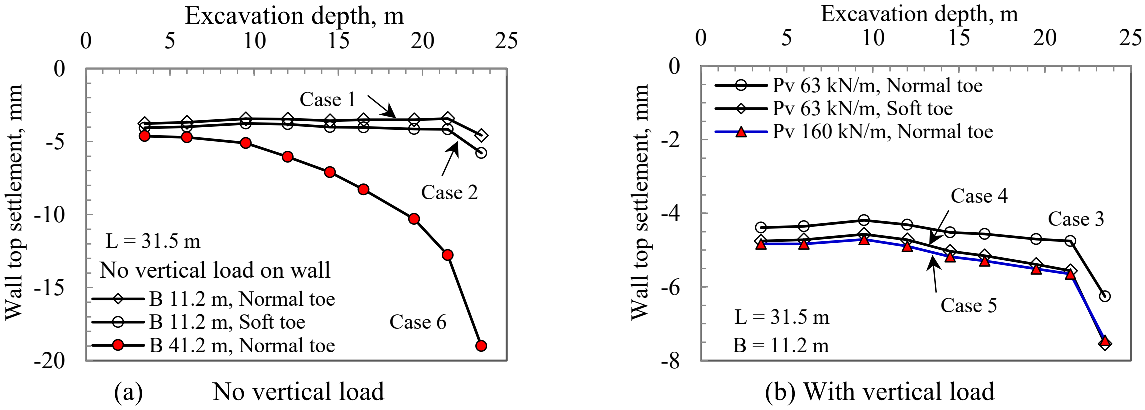

Figure 5: Computed wall settlements for cases with and without vertical loads

As can be noted from Figure 5 and Table 4, the computed settlements of the wall top for a depth of excavation of 16.5 m are 3.5 mm in Case 1, 4.6 mm in Case 3, 5.3 mm in Case 5 and 8.3 mm in Case 6. It can also be noted in Figure 5(b) that the performance of Case 4 with soft toe would be similar to that for Case 5 with normal toe. The difference in the wall settlements between Case 4 and Case 5 is within 0.2 mm.

4.3 Effects of excavation width

The settlements of the wall top obtained in Case 6 with an excavation width of 41.2 m are presented in Figure 5(a) and compared with those obtained in Cases 1 to 4 in Table 4. Compared with those cases having a width of excavation of 11.2 m, larger wall settlements would occur with a larger excavation width. At the excavation depth of 23.5 m, the settlement of the wall top would be as large as 19.0 mm, which is 4 times that of the case with the excavation width of 11.2 m.

The larger settlements at the wall top for larger excavation width for Case 6 could be caused by less earth pressures acting along the wall. Figure 6 presents the effective normal stress acting on the active and the passive sides of the wall for Case 1 and Case 6 for the excavation depths of 16.5 m and 23.5 m. At the depths between 25 m and the toe of 31.5 m, where the wall is embedded in the sandy sublayer III, the effective normal stresses developed in Case 6 are less than those developed in Case 1.

Figure 7 presents the shear stresses mobilized on both sides of the wall and the axial loads along the wall. Figure 7(a) shows that there is not much difference in shear stresses between Case 1 and Case 6 for the excavation depth of 16.5 m. Figure 7(b) however shows that the shear stresses mobilized on the passive side of the wall in Case 1 would be larger than those in Case 6 for the excavation depth of 23.5 m.

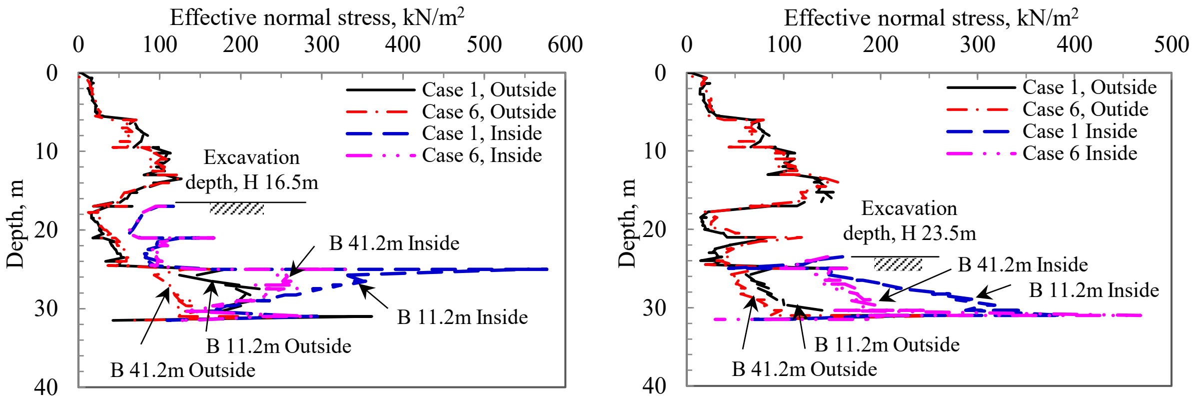

(a) Excavation depth 16.5 m (b) Excavation depth 23.5 m

Figure 6: Effective normal stresses on the active and the passive sides of wall for Case 1 and Case 6

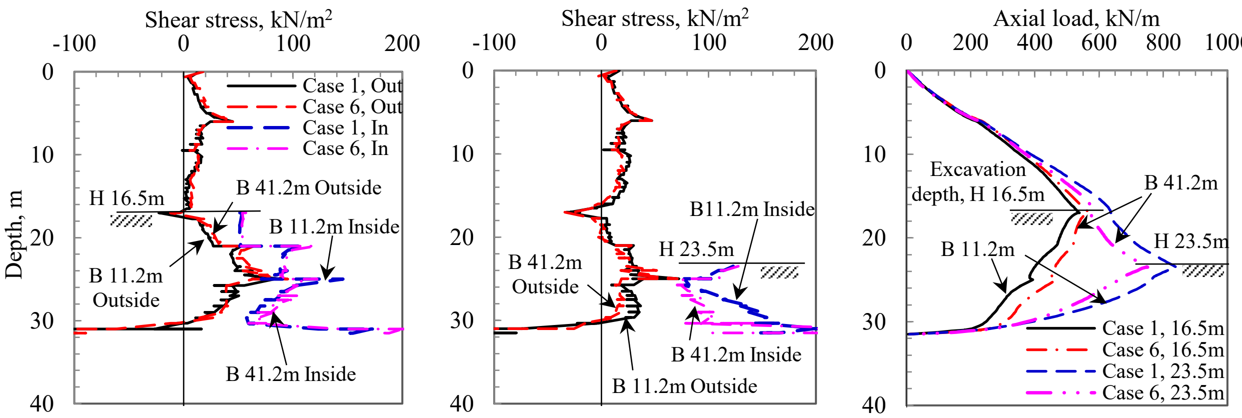

(a) Excavation depth 16.5 m (b) Excavation depth 23.5 m (c) Axial load along wall

Figure 7: Shear stresses on both sides of the wall and axial load along the wall for Case 1 and Case 6

Table 5: Mobilization of wall toe resistances for Case 1 and Case 6

Scenario	Excavation dimension, m		Axial force on wall kN/m		Ratio of axial force between Case 6 & Case 1		Wall toe settlement mm
	Width, B	Depth, H	Maximum	At toe	Maximum	At toe	
Case 1	11.2	16.5	539.0	6.4	-	-	-2.8
		23.5	841.2	10.4	-	-	-3.6
Case 6	41.2	16.5	570.5	11.1	1.06	1.73	-7.5
		23.5	751.4	27.4	0.89	2.63	-18.1

The downward wall movements, as those summarized in Table 4, would mobilize the base resistance at the wall toe. Figure 7(c) presents the variation of the axial loads on the wall with depth. The axial load profiles show that the maximum axial loads occur at the excavation depths. This load-transfer distribution indicates that the shearing stresses acting on the active side induce the negative skin friction (NSF) along the wall. That NSF is counter-reacted by the positive skin friction on the passive side of the wall below the excavation level.

Table 5 summarized the maximum axial loads acting along the wall and those transferred to the toe for Case 1 and Case 6. Compared with Case 1, the axial load at the wall toe for Case 6 increases by 82 %, from 6.4 kN/m to 11.1 kN/m for the excavation depth of 16.5 m. The toe settlement of 7.5 mm is required to mobilize the toe resistance of 11.1 kN/m. Similarly, for the excavation depth of 23.5 m, the toe settlement of 18.1 mm would be required to mobilize the toe resistance of 27.4 kN/m. For excavations with large widths and large depths, it would be prudent to monitor wall settlements.

4.4 Case history on monitoring of wall settlements

Monitoring on wall settlements was conducted for metro station BL16 of the Nangang Line located at the eastern rim of the Taipei Basin (Chen et al.1999). The site is located in the K1 Geological Zone of the Taipei Basin and the pit was retained by diaphragm walls of 1 m in thickness and 31.5 m in length. Due to the poor ground conditions, concrete cross-wall panels of 1 m in thickness, 3 m in depth, and spacing at 5 m were installed beneath the final excavation level to reduce wall deflections and ground movements. It was thus able to limit the maximum wall deflection to 25 mm as the final excavation depth of 15.2 m was reached.

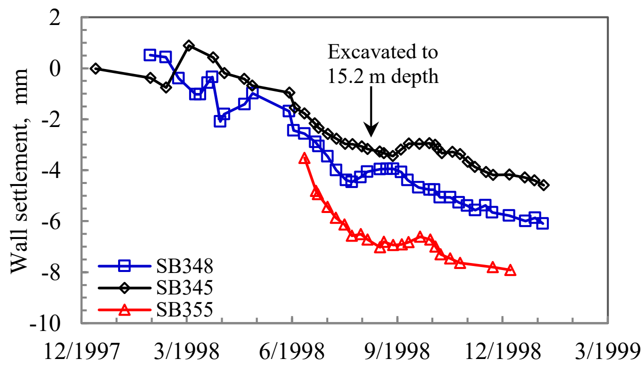

Figure 8: Wall settlement observed at Station BL16 (after Chen et al. 1999)

Figure 8 shows that the settlements recorded by 3 settlement markers installed on the wall top ranged from 3 mm to 7 mm in the final excavation stage and increased to 5 mm to 8 mm in the backfilling stage. As summarized in Table 4, the computed settlement at the wall top for Case 1 at the excavation depth of 16.5 m is 3.5 mm without soft toe. For Case 2 with soft toe, the wall top settlement at the excavation depth of 16.5 m is 4.0 mm. The computed wall top movements are in agreement with those observed in the case history of Station BL16. The prolonged wall settlements would likely be caused by the consolidation of soft clay in the Songshan Formation due to the lowering of the groundwater table.

The width of excavation for Station BL16 is approximately 25 m. Interpolating the results obtained in Case 3 and Case 6, refer to Table 4, the settlement of the wall top for an interpolated excavation width of 26.5 m with traffic deck would be around (4.6 + 8.3)/2 = 6.5 mm. As shown in Figure 8, this interpolated wall top settlement is consistent with the values ranging from 3.2 mm to 7.0 mm recorded by the 3 settlement markers at Station BL16. The consistency between the observed and computed wall settlements validates the results of the parametric studies.

5 HEAVE IN EXCAVATION TRENCH

5.1 Computed ground heaves for narrow excavation

Figure 9 presents the heaves induced along the central axis of the trench in Case 1 and Case 6. The computed results show that the maximum heave in each stage occurs at the corresponding excavation level. The heave zone propagates downward as excavation depths increase and diminishes at the base of the Songshan Formation, where the underlying gravelly Jingmei Formation has much larger stiffnesses than those for the sandy and clayey Songshan sublayers.

As shown in Figure 9(a) and summarized in Table 6, the maximum ground heave for the excavation width of 11.2 m (i.e., Case 1) would increase from 12.7 mm to 63.2 mm as the depths of excavation increase from 3.5 m to 23.5 m. It is interesting to note that, instead of heaving, the soils below a depth of 10 m actually settle in Stage 1 excavation to a depth of 3.5 m. The largest settlement in the trench is 3.3 mm, which is slightly less than the settlements of the wall of 3.8 mm. Essentially the soils sunk together with the walls due to the plugging effects because of the narrowness of the trench.

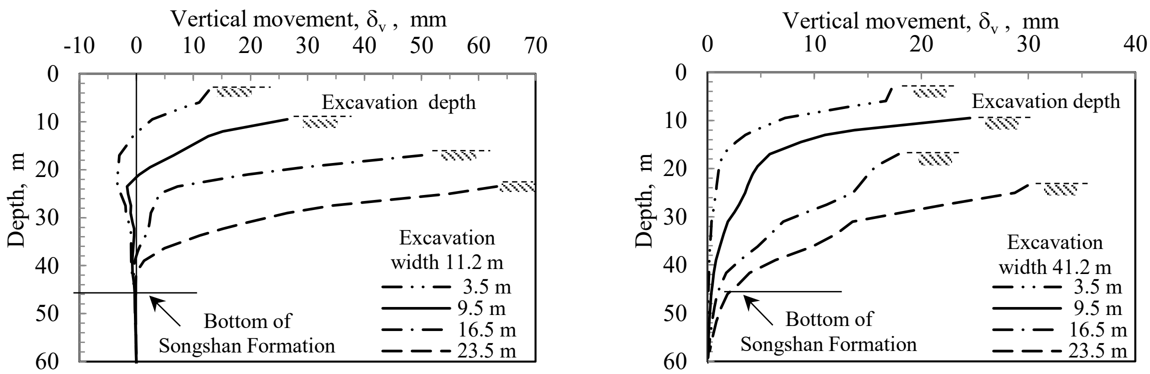

(a) Case 1 (b) Case 6

Figure 9: Profiles for heaves induced along the central axis of excavation for Case 1 and Case 6

Table 6: Computed heaves and settlements along the central axis and the wall

Studied Case	Excavation width, B, m	Excavation depth, H, m	Ground movement along axis, mm		Wall settlement, mm	
			Maximum heave	Maximum settlement	Top	toe
Case 1	11.2	3.5	12.7	-3.3	-3.8	-3.6
		9.5	26.5	-1.6	-3.5	-3.1
		16.5	50.1	-0.5	-3.5	-2.8
		23.5	63.2	-0.1	-4.6	-3.6
Case 6	41.2	3.5	17.2	0	-4.6	-4.3
		9.5	24.6	0	-5.1	-4.6
		16.5	17.9	0	-8.3	-7.5
		23.5	29.9	0	-19.0	-18.1

5.2 Computed ground heaves for wide excavation

It is envisaged that the plugging effects would diminish as the width of the trench increases. As depicted in Figure 9(b), the settlement does not occur along the axis of excavation in Case 6 with an excavation width of 41.2 m. Figure 9(b) shows that the maximum ground heave for the excavation width of 41.2 m (i.e., Case 6) would increase from 17.2 mm to 29.9 mm as the depths of excavation increase from 3.5 m to 23.5 m. For the excavation depths exceeding 16.5 m, the heaves along the axis for the wider Case 6 are 36 % (H = 16.5 m) to 47 % (H = 23.5 m) of those for the narrower excavation in Case 1.

5.3 Case history on monitoring of ground heaves

It is desirable to compare the results of analyses on ground heave inside the excavation trenches with field observations. However, the case histories on the ground heave inside the pits are rather limited. The cases on heaves subsequent to the end of excavation are even less. Nash et al. (1996) presented the observed heave profiles inside an excavation area in Gault Clay in the Cambridge area in London, UK. The over-consolidation Gault clay has the thickness of 40 m which overlies Lower Greensand, which is an aquifer at depth. Prior to excavation the initial pore pressures were about 7 mOD (metre above Ordnance Datum), which was 3 m below the ground level of 10 mOD. The excavation area was 65 m x 45 m in plan. The excavation was carried out to -0.5 mOD, giving a total depth of excavation of 10.5 m. The pit was retained by diaphragm walls of 17 m in length.

Extensometers were available at a distance of 5m from the centreline of the excavation area at depths ranging from 4 mOD to -25.1 mOD. The development of heaves in different stages of excavation is shown in Figure 10. As the excavation reached its final level of -0.5 mOD, a heave of 30 mm was recorded. Monitoring on pneumatic piezometers indicated that the piezometric levels were originally between +6 mOD and +7 mOD and dropped to around -7 mOD as the excavation reached the final level. The piezometric levels rose to -0.5 mOD in 4.8 years after casting the base slab. The extensometer monitoring showed that the ground heave continued as a result of swell of soils linearly against time (in a log scale), from 30 mm to 110 mm, during this 4.8-year period.

As can be noted from Figure 9(b), as the excavation reached a depth of 9.5 m in Stage 3 in Case 6, the heave computed was 24.6 mm, which is of a similar magnitude of 30 mm as that reported by Nash et al. (1996) for a depth of excavation of 10.5 m. Since the ground conditions at the two sites were quite different, it is unrealistic to expect the heaves to be of the same in magnitudes. Nevertheless, the similar tendency presented in Figure 9(b) and in Figure 10 is very encouraging and gives confidence to the validity of the numerical analyses.

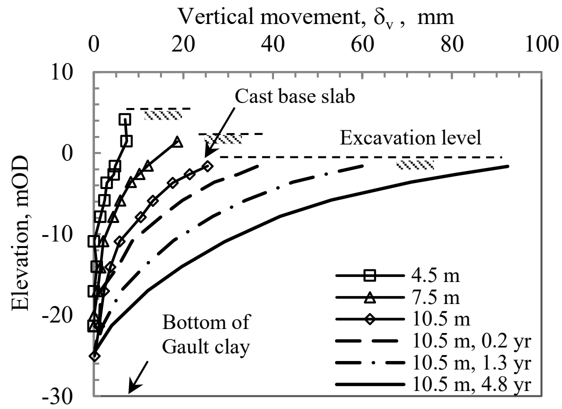

Figure 10: Heaves during excavation and subsequent heaves (Nash et al. 1996)

6. GROUND MOVEMENT IN HORIZONTAL SECTIONS

6.1 Ground movements in horizontal section for narrow excavation

The computed vertical ground movements in the horizontal sections at depths of 17 m and 24 m for Case 1 are shown in Figure 11 and summarized in Table 7. Comparing with the results for Case 2 summarized in Table 4, the largest differences in settlements between normal toe and soft toe for wall lengths of 31.5 is around 0.5 mm for the excavation depth of 16.5 m. The vertical movement profiles for Case 2 with soft toe are similar with those for Case 1 and are thus not shown for sake of clarify.

Table 7: Maximum vertical ground movements for Case 1 and Case 6

Studied case	Excavation area	Excavation depth, H, m	Maximum vertical movements, $\delta_{v\text{-}max}$ mm		Ratio of Case 1/Case 6	
			At 17 m depth	At 24 m depth	17 m depth	24 m depth
Case 1 B 11.2 m	Inside	16.5	50.2	5.7	-	-
		23.5	-	60.6	-	-
	Outside	16.5	-12.6	-3.5	-	-
		23.5	-21.2	-9.6	-	-
Case 6 B 41.2 m	Inside	16.5	30.5	14.0	0.61	2.46
		23.5	-	43.2	-	0.71
	Outside	16.5	-21.0	-8.4	1.67	2.40
		23.5	-38.7	-25.8	1.83	2.69

6.2 Ground movements in horizontal section for wide excavation

Case 6 has an excavation width of 41.2 m, which is larger than the wall length of 31.5 m. The computed vertical ground movements for Case 6 in the horizontal sections at depths of 17 m and 24 m are shown in Figure 12. In comparison with the vertical ground movement profiles for the narrow excavation in Case 1 shown in Figure 11, the wider excavation Case 6 would cause smaller heaves and larger settlements for the horizontal sections above the wall toe levels. Table 7 shows that at the excavation depth of 16.5 m, the computed heave occurring inside the excavation trench at the horizontal section of 17 m depth for Case 6 is 30.5 mm, which is 61 % of 50.2 mm for that in Case 1. At the excavation depths of 23.5 m, the computed heave inside the pit at the section of 24 m depth for Case 6 is 43.2 mm, which is 71 % of 60.6 mm for the heave for Case 1.

Outside the excavation trench, the settlements for the wider excavation Case 6 are larger than those with the narrower excavation in Case 1. For example, Table 7 shows that at the excavation depth of 16.5 m, the maximum settlement at the section of 17 m depth for Case 6 is 21.0 mm, which is 167 % of the settlement of 12.6 mm for Case 1. At the excavation depth of 23.5 m, the maximum settlement outside at the section of 24 m depth is 25.8 mm, which is 269 % of the settlement of 9.6 mm for the narrow Case 1. The finding that wider excavation would cause larger ground settlements outside and less heave inside the excavation trench in the final excavation is consistent with the common experience.

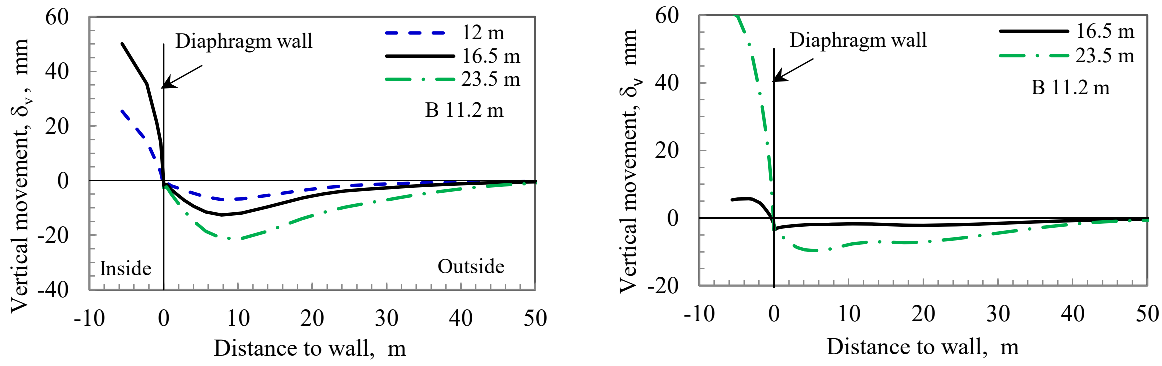

Figure 11: Vertical movements on the inner and the outer side of narrow excavation - Case 1

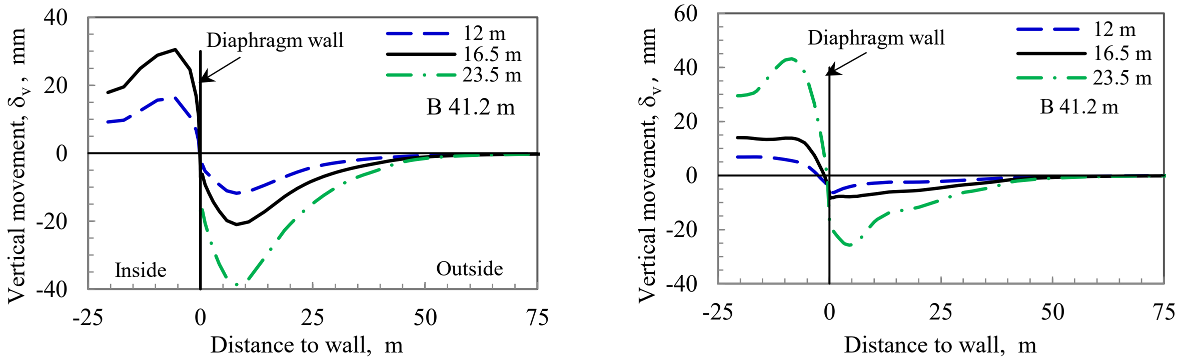

Figure 12: Vertical movements on the inner and the outer side of wide excavation - Case 6

6.3 Case history on monitoring of ground movements in horizontal section

Panchal et al. (2017) conducted a centrifuge modelling test on an underwater excavation case to study the relationship between the ground movements and basal heave below the final excavation level. The soil model comprised Speswhite kaolin clay mixed to a water content of 120 %. The excavation depth and the half-width for the prototype model were 12.0 m and 24 m respectively. The wall length was 20.8 m. The wall toe was 20 m above the base of the prototype model. The wall was deliberately very stiff, with a prototype stiffness equivalent to a 2.1 m thick concrete diaphragm wall. The LVDT and digital imaging were used to measure the ground displacements. Pore pressure transducers were embedded in the soil model on both sides of the wall.

The excavation was simulated by reducing air pressure of 202 kPa in a latex bag over a period of 3 minutes to simulate the excavation in 2 months. Measurements on displacements and pore pressures continued for a further 30 minutes, equivalent to 18 months at the prototype scale, after excavation to the observed long-term ground response. The test simulates the immediate and the long-term ground movements arising from unloading and soil softening respectively. As excavation proceeded, the 2 pore pressure transducers next to the wall on both sides recorded reduction in pore pressures. In the post-excavation stage, the negative pore pressures dissipated within 20 minutes.

Figure 13 shows the vertical ground movements on both sides of the wall in the horizontal section at the final formation level of 12 m in depth. Based on readings of the pore pressure transducers, the long-term changes in the vertical movements are a result of the dissipation of pore pressures. The trend of variations in ground heaves and settlements presented in Figures 11 and 12 is similar to that observed in the centrifuge tests presented in Figure 13.

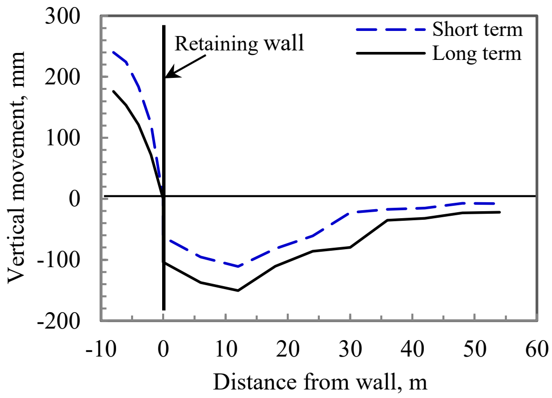

Figure 13: Vertical movement profiles obtained from centrifuge test (after Panchal et al. 2017)

7 CONCLUSIONS

Parametric studies have been conducted on excavations supported with diaphragm walls in soft ground with various excavation widths, wall toe stiffnesses and vertical loads on wall. The Hardening-Soil with small-strains stiffness is adopted for the constitutive soil model in the numerical analysis. The computed results have been verified with case histories on ground heaves and on wall settlements. The following conclusions could be drawn from the parametric studies:

(1) Narrower excavations would cause larger heave inside and smaller settlements outside the excavation trench than those occurring for wider excavations.
(2) Wider excavation width could cause lower in earth pressures acting on the passive side of the wall. The shear stresses along the wall on the passive side would then be less than those of the narrow excavations.
(3) The soft toe effects and the vertical loads on wall would be insignificant to wall deflections, ground settlements and to wall settlements.

Amongst the potential attributing factors evaluated in this study, the excavation width is the most dominant factor affecting the magnitude of wall deflections, surface settlements and wall settlements. Due to the non-linear behavior of soils, the wall-soil interaction and its effects on the wall and ground movements are complicate problems. The influences of wall lengths and excavation widths to wall and ground movements shall be the topics for the future studies.

REFERENCES

Chen, Y.W. Duann, S.W., Hwang R.H. and Kong, K.S. (1999). Influence of excavation on adjacent piles. *Proceedings of 8th conference on Current Researches in Geotechnical Engineering*, Pingtung, Taiwan, August 18~20, 1425-1432. (in Chinese)

Nash, D.F.T., Lings, M.L. and Ng, C.W.W. (1996). Observed heave and swelling beneath a deep excavation in Gault clay. *Geotechnical Aspects of Underground Construction in Soft Ground*, Mair and Taylor (Eds). 1996 Balkema, Rotterdam. ISBN 90 5410 856 8, 191-196.

Panchal, J.P., McNamara, A.M. and Stallebrass, S.E. (2017). Minimising base heave from deep excavations in soft soil conditions using underwater construction methods. *Proceedings of the 19th International Conference on soil mechanics and Geotechnical Engineering*, Seoul 2017, 3019-3022.

Wong, L. W. and Hwang, R. N. (2021). Effectiveness of cross-walls in reducing wall deflections in deep excavations. *Proceedings, 41st HKIE Geotechnical Division Annual Seminar*. 18 May 2021, 282-295.

Wong, L. W. (2022). Analyses on wall deflections and ground surface settlements in excavations using small strain stiffness soil model. *Proceedings, 42nd HKIE Geotechnical Division Annual Seminar*. 15 May 2022, 490-501.

Numerical Analyses on Wall Deflections and Ground Surface Settlements in Excavations

L W Wong
SMEC Asia Limited, Hong Kong, China

ABSTRACT

Ground movements may cause damages to structures. Accurate estimations of ground movements are therefore essential for the risk assessment programs for projects involving underground constructions. Presented herein is a study on the influence of various parameters on the magnitudes and the distributions of ground movements during deep excavations with emphasis on the shapes of settlement troughs. Two-dimensional finite element analyses were conducted on 5 cases for the east end of Xiaonanmen Station in Taipei Metro. The hardening soil with small-strain stiffness was adopted to simulate the nonlinear stress-strain relationship of soils. The results indicate that the shapes of the settlement troughs are primarily affected by the depths of excavations and are relatively insensitive to the width of excavation or the thickness of the retaining wall. Based on the results obtained, the relationship between the width of the influence zone of settlement and the depth of excavation is established.

Keywords: Excavation, Hardening Soil Model, Small Strain, Settlement Trough, Influence Zone

1. INTRODUCTION

Xiaonanmen Station of Taipei Metro was constructed by using the bottom-up cut-and-cover method of construction. Adjoining the east end of the station is a 397 m long crossover tunnel with the depths of excavations increasing from 16.5 m to 21.7 m and widths of excavation reducing from 19.2 m to 8 m. This section of the route is ideal for the evaluation of the influences of the width and the depth of the pit on ground movements induced by excavation because there are only a few low-rise structures in the vicinity of the excavation with one-level basements under some of them. This drastically reduces the complexity of the problem. The 2-Dimensional analyses will be appropriate for back analyses on the ground movements.

This section of the tunnel route was previously studied with emphasis on the effectiveness of the 3 cross-walls in reducing the lateral deflections of the diaphragm walls located in close proximity to Lizhengmen, which is the South Gate of the City of Taipei and is now a historical heritage to be preserved (Wong and Hwang, 2021). Therefore, most of the soil and structural parameters adopted in the current study have previously been verified by matching the computed wall deflections with the observed wall deflections. The study presented herein is in fact an extension of this previous study with emphasis on ground settlements induced.

2 CASE STUDIED

As depicted in Figure 1, at the junction of Xiaonanmem Station and the crossover tunnel, ground movements were monitored by 6 inclinometers, i.e., SID-2 to SID-4 and SID-6 to SID-8, embedded in the diaphragm walls. There were 20 settlement markers installed along Chongqin South Road, 6 piezometers installed at various depths outside the pit, and 7 piezometers inside the pit for monitoring the groundwater levels.

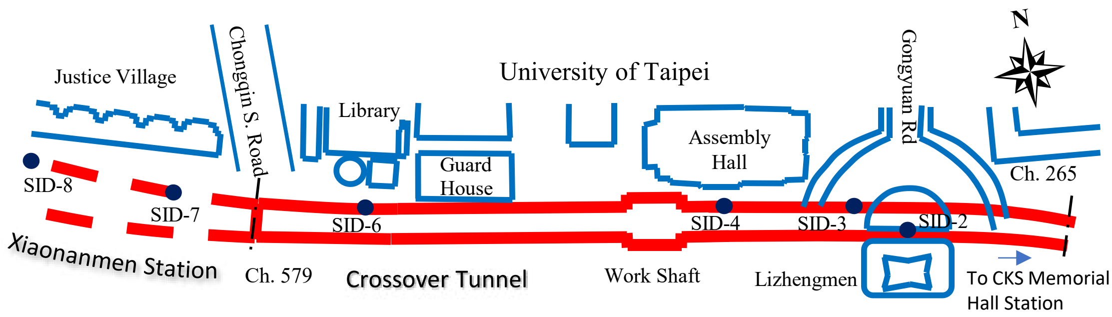

Figure 1: The crossover tunnel between Xiaonanmen Station and Chiang Kai Shek Memorial Hall Station

A representative excavation model is shown in Figure 2. The excavation was carried out to a depth of 16.5 m in 6 stages. The pit was retained by diaphragm walls of 0.8 in thickness and 31.5 m in length and was propped by steel struts at 5 levels. However, analyses were conducted to a depth of 23.5 m by adding 3 more stages to test the stability of the excavation if the excavation were continued.

2.1 Ground conditions

This section of the route is located in the T2 Geological Zone (MAA 1987) in the central Taipei Basin. As depicted in the soil profile shown in Figure 2, the Songshan Formation at the surface comprises six alternating sand (SM) and clay (CL) layers. Sublayers I, III, and V are sandy soils, and Sublayers II, IV, and VI are clayey soils. The properties of the six sublayers in the Songshan Formation have been well discussed in literatures (Moh and Ou 1979; MAA 1987). Underlying the Songshan Formation is a water-rich gravelly (GM) stratum, i.e., the so-called Jingmei Formation, which is a competent formation with very high stiffness and is frequently assumed to be the base of the numerical models. However, the base of the finite element model in this study is placed at a depth of 61 m to include a 15 m layer of the Jingmei Formation to ensure that the contribution of this formation to ground movement is accounted for.

The piezometric levels in the Jingmei Formation were lowered to a level near the bottom of the Songshan Formation in the 1970s due to excessive extraction of groundwater to supply water to the city, leading to significant reductions in water pressures in the Songshan Formation and substantial ground settlements as a result. The piezometric levels in the Jingmei Formation did not recover till the mid-1970s although pumping had been banned since 1968. The subsoils in the Songshan Formation in the central city area are thus substantially over-consolidated. This is particularly true for the clayey Sublayer II because the underlying sandy Sublayer I is so permeable that the piezometric level in Sublayer I essentially dropped by the same magnitudes as those in the Jingmei Formation

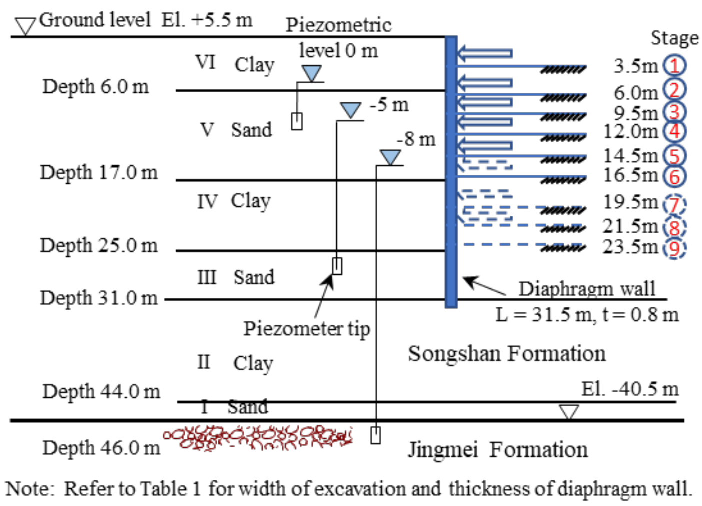

Figure 2: Soil profile of the Cross-over tunnel and excavation scheme

An advanced study was conducted by Geotechnical Engineering Specialty Consultant engaged by the Department of Rapid Transit Systems of Taipei City Government in the very early stage of the metro construction. This Designated Task studied the characteristics of the soils in the Taipei basin to provide the basic information required for the design and construction of metro facilities (Chin et al. 1994; Chin and Liu 1997). This was a research project so it was carried out under stringent supervision. Soil samples of high quality were obtained and tested with great care. The test results are therefore more reliable than those normally obtained. Hwang et al. (2013) summarized the results of the study and suggested that Figure 3 be adopted for estimating the undrained shear strengths of the clays in the T2 Zone.

The piezometric levels recorded by piezometers outside the pit are presented in Figure 2 and Figure 4. The drawdowns were small and, presumably, would not have a significant influence on wall deflections or ground settlements. Inside the pit, the groundwater table was maintained at a depth of 1m below the bottom of the excavation as the excavation proceeded.

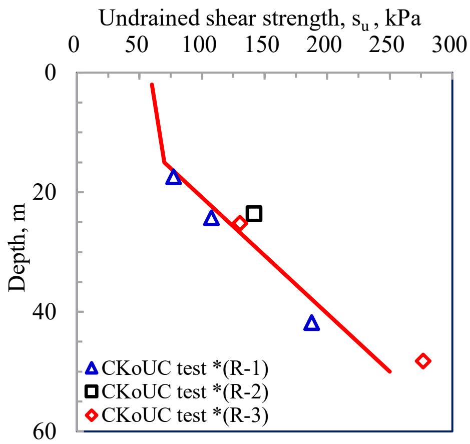

Figure 3: Estimated undrained shear strengths of clays in T2, TK2, and K1 Zones (Hwang et al. 2013)

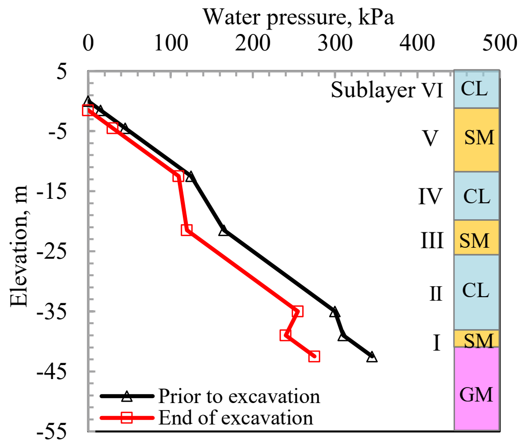

Figure 4: Groundwater pressures on the outer face of the diaphragm walls

3 NUMERICAL SIMULATION

Five cases, Case I to Case V, as summarized in Table 1, have been analyzed. Case I is the benchmark case for the verification of the stiffness parameters adopted. Cases II to Case V are conducted for assessing the effects on wall deflections and ground settlements due to variation in excavation widths and in wall thicknesses.

Table 1: Cases studied by the HSS model

Case	Excavation		Diaphragm wall			
	Width B, m	Depth H, m	Thickness t, m	Length L, m	Flexural stiffness E_cI_c, MN-m	Axial stiffness E_cA_c, MN/m
I	11.2	23.5	0.8	31.5	750	14,056
II	41.2	23.5	0.8	31.5	750	14,056
III	41.2	23.5	0.7	31.5	502	12,300
IV	41.2	23.5	0.6	31.5	316	10,540
V	41.2	14.5	2.1	31.5	13,560	36,900

3.1 Finite element mesh

The section analyzed is depicted in Figure 2. The width of the excavation is 11.2 m. Because of symmetry in geometry, only half of the section was analyzed as depicted in Figure 5. The excavation was carried out to a depth of 16.5 m. The lateral extent of the finite element model reaches a distance of 140 m from the central axis of the excavation trench. The ground model is 61 m in depth and the diaphragm wall is located at a distance of 5.6 m from the axis of the trench.

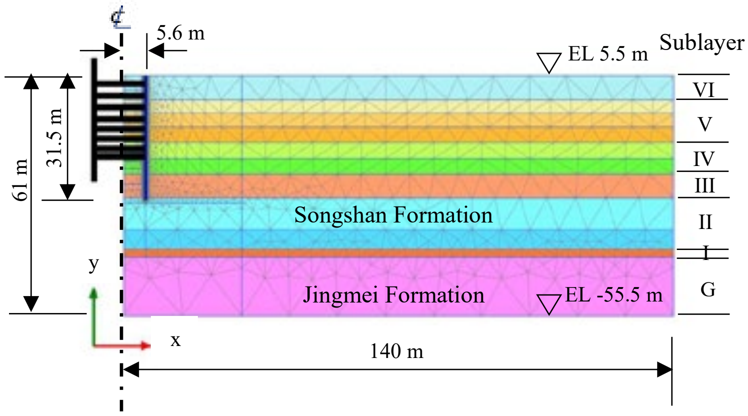

Figure 5: Finite element mesh for the analytical section for 9 stages of excavation

3.2 Nonlinearity of Soil Behavior - Hardening-Soil with Small-strain Stiffness Model

The PLAXIS-2D finite element software developed by PLAXIS BV (2013) has become a very popular tool in geotechnical analysis and design. The Hardening-Soil with Small-strain stiffness (HSS) constitutive soil model is an extension of the Hardening-Soil model (Benz 2006, Schanz and Vermeer 1998; Schanz et al. 1999) introduced in the PLAXIS program and is adopted herein to simulate the non-linear stress-strain relationship of soils under loading and unloading. In the HSS model, the parameters adopted to define the hyperbolic stress-strain relationship are as follows:

- E^{ref}_{50} is the reference secant stiffness from standard triaxial test,
- E^{ref}_{oed} is the reference tangent stiffness for oedometer primary loading,
- E^{ref}_{ur} is the reference unloading-reloading stiffness,
- m is the exponential factor for stress-level dependency of stiffness,
- R_f is the failure ratio, $R_f = q_a / q_f$,
- q_f is the asymptotic value of the shear strength and qa is the failure strength,
- G^{ref}_0 is the reference shear modulus at the level of very small strains,
- $\gamma_{0.7}$ is the reference shearing strain to define the behavior of degradation of moduli.

The stress-strain curves can be determined from laboratory tests such as the Ko-consolidated triaxial undrained compression and extension tests. In this study, the stiffness values of soils are related to the undrained shear strengths for clays and the N values for sands. The empirical relationships expressed in Equations 1 to 5 are adopted:

$$E^{ref}_{50} = 250\ s_u \text{ (for clayey soils)} \tag{1}$$
$$E^{ref}_{50} = 2\ N \text{ (in MPa for sandy soils)} \tag{2}$$
$$E^{ref}_{ur} = 5\ E^{ref}_{50} \tag{3}$$
$$E^{ref}_{oed} = E^{ref}_{50} \tag{4}$$
$$G^{ref}_0 = 1.2\ E^{ref}_{ur} \tag{5}$$

in which s_u is the undrained shear strengths of clayey soils and N is the blow-counts obtained in standard penetration tests for sandy soils. A $\gamma_{0.7}$ value of 0.8 x 10^{-4} is adopted for the various soil layers. The parameters in Equations 1 to 4 have been validated in a previous study by matching the deflection profiles observed in inclinometer SID-6 (Wong and Hwang, 2021). The parameters adopted in this study are summarized in Table 2. The effective shear strength parameters, i.e., the c' and ϕ'values, for the silty sand strata, are determined from laboratory tests conducted on thin-wall tube specimens. For the clayey layers, c' = s_u and ϕ' = 0° is assumed in the analyses. The dilation angle, ψ', of 2°, 0°, and 5° are adopted for the sandy, the clayey, and the gravelly soils respectively. The R_f equals 0.9 and an interface reduction factor, R_{inter}, of 1 is adopted. The unload-reload Poisson's ratio, υ_{ur}, of 0.2 is used as suggested by Benz (2006) and Schanz et al. (1999).

Table 2: Soil parameters for the HSS model adopted in the PLAXIS analyses

Depth m	Soil type	Unit weight γ' kN/m^3	N value	Undrained shear strength s_u, kPa	Effective cohesion c' kPa	Effective friction angle ϕ', deg	Dilation angle ψ' deg	Reference stiffness, MPa		Initial shear moduli G^{ref}_0, MPa
								Secant stiffness E^{ref}_{50}	Unload-reload stiffness E^{ref}_{ur}, MPa	
0-6	CL	18.8	4	50			0	12.5	63	75
6-17	SM	19.2	5		0	32	2	10	50	60
	SM	19.2	8				2	16	80	96
	SM	19.2	11				2	22	110	132
17-21	CL	18.6	6	53.7			0	13.4	67	80.4
21-25	CL	18.6	17	114.3			0	28.6	143	170
25-31	SM	19.4	18		0	32	2	36	180	216
31-39	CL	18.9		195.0			0	48.6	243	290
39-44	CL	18.9		241.0			0	60.2	301	360
44-46	SM	19.7	30		0	32	2	60	300	360
46-60	GM	19.9	>100		0	40	5	250	1250	1500

3.3 Determination of Small-strain Stiffness

Kung et al. (2009) presented the results of small-strain triaxial tests and bender element tests conducted on undisturbed specimens recovered from clayey Sublayer IV of the Songshan Formation. The specimens were saturated and Ko-consolidated to the in-situ effective stress states. The Ko values applied for consolidation ranged from 0.5 to 0.55. After completing the Ko-consolidation, but prior to the shearing tests, bender element tests were carried out to measure the shear moduli of the clay specimens. Compression and extension undrained triaxial shearing tests were then conducted. The undrained shear strengths profile obtained is consistent with that reported by Hwang et al. (2013) as summarized in Figure 3.

Based on the results of the small-strain triaxial tests and the bender element tests, Kung et al. (2009) obtained G_{max}/s_u ratios ranging from 738 to 788. As defined in Equations 1, 3, and 5, the G^{ref}_0/s_u ratio adopted in this study is 1500. The difference in the maximum shear moduli obtained from bender element tests and back-analysis on field cases could be attributable to the difference in the levels of the strains.

Table 3: Strut properties

Strut level	Depth m	Strut type	Area A_s, cm^2	Stiffness E_sA_s/s, MN/m	Design preload, kN/m	Strut spacing s, m
S1	2.2	1H350x350x12x19	173.9	1,188	120	3.0
S2	5.2	1H400x400x13x21	218.7	1,494	250	
S3	8.2	2H350x350x12x19	347.8	2,377	500	
S4	11.0	2H350x350x12x19	347.8	2,377	500	
S5	14.2	2H400x400x13x21	437.5	2,989	553	
S6 to S8	16 to 23	2H350x350x12x19	347.8	2,377	500	

3.4 Modeling of the retaining structures

The excavation scheme and the retaining structures are depicted in Figure 2. The diaphragm walls are simulated by plate elements and an E_c value of 25,000 MPa is adopted for concrete with a characteristic compressive strength of 28 MPa. The estimated flexural rigidity (denoted as E_cI_c where I_c is the moment of inertia) and the axial stiffness (denoted as E_cA_c where A_c is the sectional area) of the diaphragm wall of 0.8 m in thickness are 750 MN-m and 14,056 MN/m respectively. These values have already been reduced from their original values by 30 % to account for tensile cracks and creeping of concrete during excavation.

The excavation was supported by 5 levels of steel struts, i.e., S1 to S5, of which the structural properties are presented in Table 3. The struts are represented by node-to-node anchors. The steel is assumed to be an elastic material with a Young's modulus (E_s) of 210 GPa. The preloads in the struts adopted in the analyses were half of those specified in Table 3. To study the effects of excavation depths on wall and ground movements, the excavation was assumed to continue from a depth of 16.5 m further to 23.5 m in 3 stages following the same scheme of excavation adopted in Stage 6 and with the same configuration of the struts.

4 RESULTS OF NUMERICAL ANALYSIS

4.1 Validation of the Methodology and Parameters

The computed wall deflection and surface settlement profiles for Case I are presented in Figure 6. At the final excavation depth of 16.5 m, the computed maximum deflection and toe movements are 33.1 mm and 2.8 mm respectively. The results are compared with the readings of inclinometers SID-6 and SID-7 and with the settlement markers installed along Chongqin South Road in Figure 7. In consideration of the fact that the pit was wider at the locations of both inclinometers, the agreement among the 3 sets of data with Case I is reasonably well. It is noted that the settlement markers were located along Ch.570 m and Ch.584 at distances of 5 m to 9 m to the end wall of Xiaonanmem Station. The over-estimation of the computed results by around 5 mm as shown in Figure 7(b) could be attributable to the presence of this end wall, which restrained the lateral movements of the two walls but is not modelled in the 2-dimensional analysis.

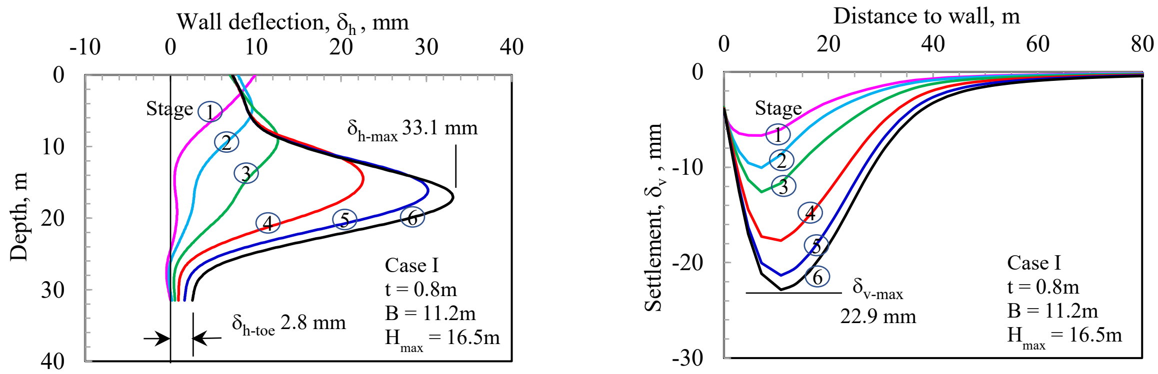

(a) Lateral wall deflections (b) Ground surface settlements

Figure 6: Computed wall deflections and surface settlements for Case I

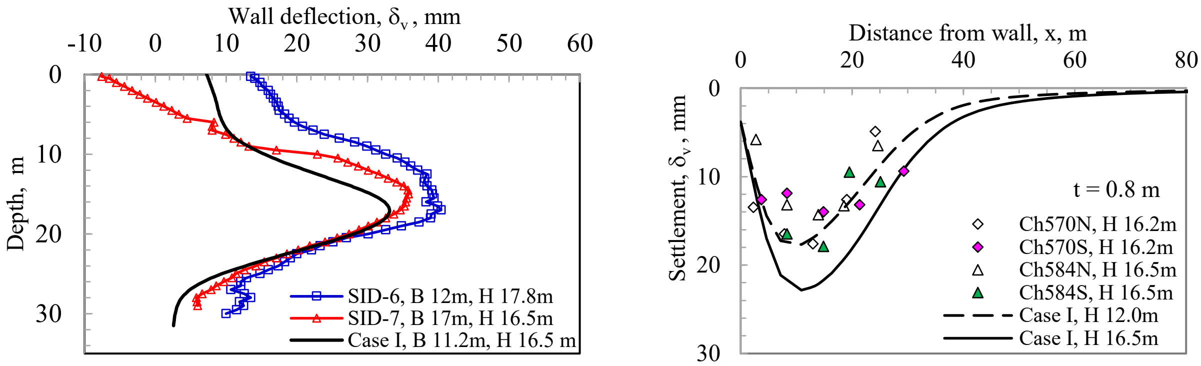

(a) Wall deflections observed in inclinometers (b) Observed surface settlements

Figure 7: Comparison between the computed and observed wall deflections and surface settlements for Case I

4.2 Effect of the widths and the depths of excavations on wall deflections and ground settlements

To study the effects of the width of excavation on wall deflections and ground settlements, the excavation is widened from 11.2 m in Case I to 41.2 m in Case II. It can be noted by comparing Figure 8 with Figure 6, the maximum wall deflection increases from 33.1 mm to 45.9 mm in Stage 6 as a result of widening the excavation while the maximum settlement increases from 22.9 mm to 36.3 mm. The maximum wall deflection for Case II would increase from 45.9 mm to 54.6 mm while the ground settlement would increase from 36.3 mm to 48.9 mm, if the excavation were carried out to a depth of 23.5 m.

Figure 9 shows the normalized settlement troughs obtained in Cases I and II. It can be noted that the settlement troughs become wider as the excavation width increases, but the differences among these cases are indeed insignificant for practical purposes.

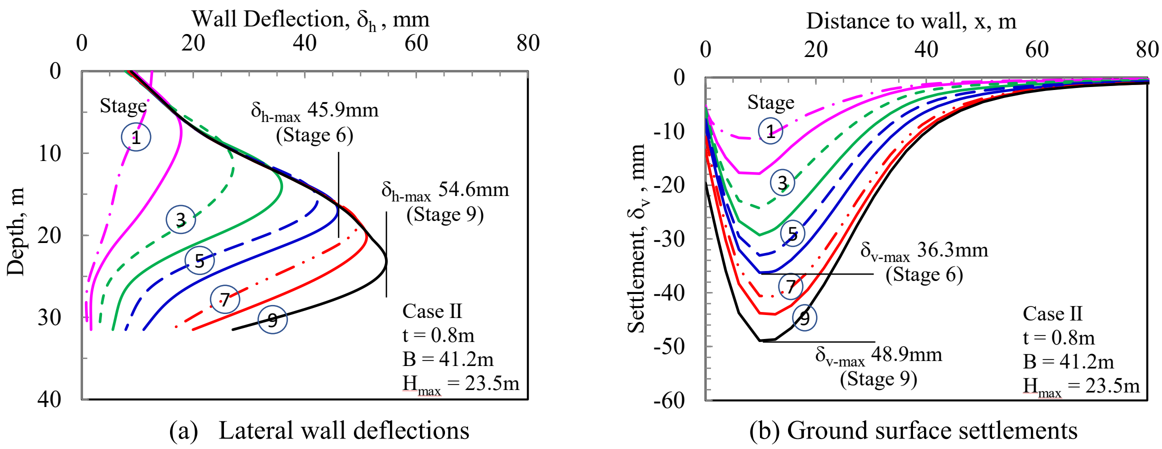

Figure 8: Computed wall deflections and surface settlements for Case II

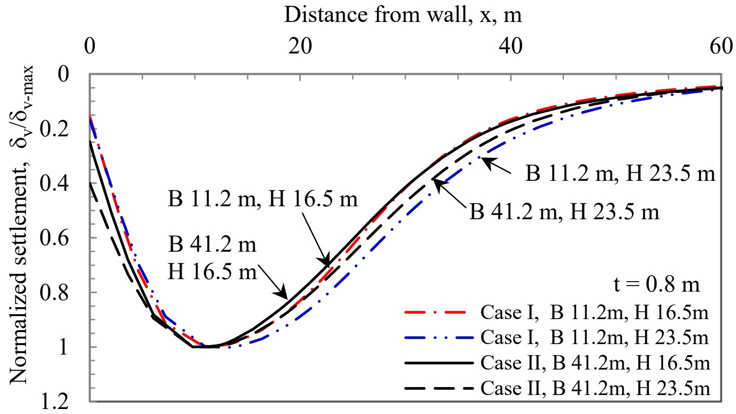

Figure 9: Effect of excavation width on the normalized settlement troughs in Case I and Case II

4.3 Effect of the wall thickness on wall deflections and ground settlements

Figure 10(a) shows the computed wall deflections profiles obtained in Stage 6 excavation for Cases II, III, and IV. The maximum wall deflection increases from 46.0 mm to 50.2 mm as the wall thickness reduces from 0.8 m to 0.7 m, and to 57.1 mm as the wall thickness reduces further to 0.6 m. The same trend can be noted from Figure 10(b) for Stage 9 excavation. Similarly, Figure 11 shows that the reduction in wall thickness, hence, the stiffness of the wall, does increase ground settlements by, say, roughly 18 %. However, the normalized settlement troughs are hardly affected by wall thickness as depicted in Figure 12.

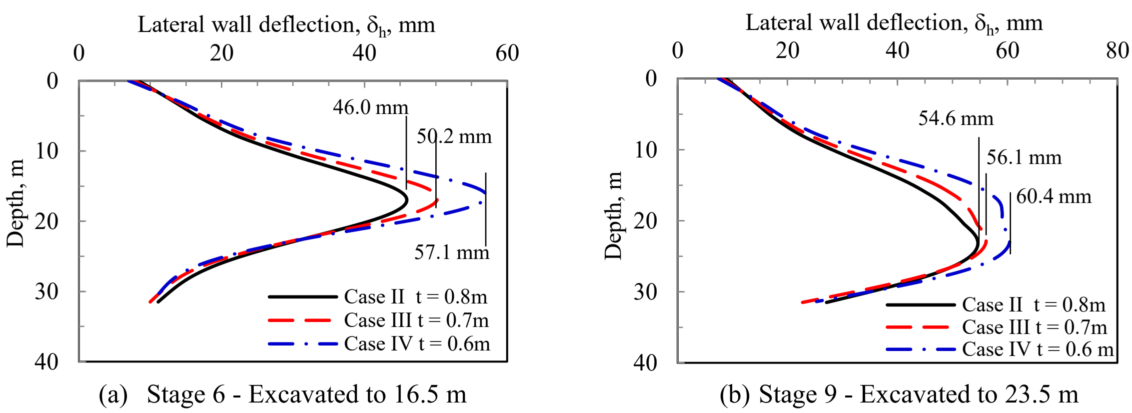

Figure 10: Effect of wall thickness – Wall deflections in Cases II, III, and IV

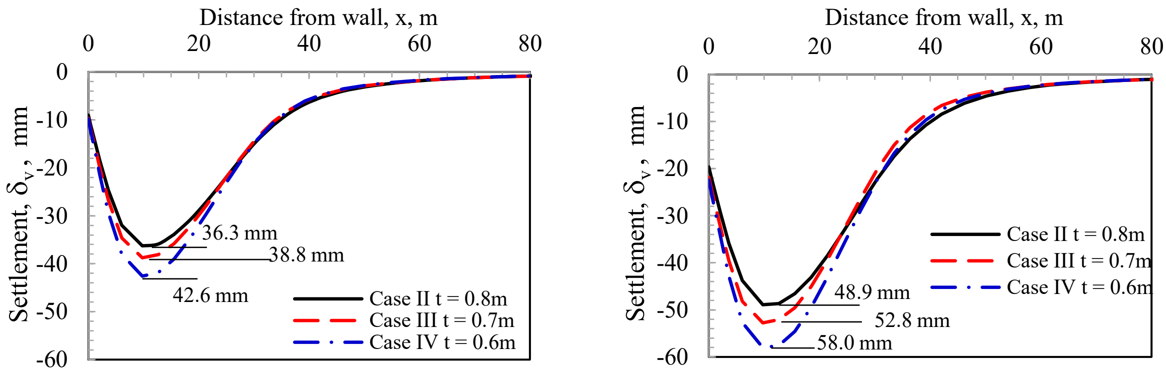

(a) Stage 6 - Excavated to 16.5 m (b) Stage 9 - Excavated to 23.5 m

Figure 11: Effect of wall thickness – Settlements in Cases II, III and IV

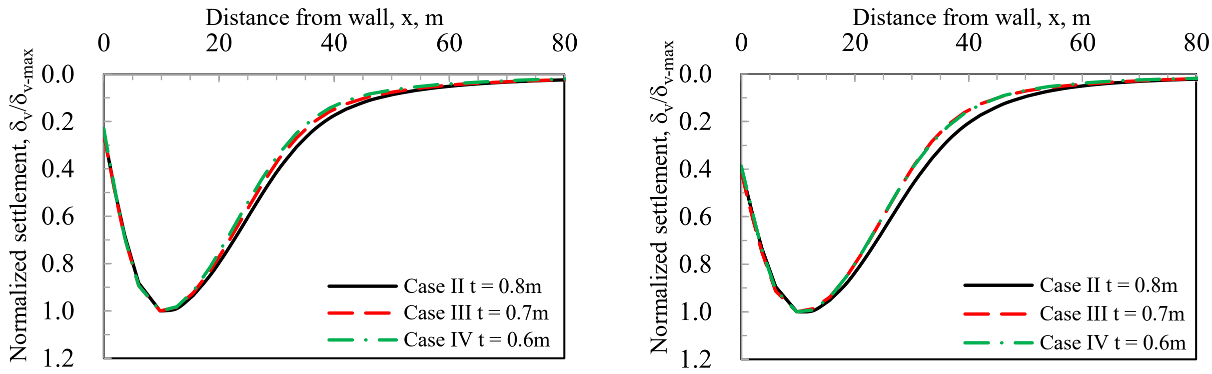

(a) Stage 6 - Excavated to 16.5 m (b) Stage 9 - Excavated to 23.5 m

Figure 12: Effect of wall thickness – Normalized settlements in Cases II, III and IV

4.4 Extent of Influence of Settlements

In addition to the magnitudes of ground settlements, the lateral spreading of the settlements is also an important element in the risk management program for protecting adjacent structures. The extent of the influence of settlements is often correlated to the depth of excavation. Taking Case II as an example, Figure 13(a) shows the settlement troughs in all the 9 stages of excavation with the settlements, δ_v , normalized by the maximum settlement, $\delta_{v\text{-}max}$, and the distance from the wall, x, normalized by the depth of excavation, H.

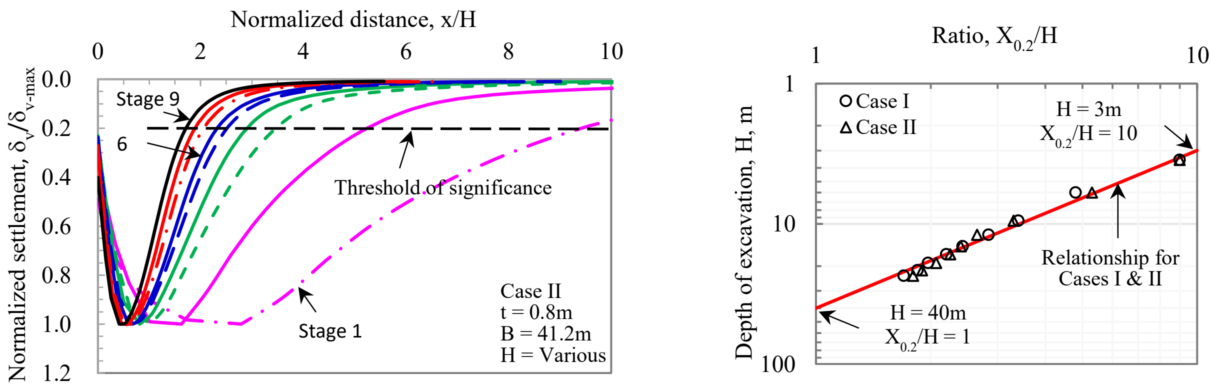

(a) Normalized settlement troughs (b) Width of settlement trough

Figure 13: Estimation of significant ground settlements

The normalized settlement troughs would become narrower and narrower as the depths of excavation increase. If 20 % is adopted to be the threshold for significance, the $X_{0.2}/H$ ratio, in which $X_{0.2}$ is the distance from the wall to where the settlement equals 20 % of the maximum settlement, can be related to the depth of excavation as depicted in Figure 13(b). The regression function can be defined in a log-log scale by two control points, at H values of 3 m and 40 m. For the excavation depths H of 3 m and 40 m, the normalized distance to the wall, i.e., the $X_{0.2}/H$ ratios, are 10 and 1 respectively. It appears that this relationship is not sensitive to the excavation widths and is expected to be applicable in general cases. Based on Figure 13(a), it is recommended to assume ground settlements drop linearly to zero at a distance of 10H for excavations shallower than 10 m in depth and 5H for deeper excavations. The proposed empirical relationship is verified by field observations and results of the centrifuge test shown in Section 5.3. It should however be noted that the results of the analyses presented are performed with consideration given only to the equilibrium of stresses induced in soils as the excavation proceeds and the balances of forces acting on the wall and struts. Consolidation settlements are not accounted for.

5 COMPARISON WTH FIELD OBSERVATIONS

To verify the applicability of the results of the analyses, the computed wall deflections and ground settlements are compared with the field observations and the centrifuge tests reported in Wong & Patron (1993), Hsieh & Ou (1998), Panchal et al. (2017) and Panchal et al. (2018) as follows.

5.1 Cases Reported in Wong and Patron (1993)

Wong and Patron (1993) reported the wall deflections and ground settlements caused by excavation in 8 cases in the T2 Zone of the Taipei Basin. As summarized in Table 4, the excavation widths for these cases range from 35 m to 61 m and the final excavation depths range from 11.1 m to 21.7 m. The diaphragm walls were 0.7 m and 0.6 m in thickness. The majority of the wall lengths are 60 % to 80 % of the length of 31.5 m adopted in the analysis. The wall deflections for the wall thicknesses of 0.7 m and 0.6 m are compared with those computed in Case III and Case IV in Figure 14 and Figure 15 respectively.

Table 4: Summary of excavation cases in T2 Zone presented by Wong & Patron (1993)

Case	Wall dimension, m		Excavation geometry, m		H/L	Strut levels	Excavation case
	Thickness, t	Length, L	Depth, H	Width, B			
A1	0.7	21	16.2	61	0.77	4	Taiwan Power
A4		27	14.7	37	0.54	5	Chun Wei
A7		34	21.7	46	0.64	7	Cathay Life
A8		30	17.1	40	0.57	5	China Times
A2	0.6	17	11.1	52	0.65	3	Kuan Min
A3		23	11.4	35	0.50	3	Central Insurance
A5		25	12.3	37	0.49	4	Chung Yang Pa Shi
A6		22	12.6	48	0.57	4	Shin-I

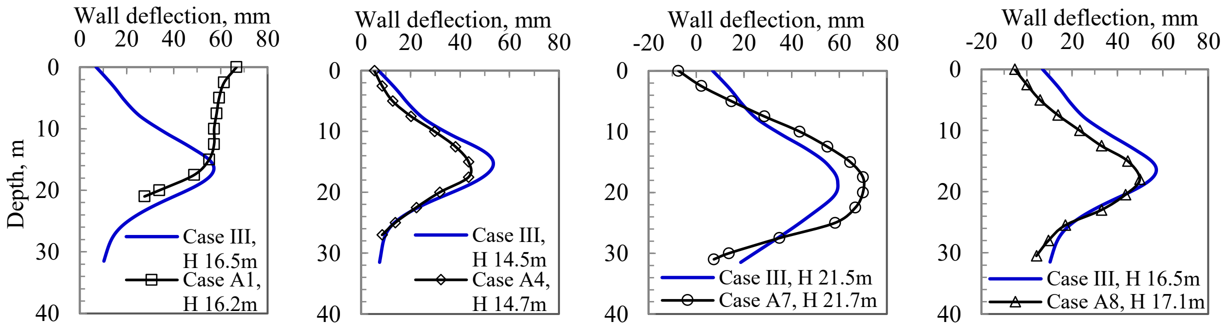

(a) A1: Taiwan Power (b) A4: Chun Wei (c) A7: Cathay Life (d) A8: China Times

Figure 14: Computed wall deflections in the final excavation stage for cases with a wall thickness 0.7 m

As can be noted from Figure 14(a), the large deflections that occurred in Case A1 could probably be due to the short wall length of 21 m, which is 70 % of the length of 31.5 m adopted in the analysis. Other than that, despite the various uncertainties associated with the field operations, such as preloading and over-excavation, the computed wall deflection profiles are reasonably close to those observed.

The settlement profiles for the eight cases are presented in Figure 16. Comparing with those computed profiles in Case III and Case IV at the excavation depths of 16.5 m and 14.5 m respectively, the observed and the computed settlement profiles are reasonably close. Based on Figures 14 to 16, it is concluded that the HSS soil model could reliably estimate the wall deflections and ground settlements simultaneously.

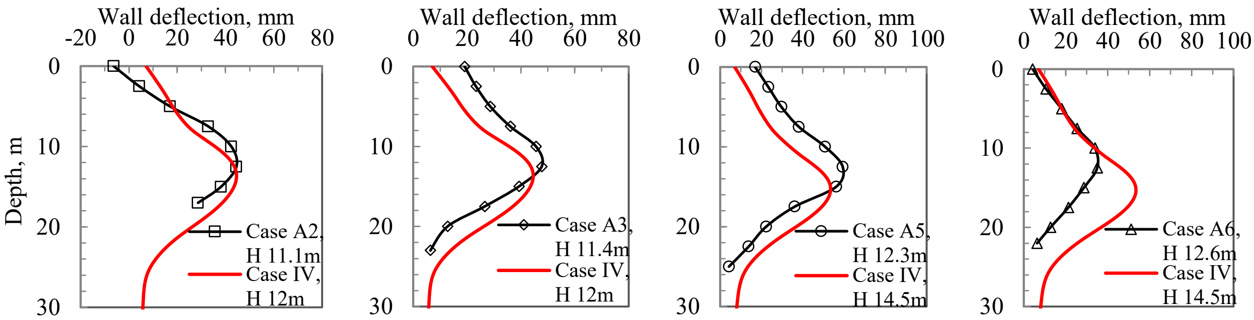

(a) A2: Kuan Min (b) A3: Central Insurance (c) A5: Chung Yang Pa Shi (d) A6: Shin I

Figure 15: Computed wall deflections in the final excavation stage for cases with a wall thickness of 0.6 m

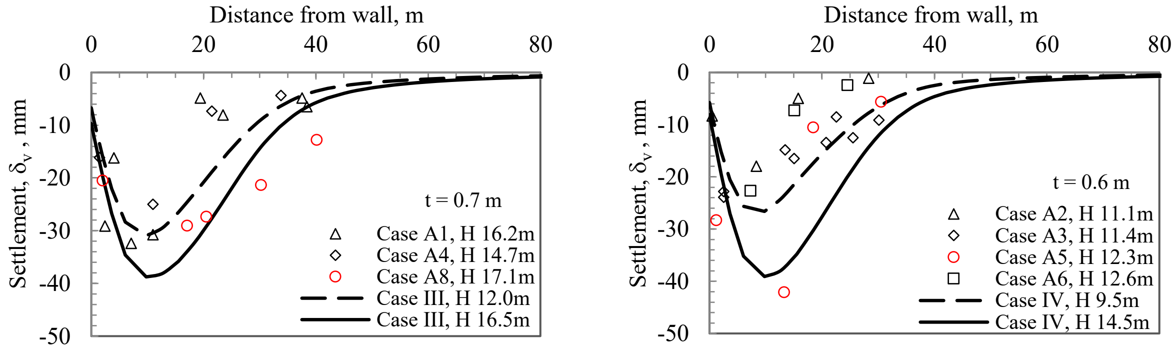

(a) Wall thickness 0.7 m (b) Wall thickness 0.6 m

Figure 16: Computed settlements in the final excavation stage for the cases reported in Wong & Patron (1993)

5.2 Cases Reported in Hsieh and Ou (1998)

Hsieh and Ou (1998) collected 7 excavation cases in soft ground located in Taipei, London, Chicago, Oslo, and in Japan. The final excavation depths ranged from 11 m to 20 m as summarized in Table 5. Among these 7 cases, Cases B1 and B3 to B4 were supported with floating walls with the toe levels at 10 m to 15 m above the competent strata. The walls for other cases, Cases B2, B6, and B7, were end bearing walls with the toes founded on bedrock or on the gravel stratum.

Table 5: Summary of excavation cases studied by Hsieh & Ou (1998)

Case	Wall dimension, m		Excavation geometry, m		H/L	Strut levels	Location
	Thickness, t	Length, L	Depth, H	Width, B			
B1	Diaphragm wall 0.9m	35	19.7	41	0.56	6	Taipei, TNEC
B2	Diaphragm wall	31	18.5	35	0.60	6	Taipei
B3	Steel concrete wall	32	17.0	30	0.53	5	Japan
B4	Diaphragm wall	30	18.5	50	0.62	5	London
B5	Steel sheet pile	19.2	12.2	12.2	0.64	4	Chicago
B6	Steel sheet pile	16	11.0	11	0.69	5	Oslo
B7	Diaphragm wall	33	20.0	70	0.61	5	Taipei, Far East Enterprise

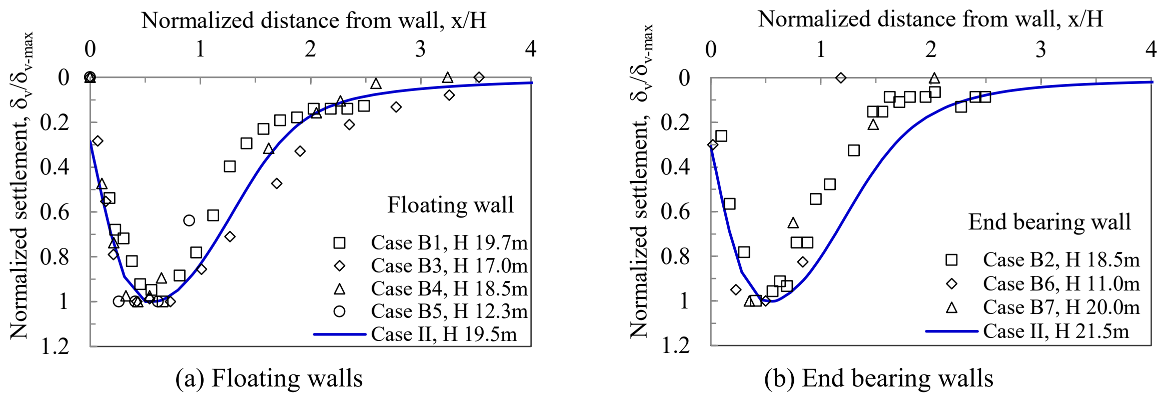

Figure 17: Computed settlements in the final excavation stage for the cases reported in Hsieh & Ou (1998)

The computed settlement profiles are compared with the settlements obtained in Case II (H = 19.5 m for Stage 7 and H = 21.5 m for Stage 8) in Figure 17. The normalized settlement profiles are reasonably close to the observed profiles.

5.3 Centrifuge tests by Panchal et al. (2017; 2018)

Ground movements associated with excavations are a complex combination of lateral and vertical wall movements, wall bending, and ground heave. Centrifuge modeling allows researchers to simply and physically simulate complex geotechnical problems, especially on nonlinear geotechnical materials. Panchal et al. (2017; 2018) reported the results of 3 centrifuge modeling tests, as summarized in Table 6, on an underwater excavation case to study the relationship between the ground movements and basal heave below the final excavation level. The model comprised half an excavation, 150 mm wide and 75 mm deep, representing 24 m and 12 m at prototype scale, respectively. The toe of the retaining wall was embedded 55 mm into the clay, equating to 8.8 m at prototype scale, giving a total length of 20.8 m of the wall.

To confirm whether the normalized settlement troughs obtained by numerical analyses are applicable to centrifuge tests, Case V, referring to Table 1, was conducted and the results are compared with those reported by Panchal et al. (2017; 2018) in Figure 18. The agreement between these 2 sets of data is very encouraging.

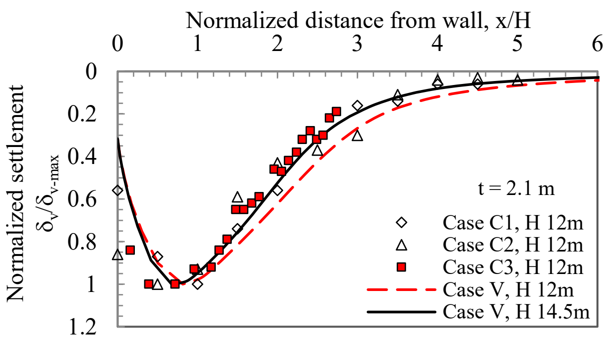

Figure 18: Comparison of settlements computed in Case V and those reported in Panchal et al. (2017 & 2018)

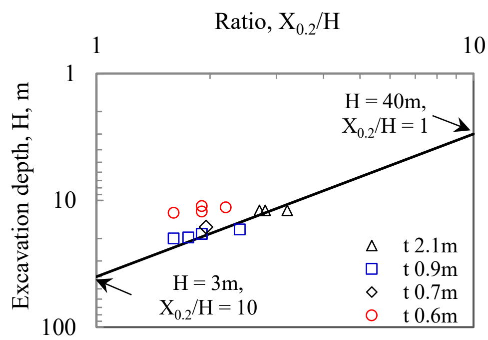

Figure 19: Width of settlement trough at 20% of maximum settlement for various case histories

Table 6: Summary of centrifuge models reported by Panchal et al. (2017; 2018)

Case	Wall dimension, m		Excavation geometry, m		Main feature	Reference
	Thickness, t	Length, L	Depth, H	Width, B		
C1	2.1	20.8	12	48	Underwater excavation	Panchal et al. (2017)
C2	2.1	20.8	12	48	Reference test	Panchal et al. (2018)
C3	2.1	20.8	12	48	Lime stabilized	

As can be noted from Figure 19, the $X_{0.2}/H$ ratios obtained in various case histories and centrifuge tests fit very well with the relationship established based on the results obtained in all other cases. The empirical relationship between the widths of the settlement trough and the excavation depths has thus been verified.

6 CONCLUSIONS

Parametric studies on a typical excavation case in soft ground supported by diaphragm walls using 2-Dimensional finite element analysis have been conducted. Various excavation widths, wall thicknesses and excavation depths have been adopted. The following conclusions could be drawn:

(1) The nonlinear Hardening-Soil with small-strain stiffness constitutive soil model could reliably estimate the wall deflections and ground settlement simultaneously in the numerical analysis.
(2) There is the trend of the larger the excavation depth, the narrower the width of the settlement trough.
(3) The shapes of the normalized settlement profiles are primarily affected by the depths of excavations and are relatively insensitive to the width of excavation or to the thickness of the retaining wall.
(4) An empirical relationship between the widths of the settlement trough and the excavation depths has been established for assessing the influence of surface settlements.

As the computed distribution of the settlement troughs and the magnitude of the settlements have agreed with those observed in the field, the stiffness parameters adopted for the Hardening-soil with the small-strain stiffness model have been validated.

REFERENCES

Benz, T. (2006). Small-strain stiffness of soils and its numerical consequence. *Dissertation of thesis*, the Institute of Geotechnics, University Stuttgart.

Chin, C. T., Crooks, A. J. H. and Moh, Z. C. (1994). Geotechnical properties of the cohesive Sungshan deposits. *Geotechnical Engineering, J. Southeast Asian Geotechnical Society*, Taipei, Taiwan 25(2), 77-103. (in Chinese)

Chin, C. T. and Liu, C-C. (1997). Volumetric and undrained behaviors of Taipei silty clay. *J. Chinese Institute of Civil and Hydraulic Engineering*, Taipei, Taiwan 9(4), 665-678. (in Chinese)

Hsieh, P.G. and Ou, C.Y. (1998). Shape of ground surface settlement profiles caused by excavation. *Canadian Geotechnical Journal* 35(6), 1004-1017.

Hwang, R., Moh, Z. C. and Hu, I-C. (2013). Effects of consolidation and specimen disturbance on strengths of Taipei Clays, *Geotechnical Engineering, J. of SEAGS & AGSSEA*, March, Bangkok, 44(1), 9-18.

Kung, G.T.C, Ou, C.Y. and Juang C.H. (2009). Modelling small-strain behavior of Taipei clays for finite element analysis of braced excavations. *Computers and Geotechnics* 36 (2009), 304-319

MAA (1987) *Engineering properties of the soil deposits in the Taipei Basin*, Report No. 85043, Ret-Ser Engineering Agency and Taipei Public Works Department, Taipei (in Chinese)

Moh, Z. C. and Ou C. D. (1979). Engineering characteristics of Taipei Silt. *Proc., 6th Asian Regional Conference on Soil Mechanics and Foundation Engineering*, Singapore, 1, 155-158.

Panchal, J.P., McNamara, A.M. and Stallebrass, S.E. (2017). Minimising base heave from deep excavations in soft soil conditions using underwater construction methods. *Proceedings of the 19th International Conference on soil mechanics and Geotechnical Engineering*, Seoul, Korea, 3019-3022.

Panchal, J.P., McNamara, A.M. and Stallebrass, S.E. (2018) Physical modelling of lime stabilization in soft soils around deep excavations, *The Journal of Deep Foundations Institute*, Volume 11, 137-147

PLAXIS, B. V. (2013). *PLAXIS reference manual*. Plaxis BV, Delft, the Netherlands.

Schanz, T. and Vermeer, P. A. (1998). On the Stiffness of Sands. *Pre-failure Deformation Behaviour of Geomaterials*, ICE, London, UK, 1998.

Schanz, T., Vermeer, P.A. and Bonnier, P.G. (1999). The hardening soil model: formulation and verification. *Beyond 2000 in Computational Geotechnics*. Rotterdam, the Netherlands, 281-290.

Wong, L. W. and Hwang, R. N. (2021). Effectiveness of cross-walls in reducing wall deflections in deep excavations. *Proceedings, 41st HKIE Geotechnical Division Annual Seminar*, Hong Kong 18 May 2021, 282-295.

Wong, L.W. and Patron B.C. (1993). Settlements induced by deep excavations in Taipei. *Proceedings of the 11th Southeast Asian Geotechnical Conference*, Singapore, 787~791.

Innovative Skidding Mega Truss Shoring System

Raymond W M Cheung, Sam H S Liu
Gammon Construction Limited, Hong Kong, China

Gavin S H Toh, Steven Jenkins, M K Chong, Michael Chak
Lambeth Associates Limited, Hong Kong, China

ABSTRACT

The construction of submerged tunnels at marine areas is a difficult challenge faced by both Contractor's and Designer's as the excavation and tunnel construction works will be carried out over water exposing workers to safety risks for marine works and the costly logistical planning required. To overcome this challenge, the proposed cut and cover tunnel with clutched pipe pile (CPP) wall cofferdam would use an innovative method where mega trusses are proposed as struts for the first and second shoring layers and also double function as support for the hanging kingposts. The trusses would be transported by barge in modules and assembled on the bulkhead temporary working platform as on-site assembly factory. Once mega truss is assembled, strand jack lifting towers will lift each mega truss onto the skidding rails installed along the top of the CPP cofferdam wall where hydraulic jacks will skid each truss in a sequence of small strokes along the rails until they reach their final position and this process is repeated for all trusses. The use of the mega truss skidding system increases the productivity and cost effectiveness of both the installation and dismantling of the ELS works in addition to reduction of the safety risks and complexity of erecting steel works above water.

1 INTRODUCTION

1.1 Project Background

In the Central Kowloon Route - Kai Tak West (CKR-KTW) project by the Highways Department Major Works Division under Contract no. HY/2014/07 and is located at Kai Tak West area. The main works are for the construction of a 900m length dual three lane carriageway by cut & cover method comprised of 125m long depressed road and 200m long underpass at the runway of former Kai Tak Airport, a 370m long submerged tunnel under Kowloon Bay and 160m long tunnel located at Ma Tau Kok Public Transport Interchange. Refer to Figure 1 below.

Figure 1: CKR-KTW Submerged Tunnel located at Kowloon Bay

The construction of the 370m length by 60m width curved submerged tunnel at Kowloon Bay is the highlight of this project and a difficult challenge faced by the Contractor and his Designer for the temporary works required of the bulk excavation and tunnel construction works over water. The works are further made more difficult due to Kowloon Bay (KWB) being a typhoon shelter and marine passage for several stakeholders in the area requiring uninterrupted access through-out the Contract. To overcome this, the submerged tunnel was planned to be constructed in two stages and maintain a 60m wide navigation channel at all times as shown in Figure 2 below:

Figure 2: Provision of 60m wide Navigation Channel within KWB

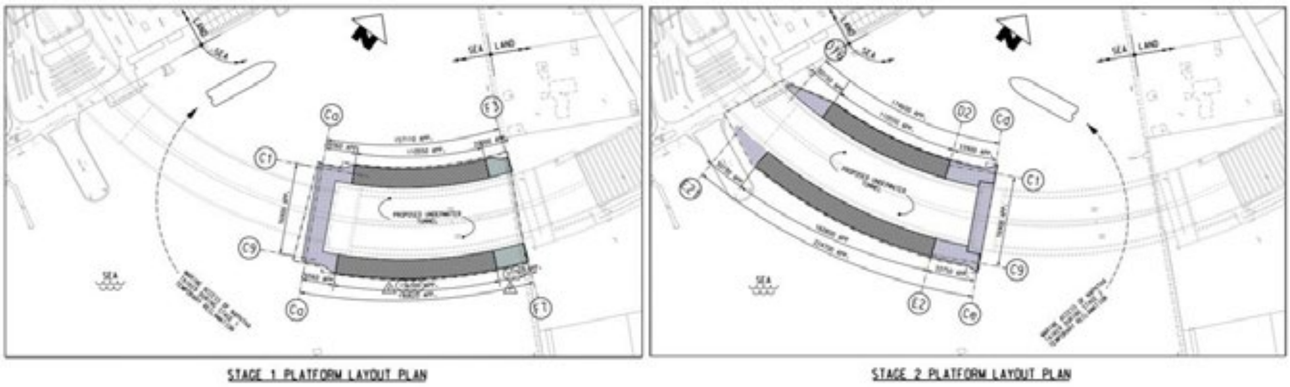

1.1 Innovative Concept for Marine Cut and Cover Tunnel Construction

An innovative scheme was proposed for the cut and cover cofferdams using Clutched Pipe Pile (CPP) cofferdam wall where the mega trusses are proposed as struts for the first and second shoring layers. The mega trusses also provide the 3 nos. of hanging kingposts used for supporting the remaining typical struts below. This sliding strut system eliminates the necessity and difficulties of driving multiple King Post piles and erecting the struts above the water prior to dewatering works. The trusses would be transported by barge in modules and assembled on the bulkhead temporary working platform located at the midpoint of KWB as on-site assembly factory. Once truss is assembled, strand jack lifting towers will lift each mega truss onto the skidding rails installed along the top of the CPP cofferdam wall where hydraulic jacks would skid each truss in a sequence of small strokes along the rails until they reach their final position and the process is repeated for all trusses. The mega truss skidding struts were developed from scheme to detailed design completely in house by the Contractor's Designer. The Designer made use of the experience gained during the use of the mega trusses in previous project in Marina Bay, Singapore and further enhanced for this project by applying skidding struts to allow for easy strut installation over water and elimination of piling works for king posts. The mega truss shown in use at Singapore in Plate 1 below.

Plate 1: Mega-Truss concept as used for ELS works in Marina Bay, Singapore

2 SKIDDING MEGA TRUSS SHORING SYSTEM

2.1 Underwater Tunnel ELS Cofferdam

The temporary works for construction of the 370m length curved submerged tunnel commenced in August 2018 and is separated into two cut and cover tunnel stages named Underwater Tunnel (UWT) Stage 1 and UWT Stage 2 with the bulkhead wall located at midpoint of KWB. The cofferdams for UWT Stage 1 and Stage 2 are approximately 160m and 210m in length, respectively. The layout plan of mega trusses for UWT Stage 1 and 2 are shown in Figure 3 below.

Figure 3: UWT Stage 1 and 2 Mega Truss Layout Plan

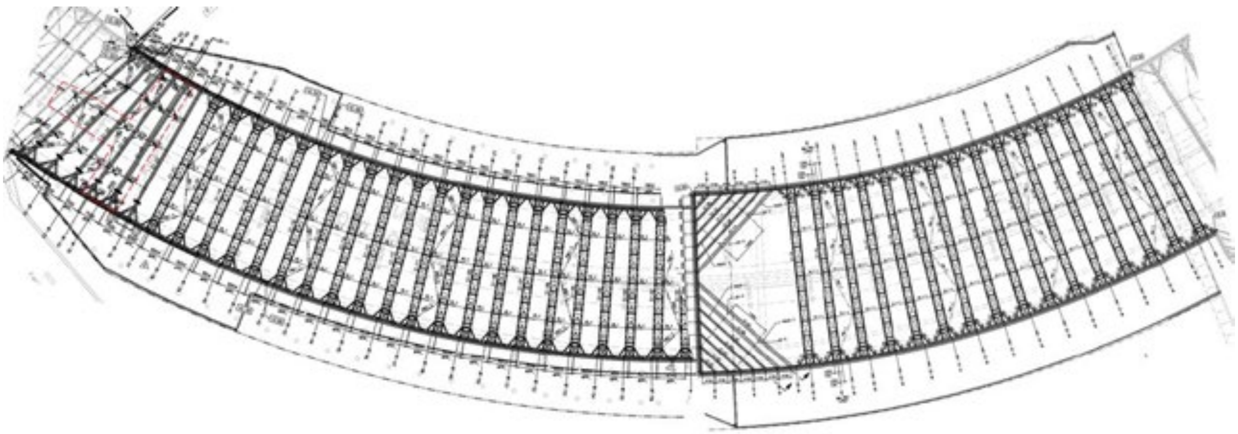

The cofferdam wall is a double wall system of 16m width with 813mm diameter x 25mm thick CPP as the inner ELS wall and FSP Type V sheet piles for the outer sea wall. Reclamation backfill is deposited in between the inner and outer walls with tie backs at at +2.5 mPD with 6m c/c spacing. Temporary marine working platforms of 16m width were erected with top level of +6 mPD over the reclamation area and supported by 2 rows of staging piles driven by 80t vibro-hammer to the top level of the CDG layer below. The lateral shoring of the ELS works comprised of maximum 6 layers of modular type struts and walers to the final excavation level of -25 mPD. The mega trusses provide the top two layers of shoring for strut layers S1 and S2. The remaining strut layers below are typical modular struts supported by three rows of kingposts hanging from the mega truss above as shown in cross section of Figure 4 below.

Figure 4: Typical Cross Section of UWT Stage 1 ELS Arrangement

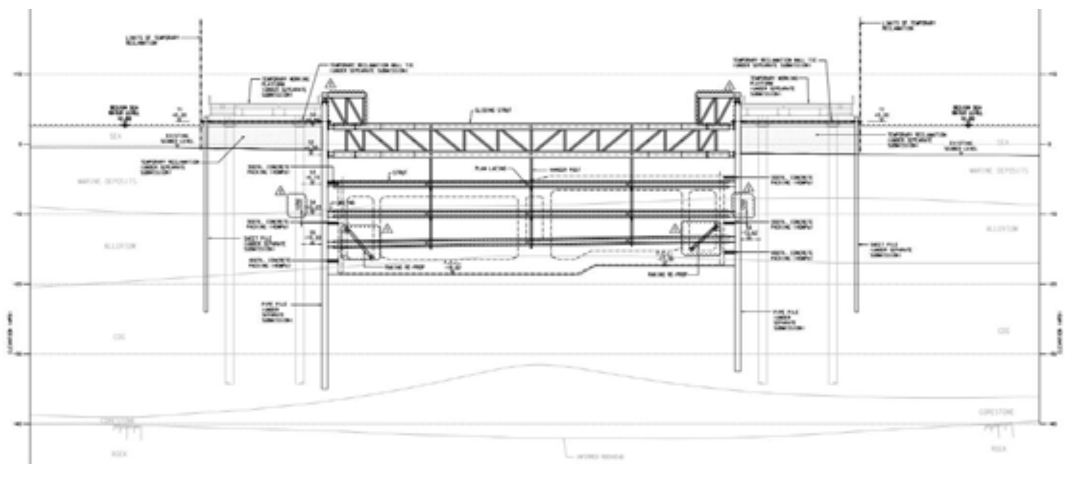

The mega trusses also allowed the earlier commencement of the pumping test as the ELS design required that the strut layers S1 and S2 be installed prior to the required pumping test in order to control the wall deflection to less than 1% of the excavation depth as required by the particular specifications of the Contract. The traditional method of driving kingposts and installing the strut layers S1 and S2 would have required an estimated 75% more time than the mega truss system.

2.2 Mega Truss / Skidding Struts

The design of the mega truss modules was based on two criteria's, first being that they would function as beam / strut combination capable of supporting vertical loads from the hanging kingpost to eliminate the need for piling rig and marine platforms of traditional king post founded in soil or rock and also the lateral shoring loads from ELS design for strut layers S1 and S2, secondly, the mega truss should be transportable by barge in modular segments onto the temporary cradle and assembled by bolt and nut into the full span for lifting by the strand jack towers onto the skidding rails. It was determined that each of the modules would be sized to be less than the SWL of 50t which is the lifting capacity of the crawler crane positioned on the temporary marine working platform at the bulkhead of UWT Stage 1 and 2 interface. The delivery of mega truss modules to assembly area is shown in Plate 2 below:

Plate 2: Mega Truss modules as arranged on transport barge

Therefore, each of the 9 nos. of modular segments was limited to be less than 30t with the completed mega truss having a gross weight of 160t and clear span of 57.7m. The mega truss cross sectional area is generally 3m width by 5m deep. The modular segments and weights are shown in Figure 5 below.

Figure 5: Modular Segments of Mega Truss (UWT Stage 1)

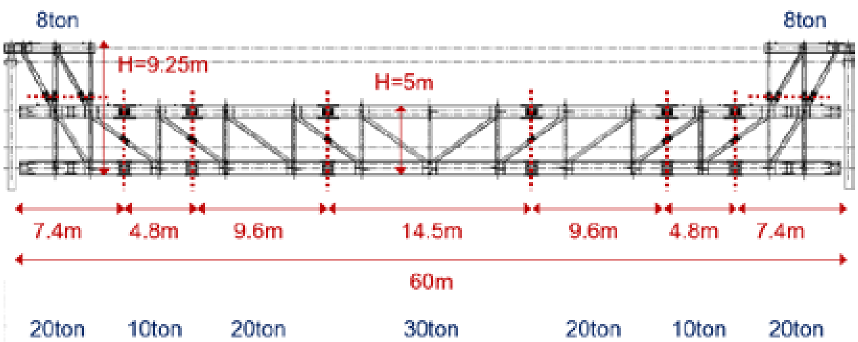

At either end of the mega truss are forks extending out 3m on each side of the strut and connected to 9m wide walers to spread the strut loads onto the CPP wall. The 9 nos. of modular segments are connected by nut and bolt on a temporary hanging cradle to avoid the necessity of carrying out hot works above water and benefit worker safety. The mega truss is pre-set at the required strut levels with the top chord for S1 at +2.5 mPD and bottom chord as S2 at -1.5 mPD. An upstand hanger frame connected at each end of the mega truss rests on the skidding rails installed at the top of CPP wall as shown in Figure 5 below. The 16 nos. of mega trusses spanning the 60m wide UWT Stage 1 cofferdam are designed as modular struts and reusable in the 50m wide UWT Stage 2 cofferdam which require 21 nos. of mega trusses for the lateral shoring works. The deletion of two 4.8m length modular segment from the UWT Stage 1 57.7m span mega truss will change the effective span from 57.7m to 48.1m and the removed modular segments can be used to build up three more nos. of mega trusses with 57.7m span allowing for high majority reuse rate in UWT Stage 2 for the mega trusses from UWT Stage 1.

2.3 Mega Truss Assembly Cradle Strand Jack Lifting Towers

The mega truss segment modules are transported by barge to the temporary marine platform located at the bulkhead of UWT Stage 1 and 2 at the midpoint of KWB where a 200t crawler crane on the marine platform lifts each segment from barge to the temporary cradle for assembly into the full span of mega truss. The platform geometry was set to maximize deck panel sizes to suit derrick lighter and also handling by the crawler cranes on the platform. This meant that the handling logistics required one lane for construction vehicle access to pass by the 200t crawler crane which drove the geometric design of the temporary marine working platforms to be 16m in width. There are 6 nos. of temporary cradles that are hung from the CPP bulkhead wall at the connection joints of each of the mega truss modular segments. Workers then fix the modular segments together by nut and bolt to form the final completed span of the mega truss strut. The marine working platform and temporary cradles are shown in Figure 6 below.

Figure 6: Mega Truss Assembly Yard - Temporary Cradle, Lifting Tower and Strand Jack Layout

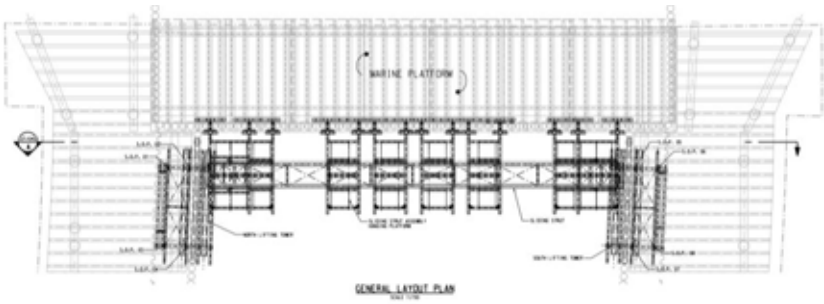

Two numbers of strand jack lifting towers are used to lift the mega truss struts onto the skidding rail and they are designed to be reusable from for UWT Stage 1 to UWT Stage 2. Each lifting tower is approximately 17m in height by 4m wide by 13m long and positioned at either ends of the temporary cradle each with a lifting capacity of 200t. The Lifting Tower and Strand Jacks arrangement are shown in Figure 7 below.

Figure 7: Lifting Tower and Strand Jacks Arrangement

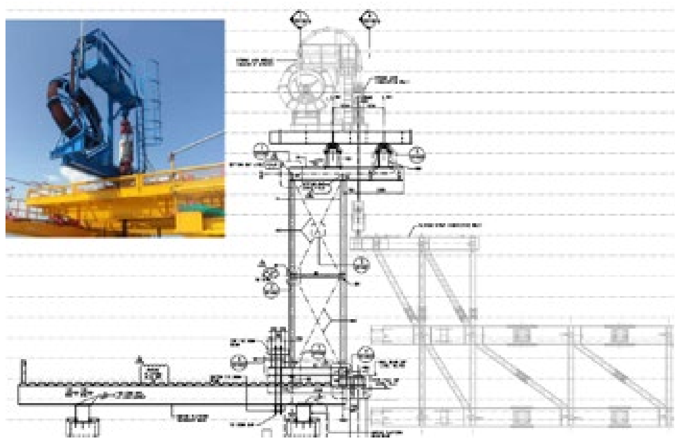

2.4 Mega Truss Skidding System

The skidding system is comprised of slotted skidding rail, slider and hydraulic jack system, mega truss skate and vertical jack system. The mega truss strut is lifted directly by the strand jack lifting tower onto the skidding rail. Rollers are provided on each side and a PTFE pad to reduce the friction of the 160t mega truss struts. Since the UWT ELS cofferdam is curved, the rollers allows the mega truss strut to maintain its alignment along the curved skidding rail while skidding with a tolerance for longitudinal movement. Next a fully retracted horizontal hydraulic cylinder jack is attached with lock pin inserted to the skidding rail slots and used to push or skid the mega truss simultaneously at both ends of the curved skidding rails. Workers at each end of the mega truss strut observe the skidding movement to ensure that both ends are skidding at the correct rate. Should one end skid too fast, the worker would cease skidding and allow the other end of the mega truss to catch up to the correct rate of advance. Both workers would be in communication with each other and another worker would observe the overall rate of skidding from the high point of strand jack lifting towers. The jacking system hydraulic power unit is placed directly onto each ends of the mega trusses. Illustration of the skidding action of the mega truss is shown in Figure 8 below.

Figure 8: Skidding mega truss from UWT Stage 1 bulkhead towards the Kai Tak seawall

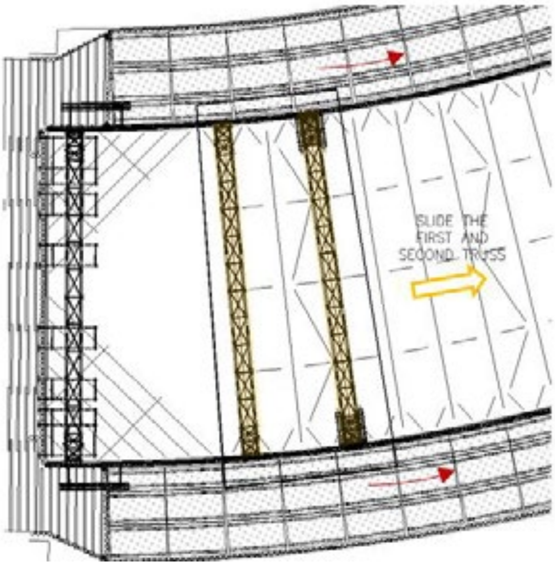

The aerial view showing all 16 nos. of skidding mega trusses in position as well as the progressive staged excavation and lateral shoring works up to strut layer S5 are shown in Plate 3 below.

Plate 3: Completed view of skidding mega trusses at UWT Stage 1

The skidding of one mega truss across a typical bay of 12m length requires approximately 1 hour. Once the mega trusses are skidded into positions, two nos. of locking pins are inserted with stoppers and welded to the mega strut to maintain its final position for the duration of the tunnel construction works. The process is repeated for the remaining mega trusses until all 16 nos. of mega trusses are in position. As the mega truss is designed to be reused, the removal of the mega trusses is done in reverse and the modification of the truss segment modules as described in *Section 2.2* above for reuse in ELS UWT Stage 2 is completed on land.

2.5 Design Considerations and Modelling

The design concepts of the skidding idea were drafted early on during the tender design stage which the detailed design drawings of the skidding mega trusses were based upon. The early concept ideas are shown in Figure 9 below.

Figure 9: Early Conceptual Design on the Development of Mega Truss Skidding System

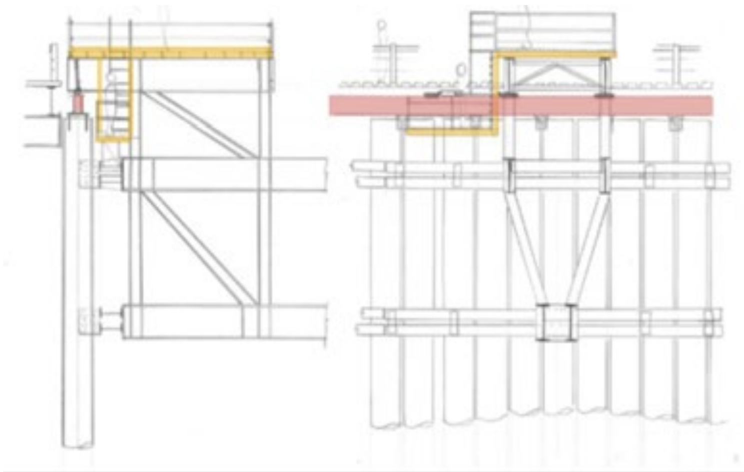

From the preliminary conceptual design, the berthing or accidental impact of ship vessels was a major consideration for the skidding truss system. In order to mitigate this impact, the 16m width of temporary marine working platforms and the reclamation backfill were tied back together at +2.5 mPD to form the double wall cofferdam and provide significant mass to mitigate berthing from the marine working barges or accidental impact collision of marine vessels operating in the KWB typhoon shelter area. The tie between outer and inner walls was envisaged as a fuse, acting only in one direction or tension without transferring direct compression loads from berthing vessels or accidental collisions to the ELS struts. The use of OASYS GSA structural computer modelling was carried out to simulate the collision from marine vessel to the temporary marine platform and impact to the skidding rails as shown in Figure 10 below.

Figure 10: OASYS GSA computer modelling of accidental collision on temporary marine working platform

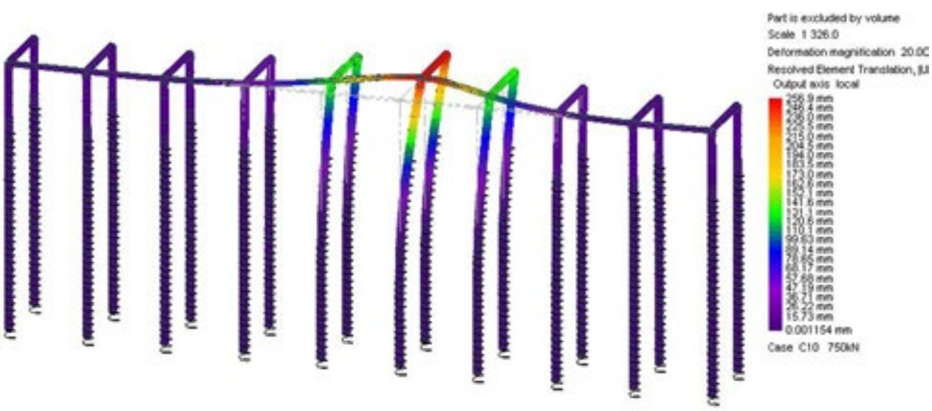

Since the CPP wall effectively functions as both a retaining wall and vertical support for the mega trusses above, the CPP wall was modelled as a retaining wall. The vertical load applied at the top was checked against the structural and geotechnical capacity of the CPP. This was modelled along with the double tie back wall and marine working platforms directly in the PLAXIS computer simulation. Additionally, the predicted maximum wall deflection at the top after would need to be known to allow suitable tolerance for the skidding system upon the time for the removal of struts. The PLAXIS model geometry is shown in Figure 11 below.

Figure 11: PLAXIS modelling of ELS and Mega Truss Strut

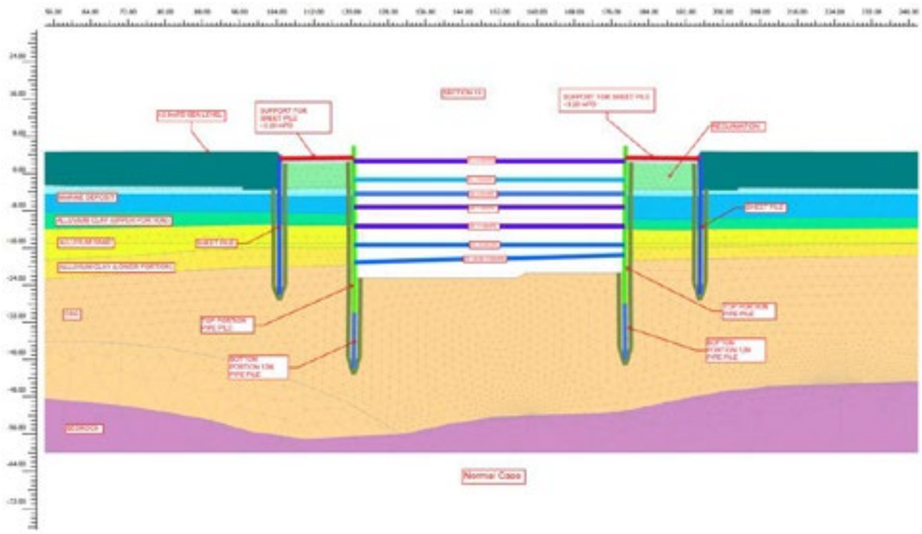

Consideration was also made for removal of the mega truss was made for the deflection of the CPP wall after completion of tunnel structure and backfilling works by including a 1m segment allowed for sacrificial cut at localized strut extension of S1 / S2 levels and walers. The ELS design also required that strut layers S1 and S2 be installed prior to pumping test and dewatering works for installation of strut S3 layers and below in order to control the cofferdam wall deflection to within the PS requirement of 1% of the excavation depth. Without the use of the skidding mega truss method, the construction programme would have been severely adversely impacted by the traditional method of vertical member installation and subsequent staged bulk excavation and dewatering works sequence. The removal of CPP in UWT Stage 1 is shown in Plate 4 below.

Plate 4: CPP Removal at UWT Stage 1

2.6 Precautionary Measures

The ELS UWT design adopted seawater level of +2.8 mPD based on the historical seawater levels for 1 in 10 year return periods. However, as a precautionary measure the ELS design also considered the Hong Kong Observatory (HKO) records for the highest historical seawater levels recorded even including the extreme storm of Typhoon Mangkhut in September 2018 where the highest seawater levels recorded up to +4 mPD. Therefore, the CPP top level of +6 mPD was adopted so that along with the outer sheet pile wall, the marine platform top level and 16m width provided margin to safely prevent seawater overtopping the cofferdam wall and flooding the UWT ELS works by standing waves up to two times the wave height due to wave interference. The design of the cofferdam wall and platform to mitigate the risk of flooding is shown in Figure 12 below.

Figure 12: Precautionary Measures for Flood Risk Mitigation

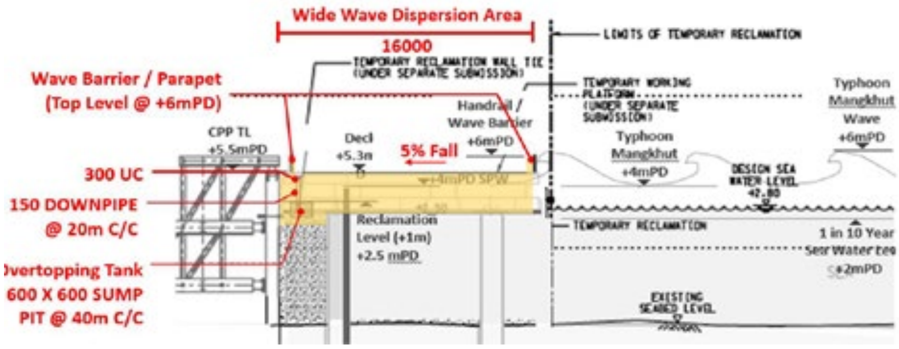

2.7 Potential Limitations

The main limitation of the skidding mega truss system is due to the width of the ELS cofferdam. As the ELS span increases, the free span of the simply supported mega trusses also increase, which proportionally increases the bulk and weight of the mega trusses and at some point it becomes structurally unfeasible and uneconomical to construct and erect such a large span.

The potential limitations and solutions for the skidding mega truss system are listed below:

- Large Span (50-60m) that is required for the mega trusses are heavier in steel tonnage for the ELS compared to traditional king post design. However, king posts would have meant additional platforms / piling cost which meant that even though the mega trusses had greater steel tonnage, they would still be faster and less costly.

- Shallow seawater obstructs the mega truss skidding since the truss structural depth of 5m requires sufficient draft for clearance between the truss soffit and the sea bed level. As the water depth is shallower nearby the shore line, some dredging of seabed within the cofferdam to below the soffit of mega truss is required.

- Transportation of the bulky and heavy mega truss modules makes delivery to the assembly area difficult. As there is no marine or land access for mega truss delivery at both ends of the cofferdam-seawall interface, an island platform at the bulk head is required for the loading and unloading of truss modules from barges. Therefore, the mega truss modules are fabricated in our strut factory in parallel with the installation works for the ELS cofferdam wall and transported to site when needed to reduce the storage area for mega trusses on site.

- Skidding Rail placement on top of the CPP wall meant that the wall alignment for individual piles that were out of tolerance wasn't critical. We pit the vertical load down the centre of the wall and the truss had to be designed for that tolerance as well as the lateral movement from deflection of the ELS cofferdam wall.

2.8 References

Clark et al. (2011)

3 CONCLUSIONS

The Employer envisaged scheme was a full reclamation, D-walls and constructed as a land operation with king posts. The Contractor's solution was quite a big departure in thinking and had many interacting benefits to simplify the construction. The use of this innovative construction method facilitated increase productivity by eliminating King Post piling works and safety to workers compared to the traditional method of ELS works at marine area and risk associated with working above water. The system benefits the environment by being reusable and reduces the quantity of marine piling works as well as the reclamation fill needed as working platform at excavation area.

ACKNOWLEDGEMENTS

Special gratitude and appreciation is expressed for all the contributions from the CKR Site Teams below:

Hong Kong Highways Department Major Works Division – LAM M.S. Roy (CE1/MW), CHAN M.K. (SE3/CKR), WONG Y.P. Arthur (E15/CKR), LEE K.S. Victor (PC1/CKR)

Arup - Mott MacDonald Joint Venture (AMMJV) – LO K.C. Patrick (CRE), WONG Y.K. Antony (SRE), LAU Jeffrey (SRE), NG M.Y. May (RE), KWOK H.Y. Kevin (RE)

Gammon Construction Limited – TAM K.F. (CM), LUI Y.F. Niki (SPM), LEE H.H. (SPM), FUNG C.S. Julian (PM)

REFERENCES

Clark & Askew, Thoren, 2011, Safety by Design – Clearance of buried sea wall at Marina Bay, Singapore, Underground Singapore

A Review of Conventional and Innovative Permanent Support Systems for Rock Cavern Development in Hong Kong

Endicott L John, Franklin K L To, Andrew K W Seto
AECOM Asia Company Ltd., Hong Kong, China

ABSTRACT

In recent years, the HKSAR government departments have been playing a leading role to study the feasibility of rock cavern development in Hong Kong. These studies include the relocation of existing surface sewage treatment works, service reservoirs, refuse transfer stations, archive centre and laboratory to rock caverns. After completion of the relocation, the previously occupied surface land can be released for other developments beneficial to the communities.

Conventional permanent support systems comprise the cast-in-situ concrete lining with sheet waterproofing membrane. These have been applied in most of the highway and railway tunnels in Hong Kong. However, it involves the use of bulky steel shutter, heavy rebar fixing and an extra set of redundant temporary supports, which leads to very expensive and time-consuming construction.

With the advance development in construction technologies, permanent rock reinforcements with sprayed waterproofing membrane could be a cost-effective engineering solution. With the integration of temporary and permanent supports, the tight daily drill-and-blast cycle and timely permanent support installation is greatly enhanced.

This paper provides a general review of different conventional and innovative permanent support systems for rock cavern development with the purpose of achieving more efficient design and construction. It also discusses the application according to the unique requirements for various cavern facilities.

1 INTRODUCTION

1.1 Rock Cavern Development Strategy in Hong Kong

Hong Kong is surrounded by hilly terrains, rural areas and statutory protected areas such as country parks and restricted areas. This provides limitations to the land development in Hong Kong. As such, only less than 25% of total land area in Hong Kong has been developed for the 7.5 million population. Traditional approaches of land development include flat land, open-cut site formation of moderately hilly terrain and large-scale reclamation. They have been playing an important role in Hong Kong's continuous land supply. However, these approaches have caused the built-up areas to be largely concentrated within the foothills of natural terrain extending towards the shoreline or the reclaimed land.

Among the various rock types of igneous, sedimentary and metamorphic origins found in Hong Kong, over 80% of them comprises hard and massive igneous rocks, such as granite and various volcanic rock types. This brings favorable conditions for underground space development such as rock caverns as an alternative source for land supply. In recent years, the HKSAR government departments have been playing a leading role to study the feasibility of rock cavern development in Hong Kong. These studies include the relocation of existing surface sewage treatment works, service reservoirs, refuse transfer stations, archive centre and laboratory to rock caverns. After completion of the relocation, the previously occupied surface land can be released for other developments beneficial to the communities.

A territory-wide Cavern Master Plan (CMP) is presented in Figure 1. It is prepared to guide and facilitate the planning and implementation of long-term cavern development. The CMP delineates 48 numbers of Strategic Cavern Areas (SCVAs) that are suitable for cavern development in terms of geological considerations and the current planning perspectives.

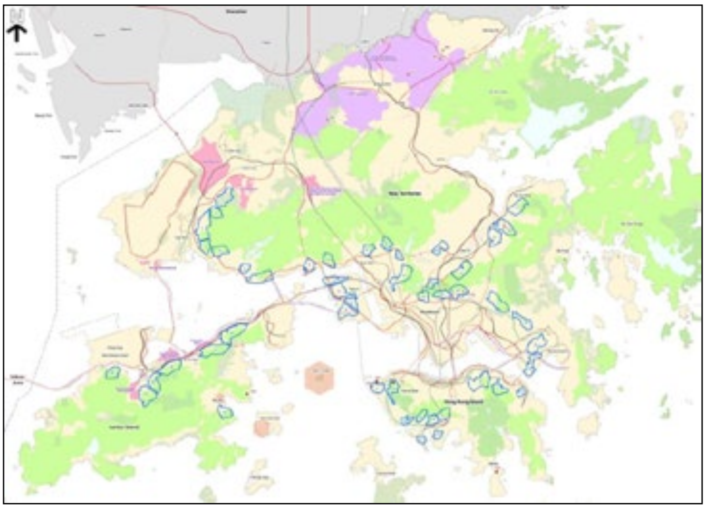

Figure 1: The Cavern Master Plan (CEDD and PlanD, 2017)

1.2 Permanent Cavern Support Systems

As suggested by GEO (2018), a cavern shall be designed and built in a way that can be maintained in a practical and economically viable manner during its service life, which could last for 100 to 120 years. The rock support elements shall be designed to be sufficiently durable and robust to guard against local deterioration of the rock mass over time, in particular at the weakness/fault zones. In consideration of the consequence of life, durability and maintenance problems, temporary supports such as rock dowels and shotcrete are usually not taken to contribute any of the long-term ground stability. The permanent support systems are installed in a later stage.

Most of the constructed rock tunnels in Hong Kong for highway and railway purposes are permanently supported by conventional cast-in-situ concrete lining. Plain concrete lining is used in good rock conditions; while heavily reinforced concrete lining is used in poor/soft ground conditions. It involves the use of bulky steel shutter, heavy rebar fixing and an extra set of redundant temporary supports, which leads to very expensive and time-consuming construction. If design optimization for permanent supports is achieved, the overall construction cost and time can be significantly reduced. With the advance development in construction technologies, permanent rock reinforcements with sprayed waterproofing membrane could be a cost-effective engineering solution.

The use of single-layer rock support system has been applied in the overseas projects for many years. For example, a composite shotcrete lining can serve both the temporary and permanent support purposes. The system is continuously improved with the introduction of new technology and materials, such as machinery, explosives and shotcrete materials. With the integration of temporary and permanent supports, the tight daily drill-and-blast cycle and lengthy support installation is greatly enhanced to save the overall construction cost and time. Yet, in order to allow the use of single-layer rock support in Hong Kong, one of the key issues to resolve is the possible blast-induced damage and cracks development to the temporary shotcrete layer during excavation. The development of new shotcrete materials with vibration resistance could be one of the possible solutions.

The permanent structures for cavern can be designed as drained or undrained. A drained structure is designed with a groundwater pressure relief system to allow groundwater ingress into the cavern in a controlled manner; while an undrained structure is designed to withstand the full in-situ groundwater pressure by preventing any groundwater ingress. For drained caverns, the groundwater pressure relief system consists of groundwater inflow control and groundwater drainage system is installed. These arrangements ensure that the groundwater can be diverted effectively and prevent the built-up of groundwater pressure surrounding the rock mass.

A general review of different conventional and innovative permanent support systems for rock caverns development is carried out. The selection shall fit the unique requirements for various cavern facilities in order to achieve the purpose of achieving more efficient design and construction.

2 CONVENTIONAL AND INNOVATIVE PERMANENT CAVERN SUPPORT SYSTEMS

2.1 Conventional Permanent Cast-in-situ Concrete Lining

For conventional cast-in-situ concrete lining, two independent sets of temporary and permanent supports are installed during the construction. Temporary support including rock dowels and a thin layer of shotcrete are first installed, then subsequently the casting of permanent support includes the cast-in-situ concrete lining with geotextile and sheet waterproofing membrane as shown in Figure 2. A movable steel shutter in form of scaffolding and timber formwork is used for concrete pouring.

Figure 2: Conventional Permanent Cast-in-situ Concrete Lining with Sheet Waterproofing Membrane

The use of permanent cast-in-situ concrete lining for large-span rock caverns has been successful in Hong Kong, such as the 24.2 m span cavern for MTR Island Line Tai Koo Station completed in 1985 as shown in Figure 3, and the 24.3 m span cavern for MTR South Island Line Admiralty Station completed in 2016.

Figure 3: Steel Shutter for the Construction of MTR Tai Koo Station
(http://dragageshk.com/project/tai-koo-mtr-station-and-tunnels/)

For permanent cast-in-situ concrete lining, the conventional "rock support" design approach is adopted in which concrete and reinforcement are used as structural materials to sustain all possible loadings. The design load involves an array of load combinations, including the overburden, groundwater and different internal facilities. They should be checked against the structural capacity of the lining such as axial, shear and bending moment accordingly.

2.2 Permanent Steel Fibre-Reinforced Shotcrete (SFRS) Lining

Steel fibre-reinforced shotcrete (SFRS) is sprayed concrete with steel fibres added as reinforcement. It has higher tensile strength than unreinforced shotcrete and is widely used for underground structure supports. The use of permanent SFRS lining has been successful at the Po Shan Road Drainage Tunnel (Lo et al 2009 and Chau et al 2011). The project consists of twin 3m-diameter bored tunnels and a series of sub-vertical drains. It was designed and constructed to form a robust system to control the groundwater levels for maintaining the overall stability of the Po Shan hillside within the Mid-Levels area. A horse-shoe shaped portal chamber of 8m (W) x 5m (H) was also constructed.

The intersection of drainage tunnels and portal chamber has a span of ~17m but with an irregular shape. Under the conforming scheme, heavily reinforced concrete lining with the need of irregular formwork was required. The fixing of reinforcements at crown and formwork erection are known as high risk works activity. Alternatively, a 700mm thick steel fibre reinforced shotcrete (SFRS) lining with cast-in-situ kicker walls and base slab was adopted as the permanent support construction, which significantly shortened the construction period, lowered the construction cost and reduced the construction risks. The intersection is shown in Figure 4.

Figure 4: Intersection at Po Shan Road Drainage Tunnel with Permanent SFRS Lining
(https://www.thestandard.com.hk/section-news/section/4/235348/Po-Shan-tunnel-debuts-landslide-sci-tech-chamber)

2.3 Permanent Rock Reinforcements in Hard Rock

The in-situ stress conditions for a rock mass at a specific depth below ground can have one or more origins. The major components usually comprise the gravitational stresses and tectonic stresses. According to GEO (2018), there is no evidence of high tectonic stresses in Hong Kong rocks. Local strong igneous rock has a typical uniaxial compressive strength (UCS) that ranges from 75 MPa to 200 MPa, which is much greater than structural concrete. Compared with the redistributed stresses after excavation, high stresses will not be a problem for local cavern construction at modest depths given the high strength of most of the rocks encountered.

An arched structural form has been widely used in civil engineering projects such as bridges and arched dams. This also applies to rock cavern engineering. After excavation, the overburden weight of loosened rock above the cavern crown is redistributed to the sidewalls. Hard rock is strong in compression but very weak in tension. With an arched roof, the best stress distribution is obtained to reduce the zone of tensile stresses in the cavern crown. This utilizes the “arching-effect” within the rock mass and therefore improves the ground stability, allows a more cost-effective support system and reduces the overbreak for excavation.

As such, the “rock reinforcement” design approach has been developed to offer a practical method to consider the hard rock as a structural material to self-support itself by utilizing the hoop stress within the arch of the rock above the roof of the cavern. Permanent rock bolts are installed as rock reinforcement to guarantee the formation of this arch, and permanent shotcrete supports the smaller rock wedges between adjacent bolts. The inherent strength of the rock mass is utilized by applying confining pressure from the rock bolts. The thrust capacity discussed by Bischoff JA and Smart JD (1977) is therefore increased and the theoretical rock arch formed around the cavern is capable to resist the hoop force and can stabilise the opening by supporting the ground above the excavation. The design load involves the field stresses in rock mass. The rock supports should be checked against individual failure modes.

The use of permanent rock bolts and shotcrete for large-span rock caverns has been successful in Hong Kong, such as the 15 m span cavern for DSD Stanley Sewage Treatment works completed in 1995 as shown in Figure 6, and the 27 m span cavern for EPD Island West Transfer Station completed in 1997. The on-going DSD project to relocate the Sha Tin Sewage Treatment Works to caverns involves the construction of a cavern complex with 7 parallel rock caverns up to 32m width x 33m height in order to handle a large sewage treatment capacity. Upon completion, the relocated STSTW will be the biggest cavern sewage treatment works in Asia.

Figure 5: Rock Bolt Installation in Hard Rock

Figure 6: Stanley Sewage Treatment Works in Caverns with Permanent Rock Reinforcements
(https://www.dsd.gov.hk/TC/HTML/20520.html)

For each class of rock support, the rock bolt length, diameter, and spacing, can determined by reference to NGI Q-system (NGI 2015), Geoguide 4 (GEO 2018) and other design guidelines. Guidelines are non-specific and are conservative, with suggested minimum values for requirements to be used. In particular for large-span rock caverns, design verifications using numerical modelling shall be adopted for the multi-stage excavation with site specific values for rock parameters. With sufficient design justifications, a less conservative approach could be adopted for a specific site and a specific use.

The guidelines for rock bolt length and spacing have largely been developed from large numbers of case histories. In theory, the bolts, together with shotcrete, provide a quantifiable support pressure. To some degree, rock bolt length could be shortened, and spacing decreased, resulting in the same support pressure being applied. However, rock reinforcement approach also requires a minimum thickness of theoretical rock arch, which would result in a minimum rock bolt length and spacing ratio proposed by Lang (1961), which might vary depending on the rock mass quality.

The effective bolt length should exclude the allowance for the expansion shell and face plate portion embedding into the shotcrete layer as shown in Figure 7. By adopting appropriate numerical modelling to validate the proposed rock bolt length and spacing, it is considered that there may be opportunity to optimize rock bolt lengths to suit either material supply, or site working practice. For example, one opportunity would be to reduce the length of systematic rock bolts such that the bolt holes could be drilled in one pass, without the need to add extension rods during the drilling process. By adopting shorter bolts, the time saved per bolt is the time taken to add a drill rod before continuing to drill. However, if the design validation proves that shorter systematic rock bolts will constitute to the increase in rock bolts quantities, the total number of installations is indeed increased. This would be doubtful if there would be an overall saving of time. A further detailed study shall be carried out with approval from relevant authorities.

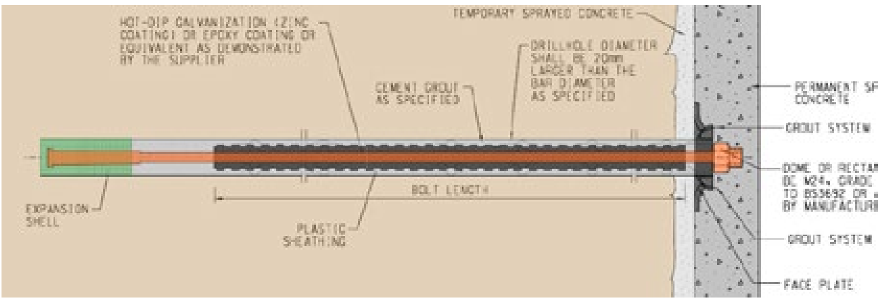

Figure 7: Typical Arrangement of Cement Grouted Permanent Systematic Bolts with Expension Shell

2.4 Integration of Permanent Cavern Supports & Internal Structures

From a structural engineering perspective, the internal structures of cavern facilities can be integrated or even replace the permanent cavern walls support. This allows a cost saving on construction materials. An example is shown in Figure 8 where the cavern sewage facilities with water tank walls and rock support walls coexist adjacently. However, if the excavation works and internal structures are carried out by two Contractors under separate contract; or the rock supports are designed by the Engineer but the inner facilities (such as special hydraulic and E&M equipment) are designed by the Contractor, the contractual issue would cease the feasibility for the integration.

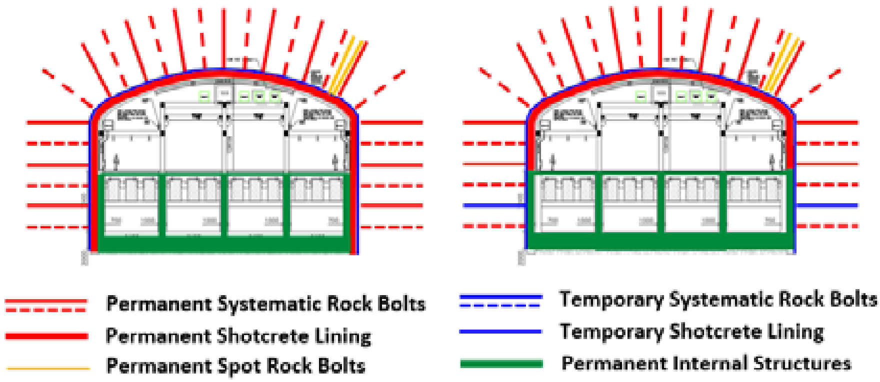

Figure 8: Integration of Cavern Support and Internal Structure (left: not integrated; right: integrated)

The integration of permanent cavern supports and internal structures have been successful at the Western Salt Water Service Reservoirs at the University of Hong Kong. It is the first service reservoirs built in rock caverns (Mackay et al 2009, Toh et al 2011 and Yeung et at 2011). The permanent support system comprises cast in-situ concrete along the sidewalls and shotcrete across the crown as illustrated in Figure 9. The cavern roof is permanently supported by a steel-fibre reinforced shotcrete lining with a plain shotcrete smoothing layer. The shotcrete arch roof was first constructed during the top-heading excavation and supported on an elephant foot founded on sound rock before full excavation of bottom beaches. SFRS lining is able achieve a quantifiable tensile strength depending upon the quantity of steel fiber reinforcement added. It doesn't require the use of formwork for installation. The shotcrete lining is rested on recesses at the crown base with additional reinforcement to the side walls using 32mm diameter rock dowels.

In order to fulfill the watertight requirement, the cavern permanent linings were designed as water retaining structures. Waterproofing layers were laid at the external face of cavern profile to avoid groundwater ingress into the salt water service reservoirs as shown in Figure 10. The service reservoir structures are monolithic reinforced concrete structures. With these mitigation measures, the possibility of groundwater leakage into the cavern would be minimized such that the contamination problem could be avoided. The permanent lining was designed as drained with a groundwater relief system.

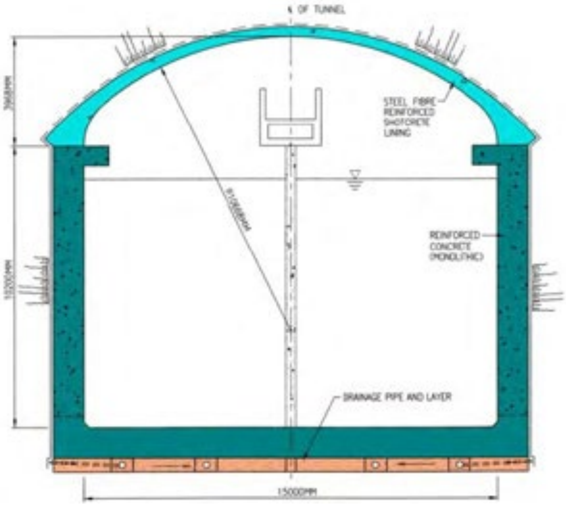

Figure 9: General Arrangement of Western Salt Water Service Reservoirs at HKU

Figure 10: Construction of Western Salt Water Service Reservoirs at HKU
(https://www.edb.gov.hk/attachment/tc/curriculum-development/kla/pshe/references-and-resources/geography/presentation%20slides%20-%20cavern%20development%20for%20wsd%20waterworks.pdf)

2.5 Modular Integration Construction (MiC) and Design for Manufacturing and Assembly (DfMA)

Modular Integrated Construction (MiC) with reinforced concrete structural components cast off-site under factory conditions adopting Design for Manufacturing and Assembly (DfMA) methods which allow elements to be imported and erected and in position can prove to be time saving for site works and can be a cost saving method of construction. Normally, cost for modular constructions might contribute savings of up to 10% of the total costs for outdoor greenfield structures but there are more constraints for caverns.

The choice of elements to be included for modular construction should be those highly repetitive members that could be pre-casted and delivered to site. An example for a rock cavern accommodating sewage treatment facilities is discussed. Internal structures such as the top slab of sewage treatment tanks, large tank covers, columns and beams, and internal buildings could be considered for modular construction. Water retaining structures requires high standard of workmanship to ensure the water tightness. They may not be as appropriate as a mandatory component for modular construction given the number of pre-cast units and constructions joints that will be involved. For large metal tank covers and mesh flooring system, they could be prefabricated off-site. The cavern facilities usually involve many E&M equipment to be installed. These could also be considered for modular construction.

Construction inside a rock cavern is limited by headroom, working space and internal access. This limits the Contractor's choice of plants for lifting operations and size of prefabricated elements. These factors will eventually contribute to the construction costs, hence undermine the cost-effectiveness of modular constructions.

Nonetheless notwithstanding the above concerns on MiC in caverns, some of the Contractors could be more capable than others in overcoming constraints inside caverns by using special machinery, while some Contractors would prefer conventional ways of cast in-situ construction depending on their availability of resources and their costs in securing materials at the time of works. Therefore, one of the cost-effective options could be to leave the option for precasting and prefabrication open for the Contractor. Moreover, if the designer/procurer of the structures are to be carried out by the Contractor, they could then decide the most cost-effective way to construct the facilities, which will be subject to a competitive tendering process and promote this consideration.

Figure 11: MiC and DfMa for Rock Cavern Facilities

2.6 Groundwater Relief System and Water Tightness Requirements

The permanent cavern support system can be designed as drained or undrained. A drained structure is designed with a groundwater pressure relief system to allow groundwater ingress into the cavern in a controlled manner; while an undrained structure is designed to withstand the full in-situ groundwater pressure by preventing any groundwater ingress. For drained caverns, the groundwater pressure relief system consists of groundwater inflow control and groundwater drainage system is installed. Drainage layer comprising crushed rock will be laid at the invert of the caverns and tunnels. The drainage layer will divert the groundwater to the public drainage system. These arrangements ensure that the groundwater can be diverted effectively and prevent the built-up of groundwater pressure surrounding the rock mass.

A rock cavern network is usually proposed under hillside and above the seawater level. Therefore, the probability of excessive groundwater inflow into the caverns is very insignificant. Considering the majority of the caverns shall be relatively dry, it is proposed that groundwater pressure relief system shall only be installed in areas with observable groundwater inflow instead of applying the systems along the entire caverns and tunnels.

A three-tier groundwater system for rock caverns is considered as a cost-effective solution:

i. During the probing from rock face, carry out permanent pre-excavation grouting (PEG) if excessive groundwater inflow is recorded;

ii. For any small groundwater inflows observed after excavation, install drainage measures to direct the flow path to the drainage layer at the cavern invert; this flow path would become embedded within the permanent sprayed concrete;

iii. In sensitive areas where equipment needs to be free from water (e.g. E&M plant rooms), install a systematic grid of groundwater drainage measures, and spray waterproofing membrane over the entire cavern roof and upper walls, covering the drainage measures. This waterproofing layer would then be covered by the final layer of permanent sprayed concrete support.

For caverns constructed in sound granite rock material, it has very low permeability and groundwater circulation can only circulate through fissures where present. Where mass weathering is extensive, such as close to rockhead, water can also seep through the decomposed zones. However, this is not expected as sufficient rock cover is required when proposing a rock cavern location. Ground investigation with rock coring shall be carried out. Limited localised flow is expected through minor rock fractures. Only at locations of faults with higher fracture frequency, these zones may have potential for higher groundwater inflow rates.

The appropriate means of dealing with potential inflow of water is to probe ahead of the excavation to identify zones where large inflows would occur and to stem these by pre-excavation grouting. By this means flows of water immediately after excavation would be limited. Where any minor seepages are subsequently observed, seepage water should be collected and drained, such as by means of band drains that conduct the water from the zone of seepage down to the drainage system at or near the invert of the tunnel or cavern. This approach is discussed in ITA tech Report No.2, section 3.3 which describes a localised drainage system option for zones made up of mainly impermeable rock. The report considers whether a waterproof membrane may be added after the primary shotcrete and invert drainage system has been applied. However, the invert drainage system is equally applicable whether a waterproof membrane is required in addition to the final shotcrete lining or not. Therefore, for very good and massive rock, there is no need for systematic weep holes and systematic circumferential band drains to be applied for zones made up of mainly impermeable rock. Localised adhoc band drains maybe required where minor seepage occurs. The actual provision and spacing shall be subject to review and agreement with the resident site staff spacing.

Figure 12: An example of Massive Granite. It can be “bone dry”, no groundwater weep holes are needed

3 CONCLUSIONS

A general review of different conventional and innovative permanent support systems for rock cavern development is carried out. These include the use of conventional cast-in-situ concrete lining, steel fibre-reinforced shotcrete (SFRS) lining, rock reinforcements in hard rock. Two innovative systems including the integration of permanent cavern supports & internal structures as well as modular integration construction (MiC) and design for manufacturing and assembly (DfMA) are also discussed. The selection shall fit the unique requirements for various cavern facilities in order to achieve the purpose of achieving more efficient design and construction.

It is essential that civil engineering works are designed and built to the required standards of safety. However, it is also important to ensure that design of civil engineering projects is not unduly conservative; whilst recognizing the inherent geological risks associated with major underground construction works.

REFERENCES

Bischoff J.A. & Smart J.D. 1977. *A method of computing a rock reinforcement system which is structurally equivalent to an internal support system*. In Proceedings of the 16th US Symposium on Rock Mechanics,

Chau, S.F., Cheuk, J.C.Y. & Lo, J.Y.C. 2011. *Innovative Approach for Landslide Prevention – A Tunnel and Sub-vertical Drain System*. Proceedings of HKIE Geotechnical Division Annual Seminar 2011, Hong Kong.

CEDD & PlanD. 2017. *Cavern Master Plan*. Civil Engineering and Development Department, Hong Kong SAR. See https://www.cedd.gov.hk/eng/topics-in-focus/index-id-27.html

GEO. 2007. GEO Publication No. 1/2007: *Engineering Geological Practice in Hong Kong*. Geotechnical Engineering Office, Hong Kong SAR.

GEO. 2018. *Geoguide 4: Guide to Cavern Engineering, Second Edition (2018)*. Geotechnical Engineering Office, Hong Kong SAR.

Kong, K.W.K. & Garshol, K.F. 2015. *Rock Reinforcement Design for Underground Openings.* Proceedings of the Underground Design and Construction Conference 2015, The Institute of Materials, Minerals & Mining Hong Kong Branch, Hong Kong 2015. pp. 51-62.

Lang, T.A. 1961. *Theory and practice of rockbolting*. Transactions of the American Institute of Mining Engineering, Vol. 220.

Lo, J.Y.C., Chau, S.F., Lau, D.T.W. & Li, E.S.F. 2009. *Design and Construction of Shotcrete Lining at Tunnel Intersection of Po Shan Road Drainage Tunnels*. Proceedings of the Hong Kong Tunnelling Conference 2009, IOM3 (Hong Kong Branch), pp. 279-289.

Mackay, A.D., Steele, D.J., Chan, T., & Chow, W. 2009. *The Design and Construction of the University of Hong Kong Centennial Campus Underground Salt-Water Reservoirs*. Proceedings of the Hong Kong Tunnelling Conference 2009 (IOM3), pp. 169-177.

NGI. 2015. *Using the Q-system: Rock Mass Classifications and Support Design (handbook)*. Norwegian Geotechnical Institute, Oslo.

Toh G. S. H. & Askew I. 2011. *The University of Hong Kong Salt Water Storage Caverns – An Overview Of Design And Constructability Considerations.* Proceedings of the joint HKIE-HKIP Conference on Planning and Development of Underground Space, 23-24 September 2011, Hong Kong, pp. 211-226.

Yeung S.K., Kam W.K., Lee A. P. N., Man, Alan H. L. & Chung Edwin K. F. 2011. *The First Service Reservoir in a Cavern*, Proceedings of the joint HKIE-HKIP Conference on Planning and Development of Underground Space, 23-24 September 2011, Hong Kong, pp. 215-220